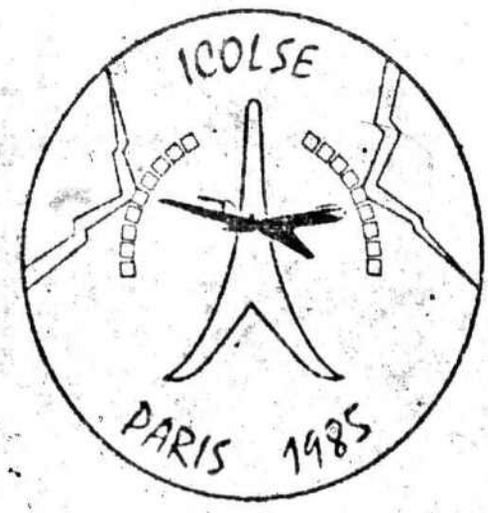
AD-A175 999

10th INTERNATIONAL AEROSPACE AND GROUND CONFERENCE on LIGHTNING AND STATIC ELECTRICITY



XVII^{e} CONGRÈS INTERNATIONAL AÉRONAUTIQUE

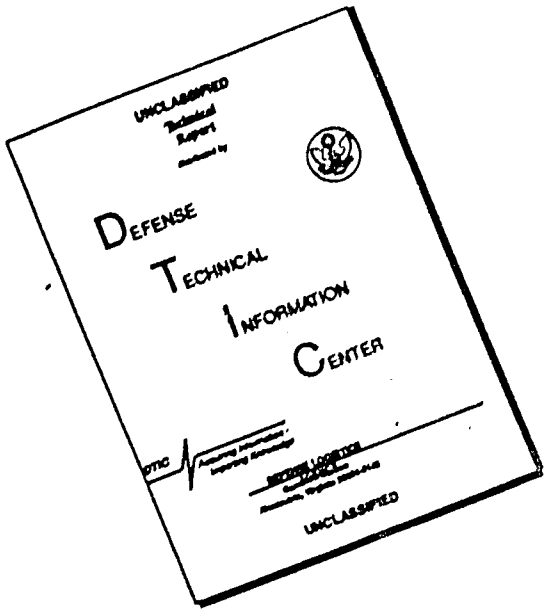
Organisés par l'ASSOCIATION AÉRONAUTIQUE ET ASTRONAUTIQUE DE FRANCE
PARIS
10-13 juin 1985

JAN 1 5 1987
A

les éditions

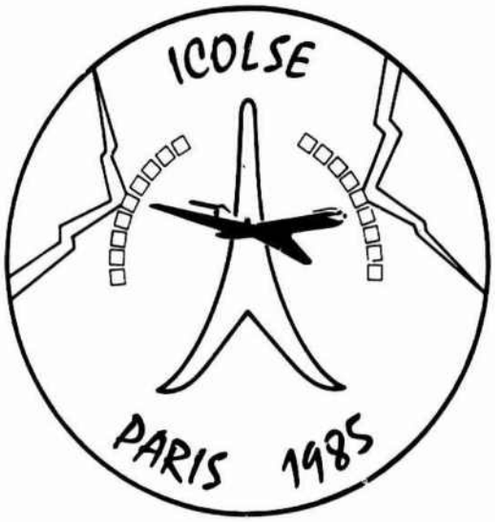
87 1 14 060

DISCLAIMER NOTICE



THIS DOCUMENT IS BEST QUALITY AVAILABLE. THE COPY FURNISHED TO DTIC CONTAINED A SIGNIFICANT NUMBER OF PAGES WHICH DO NOT REPRODUCE LEGIBLY.

10th INTERNATIONAL AEROSPACE AND GROUND CONFERENCE on LIGHTNING AND STATIC ELECTRICITY



XVII• CONGRÈS INTERNATIONAL AÉRONAUTIQUE

CONFERENCE CHAIRMAN
IGA Pierre CONTENSOU

PROGRAM COMMITTEE CHAIRMAN
Dr Joseph TAILLET

U.S. Conference Coordinator
Mr Laurence C. WALKO

DTIC
ELECTE
JAN 15 1987
S D
A

les éditions de physique

Avenue du Hoggar,
Zone Industrielle de Courtabœuf,
B.P. 112,
91944 Les Ulis Cedex, France

This document has been approved for public release and sale; its distribution is unlimited.

10th ICOLSE - XVIIe CIAé

La 10ème Conférence Internationale sur la Foudre et l'Electricité Statique (ICOLSE), jumelée avec le XVIIème Congrès International Aéronautique, est organisée par l'Association Aéronautique et Astronautique de France (A.A.A.F.) sous le Haut Patronage

- de la Délégation Générale pour l'Armement (DGA)
- de la Direction Générale de l'Aviation Civile (DGAC)
- du Centre National d'Etudes Spatiales (CNES)

le parrainage

- du National Interagency Coordination Group (NICG)*
- de l'Agence Spatiale Européenne (ASE)
- de l'International Association of Meteorology and Atmospheric Physics (IAMAP)
- de l'Union Radio Scientifique Internationale (URSI)
- de la Civil Aviation Authority (CAA) G.B.
- du Royal Aircraft Establishment (RAE) G.B.
- de la Bundesamt für Wehrtechnik und Beschaffung (BWB) R.F.A.
- de l'Académie Nationale de l'Air et de l'Espace (ANAE)
- de l'Aéro-Club de France (Aé.C.F)
- de la Société des Electriciens, des Electroniciens et des Radioélectriciens (SEE)
- de la Société Française de Physique (SFP)
- de la Société Météorologique de France (SMF)

et avec le soutien

- de la Direction des Recherches Etudes et Techniques (DRET)
- de l'European Office of Aerospace Research and Development (EOARD) U.S.A.
- du Groupe de Recherche, Développement et Standardisation - U.K. de l'U.S. Army

*qui comprend les représentants des Organismes suivants : U.S. Air Force, U.S. Army, U.S. Navy, NASA, NOAA et FAA.

10th ICOLSE - XVIIe CIAé

The 10th International Aerospace and Ground Conference on Lightning and Static Electricity (ICOLSE) joined to the XVIIe Congrès International Aéronautique (CIAé) is organized by the Association Aéronautique et Astronautique de France (A.A.A.F.) under the Patronage of

- Délégation Générale pour l'Armement (DGA)
- Direction Générale de l'Aviation Civile (DGAC)
- Centre National d'Etudes Spatiales (CNES)

the sponsorship of

- National Interagency Coordination Group (NICG)*
- European Space Agency (ESA)
- International Association of Meteorology and Atmospheric Physics (IAMAP)
- Union Radio Scientifique Internationale (URSI)
- Civil Aviation Authority (CAA) U.K.
- Royal Aircraft Establishment (RAE) U.K.
- Bundesamt für Wehrtechnik und Beschaffung (BWB) F.R.G.
- Académie Nationale de l'Air et de l'Espace (ANAE)
- Aéro-Club de France (Aé.CF)
- Société des Electriciens, des Electroniciens et des Radioélectriciens (SEE)
- Société Française de Physique (SFP)
- Société Météorologique de France (SMF)

and with the support of

- Direction des Recherches Etudes et Techniques (DRET)
- European Office of Aerospace Research and Development (EOARD) U.S.A.
- U.S. Army Research, Development and Standardization Group - U.K.

*composed of representatives of the U.S. Air Force, U.S. Army, U.S. Navy, NASA, NOAA and FAA.

Accession For
NTIS GRA&I
DTIC TAB
Unannounced
Justification
By
Distribution/
Availability Codes
Dist | Avail and/or Special
A-1

DTIC COPY INSPECTED

FOR-10A

SPONSORING COMMITTEE / COMITE DE PATRONAGE

- France

Mr CARAYOL	DRET
Mr FRANTZEN	DGAC
Mr HUSSON	CNES
Mr SAMSON	STTE (Service Technique des Télécommunications et Equipements Aéronautiques)

- United Kingdom

Mr PERRY	CAA

- U.S.A.

Mr FISHER	U.S. Navy
Mr CARRO	FAA
Mr WALKO	USAF

- West Germany

Mr ERNST	BWB

PROGRAM COMMITTEE / COMITE DES PROGRAMMES

Chairman : J. TAILLET
ONERA - 29 avenue de la Division Leclerc -
92320 CHATILLON

Members

J.L.	BOULAY (F)
B.J.C.	BURROWS (U.K.)
J.P.	CATANI (F)
M.	DILL (F)
C.	GARY (F)
J.	HAMELIN (F)
A.J.	ILLINGWORTH (U.K.)
H.	KNOLLER (U.S.A.)
J.E.	NANEVICZ (U.S.A.)
G.A.M.	ODAM (U.K.)
R.A.	PERALA (U.S.A.)
F.	PITTS (U.S.A.)
J.A.	PLUMER (U.S.A.)
J.	SKIBA (F.R.G.)

ORGANIZING COMMITTEE / COMITE D'ORGANISATION

Chairman : P. CONTENSOU
Members : J. TAILLET
L. WALKO

Liaison (U.S.A. - Canada - Mexico)	W. McKERCHAR
Secretary	Y. TIXIER

Message du Président
de l'ASSOCIATION AERONAUTIQUE ET ASTRONAUTIQUE
DE FRANCE

En 1785, il y a exactement deux cents ans, le plus illustre Américain de l'époque, Benjamin FRANKLIN, quittait la France pour regagner définitivement les Etats-Unis, au terme d'une mission diplomatique qui jetait les bases de deux siècles d'amitié et d'alliance entre les deux peuples. Ce même homme avait écrit, trente ans plus tôt, un ouvrage scientifique remarquable dans lequel il attribuait à l'électricité l'origine de la foudre.

Depuis cette époque, les applications industrielles de l'électricité ont connu un développement prodigieux, sans cependant que la connaissance de ses manifestations naturelles progresse tout à fait au même rythme, et c'est peut-être aujourd'hui dans la mesure où le phénomène naturel apparaît comme perturbateur de l'application que son étude est vigoureusement reprise.

C'est un honneur pour la France d'accueillir les lointains disciples de Benjamin FRANKLIN venus des Etats-Unis et du reste du monde pour s'entretenir des moyens de protéger l'Humanité, exposée à tant de nouveaux périls, contre celui qui lui apparut longtemps comme la manifestation privilégiée de la colère des dieux.

P. CONTENSOU

Message from the President
of the ASSOCIATION AERONAUTIQUE ET ASTRONAUTIQUE
DE FRANCE

Exactly two hundred years ago, in 1785, the most famous American of the period, Benjamin FRANKLIN, left France to return to the United States for good, at the end of a diplomatic mission which laid the foundation of two centuries of friendship and alliance between the two peoples. This same man had - some thirty years before - written a remarkable scientific work in which he attributed the origin of lightning to electricity.

Since this period, industrial applications of electricity have enjoyed a tremendous development, without, however, the understanding of its natural manifestations having kept up the same pace. But, today, in the measure that this natural phenomenon appears as a perturbing element in these applications, its study is being vigorously pursued.

It is an honor for France to welcome the present-day disciples of Benjamin FRANKLIN from the United States and from the rest of the world, to discuss together the means of protecting Humanity - which is exposed to so many new dangers - from this particular one which was for so long considered as the special manifestation of the anger of the gods.

P. CONTENSOU

CONFERENCE D'OUVERTURE

PROTECTION A LA FOUDRE DES AVIONS MODERNES

Le point de vue de l'Avionneur

D. LEROUGE
Directeur Technique Adjoint, AVIONS MARCEL DASSAULT - BREGUET AVIATION, 78, Quai Carnot, 92214 Saint-Cloud, France

INTRODUCTION

A l'instar d'autres secteurs industriels, l'industrie aérospatiale accomplit une profonde mutation technologique et technique. Celle-ci est principalement axée sur l'emploi à grande échelle de matériaux composites et l'utilisation d'une électronique omniprésente, appelée à traiter toutes les fonctions de l'avion.

Cette évolution, qui permet d'accroître les performances de l'avion et d'étendre son domaine opérationnel, ne peut être acceptée qu'au prix d'une parfaite maîtrise de la sécurité des vols pour toutes les conditions d'environnement rencontrées.

Or, la susceptibilité de l'avion moderne aux effets directs et indirects de la foudre, s'est sensiblement accrue. Trois raisons principales sont responsables de cette situation :

1 - La faible conductivité, voire l'absence de conductivité des matériaux composites (carbone, kevlar).
2 - La vulnérabilité accrue des composants micro-électroniques aux transitoires de tension ou d'énergie.
3 - Le rôle critique de l'électronique pour assurer les fonctions vitales de l'avion.

Ainsi, l'Avionneur se trouve-t-il confronté à des problèmes nouveaux en matière de protection qui réclament des solutions aptes à restaurer un équilibre qui semblait momentanément compromis.

SITUATION ACTUELLE

Dans cette période de transition où l'Avionneur manque de références (les Spécifications ne sont plus adaptées, les conditions applicables aux équipements ne sont pas encore fixées), ses efforts se sont déjà concentrés à la résolution ponctuelle des problèmes apparus lors d'essais aux effets directs ou indirects de la foudre :

- sur les matériaux composites :
  - . pour assurer une meilleure tenue mécanique des éléments situés en zones exposées (bords de fuite d'empennages ou de voilure) ou minimiser les endommagements de surface.
  - . pour renforcer la protection aux basses fréquences.
  - . pour améliorer les liaisons électriques des assemblages structuraux pseudo-isolés.

- sur les réservoirs de carburant non métalliques :
  - . afin d'éliminer les risques importants d'étincelages internes capables de provoquer une explosion.

- sur les équipements électroniques et les circuits associés :
  - . en vue de minimiser les perturbations et éviter la détérioration des circuits d'interface, sachant que la redondance d'un système peut être mise en défaut si la perturbation affecte simultanément les circuits concernés.

Il est certain que l'étude de la protection d'un avion doit être conduite selon une méthodologie rigoureuse et que les principes de protection doivent être correctement établis dès les premières étapes de la conception d'un nouvel avion : les éléments structuraux ou revêtements composites se prêtent mal aux modifications ; de même, les modifications d'une électronique de plus en plus complexe et intégrée sont coûteuses et peuvent compromettre les délais de réalisation.

POUR LE FUTUR

L'effort de recherche de ces dernières années s'est déjà concrétisé par une meilleure connaissance du phénomène naturel, notamment en vol, et de ses conséquences sur les matériaux et les systèmes de l'avion.

Pour la mise en œuvre d'une méthode globale de protection, l'Avionneur souhaite que l'action entreprise se poursuive, et même que lui soient fournis rapidement les moyens d'action et de décision, dans les domaines qui reflètent ses besoins immédiats et qui sont :

- L'étude des mécanismes de couplage direct ou par diffusion

Cette étude à la fois théorique et expérimentale doit tenir compte de la géométrie et de la répartition des nouveaux matériaux qui recouvrent des zones importantes d'un avion moderne (pointe avant, compartiment électronique, voilure, compartiment moteurs).

- L'analyse du comportement d'ensembles électroniques complexes au foudroiement naturel

L'étude du foudroiement en vol a déjà fourni des résultats très positifs tels : la trajectographie de la foudre en balayage (F-106B), les premières mesures de couplage électromagnétique à travers des ouvertures (TRANSALL04) ou encore le spectre électromagnétique émis (C-580 et TRANSALL04).
Il paraît nécessaire de poursuivre ces essais afin de compléter les informations de caractérisation de la foudre et de son interaction avec l'avion.
En complément de ces essais, il serait utile de soumettre des électroniques de techniques récentes aux conditions réelles de foudroiement et comparer ensuite les réponses obtenues à celles issues de la simulation au sol, qui laisse subsister un doute quant à sa représentativité. Une expérience de ce type conduirait à réaliser une installation capable de mettre en évidence les divers modes de couplage qui apparaîtront sur l'avion pour lequel le système est conçu.

- Les programmes de calcul électromagnétique 3D

Les formes géométriques d'un avion, l'assemblage de ses éléments constitutifs, les matériaux utilisés et les cheminements de ses circuits électriques sont d'ores et déjà informatisés.
La prochaine étape devrait conduire à y associer un programme de couplage électromagnétique dans le double but :

1) de pouvoir évaluer, dès les premières étapes de conception d'un nouveau projet d'avion, les niveaux induits sur les circuits reliant les équipements de l'avion.

2) de procéder ensuite à l'étude d'optimisation des protections, en considérant l'ensemble des exigences de protection liées aux conditions d'environnement applicables.

- La définition des niveaux de protection applicables aux équipements et des méthodes d'essais correspondantes

La protection électromagnétique globale d'un système est répartie entre :
. l'avion
. les circuits
. les équipements.

Pour fixer la part qui incombe aux deux premiers, l'Avionneur doit connaitre les niveaux que peut supporter l'équipement, niveaux auxquels il sera soumis lors des essais de qualification.
Les documents existants fixant les conditions applicables et décrivant les méthodes d'essais (DO160/ED14, SAE AE4L, MIL STD 1757, STANAG...) doivent être mis à jour ou complétés.
L'expérience actuelle montre que l'Avionneur est amené à multiplier les essais et renforcer la protection au niveau de l'avion en attendant qu'une normalisation apparaisse.

- Les moyens de contrôle initial et de maintenance

De nouveaux besoins sont apparus pour le contrôle des protections applicables aux matériaux composites associés ou non à des éléments classiques très conducteurs.
Qu'il s'agisse du contrôle des métallisations de surface ou des liaisons entre éléments voisins, les méthodes de contrôle sous courant continu appliquées aux structures métalliques s'avèrent inutilisables.
Les techniques qui seront proposées devront permettre de juger de l'état initial et de la tenue dans le temps des solutions appliquées pour la protection aux effets directs et indirects de la foudre et la protection électromagnétique générale de l'avion.

CONCLUSION

Un travail important reste à accomplir avant de fournir une réponse satisfaisante aux questions qui se posent encore concernant :

- la caractérisation de la menace
- la vulnérabilité de l'avion et de ses systèmes
- le choix des protections
- les méthodes et moyens d'essais.

L'Avionneur ne peut attendre que tout soit finalisé. Actuellement, à la lumière des plus récents travaux, il s'efforce de choisir les solutions les plus aptes à assurer la sécurité des avions de formule nouvelle qui sont déjà en construction. En l'absence de critères plus précis, ces protections sont souvent surdimensionnées, avec l'inconvénient de réduire les avantages issus des techniques nouvelles.

Dans ces conditions, il paraît urgent de définir les nouvelles règles de conception ou de réglementation s'appliquant aux avions incorporant des technologies ou techniques modernes ; ce travail devrait largement tenir compte des options ou orientations qui auront été retenues au cours de la période de transition.

KEYNOTE ADDRESS

PROTECTION OF MODERN AIRCRAFT AGAINST LIGHTNING

A manufacturer's point of view

D. LEROUGE
Deputy Technical Director, AVIONS MARCEL DASSAULT - BREGUET AVIATION, 78, Quai Carnot, 92214 Saint-Cloud, France

INTRODUCTION

Like many other industrial fields, the aerospace industry is experiencing deep technical and technological changes. These changes are mainly directed towards the use at a large scale of composite materials and generalization of active avionics to deal with all aircraft functions, including those which are critical for the flights.

This development, which improves the aircraft performance and increases its operational range, can only be accepted at the cost of a perfect control of the flight safety, for all encountered environmental conditions.

In the meantime, susceptibility of today's aircraft to lightning direct and indirect effects has noticeably increased. Three main reasons are responsible for this situation :

1 - The low or even the absence of conductivity of composite materials (carbon, kevlar),
2 - The increased vulnerability of microelectronic components to voltage or energy pulses,
3 - The critical role of electronics to insure the aircraft vital functions (fly by wire, engine control, etc...).

Thus, the aircraft manufacturer has to cope with new problems in the field of protection, requiring solutions to restore a balance which seemed temporarily compromised.

PRESENT SITUATION

In the transition period, where the aircraft manufacturer lacks references (specifications are no longer adapted and applicable requirements to equipment not yet defined) efforts have been concentrated on punctual solutions to problems which appeared during tests performed to study direct and indirect lightning effects :

- on composite materials :
  . to ensure a better mechanical behaviour of components located in exposed areas (tail or wing trailing edges), or to minimize surface damages.

- on non-metallic fuel tanks :
  . to eliminate important risks of internal sparking capable of inducing an explosion.

- on electronic equipment and associated circuits :
  . to minimize upset of electronic systems and avoid failure of interface circuits, taking into account the fact that redundancy of a system can be lost, should the disturbance simultaneously affect the concerned circuits.

It is certain that studies to harden aircraft must be conducted according to a rigorous methodology and the protection principles be well established from the first design stages of a new aircraft, as composite materials can hardly be modified ; likewise, modifications of more and more complex and integrated electronic systems are expansive and can jeopardize the program time schedule.

THE FUTURE

Research efforts of these last years have already led to a better knowledge of the natural lightning phenomenon, particularly in flight, as well as of its consequences on the aircraft materials and systems.

In order to develop a global protection method, the aircraft manufacturer wishes that the action in the fields which reflects its immediate needs be continued and means of action and of decision quickly supplied, amongst said needs are :

- Study of coupling mechanisms, through apertures or by diffusion

This study, which is theoretical as well as experimental, must take into account both the geometry and the location of new materials covering large areas of modern aircraft (nose cone, electronic compartment, wings, engine compartment).

- Analysis of the behaviour of complex electronic systems to natural lightning

Study of lightning in flight has already supplied very positive results such as : swept stroke trajectography (F-106B), measurements of electromagnetic coupling through openings (TRANSALL04), or data on the radiated electromagnetic spectrum (C-580 and TRANSALL04).
It seems necessary to continue these trials in order to complete the characterization of lightning and its interaction with the aircraft.
In addition, it would be useful to evaluate new electronic systems under real lightning conditions in order to compare the results to those gathered from ground simulations, which remain questionable. Installation of new systems would lead to reproduce all coupling modes found in modern aircraft.

- 3D electromagnetic computing codes

The aircraft geometry, the assembly of its components, the structural materials used and cables routing are already available in computer data file.
The next step could be the association of an electromagnetic code, in order to :

1) evaluate induced levels in circuits connecting the various equipment units.

2) optimize hardening of the equipment in relation with the overall protection requirements, as imposed by the environmental conditions.

- Definition of the protection levels to equipments units and related test methods

The overall electromagnetic protection of a system is shared between :
. the aircraft
. the circuits
. the equipment units

In order to determine the protection covering the two first items, the aircraft manufacturer must know the threat level the equipment can stand.
Documents listing applicable conditions and describing test methods must be either updated or completed (DO160/ED14, SAE AE4L, MIL STD 1757, STANAG...).
Present experience shows that the aircraft manufacturer is led to multiply tests and reinforce protections at the aircraft level, pending issue of a standardization.

- Initial check and maintenance equipment

New requirements came up to check protections applied to composite materials which can be associated or not to highly conductive structural elements.
Previous test procedures using D.C. methods on metal structures are unusable in tests made on composite aircraft.
Techniques to come should provide for the possibllity to measure both the initial state and the changes due to aging for any solution selected to protect the aircraft against direct and indirect effects of lightning as well as other electromagnetic threats.

CONCLUSION

An important work is still to be performed before giving a satisfactory answer to yet unsolved questions covering :

- threat characteristics
- vulnerability of the aircraft and its systems
- selection of protections
- test methods and test equipments.

The aircraft manufacturer cannot afford to wait until everything is set. For the present time, and considering the latest developments, the manufacturer must select solutions ensuring safety of new aircraft. Precise criteria not being available, these protections are often overdimensioned, thereby loosing some of the advantages coming from new techniques.

Under these conditions, it seems urgent to define new recommendations or instruction rules specific to aircraft incorporating the latest technologies or techniques ; this work should, as much as possible, take into account choices already made or trends adopted by the manufacturer during the transition period.

TECHNICAL PROGRAM

Session 1A
STATISTICAL DATA AND STANDARDS
Chairman : M. DILL

1A-1 R.L. GARDNER, L. BAKER, J.L. GILBERT, C.E. BAUM and D.J. ANDERSH.- Comparison of published HEMP and natural lightning on the surface of an aircraft..... 1

1A-2 J.C. CORBIN.- Military standard for lightning protection of aerospace vehicles..... 9

Session 2A
COUPLING AND INDIRECT EFFECTS
Chairman : R.A. PERALA

2A-1 H.D. BRÜNS and H. SINGER.- Electromagnetic interaction of external impulse fields with aircraft..... 13

2A-2 K.G. LOVSTRAND, BO WAHLGREN et al.- Finite difference analysis of lightning strike to CFC wing* .....

2A-3 E. GRORUD and M. SOIRON.- Induced surface currents and fields on a conducting body by a lightning strike (frequency domain)..... 21

2A-4 Y. BENIGUEL.- Induced current surface density after a direct lightning strike on an aircraft..... 25

2A-5 P. LEVESQUE, J. TAILLET, G. LABAUNE, S. LARIGALDIE and J.C. ALLIOT.- A study of the physical mechanisms and the perturbations created by the attachment of an arc to a conducting cylinder..... 29

2A-6 R. HESS.- The effects of finite linear characteristics inherent in the physically realizable devices associated with cable injection tests..... 37

Session 1B
METEOROLOGY AND THUNDERSTORM STUDIES : MICROPHYSICS
Chairman : A.J. ILLINGWORTH

1B-1 P. LAROCHE, M. DILL, J.F. GAYET and M. FRIEDLANDER.- In-flight thunderstorm environmental measurements during the Landes 84 campaign..... 59

1B-2 J.F. GAYET, C. DUROURE, R.G. SOULAGE and P. LAROCHE.- Location of lightning strokes on aircraft in storm field with measured electrical, microphysical and dynamical properties..... 67

1B-3 P. GONDOT and A. DELANNOY.- In-flight electrical conductivity measurements..... 71

1B-4 C.P.R. SAUNDERS and E.R. JAYARATNE.- Electric charge transfer during riming..... 77

Session 2B
METEOROLOGY AND THUNDERSTORM STUDIES : ELECTRIC PARAMETERS
Chairman : B. VONNEGUT

2B-1 E.P. KRIDER, R.J. BLAKESLEE and L.M. MAIER.- Thunderstorm currents and lightning charges at the NASA Kennedy Space Center..... 83

2B-2 M. BALA, K.C. MATHPAL and J. RAI.- Ground electrostatic field changes due to lightning..... 89

2B-3 Y. GOTO, K. NARITA, M. NAITO and R. FUNAYAMA.- Electric fields produced by winter thunderstorms..... 97

2B-4 P. PRADEEP KUMAR and J. RAI.- Electric field changes due to lightning in tropical thunderstorms..... 105

Session 3A
LIGHTNING SIMULATORS : DESIGN
Chairman : B.J.C. BURROWS

3A-1 L.H. RILEY.- United States Army missile command lightning simulation test facility..... 111

3A-2 J.L. HEBERT, L.C. WALKO and J.G. SCHNEIDER.- Design of a fast risetime lightning generator..... 115

3A-3 J.L. HARRISON, Y.G. CHEN, E. GALICKI, W. RICHARDSON, J.R. LIPPERT and D. HEIDLEBAUGH.- A severe threat-level lightning simulator*.....

3A-4 R.A. PERALA, P.M. McKENNA, T.H. RUDOLPH and J.D. ROBB.- Implementation of a crowbar switch in a Marx generator/peaking capacitor lightning simulator system..... 121

3A-5 M. MODRUSAN and P. WALTHER.- Aircraft testing with simulated lightning currents of high amplitudes and high rate of rise*.....

Session 4A
LIGHTNING SIMULATORS : MEASUREMENTS
Chairman : J.A. PLUMER

4A-1 C.J. HARDWICK and V.P. DUNKLEY.- The observation of high frequency $\dot{B}$ and $\dot{D}$ transients excited on a fuselage by an impulse generator..... 127

4A-2 C. EASTERBROOK and R. PERALA.- The utility of low level and threat level testing methods in assessing lightning hardness of composite and all metal aircraft*.....

4A-3 L.C. WALKO and J.L. HEBERT.- Lightning simulation tests in FAA CV-580 lightning research aircraft..... 137

4A-4 D.B. WALEN.- Lightning simulation tests on a graphite/epoxy airplane mockup*.....

Session 5A
FUEL IGNITION HAZARDS
Chairman : G.A.M. ODAM

5A-1 W.E. HUTCHINSON, M.L. VINCENT and J. CARTER.- Lightning protection for composite fuel tanks*.....

5A-2 R.O. BRICK.- Multipath lightning protection for composite structure integral fuel tank design..... 149

5A-3 F.J. ANDERSON, G.D. FREIER, T.S. LEE and J.D. ROBB.- Optical detection methods for testing of fuel tank lightning ignition hazards..... 157

Session 3B
PHENOMENOLOGY AND CHARACTERIZATION OF LIGHTNING :
GROUND MEASUREMENTS
Chairman : E.P. KRIDER

3B-1 K. NARITA, Y. GOTO and R. FUNAYAMA.- Bipolar lightning in winter season at Maki, Japan*.....

3B-2 E.M. THOMSON, P. MEDELIUS, M. RUBINSTEIN, M.A. UMAN, J. JOHNSON and J.W. STONE.- Horizontal electric fields from lightning return strokes..... 167

3B-3 C. WEIDMAN, J. HAMELIN and M. LE BOULCH.- Lightning VHF and UHF emissions and fast time resolved measurements of the associated electric field variations..... 175

3B-4 P. RICHARD, F. BROUTET and A. BONDIOU.- Spatial characterization of the VHF-UHF lightning radiation*

3B-5 A. BONDIOU, I. TAUDIERE and P. RICHARD.- Temporal characterization of the VHF-UHF lightning radiation*

3B-6 C. LETEINTURIER, E.P. KRIDER and J.C. WILLETT.- Submicrosecond structure of the radiation fields produced by lightning..... 185

Session 4B
PHENOMENOLOGY AND CHARACTERIZATION OF LIGHTNING : MODELIZATION
Chairman : P.L. RUSTAN

4B-1 B. HUTZLER, C. RIQUEL and J.-P. RIU.- High voltage laboratory tests and lightning phenomena..... 191

4B-2 S. LARIGALDIE.- High current surface discharge propagation analysis - Application to the lightning leader..... 197

4B-3 P.R.P. HOOLE and J.E. ALLEN.- Lightning magnetic field calculation using finite element method..... 205

4B-4 P. HUBERT.- A new model of lightning subsequent stroke - Confrontation with triggered lightning observations..... 211

4B-5 T.S. VERMA.- On the regeneration of multiple strokes in lightning flashes*.....

4B-6 J.A. BICKNELL and R.W. SHELTON.- The energy requirements of an aircraft triggered discharge..... 217

4B-7 A. BONDIOU, G. LABAUNE and J.P. MARQUE.- Electromagnetic radiation associated with the breakdown of air at atmospheric pressure..... 223

Session 6A
PHENOMENOLOGY AND CHARACTERIZATION OF LIGHTNING : TRIGGERED LIGHTNING
Chairman : M.A. UMAN

6A-1 H.W. KASEMIR.- Differences and similarities of cloud to ground discharges and lightning discharges triggered from the ground*.....

6A-2 P. LAROCHE, A. EYBERT-BERARD and L. BARRET.- Triggered lightning flash characterization..... 231

6A-3 Z.I. KAWASAKI, M. NAKANO, T. TAKEUTI and T. NAKAI.- Group velocity of lightning return stroke currents 241

Session 7A
PHENOMENOLOGY AND CHARACTERIZATION OF LIGHTNING : AIRBORNE MEASUREMENTS
Chairman : J.L. BOULAY

7A-1 N.O. RASCH and M.S. GLYNN.- Survey of lightning hazard and low altitute direct lightning strike program.... 247

7A-2 P.L. RUSTAN Jr., B.P. KUHLMAN and J.M. REAZER.- Airborne and ground electromagnetic field measurements of lightning..... 253

7A-3 P.L. RUSTAN Jr. and J.P. MOREAU.- Aircraft lightning attachment at low altitudes..... 259

7A-4 B.D. FISHER, P.W. BROWN and J.A. PLUMER.- Research in lightning swept-stroke attachment patterns and flight conditions with the NASA F-106B airplane..... 267

7A-5 V. MAZUR, B.D. FISHER and J.C. GERLACH.- Lightning strikes to an airplane penetrating thunderstorms at low altitudes*.....

7A-6 J.P. MOREAU and J.C. ALLIOT.- E and H fields measurements on the transall C160 aircraft during lightning flashes..... 281

Session 8A
SUSCEPTIBILITY AND PROTECTION OF AVIONICS
Chairman : J. BISHOP

8A-1 W.W. EVERETT III and W.W. EVERETT Jr.- Microprocessor susceptibility at RF power levels associates with lightning strokes*.....

8A-2 R.L. VAUGHN.- Airworthiness considerations of lightning strike protection for helicopter digital engine controls*

8A-3 R. HESS.- Implications associated with the operation of digital data processing in the presence of the relatively harsh EMP environments produced by lightning 289

8A-4 B.I. WOLFF and R.A. EARLE.- A new form of transient suppressor 293

Session 5B
GROUND SYSTEMS PROTECTION
Chairman : C. GARY

5B-1 R.B. CARPENTER Jr. and M.D. DRABKIN.- A 12 year study of lightning strike prevention systems 299

5B-2 YAN MUHONG.- A numerical calculation of space charge layer created by corona due to a ground artificial point beneath thunderstorm 305

5B-3 CHANGMING GUO.- Can lightning strike inhibitor inhibit lightning ?*

5B-4 N. KITAGAWA, K. ISHIKURA and H. OHTA.- The evaluation of the step voltage caused by lightning flashes to ground*

5B-5 B.G. MELANDER.- The effects of termination impedance on lightning current measurements and lightning threat definition*

5B-6 R.T. HASBROUCK.- Investigation of the lightning vulnerability of nuclear explosive test systems at the Nevada test site 311

5B-7 I. MLADENOVIĆ and A. VORGUČIĆ.- Stepped leader and striking distance 321

5B-8 A. VORGUČIĆ and I. MLADENOVIĆ.- Exposition to the lightning current of objects situated near to the vertical lightning rod 325

5B-9 C.N. GOLUB.- Lightning and logistics. Cape Canaveral - A proving ground for lightning research 329

Session 6B
LIGHTNING LOCATORS
Chairman : J. HAMELIN

6B-1 R.E. ORVILLE Sr., R.B. PYLE, R.W. HENDERSON, R.E. ORVILLE Jr. and R.A. Weisman.- Characteristics of cloud-to-ground lightning flashes along the east coast of the United States 333

6B-2 M.W. MAIER and W. JAFFERIS.- Locating rocket triggered lightning using the LLP lightning locating system at the NASA Kennedy Space Center 337

6B-3 W.A. LYONS, R.B. BENT and W.H. HIGHLANDS.- Operational uses of data from several lightning position and tracking systems (LPATS) 347

6B-4 L.W. PARKER and H.W. KASEMIR.- Ranging and azimuthal problems of an airborne crossed loop used as a single-station lightning locator 357

Session 9A
AIRCRAFT SYSTEMS PROTECTION
Chairman : H. KNOLLER

9A-1 J.R. LIPPERT, R.C. BEAVIN and J.E. LAVOIE.- Development and demonstration of atmospheric electricity hazard protection*

9A-2 W.W. COOLEY.- Lightning protection tradeoffs for indirect effects protection*

9A-3 A.R. CARLSON and D.L. TAGUE.- A study of EMP/lightning on F-16 aircraft*

9A-4 J.L. TER HASEBORG and H. TRINKS.- Special protection circuits against transient currents for aircraft systems 363

9A-5 J. BISHOP, A. AKED, C.W. POWELL and H.M. RYAN.- Aspects of lightning protection schemes for radomes (Paper received too late to be included in its session) 499

9A-6 C. KING.- Lightning-induced transient test on a transport aircraft..... 367

Session 10A
STRUCTURES AND MATERIALS
Chairman : J. SKIBA

10A-1 T.S. LEE and W.Y. SU.- Time-convoluted hotspot temperature field on a metal skin due to sustained arc stroke heating..... 371

10A-2 T.S. LEE and J.D. ROBB.- Ring discharge on the backsurface of a composite skin with ohmic anisotropy in response to frontal high current injection..... 377

10A-3 H.-P. WENTZEL, C.M. HERKERT, Th. THIELE and G. BOES.- Development and testing of protection measures for reinforced composites against lightning strike..... 383

10A-4 Th. THIELE and G. BOES.- Lightning stroke tests at the CFRP horizontal stabilizer of alpha jet..... 395

10A-5 H. EBNETH.- Simulated lightning tests on Baymetex C protected graphite-epoxy laminates..... 403

Session 7B
ELECTROSTATICS
Chairman : J.E. NANEVICZ

7B-1 A.J. ILLINGWORTH and S.J. MARSH.- Static charging of aircraft by collisions with ice crystals*.....

7B-2 B. GARDINER, J. HALLETT and C.P.R. SAUNDERS.- Field observations of aircraft charging in convective clouds..... 423

7B-3 P. LAROCHE.- Airborne measurements of electrical atmospheric fields produced by convective clouds*.....

7B-4 M.L. PRICE, R.A. PERALA, G. EDLIN and C.B. MOORE.- Dust electrification during large explosions..... 431

7B-5 J.E. NANEVICZ and E.F. VANCE.- Corona threshold determination by three-stage physical modelling of aircraft..... 441

7B-6 H. SCHNEIDER.- Live tests on static electricity in fuelling of aircraft..... 451

7B-7 D. KÖNIGSTEIN.- Hand-held electrostatic charge distribution measuring system..... 461

Session 8B
SPACECRAFT PROTECTION AGAINST STATIC ELECTRICITY
Chairman : J.P. CATANI

8B-1 L. LEVY.- A new understanding of breakdowns in the day sections of geosynchronous orbit..... 467

8B-2 J.E. NANEVICZ and R.C. ADAMO.- Status of critical issues in the area of spacecraft charging..... 475

8B-3 J.P. MARQUE.- Propagation mechanisms analysis of electrostatic discharges on satellites*.....

8B-4 B.M. SHUMAN and H.A. COHEN.- A charge control system for spacecraft protection*.....

8B-5 M. BLEZ, J. THAYER and J.E. NANEVICZ.- Spacecraft materials test in a continuous, broad energy-spectrum electron beam..... 485

AUTHOR INDEX..... 509

*Paper not available for incorporation into this book.

COMPARISON OF PUBLISHED HEMP AND NATURAL LIGHTNING ON THE SURFACE OF AN AIRCRAFT

R.L. Gardner, L. Baker, J.L. Gilbert, C.E. Baum* and D.J. Andersh*

Mission Research Corporation, 1720 Randolph Road S.E., Albuquerque, New Mexico 87106, U.S.A.
**Air Force Weapons Laboratory, Kirtland Air Force Base, New Mexico 87117, U.S.A.*

Abstract - High Altitude EMP, (HEMP) and Lightning are both electromagnetic environments which threaten aircraft. These environments interact with aircraft in different ways, however. In this paper, we compare currents and changes on the surfaces of various simple aircraft-like geometries. We use these resulting currents and charges to compare lightning and HEMP.

I. INTRODUCTION

High altitude EMP (HEMP) and its concomitant electromagnetic environment potentially threaten an aircraft. HEMP, a short (~ 0.1 μs) pulse of large amplitude (~ 50 kV/m) arrives at aircraft essentially as a plane wave. Although this pulse generally contains no oscillations (zero crossings), it's Fourier transform shows frequency content over a wide band, with significant content up to 100 MHz. For present purposes we use a well-known public domain HEMP waveform.

Lightning, another potential threat, can interact with an aircraft in two essentially different ways. First, for a nearby strike, the electromagnetic fields generated in and near the stroke channel impinge on the aircraft. Second, for a direct strike on the aircraft, the stroke current actually flows on the conducting structure of the aircraft. The first of these effects may be called field interaction and the second, current injection. It is reasonable to expect that the latter may have larger effects than the former because the strike current path is along the aircraft.

Because of the increasing concerns about these two threats, this study assessed the differences between the electromagnetic environment associated with HEMP and that associated with natural lightning, including the manner in which they affect aircraft. The investigation was based on the environments suggested by public domain literature for HEMP and by published data for natural lightning. These environments are described in Section 2 of this paper. The comparison of the two threats was based on the currents and charges on a simple geometry representative of the characteristics of an aircraft that were caused by the two electromagnetic environments. In Section 3 several simple analytical models are presented to relate the currents and charges to the environments. These models are then used to compare the two threats to aircraft in Section 4.

In Section 5, operational considerations for the two threats are presented. Lightning is improbable but damaging to aircraft. Exposure to HEMP is essentially certain for military aircraft in war but is more likely to cause indirect damage to electronic systems than the direct damage often caused by lightning.

Section 6 presents the conclusions of the study, that below about 1 MHz lightning dominates, above 10 MHz HEMP dominates, and between the two limits the interaction of the environment with the aircraft is sufficiently complex that either may dominate, depending on the details of the aircraft.

II. ENVIRONMENTS

This section presents the electromagnetic environments produced by HEMP and lightning. The environment for HEMP is that presented in the public domain [Ref. 1]. The lightning environment is derived from a number of references which present actual measurements of lightning electrical characteristics. In this paper the mechanism of HEMP and the various arguments used for determining a lightning environment are only summarized. For more detail see reference 2.

HEMP Environment

The generation of HEMP by a nuclear device is described in detail in an article by Longmire [Ref. 1]. In this paper we are primarily concerned with high altitude EMP which is characterized by an exoatmospheric nuclear detonation and a source region which extends from 20 to 40 km altitude and geographically over regions as large as the continental United States.

HEMP is generated by the interaction of weapon gamma rays with the atmosphere. Weapon gammas scatter electrons from molecules in the atmosphere and produce a radial current. This radial current would not radiate if the weapon is immersed in a uniform atmosphere. Since the weapon is above the earth's atmosphere the symmetry is broken and the EMP radiated field is produced. These forward scattered electrons are bent in the earth's magnetic field and produce a transverse current which radiates efficiently. The primary electrons produce a number of secondary electron-ion pairs which form a background conductivity. The air conductivity limits the electric field to a saturation value. For this study, the saturation field is about 60 kV/m. Sophisticated codes are used to calculate the field levels for HEMP and these calculations agree well with experimental data.

The incident HEMP waveform depends on a number of factors including: height of burst, device type,

atmospheric conditions, and distance from the explosion. To avoid this complexity during the system design process a guideline waveshape is used. A waveform presented in reference 1 is:

$$E(t) = \frac{E_0}{e^{-(t-t_0)/\tau_r} + e^{(t-t_0)/\tau_f}} \qquad (1)$$

where

E_0 = 60 kV/m (saturation field)

τ_f = 250 ns is the fall time

τ_r = 2 ns is the rise time constant

and u(t) is unit step function.

In this comparison of HEMP and lightning, HEMP will treated as an incident plane wave with the waveform described by Equation 1. With this waveform, the peak amplitude is the predicted saturation value of 60 kV/m. While the peak field of HEMP depends strongly on device design and burst height, this field provides a reasonable representation of an expected HEMP wave-form.

Lightning Environment

In this report, the current, that is the electromagnetic environment for direct and nearby strikes, is assumed to be produced in a return stroke because it typically has the largest currents and rates of rise. Detailed descriptions of the sequence of events in a lightning discharge and relevant definitions are contained in Uman [Ref. 3] and Golde [Ref. 4].

To characterize the lightning environment, which is the lightning current, three figures of merit are sufficient to specify the double exponential waveform of Equation (1). The three figures of merit considered here are:

(1) Peak Current
(2) Peak rate of rise of the current
(3) Integral of the pulse

Since the detailed theoretical modeling effort applied to HEMP has not been applied to lightning, it was necessary to use empirical techniques to determine the figures of merit listed above. All of the available measurements from which estimates of lightning current parameters are derived may be divided into three classes:

(1) Tower measurements
(2) Measurements on aircraft in flight
(3) Radiated field inference of current

Data from each of these sources were used to estimate the current in the lightning channel. This current within the channel establishes the lightning current waveform that constitutes the threat.

Tower Measurements.

Tower measurements of lightning currents are made using current sensors installed on metal towers located where there is normally a great deal of lightning activity, generally mountain peaks. Since the tower is part of the lightning discharge circuit, the effect of the tower itself on the measurements must be considered.

Useful summaries of lightning currents and rates of rise of the current are given in Uman [Ref. 3], Golde [Ref. 4], and Garbagnati [Ref. 5]. Of those summaries, only the data presented by Garbagnati is fast enough to see characteristic times of 100 ns or less, so that data will be shown here. The longer version of this paper [Ref. 2] contains a more complete presentation of the data. The maximum rate of rise reported is less than 10^{11} A/s. Other sets of tower measurements confirm this data. When corrected for ground reflection even the maximum rate of rise observed by Ericsson [Ref. 6] is very near 10^{11} A/s, as well.

At this time, tower measurements constitute the only low altitude, cloud to ground lightning current measurements available.

Aircraft Measurements.

Electromagnetic measurements made on an aircraft in flight represent another useful data base for determining the electromagnetic environment caused by lightning. Two recent sources provide data on the effects of lightning direct strikes on aircraft.

The peak rate of rise measured on the boom in front of the F-1068 [Ref. 7] is particularly interesting since it has the largest rate of rise of the current. In spite of the low (13.9 kA maximum) peak currents, the peak rate of rise found by taking a graphical derivative of the current records was 1.3×10^{11} A/s. Significantly, the maximum value closely approximate the 10^{11} A/s maximum rate of rise seen in the tower measurements.

Currents Inferred from Field Measurements.

Another method of determining the current in a discharge is to derive the current from distant field measurements. The difficulty with this method is that the current derived from the fields is not unique and unfolding the very complicated early time current evolution of lightning is not a trivial task since no quantitative model exists for the early part of the return stroke.

Since the recently published research using this method suggests very fast rates of rise in return strokes the methods used will be more closely examined.

Uman, et al. [Ref. 8] derive the relationship between the electric field and the current in the lightning channel under a restrictive set of assumptions. The initiation point must be at the ground and the current waveform must propagate up the channel at uniform velocity and without distortion of the waveshape as it propagates. It is also assumed that the fields are entirely in the radiation zone.

Correcting the above modeling to account for the return stroke currents that initiate from a point about 100 m from the ground rather than at the ground reduces the current and derivative values by a factor of two.

For subsequent strokes there is no initiation region as described here. However, for subsequent strokes there is a memory of the location of the channel. The breakdown wave is limited in propagation velocity by the velocity of light rather than the velocity of propagation for return strokes. Near the

ground, i.e., at early times the appropriate velocity for the Uman model is that of light. Corrections for the data reported in reference 9, which shows the distribution of the derived rates of rise from the fields, brings the data from the fields into much closer agreement with the data reported from tower measurements.
During the initial stages of a return stroke, the return stroke channel radius is small; consequently the channel is simultaneously resistive and inductive [Ref. 2]. Detailed numerical simulation of the evolution of the channel indicates that the channel diameter is less than about 2 mm. The impedance of the initial channel for high frequency does allow current waveforms with high rates of rise to propagate without distortion along the channel, thus violating the assumptions of the Uman model [Ref. 2]. A model consistent with this small channel at early time is that of a local current source rather than a propagating wave.

A final item to consider in deriving currents from electromagnetic fields of lightning is the possible branched configuration near the ground. A conceptual picture is shown in Fig. 1 which is supported by photographic evidence [Ref. 2]. The effect of this branched configuration is that currents derived from the fields of lightning, at early times, are potentially a factor of two to three too high.

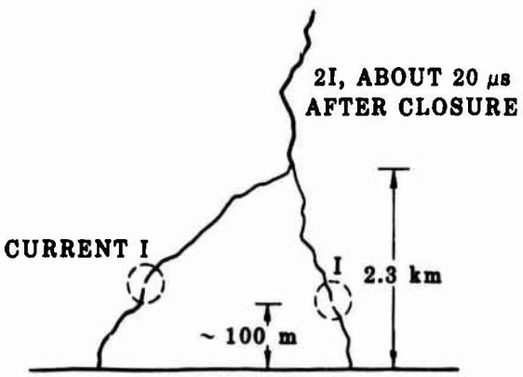


Fig. 1. Possible branched configuration showing closure region where the transition from leader to return strokes occurs.

Summary of the Lightning Threat.

A review of the available data on lightning suggests a particular waveform for the lightning return stroke current. The waveform is similar to Equation (1) for the HEMP fields but has different parameter values. We conclude the lightning current should be represented by:

$$I(t) = \frac{I_{pk}}{e^{-(t-t_0)/\tau_r} + e^{(t-t_0)/\tau_f}} \qquad (2)$$

where k is 1.025 and I_{pk} = 100 kA

τ_r is the rise time constant = 2.5×10^{-7} chosen to give a maximum rate of rise 10^{11} A/s at $t = t_0$

τ_f = 50 μs is the fall time constant

τ_0 is an offset time

Figure 2 is a plot of the current described by Equation 2. Fig. 3 shows the corresponding frequency spectrum for the waveform described in Equation 2. Based on an examination of available data, there is a severe threat described by Equation 2 with a maximum rate of rise of 10^{11} A/s and a maximum current of 100 kA. Also an expected threat should be represented by the same rate of rise but a maximum current of 10 kA. It should be noted that the lower current results in a larger frequency content above a few MHz.

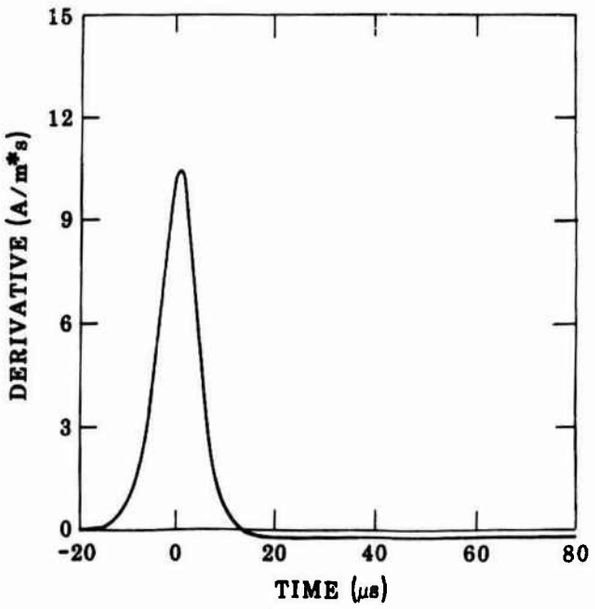


Fig. 2. Time derivative of current described by Equation 2.

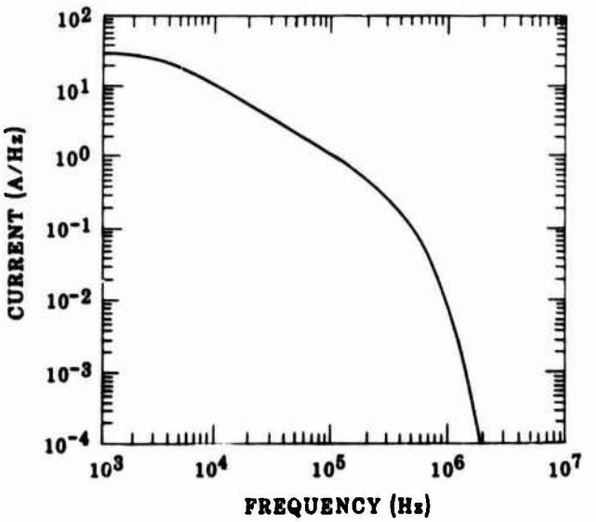


Fig. 3. Frequency spectrum of current from a Fourier transform of Equation 2.

III. INTERACTION

In addition to the differences in the electromagnetic environments produced by lightning and HEMP, these two threats differ in the way they interact with an aircraft. This section describes both qualitatively and quantitatively, using simple analytical models, the interaction of lightning and HEMP with aircraft.

Physics Of Interaction of Lightning and HEMP With Aircraft

Direct Strike Lightning.

Direct strike lightning and incident electromagnetic waves like HEMP and waves from nearby lightning strikes interact with aircraft in physically different ways.

While understanding of the physics of interaction of direct strike lightning with aircraft is still in its early stages, a qualitative description of the interaction may be given. When an aircraft enters a thunderstorm, it is under the influence of an electric field which by polarizing the aircraft induces image changes and causes currents to flow on the aircraft's skin. If a leader streamer approaches the aircraft, those fields become much larger, particularly around sharp corners and edges near the streamer. As the local fields approach a level of about 3 MV/m the air begins to break down in the field enhanced region or forms a corona. This corona exhibits non-linear characteristics which complicate the electromagnetic behavior of the aircraft under the influence of the nearby streamer. A very qualitative description of the macroscopic coronal behavior is that it exhibits the conductivity of wood until the fields begin to exceed approximately 3 MV/m. At this point, the conductivity of the air is increased substantially by electrons produced through avalanching on a time scale that is short when compared to lightning's. The increased conductivity tends to clamp the field at the 3 MV/m value.

As the leader attaches to the aircraft, coronal activity increases and a channel forms. As current flows through the channel, the air gets hotter and the number of active physical processes increases dramatically, Hydrodynamic expansion, radiative transfer, thermal conduction, joule heating, and field emission from the metal surfaces all play a part in developing the channel that in turn forms the current carrier of the lightning direct strike.

The system of clouds, channel, and aircraft should by viewed as an electrical circuit. Initially, because the channel is cool and narrow, it is both resistive and inductive; consequently it limits both the current and its rate of rise. As the lightning channel forms and as the return stroke current flows, the channel becomes hotter and larger in diameter. These increases, in turn, diminish the resistance and inductance of the channel, allowing more current to flow more rapidly. The channel expansion obeys a complex set of simultaneous differential equations that determine channel growth that is controlled by phenomena like radiative heat transfer and complex air chemistry. Since the aircraft, itself, is part of the electrical circuit under examination, it must be considered when developing an understanding of the entire interaction problem. Consequently, researchers must include both the effect of the aircraft on the formation of the lightning channel as well as the effects of the channel formation and the corona surrounding the aircraft when they analyze the current flow's effect on the aircraft, itself. In other words, the complete interaction of direct strike lightning with an aircraft is a nonlinear interaction of a large current with the air, the aircraft and the region of the thunderstorm local to the aircraft. Many of the details of the physical processes, however, are not completely understood because of the range of length scales in the problem and the large variation in the physical variables. The problem is not susceptible to either brute force numerical or to empirical techniques.

One way the surrounding corona and the attached channels manifest themselves is by altering the resonant frequencies of the aircraft. These resonant (or natural) frequencies of a structure are useful in describing the electromagnetic response of a conducting or partially conducting body. In a normal electromagnetic scattering problem, such as HEMP, the natural frequencies are functions solely of the geometry and the material of the scatterer from those of the exciting field which, of course, results in a linear problem. Since the corona and channel sheft (which in some approximation may be treated as conductors loading the aircraft) the resonant frequencies, (as will be shown later in the section), in a way that depends on the current in the channel, that separation is no longer valid and the problem becomes nonlinear. Because the natural frequencies (the geometry of the conducting body in question) now lightning, the analysis techniques used for the direct strike problem must be used with care.

The difficulty caused by the large range of length scales deserves further comment. The interaction of electrical conductivity produced by the charged particle densities and the local electric field, that produces the collisional ionization dominating the production of the electrical conductivity, occurs on length scales of the order of 0.0001 m. The macroscopic interaction problem determiing those local electric fields is of the order of tens of meters and includes the aircraft and the lightning channel, as well as the charge stored in the surrounding clouds. This combination gives a range of length scale of at least 10^5 per dimension. Electromagnetics codes designed to solve less difficult linear electromagnetics problems can handle length scale variation ratios on the order of 100 per dimension. However, even with subgridding techniques, the problem requires more zones for its solution than are now available in the state-of-the-art finite difference codes. Additionally, the problem would also require simple analytical or semi-empirical methods to circumvent the remaining numerical problems.

In a comparison of HEMP and lightning, high frequency signals affecting system electronics should also be considered. It must be noted, however, that the total energy content delivered to an aircraft by a lightning direct strike is much larger than that delivered by HEMP. Lightning's energy is mostly in the sub-MHz frequency band and consequently does not couple to system electronics as efficiently as higher frequency signals. Although low frequency energy can significantly damage an aircraft, that damage is likely to be structural or direct, rather than indirect effects on electronics. However,

indirect effects, usually associated with super-MHz frequencies, can cause far more subtle difficulties such as upset and damage to individual electronic components. Direct damage from lightning, of course, may be quite severe; there are, in fact, documented cases of fuel tank explosion and complete loss of flight control systems. Since the interaction of HEMP seldom directly affects the aircraft, the subject of direct effects does not need to be explored further for a complete comparison of HEMP and lightning.

Free Field Interaction.

HEMP and nearby lightning both interact with aircraft as a superposition of plane waves. When the electromagnetic wave inter acts with the aircraft, it induces currents and charges on the aircraft as if the aircraft were an antenna. While non-linear behavior near sharp points and edges may occur in free field interaction, the effects are not as dominant as they are in the direct strike case since the coupling is not as efficient and there is not the direct charge transfer that exists in the direct strike case.

The incident fields penetrate in the air craft through apertures and along system cables entering the electrical enclosures of the fuselage.

Internal system cables may be excited by several apertures. For HEMP excitation, the cable drive from these various apertures will in general be in-phase, such that the various drives from the apertures reinforce. This "in phase" drive is in contrast to the aperture drive from direct strike lighting where the phase of the aperture excitation depends of the velocity of propagation of the direct strike along the aircraft. In this complicated situation either environment may dominate.

Basis For The Comparison.

Comparison of the effects of HEMP and lightning on aircraft requires that a point in the interaction process be chosen such that like quantities may be compared. That is, incident fields compared with incident fields and surface currents compared with surface currents. In addition, the comparison should take place as close to the outside of the aircraft as possible to make the comparison as simple as possible. When comparing electromagnetic threats to aircraft is is necessary to compare those fields which are important in determining the penetration of the fields into the aircraft. Those fields are the normal electric field or equivalently the surface charge density and the tangential magnetic field or equivalently the surface current density. Certainly, it is desirable to choose only the dominant threat for the comparison if one exists. The relative effectiveness of the two types of threats at penetrating the aircraft is indicated by the wave impedance $Z = E/H$ at the surface of the aircraft and the surface charge and current are of equal importance when Z=377 Ohms, the impedance of free space. For an incident plane wave, like HEMP or nearby lightning, the wave impedance is always 377 Ohms. For direct strike lightning the impedance may vary and must be estimated for the particular problem.

In the upper limits of the parameters describing direct strike lightning the impedance may be calculated directly by dividing the largest expected value of E by the largest expected value of H. The upper limit of E is the breakdown value for air, $E = 3 \times 10^6$ V/m. For the largest expected value of H we are forced to use the reasonable worst case current, 100 kA described above and assume it is propagating along a 1 m radius cylinder. The resulting impedance is about 200 Ohms, indicating a dominance of the surface current density. A review of the natural lightning data gathered on the surface of an aircraft indicates that the impedance is as much as 2000 Ohms, indicating a dominance of the surface charge.

Since both surface charge and current are important to the process of coupling energy into the aircraft both must be considered when comparing electromagnetic fields or when simulating the effects of lightning on systems.

There are a number of simple interaction models that may be used for the comparison for simple geometric shapes that may be used to represent some of the important features of aircraft. The ones used here are shown in Table 1 and described in more detail in [Ref. 2].

TABLE 1. INTERACTION MODELS

		Model		
		Frequency Domain		
Effect	Variable	Low	Medium	High
HEMP/ Nearby	Current	Slab	Sassman	Slab, GTD
Direct Strike	Current	Continuity	T-Line	
	Charge	Ellipsoid	T-Line	

In this table, low frequency means subresonant or below about 1 MHz. Medium frequency means in the resonant or 1-10 MHz region. Finally, high frequencies are those for which aircraft structural details become important, or above 10 MHz.

IV. COMPARISON

In this section the actual comparisons will be presented along with the effect of the corona on the natural frequencies of the aircraft by the surrounding corona and attached streamer.

Natural Frequencies and Evidence for Corona.

In investigations of the F-106B data [Ref. 10] Trost and Turner have extracted the natural frequencies of the currents on the F-106 and models of it in configurations representative of both nearby and direct strikes. Attachment of wires and the direct strike data show natural frequencies with much higher loss components than those of the bare aircraft described in more detail in [Ref. 2.].

The importance of this shift in natural frequencies may be seen by examining the curves in Fig. 4. This figure shows a hypothetical transfer function. Two possible exterior environments are superimposed on the transfer function. The threat to the system is found by multiplying the transfer function by the threat environment. For example, suppose environment A is HEMP and environment B is lightning.

Because environment A has peaks at the same frequencies as the transfer function, and environment B has peak at the minima of the transfer function, environment A results in far higher currents at the interior system.

For the choice of environments given above, HEMP would be the dominant threat. The opposite conclusion, however, would be drawn if environment A were lightning and environment B, HEMP. Since the a priori knowledge of the identity of the environment is not available the result is a region of uncertainty in the 1-10 MHz region when the two threats are compared.

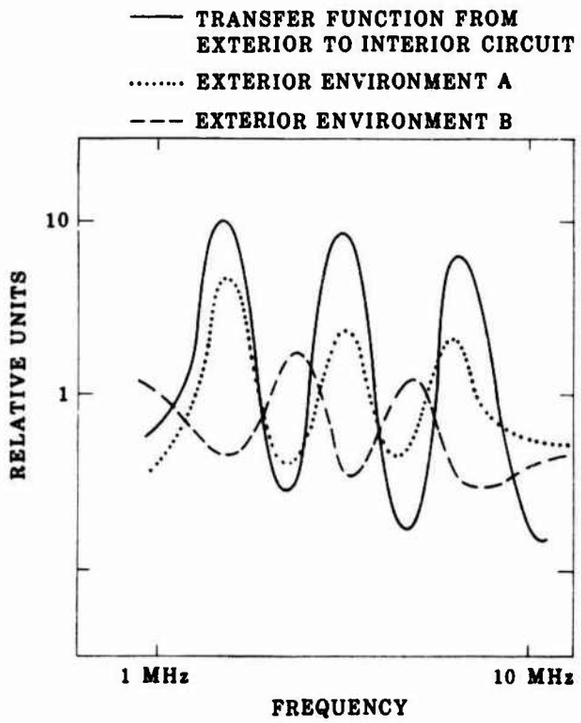


Fig. 4. Transfer function products.

Comparison of Simple Models.

The first comparison of HEMP and lightning to be presented uses the slab model for HEMP and the continuity of current model for lightning. In Fig. 5, the two models are used to compare the surface magnetic field, on a 1 m radius cylinder, generated by HEMP and by direct strike lightning. HEMP is calculated from the incident waveform in Equation (2) with a peak field of 60 kV/m, as the saturation field. The surface magnetic field is then doubled to account for reflection. Both reasonable worst case and moderate threat lightning waveforms are used in the comparison. In Fig. 5, it is clear that lightning dominates at low frequencies and HEMP dominates at high frequencies. At intermediate frequencies there is a region of uncertainty.

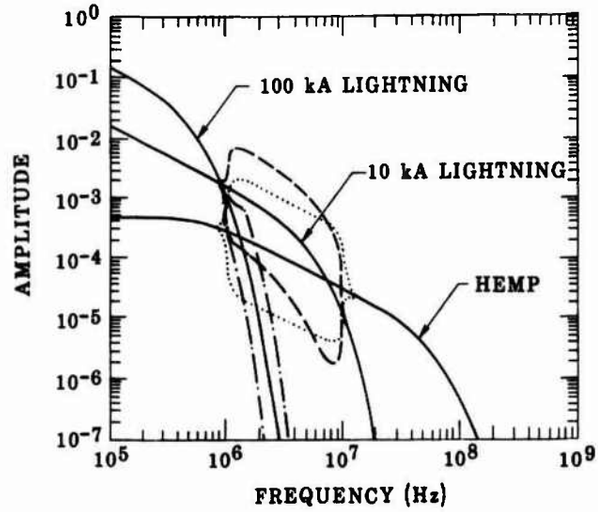


Fig. 5. Spectrum of H for two waveforms for direct strike lightning and for HEMP. The uncertainty envelopes show the effect of the resonant region.

For more complex models, such as transmission line models (see Ref. 2 for details) the conclusions are the same for both magnetic field and normal electric fields as shown in Figs. 6 and 7.

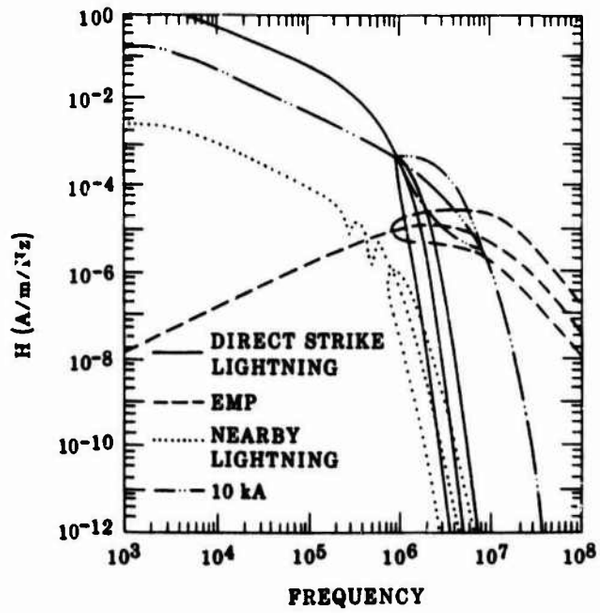


Fig. 6. Comparison of magnetic field intensity H for HEMP and lightning using the more sophisticated models.

V. OPERATIONAL ENVIRONMENTS

A comparison of HEMP and lightning is not complete without considering differences in the operational environments for aircraft exposed to these two threats.

Aircraft must be protected from lighting during the peacetime operational environment, that is, for training flights and normal cargo and passenger runs. During peacetime the schedules for these missions are not usually critical; therefore delays due to thunderstorm avoidance are regularly permitted and in most cases required. Such avoidance procedures help keep the incidence of reported lightning strikes down to one in approximately one million flight hours. Commercial aircraft have about an order of magnitude higher incidence of lightning strikes because of a stricter adherence to schedule; consequently, a somewhat higher incidence of lightning strikes to military aircraft might be expected during wartime.

If a strike occurs, there is a relatively high probability of an effect on mission accomplishment. The summary of the Air Force data base on lightning strikes given by Corbin [Ref. 11], shows that 37 percent of the reported lightning strikes resulted in at least a precautionary landing that became a mission abort. In less than 1 percent of the reported mishaps, there was a forced landing; additionally, in less than 1 percent of the mishaps, the aircraft was lost. As these data indicate, for each reported lightning strike mishap there was: a 37 percent chance of a precautionary landing; less than 1 percent (0.8 percent chance from Ref. 12) chance of a forced landing; and less than 1 percent chance (0.8 percent from Ref. 12) of an aircraft loss. In addition, there is about an 8 percent probability of damage to system electronics. Experience for electrical outages for civilian aircraft is similar with 11 percent of 783 strike reports requiring ground crew maintenance of particular electronic components [Ref. 12]. Coupled with the small probability of a mishap, approximately 10^{-6} per flight hour, these various degrees of mishap are rarely observed in peacetime.

A HEMP environment is experienced by an aircraft during wartime. In all probability an aircraft will experience HEMP environment at least once during each mission. In fact, some scenarios indicate that there may be multiple high altitude bursts. Significantly, unlike the relatively complete data base for lightning, no statistics on the probability of a certain type of failure per HEMP exposure are presently available. However, the data base for lighting does provide some guidance for estimating the probability of failure per HEMP event.

While the 37 percent precautionary landing rate for military aircraft does not directly indicate that there would be a 37 percent abort rate in wartime it does indicate a non-trivial abort rate. Assume, for the moment, that the abort rate is equal to the electronics damage rate for civilian aircraft, 8 percent. If that same abort rate per exposure held for HEMP then 8 percent of our aircraft fleet would be out of action for each HEMP exposure. Of course, the HEMP abort rate is not known, but a rate as high as eight percent would be very damaging.

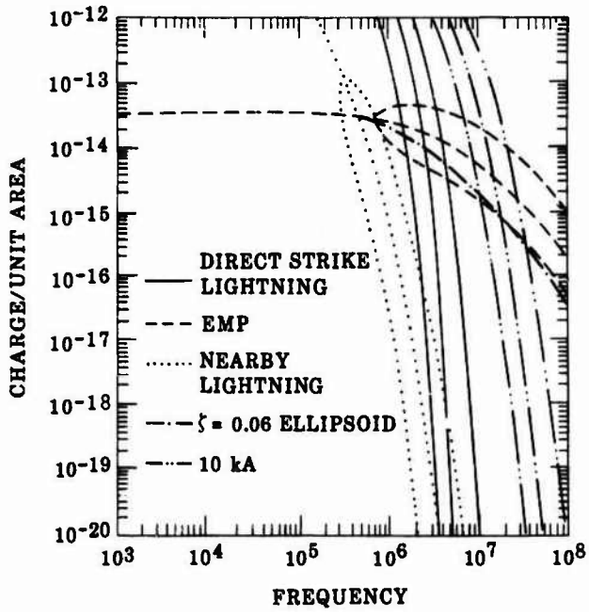


Fig. 7. Comparison of the surface charge density for HEMP and lightning.

VI. CONCLUSIONS

For several methods of comparison of HEMP and lightning the conclusion is the same. Lightning dominates at frequencies below about 1 MHz. HEMP dominates above 10 MHz. Finally, in the region between 1 and 10 MHz the inter action between the two threats and aircraft is so complex that either threat may dominate.

In addition, the two threats of direct strike lightning and HEMP interact with air craft in fundamentally different ways requiring different hardening techniques.

Finally, the operational impact of particular vulnerability levels for lightning and HEMP have very different effects on aircraft operations. In particular, only very low levels of failure probability may be tolerated for HEMP since the entire fleet may be exposed to the threat simultaneously.

REFERENCES

1. EMP Interaction Principles: Techniques, and Reference Data, K. S. H. Lee, editor, AFWL TR-90-402, Air Force Weapons Laboratory, Kirtland Air Force Base, NM, 1980.

2. R. L. Gardner, et. al., "Comparison of Published HEMP and Natural Lightning on the Surface of an Aircraft," Lightning Phenomenology Note 12, Air Force Weapons Laboratory, Kirtland Air Force Base, NM, 1984.

3. Uman, M. A., Lightning, McGraw-Hill, New York, 1969.

4. Golde, R. H., "Lightning Currents and Their Parameters," in Lightning, Vol. I, Physics of Lightning, R. H. Golde, ed., Academic Press, London, 1977.

5. Garbagnati, E., et al., "Lightning Parameters--Results of 10 Years of Systematic Investigation in Italy" in Proceedings of the International Aerospace Conference on Lightning and Static Electricity, Oxford, England, 23-25 March 1982.

6. Melander, B. G., "Effects of Tower Characteristics on Lightning Arc Measurements," in International Aerospace and Ground Conference on Lightning and Static Electricity, June 26-28, 1984, Orlando, Florida.

7. Trost, T. F. and F. L. Pitts, "Analysis of Electromagnetic Fields on an F-106B Aircraft During Lightning Strikes, "Proceedings of International Aerospace Conference of Lightning and Static Electricity, St. Catherine's College, Oxford, England, 2325 March 1982.

8. Uman, M. A., D. K. McLain, and E. P. Krider, "The Electromagnetic Radiation from a Finite Antenna," Amer. J. Phys. 43, 33-38, 1975.

9. Krider, E. P. and E. D. Weidman, "The Submicrosecond Structure of Lightning Radiation Fields," in Proceedings of the 8th International Aerospace and Ground Conference on Lightning and Static Electricity, DOT/FAA/CT-83/25, Federal Aviation Administration, Technical Center, Atlantic City Airport, NJ.

10. Turner, C. D. and T. F. Trost, "Laboratory Modeling of Aircraft-Lightning Interactions, Final Report, "NASA Grant, NAG-1-28.

11. Corbin, J. C., "Lightning Interaction with Aircraft," in Proceedings of the 8th International Aerospace Conference on Lightning and Static Electricity, DOT/FAA/CT-83-25, Conference Publication,

12. Rasch, N. O., M. S. Glynn, and J. A. Plumer, "Lightning Interaction with Commercial Air Carrier Type Aircraft," in International Aerospace and Ground Conference on Lightning and Static Electricity, June 1984.

MILITARY STANDARD FOR LIGHTNING PROTECTION OF AEROSPACE VEHICLES

J.C. Corbin

Air Force Aeronautical Systems Division, Directorate of Avionics Engineering, Wright-Patterson AFB, Ohio 45433, U.S.A.

Abstract - The U.S. Air Force, in conjunction with SAE Committee AE4L which is comprised of lightning experts from Government, industry, and test laboratories, is presently developing a new military standard which establishes requirements and verification criteria for lightning protection of aerospace vehicles (fixed/variable wing aircraft, helicopters, missiles, and spacecraft). The standard, when approved, will be applicable to aerospace vehicles including all associated subsystems, equipments, components and stores. The standard is to be used in conjunction with Department of Defense (DoD)-approved MIL-STD-1757A which establishes required lightning qualification test techniques for aerospace vehicles and associated hardware. These standards will supersede lightning protection requirements and tests specified in MIL-B-5087B which will continue to be used to specify electrical bonding requirements.

I - INTRODUCTION

For over twenty years, specification MIL-B-5087B, dated 15 October 1964 and amended 6 February 1968, has been the principal document used in the Department of Defense (DoD) to specify the requirements for lightning protection of aerospace vehicles and systems. The document presumes that all lightning protection (except for antenna systems) can be achieved if certain electrical bonding requirements are met. These requirements are specified under paragraph 3.3.4, Class L Bonding (Lightning Protection). The bonding requirements are designed to achieve protection against lightning discharge current carried between vehicle extremities without risk of damaging flight controls or producing sparking or voltages within the vehicle in excess of 500 volts. The bonding requirements are based upon a lightning current waveform of 200,000 amperes peak with a width of 5 to 10 microseconds at the 90-percent point, not less than 20 microseconds at the 50-percent point, and a rate-of-rise of at least 100,000 amperes per microsecond. The requirements may be reduced when flight safety is not a factor. Under this paragraph, laboratory tests of lightning protection provisions for external sections, such as radomes and canopies, are required using the test waveform specified above. The paragraph also states that lightning protection shall be provided at all possible points of lightning entry into the aircraft and shall be proven by test (presumably the test mentioned above).

Although many people recognized the shortcomings of MIL-B-5087B in terms of lightning protection requirements and verifications, it was 1972 before an organized effort was undertaken to better define and establish generally accepted lightning simulation test measures. In 1972, a committee comprised of individuals from lightning simulation laboratories, Government agencies, and aircraft manufacturers with experience in lightning phenomenology, simulation, and testing was organized under the auspices of the Society of Automotive Engineers (SAE) Committee AE4 on Electromagnetic Compatibility to define, establish, and document test measures that would be widely accepted and put into practice. Beginning with a survey of extensive lightning-related literature, the committee proceeded to define the possible lightning strike zones to aircraft, the lightning environment to be experienced in each zone, and the techniques for simulating this environment in the laboratory. In 1976, the committee published its recommendations in a report entitled, "Lightning Test Waveforms and Techniques for Aerospace Vehicles and Hardware" [1]. The report, referred to as the "red book," was quickly adopted by lightning test laboratories and put into practice.

In 1978, the committee (now designated SAE Committee AE4L) revised its "red book" and published a "blue book" with the same title [2]. It incorporated suggestions from British lightning test laboratories that modified some of the test procedures and wording in the document. The principal change in the report was the establishment of two categories of tests: (1) Qualification Testing and (2) Engineering Testing and inclusion of all the protection verification tests within the qualification test category. Qualification tests included (a) full-size hardware attachment point test (zone 1), (b) direct effects (structural), (c) direct effects (combustible vapor ignition via skin or component puncture, hot spots, or arcing), (d) direct effects (streamers), (e) direct effects (external electrical hardware) and (f) indirect effects (external electrical hardware). Engineering tests included (a) model aircraft lightning attachment point test, (b) full-size hardware attachment point test (zone 2), and (c) indirect effects (complete vehicle). Engineering tests were designed to provide data useful in achieving a qualification design, but were not considered necessary for protection verification.

MIL-STD-1757

In June 1978, the qualification test criteria in the "blue book" were incorporated in a draft of a proposed new military standard entitled, "Lightning Qualification Test Techniques for Aerospace Vehicles and Hardware" [3] at the request of the Department of Defense. It was not until 17 June 1980 that the document was finally approved and issued for use by all

departments and agencies of the DoD as MIL-STD-1757.

MIL-STD-1757 defines the lightning strike zones, lightning voltages and currents applicable to each zone, and the methods to be used to test components located in each zone. However, it does not specify (1) the location of the lightning strike zones on a particular vehicle, (2) the systems or components that must be tested, (3) protection techniques, and (4) pass-fail criteria. These items depend upon the mission and characteristics of the particular aerospace vehicle (fixed/variable wing aircraft, helicopter, missile, or spacecraft). The Government procuring agency, vehicle manufacturer/integrator, and/or equipment supplier must establish and agree upon the above items for each particular procurement.

In order to provide guidance in the application of MIL-STD-1757 and the rationale for establishing the various test techniques, a handbook was added to the standard as Appendix A, minor additions and corrections were made, and a revised document with the same title was approved and issued on 20 July 1983 by the DoD as MIL-STD-1757A.

MIL-STD-XXXX

In 1983, the U.S. Air Force proposed to the SAE Committee AE4L that it undertake, as its next major task, the preparation of a new military lightning protection standard for aerospace vehicles that would provide a much more comprehensive document in terms of lightning protection requirements and verification criteria than that contained in MIL-B-5087B [4]. The committee accepted the challenge. In 1984, a draft standard prepared by the committee was reviewed by the Air Force and, with minor corrections and additions, approved by an Ad Hoc Technical Review Committee established by the Aeronautical Systems Division.

Principle features of the new standard are reviewed in the following paragraphs:

Scope and Application

The standard establishes requirements and verification criteria for lightning protection of aerospace vehicles which includes fixed/variable wing aircraft, helicopters, missiles, and spacecraft and all associated subsystems, equipments, components, and stores. It is to be used in conjunction with MIL-STD-1757A which established lightning qualification test techniques for aerospace vehicles and hardware as previously described. Lightning protection requirements and tests specified in MIL-B-5087B are superseded by this standard and MIL-STD-1757A.

Requirements

Lightning protection program. The standard establishes a lightning protection program. Under the program, the standard requires contractors to prepare a comprehensive lightning protection plan (LPP). If program documentation calls for an Electromagnetic Compatibility (EMC) Control Plan under MIL-E-6051D, "Systems Electromagnetic Compatibility Requirements," the LPP becomes part of the EMC Control Plan. The LPP will include, but not be limited to, the following items:

a) Management control
b) Lightning zone identification
c) Lightning component identification
d) Criticality of structures and subsystems to flight safety and mission success
e) Hazards assessment
f) Direct effects protection approach
g) Indirect effects protection approach
h) Electrical bonding and corrosion control
i) Other effects
j) Design analysis/developmental testing
k) Verification criteria
l) Life cycle aspects
m) Configuration/documentation control
n) Initial lightning protection survey (LPS)

Lightning protection survey (LPS). A lightning protection survey (LPS) of the aerospace vehicle, its subsystems and components will be made to determine lightning damage susceptibility. The survey will be initiated early in the program to identify the potential lightning effects to the vehicle and to categorize them based upon the criticality of the lightning hazard and the zone or zones within which the subsystem is located. The potential effects of lightning (direct effects such as pitting, melting, puncture, internal arcs and welding, and indirect effects such as transient pulses coupling into wires and cables) will be a part of the survey. The survey will specify portions of the vehicle, its subsystems and components requiring protection consideration. The survey will be initially included in the LPP. It will be updated as necessary and the updated versions will be presented during appropriate design reviews. The final results of the survey will be documented in the Lightning Protection Verification Plan (LPVP).

Lightning protection categories for the vehicle and its subsystems will be based upon the impact of lightning on the overall performance of the vehicle. Three categories are identified:

a) Category I - flight safety. Lightning effects that would result in loss of life or loss of vehicle.

b) Category II - system safety and mission essential. Lightning effects that would result in personnel injury and/or would endanger mission success.

c) Category III - minor effects. Lightning effects that would not significantly reduce system effectiveness.

The contractor will identify all systems, subsystems, and/or components which are designated lightning Category I or II. Systems or subsystems to be considered for Categories I and II will include, but not be limited to, structural/mechanical, fuel/hydraulic, electrical/electronic, personnel, ordnance, and external stores.

Lightning protection design requirements. The aerospace vehicle, subsystem, or component will be protected against Category I effects and, unless otherwise specified, Category II effects when subjected to the lightning environment described in MIL-STD-1757A. In addition, design considerations will include redundant subsystems, electrical bonding, corrosion control, life cycle aspects (maintenance, repair, cumulative strike effects), compatibility with other requirements, and configuration control.

Verification

Lightning protection verification program. The contractor will be responsible for verifying the adequacy of the vehicle, subsystem, or component lightning protection design measures used to satisfy the requirements of the standard. Verification will be accomplished by qualification tests, analyses based on development test data, basic principles, or previously verified designs, or a combination of these methods.

The contractor will prepare a lightning protection verification plan (LPVP). The LPVP will include the final results of the LPS and the test/analysis data and methods to be employed as well as the success criteria for each subsystem/component. Qualification testing will be in accordance with MIL-STD-1757A. The plan will describe the methods to be used for verifying lightning protection design measures for those items identified in the LPS.

Lightning protection verification report. The contractor will prepare a lightning protection verification report (LPVR) describing the analyses and tests used to verify the adequacy of Category I and Category II lightning protection designs.

Handbook

Guidance, rationale, and lessons learned. An appendix (yet to be prepared and approved) will provide guidance, rationale, and lessons learned for the benefit of Government procuring agencies and prospective contractors in the application of MIL-STD-XXXX.

REFERENCES

[1] Lightning Test Waveforms and Techniques for Aerospace Vehicles and Hardware, report of SAE Committee AE4 on Electromagnetic Compatibility, Special Task F, May 1976.

[2] Lightning Test Waveforms and Techniques for Aerospace Vehicles and Hardware, report of SAE Committee AE4L, June 1978.

[3] Lightning Qualification Test Techniques for Aerospace Vehicles and Hardware, Proposed MIL-STD, SAE Committee AE4L, 20 June 1978.

[4] U.S. Air Force letter to Mr. J. A. Plumer, co-chairman, SAE Committee AE4L, 29 April 1983.

ELECTROMAGNETIC INTERACTION OF EXTERNAL IMPULSE FIELDS WITH AIRCRAFT

H.D. Brüns and H. Singer

Hochschule der Bundeswehr Hamburg, Holstenhofweg 85, 2000 Hamburg 70, F.R.G.

Abstract - The paper deals with the coupling of LEMP and NEMP type fields into aircraft. The theory is based on the method of moments, with a special technique for the treatment of wire junctions. The aircraft is simulated by a stick model or a wire junction model. The calculations are performed in the frequency domain with a spectrum of 0.006...60 MHz and 0.1...100 MHz respectively, using a Fourier transformation for the transition to the time domain. By means of these calculations resonance frequencies along the structure and the time-dependent behaviour of the currents are determined, comparing the results for LEMP and NEMP type fields. It is also investigated how the results are changed by using composite materials (CFRP) instead of metals for the aircraft.

1. INTRODUCTION

The electromagnetic phenomena occuring by excitation of complicated electrical systems such as aircraft by means of transient impulse fields produce a variety of individual problems. Considerable effort is spent in predicting how a system will respond on the fields of LEMP (Lightning Electromagnetic Pulse) and NEMP (Nuclear Electromagnetic Pulse). Both types of pulses show the characteristics of plane waves in a great distance from their source.

The total interaction process can be subdivided into three parts [1]: First, on metallic surfaces transient currents, charges, and fields are generated (external interaction). Second, it has to be expected that some portions of the field energy penetrate into the interior of the external structure by windows, antennas or signal cables (internal interaction). Then, this penetrated energy can spread over data lines or hydraulic leads et cetera and can excite elements of the electric systems and damage them (internal propagation). As the mutual coupling between these processes is weak, they can be viewed as being independent, in a good approximation, and solved separately [2]. This paper deals with the calculation of the external interaction problem and compares the respective effects of LEMP and NEMP.

2. METHOD OF CALCULATION

In order to calculate the interaction of aircraft with transient impulse fields or currents, several methods can be applied [3-7]:

- Integral equation method (EFIE and MFIE)
- Finite difference solution
- Singularity expansion method
- Impulse propagation calculation (transmission line theory, lumped-parameter network model).

In this paper we use an integral equation approach (EFIE), the method of moments, which is able to regard transient effects on linear systems.

Starting point is the boundary condition

$$\vec{E}^{s}_{tan} + \vec{E}^{i}_{tan} = 0, \qquad (1)$$

where $\vec{E}^{i}_{tan}$ denotes the impressed electric field, $\vec{E}^{s}_{tan}$ the tangential component of the field, caused by all charges and currents of the considered system. All conductors are assumed to be wirelike with a circular cross-section, which is very small compared to the wave length of the highest frequency applied by the exciting system. Each conductor of the system is subdivided into a certain number of segments, shown in Fig. 1.

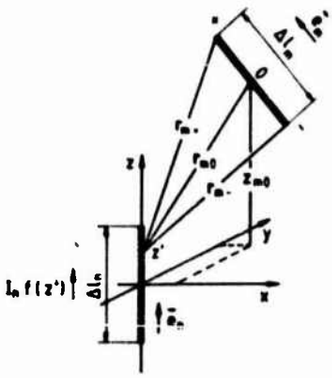


Fig. 1: Geometric relations of field point segment Δl_m and source segment Δl_n in cartesian coordinates

The expression for the voltage over the field point segment Δl_m due to the current in the source segment Δl_n is

$$U_m \approx \vec{E}^i_m \cdot \Delta l_m \cdot \vec{e}_m =$$

$$= j\omega\mu_o \cdot \int_{\Delta l_n} I(z') \cdot \psi(r_{mo}) \cdot dz' \cdot \vec{e}_n \cdot \vec{e}_m \cdot \Delta l_m +$$

$$+ \frac{j}{\omega\varepsilon_o} \cdot \left[\int_{\Delta l_n} \frac{dI(z')}{dz'} \cdot \psi(r_{m+}) dz' - \int_{\Delta l_n} \frac{dI(z')}{dz'} \cdot \psi(r_{m-}) dz' \right] \quad (2)$$

with $\psi(r) = \frac{1}{4\pi} \cdot \frac{e^{-jkr}}{r}$,

$k = \sqrt{\omega^2 \mu_o \varepsilon_o}$,

$I(z') = I_n \cdot f(z')$.

The current distribution I(z') is approximated by a linear combination of elementary expansion functions with unknown amplitudes. Each expansion function exists only over one segment of the structure. For the distribution f(z') triangular functions are assumed, because they give more accurate results with fewer segments per wave length than pulse functions; in the case of triangular functions 8 segments per wave length are sufficient in general, which is a good standard value for high frequencies. For low frequencies it has been experienced that at least 3 segments at a conductor are necessary in order to get a realistic, convergent current distribution. The developed computer program is based on these principles and uses an automatic, variable segmentation, in general with less segments for low frequencies and more segments for high frequencies.

From eqn. (2) we get for the voltage U in a shorter form:

$$U_m = Z_{mn} \cdot I_n \quad (3)$$

with the coupling impedance Z_{mn} between the two elements Δl_m and Δl_n. Regarding all the N source elements Δl_n, the resulting voltage over segment Δl_m becomes

$$U_m = \sum_{n=1}^{N} Z_{mn} \cdot I_n. \quad (4)$$

Finally, all mutual couplings are taken into account and give a set of N equations, which can be written in matrix form:

$$[Z] \cdot [I] = [U]. \quad (5)$$

The solution of this equation system delivers the current amplitudes I_n and in consequence the current distribution, which is the basis for further calculations such as electromagnetic fields in fixed points or voltages at lumped loads.

The elements of the right hand side of the equation system (5) can be caused by generators with known source voltages and have nonzero values only at such source elements. In the case of an incident field, however, a voltage over each segment has to be regarded, dependent on the spatial orientation of the conductors and on the direction of the field. Only if the field is directed perpendicular to a segment, then the line integral along the conductor and therefore the corresponding element of the right hand side is zero. With the vector $\vec{E}^i_m$ of the incident electric field at segment m, [U] is

$$[U] \approx \begin{bmatrix} \vec{E}^i_1 \cdot \vec{e}_1 \cdot \Delta l_1 \\ \vdots \\ \vec{E}^i_m \cdot \vec{e}_m \cdot \Delta l_m \\ \vdots \\ \vec{E}^i_N \cdot \vec{e}_N \cdot \Delta l_N \end{bmatrix} \quad (6)$$

with $\vec{E}^i_m = \hat{E} \cdot \vec{p} \cdot e^{-j\vec{k} \cdot \vec{r}_m}$.

$\vec{p}$ is the polarization unit vector of the incident electric field; the wave vector $\vec{k}$ shows the direction of the incident wave (Poynting vector). The vector $\vec{r}_m$ is directed from the coordinate origin to the center of segment m.

The investigated structure of aircraft is simulated by arbitrarily oriented and interconnected conductors. It is possible to regard the resistance of the conductors and also the skin effect. In order to treat conductor connections a special wire-junction technique has been developed [7,8]. This method is based on the continuity equation, which can be written as

$$\sum_{\kappa=1}^{K} I_\kappa = -j\omega \cdot \sum_{\kappa=1}^{K} \int_{\Delta l_\kappa} \lambda(l') dl' \quad (7)$$

with K as the number of conductors which are connected at the nodal point, and the line charge density λ of these wire conductors. For $\omega = 0$ the Kirchhoff current law results from this equation. The triangular functions, which are used in this paper, have to be located in the proximity of a junction as depicted in Fig. 2, which shows a joint of three wires (K=3).



Fig. 2: Junction geometry of connected wires

Every current portion, which contacts the junction, is split on the other wires in the shown manner. An advantage of treating the junction problem in this way is that no assumptions on the amplitudes of the involved currents or other additional constraints are needed. Thus the method is ideal for programming purposes.

Up to the present all the considerations were made with regard to the frequency domain. In order to get the desired transient responses in the time domain, it is necessary to compute all currents, voltages and fields for a sequence of increasing discrete frequency values of the transfer function $G(\omega)$ up to a limiting frequency ω_c. All the complex system responses are multiplied by the corresponding values of the spectrum of the exciting voltage $H(\omega)$. Subsequently, an inverse Fourier transform is performed by means of the following equations

$$f(t) = \frac{1}{\pi} \int_0^{\omega_c} (R(\omega)\cos\omega t - X(\omega)\cdot\sin\omega t)\, d\omega; \quad (8)$$

$$F(\omega) = H(\omega) \cdot G(\omega) = R(\omega) + jX(\omega). \quad (9)$$

The evaluation of the integral of eqn. (8) has to be performed numerically, so that $G(\omega)$ at fixed support frequencies ω_n must be calculated. Investigations of the transfer functions $G(\omega_n)$ have shown that it is not necessary to compute the complete series of $G(\omega_n)$. Indeed, many transfer functions have extreme variations with pronounced resonances, but in general a significant change of the function occurs only after some frequency values ω_n. Therefore, an interpolation procedure is advisable in order to save computer time. Dependent on the arrangement it has proved to be sufficient to regard only $G(\omega_n)$ of every second or third (or more) support frequency without any evident loss of accuracy. The missing values $G(\omega_n)$ can be added subsequently to a good approximation. A cubic spline function was used for this purpose.

LEMP and NEMP are commonly described by the double exponential time function

$$E(t) = E_o \cdot (e^{-t/T_1} - e^{-t/T_2}).$$

For the NEMP the values $T_1 = 500$ ns, $T_2 = 5$ ns are used in this paper in order to simulate an EXO-NEMP. Concerning the LEMP, previously interaction with aircraft has been investigated only by means of low frequency models without any dynamic current distributions or airframe resonances [2]; during the last years attention has been drawn upon the fast transient field components, having significant spectral content in the aircraft region, because it has become known that LEMP fields have fast time components in the order of 100 ns [9-13]. In this paper LEMP fields are simulated by $T_1 = 15000$ ns and $T_2 = 100$ ns or $T_1 = 1000$ ns and $T_2 = 100$ ns.

All the following results refer to $E_o = 50$ kV/m, in order to make comparable the currents due to LEMP and NEMP fields. In reality this value of 50 kV/m will occur in the case of lightning field only at small distances from the lightning channel where a circular field exists. So in general this value has to be reduced according to the inverse value of the distance. This can be done because all the here described computations are based on the principle of linearity.

The aircraft exposed to these fields is simulated either by a simple stick model or by a mesh of thin wires using the technique for wire-junction modelling described above. Both models can be used to calculate roughly aircraft resonances and the order of magnitude of currents which flow on the real structure during a lightning event for example. It can be expected that the simulation of the actual surface by a greater number of rods will give more detailed results.

3. STICK MODEL

Details of the stick model used for the calculation are shown in Fig. 3. The length of the aircraft is 10.5 m and the wing-span 8 m. In this paper the incident field was propagating parallel to the x-z-plane (Fig. 3) with the E-field 30° inclined with reference to the x-axis. A variable segmentation with a maximum number of 43 segments was applied; taking advantage of the symmetry between field and stick model only 35 segments were needed. The radii were $r_1 = 20$ cm, $r_2 = 15$ cm, $r_3 = 10$ cm. The conductivity was chosen so that the d.c. value of the resistance over the total length was 10 mΩ, in another case 100 Ω in order to approximate roughly reinforced fiber composites like CFRP.

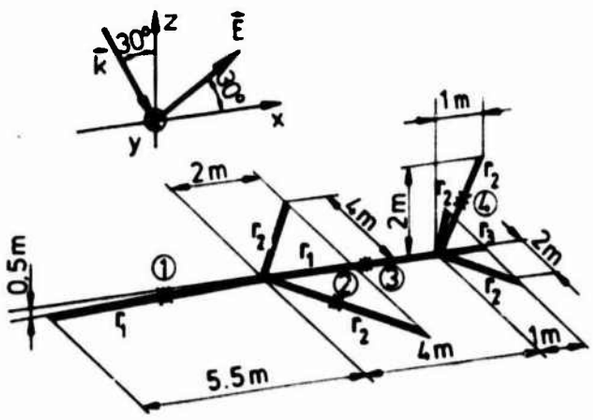


Fig. 3: Stick model of the calculated aircraft (d.c. resistance 10 mΩ and 100 Ω resp.)

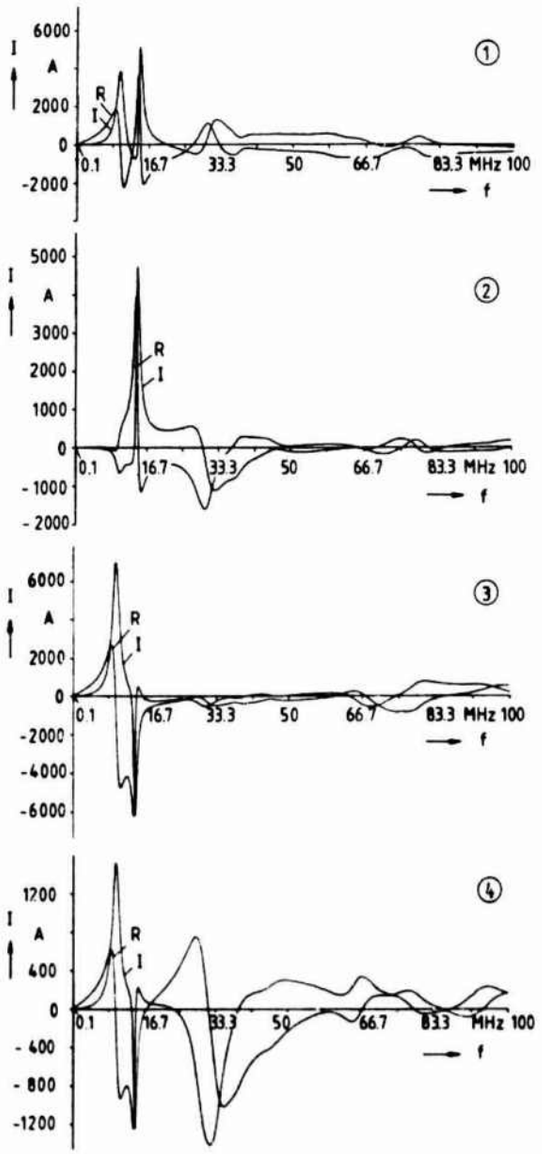


Fig. 4a: Real part (R) and imaginary part (I) of the current distribution over the frequency at the points ① to ④ of Fig. 3 for a d.c. resistance of 10 mΩ of the aircraft model

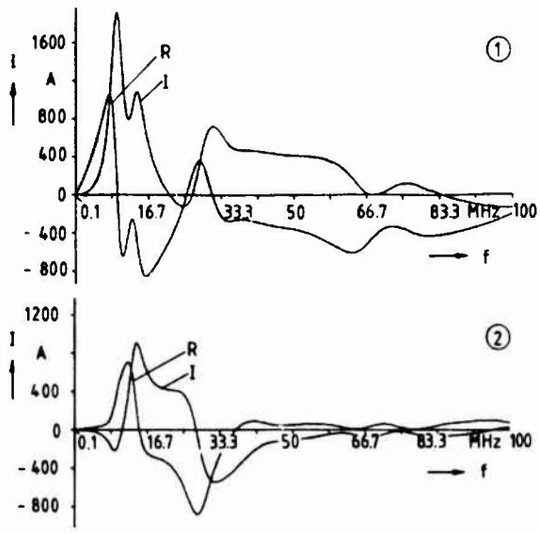


Fig. 4b: Real part (R) and imaginary part (I) of the current distribution over the frequency at the point ① and ② of Fig. 3 for a d.c. resistance of 100 Ω of the aircraft model

Fig. 4a shows the real part (R) and the imaginary part (I) of the current distribution in the frequency domain for the points ① to ④ marked in Fig. 3. Apparently conspicuous resonances occur at frequencies of around 10, 15, and 30...35 MHz, associated with the longitudinal extension of the aircraft and its parts. Whereas Fig. 4a refers to a d.c. resistance of 10 mΩ (metal skin), Fig. 4b shows the current distribution of points ① and ② in the frequency domain for a d.c. resistance of 100 Ω (related to fiber composites like CFRP). The comparison between Fig. 4a and Fig. 4b illustrates that the resonances occur at the same frequencies, but the amplitudes of Fig. 4b are evidently lower.

The lightning field with T_1 = 15000 ns and T_2 = 100 ns (10%-90%-rise time = 200 ns) was simulated in the frequency domain by frequencies from 6 kHz to 60 MHz with intervals of 192 kHz, that means 5000 harmonics. The integration was started at 6 kHz in order to take into account the relative long tail of 15 µs. The NEMP field was described by the parameters T_1 = 500 ns and T_2 = 5 ns (10%-90%-rise time = 9,7 ns) and simulated by frequencies from 100 kHz to 100 MHz with intervals of 0.2 MHz in the lower and 0.4 MHz in the upper frequency domain.

The results of the lightning field are sketched in Fig. 5, which demonstrates the time-dependent current distribution at points ① to ④ of the stick model. Fig. 5a refers to 10 mΩ d.c. resistance, Fig. 5b to 100 Ω. All the curves show oscillations in cycles of 70...105 ns, corresponding to length extensions of 21...32 m. The oscillation times at the wing, point ② , are exceptionally uniform. All the currents get positive values at the first moment, which is necessary in the case of the given field direction; in order to fulfil the boundary condition $E_{tan} = 0$ at the conductor surfaces, the current polarity must agree with the direction of E^i_{tan}. The maximum current peaks (≈ 291 A) occur at point ③ . In Fig. 5b strong attenuation

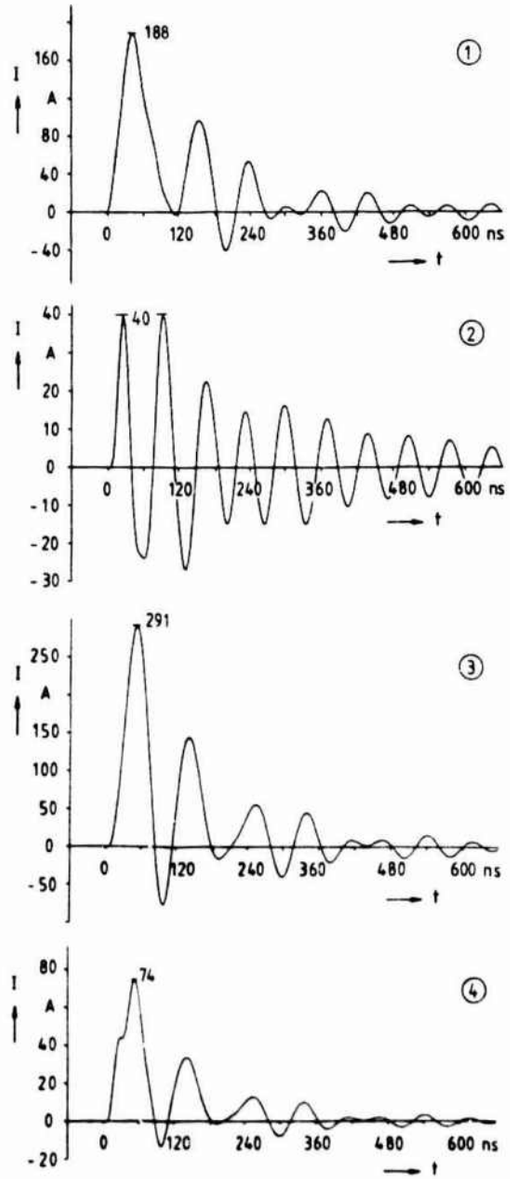


Fig. 5a: Time-dependent current distribution due to a fast lightning field at points ① to ④ of Fig. 3 for a d.c. resistance of 10 mΩ of the aircraft model

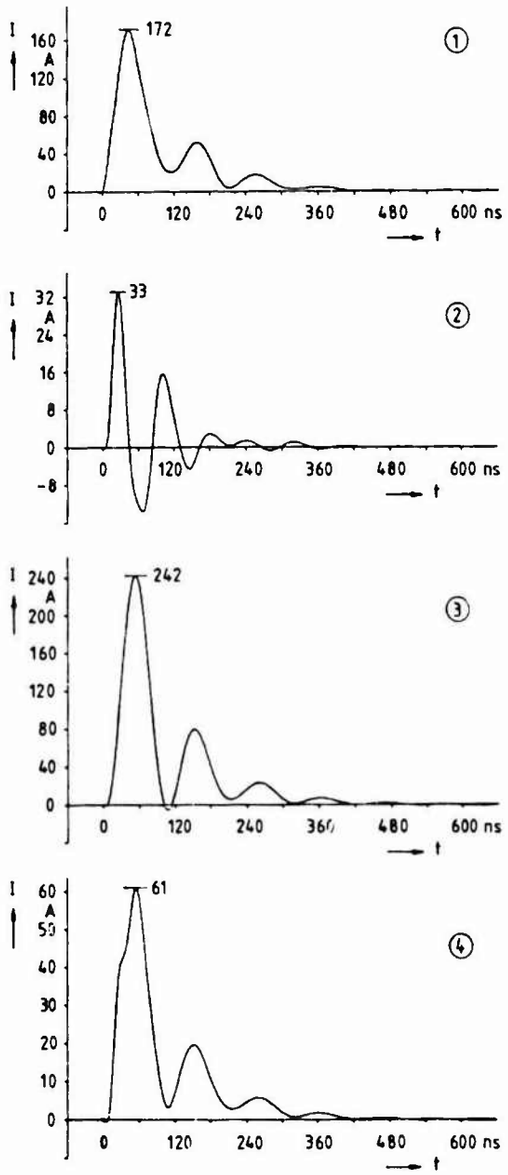


Fig. 5b: Time-dependent current distribution due to a fast lightning field at points ① to ④ of Fig. 3 for a d.c. resistance of 100 Ω of the aircraft model

over the time appears, in comparison with Fig. 5a. On the other hand the amplitudes of the first oscillations of corresponding points of both figures do not differ very much, although the resistances have the ratio 1:10000, that means that obviously the characteristic impedance of the aircraft mainly determines this first amplitude and its slope.

Corresponding results of the NEMP field effects are given in Fig. 6a/b, which shows the time-dependent current distribution at the same points of the stick model. The curves are similar to those of Fig. 5a/b, the corresponding amplitudes appear at the same moments, but the NEMP field yields higher amplitude values (factor 3...6). The comparison between Fig. 6a and Fig. 6b shows a stronger attenuation in the case of higher resistance again.

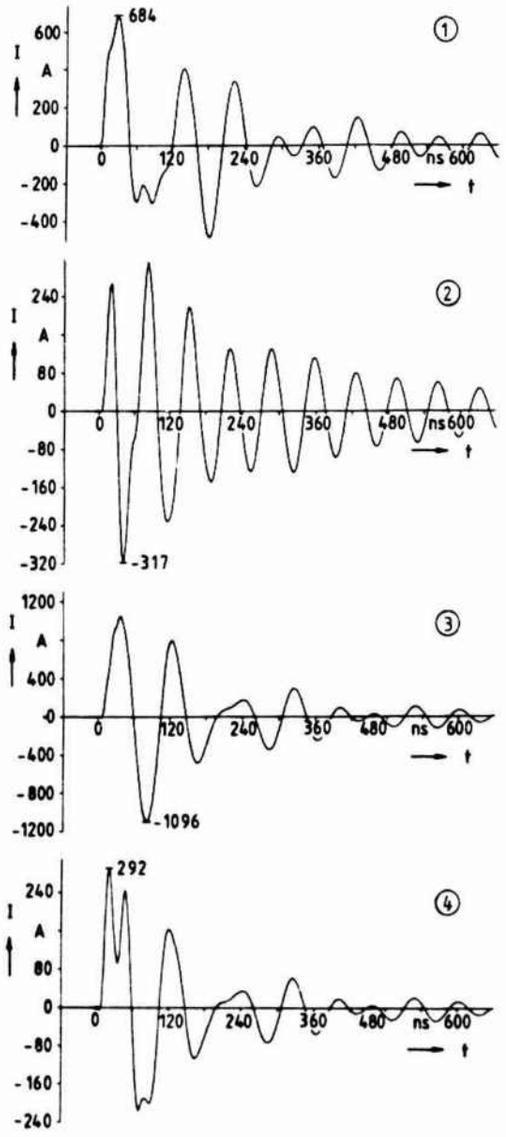


Fig. 6a: Time-dependent current distribution due to a NEMP field at points ① to ④ of Fig. 3 for a d.c. resistance of 10 mΩ of the aircraft model

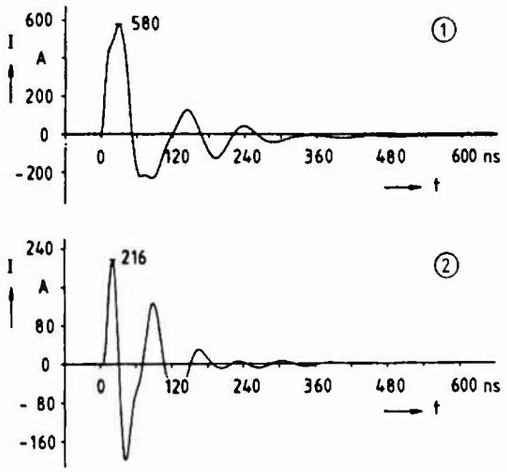


Fig. 6b: Time-dependent current distribution due to a NEMP field at points ① , ② of Fig. 3 for a d.c. resistance of 100 Ω of the aircraft model

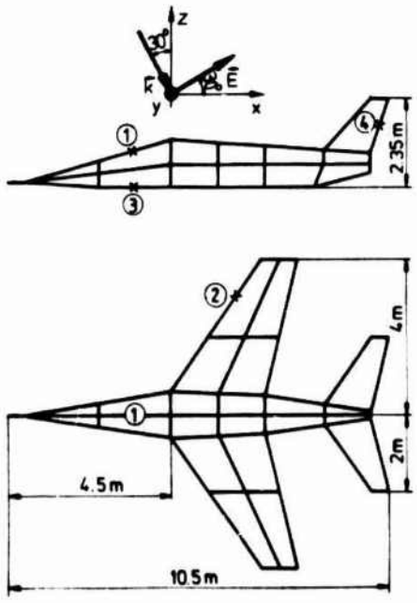


Fig. 7: Wire-junction model of the calculated aircraft (d.c. resistance 10 mΩ)

4. WIRE-JUNCTION MODEL

Using the developed wire-junction technique [7,8] a wire-junction model of the same aircraft was composed, as it is shown in Fig. 7. The incident field has the same direction as in the case of the stick model. A variable segmentation was applied again, with 78 conductors and a maximum number of 161 segments, utilizing fully the symmetry of the field arrangement. The conductivity of the wires was chosen so that again a value of 10 mΩ resulted for the d.c. resistance of the total model from nose to tail.

The lightning field component was regarded by the parameters T_1 = 1000 ns and T_2 = 100 ns, the EMP field by T_1 = 500 ns and T_2 = 5 ns. In both cases frequencies from 0.1 MHz to 102 MHz were taken into account with intervals of 0.2 MHz near the resonances, to 0.8 MHz in not critical parts of the frequency spectrum.

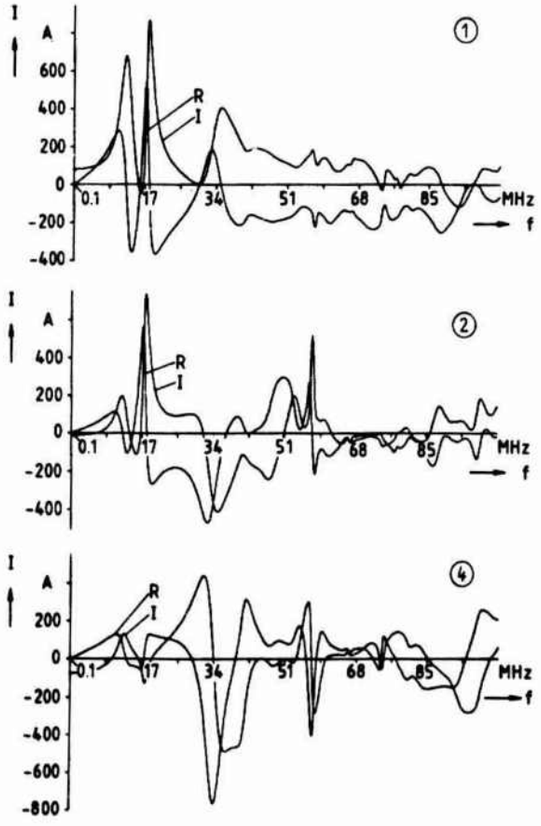


Fig. 8: Real part (R) and imaginary part (I) of the current distribution over the frequency at the points ① , ② , ④ of Fig. 7

In Fig. 8 the current distribution in the frequency domain with real part (R) and imaginary part (I) has been drawn, for the points ① , ② , ④ , marked in Fig. 7.

The rough structure of Fig. 8 is similar to that for the corresponding points of Fig. 4a, with resonances at nearly the same frequency values: ≈ 12, 17, 34 MHz. The most important resonances, for instance near the cockpit (point ①), are already detected by the stick model. Additional resonances are produced by the here occuring loops with smaller lengths than those of the stick model; so the fine structure of the current distribution over the frequency is more evident in the case of the wire-junction model. The current amplitudes are higher in the stick model, because in the wire-junction model the current is distributed over several, parallel conductors. At low frequencies (< 1 MHz) the wire-junction model exhibits comparatively high current values, because in this model loop currents can flow on account of the magnetic flux $d\phi/dt$ in any loop; the stick model yields almost zero values for these frequencies, as in this model an inductive effect appears only by means of the electric field E.

The time-dependent currents have been drawn in Fig. 9 (LEMP) and Fig. 10 (NEMP). Similar to the case of the stick model the amplitudes of the NEMP produced currents are higher (factor 3...8). The LEMP induced currents show less oscillations. However, the individual oscillations have nearly the same rise times (≈ 15 ns) in the cases of LEMP and NEMP, corresponding to a quarter of the double propagation time along the aircraft; that means that these rise times are strongly determined by the aircraft dimensions.

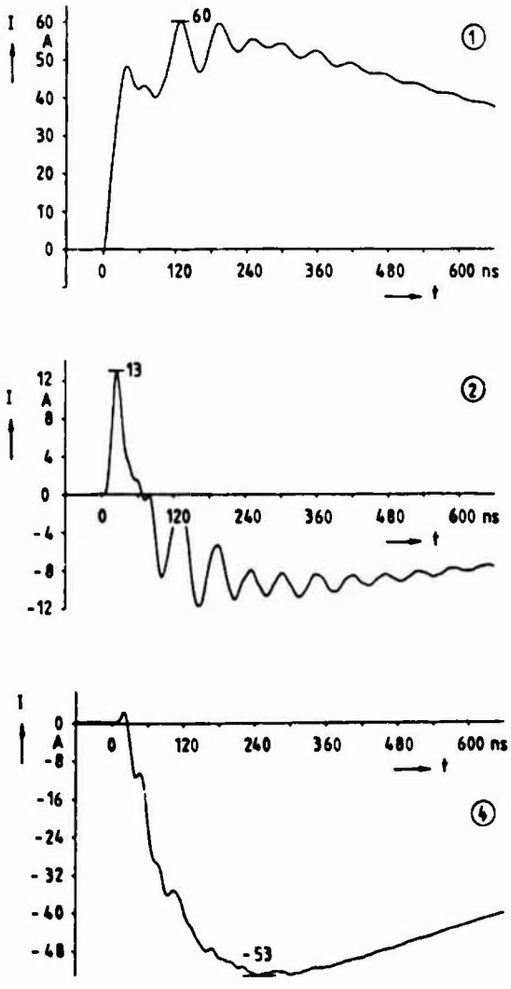


Fig. 9: Time-dependent current distribution due to a fast lightning field component (T_1 = 1000 ns, T_2 = 100 ns) at points ① , ② , ④ of Fig. 7

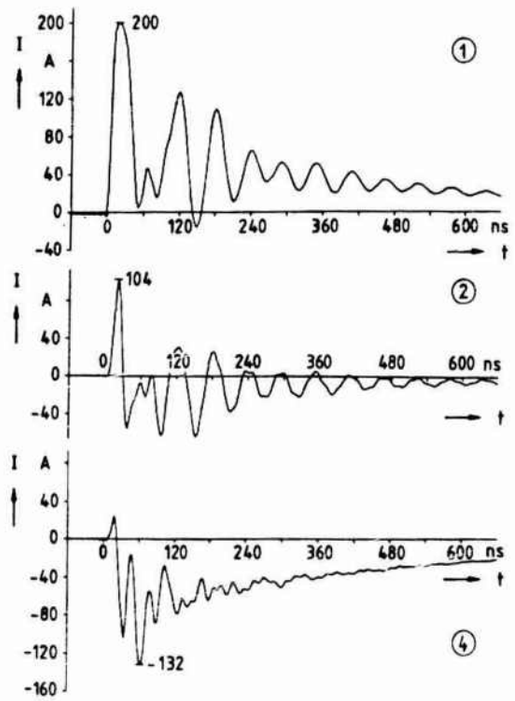


Fig. 10: Time-dependent current distribution due to a NEMP (T_1 = 500 ns, T_2 = 5 ns) at points ① , ② , ④ of Fig. 7

5. SUMMARY

The integral equation method has proved to be an efficient procedure in determining fields and current distributions at aircraft. Especially the wire-junction technique has been successful, and also the interpolation procedure in order to calculate very fast transient phenomena with reasonable computer times. The following essential results can be summarized:

- The stick model describes the rough structure of the curve shapes relatively well; by means of the wire-junction models a better resolution of the fine structure (ripples) can be seen.
- Transition to higher resistances (for instance 100 Ω at CFRP) leads to a stronger attenuation of the currents, but the first amplitudes are scarcely influenced. Apparently the characteristic impedance of the aircraft determines this first amplitude and its slope.
- LEMP fields yield lower current amplitudes and often fewer oscillations than faster field pulses, even if in both cases the same value E_0 for the exciting field pulse is assumed, which is only realistic for the near field of the lightning. The rise times of the individual oscillation components, however, are similar for both field types (≈ 15 ns), they are mainly influenced by the aircraft dimensions. It could be seen that also by the LEMP very fast processes with very steep slopes are excited.

6. REFERENCES

[1] C.D. Taylor: "External Interaction of the Nuclear EMP with Aircraft and Missiles", IEEE Trans. EMC 20 (1978), pp. 64-76

[2] R.A. Perala, T. Rudolph, F. Eriksen: "Electromagnetic Interaction of Lightning with Aircraft", IEEE Trans. EMC 24 (1982), pp. 173-203

[3] F.M. Tesche, J.P. Castillo: "Computational Techniques for EMP Interaction", Int. Symp. EMC, Rotterdam 1979, Paper 56J1

[4] T.W. Armour: "Modelling of Aircraft Responses to EMP", Int. Symp. EMC, Rotterdam 1979, Paper 57J2

[5] L. Marin: "External Interaction Problems Made Simple with the Singularity Expansion Method", 4th Int. Symp. and Techn. Exhib. EMC, Zürich 1981, Paper 42H4

[6] D.T. Auckland, R.F. Wallenberg, J.A. Birken: "Modelling of Direct-Strike Lightning Coupling by a Transfer Function Technique", 1983 Int. Aerospace and Ground Conf.on Lightning and Static Electricity, Fort Worth/Texas, Paper 16

[7] H.-D. Brüns: "Pulserregte elektromagnetische Vorgänge in dreidimensionalen Stabstrukturen", Doctoral thesis HSBw Hamburg 1985

[8] H.-D. Brüns: "Berechnung der Strombelegung auf dreidimensionalen Stabstrukturen", Archiv für Elektronik und Übertragungstechnik, 38 (1984), pp. 219-226

[9] C.D. Weidman, E.P. Krider: "The Fire Structure of Lightning Return Stroke Waveforms", J. of Geophys. Research 83 (1978), pp. 6239-6247

[10] E.P. Krider, C.D. Weidman: "The Submicrosecond Structure of Lightning Radiation Fields", 1983 Int. Aerospace and Ground Conf. on Lightning and Static Electricity, Fort Worth/Texas, Paper 69

[11] C.E. Baum, E.L. Breen, J.P. O'Neill, C.B. Moore, D.L. Hall: "Measurements of Electromagnetic Properties of Lightning with 10 Nanoseconds Resolution", Lightning Phenomenology Notes, Note 3, 5.2.1982

[12] T.F. Trost, F.L. Pitts: "Analysis of Electromagnetic Fields on an F-106 B Aircraft during Lightning Strikes", Int. Aerospace Conf. on Lightning and Static Electricity, Culham 1982, Paper B3

[13] P. Rustan, B. Kuhlman, G. DuBro, J. Reazer: "Airborn Measurements of the Risetimes in Lightning Return Stroke Fields", 1983 Int. Aerospace and Ground Conf. on Lightning and Static Electricity, Fort Worth/Texas, Paper 46

INDUCED SURFACE CURRENTS AND FIELDS ON A CONDUCTING BODY BY A LIGHTNING STRIKE (FREQUENCY DOMAIN)

E. Grorud and M. Soiron

Laboratoire Central de Télécommunications, 18-20, rue Grange-Dame-Rose, 78140 Vélizy-Villacoublay, France

Abstract - A method is presented for simulating the electromagnetic excitation of a conducting body of arbitrary shape by a direct lightning strike. The Electric Field Integral Equation (E.F.I.E.) is solved in the frequency domain by the method of moments.
The modeling of the conducting body uses planar triangular patches and is done automatically by a mesh generation procedure from a given set of data points.
For direct strike simulation, the lightning attachment points are modelized by "wire-surface" junction type triangles.
Some time domain results are obtained on an aircraft using an inverse Fourier Transform (FFT).

I - INTRODUCTION

The effects of lightning arise through either a direct or nearby strike. In the first case the total current flow is known and goes through the body. In the second case, an electromagnetic pulse of radiation is scattered by the body, the excitation being an impressed E Field. Both direct and indirect discharges can be analysed by numerical methods developed for the problem of the nuclear EMP-scattering.

A computer program bas been developed at the Laboratoire Central des Telecommunications for the NEMP problem. This code computes the induced currents, surface currents and fields on composite wire and surface geometries by an impressed incident E Field. The arbitrarily shaped surfaces are assumed to be perfectly conducting. The Electrical Field Integral Equation (E.F.I.E.) is expressed in the frequency domain.

This program can also compute the surface current distribution from any type of excitation : voltage, injected current.
The effects of a direct lightning strike on a perfectly conducting body can then be analysed by such a code.

II - LIGHTNING CHANNEL AND CURRENT WAVEFORM

The return stroke channel is usually modelized by a succession of radiating dipoles carrying a travelling current pulse. When one wants to obtain fields close to the channel, it is necessary to perform an integral summing radiation from elements along the whole length. For a straight channel, a travelling current pulse radiates as if the fields emanated from the end of the filament. When one considers a conducting body struck by a straight return stroke channel, the segmentation of the channel itself into elementary radiating dipoles is superfluous since the excitation level created by the injection of the current pulse onto the body is far more important than the excitation created by the channel radiated E Field.
It is then sufficient to modelize the channel by two short dipoles connected to the body at some predefined entry and exit points, where the strike is most likely to occur.

One of the most widely used empirical approximation of the return stroke current waveform is :

$$I(t) = I_0 \left(e^{-\alpha t} - e^{-\beta t}\right) \qquad (1)$$

Typical values of I_0, α, β are :

$I_0 = 10kA \qquad \alpha = 10^4 s^{-1} \qquad \beta = 3.10^5 s^{-1}$

The frequency range of a lightning pulse is then much narrower than the NEMP one.
In particular, the NEMP frequency range extends over the body resonances when one considers an average size air-craft for example (2 MHz to 10 MHz) (fig.1)

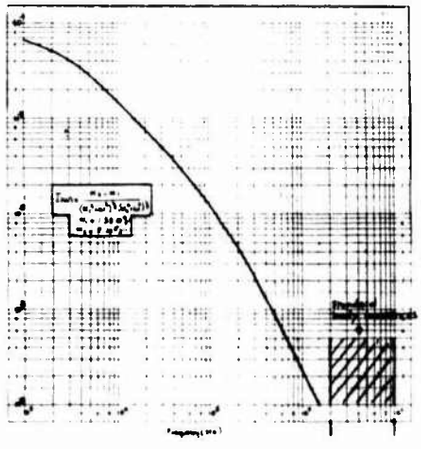


fig.1 - Frequency range of a lightning pulse

With such a low frequency range, the current waveform injected onto body surface is not affected and it will be transmitted from the entry point to the exit point without much change in its shape. The time dependence of the exit current is then assumed to be given by eq. (1).

III - PROBLEM FORMULATION

The E.F.I.E. for a perfectly conducting body of surface S can be written as :

$$\hat{n} \times \bar{E}^s(\bar{r}) = -\hat{n} \left[j\omega\mu_0 \int_S \bar{J}(\bar{r}')\,\varphi\,ds' - \frac{1}{4\pi j\omega\varepsilon_0} \int_S \nabla_s' \cdot \bar{J}(\bar{r}')\,\nabla'\varphi\,ds' \right]$$

where $\varphi = \frac{e^{-jk|\bar{r}-\bar{r}'|}}{4\pi|\bar{r}-\bar{r}'|}$ and $\bar{r} \in S$. E^{inc} is the incoming impressed electric field. (2)

$$\hat{n} \times \bar{E}^s(\bar{r}) = -\hat{n} \times E^{inc}(\bar{r})$$

The E.F.I.E. is solved by the moment method applied to surfaces and wires. The set of expansion and test func-

tions used for the surface currents are due to GLISSON [1] (fig.2). The surface is modeled by triangular patches. The current on the dipoles is expanded into standard pulse functions. The connection between wires and surfaces is done by "junction type" triangle patches whose common vertex is a node of the triangular patch modeling and the attachment point of the wire to the surface (fig.3). The current flowing from the wire onto the surface is assumed to have a radial behaviour and a 1/r decrease in amplitude. A set of junction type basis functions [2] insures the continuity of the current flow from the wire to the surface (fig.4).

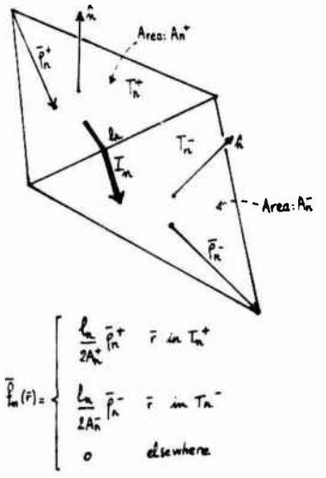


fig.2 - Expansion function for triangular patches

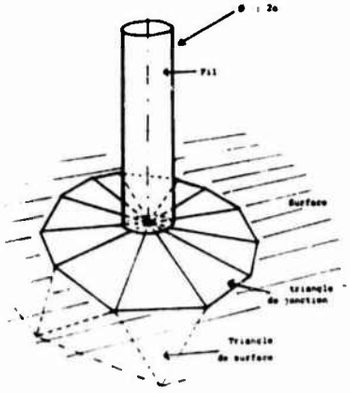


fig.3 - Wire attachment to surface modeled by triangular patches

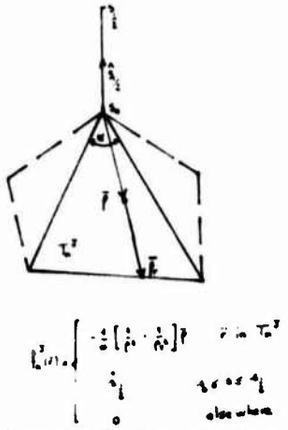


fig.4 - Expansion function for "junction-type" triangles

The equation (2) is transformed into a linear system of equations. The number N of unknown currents is the sum of Ns non-aperture edges of the triangular patches of the surface, N_J junction-type triangles and N_W thin dipoles.

In the lightning strike configuration, there are two dipoles attached at the entry and exit point of the surface. As stated earlier, these currents are assumed to be known.

The actual number of unknown currents is then :

$$N = N_S + N_J + N_W \qquad (3)$$

The current injection scheme consists of computing the impedance matrix over $N_S + N_J + N_W$ elements with only $N_S + N_J$ unknown to be found.

The following linear system is then solved :

$$\begin{aligned} Z^{SS} I_S + Z^{SJ} I_J &= -Z^{SW} I_W \\ Z^{JS} I_S + Z^{JJ} I_J &= -Z^{JW} I_W \end{aligned} \qquad (4)$$

where $Z^{SS}, Z^{SJ}, Z^{JS}, Z^{JJ}, Z^{SW}, Z^{JW}$ are the self and mutual impedance matrices between surface, junction part and wires.

This system can also be written as :

$$\begin{bmatrix} Z^{SS} & Z^{SJ} & Z^{SW} \\ Z^{JS} & Z^{SS} & Z^{JW} \\ 0 & 0 & [1] \end{bmatrix} \begin{bmatrix} I_S \\ I_J \\ I_W \end{bmatrix} = \begin{bmatrix} 0 \\ 0 \\ I_W \end{bmatrix} \qquad (5)$$

The excitation term can be seen as the voltage across each element of the surface and junction part created by the entry and exit currents on the two dipoles.

IV - RESULTS

An aircraft 30 m long with 40 m wing span bas been modeled into a triangular patch surface including 80 nodes, 282 edges and 188 patches. The two attachment points (entry and exit) were respectively put at the nose and tail of the aircraft. The code was run at several frequencies ranging from 50 kHz to 5 MHz. The two first aircraft resonances appear at 3.8 MHz and 4.5 MHz. From 50 kHz to 1 MHz, the induced surface currents are essentially real and relatively unsensitive to the frequency. Above this range, the resonance effect starts to be noticeable and the imaginary part of the currents start growing.

The surface current distribution taken at 50 kHz is shown on fig.5. Arrows show the direction of current.

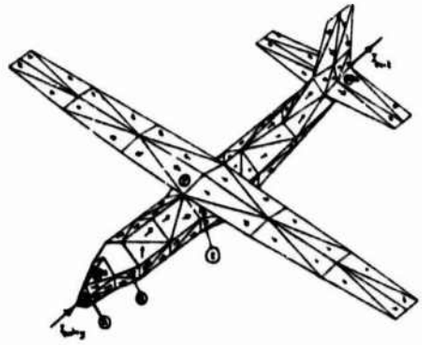


fig.5 - Surface currents distribution on an aircraft patch model at 50 kHz

High values of current occur mainly near the nose and by the tailplane. The current flow from the entry point to the exit is quite visible.
Since the frequency spectrum of the current pulse is two decades below its maximum value at 50 kHz (see fig.1) the frequency sweep necessary to obtain time domain results was limited to this value. Six points were chosen on the aircraft surface (point A to F) in order to obtain time domain results, by a FFT procedure. The induced surface currents (fig. 6,7) have the same time dependence as the injected current pulse since no aircraft resonance is excited.

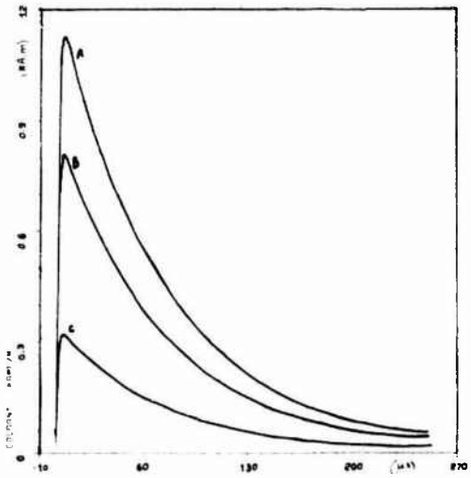


fig. 6 - Time domain surface currents induced on an aircraft (10 kA injected current).

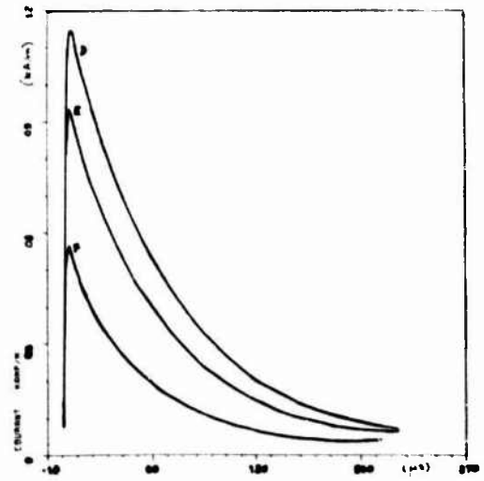


fig. 7 - Time domain surface currents induced on an aircraft (10 kA injected current).

A good check of the validity of the injection technique adopted here, is to sum over the number of junction triangles at the entry or exit points, the junction currents obtained after inversion of the impedance matrix.
Recalling that 10 kA have been injected which correspond to a maximum amplitude of 9.25 kA at 4.7 μs the injection technique works reasonably well when one sees the time domain result shown on fig.8 which corresponds to the sum of all the junction currents at the entry point.

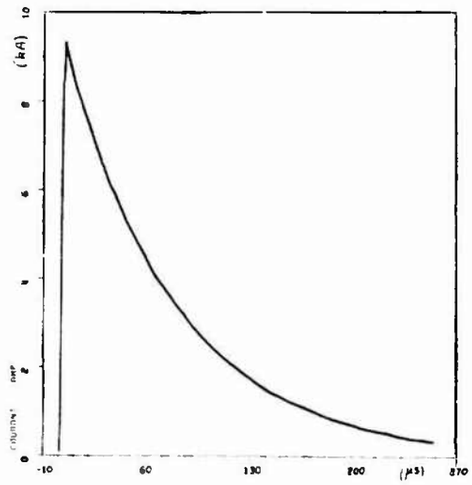


fig. 8 - Time domain junction current at the entry point

The normal component of the total electric field at the surface of the scatterer can be written as :

$$\hat{n}.\bar{E} = -\frac{1}{j\omega\varepsilon_0}\nabla_s.(\hat{n}\times\bar{H}) = -\frac{1}{j\omega\varepsilon_0}\nabla_s.\bar{J} \quad (6)$$

It is then straightforward to obtain this quantity all over the surface. The time domain normal component of E is plotted on fig.9 at point A and B. The E field at the nose of the plane, near the attachment point is far more important than elsewhere on the surface, which is to be expected.

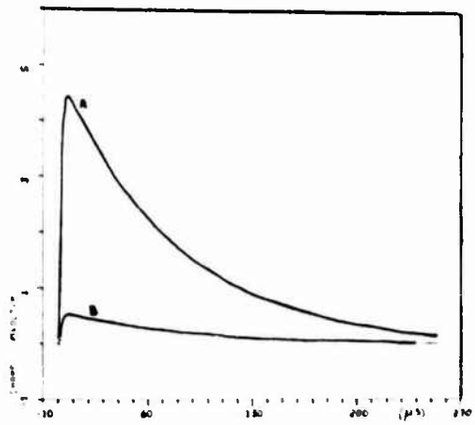


fig.9 - Time domain normal E field component on the aircraft surface

V - CONCLUSION

The triangular patch modeling of surfaces associated with special wire-surface junction techniques is quite suitable for solving the E.F.I.E. in the frequency domain. Direct current injection onto the surface works quite well.
The results obtained so far are promising and the versatility of the numerical code allows to modelize a large

number of configurations.
The next step will be to apprehend the penetration of fields into aperture (cockpit for example) which is of primary interest.

REFERENCES

1 *AW. GLISSON*

On the development of numerical techniques for treating arbitrarily shaped surfaces. Ph.D. Dissertation. Univ.of Mississipi, 1978.

2 *S.M. RAO*

Electromagnetic scattering and radiation of arbitrarily shaped surfaces by triangular patch modeling.
Univ. of Mississipi, Ph. D. Thesis.

INDUCED CURRENT SURFACE DENSITY AFTER A DIRECT LIGHTNING STRIKE ON AN AIRCRAFT

Y. Beniguel

Laboratoire Central de Télécommunications (L.C.T.), B.P. 40, 78141 Vélizy-Villacoublay, France

Abstract - This paper describes a method to calculate the current after a direct lightning strike on an aircraft. To solve this problem we have developped a time domain algorithm which compute the current surface density on a structure of arbitrary shape.We examine in this paper its mathematical and numerical aspects. The lightning strike is represented by a source current in one point of the aircraft, an exit at another point and we calculate the effects of this current travelling along the structure.

1 - INTRODUCTION

In the past years LCT has developped computer codes to solve electromagnetic problems in the field of NEMP interactions. Two families of codes are available, one in the time domain and the other in the frequency domain. These codes allows to study interaction of NEMP signals with targets of arbitrary shape (aircrafts, ships, wire antennas, including more complicated configurations as mixed wires and surfaces (U.S. TACAMO for example)). The time domain may vary from some ns to some µs or correlatively the frequency domain may vary from 0 to about 100 MHz.

The purpose of this study is to use such a code to study the effects of a direct lightning strike on an aircraft.

The frequency domain algorithm is presented in a companion paper [1] . The time domain algorithm is presented hereafter. The Maxwell equations are used on their integral formulation preferably to the finite difference one. This allows to use a surface approximation close to the true shape of the aircraft and obtain a better estimate of the results. In the integral formulation the current is computed in local coordinates so that we take into account the local properties of the structure i.e. the curvature radius at each point on this one.

In the case of the direct lightning strike, we take the a priori hypothesis that the source current is impinging on the aircraft at one point and flows out by another point. More generally we could imagine these two points (entry and exit) be located as a discrete function of time. In this hypothesis, consequently, we suppose no reaction from the aircraft on the lightning channel. This is a first approach on a simplified physical model, using a rigorous formulation.

2 - TECHNIQUE FOR OBTAINING TIME-DOMAIN RESULTS

We distinguish two kinds of surfaces on the aircraft (a TRANSALL C160 in this study) :

- the fuselage which is a closed surface,
- the wings and the tail. These parts of the aircraft have been approximated by planes.

Two equations have been solved and two algorithms developped corresponding to the two kinds of surfaces indicated above. The use of one or the other of these equations in an electromagnetic scattering problem depends on the geometry of the target, these two equations being not equivalent from a numerical point of view.

1. Current density on the fuselage

On such a closed surface we use the magnetic field integral equation (M.F.I.E.) whose expression is :

$$\vec{J}_m(t) = 2\,\hat{n} \times \vec{H}^i(t) + \frac{\hat{n}}{4\pi} \times \iint_S \left(\frac{1}{R^2} + \frac{1}{Rc} \frac{\partial}{\partial \tau} \right) \vec{J}(\tau) \times \hat{R}\, ds \qquad (1)$$

The current at time t at a point m on the surface can be computed using the magnetic incident field at the same time and the values of current densities on the surface at retarded times τ where $\tau = t - R/c$ and R is the distance from the point m to any other point i on the surface.

The first term $2\,\hat{n} \times \vec{H}^i(t)$ is the physical optic approximation term.

The second term represents the radiation of currents at the different patches of the structure at retarded times.

In particular, if i=m, $\tau = 0$ and the delay is zero. The value of the self patch integral can be computed if we know the principal curvature radius ρ_m and ρ_n at the center of this patch. We obtain the result :

$$\int_{S_m} \left(\frac{1}{R^2} + \frac{1}{Rc} \frac{\partial}{\partial \tau} \right) \vec{J}_i(\tau) \times \hat{R}\, ds = \frac{\gamma}{4} \left(\rho_m - \rho_n \right) \left[\hat{a}_m \times J_m(t) - \hat{a}_n \times J_n(t) \right] \qquad (2)$$

where γ is the radius of the patch approximated by a circle.

The preceeding equstion is thsn :

$$\bar{J}_m(t)(4+c) + \bar{J}_m(t)(4-c) = c\,\hat{n}\times\bar{H}^i_m(t) + \frac{\hat{n}}{2\pi}\times\int_{S-S_m}\left(\frac{1}{R^2}+\frac{1}{Rc}\frac{\partial}{\partial t}\right)\bar{J}_i(t)\times\bar{R}\,ds \quad (3)$$

with : $$c = \frac{\gamma}{4}(\rho_m - \rho_m) \quad (4)$$

The fuselsge of the aircraft is modeled by three surfaces :
- hslf s sphere at the nose,
- s cylinder in plsce of the csbin,
- s cone st tha aft.

On esch of these particular surfsces we use a proper systam of coordinstes (spherical, cylindricsl). The patches on each of these surfsces are approximately squsre in the corresponding coordinstes.

This is a first approach to solve the problem. It can be improved using at each discretization point on the surface the vslues of its right curvsture rsdius st this point.

In the csse of the sphere, the two curvsture radius being equsl e is zero. In the case of the cylinder snd the cone one of the principsl curvsture radius is zero and the vslue of e is :

$$c = \frac{\gamma\rho_m}{4} \quad (5)$$

The integrsl over the other patches requires to compute the velues of the current snd its time derivstive. Both hsve been computed using Legrengien polynomial interpoletion.

Moreover we need to sdd the contribution of current densities of perts of the eircraft other then fuselege (winge, tail) to compute the right value of the potentiel vector. The other valuee are computed simultaneously.

Convergence and stability of the cloeed curfeces elgorithm.

The algorithm is etable if the petches heve approximetely equal areas. The time increment correaponds to the shortest dietance between any two points.
The area of the patches is not a critical factor to obtain the convergence of the resulte.

2.2. Current density on the wings and the tail on the aircraft.

On e plane aurface we uae the Electric Field Integral Equation (E.F.I.E.) which permits to take into account epecial conditione in case of curvature radius discontinuities (the edgee of planes for example). This special case will be documented later on.

The equation we solve is the following :

$$\hat{n}\times\frac{\partial\bar{E}^i(t)}{\partial t} = -\frac{1}{\mu\varepsilon}\,\hat{n}\times\nabla\nabla\cdot\bar{A}_m(t) + \hat{n}\times\frac{\partial^2\bar{A}_m}{\partial t^2}(t) \quad (6)$$

with: $$\bar{A}_m(t) = \frac{\mu_0}{4\pi}\int_S\frac{\bar{J}_i(\tau)}{R}\,ds \quad (7)$$

As in the preceeding csse (M.F.I.E. equstion), the surface is divided in pstches which sre spproximstely squsre snd of equsl sress. Tha current density is computed st the center u of esch one from tha vslue of the vector potantisl $\bar{A}_m(t)$ at this point. $\bar{A}_m(t)$ is computed in fonction of values of currant density st delsyed times τ with $\tau = t - R_{iu}/c$ and R_{iu} is the distance between u snd tha center i of any other patch on the surfsce.

$$A_m(t) = \frac{\mu_0}{4\pi}\sum_i\int_{S_i}\frac{\bar{J}_i(\tau)}{R}\,ds \quad (8)$$

with :

$$R = |R_m - R_i| \quad (9)$$

In the csse where the points i snd u sre identicsl (self pstch contribution to $\bar{A}_m(t)$) the integrsl is not singulsr snd is found to be equal to :

$$\int_{S_m}\frac{\bar{J}_i(\tau)}{R}\,ds = 4\Delta\,\mathrm{Log}\left(1+\sqrt{2}\right)\bar{J}_m(t) \quad (10)$$

Consequently the vector potential $\bar{A}u(t)$ ie a fonction of the current density et the point u and time t end the other points st retsrded times.

If we choose s coordinste system such thet x = 0 on the plane we have :

$$\hat{n}\times\nabla\nabla\cdot\bar{A}_m = -\hat{y}\left(\frac{\partial^2 A_y}{\partial y\partial y}+\frac{\partial^2 A_z}{\partial y\partial z}\right)+\hat{y}\left(\frac{\partial^2 A_y}{\partial y^2}+\frac{\partial^2 A_z}{\partial y\partial z}\right) \quad (11)$$

The time derivetive of the current is computed from the following formula :

$$\frac{\partial^2\bar{A}_m(t)}{\partial t^2} = \frac{\bar{A}_m(t_{n+1}) - 2\bar{A}_m(t) + \bar{A}_m(t_{n-1})}{\delta t^2} \quad (12)$$

Equetion (6) gives two equetione for esch one of the vector potentiel componente.

a/ On $\hat{y}$

$$A_{m,y}(t_{n+1}) = \frac{\delta t^2}{\mu\varepsilon}\left[\frac{\partial^2}{\partial y\partial y}A_{m,y}(t)+\frac{\partial^2}{\partial y\partial z}A_{m,z}(t)\right] + 2A_{m,y}(t) - A_{m,y}(t_{n-1}) + \delta t^2\frac{\partial E^i_{m,y}(t)}{\partial t} \quad (13)$$

b/ On $\hat{z}$

$$A_{m,y}(t_{n+1}) = \frac{\delta t^2}{\mu\varepsilon}\left[\frac{\partial^2 A_{m,y}(t)}{\partial y\partial z}+\frac{\partial^2 A_{m,z}(t)}{\partial z\partial z}\right] + 2A_{m,y}(t) - A_{m,y}(t_{n-1}) + \delta t^2\frac{\partial E^i_{m,y}}{\partial t}(t) \quad (14)$$

For the mixed derivative we uee :

$$\frac{\partial^2 A_{m,\ell}}{\partial y\partial z}(y_j,z_k,t) = \frac{1}{4\Delta y\Delta z}\left[A_{m,\ell}(y_{j+1},z_{k+1},t) - A_{m,\ell}(y_{j-1},z_{k+1},t) + A_{m,\ell}(y_{j-1},z_{k-1},t) - A_{m,\ell}(y_{j+1},z_{k-1},t)\right] \quad (15)$$

The equations (13) and (14) allows us to compute the current at the center of each patch. The equation is explicit for each component of the current density due to the fact that the time derivative on $\bar{A}$ makes appear $\bar{A}u(t+1)$ and consequently $\bar{J}u(t+1)$, all other terms being evaluated at t.

Special treatment on edges of planes

The ending conditions we use are Meixner conditions at the vicinity of an edge which states that the two current density components perpendicular and parallel to the edge behave as the square root of the distance from the observation point to the edge or the inverse depending on the case.

To take into account these special conditions, we set discretization points on the edge. Doing this, we calculate an equivalent current and the potential vector on these patches. It has been shown [2] that these integrals can be evaluated in spite of their apparent singularity for the parallel component case.

Several cases have to be considered :

- the edges of the wings,
- the intersection between the horizontal and vertical stabilizers.

At each case corresponds a particular solution.

Convergence and stability of the plane surface algorithm.

Convergence conditions require that the distance between discretisation points be a fraction of the rise time of the signal. On the wings which are 40 meters long and about 160 m2 of surface we use patches of 0.8 m2 each.

Source current

We want to impose the current at one entry point and at one exit point on the aircraft. To do this, we add to the structure two short wire antennas (two dipoles). The current at the entry point (middle of the dipole) is :

$$I(t) = 10^4 \left(e^{-\alpha_1 t} - e^{-\alpha_2 t} \right) \qquad (16)$$

with : $\alpha_1 = 1.10^8 s^{-1}$ and : $\alpha_2 = 9.52.10^8 s^{-1}$

The current at the exit point is the same than that of entry point with a delay which corresponds to the propagation of the current along the structure.

In the computer simulations the current enters the aircraft at the nose and leaves at the aft.

The current at the entry point creates a field whose value is :

$$\bar{H}(M,t) = \frac{1}{4\pi} \int_c \left(\frac{1}{R^2} + \frac{1}{Rc} \frac{\partial}{\partial \tau} \right) \bar{I}(l,\tau) \times \hat{R} \, dl' \qquad (17)$$

which depends on the current and not of the dipole radius.

The solution is explicit, the current density at one point on the aircraft being calculated from those obtained at all other points at retarded times. This is a major difference with a frequency domain method which is necessarily implicit.

4 - RESULTS

A computer program was obtained which solves the preceding equations. Simulations conducted with this program show that the current density at any point on the aircraft have the same time dependance than the source current. The value obtained at one particular point depends on the location of this point on the aircraft.

Shown on figure 1 is the value of the current density near the nose of the aircraft and about 6 m from the nose. High values of the current density are obtained near the attachment point.

This method gives precise values of the current density at the beginning of the phenomena. In return it costs a lot of computer time to obtain the far time response for which a frequency method is best suited.

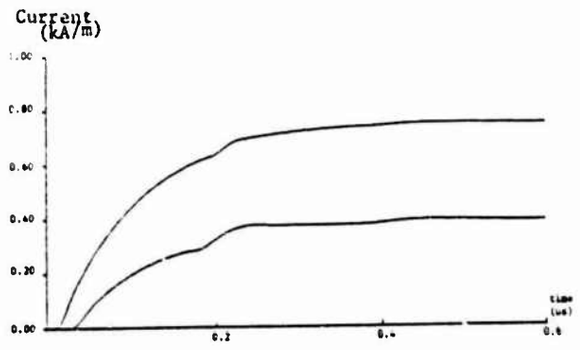


Figure 1 . Time domain surface current densities induced on an aircraft (10 kA injected current).

5 - SUMMARY

The computer simulations executed with our code show that the current density at any point on the aircraft have the same time dependance than the source current. The aircraft's resonant frequencies are far too high to be excited so that no oscillations appear in the response. The level of the current at one point depends on its location on the aircraft.

We comment this result saying that this problem is a quasi-static problem and the results may be obtained using such a less complicated method. However it was necessary to use an electrocinetic method as ours to justify this result.

One other question we can ask and one other developpement which could be conducted in the future concerns the problem of the reaction of the aircraft on the lightning channel and the modifications resulting on this channel. Studies on this subject require to have access to precise data and have to be pursued under collaboration with experimentators. From a theoritical point of view, our code permits to take into account the field diffracted by the aircraft on antennas which can model the lightning channel. This effect has been ignored in the present study. Moreover no comments have been made on the non linearity of the source current. In such a method it is not a problem to introduce it.

References:

[1] E. Grorud and M. Soiron
Induced surface current and field on a conducting body by a lightning strike. Frequency domain. See this conference.

[2] C.L. Bennet et H.Mieras
Time domain scattering from open thin conducting surfaces.
R.S. Vol 16, N6, Nov-Dec. 1981

A STUDY OF THE PHYSICAL MECHANISMS AND THE PERTURBATIONS CREATED BY THE ATTACHMENT OF AN ARC TO A CONDUCTING CYLINDER

P. Levesque, J. Taillet, G. Labaune, S. Larigaldie and J.C. Alliot

Office National d'Etudes et de Recherches Aérospatiales, B.P. 72, 92322 Châtillon Cedex, France

Abstract - The typical phenomena related to voltage shock excitation of a suspended cylinder are analyzed in comparison with previous interpretations. The respective role, on the external electric field and on the internal voltage transients, of capacitive currents, streamers, leaders and arc transitions are emphasized.
The rationale for voltage shock excitation aircraft testing is deduced from the conclusion of the study. Use of a medium-voltage fast rise-time Marx generator (300 kV, 50 ns) rather than a high voltage slow rise-time one (1.4 MV, 1 µs) is recommended.

I - INTRODUCTION

Indirect effects of lightning are characterized by fast transients internal to the structure and affecting the electronic circuits. The coupling of these circuits with the external source of electro-magnetic radiation proceeds by the following ways:

a) aperture coupling of the external magnetic field associated with the aircraft skin currents (diffusion coupling through the metallic skin is negligible at high frequency); this has been for a long time recognized as an important source of interference and standard methods are currently applied for predicting and simulating the internal disturbances associated with this mode of coupling;

b) aperture injection of displacement currents generated by the changes of the quasi-static electric field normal to the aircraft skin; these changes occur when a lightning leader approaches the aircraft, and when the associated streamers reach its skin, or when streamers emerging from the structure connect to the lightning streamers. This is the situation that voltage shock excitation is intended to simulate. This type of coupling has been recognized more recently as a possible threat, and the related phenomenology as well as the rationale for testing are still open to discussion;

c) injection of extra currents associated with breakdown phenomena at the apertures; this is typically a non linear effect and its evaluation requires a full scale test; this case is not considered in this paper.

The aim of the present study is to analyze, in relation with the choice of the selected parameters, the relevance of the laboratory simulation of voltage shock excitation. As the final objective is to protect the internal circuits against indirect effects of lightning, any external excitation not related to an internal disturbance will be discarded as irrelevant.
This type of simulation is performed with a high-voltage Marx generator of a given polarity, voltage and rise time; the fuselage is approximated by a cylinder having a given capacitance to ground; this cylinder is excited by the generator through a first spark gap (upper gap); a second spark gap (lower gap) is located between cylinder and ground. The following questions will be examined: choice of the polarity; choice of the gap length; role of the cylinder dimensions and of its capacitance to ground; best compromise between voltage and rise-time.
Although the majority of the cloud-to-ground strokes is of the negative polarity, if we assume that the interior problem is essentially linear, the sign of the excitation is irrelevant; the same is true if non linear phenomena are produced by the currents circulating at the junction of metallic skin and composite panels: if these currents are driven by voltage shock excitation, the response is generally a slightly damped oscillation of the same type for both polarities. Note that a positive excitation has the advantage of making easier the simulation of an incoming leader if a point is used at the generator side of the upper gap, and of a departing leader if a point is used at the cylinder side of the lower gap. According to K.Feser [1], if the gap is more that 5 cm long, and if the rise time of the generator is short enough (<50 ns) , high current streamers (I > 100 A) are first generated; a leader is produced after this first phase and before the arc transition. This phenomenology resembles the most the phenomenology expected from the real lightning. This is why, in the work described here, gap lengths between 5 and 35 cm, a positive polarity, and a fast rise-time (<50 ns) 300 kV Marx generator have been used. Particular attention is devoted to the characterization of the physical mechanisms related to the behaviour of the system, and a comparison is made with an earlier experiment.

II - THE CLIFFORD-ZEISEL EXPERIMENT AND ITS INTERPRETATION

A pioneering work in high-voltage shock excitation was published in 1979 by Clifford and Zeisel [2] . In this experiment, the gap length varies from 2.5 to 63 cm. The cylinder to ground capacitance is 140 pF. The Marx generator voltage is 1.4 MV but a reduced voltage of 600 kV is typically used; the corresponding rise time is 400 ns. The recordings of the external electric field E, as measured by a sensor placed in a stand in front of the cylinder, of the current and of an internal voltage disturbance, are shown in Fig. 1.
The different steps of the discharge process are

explained as follows by Clifford and Zeisel:

a) a pulse of typically 600 kV is delivered at time T1 by the Marx generator; the cylinder acquires a voltage due to charging by displacement currents the electrode-to-cylinder (C1) and the cylinder-to-ground (C2) capacitances; the related event is designated as the E-dot event;

b) from time T1 to time T2, streamers emerging from the high-voltage electrode approach the cylinder, increasing steadily its electric charge and the field E; this is equivalent to say that the capacitance C1 between streamers connected to the high voltage and the cylinder decreases steadily as the effective gap length decreases;

c) at time T2, the streamers connect to the cylinder, producing a sudden increase of E; the corresponding event is designated as the V-dot event;

d) from time T2 to time T3, as a consequence of the increase of voltage, streamers are produced at the other gap; the capacitance C2 of this gap increases and E decreases slightly;

e) at time T3, the streamers reach the ground and the arc transition occurs, analog to the lightning return stroke; the electric field E vanishes as the generator is short-circuited by a very low impedance; a large current flows through the loop formed by the generator, the upper gap, the cylinder, the lower gap, and the ground return path; the related resonant frequency is observed in the current waveshape.

It is important to point out that the internal disturbance only appears at times T1, T2, and T3 and not during the intermediate phases.

This interpretation can be questioned for the following reasons:

a) the field value measured at T1 is about one third the value obtained at the attachment of the streamer, which corresponds to a direct connexion with the generator; this is not consistent with the value of C1 and C2;

b) the streamers produced in the upper gap travels during 8 μs an unspecified distance having an upper bound of 62 cm; the corresponding velocity is therefore smaller than 8.10^4 ms^{-1}, an excedingly low value for a streamer velocity.

III - EXPERIMENTAL SET-UP .

Fig. 2 shows the experimental arrangement. The aircraft fuselage is simulated by a AG3 cylinder 2.6 m long and 26 cm in diameter, suapended at about 3 m from ground. A aquare aperture 20 x 20 cm is cut in its side wall. Two gaps having a length variable between 5 and 35 cm are located between the high voltage terminal and one end of the cylinder, and the ground and the other end. The capacitance C1 between cylinder is about 2 pF. The positive aide of each gap is fitted with a point. A 530 Ω resistor ia inserted between generator and high-voltage point in order to limit the current during the arc phase.

The following diagnoatics have been implemented:

a) a high voltage divider bridge, for the measurement of the generator output voltage;

b) a Pearaon probe around the generator gound connexion, for the measurement for the current (type 110 A, bandwidth 1 Hz - 30 MHz);

c) an E field sensor, located on the external skin of the cylinder, in front of the ground (bandwidth 50 Hz - 130 MHz);

d) a voltage amplifier connected to an internal wire line (bandwidth 500 Hz - 130 MHz);

e) an Imacon image converter, used to visualize (single shot or streak mode) the discharges obtained in the two gaps.

Note that the E field is proportional to the voltage applied to the cylinder only if the geometry is unchanged: this is not the case when different configurations are compared or when a discharge develops in the cylinder environment.

All the signals are transmitted by opto-electronic links (Electro Optic Development FOL 100, bandwidth 1.5 MHz - 100 MHz and ONERA, bandwidth 1 kHz - 150 MHz) and digitalized by fast analysers (Tektronix 7612); the data are then reduced and stored with a Tektronix 4052 mini-computer.

The shock excitations have been applied with three values of the positive voltage: 168, 240 and 300 kV;

IV - EXPERIMENTAL RESULTS: BEHAVIOUR OF THE DISCHARGE THROUGH A GAP .

When the excitation is applied, it is expected that the ratio of the cylinder voltage to the excitation voltage reaches in a very short time a value determined by the ratio C1/(C1+C2) or approximately 0.05. Actually, the measured value is close to 0.3; it has been verified that at low excitation voltage, i.e. without discharge formation, this ratio is 0.05 as expected: this means that at the operating voltage the discharge is formed and is in contact with the cylinder at very early times. This suggests that the so-called E-dot event of Clifford and Zeisel is more properly a V-dot event, the E field change being obtained by conduction charging and not by a capacitive current. To verify this hypothesis, it was decided to study the discharge generated in the upper gap when the cylinder is grounded.

A typical streak camera recording correlated with a current recording is shown in Fig. 3. The gap length is 15 cm and the applied voltage V is 168 kV.

A first current peak is observed at the application of the voltage, and, at the same time, a brush discharge constituted by a great number of streamers is seen across the gap; at the time scale of the recording (about 1 μs full scale) it is difficult to evaluate preciaely the delay after the applicstion of the voltage which is necessary for the streamers to bridge the gap; their speed is of the order of 3.10^6 ms^{-1} ; the firat peak of current is approximately 120 A; dV/dt is about 5.10^{12} Vs^{-1} ; with a gap capacitance of 2 pF, the displacement current CdV/dt cannot account for this peak which is consequently due to conduction by the streamers ; a resonance is observed in the current, which average value, always positive, decreases first for 300 ns; during this time a conduction current flows through the gap along the streamers; at 300 ns, a leader, characterized by its luminous tip, leaves the high-voltage electrode with a velocity of 4.10^5 ms^{-1}; in the same time, the average current increases slightly. When the leader reaches the cylinder, the arc transition is triggered, characterized by an intense luminosity and by a steep increase of the current to the value of 300 A determined by V/R.

By varying the gap length and the applied voltage, the limits of the regime described above can be measured; the streamers appear when the field is sufficient to provoke the breakdown; their velocity varies between 10^6 and 10^7 ms^{-1} , and the total current carried is of the order of few hundred Amperes (this is probably due to the short rise-time; with long rise-time generators, the current is

generally weaker). The average vslue of this current has been plotted in Fig. 4 as a function of the electric field across the gap and of the applied voltage.
The leader, which has a velocity between 10^4 and 10^6 ms^{-1} appears only for intermediate values of the field: if the field is higher than a critical value, the arc transition occurs rapidly without leader propagation; it can also be observed that for the lower values of the field, the arc appears only a certain time after the leader has reach the cylinder: in this case, the conductivity of the leader is to low for triggering the transition. In accordance with an observation by Sigmund and Goldman [3], it has been verified that, for a given generator voltage, the arc transition occurs when a given energy density per unit length has been deposited in the gap; the measured values of this density is 0.2 J cm^{-1} for a voltage of 168 kV and 0.6 J cm^{-1} for 300 kV.

V - EXPERIMENTAL RESULTS: CASE OF THE FLOATING CYLINDER .

In a typical experiment, the upper gap is 15 cm long and the lower gap 7 cm long.
Fig. 5 shows the evolution of the electric field at the wall of the cylinder, which permits to appreciate the cylinder voltage, and of the ground return current (lower gap current); the upper gap current is not measured and can only be estimated from the other parameters. The streak camera recordings associated with these curves show the upper and lower gap discharges.

The succession of the different events can be described as follows:

1 - Time T1: when the Marx generator is triggered, the streamer phase appears in the upper gap; the corresponding current charges up the cylinder; it has been verified that, during this phase, the relation mentioned above between the streamer current and the field applied to the gap is still valid. The cylinder acquires a voltage superior to the value corresponding to the case where the two gaps have the same resistance per unit length: this is due to the fact that the voltage increases during the delay necessary for the streamers to bridge the lower gap.

2 - Time T1 to time T2: the corresponding phase is a slow decrease of the cylinder voltage; this is due to the fact that the current in the lower gap is greater than the current of the upper gap; the difference is only about 10 A. This difference could be due to the larger overvoltage obtained in the lower gap as a consequence of the delay mentioned above; a leader can be observed in this gap, and if its resistance per unit length is smaller than that of the streamer, the gap conductivity increases during its propagation. This is not observed for the lower values of the field since in this case the leader conductivity is low, and the arc transition does not appear when the leader bridges the gap (Fig. 6).

3 - Time T2: the lower gap experiences the arc transition, and the cylinder voltage vanishes; the transition being associated with a given energy density per unit length, and the corresponding value being larger for the lower gap, it is not surprising to obtain the transition first in this gap.

4 - Time T2 to time T3: as soon as this transition occurs, the energy deposited in the upper gap increases and a process similar to the one described above appears also in this gap.

5 - Time T3: the arc transition is obtained in the upper gap and the generator delivers the full arc current to the circuit.

An experiment performed with an upper gap length of only 7 cm and a lower gap length of 15 cm displays the same phenomenology with a larger delay T2-T1. In all cases, the streak camera recordings show clearly that at time T1 the jump in voltage is due to the streamers and not to a capacitive current.

A surprising result is the observation that the lower gap is activated, in our experiment, before the upper gap, contrary to the case of the Clifford-Zeisel experiment. This is due to the fact that the cylinder to ground capacitance is only 40 pF in this experiment instead of 140 pF in the Clifford-Zeisel experiment. Adding an extra cylinder-to-ground capacitance restitute the positive slope of the field curve between T1 and T2. If the capacitance is large enough, the lower gap cannot be energized with a sufficient overvoltage to trigger a leader in this gap before the formation of the leader in the upper gap. It seems therefore that a good simulation should use a cylinder more representative of the actual dimensions and capacitance of an aircraft. This point will be discussed later.

VI - TRANSIENTS INDUCED ON THE INTERNAL LINE .

The test line is placed axially inside the cylinder; the induced transients have been measured on a 50 Ω resistor, in the short circuit case and also with a 10 kΩ termination. The cylinder wall is thick enough (1.5 mm of AG5) to eliminate any diffusion coupling for the considered frequency range: the rise time of the diffused field is 10 μs and the times of interest in this work are shorter than 1 μs [4].
The analysis of the transients obtained on the line will be performed with reference to the external problem (structure of the electromagnetic field in front of the aperture) and to the internal problem (coupling between the test line and the electric and magnetic dipoles equivalent to the electro-magnetic configuration at the aperture [5]).
Fig. 7 and 8 display the transients obtained with the floating cylinder. The following remarks can be made:

a) as in the case of the Clifford-Zeisel experiment, no transient is induced in the phases between the times T1, T2 and T3; this means that, in the exterior electro-magnetic configuration, the changes associated with the motion of the leaders are too slow to produce any E-dot effect; for this reason, the fact that in our experiment the lower gap leader is propagated before the upper gap leader is irrelevant;

b) the pattern obtained for the short-circuited line, which is sensitive only to the internal magnetic field changes, show that the electric dipole at T1 and T2 gives shock excited magnetic disturbances at the line location; the current rise at T3 gives a magnetic disturbance reproducing the current slope plus some shock excitation;

c) the pattern obtained for the high impedance line, which is essentially sensitive to capacitive pick-up, reproduce at T1 and T2 the derivative of the voltage waveform, i.e. the displacement currents injected into the interior volume by the electric dipole; the magnetic excitation at T3 gives also a small signal associated with the voltage induced in the interior between wire and wall.

d) if we analyze in Fig. 8 the magnitude of the transients, it appears that a V-dot excitation corresponding to an electric field of 180 kV m gives approximately the same amplitude that a I-dot excitation corresponding to a current step of 300 A; if the current distibution is symmetrical, the latter corresponds to 367 A m^{-1} ; interpretation of these values requires an understanding of the transfer functions from the external sources to the internal circuit. These transfer functions are plotted versus frequency in Fig. 9 (for the short-circuited line) and 11 (for the high-impedance line); the input functions are, for both cases, the electric and magnetic dipoles associated with an unit excitation (1 V m^{-1} and 1 A m^{-1}).

VII - CONCLUSION

This experiment shows that the voltage shock excitation is a possible threat for indirect effects of lightning; in particular, such effects could be important at the time of attachment of a streamer to the aircraft structure (or of the junction of an aircraft streamer with the streamers associated with the step leader);
Discussing the possibility of predicting the amplitude and spectrum of the corresponding excitation is out of the scope of the present paper, but, if this evaluation can be performed, the resulting internal transient depends only on the solution of the internal problem; if this problem is linear, it can be solved by computational methods or by measuring the small signal harmonic transfer function between excitation and internal induced voltage, but it is likely that non-linear effects are generated at the junctions between panels. The sensitivity of an internal wiring to voltage shock excitation must therefore be checked with full excitation; this can be made on a suspended aircraft with a Marx generator.
The result of this study shows that E-dot transients or leader propagation are not generating any internal disturbance and that only V-dot transients have to be simulated. On the one hand, the condition stated by Clifford and Zeisel that V-dot and I-dot temporal responses shall be separated is also met with voltages as low as 300 kV and gap lengths of 15 cm. On the other hand the excitation obtained, which is proportional to dV/dt, can be stronger with a short rise-time medium-voltage Marx generator than with a long rise-time high-voltage one: for this reason, we recommend the use the former and 15 to 30 cm long air gaps.

Clifford and Zeisel, at the end of their paper, suggest the use of charging the test vehicle like a capacitor and then letting it discharge to ground for having a large I-dot transient. In the same way, the superposition of an initial charge and of a pulse delivered by a fast rise-time medium-voltage Marx generator can, with the proper arrangement, produce a very large and very fast V-dot transient. This suggestion has still to be verified by future experiments.

VIII - AKNOWLEDGEMENTS .

This work has been largely supported by DRET (Direction des Recherches, Etudes et Techniquea of the French Defense Ministry); the authors are also grateful to Professor J. Ueberafeld, Mr R. Moreau and Dr J.L.Boulay for their help and their fruitful advices.

IX - REFERENCES

[1] - K. Feiser
"Breakdown behaviour of air spark-gaps with homogeneous field at bias voltages", Bulletin ASE 62, n° 6, p. 320-329 (1971).

[2] - D.W. Clifford and K.S. Zeisel
"Evaluation of lightning-induced transients in aircraft using high-voltage shock excitation techniques", Proceedings IEEE Int. Symp. on Electromagnetic Compatibility, San Diego, p. 160-166 (1979).

[3] - M. Goldman and R.S. Sigmond
"Positive streamers decay and transition to spark in short corona gaps in ambient air", XVth Int. Conf. on Phenomena in Ionized Gases, Minsk (1981).

[4] - J.C. Alliot and P. Levesque
"Etudes théoriques et expérimentales des mécanismes de couplage électromagnétique", 2ème Colloque sur la Compatibilité Electromagnétique, Trégastel (1983).

[5] - H.A. Bethe
"Theory of diffraction by small holes", Phys. Rev., 2nd series, vol. 66, 7-8, p. 163-182 (1944).

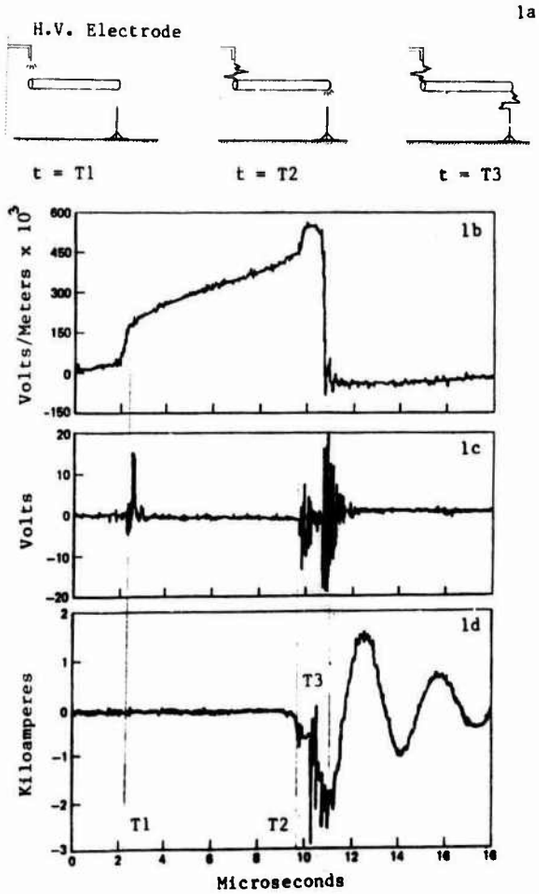
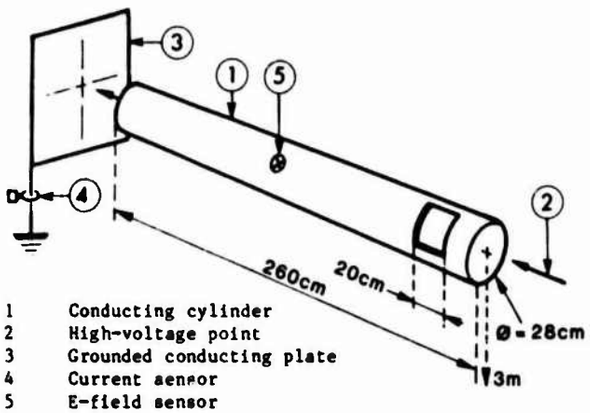


Figure 1. The Clifford-Zeiael experiment: time history of the transient events (from ref.2).

1a Schematic representation of the various phases of the experiment
1b E-field recording
1c Induced transients
1d Current recording



1 Conducting cylinder
2 High-voltage point
3 Grounded conducting plate
4 Current sensor
5 E-field sensor

Figure 2. Experimental set-up.

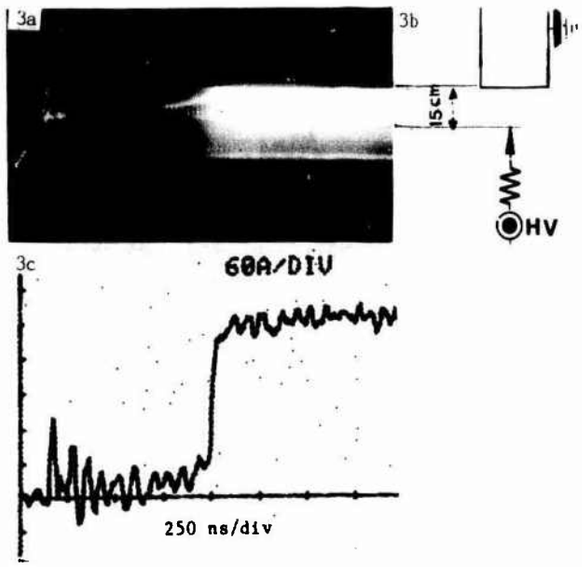


Figure 3. Brush discharge, leader and arc transition.

3a Discharge geometry
3b Streak camera recording
The streamers forming a brush discharge are visible at the left end; the arc phase is characterized by the strong illumination seen at the right side; the curved line in the middle shows the leader progression
3c Current recording
Total duration of breakdown phase from application of the voltage to arc transition is 1 µs

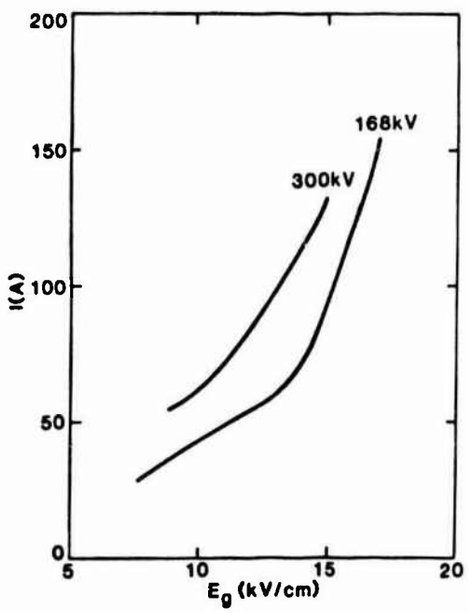


Figure 4. Variation of the streamers average current I as a function of the average longitudinal electric field in the gap Eg and the Marx generator voltage V

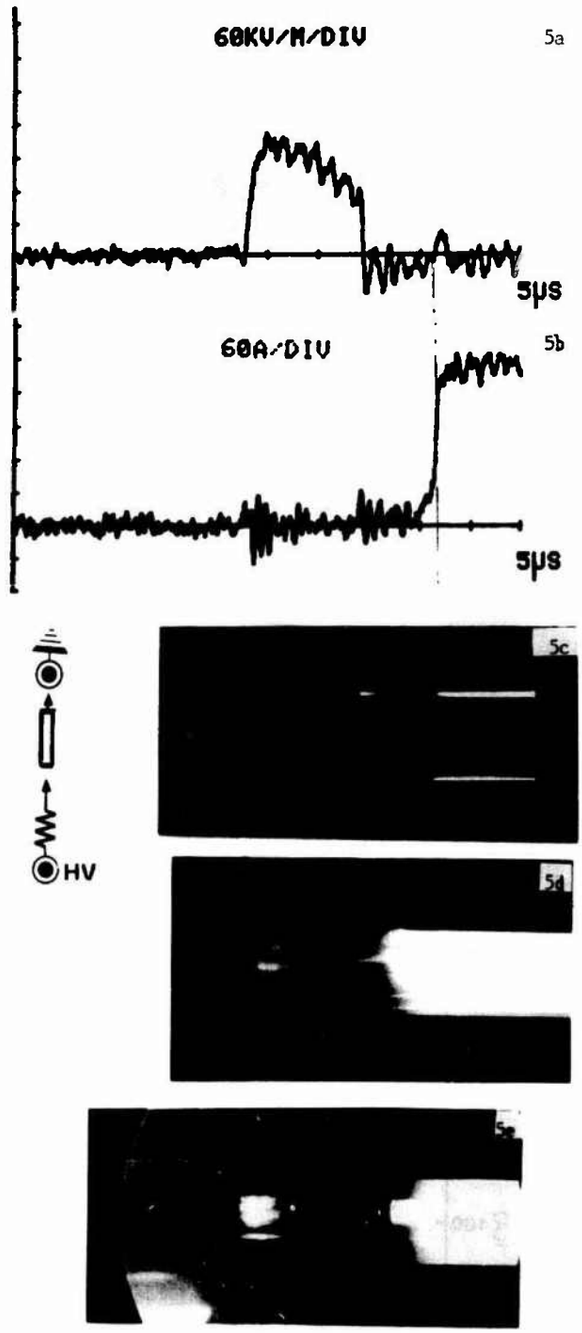


Figure 5. Time history of transient events with the floating cylinder.

5a E-field recording
5b Lower gap current
5c Streak camera recording (visible light); the two gaps have been simultaneously recorded.
5d Streak camera recording (UV and visible light) of the lower gap.
5e Streak camera recording (UV and visible light) of the upper gap.
In the streak camera recordings, note that UV light is emitted by the streamera and visible light by the leader tip and the arc phases.

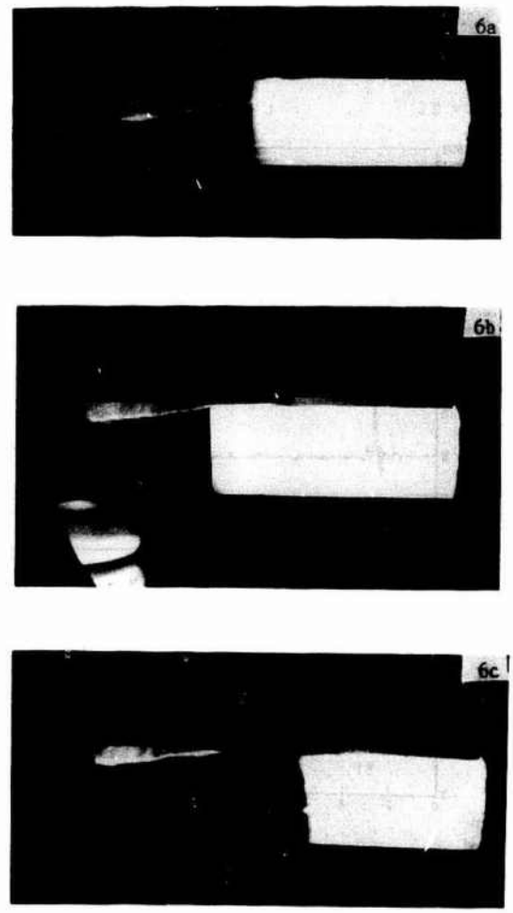
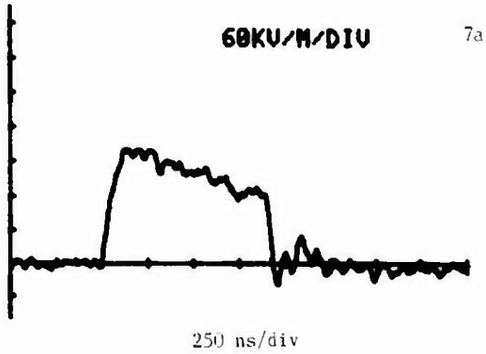
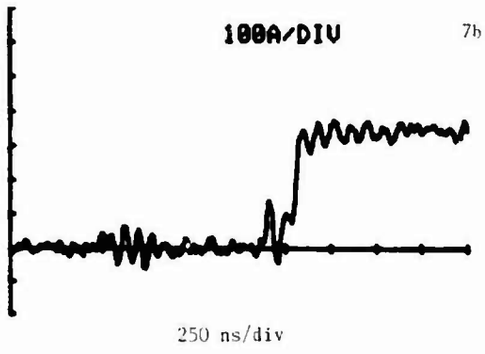


Figure 6. Streak camera recordings of arc transitions.

In the first recording (6a), the transition occurs before the junction of the leader and the electrode; in the second case (6b), the transition is triggered by the junction of the leader; in the third case (6c), the plasma suffers an extinction between leader junction and arc transition. The type of situation obtained depends on the gap overvoltage.





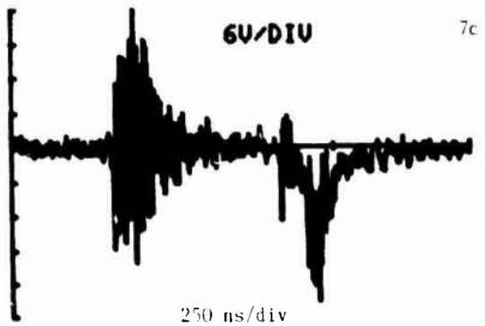
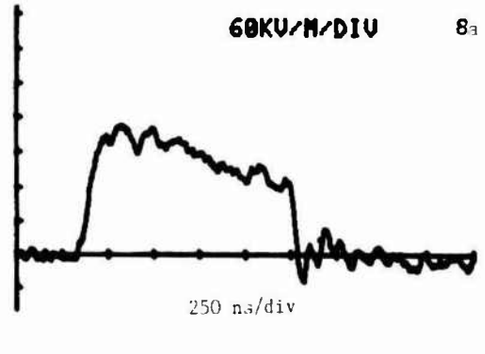


Figure 7. Disturbance obtained on an internal short-circuited line

7a External E-field signal
7b Lower gap current
7c Voltage induced across a 50 Ω resistor inserted in an axial short-circuited line.



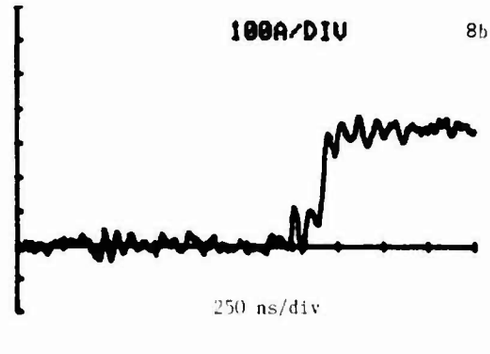
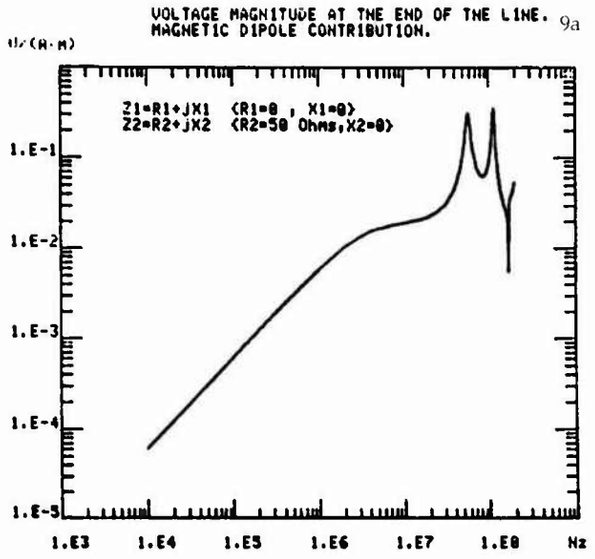
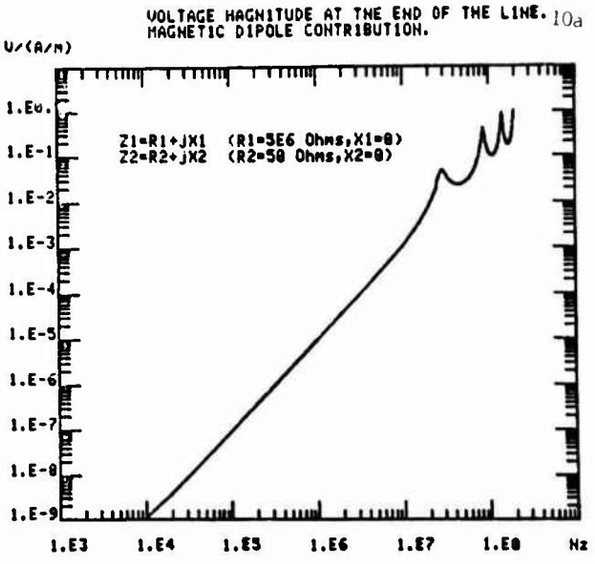


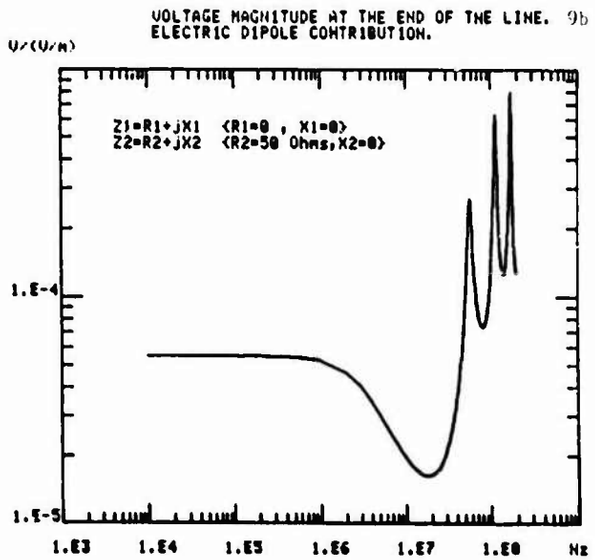


Figure 8. Disturbance obtained on an internal high-impedance line

8a External E-field signal
8b Lower gap current
8c Voltage induced across a 50 Ω resistor inserted in an axial high-impedance line.







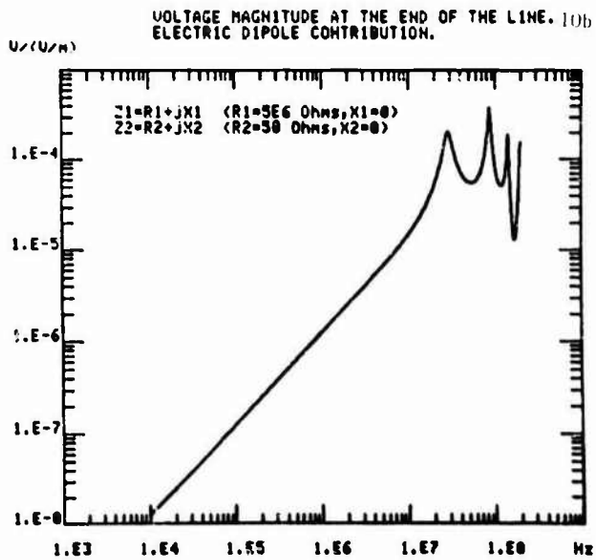


Figure 9. Transfer function relative to the interior problem in the linear regime; the output is the voltage induced across a 50 Ω resistor inserted in an axial short-circuited line.

9a Magnetic dipole contribution
9b Electric dipole contribution

Figure 10. Transfer function relative to the interior problem in the linear regime; the output is the voltage induced across a 50Ω resistor inserted in an axial line having a 10 kΩ termination.

10a Magnetic dipole contribution
10b Electric dipole contribution.

THE EFFECTS OF FINITE LINEAR CHARACTERISTICS INHERENT IN THE PHYSICALLY REALIZABLE DEVICES ASSOCIATED WITH CABLE INJECTION TESTS

R. Hess

Principal Engineer, Sperry Corporation, Aerospace & Marine Group, Phoenix, Arizona 85027, U.S.A.

ABSTRACT

When an aerospace vehicle/lightning interection occurs, electrical power trensients cen be produced throughout the wiring within the vehicle. The transients cen be substentiel, and thorough design end verificetion measures must be teken to ensure the immunity of vehicle electricel/electronic equipment to such transients. This paper presents the results of an anelysis that considered the effects of varying only the lineer properties of the transfer functions (break frequencies) of the devices used es pert of the errangements for cable injection tests. The distinct possibility of e significant effect on the results of tests that involved applying the double exponential or demped sinusoid pulse weveform is demonstreted by varying specific characteristics of such trensfer functions.

I – INTRODUCTION

When an aerospace vehicle/lightning interaction occurs, electrical power transients can be produced throughout the wiring within the vehicle. These transients can be substantial, and thorough design and verification measures must be taken to ensure the immunity of vehicle electrical/electronic equipment to such transients, (Ref. 1, 2, 3). This is particularly the case because the technological trends relative to aerospace vehicle design are toward increasing vulnerability to the effects of lightning (Ref. 4). One such trend, which is currently the subject of intensive investigation/evaluation (Ref. 5, 6, 7, 8, 9), is the increasing reliance on digital data processing to provide functions that are considered "flight critical."

II – DISCUSSION

Design and verification measures include analysis and test activity. For electrical/electronic equipment, analyses may be performed and testing may be conducted at the system, subsystem, equipment, circuit or device level. The waveforms of the transients induced in vehicle wiring by lightning are relatively complex and, for tests involving the injection of transients into cable wiring (laboratory tests), this complex waveform would be decomposed into representative components (Ref. 10). A waveform component would be developed using a particular test arrangement, and care must be exercised to preserve the fidelity of the particular waveform that appears at the equipment interface under test.

All devices that are physically realizable have finite limitations. This paper reviews only linear (transfer function) aspects that result from the arrangement of test apparatus. By arrangement, I mean the pulse generator or source of the transient, the coupling device that transfers energy from the generator to the cable through the medium of electric or magnetic fields, and any other elements that contribute to the overall transfer function of the test arrangement. In addition to the process producing the transient, the high-fidelity measurement of the transient that actually occurs is also an essential element in conducting cable injection tests.

Even though the following concepts are illustrated by considering magnetic field devices for coupling the cable injection and for injected waveform monitoring, they are general in nature and apply to any coupling technique. The first identified issue is the preservation of pulse fidelity through the magnetic coupling portion of the test arrangement. In practice, the element that has the largest impact on the cable injection transfer function is the injection transformer. The second issue that has been identified is the high-fidelity measurement of the transient. In practice, the monitoring probe (if it is a magnetic field device) will have the largest impact on the measurement transfer function. The overall transfer function would include the transfer functions of all elements in the test arrangement (Fig. 1), from the pulse generator to the measurement instrumentation (e.g. oscilloscope, digitizing equipment). Ideally, the injection transformer would have a transfer function that is independent of frequency; in other words, a straight line over the entire frequency spectrum (Fig. 2).

If the hysteresis of magnetic materials is ignored, in realizable injection transformers the linear electromagnetic characteristics of the transformer, such as inductance, capacitance, resistance which are a function of material electromagnetic properties and the geometries of material arrangements, will result in a transfer function through the device that is not ideal and which exhibits at least two break points (Fig. 3).

For the injection transformer, Φ_i is proportional to i_i and v_o is equal to $d\Phi_o/dt$ (if output feeds into an open circuit). Thus, Φ_o will be proportional to $\int v_o dt$. Consequently, in terms of Φ_o/Φ_i, the general shape of the frequency domain plot will be flat at lower frequencies and exhibit at least two breaks as frequency increases (Fig. 4).

For cable injection tests, two types of broadband pulses are identified in the AE4L committee report - AE4L-81-2: 1) double exponential, and 2) damped sinusoid, as illustrated in Fig. 5 and 6.

The frequency spectrum for the double exponential pulse is flat at lower frequencies and exhibits two breaks as frequency increases. The frequency spectrum for the damped sinusoid pulse is flat at lower frequencies, exhibits a peak at the fundamental frequency (f_{RS}--resonant frequency of a relatively high Q circuit), and has a slope of -40 dB as frequencies increase beyond f_{RS}.

The frequency spectrum of the transient that appears at the output of the magnetic coupling portion of the test arrangement transfer function and at the input to the equipment interface under test is obtained by multiplying the value of the transfer function times the value of the input spectrum at each frequency line over the range of significant frequencies. The corresponding time domain response is obtained by a numeric Fourier inversion (classical Fourier transform method).

An alternate method, and the one used to obtain the results reported in this paper and shown in the various figures containing time domain plots, converts the frequency domain transfer function into its corresponding time domain differential equation. Using the SCEPTRE computer program, the differential equation is then evaluated for both a double exponential input and a damped sinusoid input.

The magnetic field pulse ϕ_i--double exponential or damped sinusoid--is developed in the input of the injection transformer by the current flowing in its primary windings due to the energy stored in a capacitor being discharged through a path that includes the primary windings. The double exponential and the damped sinusoid waveform of the current developed in the primary windings are the natural result when the discharge circuit consists of a simple series connection of capacitive, inductive, and resistive elements. The particular waveform, and thus the corresponding frequency spectrum that develops, is determined by the values of those elements. The fidelity of the magnetic field pulse developed in the output of the injection transformer can be assessed as a function of where break frequencies in the transformer transfer function are in relation to the break frequencies in the frequency spectrum of the input pulse. The effect of the injection transformer break frequencies is illustrated from the perspective of open-circuit output voltage in Fig. 8 through 17 (where the computer plot v_o is labeled as VOUT and i_i is labeled as I).

It is evident from Fig. 8 through 10 that the relationship

$$|v_o| = |d\phi_o/dt| = M|di_i/dt| = (M/L_i)|d\phi_i/dt| \text{(time domain representation)}$$

achieved with an ideal injection transformer is closely approximated in the physically realizable device (in regards to general waveshape) when f_L/f_r or f_L/f_{RS} is 10 or greater. That is, when the lower break frequency of the transfer function (f_L) is greater than the upper break frequency of the input spectrum (f_r or f_{RS}) by a factor of 10 or more, the waveform of the injection transformer's open-circuit output voltage closely approximates the "classical" first derivative response to the magnetic field produced by lightning. The implication for injection transformers is that they will have to be relatively high frequency devices:

- f_L should be 100 MHz or greater for the 10 MHz damped sinusoid pulse
- f_L should be 20 MHz or greater for the double exponential pulse.

From the classical first derivative response perspective, as f_L/f_r decreases below 10, waveform deterioration (distortion) is evident in Fig. 11 through 17 (the amplitudes of the output waveforms are a result of normalizing the input waveform's peak amplitude and the transfer functions' "ideal" midband gain to unity).

Basically, both the injection transformer and the monitoring probe for current are the same type of magnetic field device, commonly referred to as a current probe. Traditionally, the characteristics (transfer function) of a current probe are provided in the form of the frequency domain plot of Fig. 3. However, the probe for monitoring current needs to provide a significantly different function than that provided by the injection transformer. As a result, the relationship desired between the transfer function break frequencies and the break frequencies of the waveform spectrum being applied to the monitoring probe input will be different from those determined for the injection transformer.

Specifically, the monitoring probe monitors the waveform of the current actually injected into the cable. The ideal monitoring probe would have a transfer function that is independent of frequency. Also, v_o would be proportional to ϕ_o rather than the $d\phi_o/dt$ relationship required for the injection transformer (Fig. 7).

The responses illustrated in Fig. 14 and 15 show that the v_o waveform induced by i_i (the current flowing through the monitoring probe input) will be a reasonably good reproduction of the i_i waveform when $f_L/f_d<.01$ and $f_H/f_r>10$ (double exponential) or $f_L/f_{RS}<.1$ and $f_L/f_{RS}>10$ (damped sinusoid). That is, when the lower break frequency of the transfer function (f_L) is less than the lower break frequency of the input spectrum (f_d or f_{RS}) by a factor of 10 or more, and the upper break frequency of the transfer function (f_H) is greater than the upper break frequency of the input spectrum (f_r or f_{RS}) by a factor of 10 or more, the waveform of the monitoring probe's output voltage closely approximates the monitoring probe's input current. The implications for the monitoring probe are:

- The flat portion of the transfer function (the portion between f_L and f_H) will probably have to extend over a frequency range of 10^4 or greater.
- The lower break frequency will be in the less than 500 Hz range.

As shown in Fig. 16 and 17, a lag distortion departure from the i_i waveform is evident in the v_o waveform when $f_H/f_r<1$ or $f_H/f_{RS}<1$. As previously observed, when considering injection transformer characteristics, a derivative distortion departure from the i_i waveform (from a current monitoring perspective) is evident in the v_o waveform when $f_L/f_r>1$ or $f_L/f_{RS}>10$. If only the preservation of the general shape of the damped sinusoid waveform is

desired, any of the transfer function responses would be acceptable since the reproduction of the general features (fundamental frequency, exponential decay) of the damped sinusoid is relatively insensitive to the effects of the current monitor's transfer function.

III – CONCLUSIONS

When physically realizable devices are used in a cable injection test arrangement, especially where classical results are expected (the test arrangement is considered electrically short), care must be taken that the influence of device characteristics on the test results will be insignificant. An analysis that considered the effects of varying only the linear properties of the transfer functions (break frequencies) of devices used as part of arrangements for cable injection tests, demonstrated the distinct possibility of a significant effect on the resulting waveforms produced and measured during a test by the specific characteristics of the transfer function when the application of the double exponential or damped sinusoid pulse waveform was involved. It was also shown that to preserve test integrity, injection devices using field-coupling isolation require the use of relatively high frequency devices. Also, waveform monitoring devices that use field-coupling isolation need to be relatively broadband devices where the associated lower break frequency occurs at a relatively low frequency.

When considering cable injection using field coupling, an additional observation relative to testing that specifically involves magnetic field injection seems appropriate. In the AE4L-81-2 report, the voltage and current amplitudes associated with the various levels defined in the document are those that occur if the equipment interface cable is opened or shorted. As such, they are general quantities that relate to a system's response to a lightning/vehicle interaction. They should not be interpreted as appropriate for individual inputs per se. However, because of the electromagnetic mechanisms that produce cable voltages (magnetic field induction/cable resonance), the voltage level is appropriate, and represents a maximum level for specific application to individual inputs that possess relatively high impedances (greater than 1K). The proposed current level should not be interpreted as appropriate for individual inputs, except possibly in an extreme case where only one input (loop) impedance is virtually zero and all others are virtually open.

Thus, cable current amplitudes will have to be translated into wire currents, using analysis guidelines that achieve a reasonable balance between the design measures that can be taken at the equipment level (larger input impedances, larger output devices, input protection devices) and design measures that can be taken at the system/subsystem level (cable routing/shielding, shielded equipment bays, surge protection devices). To literally apply the amplitudes of current specified for the cable to each equipment input would result in excessive equipment penalties involving price, size, weight, power dissipation, functional performance, and reliability. In the case of the equipment input circuits that interface with long and/or exposed wiring, it may be necessary to specify levels higher than those that would be considered appropriate for a baseline. When this is the case, it would be cost effective if the choices for the upper levels could be from standardized levels (levels 4 and 5 in AE4L-81-2, for instance).

Design objectives should be the result of tradeoffs that optimize shielding versus equipment hardening for a particular subsystem. The proposed waveform amplitude levels can then be used to translate design objectives into equipment hardening requirements. The amplitude levels cannot be used as a substitute for the basic analysis effort necessary for the subsystem hardening decisions that result in a balanced hardening approach.

IV – REFERENCES

1. R. F. Hess. "EMP-Coupling Analysis Using the Frequency (Transfer Function) Method with SCEPTRE Computer Program," IEEE Trans. Electromagnetic Compatibility (August 1975).

2. R. F. Hess. "Properties of Induced Transients Associated with EM Fields Produced by Lightning or Other Relatively Slow Rise-Time EMP," IEEE International Symposium on EMC, Atlanta, Georgia (June 1978).

3. J. C. Corbin. "Aircraft Electromagnetic Threat Protection," IEEE International Symposium on EMC, San Antonio, Texas (April 1984).

4. D. T. Auckland, R. F. Wallenberg, and J. A. Birken. "The Effects of New Technology Trends on Aircraft Lightning Vulnerability and the Capability to Identify Technology Deficiencies," International Aerospace and Ground Conference on Lightning and Static Electricity, Fort Worth, Texas (June 1983).

5. R. F. Hess. "Implications Associated with the Operation of Digital Data Processing in the Presence of the Relatively Harsh EMP Environments Produced by Lightning," International Aerospace and Ground Conference on Lightning and Static Electricity, Paris (June 1985).

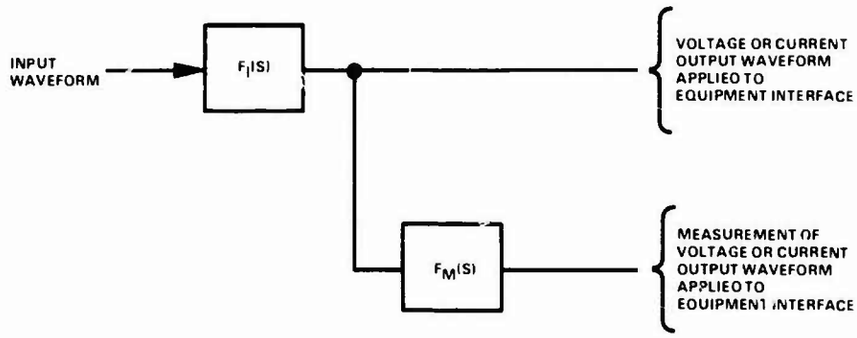
6. M. E. Schmid, R. L. Trapp, G. M. Mason, and A. E. Davidoff. "Monitors for Upset Detection in Computer Systems," International Aerospace and Ground Conference on Lightning and Static Electricity, Fort Worth, Texas (June 1983).

7. G. M. Mason. "Upset Experimentation in Computer-Based Systems," International Aerospace and Ground Conference on Lightning and Static Electricity, Fort Worth, Texas (June 1983).

8. V. A. Carreno. "Upset Susceptibility Study Employing Circuit Analysis and Digital Simulation," International Aerospace and Ground Conference on Lightning and Static Electricity, Orlando, Florida (June 1984).

9. C. M. Belcastro. "Data and Results of a Laboratory Investigation of Microprocessor Upset Caused by Simulated Lightning-Induced Analog Transients," International Aerospace Ground Conference on Lightning and Static Electricity, Orlando, Florida (June 1984).

10. "Test Waveforms and Techniques for Assessing the Effects of Lightning-Induced Transients," AE4L Committee Report AE4L-81-2, SAE (December 1981).



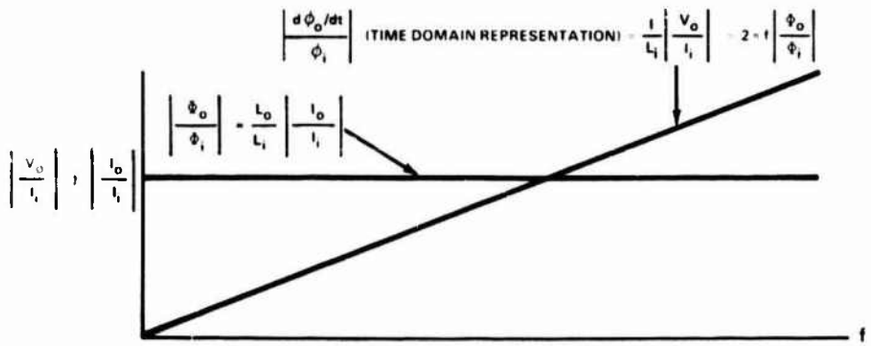
WHERE

$F_T(S)$ = OVERALL TRANSFER FUNCTION = $(F_I)(F_M)$

$F_I(S)$ = INJECTION TRANSFER FUNCTION = FREQUENCY DOMAIN RATIO OF OUTPUT VOLTAGE OR CURRENT TO INPUT CURRENT (INJECTION TRANSFORMER)

$F_M(S)$ = MEASUREMENT TRANSFER FUNCTION = FREQUENCY DOMAIN RATIO OF OUTPUT VOLTAGE TO INPUT CURRENT (CURRENT PROBE) OR OUTPUT VOLTAGE TO INPUT VOLTAGE

Fig. 1 Injection and measurement transfer functions comprising an arrangement for cable injection tests.



WHERE

Φ_i = INPUT FLUX (FREQUENCY DOMAIN)

Φ_o = OUTPUT FLUX (FREQUENCY DOMAIN)

ϕ_i = INPUT FLUX (TIME DOMAIN)

ϕ_o = OUTPUT FLUX (TIME DOMAIN)

I_i = INPUT CURRENT

I_o = OUTPUT SHORT-CIRCUIT CURRENT

V_o = OUTPUT OPEN-CIRCUIT VOLTAGE

L_i = SELF-INDUCTANCE OF INJECTION TRANSFORMER INPUT WINDING

L_o = SELF-INDUCTANCE OF INJECTION TRANSFORMER OUTPUT WINDING

NOTE:

M – IS MUTUAL INDUCTANCE BETWEEN INPUT AND OUTPUT WINDINGS OF INJECTION TRANSFORMER

Fig. 2 Frequency domain response of an injection transformer that has an ideal transfer function for $|V_o/I_i|$ and $|I_o/I_i|$.

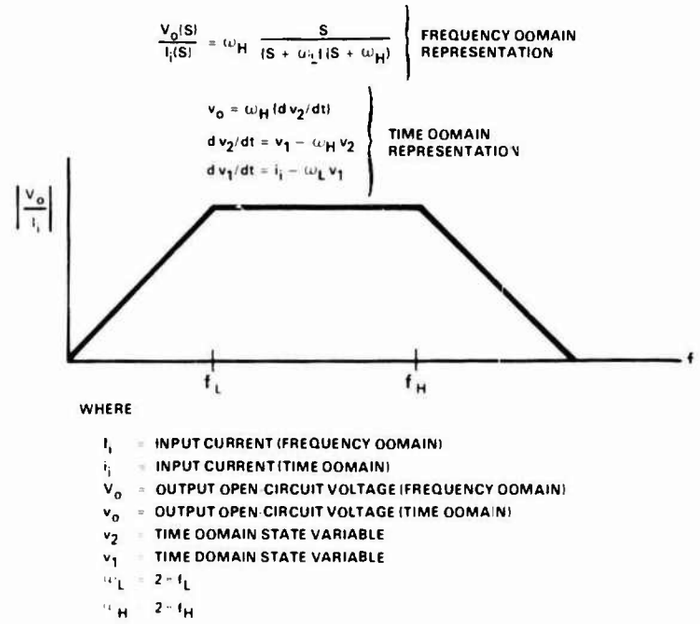


Fig. 3 Frequency domain response of a current probe (injection transformer or current monitor) in terms of V_o and I_i.

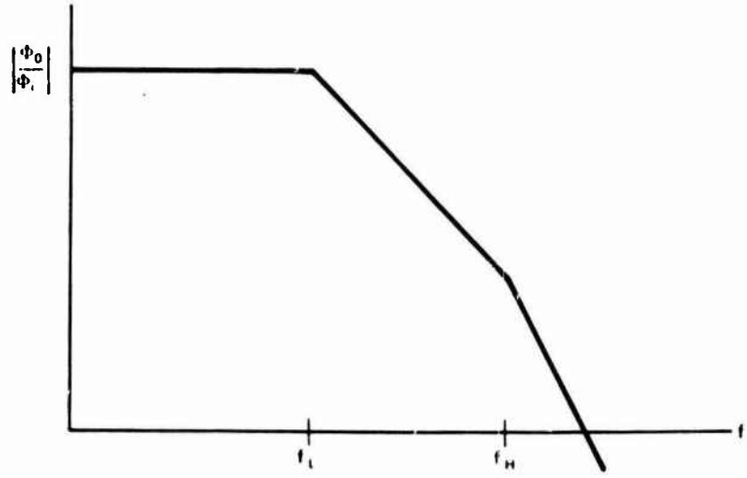


Fig. 4 Frequency domain response of a current probe in terms of Φ_o and Φ_i.

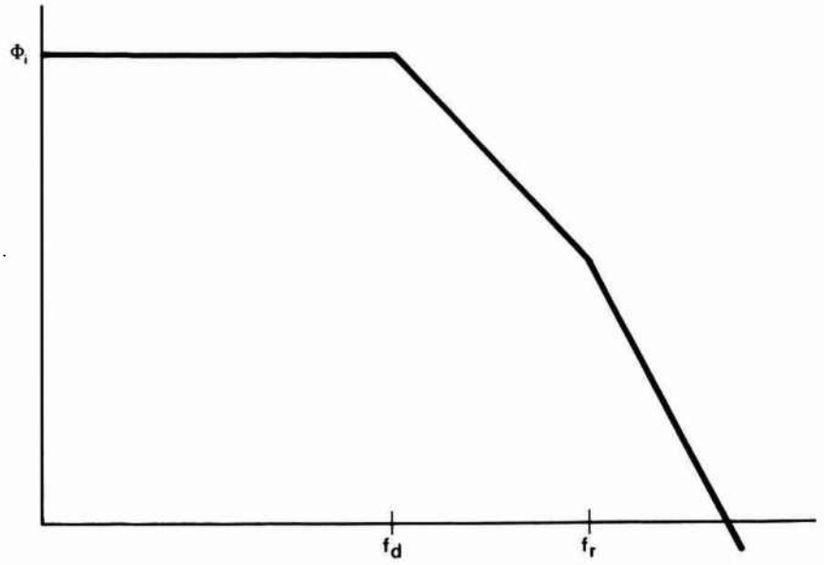


Fig. 5 Frequency spectrum of a doubie exponential pulse in terms of Φ_i.

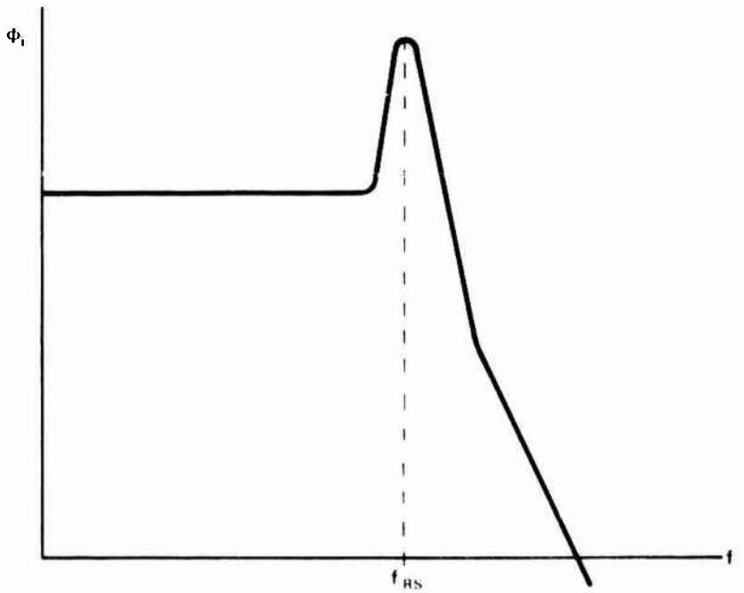


Fig. 6 Frequency spectrum of a damped cosine sinusoid pulse in terms of Φ_i.

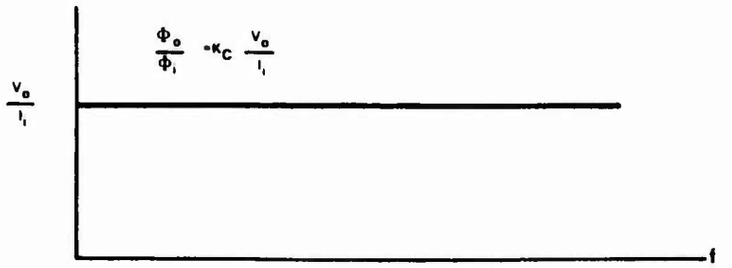


Fig. 7 Frequency domain response of a current monitor that has an ideal transfer function.

PLOT-1

UNITS-SECONDS

I ******* CHARACTER – A
VOUT ******* CHARACTER – B

I	0.000	4.000-01	8.000-01	1.200+00	1.600+00	2.000+00
VOUT	-2.000-02	2.000-02	6.000-02	1.000-01	1.400-01	1.800-01

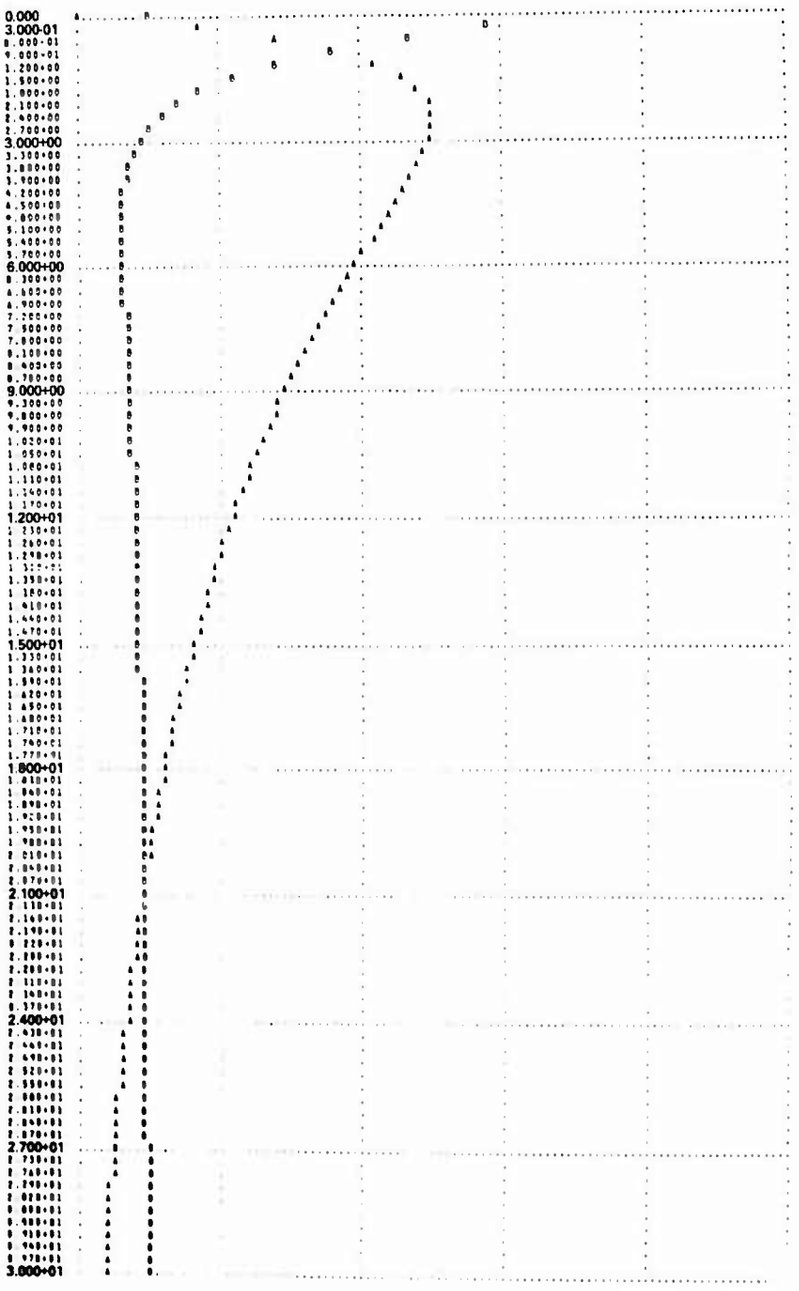


Fig. 8 Computer plot of transfer function input and output waveforms for a double exponential with f_L/f_r = 10 and f_H/f_r = 100, and damped sinusoid with f_L/f_{RS} = 100 and f_H/f_{RS} = 1000. (Sh. 1 of 2)

PLOT-1

UNITS-SECONDS

I ******* CHARACTER – A
VOUT ******* CHARACTER – B

I	-8.000-01	-4.000-01	0.000	4.000-01	8.000-01	1.200+00
VOUT	-9.000-03	-3.000-03	3.000-03	9.000-03	1.500-02	2.100-02

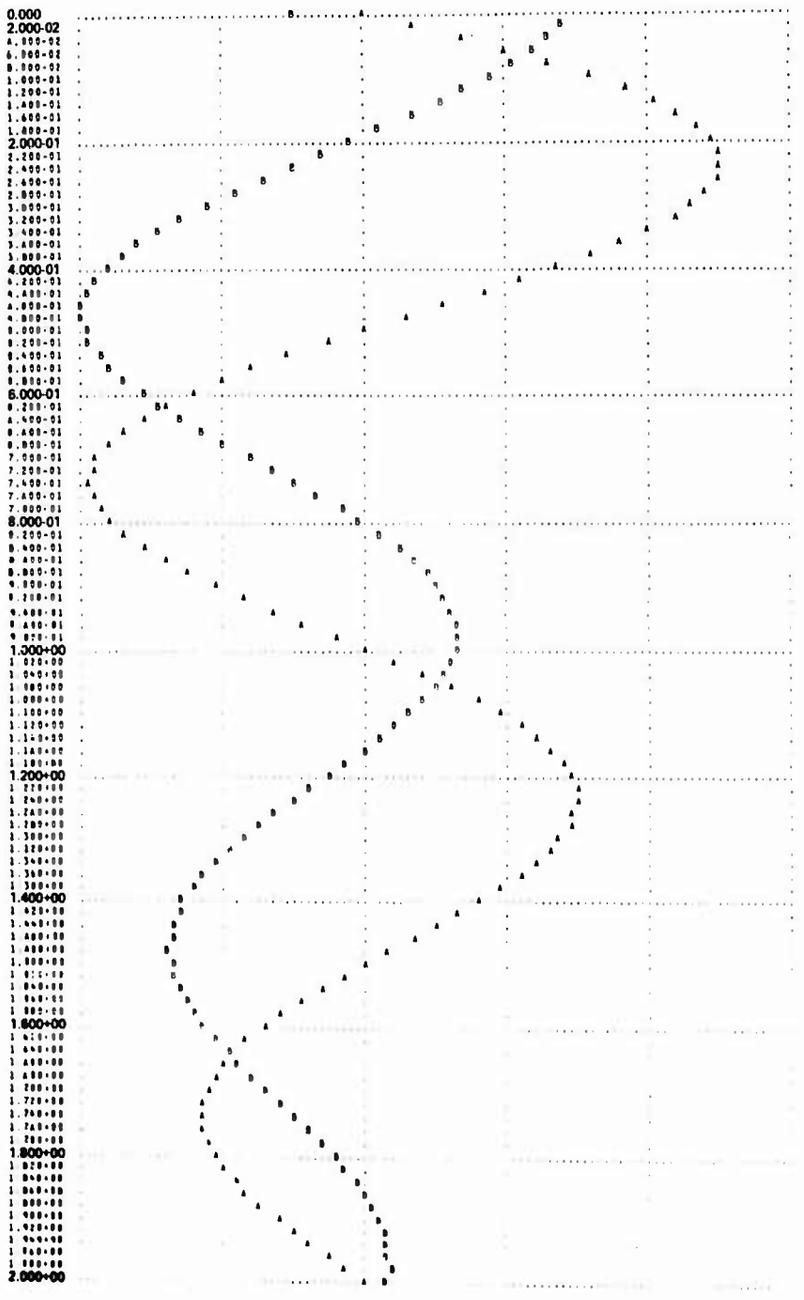


Fig. 8 Computer plot of transfer function input and output waveforms for a double exponential with f_L/f_r = 10 and f_H/f_r = 100, and a damped sinusoid with f_L/f_{RS} = 100 and f_H/f_{RS} = 1000. (Sh. 2 of 2)

PLOT – 1

UNITS-SECONDS

I ..... CHARACTER – A
VOUT ..... CHARACTER – B

I	0.000	4.000-01	8.000-01	1.200+00	1.600+00	2.000+00
VOUT	-1.000-02	1.000-02	3.000-02	5.000-02	7.000-02	9.000-02

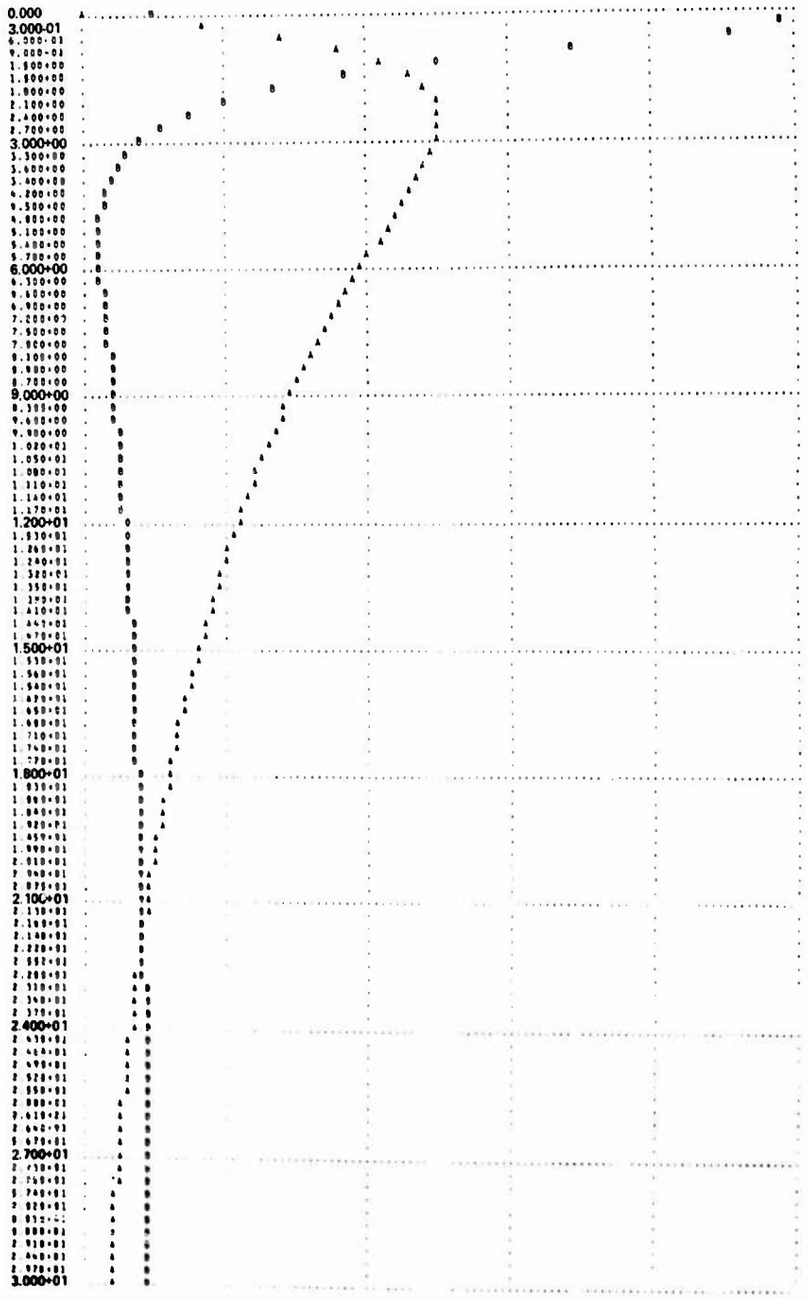


Fig. 9 Computer plot of transfer function input and output waveforms for a double exponential with $f_L/f_t = 10$ and $f_\mu/f_t = 10$.

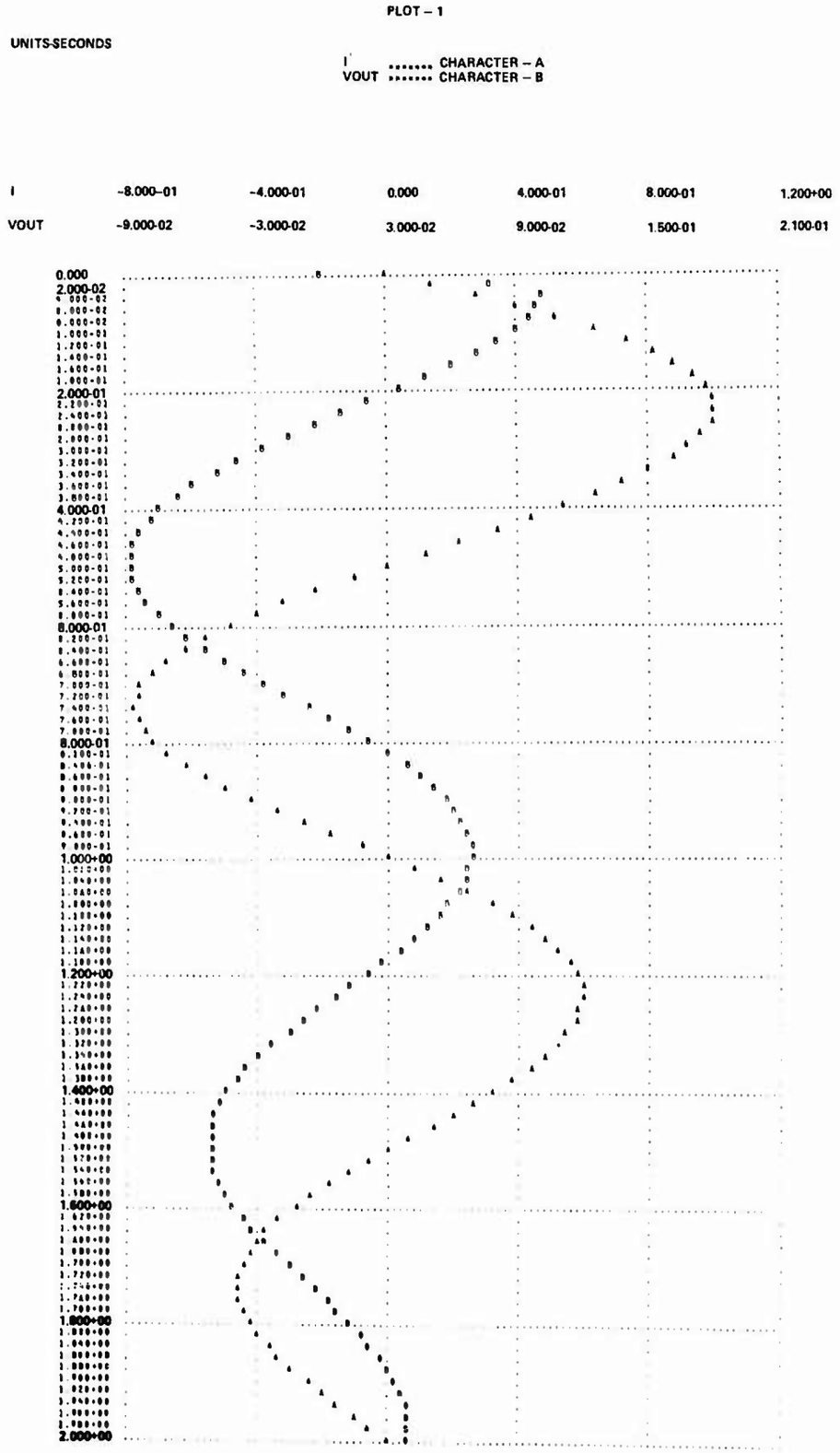


Fig. 10 Computer plot of transfer function input and output waveforms for a damped sinusoid with $f_L/f_{RS} = 10$ and $f_H/f_{RS} = 100$.

PLOT – 1

UNITS-SECONOS

I ••••••• CHARACTER – A
VOUT ••••••• CHARACTER – B

I	0.000	4.000-01	8.000-01	1.200+00	1.600+00	2.000+00
VOUT	-1.200-01	0.000	1.200-01	2.400-01	3.600-01	4.800-01

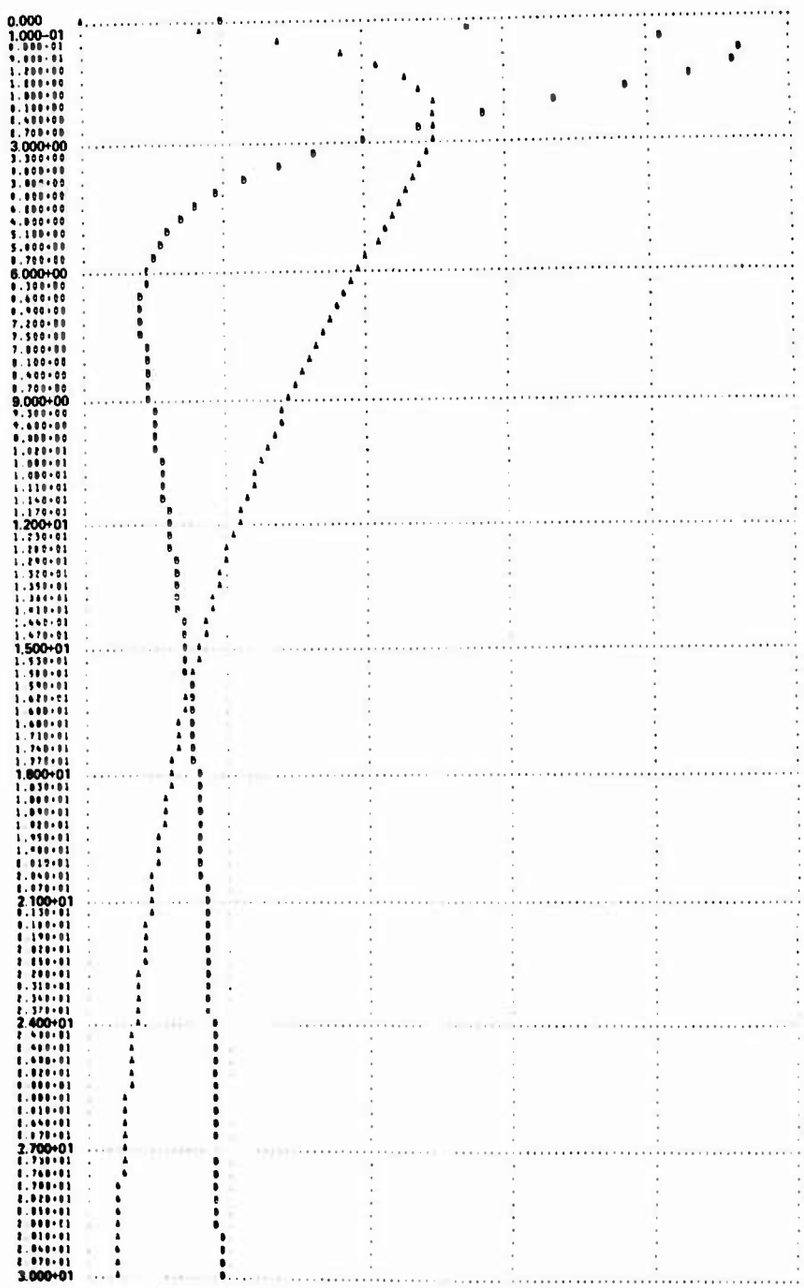


Fig. 11 Computer plot of transfer function input and output waveforms for a double exponential with $f_L/f_r = 1$ and $f_H/f_r = 10$.

PLOT – 1

UNITS-SECONDS

I ******* CHARACTER – A
VOUT ******* CHARACTER – B

I	0.000	4.000-01	8.000-01	1.200+00	1.600+00	2.000-01
VOUT	-2.000-01	2.000+00	6.000-01	1.000+00	1.400+00	1.800+00

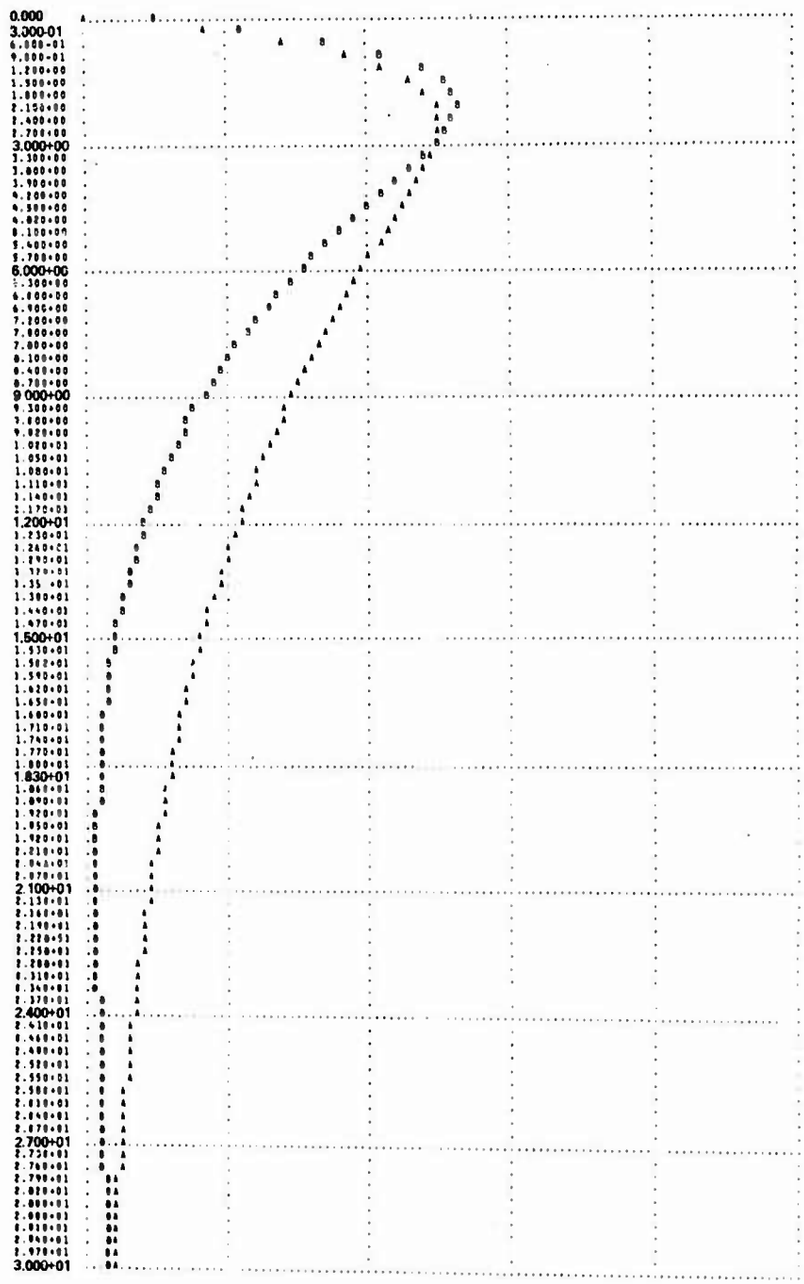


Fig. 12 Co.nputer plot of transfer function input and output waveforms for a double exponential with $f_L/f_d = 1$ and $f_H/f_r = 10$ and a damped sinusoid with $f_L/f_{RS} = 1$ and $f_H/f_{RS} = 10$. (Sh. 1 of 2)

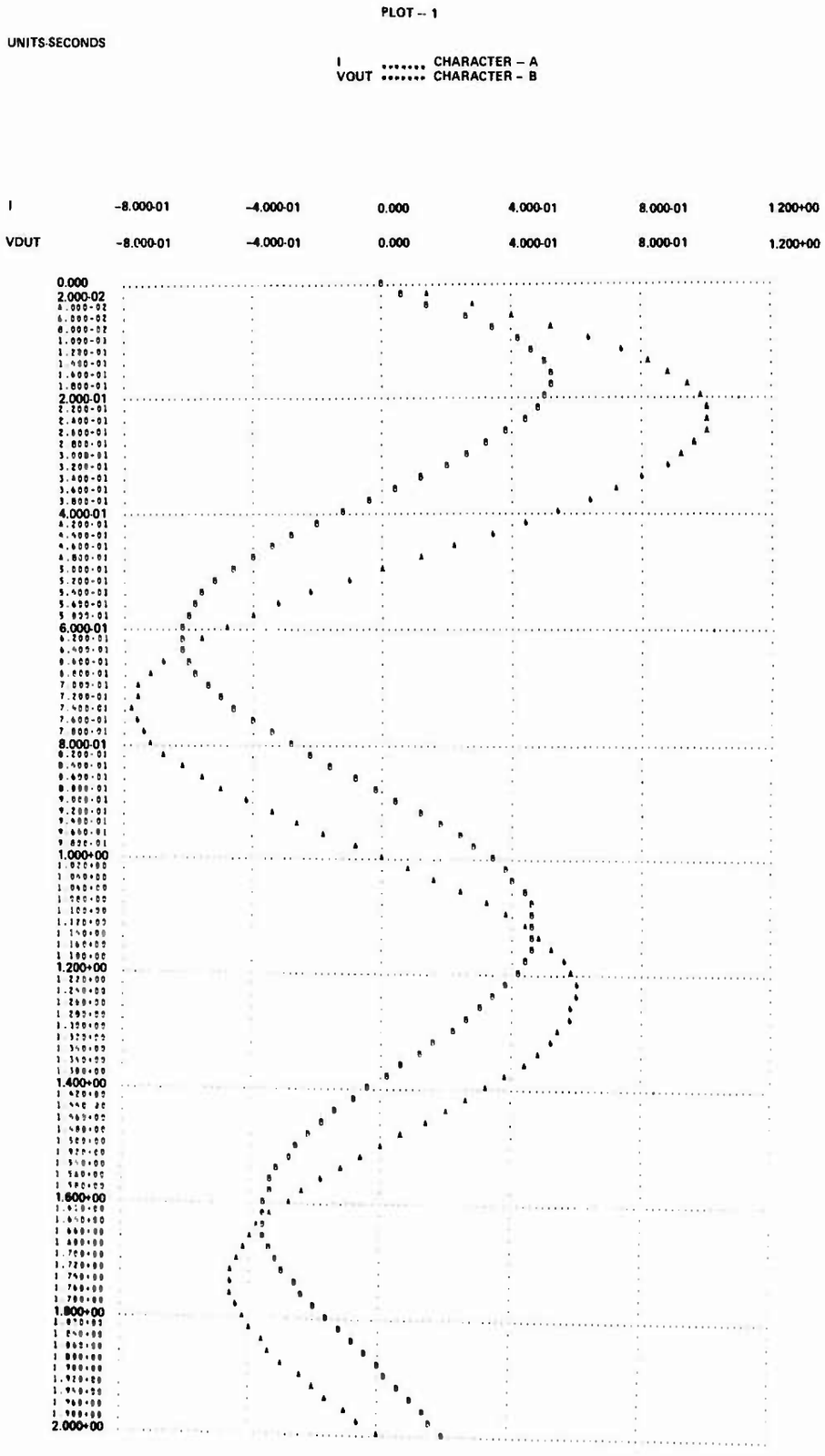


Fig. 12 Computer plot of transfer function input and output waveforms for a double exponential with $f_L/f_d = 1$ and $f_H/f_r = 10$ and a damped sinusoid with $f_L/f_{RS} = 1$ and $f_H/f_{RS} = 10$. (Sh. 2 of 2)

PLOT – 1

UNITS-SECONDS

I ••••••• CHARACTER – A
VOUT ••••••• CHARACTER – B

I	0.000	4.000-01	8.000-01	1.200+00	1.600+00	2.000+00
VOUT	0.000	4.000-01	8.000-01	1.200+00	1.600+00	2.000+00

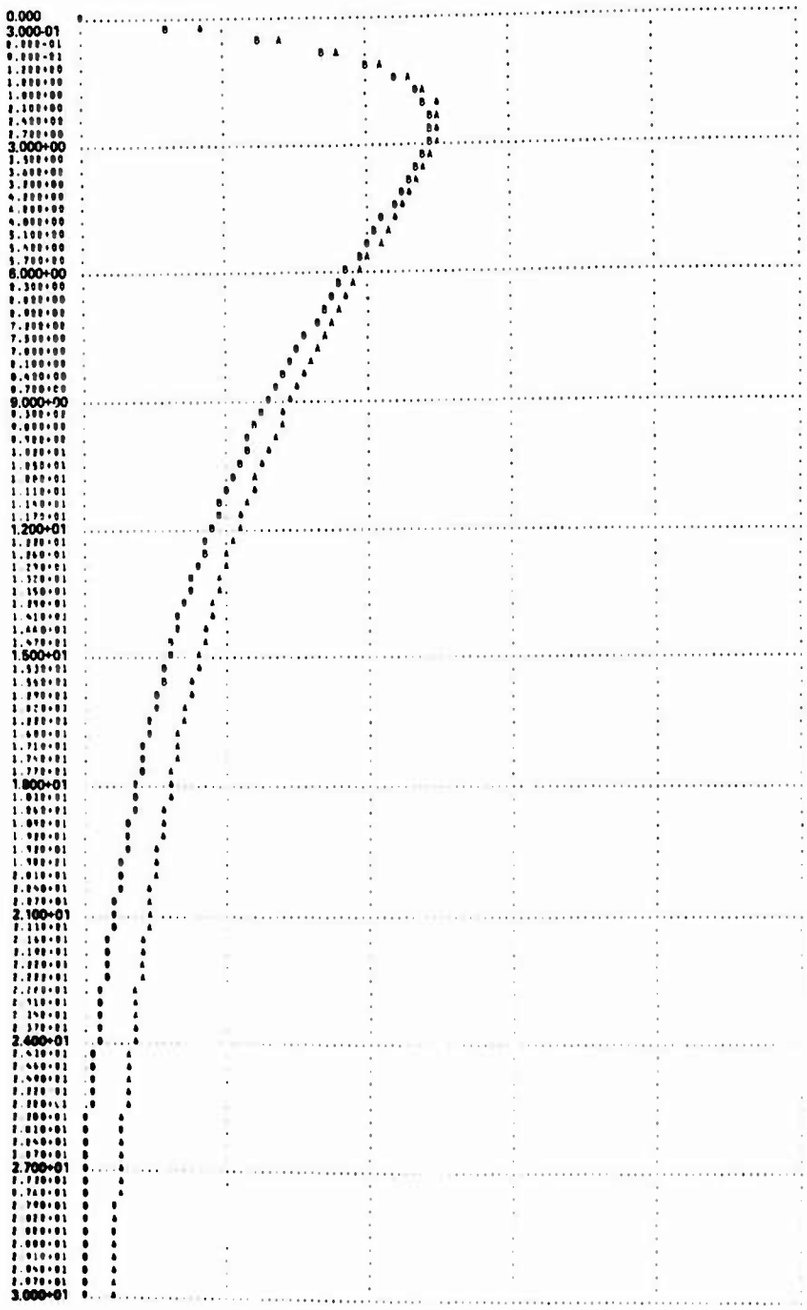


Fig. 13 Computer plot of tranfer function input and output wavaforms for a double axponantial with f_L/f_d = .1 and f_H/f_r = 10 and a damped sinusoid with f_L/f_{RS} = .1 and f_H/f_{RS} = 10. (Sh. 1 of 2)

PLOT – 1

UNITS-SECONDS

I ******* CHARACTER – A
VOUT ******* CHARACTER – B

I	-6.000-01	-4.000-01	0.000	4.000-01	8.000-01	1.200+00
VOUT	-1.000+00	-8.000-01	-2.000-01	2.000-01	6.000-01	1.000+00

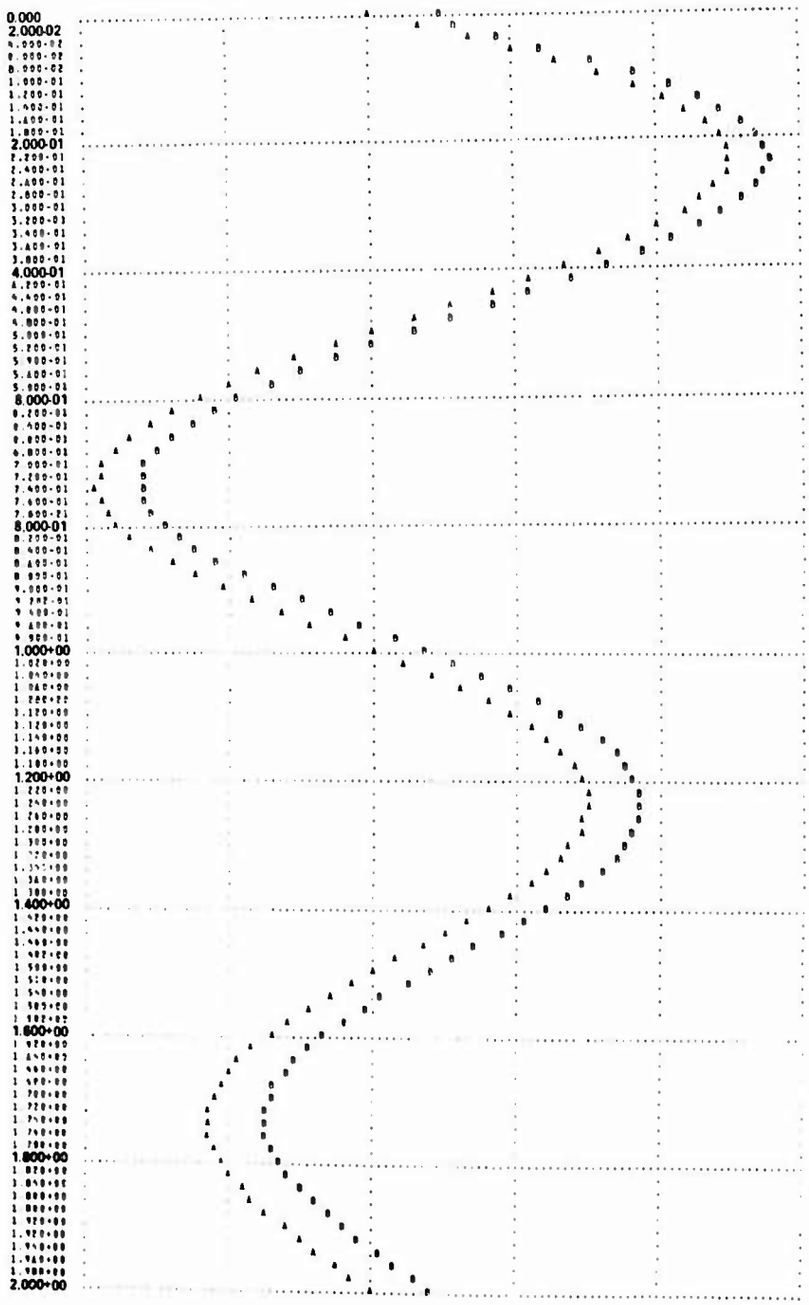


Fig. 13 Computer plot of transfer function input and output waveforms for a double exponential with f_L/f_d = .1 and f_H/f_r = 10 and a damped sinusoid with f_L/f_{RS} = .1 and f_H/f_{RS} = 10. (Sh. 2 of 2)

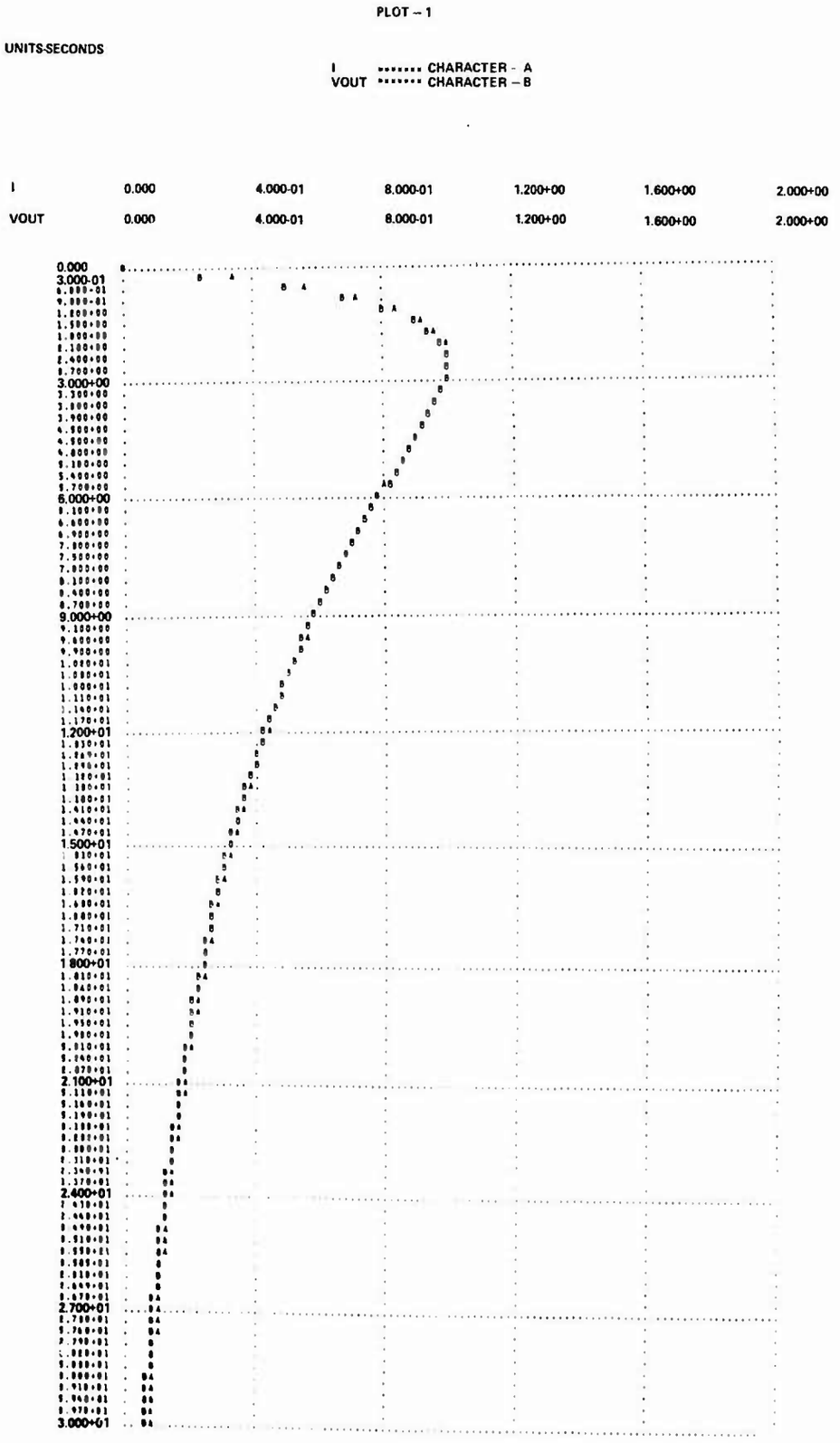


Fig. 14 Computer plot of transfar function input and output wavaforms for a doubla axponantial with f_L/f_d = .01 and f_H/f_r = 10.

PLOT – 1

UNITS-SECONDS

I ..... CHARACTER – A
VOUT ..... CHARACTER – B

I	0.000	4.000-01	8.000-01	1.200+00	1.600+00	2.000+00
VOUT	0.000	4.000-01	8.000-01	1.200+00	1.600+00	2.000+00

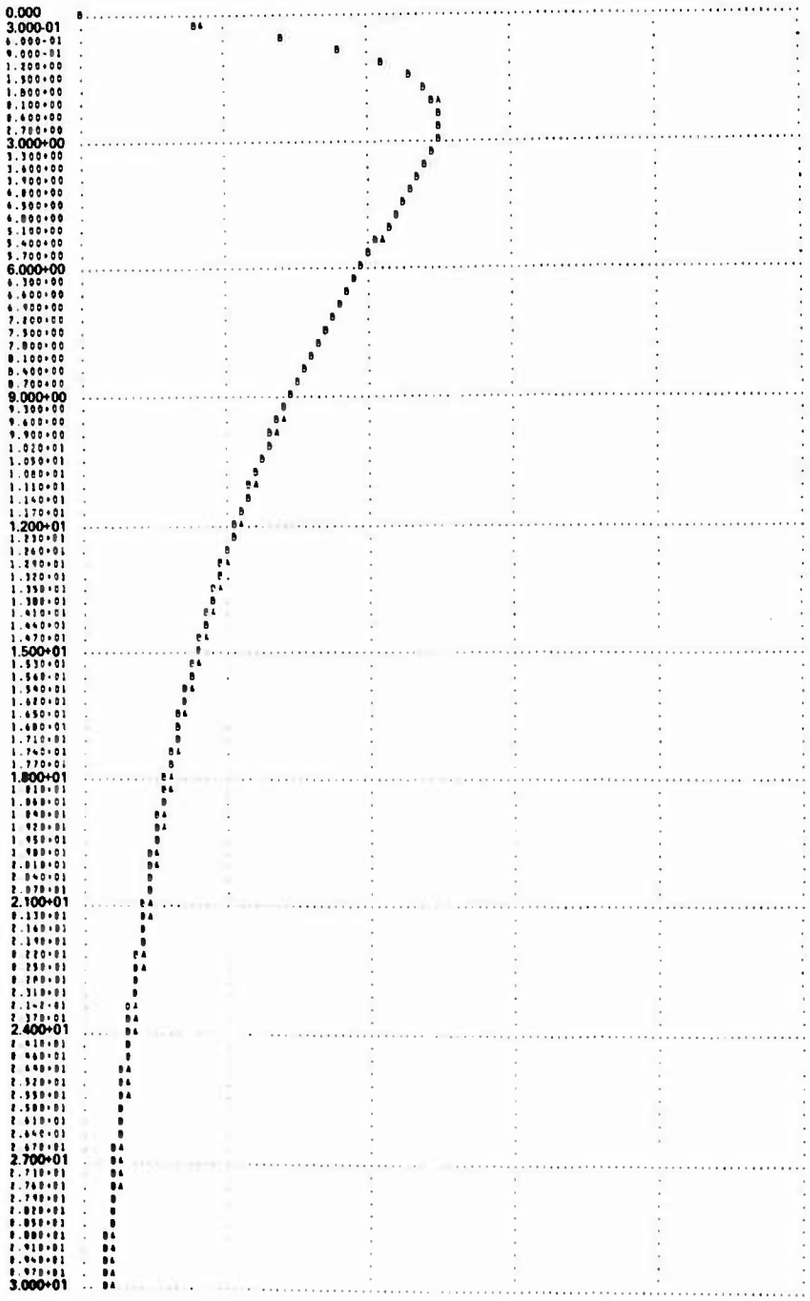


Fig. 15 Computar plot of transfer function input and output waveforms for a double exponantial with f_L/f_d = .01 and f_H/f_r = 100 and a damped sinusoid f_L/f_{RS} = .01 and f_H/f_{RS} = 100. (Sh. 1 of 2)

PLOT – 1

UNITS-SECONDS

I ******* CHARACTER – A
VOUT ******* CHARACTER – B

I	-8.000-01	-4.000-01	0.000	4.000-01	8.000-01	1.200+00
VOUT	-8.000-01	-4.000-01	0.000	4.000-01	8.000-01	1.200+00

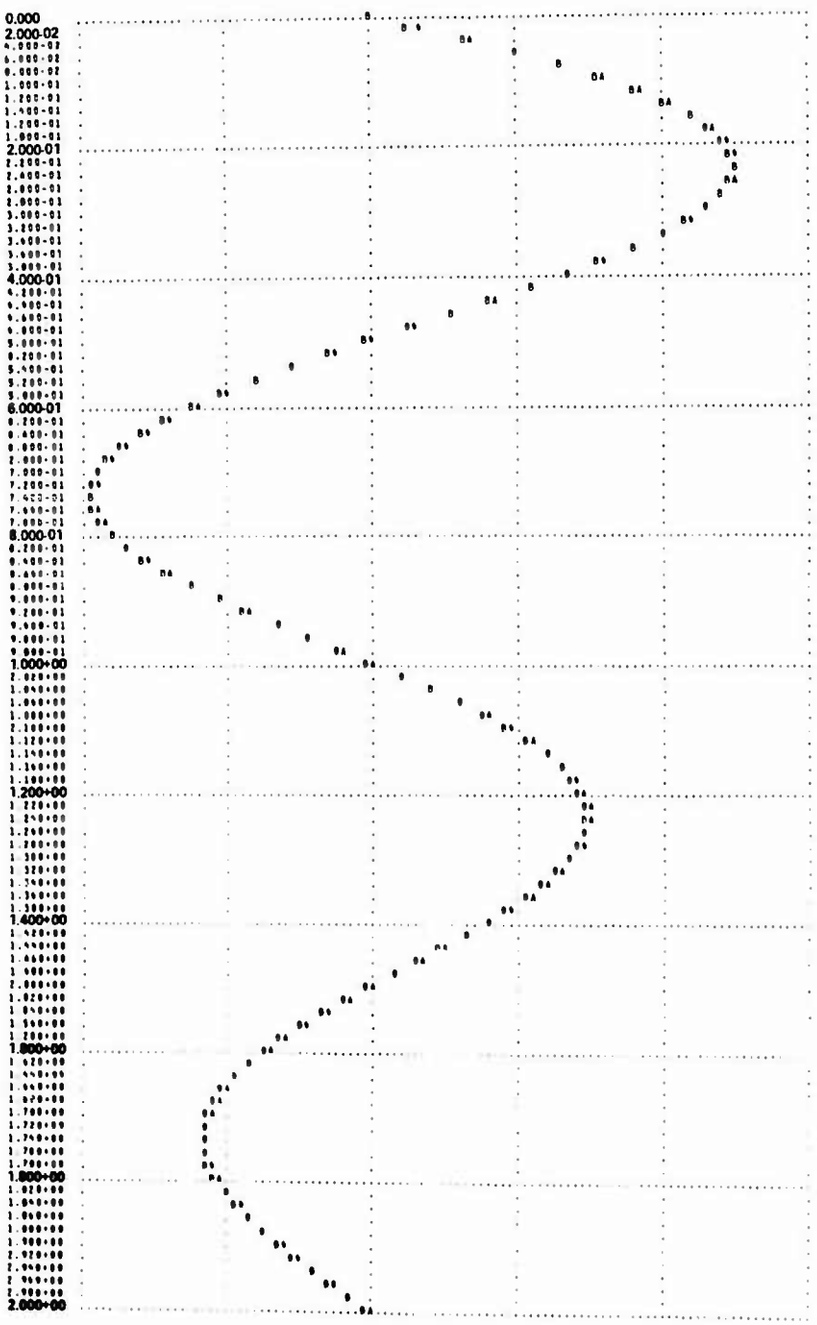


Fig. 15 Computer plot of transfer function input and output waveforms for a double exponential with f_L/f_d = .01 and f_H/f_r = 100 and a damped sinusoid f_L/f_{RS} = .01 and f_H/f_{RS} = 100. (Sh. 2 of 2)

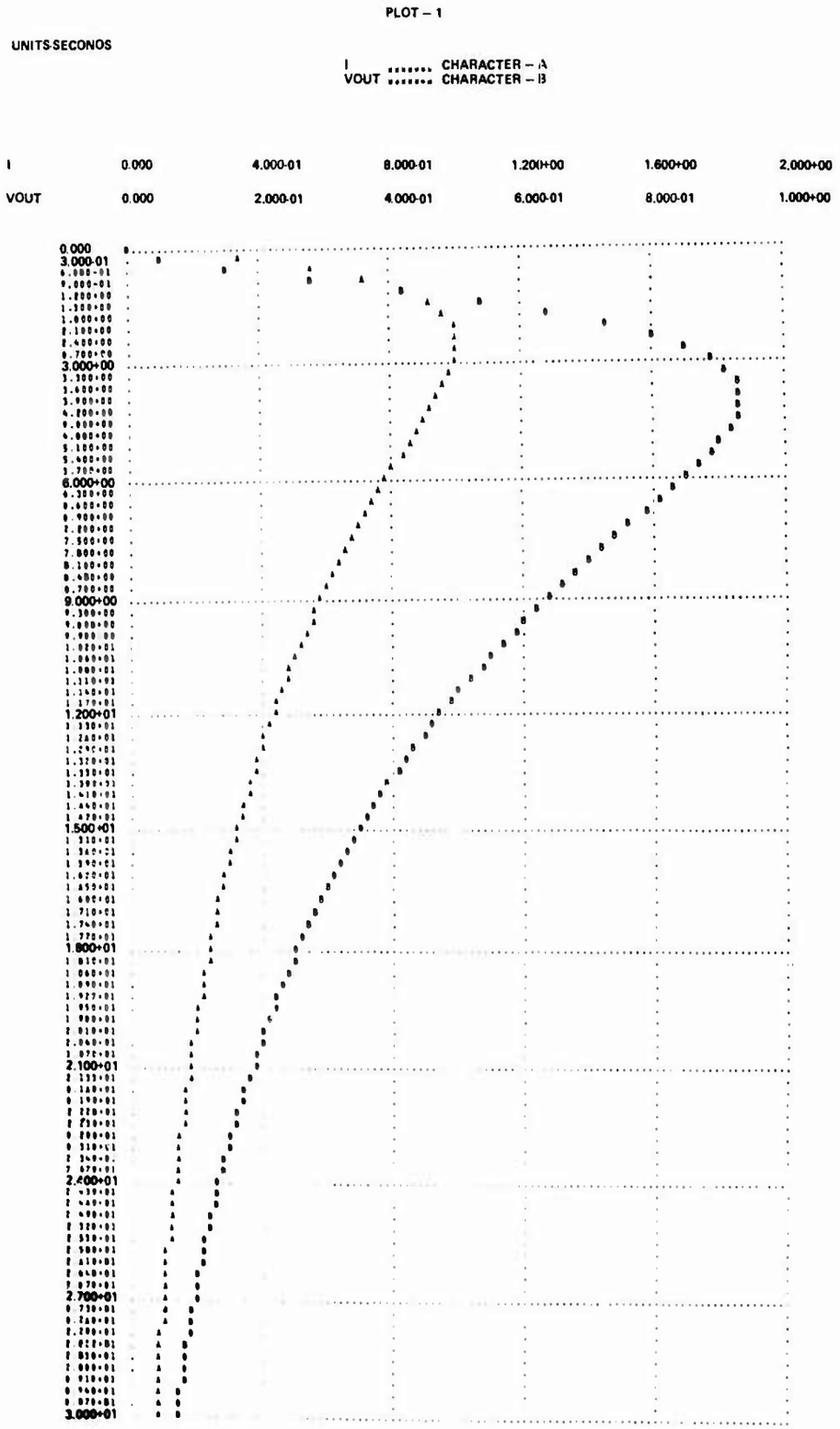


Fig. 16 Computer plot of transfer function input and output waveforms for a double exponential with f_L/fd = .01 and f_H/f_r = 1 and a damped sinusoid with f_L/f_{RS} = .3 and f_H/f_{RS} = 3. (Sh. 1 of 2)

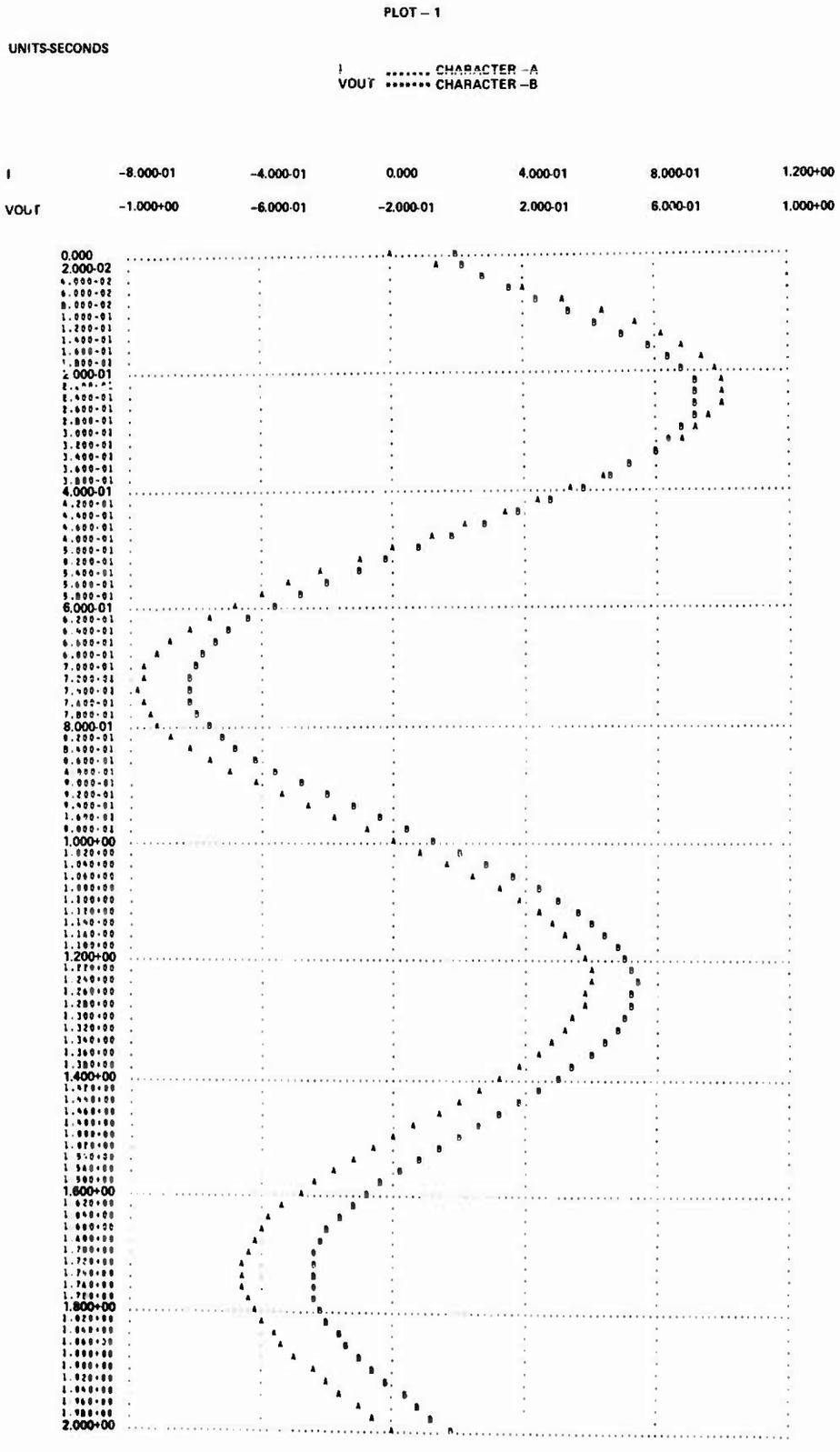


Fig. 16 Computer plot of transfer function input and output wavaforms for a double axponantial with f_L/fd = .01 and f_H/f_r = 1 and a damped sinusoid with f_L/f_{RS} = .3 and f_H/f_{RS} = 3. (Sh. 2 of 2)

PLOT -- 1

UNITS-SECONDS

I ••••••• CHARACTER – A
VOUT ••••••• CHARACTER – B

I	0.000	4.000-01	8.000-01	1.200+00	1.600+00	2.000+00
VOUT	0.000	1.000-01	2.000-01	3.000+00	4.000-01	5.000-01

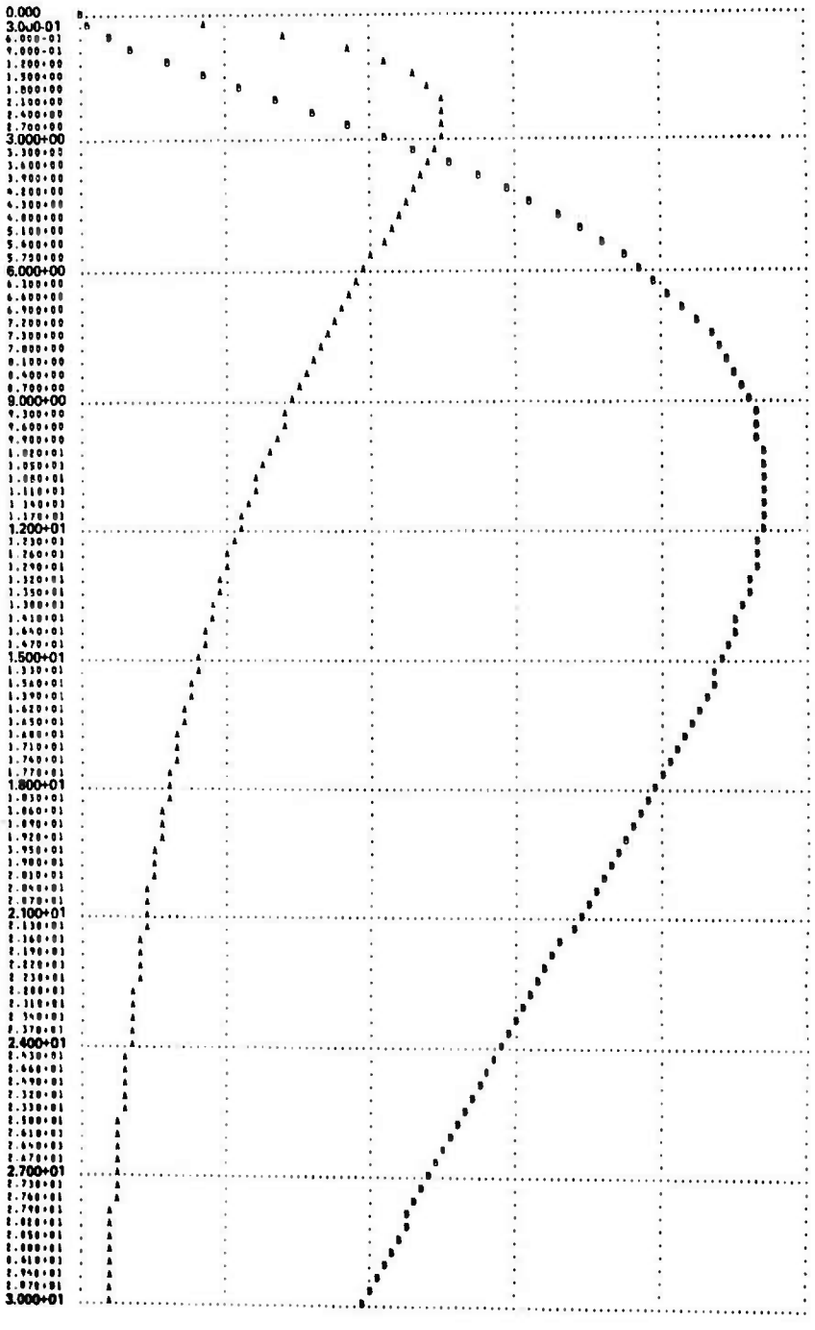


Fig. 17 Computer plot of transfer function input and output waveforms for a double exponential with f_L/f_d = .01 and f_H/f_r = .1 and a damped sinusoid with f_L/f_{RS} = .01 and f_H/f_{RS} = .01. (Sh. 1 of 2)

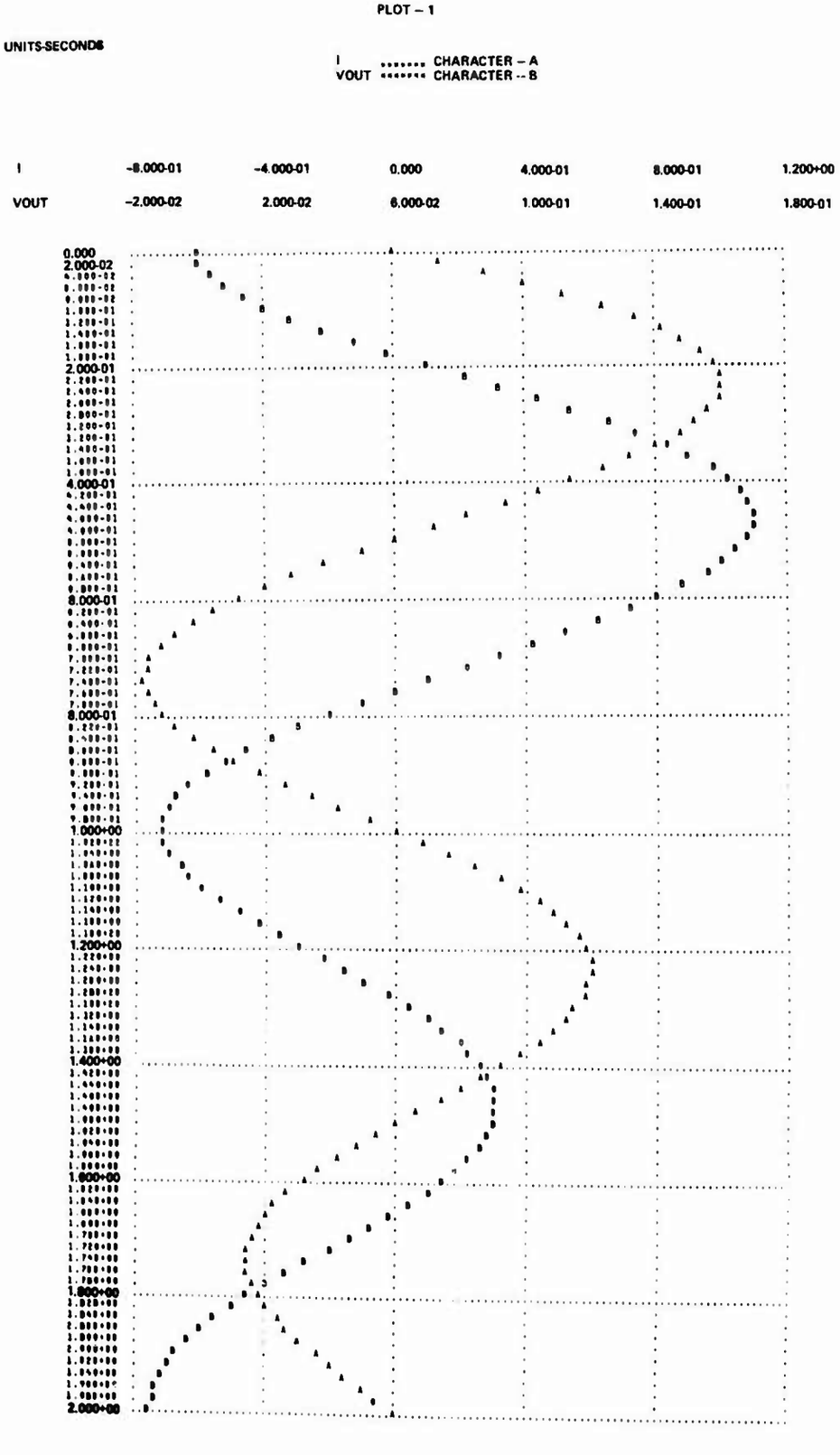


Fig. 17 Computer plot of transfer function input and output waveforms for a double exponential with f_L/f_d = .01 and f_H/f_r = .1 and a damped sinusoid with f_L/f_{RS} = .01 and f_H/f_{RS} = .1. (Sh. 2 of 2)

IN-FLIGHT THUNDERSTORM ENVIRONMENTAL MEASUREMENTS DURING THE LANDES 84 CAMPAIGN

P. Laroche, M. Dill*, J.F. Gayet** and M. Friedlander***

Office National d'Etudes et de Recherches Aérospatiales, B.P. 72, 92322 Châtillon Cedex, France
**Centre d'Essais Aéronautiques de Toulouse, 23, rue André Guillaumet, 31056 Toulouse, France*
***Laboratoire Associé de Météorologie Physique, B.P. 45, 63170 Aubière, France*
****Centre d'Essais en Vol, 91220 Brétigny, France*

Abstract - A campaign devoted to lightning and convective clouds properties studies was held in spring 84 in South West of France. Ground experiments consisted in meteorological radar observations associated with classical meteorological measurements. Airborne measurements on a Transall aircraft consisted in electrostatic and electromagnetic experiences on direct and nearby lightning, microphysical, thermodynamical and dynamical studies of convective clouds. This paper describes the in-flight experiments.

1 - INTRODUCTION

In-flight measurements on direct and nearby lightning had began in France few years ago, on board a Transall C160 aircraft belonging to the French Air Force and flown by the French Flight Test Center (CEV). In 1984, the aircraft instrumentation was improved to allow a wider range of investigations related to thunderstorm environmental parameters. This campaign (LANDES 84) was the first of this kind in France; it gathered in a joined experiment, measurements on lightning, atmospheric electricity, microphysic, thermodynamic and dynamic. The LANDES 84 campaign was hold at the same time that the FRONTS 84 experiment whose main objectives were about dynamic and thermodynamic of cold fronts hapenning in the South West part of France during spring. LANDES and FRONTS 84 gathered the operation concerning the deep convection phenomena associated with fronts.
The experiment was supported by DRET[1], DCA[2] and INAG and many laboratories were involved in it:
Abidjan University,
Centre d'Essais Aéronautique de Toulouse (CEAT)
Centre d'Essais en vol (CEV)
Centre National d'Etudes des Télécommunications (CNET)
Centre de Recherche en Physique de l'Environnement (CRPE)
Etablissement d'Etude et de Recherche Météorologique (EERM)
Institut National d'Astronomie et de Géophysique (INAG)
Institut et Observatoire de Physique du Globe (IOPG)
Laboratoire d'Aérologie (LA)
Laboratoire Associé de Météorologie Physique (LAMP)
Laboratoire de Physique de l'Atmosphère (LPA)
Laboratoire de Sondages Electromagnétiques de l'Environnement Terrestre (LSEET)
Office National d'Etudes et de Recherches Aérospatiales (ONERA).

[1]Direction des Recherches, Etudes et Techniques (Ministry of Defense)
[2]Direction des Constructions Aéronautiques (Ministry of Defense)

The aim of this paper is to describe shortly the overall experiment but to give more details on the measurements made on board the Transall aircraft. Other papers in this conference are specifically devoted to results about particular experiments. We describe here the method of operations and simply expose and comment the general results of the experiment.

2. DESCRIPTION OF THE EXPERIMENT

2.1 Technical and scientific objectives

There is a lack of in-flight data about direct lightning on aircraft. Those previously obtained on the Transall, on the C130 experienced by USAF and on the F106 from NASA [1-3] confirm that intracloud flashes triggered or intercepted by an aircraft, have electrical properties quite different from those of cloud-to-ground flashes which were used to elaborate standart regulations. The french program for in-flight studies of lightning aims on the one hand to obtain statistical informations about current magnitude and waveform of direct lightning and on the other hand to study the lightning-aircraft interaction whose indirect effects like coupling by dielectric apertures or currents pattern on the fuselage are of the most significative importance.
The overall electrical structure of a convective cloud like cumulus-congestus or cumulo-nimbus may be equivalent to a vertical dipolar or tripolar charge, as far as we observe the phenomena from the outside; the typical equivalent charge for a mid latitude storm cloud is + 40°C in the upper part, -40°C in the lower part and few coulombs positive charge at the cloud base. In fact the charge content and repartition in the cloud is much more complicated [4]. The aim of the on board experiment on atmospheric electricity [5] is to describe more precisely in relation with microphysical and dynamical analysis, the electrical structure of the cloud, the mechanisms of cloud electrification, and the influence of these parameters on lightning flashes behaviour and occurence.

We try also, to look for an eventual relationship between location of striking of plane and thermodynamical, dynamical and microphysical structure of cloud systems [6]. The other objectives of microphysical measurements are:
- intercalibration of airborne and radar measurements at ground in order to use the last one to study the temporal and spatial evolution of the cloud microstructure;
- check in high ice crystal concentration at low levels (-5°, -10°) in some cumulus clouds;
- investigation of the efficiency of the feeder seeder mechanisms between clouds at different levels on the precipitation genesis.

2.2 FRONTS 84 network [7]

The dynamical and thermodynamical characteristics of cold fronts and associated convective clouds were basically studied with a ground network of meteorological radars. A set of two doppler radars, the RONSARD system, separated by a distance of 30 km, performed simultaneous coplan exploration (wavelength 5 cm). Data processing delivers reflectivity and the three dimensional field of wind velocity. A 10 cm radar performed exploration of the clouds with a cross polarization system; with data delivered by this device one's may calculate the absolute and differential reflectivity. This last parameter contains informations on the phase of precipitations (solid or liquid) and on the deformation of hydrometeores (crystal of ice or liquid water drop).

A 8 mm wavelength doppler radar detects smaller cloud particles. A 60 m stratospheric radar, performing vertical soundings of clear air, gives informations on vertical wind profil, up to the tropopause.

Several 10 cm radars, belonging to official survey systems, for aeronautical and general forcast were available at the time of the experiment.

Those radar experiments were supported by ground meteorological measurements (rain, temperature, wind, humidity and thermal flux) and classical aerological soundings performed at several points at high rate during storms occurence (one each two hours). Stratiform ano weak convective clouds were explored by a Piper Aztec aircraft equipped with thermodynamical and microphysical sensors. Electrostatic and electromagnetic measurements at ground were installed near the middle of the aera observed by radars. The VHF radiation sources due to natural lightning are localized and analysed on a time scale less or egal to one microsecond [8]. Figure 1 shows the arrangement of the overall network.

2.3 Transall aircraft implementation

Basic modifications of the aircraft - The aircraft has been modified for different purposes, including lightning or atmospheric study so it became a polyvalent test bed, like the LOCKHEED HTTB (High Technology Test Bed) C130.

To achieve this, an important hardware modification program necessitated several months groundings, in order to install:
- an electrical power station providing
  - 6 kVA in 220 V/50 Hz,
  - 40 kVA in 115 V/400 Hz,
  - 4 kW in 28 V-DC;
- a general protection and distribution box for electrical equipment;
- 500 different electrical wires and cables all over the aircraft for sensors connection, power and parameters distributions;
- two polyvalent pods equipped with all types of electrical distribution and connection circuits;
- different sensor mountings or housings along the skin of the aircraft and the wings;
- extra antennas;
- extra NAV-COM facilities;
- safety devices.

Performances of the aircraft - The C160 is a germanfrench cargo aircraft whose span and length are approx. 40 m (which are about the Hercules C130 dimensions). The aircraft is propulsed by two Rolls Royce Tyne turbo props. Its speed with no flap in turbulence may varies from 70 to 120 m/s. Its range is between four and eight hours, depending on the cargo. The Transall is certificated for high levels of turbulence.

All classical measurements are performed, on board, to determine the flight conditions: velocity, static and dynamic pressure, incidence, side slip, three axis accelerometer, total temperature.

The absolute aircraft position regarding ground network is determined by use of an inertial navigation plateform, classical radionavigation system and a ground air location system which has a precision of ten meters. Ground speed and horizontal wind component are also delivered by an on board doppler radar.

Two video screen of a 3 cm weather-radar are available: one is recorded during the flight and the other is in the cockpit.

Measurements on direct and nearby lightning - High level electromagnetic signals due to direct or nearby lightning are measured in several places of the aircraft and transmitted by wide bandwidth optic fiber links (typical up to 100 MHz) to on acquisition unit which is a high performance Faraday cage.

A lightning rod is installed under the nose and at the tail of the aircraft. Rods are equipped with coaxial resistive shunt with a 100 MHz bandwidth and a resistance of 1 mΩ. Skin currents are measured on several points of the fuselage to study current pattern during direct lightning strike.

Electric and magnetic sensors are installed inside or along the wing and in the fuselage to determine the electromagnetic field produce by the strikes.

A specific experiment (see Fig. 2) about coupling by dielectric aperture is installed near the right side fuselage window [9]; it is made of E and H sensors with respective full range of 300 kV/m and 840 A/m. Signals are recorded on transient digitizers (Tektronix 7612 and 7912) and on wide-band analog recorders (10 and 2 MHz bandwidth). A synchronization between the two recording process allows to determine in what period of a flash a transient signal happens.

Atmospheric electricity - Local elecrical parameters measured on the aircraft are gazeous ions characteristics, drop charges [10] and triboelectric current.

Ions conductivity is measured by three gerdien type sensors; they consist in a cylindrical capacitor in which an unperturbated air flow is organized.

The ions are deviated towards a collecting electrode by the electric field produced by a biased electrode (Fig. 3). The biased voltage is manually adjustable for one sensor, automatically applied by steps for an other one, and adjustable with plus and minus polarity for the last one. The sensors are installed

on the profiled pod under the extremity of the wings (Figs. 4 and 5); it is expected that at this place, there are no perturbations due to propellers. The minimum ionic current detected is about 1 pA, the measuring range being ± 1 nA.

Charge of drops or ice crystals are sampled by a Faraday cylinder; corresponding bipolar current pulses are individually and automatically analyzed to obtain histograms of charge versus time. Data acquisition method is similar to this used for microphysical data, so the results of the two measurements may be easily compared. Fifteen class of values of both sign are linearly extended from about 10^{-12} to 10^{-10}C.

The triboelectric current is detected on three points on the aircraft. Two identical sensors (Fig. 4) are installed on the leading edge of each instrumented pod: they consist in a metallic isolated sheet, connected to a current amplifier. The front section of the two sheets is about 8.10^{-2} m^2, and the measuring range is ± 50 µA. The third sensor is made of a frontal windscreen panel, coated with a transparent conducting material, and connected to a current amplifier (measuring range ± 50 µA). None of the three sensors are supposed to be influence by the propellers. The current they collect is due to triboelectric effects and to impact of charged particules. The three measurements cannot be easily related to the actual total input current on the aircraft but they can be qualitatively associated with other electrical or microphysical parameters.

Global electrical activity is characterized by the atmospheric electrostatic field. This parameter is produced by the electrical charges separated in the clouds.

The horizontal and vertical components of the field, as well as the aircraft potential, are determined by calculations from five independent electrostatic field measurements made on the aircraft fuselage. The relation between the field at a measuring point and the potential and outside field, is initially determined by electrostatic measurements on a conductive mock up of the aircraft. Each sensor is of the field mill type, with a bandwidth of 0 to 20 Hz and a measuring range of ± 100 kV/m (see Fig. 3).

Field magnitude and direction are compared to storm cell location deduced from the various radar measurements which give reflectivity and wind velocity pattern and to local microphysical and electrical measurements.

Potential value is compared to local events and parameters, as direct lightning or triboelectric current.

The low frequency current emitted by passive discharges installed on wing trailing edges and in other high electrostatic field places of the aircraft are recorded.

Cloud physics instrumentation - The available cloud physics instrumentation is summarized in figure 6.

Microphysical probes. This instrumentation and mounting location are as follow:

- three PMS* 1D probes which measure the particle spectra with diameter ranges: 3-45 µm (FSSP), 80300 µm (1D-C), 300-4500 µm (1D-P),
- Two PMS 2D probes which give the images of particles with dimension ranging from 25 to 800 µm (2D-C) and from 200 to 6400 µm (2D-P),
- two hot-wire liquid water content devices (Johnson-Williams and King probe),

  These probes were mounted on the two pods located under the wings (see Figs. 4 and 5);
- a total water content probe and a second Johnson-Williams probes mounted on the airplane flank in front of the wing.

Thermodynamical probes. This instrumentation provides three total temperature measurements (de-iced Rosemount, non de-iced Rosemount and Reverse Flow), a dew-point temperature (Cambridge) and static and dynamic pressures.

The total temperature probes are located on the left pod (Fig. 5).

Dynamical and localization devices. A doppler radar, an inertial plateform and three accelerometers provide the dynamical and navigational parameters (Fig. 6). The navigational parameters are complemented by a localization system working from ground based radio-beacons.

Cells location. The screen of the on board 3 cm PPI radar is video recorded to obtained the position of the aircraft regarding the storm cell.

Recording systems. The Transall was equipped with various and sophisticated acquisition systems. We have on the one hand systems protected during flashes by the Faraday cage and on the other hand those simply installed in the cargo without special shielding precaution.

Unprotected acquisition system. All the microphysical, thermodynamical, dynamical, and low frequency electrical parameters are processed by an on board computer (HP-A 900) which continously dumps the data on magnetic tape (two 1600 BPi magnetic tape, recorders run "Flip Flop") and give a real time visualization of measurements on two console devices. The maximum sample rate used is 128 words/s for one parameter and a total of 70 parameters are recorded. A third 1600 Bpi mag-tape recorder is devoted to the acquisition of the 2D microphysical parameters which run as fast as 10^5 bytes/s.

A serial PCM signal including electrical and general information parameters is recorded on a 14 channels analog recorder.

Medium bandwidth electromagnetical and electrical signala are recorded on a 0-2 MHz, 28 channela analog recorder.

Protected acquiaition aystem. A double skin HF shelter (Faraday cage) was especialiy designed, manufactured and equipped for these types of tests. The "box" was made of walls comprising a balss core included between two aluminium alloy sheets.

The double skins were really isolated, but connected in a unique point. One door and one gridded window allowed communication between outside and inside, and all seals were of the HF type. The electrical power was introduced through a "broken circuit" tranaformer (400 Hz, 10 kVA). Inside the shelter, rectifiers and 50 Hz inverters produced the adequate electricity, in conjunction with dry batteries.

All the parameters or remote central transmiasion linea were fiber optics and went through the walls via special HF "organ pipe" tubea.

Inside the shelter were six magnetoscopes used as single parameter analog recorders (3 and 10 MHz bandwidth), two 14 channels data recorders, two digital analyzers (Tektronix 7612 and 7912) and a basic clock.

*PMS: Particle Measuring System, Boulder, Co, USA

3. GENERAL RESULTS

3.1 - Survey on the Transall activities during the campaign

The meteorological situations in which, basically, we were expected to fly were deep convections associated or not with cold fronts. From may to beginning of July we have had twenty four situations to study and eleven of them happened near the ground radar system. Flight objectives were devoted either to lightning studies in storm either to microphysical studies in low convective or stratiform clouds or to both objectives in coordinate flights. The basic crew for this campaign was 2 pilots, 2 mechanical engineers, 2 system engineers and 3 scientists.

The lightning strike studies flight consisted in cells penetration from - 10°C to 0°C, the trajectory of the aircraft beeing chosen by the pilots, regarding on board radar informations, to avoid the most dangerous hail regions.

The microphysical and dynamical studies flight consisted in trajectories adapted to each type of clouds.

The coordinated flights consisted in organized patterns in cumulonimbus, typically beginning by a tail wind penetration at low temperature (-20° to - 10°C) and horizontal explorations each 5°C (Fig. 7). A medium scale cell, about 10 km wide was explored, that way, within less than 20 minutes.

3.2 - Occurence of lightning

The explorations of clouds were limited by the flight range of the aircraft. Attempts of penetration were made at several levels, depending of the clouds characteristics, at temperature between - 20° and 0°C. Direct and close nearby lightnings were observed during the campaign. More than 20 direct flashes were obtained inside 7 different storms. Figure 8 is video picture of flashes sweeping on the front rod and from one wing to the other. Microphysical properties of the medium where flashes were observed are described in an other paper [6].

3.3 - Example of availabled data

Electromagnetic measurements - Fast pulses produced by a direct lightning are represented on figure 9 together with the slow electric field indicated by a field mill; those signals are analyzed in [9].

Electrical and atmospherical measurements - We present on figures 10 and 11 an example of a measuring sequence, in order to emphasize the kind of investigations permitted by those experiments. Figure 10 is the cell reflectivity in dBZ, in a plane containing the two radars of the RONSARD system and the aircraft trajectory indicated by the curve A-B and corresponding to 2 minutes of flight (about 12 km). During that sequence, the aircraft leaves a high reflectivity core underneath, and has a medium reflectivity cell on its right. The atmospheric field values are somewhat relevant with radar informations (Fig. 11): when the aircraft enters the higher reflectivity portion of its trajectory the longitudinal compcnent became lower and the transversal one higher pointing toward the core of the cell. The radar reflectivity give a representation of the geometry of the cell, which actual symetry is indicated by its dynamical structure.

Aircraft electrical potential is closely related to impact current and cloud particles concentrations as can be seen on figure 11.

CONCLUSIONS

For the first time in France, a sophisticated ground and in-flight experiments about thunderstorm environmental studies, was held in South West of France during spring and beginning of summer 1984.

All the data about lightning, static electricity, microphysic, thermodynamic and dynamic are still under analysis. But, at that time, we can say that the Transall aircraft, with its measuring equipments, is well adapted to elecrical and microphysical experiments into deep convective clouds; this is mainly due to its range, volume, safety and typical speed of 100 m/s.

The results of the 84 campaign indicate also that a successfull experiment on lightning may be conducted in France even if the occurence of storms is poor, in spite of the fact that simultaneous events in flight and at ground have a small probability to occur when the measuring range is small (inferior to 30 Km).

ACKNOWLEDGEMENTS

This work has been carried out with the support of the Direction des Recherches Etudes et Techniques and of the Direction des Construction Aéronautiques of the Defense Ministry.

REFERENCES

[1] - CEAT, "Mesure des caractéristiques de la foudre en altitude", C.R. d'Essais n° 76/65 0000 P, Juillet 1979.

[2] - P.L. Rustan, B. Kuhlman, J. Showalter, J. Reazer, "Electromagnetic measurements of lightning attachment to aircraft", Int. Aerospace and Ground Conference on Lightning and Static Electricity, Fort Worth (Texas, USA), June 21-23, 1983.

[3] - T.F. Trost and F.L. Pitts, "Analysis of electromagnetic fields of an F 106 B aircraft during lightning strikes", Int. Aerospace and Ground Conference on Lightning and Static Electricity, Oxford (England), March 1982.

[4] - I.M. Imianitov, B.F. Evteer, I.R. Kamaldina, "Planetary electrodynamics", London, Gordon and Breack, p. 401, 1969.

[5] - P. Laroche, "Airborne measurements of electrical atmospheric fields produce by convective clouds", In this conference.

[6] - J.F. Gayet, C. Duroure, R.G. Soulage, P. Laroche, "Location of lightning strokes on aircraft in storm field with measured electrical, microphysical and dynamical properties", In this conference.

[7] - J.P. Chalon, "Projet d'expérience LANDES-FRONTS 84", EERM Note, November 1983.

[8] - P. Richard, F. Broutet, A. Bondiou, "Spatial characterization of the VHF-UHF lightning radiation", In this conference.

[9] - J.P. Moreau, J.C. Alliot, "E and H fields measurements on the Transall C 160 aircraft during lightning flashes", In this conference.

[10] - P. Gondot, A. Delannoy, "In-flight electrical conductivity measurements", In this conference.

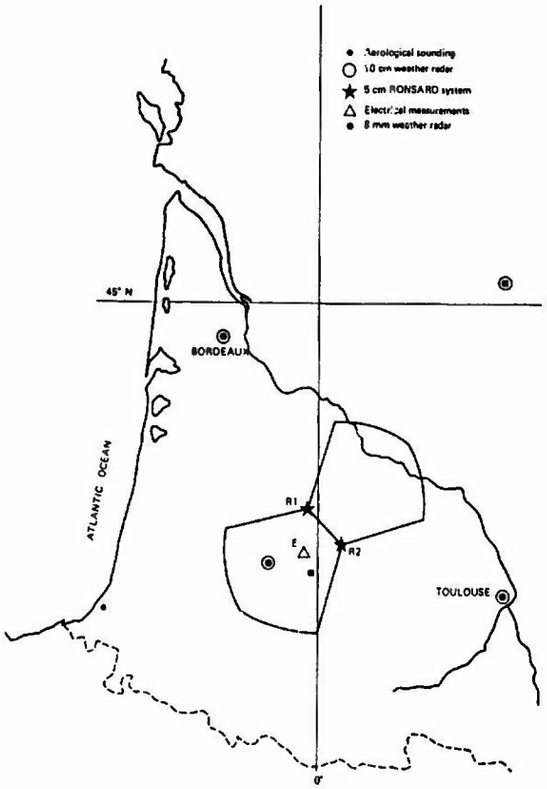


Fig. 1 - FRONTS 84 network.

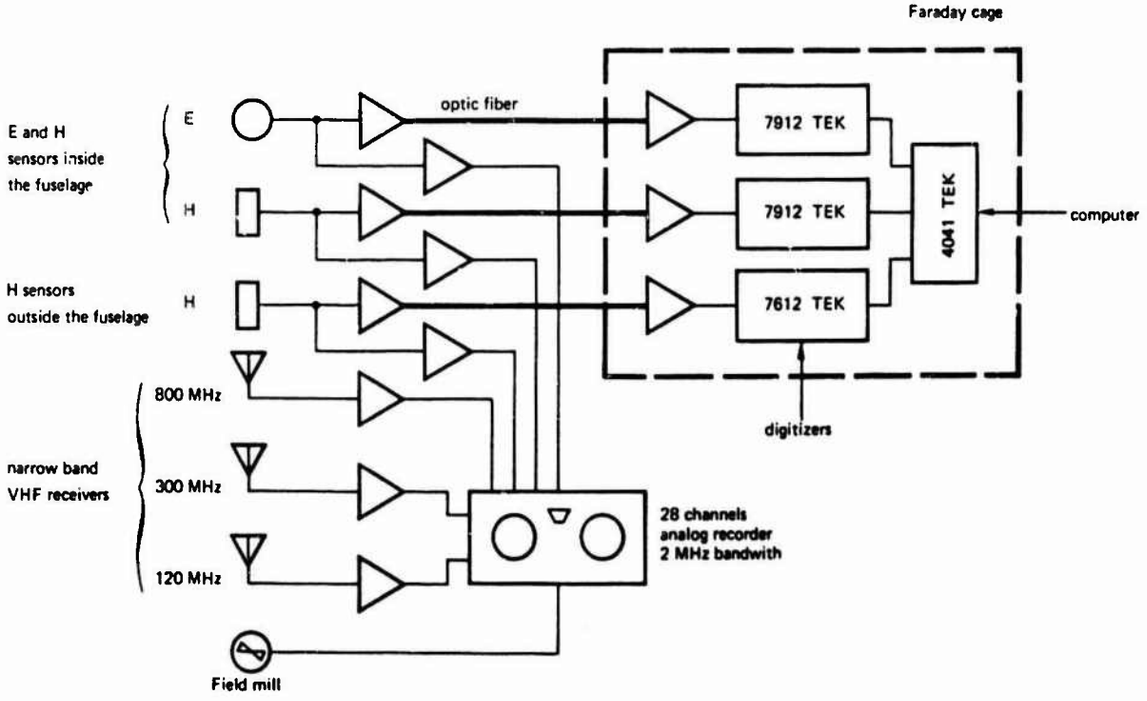


Fig. 2 - Coupling by dielectric aperture experiment.

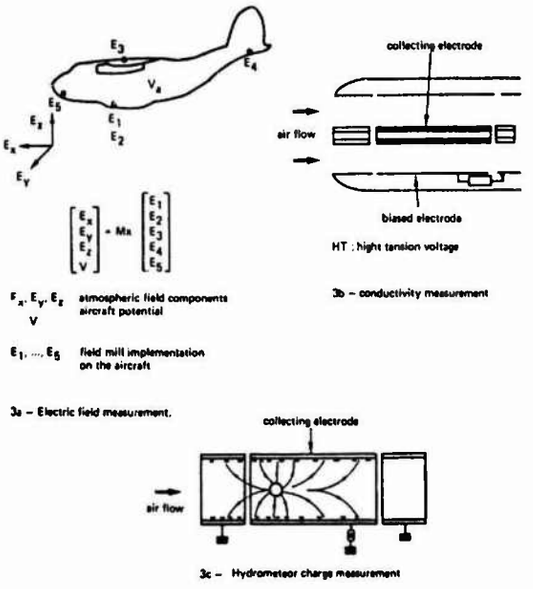


Fig. 3 - Electrostatic measurement.

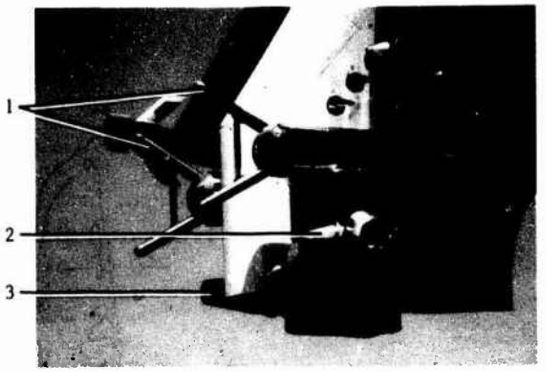


Fig. 5 - Left side instrumented pod.
1.Conductivity cell
2.Faraday cylinder
3.Microphysical sensors

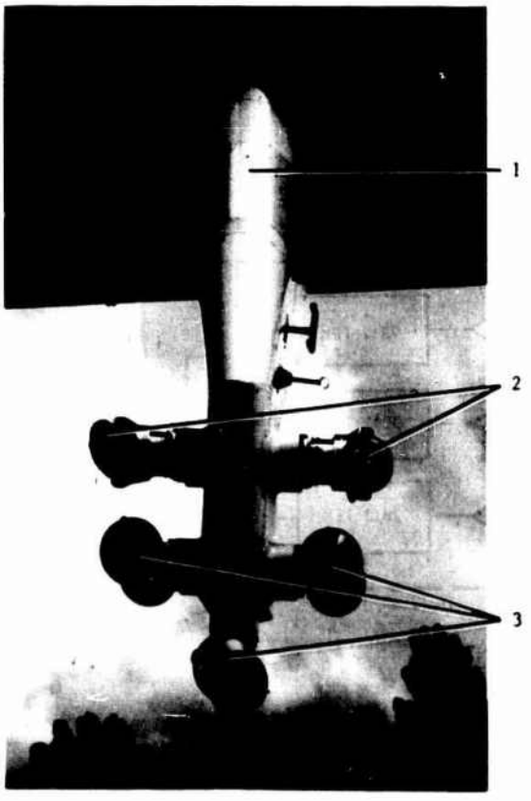


Fig. 4 - Right side instrumented pod.
1.Impact current sensor
2.Conductivity cells
3.Microphysical sensors

	Probes	Parameters	Acquisition Frequency (Hz)
Microphysical parameters	PMS FSSP - 100	Droplet spectra (3 < D < 45 μm)	16
	PMS 1D - C	Particle spectra (20 < D < 300 μm)	16
	PMS 1D - P	Particle spectra (300 < D < 4 500 μm)	4
	PMS 2D - C	Particle image (25 < D < 800 μm)	–
	PMS 2D - P	Particle image (200 < D < 6 400 μm)	–
	2 α Johnson - Williams	Liquid Water Content	16
	King Probe	Liquid Water Content	16
	Ruskin	Total Water Content	128
		Dew - Point Temperature	8
Thermodynamical parameters	De Iced Rosemount	Total temperature	64
	Non de Iced Rosemount	Total temperature	64
	Reverse - Flow	Total temperature	16
	Cambridge	Dew - Point temperature	8
	Crouzet	Static pressure	16
	Pitot Crouzet	Dynamic pressure	16
Dynamical and localization parameters	De iced sideslips	Attack angle	32
		Yaw angle	32
	Compass system	Magnetic head	32
	Inertial Plateform	Roll angle	32
		Pitch angle	32
		True head	32
		Ground speed	4
		Route	4
		Vertical acceleration	64
	Doppler radar	Ground speed	32
		Drift angle	32
	Accelo - meters	x, y, z accelerations	32
	Radio - altimeters	Altitude	32
	Trident systems	Localisation	8
	Chronometry station	Detection	1

Fig. 6 - List of the cloud physic probes and parameters of the Transall-04 aircraft and acquisition rates.

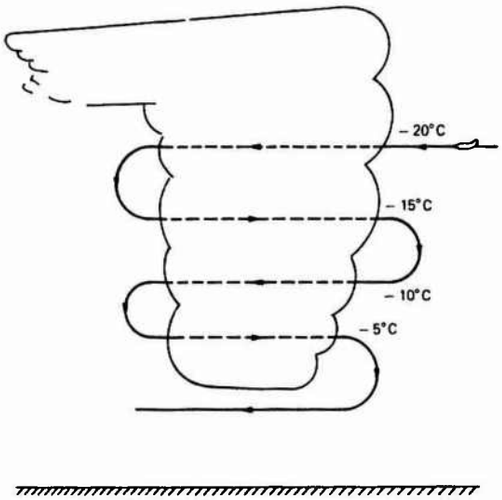
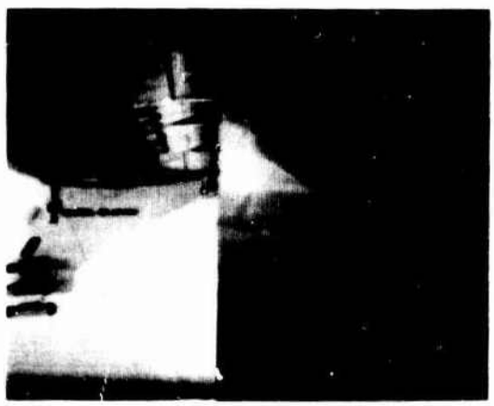


Fig. 7 - Aircraft pattern in cumulonimbus.



Flash on the front rad



Wing to wing flash

Fig. 8 - Direct strikes on the Transall.

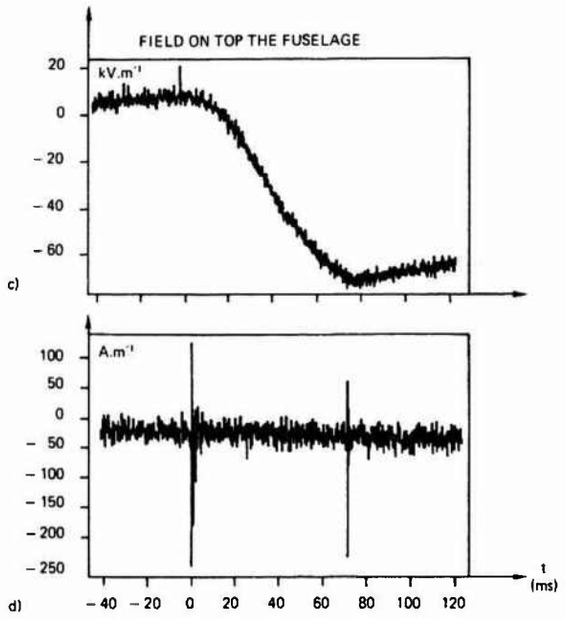


Fig. 9 - Direct lightning: time correspondance between slow E field and H field pulses.

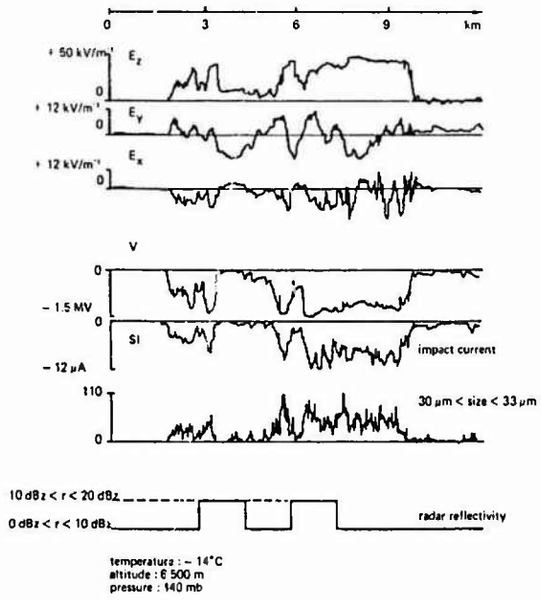


Fig. 11 - Flight n° 27: trajectory A-B.

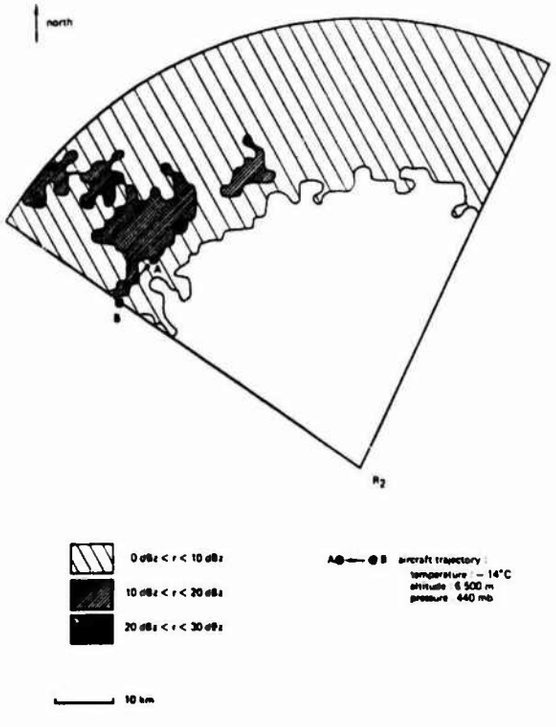


Fig. 10 - Flight n° 27: 10 cm radar reflectivity.

LOCATION OF LIGHTNING STROKES ON AIRCRAFT IN STORM FIELD WITH MEASURED ELECTRICAL, MICROPHYSICAL AND DYNAMICAL PROPERTIES

J.F. Gayet, C. Duroure, R.G. Soulage and P. Laroche*

LAMP, University of Clermont II, France
**ONERA, France*

Abstract - This paper will show the results of microphysical, dynamical and electrical measurements of the characteristics of clouds when the Transall 04 plane was struck by lightnings during the Landes-Fronts 1984 experiment above described by P. Laroche et al. The measurements were carried out during cloud penetrations between + 3 and - 20°C. They concern the size spectrum of cloud droplets and drops between 3 µm and 4500 µm, the size spectrum and feature of ice crystals between 50 µm and 6500 µm, the liquid water content of cloud, its vertical velocity. The results show that the striking of the plane occured in preferential regions and stage of growth of the clouds.

Only a few studies have been carried out on the location of lightning strokes on an aircraft in storms (Mazur et al., 1984 ; Kuhlman et al., 1984).

This location depends upon the space and time distribution of natural lightnings in a cumulonimbus and the part played by the plane by triggering special strokes.

One objective of the Landes-Fronts experiment above described by Laroche et al. (1985) was to investigate the preferential period and regions in the life of a thundercloud for lightning strokes on an aircraft and to determine the electrical, microphysical and dynamical cloud properties in these periods and regions.

The process that we intended to use consisted in :
- drawing the flight path of the Transall plan given by an inertial platform and/or a tracking radar (Mistral radar) ;

- marking the location of the lightning strokes, taking into account only the strokes on the boom or the wings of the plane seen by video cameras in order to consider only lightning strokes on the plane and not lightning at variable distances of the plane ;

- drawing the echoes of the cloud field given by the onboard 3 cm radar ;

- comparing these echoes to the pictures of clouds taken from the aircraft or from the ground ;

- displaying the time variation of the following parameters along the flight path of the aircraft before and after the lightning stroke :
  . thermodynamical and dynamical parameters (temperature, pressure, vertical velocity of the air, the last one giving the activity of the cloud and being evaluated by integrating the vertical acceleration with a correction of roll and pitch angles) ;
  . electrical parameters (potential of the plane, horizontal and vertical components of the electric field which can give the direction of the charged regions ; the accuracy can be about 20 % for the vertical component, much less for the horizontal components) ;
  . microphysical parameters (size spectrum of cloud droplets and ice crystals, feature of ice crystals given by PMS probes (FSSP, 1D-C, 1D-P, 2D-C, 2D-P), liquid water content given by Johnson-Williams probe. These last parameters are usable to explain the lightning strokes only if the electric field and the lightning is horizontal and parallel to the flight path. In the case of a vertical field and lightning, they have to be extrapolated to have an idea of the microphysical properties of the below and above regions containing the electrical charge responsible for the electric field and the lightning. In the case of a cloud system stationary during several hours, with the same kind of cumulonimbus repeating, measurements carried out in different times, levels and locations at different stages of the evolution of the clouds, permit to qualitatively reconstruct the microphysical field. In the other cases, the microphysical measurements on the plane are not easily usable.

Besides these onboard measurements, we have at our disposal in some cases and intend to use in the future in order to situate the lightning stroke on the plane, in the cloud system, at a large scale :
- the field of reflectivity of the cloud system given by radars at the ground (Melodi 10 cm radar, Ronsard 5 cm doppler radars, Rodin 5 cm radars, Rabelais 0.8 cm radar). These data are specially important to follow the time evolution of the clouds and to extrapolate or interpolate the aircraft measurements ;

- the field of rain at the ground.

The campaign of measurements was carried out in June 1984. All data are not yet processed. So we describe hereafter only two cases of aircraft cloud penetrations to show the difficulty of the problem and to give a partial and preliminary answer for it.

The first case concerns a small cloud system formed by 3 adjacent cells labelled A, B, C that Transall plane has penetrated along 19 km at 3500 m (MSL) with an air temperature of - 10°C (Fig. 1). These 3 cells (the boundary of which are not perfectly defined and a little arbitrary) and their microphysical, dynamical and electrical properties are revealed by the Figure 2 which displays the time variation of a part of the parameters measured from the plane. They correspond, at 3 stages of evolution of cumulonimbus previously described by Gayet (1979). The cell A is in a dissipating stage with a vertical velocity of air very weak, no small droplets, except in the zone of mixing with the cell B, ice crystal agglomerates (Fig. 3), the concentration of which reaches 3 l^{-1} and the size 3 mm. An electrical field vertical and downward is observed along 5 km due to a vertical dipole with positive charges upward in agreement with microphysical observations.

The cell B is in a mature stage with not negligible

vertical motions (updraft of about 5 m s^{-1} bordered by 2 downdrafts), small droplets (about 500 cm^{-3}) bearing a liquid water content of about 2.0 g m^{-3}, ice crystals (columns (Fig. 4-a) and graupels (Fig. 4-b) with a maximum diameter of about 10 mm).

The electric potential of the plane is high. The vertical component of the electric field is weaker than in the cell A. Its fluctuations are in agreement with a mature cell. The horizontal components along the flight path oscillates and increases on the boundary between the cells B and C.

The cell C is a young cell with and updraft of 10 m s^{-1}, small droplets (500 cm^{-3}) bearing a liquid water content of 2.0 g m^{-3} without or with only a few ice crystals in a small region, no electric potential of plane.

In this first case, we observe that the plane was stroken by lightning on the boundary between the cells B and A that is to say between two active cells on of them containing ice crystals and with an horizontal electric field between the two cells. We note that the electric potential decreases and becomes equal to zero just before the lightning,when the plane passes from a cell with many ice crystals to a cell with mainly cloud droplets.

The second case is the one of a more isolated cell B growing beside the skeleton of an older cloud. The Transall plane penetrates at - 15°C/3500 m MSL level (Fig. 5) firstly the precipitation of this old cloud characterized (Fig. 6) by big particles, then the growing cell A characterized by upward vertical velocity (5 to 10 m s^{-1}), small droplets (200 cm^{-3}) bearing a liquid water content of 0.2 to 1 g m^{-3} and ice crystals (columns of 500 µm) with a concentration of 300 l^{-1} and agglomerates (maximum diameter of 5 mm), a potential of the plane of -1000 kV which becomes positive during the lightning stroke, an electrical field variable but rather vertical. In this second case the plane was stroken by lightning almost in the middle of the cell.

CONCLUSION

From the study of the two above cases and a very fast review of the other cases that we have observed, with or without lightning stroke on the aircraft, we cannot evidently conclude for the moment.

The cases of lightning on the aircraft seem various. However, it appears that one find in the most part of the cases some identical characteristics :

- an activity of the cloud (that is to say vertical velocity),
- large ice crystals (graupels, agglomerates),
- discontinuities between parts of clouds with different microphysical, electrical and dynamical properties.

The plane seems to have been stroken by lightning, neither in very young cells, nor in very old dying cells, but in, near or between mature and yet active cells.

These results are in good agreement with the idea of Moore and Vonnegut (1977), Lhermitte (1978). Their merit is to bring qualitative and sometimes quantitative simultaneous measurements of electrical, microphysical and dynamical parameters to support them, but they must be completed by additional investigations. These investigations are going on ; they concern mainly the relationship between the microphysical and dynamical phenomena and the electrical phenomena. We hope to be able to present their results for the conference.

ACKNOWLEDGEMENTS

This work has been carried out with the support of the Division "Sciences du Globe" de la Direction des Recherches Etudes et Techniques du Ministère de la Défense, under the contract DRET/INAG/LAMP n° 83-308 and the contract DRET/ONERA n° 84.34.001 poste 331.

It is a duty and a pleasure for us to thank this organization, the Centre d'Essais en Vol de Brétigny which operated the Transall plane, and the participants of the Landes-Fronts experiment who helped us in many opportunities.

References

Gayet, J.F., 1979 : "Cloud microphysical parameters obtained with the DC7 aircraft", Workshop on Weather Modification, PEP Report n° 13, O.M.M.

Kuhlman, B.P., P.L. Rustan and J.S. Reazer, 1984 : "Characterization of a fast risetime electromagnetic pulse recorded inboard a airborne measurements during Florida thunderstorm", Intern. Aerospace and Ground Conference on Lightning and Static Electricity, June 26-28, 1984, Orlando, Florida, USA.

Laroche, P. et al., 1985 : "In-flight thunderstorm environmental measurements during the Landes 84 campain", paper presented at the 10th Intern. Aerospace and Ground Conference on Lightning and Static Electricity, Paris, 10-13 June 1985.

Mazur, V., B. Fisher and J. Gerlach, 1984 : "Lightning strikes to an airplane in a thunderstorm", Journal of Aircraft, vol. 21, n°8.

Moore, C.B. and B. Vonnegut, 1977 : "The thundercloud", Physics of Lightning (Vol. 1), Edited by R.H. Golde, Academic Press.

Lhermitte, R., 1978 : "Doppler radar and electrical radiation observations of thunderstorms", Preprint of Conf. on Cloud Physics and Atmospheric Electricity, Issaquah, Wash., July 31 - August 4 1978.

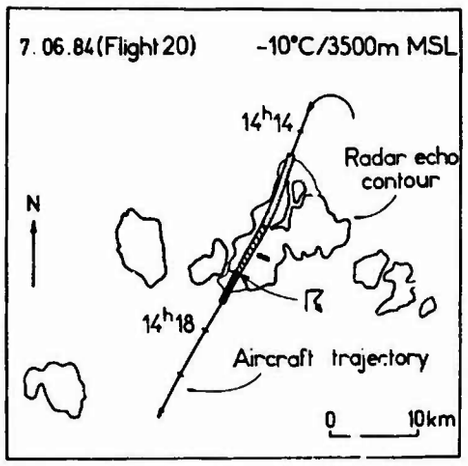


Figure 1 : Field of cloud echoes detected by the onboard meteorological radar and aircraft flight path given by the inertial platform. The trajectory portion represented by a thick line corresponds to the cloud limits detected by the microphysical probes. Dotted, hatched and darked portion represent the cells A, B and C respectively (see text). ⚡ symbol indicates the location of aircraft lightning strike.

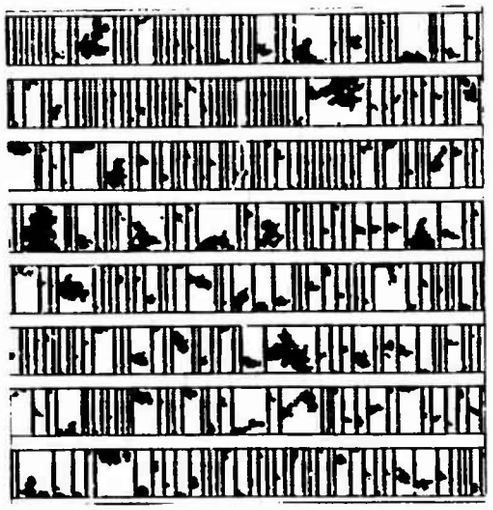


Figure 3 : Typical ice crystal agglomerats recorded by the 2D-P probe in the cell A. The distance between the horizontal lines is 6400 µm and the resolution is 200 µm. The vertical lines between images are time bars which give in a binary code the time during which the probe was not recording because no image was present.

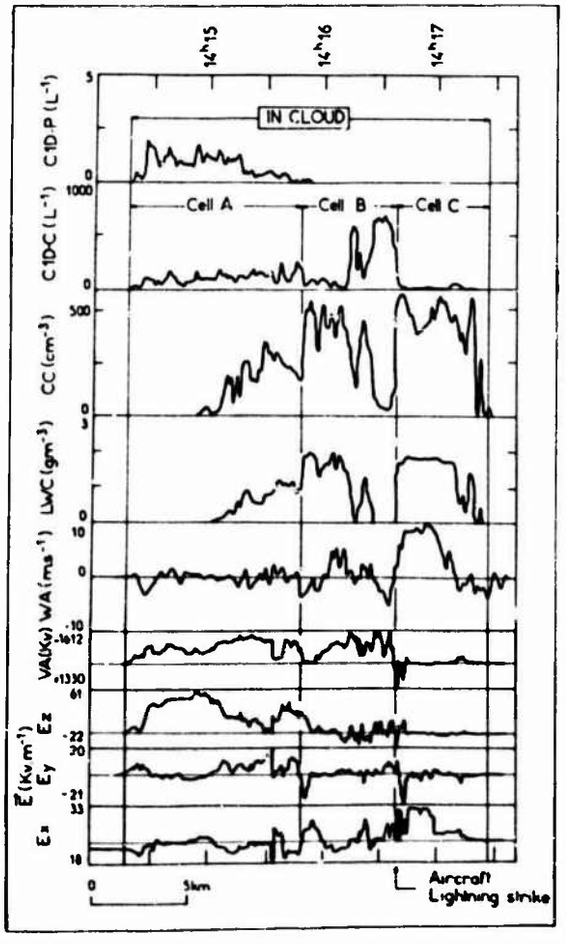


Figure 2 : Time variation along the flight track of the microphysical, dynamical and electrical parameters during the cloud penetration at - 10°C/3500 m MSL level. From the top to the bottom :

- C1D-P : concentration (l^{-1}) of particles ranging from 300 to 4500 µm size ;
- C1D-C : concentration (l^{-1}) of particles ranging from 60 to 300 µm size ;
- CC : concentration (cm^{-3}) of supercooled cloud droplets ranging from 3 to 45 µm diameter ;
- LWC : liquid water content ($g\ m^{-3}$) ;
- WA : vertical air velocity ($m\ s^{-1}$) ;
- VA : electrical potential of the aircraft (kV) ;
- Ex, Ey, Ez : components of the electrical field ($kV\ m^{-1}$).

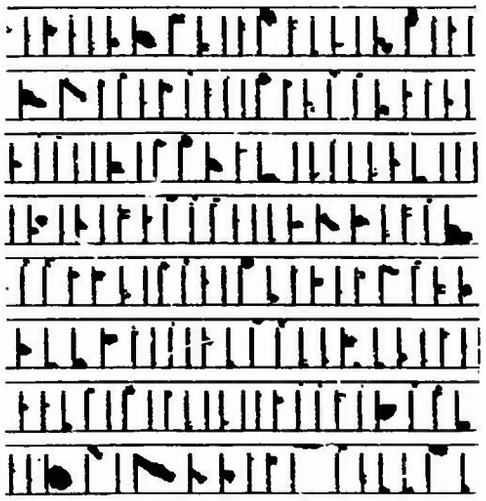


Figure 4-a : Example of ice columns measured by the 2D-C probe in the cell B. The distance between the norizontal lines is 800 µm and the resolution is 25 µm.

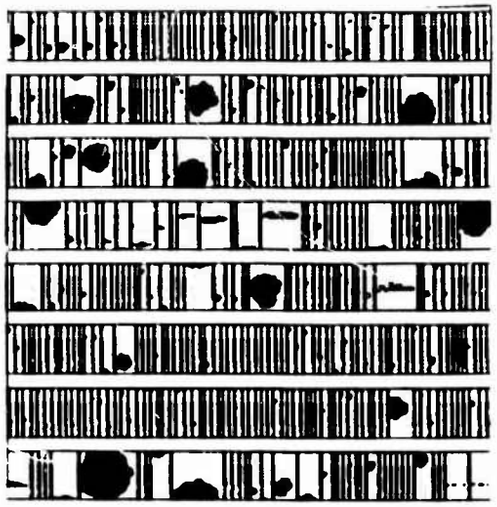


Figure 4-b : Typical large graupels sampled by the 2D-P probe in the cell B.

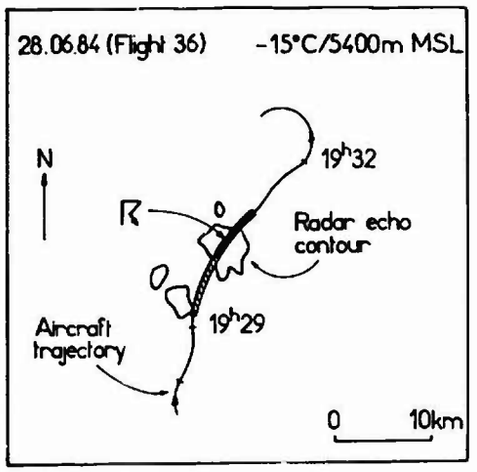


Figure 5 : Same caption as Fig. 1 for the second example of lightning strike on the aircraft.

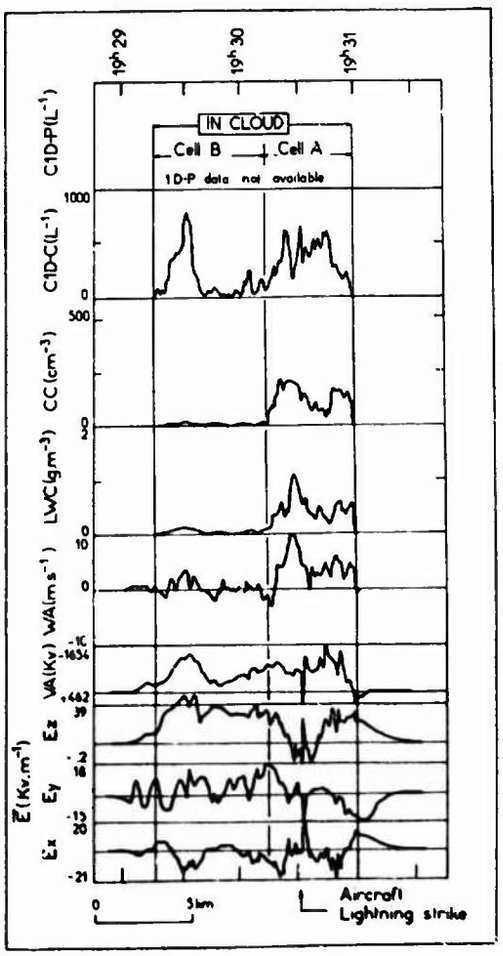


Figure 6 : Same caption as Fig. 2. Cloud penetration performed at -15°C/5400 m MSL level.

IN-FLIGHT ELECTRICAL CONDUCTIVITY MEASUREMENTS

P. Gondot and A. Delannoy

Office National d'Etudes et de Recherches Aérospatiales, B.P. 72, 92322 Châtillon Cedex, France

Abstract - The electrical behaviour of a convective cloud is related to global parameters as the atmospheric electric field and to local phenomena as the electrical charge of drops and droplets and the electric ionic conductivity. Conductivity around and inside clouds is not for the moment a well-known parameter but it plays an important role specially in the screening layers arrangment.
At the ONERA, sensors of conductivity of the Gerdien type were designed, to be installed on a Transall aircraft involved in a measuring campaign concerning thundercloud and lightning flashes studies. This campaign was held in South West of France during spring 84.
Three different sensors were used for the in-flight experiment:
a - a first cell of conductivity with an automatic bias device for conductivity, ionic density and mobility measurements,
b - a high voltage bias cell with a multi receiving electrode for the fast analysis of the cloud transition zones,
c - an adjustable bipolar high voltage bias.
We present in this paper typical sequences obtained during the experimental campaign, and we discuss the main results corresponding to electrical conductivity measurements.

I - INTRODUCTION

Electrical conductivity still remains one of the least understood factors in storm activity. The only experimental results available date from 1972 (Rust and Moore, 1974). The role of electrical conductivity in storm clouds is still a subject of controversy. Inside a cumulonimbus, electrical conductivity characterizes the capacity of the atmosphere to sustend an increase in electrical charge; electrical conductivity is a therefore important parameter in electrification.
The difference of values between clear air conductivity and conductivity along the surface of a thundercloud is at the origine of screening layers and is responsible for their growth.
The presence of screening layers has not yet been clearly established experimentally but is indicated by certain E field measurements as those by Marshall et al (1974).
For the LANDES-FRONTS 84 experiment, ONERA developed new types of sensors at ONERA to measure electrical conductivity in thunderclouds. We present here a brief description of the measuring principle of the devices developed, and a commentary on results obtained in the laboratory and in flight.

II - INSTRUMENTATION AND RESULTS OBTAINED

The sensor basic diagrams are given in figure 1. The operating principle is the Gerdien principle; the measuring chamber contains two coaxial cylindrical electrodes.
Air penetrates the capacitor and the ion paths are governed by their inlet speed and the air flow speed. Their drift speed is defined by the difference in potential applied to the electrodes 2 and 3. The ions are collected on an internal electrode 2. The sensor is installed on the airplane and operates by direct intake, i.e. without a suction device, the air flow being governed by the aircraft speed.
The conic air inlet 4 operates as an inertial filter by limiting hydrometeors penetration into the measuring chamber.
A clear air conductivity measurement was made with a prototype sensor on board the Transall 04 aircraft in the fall of 1984. The measurement results are given in figure 2. Comparison can be made of the Gish and Wait curve (1950; broken line), the positive conductivity measurements obtained by Gringel (dotted line) and our results (plured line); it is noticed that the three types of indications are equivalent. This preliminary experiment was instrumental in validating the cell operation in flight.
A second series of measurements was made during 1984. The measurements were performed in a cloudy flow in the Puy de Dôme wind tunnel at an altitude of 1465 m. This series of experiments enabled testing of the device in clear air, in cloudy and in icing conditions. Several distributions of ion mobility were obtained in clear sky (Gondot, 1985). Several measuring sequences were run in a flow originating from clouds covering the top of the mountain; they showed a reduction of 60 % in electrical conductivity with respect to clear air for a liquid water content of 0.3 gm^{-3}. We also observed that the mean ion mobility was reduced by 40 % inside the cloud. This reduction is attributed to ion hydration. However, the most important feature of this series was the confirmation of the sensor satisfactory operation in a non electrified cloud environment.
Three conductivity sensors were installed on the Transall aircraft for the LANDES-FRONTS 84 experiments.
- The first conductivity sensor was extended by using an annular Venturi device to measure the flow rate; the sensor was provided with an automatic cyclic variation of the high voltage bias to perform a detailed analysis of the environment by measuring three parameters

(conductivity, density and average mobility) at a mean spatial resolution of 100 m.

- The second sensor can operate alternatively at positive or negative polarity with a constant voltage. The voltage level can be set in flight.
- The third sensor's design is less standard; it contains a measuring electrode divided into four sections. The simultaneous measurement of ionic currents from each section enables reconstruction of characteristic I = f(V) using 4 points; the voltage difference between the electrodes is held constant.

The sensors are supported on bases fixed to the pods under each wing of the Transall (Fig. 3). The preamplifier stage is housed in the sensor bare and the preconditioning packages containing the high voltage modules are installed in the pods. The signals are output from the packages under low impedance and flow through the wings to the interior of the fuselage where they are acquired and digitized by an HP-A900 computer at a rate of 128 words/s. They are also acquired, in parallel, by an analog wideband system (0-500 kHz).

Signal analysis from the divided electrode sensor is identical with that of the characteristic I = f(V) sensor obtained by polarization drift. The following relations are used for:

- conductivity : $\lambda = \frac{\varepsilon_o}{C} \frac{dI}{dV}$
- ion total density : $n = \frac{I_s}{Q_e}$

mobility distribution : $f(k) = \frac{CV^3}{\varepsilon_o Q_e} \left| \frac{d^2I}{dV^2} \right|$

with C : capacitor capacitance,
I_s : saturation current,
Q : flow rate,
e : elementary charge,
ε_o : air permittivity.

The clear air operation of the divided electrode is shown in figure 4, on which we plotted an equivalent global characteristic I(V) from the current values acquired simultaneously by the 4 electrodes. For this sequence the mean results over 4 s are: positive conductivity: $1.10^{-14}\ \Omega^{-1}m^{-1}$, positive ion density: 600 cm^{-3}, and mean ion mobility: $10^{-4}\ m^2.V^{-1}.s^{-1}$.

During the Landes 84 experiment, the Transall aircraft made several active cumulonimbus explorations. In most of the cumuliform cloud penetration sequences we observed s characteristic development of the conductivity signal. The microphysical parameters, the electric potential of the aircraft and the current signals acquired by all the conductivity sensors are plotted as a function of time and distance covered by the aircraft (Fig. 5).

The aircraft penetrated a cumulonimbus at an altitude of 5400 m (-15°C) under the conditions given in figure 5. All the conductivity sensors delivered current pulses A with a width of 200 ms, at a distance of 20 m before effective cloud penetration. Inside the cloud, measurements are disturbed by the impact of fine cloud droplets on the sensitive electrode to be of use. Figure 5 shows the effect of a clear air layer at an altitude of 6000 m separating two storm cells belonging to the same storm system.

During the cloud/clear-air transitions, the 4 measuring channels on the divided electrode sensor provided coherent measurement of type A pulses and an ionic current density gradient (B) of 2 pAm^{-1} over 70 m, which corresponds to an increase in positive ion density of 50 cm^{-3} per meter and to an ionic space charge of about 0.3 nCm^{-3} in the close vicinity of the cloud. The pulse associated with the change in the physical nature of the aircraft environment is visible during the cloud/clear-air transition as well as during the clear-air/cloud transition. This removes the doubt on an artifact due to degradation of sensor operation following penetration of cloud air into the measuring chamber.

Figure 7 emphasizes the systematic character of this observation. This experiment concerned very active cloud explored at an altitude of 3000 m (-2°C). The 250 ms wide type A pulse is practically synchronized with the clear air-cloud transition. Analysis of these same signals recorded simultaneously by an analog system, 500 kHz passband, confirms the presence of zone A and its isolation from the rest of the cloud (Fig. 9).

Finally, note that these pulses are independent of the electric potential of the aircraft cannot be attributed to an artifact generated by the electrostatic field at the outer surface of the probe.

III - DISCUSSION

Figure 6 illustrates an observed phenomenon associated with an increase in positive ion density. We may assume that the positive ions are drawn to the cloud, the negative ions repelled and an electrically monopolar air layer is created near the clear air-cloud interface. In this case, an additional increase in positive ion density may result from the elimination of recombination of ions of opposite polarity hence the formation of zones A and B. Unfortunately, we were not able to take a simultaneous measurement of negative ion denaity to collaborate our hypothesis.

Considering all of these measuring sequences, the location of zones A and B with respect to the clear air-cloud boundary seems to be related to altitude and perhaps more directly to the variation with altitude of clear air conductivity. The invariable width of the pulse (between 200 and 300 ms) should also be borne in mind.

Although we have not fully analyzed all the flight sequences of the LANDES-FRONTS 84 experiment to provide an irrefutable argument in favor of our assumption, we can state at the present time that out electrical characterization of the peripheral structure of the charge distribution of convective clouds has been validated by two techniques of measurement of the electric conductivity: simultaneous measurement of two ionic polarities ad rapid measurement of the divided cell type.

Furthermore, measurement of electric conductivity on the basis of this principle proved to be difficult inside the cloud mainly due to interference from droplets or ice crystals. We are not yet in a position to attribute the cause of this interference to charged droplets or ice particles, to contact electrification due to solid particles, or to fragmentation of liquid droplets.

Nevertheless, we have observed that over a large number of cloud penetration sequences, the signal reliability has been maintained over a few meters as long as the droplet water content does not exceed a critical threshold, whilst the presence of precipitation had only a slight influence on the measurements.

IV - CONCLUSION

The major result of these experiments is that two monopolar ionic density zones A and B located in clear air at the perimeter of convective clouds have been shown up by conductivity measurements. The presence of the clouds was also detected by hydrometeor density measurements.
In addition, electric field measurements performed on the perimeter of convective clouds in other experiments (Marshall, T.C. et al, 1984) tends to confirm the existence of a screening layer formed by cloud droplets charged by a ion flow drained by the cloud. This flow would hence condition the existence of zones A and B mentioned above; conversely, the screening layers most probably control the transfer of electrical charges to the cloud and largely condition its electrical activity.
The modelization of charge transfer between the cloud and its environment requires an accurate knowledge of the medium: peripheral dynamic structure, detailed hydrometeor population, electric conductivity values, cloud state of maturity, etc.
This is why it is anticipated that improving this type of measurements is a worthwhile effort for collecting the basic data necessary for model development.

V - ACKNOWLEDGEMENTS

This work has been carried out with the support of the Direction des Recherches Etudes et Techniques of the Defense Ministry.

REFERENCES

Gish, O.H. and Wait, G.R., "Thunderstorms and the Earth's general Electrification", J. Geophys. Res., 55, 473-484, 1980.

Gondot, P., "Définition et exploitation de capteurs destinés à la mesure de la conductivité électrique dans les nuages d'orage", Thèse de 3ème Cycle, Paris VI, 1985 (to be published).

Laroche, P., Dill, M., Gayet, J.F., and Friedlander, M., "In-flight thunderstorm environmental measurements during the Landes 84 Campaign", In this conference.

Markson, R., "Measurement of the Global Circuit", International Conference on Atmospheric Electricity, Albany (New York, June 1984.

Marshall, T.C. et al, "Screening Layers at the Surface of Thunderstorm Anvils", International Conference on Atmospheric Electricity, Albany (New York), June 1984.

Rust, W.D., and Moore, C.B., "Electrical conditions near the Bases of Thunderclouds in the South Western United States", 5th International Conference on Atmospheric Electricity, Garmisch-Partenkirchen, Sept. 1974.

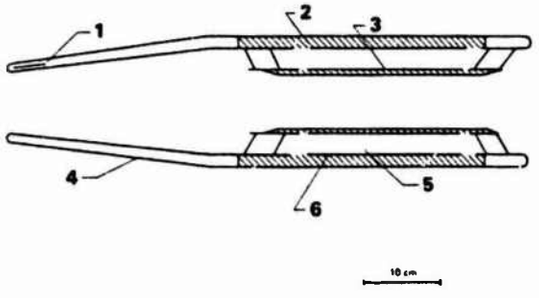


Fig. 1 - Conductivity sensor diagram.
1 - deicing
2 - insulation
3 - measurement electrode
4 - cone
5 - measuring chamber
6 - bias electrode.

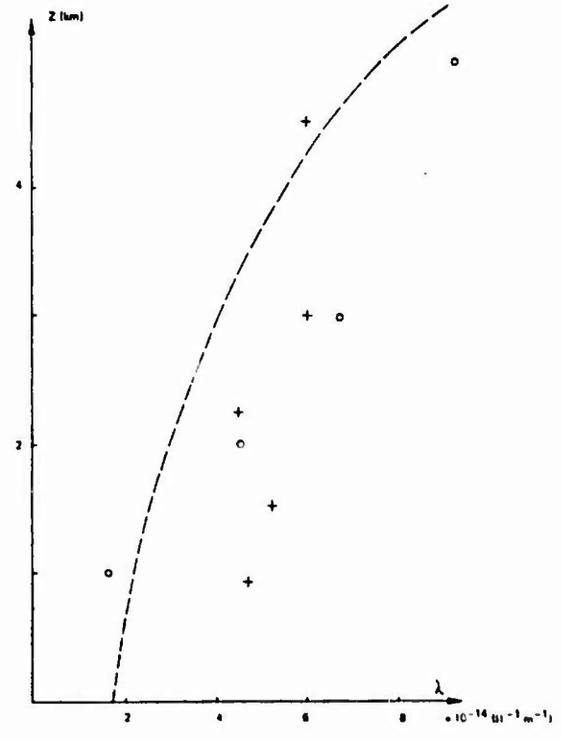


Fig. 2 - Positive conductivity profiles in clear air
--- Gish and Wait (1950)
o Gringel (1970) according to Markson (1984)
+ ONERA 83 measurements

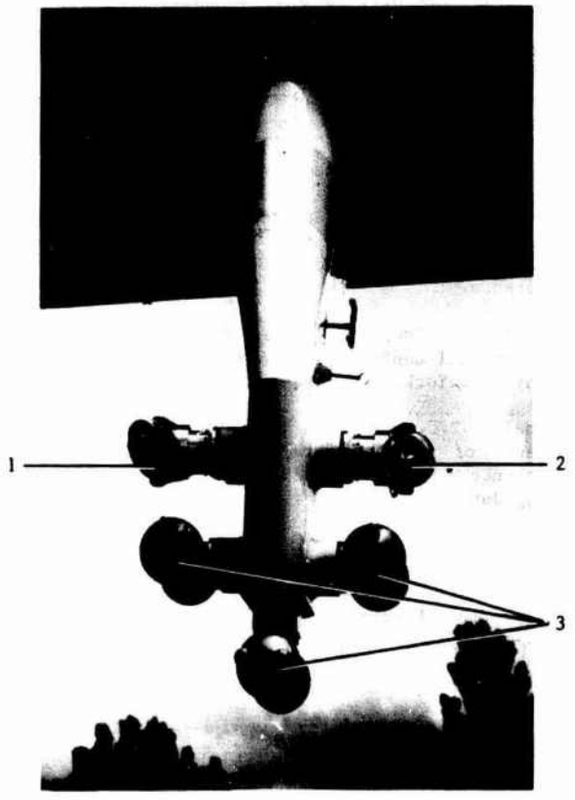


Fig. 3 - Microphysical and electric sensors locations on the aircraft.
1. Ionic conductivity sensor
2. Ionic conductivity sensor
3. Microphysical sensors

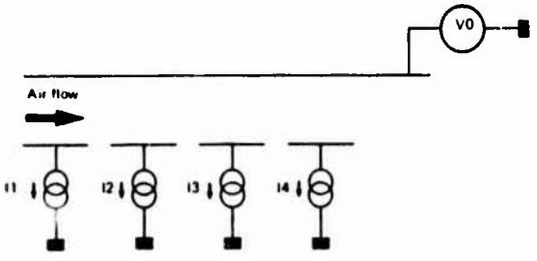


Fig. 4

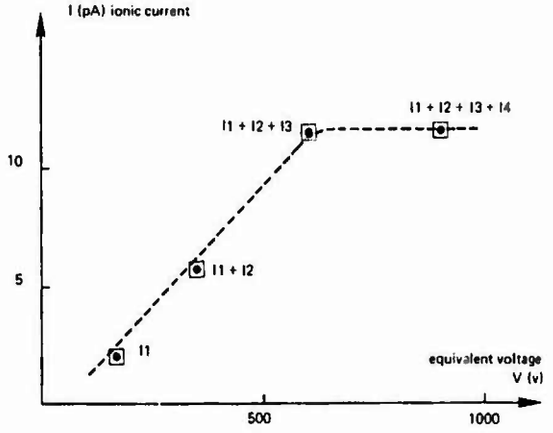


Fig. 4 bis

Fig. 4 - Example of the divided electrode cell operation: construction of a characteristic using the 4 signals delivered by the sensor.

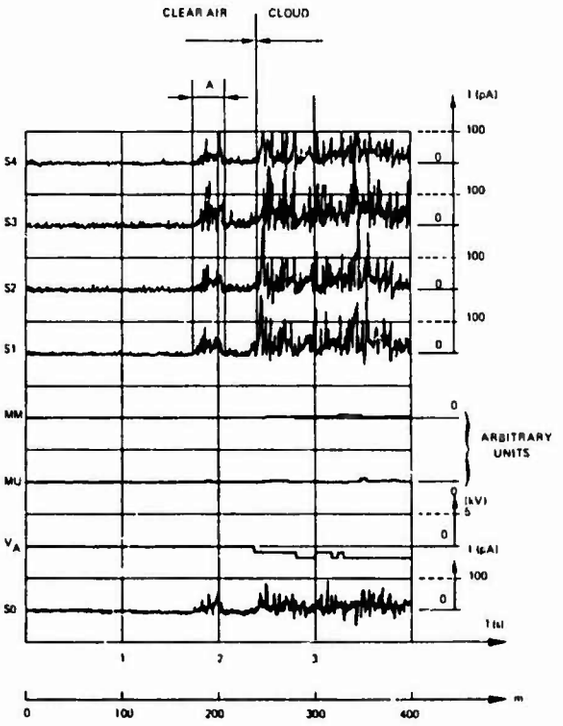


Fig. 5 - Penetration of a cumulonimbus at level -15°C
S_1 to S_4: the 4 divided electrode sensor signals,
S_0 : single electrode sensor signal,
V_A : aircraft potential,
MU : droplets liquid water content (3 to 40 µm in radius),
MM : precipitation liquid water content.

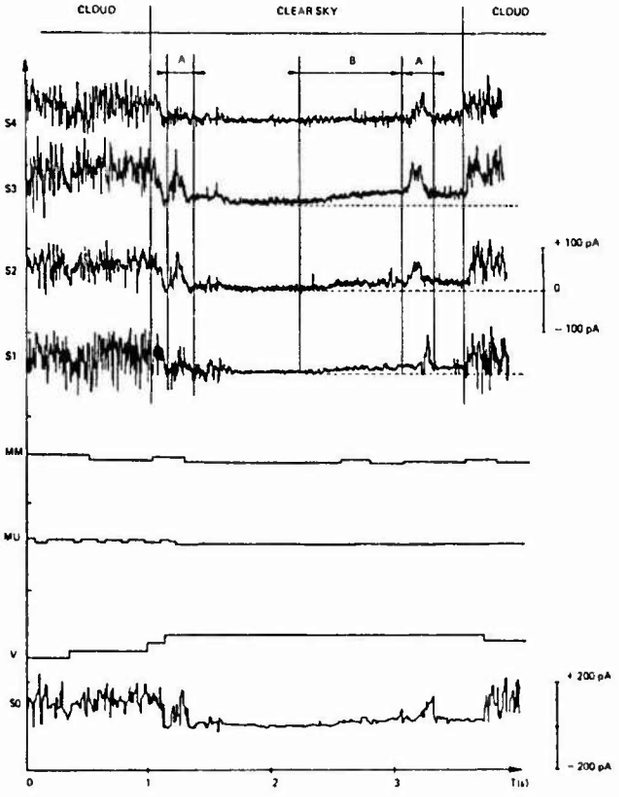


Fig. 6 - Crossing of two thunderclouds at an altitude of 6000 m.

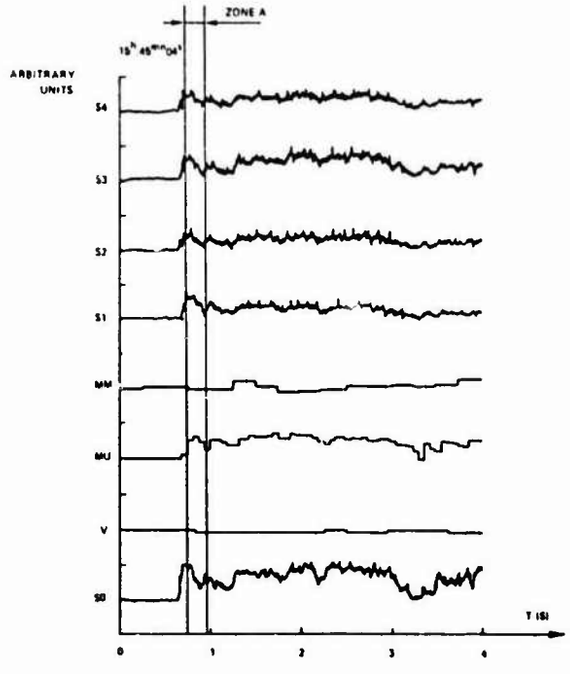


Fig. 7 - Penetration of a thundercloud at an altitude of 3000 m (same caption as Fig.5).

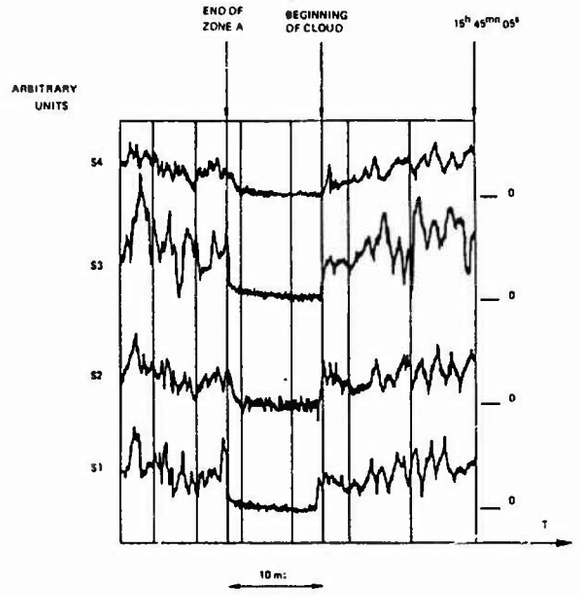


Fig. 8 - Detailed analysis of zone A from figure 7.

ELECTRIC CHARGE TRANSFER DURING RIMING

C.P.R. Saunders and E.R. Jayaratne

Department of Pure and Applied Physics, UMIST, Manchester M60 1QD, U.K.

Abstract - Electric charge transfer to an ice covered target due to ice crystal interactions has been studied in the laboratory and the charge transfer has been found to be a function of the impact speed, ice crystal size, environment temperature, impurity content of the ice and the presence of liquid water in the cloud. These studies simulate the fall of a hailstone through a thunderstorm cloud but also are applicable to charge transfer to ice coated metal targets which collide with ice crystals.

1. - Introduction

This work was prompted by reports of field based observations of thunderstorms in which the location of lightning charge centres has been determined. (Lhermitte and Krehbiel, 1979; Krehbiel et al, 1979, 1980). These authors provided radar, electric field and radiation data that indicates that the negative charge centres within thunderclouds are co-located with precipitation within well-defined temperature zones above the freezing level. The implication is clear that one of the principal thunderstorm charge transfer mechanisms involves collisions between soft-hail pellets (graupel) and ice crystals in the presence of supercooled water droplets. Airborne measurements have shown that precipitation sized particles in thunderclouds carry substantial charge, Christian et al (1980), Gardiner et al, (1984) and Vali et al (1984), adding credibility to the concept of particle charge giving rise to the major centres in thunderstorms.

Several laboratory studies of thunderstorms have shown that a significant charge is separated when ice crystals bounce off a hailstone leaving it charged. If this mechanism may be extended to natural thunderstorms, subsequent gravitational separation of the oppositely charged particles would set-up an electric field which is augmented by large numbers of similar collisions and charge separation events. Some discrepancies between reports of the early laboratory experiments, for example, those of Reynold et al (1957) and Latham and Mason (1961, a, b) were resolved by Jayaratne et al (1983) in terms of the requirement for the presence of liquid water in the cloud in order to obtain substantial charge transfer. Theoretical work by Illingworth and Latham (1977) and Rawlins (1982) has shown that the laboratory measured charge transfers are adequate when integrated over the whole active cloud volume to account for the magnitude of the charge values observed in thunderclouds which give rise to lightning strokes in which tens of coulombs of charge are transferred.

The present work is an extension of the studies by Jayaratne et al and has as its long term intent the isolation of the specific conditions under which charge is transferred between ice crystals and ice targets representing hailstones.

2. - The Experiments

Experiments have been conducted in a large, walk-in, cold chamber with temperature control down to -30°C and also in a deep-freeze. The experiments consist either of moving a target through a cloud on a rotating frame or of drawing a cloud past a stationary target. Figure 1 shows the rotating frame in the cold chamber. The target rod is gold-plated stainless steel and is connected to a high input impedance amplifier. The output passes via slip-rings out of the chamber to a data recorder. A cloud is produced in the chamber by introducing water vapour from a steam generator. Droplets form on cloud condensation nuclei and analysis has shown them to have sizes up to about 30μm with a median value at the start of an experiment of about 8μm. By briefly inserting a wire which has been dipped in liquid nitrogen, ice crystals are produced and they grow directly from the water vapour made available by the water droplets which evaporate. (The equilibrium vapour pressure over water is greater than that over ice at the same temperature.) Hence the conditions in the cloud change continuously throughout an experiment. As the ice crystals grow, so the water droplet sizes decrease until the concentration of crystals is sufficiently depleted by fall-out that the incoming water vapour is able to deposit on the droplets once more and increase their sizes back to the original values. Figure 2 shows a time sequence of droplet concentration, ice crystal concentration and mean size throughout an experiment. The ice crystals are nucleated at time t=0 and continuously fall out of the cloud attaining a maximum size of about 100μm. The liquid water content of the cloud also changes throughout a run, starting with a maximum value of 2gm^{-3} and falling to a fraction of a gm^{-3} during the experiment before rising again to its

initial value. The cloud particle concentrations and sizes are determined by means of a formvar replicator: a tube protrudes into the cloud chamber carrying within it a 16mm wide plastic film onto which is coated wet formvar solution (polyvinal formal dissolved in chloroform). At the end of the tube, a slot cut into the tube wall exposes the wet film to the cloud. The film is moved past the slot on rollers and air is drawn through the slot from an air pump. Cloud particles impinge on the film and their shapes are replicated in the plastic film which dries to make a permanent impression for later analysis.

Throughout a run the cloud was illuminated and visual observations of the cloud were maintained through a window in the chamber. When water droplets were present, the visibility was low; when the droplets were depleted by the growing crystals, the visibility improved and the crystals could be seen as isolated points of light. A stage was reached during each experiment when the droplets re-appeared in the cloud, this situation was readily observable and analysis of the replicator showed that the liquid water content was less than $1gm^{-3}$. This stage has been called the reference stage of the experiment and its use permits comparison of data, at different temperatures for example, because it provides a fixed set of experimental parameters that occur at one moment in all the experiments conducted.

Figure 1 also shows the stationary target past which the cloud could be drawn. The stationary target could be used with velocities up to about $10ms^{-1}$ while the rotating target was limited to $3.5ms^{-1}$ in order to prevent possible spurious effects due to high rotational forces. When operated at the same speed, both stationary and rotating targets gave the same result. Another experiment in a deep freeze was conducted with high speed revolutions up to $20ms^{-1}$ in order to compare with other worker's results. The charge that was transferred to the targets was converted to a measurable voltage such that a charging current of 10^{-13}A produced an output of 1mV. From a knowledge of the crystal concentration, and with an assumption of the target collection efficiency for colliding crystals, a value of the charge removed per separating crystal could be determined; this value is called the charge per event.

3. - Results

Having been used to provide vapour for crystal growth, the steam generator was turned off which permitted some experiments to be performed with no liquid water present. In these experiments the surface state of the ice-covered stationary target and the crystals could be controlled by heating the target externally or internally, or by cooling the target before the experiment, or by passing the crystals through a heated tube or through a heated tube lined with moist blotting paper. The results showed that the target charged negatively when the target ice was evaporating and the crystals were also evaporating. The target charged positively when its surface was growing by vapour deposition for both growing and evaporating ice crystals. Thus it was concluded that a growing surface charges positively while an evaporating surface charges negatively. This result produced charge transfers of very low magnitude, typically below 0.25fC where $1fC = 10^{-15}C$ and required high velocities of $\sim 10ms^{-1}$ to obtain a detectable signal. Such high velocities and small charge transfers are not relevant to thunderstorms where the relative velocities between small hail and ice crystals is around $3ms^{-1}$. Other workers have also noted this charge-sign dependence on the evaporation or growth of the ice target and have suggested that a contact potential mechanism is active. (Buser and Aufdermaur, 1977; Marshall et al 1978). However, Caranti and Illingworth (1980) did not observe a change in the contact potential of ice when it changed from a growing to an evaporating state.

The major part of the studies was performed in the presence of supercooled water droplets. Figure 3 shows the current measured to the riming target at three temperatures. The results have distinct characteristics and were quite reproduceable. The initial positive peak occurs shortly after the cloud is seeded and is associated with a high concentration of very small ice crystals ($\sim 10\mu m$) together with a high value of liquid water content. After this peak the cloud is rapidly depleted of water droplets and vapour which results in a low liquid water content; then the charging current decreases. When the liquid water content increases again, the charging current increases positively at warm temperatures (above -20°C) and negatively at colder temperatures. When the crystal cloud is exhausted due to fall out, the current returns to zero. At -20°C, the charging current reverses sign again at about 2.5mins after seeding. These data and results of other similar experiments over a range of temperatures have been used to generate Figure 4 which indicates the charge gained by the target for each separating crystal as a function of temperature at the reference stage of the experiment. The velocity used was a realistic value of around $3ms^{-1}$. Figure 3 indicates that the presence of a water cloud is important; the second positive peak at -20°C is associated with the re-established liquid water content. The tendency for positive charging to be promoted in the presence of liquid water is evidently swamped at -25°C where the cold temperature is dominant even though the liquid water increases again at the end of a run. In other experiments, the water vapour supply was reduced during a run and in general this caused charge transfer to the target to change in the negative sense, becoming negligible once all the vapour in the cloud was exhausted. Experiments over a range of velocities at -11°C with positive rime charging showed a rapid increase of charge transfer per crystal separation event with velocity. (Figure 5). The average slope was 3.2 and is due to at least two effects; namely, the effect of the velocity

itself and the increased collection of liquid water at higher velocities due both to increased collision efficiency and to higher sweep-out rate. The higher rime accretion rate with higher velocity has the same effect as increasing the liquid water content which has been shown to promote positive charge transfer. This powerful dependence on velocity throws doubt on the relevance of the results of other workers who used velocities of ~10ms^{-1} and obtained significantly higher charge transfers than those reported here.

Figure 6 shows the charge per event as a function of the crystal size during two typical runs. It is clear that the slope for positive rime charging at warmer temperatures is greater than that for negative rime charging at colder temperatures. The difference may be attributable to the rime accretion rate which is higher when the crystal size is larger due to the increase of the liquid water content during the run after its initial decline. However, the very large dependence of charge transfer on crystal size indicates that in real clouds with crystals of several hundred microns in size, the charges transferred will exceed those measured here even though the relative velocity between the hail particle and crystal will be reduced.

Some experiments with a high rotation rate produced some surprising results. (Figure 7.) These results have since been verified with a stationary target and high crystal and cloud velocity. As the liquid water content becomes re-established in the cloud, the rimer charge reverses to negative. So, despite the expected effect of an increased rime accretion rate which usually favours positive charging, the high velocity leads to negative charging. The enhanced positive charging within the first two minutes of the experiment are not consistent with Figure 3. These experiments may indicate that high speed interactions do not provide results representative of thunderstorm conditions.

Experiments with cloud droplets carrying impurities were performed by spraying droplets from an ultrasonic atomiser. Firstly, it was confirmed that pure spray droplets gave similar results to the steam generated cloud. Figure 8 shows that ammonium sulphate promotes positive rime charging and sodium chloride leads to negative charging with an increased effect at lower temperatures. The solution strengths used are typical of those found in real clouds.

4. - Discussion

These results have shown that the sign and magnitude of the charge transferred to an ice target by interacting ice crystals is dependent on the temperature, the water content of the environmental cloud, the velocity of impact and the impurity content of the droplets; the magnitude of the charge transfer is highly dependent on the ice crystal size.

Experiments with ice crystals alone hitting an evaporating or growing target showed that the surface state of the target ice controls the sign of the charge transfer. The experimental result that the contact potential is not affected by whether the surface is growing or evaporating implies that this mechanism cannot explain the sign of the charge transfer. The present experiments also showed that the temperature difference between the interacting surfaces played no role in the charge transfer. When liquid water droplets are present in the cloud, the charge transfer is typically two orders of magnitude larger than with ice crystals alone. Here, the liquid water must be playing an important part in controlling the way in which the crystals interact on the rime surface. The water droplets themselves will collide with the target (if above a certain size for a given airstream velocity) and will freeze on impact with the riming surface. At cold temperatures, the droplets freeze very rapidly and Caranti and Illingworth (1980) have shown that there is a contact potential difference between a rimed ice surface and an unrimed surface. Such a potential difference may explain the negative charge transfer to riming surfaces at cold temperatures. At warmer temperatures, or at higher rime accretion rates, the droplets take longer to freeze on the rime surface and while freezing with their surface temperature close to 0°C, they may provide a local super-saturation (Nix, Fukuta 1974) that causes growth of the regions of the surface being bombarded by ice crystals. Here the positive charging of a growing surface may be the dominant effect which swamps the contact potential effect. Further analysis of these two competing mechanisms is required - they follow from discussions with Caranti, Illingworth and Hallett and are only tentative suggestions at present.

References

Buser O. and Aufdermaur A. N. 1977 Electrification by collision of ice particles on ice or metal targets. Electrical processes in atmosphere, Steinkopf, Darmstadt.

Caranti J. M. and Illingworth A. J. 1980 Surface potentials of ice and thunderstorm charge separation. Nature, 284, 44-46.

Christian H., Holmes C. R., Bullock J. W., Gaskell W., Illingworth A. J. and Latham J. 1980 Airborne and ground-based studies of thunderstorms in the vicinity of Langmuir Laboratory. Quart. J. Roy. Met. Soc., 106, 159-174.

Gardiner B., Lamb D., Pitter R., Hallett J. and Saunders C. P. R. Measurements of initial eletric field and ice particle changes in Montana summer thunder-

storms. (Jour. Geophys. Res., 1985 In Press)

Illingworth A. J. and Latham J. 1977 Calculations of electric field growth field structure and charge distribution in thunderstorms. Quart. J. Roy. Met. Soc., 103, 281-295

Jayaratne E. R., Saunders C. P. R. and Hallett J. 1983 Laboratory studies of the charging of soft-hail during ice crystal interactions. Quart. J. Roy. Met. Soc., 109, 609-630

Lhermitte R and Krehbiel P. R. 1979 Doppler radar and radio observations of thunderstorms, IEEE Trans. Geosci. Electronics, GE17, 162-171

Krehbiel P. R., Brook M. and McCrory R. A. 1979 An analysis of the charge structure of lightning discharges to ground. J. Geophys. Res., 84, 2432-2456

Krehbiel P. R., Brook M., Lhermitte R. L. and Lennon C. L. 1980 Lightning charge structure in thunderstorms, in Proc. Int. Conf. Atmos. Elec., Manchester

Latham J. and Mason B. J. 1961a Electric charge transfer associated with temperature gradients in ice. Proc. Roy.Soc., A260, 523-536

Latham J. and Mason B. J. 1961b Generation of electric charge associated with the formation of soft hail in thunderclouds, ibid, 537-549

Marshall B. J. P., Latham J. and Saunders C. P. R. 1978 A laboratory study of charge transfer accompanying the collision of ice crystals with a simulated hailstone, Quart. J. Roy. Met. Soc., 104, 163-178

Nix N. and Fukuta N. 1974 Nonsteady-state kinetics of droplet growth in cloud physics. Journ. Atmos. Sci., 31, 1334-1343

Rawlins F. 1982 A numerical study of thunderstorm electrification using a three dimensional model incorporating the ice phase. Quart. J. Roy. Met. Soc., 108, 779-800

Reynolds S . E., Brook M. and Gourley M. F. 1957 Thunderstorm charge separation. J. Met., 14, 426-436

Vali G., Cupal J., Saunders C. P. R., Winn W. P. 1984 Airborne measurements of the electrical charges of hydrometeors. Proc. Int. Conf. on Cloud Physics, Tallin

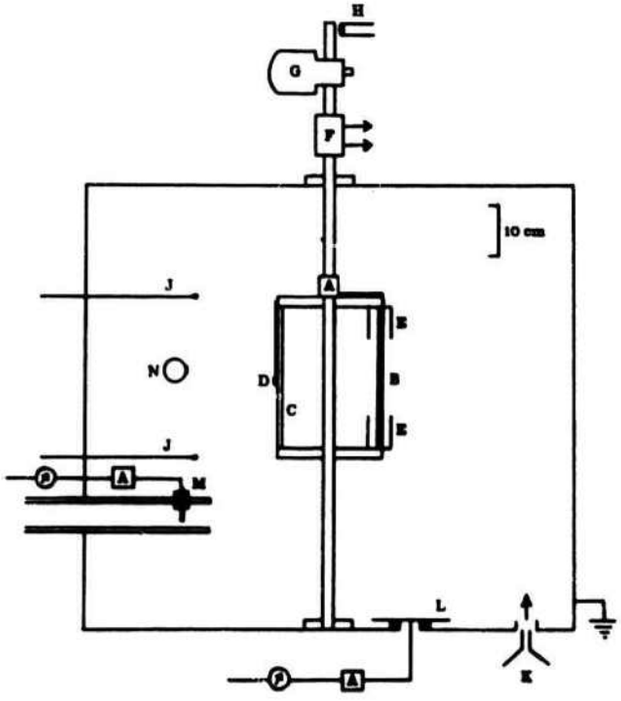


Figure 1. The experimental cold chamber A, amplifiers; B, target rod; C, control rod; D, thermistor; E, shielding cups; F, slip rings; G, motor; H, revolution counter; J, thermocouples; K, steam kettle; L, crystal collector plate; M, stationary target; N, formvar replicator.

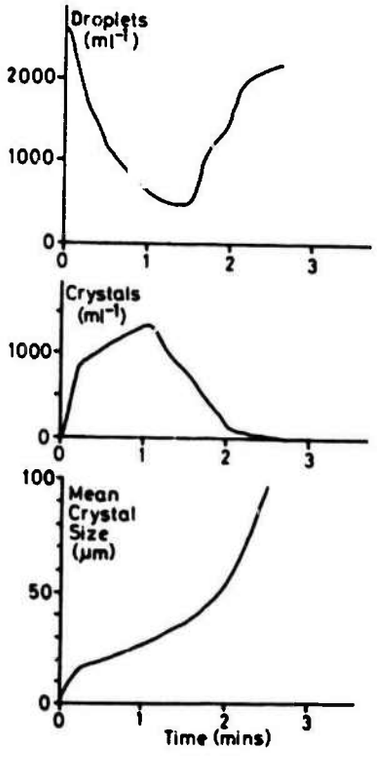


Figure 2. Particle concentrations and sizes observed on the formvar replicator. Temperature -6°C; rod speed 2.9 ms^{-1}; initial liquid water content 2gm^{-3}.

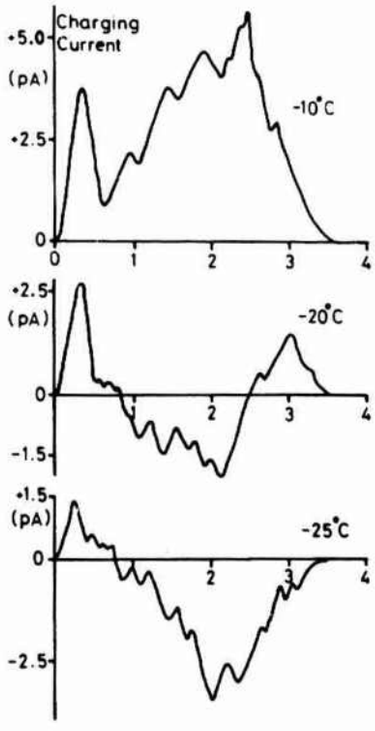


Figure 3. The rotating rod charging current as a function of time at three temperatures. The reference stage is marked by three arrows. Rod speed $3ms^{-1}$.

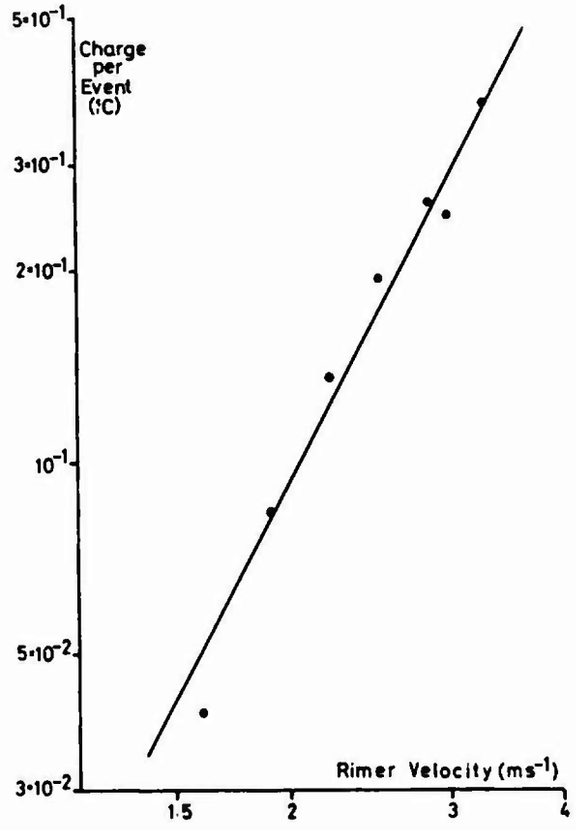


Figure 5. The charge per event as a function of rod speed at the reference stage of experiments conducted at $-11^{0}C$ and liquid water content $1gm^{-3}$.

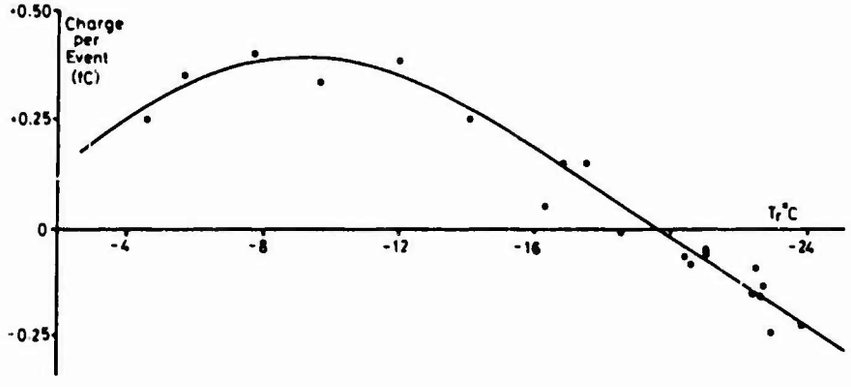


Figure 4. The charge per event at the reference stage of runs conducted at various rime temperatures. Rod speed, $2.9ms^{-1}$; liquid water content, $1gm^{-3}$.

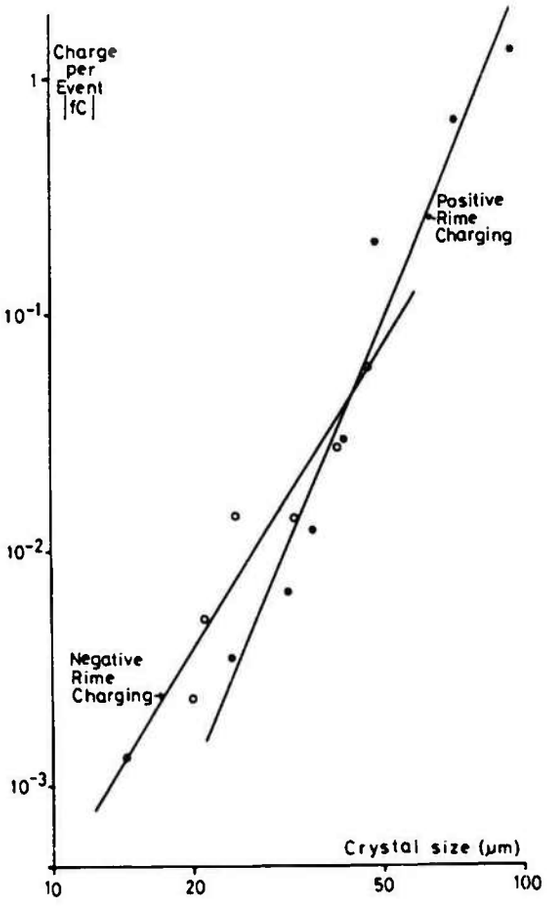


Figure 6. The charge per event as a function of crystal size for positive rime charging at a rime temperature -6°C, and negative rime charging at a rod speed 2.3ms^{-1} and rime temperature -21°C.

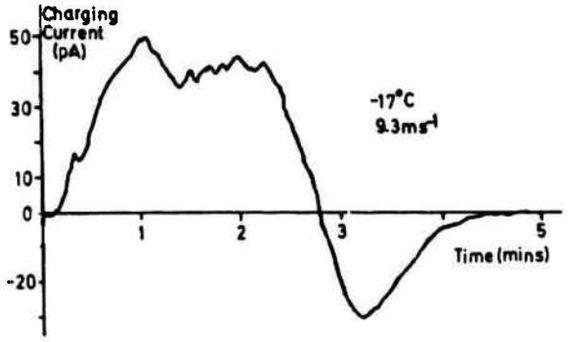


Figure 7. Rime charging produced by high speed rotation

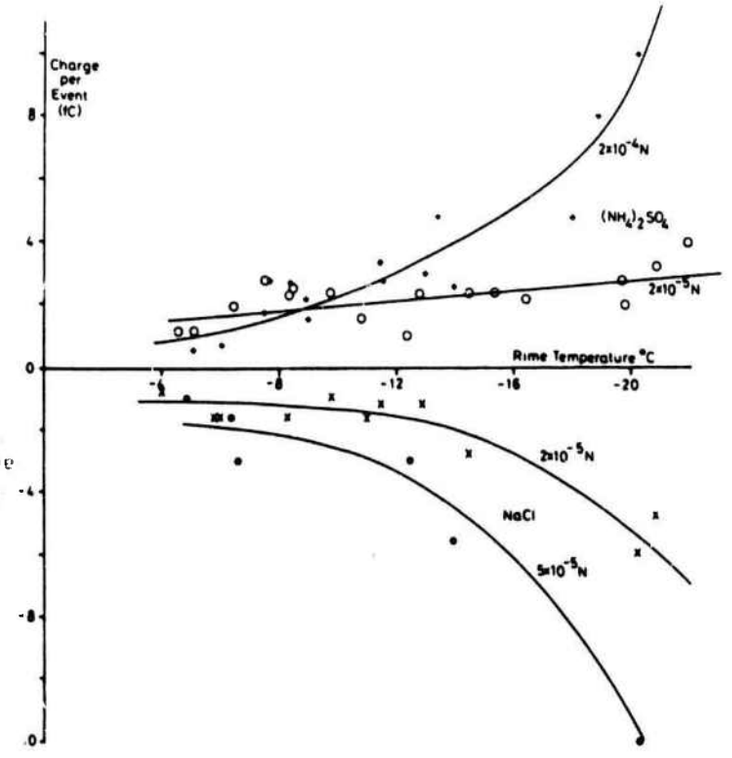


Figure 8. The charge per event at the reference stand as a function of rime temperature when the droplets in the cloud contained dilute $(NH_4)_2SO_4$ or $NaCl_2$ solution; rod speed, 3ms^{-1}.

THUNDERSTORM CURRENTS AND LIGHTNING CHARGES AT THE NASA KENNEDY SPACE CENTER

E.P. Krider, R.J. Blakeslee* and L.M. Maier

Institute of Atmospheric Physics, The University of Arizona, Tucson, Arizona 85721, U.S.A.

Abstract - The NASA Kennedy Space Center (KSC) and the U. S. Air Force are currently operating an extensive network of ground-based electric field milla in order to detect atmospheric electrical hazards to ground operations, launches, and landings of spacecraft. Over the past 10 years, the University of Arizona haa utilized data provided by this network, and other instrumentation, to investigate the electrical atructure of thunderstorma and lightning in Florida. Recent analyses have included estimates of the Maxwell current density that thunderstorms produce at the ground and computations of the locations and magnitudes of lightning-caused changea in the cloud charge distribution. In thia paper, we will review this work and will ahow an example of how thunderatorm current patterns and lightning charges develop in both space and time.

I - INTRODUCTION

Over the years, many authors have aasumed that thunderclouds are relatively stationary distributions of electric charge with a region of diffuse positive charge above a more concentrated volume of negative charge [1-3]. When the cloud is producing lightning, however, this concept must be modified because, whenever a discharge occurs, the cloud electric field undergoes a large change, and between flashes this field usually recovers back to a value close to that before the discharge occurred. Clearly, if the cloud field is not steady, either when there is lightning or between flashes, then the cloud charges that produce this field cannot be steady.

A much better approximation is to asaume that the cloud is a steady current source [4-6], and, in this case, the observational quantity that is of primary interest between discharges is the Maxwell current density, $\vec{J}_m$ [7]. Note that

$$\vec{J}_m = \vec{J} + \partial\vec{D}/\partial t \ , \qquad (1)$$

where $\vec{J}$ is the current density produced by the motion of free charges, i.e., all field-dependent currents plus precipitation and convection currents, and $\partial\vec{D}/\partial t$ is the displacement current density. In order to conserve electric charge, $\vec{J}_m$ must be a solenoidal vector field, i.e.,

$$\vec{\nabla} \cdot \vec{J}_m = \vec{\nabla} \cdot \left(\vec{J} + \frac{\partial\vec{D}}{\partial t}\right) = 0 \ ; \qquad (2)$$

therefore, the lines of $\vec{J}_m$ will form closed loopa within and outside the cloud. Below a thunderstorm, many of the lines of $\vec{J}_m$ will close in the ground and will be vertical just above the ground.

Simultaneous measurements of $\vec{J}_m$ and $\vec{E}$ under active thunderstorms [8,9] show $\vec{J}_m$ to be closely approximated by $\partial\vec{D}/\partial t$ when $\vec{E}$ is close to zero, and the relative contributions of convection and conduction currents to $\vec{J}_m$ at these times to be usually small. This result was predicted by Krider and Musser [7] and can be expressed mathematically as

$$\vec{J}_m \approx \partial\vec{D}/\partial t \Big|_{\vec{E}\approx 0} = \varepsilon_0 \partial\vec{E}/\partial t \Big|_{\vec{E}\approx 0} \ . \qquad (3)$$

The significance of Equation (3) is that a measurement of just $\vec{E}$ as a function of time can often be used to estimate $\vec{J}_m$. We note that Equation (3) will not usually be valid within regions of heavy precipitation because of the contributions to $\vec{J}_m$ due to precipitation currents.

The changes in the cloud electric field that are caused by lightning have been studied by many investigators who have used them to infer characteriatics of both the discharges themselves and the associated changes in the cloud charge distribution [1,10-12]. In the most recent work [10,11], field changes were measured simultaneously at a number of different sites on the ground, and the results were interpreted in terms of an assumed model of the cloud charge distribution that was altered by the flash. The model that is usually assumed for cloud-to-ground lightning is that the change in the cloud charge is spherically symmetric or, equivalently, that the change can be described by the well-known point-charge relation. With thia assumption, the field change, ΔE_i, at a given horizontal distance, D_i, is given by

$$\Delta E_i = \frac{2QH}{4\pi\varepsilon_0 (H^2 + D_i^2)^{3/2}} \ , \qquad (4)$$

where Q is the net change in the total cloud charge, and H is the height of the center of this charge. The horizontal distance D_i is given by

$$D_i = \left[\left(X - X_{0i}\right)^2 + \left(Y - Y_{0i}\right)^2\right]^{1/2} \ , \qquad (5)$$

where X, Y are the coordinates of the cloud charge in the plane of the earth, and X_{0i}, Y_{0i} are the

* Present address: NASA Marshall Space Flight Center, Huntsville, Alabama 35812

coordinates of the measuring site. This model is certainly not unique, but it does contain just 4 unknown parameters, Q, H, X, and Y. If the number of measurements exceeds the number of unknowns, then the values of the unknowns can be found using a standard least-squares optimization procedure [10].

Following [11], we assume an intracloud field change can be described by a point dipole model, i.e., the field change, ΔE_i, at site i is given by

$$\Delta E_i = \frac{1}{2\pi\varepsilon_0 R_i^3}\left[\frac{3H(\vec{P}\cdot\vec{R}_i)}{R_i^2} - P_z\right] , \qquad (6)$$

where

$$\vec{P} = P_x\hat{x} + P_y\hat{y} + P_z\hat{z}$$

is the change in the three-dimensional dipole moment vector and

$$\vec{R} = (X - X_{0i})\hat{x} + (Y - Y_{0i})\hat{y} + H\hat{z}$$

is the three-dimensional position vector pointing from the measuring site to the dipole. If this model produces a better agreement with the measurements than the point-charge model, then we assume the lightning was an intracloud discharge.

Initial applications of the least-squares method by Jacobson and Krider [10] indicate that cloud-to-ground lightning in Florida effectively neutralizes tens of Coulombs of negative cloud charge, and that these charges are centered at altitudes where the ambient air temperature is -10° to -34°C. In a more detailed study of 4 flashes, Krehbiel et al. [11] have reported that individual return strokes in New Mexico neutralize charge that is centered at altitudes of -10 to -20°C, values that are consistent with but somewhat lower than the results of Jacobson and Krider.

In this paper, we will illustrate some attempts to use Eq. (3) to estimate Maxwell current densities under thunderstorms and Eqs. (4) and (6) to describe changes in the cloud charge that are caused by lightning. Our example will be a relatively small thunderstorm that occurred at the NASA Kennedy Space Center, Florida, on July 11, 1978.

II - DATA

The NASA Kennedy Space Center and the Cape Canaveral Air Force Station have been operating the network of field mills for about 10 years to identify atmospheric electrical hazards to ground operations, launches, and landings. These sensors measure the vertical electric field at 25 or more sites, and the network covers a total area of about 15×25 km^2. The instruments, the data acquisition system, and various scientific applications of the data have been described previously [7,10,12-14].

Figure 1 shows a map of the field-mill sites that were used during the summers of 1976, 1977, and 1978, the years of the Florida Thunderstorm Research International Program (TRIP) experiments [15]. Basically, the field at each site was digitized at a rate of 10 samples per second and stored on magnetic tape together with an accurate time code. The digitization accuracy was 30 V/m, and the dynamic range of the instruments covered field values from -15 kV/m to +15 kV/m with an accuracy of about 10% or better.

To provide both accuracy and rapid data processing, a computer algorithm very similar to that devised by Piepgrass et al. [14] was used to identify lightning. First, there was a coarse search for a field discontinuity in successive 1-second intervals; then when a discharge was detected, there was a careful determination of the flash time and the field-change value at each site.

Between flashes, the values of the displacement current when the field was close to zero [i.e., Eq. (3)] were accumulated and then averaged over consecutive 2.5-minute intervals to estimate the average Maxwell current density, $\bar{J}_m$, at each field-mill site.

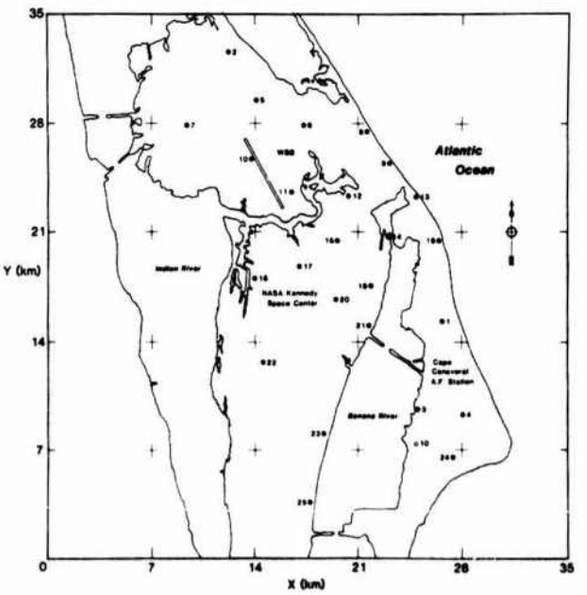


Fig. 1. The locations of electric field-mill sites at the NASA Kennedy Space Center.

III - RESULTS

Maps of the average Maxwell current density and the locations and magnitudes of lightning-caused changes in the cloud charges have been derived for several storms at KSC using the field-mill data. Figure 2 shows a sequence of Maxwell current maps for a small isolated thunderstorm on July 11, 1978. Here, the thin solid lines show isocurrent densities in increments of 0.5 nA/m^2, and the thin dashed contour is 0.25 nA/m^2. The Qs show the locations of cloud-to-ground lightning charges (point-charge model) and the Ps show intracloud discharges (point-dipole model). The heavy dashed and solid contours show plan views of the radar echoes at altitudes of 7.5 km and 10 km, respectively. Note in each panel of Figure 2 how the patterns of $\bar{J}_m$ are consistent with the locations of the lightning charges and the radar echoes. Note also how these patterns develop and change shape slowly with time.

An area-integration of a map of $\bar{J}_m$ provides an estimate of at least a lower limit for the total current produced by the cloud aloft and an upper limit to the total rate of charge transport to the earth [8,9].

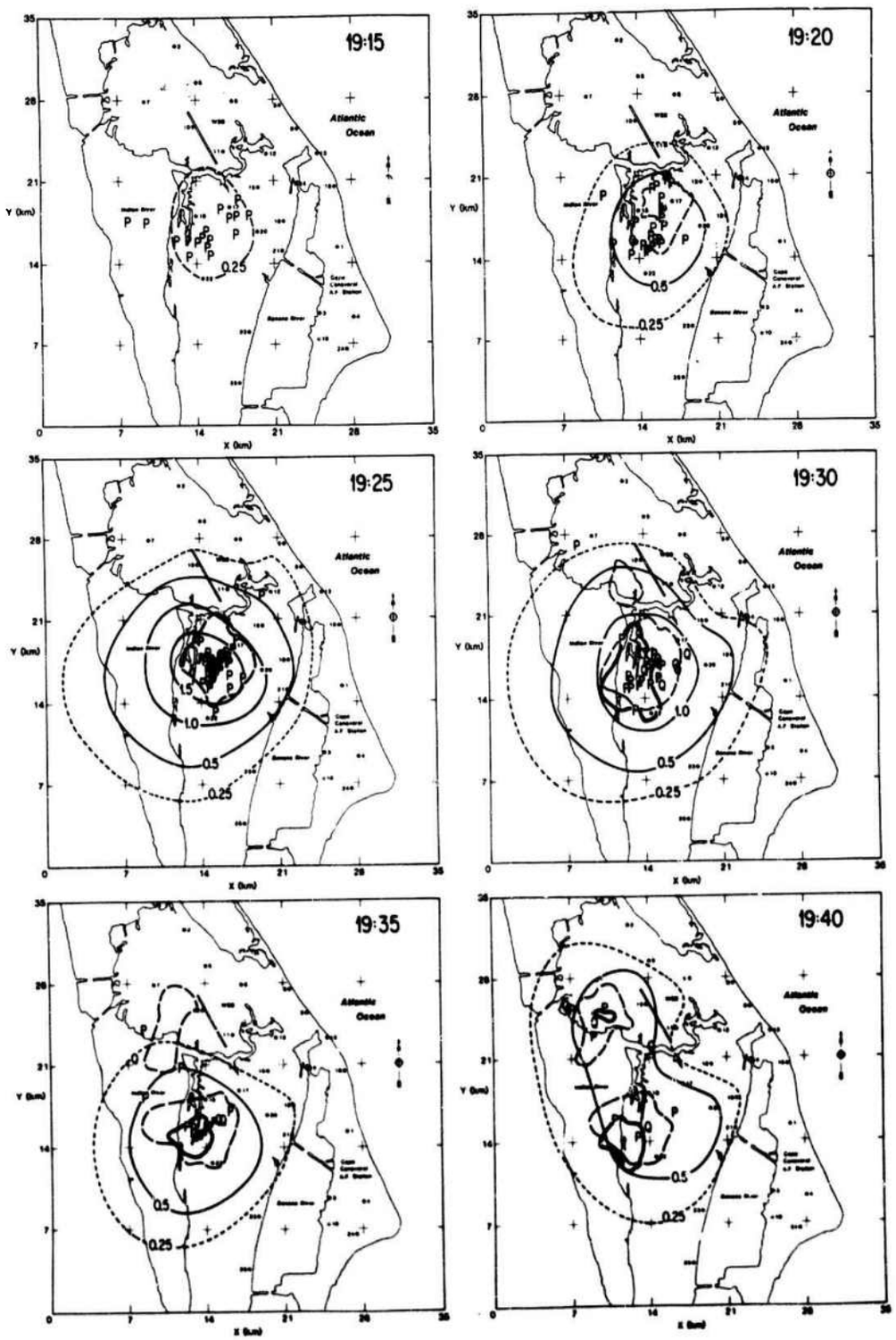


Fig. 2. A sequence of maps of $\bar{J}_m$ derived from field-mill data for a storm on July 11, 1978. The ending times (UT) of the averaging interval are shown in the upper right corner of each plot, and the locations of the active field-mill sites are shown as dots. Contours of iso-$\bar{J}_m$ are shown as thin solid lines in increments of 0.5 nA/m^2, and the dashed contour is 0.25 nA/m^2. The locations of lightning charges are marked with Qs and Ps, and the heavy dashed and solid lines show the locations of radar echoes at 7.5 km and 10 km, respectively, at 5-min intervals.

Curve 1 in Figure 3 shows the total current that has been derived for the storm on July 11, 1978. Note that there are two peaks in this current that are due to separate storm cells (see Figure 2) and that the larger of these cells peaks at about 0.45A.

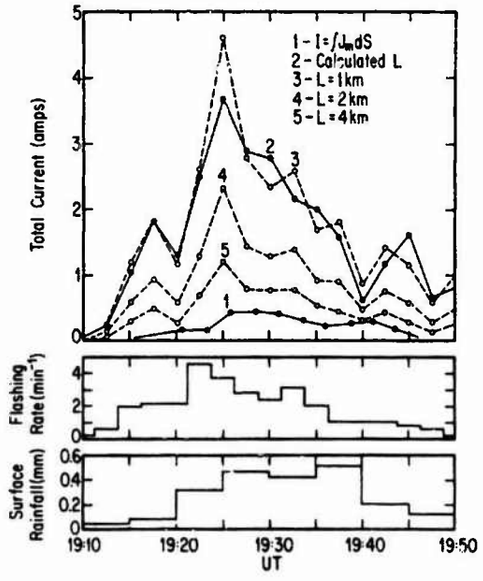


Fig. 3. The area-integrated Maxwell current density (curve 1) and estimates of lightning current (curves 2-5) as a function of time. The lightning rate and area-integrated rainfall are also shown. The lightning rate is averaged over 2.5-min intervals, and the rainfall is averaged over 5-min intervals.

The remaining curves in Fig. 3 show preliminary estimates of the total lightning current to (or from) the negative charge region. These curves have been derived by summing the charges for optimum Q and P solutions in successive 2.5-min intervals and then dividing by the duration of the interval (150 sec). In the case of P solutions, the charges were estimated by dividing each dipole moment by an estimate of the length of the dipole, L. In cases where L could be computed using a constrained 2-charge model, the mean length was 1.3 km, and it is this current that is shown in Curve 2. Curves 3, 4, and 5 show lightning currents where the L for each P solution have been assumed to be 1, 2, and 4 km, respectively.

Although the data in Figure 3 are preliminary, it should be noted that the average lightning current is substantially higher than the area-integrated J_m at the ground. Clearly, the overall charge budget of a thunderstorm is an important problem that needs further study.

As a final illustration, Figs. 4 and 5 show the altitudes and magnitudes of the changes in cloud charges and in the dipole moments for the Q and P solutions that were plotted in Fig. 2. Note in Fig. 4 that most Qs fall in a rather narrow range of altitudes, where the ambient air temperature is in the range from -15° to -30°C. These altitudes also tend to be constant throughout the development of the storm.

Most P solutions in Fig. 4 tend to be located above the Q altitudes, as would be expected for intracloud discharges between the negative charge level and an upper positive region. Some P solutions are below the Q level, and these tend to be reversed in polarity.

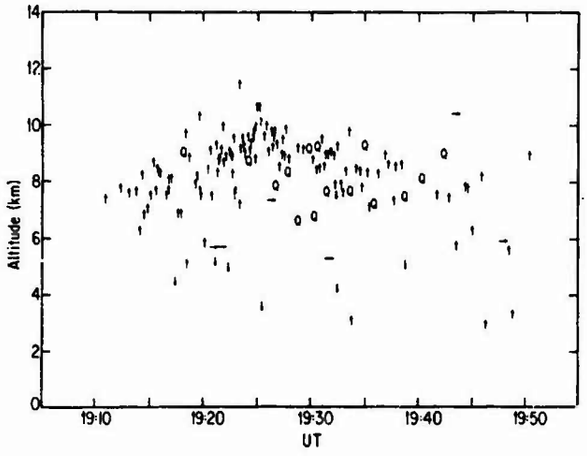


Fig. 4. The altitudes of lightning-caused changes in the cloud charge distribution that could be described by the point-charge model (Q) and the point-dipole (arrow). The polarities of all Q solutions are in the sense of negative charge being neutralized by the discharge, and an upward-directed arrow is in the sense of a P solution that had a positive charge above a negative charge being neutralized by the discharge. Horizontal arrows show those P solutions that had a horizontal component of $\vec{P}$ that was 90% of the total dipole moment or larger.

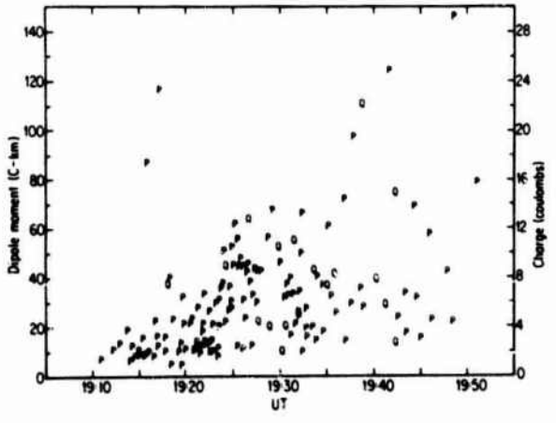


Fig. 5. The magnitudes of the charges and total dipole moments of Q and P solutions plotted in Figures 2 and 4.

During the early part of the storm, from 19:10 to 19:25 UT, the average altitude of the P solutions increased from about 8 km to 9.5 km. This increase ceased after there was a maximum in the lightning

rate and then gradually subsided to approximately 8 km at about 19:40 UT.

In Fig. 5, the charge values associated with cloud-to-ground lightning (Q) average 9.5 C with a large standard deviation. The magnitudes of the total dipole moments in cloud discharges (P) start at rather low values near 10 C/km and then increase to an average of about 30 C/km at about 19:25 UT. After this time, there may even be a future increase, but the number of discharges is limited.

IV - SUMMARY

Our studies to date show that Maxwell current patterns provide a good indication of the location and relative intensity of electrical storms and that there is good agreement between these patterns and the locations of lightning and radar echoes. There are also some new questions about how the average lightning current is related to the area-integrated Maxwell current and what is the electrical budget of a thunderstorm.

ACKNOWLEDGMENTS - This research has been supported in part by NASA contracts NAS8-34734, NAS10-10082, NAS8-36748, and NAS10-10958. The authors are particularly grateful to the NASA Kennedy Space Center for the use of their facilities, to W. Jafferis for his assistsnce during the field program, and to Msrgaret Ssnderson Rae for editing the manuscript.

REFERENCES

1. C.T.R. Wilson, Phil. Trans. Roy. Soc. London, A221 (1920) 73-115.
2. G. Simpson and G.D. Robinson, Proc. R. Soc. London, Ser. A, 177 (1941) 281-329.
3. C. Magono, Thunderstorms, Elsevier, Amsterdam, 1980.
4. R.E. Holzer and D.S. Saxon, J. Geophys. Res., 57 (1952) 207-216.
5. H.W. Kasemir, Zeit. f. Geophys., 25 (1959) 33-96.
6. H.W. Kasemir, in Problems of Atmospheric and Space Electricity, Elsevier, New York, 1965.
7. E.P. Krider and J.A. Musser, J. Geophys. Res., 87 (1982) 11171-11176.
8. R.J. Blakeslee and E.P. Krider, in Proceedings VIIth International Conference on Atmospheric Electricity, Am. Meteorol. Soc., June 3-8, 1984.
9. R.J. Blakeslee and E.P. Krider, submitted to J. Geophys. Res., 1985.
10. E.A. Jacobson and E.P. Krider, J. Atmos. Sci., 33 (1976) 103-117.
11. P.R. Krehbiel, R. Tennis, M. Brook, E.W. Holmes, and R. Comes, in Proceedings VIIth International Conference on Atmospheric Electricity, Am. Meteorol. Soc., June 3-8, 1984.
12. L.M. Maier and E.P. Krider, submitted to J. Geophys. Res., 1984.
13. J.M. Livingston and E.P. Krider, J. Geophys. Res, 83 (1978) 385-401.
14. M.V. Piepgrass, E.P. Krider, and C.B. Moore, J. Geophys. Res., 87 (1982) 11193-11201.
15. E.T. Pierce, Bull. Am. Meteorol. Soc., 57 (1976) 1214-1216.

GROUND ELECTROSTATIC FIELD CHANGES DUE TO LIGHTNING

M. Bala, K.C. Mathpal* and J. Rai

Department of Physics, University of Roorkee, Roorkee 247667, India

Abstract - In computing the electrostatic field and field changes due to lightning discharges, earlier workers have assumed thundercloud as the dipole model of point charges. In this paper the authors have improved the point charge model by considering a thundercloud of finite dimensions with spatially inhomogeneous charge distribution with positive and negative charges at the upper and lower regions respectively. Further, the finite width of the cloud was also taken into account. Such considerations provided more realistic computations of the electric field and field changes. The calculations are in good agreement with the experimental observations and theoretical predictions made by different workers so far.

I - INTRODUCTION

For calculating electric fields, dipole model of lightning is generally taken into account where it is assumed that the point of observation is at the same distance from every point of the discharge channel. This assumption is valid only for distances greater than about 10 km. Comparatively very little attention has been paid to the field changes very close to a lightning channel. Wilson /1,2/ considered a point charge which moves within the cloud or from cloud to the ground and then determined the electrostatic field changes. Pierce /3/ suggested the variation in the ground electric field in the intracloud discharges to be due to the vertical movement of charges within the cloud. Based on this argument, elementary theoretical calculations of electrostatic field changes, using simple bipolar point charges with upper positive and lower negative within a thundercloud were made by several workers /4,5,6,7/. Tiller et. al. /8/ measured the electrostatic field changes due to return strokes of lightning at distances from 1 to 15 km. Lin et. al. /9/ also reported the observations at 9 km. Krehbiel aet al. /10/ measured electrostatic field changes due to overhead lightning discharges. The dipole model of point charges as used by earlier workers is an over simplified approach and far from reality. Thus, Mathpal and Varshneya /11/ have improved the point charge model by considering a thundercloud of finite dimension with spatially inhomogeneous charge distribution with a net positive charge at the upper region and negative charge at the lower region. Further, the finite width of the cloud was also taken into account. Such considerations provided more realistic computations of the electric field changes. In this paper theoretical computations for the electrostatic field changes at a point on the ground surface as produced by an upward propagating streamer within the cloud (K-change) and an upward propagating positive streamer from ground to the cloud (return stroke) have been made for finite dimensions of the cloud.

II - THEORY

The theory considers a finite cloud dimension. The cloud is idealized of having a cylindrical shape with radius W /11,12,13/. The positive and negative charge regions, both have a width H. The origin of the coordinate is assumed to lie at the centre of the cloud (Fig. 1). The length of the charging zone is 2L. The radius of the streamer has been designated by R_s and the cloud base has been assumed to be at an altitude h from the ground. Caloulations have been made for K-changes and return strokes.

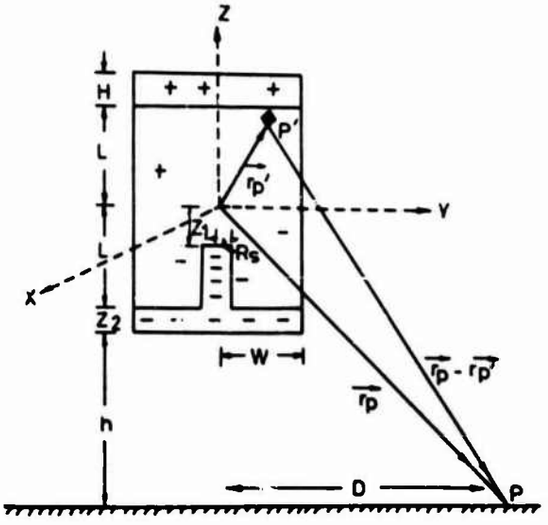


Fig. 1 - Cloud structure and charge distribution

*Present address - Sahu Jain College Najibabad (U.P.), India.

III - ELECTROSTATIC FIELD DUE TO K-CHANGES

Smith /14/ was first to have a detailed study of the intracloud discharges. He measured the electric field changes at two stations 13.5 km apart. From the measurements hs concluded that the intracloud discharges raised negstive charge from N-region to the P-region of the cloud. However, Takagi /15/ from his statistical studiss of the intracloud discharges gave a contrary view. The situation was clarified by Ogawa and Brook /5,16/ who showed that the K-changes sre preceded by downward positive streamers. Thus the K-changes are the counterpart of a return stroke in cloud to ground lightning. In this case the negative charge moves upward. The K-charges are known to be prsdominantly vertically oriented/17/.

The propagating streamer draws its charge from the N-region. The thicknsss of this region decreases with increase in the length of the strsamer. Let at any time t, Z_1 be ths vertical position of the tip of ths streamsr from the origin and the oorresponding thickness of the N-region be Z_2 (Fig. 1). Initially, when t = 0, $Z_1 = L$ and $Z_2 = H$. Thus, following Mathpal and Varshney /11/, the vertioal oharge distribution $\rho(Z')=\rho(\bar{r}_p')$ at point p' within the oloud at an instant t, can be written as -

(i) For region of cloud having streamer (the cloud width lying in between $-R_s$ and $+R_s$)

$$\rho(\bar{r}_p')=\rho(\bar{Z}',t)=\rho_o, \text{ for } L < Z' < L+H$$
$$=\rho_o\, Z'/L, \text{ for } Z_1 < Z' < L$$
$$= -\rho_o, \text{ for } -(Z_2+L) < Z' < Z_1 \quad ..(1a)$$

(ii) For region of oloud othsr thsn streamsr region (the oloud width lying in betwesn R_s and W on one side and in betwesn $-R_s$ and -W on the other side)

$$\rho(\bar{r}_p')=\rho(\bar{Z}',t)=\rho_o, \text{ for } L < Z' < L+H$$
$$=\rho_o\, z'/L, \text{ for } -L<Z'<L$$
$$= -\rho_o, \text{for } -(L+Z_2)<Z'< -L \quad ..(1b)$$

whsrs $\bar{r}_p'$ is the position vsotor of point p' and ρ_o is the maximum oharge density of each polarity. Consider a volume slemsnt $d^3 r_p'$, at p'. The potential funotion $d\phi(\bar{r}_p)$ at point p on the ground surfaoe, whoss position vsotor is r_p, due to this oharge element is g'ven by -

$$d\phi(\bar{r}_p)=\rho(\bar{r}_p')\, d^3 r_p' / (4\pi\varepsilon_o|\bar{r}_p-\bar{r}_p'|) \quad ..(2)$$

Expending $1/|\bar{r}_p-\bar{r}_p'|$ in terms of the sphsrioal harmonics, $Y_{\ell m}(\theta,\phi)$, one may get /17/

$$1/|\bar{r}_p-\bar{r}_p'|=4\pi \sum_{\ell}\sum_{m} \frac{Y_{\ell m}(\theta,\phi)\, Y^*_{\ell m}(\theta',\phi')(\bar{r}_p')^{\ell}}{(2\ell+1)\,(\bar{r}_p)^{\ell+1}} \quad ..(3)$$

Substituting Eq. (3) in Eq. (2), one gets

$$\phi(\bar{r}_p)= \frac{1}{\varepsilon_o} \sum_{\ell}\sum_{m} \frac{Y_{\ell m}(\theta,\phi),\ Y^*_{\ell m}(\theta',\phi')\rho(\bar{r}_p')\,(\bar{r}_p')^{\ell}\, d^3\bar{r}_p'}{(\bar{r}_p)^{\ell+1}(2\ell+1)} \quad ..(4)$$

Thus the potential function, $\phi(\bar{r}_p)$, at point p on the ground oan be written as-

$$\phi(\bar{r}_p) = \frac{2}{\varepsilon_o} \sum_{\ell}\sum_{m} \frac{Y_{\ell m}(\theta,\phi)\ q_{\ell m}}{(2\ell+1)(\bar{r}_p)^{\ell+1}} \quad ..(5)$$

The factor 2 is due to the effect of the electrical image of ths oharged region of the oloud. The multipole moments ($q_{\ell m}$) are given by-

$$q_{\ell m} = \int\int\int Y^*_{\ell m}(\theta',\phi')(\bar{r}_p')^{\ell}\rho(\bar{r}_p')d^3\bar{r}_p' \quad ..(6)$$

where the parameter ℓ must bs zero or a positive integsr and that the integer m oan take only the valuss $-\ell$, $-(\ell-1)$,--- -1, 0,1, ---$(\ell+1)$, ℓ.

Thus for $\ell = 0$, $m = 0$

and for $\ell = 1$, $m = -1, 0, 1$

The values of sphsrioal harmonios, $Y_{\ell m}$, for $\ell = 0$ and $\ell = 1$ are given by (Jaokson, /17/.

If one oonsiders only upto the dipole terms, the Eq. (5) reduoes to

$$\phi(\bar{r}_p)= \frac{2}{\varepsilon_o}\left[\frac{Y_{oo}q_{oo}}{r_p} + \frac{Y_{1,-1}\ q_{1,-1}+Y_{10}q_{10}+Y_{11}q_{11}}{3r_p^2}\right] \quad ..(7)$$

and

$$q_{oo} = \int_o^W \int_{-(L+Z_2)}^{(L+H)} \int_o^{2\pi} Y^*_{oo}(\theta',\phi')\rho(\bar{r}_p')\rho'd\rho'dZ'\, d\phi' \quad ..(8)$$

$$q_{oo}=\pi\left(\frac{1}{\pi}\right)^{1/2}\rho_o\left[W^2(H-Z_2)-R_s^2\left(\frac{Z_1^2}{2L} + Z_1 + \frac{L}{2}\right)\right]$$

One may find

$$W^2(H-Z_2) = R_s^2\left(\frac{Z_1^2}{2L} + Z_1 + \frac{L}{2}\right) \quad ..(9)$$

Thus $q_{oo} = 0$ and

$$Z_2 = H - \frac{R_s^2}{W^2}\left(Z_1 + \frac{L}{2} + \frac{Z_1^2}{2L}\right)$$

and $Z_1 = \int v_t dt - L$

$$q_{1,-1} = \int\int\int Y^*_{1,-1}(\theta',\phi')\bar{r}_p,\rho(\bar{r}_p,)\rho' d\rho' dZ' d\phi' \quad ..(10)$$

We know that

$$\int_0^{2\pi} \exp(-i\phi')\, d\phi' = 0 \quad ..(11)$$

hence

$$q_{1,-1} = 0 \quad ..(12)$$

and

$$q_{11} = \int\int\int Y^*_{11}(\theta',\phi')\bar{r}_p,\ \rho(\bar{r}_p,)\rho'\ 1\rho' dZ' d\phi' \quad ..(13)$$

Further

$$\int_0^{2\pi} \exp(i\phi')\, d\phi' = 0 \quad ..(14)$$

hence

$$q_{11} = 0 \quad ..(15)$$

and

$$q_{10} = \int\int\int Y^*_{10}(\theta',\phi')\bar{r}_p,\ \rho(\bar{r}_p,)\ \rho' d\rho'\ dZ'\ d\phi' \quad ..(16)$$

or

$$q_{10} = 2\pi\left(\frac{3}{4\pi}\right)^{1/2}\left[\frac{R_e^2\rho_o}{2}\left(-\frac{Z_1^3}{3L} - \frac{Z_1^2}{2} + \frac{L^2}{6}\right) + \frac{W^2\rho_o}{2}\left(\frac{(L+H)^2}{2} - \frac{L^2}{3} + \frac{(L+Z_2)^2}{2}\right)\right] \quad ..(17)$$

or

$$q_{10} = \pi(3/4\pi)^{1/2}\ \rho_o[I_1R_s^2 + I_2W^2] \quad ..(18)$$

where

$$I_1 = \left[-\frac{Z_1^3}{3L} - \frac{Z_1^2}{2} + \frac{L^2}{6}\right] \quad ..(19)$$

and

$$I_2 = \left[\frac{(L+H)^2}{2} - \frac{L^2}{3} + \frac{(L+Z_2)^2}{2}\right] \quad ..(20)$$

Now,

$$\bar{\phi}(\bar{r}_p) = \frac{2}{\varepsilon_o}\frac{1}{3r_p^2}(3/4\pi)^{1/2}\ \mathrm{Cos}\theta\ \pi(3/4\pi)^{1/2}\ \rho_o[I_1R_s^2 + I_2W^2]$$

or

$$\bar{\phi}(\bar{r}_p) = \frac{\rho_o}{2\varepsilon_o}[I_1R_s^2 + I_2W^2]\frac{\mathrm{Cos}\theta}{r_p^2} \quad ..(21)$$

From coordinate system

$$\mathrm{Cos}\theta = Z/r_p \quad ..(22)$$

and

$$r_p = (Z^2+D^2)^{1/2} \quad ..(23)$$

hence

$$\bar{\phi}(\bar{r}_p) = \frac{\rho_o}{2\varepsilon_o}[I_1R_s^2 + I_2W^2]\frac{Z}{(Z^2+D^2)^{3/2}} \quad ..(24)$$

where D ie the dietance between the cloud base to the point of observation and Z ie the vertical position of the origin of oo-ordinate eyetem from the ground. Thus

$$Z = h + H + L \quad ..(25)$$

The vertical electric field, E at a point at the ground is given by

$$E = -\frac{\partial\bar{\phi}}{\partial Z} \quad ..(26)$$

Aoooording to the convention used in the formulation of $\bar{\phi}(r_p)$, the electric field is poeitive when it ie direoted upward. However, in most works in atmoepheric electrioity, downward fielde are taken as positive. Therefore, following the later oonvention, Eq. (26) reduces to

$$E \quad \frac{\partial\bar{\phi}}{\partial Z} \quad ..(27)$$

where the elootric field E ie positive when it is direoted downward.

or

$$E = \frac{\rho_o}{2\varepsilon_o}[I_1R_s^2 + I_2W^2]\frac{D^2 - 2Z^2}{(Z^2+D^2)^{5/2}} \quad ..(28)$$

If Q' is the total negative oharge in the lower half region of the cloud, then

$$Q' = \int_0^W \int_o^{-(L+H)} \int_0^{2\pi} \rho' d\rho' \rho(\bar{r}_p,) dZ' d\phi' \quad ..(29)$$

or

$$Q' = -\pi W^2 \rho_o \left(H + \frac{L}{2}\right)$$

For calculating electric field and the field change, the current density and length of the channel for the K-change have been obtained using current and velocity expressions given by

$$I_t = I_o(\exp(-\alpha t) - \exp(-\beta t)), \quad V_t = V_o(\exp(-at) - \exp(-bt))$$

where I_o, V_o, α, β, a and b are the constants and their values are taken from Wadehra and Tantry /18/.

$I_o = 21$ K Amp., $V_o = 3\times10^7 ms^{-1}$, $\alpha = 5\times10^4\ s^{-1}$

$\beta = 2\times10^5 s^{-1}$, $a = 1\times10^4 s^{-1}$ and $b = 1.2\times10^5\ s^{-1}$

IV - ELECTROSTATIC FIELD CHANGES DUE TO RETURN STROKES

Return stroke is a ground to cloud discharge. In this case we consider the positive charge from the ground moving upward and obtain an expression for electrostatic field at a distance D on the ground surface. The effect of static charge of thunderoloud has also been taken into account. The total electric field E is given by

$$E = E_1 + E_2 \qquad ..(30)$$

where E_1 is the electric field due to the static charge on the cloud and E_2 is the electric field due to the propagation of upward positive streamer. The expression for E_1 as obtained by Mathpal /12/, is given as-

$$E_1 = -\frac{1}{2\pi\varepsilon_o}\left[\frac{(L+H)^2 - \frac{L^2}{4}}{H+L/2}\right]\left[\frac{(D^2-2Z^2)}{(Z^2+D^2)^{5/2}}\right]Q \qquad ..(31)$$

where Q is the total charge on the cloud.

For calculating electrostatic field due to the return stroke we used double exponential current and velocity expressions

$$I_t = I_o(\exp(-\alpha t) - \exp(-\beta t)), \quad V_t = V_o(\exp(-at) - (-\exp(-bt))$$

The values of constants for return stroke are given by-

$I_o = 22\times10^3 A$, $V_o = 9\times10^7\ ms^{-1}$, $\alpha = 1.6\times10^4\ s^{-1}$

$\beta = 5\times10^5\ s^{-1}$, $a = 3\times10^4\ s^{-1}$ and $b = 7\times10^5\ s^{-1}$

Here further as in the previous section,

$$q_{10} = \int_0^{R_e}\int_{-Z}^{-Z_1}\int_0^{2\pi} Y_{10}^*(\theta',\phi')\,\rho_o(\bar{r}_p,)\rho'\,d\rho'\,dZ'\,d\phi'$$

or

$$q_{10} = \rho_o 2\pi\sqrt{\frac{3}{4\pi}}\,\frac{R_s^2}{4}\,[Z_1^2 - Z^2] \qquad ..(32)$$

$$q_{oo} = \int_0^{R_s}\int_{-H}^{-Z_1}\int_0^{2\pi} Y_{oo}^*(\theta',\phi')\,\rho(\bar{r}_p,)\rho'\,d\rho'\,dZ'\,d\phi'$$

r

$$q_{oo} = \frac{R_s^2}{2}\,2\pi\,\frac{1}{\sqrt{4\pi}}\,\rho_o(-Z_1+H) \qquad ..(33)$$

and

$$[(\bar{r}_p) = \frac{2}{\varepsilon_o}\left[\frac{q_{10}Y_{10}(\theta,\phi)}{3r_p^2} + \frac{q_{oo}\,Y_{oo}(\theta,\phi)}{r_p}\right]$$

or

$$\frac{1}{2\varepsilon_o}\rho_o R_e^2(Z_1^2 - Z^2)\frac{Z}{(Z^2+D^2)^{3/2}} + \frac{2}{\varepsilon_o}\rho_o R_s^2(-Z_1+Z)\frac{1}{(Z^2+D^2)^{1/2}} \qquad ..(34)$$

Now,

$$E_2 = -\frac{\partial I}{\partial Z}$$

$$E_2 = -\frac{1}{2\varepsilon_o}\rho_o R_s^2\left[\frac{3Z^4 - 3Z^2Z_1^2}{(Z^2+D^2)^{5/2}} + \frac{Z_1^2 - 3Z^2}{(Z^2+D^2)^{3/2}}\right] + \frac{2}{\varepsilon_o}\rho_o R_s^2\left[\frac{2Z_1+Z^2}{(Z^2+D^2)^{3/2}} + \frac{1}{(Z^2+D^2)^{1/2}}\right] \qquad ..(35)$$

where $Z_1 = Z - \int V_t\,dt$

V - RESULTS AND DISCUSSIONS

In the present work the electrostatic field and field changes for K-changes and return-strokes have been calculated in time domain. We found that the total electrostatic field during an intracloud lightning discharge (negative charge moving up) decreases with the increase of either charge or distance or both. Though, the present calculations are in time domain, the results can be compared with those of Khastgir and Saha /4/. Khastgir and Saha /4/ reported the field about -25 KV m^{-1} and about -6 KV m^{-1} at a distance of 2 km and 5 km respectively. In the present case, the field at 1 km is -15.4 KVm^{-1} and at 5 km it is -6.3 KVm^{-1} for

a cloud charge of 40C. Thus the present values are in accordance with those given by Khastgir and Saha /4/.

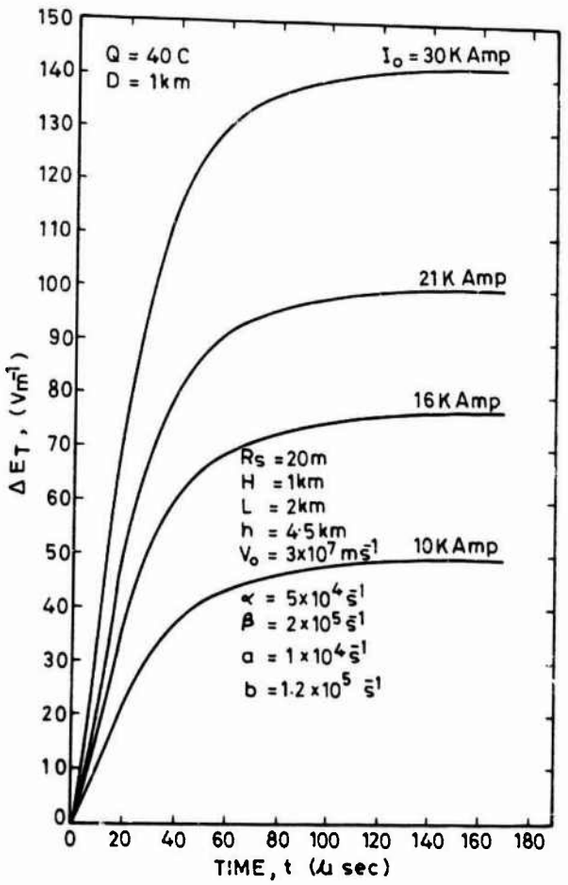


Fig.2 - Variation of total electrostatic field change ΔE_T with time at D=1 km and Q=40C, for various values of current I_o, for a K-change

Figure 2 shows the variation of total electrostatic field change ΔE_T due to a K-change above ambient level with time for different values of I_o(10-30 Kamp). The field change increases with increasing current. The instantaneous electrostatic field changes(for different values of I_o and α) with time for K-change have been shown in Fig. 3. The calculations for distances greater than 7 km have not been made because beyond the above distance the induction field may also contribute to the field changes. Our values are in good agreement with the results of Ogawa and Brook /5/ and Khastgir and Saha /4/.

The instantaneous electrostatic field change has also been calculated with time for different values of the streamer radius R_s. The field is found to be insensitive to the

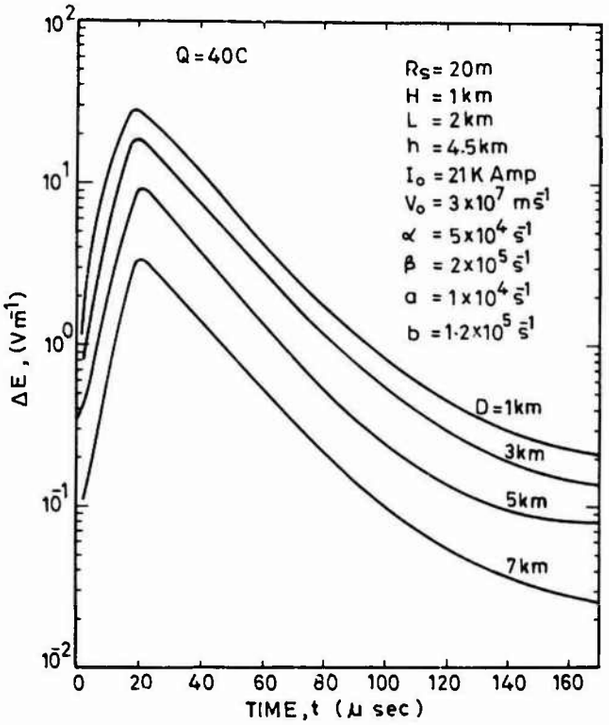


Fig.3 - Variation of instantaneous electrostatic field change ΔE with time at Q=40C, for various values of distance D, for a K-change

radius upto about 20 μ sec and beyond this limit it is highly dependent on R_s. For larger radii the field change decreases slowly in comparison to that for smaller radii. The radius of K-change is not precisely known. But it is argued that the K-change radius may be equal to or more than the radius of a stepped leader. Hence calculations have been done for radii ranging from 10-100 metres.

Another important parameter is the charge Q on the cloud. We have used the value of Q ranging from 20 to 80 coulombs. The negative charge as estimated by various workers lies between 20 to 60C. Mathpal and Varshneya /11/ made calculations for 40C of charge which gave a value of field close to the experimental observations.

The electrostatic field during a return stroke on the ground surface increases with time and attains a maximum value at the end of the discharge for any amount of charge Q. After entering into the cloud the discharge structure becomes complicated and the return stroke probably becomes horizontal. Such a case has not been taken into consideration. The electric field decreases with decreasing amount of charge on the cloud. It also decreases with increasing distance.

The variation of total electrostatic field change ΔE with time for return stroke for

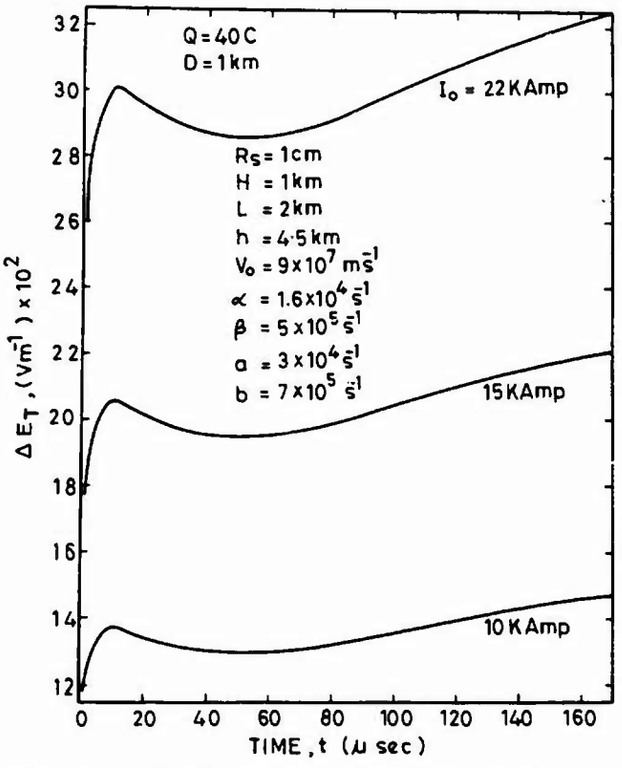


Fig.4 - Variation of total electrostatic field change ΔE_T with time at Q=40C and D=1 km for various values of current I_o, for a return stroke

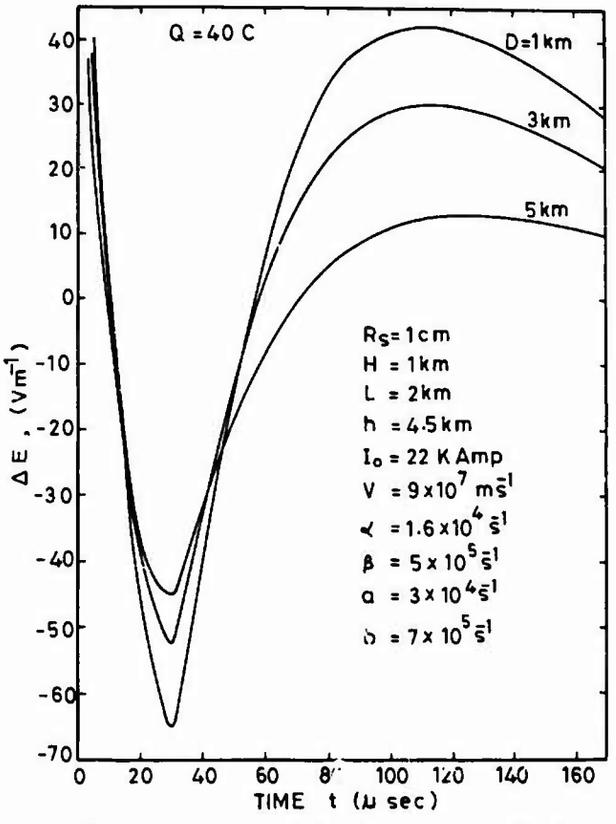


Fig. 5 - Variation of instantaneous electrostatic field change ΔE with time at Q=40C for various values of distance D, for a return stroke

various values of I_o is shown in Fig. 4

Calculations have been made for maximum currents ranging from 10 to 22 K Amp. However, as suggested by various workers I_o varies from 10 to 50 K Amp. A value of 22 K Amp. was suggested by Srivastava and Tantry /23/ which has been extensively used by various workers /21,22,24/. The maximum field change at 170 μsec at a distance of 1 km is 3.2 KVm^{-1}. Tiller et al. /8/ from their records of the return stroke electric fields at various distances near Gainesville, Florida found the total electric field change to be 10 KVm^{-1} at a distance of 1 km and at 170 μsec after the initiation of the return stroke. The field change was observed to be 6 KV m^{-1} at the same distance and for the same time by Serhan et al. /20/. Krehbiel et al. /10/ found that for overhead lightning discharges thetotal electric field change ranges from 1.37 to 22.1 KV m^{-1}. Thus the maximum electric field of 3.26 KV m^{-1} in the present case is in good agreement with the experimental observations of different investigators.

The variation of instantaneous electric field change ΔE with time for a return stroke is shown in Fig. 5. The field change is negative for all distances. The total field change for the returnstroke is about 10 times that for a K-change. The field changes in both the cases are similar in nature. Rai and Varshneya /21/ observed that the radiation field due to a return stroke is about 10 times that of a K-change. Similar results were obtained by Wadehra and Tantry /19/ also.

REFERENCES

/1/ C.T.R.Wilson, Proceedings of the Royal Society (London), Ser. A, 92, 555-574 (1916).

/2/ C.T.R. Wilson, Phil. Trans. R. Soc. (London), Ser. A., 221, 73-115 (1920)

/3/ E.T.Pierce, Report of Meeting on Atmospheric Electricity during the IGY at Aachen May' 11/12, 1956, 28-37, ed. H.Israel, Meteorological Observatory, Aachen (1957).

/4/ S.R.Khastgir and S.K.Saha, J.Atmos. Terr. Phys. 34, 115-126 (1972).

/5/ T.Ogawa and M.Brook, J.Geophys. Res., 69, 5141-5150 (1964).

/6/ E.T.Pierce, Quart. J.Roy. Meteorol. Soc. 81, 211-228 (1955).

/7/ E.T.Pierce, Quart J.Roy. Meteorol. Soc., 81, 229-240 (1955).

/8/ J.A.Tiller, M.A.Uman, Y.T.Lin, R.D. Brantley and E.P.Krider, J.Geophys. Res. 81, 4430-4434 (1976).

/9/ Y.T.Lin, M.A.Uman and R.B.Standler, J.Geophys. Res., 85, 1571-1583 (1980).

/10/ P.Krehbiel, M.Brook and R.McCrory, J.Geophys. Ree., 84, 2432 (1979).

/11/ K.C.Mathpal and N.C.Varshneya, J. Meteorol. Soc. Japan, 61(6), 909-920 (1983).

/12/ K.C.Mathpal, Ph.D.Theeis, University of Roorkee, Roorkee, India (1982).

/13/ A.J.Illingworth and J.Latham, Quart. J. Roy. Meteorol. Soc., 103, 281-295 (1977).

/14/ L.G.Smith Quart. J.Roy. Meteorol. Soc., 83, 103-111 (1957).

/15/ M.Takagi, Proc. Res. Inst. Atmoe. Nagoya University, 8B, 1-106 (1961).

/16/ T.Ogawa and M.Brook, Paper presented at American Geophysical Union, Pacific South West Regional Meeting, Tueson, Arizona, Feb. 1 (1962).

/17/ J.D.Jackson, Classical Electrodynamice, John Willy and Sone Inc., New York, Eaetern Ltd., New Delhi, 84-167(1975).

/18/ Madhubala, K.C.Mathpal, J.Rai, and N.C.Varshneya, Ann. Geophys 38, 177-188 (1982)

/19/ N.S.Wadehra and B.A.P.Tantry, Ind. J. Pure, Appl. Phys., 5(20), 447-449 (1967).

/20/ G.I.Serhan, M.A.Uman, D.G.Childer and Y.T.Lin, Radio Sci., 15, 1089-1094 (1980).

/21/ J.Rai and N.C.Varshneya, J.Atmos. Terr. Phys., 44(3), 291-299 (1982).

/22/ J.Rai, J.Atmos. Terr. Phys., 40, 1275-1280 (1978).

/23/ K.M.L. Srivastava and B.A.P. Tantry, Ind. J.Pure. Applied Phys., 4, 272-275 (1966).

/24) P.P.Pathak, J.Rai and N.C.Varshneya, Ann. Geophys., 36, 613-621 (1980).

ELECTRIC FIELDS PRODUCED BY WINTER THUNDERSTORMS

Y. Goto, K. Narita, M. Naito and R. Funayama*

Department of Electrical Engineering, Tohoku University, Sendai 980, Japan
**General Research Center, Tohoku Electric Power Co., Inc., Sendai 980, Japan*

Abstract - The electric field changes produced by winter thunderstorms have been measured at two points Maki and Hamochi. The field strength observed at Hamochi of Sado Island in the Japan Sea were very large and frequently more than +50 kV/m. When the western winds blow, the field changes measured at two points compares with each other, and the moving mean velocity of thundercloud has been nearly equal to the wind speed obtained at the tower top of Maki. Moreover the deformations of thunderclouds are discussed with the radar echo figures and the field variations measured at Maki. The scale of clouds in the wind direction coincides to the scale estimated from the electric field change.

1. INTRODUCTION

It is well known that many winter thunderstorms occur over the Japan Sea coastal regions. As the winter lightning discharges are very anomalous [1] [2], its characteristics must be made clear for the design of lightning protection of power system and tall structures.

The winter lightning currents which flowed through an isolated tower for meteorological observation have been measured by magnetic links, a magnetic tape recording device and an oscilloscope with a recording camera since the winter of 1976 [3], and by a digital recording system using Rogowsky coil set at the tower top as a current sensor at Maki of Japan since the winter of 1982 [4].

To clarify the characteristics of winter thunderstorms which attack Maki area, surface electric field changes have been measured by a field mill near the tower since the winter of 1982.

Moreover a video camera system has been set up to take the images of lightning discharges struck the tower. It is operated automatically when thunderstorms attack the area since the winter of 1983 [5].

The data of slow electric field changes were processed with a low path filter and analyzed to spectral distributions by Maximum Entropy Method considering that the meteorological conditions.

Assuming that thunderclouds move across over Maki at the wind speed measured at the tower top, the periodical time variation of field strength can be converted to horizontal wave length. It can be thought that wave length relates to the horizontal distance between the charge centers in the cloud and it may mean the size of convection cells.

From the results of analysis, it has been made clear that the cell size is about 4-20 km and in proportion to the heat and water vapour supplied from the sea surface to the atmosphere [6] [7].

In order to study more fully the winter thunderstorms, the measurements of the electric field changes have been continued at two points(Maki and Hamochi) since the winter of 1983.

In this paper, we describe the results of the electric fields produced by winter thunderstorms at the two points and discuss the movement and deformation of thunderclouds in the period of 45 km travelling.

2. OBSERVING POINTS AND ELECTRIC FIELD MEASURING SYSTEM

The main lightning observing point "Maki" is located at about 28 km SW from Niigata city facing the Japan Sea as shown on a map in Fig.1.

The meteorological observation tower at Maki is 150 m in height and constructed on a hill at an altitude of 125 m above sea level. The meteorological data at Maki have been measured at the point of EL 270 m on the tower where lightning currents have been measured too. Moreover the aerological data at Wajima about 180 km WSW(256 deg. directional angle of Maki) from Maki have been used for the reference.

The second observing point "Hamochi" is located at about 45 km W(281 deg. directional angle of Maki) in Sado Island from Maki. There is the point in the middle of paddy field.

Electric field have been measured since the winter of 1983 at Hamochi. Since the winter of 1984, wind parameters have been measured by an anemometer installed on the top of a power pole at 8.6 m in height.

The third measuring point of electric field "Shirone" started since the end of 1984 is located at about 20 km E inland area from Maki in the Niigata plain. There are the radar site of Mt.Yahiko(EL 638 m) at about 1 km S from Maki point and the Fukui radar site at about 290 km SW from Maki. The radar echo figures obtained at multi radar sites(mainly Yahiko radar and Fukui radar) are used in discussion.

The field mills used at each point have a response time of about 0.14 sec. and its output signals have been recorded on a per recorder only in the early stage. To simplify the data analysis and to avoid the data lacks caused by troubles on recorder, a digital recording system has been developed and used together at each observation point.

The system consists of a field mill, opto-electronic transmission system, A-D converter, a digital cassette recorder and simple micro-computer with a timer. The dynamic range of the system covers from +60 kV/m to -60 kV/m of the electric field strength. To record the field data automatically for long period, the field signals are sampled at 1 sec. intervals. They have been registered on memory of the computer with time index when the difference between one sampled value and next exceeds a certain threshold. When the field do not change, the field

data are registered once for about 9 hours(32385 sec.) interval only.

3. RESULTS OF ELECTRIC FIELD MEASUREMENTS AT TWO POINTS

When a cyclone is located on the northeastern Japan Sea, severe phenomena such as thunderstorm or gust are observed towards south of the cyclone center. It is a notable feature that the surface disturbances are observed inside of the polar air bounded by the cold dome boundary layer.

When a storm moves through the our observation areas, the electric field rises to over 2 kV/m, sometimes exceeds more than 20 kV/m varying highly in both magnitude and polarity then subsides to a zero value again at Maki. The other hand, the field strength exceeds frequently more than ±50 kV/m at Hamochi. The difference between oscillating amplitudes at the two points is considered by the following reasons:

(a) Thunderclouds occur on the adjacent seas of Hamochi, so charge centers in the thundercloud are very lower at Hamochi than at Maki.

(b) Space charge effects of charged particles generated by thundercloud field or shielding effects are much at Maki than at Hamochi, because there are the high tower and many trees from which intense corona discharges are induced around the field mill at Maki, but there is little hill or tall structure around the mill at Hamochi.

One result of the field measurements at the two points is shown in Fig.2. Several thunderstorms develop and attack to the regions of the observing points periodically over a long period of time during one day or over. If there is more than 1/2 hour interval of zero field between such storms, they are regarded as each another one. In the period there are large amplitude and abrupt changing polarity alternations before and after the lightning flashes to the tower. So these abrupt changes may represent the rapid electrical processes which occur during intracloud or ground discharges and precipitations. But slow changes of the field are considered due to the thundercloud charges moving with wind speed.

The time length of continuous field variation, which means the duration of a thunderstorm or a fluctuation of meteorological conditions, and the period of slow field oscillation, which means the duration of convection cells, depend on wind speed.

When the wind directions at the two points are same and western, the storm which moves over Hamochi attacks to Maki area. Then the durations of continuous field variation at the two points are roughly equal but the periods and patterns of oscillatory variation are different. The differences of field variations are thought due to the deformation of convection cells and the change of charge distribution in the cloud .

The period can be obtained in dividing the distance of the two points with the wind speed at tower top. It nearly coincides with the time lag of the field change start at the leeward point Maki. Therefore it is seemingly adequate that the travelling velocity of thunderclouds are the same of wind speed measured at the tower top.

The scale of thunderclouds and inner cells have been deduced on the assumption that the cloud velocity is equal to the wind speed observed at Maki. The time variations of field converted to the distant variations are shown in Fig.3. They are the same one as in Fig.2. The wind speeds are used the average values in every ten minutes which are calculated by the supplemental method with the average values in ten minutes measured on the hour.

S.Matsumoto et al. have emphasized in their paper as following: The fluctuations of weather conditions such as wind, pressure and precipitation for a period of 2-3 hours occur with the passage of mesoscale disturbances which develop in the vicinity of the cold dome center one after aother. A series of mesoscale disturbances whose horizontal scale and life time are 100-200 km and several hours respectively can be analyzed during the process in which cold air outbreak is accomplished. The phase velocity of the mesoscale disturbance is 55 km/hour [8].

The measured periods of continuous field variation and scales of thundercloud correspond to them of mesoscale disturbances described by S.Matsumoto et al..

Most winter thunderstorms develop at and behind the frontal surface of trough moving across the Japan Sea. As troughs pass over the observatory, wind direction and its speed change with time in a wide range.

When the wind direction is not west, sometimes violent changes of electric field have been observed at one point only. But they have not observed at another point. So the field changes at the two points do not correspond to each other in this case.

4. THE SCALE OF THUNDERCLOUDS DEDUCED FROM THE FIELD VARIATIONS AND RADAR ECHO FIGURES

To clarify the form and scale of thundercloud, weather radar echo figures made by Japan Meteorological Agency are used. In weather radar, echoes are received from precipitation elements whose in thus located. Weather radar, especially when a PPI presentation is used, is excellent for tracing precipitation areas over a range of perhaps 15 to 200 km. Sometimes distant returns can be masked by echoes from close precipitation but this case is seldom serious. It is important to reiterate that weather radar detects precipitation elements not lightning. It does not therefore distinguish between a shower and a thundercloud.

In spite of the above mention, most clouds formed by strong cumulus convections are observed as radar echoes, when cyclones have passed away from southwest to northeast over the Japan Sea in winter. They are estimated as thunderclouds. Because air temperatures over EL 1 km are below the freezing point and below -20°C at EL 4 km. It should be thought that vigorous charge separations occur at the altitude in the clouds and thunderclouds are formed.

The radar echo figures in the period from 20 Dec. 1984 to 24 Dec. 1984 have been compared with the data of the field variation for the same period. In the period a lightning flash struck the tower at Maki was observed at 23:50 LST in 20 Dec. 1984 and the field variation in the period were violent and maintained periodically over a long period during five days.

A series of the radar echo figures at intervals of three hours is shown Fig.4. In the figure, the wind directions measured at the tower top of Maki with arrow heads, the heights of cloud top observed by radar echoes with ranked number (1: under 2 km, 2: 2-4 km, 3: 4-6 km, and so on, 9: unknown) and precipitation level with symbol are shown.

The time variations of electric field corresponding to Fig.4 is shown in Fig.5.

The field variations which were converted from the time dependence to distance dependence are shown

in Fig.6.

From Fig.4 and Fig.6, it is clear that the scale of clouds in the wind direction coincides to the scale estimated from the electric field change.

Although they are not shown here, the radar echo figures at intervals of one hour and the patterns of field variation have shown that the shape of thundercloud deforms with time and the growth and extinction of convection cell in the cloud or the change of electric charge distribution in the cloud successively occur.

Sometimes field change is measured although there is no cloud on the radar echo. This can be estimated that there are the transparent charged elements for radar pulse wave around the clouds observed radar.

5. CONCLUDING REMARKS

In order to make clear the characteristics of winter thunderstorms, the changes of electric field have been measured at the two points since the winter of 1983. The field strength observed at Hamochi (Sado Island) in the Japan Sea were very largeer in comparison with one at Maki and exceeded frequently more than ±50 kV/m in the period of the winter thunderstorms.

When the westerly wind blows, the field variations observed at the two points correspond to each other. The time lag of the field variation at the leeward point can be explained the distance between two observation points. It depends on the wind speed measured at the tower top of Maki.

Moreover, the scale and deformation of thundercloud have been discussed with the field variation observed at Maki and the radar echo figures.

The scale of the cloud in the wind direction at Maki obtained with the echo is nearly equal to the scale estimated from the field variation. Sometimes field change is observed in spite of no cloud on the radar echo. This can be estimated that there are the transparent charged elements for the radar pulse.

To clarify the winter thunderstorms, further accumulation of data in a various conditions is needed. We observed the lightning flashes struck the tower at Maki in 31 Jan., 1 Feb. and 21 Feb. 1985. So we will discuss the characteristics of thunderstorms for the period involved the lightning flash days.

Moreover, as the field variations have been measured at Shirone since the end of 1984, the relations of field variations at three points must be analyzed.

ACKNOWLEDGEMENTS

The authors wish to express their hearty thanks to the associates of Nuclear Power Department, Tohoku Electric Power Co.,Inc. for a support. The authors also wish to thank Mr. R.Shimanuki, the head of Wajima Meteorological observatory who offered kindly many aerological data at Wajima and Mr. K.Ando, the section head and Mr. Y.Kuzumaki, a chief clerk of weather forecast section, Sendai District Meteorological Observatory who showed kindly the radar echo figures.

REFERENCES

[1] T.Takeuti, M.Nakano and Y.Yamamoto,"Remarkable Characteristics of Cloud-to-Ground Discharges Observed in Winter Tunderstorms in Hokuriku Area, Japan" J. Meteorol. Soc. Jap., 54, 436-429 (1976)

[2] T.Takeuti, M.Nakano, M.Brook, D.J.Raymond and P.Krehbel, "The Anomalous Winter Thunderstorms of the Hokuriku Coast" J. Geophys. Res., 83, 2385-2394 (1978)

[3] Y.Goto, F.Naito, K.Narita and T.Sato, "The Observation of Lightning Discharges in Winter Thunderstorms at the Niigata Coast,Japan" Proc. Int. Aerospace Conf. on Lightning and Static Electricity, A-3 (1982)

[4] Y.Goto, K.Narita and F.Naito,"The Digital Recording System for Lightning Currents and Some Results Obtained for Winter Thunderstorms" Res. Let. Atmospheric Electricity Jap., 3, (1983)

[5] K.Narita, Y.Goto and R.Funayama,"Measurement of Lightning Stroke Current in Winter Season at Maki, Japan" Proc. Int. Aerospace and Ground Conf. on Lightning and Static Electricity, 33, (1984)

[6] Y.Goto, F.Naito, K.Narita and M.Naito,"Sureface Electrostatic Field and Meteorological Conditions in the Period of Winter Thunderstorms" Proc. Int. Aerospace and Ground Conf. on Lightning and Static Electricity, 28, (1984)

[7] Y.Goto, K.Narita and M.Naito,"Spectral Analysis for Electrostatic Field Changes Produced by Winter Thunderstorms" Res. Let. Atmospheric Electricity Jap., 4, 21-28

[8] S.Matsumoto, K.Ninomiya and T.Akiyama,"Cumulus Activities in Relation to the Mesoscale Convergence Field" J. Meteorol. Soc. Jap., 45, 292-305 (1967)

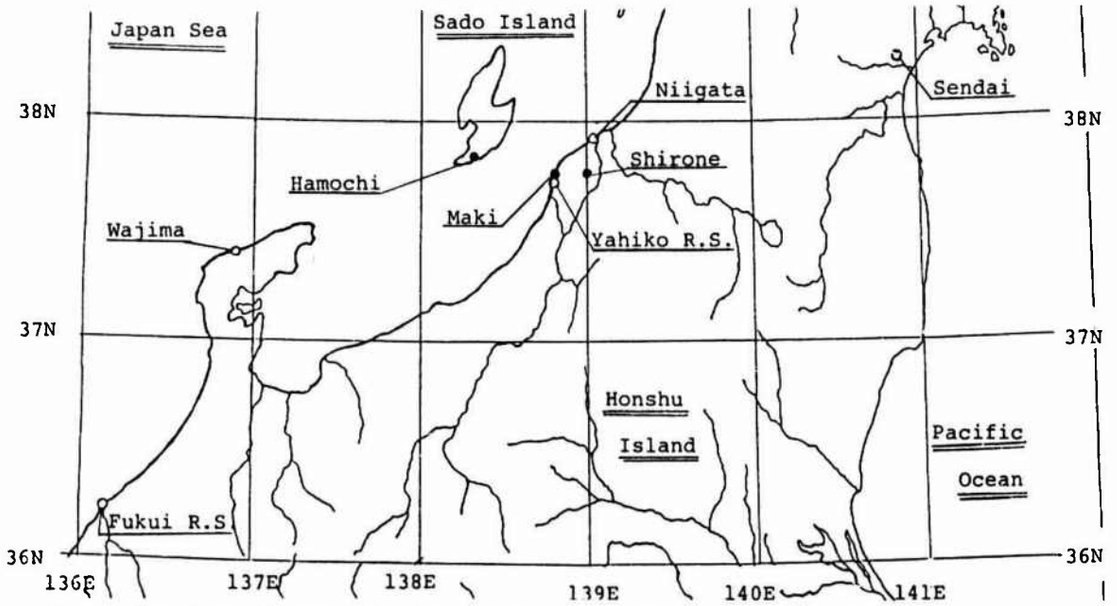


Fig. 1. Locations of observing points for winter thunderstorms on a map of central Japan.

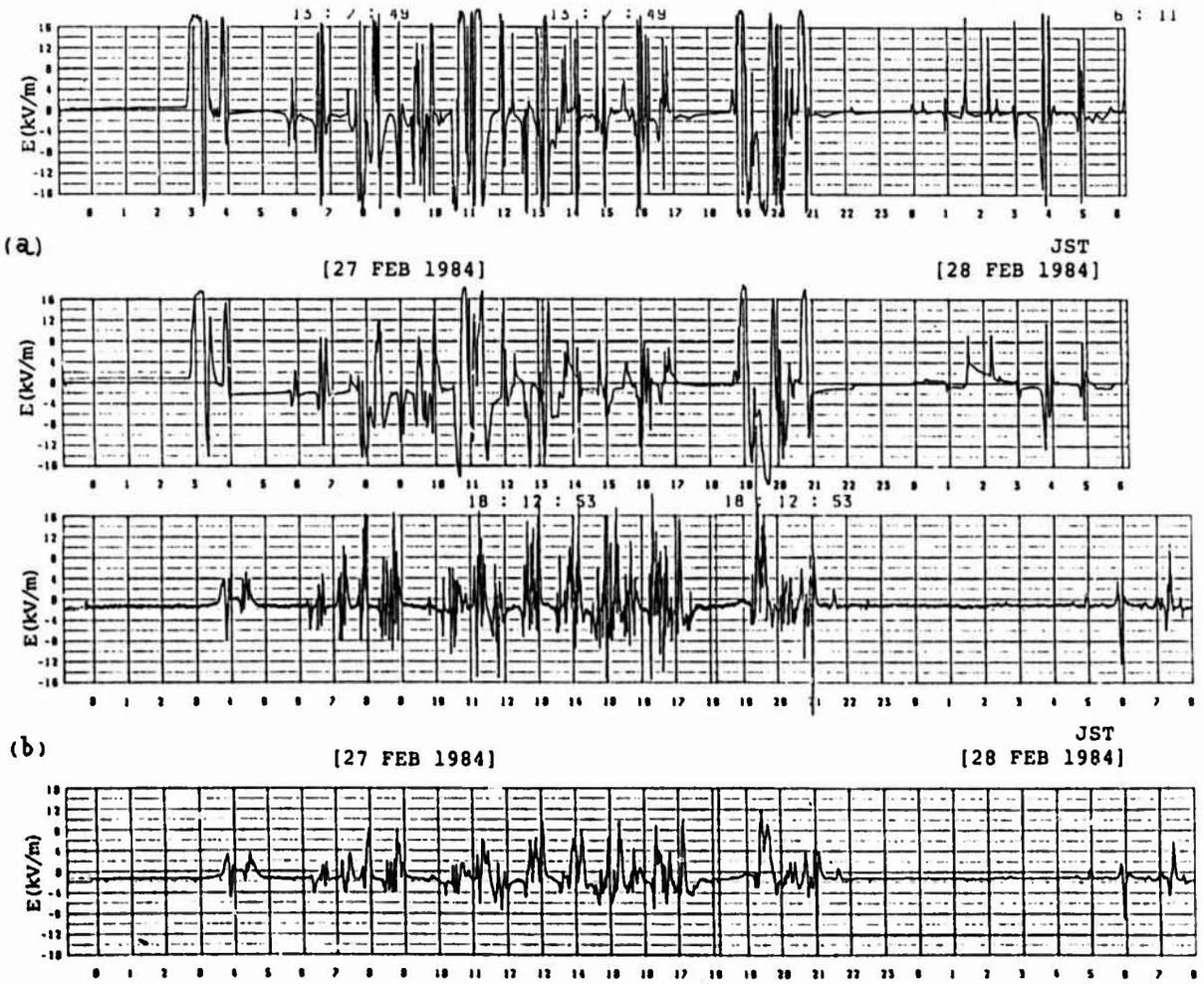


Fig. 2. One example of electric field variations measured at two points, (a) at Hamochi, (b) at Maki. Lower records of the pair are the field slow variations processed with a low pass filter(f_c=0.01 Hz).

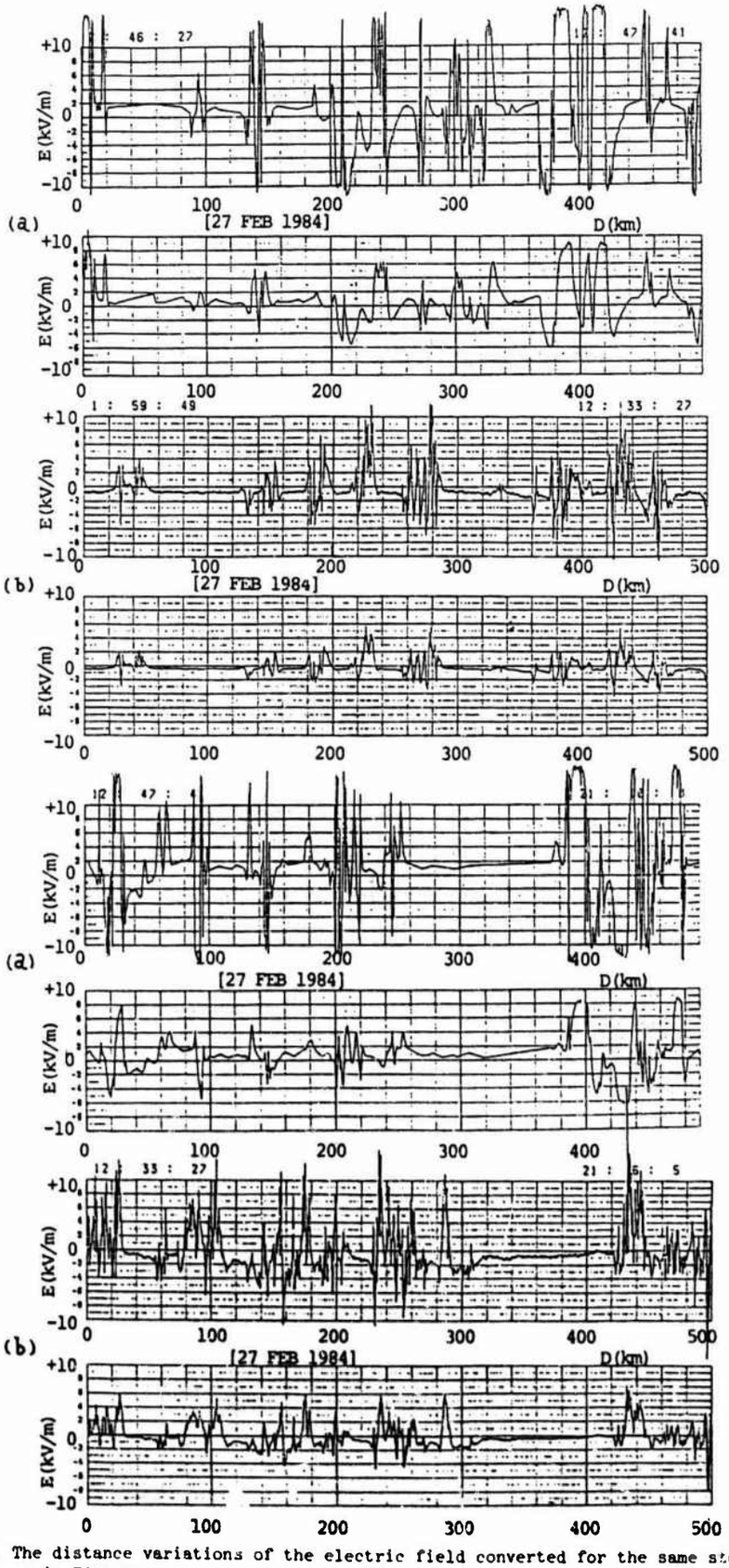


Fig. 3. The distance variations of the electric field converted for the same storms as in Fig. 2.

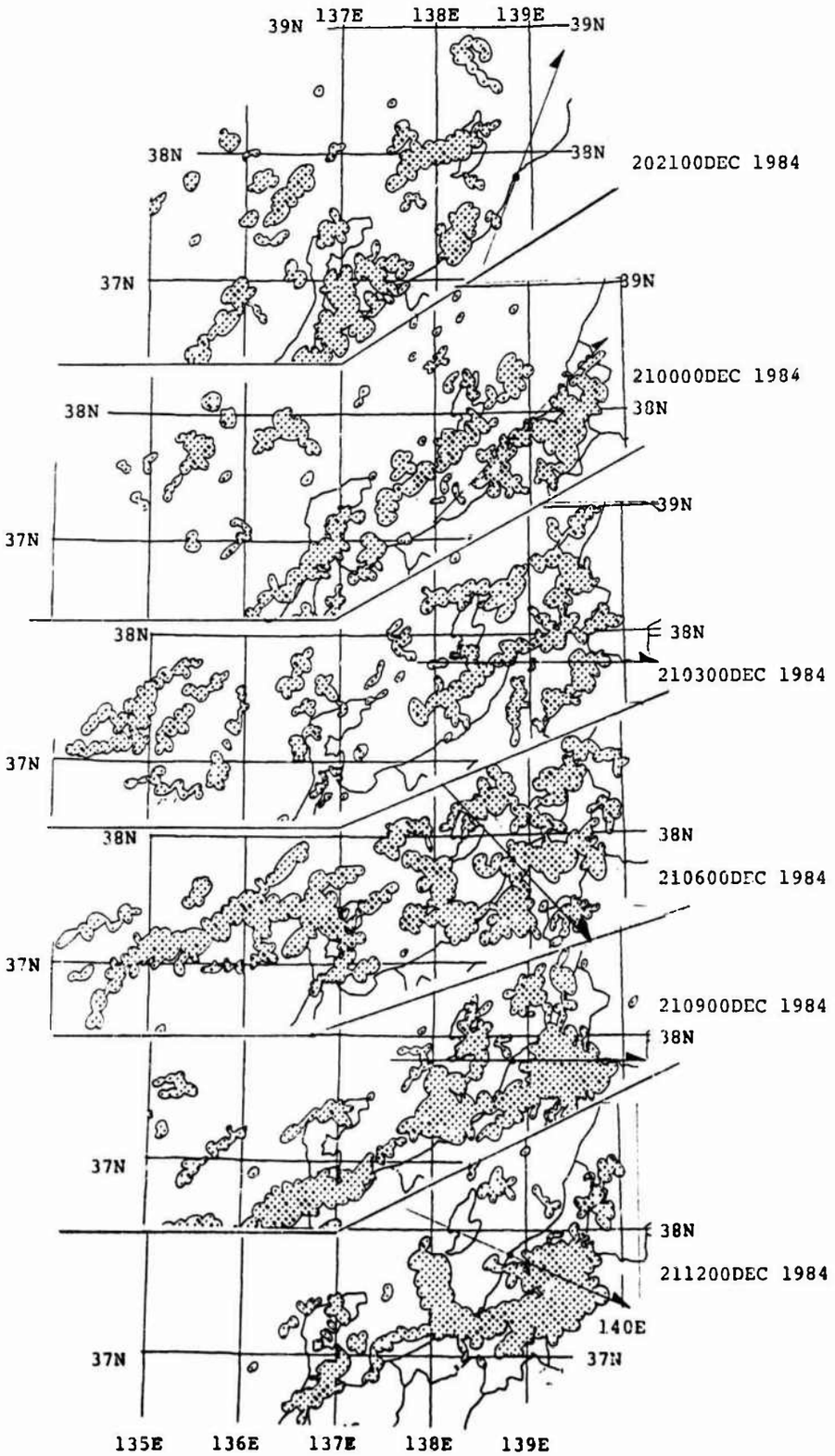


Fig. 4. A series of the radar echo figures at intervals of three hours.

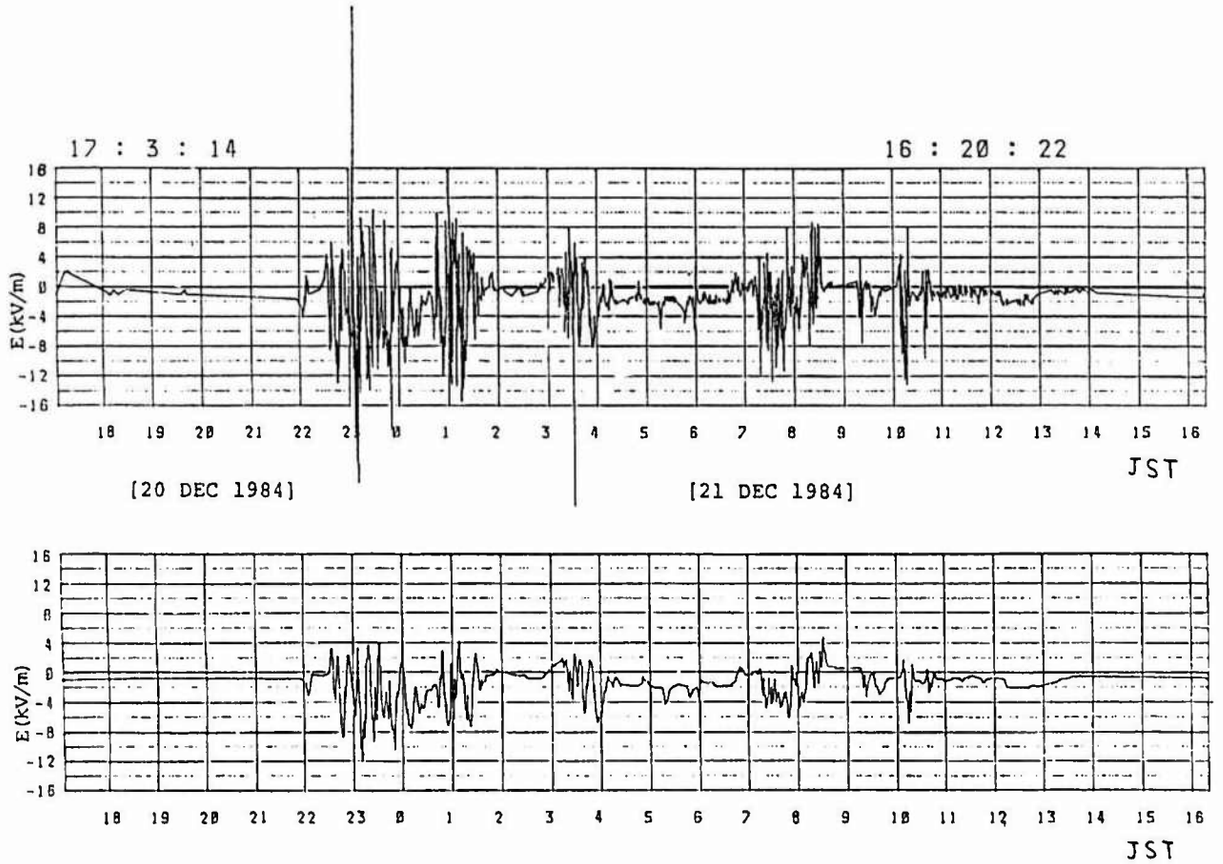


Fig. 5. The field variations for the same storms as in Fig. 4.

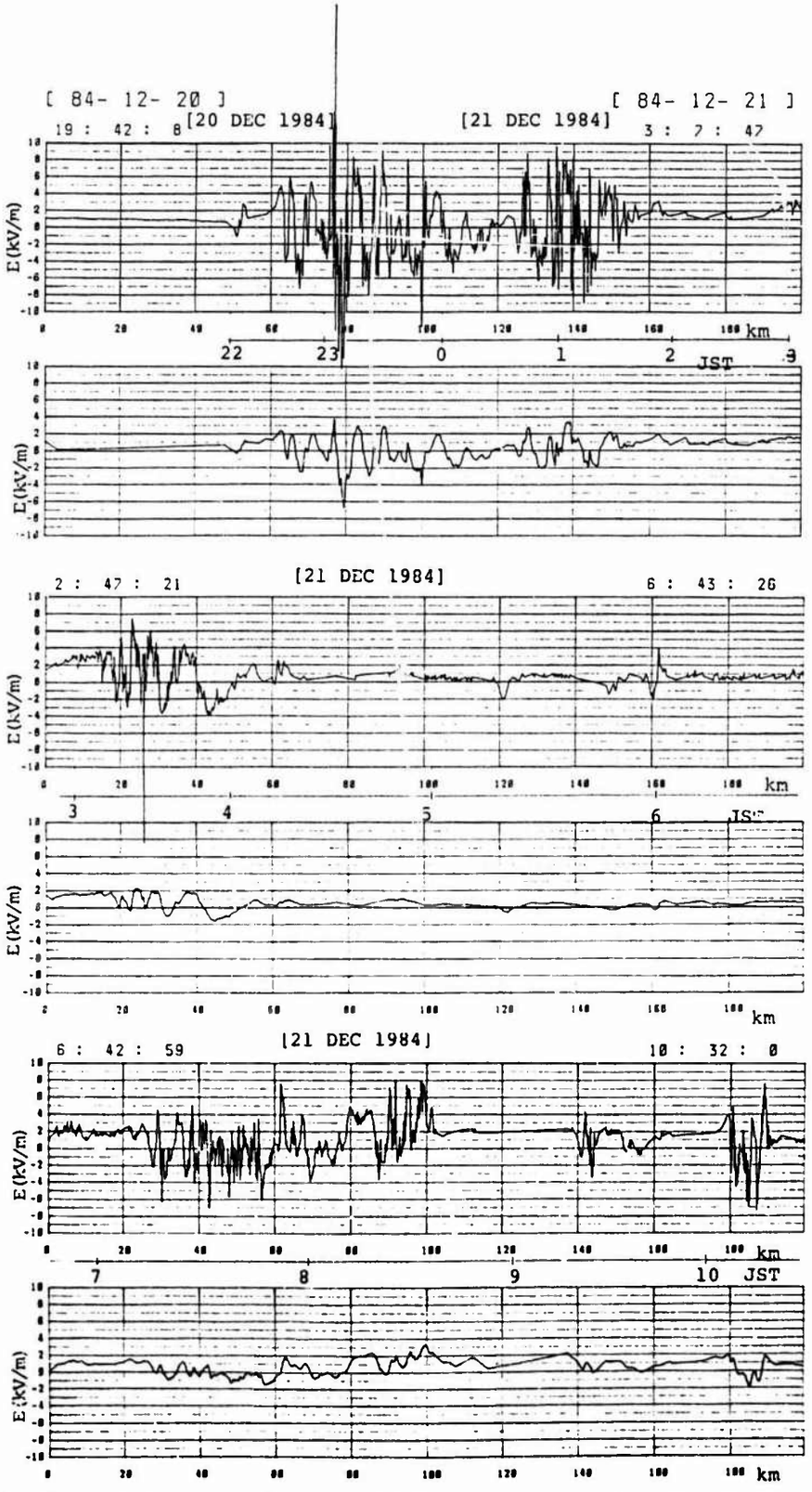


Fig. 6. The distance variations converted from the time variations shown in Fig. 5.

ELECTRIC FIELD CHANGES DUE TO LIGHTNING IN TROPICAL THUNDERSTORMS

P. Pradeep Kumar and J. Rai

Department of Physics, University of Roorkee, Roorkee 247667, India

Abstract - Using a plate antenna the electrostatic field changes due to overhead lightning discharges were carried out for the summer thunderstorms of 1983-84 at Roorkee. Simultaneous measurements of thunder was also carried out to find the distance to the discharge. Statical analysis of electric field changes, interflash time interval, charge destroyed and distance to the discharge are presented in this paper.

I - INTRODUCTION

Most of the measurements on lightning have been carried out in the higher and middle latitudes, comparatively little work has been done at low latitudes. The work on intracloud discharges has lagged behind because of the fact that, it is the cloud to ground discharges that is harmful for the electrical installations, buildings and human life. Moreover, the intracloud discharges are hidden behind the clouds making their photographic studies difficult and therefore not much has been known regarding the mechanism of these discharges. More than 75% of the discharges in the tropics are intracloud discharges /1/ and very few observational data are available from this region /2, 3, 4, 5/. To test the existing theories of intracloud discharges simultaneous measurements of electrostatic field changes, thunder and VLF radiations are being made at Roorkee (29.52°N, 77.53°E). Statistical analysis of the electrostatic field changes, interflash time interval, charge destroyed and distance to the discharge for the observations made during the summer thunderstorms of 1983-84 has been presented in this paper.

II - EXPERIMENTAL SETUP

A field change recorder (FCR) was constructed for the purpose of recording the electrostatic field changes due to lightning discharges. A plate antenna was kept at a height of 1m. above the ground, a potential difference is thus developed between the antenna and the ground, this potential difference was measured using a RC network. The value of C was so selected that it was much than the capacitance (C_g) formed between the antenna and the ground. The value of R was kept much larger than the value of C, so that the whole potential difference is developed across C, and the time constant RC was large enough to measure individual events /6/. The output from the RC network was given to a multistage amplifier system, the output of which was recorded on a pen-chart recorder. Fig.1 gives the schematic representation of the whole setup.

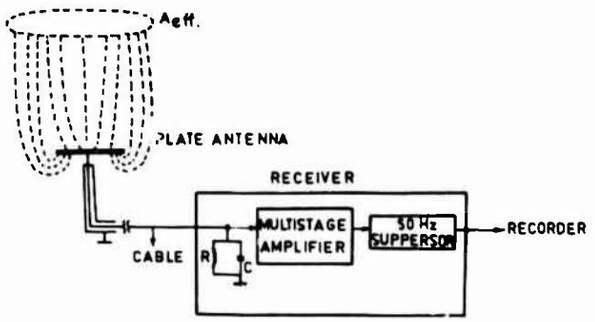


FIG.1

Fig.1 Plate antenna with associated electronics.

The change in voltage due to the change in the induced charge on the plate antenna during a lightning discharge was recorded and the electric field change was calculated using Eq.1,

$$\Delta V = \varepsilon_o A_{ef} \Delta E/C \qquad \ldots (1)$$

where ΔV is the voltage change at the amplifier input, A_{ef} is the effective area of the plate antenna, ΔE is the electric field change, C is the capacitance of the RC network and ε_o is the permittivity of free space.

To estimate the distance to the lightning discharge and length of the channel, thunder accompanying the electrostatic field change was recorded on a tape recorder using a condeser microphone. The onset of thunder after the electrostatic field change provided information regarding the distance of lightning from the point of observation. The duration of thunder gave information regarding the channel length.

Observations were made during the summer months of 1983-84 for overhead thunderstorms only. Twenty one thunderstorms consisting

of approximately 5700 discharges w e used in the study.

III - RESULTS AND DISCUSSIONS

Frequency of Lightning discharges :- The interflash time interval (in seconds) for the total number of discharges observed during 1983-84 is plotted as a histogram in Fig.2. It is seen that maximum number of flashes occured in the interflash time interval of 1 to 2 seconds. The flash rate in the initial and final stages of a thunderstorm is low and in the active stage very high. The duration for which the lightning activity was recorded for each thunderstorm varied from 12 minutes for a storm on April 17, 1983 to 81 minutes for a storm on June 18, 1984. Total number of observed discharges varied from 32 discharges in 24 minutes for a storm on June 18, 1984 to 1644 discharges in 81 minutes for the storm on June 18, 1984 and a maximum flashing rate of 49 discharges perminute was also observed in this storm. The average flash rate per minute for each storm was calculated and it was found to vary from 1.3 flashes per minute to 20.3 flashes per minute. The average of the averages comes out to be 8 flashes per minute.

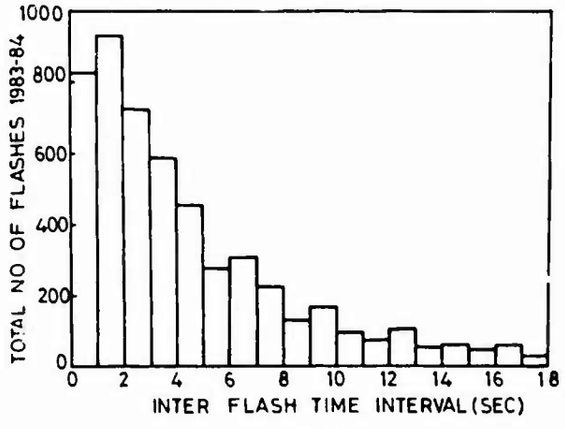


FIG. 2

Fig.2 Interflash time interval versus Number of discharges.

Global values of flash rate given in /7/ is 3 flashes per minute, in /8/ 50 flashes perminute (maximum value), from satellite observations over 30°± of equator /9/ a value of 5 flashes per minute was reported. From the tropical zone the only available values are in /2/ 3 flashes per minute and in /3/ 8 flashes per minute (median value). Our average value of 8 flashes per minute agrees very well with the value reported in /3/ for thunderstorms over Banglore.

Electric field changes :- In all the storms recorded the reversal of the sign of the electric field took place as the storms approached the observing station and the field again reversed its sign as the storm receded from the station. It was seen that in all the overhead discharges the electric field observed was negative and this is in good agreement with the observations reported in /10/. Fig.3 gives the histogram of the negative field changes observed to the total number of flashes. It is seen that most of the flashes produced a field change ranging from 0-1 KV/m and the maximum observed field change was in the range 6.5 to 7 KV/m. Fig.4 shows a histogram of the observed positive field changes to the total number of flashes. Most of the flashes produced field changes ranging from 0-500 V/m and the maximum observed field change ranged from 1.5-2 KV/m.

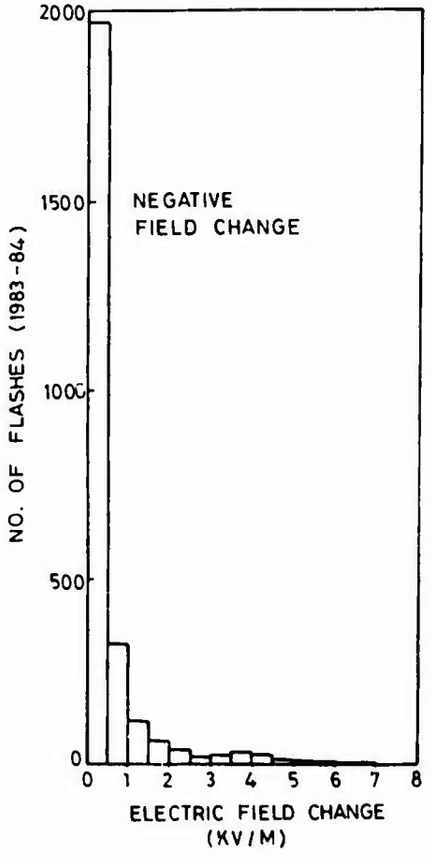


FIG. 3

Fig.3 Electric field change (negative) for the observed discharges.

From the theortical calculations given in /6/ cloud to ground discharges lowering negative charge to the ground exhibt positive field change at all distances from the point of observation. The works of numerous other workers in the middle and higher latitudes show that negative charge is lowered in a cloud to ground discharge.

For cloud to ground discharges very near to the observing point the value of field change should be much larger than 1 KV/m. The value decreases with increasing distance. The number of observed positive field changes with values greater than 1 KV/m when the storm was overhead were quite small. It can then be very correctly said that more than 75% of the lightning discharges in the tropics are intracloud discharges.

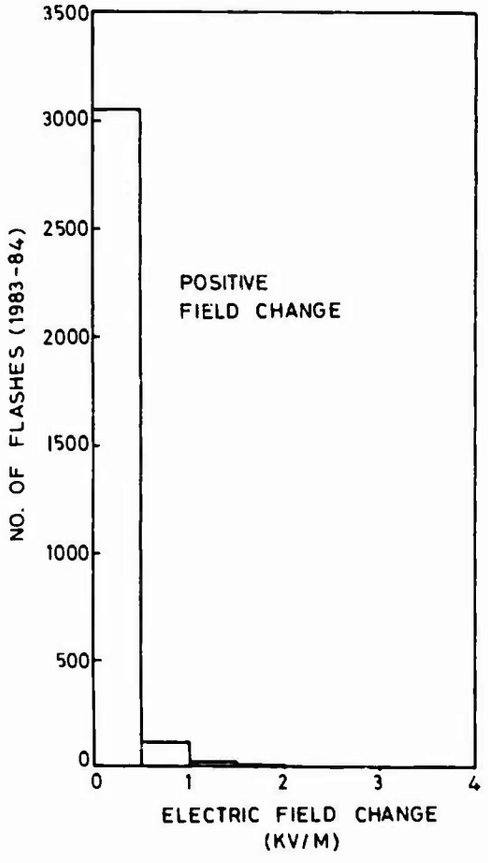


FIG. 4

Fig.4 Electric field change (positive) for the observed discharges.

Field reversal distance :- Distance to the discharges were obtained from the simultaneous records of electrostatic fields and thunder. In Fig.5 the negative field changes have been plotted as a function of distance. The straight line represents the least square fit to the observed data. This straight line cuts the X axis at 11.2Km, which is field reversal distance. For tropical thunderstorms a value of 11.2 Km, has been reported in /5/.

Charge destroyed :- From the measurements of magnetic fields produced by intracloud discharge for tropical thunderstorms an average inclination of lightning discharge was reported in /11/ to be 20° from the vertical with a median value of 13°. In our observations we have obtained the maximum length of the channel to be 14 Km. Such channel lengths are unusual and they can be attributed to horizontal lightning. Such horizontal channels have actually been observed and have been reported /12, 13/. For the calculation of the charge destroyed in intracloud discharges we have assumed that the channel is vertically oriented and therefore have neglected those discharges for which the observed channel length was greater than 5 Km.

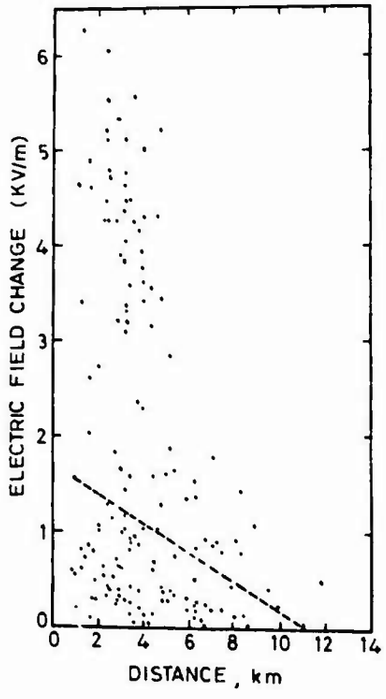


FIG.5

Fig.5 Electric field change versus distance to the discharge.

Our records show that for overhead intracloud discharges the field change produced was predominantly negative. This could only be possible if the negative charge was being transported from the lower negative charge centre to the upper positive charge centre of the cloud /10, 14/. To estimate the value of charge destroyed in an intracloud discharge we have used the model given in /14/ for a discharge propagating from the lower negative charge centre to the upper positive charge centre. The net electrostatic field can be written as

$$E = 2\rho\left[\frac{1}{\sqrt{(h+x)^2+D^2}} - \frac{1}{\sqrt{h^2+D^2}} - \frac{(H-h-x)\,h}{\sqrt{(h^2+D^2)^3}} + \frac{(H-h)\,h}{\sqrt{(H^2+D^2)^3}}\right] \quad ..(2)$$

where H and h are the distances of the upper positive and lower negative charge centres from the ground, D the horizontal distance from the point of observation to just below the charge centre, and x the distance of a channel segment from the lower negative charge centre. The maximum value of x can be L. The geometry of such a model is shown in Fig.6.

From the geometry of the figure one can write

$$H-h = L \quad ..(3)$$

$$D^2+h^2 = r_h^2 \quad ..(4)$$

$$D^2+H^2 = r_H^2 \quad ..(5)$$

$$\rho L = Q \quad ..(6)$$

Substituting equations 3-6 in Fig2 we have

$$E = \frac{2Q}{L}\left[\frac{1}{\sqrt{(h+x)^2+D^2}} - \frac{1}{r_h} - \frac{(L-x)h}{r_h^3} + \frac{L\,H}{r_H^3}\right] \quad ..(7)$$

The net electrostatic field change is obtained from the difference in the field at x=0 and x=L and comes out to be

$$\Delta E = 2\,\Delta Q\,L\left[\frac{1}{r_h} - \frac{1}{r_H} - \frac{h\,L}{r_h^3}\right] \quad ..(8)$$

If the time difference between the onset of electrostatic field change and the first arrival of thunder is T_1 and that of the arrival of the last pulse is T_2 then one can write

$$r_h = v\,T_1$$

$$r_H = v\,T_2$$

$$L = v\,(T_2-T_1)$$

where v is the speed of sound. The emission of thunder from a given segment of the channel is assumed to be instantaneous. It has been found out that the error due to the persistence of the thunder is negligibly small. As the velocity of the lightning discharge ($\sim 10^6$ m/sec) being much larger than the velocity of sound (330 m/sec), thunder from the first segment near the lower negative charge centre is received earlier than from the last segment of the channel. From equations 3-5 one can readily write that

$$h = \frac{r_H^2 - r_h^2 - L^2}{2\,L} \quad ..(9)$$

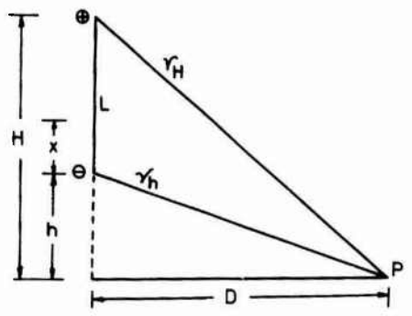


FIG.6

Fig.6 Geometry of the model for vertical discharge.

Substituting the values of E, L, r_H and r_h for each lightning discharge, the value of the charge destroyed were calculated. The values of the charge destroyed varied from 0.14 C to 26.03 C with an average value of 6 C. After reviewing the available literature the average value was reported in /15/ to vary from 6 C to 60 C for intracloud discharges.

REFERENCES

/1/ Prentice S.A. and Mackerras D., 'The ratio of cloud-ground lightning flashes in thunderstorms', J. Appl. Meteor., 545-550, 1977.

/2/ Aiya S.V.C. and Sonde B.C., 'Spring thunderstorms over Bangalore', Proc. IEE, 1493-1501, 1963.

/3/ Aiya S.V.C., 'Lightning and power systems', Electrotechnology (Bangalore), 1-12, 1968.

/4/ Harris D.J. and Salaman Y.E., 'The measurement of lightning characteristics in northern Nigeria', J. Atmos. Phys., 775-786, 1972.

/5/ Wang C.P., 'Lightning discharges in the tropics', J. Geophys. Res., 1943-1949, 1963.

/6/ Uman M.A., 'Lightning', 1969.

/7/ Cianos N. and Pierce E.T., 'A ground lightning environment for engineering usage, Stanford research institute', Project, 1834, 1972.

/8/ Dennis A.A., 'Final report of Stanford research institute', Project, 4877, 1964.

/9/ Sparrow J.G. and Ney E.P., 'Lightning observations by satellite', Nature, 540-541, 1971.

/10/ Ogawa T. and Brook M., 'The mechanism of intracloud lightning discharges', J. Geophys. Res., 5141-5150, 1964.

/11/ Wong C.M. and Lim K.K., 'The inclination of intracloud lightning discharges', J. Geophys. Res., 1905-1912, 1978.

/12/ Brantley R.D., Tiller J.A. and Uman M.A., 'Lightning properties in Florida thunderstorms from video tape records', J. Geophys. Res., 3402-3406, 1975.

/13/ Teer T.L. and Few A.A., 'Horizontal Lightning', J. Geophys. Res., 3436-3441, 1974.

/14/ Khastagir S.R. and Saha S.K., 'On intracloud discharges and their accompanying electric field changes', J. Atmos. Phys. 115-126, 1972.

/15/ Ogawa T., 'Lightning current', CRC Handbook of Atmos. 23-63, 1982.

UNITED STATES ARMY MISSILE COMMAND LIGHTNING SIMULATION TEST FACILITY

L.H. Riley

U.S. Army Missile Command, Redstone Arsenal, Alabama 35898-5240, U.S.A.

Abstract - This paper describes the United States Army Missile Command Lightning simulation Test Facility located at Redstone Arsenal, Alabama. The Lightning Test Facility is used to qualify missile systems to their design specifications.

The facility can simulate a high rate of rise near strike by providing 200 Kiloampere/microsecond through a vertical column near the system under test.

The facility can provide a high rate of rise direct strike by providing 200 Kiloampere/microsecond through a plasma arc directed on to the system under test.

The facility can provide for direct strike high current testing by injecting up to 200 Kiloamperes of peak current into the system.

The facility can provide for direct strike attachment point studies utilizing electrical arcs up to 12 feet in length.

The high rate of rise (200 Kiloampere/mirosecond) forms the leading edge of a pulse that extends beyond a peak current of 30 kiloamperes. There is no other known lightning simulation test facility capable of providing these current characteristics.

These currents and amplitudes are made possible by a large peaking capacitor. The capacitor is formed by a square wire mesh 50 meters long on each side suspended 10 meters above a metal ground sheet. A high voltage (up to 3 million volts) capacitor bank is located within the peaking capacitor. A large electrode provides a discharge current path from the elevated mesh through a plasma arc to the metal ground sheet. During near strike tests the electrode is mounted at the edge of the peaking capacitors. Electromagnetic fields radiating from the electrode illuminates test specimens located nearby and outside the peaking capacitor. During direct strike tests the test specimens are located beneath the electrode such that currents pass from the mesh through the electrode, through a plasma arc, through the test specimen and into the metal ground sheet.

Glass fiber optic data links provides for remotely monitoring the characteristics of the simulated lightning and its impact on the equipment under test. A unique two (2) fiber link is normally used. One fiber transmits data and the other is for remote control of the instrumentation within the equipment under test.

All data is normally acquired in a digital format by transient waveform digitizers. The data is stored on computer disks.

Computer analysis is available immediately after each simulated lightning strike. Plots and tables of measured voltage and current wave forms in report quality final form may be reviewed and testing redirected if necessary. Extrapolations, interpolations and other data analysis techniques common to computers can be utilized interactively during the testing to provide maximum test results during minimum test times.

LIGHTNING SIMULATION TEST FACILITY: The purpose of this paper is to describe the lightning simulation test facility at the US Army Missile Command (MICOM). This facility consists of a unique lightning simulator and the unique instrumnetation for data collection and analysis. The lightning simulator (Figure 1) is essentially the same as that previously used as reported in the 1984 Conference Procedures (1). One noticeable difference in this arrangement and that previously reported on is the rectangular shape of the Marx generator and its physical location and attachment point. The Marx generators - there are two (2) generators now available at MICOM - will be mounted in a horizontal position at the side of the complex and then erected and attached to the side of the upper plate when in use. The parallel plate screen is identical in size (i.e. 50m x 50m) and it remains ten (10) meters above the ground plane. The tapered feed (Figure 2) remains the same.

The Marx generator, previously made available through Lightning and Transients Research Institute of St. Paul, Minnesota, has been replaced by two (2) Marx generators built by MICOM (see Figure 3). The larger of these two generators is capable of high voltage (3.6 MV) and high rate of rise and will be used for destructive testing. The smaller generator is capable of 1.5 MV and twice the current and can be used for non-destructive testing. Figure 4 shows the test facility with one pad partially completed for accommodating the larger Marx generator. The smaller generator will be located on a pad parallel to the one seen here.

UNIQUE INSTRUMENTATION REQUIREMENTS: The instrumentation used for simulated lightning testing must be capable of making precise measurements during an electrical energy discharge of millions of volts potential and hundreds of thousands of amperes of current. The ranges of these measurements include volts to megavolts, amperes to hundreds of kiloamperes and time intervals from nanoseconds to seconds for multiple strokes. High levels of electrical interference, commonly called radio frequency interference (RFI), are generated. This RFI makes packaging of the instrumentation difficult. The package must provide sensor sensitivities in the volt and ampere region and at the same time provide isolation of instrumentation electronics from the simulated lightning discharges of megavolts and hundreds of kiloamperes. Telemetering data from the equipment under test (EUT) to remote data recording and processing devices is necessary. High speed recording equipment capable of recording large quantities of data to nanosecond resolution cannot normally be located within the EUT. The electrical character of the lightning simulation precludes the use of hard wired or standard electrical telemetry. Acoustic or pneumatic telemetry links do not provide the necessary frequency response. Telemetry utilizing modulated light conducted through glass fiber optics appears to be the best technique presently available for telemetering data.

GLASS FIBER OPTIC DATA LINK: Most present fiber optic telemetry data links utilze a time based modulation scheme to eliminate errors introduced by variations in the light conducted through the fiber optic path due to such things as connectors, fibers, ambient conditions, and etc. Also they are used to provide for transmission of steady state or direct current voltage (DC) values without being effected by DC drift of the data link. Fiber optic links utilizing Pulse Code Modulation (PCM) techniques are the most popular because of their large dynamic range. Unfortunately, at this time PCM analog to digital (A/D) encoders fast enough to provide the required time resolution cannot be made small enough to be located within the EUT. However, the state of the art is changing rapidly such that these encoders may be available in the very near future. Fiber optic links utilizing Frequency Modulation (FM) techniques are available in sufficiently small sizes and have been utilized by the US Army Missile Command (USA MICOM) for twenty (20) years in the measurement of missile RFI as the result of adjacent radio and radar operations. Presently, these links cannot provide the necessary frequency response and have dynamic range limitations.

An amplitude modulated (AM) fiber optic data link utilizing two fibers appears to be the best telemetry link presently available for lightning testing. Such a system is presently available and is currently being used by USA MICOM. These links can be used for simulated or directed lightning tests. The two fibers are necessary to provide compensation for inadvertent variation in the light data transmissions and to provide adjustments in system sensitivity as required for the dynamic range. One fiber (first fiber) is used for data transmission for the telemetry transmitter located in the EUT to the remote receiver/controller located in the data recording and processing area. The other fiber (second fiber) is used for system control between the telemetry receiver/controller and the telemetry transmitter. The telemetry receiver/controller can sense inadvertent variations in the data transmission through the first fiber and can provide compensation for this variation utilizing the second fiber. This can be done automatically and provide automatic optical gain control. Dynamic range changes can be made by changing control setting at the telemetry receiver/controller. The second fiber can transmit sensitivity change commands from the telemetry receiver/controller to the telemetry transmitter where attenuators are inserted or removed. These control settings can be entered manually or by computers utilizing a variety of techniques (IEE 488, etc.). A special low frequency version of the data link is available with a low frequency limit of 0.1 Hz. The upper bandwidth limit is approximately 150 MHz. The transmitter reportedly has been tested by electrostatically discharging two-inch to three-inch arcs without introduction of interference into the telemetry data. Unique differential or single ended voltage probes are available from fiber optic telemetry manufacturers. Current probes are available from a variety of manufacturers.

DATA RECORDING/ANALYSIS: Analog data from the fiber optic data links can be digitized by high speed A/D converters in the data recording and processing areas. The combined fiber optic A/D converter system can provide data with a frequency response exceeding 150 MHz. The digitized data can be stored in computer memory. A computer utilizing specialized programs provides processing and presentation of data in report quality.

PRESENT SYSTEM DESCRIPTION: A block diagram of the present USA MICOM lightning instrumentation system is shown in Figure 5. A

picture of a complete fiber optic data link (current probe, fiber optic transmitter, optional fibers, and receiver/controller) is shown in Figure 6. A picture of a complete fiber optic data link with the current probe and transmitter located in a break out box for testing is shown in Figure 7. A picture of a fiber optic receiver/controller installation with A/D system is shown in Figure 8. The computer installation for data recording, processing, and analysis is shown in Figure 9.

REFERENCES:

1. R.A. Perala, T.H. Rudolph and P.M. Kenna "The Use of a Distributed Peaking Capacitor and Marx Generator for Increasing Current Rise Rates and the Electric Field for Lightning Simulation" Proceedings of International Aerospace and Ground Conference on Lightning and Static Electricity, Oralando, Florida 1984.

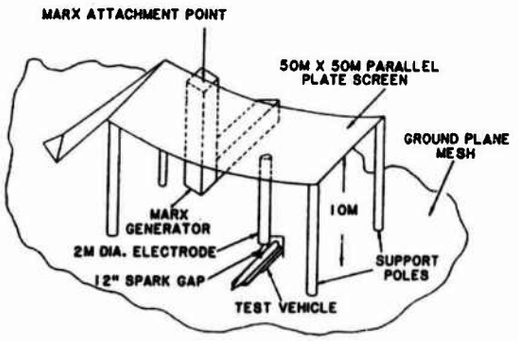


FIGURE 1. DIRECT STRIKE TEST CONFIGURATION

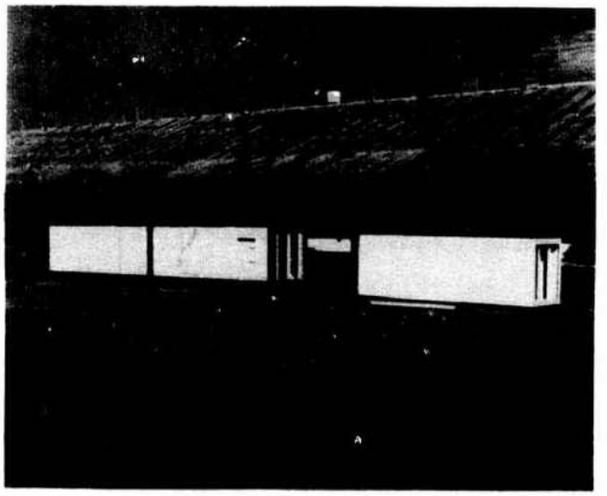


FIGURE 3. MARX GENERATORS

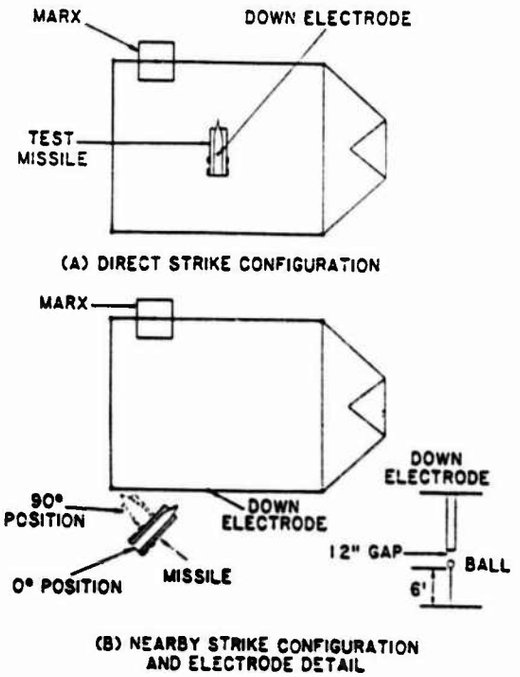


FIGURE 2. PLAN VIEWS - TEST CONFIGURATION

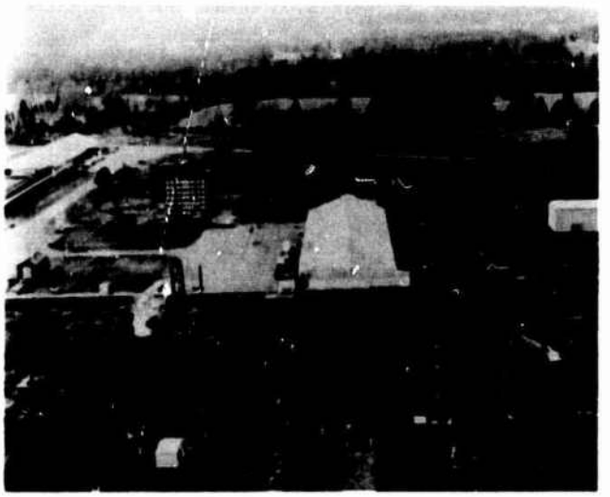


FIGURE 4. TEST FACILITY - LIGHTNING SIMULATOR

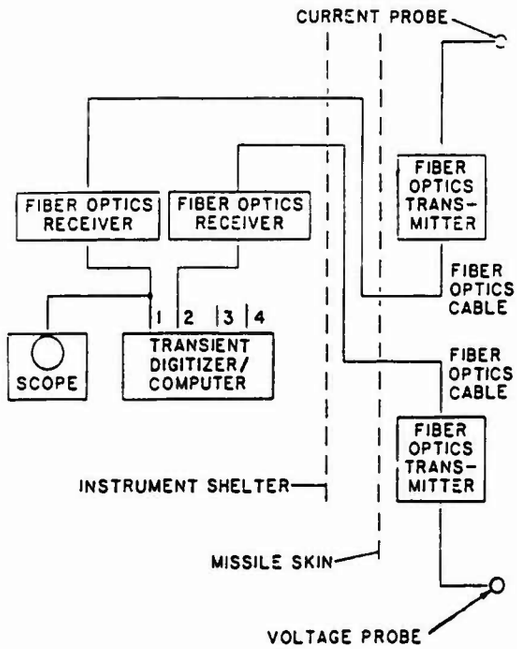


FIGURE 5. INSTRUMENTATION BLOCK DIAGRAM

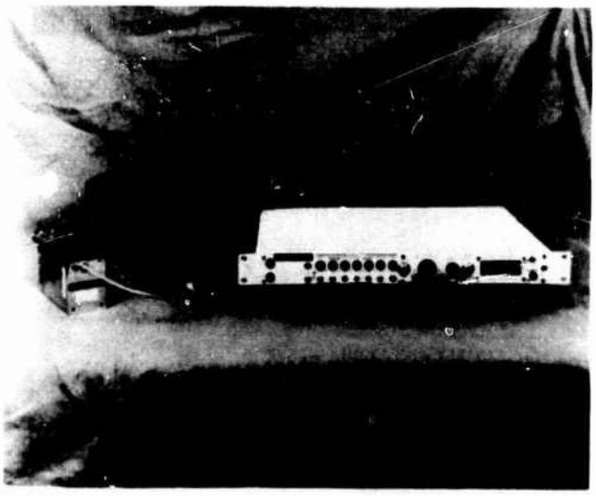


FIGURE 6. FIBER OPTIC DATA LINK

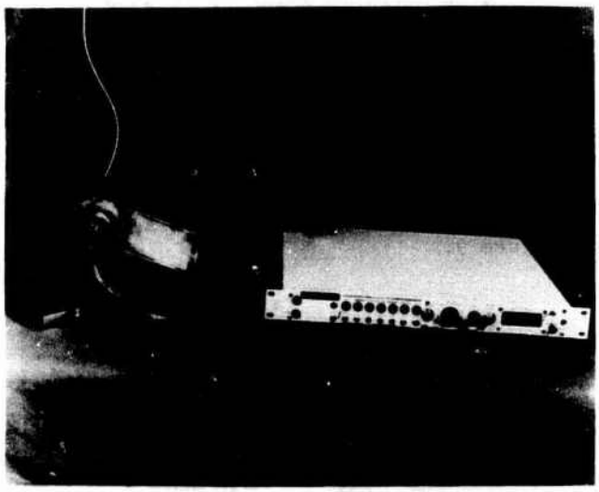


FIGURE 7. FIBER OPTIC DATA LINK WITH BREAK-OUT BOX

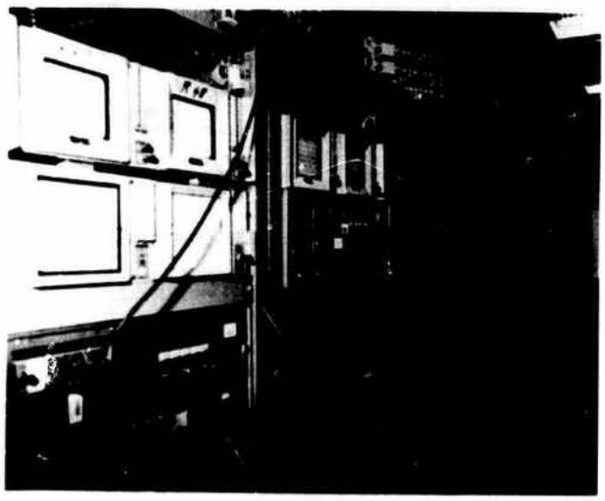


FIGURE 8. FIBER OPTIC RECEIVER/CONTROLLER WITH A/D SYSTEM

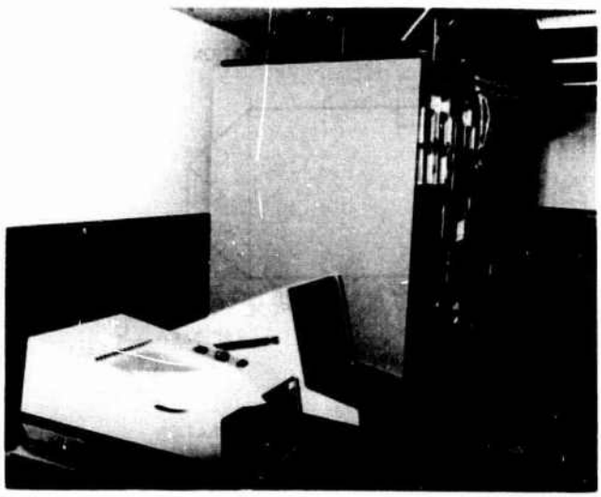


FIGURE 9. COMPUTER INSTALLATION

DESIGN OF A FAST RISETIME LIGHTNING GENERATOR

Lt. J.L. Hebert, L.C. Walko and J.G. Schneider*

U.S. Air Force Wright Aeronautical Laboratories, AFWAL/FIESL, Wright Patterson AFB, Ohio 45433, U.S.A.
**Technology/Scientific Services Inc., Dayton, Ohio 45431, U.S.A.*

Abstract

It has been verified through analytical and smaller scale experimental studies that a NEMP-type peaking capacitor could be coupled with a high voltage EMP simulator to provide the fast current risetimes that have been observed during recent ground and in-flight lightning research programs. The Atmospheric Electricity Hazards (AEH) Group of the Air Force's Wright Aeronautical Laboratories has built and demonstrated a fast risetime generator, using a peaking capacitor which is capable of applying currents of 20 kA to 40 kA with risetimes of 100 nsec to 200 nsec onto an operational aircraft. The generator was used during 1984 for lightning simulation tests on the specially instrumented FAA CV-580 lightning research aircraft, a GF-16 prototype aircraft and a specially instrumented lightning strike object (LSO) in a coaxial geometry return path.

Introduction

Recent lightning characterization programs by the Flight Dynamics Laboratory of the Air Force Wright Aeronautical Laboratories and NASA have revealed that the risetimes of lightning return stroke components can be on the order of 100 nano seconds (1,2), a full order of magnitude faster than the previously accepted risetime of one microsecond. The faster risetimes can excite natural aircraft resonant frequencies resulting in more energy at these frequencies coupling into the aircraft via aperture penetration of electric and magnetic fields. Most impulse generators for lightning simulation are designed for risetimes of 1 to 2 microseconds and because of inherent generator resistances and inductances cannot readily achieve the faster risetimes of the newly revealed threat. The addition of NEMP type distributive peaking capacitors provides an economical approach to modifying the generators to produce the faster risetimes.

Design Approach

The basic design of the fast risetime generator was provided under contract by Lightning and Transients Research Institute (LTRI) and Electro Magnetic Applications, Inc. (EMA) (3). The actual design of the final peaking capacitor was developed by the Air Force AEH Group.

LTRI and EMA conducted analytical and smaller scale experimental studies on the full scale NEMP type lightning simulator for aerospace vehicles. These studies verified that the NEMP type capacitor approach could be used for lightning simulators and provide an order of magnitude improvement in current risetimes over existing lightning simulators.

With this confidence, the AEH Group performed a parametric study of the generator using a three branch lumped parameter RLC representation of: the generator with resonant charging inductance, L_s, and resistance R_s; the peaking capacitor; and the load as shown in Figure 1.

Although the approach neglects the coaxial transmission line characteristics of a typical aircraft and return paths, it does provide a first order parametric analysis of the effects of changing various circuit values.

A bulk inductance of 6 μH to 12 μH and a characteristic surge impedance of 75 Ω to 130 Ω are common in many simulator set-ups involving a complete aircraft as the test object. The RLC parameters of the high voltage Marx generator were set by the generator's design. The value of the distributive peaking capacitor, 1 nanofarad, was suggested by the LTRI and EMA study. The value of 10 μH for the resonant charging inductor between the Marx and peaking capacitor was chosen based on the results of the overall parametric study. The results of the study for the load representations of L_L = 6 μH, 12 μH and Z_o = 75 Ω, 130 Ω are presented in Table 1 through 4. The predicted waveforms for these values are presented in Figures 2 through 5.

From these tables one can see that, due to resonant charging, the peaking capacitor charges to a voltage 1.6 times the original voltage on the Marx. Careful consideration is required not to overvoltage the peaking capacitor. In the ideal case, no resistances, the peaking capacitor voltage can approach 2 times the Marx voltage, if Cp << Cm.

The typical computed waveforms for two cases are compared with actual test waveforms from the CV-580 lightning simulation tests in Figures 6 and 7. In the first case, Figure 2, the output gap of the peaking capacitor is shorted such that the peaking capacitor has little effect on the output of the generator. Without the peaking capacitor, the Marx produces a current pulse of 23.4 kA with a risetime, 10% to 90%, of 500 nanoseconds. In the second case, Figure 7, an output gap of 45 inches is inserted at the output of the peaking capacitor.

The output peaking capacitor gap of 45 inches results in gap breakdown at a little over 2 million volts, about the same as the original voltage on the Marx. Had the peaking capacitor charged to its maximum voltage, it would have charged to 3.2 million volts. With the peaking capacitor charged to 2 million volts the generator produces an output of 34 kA with a risetime, 10% to 90%, of 165 nanoseconds. Comparing the two waveforms, the effects of adding the NEMP type distributive peaking capacitor is dramatically illustrated. Once the Marx has erected the peaking capacitor charges, while the shorted signal has already begun to rise. After approximately 600 nsec the peaking capacitor is charged and self-breakdown of the output gap occurs, providing an impulse with a much faster risetime.

Construction of the Peaking Capacitor

Two engineering constraints strongly influenced the final design of the fast risetime generator. The first was the requirement to stand-off 4 million volts. The second was the need for the generator to operate in the AEH Group's test facilities with ceilings as low as 22 feet high. The final design of the peaking capacitor is shown in Figure 8.

The peaking capacitor is a 4 million volt distributive capacitor comprised of four parallel legs of forty 100 KV, .01MFD capacitors arranged in series (4 million volts). The 160 capacitors have an equivalent capacitance of 1 nanofarad. The capacitors are mounted in a zig-zag fashion for space economy, between fiberglass channels which are compressed together using permali rods as bolts. A copper sleeve couples the high energy ends of the four series arrays at the Marx input to the peaking capacitor. The series legs first are oriented towards the Marx and then expand outward surrounding the final output spark gap to points on a concentric circle from the output of the gap, where they meet the return paths of the simulator set-up.

The final output spark gap that ultimately determines the final charge of the peaking capacitor uses 18 inch diameter spherical brass electrodes enclosed in a 500 gallon fiberglass storage tank. The tank rests on scissor jack-like stands that can be lowered for transportation of the peaking capacitor or mating the peaking capacitor to other test objects.

The 10 μH resonant charging inductor is comprised of soft copper tubing rolled around a varnished cardboard concrete column mold. The peaking capacitor also incorporates a current shunt in the pipe which forms the final output connection from the output spark gap to the aircraft being tested. This shunt uses a pneumatically operated fiber optics transmitter to bring the output waveform from the peaking capacitor. For shielding, the transmitter itself is mounted inside the output pipe.

Future Development

LTRI is presently under contract to the Air Force AEH Group to develop a crowbar switch that is capable of being used with the peaking capacitor. The inclusion of this crowbar switch will result in a waveform that will have a fast risetime, but have a slower decay time that would more closely approximate the classic double exponential lightning threat waveform used in lightning simulation testing. (4).

Conclusion

The AEH Group of the Air Force Wright Aeronautical Laboratories has built and demonstrated a NEMP type peaking capacitor to provide an order of magnitude improvement in current risetimes over existing lightning simulators. The peaking capacitor has been coupled with a high voltage Marx bank to form a fast risetime generator. Risetimes on the order of 100 to 200 nanoseconds have been achieved with magnitudes between 20 and 40 kA. Future development of the fast risetime generator includes the addition of a crowbar switch to the peaking capacitor.

References

1. P.L. Rustan, B.P. Kuhlman, A Serrano, J Reazer, and M. Risley, "Airborne Lightning Characterization", USAF Report AFWAL-TR-83-3013, January 1983.

2. B.P. Kuhlman and M.J. Reazer, "Characterization of Fast-Risetime Electromagnetic Field Pulses Recorded in Airborne Measurements During Florida Thunderstorms", presented at the International Aerospace and Ground Conference on Lightning and Static Electricity, Orlando, FL, June 1984.

3. J.D. Robb, "An Experimental and Theoretical Investigation of an NEMP Type Fast Rise Lightning Simulator", USAF Report AFWAL-TR-84-3007, March 1984.

4. "Lightning Qualification Test Techniques for Aerospace Vehicles and Hardware", Military Standard MIL-STD-1757, 20 July 1983.

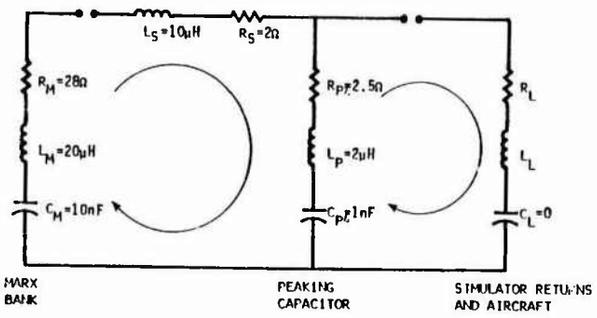


Fig. 1 Lumped RLC Representation of the Generator and Load

TABLE 1

LOAD RESISTANCE= 2.5000000000000 OHMS
LOAD INDUCTANCE= .0000060000000 HENRIES
LOAD CAPACITANCE= .0000000000000 FARADS

VMARX CHRG (MV)	VMARX LOOP1 (MV)	VPEAK LOOP1 (MV)	TIME ONE (NS)	PEAK CURR (KA)	RTIME 10T090 (NS)	T TO CREST (NS)
2.000	1.680	3.202	537.9	34.02	91.00	140.00
2.100	1.764	3.362	537.9	35.72	91.00	140.00
2.200	1.848	3.522	537.9	37.42	91.00	140.00
2.300	1.932	3.682	537.9	39.12	91.00	140.00
2.400	2.016	3.842	537.9	40.82	91.00	140.00
2.500	2.100	4.002	537.9	42.52	91.00	140.00
2.600	2.184	4.162	537.9	44.22	91.00	140.00
2.700	2.268	4.322	537.9	45.92	91.00	140.00
2.800	2.352	4.483	537.9	47.62	91.00	140.00
2.900	2.436	4.643	537.9	49.32	91.00	140.00
3.000	2.520	4.803	537.9	51.02	91.00	140.00

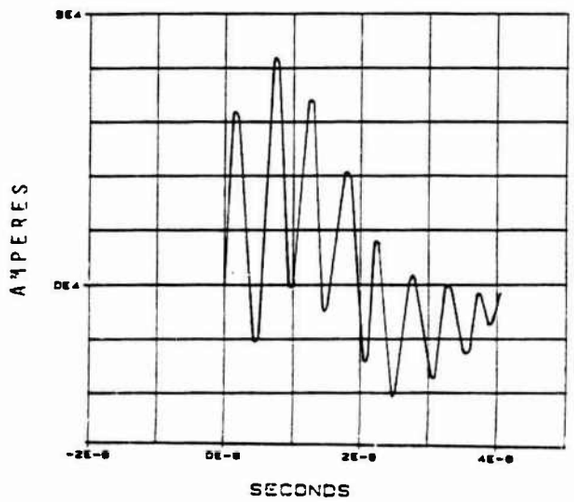


Fig. 2 Computed Waveform For: L_L= 6μH, R_L=2.5Ω

TABLE 2

LOAD RESISTANCE= 2.5000000000000 OHMS
LOAD INDUCTANCE= .0000120000000 HENRIES
LOAD CAPACITANCE= .0000000000000 FARADS

VMARX CHRG (MV)	VMARX LOOP1 (MV)	VPEAK LOOP1 (MV)	TIME ONE (NS)	PEAK CURR (KA)	RTIME 10T090 (NS)	T TO CREST (NS)
2.000	1.680	3.202	537.9	25.07	117.00	183.00
2.100	1.764	3.362	537.9	26.32	117.00	183.00
2.200	1.848	3.522	537.9	27.57	117.00	183.00
2.300	1.932	3.682	537.9	28.83	117.00	183.00
2.400	2.016	3.842	537.9	30.08	117.00	183.00
2.500	2.100	4.002	537.9	31.33	117.00	183.00
2.600	2.184	4.162	537.9	32.59	117.00	183.00
2.700	2.268	4.322	537.9	33.84	117.00	183.00
2.800	2.352	4.483	537.9	35.09	117.00	183.00
2.900	2.436	4.643	537.9	36.35	117.00	183.00
3.000	2.520	4.803	537.9	37.60	117.00	183.00

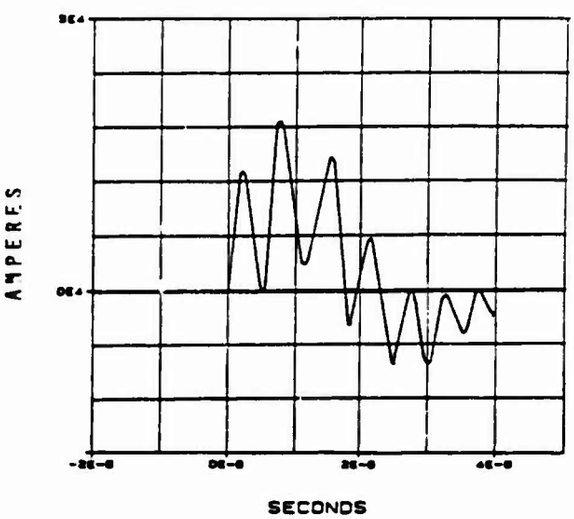


Fig. 3 Computed Waveform For: L_L=12μH, R_L=2.5Ω

TABLE 3

LOAD RESISTANCE= 75.000000000000 OHMS
LOAD INDUCTANCE= .000002000000 HENRIES
LOAD CAPACITANCE= .000000000000 FARADS

VMARX CHRG (MV)	VMARX LOOP1 (MV)	VPEAK LOOP1 (MV)	TIME ONE (NS)	PEAK CURR (KA)	RTIME 10TO90 (NS)	T TO CREST (NS)
2.000	1.680	3.202	537.9	24.72	43.00	73.00
2.100	1.764	3.362	537.9	25.96	43.00	73.00
2.200	1.848	3.522	537.9	27.20	43.00	73.00
2.300	1.932	3.682	537.9	28.43	43.00	73.00
2.400	2.016	3.842	537.9	29.67	43.00	73.00
2.500	2.100	4.002	537.9	30.91	43.00	73.00
2.600	2.184	4.162	537.9	32.14	43.00	73.00
2.700	2.268	4.322	537.9	33.38	43.00	73.00
2.800	2.352	4.483	537.9	34.61	43.00	73.00
2.900	2.436	4.643	537.9	35.85	43.00	73.00
3.000	2.520	4.803	537.9	37.09	43.00	73.00

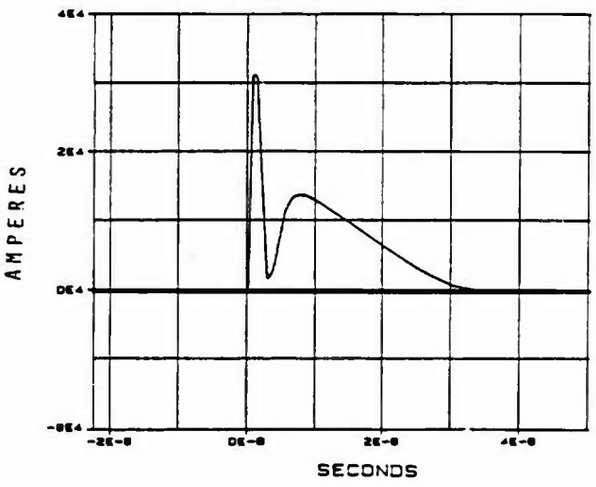


FIG. 4 COMPUTED WAVEFORM FOR: $L_L = 2\mu H$, $Z_0 = 75\Omega$

TABLE 4

LOAD RESISTANCE= 130.000000000000 OHMS
LOAD INDUCTANCE= .000002000000 HENRIES
LOAD CAPACITANCE= .000000000000 FARADS

VMARX CHRG (MV)	VMARX LOOP1 (MV)	VPEAK LOOP1 (MV)	TIME ONE (NS)	PEAK CURR (KA)	RTIME 10TO90 (NS)	T TO CREST (NS)
2.000	1.680	3.202	537.9	17.72	35.00	61.00
2.100	1.764	3.362	537.9	18.60	35.00	61.00
2.200	1.848	3.522	537.9	19.49	35.00	61.00
2.300	1.932	3.682	537.9	20.37	35.00	61.00
2.400	2.016	3.842	537.9	21.26	35.00	61.00
2.500	2.100	4.002	537.9	22.15	35.00	61.00
2.600	2.184	4.162	537.9	23.03	35.00	61.00
2.700	2.268	4.322	537.9	23.92	35.00	61.00
2.800	2.352	4.483	537.9	24.80	35.00	61.00
2.900	2.436	4.643	537.9	25.69	35.00	61.00
3.000	2.520	4.803	537.9	26.57	35.00	61.00

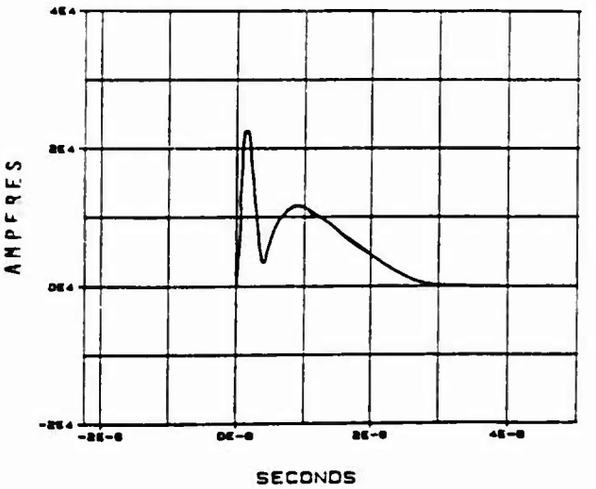


FIG. 5 COMPUTED WAVEFORM FOR: $L_L = 2\mu H$, $Z_0 = 130\Omega$

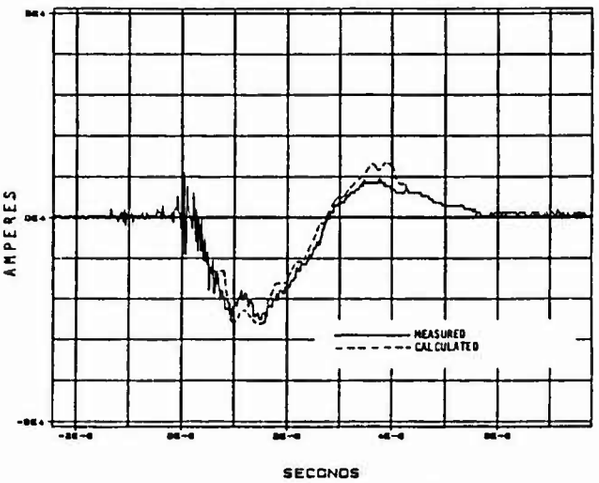


FIG. 6 ACTUAL MEASURED AND COMPUTED WAVEFORMS FROM THE CV-590 TESTS, NOSE-TO-TAIL, PEAKING CAPACITOR SHORTED

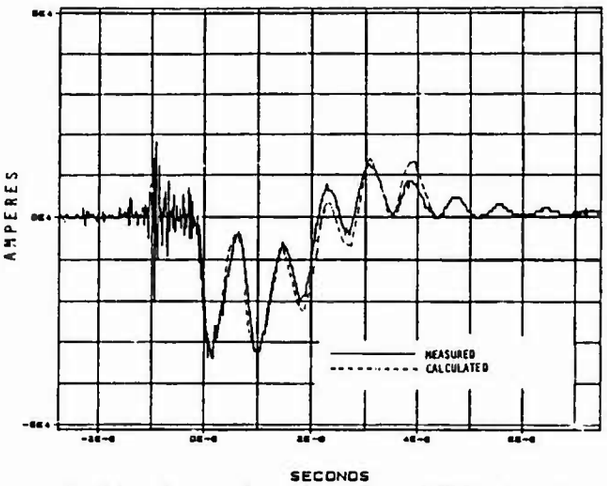


FIG. 7 ACTUAL MEASURED AND COMPUTED WAVEFORMS FROM THE CV-590 TESTS, NOSE-TO-TAIL, PEAKING CAPACITOR GAP AT 45 INCHES.

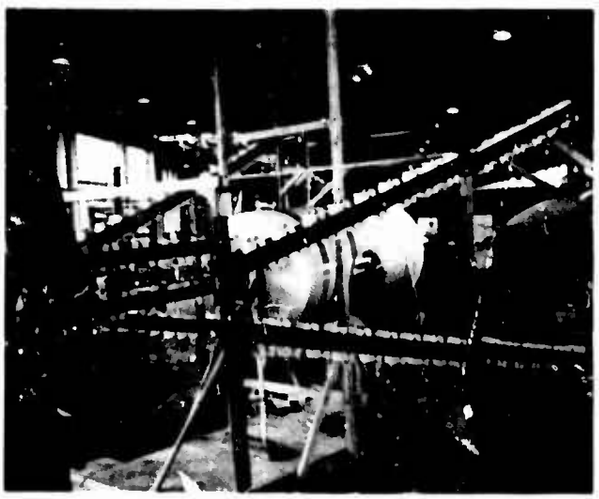


Fig. 8 The Actual Peaking Capacitor

IMPLEMENTATION OF A CROWBAR SWITCH IN A MARX GENERATOR/PEAKING CAPACITOR LIGHTNING SIMULATOR SYSTEM

R.A. Perala, P.M. McKenna, T.H. Rudolph and J.D. Robb*

Electromagnetic Applications, Inc., P.O. Box 26263, Denver, Colorado 80226, U.S.A.
**Lightning and Transients Research Institute, 2531 W. Summer Street, St. Paul, Minnesota 55113, U.S.A.*

ABSTRACT - There is a growing interest in the development of simulators which can properly excite an aircraft with a lightning-like current and voltage pulse. In previous investigations [1-5], the use of a high voltage Marx generator with a peaking capacitor output has been shown to provide sufficiently large values of $\dot{I}$, $\dot{H}$, and $\dot{E}$. There are two problems which exist, however, with that approach. First, there are some spurious resonances introduced by the interaction of the test object with the simulator, and, second, the late time waveform is a damped sinusoid with a frequency too high to investigate low frequency coupling effects in composite aircraft. In the work reported in this present paper, these two problems are addressed. A method for terminating the test object to minimize the spurious resonances is presented, and a crowbar switch is implemented to provide a long late time damped exponential current.

1 - INTRODUCTION

The electromagnetic interaction of lightning with aircraft has received an increasing amount of interest in recent years for several reasons. The first reason has to do with the knowledge of the environment. Recent studies have shown that the frequency content of lightning waveforms has significant amplitude in the aircraft resonance region, which is in sharp contrast to previous understanding of the lightning environment.

A second set of reasons has to do with aircraft technology. New and existing aircraft are being made out of advanced composite materials because of their advantageous strength to weight ratios when compared with metals. A third reason is that modern aircraft are being equipped with low-level semiconductor circuitry which have critical roles in functions such as stores management and fly-by-wire systems. Therefore, a great concern arises for preventing upset of these critical digital systems.

Because of these reasons, it is necessary to develop techniques which can be used to test aircraft with an appropriate lightning environment.

An approach based on the use of a Marx generator with a peaking capacitor has previously been reported [1-5]. This approach makes it possible to inject a current with a rate of rise exceeding 2×10^{11} A/s into a full scale fighter size aircraft, and with a peak current level on the order of 40 kA.

One of the problems of the above approach is that the late time waveform is a damped sinusoid whose ringing frequency is determined by the Marx generator capacitance and the combined inductance of the Marx plus the aircraft under test. The frequency of oscillations is too high to permit experimental investigations into redistribution times of current on mixed metal composite aircraft, and other late time effects.

This limitation can be overcome by shorting out the Marx generator when the energy in the aircraft is close to the maximum. The decay will then be exponential, because the Marx capacitance is no longer part of the circuit. This shorting of the Marx is accomplished by a "crowbar" switch, which physically consists of a triggered gap which turns on at a predetermined time. The late time currents are therefore sufficiently long to investigate coupling effects regarding carbon fiber composite (CFC) aircraft.

In this paper, numerical modeling results are presented which indicate the usefulness of the crowbar switch approach. First, the approach is applied to a uniform cylindrical test object, in order to study responses which are not confused by the presence of variations in a real aircraft geometry. Next, the approach is applied to a three dimensional (3D) model of an F-16 aircraft.

The analysis shows that the crowbar switch can be used to accomplish the desired objectives. The test approach does introduce spurious resonances from the test fixture/aircraft interaction. An approach is also given for terminating the aircraft such that these resonances are minimized. It is found that the approach works quite well for a uniform cylinder, but is not as effective for a real aircraft geometry.

Experiments are planned by Lightning and Transients Research Institute of Minneapolis, Minnesota, to verify the analytical results. Unfortunately, they were not yet available at the time of publication.

2 - RESPONSE OF A UNIFORM CYLINDRICAL TEST OBJECT

A right circular cylinder test bed is used to provide basic information for the response of an object in a candidate simulator design configuration. The basic cylinder configuration is shown in Figure 2.1, which includes the Marx generator, geometrical information, spark gaps, and terminations. This response is obtained by treating the configuration as a uniform transmission line.

The model combines the solutions for the telegrapher's equations in the test fixture itself with the solutions for the circuit which represents the Marx generator. The solution is accomplished in the time domain using finite difference techniques [6].

The results for the injected current, I, are shown in FIgures 2.2 and 2.3.

In Figure 2.2, the responses with and without a crowbar are indicated for a short circuited termination ($R_T = 0$). When there is no crowbar, 3 resonances are indicated:

1. The 1.45 kHz oscillation due to the resonance of the Marx generator with the test object.

2. The 1.5 MHz oscillation due to the resonance of the peaking capacitor with the test object.

3. The 6.7 MHz oscillation of the test object shorted on one end and loaded in a 2.5 nf capacitor on the other.

The crowbar is switched on at the time of the largest peak current. It is clear that the crowbar eliminates the lowest frequency oscillation.

The other oscillations are troublesome because they, too, are caused by simulator/test object interactions. One approach to minimize these resonances is to provide a matched termination impedance (71.4Ω) on the transmission line. The disadvantage of this approach is that the peak current level will be limited to approximately 4 kA (300 kV divided by 71.4Ω). An alternate approach is to put a shunt termination inductance L_T in parallel with the resistance R_T. The objective in doing this is that at high frequencies, the line is nearly perfectly matched, but at low frequencies, the termination is inductive. Thus the high frequency oscillations are heavily damped, and the low frequency current discharge of the Marx generator is limited by the termination inductance and not the termination resistance.

Results for L_T = 1 and 10 μH are shown Figure 2.3. A 1 μH inductance allows the highest frequency resonances to be damped fairly well, but the lower frequency resonances are not. A 10 μH inductance will significantly damp even the lower frequencies. The price that is paid for damping the oscillations is reduction of the injected current amplitude. However, even with 10 μH, the peak current is nearly 11 kA, significantly higher than the 4 kA one could obtain with a matched resistive termination.

One other approach which could be done would be to switch the crowbar on at the earliest main peak. Although no analysis of this case was done, it is clear from Figure 2.3 that the peak current would be about 9 kA for 1 μH inductance, but only about 6 kA for the 10 μH inductance. The late time response would be a damped exponential with superimposed high frequencies of about the same amplitude as indicated in Figure 2.3

The results show that the crowbar switch can be used to provide the desired late time response.

3 - THREE DIMENSIONAL AIRCRAFT RESPONSE IN A FULL SCALE SIMULATOR

The modeling approach is the same as in the previous study [1,2], but is repeated here for convenience.

The three dimensional finite difference technique [6] is used to model the response of a full size aircraft in a full scale simulator. The configuration is shown in Figure 3.1. The large clearances are required to provide sufficient voltage stand off such that arcing of the aircraft to the fixture does not occur. Voltages exceeding 6 MV are expected on the aircraft.

The aircraft is an F-16, and the shape of the computer model is shown in Figure 3.2. The cell size is 1 meter in the longitudinal direction, and is 1/2 meter in the other directions. The time step is 1 ns. Because approximately 5 cells are required to resolve a wavelength, the upper frequency limit of the computation is 60 MHz. The erected Marx voltage is 4 MV, and the output spark gap is adjusted to arc over when the gap voltage exceeds 6 MV. The measurement point is the injected current I.

The results are shown in Figures 3.3 - 3.5.

Figure 3.3 shows the injected current for a shorted termination with and without a crowbar. The effect of the crowbar is clearly seen and extends the current out in time. There is a resonant structure on the waveform due to the natural resonances of the aircraft in the test fixture and the interaction of the aircraft with the test configuration. They may be summarized as follows:

1. The 4 MHz resonance is the resonance of the aircraft shorted to the fixture on one end and terminated in the peaking capacitance on the other end. This is roughly a quarter wave resonance.

2. The roughly 250 kHz resonance of the Marx capacitor discharging into the aircraft and Marx inductances.

3. Higher frequency resonances on the order of 10 MHz which are related to aircraft structure dimensions.

It is desirable to damp out the aircraft/test fixture resonances, in the same manner as was described Section 2. Figure 3.4 shows the injected current for different values of L_T and with $R_T = 78\Omega$. Figure 3.5 shows the same thing for $R_T = 150\Omega$. The 78Ω case seems to be a better march, but the match is not very good in any case. The spurious oscillations are not greatly damped in any case, although the 30 μH inductance with 78Ω seems to be the best. The damping is not nearly as good as was possible with the cylindrical geometry previously discussed. This is because the aircraft is not a uniform transmission line, and the aircraft impedance seen at the termination is a frequency dependent complex number, and cannot be completely damped with a resistor, as is possible with a uniform transmission line.

4 - SUMMARY AND CONCLUSIONS

The intent of the work reported here has chiefly been to demonstrate the applicability of a crowbar switch to a fast risetime simulator configuration. The results indicate that the approach can be successfully used to increase the pulse width beyond the time constants of interest for testing composite aircraft.

A separate but related issue concerns the presence of resonances in the injected current which are caused by interaction of the test object with the simulator. An approach was studied to minimize these resonances. It was found that for a uniform transmission line, they could be damped by terminating the line in its characteristic impedance, and shunting this with an inductor which still allows a rather large late time current. When applied to an actual aircraft, this approach does reduce these resonances, but not to the same degree as was possible with a uniform line. This is because the aircraft geometry cannot really be represented by a uniform transmission line. However, it is believed that these spurious resonances might be reduced with more judicious choices for termination impedances and a more detailed test fixture design.

REFERENCES

1. Robb, J.D. and R.A. Perala, "Measurements with Theoretical Analysis of a Full Scale NEMP Type Lightning Similator for Aerospace Vehicles," published in the 1983 Proceedings of the International Aerospace and Ground Conference on Lightning and Static Electricity."

2. Perala, R.A. and S.L. Parker, "Numerical Modeling of the Response of an Aircraft in a Fast Risetime Threat Level Lightning Simulator," EMA 83-R-18, March 1983.

3. Robb, J.D. and R.A. Perala, "Experimental and Theoretical Evaluation of a Fast Risetime, High Current Lightning Indirect Effects Simulator," Presented at and Published in the Proceedings of the International Aerospace Conference on Lightning and Static Electricity, Oxford England, March 1982.

4. Robb, J.D. and R.A. Perala, "NEMP Type Lightning Indirect Effects Simulation for Aerospace Vehicles," Proceedings of the 1981 EMC Conference, Boulder, Colorado, August 1981.

5. Robb, J.D., "An Experimental and Theoretical Investigation of a NEMP Type Fast Rise Lightning Simulator," AFWAL-TR-84-3007, 15 March, 1984.

6. Merewether, D.E., and R. Risher, "Finite Difference Solutions of Maxwell's Equations for EMP Applications," Electro Magnetic Applications, EMA-79-R-4, 24 July, 1980.

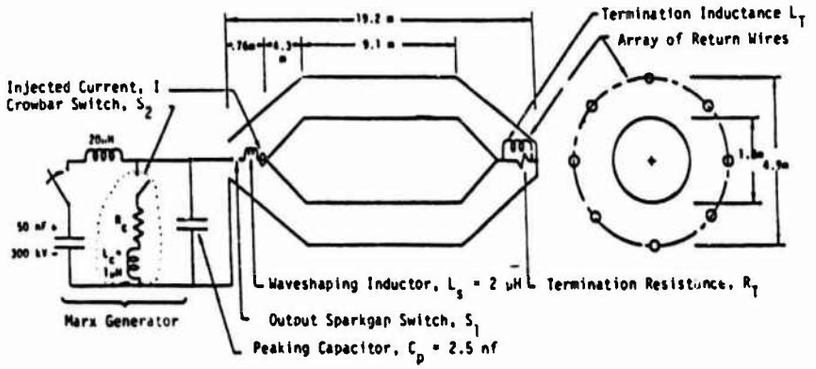


Figure 2.1 Basic Cylinder Configuration. S_1 Turns On When the C_p Voltage Reaches 300 kV.

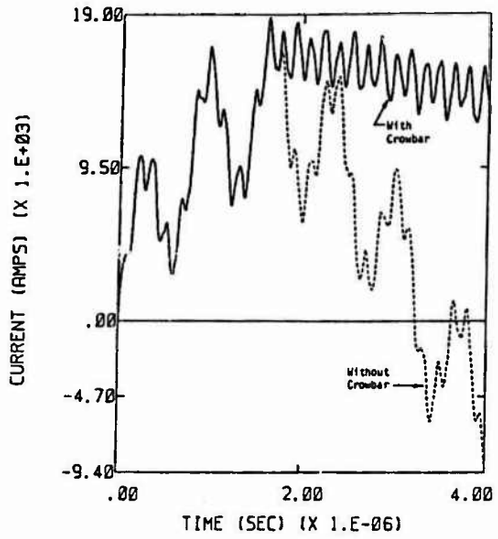


Figure 2.2 Current I for a Shorted Termination, With and Without a Crowbar Switch.

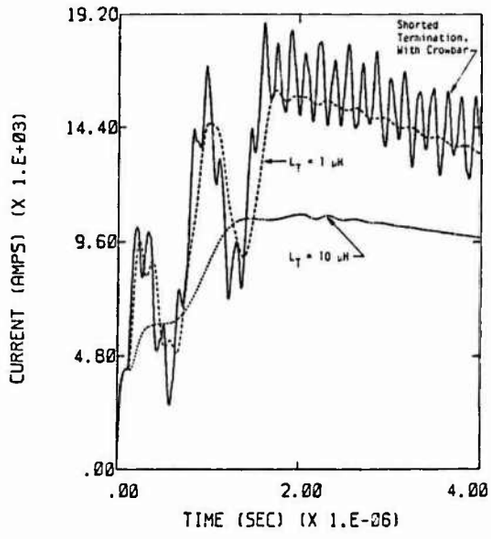


Figure 2.3 Current I with R_T = 71.4Ω and L_T = 10 ΩH, Both With a Crowbar, Results for Shorted Termination With Crowbar Also Shown For Comparison.

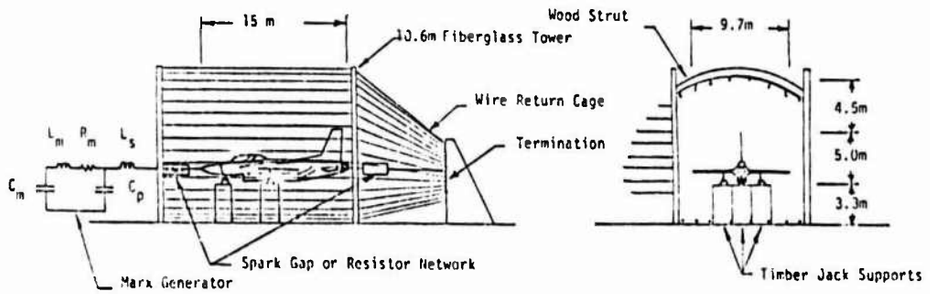


Figure 3.1 F-16 Aircraft in Full Scale Simulator.

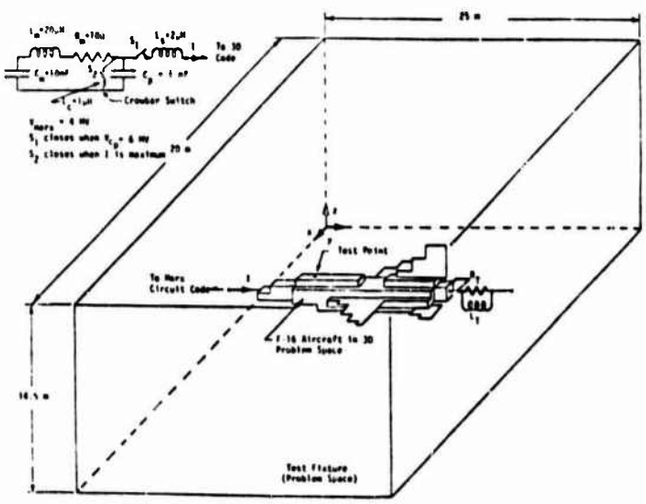


Figure 3.2 Three Dimensional Finite Difference Model of F-16 Aircraft in Test Fixture.

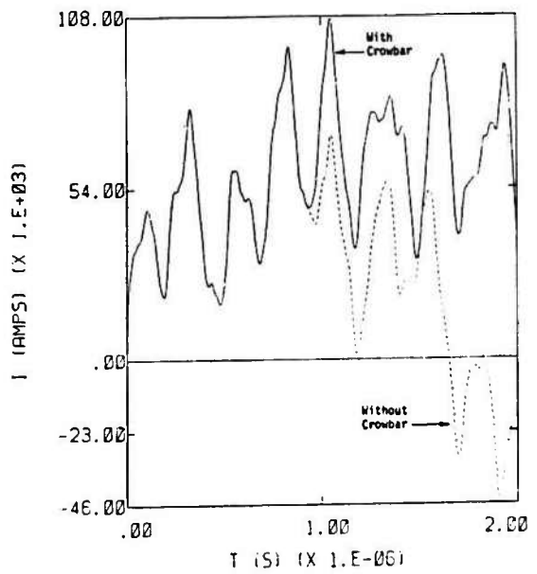


Figure 3.3 I for Short Circuited Termination With and Without a Crowbar.

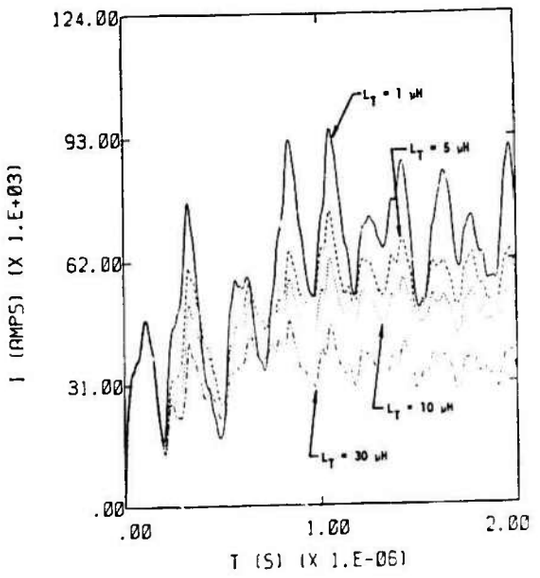


Figure 3.4 I with 78 Ω Termination and Different Values of the Shunt Inductance.

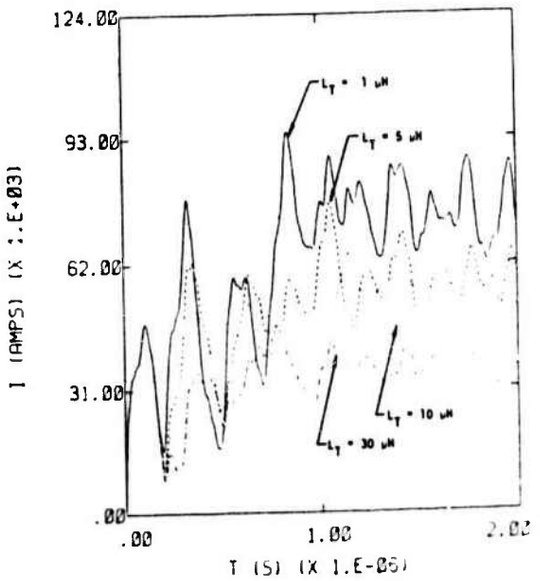


Figure 3.5 I with 150 Ω Termination and Different Values of the Shunt Inductance.

THE OBSERVATION OF HIGH FREQUENCY $\dot{B}$ AND $\dot{D}$ TRANSIENTS EXCITED ON A FUSELAGE BY AN IMPULSE GENERATOR

C.J. Hardwick and V.P. Dunkley

UKAEA Culham Laboratory, Abingdon, Oxon OX14 3DB, U.K.

Abstract

High frequency transients in the MHz range of both $\dot{B}$ and $\dot{D}$ on a Hawker Hunter fuselage subjected to a simulated lightning strike have been observed. The magnitude and frequency content of the waveforms and their variation with position on the fuselage have been measured and a comparison is made with various models of the fuselage-lightning simulator system. Both distributed and lumped models of the transmission line formed by the fuselage and the conductors connecting it to the lightning generator give a reasonable description of the transients. The $\dot{D}$ transients occuring were quite large and can induce large voltages on exposed, high impedance circuits.

INTRODUCTION

Investigations of induced voltages on aircraft wiring during whole aircraft simulated lightning tests, for example on the Fly-by-Wire Jaguar (Ref. 1), the Saab Viggen (Ref. 2), on the Hawker Hunter fuselage at Culham (Ref. 3), and in tests done in the USA (Ref. 4) have shown the existence of bursts of HF oscillations in the MHz range at the beginning of the waveform. These high frequency transients are due to both capacitive coupling (proportional to rate of change of electric field $\dot{D}$) and inductive coupling (proportional to the rate of change of magnetic field $\dot{B}$). In order to predict what values of induced voltage might be expected it is important to have a knowledge of the values of $\dot{B}$ and $\dot{D}$ on the aircraft.

Essentially a simulated lightning strike to an aircraft is obtained by discharging a capacitor bank into a circuit consisting of the aircraft and its return conductors. The resulting aircraft current waveform contains low frequency oscillations, in the 10-200 kHz range, arising from the resonant circuit of the bank capacitance and the total circuit inductance, and high frequency oscillations in the 10-50 MHz range during the first few microseconds, arising from the shock excitation of the natural resonances of the aircraft.

Recent work by Burrows (Ref. 5) and Evans (RAE Farnborough, Private Communication) has attempted to calculate in some detail the magnitude and shape of these high frequency current transients in an idealized aircraft structure and the resultant $\dot{B}$, $\dot{D}$ waveforms. This present paper describes measurements of $\dot{B}$ and $\dot{D}$ at various positions along the Hawker Hunter fuselage and compares the results with the predictions.

Until recently assessment of lightning induced effects has concentrated mainly on the effects of magnetic fields. It is now thought that during a natural lightning strike, there are large values of $\dot{D}$ during the leader attachment to the aircraft and a significant proportion of induced effects can be due to this process especially in circuits of high impedance.

Therefore, measurements of the induced voltage on an open circuit wire on the Hunter fuselage have been made and we compare these measurements with predictions calculated from the measured $\dot{D}$ values.

THE HAWKER HUNTER TEST ASSEMBLY

The test assembly at Culham consists of a Marx generator connected to the Hawker Hunter fuselage with a quasi coaxial system of return conductors shown schematically in Figure 1a.

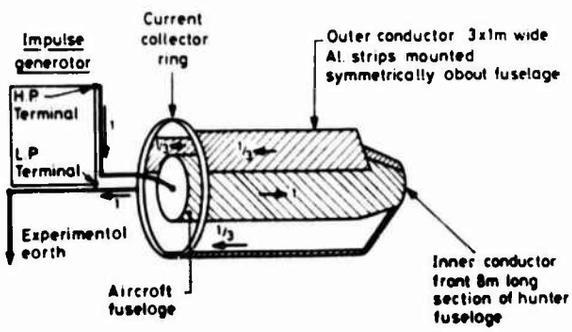


Fig. 1a

The wings and tail fin had been removed from the fuselage and the cockpit canopy had been replaced by an aluminium sheet cover. The fuselage and return conductor system is electrically similar to a transmission line with a short circuit at the remote end, and an equivalent circuit is shown in Figure 1b.

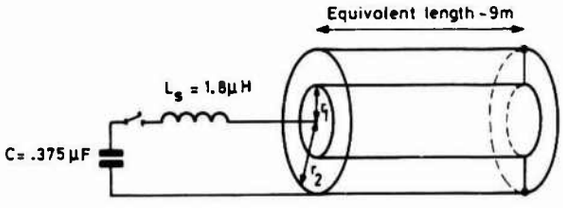


Fig. 1b

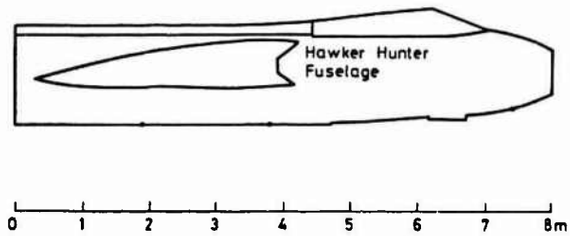


Fig. 2

As we are interested in comparing the effect of applying a theoretical step impulse of voltage to the fuselage with experimental behaviour, only a single stage of the Marx generator was used in order to simplify the actual shape of the impulse applied. The high voltage switch was a triggered spark gap. The parameters of the system were as follows:-

Capacitance	= .375 μF
Voltage	= 50-150 kV
Total inductance, L	= 3.1 μH
Series damping resistance	= 150 mΩ at 147 kHz

The inductance, L_o and capacitance C_o per unit length of a concentric pair of cylinders are given by:

$$L_o = 0.2 \ln \frac{R_2}{R_1} \ \mu H/m$$

$$C_o = \frac{2\pi\varepsilon o}{\ln \frac{R_2}{R_1}} \ F/m$$

With our geometry R_2 = 1.3 m and R_1 = 0.64

giving L_o = .14 μH/m

$$C_o = 79 pF/m$$

and a characteristics impedance,

$$Z_o = \sqrt{\frac{L_o}{C_o}} = 42 \ \Omega$$

The fuselage is 8 m long, however, the protruding wing stubs and finite diameter of the coaxial assembly will effectively increase the length of the transmission line. Therefore we have approximated our system by a 9 m length of line of the above characteristic impedance. Hence, we estimate a source inductance Ls of about 1.8 μH and a "bothway travel time" of 50-60 ns.

Measurements of $\dot{B}$ and $\dot{D}$ were made with diagnostic probes attached to the underside of the fuselage along the bottom centre line. A side view of the fuselage with a distance scale is shown in Figure 2.

DIAGNOSTIC PROBES AND DATA ACQUISITION

$\dot{D}$ Probe

The $\dot{D}$ probe used was an EG&G conforming flat dipole CFD-1B. Manufacturers paramters for the probe are: rise time 1.1 ns; frequency response 300 MHz; an effective area of 10^{-3} m^2; and it requires a load impedance of 50 Ω giving an output of 1 V for a $\dot{D}$ of 20 A/m^2. The ground plane of the dipole was attached to the underside of the fuselage. Signals from the probe were conveyed to a FOL 200 fibre optic transmitter located inside the fuselage via 50 Ω coaxial cable.

J_s Probe

The J_s probe was a small 6 turn coil of cross-sectional area 0.7 x 10^{-4} m^2. The axis of the coil was aligned at 90^0 to the axis of the fuselage, parallel to the lines of magnetic field around the fuselage. The signals from the coil were conveyed to a FOL 100 transmitter located inside the fuselage with an 8 m length of 80 Ω screened, twisted pair cable with appropriate termination and 2 x 0-31 dB variable attenuators. The 8 m length of cable was attached close to the fuselage surface. The 3 dB point on the frequency response curve for the probe-cable assembly was 30 MHz. The probe gives about 1 V output for a $\dot{B}$ of 2300 T/s.

$\dot{B}$ Probe

During the later stages of the program an EG&G multi gap loop ground plane MGL-2A $\dot{B}$ probe was obtained. This was connected to the FOL 200 in a similar way to the $\dot{D}$ probe. The probe was used as a check on the frequency content and magnitude of the waveforms obtained with the J_s probe. The probe has a frequency response > 2 GHz, an equivalent area of 10^{-4} m^2 and gives 1 V output for a $\dot{B}$ of 10^4 T/s. The waveforms obtained from the J_s and $\dot{B}$ probes were similar except for the better frequency response of the $\dot{B}$ coil.

The FOL 100 and 200 transmitters of bandwidths 100 and 200 MHz respectively, were connected via fibre optic cables to their corresponding receiver/control units in the screened room. Signals from them were connected to a Tektronix 7612 D ditigiser via appropriate plug-in units. The digitiser has a maximum of 2048 samples per channel and a minimum time between samples of 5 ns.

EXPERIMENTAL RESULTS AND COMPARISON WITH "LUMPED ELEMENT" AND "LUMPED SOURCE" MODELS

Typical $\dot{D}$ and $\dot{B}$ waveforms at 10 cm along the fuselage, essentially at the input end, are shown in Figure 3a and b. Waveforms were also recorded at other positions along the fuselage. The basic shape remained the same but the magnitude of the different frequency components varied. The magnitudes were repeatable to better than 10% and also scaled linearly with the generator voltages to within 15% over the range of 50-150 kV.

The main features of the $\dot{B}$ waveforms are a low frequency cosine wave oscillation at 147 KHz and a large high frequency component at 9.4 MHz. The $\dot{D}$ waveform shows no low frequency component. The high frequencies decay after about 5 microseconds. The time constant for the decay is 2.0 μs giving a HF resistance of about 2 Ω. This is consistent with the increase in resistance in going from 147 kHz to 9.4 MHz due to the decrease of skin depth.

A fast Fourier transform of both $\dot{B}$ and $\dot{D}$ waveforms shows a second high frequency at 25 MHz generally less then one tenth the 9.4 MHz component. Also some waveforms show enhancements in the range 10-12 MHz.

The simplest model of a simulated lightning rig is a "lumped element" model where a capacitor C at potential V_o is discharged through a load inductor L, and series resistor R as discussed by Burrows in Ref. 5. This results in a damped low frequency oscillation, the frequency given by $1/2\ \pi\sqrt{LC}$. The peak value of $\dot{I}$ is given by V_o/L. Clearly this model cannot predict the high frequency behaviour or the variation of $\dot{I}$ at positions down the fuselage.

An alternative approach proposed by Burrows is the "lumped source model". Provided the impulse generator and its connecting plates to the aircraft/return conductor assembly are kept small, compared to the length of the aircraft/return conductor transmission line (TL), then the circuit can be considered as shown in Fig. 1b. The generator is composed of a lumped source inductance, Ls, representing the generator and connecting plate inductance and a voltage source producing a voltage step, V_o when the switch is closed. The generator capacitance is not represented as for times short compared to the lumped element model low frequency period of oscillation, the capacitance will not discharge appreciably. The load is the transmission line and the voltage step will travel down the line towards the short circuit end. The impedance is essentially purely resistive and equal to Zo, the characteristic impedance of the TL, until the arrival of the reflected voltage step from the short circuit end at the source modifies the apparent impedance of the line. Using this model the initial HF transient value can be calculated and is given by:

$$\dot{I} = \frac{V_o}{Ls}\ e^{-t/\tau s}$$

$$\text{where } \tau s = \frac{Ls}{Z_o}$$

Hence the peak $\dot{I}$ value is greater than the lumped element model by the ratio L/Ls. In our particular example we have a ratio of 3.1/1.8 = 1.7.

The initial peak $\dot{D}$ and $\dot{B}$ values can he calculated from the formulae:

$$\dot{B} = \frac{\mu_o \dot{I}}{2\ \pi\ R_1}\ T/s$$

TABLE 1

CALCULATED VALUES OF $\dot{I}$, $\dot{D}$ AND $\dot{B}$ FROM LF LUMPED ELEMENT AND LUMPED SOURCE MODELS AND OBSERVED VALUES OF $\dot{D}$ AND $\dot{B}$ AT INPUT END OF LINE FOR DIFFERENT BANK VOLTAGES

Bank voltage	LF Lumped element model predictions L = 3.1μH			Lumped source model predictions L_s = 1.8μH			Observed values at input end	
kV	$\dot{I}$ kA/μs	$\dot{D}$ A/m^2	$\dot{B}$ T/s	$\dot{I}$ kA/μs	$\dot{D}$ A/m^2	$\dot{B}$ T/s	$\dot{D}$ A/m^2	$\dot{B}$ T/s
50	16.1	13.2	5031	27.8	22.8	8688	31.0	8300
100	32.3	26.5	10094	55.7	45.7	17406	63.6	19000
150	48.4	39.7	15125	83.3	68.3	26031	102.4	27800

Fig. 3a

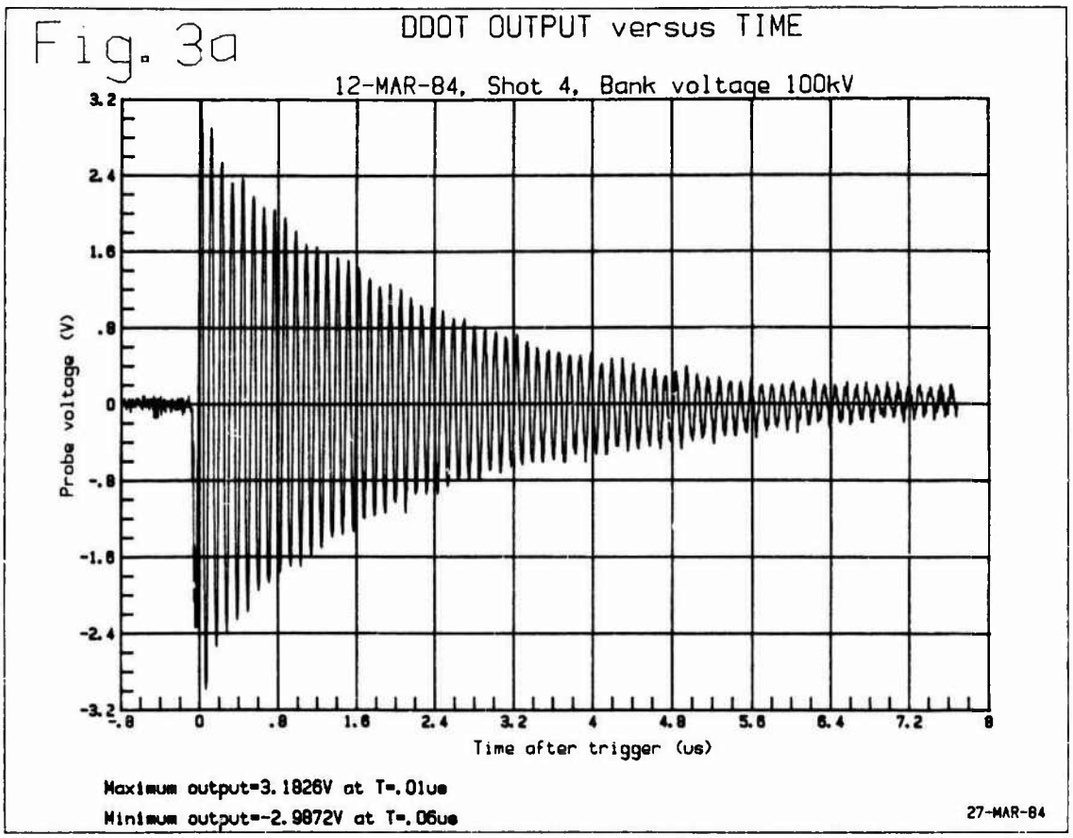
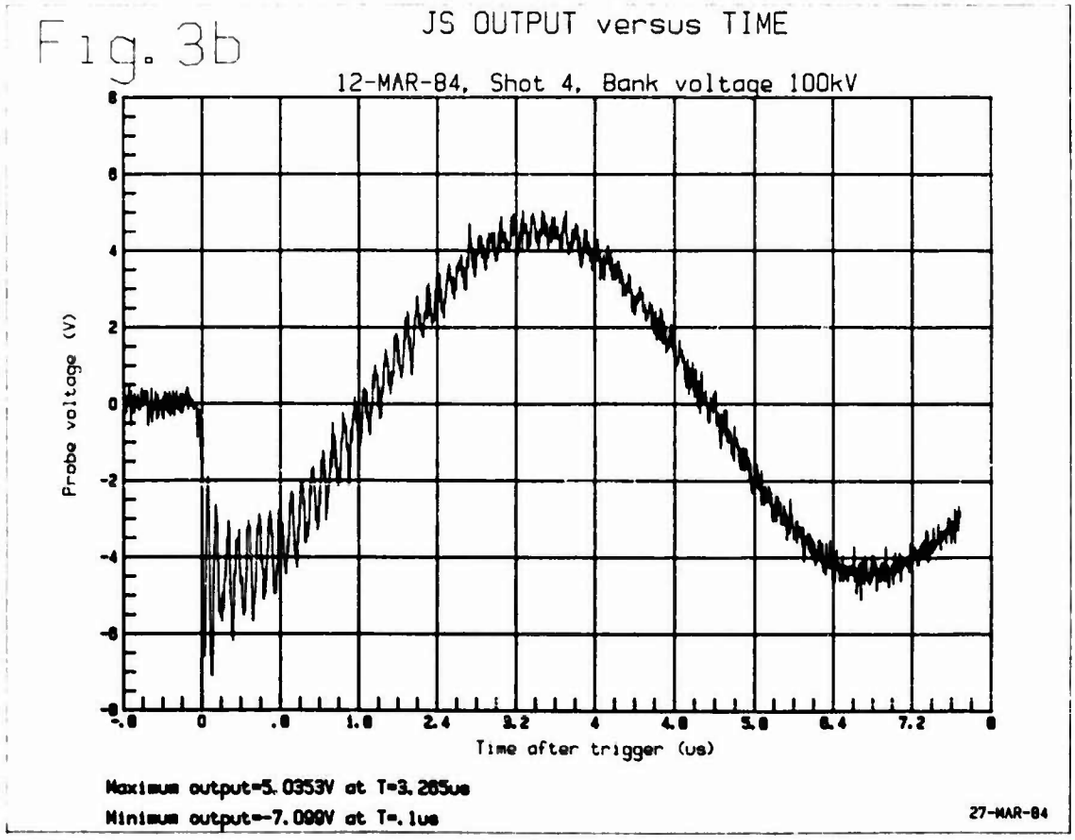

DDOT OUTPUT versus TIME
12-MAR-84, Shot 4, Bank voltage 100kV
Probe voltage (V)
3.2
2.4
1.6
.8
0
-.8
-1.6
-2.4
-3.2
-.8
0
.8
1.6
2.4
3.2
4
4.8
5.6
6.4
7.2
8
Time after trigger (us)
Maximum output=3.1826V at T=.01us
Minimum output=-2.9872V at T=.06us
27-MAR-84

Fig. 3b


JS OUTPUT versus TIME
12-MAR-84, Shot 4, Bank voltage 100kV
Probe voltage (V)
8
6
4
2
0
-2
-4
-6
-8
-.8
0
.8
1.6
2.4
3.2
4
4.8
5.6
6.4
7.2
8
Time after trigger (us)
Maximum output=5.0353V at T=3.265us
Minimum output=-7.099V at T=.1us
27-MAR-84

$$\dot{D} = \frac{\varepsilon_o \dot{V}}{R_1 \ln \frac{R_2}{R_1}} \quad A/m^2$$

and $\dot{V} = \dot{I} Z_o$ for the initial peak values.

The low frequency component of V across the transmission line will be given by $V = I\omega L$ where L is the aircraft/return conductor inductance. In our case, with a frequency of 147 kHz and L = 1.3 μH we have an impedance of 1.2 Ω which is 35 times less than Z_o. Hence the low frequency content of the $\dot{D}$ waveform will be much smaller than the HF content.

Table 1 summarises the peak, $\dot{I}$, $\dot{D}$ and $\dot{B}$ values calculated with lumped element and lumped source models for different bank voltages and, for comparison, the observed peak values of $\dot{D}$ and $\dot{B}$ at the input end of the fuselage are also shown.

We see from the experimental data that the peak values are greater than the LF values and are more in agreement with the predictions of the lumped source model. The observed values of $\dot{D}$ at the input end are 3 dB greater than the predicted values of the model but this is probably due to distortion of the electric field at the feed-in end. The $\dot{B}$ values agree to within ± 1 dB.

Variation of peak values of $\dot{B}$ and $\dot{D}$ with position along fuselage

The variation of the peak values for $\dot{D}$ and $\dot{B}$ along the fuselage is illustrated in Figures 4 and 5 respectively for data taken at 50 kV bank voltage. Also indicated in the graphs by horizontal lines are the values of $\dot{B}$ and $\dot{D}$ at the input end, calculated from the lumped element (total inductance, L = 3.1 μH) and lumped source (L_s = 1.8 μH) models as discussed above.

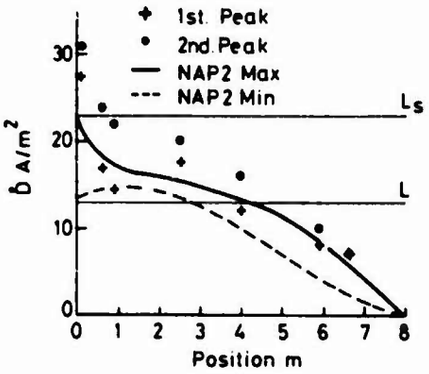


Fig. 4 Variation of peak $\dot{D}$ with position along fuselage. The experimental data points are the absolute values of the first and second peaks of the waveform. The curves are the first and second peak values calculated from the NAP2 computer code (see key).

We note that $\dot{D}$ is a maximum at the high voltage end and minimum at the short circuit end as indeed it has to be as the voltage here is zero. Similarly $\dot{B}$ is a maximum at the short circuit end as the current is maximum here. There is a minimum of the peak $\dot{B}$ at 2 m and at 1 m for the 9.4 MHz component.

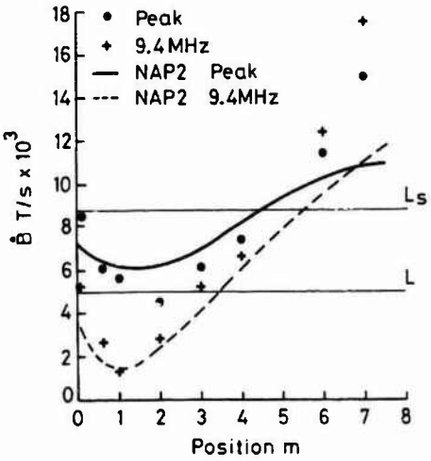


Fig. 5 Variation of peak $\dot{B}$ with position along fuselage. The experimental data points are the absolute value of the maximum peak of the waveform and the maximum value of the 9.4 MHz component. The 9.4 MHz component is the difference between successive maxima and minima and hence can be greater than the maximum peak if the following minimum has a different sign.

We will now discuss more complex models required to calculate the variation of $\dot{B}$ and $\dot{D}$ along the fuselage.

The Distributed TL Model

To evaluate possible resonant frequencies we may get in the fuselage we can consider the rig as a resonant circuit formed by the TL and the source inductance, Ls. In the case of a loss-less TL with a short circuited load the impedance is given by $Z = Z_o \tan \frac{2\pi l}{\lambda}$, where l is the length of line, Z_o its characteristic impedance and λ the wavelength, and is entirely reactive. If $(n+1)\frac{\lambda}{4} > l > \frac{n\lambda}{4}$, for n odd then the reactance is capacitive. In addition there will be some stray capacitance, C, in connecting plates from the Marx generator giving a total capacitive reactance of $\frac{1}{\omega C + \frac{1}{Z_o \tan 2\pi l/\lambda}}$ and this will be resonant with the source inductance. Figure 6 shows the variation of the total capacitive reactance and the source reactance, ωLs with frequency. Using 22pF for C, 9 m for l and 1.8 μH for Ls we see that a reasonable fit to the observed resonances of 9.4 MHz (n = 1) and 25.4 MHz (n = 3) is obtained. For 9.4 MHz, λ/4 = 8 m, hence there will be a node about 1 m in from the feed-in end of the fuselage. That is, at this point there will be a minimum in the HF component of current and a maximum in the HF

component of voltage. This is indeed observed with $\dot{B}$ which is proportional to $\dot{I}$ and hence peak I.

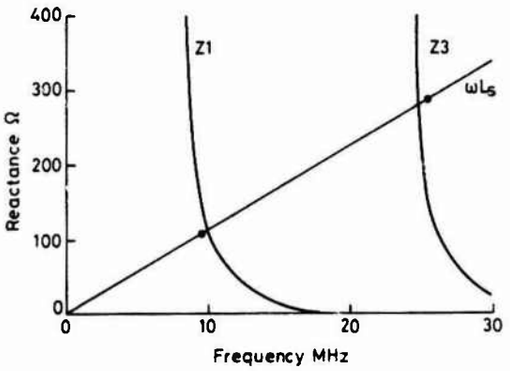


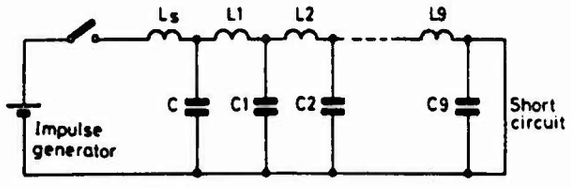
Fig. 6 The variation of source impedance (ωL_s) and the transmission line capacitive reactance for the first and third harmonics (Z1 and Z3 respectively) with frequency. The observed resonant frequencies at 9.4 and 25.4 MHz are marked on the ωL_s line by dots.

$\dot{D}$ does not show a maximum here probably due to the fact that, near the high voltage feed-in, the fuselage cylinder ends abruptly in an end plate, hence the electric field can be distorted at the edge and made larger.

The shape of the waveforms can be calculated by summing successive reflections from either end of the TL and is discussed further below.

The discrete element transmission line model

In this model the generator/fuselage system is represented by a circuit as shown in Figure 7. The fuselage is approximated by 9 equal "L" sections of L = .14 μH and C = 78pF which are the estimated inductance and capacitance per metre of the fuselage. The generator is approximated by an L section with an L = 1.8 μH and C = 22pF. The result of applying a step impulse to this circuit was analysed by a network analysis computer code (NAP2, Ref. 6) discussed in Ref. 5.



L1 = L2 = Ln = .14 μH

C1 = C2 = Cn = 78pF

Fig. 7 Representation of fuselage-generator system by a 10 section discrete element LC network.

The 1st peak and 2nd peak $\dot{D}$ values obtained are shown by the curves in Figure 4. The first peak value is always greater than the second peak value, unlike the observed values shown in the same figure, which have a maximum value at the second peak. However, the variation of the values is fairly well reproduced. The second peak shows a maximum at about 1 m as expected from the TL model but the first peak is maximum at the input end of the fuselage, due the sharpness of the impulse applied and the small value of stray capacitance used for the feed-in plates.

The model has no resistive damping and the closure time of the spark gap is assumed to be zero, hence the rise to the first peak at the input end occurs almost instantaneously whereas in practice $\dot{D}$ takes 40 ns to reach its first maximum, presumably due the closure time of the gap and perhaps, more stray capacity in the generator-fuselage connection than estimated. A finite closure time will decrease the calculated values.

The peak and HF values of $\dot{B}$ obtained from the model are shown by the curves in Figure 5. The curves fit reasonably well to the experimental data, also shown in the figure. In particular the minimum in the HF value is well reproduced. The measured values are greater than the calculated values towards the nose end of the fuselage as no allowance for the decrease in radius of the fuselage has been made.

Comparison of distributed and lumped models of the transmission line

Another approach to calculate the shape of the waveforms is due to Evans. (RAE Farnborough, Private Communication). Here the fuselage is represented by an idealized transmission line as discussed above. The waveforms are calculated by adding successive reflections from either end of the line. Again the model does not take account of resistive effects or the switch closure time.

As the line is loss-less all frequencies are equally well transmitted, hence the initial sharp rises of $\dot{D}$ and $\dot{B}$ are maintained after any number of reflections, and the resulting waveforms are fairly spiky, especially the $\dot{D}$ waveform, unlike those actually observed and those calculated by the NAP2 computer program.

In fact the impulse applied has about a 40 ns rise to maximum $\dot{D}$ and $\dot{B}$, hence the discontinuities in the waveforms due to summation of the reflected waves will be smoothed out. Moreover, the fuselage return conductor assembly has protruding wing stubs, a protruding cockpit and a tapered section of the return conductors near the nose of the fuselage where the short circuit is made. All these features will produce changes in the impedance of the line in a distance much less than 1 wavelength, hence reflections will occur at these features smoothing out even more the waveforms. Therefore the uneven nature of the fuselage is better represented by the discrete element model in which the dominant high frequency component is the fundamental λ/4 resonance and the higher harmonics are suppressed.

Figure 8 shows a comparison of the observed waveforms of $\dot{D}$ at the input end together with the predicted waveforms from the two models. Figure 9 shows similar waveforms for $\dot{B}$.

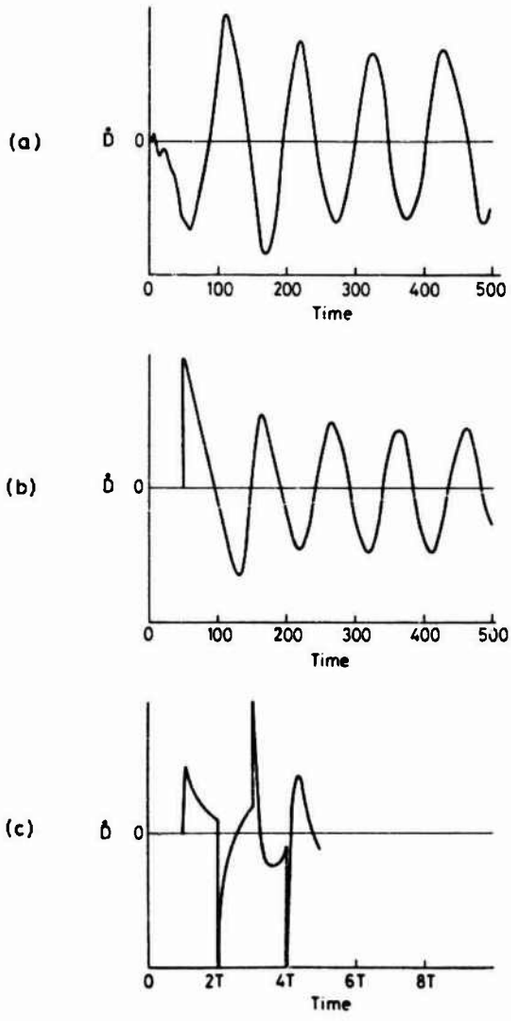


Fig. 8 Comparison of observed and calculated $\dot{D}$ waveforms at the input end of fuselage. The amplitude scale is abitrary.

(a) The observed waveform. The phase is reserved compared to b. and c. due to instrumentation.

(b) Waveform calculated from NAP2 computer code.

(c) Waveform taken from Evans. For this plot the timescale is in multiples of T (= 53ns), the bothway travel time of signals on the fuselage. The waveform is for L/Ls = 1. In our case L/Ls = 1.7. This will increase even more the sharpness of the waveform.

$\dot{D}$ COUPLING TEST

In real aircraft, unlike the Hunter fuselage which was completely closed, D fields can penetrate apertures which are not covered by conducting sheets, for example the cockpit and bays which are covered by GFRP or Kevlar. Wiring circuits which are un-terminated, for example wires ending in the cockpit at open switches, are especially susceptible to $\dot{D}$.

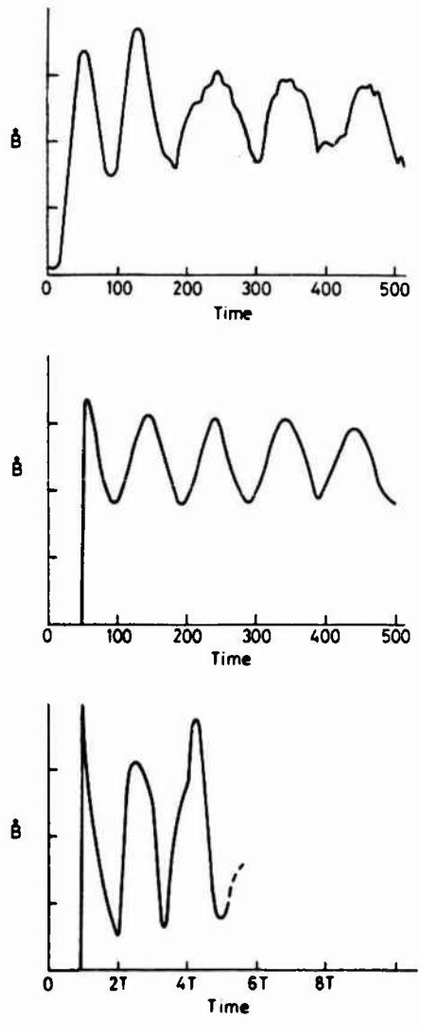


Fig. 9 As figure 8 but for $\dot{B}$ waveforms.

A test on induced voltages on open circuit wires was made by suspending 70 cm long wires of two different diameters and hence capacitance about 4 cm from the underside of the fuselage. One end of the wire was connected to the FOL 200 and terminated into 440 Ω, a typical avionic system impedance; the other end was left open circuit. The arrangement is shown schematically in Figure 10. Very large voltages, up to 1 kV, were induced on the wire when a pulse from the Marx generator was applied to the fuselage.

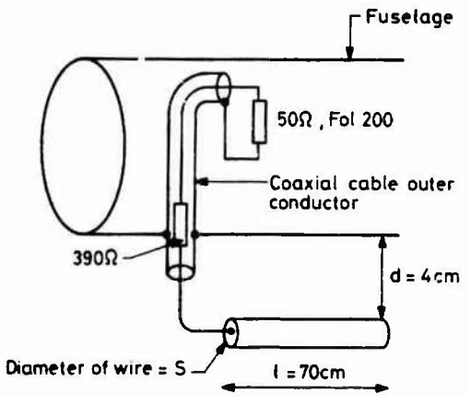


Fig. 10 Schematic diagram of fuselage with suspended open circuit test wire.

The voltage induced on the wire can be calculated as follows:

The charge Q, stored per unit length of wire is related to the voltage between it and the fuselage by:

$$Q = CV$$
$$\therefore I = C\dot{V} \text{ for } \ell \ll \lambda$$

where C is the capscitance per unit length between the wire and the fuselage.

As the dimater of the fuselage $\gg$ diameter of wire, the capacitance C per unit length is given by:

$$C \sim \frac{2\pi\varepsilon_o}{\ln \frac{4d}{s}}$$

where d is the distance between the wire and the fuselage and s is the diameter of the wire (see Figure 10).

$C \sim 20$pF/m for s = 12mm
~ 11pF/m for s = 1 mm

$$\therefore \text{Voltage measured} = RC\dot{V} = \frac{RC\dot{D}d}{\varepsilon_o}$$

$$= \frac{2\pi Rd\,\ell\dot{D}}{\ln \frac{4d}{s}}$$

where ℓ is the length of wire and R is the impedance.

The measured $\dot{D}$ at the position of the wire was .46A/m^2/kV.

A comparison of observed and calculated values is made in Table 2. The values agree to within 2 dB. The shape of the waveform also follows the $\dot{D}$ waveform as would be expected. The predominant frequency is the 9.4 MHz resonance with a smaller peak at 25 MHz.

TABLE 2

COMPARISON OBSERVED AND CALCULATED INDUCED VOLTAGE ON TEST WIRE

	Diameter of wire			
	1mm		12mm	
	Bank voltage kV			
	50	100	50	100
Observed voltage volts	422	813	554	1390
Calculated voltage volts	351	702	687	1374

SUMMARY

Extensive measurements of $\dot{B}$ and $\dot{D}$ on the Hunter Fuselage excited by 50 to 150 kV impulses from a single stage Marx generator have been made.

The peak values of $\dot{B}$ and $\dot{D}$ at the input end of the fuselage are in approximate agreement with the lumped source model of Ref. 5.

The resonant frequencies and the variation of the transient magnitudes with fuselage position can be understood in terms of a TL model of the fuselage and return conductors.

The detailed shapes of the waveforms observed at different positions along the fuselage are more similar to those predicted by the discrete element TL model using ten L-section filters than a more idealized distributed model of the fuselage. Remaining discrepancies are probably due to the non-uniform shape of the fuselage, resistive damping and switch closure time effects.

The voltage induced on an open circuit wire near the fuselage agreed well in both magnitude and time structure with that calculated from the measured $\dot{D}$ values. In view of the large values of voltage induced (~ 1000 V) it is important to agree on an international standard for $\dot{D}$ values and to measure $\dot{D}$ values on the airframe during whole aircraft tests.

REFERENCES

1. R Evans, J Bishop: Induced Transients in Simulated Lightning Test of Fly-by-Wire Jaguar Aircraft: Proc. International Conference on Lightning & Static Electricity, Fort Worth, Texas, June 1983.

2. B Walgren, B Olsson, C Luther: Lightning Testing of Viggen Aircraft; Proc. International Conference on Lightning & Static Electricity, Oxford, March 1982.

3. B Burrows, C Luther, P Pownall, 'Induced Voltages in Full Sized Aircraft at 10^{11} A/s' Proceedings of IEEE Symposium on EMC Seattle Washington 1977.

4. W Butters, D Clifford, K Murphy, K Zeisel, B Kuhlman, 'Assessment of Lightning Simulation Test Techniques'. Proceedings of the International Conference on Lightning and Static Electricity, Oxford, March 1982. Published by Culham Laboratory.

5. B Burrows: Nanosecond Resolution of $\dot{E}$, $\dot{H}$ and $\dot{I}$ in Aircraft Lightning Test Rigs; Proc. International Conference on Lightning & Static Electricity, Fort Worth, Texas, June 1983.

6. T Rubner-Peterson, 'NAP2 - A nonlinear Analysis Programe for Electronic Circuits' Users Manual 16/5-73. Institution of Circuit Theory Telecommunications Technical University of Denmark.

ACKNOWLEDGEMENTS

The authors would like to acknowledge the support given by the Procurement Executive, Ministry of Defence, UK for the work reported in this paper.

LIGHTNING SIMULATION TESTS ON FAA CV-580 LIGHTNING RESEARCH AIRCRAFT

L.C. Walko and Lt J.L. Hebert

U.S. Air Force Wright Aeronautical Laboratories, AFWAL/FIESL, Wright Patterson AFB, Ohio 45433, U.S.A.

Abstract

Lightning simulation tests were performed by the United States Air Force Wright Aeronautical Laboratories Atmospheric Electricity Hazards Group on a specially instrumented Federal Aviation Administration Convair CV-580 aircraft. The mission of this aircraft is to obtain information on the characteristics of airborne lightning attachment to the aircraft. In June 1984, the aircraft was subjected to high current pulses such as would be encountered from lightning return strokes during lightning attachment. During these tests current pulses of up to 115 kA were applied to the aircraft. In October 1984, after the summer CV-580 in-flight program , additional simulation tests were performed. A fast risetime lightning generator was used to apply current pulses of up to 46 kA, with risetimes of under 200 nanoseconds. This paper describes the tests performed, the test setups and a comparison of the results from each of the tests.

Introduction

In June 1984, the CV-580 aircraft was flown to Wright-Patterson AFB for installation of the data acquisition equipment needed for the in-flight lightning measurements program that was to begin in Summer of 1984. The aircraft was instrumented for the in-flight program to measure the lightning current flow on the wing tips, the normal and horizontal component of current density on the fuselage and on the wings, the electrostatic field, and the VHF radiation during direct lightning attachment. More details on these sensors and data acquisition equipment can be found in Reference 1.

The objectives of the lightning simulation tests that were performed in June 1984 were:

a. To verify shielding integrity of sensor signal cables, data acquisition equipment and instrumentation power sources and lines.

b. To record electromagnetic signals resulting on the aircraft from a medium level current pulse to gain operational experience and to provide baseline data for comparison with succeading lightning measurements.

c. To verify effectiveness of hardening measures used to protect the CV-580.

In October 1984, after the in-flight measurements program in Florida, the aircraft was returned to Wright-Patterson for removal of the data acquisition equipment. Before this was accomplished, another series of lightning simulation tests was performed on the aircraft. A major difference in this test effort was the use of a current impulse generator capable of applying a sub-microsecond risetime current waveform to the aircraft. This generator was developed by the Atmospheric Electricity Hazards Group to investigate the electromagnetic indirect effects of a very fast changing current pulse on aircraft electrical circuits (2,3). In addition to the use of the fast risetime generator, a coaxially-configured current return path was fabricated around the aircraft. This was used to aid in keeping total test circuit inductance low and rate of rise of the applied waveform very fast. The signal outputs of the electromagnetic sensors on the aircraft were again measured. A number of representative lightning current paths were used. In a few cases, the method of generator attachment to the aircraft was varied from direct to arc attachment.

The following is a more detailed account of the test efforts.

June 1984 Tests

Figure 1 shows the June 1984 test setup. The impulse current generator used was a four stage capacitor bank equivalent to 4 μF, 200 kV. A heavy wire mesh screening was placed under the fuselage and wings. The aircraft was isolated from ground by Lexan sheets. The aircraft fuel tanks were topped up with JET-A fuel at Dayton International Airport and the aircraft was flown to Wright-Patterson AFB, where the ullage in the fuel tanks was inerted by injecting nitrogen into the tanks to replace fuel/air vapors. This insured a non-explosive atmosphere in the tanks during the test. Table 1 lists the simulation tests performed over a three day period.

The tests began with instrumentation noise tests at applied current pulses of 11 kA to 16 kA. Power was generated by the aircraft APU for the on-board instrumentation. These noise measurements were made with the sensors disconnected from their cables. The cables were either terminated in open circuit for the E-field sensors, or short circuit for the magnetic field and current sensors. A shielded cap was placed over the cable end in both cases to insure all

extraneous noise pickup would be characteristic of the cable itself. Risetime on the unidirectional waveform was 14 μs. Current paths chosen for the noise tests were nose-to-tail and nose-to-right wing.

All sensors were reconnected and the aircraft was then subjected to higher current levels by applying oscillatory current pulses of from 50 kA to 115 kA peak. This was done to test the basic protection integrity of the aircraft and, therefore, was performed without nitrogen injected into the fuel tanks. The left engine was operated to provide power to the on-board measurement systems for a more realistic test. All measurement systems were unaffected by the high current safety tests.

The operation of the on-board measurement systems was then observed with various current flow paths on the aircraft. A number of current path configurations were used to provide sensor data, given any combination of major lightning attachment points. An example of the applied current pulse waveform and the signals from the magnetic field sensors located on the fuselage and wings of the aircraft are shown in Figure 2. The current rises to a peak of 20 kA in approximately 14 μs. The current was applied wing-to-wing. The magnetic field measured on the wings is observed to be proportional to the applied current in waveshape and magnitude. The risetime of the magnetic field waveform appears to be slightly faster than the applied. This is due to a limitation in the response of the magnetic field sensor, which actually measures the rate of rise of the magnetic field and is then integrated. Magnetic field for a uniform current distribution is $I/2\ell$ where I is the applied current and 2ℓ or 8.3 meters is the wing cross section at the location of the wing magnetic field sensors. Assuming uniform disbribution, the magnetic field for a 20 kA peak current should theoretically be 2410 amps/meter. From Figure 2 the magnetic fields measured of 3674 amps/meter and 4310 amps/meter on the wings are within a factor of 2 of the theoretical value.

At the end of the June ground tests, the aircraft left Wright-Patterson with the major ground test objectives accomplished. The shielding integrity of the sensor signal cables, instrumentation and power sources were observed and recorded. Any inherent pickup was noted and compensated for during in-flight data acquisition. The protection hardening measures applied to the aircraft were given a final test and no problems were observed. Most important, the operation of the data acquisition system and the sensors was monitored. The tests were most helpful for system setup, choosing trigger levels and times, and establishing an operating procedure for the actual in-flight measurement program.

October 1984 Tests

After the conclusion of the Summer in-flight lightning measurement program the CV-580 aircraft was again flown to Wright-Patterson AFB in October 1984 for removal of the on-board data acquisition equipment. By this time the Atmospheric Electricity Hazards Group had constructed and operationally tested the fast risetime lightning current generator. This generator achieves the sub-microsecond risetimes by using a 4 megavolt 1 nanofarad peaking capacitor coupled with a 6 megavolt 10 nanofarad Marx generator.

The fast risetime generator was used, along with the 4 μF, 200 kV, generator, for additional tests on the aircraft. These tests were performed to recheck the operation of the aircraft sensors and the data acquisition equipment. The response of the aircraft sensors to the various applied waveforms was of primary interest. Table 2 lists the variations in test set up for the October Tests. Figure 3a and 3b show some detail of the test setup.

Figure 4 shows the fast risetime generator applied nose-to-tail. The risetime on this waveform is 200 nanoseconds with a peak current of 39 kA. Assuming $H=I/2\pi r$, where r is the radius of the fuselage, the calculated H field measured at a location on the fuselage of 10 meters circumference is 3800 amps/meters. The magnetic fields measured on the forward fuselage and aft fuselage are respectively 2225 amps/meter and 2943 amps/meter, within a factor of 2 of the calculated value. The wing sensors detected much lower fields proportional to the smaller value currents that flow on the wings during a nose-to-tail attachment.

Another nose-to-tail attachment is shown in Figure 5. The faster risetime waveform was produced by discharging the high voltage Marx generator with the peaking capacitor shorted. In this case, the comparison of theoretical to measured magnetic fields is very good. The theoretical value assuming uniform current distribution is 2000 amps/meter. The measured magnetic fields on the forward and aft fuselage are 2125 amps/meter and 1859 amps/meter, respectively.

Figure 6 shows an oscillatory current, supplied by the 4 μF, 200 kV, capacitor bank, applied nose-to-tail. The calculated magnetic field at the location of the magnetic field sensors on the fuselage is 7000 amps/meter for a peak current of 70 kA. The magnetic fields measured on the forward and aft fuselage are 3340 amps/meter and 3840 amps/meter, respectively. Again using our simple uniform current distribution the calculated and measured results are about a factor of 2 apart.

The fast risetime generator with a 16 kA peak current was applied to the aircraft in a wing-to-wing configuration as shown in Figure 7. The calculated magnetic field for the wing sensors was 1928 amps/meter. The measured values were 1788 amps/meter for the left wing and 1881 amps/meter for the right wing, a very good correspondence. A substantial amount of current was observed to flow on the aft fuselage, where 1288 amps/meter was measured. This could be due to the influence of the current return path for the test setup, which was in close proximity to the fuselage.

Test Analysis

In conjunction with these ground tests an Electromagnetic Analysis was performed for the CV-580 aircraft using a three-dimensional finite difference code (4,5). The aircraft and the lightning channel were modelled in Cartesian 3-D space as illustrated in Figure 8. The electromagnetic analysis was performed for nose-to-tail lightning strike which was modelled as a double exponential as shown in Figure 9. This waveform has a peak value of 5.3 kA and a risetime of 1 microsecond and propagated onto and off of the aircraft at the speed of light. The waveforms for the resulting fields on the aircraft shown in Figure 10 is the waveform for the integrated magnetic field at the location of the J_{SFUF} sensor on the top

of the forward fuselage and shown in Figure 11 is the electric field on top of the forward fuselage. The time step in the analysis was 1 nanosecond and the program was run for the first 2 microseconds of the pulse.

One reassuring observation from these plots is that, after some initial oscillations, the H fields which correspond to the skin current densities, basically follow the shape of the input wave. This was also shown in the waveforms of the simulated ground tests presented in this paper. Analysis of the CV-580 simulation test data and inflight data shall continue.

Conclusions

The lightning simulation tests performed on the CV-580 aircraft were very useful for providing baseline information on the operational characteristics of the data acquisition systems installed on the aircraft. The tests provided the personnel responsible for the data acquisition with experience in operating the multi-channel recording systems under simulated in-flight conditions. In addition, a final safety check of the aircraft was made by applying very high current pulses. This final check, along with the safety inspection and recommendations made by Lightning Technologies Inc. insured no problems would occur during flight.

The ground tests performed after the in-flight program came at an opportune time for not only reassessing the aircraft data instrumention but also assessing the operation of the newly configured fast risetime generator. The opportunity to apply a number of different current waveforms to the aircraft added to the knowledge of the sensor characteristics.

We have shown a comparison between the measured magnetic field values on the fuselage and on the wings and the calculated magnetic field values assuming a uniform current distribution on the aircraft. For a wing-to-wing configuration with the wire mesh return path the measured fields exceeded the calculated field by 52% to 78%. However, when a coaxial return path was used the measured values were between 92% and 98% of the calculated values. These data show the type of approximation made when the current in the lightning discharge is estimated based on the measured magnetic field values in the aircraft.

REFERENCES

1. P.L. Rustan, Jr., "The Lightning Threat to Aerospace Vehicles", Presented at the AIAA 23rd Aerospace Science Meeting, Reno, Nevada, January 1985.

2. J.D. Robb, "An Experimental and Theoretical Investigation of an NEMP Type Fast Rise Lightning Simulatior", USAF Report AFWAL-TR-84-3007, March 1984.

3. J.L. Hebert, L.C. Walko, and J.G. Schneider, "Design of a Fast Risetime Lightning Generator", Presented at the International Aerospace and Ground Conference on Lightning and Static Electricity, Paris, France, June 1985.

4. Rymes, M.D., "T3DFD User's Mannual", Electromagnetic Applications, Inc., prepared for Air Force Flight Dynamics Laboratory, Wright-Patterson AFB, OH under contract F33615-79-3412, April 1981.

5. Hebert, J. L. and Sanchez-Castro, C., "Implementation of a Three-dimensional Finite Difference Electromagnetic Code for Analysis of Lightning Interaction with a FAA CV-580 Aircraft", AFWAL-TR, Air Force Flight Dynamics Laboratory. In Publication.

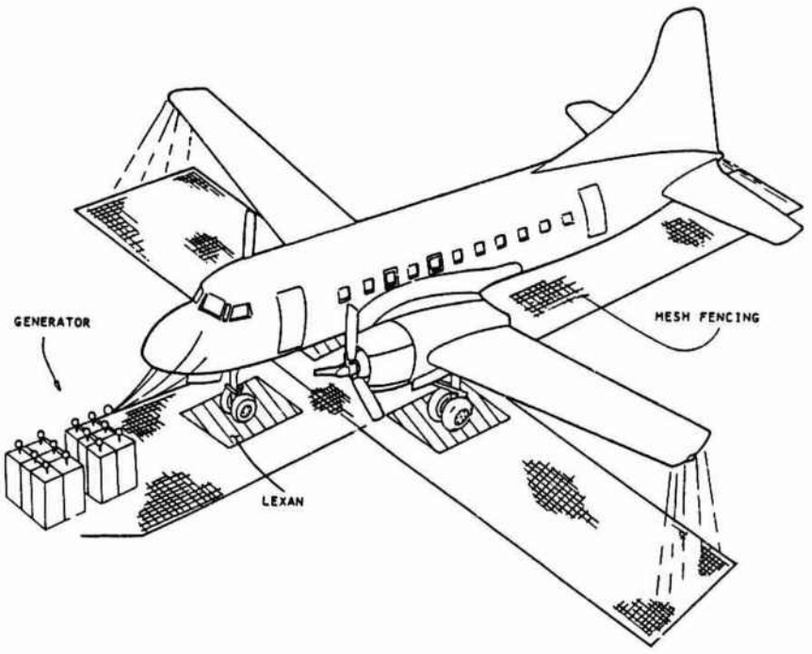


Figure 1 - Simulated Lightning Test Setup on the CV-580 Aircraft, June 1984.

Table 1 - Variations in Setup for June 1984, CV-580 Ground Tests

Current Path	Impulse Generator	Peak Current Kiloamperes	Notes
Nose-to-tail	4 μF, 200 kV Unidirectional	11 kA to 16 kA	System noise measurements
Nose-to-Right Wing	" "	14 kA	" "
Nose-to-tail	4 μF, 200 kV oscillatory	50 kA to 70 kA	Safety test Engine running
Nose-to-right aileron	" "	75 kA	Safety test Engine off
Nose-to-horizontal stabilizer	" "	55 kA	" "
Nose-to-rudder	" "	50 kA to 70 kA	" "
Nose-to-right sensor boom	" "	115 k	" "
Nose-to-tail	4 μF, 200 kV unidirectional	11 kA to 16 kA	All onboard systema functioning
Left Wing-to-Nose	" "	" "	" "
Left Wing-to-Right Wing	" "	" "	" "
Nose-to-Right Wing	" "	" "	" "
Left Wing-to-tail	" "	" "	" "

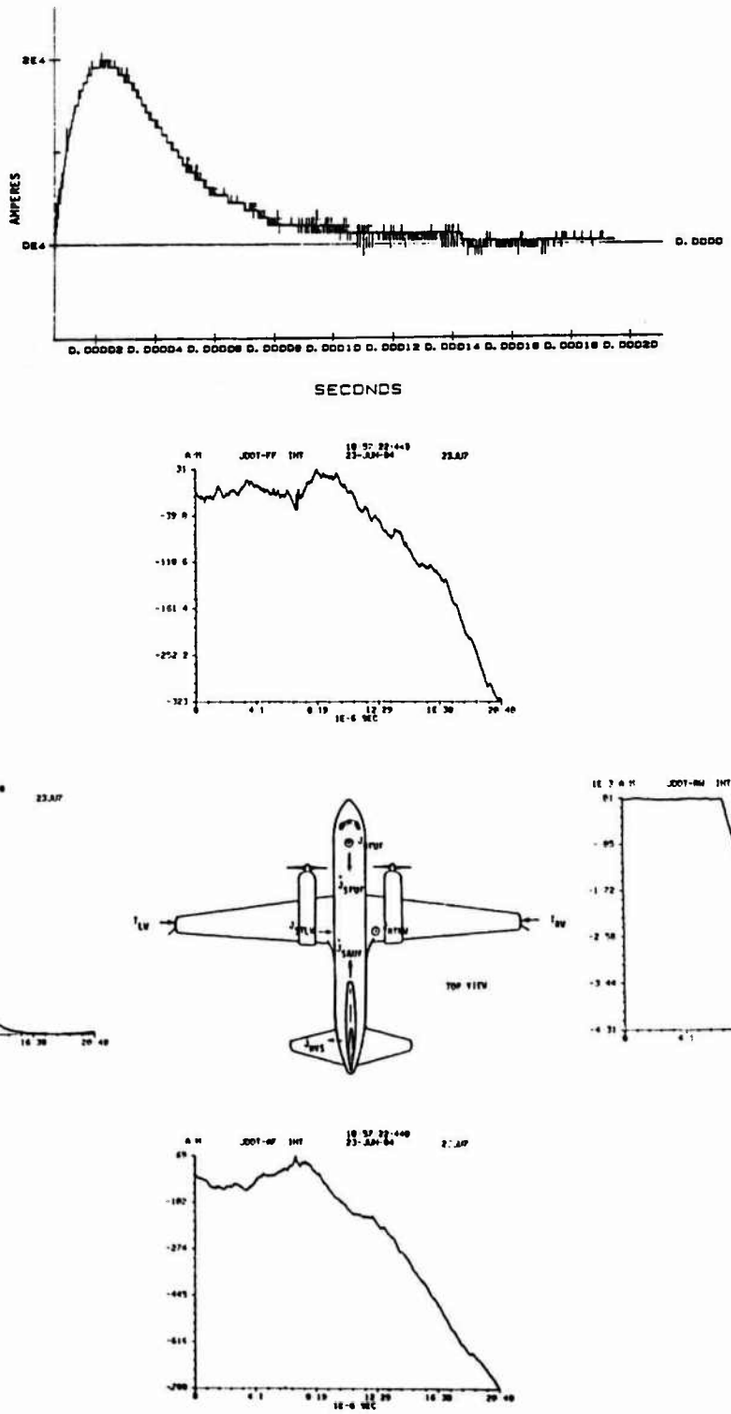
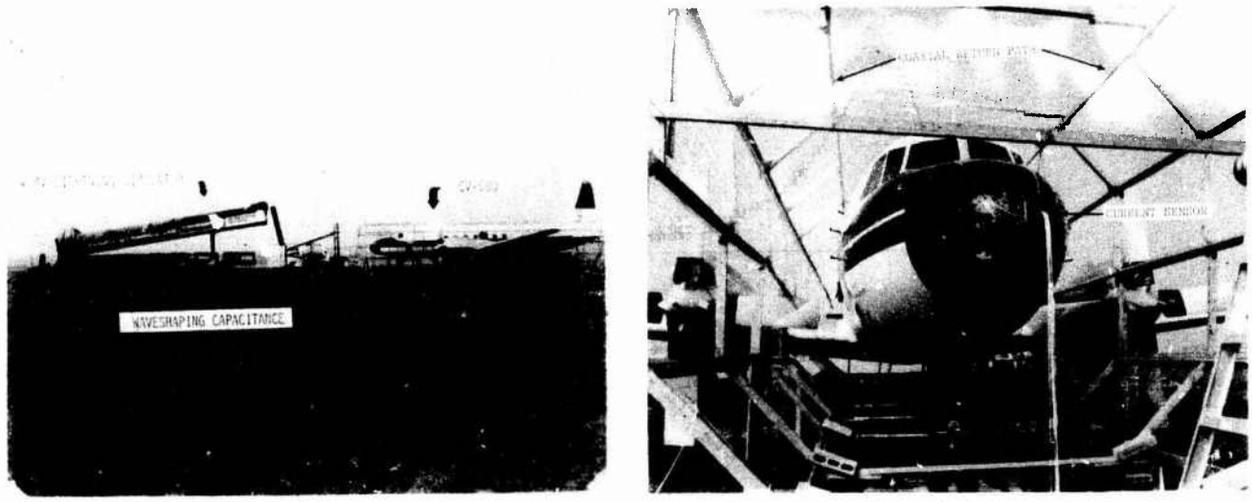


Figure 2 - 4 μF, 200 kV Generator, Unipolar Applied Current Waveform, Wing-to-Wing, and Magnetic Field Sensor Response on CV-580 Aircraft, June 1984.



(a) (b)

Figure 3 - Simulated Lightning Test Setup on the CV-580 Aircraft, Oct 1984.

Table 2 - Variations in Setup for October 1984, CV-580 Ground Tests

Current Path	Impulse Generator	Peak Current Kiloamperes	Note
Nose-to-tail	Fast Rise Generator	20 kA to 40 kA	All Onboard Data Acquisition systems functioning
Upper Radome-to-aingle point tail exit	" "	" "	" "
Gap at Radome-to-tail	" "	20 kA	" "
Gap at Radome-to-gap at tail	" "		Unauccesaful due to arcing to return patl
Noae-to-tail	4 μF, 200 kV unidirectional	20 kA	Regular connections for return path
Noae-to-tail	4 μF, 200 kV oacillatory	70 kA	" "
Top of fuaelage-to -vertical atabilizer	4 μF, 200 kV unidirectional	16 kA	Change in current distribution
Top of fuselage-to -vertical atabilizer	Fast Riae generator	30 kA	" "
Noae-to-tail	Marx generator peaking capacitor ahorted out	20 kA	Unidirectional pulae
Left Wing-to-tail	" "	20 kA	" "
Left Wing-to-tail	Fast Rise generator	30 kA	Current meaaured at left wing
Wing-to-wing	" "	20 kA	" "
Wing-to-wing	4 μF, 200 kV unidirectional	20 kA	" "
Wing-to-wing	4 μF, 200 kV oacillatory	70 kA	" "

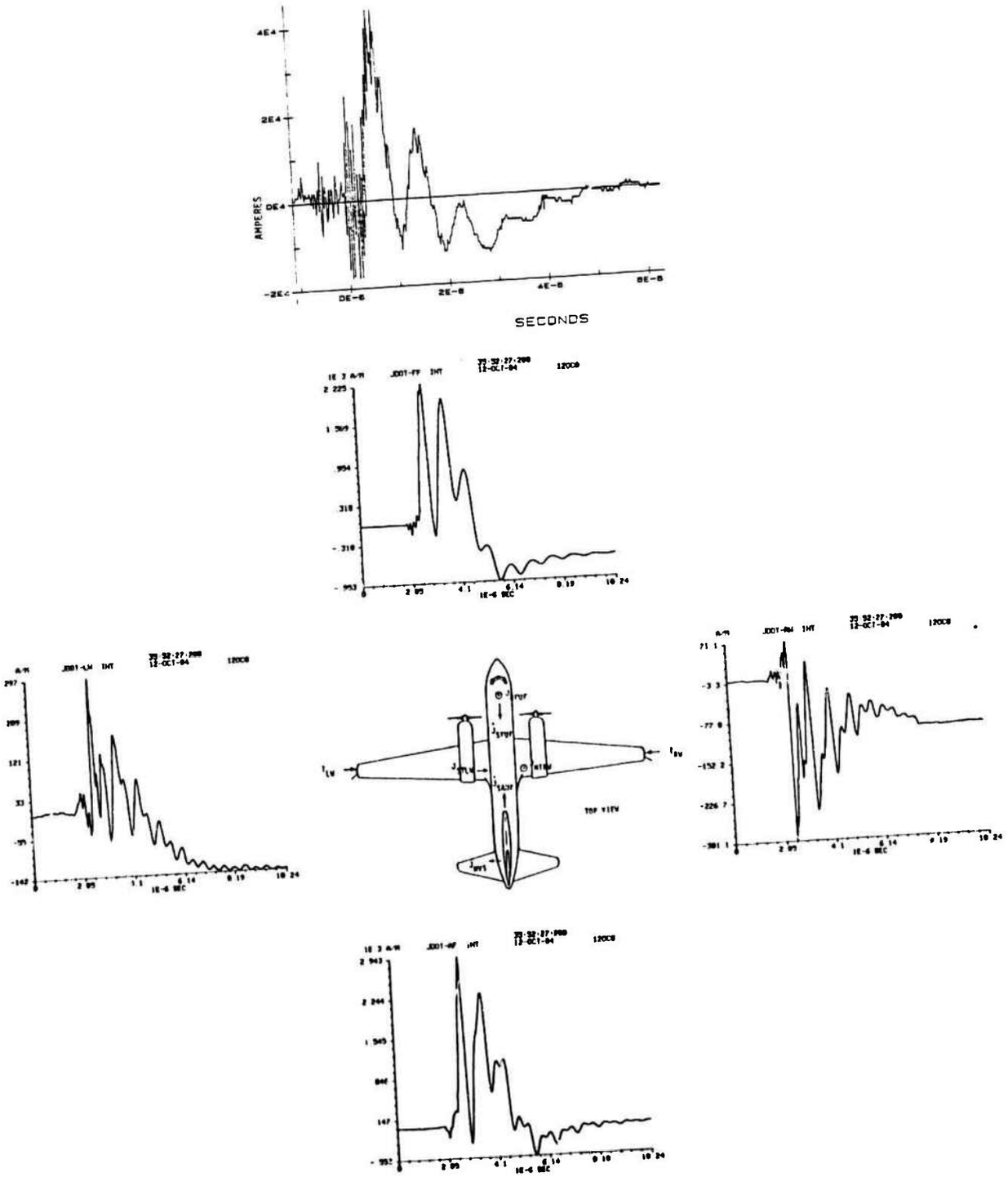


Figure 4 - Fast Risetime Applied Current Waveform, Nose-to-Tail, and Magnetic Field Sensor Response on CV-580 Aircraft, Oct 1984.

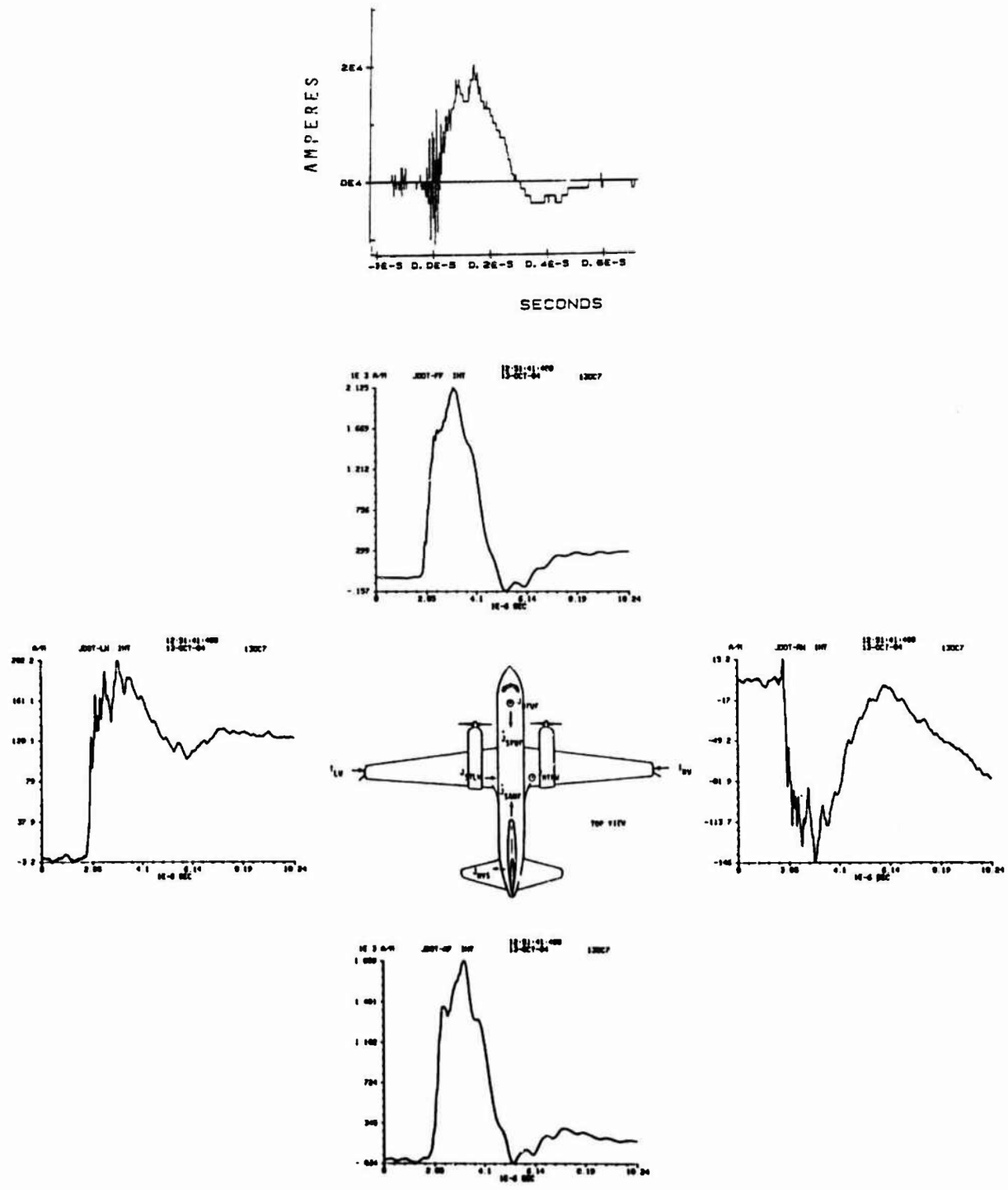
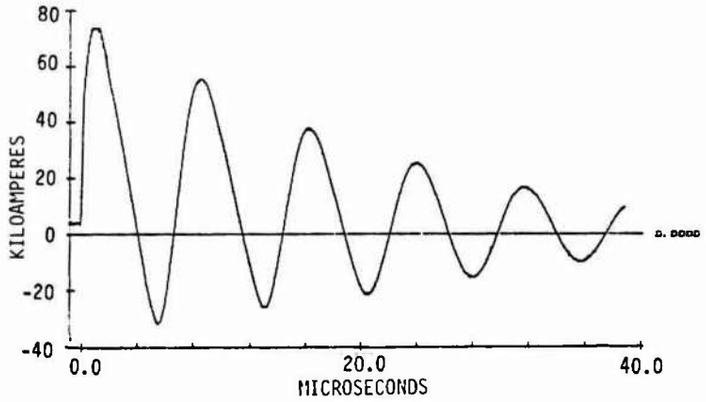


Figure 5 - Fast Risetime Generator, Peaking Capacitor Shorted, Applied Current Waveform, Nose-to-Tail, and Magnetic Field Sensor Response on CV-580 Aircraft, Oct 1984.



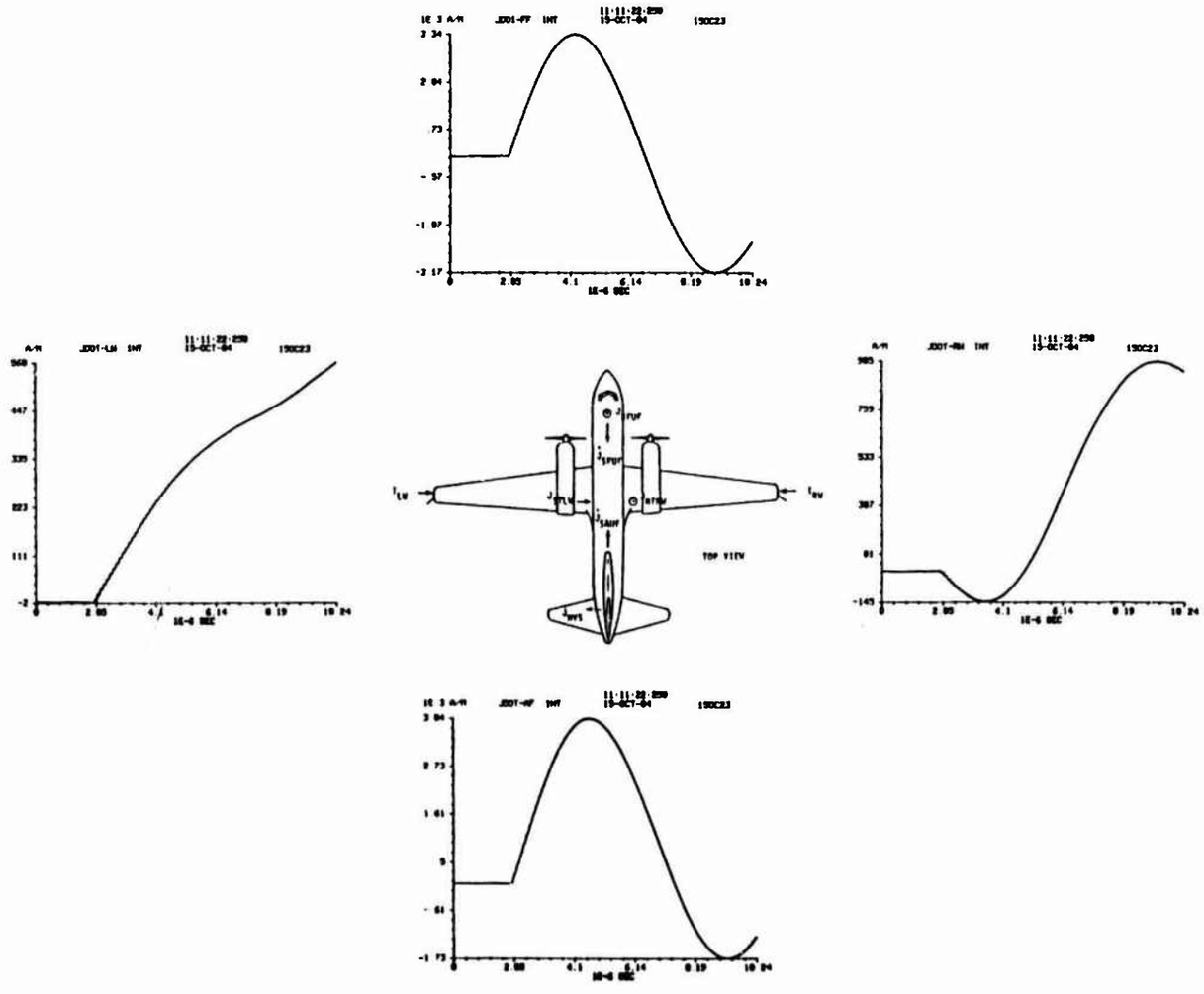
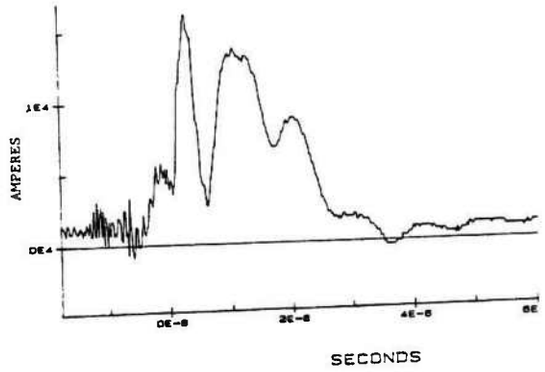


Figure 6 - 4 μF, 200 kV Generator, Oscillatory Applied Current Waveform, Nose-to-Tail, and Magnetic Field Sensor Response on CV-580 Aircraft, Oct 1984.



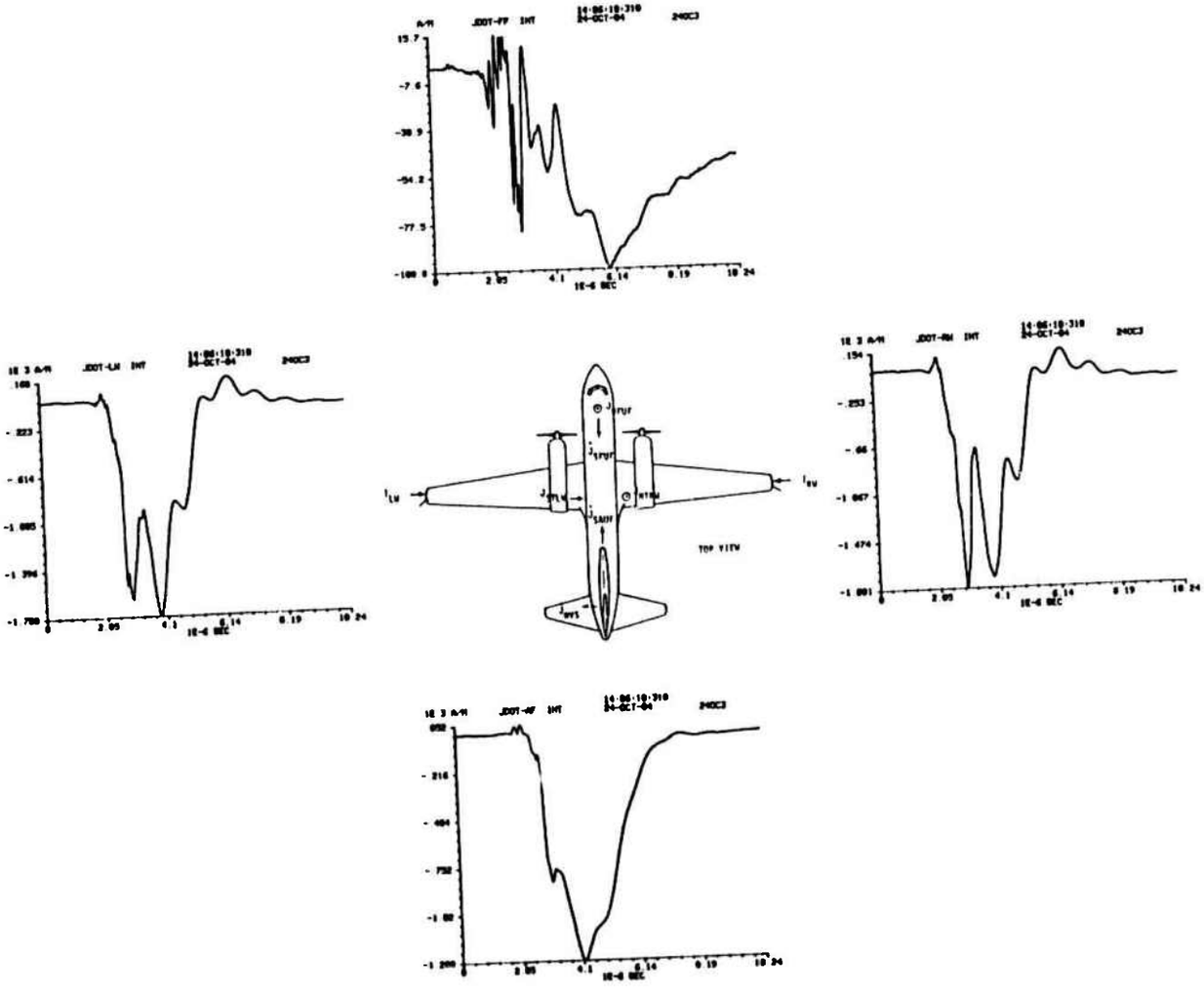


Figure 7 - Fast Risetime Applied Current Waveform, Wing-to-Wing, and Magnetic Field Sensor Response on CV-580 Aircraft, Oct 1984.

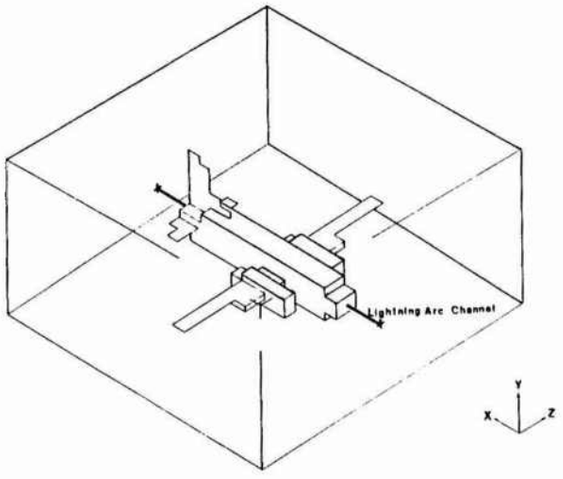


Figure 8 - The CV-580 Aircraft and Lightning Channel, Modelled in Cartesian 3-D Space.

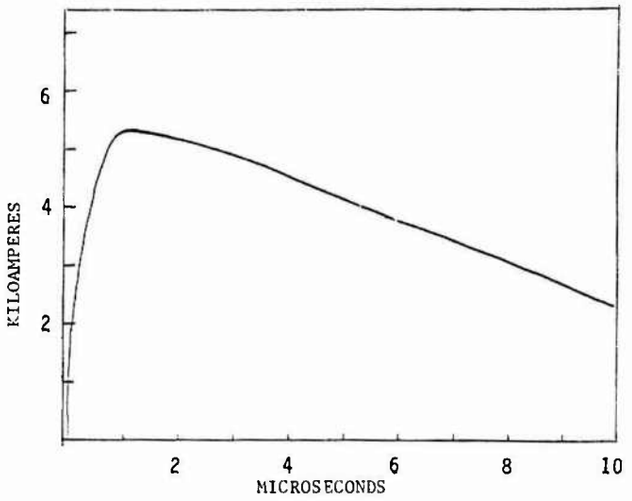


Figure 9 - The Double Exponencial Lightning Waveform.

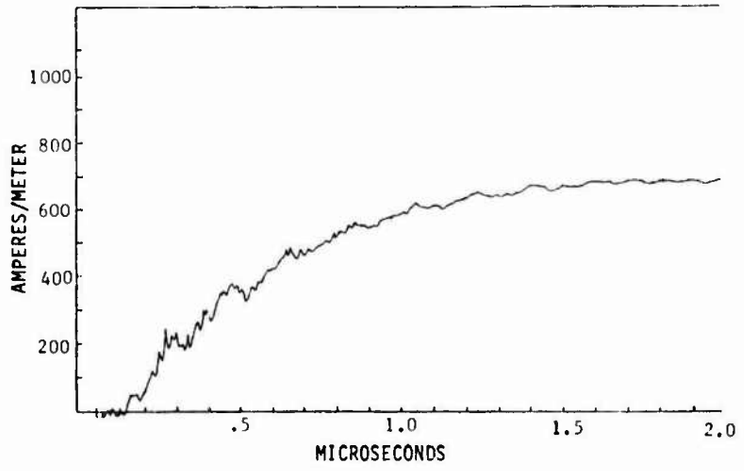


Figure 10 - Magnetic Field, Top Forward Fuselage CV-580 Aircraft.

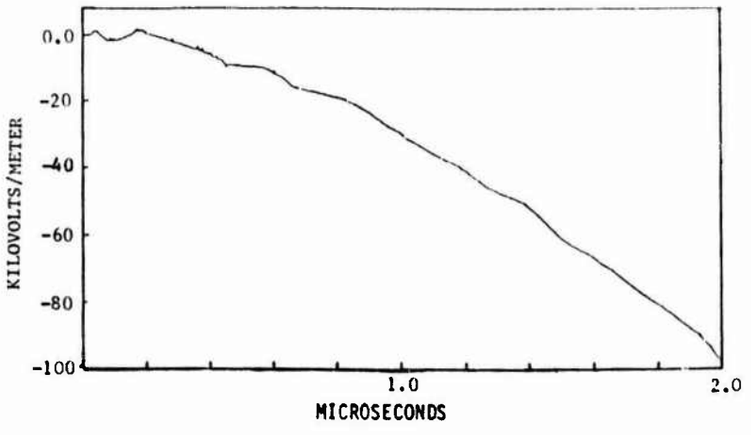


Figure 11 - Electric Field, Top Forward Fuselage CV 580 Aircraft.

MULTIPATH LIGHTNING PROTECTION FOR COMPOSITE STRUCTURE INTEGRAL FUEL TANK DESIGN

R.O. Brick

Boeing Commercial Airplane Co., Advanced Composites Development Program, P.O. Box 3707, M/S 6C-16, Seattle, Washington 98124, U.S.A.

ABSTRACT

This paper presents a design development approach to identify failure modes and incorporate a minimum dual path lightning protection system for composite structure integral fuel tanks.

Lightning protection for integral fuel tank structure against the potential ignition hazards of direct lightning attachment has been relatively straightforward for metal structure. Due to the homogeneity and excellent electrical conductivity of metal skin surfaces, single path protection systems can be employed. For example, aluminum skins can be protected by sizing the skin thickness to prevent skin puncture. In this case, skin puncture is the potential ignition mechanism. Since the material properties of aluminum are uniform and predictable, reliable, safe, single path protection designs can be easily developed. These designs are essentially maintenance free for the life of the airplane.

Composite structure is nonhomogeneous and the potential ignition producing failure modes are more complex. For example, there is a greater possibility of undetected damage such as fiber breakout and ply delamination during the installation of fasteners. Design factors that may be structurally inconsequential are critical in the case of lightning induced failure. Fiberglow, for instance, may ignite fuel vapor. The structure may not have aluminum structure's inherent "lightning protection." A design development process is required to identify the more complex lightning induced failure modes.

A multipath lightning protection system can provide a lightweight, low cost design. This design approach has the advantage of using protection methods that were previously considered impractical in a single path protection system. The use of a minimum dual path protection system allows protection methods to be used that are more compatible with inspection and maintenance practices.

The advantages and disadvantages of the multipath lightning protection concept are detailed for a graphite-epoxy skin-spar joint located in a lightning Zone 2 swept stroke area.

INTRODUCTION

The use of composite materials in primary aircraft structure has increased over the past decade. With the recent advancements in fiber technology and improved resin systems, the application of composites to the primary wing structure of large commercial transport airplanes is now being considered.

The need for lightning protection for primary structure must be evaluated early in the preliminary design phase so that cost effective, reliable designs can be developed. Since the structural wingbox is also an integral fuel tank, design details relating to lightning induced fuel ignition are of primary importance.

For design purposes it is assumed that a combustible mixture is present in the fuel tank at all times, and the main effort in the development of lightning protection systems is to produce designs that eliminate all lightning induced ignition sources in the tank area [1]. Potential ignition sources such as hot spots, skin punctures, and electrical arcing and sparking between conductive components are of particular concern for graphite composite structure. The elimination of ignition sources is accomplished by a detailed study of the structural design followed by test and analysis to determine the sensitivity of the primary structure to direct lightning attachment. Critical design factors are then identified and candidate lightning protection techniques are developed and incorporated into the final design.

DISCUSSION

The location of the wingbox primary structure and the fuel tank for a typical two-engine airplane configuration (one of many configurations being considered) is shown in Figure 1. The primary structural wingbox extends out to the tip. However, the fuel tank portion of the wingbox ends considerably inboard of the Zone 1 lightning strike attachment area where the most severe lightning attachments can occur [2]. Lightning strikes in this area are not a major fuel ignition concern because no fuel system components are located in this area. The current from wingtip lightning strikes will flow inboard along the wing and distribute throughout the cross section of the conductive structure. The normal structural design will be capable of carrying these lower currents safely in the fuel tank area, and lightning strikes to the wingtip do not present a critical structural design problem.

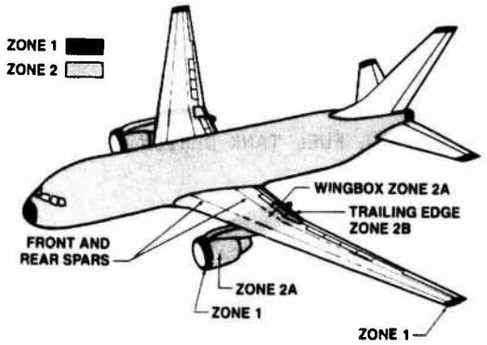


Figure 1. Wing and Engine Nacelle Lighlning Strike Zones

Lightning Attachment to Integral Tank Structure

The most critical situation occurs when the lightning channel can attach to the fuel tank skin surfaces. One such area is located aft of the engine nacelle. The forward area of the engine nacelle is also a Zone 1 area. However, in this case, lightning attachments can be swept aft over the primary wingbox structure and reattach to the fuel tank skin surfaces. This area, as shown in Figure 1, is defined as a Zone 2A area per AC20-53A [2]. This is the most critical area of the wing in that both fuel vapor and the possibility of lightning attachment are present. It is assumed that the lightning channel can attach at any point in the Zone 2A area. The time that the attachments remain at any one point is referred to as the dwell time [3]. The times vary from less than 1 ms to 20 ms for typical conductive surfaces [1]. The shortest times occur for unpainted surfaces and the longer times occur for painted surfaces. The insulative properties of the paint can impede the reattachment process, and skin surface preparation can be a very important design factor in developing lightning protection systems. On surfaces where the aerodynamic boundary layer is thick, longer dwell times can occur [4]. Normally the boundary layer is thin in this area of the wing, and the lightning channel will lay close to the skin surface during the sweeping and reattachment process [3].

The amount of damage produced at any one attachment in the swept-stroke Zone 2A area is highly dependent upon the type of material, surface preparation, dwell time, and current flow during the attachment. Lightning attachments in Zone 2A areas are less severe than Zone 1 areas. Lightning strike test waveforms to simulate the worst case lightning conditions for the various lightning strike zones are specified in several documents [1,2,5]. The test waveforms, shown in Figure 2, for Zone 2A have half the peak current and one-eighth of the high current action integral of the Zone 1 test waveform. The minimum skin thickness of 0.61 cm used in the Zone 2A area is more than adequate to resist puncture and hot spot ignition hazards. Basic skin thickness is not a critical design factor, but the use of fasteners in joints presents a potential ignition hazard. The most critical situation for the designs studied is the possibility of lightning attachment to fasteners located in the skin surface of the Zone 2A integral tank area, as shown in Figure 3.

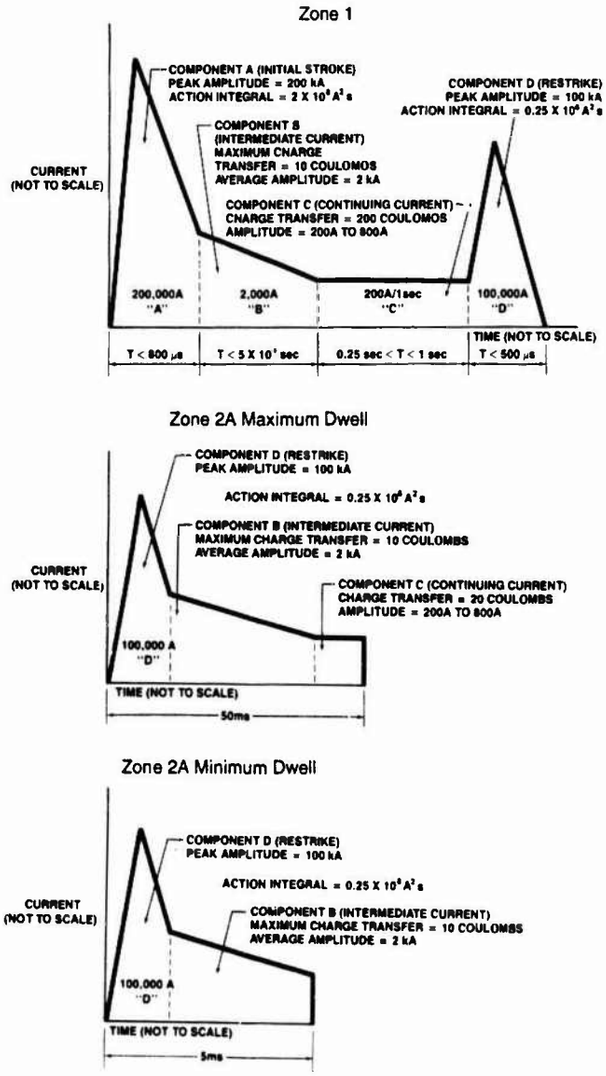


Figure 2. Lighlning Current Test Waveforms

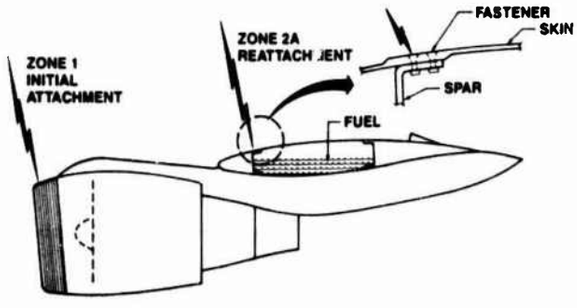


Figure 3. Lightning Attachment to Engine Nacelle and Wing Integral Tank Skin-Spar Joint

Lightning Attachment to Fasteners

When the lightning channel attaches to a fastener head, extremely high current densities are produced at the fastener-to-structure interface. Aluminum structure used in transport airplane integral fuel tank design has an inherent lightning protection with regard to "spark free" fastener installations. This is due to the excellent low electrical resistance at the fastener and aluminum skin interface, which allows very high current transfer to occur with minimal heating.

However, for graphite composite integral fuel tank structure, the type of fastener normally used will fail the lightning tests. The failure is attributed to the more than 1000X increase in resistance at the fastener composite interface and the requirement to install the fasteners in clearance-fit holes to prevent fiber delamination. Lightning tests of typical skin to spar, rib shear tie, and stringer runout configurations made of graphite composite structure produced ignition of fuel vapor and or profuse spark displays when the simulated lightning was directed to the fastener head.

Since the original composite structure design concept did not have the inherent lightning protection that is typical of aluminum structure, a lightning protection design development program was implemented to identify the failure modes and develop lightning protection that is reliable and cost effective for large commercial aircraft.

Examination of failed test parts indicated that the basic ignition mechanism was hot arc plasma blowby from under the fastener collar and between the skin and spar mating surfaces. Black soot residue from the arc plasma blowby is shown in Figure 4 for a skin spar test part.

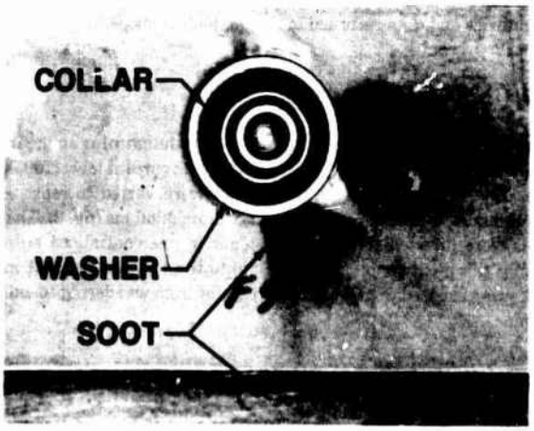


Figure 4. Arc Plasma Blowby for Skin-Spar Joint

Removal and inspection of fasteners showed that the arc plasma was generated at the interface between the graphite and the fastener countersink-shank area. There was no indication of arcing at the washer-to-graphite interface surface or the skin-spar mating surfaces on the graphite. The bare titanium fastener was slightly pitted and blackened due to the arcing at the interface. However, no significant structural degradation of the fastener occurred. Examination of the test parts also indicated that structural damage of the graphite was not critical, and only fasteners that showed severe direct attachment would require replacement. An oversized fastener and cosmetic repairs of the outer plies and paint finishes may be required for severe strikes. Since structural damage was not considered to be critical for the thick skins tested, only the design aspects that related to potential fuel ignition hazards were addressed during these early phases of the design development program.

DESIGN DEVELOPMENT APPROACH

The design development program consisted of the following:

1. Select a joint configuration for detailed study
2. Produce design drawings for baseline configuration and variations of the baseline as required to investigate single path lightning protection techniques.
3. Fabricate and assemble test panels per the drawings using production manufacturing methods and shops.
4. Test the various designs for worst case simulated lightning strike inputs for Zone 2A using simulated lightning test waveforms .
5. Analyze test results and select candidate single path protection systems for additional development and or incorporation into design standards.
6. Select multipath protection system(s) for additional analysis and trade studies.
7. Select final multipath protection system(s).

JOINT CONFIGURATION SELECTION

The configuration selected for detailed study was a skin-spar joint. This joint consists of a double row of fasteners that attach the skin to the spar. Table 1 shows the approximate skin fastener counts for the various types of joints in the lightning Zone 2A of the wingbox. A series of skin-spar joint test panels with design variations were fabricated to make a detailed study of the critical design factors. The skin-spar joint configuration was selected because it represented the joint with the greatest number of fasteners located in a lightning Zone 2A where the lightning channel could attach directly to a fastener head. It also provided a configuration that could be assessed for qualities of inherent lightning protection capability due to current sharing by adjacent fasteners. The panels were fabricated with skin thicknesses that represented structure aft of a wing-mounted engine.

JOINT TYPE	FASTENERS		
	DIAMETER cm (in)	NUMBER	TOTALS
SKIN-SPAR	0.953 (3/8)	712	712
SHEAR TIE RIBS	0.635 (1/4)	168	
	0.794 (5/16)	224	
	0.953 (3/8)	32	
	1.111 (7/16)	16	
INTERMEDIATE RIBS	0.635 (1/4)	104	
	0.953 (3/8)	32	
ENGINE SUPPORTS	0.794 (5/16)	20	
	0.953 (3/8)	92	
			688
		GRAND TOTAL	1 400

Table 1. Skin Fastner Count for Joints Used in Zone 2A

SKIN-SPAR PANEL DESIGN

The basic skin-spar panel design is shown in Figure 5. Graphite AS-6 fiber preimpregnated with Epoxy 3501-6 resin was used to fabricate the panels. The unidirectional tape is about .0185 cm per ply. The plies were oriented in a 0/±45/90 layup with 0 deg parallel to the spar. The outer two plies were oriented at ±45 deg. Titanium fasteners were used to assemble the panel.

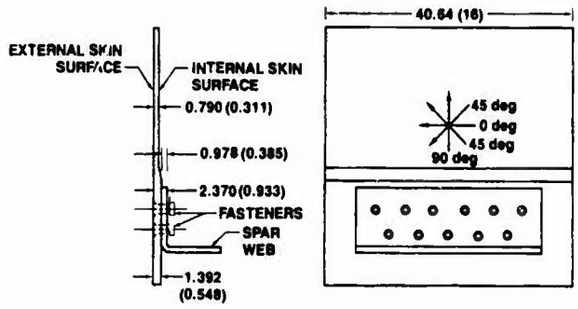


Figure 5. Skin-Spar Joint Design

Baseline Panel Design

A baseline configuration of the basic design used the maximum skin thickness of 0.79 cm. The stackup thickness of the skin plus padup plus the spar flange in the fastener area was 2.37 cm. Oversized 1.11 cm dia bare titanium 100 deg shear head fasteners are dry-installed in clearance-fit holes. A minimum of one corrosion resistant steel washer is used under a corrosion resistant steel preload self-locking collar. The graphite parts were painted with primer prior to assembly. Sealant was applied to the spar angle ends and other locations to suppress sparking in areas that do not represent the tank interior. The exterior skin surface was painted after assembly with a second coat of primer and a polyurethane enamel decorative finish coat. Tank sealants, which would normally be applied over the fastener collars and at the spar edge skin surface area, were not used since these materials can be considered as lightning protection techniques and would mask the effectiveness of other single path protection techniques being investigated.

Design Variations

Variations of the baseline panel were made to incorporate single path lightning protection techniques. Only one protection technique was used at a time so that the individual merits of each could be determined.

Table 2 lists some of the protection techniques used and the potential improvement expected.

	SINGLE PATH PROTECTION	POTENTIAL IMPROVEMENT
1.	INSTALL FASTENER WET WITH SEALANT	PREVENT ARC PLASMA BLOWBY
2.	INSTALL IGNITION BARRIER OVER COLLAR AND AT SKIN-SPAR JOINT EDGE	"
3.	INSTALL SWAGE COLLAR LOCKBOLT	"
4.	INSTALL FASTENER WET WITH SILVER CONDUCTIVE SEALANT	IMPROVE ELECTRICAL CONTACT BETWEEN FASTENER AND GRAPHITE TO ELIMINATE OR MINIMIZE ARC PLASMA
5.	INSTALL FASTENER WET WITH CARBON LOADED SEALANT	"
6.	INSTALL TENSION HEAD FASTENER	"
7.	INSTALL SILVER CONDUCTIVE SEALANT IN COUNTER SINK	"
8.	INSTALL SLEEVED LOCKBOLT WITH SWAGED COLLAR (EQUIVALENT TO INTERFERENCE FIT FASTENER)	"
9.	ADD METALLIC OUTER PLY TO EXTERIOR SKIN (PLY DOES NOT COVER FASTENER HEAD)	IMPROVE CURRENT SHARING BY ADJACENT FASTENERS

Table 2. Lightning Protection Techniques

FABRICATION AND ASSEMBLY

The skin panels were fabricated and assembled from design drawings using production planning shops and quality control methods. In some cases, where special fasteners were used and special tools were required, the panels were assembled by the materials technology laboratories and then returned to the production shops.

LIGHTNING TESTS

The skin-spar panels were tested with lightning strike inputs simulating the worst case lightning strike peak current level (100,000A) for a Zone 2A area [5]. The dwell times were varied to represent a minimum dwell time of 5 ms and a maximum of 50 ms (fig. 2). The test pulses were directed to a single fastener in one continuous pulse by locating the input probe close (0.97cm) to the fastener head. A mylar mask was also used to prevent the arc input from wandering to another fastener.

Panel Grounding

The skin panels were grounded to a metal test box on three sides to simulate the continuation of the skin structure. The grounds were made to the fiber ends along the edges of the panel. In addition, the spar was also grounded to allow current flow to substructure as shown in Figure 6. The fourth side representing the leading edge or trailing edge of the wingbox was not grounded, thereby simulating the current discontinuity that occurs in this area where nonconductive materials are used for leading edge and trailing edge structure.

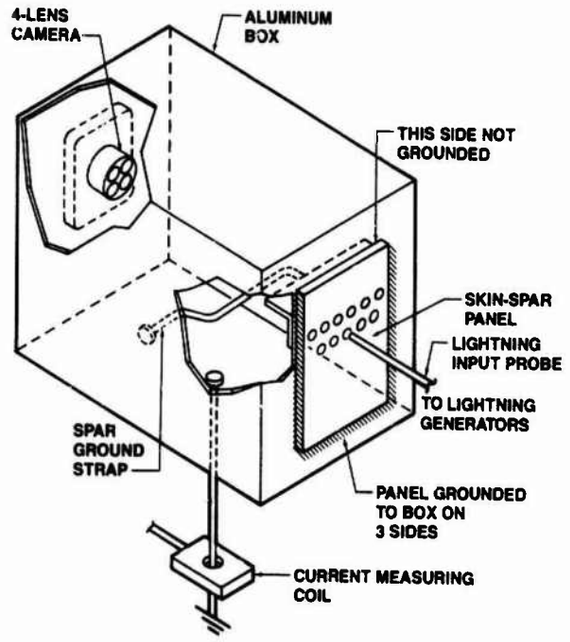


Figure 6. Skin-Spar Panel Lightning Test Setup

The above grounding technique is particularly important for this configuration to properly assess the current carrying capability of the fastener for direct arc attachment when other fasteners are adjacent or very close. This should be a better simulation of a natural lightning strike attachment to a single fastener on actual wing structure than a single side ground. The multiple side grounding also allows all of the conductive graphite fibers in the countersink and hole to carry their proper share of current. Since the test pulse is so severe to begin with, the proper grounding of the panel during test can be critically important for nonhomogeneous structure. Graphite composites typically have a higher resistance when measured transverse to the fibers than when measured along the fibers [6]. The RF impedance variations are probably greater when one considers the high frequency content of lightning.

Pass Fail Criteria

For the design development tests, photographic techniques [5] were used to determine the acceptability of a protection technique as a candidate for additional study. A protection technique was considered to be an acceptable candidate if no visual display was detected on the tankside by a camera using high speed ASA 3000 film. Polaroid film was used and film defect problems were eliminated by a special split lens that could provide four identical views of the panel in the same picture. Two of the lenses used filters and two were clear. Film defects were determined by noting if a suspected false exposure spot was observed in both frames. If the spot occurred in only one frame, it was considered to be a film defect.

Dwell Time

Each protection technique was tested for two dwell times. The actual dwell time is not known for the skin surfaces tested. However, the need for developing surfaces that minimize the dwell time becomes more evident if the selection of protection techniques that pass the severe maximum dwell tests becomes too limited or are not practical for production.

Normally a dwell time of 50 ms is used for testing if the dwell time is not known [5] for the particular surface studied. However, the longer dwell times are considered to be severe. Other investigators have shown dwell times of less than 20 ms for painted graphite composite surfaces. By including the short dwell time of 5 ms in the test program, protection techniques that failed the maximum dwell tests could be assessed.

TEST RESULTS

Clearance Fit Fasteners

Tests of the baseline panel with the oversize shear head fasteners to increase the electrical contact area failed the minimum dwell tests. Profuse arc plasma showers were photographed and visual signs of sooting were evident. This failure becomes more understandable if the area of the countersink is considered to be the only good current transfer area for clearance-fit fasteners. The maximum current carrying capability of graphite laminates is reported to be approximately 55 kA/cm² [8]. The current density for the 1.111-cm-dia shear head fastener with a countersink area of 1.21 cm² and peak current of 100 kA is 83 kA/cm². This exceeds the current carrying capability of the composite material by 150%. Subsequent tests, using tension head fasteners to increase the countersink area, passed the minimum dwell tests. The smallest tension fastener tested that would pass the minimum dwell tests was a 0.953-cm-dia fastener with a countersink area of 2.53 cm². The peak current density would be 40 kA/cm² which is approximately 27% below the current carrying capability of graphite composite material.

If a perfect electrical connection could be made from the fastener countersink area to the graphite, an area of approximately 1.8 cm² would be required. The next smaller size tension head fastener of 0.794-cm dia has a countersink area of 1.7 cm² and would not be expected to pass the minimum dwell tests. The 0.953-cm-dia tension head fastener with a countersink area of 2.53 cm² tends to set a lower limit for the electrical contact area required to pass the minimum dwell Zone 2A tests.

A special fastener, which upon installation expands a metal sleeve in a clearance hole to give the electrical equivalent of an interference-fit fastener installation, was tested in skin-spar panels that represented the minimum skin thickness for the Zone 2A area. The panels passed the worst case maximum dwell tests. The total electrical contact area between the 0.953-cm-dia fastener and the graphite composite material is 6.44 cm².

Due to the limited number of test panel variations, the lower limit for the fastener contact area required to pass maximum dwell conditions has not been established at this date.

Single Path Protection Techniques

The most promising single path protection techniques of those studied for the skin-spar joint are shown in Table 3. They fall into three general categories.

PROTECTION TECHNIQUE	PASS CONDITION
1. PREVENTION OF ARC PLASMA BLOWBY	
(a) INSTALL IGNITION BARRIER OVER COLLAR AND AT SKIN-SPAR JOINT EDGE	MAXIMUM DWELL
(b) INSTALL SWAGE COLLAR-LOCKBOLT (NO WASHER) TO PROVIDE BETTER SEAL AT COLLAR-GRAPHITE INTERFACE	MAXIMUM DWELL
2. IMPROVE ELECTRICAL CONTACT BETWEEN FASTENER AND GRAPHITE FIBER ENDS	
(a) INSTALL FASTENER WET WITH SILVER CONDUCTIVE SEALANT	MINIMUM DWELL
(b) INSTALL TENSION HEAD FASTENERS TO INCREASE COUNTER SINK AREA	MINIMUM DWELL
(c) INSTALL SLEEVED LOCKBOLT WITH SWAGED COLLAR (EQUIVALENT TO INTERFERENCE FIT FASTENER)	MAXIMUM DWELL
3. IMPROVED CURRENT SHARING OF ADJACENT AND NEAR BY FASTENERS	
(a) ADD METALLIC OUTER PLY	MINIMUM DWELL

Table 3. Single Path Protection for Graphite Composite Skin-Spar Configuration

1. Prevention of arc plasma blowby.
2. Improvement of electrical contact between fastener and graphite to minimize or prevent arc plasma.
3. Improvement of current sharing by other fasteners to minimize or prevent arc plasma.

Categories 2 and 3 could probably be combined since the intent is to prevent or minimize the generation of the arc plasma. However, it is desirable to keep them separate because of the marked difference in the techniques to accomplish minimization or elimination of the arc plasma.

In category 2, the critical design factors relate to the fastener installation, while in category 3 the critical design parameter is the conductivity of the outer ply, which is independent of the fastener installation process.

There are other protection techniques that were not examined during the early phases of this program but should be considered, particularly in areas where there may be only one adjacent fastener in the immediate vicinity. These other techniques include:

1. Insulative treatments to prevent lightning attachment directly to the fastener head.
2. Multiattach surface preparations that would cause the channel to split or easily reattach downstream of the original attachment point.
3. Current dispersion surface coatings that will ensure current sharing by more than one fastener.

Some of the above concepts will be investigated in future studies and should offer other single path protection techniques for incorporation into multipath lightning protection systems.

MULTIPATH PROTECTION SYSTEMS

The concept of a multipath lightning protection system is similar to the concept used in structures design where structural load carrying members are redundant. If failure occurs for a particular item, such as a spar, the remaining members can carry the load. The structure must be designed with the failure modes in mind to arrive at the optimum design. No single member failure will cause catastrophic failure of the system. The same concept can be applied to lightning protection.

Multipath lightning protection can be achieved by combining two or more known single path protection techniques to achieve a redundant protection system. For example, in the case of a fastener installation for the skin-spar joint discussed in this paper, two single path protection techniques can be combined: (1) the use of an interference fit fastener as one protection technique and (2) the use of an ignition barrier over the collar (e.g. tank sealant) as the second protection technique. Each of these protection techniques will pass the worst case Zone 2A maximum dwell time lightning strike test. Another combination of a dual path protection system would be to use: (1) a dielectric barrier over the fastener head to prevent direct attachment to the fastener and (2) the ignition barrier over the collar. In the two cases above, the use of tank sealant over the fastener collar and the dielectric overlay would probably not be considered as an adequate single path protection system. Both of these protection techniques would be difficult to inspect to verify the integrity of the system. It would not be desirable to require mandatory periodic draining and opening of fuel tanks to inspect the integrity of the lightning protection aspects of the sealant. However, if sealant or sealant caps are a part of a multipath protection system, it is highly unlikely that both protection systems would fail at the same fastener. Only the normal inspection to verify the integrity of the sealant as a fuel sealant would be required.

The dielectric overlay would be easier to inspect because it would be on the exterior surface. Small punctures would probably not be detected and special inspection procedures would be required if it were used as the only protection system.

If a second protection system is combined with the dielectric overlay, then one only needs to inspect for severe damage such as cracks, peeling, or scratches, since it would be unlikely than an undetected pin hole would be over a fastener that also had a failure of the other component of the dual protection system.

Other combinations could also be made to achieve a multipath protection system. For example, a technique that passes a minimum dwell test could be combined with a technique that passes a maximum dwell test.

If this is done, more must be known about the dwell characteristic of the skin surface. One can either measure the dwell time of the surface coatings and use that time for testing if it exceeds 5 ms, or use surfaces that will give dwell times of approximately 5 ms or less.

The main advantage of the multipath lightning protection concept is that it allows the use of single path protection techniques that have been considered unacceptable by the designer for use in critical integral fuel tank areas. The reluctance to use a single path protection system that may require special inspection and or maintenance procedures to keep the system 100% is understandable. Extensive qualification and certification programs may be required for single path systems that do not have a long historical record of acceptability.

The concerns relating to inspectability, maintenance, and environmental aging factors would not be critical for well designed multipath protection systems. Multipath protection concepts would be more compatible with the qualification, certification, and operational aspects of advanced composite primary structure.

CONCLUSIONS

A design development program to eliminate potential lightning induced ignition sources for a graphite composite integral fuel tank skin-spar joint has been described.

The lightning protection techniques developed are capable of withstanding the severe direct lightning attachment to a skin-spar fastener.

The proposed combination of two or more protection techniques into a multipath protection system offers a greater range and flexibility of designs to provide safe, reliable, cost effective lightning protection for transport aircraft composite structure.

REFERENCES

[1] N. Rasch, "User's Manual for AC 20-53A Protection of Airplane Fuel Systems Against Fuel Vapor Ignition Due to Lightning," U.S. DOT FAA Technical Center Report DOT/FAA/CT-83/D, October 1984.

[2] "Protection of Airplane Fuel Systems Against Fuel Vapor Ignition Due to Lightning," U.S. DOT FAA Advisory Circular AC 20-53A.

[3] R.O. Brick, L.L. OH, S.D. Schneider, "The Effects of Lightning Attachment Phenomena on Aircraft Design," 1970 Lightning and Static Electricity Conference, December 9-11, 1970 at Wright Patterson AFB, Ohio.

[4] J.A. Dobbing, A.W. Hanson, "A Swept Stroke Experiment with a Rocket Sled," Proceedings 1978 IEEE International Symposium on Electromagnetic Compatibility, Atlanta, GA, July 1978.

[5] "Lightning Test Waveforms and Techniques for Aerospace Vehicles and Hardware," SAE Committee AE4L Report Dated June 20, 1978; or "Lightning Qualification Test Techniques for Aerospace Vehicles and Hardware," MIL-STD-1757A, July 20, 1983.

[6] R. Force, et. al. "Investigation of Effects of Electromagnetic Energy on Advanced Composite Aircraft Structures and Their Associated Avionic/Electrical Equipment," Naval Air Systems Command Report D180-20186-4, September, 1977.

[7] E.H. Shulte, W.T. Walker, "Rear Surface Temperature Measurement of Aircraft Materials Subjected to Zone 2A Lightning Strikes," Proceedings International Aerospace and Ground Conference on Lightning and Static Electricity, Orlando, Florida, USA, June 26-28, 1984.

[8] W.E. Howell, "Effects of Simulated Lightning Currents on the Tensile Strength of Graphite/Epoxy," Proceedings Addendum to International Aerospace and Ground Conference on Lightning and Static Electricity, DOT/FAA/CT-83/25A, October, 1983.

OPTICAL DETECTION METHODS FOR TESTING OF FUEL TANK LIGHTNING IGNITION HAZARDS

F.J. Anderson, G.D. Freier*, T.S. Lee** and J.D. Robb

Lightning and Transients Research Institute, St. Paul, Minnesota 55113, U.S.A.
**Physics Department, University of Minnesota, Minneapolis, Minnesota 55455, U.S.A.*
***Institute of Technology, University of Minnesota, Minneapolis, Minnesota 55455, U.S.A.*

Abstract - A theoretical and experimental investigation has been undertaken to evaluate briefly the optical methods currently in use or considered for detecting sparking and hot spots in fuel tanks. The methods investigated have included a) photography, b) photomultipliers, c) image intensifiers, d) photomultipliers with optical light pipe, e) photomultipliers with spherical mirrors for spark detection, as compared with the human eye, and f) infrared photo detectors and heat sensitive paints for hot spot detection.

The investigations have focused on a theoretical spark with a 10 nanosecond duration and a 200 microjoule energy which could occur but which have never been observed in many years of testing graphite composite and metal fuel tanks to the best of our knowledge. The spark showers, when they occur, are usually bright and easily photographed.

The investigations confirm that the present photographic methods with polaroid film are adequate but marginal for fuel tank component testing at distances of less than one meter for the 10 nanosecond spark referred to above. Therefore, the faster 35 mm photography is preferred because of the reduced film blemishes and the easy availability of faster lenses. A combination of both conventional cameras using negative film and polaroid cameras is optimum for obtaining immediate results but with assurance that the 10 nanosecond spark could be detected if it occurred.

For transluscent fuel tanks, optical methods will probably be impractical and the use of flammable fuel vapors will be required. Qualification methods using flammable vapors for some composite aircraft fuel tanks will therefore be required, as discussed in a separate paper. Further development of some of the above optical methods will be required for testing of full size fuel tanks which have extensive internal plumbing and wiring.

INTRODUCTION

This paper presents the results of experimental and theoretical investigations on optical methods of spark detection, which are presented in more detail in Reference 1.

Optical methods of spark detection were studied:photographic;photomultipliers, as used alone, with optical cable, or with spherical mirrors; and image intensifiers. Electromagnetic detection with magneto-optical rotational crystals was considered, but not studied at this time (Johnson, Ref. 2). The uses of infra-red detectors and heat sensitive paints to detect hot spots and hot particle showers were investigated. The detection methods are presented in the following sections in terms of the margins between the light emission of the spark and the sensitivity of the detection method being used.

The principal conclusions drawn from the investigations are that photographic detection of incendiary sparks can be used out to distances of 9 feet with 35 mm cameras (and possibly to greater distances with new faster films and lenses) and that electronic detection systems such as photomultipliers can be used in larger fuel tanks with mirrors and possibly optic fiber out to distances of 24 feet or greater with some additional development work. Polaroid cameras can be used out to distances of three feet with lenses faster than F 4.7 and/or films faster than ASA 3000.

SPARK SOURCE

A standardized spark source was used for the tests of the various detection systems. A 10 picofarad capacitor, charged to 6500 volts was used to generate the minimum ignition energy spark of about 200 microjoules. These sparks are similar to those studied by Barreto (Ref. 3). The spark had a current peak of 12 amperes and a time duration of about 10 nanoseconds. A sketch of the spark source used in the experiments and a typical current-time trace of the spark are shown in Figures 1a and 1b.

An important question remains as to whether these short duration sparks could be generated inside a metal or graphite fuel tank because the fuel tank acts as a low pass filter in which diffusion effects lengthen the typical lightning current waveform rather than shortening it. This may also be demonstrated by simple linear circuit theory as illustrated in Figure 2. With a two microsecond rise time for the lightning current, the internal short circuit current has a rise time determined by the ratio of the inductance and resistance of the internal wire. For the short circuit current which is of interest for sparking, this rise time is of the order of milliseconds rather than microseconds. Thus, the nanosecond low energy spark, if a mechanism could be determined for generating it, would in effect be limited by the slow rise time of the short circuit current.

Also, it has been observed in the LTRI laboratories where observers are used along with the cameras that sparking, when it occurs, is quite energetic and easily observed by the polaroid camera.

However, the assumption was made in these studies that such a spark could exist as a worst possible case and therefore it was used as the "Standard Spark" in the evaluations of the various test methods.

INDIVIDUAL OPTICAL DETECTION METHODS

PHOTOGRAPHY

DESCRIPTION OF THE TECHNIQUE - The test arrangement for the photographic detection of sparking from a fuel tank component is illustrated in Figure 3.,as reproduced from MIL-STD-1757. The procedure is as follows. The item to be tested is mounted in one wall of the fuel tank mockup, a high current discharge is fired to the component and a camera is used to record any internal sparking. The camera can be either of the Polaroid type or of the conventional type with negative film. Currently, an aperture of F 4.7 and a film speed of ASA 3000 is specified in Mil-STD-1757. Special care is required when using polaroid cameras because of the much greater tendency for flaws to be found on the print and these flaws make accurate identification of sparking more difficult. An observer can also be located inside the cabinet to observe the sparking and this is a standard practice for some organizations. The dark adapted eye has a light sensitivity exceeding that of a polaroid camera with an F 4.7 lens opening and ASA 3000 film by a factor of about 20 as determined both theoretically and experimentally.

THEORETICAL ANALYSIS - The calculations of G. Freier and F. Anderson (Ref. 1) have shown that the photographic method is theoretically marginal with the Polaroid film sensitivity of 3000 ASA and a lens opening of F 4.7. The "Standard" 200 microjoule spark with a 10 ns time duration produces a total of 4.1×10^{8} photons and 1.8×10^{4} photons reach the lens opening of 0.00057 square meters in area for a typical lens used in fuel tank testing (focal length of 127 mm) and a test object distance of one meter. These photons are focused by the lens to a spot of 1.6×10^{-8} square meters. Assuming a loss through the glass of about 15 percent, the photon density on the film would be increased to 9.8×10^{11} photons per square meter. Anderson found a film sensitivity of 1.05 of 10^{12} photons per square meter for a margin of -0.3 dB and Freier about one dB. Experiments approximately confirm this calculation and show that the sparks can be detected on the photographs only with careful examination as illustrated in Figure 4. For routine test use, thisis a marginal test method for the short 10 nanosecond, 200 microjoule sparks.

The sensitivities and margins may also be presented in terms of the required photographic ASA number and lens aperture for detection of the spark. The following equation permits calculations of the required ASA film number as a function of the camera F stop and the charge transfer in microcoulombs for the detection threshold (assuming a 15% transmission loss in the lens).

$$ASA = 9.60\ (\text{F Stop No.})^{2}\ A \times 10^{6}\ /Q$$

where A = current in amperes
Q = charge transfer in μCoulombs

Thus, with a ten nanosecond spark, spark photography is marginal for ASA 3000 film and F4.7. For an aperture of F2.0 or a film speed of ASA 10,000, the spark can be detected with a margin of about five dB at a distance of one meter.

EXPERIMENTAL TESTS - Shown in Figure 5 are test discharges with the 200 microjoule "standard spark". The discharge has a ten nanosecond duration and a peak current of 12 amperes. Shown on 35 mm film, ASA 3000 equivalent, are discharges at 3 feet at F 2.0, 3 feet at F 4.7, and 9 feet at F. 2.0. All are visible on the photographs except at 9 feet, in which case the image is probably too faint for routine test use. The tests showed that the Polaroid ASA 3000 film with a lens opening of F 4.7 is marginal but that the technique can provide a reasonable margin, if a faster lens opening or faster film is used.

SUMMARY - The theoretical and experimental investigations have shown that the photographic method does provide a method of evaluating all fuel tank component sparking, even if of ten nanosecond duration, if a), used at distances of one meter or less, b) if proper measures are taken to insure that the film development is standard, and c) if an ASA 10,000 speed film is used with an F 4.7 lens opening or if a 35 mm film is

used with an equivalent speed, (F 2.0 with ASA 1000 speed film pushed three stops in the development.)

PHOTOMULTIPLIERS

DESCRIPTION OF THE TECHNIQUE - A photomultiplier can be used to view a fuel tank interior or to view components mounted in a fuel tank mock up, either by itself or in combination with a camera. As shown in Figure 6, the required equipment includes the photomultiplier and its power supply and the oscilloscope for recording the output. This is all located in a shielded chamber with extra shielding for the photomultiplier assembly and its isolated power supply. The major application is for complete fuel tanks where the dimensions are too great for minimum spark detection with the photographic technique. Since the photomultiplier tube alone doesn't see the entire fuel tank, nor does it specify the location of a spark, it is necessary to augment the photomultiplier tube with an optic fiber cable or spherical mirrors.

THEORETICAL ANALYSIS - The photomultiplier (PM tube) is different from a camera in that it records the rate of photon impingement rather than total quantity of photons. When the photons fall on the photocathode in a very short time, the rate of impingement is very high and the sensitivity is also accordingly very high. PM tubes have current gains of the order of 2,000,000 and thus are extremely sensitive. Freier and Anderson show that they provide a margin above the light output from the standardized spark of at least 40 dB.

The theoretical analysis of the light coupling into the optical cable presents considerable difficulties. It requires further work.

EXPERIMENTAL TESTS - Some experimental measurements were made with a photomultiplier to confirm the above data as shown in Figure 6. The measurements with the photomultiplier confirm the Freier and Anderson calculations of great sensitivity and the ability to measure faint sparks at great distances.

Experiments were performed using only one type of optical cable, and were not very successful. However, they have been used successfully to monitor sparking in aircraft fuel tanks by the staff at Culham Laboratories in England.

Tests were also carried out by locating a 5" sphere at a distance of 24 feet from the photomultiplier and providing the "Standard" 200 microjoule spark source shielded from the photomultiplier but not from the sphere. For a spark one foot from the sphere, the test results showed a signal 10 times the minimum signal detectable corresponding to a 10 dB signal to noise ratio. The experiments were conservative because the spherical mirror was surrounded with black cloth in order to kill reflections. In an actual fuel tank the plumbing and wall of the tank are usually covered with semi-reflective coatings which greatly increase the total light collected by the photodetector.

SUMMARY - Photomultipliers offer a means of testing full size fuel tanks with plumbing and conduit, but only in conjunction with spherical mirrors and possibly optical cable to provide coverage of the entire tank. Its use in conjunction with a camera permits location of most sparking if it does occur.

IMAGE INTENSIFIERS

DESCRIPTION OF THE METHOD - The image intensifier is used to increase the sensitivity of cameras. The basic test arrangement, includes a camera and an image intensifier to, in effect, increase the film speed and permit the photographing of weaker sparks and sparks at greater distances. Image intensifiers are used in astronomy to photograph weak stars. and have sensitivities equal or greater than photomultipliers. They can be used in series to further increase the system sensitivity.

THEORETICAL ANALYSIS - Image intensifiers are inherently at least as sensitive as photomultiplier systems. By cascading the units they can be made more sensitive. However, the photocathode must be selected so that it is sensitive in the ultra-violet region.

EXPERIMENTAL TESTS - The experimental measurements, with the available image intensifier, disclosed that it was not capable of resolving sparks at even six feet away because of the incorrect spectral sensitivity. The emphasis in the program was on economical and available devices which are of primary interest in fuel hazards testing. The image intensifiers used for astronomy cost tens of thousands of dollars and for this reason were not evaluated. Low cost and ready availability were major parameters in evaluating the various approaches. The requirement is therefore for higher resolution and greater spectral sensitivity in a reasonably priced device.

SUMMARY - The image intensifier provides great promise in conjunction with cameras and spherical mirrors for qualification of aircraft fuel tanks because of its sensitivity. The basic drawback with all of the electromagnetic detectors is the complexity in comparison with a camera. There is considerable work required to develop this method in terms of developing a specific test method and hardware.

HOT SPOT DETECTION

INFRARED DETECTORS

For hot spot detection, the work of

Demetri (Ref. 4) has shown that a temperature of 1650 degrees F. is required for ignition of flammable fuel vapors by even a large hot spot (approximately 1 cm by 2 cm). Most of the infrared cameras for measurement of temperature are complex and expensive. For fuel tank applications, where the hot spot minimum ignition temperatures have, as noted, been found to be very high, simple infrared photodetectors can be used as they easily detect typical lightning hot spots with diameters of one centimeter and temperatures of 450 degrees F which is well below the minimum ignition temperature of 1650 degrees F shown by Demetri.

HEAT SENSITIVE PAINTS

Heat sensitive paints have been successfully used for many years for qualification of fuel tanks and components. The tests have been carried out by using relatively low temperature paints, 450 degrees F. If the temperature exceeds the sensing temperature, the paints indicate that the 450 degree temperature has been exceeded. This approach continues to be a satisfactory but conservative method of testing fuel tanks for hot spot ignition. Data as indicated in Ref. 4 on hot spot ignition indicates as noted in previous section that extremely high temperatures of 1650 degrees F are required to ignite flammable fuel vapors for the time duration of lightning events of seconds. Therefore, the use of the temperature sensing paint of 450 degrees F sensitivity level does provide considerable margin for fuel systems testing. Its principal fault is that it is too sensitive and that higher temperature paints could be used, if more data were available.

Thus the present state of the art technique of using temperature sensing paints for hot spot detection is satisfactory but over conservative.

HOT SPOT CALCULATIONS

It is useful to be able to calculate approximate hot spot temperatures. A very early LTRI report (Ref. 5) presented solutions for calculating the hot spot time temperature profiles. In this new program, a simpler form of solution was developed for this investigation. An energy input may be expressed roughly as the product of the cathode drop voltage of 10 volts, the current and the time. For a current of 30,000 amperes for a period of 50 microseconds and 10 volts (15 joules), this gives a temperature peak in aluminum of 300 degrees C as shown in Appendix .

CONCLUSIONS

The relative sensitivity of the various detection techniques are given in Table 1.

The investigations confirmed that a 200 microjoule spark is detectable only marginally by present photographic methods. The tests showed that the film speed or the lens opening need to be increased over the present standard of a F 4.7 lens aperture and a film speed of ASA 3000 and that, most important, 35 mm film with its greater resolution should preferably be used for fuel tank qualification testing. A number of other methods were shown to provide more than sufficient sensitivity for sensing fuel tank sparking such as the use of photomultipliers and image intensifiers, although they have technical problems which should be addressed.

The most commonly used hot spot detection technique at the present time, is temperature sensitive paint and it works satisfactorily. In some cases, fuel tanks may fail the test but would present no threat of flammable fuel vapor ignition. Therefore, some further work is needed that would provide more detailed time temperature data for minimum ignition.

What remains in question is the probability of generating these shorter duration sparks inside a fuel tank during a lightning strike. Generally diffusion effects and simple circuit effects tend to lengthen the current waveform from the typical 50 microseconds duration rather than shorten it. And it has been observed over many years of fuel tank testing by LTRI that sparking, when it occurs, is energetic and easily detected as verified by the use of visual observers in all fuel tank testing.

ACKNOWLEDGEMENT

Support by the USAF Wright Aeronautical Laboratories, Wright-Patterson Air Force Base, Ohio and the Naval Air Development Center, Warminster, Pennsylvania, in the area of optical detection techniques is appreciated.

REFERENCES

1. Crouch, K. and Robb, J., et. al., "Aircraft Fuel System Lightning Protection, Design and Qualification Test Procedures Development, Phase I Final Report, State of the Art Review", Lightning Technologies, Inc. and Lightning and Transients Research Institute, NADC Contract N62269-83-R-066, Naval Air Development Center, Warminster, PA 18974, February 1985.

2. Johnson, M., "Opto- Rotational Crystals for Electromagnetic Field Detection." Southwest Research Institute, Dallas, Texas, 1983.

3. Barreto, E., Reynolds, S. I., Jurenka, H., "Ignition of Hydrocarbons and the Thermalization of Electrical Discharges." Journal of Applied Physics, 45, 3317-3327, (1974).

4. Demetri, Elia P., and White, Bruce F. , "Development of a Model for Hot-Surface Ignition of Combustible Material, Phase I Final Report", Advanced Mechanical

Technology, Inc., AFWAL Contract No. F33615-83-C-2380, Air Force Wright Aeronautical Laboratories, Wright-Patterson AFB, Ohio 45433, May 1984.

5. Robb, J. D., Hill, E. L., Newman, M. M., and Stahman, J.R., "Lightning Hazards to Aircraft Fuel Tanks." National Advisory Committee for Aeronautics, Technical Note 4326. Comments: First study of lightning hazards to aircraft fuel tanks with theoretical calculations of fuel tank hot spot time-temperature profiles.

TABLE 1

Sensitivity of the Various Detection Techniques for the Standard Spark

The standard spark emits 4.06×10^{8} photons, the number of photons/square meter-second entering the detector is 3.25×10^{15}, corresponding to 1170 microwatts per square meter.

Detection Technique	Sensitivity in photons per sq. meter-sec	Sensitivity in microwatts per sq. meter	S/N dB
eye	1.60×10^{14}	62.4	13.1
film, ASA 3000			
f/4.7	3.5×10^{15}	1260	-0.3
f/2	6.34×10^{14}	228	6.3
photomultiplier tube	2.41×10^{11}	.09	41.3
image intensifier	1.43×10^{10}	.005	53.5

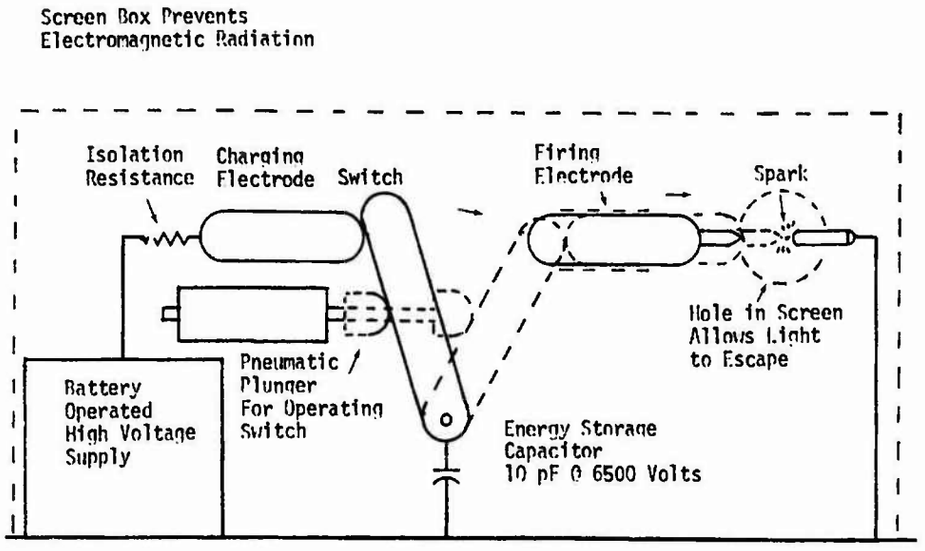


Figure 1a Sketch of Screened Switch for 10 Nanosecond Standard Spark Generator.

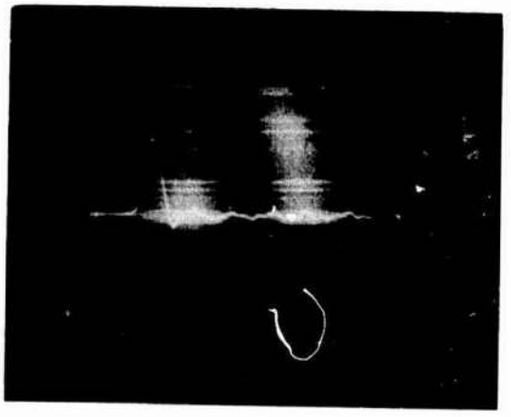


Figure 1b Oscillogram of Discharge from 10 Picofarad Capacitor Charged to 6,500 Volts. The Ordinate is the Current in Units of 6 Amperes/Division and the Abscissa is Time in Units of 10 Nanoseconds/Division.

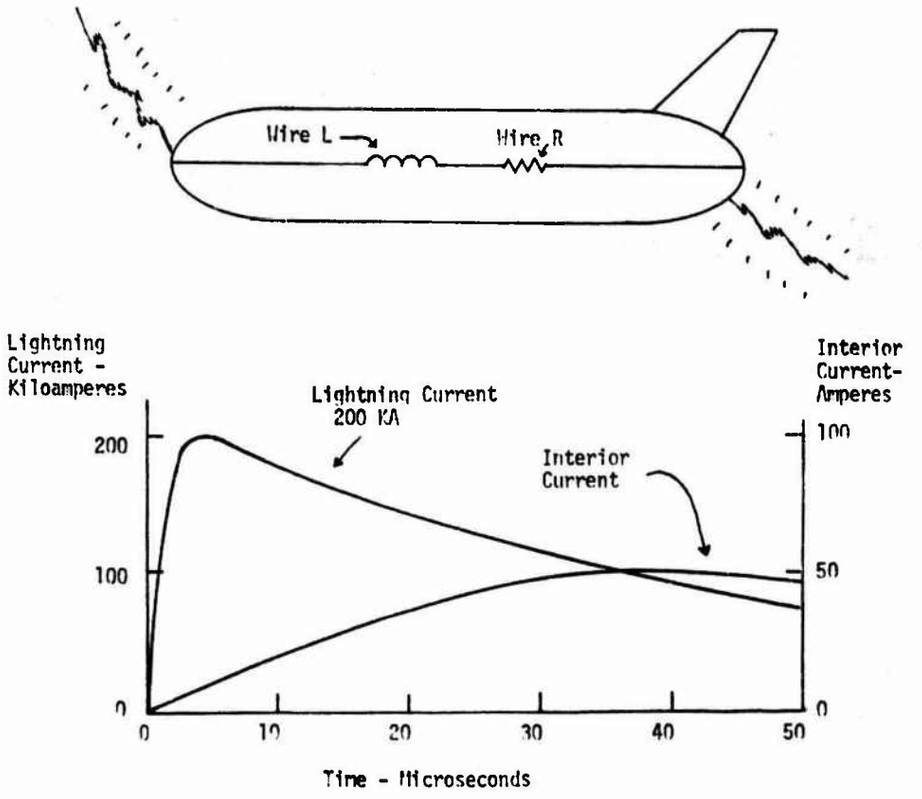


Figure 2 Lumped Constant Calculation Shows Lengthening of Current Waveform on Interior Wire.

MIL-STD-1757A
APPENDIX A
20 July 1983

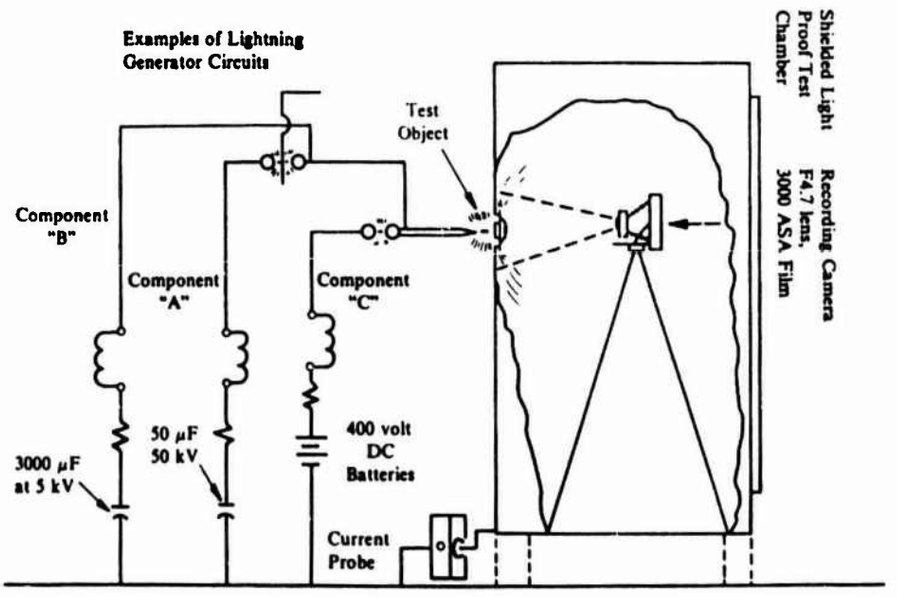


Figure 3 Test Arrangement for Sparking Tests using Cameras from Mil. Std. 1757A (Page A-43).

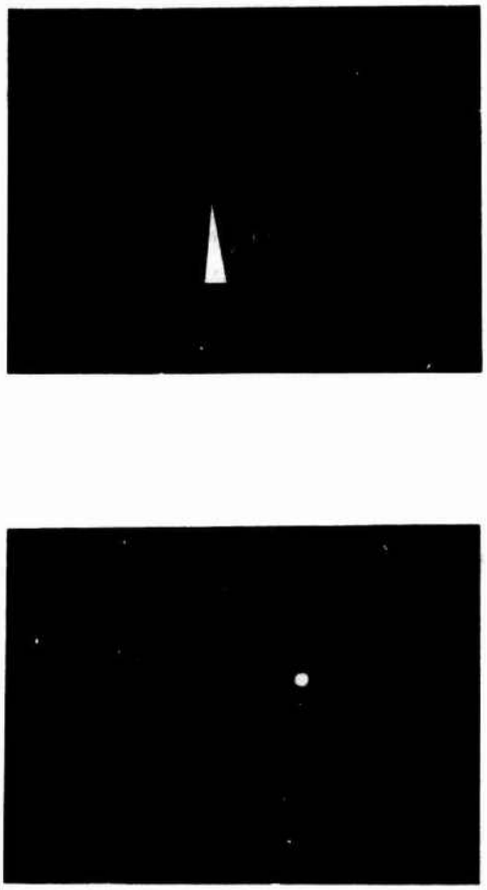


Figure 4 Photographs of Standard Spark using Polaroid Film (above) and 35mm Film (below).

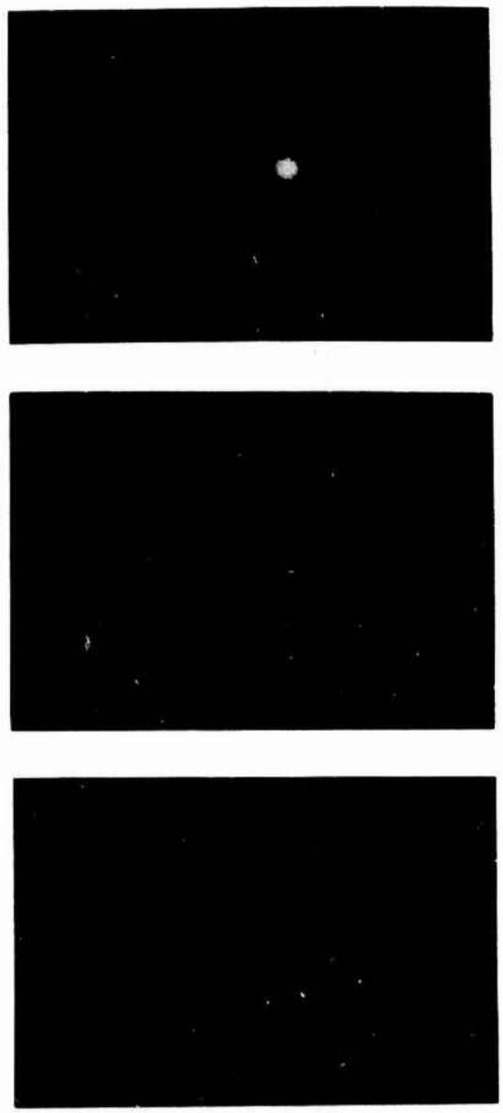


Figure 5 Photographic Tests of Standard Spark. The Photographs are enlarged by a Factor of 23 from the 35mm Negatives. The Conditions for the Photographs are from Top to Bottom, a) f/2.0 at 3 Feet, b) f/4.7 at 3 Feet, and c) f/2.0 at 9 Feet.

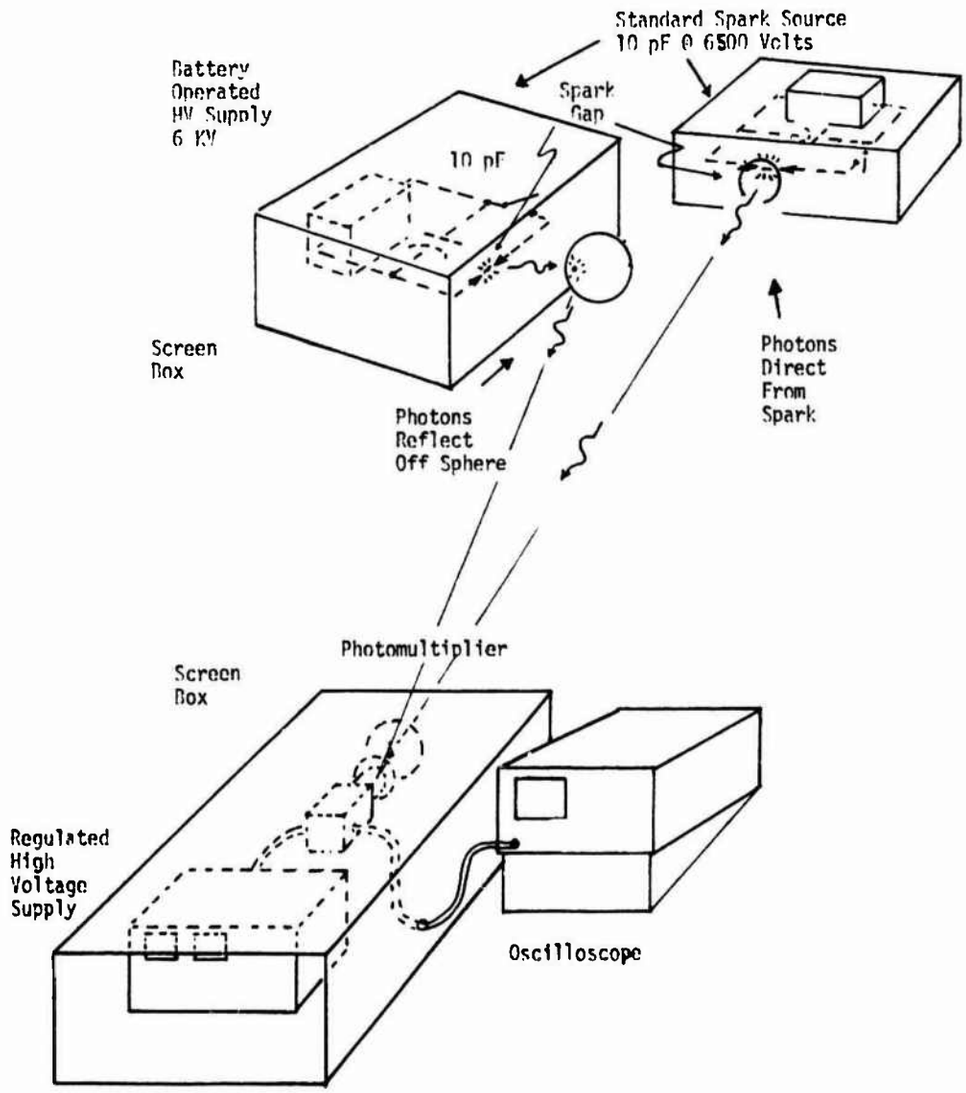


Figure 6 Test Arrangement for Measurement of Light Output from Sparks - Direct and Reflected from Spherical Mirror.

HORIZONTAL ELECTRIC FIELDS FROM LIGHTNING RETURN STROKES

E.M. Thomson, P. Medelius, M. Rubinstein, M.A. Uman, J. Johnson and J.W. Stone

Department of Electrical Engineering, University of Florida, Gainesville, FL 32611, U.S.A.

Abstract - Measurements are presented of simultaneous horizontal and vertical electric fields from both close and distant lightning return strokes. The data were obtained during summer 1984 at the Kennedy Space Center, Florida using an electrically isolated spherical antenna having a system bandwidth of 3 Hz to 5 MHz. Lightning signals were obtained from flashes at distances from a few to 100 kilometers. Since the horizontal electric field is in part determined by the local ground conductivity, that parameter was measured as a function of depth. The horizontal fields from lightning return strokes had typically 1/50 the peak amplitude of the vertical fields and waveshapes which were consistent with available theory, as expressed by the "wavetilt" formula.

I - Introduction

The horizontal electric field from lightning has not been previously measured with a wideband system. In contrast, the vertical component of the electric field from lightning has been thoroughly investigated, starting with the work of C.T.R. Wilson in the early part of this century, and, of particular interest to the present study, return stroke vertical electric fields have been very well characterized of late [1-4]. According to Master and coworkers [5-6] the horizontal electric field in many circumstances is more important than the vertical in coupling to overhead power lines and to horizontal cables on and beneath the earth's surface. It follows that an understanding of the horizontal field is essential for the proper modeling of lightning induced voltages on horizontal lines and cables. Over a homogeneous lossy ground it is possible to calculate the horizontal electric field from the vertical using a wave-tilt transfer function [7] which assumes a relatively simple analytical form if the electric field approximates that of a vertically polarized plane wave at grazing incidence to the earth, an assumption that we might expect to be reasonably valid for fields from distant lightning.

In this paper we describe our experiment to measure wideband horizontal and vertical fields simultaneously, present waveshapes of the horizontal and vertical fields of return strokes, and compare the measured horizontal return stroke fields with calculated horizontal fields found by applying the wavetilt formula to the vertical field.

Experiment

Data were obtained from lightning at distances from 3 to 100 km at Kennedy Space Center, Florida, during July and August 1984. The electric field measurement system (Fig. 1) consisted of a spherical metallic sensor connected via fiber optics signal cables to three recording devices - Biomation transient waveform recorders interfaced with an IBM personal computer, a Honeywell 101 instrumentation tape recorder, and Biomation recorders displayed on a Tektronix 555 oscilloscope screen and recorded with a moving film camera. We also measured the ground conductivity as a function of depth.

The 46 cm diameter spherical sensor (Fig. 2) was suspended from a plastic support with the sphere center 145 cm above a flat area of earth approximately 150 m x 200 m in extent. At this height the effect of the conducting sphere on the ground surface charge density was about one percent. Since the sphere was effectively isolated electrically from ground, the electric field on the surface of the sphere was simply related to the incident field, the enhancement factor being a factor of three. We measured the electric field components in three orthogonal directions by electronically integrating the displacement current through three disks centered on the vertically down, northerly, and easterly axes. The bandwidth of the sensor was 3 Hz to 5 MHz. A calibration signal and the gain of each integrator in the sphere was controlled via a VHF FM radio link. The alignment of the sensor was particularly important since the horizontal fields we measured were much smaller than the vertical and any tilt caused a component of the vertical to appear in the horizontal field signals. We oriented the sphere vertically initially with respect to a gravitationally-based vertical axis and then, with reference to the signals from distance lightning, further adjusted the tilt so that the horizontal field components had essentially similar waveshapes and that no component of the vertical field was obviously evident in the horizontal fields.

All data shown in the figures were digitized and stored using the system consisting of a Biomation transient waveform recorder for each field component (Biomation 8100's for the vertical and North components, Biomation 1010 for the East component) interfaced to an IBM PC. Each data event was triggered from the vertical field and digitized at 100 ns per sample for a duration of 200 μs per trigger. The digitized data were transferred to the PC RAM within 50 ms. Thus it was possible to record several strokes within a flash. The data were ultimately stored on both a 20 mb hard disk and a magnetic tape cassette.

Since the horizontal electric field theoretically depends on the ground conductivity, we measured this parameter using a Bison 2350 B conductivity meter. The depth dependence of conductivity was obtained by considering the earth as being horizontally stratified in three layers and modeling the effective ground conductivity as a function of the horizontal separation of the conductivity probes. The layer

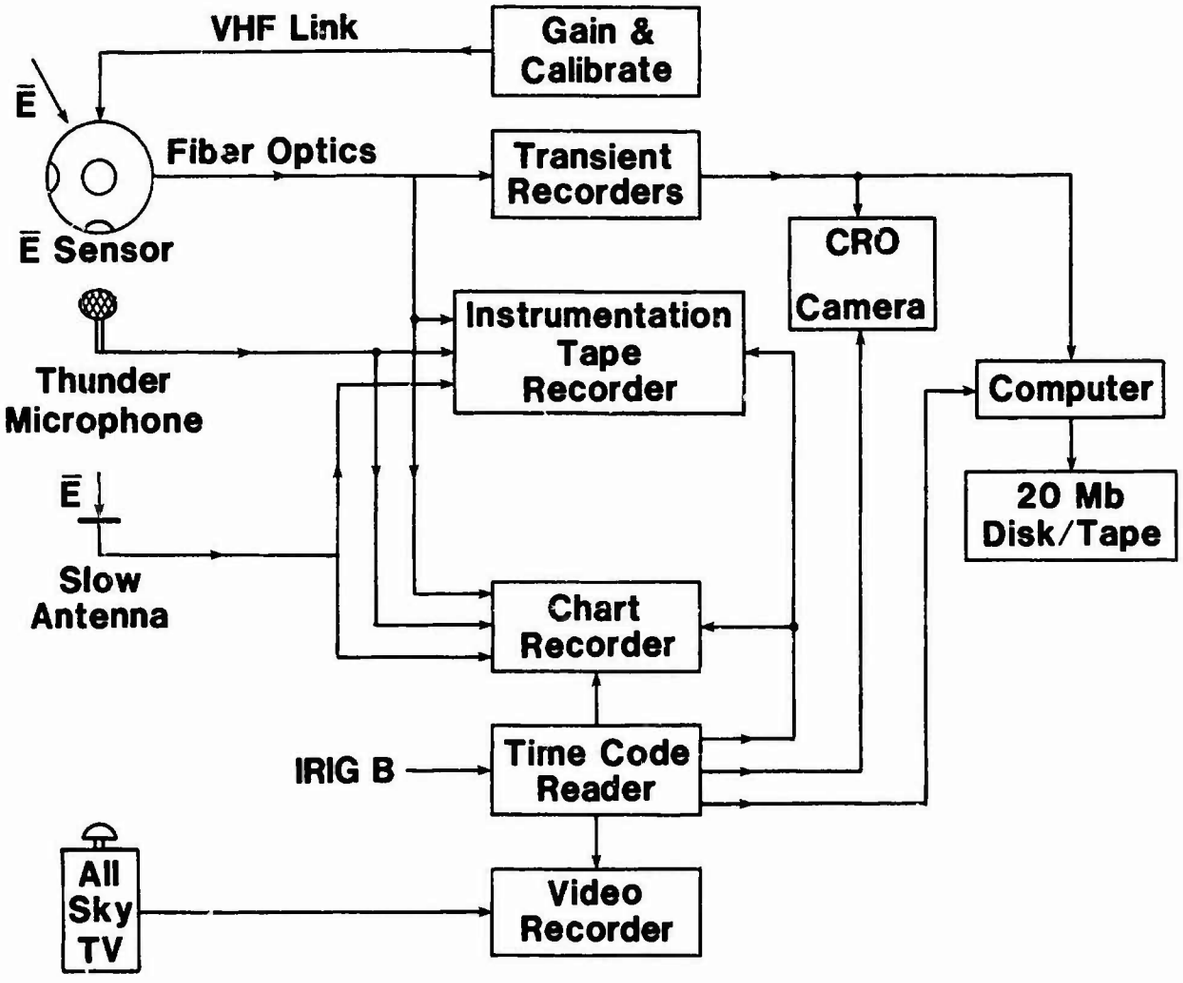


Fig. 1 Block diagram of experimental system

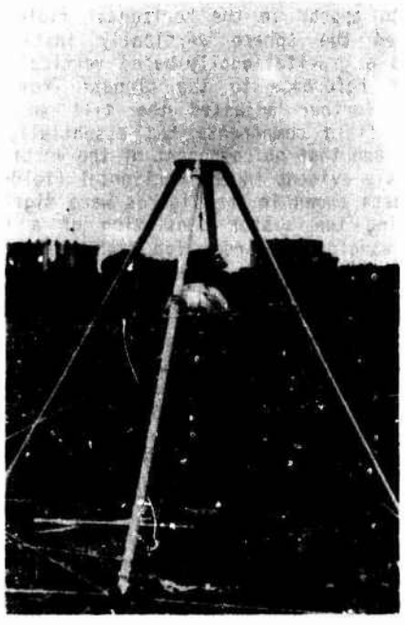


Fig. 2 Electric field sensor and PVC support

conductivities and depths found this way were 8.2×10^{-3} mho/m between ground level and 2.2 m, 3.1×10^{-2} mho/m between 2.2 m and 8.5 m, and 0.19 mho/m below 8.5 m.

II - Results

Figures 3 and 4 show the three components - vertical (EV), northerly (EN) and easterly (EE) - of the electric fields from the first and second strokes in ground flashes at distances of 7 km and 38 km, respectively. Each stroke field is plotted against time on two different time scales. The polarity convention for these fields is consistent with that generally used for lightning: for a positive field (an upward deflection in the figures) the field lines point vertically down, towards the North, or towards the East, respectively. The distances and compass bearings for the flashes were found from the location given by the Lightning Location System at Kennedy Space Center. The wave forms in Figures 3 and 4 were obtained from the raw data by first compensating for the AC coupling in the Biomations and then removing any remaining component of the vertical field that was detected along a horizontal-sensor axis as a result of previously uncorrected sensor tilt. This component, as a fraction of the vertical field, was found from the slope of a plot of the horizontal field versus the

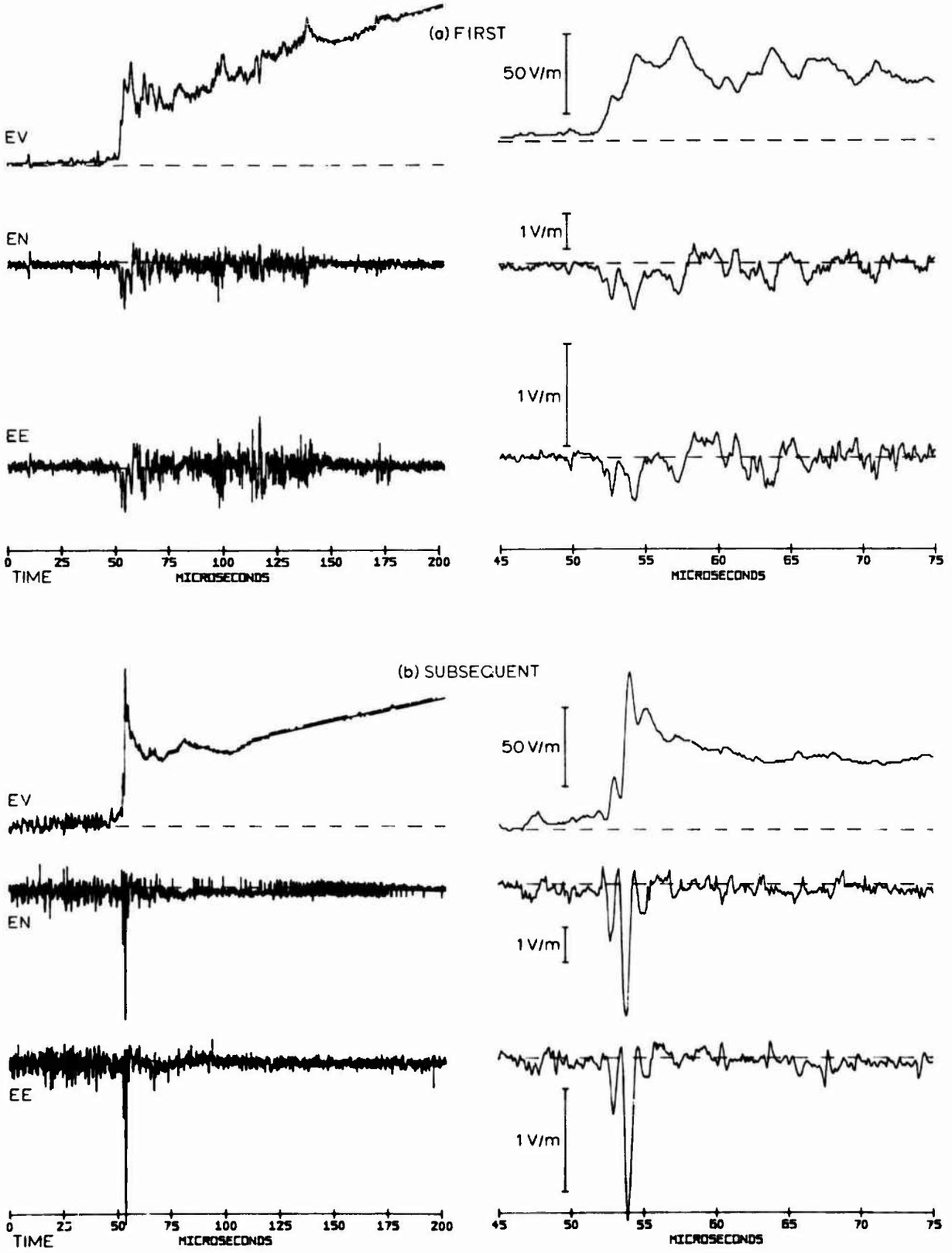


Fig. 3 Electric fields (EV, EN and EE) from strokes occurring at a distance of 7 km on Julian day 224, 1984 at (a) 18 hr. 52 min. 43.231 sec., and (b) 18 hr. 52 min. 43.340 sec.

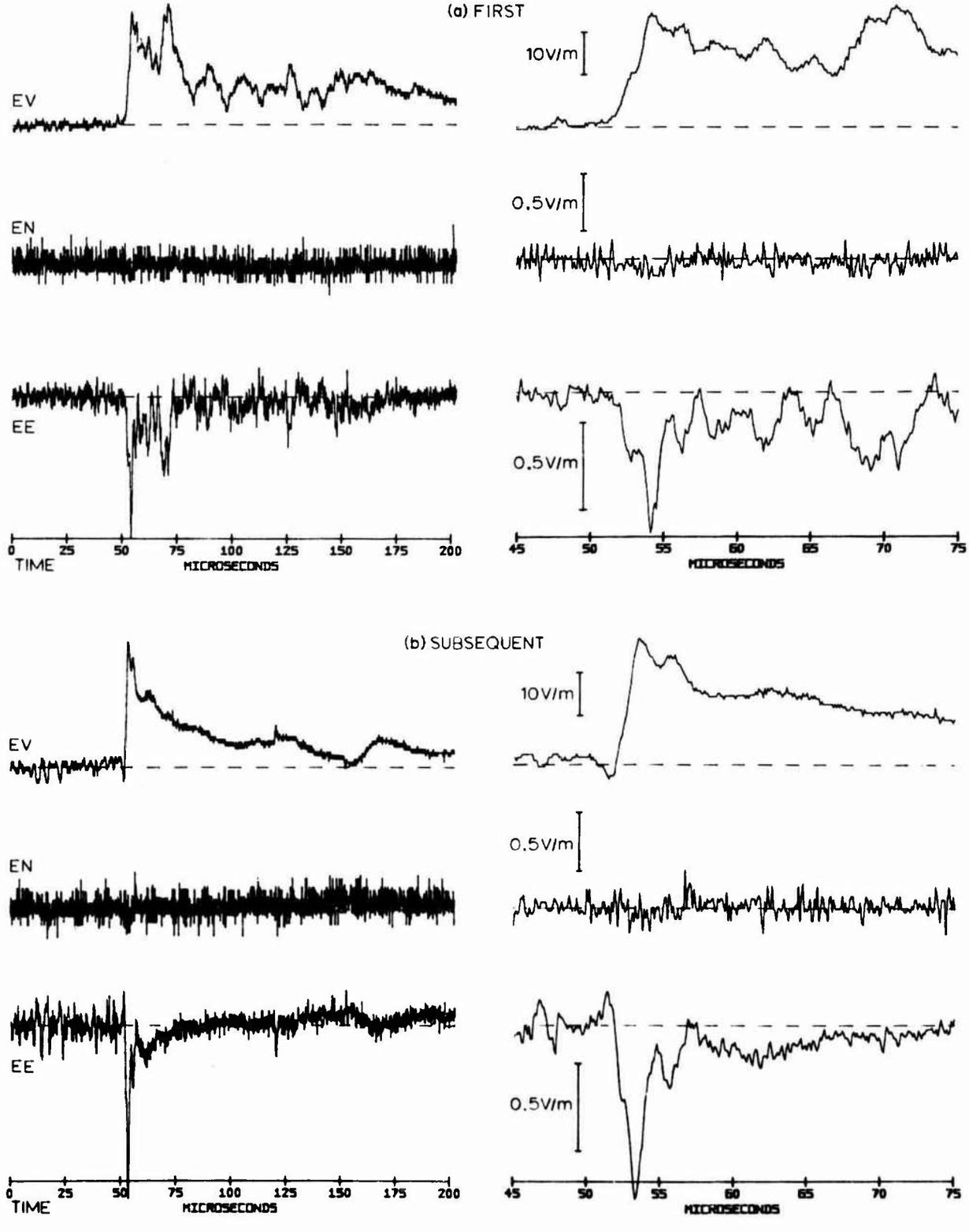


Fig. 4 Electric fields (EV, EN and EE) from strokes occurring at a distance of 38 km on Julian day 223, 1984 at (a) 23 hr. 3 min. 32.466 sec., and (b) 23 hr. 3 min. 32.529 sec.

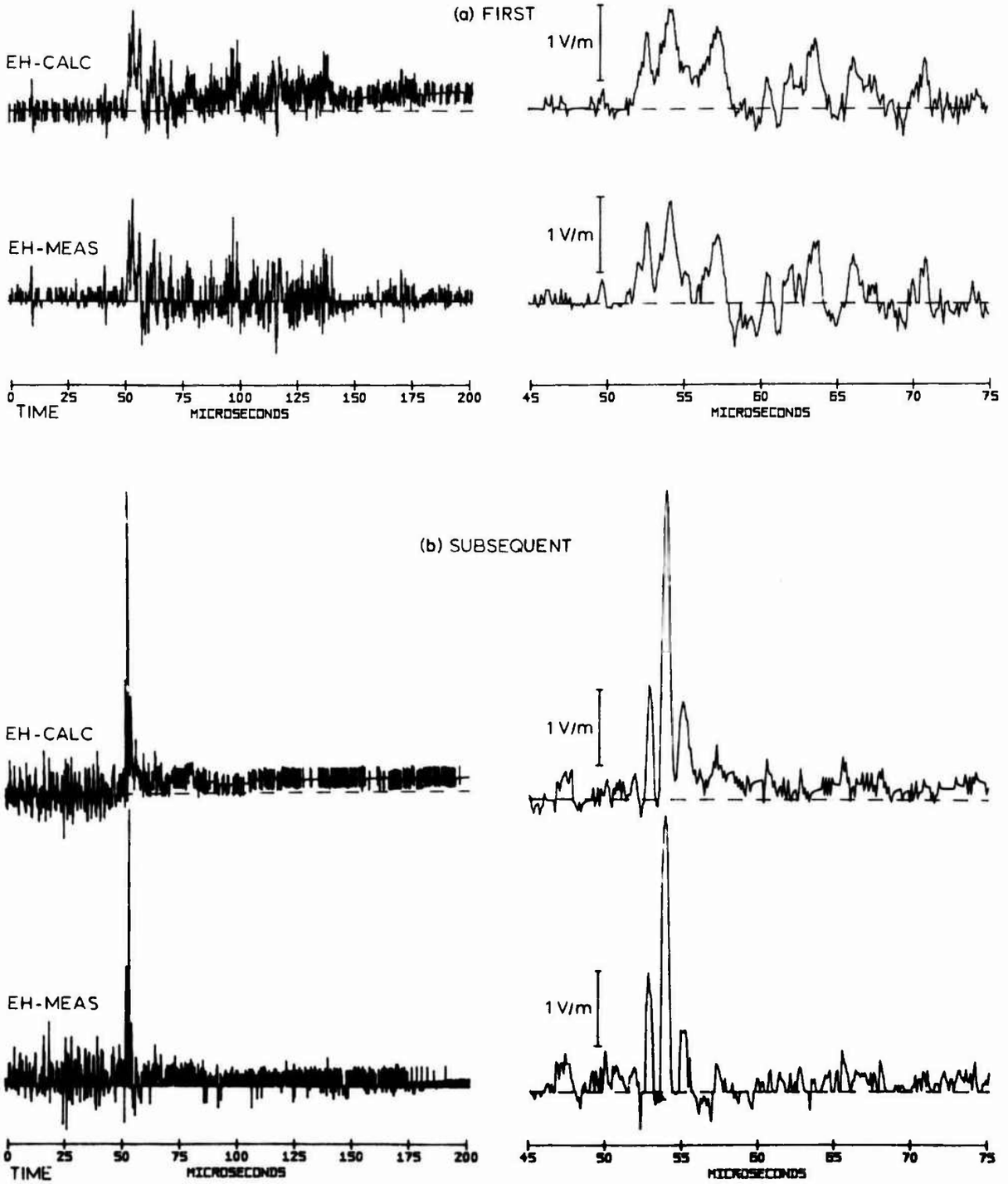


Fig. 5 Calculated (EH-CALC) and measured (EH-MEAS) horizontal electric field magnitudes for strokes occurring on Julian day 224, 1984 at (a) 18 hr. 52 min. 43.281 sec., and (b) 18 hr. 52 min. 43.340 sec.

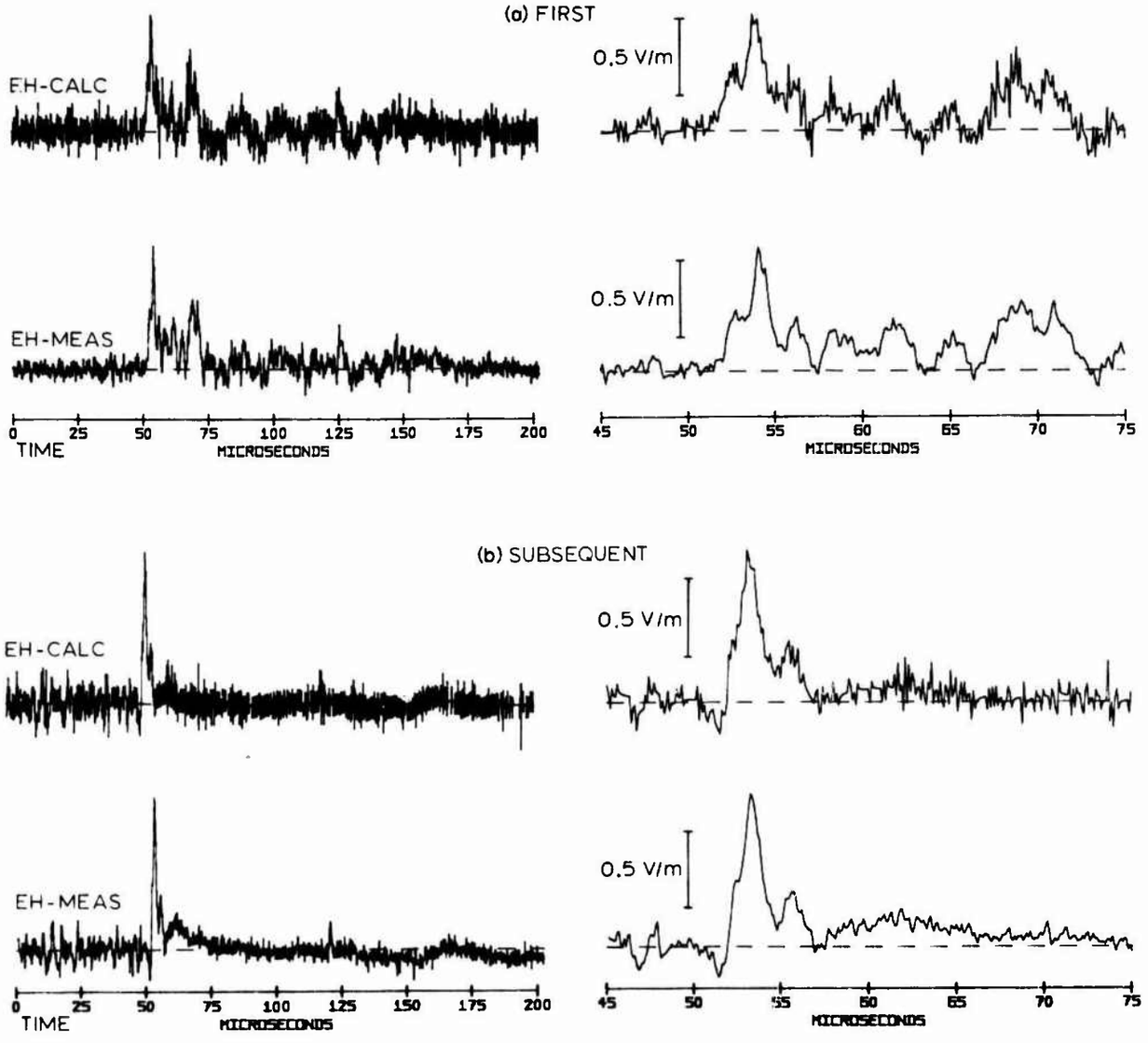


Fig. 6 Calculated (EH-CACL) and measured (EH-MEAS) horizontal electric field magnitudes for strokes occurring on Julian day 223, 1984 at (a) 23 hr. 3 min. 32.466 sec., and (b) 23 hr. 3 min. 32.519 sec.

vertical field for frequencies sufficiently low that theory predicts the horizontal field to be negligible. To find the tilt for the particular data runs in question we plotted northerly and easterly fields versus vertical field averaged over several strokes at distances of 15 to 30 km.

The two strokes in Figure 3 were separated by a time interval of 59 ms, not unduly long for an interstroke interval. Even so, the subsequent stroke (Figure 3(b) appears to be preceded by a dart-stepped leader. Each stroke produced a field change of roughly the same magnitude from the start of the return stroke (t = 50 μs) until t = 200 μs, 150 μs later. However, the peak vertical field for the subsequent stroke is roughly twice the size of that for the first stroke, and the horizontal peak fields for the subsequent stroke are about four times the size of those for the first stroke, apparently because the subsequent stroke vertical-field has a faster rate-of-rise to peak than the first stroke.

A common feature of both Figure 3 and 4 is the more highly structured character of the first stroke electric fields (Figures 3(a) and 4(a)) compared with the subsequent stroke fields (Figures 3(b) and 4(b)) for times between the start of the return stroke and 100 μs following. This structure is more evident on the horizontal field waveshapes than on the vertical waveshapes and probably arises from the branches on the first stroke channel.

III - Discussion

We found the theoretical horizontal field magnitude, E_H, from the vertical electric field, E_V, by applying a wave tilt transfer function valid for vertically polarized fields at grazing incidence

$$\frac{E_H(\omega)}{E_V(\omega)} = \frac{1}{\sqrt{\varepsilon/\varepsilon_0 + \sigma/j\omega\varepsilon_0}}$$

to the measured vertical field. In this formula σ is the conductivity and ε the permittivity of the ground, ε_0 is the permittivity of free space, and ω the angular frequency. Agreement between theoretical and measured horizontal fields was good if we assumed a uniform earth with $\sigma = 8 \times 10^{-3}$ mho/m, the value found for the top layer of ground (between the surface and a depth of 2.2 m). For the range of observed conductivities and a ground permittivity of 40 ε_0 or less, the wave shape of the computed horizontal field was insensitive to either the magnitude of the ground conductivity or the permittivity while the magnitude of the computed horizontal field varied inversely as the square root of the conductivity. This is the case because the second term under the square root in the wave tilt expression dominates the first for frequencies below the upper frequency limit of the experiment, about 5 MHz.

Figures 5 and 6 give the calculated horizontal fields (EH - CALC) found from the vertical using the wavetilt expression assuming $\sigma = 8 \times 10^{-3}$ mho/m and $\varepsilon = 40\ \varepsilon_0$, along with measured horizontal field (EH - MEAS). The close agreement between the theoretical and measured horizontal fields show that this theory is applicable, at least for frequencies represented in the waveforms studied here, even for close return strokes.

Acknowledgement

This research was sponsored by the Office of Energy Storage and Distribution, Electric Energy Systems Program, U.S. Department of Energy, under contract no. DE-AC05-840R21400 with Martin Marietta Energy Systems, Inc. and supported by NSF grant ATM-8217036, and NASA contract NAS10-11020.

References

[1] Weidman, C.D., and E.P. Krider, The fine structure of lightning return stroke wave forms, J. Geophys. Res., 83, 6239-6247, 1978.

[2] Weidman, C.D., and E.P. Krider, Submicrosecond risetimes in lightning return-stroke fields, Geophys. Res. Lett., 7, 955-958, 1980.

[3] Weidman, C.D., and E.P. Krider, Correction to the 'fine structure of lightning return stroke waveforms', J. Geophys. Res., 87, 7351, 1982.

[4] Lin, Y.T., M.A. Uman, J.A. Tiller, R.D. Brantley, E.P. Krider, and C.D. Weidman, Characterization of lightning return stroke electric and magnetic fields from simultaneous two-station measurements, J. Geophys. Res., 84, 6307-6314, 1979.

[5] Master, M.J., and M.A. Uman, Lightning induced voltages on power systems: theory, IEEE Trans. Power Apparat. and Systems, PAS-103, 2502-2518, 1984.

[6] Master, M.J., M.A. Uman, W. Beasley, and M. Darveniza, Lightning induced voltages on power lines: experiment, IEEE Trans. Power Apparat. and Systems, PAS-103, 2519-2529, 1984.

[7] Vance, E.F., Coupling to shielded cables. John Wiley and Sons, New York, 1978.

LIGHTNING VHF AND UHF EMISSIONS AND FAST TIME RESOLVED MEASUREMENTS OF THE ASSOCIATED ELECTRIC FIELD VARIATIONS

C. Weidman, J. Hamelin and M. Le Boulch

Centre National d'Etudes des Télécommunications, B.P. 40, 22301 Lannion, France

ABSTRACT : Measurements of 60, 175, 300 and 500 MHz radiation emitted by close, naturally occurring, lightning discharges are presented and compared with simultaneous recordings of electric and magnetic fields and photoelectric data. Cloud-to-ground and intracloud discharge RF emissions begin abruptly and shape parameters such as amplitude, pulse width and interval time vary considerably. Large amplitude E and B field variations below 1 MHz often accompany important RF emissions, and, thus, stepped leaders, return strokes and certain intracloud discharge processes are shown to radiate strongly at VHF and UHF. These signals are generally similar to previously published data except that we do not observe a cessation of RF radiation immediately after first return strokes.

350 kHz RF receiver bandwidths, temporal resolutions of about 3 μs, prevented direct study of RF submicrosecond time scale structures. Additional, precisely time synchronized, measurements were therefore made using a wideband, 10 MHz-1 GHz, E field antenna connected to a fast transient recorder. This system was triggered externally by either large dE/dt or VHF signals. In the first case, wideband antenna signals consisted of 3, 4 or 5 impulses spaced 0.2 to 1 μs apart which may have been radiated during intracloud leader discharges. Single 3 μs wide impulses were observed at 60 and 175 MHz ; no emissions were visible at 500 MHz. In the second case, triggers occurred during longer, 0.5 to 1 ms, duration bursts of RF radiation emitted at 60, 175 and 500 MHz during first return stroke and perhaps "K change" discharges. The associated wideband antenna signals were complex and difficult to intepret, partly because the antenna receiving transfer function has not yet been determined accurately and the incident E fields have not been calculated.

1 - INTRODUCTION

Much of what we have learned about lightning is based on measurements of electric (E) and magnetic (B) fields at frequencies between zero and a few or a few tens of megahertz /1,2/. There is currently a lot of interest in the strong emissions which lightning produces at VHF and UHF frequencies. This is partly because we still do not understand very well what kinds of discharges or physical processes generate these signals. Also, several researchers are using lightning RF fields, and time of arrival or interferometry techniques, to locate discharge sources and follow channel development in time within the cloud and to relate this to thunderstorm dynamics and structure /3-11/.

Lightning RF emissions are impulsive and their large amplitudes represent a potential hazard to any system which is sensitive to transient fields. RF signals generated during lightning discharge might perturb radio or microwave telecommunications links, for example. Past measurements have often been made with narrow bandwidth receivers, which do not resolve the fastest variations, and are thus not suitable for a proper evaluation of this risk.

With these two different objectives in mind, that is to better understand the lightning processes which radiate at VHF and UHF and to characterize the lightning electromagnetic environment between a few tens of megahertz and a few gigahertz, the Electromagnetic Environment Group at the French National Telecommunications Research Center (CNET) has recorded natural and triggered lightning RF emissions at 60, 100, 175, 300, 500 and 900 MHz during summer field experiments in New Mexico (1982) and at the St Privat d'Allier station in south central France (1983). Recordings of natural lightning RF radiation were made in 1984 in south west France as part of the FRONTS 84 experiment. 350 kHz bandwidth receivers were used and RF signals were recorded in precise time correlation with E field, B field and optical data. A detailed discussion of 1982 and some of the initial 1983 results has been given by /12/.

In this report, we will discuss the continuation and extension of this work, in particular of measurements made in 1984 using a specially designed 10 MHz - 1 GHz conical antenna connected to a fast transient digitizer. These measurements were motivated by /12/ who observed that, when viewed on a microsecond time scale, the lightning RF recorded then consisted of either single 3 μs wide impulses or superpositions of these impulses. The 3 μs wide pulse is, of course, the impulsive response of a 350 kHz bandwidth RF receiver. Frequently, these impulses could be identified at each of the six frequencies studied and, in these cases, /12/ measured peak amplitudes and plotted relative amplitude spectra ; an example is shown in Figure 1. These spectra are interesting because they do not vary monotonically with frequency but have fairly well defined maxima and minima which may tell us something about the submicrosecond structure of the lightning fields. /12/ has suggested, for example, that these spectra could be produced by either :

(a) a single current impulse in a source volume with dimensions approximately equal to the wavelength of the RF radiation. In this way constructive and destructive interference would occur at the different frequencies studied between signals originating at different parts of the source volume. A cylindrical volume would need to be a few meters in diameter to produce the observed spectra.

(b) a sequence of impulses whose durations and interval times were less than the receiver response time. A sequence containing more than just a few impulses would need to be spaced very uniformly in time for peaks to appear in the frequency spectrum.

We hope eventually, by making fast time resolved measurements of wideband E fields, to be able to investigate directly these different hypotheses. This paper reports on our initial experiments and results.

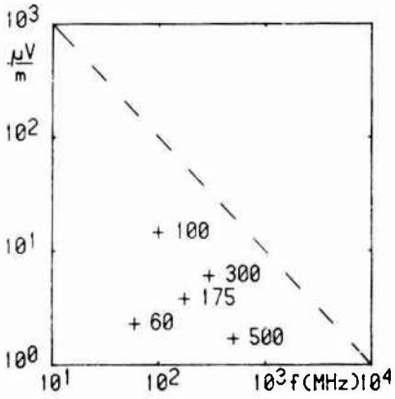


Fig. 1 An example of a lightning relative amplitude spectrum which does not decrease monotonically with frequency (adapted from /12/). Amplitudes have been normalized to 10 km and 1kHz bandwidth using 1/(distance) and $1/(BW)^{1/2}$ dependencies, respectively. The dotted line shows the 1/(freq.) fit to other data given by /32/.

2 - EXPERIMENT

A schematic diagram of the measuring equipment is shown in Figure 2. Lightning RF emissions at 60, 100, 175, 300, 500 and 900 MHz were measured using six tuned, vertically polarized, dipole antennas mounted on a grounded 9 m metal mast. For simplicity, only one of these antennas is shown in Fig. 2. Antenna spacing was such that effects due to mutual coupling between adjacent antennas and due to reflections from the ground were minimized /12/. Antennas were connected to receivers, located 10 m away in a metal trailer, using semi-rigid coaxial cables. Receiver characteristics at each of the six frequencies are summarized in Table 1. Logarithmic amplifiers were used to amplify and detect the intermediate frequency signal giving a receiver dynamic range of about 80 dB.

TABLE 1
RF Receiver Characteristics

Frequency (MHz)	Bandwidth (kHz)	Sensitivity* (μV/m)
60	330	30
100	337	90
175	348	30
300	360	50
500	350	90
900	385	600

* Sensitivities indicate the minimum field necessary at each center frequency to produce an observable signal at the receiver output.

Horizontal magnetic fields were measured using two orthogonally mounted, wideband (150Hz-20MHz) antennas /13/. A "fast E" field antenna system like that described by /14/ was used to measure lightning electric fields. System risetime and decay time constant were 0.2 and 200 μs, respectively. Luminous emissions at elevation angles of 1° and 10° were made using two photoelectric detectors similar to those described by /15/. Each detector had an angular resolution of about 1°, a risetime of less than one microsecond and a nearly 360° horizontal field of view.

Continuous recordings of the RF signals, E and B fields, the two optical signals, a time code signal and a pulse indicating a 500 MHz waveform recorder trigger were made using a 400 kHz bandwidth instrumentation tape recorder (FM mode). Time mark signals were superimposed on all channels at the recorder input to permit precise correlation in time.

The fast time resolution recording system occupies most of the right half of Fig. 2 and consists of a specially designed 10 MHz - 1 GHz conical antenna connected through 1 or 1.5 μs of RG-8 50Ω. coaxial cable delay line to a 500 MHz transient recorder. This recorder was triggered externally by an oscilloscope in the following manner : Either a dE/dt or a 60, 175 or 500 MHz signal was connected to the oscilloscope input and time base A (TB A) was set to trigger internally on that signal. TB B was operated in the "trigger after delay" mode. That is, when TB A was triggered and after a prechosen delay, which ranged from 10 to 200 ms, TB B was armed. If the signal again crossed trigger threshold before the end of the TB A sweep (the TB A sweep was typically 200 to 500 ms long) a TB B gate pulse was generated and triggered the 500 MHz recorder. If not, TB B was disenabled, TB A reenabled and the whole procedure began again. In this way we hoped, by choosing among the different triggering signals and by varying the delay before the TB B enable, to be able to record conical antenna signals from a wide variety of discharge processes. Note also that, by using one of the RF signals, the oscilloscope trigger did not depend on polarity.

When the 500 MHz recorder was triggered, it generated a gate pulse which then triggered a four channel 2 MHz recorder, operating in pretrigger mode, thus giving precisely time synchronized records of simultaneous E field and 60, 175 and 500 MHz radiation. The 500 MHz recorder gate pulse also stopped a clock, which was subsequently read by the computer, and was written onto the magnetic tape.

The 500 MHz recorder was in reality a Tektronix 7912AD programmable digitizer. The 7912 operates in many respects like a storage oscilloscope. The essential difference is the target which, in the case of the 7912, is an array of diodes. The recorded signal is subsequently read in a 512 by 512 point (horizontal by vertical) format. A very high velocity writing beam can be used because the target size is small and because very few electrons need to strike the target to record a wareform ; an effective sampling frequency of 100 GHz is possible. In our application, the 7912 was equipped with a 500 MHz input amplifier and the time base sweep speed was either 200 or 500 ns/div, effective sampling frequencies of about 250 and 100 MHz, respectively (250 MHz = 512 points / 10 divs x 200 ns/div). The uppermost curves in Figures 9, 12, 13 and 15 show 7912 records. These data were recorded in mode "edge", that is, plotted data show the upper and lower edges of the signal which was read off the 7912 diode matrix target.

The 4 channel waveform recorder sampling frequency was 2 MHz and each record contained 256

points. The delay line shown in Fig. 2 was necessary because of the 500 MHz recorder could not operate in a "pretrigger" mode and because of the external triggering method used. The delay line attenuated, significantly, higher frequency conical antenna signals. With a 1.5 μs delay line, for example, 10 and 100 MHz signals were attenuated by 6 and 20 dB, respectively.

2.1 - Conical Antenna Design and Calibration

The 10 MHz - 1 GHz antenna developed for this study has a conical form, a geometry commonly used in measurements of fast, impulsive fields where wideband response is necessary. The antenna is shown schematically in Figure 3. Basically, the lower 0.27 m consists of a solid cone which provides the high frequency response. A 43° cone angle fixes the antenna impedance at 50Ω. Extension of the solid cone to the dimensions necessary for low frequency response was mechanically unrealistic so this structure was approximated by six "wire" elements. These elements were actually constructed out of 12 mm diameter copper tubing to insure that corona discharge would not occur off the surfaces of the antenna in thunderstorm E fields. Careful placement of 250 Ω resistances damped certain antenna resonances and effectively extended low frequency response to 10 MHz while minimizing overall antenna height. The antenna was mounted on a 12 m by 12 m wire mesh ground plane.

This design represents a choice of several variants which were studied in order to best satisfy the following requirements between 10 MHz and 1 GHz :

(a) constant 50Ω impedance
(b) a lineaire phase response.
(c) minimal variation of the radiation diagram with frequency.

A detailed theoretical discussion is given by /16/.

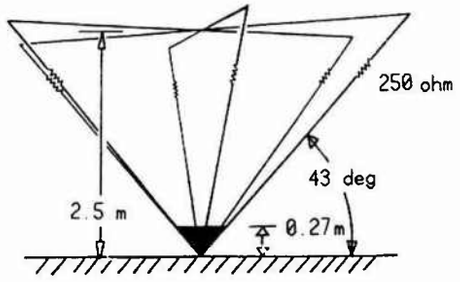


Fig. 3 A schematic, side view of the conical, electric field antenna.

When a linear antenna is used for receiving, the receiving transfer function, which relates the received voltage V(f) measured across a load impedance Z_o and the incident electric field E(f), is

$$S(f) = \frac{V(f)}{E(f)} = - \frac{h(f)\, Z_o}{Z_a(f) + Z_o} \qquad (1)$$

where h(f) is the effective height of the antenna, Za(f) the antenna impedance and f frequency /17/. Since we are interested in determining incident fields from measured antenna load voltages, we will define K(f) = 1/(S(f)) then

$$E(f) = K(f)\, V(f) \qquad (2)$$

E(t) can be determined by calculating the inverse Fourier transform of Egn. 2.

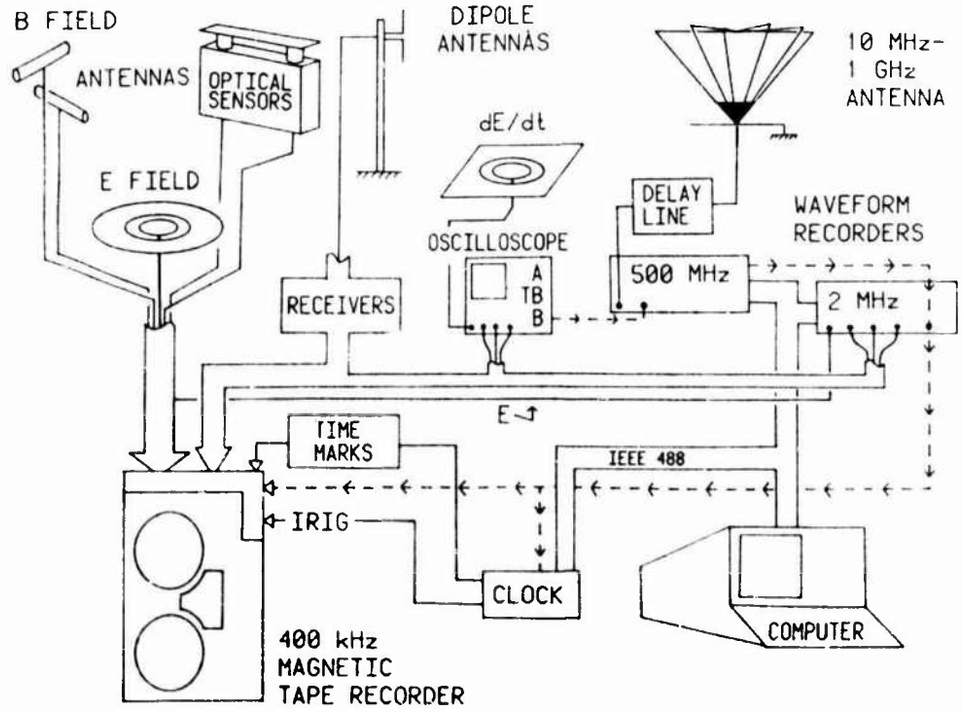


Fig. 2 A block diagram of the measuring system. The dotted lines indicate triggering signals.

/16/ has determined, experimentally, the magnitude of the complex function K(f) using the "two identical antenna method" /18/. K(f) was also determined independantly by us using a large EMP simulator. The incident test field, a square 100 ns wide pulse, was measured with a separate antenna standard and is shown in Figure 4(a). The conical antenna output signal is given in Fig. 4(b). The data aquisition system used in this test had a bandwidth of 128 MHz. K(f) was then determined by dividing the Fourier transform of the reference field by the transform of the antenna output voltage. The magnitude functions of K(f) determined in these two ways are plotted in Figure 5.

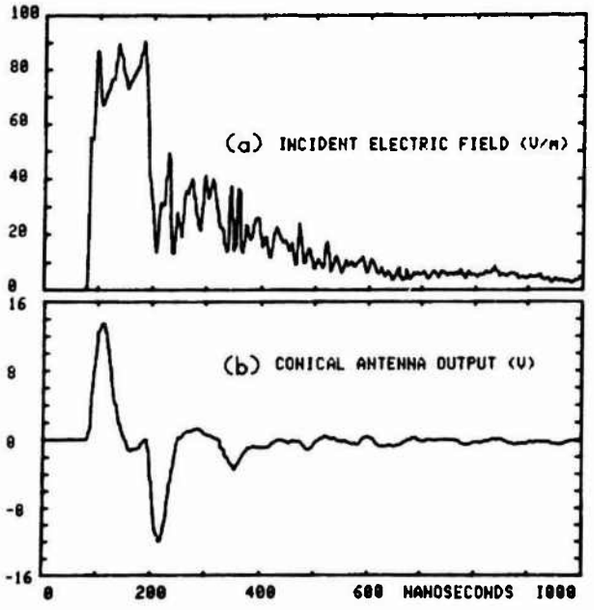


Fig. 4 Conical antenna response (curve (b)) to a 100 nanosecond wide "square pulse" vertical electric field (curve (a)).

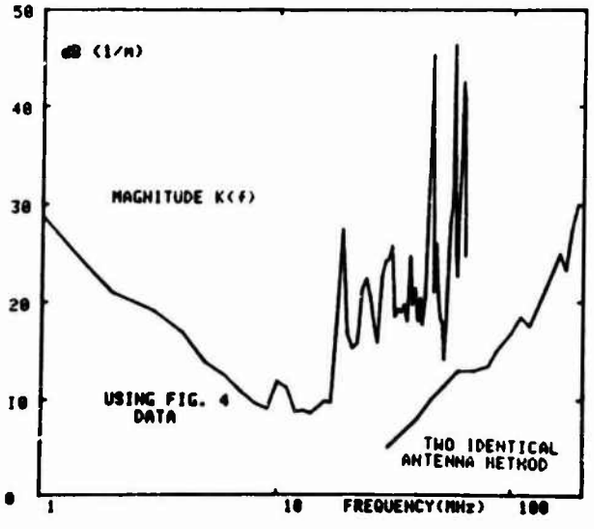


Fig. 5 Plots of two different determinations of the magnitude of the complex antenna receiving transfer function, K(f). Note that increasing antenna sensitivity is in a downward direction.

We note first in Fig. 5, that there is about a 10 dB difference between these two determinations of K(f) , which we cannot yet explain. Also, because of the superimposed high frequency variations, the Fig. 4(a) square wave E field has not permitted a good estimate of K(f) above about 45 MHz.

Even with this unsatisfactory antenna calibration we would like to have inverted conical antenna signals to determine approximate incident E field shapes. A second difficulty has kept us from doing this. This second problem is concerned with extracting higher frequency information from the 7912 "storage oscilloscope-like" records. Consider what happens if we try to record a sinusoidal signal on a storage oscilloscope.We obtain an accurate representation if one period of the sinusoid is longer than t', the time it takes to oscilloscope to sweep across one electron beam "spot width". If, however, one or more cycles occur in a time less than t', successive signal oscillations overlap and we obtain a thick trace which gives a good indication only of peak amplitude. In our application, the 7912 was operated at a relatively slow sweep speed with a high beam intensity and t' is longer than many of the conical antenna signal variations. The antenna signals were not simple sinusoids and spot width is not constant, but depends on the two-dimensional beam velocity. Recovery of the higher frequency information thus seems a complex problem and has not yet been attempted.

3 - DATA

3.1 - Millisecond Time Scale Structures

Examples of 175 MHz radiation and simultaneous "fast E" fields produced during four lightning discharges are shown in Figure 6. These records reproduce signal variations as fast as 100kHz, and were obtained by replaying analog data tapes at reduced speed and rerecording the data on a second recorder. These rerecordings were then displayed , again after reducing the playback speed, on a strip chart recorder. The RF signals produced by these discharges at the other frequencies had similar overall appearances and are not shown. Distances were determined by timing the first arrival of thunder. In Fig. 6 and throughout this report, movement of negative charge from cloud to ground produces a positive polarity E field change.

The "fast E" signals, which are shown on a fairly sensitive scale in Fig. 6, indicate only one or a few large amplitude field producing discharges per flash. At 175 Mhz, some of the strongest emissions also occur at these times, but appreciable radiation also precedes, occurs between, and follows the large "fast E" impulses. An interesting feature is the abrupt onset of the RF emissions. This is true of essentially all events we have studied, and large amplitude E and B fields often occur simultaneously (see event 022415, for example). The initial few hundred milliseconds of activity in each discharge then appears, on this time scale, to consist of impulses closely spaced in time. The rate of occurrence can be quite rapid. Especially high occurrence rates (pulses which occur at interval times too short to be individually resolved by the RF receiver) appear in Fig. 6 as a 175 MHz signal which is offset from zero. This occurs near 50 ms in events 021729 and 022017, for example, and is accompanied by a slow E field variation. Late in the discharges, emissions occur in more isolated, often intense bursts. Some of these are probably the "Q noise" the "solitary pulses" and the

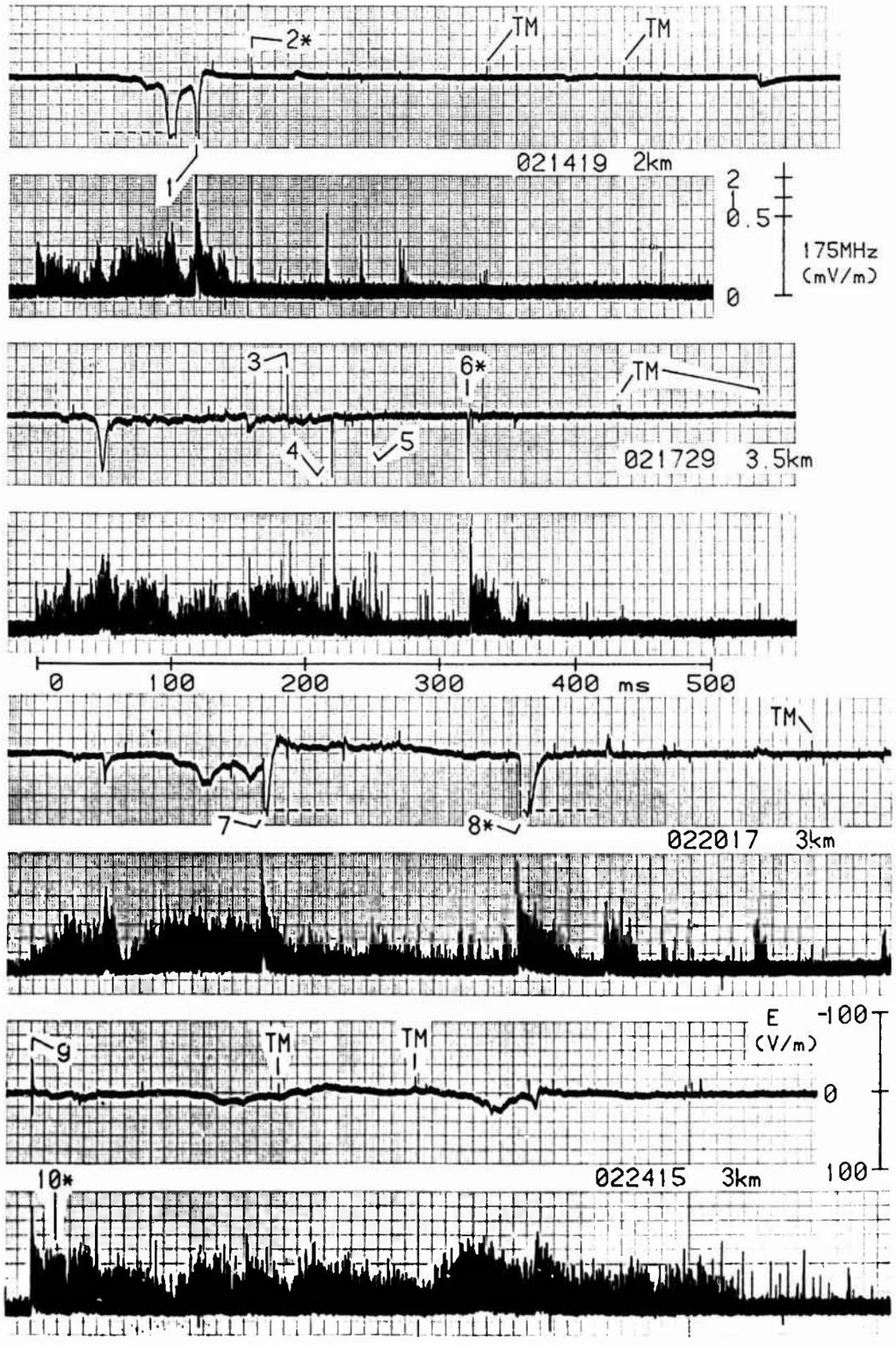


Fig. 6 "Fast E" fields and 175 MHz radiation produced during four different lightning discharges. Some of the numbered events are discussed in detail in the text (a star indicates a 500 MHz recorder trigger). The amplitude calibrations shown apply to all four discharges; note that a positive E field change is in a downward direction. The 175 MHz noise level is about 0.05 mV/m. Horizontal dotted lines show saturation levels, and "TM" indicates a time mark signal superimposed on all records at intervals of 100 ms.

"fast bursts" described by /7/, /6/ and /B/, respectively.

We note finally, that with our experience, it is not possible to identify with certainty different types of discharge processes using these slow time scale E field and 175MHz signatures. The strong emissions at points 1, 7 and B in Fig. 6 were produced by first return strokes (determination made using faster time scale E and B field shapes). There are no large amplitude E field changes in event 022415 and those in event 021729 do not have characteristic return stroke forms, and, therefore, these two events appear to have been intracloud discharges.

3.2 - Microsecond and Submicrosecond Time Scale Structures

In Figures 7 and 8 we show, with faster time resolution, the simultaneous (± 10 μs) E and B fields, luminous emissions and 60, 175, 300 and 500MHz RF radiation which occurred at points 1 and B, respectively, in Fig. 6. These E and B fields begin with an abrupt positive transition and have shapes and amplitudes which are characteristic of fairly close first return stroke discharges /19/. The initial radiation field peak is visible in all cases and is followed, on E field records, by a strong electrostatic field component which saturated the recorder. Fig. 7 illustrates particularly well, the magnetic field "hump" described by /19/ which follows the B radiation field peak on close discharges.

Significant RF activity precedes the return stroke E and B field changes at 60 and 175 MHz in Figures 7 and B and is probably associated with the stepped leader process which initiates first return stroke discharges. The 100 kHz bandwidth of the system used to reproduce these data was probably not adequate to reproduce stepped leader E and B fields, which typically have widths of only 1 or 2 μs /14/. Large "bursts" of RF radiation occur at all frequencies in association with the return stroke. Close inspection reveals that peak RF emissions generally follow the E and B radiation field peaks by a few tens of microseconds in agreement with /20,21,22/. Also, RF peaks do not always coincide at the different frequencies (see Fig. 8). Note that at 60 and 175 MHz, first

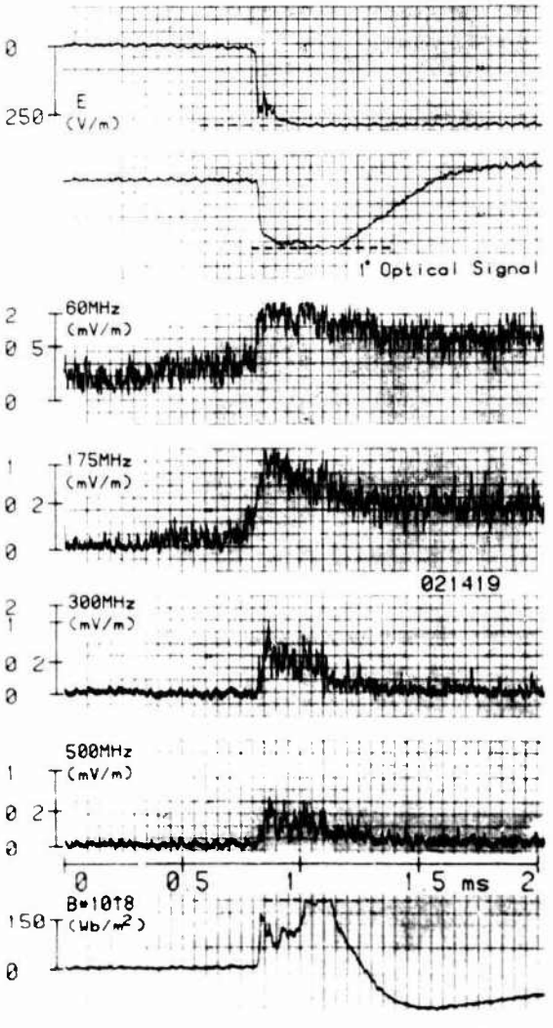


Fig. 7 Faster time resolved records of the (top to bottom) "fast E" fields, the 1° optical and the 60, 175, 300 and 500 MHz emissions and one component of the horizontal magnetic field produced during a first return stroke discharge (point 1 in Fig. 6). Horizontal dotted lines indicate saturation.

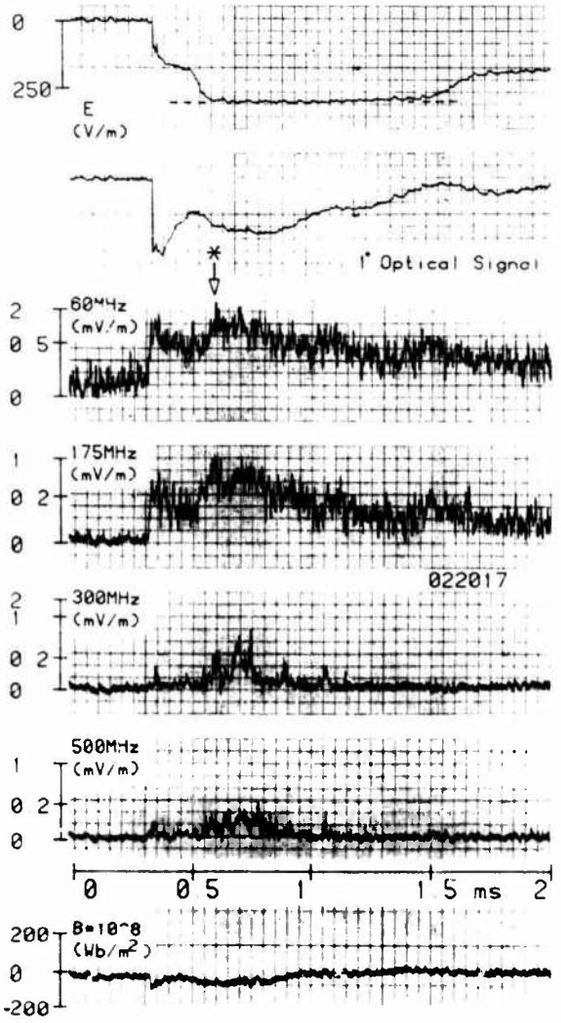


Fig. 8 Fast time resolved records of electromagnetic radiation produced by a first return stroke discharge (point 8 in Fig. 6). Fig. 7 comments apply here also. The downwardly pointing arrow indicates the moment at which the 500 MHz recorder was triggered.

return stroke RF bursts last well over 1 ms. Durations at 300 and 500MHz are shorter, about 500 μs.

The 500 MHz recorder was triggered by a large 60 MHz impulse that occurred during the return stroke discharge in Fig. 8. That record is shown in Figure 9 (upper most curve) together with recordings of the simultaneous "fast E" and 60, 175 and 500 MHz signals made with the 2 MHz recorder. Horizontal and vertical scale calibrations and zero levels are indicated. The upwardly pointing arrow indicates the moment at which the 500 MHz recorder was triggered by the oscilloscope TB B gate pulse. A dotted vertical line drawn through the lower four curves in Fig. 9 shows the time of the 2 MHz recorder trigger. We should repeat that the upper curve in Fig. 9 is the conical antenna output and not the incident E field. The incident field was not calculated, for reasons discussed in Section 2.1, and probably has a very different overall appearance. Discussion of this and other fast time resolved recordings is given in Section 4.

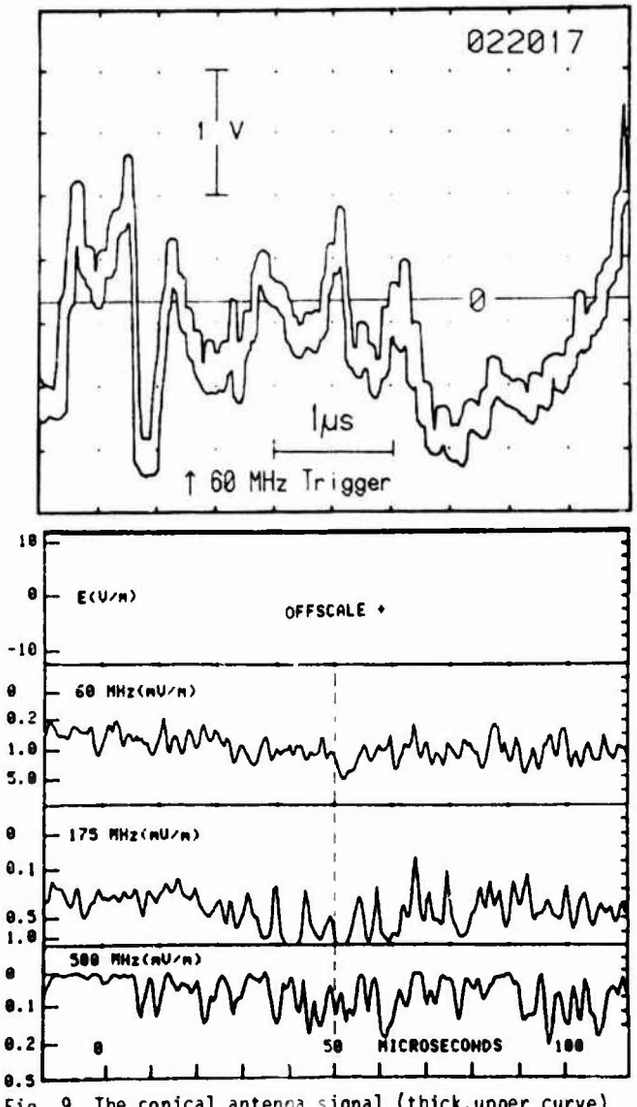


Fig. 9 The conical antenna signal (thick,upper curve) and simultaneous E field and 60, 175 and 500 MHz radiation (lower four curves; E field is offscale) produced during the return stroke discharge shown in Fig. 8.

Bipolar E field impulses, which occurred at the beginning of discharge 022419 (point 9 in Fig. 6), and the simultaneous RF emissions are shown in Figure 10. Bipolar E field waveforms like these, whose initial polarity is negative, are typical of the larger radiation field pulses produced by intracloud lightning and are discussed in detail by /23,24/. The largest RF signals have widths of a few tens of microseconds and occur in time coincidence with the E field pulses. In agreement with /25/ there is a tendency for the RF signals to peak during the initial half cycle.

Figure 11 illustrates the "fast E" and 175 MHz signals that were emitted at point 10 in Fig. 6. While appreciable 175 MHz radiation is present, simultaneous E fields were either too weak or too rapid to be recorded. The 500 MHz recorder was also triggered during this sequence, in this case by a positive dE/dt signal. That record and those obtained with the 2 MHz recorder are shown in Figure 12. This example is considerably simpler than Fig. 10. Three, perhaps four, impulses are clearly distinguishable. Here, a downward conical antenna signal deflection indicates a positive incident E field transition. Also, judging from the conical antenna response to a square wave incident field, Fig. 4(b), we suspect that the incident E field impulses, here, may have been nearly unipolar. Thus, we would suggest that this was a sequence of 3 or 4 nearly unipolar, positive polarity, E field impulses. Note that a positive E field pulse is also visible on the 2 MHz recorder E field trace.

A second fast conical antenna signal, obtained during very similar activity in another discharge is shown in Figure 13.

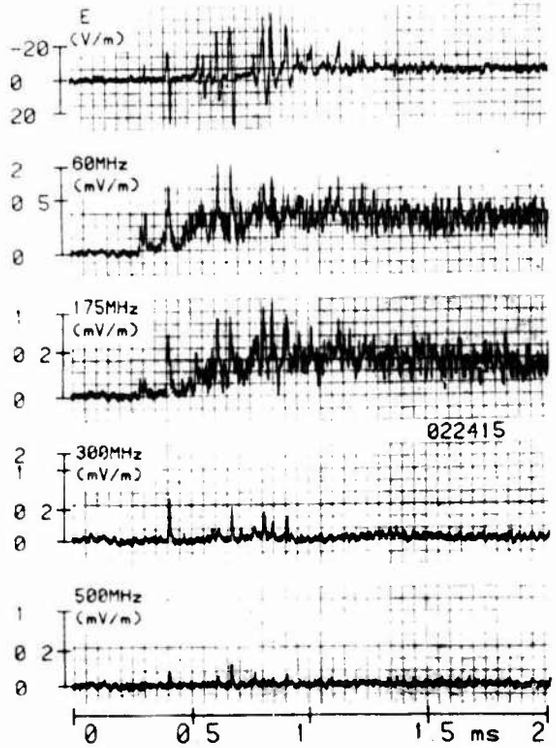


Fig. 10 The negative polarity bipolar E field impulses and simultaneous 60, 175, 300 and 500 MHz radiation which occurred at the beginning of event 022415, an intracloud discharge (point 9 in Fig. 6).

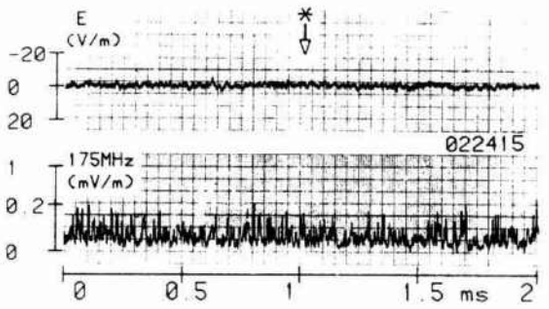


Fig. 11 Fast E field and simultaneous 175 MHz activity occurring at point 10 in Fig. 6. The downwardly pointing arrow indicates the moment at which the 500 MHz recorded was triggered.

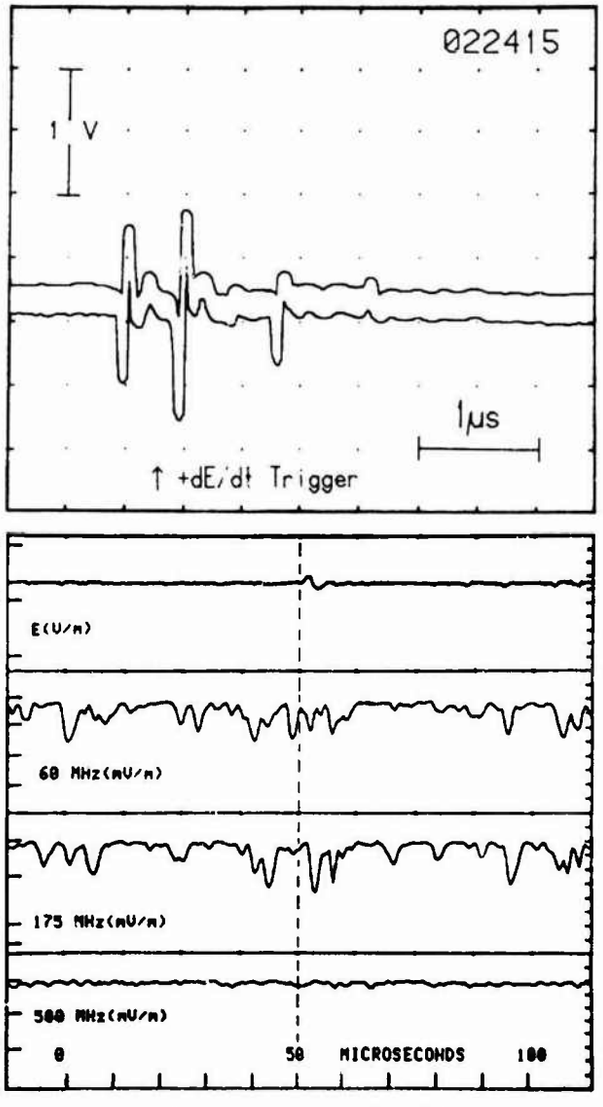


Fig. 12 The conical antenna signal (thick, upper curve) and simultaneous E field and 60, 175 and 500 MHz radiation (lower four traces) produced during the intracloud discharge activity shown in Fig. 11.

Returning now to Fig. 6, we note that a short duration, but very strong, 175 MHz impulse occurred at point 2 in event 021419. Figure 14 shows

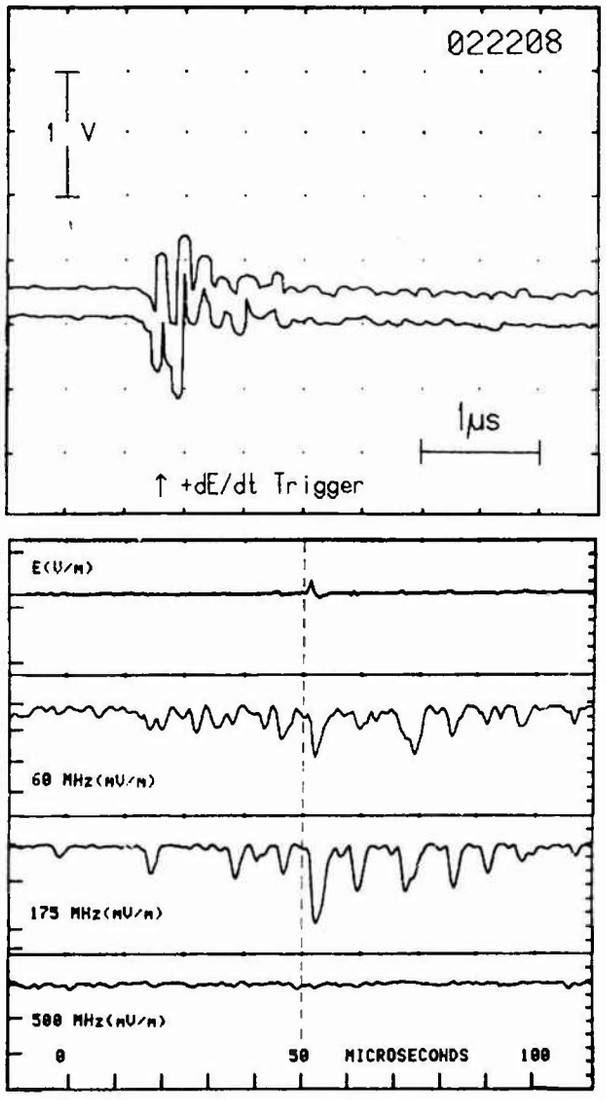


Fig. 13 The conical antenna signal (thick, upper curve) and simultaneous E field and 60, 175 and 500 MHz radiation (lower four traces) produced during lightning discharge activity very similar to that shown in Fig. 11.

the associated E field and RF emissions on a faster time scale. We do not believe this was a return stroke discharge. The E field change is negative and has a shape not at all typical of a close return stroke discharge. The durations of the RF bursts are considerably less than for the first return stroke examples given in Figs. 7 and 8. If this had been a subsequent return stroke we would have expected the peak RF radiation to have preceded the E radiation field peak /21/, which is not the case here. This may have been a "K change" /26,27/. /28/ has indicated that K changes may produce very strong RF radiation.

The 500 MHz recorder was triggered by a large amplitude 60 MHz impulse during this discharge ; those data are shown in Figure 15. A second fast trace, labelled "noise", has been added for comparison, and shows the conical antenna noise level measured during a time when there was no thunderstorm activity.

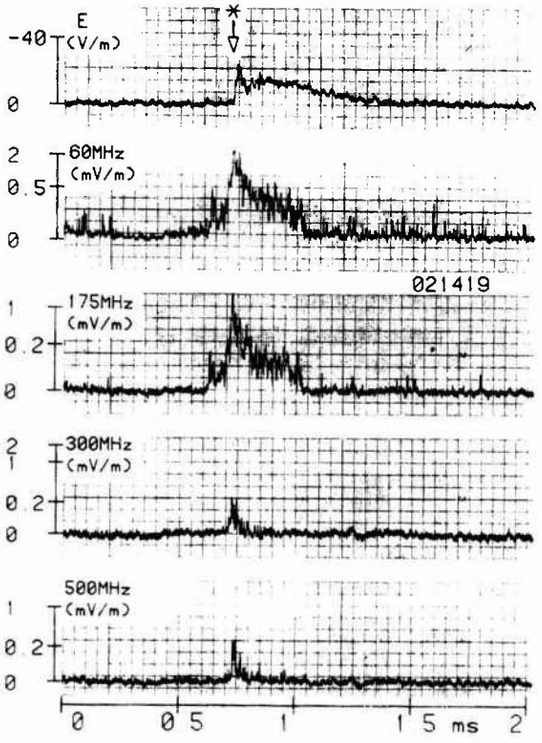


Fig. 14 Faster time resolved recordings of the E fields and simultaneous 60, 175, 300 and 500 MHz radiation at point 2 in Fig. 6, perhaps a "K change". The downwardly pointing arrow indicates the moment at which the 500 MHz recorder was triggered.

4 - DISCUSSION

In general, the lightning RF signals discussed in this report agree with previously published data. We have found no mention of the abrupt way in which the RF emissions start, but see what seem to be similar beginnings on 34 MHz data in /5/, /8/ and /22/. A sequence of negative polarity bipolar E field impulses coincided with the initial RF radiation in event 022415, an intracloud discharge. Bipolar E fields, usually of positive polarity, have also been observed tens of milliseconds before the first return stroke in cloud-to-ground discharges /24, 29/ and sometimes these fields also coincide with the initial RF radiation. These cases and events like 022415 are interesting because the large bipolar field amplitudes imply large channel currents which occur without any evidence at VHF and UHF of earlier, "preparatory", activity. Is this true or were the vertical RF fields which arrived at our site just too weak to be measured ?

Several authors have noted that very little or no RF radiation occurs during a period of a few milliseconds duration immediately following return strokes /6, 22, 30, 31/. These "quiet periods" were not observed following the three first return strokes examples presented here (points 1, 7 and 8 in Fig. 6). It is difficult to explain why this is so ; we do not believe it is an effect introduced by the instrumentation. It is possible that intracloud activity was occurring before and continued to occur during and after the return stroke discharge. In one case (point 8) it seems almost as if RF emissions we restarted after the occurrence of the return stroke.

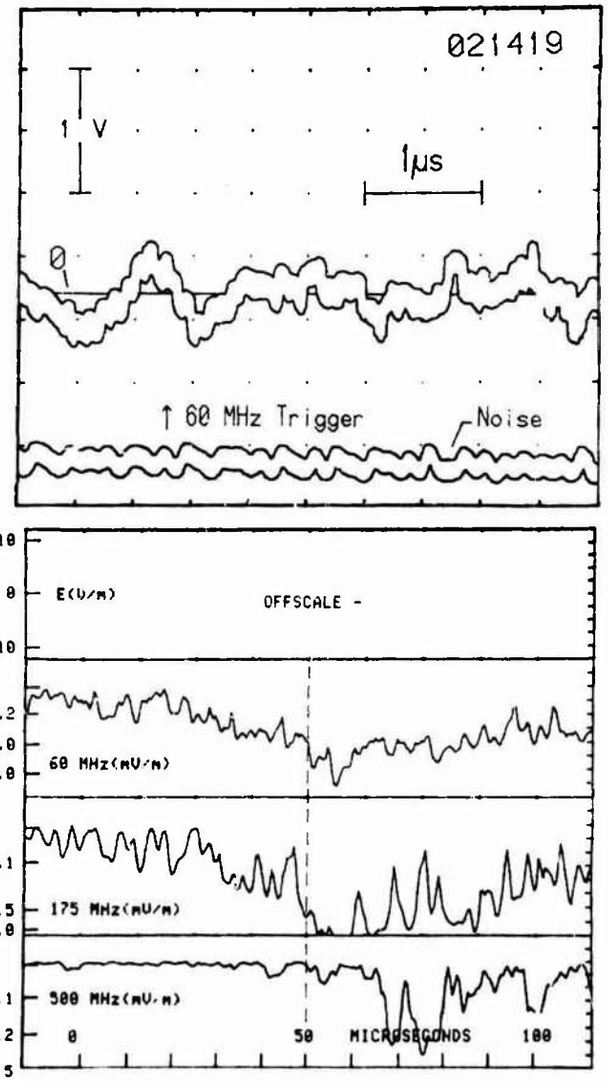


Fig. 15 The conical antenna signal (thick, upper curve) and simultaneous E field and 60, 175 and 500 MHz radiation (four lowermost traces) produced during the intracloud discharge shown in Fig. 14. A recording of the conical antenna noise level is also shown (trace labelled "noise") and is composed, predominantly, of shortwave and FM radio transmissions.

Our results show, in agreement with other authors, that intracloud discharge processes are a source of strong RF emissions. Point 2 in Fig. 6 was examined in Section 3. Points 4 and 6 in event 021729 also produced strong 175 MHz signals and were, to the best of our knowledge, intracloud discharge processes.

Let's consider briefly the conical antenna measurements. Two very different kinds of signals have been obtained depending on the triggering method used. The complex examples in Figs. 9 and 15 were obtained by triggering the 7912 recorder externally on a large amplitude 60 MHz signal (in the manner described in Sect. 2). Examining the 60 MHz fields in Figs. 9 and 15 near the trigger time, we see that it wasn't a single, large 60 MHz pulse which triggered the 7912, but, rather, a high pulse occurrence rate which meant that the receiver effectively integrated or summed a

sequence of several impulses. These separate impulses, may have come from multiple, even widely separated sources. We note, in addition, in Figs. 9 and 15 that the RF signals were not necessarily similar at the different frequencies and that appreciable radiation was present at 500 MHz. Considering the decreasing conical antenna sensitivity with increasing frequency, the delay line attenuation and the high noise levels, it is clear that the E field variations which produced these 500 MHz and perhaps even the 175 MHz emissions may not be visible on the 7912 records in Figs. 9 and 15.

The records in Figs. 12 and 13 were obtained after the 7912 digitizer had been triggered by a dE/dt signal crossing a threshold of about + 400 V/m/μs. Single, 3 μs wide, pulses of 60 and 175 MHz radiation occurred simultaneously. Here, we note that the time sequences of 60 and 175 MHz radiation are often very similar (between 50 and 100 μs in Fig. 13, for example). We would suggest, therefore, that both the 60 and 175 MHz emissions were produced by the same discharge process. Perhaps, because these signals occurred relatively early in their respective discharges and because the RF activity resembles stepped leader activity, this was an intracloud leader process. The 7912 recordings might correspond, then, to one step of that discharge. If this were true, the conical antenna signals would indicate that a leader step was in reality not just a single discharge but perhaps 3, 4 or 5 separate discharges which occur in a period of 1 to 3 μs. Note also in Figs. 12 and 13 that there is very little radiation at 500 MHz. In this respect, the discharge process which produced the signals in Figs. 12 and 13 is different from that (those) responsible for the Figs. 9 and 15 records.

Finally, it was with single impulses of RF radiation like in Figs. 12 and 13 and the associated conical antenna signals that we wished to test the two hypotheses discussed in Sect. 1. An equipment malfunction has prevented us from determining relative amplitude spectra for these two events. We cannot, therefore, say whether they resemble Fig. 1 and thus whether such a test is appropriate.

5 - REFERENCES

/1/ Uman, M.A., and E.P. Krider, "A Review of Natural Lightning: Experimental Data and Modeling," IEEE Trans. Electromag. Com., EMC-24, 79-112, 1982.

/2/ Djebari, B., J. Hamelin, C. Leteinturier and L. Nicot, "Electromagnetic Pulses Emitted by Lightning," presented at the Intl. Aerospace Conf. on Lightning and Static Electricity, Oxford, England, March, 1982.

/3/ Proctor, D.E., "A Hyperbolic System for Obtaining VHF Radio Pictures of Lightning," J. Geophys. Res., 76, 1478-1489,1971.

/4/ Taylor, W.L., "A VHF Technique for Space-Time Mapping of Lightning Discharge Processes," J. Geophys. Res., 83, 3575-3583, 1978.

/5/ Warwick, J.W., C.O. Hayenga and J.W. Brosnahan, "Interferometric Directions of Lightning Sources at 34 MHz," J. Geophys. Res., 84, 2457-2468, 1979.

/6/ Rustan, P.L., M.A. Uman, D.G. Childers and W.H. Beasley, "Lightning Source Locations from VHF Radiation Data for a Flash at Kennedy Space Center," J. Geophys. Res., 85, 4893-4903, 1980.

/7/ Proctor, D.E., "VHF Radio Pictures of Cloud Flashes," J. Geophys. Res., 86, 4041-4071, 1981.

/8/ Hayenga, C.O. and J.W. Warwick, "Two-Dimensional Interferometric Positions of VHF Lightning Sources," J. Geophys. Res., 86, 7451-7462, 1981.

/9/ Richard P., A. Delannoy, G. Labaune and P. Laroche, "UHF Interferometric Imaging of Lightning," in Addendum 8th Intl. Aerospace and Ground Conf. on Lightning and Static Electricity, DOT/FAA/CT-83/25(A), Fort Worth, Texas (USA),June,1978.

/10/ Proctor, D.E., "Lightning and Precipitation in a Small Multicellular Thunderstorm," J. Geophys. Res., 88, 5421-5440,1983.

/11/ Taylor, W.L., E.A. Brandes, W.D. Rust and D.R. MacGorman, "Lightning Activity and Severe Storm Structure," Geophys. Res. Lett., 11, 545-548, 1984.

/12/ Le Boulch, M., "Caracterisation et Mecanismes du Rayonnement VHF-UHF des Décharges Orageuses," Thesis, Université de Clermont II, Clermont-Ferrand, France, 1984. (in French)

/13/ Hamelin, J., J. Karczewsky and F. Sene, "Sonde de Mesure du Champ Magnétique dO à une Décharge Orageuse," Annales des Télécomm., 33, 198-205, 1978. (in French)

/14/ Krider, E.P., C.D. Weidman and R.C. Noggle, "The Electric Fields Produced by Lightning Stepped Leaders," J. Geophys. Res., 82, 951-960, 1977.

/15/ Weidman, C.D. and E.P. Krider, "Time and Height Resolved Photoelectric Measurements of Lightning Return Strokes," Trans. Am. Geophys. Union, 61, 978, 1980. (abstract only)

/16/ Besnault, B., G. Fine,P. Lartique and D. Vuillet-Laurent, "Etude d'Antennes VHF-UHF Large Bande Destinées à l'Observation des Décharges Orageuses," Contract Report, CNET 83-88-051-00-790-92-45 LAB/MER/GER, Ecole Supérieure d'Electricité, Gif sur Yvette, France, 1983. (in French)

/17/ Harrison, C.W. and C.S. Williams, Jr., "Transients in Wide-Angle Conical Antennas," IEEE Trans. Ant. Prop., AP-13, 236-246, 1965.

/18/ Williams, H.P., Antenna Theory and Design, Vol. 2, Sir Isaac Pitman and Sons Ltd., London, 1966.

/19/ Lin, Y.T., M.A. Uman, J.A. Tiller, R.D. Brantley, W.H. Beasley, E.P. Krider and C.D. Weidman, "Characterization of Lightning Electric and Magnetic Fields From Simultaneous Two-Station Measurements," J. Geophys. Res., 84, 6307-6314, 1979.

/20/ Brook, M. and N. Kitagawa, "Radiation from Lightning Discharges in the Frequency Range 400 to 1000 Mc/s," J. Geophys. Res., 69, 2431-2434, 1964.

/21/ LeVine, D. and E.P. Krider, "The Temporal Structure of HF and VHF Radiation During Florida Lightning Return Strokes," Geophys. Res. Lett., 4, 13-16, 1977.

/22/ Hayenga, C.O., "Characteristics of Lightning VHF Radiation near the time of Return Strokes," J. Geophys. Res., 89, 1403-1410, 1984.

/23/ Leteinturier, C. and J. Hamelin, "Analyse Expérimentale des Caractéristiques Electromagnétiques des Décharges Orageuses dans la Bande 200 Hz - 20 MHz," Annales des Télécomm.,39, 175-184, 1984. (in French)

/24/ Weidman, C.D. and E.P. Krider, "The Radiation Field Wave Forms Produced by Intracloud Lightning Discharge Processes," J. Geophys. Res., 84, 3159-3164, 1979.

/25/ Krider, E.P., C.D. Weidman and D.M. LeVine, "The Temporal Structure of the HF and VHF Radiation Produced by Intracloud Lightning Discharges," J. Geophys. Res., 84, 5760-5762, 1979.

/26/ Uman, M.A., Lightning, McGraw-Hill, New York, 1969.

/27/ Brook, M. and T. Ogawa, "The Cloud Discharge," in Lightning, Vol. 1, chap. 6, ed. by R.H. Golde, Academic Press, New York, 1977.

/28/ LeVine, D.M., "Sources of the Strongest RF Radiation From Lightning," J. Geophys. Res., 85, 4091-4095, 1980.

/29/ Beasley, W., M.A. Uman and P.L. Rustan, Jr., "Electric Fields Preceding Cloud-to-Ground Lightning Flashes," J. Geophys. Res., 87, 4883-4902,1982.

/30/ Malan, D.J., "Radiation from Lightning Discharges and its Relation to the Discharge Process," in Recent Advances in Atmospheric Electricity, Pergamon, London, 1958.

/31/ Clegg, R.J. and E.M. Thomson, "Some Properties of em Radiation from Lightning," J. Geophys. Res., 84, 719-724, 1979.

/32/ Oetzel G.N. and E.T. Pierce, "Radio Emissions From Close Lightning," in Planetary Electrodynamics, Vol. 1, Gordon and Breach, New York, 1969.

Copies of references /2/, /9/, /12/ or /16/ may be obtained directly from the authors at the mailing address shown.

SUBMICROSECOND STRUCTURE OF THE RADIATION FIELDS PRODUCED BY LIGHTNING

C. Leteinturier[**], E.P. Krider [+] and J.C. Willett[**]

[+] *Institute of Atmospheric Physics, University of Arizona, Tucson, Arizona 85721, U.S.A.*
**CNET MER/GER, 22301 Lannion, France*
***Naval Research Laboratory, Washington, D.C. 20375, U.S.A.*

Abatract - An experiment to measure the electric field, E, dE/dt, and HF signatures that are produced by lightning return strokes, leader steps, and intracloud discharge processes was conducted at the NASA Kennedy Space Center, Florida, under conditions where the lightning locations were known and where there was minimal distortion in the signals due to ground-wave propagation or the recording equipment. Values of the maximum dE/dt during the initial, fast-rising portion of first return strokes have a mean and standard deviation of 45.4 ± 13.4 V/m/μsec when range-normalized to 100 km and a full width at half maximum of 97 ± 18 nsec. If the initial return atroke velocity is 10^8 m/sec, these dE/dt results imply that the mean maximum dI/dt at the lightning source is about 230 kA/μsec, a value that is substantially larger than most tower measurements a... current test standards. The Fourier amplitude spectrum of the fast field transition in first strokes is in good agreement with previous eatimates in the interval from 1-4 MHz, but then decreases more rapidly with frequency above 4 MHz.

I - INTRODUCTION

Recent measurements have shown that the electric and magnetic fields that are radiated by leader atepa and return strokes in cloud-to-ground lightning and by various intracloud discharge processes all contain large submicrosecond variations when there is minimal distortion in these fields due to ground wave propagation or the recording equipment [1-10]. Because submicrosecond fields have important implications for the design of lightning protection systems, a new experiment was conducted during the aummer of 1984 to determine better the submicrosecond structure of E and dE/dt fields with particular emphasis on those lightning discharge processes that might represent the greatest hazard to aircraft and the strongest source of interference in HF communications systems. In this paper, we will describe the design of the experiment, and we will give some initial results for one Florida thunderstorm.

II - EXPERIMENT

Lightning electric field, E, and dE/dt waveforms were recorded, together with the output of a wideband HF receiver, at an experiment site that was located on the eastern tip of Cape Canaveral, Florida. A block diagram of the antennas and recording equipment is shown in Fig. 1, and a map showing the location of the site is given in Fig. 2. The antennas were mounted on the roof of a grounded metal truck and trailer [maximum dimensions 14.3m L x 4.4m W x 3.6m H] that were part of a U.S. Air Force lightning experiment [11]. The antennas and signal processing electronics were designed to provide a time-resolution of about 10 nsec on a dE/dt signal and 125 nsec on E. The HF receiver could be tuned to any frequency between 3 and 18 MHz, and the bsndwidth was 1 MHz. Great care was taken to maintain a precise time-synchronization of all records.

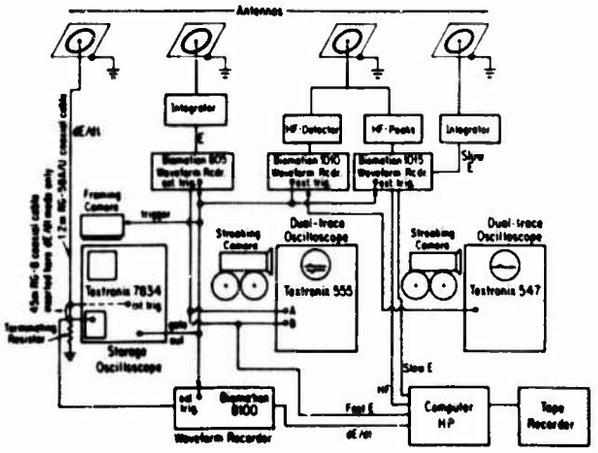


Fig. 1. A block achematic diagram of the antennas and waveform recording systems.

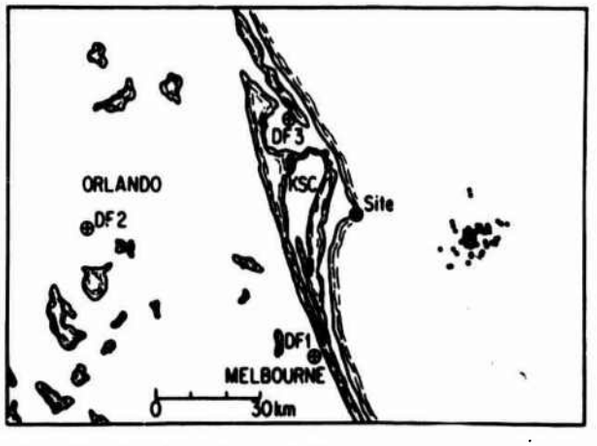


Fig. 2. The locations of the experiment site at Cape Canaveral, Florida; the lightning direction-finder sites (DF); and cloud-to-ground dischargea on Sept. 5, 1984.

The dE/dt signals were recorded on a Tektronix 7834 storsge oscilloscope snd a Biomation 8100 waveform recorder. E and HF signsls were digitized on Biomation 805 snd 1010 waveform recorders, snd the anslog outputs were photographed on oscilloscopes using both fsst and slow time scsles.

The recording system could be triggered either on the dE/dt signsl (ss shown in Fig. 1), E, or the output of the HF receiver. The type of lightning process thst produced s particulsr field impulse (e.g. leader step, return stroke, or cloud dischsrge) was determined from the oversll shape of the E signsture, snd the HF triggers were used to investigste which lightning process produced the strongest source of interference at HF frequencies.

The experiment trsiler wss locsted as close ss possible to the Atlantic Ocean so that the field from sny lightning discharge that occurred over the ocean could be messured with minimum distortion due to ground-wave propagation. The locstions of the strike points of cloud-to-ground discharges were provided in resl-time by a network of widebsnd magnetic direction finders* that was operated by the U. S. Air Force and the NASA Kennedy Space Center. The locations of the direction-finder (DF) sites are shown in Fig. 2. The principles of operation of the DFs and the lightning locating system have been described by [12-14], and the location accuracy has been verified using rocket-triggered lightning st KSC [15].

III - DATA

During the summer of 1984, records were obtained from sbout 4 thunderstorms that occurred over the ocean within 100 km of the experiment site. One of these, a large storm on September 5, contained a cell that was centered about 35 km to the east, a region of optimum accuracy for the lightning locating system. During the interval from 20:46 to 21:18 UT, about 112 correlated records were obtained using an HF trigger at 5 MHz, and 64 of these were from first return strokes. The locations of these discharges are shown in Figure 2.

Figure 3 shows an example of the dE/dt, E, and HF waveforms that were produced by the first return stroke in a cloud-to-ground discharge at a range of 36.2 km. Note that the dE/dt signal has a maximum of about 125 V/m/μsec and that the full-width at half-maximum (FWHM) of this signal is about 90 nsec. The E signal has a peak of about 22 V/m, and the arrow below the peak ahows the time of the dE/dt trigger. The HF record has a large peak at the same time as the dF/dt record, and there is a second peak in the HF signal about 35 μsec after the first peak.

IV - RESULTS

Return Strokes

In general, the shape of the electric field that is radiated by a return stroke depends on whether it is the first return stroke in a flash, a subsequent return stroke, or a subsequent return stroke that is preceded by a dart-atepped leader [1]. First stroke fields begin with a relatively slow "front" that rises for 2 to 8 μsec to about half the peak field

* Manufactured by Lightning Location and Protection, Inc., Tucson, Arizona 85719.

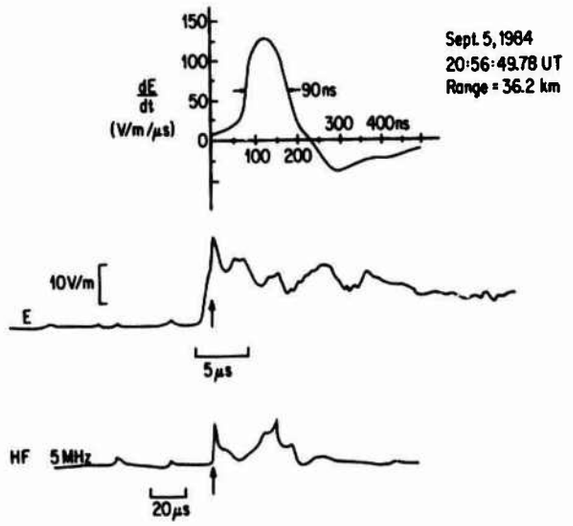


Fig. 3. Examples of the dE/dt signature (top), E waveform (middle), and HF emission produced by a first return stroke at 36.2 km.

amplitude. This front is followed by s fast trsnsition to peak, and it is this fast transition that is of primary interest in this report. Subsequent strokes produce fields that have fast tranaitions very similar to first strokes, but fronts that last only 0.5 to 1 μsec and that rise to only sbout 20% of the peak field amplitude.

The values of the maximum dE/dt during the fast field transition, the FWHM of dE/dt, and the electric field peak, E_p, are summarized in Table 1 for first return strokes, normal subsequent return strokes, snd subsequent strokes that were preceded by s dart-stepped leader. In each entry, N is the total number of records that were analyzed, and σ is the standard deviation. All values of dE/dt and E have been normalized to a range of 100 km, assuming that the measured amplitudes have an inverse distance dependence on range, and a histogram of the first-stroke values is shown in Figure 4. It should be noted in Table 1

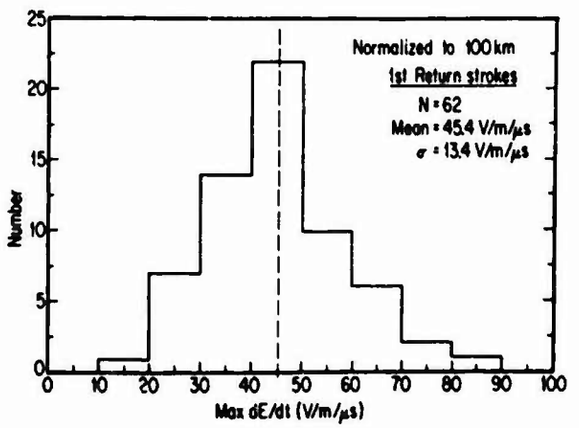


Fig. 4. Histogram of the peak dE/dt values produced by 62 first return strokes after they are range-normalized to a diatance of 100 km.

that the largest values of dE/dt are produced by subsequent return strokes that are preceded by dart-stepped leaders.

TABLE 1

Summary of the Maximum dE/dt, FWHM, and Peak E Values for Return Strokes with Range-Normalization of 100 km

Type of Stroke	Max dE/dt (V/m/μsec)	FWHM (nsec)	Peak E* (V/m)
First	N = 62	N = 64	N = 48
Return	$\overline{dE/dt}$ = 45.4	$\overline{FWHM}$ = 97.2	$\overline{E_p}$ = 11.1
Strokes	σ = 13.4	σ = 18.4	σ = 3.7
Normal	N = 6	N = 7	N = 5
Subsequent	$\overline{dE/dt}$ = 40.6	$\overline{FWHM}$ = 81.4	$\overline{E_p}$ = 4.5
Strokes	σ = 18.0	σ = 10.7	σ = 1.9
Dart-Stepped	N = 7	N = 7	N = 6
Subsequent	$\overline{dE/dt}$ = 51.7	$\overline{FWHM}$ = 98.6	$\overline{E_p}$ = 8.7
Strokes	σ = 11.5	σ = 16.8	σ = 2.2

* Some E fields exceeded the dynamic range of the recording system; therefore, the values of $\overline{E_p}$ should be regarded as lower limits.

TABLE 2

Summary of the Maximum dE/dt Values of Leader Steps and Cloud Pulses with a Range-Normalization of 100 km

	Max dE/dt (V/m/μsec)	FWHM (nsec)
Leader Steps	N = 17	N = 8
	$\overline{dE/dt}$ = 15.2	$\overline{FWHM}$ = 68.8
	σ = 6.0	σ = 6.4
Cloud Pulses	N = 22	
	$\overline{dE/dt}$ = 9.2	
	σ = 5.4	

Leader Steps

The overall shapes of the fields that are radiated by individual steps of the stepped-leader have been discussed in [3] and [4]. As the leader nears the ground, the amplitude of an individual step impulse increases, and occasionally such a step triggered the recording system just before there was a return stroke. The maximum dE/dt occurs during the initial rise of the step waveform, and values of this quantity, range-normalized to 100 km, and the FWHM are summarized in Table 2. Although the values of the maximum dE/dt and FWHM for leader steps are smaller than those for return strokes, the shapes of the dE/dt signatures are very similar.

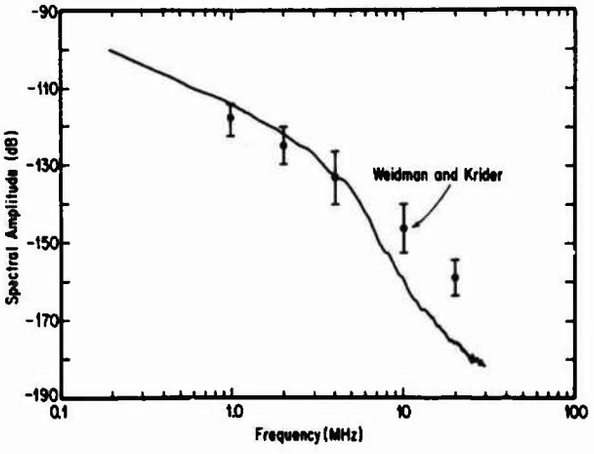


Fig. 5. The mean amplitude spectrum of 59 first return strokes during the initial, fast-field transition. The standard deviations are about 3 db at 1 MHz and increase uniformly to about 6 dB at 10 MHz. The data of Weidman and Krider [23] are shown for comparison.

Cloud Pulses

The overall shapes of the radiation fields that are produced by intracloud discharge processes have been discussed by [7] and [8]. In general, the shapes of the larger pulses tend to be bipolar with several fast, unipolar impulses superimposed on the initial half-cycle. The unipolar structures have fast rise-times, and the shapes of the dE/dt signatures during these transitions are very similar to the shapes of the signatures produced by return strokes and leader steps. Values of the maximum dE/dt, range-normalized to 100 km, of 22 cloud pulses that preceded the first return stroke in a ground discharge are also summarized in Table 2.

Amplitude Spectrum of First Return Strokes

The interactions of lightning fields with aircraft, space vehicles, and many other systems depend on the amplitudes of these fields at frequencies that correspond to the structure resonances [16-19]. Since the physical dimensions of many objects of interest are in the range from 10 to 100 m, frequencies in the range from about 1.5 to 15 MHz (i.e., frequencies for which half the associated wavelength equals the structure dimension) are of primary importance. In order to determine the amplitude spectrum in this frequency interval, we have Fourier analyzed the time-domain dE/dt waveforms that were recorded on the Biomation 8100. First, each waveform was range-normalized to a distance of 50 km, assuming an inverse distance dependence on range, and then a 5.12 μsec interval (512 points at 10 nsec per point) that was centered on the peak of the dE/dt signal was selected for analysis. The waveform was multiplied by a Hanning (cosine) windowing function to eliminate

truncation errors and then analyzed using a fast Fourier transform (FFT). We assume that the spectral amplitude of E at a particular frequency, $\mathcal{E}(f)$, is related to the amplitude of the transform of dE/dt through the relation

$$|\mathcal{E}(f)| = |\frac{d\mathcal{E}}{dt}|/2\pi f \ .$$

Figure 5 shows the average amplitude spectrum of the initial, fast transition in 59 first return strokes. Here the amplitudes are shown in dB from a reference level of 1 V/m/Hz, i.e., 20 times the logarithm (base 10) of $\mathcal{E}(f)$. By plotting the data in this way, we obtain a graphic representation of the spectral energy density vs. frequency that can be compared directly with previous work [20-23]. Note in Fig. 5 how the average spectrum is in good agreement with Weidman and Krider [23] below about 4 MHz, but that at higher frequencies the decrease with frequency is substantially more rapid.

V - DISCUSSION

The mean maximum dE/dt that we have given for first return strokes is 45.4 V/m/μsec at 100 km. This value is about 33% larger than the 33 V/m/μsec previously reported by Weidman and Krider [9,10] and clearly confirms the presence of large, submicrosecond variations in the fields produced by return strokes. Our value is larger than [9,10] possibly because the results of [9,10] were derived almost entirely from E measurements, rather than dE/dt, and the measurements of the initial slopes of E may have underestimated the true peak values. Another reason might be that our data were obtained using a trigger signal that was derived from an HF receiver, and this may have biased our data toward higher values of dE/dt. In any case, it seems clear that a large fraction of all types of return strokes, leader steps, and cloud pulses produce large dE/dt signals with a FWHM on the order of 90 nsec. We will now examine the implications of these results for the current at the lightning source.

The implications that lightning fields have for lightning currents have been discussed previously by [24] and others. If we assume that the initial, fast-field components that are produced by leader steps, return strokes, and cloud pulses can all be described by a transmission-line model, then the maximum rate of change of the channel current is related to the maximum field derivative through the relation:

$$\frac{dI(t)}{dt} = \frac{2\pi D\varepsilon_0 c^2}{v} \frac{dE(t + D/c)}{dt},$$

where D is the distance to the discharge, v is the velocity of the current pulse, and where the channel has been assumed to be perpendicular to a flat, perfectly conducting ground [24]. This relation also assumes that the measured field is produced by a single current pulse that propagates without distortion up a single channel at a constant velocity.

If we assume that v for first return strokes near the ground is about 10^8 m/sec [25], then a mean dE/dt of 45.4 ± 13.4 V/m/μsec at 100 km (Figure 4) implies that the associated mean maximum dI/dt is 227 ± 67 kA/μsec, a value that is considerably larger than most measurements during strikes to instrumented towers [26-28]. The reason for this might be due to limitations in the tower data recording systems or reading these data, or perhaps because the towers, which are located on mountains of rock, or the upward connective leaders which originate from the towers, limit the maximum rate of rise of current that can be measured with this technique. Another reason, again, might be that our dE/dt recording system may not have recorded all of the smaller return strokes. Finally, if the fast-field transitions are produced by more than one current pulse radiating at the same time, then our inferred values of dI/dt will overestimate the true value for one pulse. Since a mean dI/dt of about 230 kA/μsec is larger than the dI/dt used in most lightning test standards, we think that these problems warrant further study.

ACKNOWLEDGMENTS - We are grateful to Maj. P. Rustan of the U. S. Air Force for the use of his research vehicle, to W. Jafferis of the NASA Kennedy Space Center for his enthusiasm and support, and to W. Hiscox of Lightning Location and Protection, Inc., for computations of the lightning locations. Margaret Sanderson Rae provided editorial assistance in preparing the final manuscript.

REFERENCES

1. C.D. Weidman and E.P. Krider, J. Geophys. Res., 83 (1978) 6239-6247.
2. C.D. Weidman and E.P. Krider, Geophys. Res. Lett. 7 (1980) 955-958.
3. E.P. Krider and G.J. Radda, J. Geophys. Res., 80 (1975) 2653-2657.
4. E.P. Krider, G.J. Radda and R.C. Noggle, J. Geophys. Res., 82 (1977) 951-960.
5. C.E. Baum, E.L. Breen, D.L. Hall, C.B. Moore, and J.P. O'Neill, in Proc. Lightning Technology, NASA Conf. Pub. 2128 and FAA-RD-80-30 (1980) 39-82.
6. C.E. Baum, E.L. Breen, F.L. Pitts, G.D. Sower, and M.E. Thomas, IEEE Trans. on EMC, EMC-24 (1982) 123-137.
7. C.D. Weidman and E.P. Krider, J. Geophys. Res., 84 (1979) 3159-3164.
8. W. Beasley, M.A. Uman, and P.L. Ruatan, Jr., J. Geophys. Res., 87 (1982) 4883-4902.
9. E.P. Krider and C.D. Weidman, in Proceedings 8th International Aerospace & Ground Conference on Lightning & Static Electricity, Ft. Worth, TX, June 21-23 (1983) DOT/FAA/CT-83/25, 69.1-69.8.
10. C.D. Weidman and E.P. Krider, in Preprints VIIth International Conference on Atmospheric Electricity, Am. Meteorol. Soc., June 3-8, 1984.
11. P. Rustan, B.P. Kuhlman, and J.M. Reazer, Proceedings 10th International Aerospace and Ground Conference on Lightning and Static Electricity, Paris, June 10-13, 1985.
12. E.P. Krider, R.C. Noggle, and M.A. Uman, J. Appl. Meteorol., 15 (1976) 301-306.
13. E.P. Krider, R.C. Noggle, A.E. Pifer, and D.L. Vance, Bull. Amer. Meteorol. Soc., 61 (1980) 980-986.
14. R.C. Binford, L.G. Byerley, E.P. Krider, M. W. Maier, A.E. Pifer, and M.A. Uman, Proceedings 8th International Aerospace and Ground Conference on Lightning and Static Electricity, Fort Worth, TX, June 21-23, 1983.
15. M.W. Maier and W. Jafferis, 10th International Aerospace and Ground Conference on Lightning and Static Electricity, Paris, June 10-13, 1985.
16. D.W. Clifford, E.P. Krider, and M.A. Uman, Proceedings International Symposium on EMC, San Diego, CA, Oct. 9-11, 1979.
17. F.M. Tesche, IEEE Trans. on EMC, EMC-20 (1978) 60-64.
18. C.D. Taylor, IEEE Trans. on EMC, EMC-20 (1978) 64-76.

19. C.M. Butler, Y. Rahmat-Samii, and R. Mittra, IEEE Trans. on EMC, EMC-20 (1978) 82-93.
20. G.I. Serhan, M.A. Uman, D.G. Childers, and Y.T. Lin, Radio Sci., 15 (1980) 1089-1094.
21. C.D. Weidman, E.P. Krider, and M.A. Uman, Geophys. Res. Lett., 8 (1981) 931-934.
22. J. Preta, M.A. Uman, and D.G. Childers, Radio Sci., 20 (1985) 143-145.
23. E.P. Krider and C.D. Weidman, 9th International Aerospace and Ground Conference on Lightning and Static Electricity, Orlando, FL, June 26-28, 1984
24. M.A. Uman and E.P. Krider, IEEE Trans. on EMC, EMC-24 (1982) 79-112.
25. V.P. Idone and R.E. Orville, J. Geophys. Res., 87 (1982) 4903-4915.
26. K. Berger, R.B. Anderson, and H. Kroninger, Electra, 80 (1975) 23-37.
27. R.B. Anderson and A.J. Eriksson, Electra, 69 (1980) 65-105.
28. E. Garbagnati, F. Marinono, and G.B. LoPipero, Proceedings 16th Conf. on Lightning Protection, Szeged, Hungary, July 1981.

HIGH VOLTAGE LABORATORY TESTS AND LIGHTNING PHENOMENA

B. Hutzler, G. Riquel and J.-P. Riu

Laboratoires d'Essais à Haute Tension, Electricité de France, Les Renardières, B.P. N°1, 77250 Moret-sur-Loing, France

Abstract - It is recognized that the physical processes of the lightning stroke and of the laboratory long spark present similarities, but a complete simulation is not conceivable. However the laboratory spark can be used to simulate some features of lightning and to study their consequences on aircrafts and structures. On the basis of the physics of the phenomena, the possibilities and limitations of the simulation are discussed.

1 - INTRODUCTION

Is it possible to learn something about lightning and its effects, through laboratory tests ? It is a platitude to say that the study of lightning is difficult because it occurs at time and location which are not controlled. On the contrary, in a high voltage laboratory, the long spark can be studied in details because its occurence is controlled, because it can be repeated and because sophisticated measuring techniques can be used. As a consequence, the level of knowledge is different and direct comparison may not be convincing. Furthermore, the scale is obviously different and, as most of the processes are not linear, it is rather difficult to identify identical phenomena in both discharges.

However, even if a complete simulation of lightning is not conceivable, it is recognized for years /1/ that the physical mechanisms of the lightning stroke and of the laboratory long spark present similarities. Some features can be reproduced and used to evaluate some consequences of natural lightning, namely on aircrafts or grounded structures.

After a brief review of the laboratory test facilities and measuring techniques, the main features of the long spark will be presented together with the influence of experimental conditions. Then, the final stage of the discharge will be described in connection with the striking of earthed structures. Finally, some characteristics of the discharge, when it interacts with a free potential electrode inside the gap, will be given.

2 - THE HIGH VOLTAGE LABORATORIES FACILITIES

This is not the aim of this paper of describing high voltage laboratory facilities. However, it is necessary to introduce the tools available for the long spark study.

The voltage supply is usually a multistage Marx generator which delivers biexponential voltage impulses. The impulse shape is characterized by two parameters : T_{cr} and T_2. T_{cr} is the duration of the impulse front, T_2 is the time at which the voltage reaches half of the impulse amplitude (on the impulse tail).

The shape of these impulses can be varied in a large range by changing the front and tail resistors of the generator or by adding a front capacitor. Their amplitude are directly proportional to the charging voltage which can reach 6 MV. The energy stored in the capacitors can reach 300 to 500 kJ.

The shape and amplitude of the generated impulses are measured thanks to voltage dividers and the associated recording devices. An example of experimental arrangement is given by Figure 1.

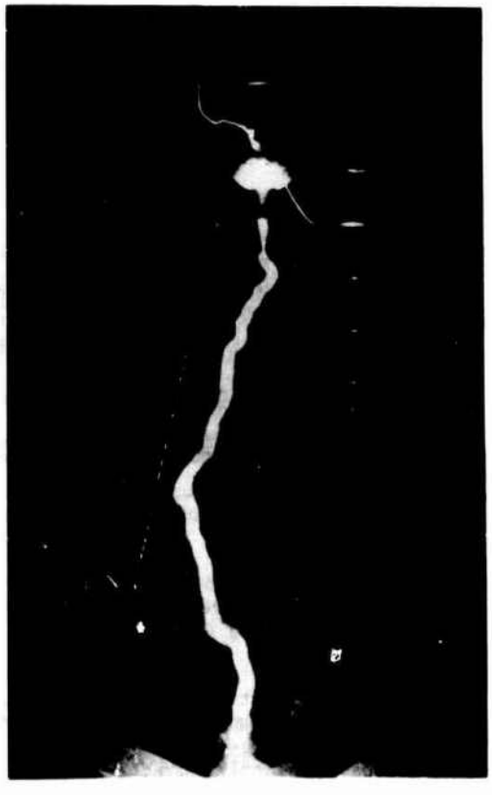


Figure 1 : U.H.V. Laboratory at Les Renardières (France) View of the experimental test circuit used for the physical study of a 17 m rod plane gap.

Provided that the laboratory can be darkened, optical measuring devices such as cameras, photomultipliers, image converters, strioscopic and spectroscopic apparatuses can be used. This allows, for instance, to build a four dimensional picture of the discharge (x, y,z,t), to measure the thermal diameter of the channel and to analyse the spectrum of the radiated light.

Furthermore, the experimental study of the spark can be completed by the use of field probes and current or charge measurements. By using optical fiber transmissions, these measurements can be performed at the energized electrode but also at a free potential electrode. They can be used to evaluate the position and the quantity of space charge present in the gap.

These techniques have been widely used by the "Les Renardières Group" /2-5/ and will not be anymore detailed here.

3 - PHYSICAL FEATURES OF THE LABORATORY SPARK

3.1 The Positive Spark

Conventionally, the positive spark is a discharge which develops in the field direction. This is the discharge which develops from the rod toward the plane when a positive impulse is applied to the rod of a rod plane gap. Its structure is illustrated by Figure 2. A narrow channel, called leader, elongates from the rod thanks to a corona, composed of streamers and located at its tip. The leader channel is a medium where thermalization is in progress. It radiates in the red /3/. On the contrary, the streamer zone where energetic electrons are moving in a cold gas, is characterized by a U.V. spectrum. The discharge characteristics (leader velocity, current, streamer length) depend on the gap length and on the shape and amplitude of the voltage impulse.

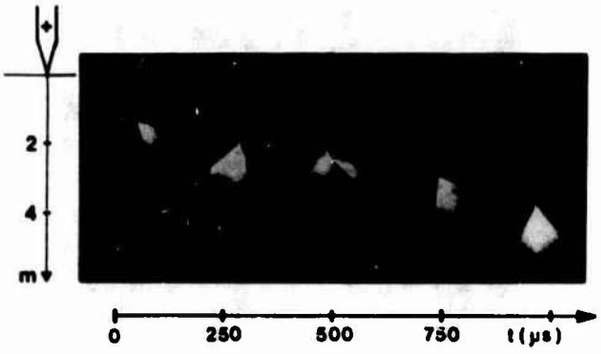


Figure 2 : Five different stages of the positive discharge recorded by an image converter camera operating in the frame mode.

For a given gap length, it exists a value of T_{cr}, said as critical, for which the breakdown voltage is minimum. This critical time-to-crest is generally taken as reference and can be roughly characterized by /6/ :

$$T_{cr.crit} = 40\ (d + 1) \quad \mu s,\ m \qquad (1)$$

For gap length of several meters, this critical time-to-crest is of the order of several hundreds of μs, corresponding to rather long front impulses, usually called switching impulses in network terminology.

In these conditions, the leader elongates continuously and the breakdown voltage of the rod-plane configuration is given by /7/ :

$$U = \frac{3\ 400}{1 + 8/d} \quad kV,\ m \qquad (2)$$

This means that in order to create a 15 m spark, a voltage impulse of at least 2.5 MV is needed. Taking into account the generator possibilities, much longer sparks can be easily obtained. However, due to limited clearances to the walls in the existing indoor laboratories, this is the order of magnitude of the longest positive spark which can be created.

As far as the physical characteristics are concerned, the following orders of magnitude can be given /3,4/ according to the experimental conditions :

- leader diameter :	1 to 10 mm
- electric field along the leader :	500 to 1000 V/cm
- streamer zone length :	0.5 to 3 m
- current :	0.5 to 1 A
- leader velocity :	1.2 to 2 cm/μs
- mean electric field along the streamer path :	4 to 5 kV/cm

If the rate of rise of the applied voltage is decreased ($T_{cr} > T_{cr.crit}$), the leader propagation becomes discontinuous. As far as the authors know, the lightning discharge never exhibits such a behaviour. Consequently, this propagation mode will not be detailed.

On the contrary, if the rate of rise of the applied voltage is higher than critical, the leader elongation remains continuous with a higher velocity and a higher current. As velocity and current are linked with a relationship like :

$$v = K \cdot I^n \qquad \text{with } n < 1$$

at a given increase of current corresponds a much smaller relative increase of the velocity. The streamer length is also significantly increased so that it is quite easy to make them bridge the whole gap. At this stage, the cathode starts to play a role in the processes and the leader propagation is no more "free". This means that, in laboratory conditions, it is not possible to increase the leader velocity beyond values of about 2 cm/μs without the cathode intervening in the mechanism.

3.2 The Negative Spark : A Stepped Discharge

Using the same convention as for the positive spark, the negative spark is observed in a negative rod plane gap. It propagates against the electric field. Depending on the gap length, the breakdown voltage under negative polarity is 2 to 3 times higher than that in positive polarity /5/. Consequently, for a given laboratory size, the longest possible negative spark will be shorter than the longest positive one. Furthermore, some precautions have to be taken. As a matter of fact, in such a case the earthed structures act as anode and can be the origin of positive sparks. As a result, for a negative rod-earthed rod gap, in most cases, the spark will be a positive one elongating from the earthed rod toward the negative rod, rather than a negative spark elongating in the other direction.

Nevertheless, as the positive spark, the negative spark is characterized by a critical value of T_{cr} for which the breakdown voltage is minimum. This value is smaller than that of the positive spark for a given distance. For T_{cr} values higher than the critical va-

lue, the leader elongation proceeds clearly by steps (Figure 3). Between successive steps, no luminous event can be detected in the gap. The time between successive steps is of some tens of microseconds. Each step elongates the leader of some tens of centimeters so that the negative leader elongates at an average velocity of about 1 cm/µs. The current impulse associated to each step reaches some tens of ampères. The rise time of these current pulses is very short, some tens of nanoseconds, so that the dI/dt value reaches probably 1 kA/µs or more. The limitation of the bandwidth of the measuring devices generally used does not allow to give a more precise value. These fast developing ionization phenomena are presumably the source of an intense electromagnetic radiation. However, as far as the authors know, no specific work was done in order to correlate these processes to the RF signals generated by the spark.



Figure 3 : Negative discharge corresponding to $T_{cr} > T_{cr.crit}$ recorded by an image converter camera operating in the streak mode. D = 4 m.

If the time-to-crest of the applied impulse is equal to or lower than the critical value, the structure of the discharge is much more complicated (Fig. 4). Basically, the discharge keeps its stepped nature. However, a complex sequence of negative streamers, spatial stem, spatial leader and positive streamers exists between successive steps /5/. When a spatial leader meets the negative leader, the whole channel reilluminates violently and the leader is lengthened by the spatial leader length. These reilluminations have characteristics similar to those existing for long T_{cr}. However, between steps, the current is formed of sharp pulses with an average value of about 1 A, the negative leader continues to elongate so that the overall velocity of propagation is higher than for long T_{cr}. As the large current pulses associated to the steps, these smaller pulses participate probably in the emission of RF signals.

From a physical point of view, it can be concluded that positive and negative leader channels have identical properties. The difference between the positive and the negative discharge is in the structure of the leader corona. As a consequence, the electric field in the corona region is also different. For the negative streamers, values of 11 to 16 kV/cm have been proposed /5/.

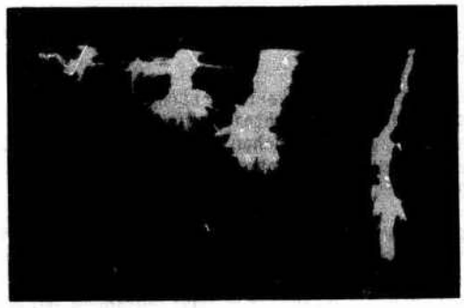


Figure 4 : I.C. streak cameragram of a negative discharge corresponding to $T_{cr} < T_{cr.crit}$. D = 7 m.

3.3 Similarities with the lightning stroke

The lightning stroke exhibits different features depending upon the cloud charge and on the shape of the earthed structures. A classification has been proposed by K. BERGER /8/. Basically, two different types of discharge are clearly identified.

. The more common is the well known stepped leader /8, 9/, which propagates downward from negatively charged clouds, by steps of some tens of meters each 50 µs. The average velocity reaches 15 to 20 cm/µs. It is clear that these orders of magnitude are different from those measured in a laboratory. In fact, these difference may be due to the fact that in laboratory, there is not enough space to allow the development of a strong corona. Furthermore, due to the lack of detailed knowledge of the lightning stepped leader, it is not possible to select the laboratory mechanism (with or without the mechanism of spatial leader described above) which better fits the lightning processes. As corona radiates essentially in the U.V. range, which is strongly absorbed by air, it will be difficult to solve this problem. As far as the RF signals generated by lightning are concerned, a lot of work has been done/10/. Unfortunately, in this case, the data relevant to the long spark are not available. Nevertheless, the similarities are so obvious that it is highly probable that the basic mechanisms are comparable.

. The second type of lightning discharge is the downward leader propagating from positively charged clouds. This type is also observed for negatively charged clouds, either during the final stage of lightning when an upward leader, starting from a grounded structure, goes to meet a downward negative leader, or, when lightning is the consequence of an upward leader starting from a very high tower /8/ or a rocket in case of triggered lightning /11/. In all these cases, this is a continuous discharge which develops in the field direction at a velocity of 5 to 10 cm/µs with an associated current of some tens or hundreds of ampères. Again, the orders of magnitude for lightning are significantly higher than the corresponding figures which relate to the long spark. This has been already ascribed to the small extension of the laboratory corona. The other difference is in the brightness of the leader corona, which is much lower for lightning than for the spark, and this may be due to air absorption of the U.V. light. Globally, as the discharge structure looks the same, it can be concluded that the laboratory positive spark is a good image of the lightning discharge which propagates in the field direction.

4 - TRANSITION TO ARC : THE ROLE OF THE GROUNDED ELECTRODE

As the protection of earthed structures is one of the main objectives of lightning studies, it is of interest to describe the mechanisms which occur in the vicinity of grounded electrodes in laboratory and which determine the choice of the stricken structure.

In fact, the previously described discharges are pure or "free discharges". They start from an electrode and propagate through the gas toward the opposite electrode. At a given instant, the most advanced part of the discharge starts to interact either with the opposite electrode or with a counter discharge which originates from it. The discharge is no more free. The physical processes are modified and the discharge enters a "forced regime", generally called final jump in the long spark terminology. It can take several forms, depending on the electrode shape and polarity.

For the positive discharge, the cathode has a passive role if it is a plane (Fig. 5a). If a rod is installed on the plane, a negative leader is able to develop toward the positive leader, but only after the arrival of the positive streamers at the cathode (Fig. 5b). As rather long gaps (15 m) can be studied in this case, a positive leader propagating freely - i.e. without the intervention of the cathode - over 10 metres can be easily analysed. It is important to note that, as the cathode plays only a passive role, the stricken point is choosen by the positive streamers of the leader corona. This point may not correspond to the part of the earthed structure where the electric field is maximum.

For the negative discharge, even if the anode is a plane, a positive leader develops toward the negative leader as soon as the negative streamers reach the plane (Fig. 5c). If a rod is installed on the plane, positive streamers are able to develop from the rod, toward the negative discharge, before the arrival of the negative streamers at the rod (Fig. 5d) /5/. In fact, the positive streamers develop from the points of the earthed structure where the field reaches a critical level. As this field is due both to the applied voltage and to the negative leader, the starting point of the streamers may be out of the rod if the negative leader is too far from it (Fig. 6). The region of the space where the positive and the negative discharges meet together is characterized by a "loop" formed by the branches of the two leaders (Fig. 6). Due to the existence of a positive counter discharge which is rather developed and also due to the fact that shorter gap length can only be studied, the maximum length of a negative leader propagating freely is only 2 to 3 m in a laboratory.

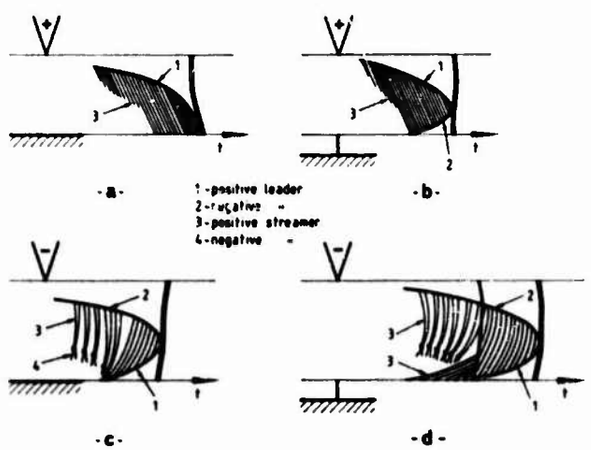


Figure 5 : Different patterns of the discharge at the final jump according to the polarity and the configuration of the earthed-electrode.

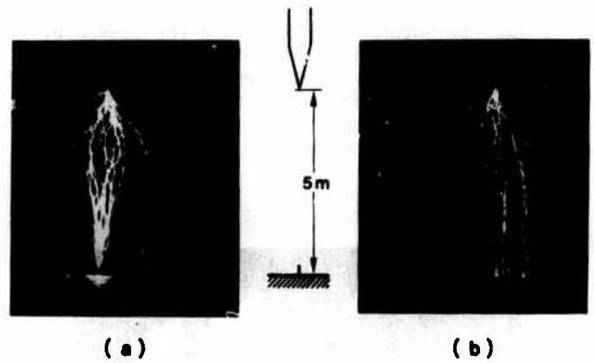


Figure 6 : Still protographs of a series of discharges in a 5 m gap, with 18 cm earthed rod (a) and without rod (b).

Whatever the polarity is, as soon as the leader channel reaches the opposite electrode, or alternatively the counter channel, a highly luminous front propagates at about 50 m/µs from the meeting point of the leaders toward the electrodes /12/. This is the return stroke which initiates a phase where the characteristics of the discharge are completely ruled by the external circuit. This is the discharge of the generator capacitances in the low impedance leader channel. The diameter of the discharge channel is suddenly increased from some millimeters up to 1 to 2 cm. The current pulse corresponding to this phase has typically a 2/10 µs shape and an amplitude of 5 to 10 kA.

The preceding description recalls some features of the lightning channel. In particular, Figure 6 illustrates the protective action of a lightning rod. However, a general observation can be made. In a laboratory, two free leaders, a positive one and a negative one, elongating toward each other, were never observed if we except the case where both electrodes are energized. In case of lightning, this situation is quite common as it is the case of a negative lightning leader approaching the ground where prominent structures (chimneys, towers, mountains) exist. This difference can be ascribed to the fact that in a laboratory, there is not enough space for the discharge to develop and to become strong enough to create an electric field sufficient for initiating a counter leader at the opposite electrode before its own arrival. In fact, the laboratory case illustrated by Figure 5d justifies clearly this assumption : the positive discharge (streamers) is initiated before the arrival of the negative streamers at the earthed rod but there is not enough time (and space) before their arrival to allow the evolution of streamers into leader. In spite of this difference, the laboratory spark can be used to study the striking distance, which is an essential parameter of the electrogeometrical model of impact provided that care is taken of the aforementioned scale effect.

5 - INTERACTION OF A DISCHARGE WITH A FREE POTENTIAL ELECTRODE

One of the major problem posed by lightning is its interaction with aircrafts. Consequently, it is interesting to examine what can be simulated in a laboratory.

From a physical point of view, it is interesting to note that the mechanism of interaction is very much dependent on the shape of the free potential electrode. An example is presented by Figure 7 which corresponds to a 1.68 m rod plane gap where a sphere (8 cm in diameter) is suspended in the gap axis with nylon ropes /13/. The shape of the sphere is modified with one or two nails sticked on the sphere. Let us define a cathodic nail as a nail sticked on the sphere side which faces the anode of the main gap. This nail acts as a cathode. A similar definition holds for the anodic nail.

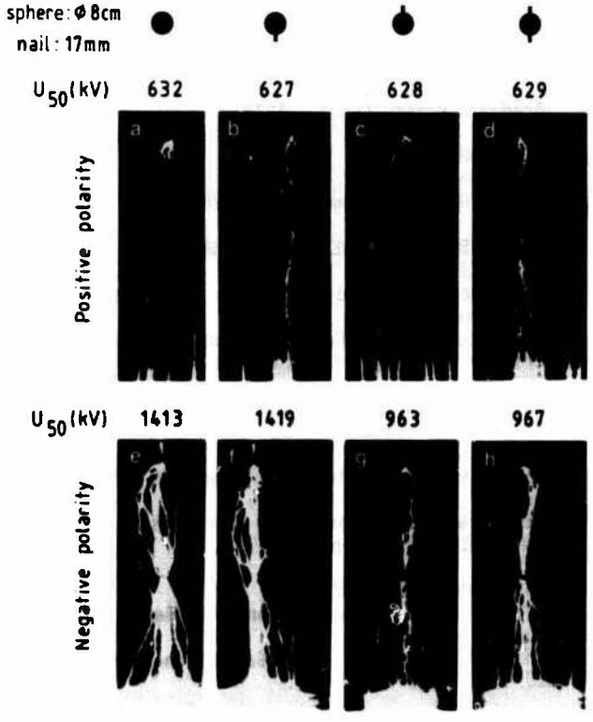


Figure 7 : Influence of a free potential object placed in a 1.68 m rod plane gap.

In positive polarity, the presence of the sphere, with or without nail, does not change the breakdown voltage of the gap. However, it is clear that if an anodic nail is added on the sphere, nearly all the discharges pass through the sphere (Fig. 7b). On the contrary, a cathodic nail does not have any influence on the discharge path (Fig. 7c). This phenomenon has been ascribed /13, 14/ to the fact that without anodic nail, the free potential object is not able to eliminate (or neutralize) the positive charges that it collects (Fig. 7a).

In negative polarity, the breakdown voltage and the percentage of discharges which pass through the object are not modified (Fig. 7f) by a cathodic nail. However, if an anodic nail is sticked on the sphere, all the discharges pass through the sphere (Fig. 7g) and the breakdown voltage is lowered by more than 30 %. This is due to the fact that an upward positive discharge is able to elongate from the sphere toward the cathode. In both cases, an anodic nail increases the percentage of discharges which pass through the isolated object : the breakdown voltage is lowered or not, depending on the polarity. A cathodic nail does not change anything.

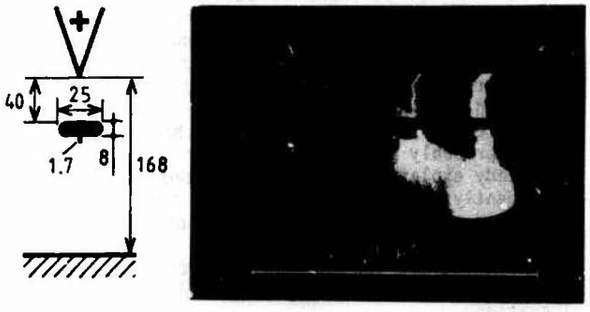


Figure 8 : I.C. streak cameragram of the positive discharge, when a free potential object equipped with an anodic nail is placed in the gap.

For aerospace applications, it is clear that the shape of the objects has not to be discussed. Generally speaking, the object must be considered as including protrusions. In such a case, the interaction between the discharge and the objects can be analyzed as shown by Figures 8 and 9 according to the polarity.

In both cases, it can be seen that the object begins to be the origin of a positive discharge (elongating downward if the main discharge is positive (Fig. 8) and upward for a negative discharge (Fig.9)) as soon as it is stricken by the streamers associated to the main discharge. This positive discharge is accompanied by a rather continuous corona in case of positive polarity and by a succession of bursts in case of negative polarity. When the object is connected to the main leader, a large corona is observed. The associated current pulse is steeper and higher in the case of negative polarity. Then, the discharge continues to propagate, as before it interacts with the object, till it meets either the ground for a positive discharge or a positive upward leader for a negative one. At that time, and as it would be the case without any object, the return stroke is triggered.

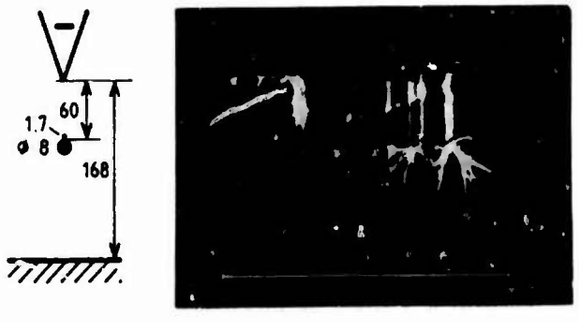


Figure 9 : I.C. streak cameragram of the negative discharge when a free potential object equipped with an anodic nail is placed in the gap.

As far as the object is concerned, the main conclusion is that large dI/dt are expected before the occurence of the return stroke, specially in the case of the negative discharge which is the most common type of natural lightning discharge.

Does this description represent satisfactorily what happens when an aircraft is stricken by lightning ? Strictly speaking, probably not. It has been previously mentioned that due to the fact that the available space in a laboratory is limited, the main discharge can not grow enough to create, at a distance, an electric field sufficient for initiating a discharge without a direct interaction between discharge and object. This is probably possible in case of natural lightning, as already explained for the final stage of lightning. Consequently, it can be anticipated that in the case of the aircraft-lightning interaction, the aircraft will be the origin of discharges and the seat of currents even before the instant at which it is stricken by the streamers associated to the lightning channel elongation.

6 - CONCLUSION

The laboratory spark presents a lot of similarities with lightning.

. From a physical point of view, it is quite sure that the basic processes are identical. However, some orders of magnitude, especially for current and leader velocity, differ significantly. This is ascribed to the space limitation of a laboratory. The discharges have not enough time (or space) to develop as strongly as for natural lightning. Nevertheless, the laboratory discharge can be used to study the physics of the lightning channel in better conditions than in nature.

. As a consequence of these similarities, the study of the RF signals radiated by a spark could improve the understanding of the causes of the RF signals emitted by lightning.

. Taking into account the scale effect, the striking of earthed structures is satisfactorily reproduced by laboratory tests.

. As far as the interaction of lightning with aircrafts is concerned, no direct comparison is available. However, the laboratory spark seems to be a good tool for a better understanding of these phenomena.

Generally speaking, if the laboratory facilities do not allow to solve all the questions raised by lightning, there is no doubt that it could help the comprehension the basic phenomena and the research of practical solutions.

REFERENCES

/1/ T.E. ALLIBONE, B.F.J. SCHONLAND
Development of the Spark Discharge
Nature, 134, pp. 735-736, 1934

/2/ Les Renardières Group
Research on Long Air Gap Discharges at Les Renardières.
Electra, n° 23, pp. 53-157, 1972.

/3/ Les Renardières Group
Research on Long Air Gap Discharges at Les Renardières. 1973 Results.
Electra, n° 35, pp. 49-156, 1974.

/4/ Les Renardières Group
Positive Discharges in Long Air Gaps at Les Renardières. 1975 Results and Conclusions.
Electra, n° 53, pp. 31-153, 1977.

/5/ Les Renardières Group
Negative Discharges in Long Air Gaps at Les Renardières. 1978 Results.
Electra, n° 74, pp. 67-216, 1981.

/6/ G. LE ROY, C. GARY, B. HUTZLER, J. LALOT, C. DUBANTON
Les propriétés diélectriques de l'air et les très hautes tensions.
Editions Eyrolles, Paris, 1984.

/7/ G. GALLET, G. LEROY, R. LACEY, I. KROMER
General Expression for Positive Switching Impulse Strength Valid up to Extra Long Air Gaps.
IEEE Transactions on Power Apparatus and Systems, vol. PAS 94, n° 5, pp. 1989-1993, 1975.

/8/ K. BERGER
The Earth Flash - Chapter 5 in Lightning.
Edited by R.H. GOLDE
Academic Press, London, 1977.

/9/ M. A. UMAN
Lightning. 1969
McGraw Hill Book Company, New York.

/10/ M. LE BOULCH, C. WEIDMAN, J. HAMELIN, C. LETEINTURIER
Characteristics and Mechanisms of VHF/UHF Radiation from Lightning Processes.
7th International Conference on Atmospheric Electricity, Albany, U.S.A., June 1984.

/11/ R.P. FIEUX, C.H. GARY, B.P. HUTZLER, A.R. EYBERT-BERARD, P.L. HUBERT, A.C. MEESTERS, P.H. PERROUD, J.H. HAMELIN, J.M. PERSON
Research on Artificially Triggered Lightning in France.
IEEE Transactions on Power apparatus and Systems, Vol. PAS 97, n° 3, pp. 725-733, May 1978.

/12/ H.N GARCIA, B. HUTZLER
Electrical Breakdown of Long Air Gaps. The Final Jump.
Third IEE Conference on Gas Discharges, London, 1974, pp. 206-210.

/13/ P. SIREAU
Etude de l'amorçage des intervalles fractionnés.
Mémoire C.N.A.M. 1982.

/14/ B. HUTZLER, P. SIREAU
Some Properties of Air Gaps Containing Additional Floating Electrodes.
4th I.S.H. · Athens 1983, paper 44.06.

HIGH CURRENT SURFACE DISCHARGE PROPAGATION ANALYSIS - APPLICATION TO THE LIGHTNING LEADER

S. Larigaldie

Office National d'Etudes et de Recherches Aérospatiales, BP 72, 92322 Châtillon Cedex, France

Abstract - The fast propagation ($v \approx 10^6$ ms^{-1}) of a ionized and thermalized channel ($n_e \approx 10^{18}$ cm^{-3}, $T \approx 2.8 \times 10^4$ K) is studied in virgin air at atmospheric pressure, using a device comprising a gliding discharge produced at the upper surface of a dielectric slab electrically charged by corona effect. For a corona voltage of about 100 kV, and without any pre-ionization of the gas, the gliding spark travels over one meter along a predetermined straight line. This allows to investigate experimentally the discharge with a full set of diagnostics, including measurements of the current and of the propagation speed, recording of the light emission (electronic image converter, spectroscopy, Lichtenberg figures), optical study of the width of the arc channel by interferometric holography, and detection of transient electric fields by capacitive probes. The various measurements are synchronized from optical fiber devices located close to the spark.

The study concerns mainly the negative spark, and shows that the thermalized arc channel is produced by the following three stages:

1) a preliminary discharge stage, similar to a positive glow, where the electronic temperature - about 2 eV - is much greater than the gas temperature, which increases continuously from 300 to 1500 K;
2) a transient arc stage, with a constant duration of about 10 ns, where the major part of the energy of the electric field is transformed into ionization energy of the gas; the spark velocity is directly proportional to the voltage drop along this zone;
3) a heating stage, with a duration included between 25 and 60 ns, where the electric field has been largely reduced, and where the ionization energy is partially restituted in form of heat to the neutrals.

I - INTRODUCTION

From the eighteenth century, physicists have questioned the similarities between lightning and sparks propagating along the surface of an insulating material [1-3]. This is why ONERA has pursued, since 1978, an investigation of the mechanisms related to the propagation of gliding discharges, with the help, in spectroscopy, of the Laboratoire de Physique des Décharges of CNRS.

The scope of this paper is to present the main results obtained, with emphasis both on the prevailing role of the region of the discharge where the ionized medium transits from glow to arc, and on the similarities of such a discharge with the lightning stroke.

II - EXPERIMENTAL ARRANGEMENT

The possibility of producing a spark having, without any pre-ionization, a well determined path is a major advance of the type of experimental arrangement selected. A number of optical or electrical sensors can be placed along this path with full probability of having the spark channel into their field of view. The experimental arrangement has been described in details in former publications [4-9].

The principle of the experiment is summarized shortly as follows (fig. 1): corona discharges, produced at the points of a metallic comb (1) connected to a high voltage power supply adjustable from 0 to + 180 kV, spread unipolar ions over the surface of a plexiglass slab (2) and over the floating electrode (3) traversing this slab. The potential of the charged surface and of the electrode reaches a steady value $V_0 = V_{ch} - V_{sc}$, where V_{sc} is the threshold of the corona produced on the teeth of the metallic comb.

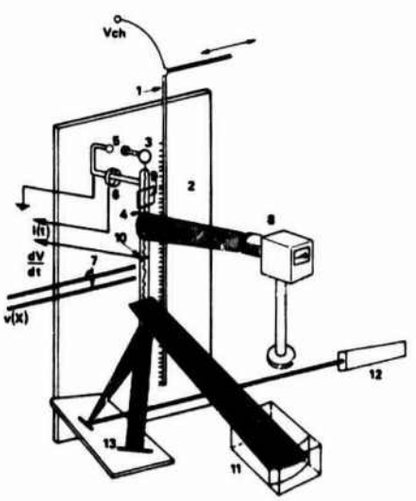


Fig. 1 - Experimental arrangement
1 - Metallic comb connected to the high voltage V_{ch}.
2 - Dielectric slab
3 - Floating electrode
4 - Grounded metallic strip
5 - Triggered spark gap.
6 - Current sensor
7 - Fiber optics pulser
8 - Electronic image converter
9 - Photographic film
10 - Capacitive probe
11 - Spectroscope
12 - Q switched YAG laser
13 - Holographic bench.

In contact with the back of the dielectric slab, a grounded metallic strip 1050 mm long and 15 mm wide (4) parallel to the comb, is used for guiding the discharge.

This discharge is triggered when the floating electrode (3) is suddenly connected to ground by a controlled spark gap (5). At this precise time the electric field close to the electrode is much higher than the breakdown field in air; the resulting ionization generates around the electrode a conducting medium which pushes further the electric field and the related ionization zone, etc. In this way, a spark channel is formed and the discharge propagates in air, over all the length of the strip guide, in close contact with the charged face of the dielectric slab.

This configuration has permitted to place, in close proximity of the channel, the following diagnostics:

- the current I(t) of the spark is measured with a Rogowski loop (6), located around the spark gap return wire;
- an optical fiber (7), with one end located adjacent to the spark path, at a distance X from the electrode, is used to generate, through an electro-optic converter, a pulse when the spark reaches the length X; this pulse is used to calibrate I as a function of X [5];
- using two identical fibers located at $X \pm \Delta X$, the local propagation velocity $v(X) = \Delta X/\Delta t$ can be inferred from the difference Δt of the arrival time of the spark at the two fibers ends;
- the light emitted by the spark is recorded by a IMACON 790 electronic image converter (exposure time 10 ns) (8);
- the luminous track of the spark are photographed with high space resolution by placing a film on the face of the dielectric slab in such a way that the spark is in direct contact with the sensitive emulsion (photographic Lichtenberg figures);
- a capacitive probe (10) is located inside a 0.5 mm wide slit cut in the strip guide perpendicularly to the discharge path; it is sensitive to the fast variations of electrical potential induced by the advancing tip of the spark;
- spectroscopic analysis of the spark plasma is obtained by focusing on a monochromator the light emitted through a virtual slit located at a fixed distance from the electrode; this is equivalent to analyse the spark plasma, going backward from the head at a velocity v;
- illuminating the spark channel with a pulse of coherent light of duration 15 ns, produced by the YAG laser (12), through the holography bench (13) the cross-section of the channel can be measured at different times Δt after the passage of the head. The fiber optics device (7) permits to select Δt by triggering the laser pulse when the spark head reaches a given distance X.

III - STRUCTURE OF THE DISCHARGES

The photographic patterns (Fig. 2) show, for $V_o < V_s$, a luminous track surrounding the electrode (polar pre-discharge), radially divided by dark lines; its radius is proportional to the voltage V_o and independent from the slab thickness. For $V_o \geq V_s$, bright spark channels (2) branch out from the electrode, topped by gliding pre-discharges (3) characterized by a track differing to the case of the polar pre-discharge by the ear shaped configuration of the dark lines.



Fig. 2 - Photographic electric figure of a gliding spark of negative polarity
1 - Polar pre-discharge
2 - Spark channel
3 - Gliding pre-discharge

The following laws, expressed by M. Töepler, describe the behaviour of these discharges [11-12].

$$\text{Negative spark: } r_{(cm)} = V_{o(kV)}/11.5 \qquad (1)$$

$$\text{Positive spark: } r_{(cm)} = V_{o(kV)}/5.5 \qquad (2)$$

The threshold voltage V_s, quite independent from the spark polarity, is a function of the surface capacitance of the dielectric; for plexiglass (relative permittivity $\varepsilon_r \simeq 3$):

$$V_{s(kV)} = 69(e_{(cm)})^{\frac{1}{2}} \qquad (3)$$

where e is the thickness of the dielectric slab.

Recorded with the image converter (exposure time 10 ns), at the advancing tip of the spark, a shimmering gliding pre-discharge can be observed (Fig. 3). For negative sparks, it will be shown that the head of the spark, located before the channel, is actually constituted by two different parts; the first is the properly so called pre-discharge; the second, inserted between the pre-discharge and the spark channel is comparable to the transient arc phase of the breakdown of a short monodimensional gap [13-14].



Fig. 3 - Electronic image converter snapshot (exposure time: 10 ns) of the advancing head of a gliding spark.

Let us note that, according [5], the voltage drop V_{lt} along the spark channel can be evaluated in all configurations by the mean of a simple electrical model and by measuring the currents I(X). This

method is verified by comparing the experimental results with the numerical prediction of I(t) as a function of V_0 (Fig. 4). The instantaneous propagation velocity of the spark as a function of $V_0 - V_{lt}$ (voltage drop available in front of the channel) and of the slab thickness e is plotted in Fig. 5.

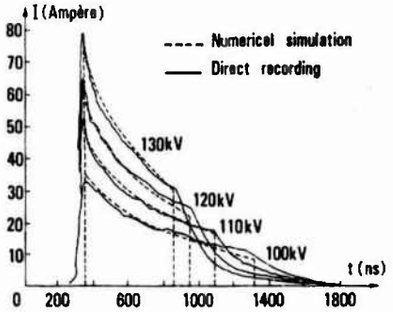


Fig. 4 - Numerical simulation of the negative gliding spark current. Comparison with the direct recording.
Dielectric slab thickness: 2 mm
Charging voltage : 100, 110, 120, 130 kV.
(The simulation does not take into account the phenomena occuring after the arrival of the spark at the end of the metallic strip).

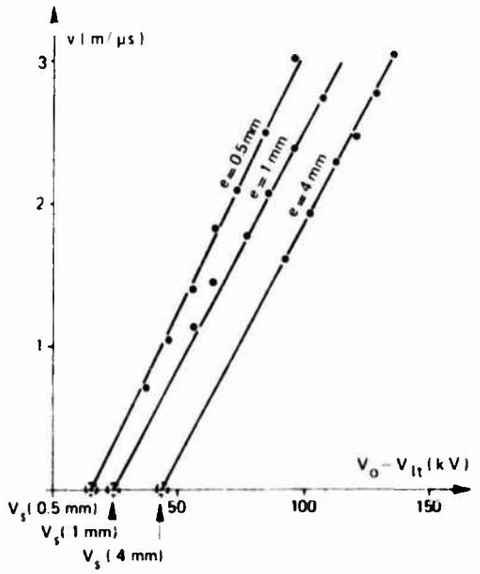


Fig. 5 - Propagation velocity of the negative gliding spark as a function of the voltage $V_0 - V_{lt}$ and of the dielectric slab thickness e.

The important reaults shown in this figure are:
a) the linesrity and the psrallelism of the curves $v(V_0 - V_{lt})$;
b) the identity of the threshold voltages V_s (e) defined by (3) with the abscissae of the points of intersection of the lines $v(V_0 - V_{lt})$ with the V axis; this shows that, no matter the voltage V_0, the information concerning V_s is included in the behaviour of the negative spark.

The relationship between velocity and voltage can therefore be written:

$$v = (V_0 - V_s(e) - V_{lt}(X,I)) \qquad (4)$$

with $\alpha = 35$ m $V^{-1}s^{-1}$.

The photographic electric patterns show, on the other hand, that the geometrical width of the gliding pre-discharges is independent from the voltage V_0, but noticeably increases with e. It can be concluded, by sifting the above mentioned experimental facts, and by assuming that the relation (1) holds for both the polar and gliding pre-discharges, that the voltage drop in the gliding pre-discharge is always equal to $V_s(e)$.
The electric patterns obtained on thin sheets ($e \leq 100$ μm) reveal that extra radial discharges show up along the channel for the highest values of V_0 (Fig. 6a and 6b). The enlargment presented Fig. 6c shows that these extra tracks do not disturb the arrangement of the symmetrical network of ears due to the gliding pre-discharge, and, consequently, that they appear after the passage of this pre-discharge. They have therefore been generated when $V_0 > V_s$ by a voltage drop attached to a zone located behind the gliding pre-discharge; this zone can be located between the pre-discharge and the tip of the conducting spark channel, and it can be characterized by other diagnoatic means.



Fig. 6a - Photographic electric figure of an unguided negative gliding spark, over a thin dielectric sheet (e = 100 μm) and with a low charging voltage (V_{ch} = 15 kV).



Fig. 6b - Photographic electric figure of an unguided negative gliding spark, over a thin dielectric sheet (e = 100 μm), V_{ch} = 30 kV.



Fig. 6c - Details of Fig. 6b.

IV - OUTLINE OF THE EXPERIMENTAL RESULTS

Fig. 7 displays a typical recording of the current at the onset of a negative spark. If it is assumed that the transient arc region controls the gliding spark propagation, it can be inferred that the rise time of the current shown in Fig. 7 corresponds to the formation time of this region. This time, of the order of 10 ns, is independent from V_0 and e.

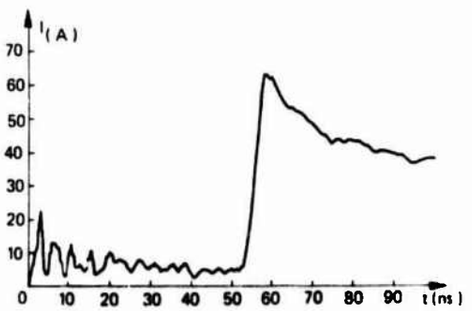


Fig. 7 - Recording of the currant rise at the onset of a negative gliding spark V_{ch} = 120 kV, e = 2 mm.

When the head of the discharge passes over the capacitive probe inserted in the strip guide, the signal recorded, due to the decrease of the local voltage of the spark, has also a duration of approximately 10 ns (Fig. 8). This time is therefore characteristic of the transient arc region; it is broadly the same as the duration of the transition in voltage drop associated with the breakdown of a spark gap in ambient air, as measured by Andreav and Vanyukov [15].

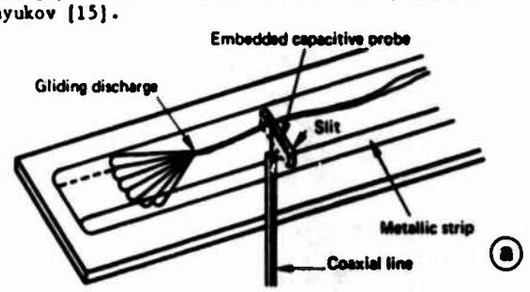


Fig. 8a- Experimental device



Fig. 8b - Probe signal.

It can be deduced from (4) that the average longitudinal electric field in the transient arc region is about 26 kV cm^{-1}, of the order of the breakdown field in air at normal temperature and pressure.
The voltage along the direction of propagation of the discharge is plotted schematically in Fig. 9, where the main experimental data have also been specified.
If AB, BC, CD and DE are respectively the pre-breakdown, transient arc, thermalization and thermalized arc regions, the main characteristics of these zones are as follows:

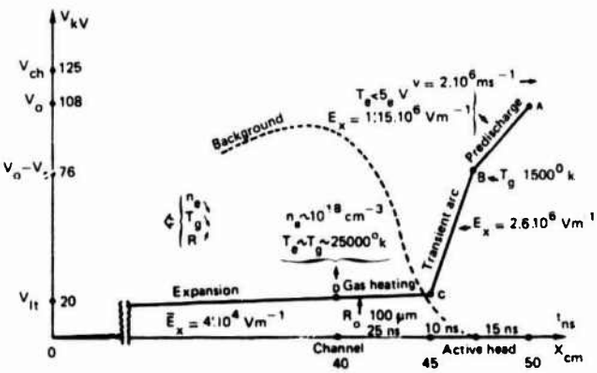


Fig. 9 - Voltage distribution and value of the main parameters along the various zones of a typical negative spark in the moving reference frame.

AB (Pre-discharge):
$T_e \simeq 2$ eV,
T_g increasing from ambient to 1500 K,
Lenght of AB independent of V_0.

BC (transient arc):
The spectroscopic investigation shows that the ratio N^*/N displays a peak in this zone, which reveals the beginning of a dissociation of the gas and a strong ionization [7].
Its duration $\tau_{BC} \simeq 10$ ns is invariant. The velocity of propagation of the discharge is proportional to the voltage drop between B and C (see relation 4).

CD (thermalization):
This region is characterized by the large increase of the continuum background radiated by the discharge in the visible range.
The corresponding time τ_{CD} is comprised between 25 and 60 ns.
The radius R_0 of the channel is 100 µm for v = 2.10^6 ms^{-1} and a = 2 mm.

DE (thermalized channel):
The desorption of hydrogen from the plexiglass permits the measurement in this region of the electronic density by using the Stark effect.
The density n_e varies from 7.10^{17} to 2.10^{16} cm^{-3} during 800 ns. In the same time, T_e is approximately equal to T_o and decreases from 28000 to 16000 K [7-8].
It should be pointed out that the transition time τ_{BC} is smaller than the thermalization time τ_{CD}.

V - MODELLING

a) Pre-discharge region AB.
When the pre-discharge is passing, let dW(t) be the energy spent by Joule heating in the volume element h dx dy attached to the insulating surface (laboratory frame of reference); h is the thickness of the ionized gas and dx dy an elementary area of the charged surface (fig. 10). $E_{x(AB)}$ is the longitudinal field assumed to be constant.

$$dW(t) = E_{x(AB)}\, dx \int_0^t J(t)dt \qquad (5)$$

where J(t) is the contribution, at the time t after the arrival of A over the volume element h dx dy, of all the current elements dJ generated by the discharge of the elementary capacitances $1/e\ \varepsilon_o\varepsilon_r$ dx dy located above this volume element. We have:

$$dJ = \frac{1}{e}\varepsilon_o\varepsilon_r .dx\ dy.\frac{\partial V}{\partial t} \qquad \frac{\partial V}{\partial t} = v.E_{x(AB)}$$

$$J(t) = \int_0^{x=vt} dJ = \frac{1}{e}\varepsilon_o\varepsilon_r v^2 E_{x(AB)}\, dy.t \qquad (6)$$

and:
$$dW(t) = \frac{1}{2e}\,(E_{x(AB)} v.t)^2\ dx\ dy \qquad (7)$$

and, when the zone AB has entirely passed across the volume element h dx dy:

$$dW_{(AB)} = \frac{1}{2e}\,\varepsilon_o\varepsilon_r V_{AB}^2\ dx\ dy \qquad (8)$$

We will assume, with I. Gallimberti [16], that at the end of the pre-discharge region (point B), the sudden change of the properties of the ionized medium is due to the thermal detachment of the electrons from the negative molecular ion O_2^-.

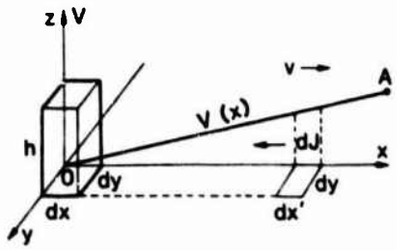


Fig. 10 - Modelling of the gliding pre-discharge zone (AB).

In reference [16], one can also find the relative value of the transfer rate of electronic energy to the gas translational and rotational energy via electronic excitation by the effect of the superelastic quenching collisions; for the field $E_{x(AB)}$ of our experiment, this value is 20%; the rest of the energy is stored in the vibrational levels of N_2. With C_V, specific heat of air at constant volume, equal to 928 JK^{-1}, the energetic balance of AB gives, as a function of h and of the translation and rotation temperature $T_{o(B)}$ = 1500 K, the value of the voltage drop V_{AB}:

$$V_{AB} = \left[\frac{C_v\, T_{o(B)}\, h}{0.1\ \varepsilon_o\varepsilon_r}\right]^{\frac{1}{2}} .e^{\frac{1}{2}} \qquad (9)$$

As $V_S \equiv V_{AB}$, the expression (9) is identical to the experimental law (3) if the thickness h is assumed to be constant and of the order of 1 m.
In these conditions, one can also evaluate, as a function of the mobility μ_e of the electrons in air, [17] the electronic density averaged over the section h dy at point B; from (6), by writing

$$v.t_{AB} = X_{AB} = V_{AB}/E_{xAB}$$

one gets:

$$n_{eB} = \frac{\varepsilon_o\varepsilon_r}{e}\,\frac{V_{AB}}{E_{xAB} h\, e_-\mu_e}.\ v \qquad (10)$$

where e_- is the electronic charge.

The density varies therefore as v and $e^{-\frac{1}{2}}$; for e = 2 mm and $v = 2.10^6\ ms^{-1}$, one gets: $n_{eB} \simeq 10^{17}\ cm^{-3}$.

The major problem of this model is to imply an increase of n_e in AB, which is not consistent with the value of $E_{x(AB)}$ given by (1). One possibility is that the increase of the ionization in this zone is due to the presence of local transverse fields; the presence of these fields is revealed by the inhomogeneity of the light emission pattern in the predischarge region.

b) Transient arc BC.

The formula (10) shows that the electronic density at the beginning of BC is high enough for making the de-excitation of the gas dependent quite exclusively from the electronic fluid. In these condition, in BC, the electronic energy stays quite totally unchanged and the power acquired from the electric field is essentially used to increase the ionization [18]. The local balance of power in the BC plasma can therefore be written with a formalism close to the one used by Rompe and Weisel [19]:

$$n_e\, e_-\, v_{de}\, E_{xBC}\, dt = dn_e\,(e_-\,\Phi_i - \tfrac{3}{2}\,KT_e) \qquad (11)$$

If it is assumed that the drift velocity of the electrons v_{de} is partically invariant in BC, and that the thermal energy per electron 3/2 KT_e is smaller than the ionization energy $e_-\,\Phi_i$ ($\simeq$15 eV in air), integration of (11) along BC gives, with dt = dx/v,

$$\frac{1}{v}\int_B^C .E_{xBC}.dx = V_{BC}/v = \left(\frac{e_-\Phi_i + \frac{3}{2}\,KT_e}{e_-\,v_{de}}\right).Ln\,\frac{n_{eC}}{n_{eB}} \qquad (12)$$

If the preceeding assumptions hold, the relationship (12) is similar to the experimental law (4) (where $V_{BC} \equiv V_o - V_s - V_{it}$) with a weak dependence on the boundary conditions n_{eC} and n_{eB}.

Conversely, if we assume $T_e \simeq 2$ eV and $n_{eC}/n_{eB} \simeq 10^2$ (see § V1) the measurement of the slope $\alpha = v/V_{BC}$ gives the electronic drift velocity v_{de}, that is to say numerically:

$$v_{de} = 2.9x10^3 ms^{-1} \simeq c_{si} = (KT_e/M_i)^{\frac{1}{2}}$$
$$= 2.6x10^3 ms^{-1} << \mu_e\, E_{xBC} \simeq 1.2x10^5\ ms^{-1}$$

(M_i : ion mass; c_{si} : ionic sound velocity).

The orders of magnitude above suggest that an anomalous resistivity phenomenon, due to the development

of an acoustic ion wave instability, reduces the drift velocity of the electrons inside the transient arc region. The region BC meets indeed the conditions for the development of this type of instability:

$$T_e > T_o \text{ and } \nu_{pe} > \nu_{eo}$$

where ν_{pe} is the electron plasma frequency $\nu_{pe} = 1/2\pi(n_e e^2/\varepsilon_o m_e)^{\frac{1}{2}}$ where m_e is the electron mass, and $\nu_{eo} \simeq 4.10^{12} s^{-1}$ is the electron-neutral collision frequency. Acoustic ion waves, with a characteristic frequency of the order of the ionic plasma frequency $\nu_{pi} = \nu_{pe}(m_e/M_i)^{\frac{1}{2}} \simeq 10$ GHz have actually been experimentally detected during the passage of BC over the sensing electrode of the capacitive probe connected to a microwave detection bench [6].

c) The heating region CD

The above-mentioned model implies that the electric field energy is essentially transformed into ionization energy after the passage of the transient arc region BC. The subsequent gas heating taking place in a region of weak field ($E_{canal} \simeq 4.10^2$ V cm^{-1}) [5], the electronic density drop in CD provides, via the three body recombination:

$$e_- + e_- + M_+ \rightarrow e_- + M,$$

the energy required for heating the gas; the energy transfer proceeds through electron-neutral, electron-ion and ion-neutral elastic collisions. The numerical model presented below permits the simulation of the evolution of the parameters n_e, T_e, T_o in the laboratory frame of reference after the passage of the head of the negative spark.

VI - EVOLUTION OF THE PLASMA AFTER THE PASSAGE OF THE HEAD OF THE SPARK.

The coupled hydrodynamic equations of the plasma in fast evolution, used by Tholl to study the heating of a transient hydrogen plasma [20], have been applied here to the above-mentioned models. The relationships written as follows express the evolution of the electronic density (13), of the electronic temperature (14) and of the gas temperature (15):

$$\frac{dn_e}{dt} = n_e(\nu_i - \nu_{rc}) \qquad (13)$$

$$\frac{3}{2}\frac{dT_e}{dt} = \nu_{oe}E - (\nu_i - \nu_{rc})(\phi_i + \frac{3}{2}T_e) - \frac{2m_e}{M_o M_o}(\nu_{eo} + \nu_{ei})\frac{3}{2}(T_e - T_o) \qquad (14)$$

$$N_o \cdot \frac{5}{2} \cdot \frac{dT_o}{dt} = \frac{2m_e}{M_o}\frac{n_e}{N_o}(\nu_{eo} + \nu_{ei})\frac{3}{2}(T_e - T_o) \qquad (15)$$

with: T_e and T_o expressed in eV

air density:

$$N_o = 2.7 \times 10^{19} \text{ cm}^{-3},$$

ionization frequency:

$$\nu_i = 1.5 \times 10^{11} T_e^{\frac{1}{2}} (1 + \frac{2T_e}{\phi_i}) \exp - \frac{\phi_i}{T_e},$$

three body recombination frequency [21]:

$$\nu_{rc} = 8.75 \times 10^{-27} T_e^{-9/2} n_e^2,$$

electron-ion collision frequency:

$$\nu_{ei} = 1.5 \times 10^{-6} n_e T_e^{-3/2} \text{Ln}\Lambda,$$

where $\text{Ln}\Lambda$ express the Coulomb interaction cut-off beyond the Debye radius.

In agreement with the estimations of §V, the following conditions are obtained:

$n_{eB} = 10^{17} \text{cm}^{-3}$, $T_{eB} = 1.4$ eV, $T_{oB} = 0.13$ eV(1500 K)

$E_{BC} = 26$ kV cm^{-1}, $v_{deBC} \simeq (KT_e/M_i)^{\frac{1}{2}} = c_{si}$,

$n_{eC} = 10^{19}$ cm^{-3} (this condition comes from the energy balance of the spark and from the value of the channel radius obtained by the holographic measurements [6-7]).

$E_{CD} = 4.10^2$ V cm^{-1}, $v_{deCD} = E_{CD} \cdot e \left[m_e(\nu_{ei} + \nu_{eo})\right]^{-1}$,

which assumes that the normal transfer coefficients apply to region CD.

The computational results, marked on Fig. 11, show the fair agreement of the theoretical predictions of the times τ_{BC} and τ_{CD} with the experimental results (Fig. 9). The computed electronic density n_{eD}, is very sensitive to the initial conditions; it is found only slightly superior to the value measured by spectroscopy. Equations (13) to (15) account therefore in a satisfactory way for the evolution of the discharge plasma, which strengthen the credibility of this model characterized by the fact that the heating phase follows a fast phase of intense ionization.

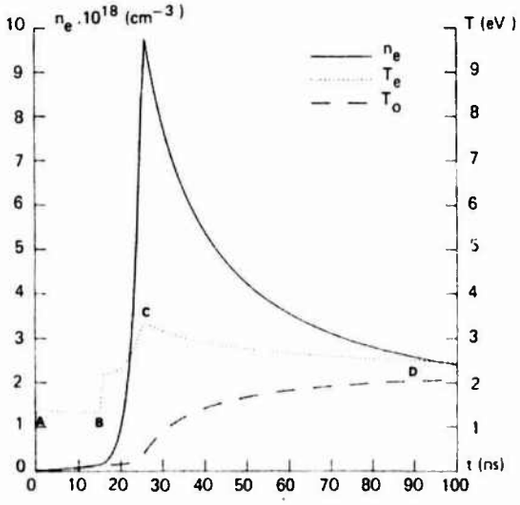


Fig. 11 - Computation of the temporal evolution of the parameters n_e, T_e, T_o during the gliding spark passage.

VII - CONCLUSION

The systematic study of the surface spark helps to understand the physical mechanisms common to high current precursors. The studied discharges and the lightning precursors (stepped and dart leaders) are similar as far as the values of the transported currents, of the propagation velocities and of the channel temperatures are concerned (see for example [23]).

The invariance of the time $\tau_{BC} \simeq 10$ ns for the formation of the transient arc, which is of same duration that the electromagnetic pulses emitted by the lightning precursors [24], suggests that the two phenomena are connected, the lightning pulses coming from the formation of transient arcs associated with branching or discontinuities in the pre-breakdown and leader phases of lightning.

ACKNOWLEDGMENTS :

This study has been partly supported by DRET. The author is grateful to Dr J. Taillet for helpful discussions, to Dr M.C. Proux-Bordage and to Dr G. Hartmann for the spectroscopic measurements, and to Mr P.O. Lagage for his participation to the theoretical analysis.

REFERENCES

[1] - Wall W., Phil. Trans. Royal Soc. 26, 67 (1708).
[2] - Merrill F.H. and Von Hippel A., J. Appl. Phys., 10, 813 (1939).
[3] - Chiba M., Kuono T., Fujika M., Third Int. Symp on High Voltage Engineering, Milan (1979).
[4] - Larigaldie S., J. Phys. (Paris), Colloque C7.40, 429 (1979).
[5] - Larigaldie S., Labaune G. and Moreau J.P., J. Appl. Phys., 52, 12 (1981).
[6] - Larigaldie S. Thèse d'Etat (to be published).
[7] - Bordage M.C., Thèse Docteur Ingênieur, Orsay n° 503 (1981).
[8] - Bordage M.C., and Hartman G., J. Appl. Phys., 53, 12 (1982).
[9] - Bondioux A., Thèse Docteur Ingênieur, Orsay n° 672 (1984).
[10] - Surget J., Int. Symp. on Flow Visualization, Ann Arbor, (1983).
[11] - Töepler M., Ann. Phys., 21, 193 (1906).
[12] - Töepler M., Arch. Für Elektrotechnik X band, 5 and 6 Heft (1921).
[13] - Haydon S.C., "A survey of phenomena in ionised gases", VIIth I.C.P.I.G., Vienna (1967).
[14] - Freeman R.A. and Craggs J.D., Brit J. Appl. Phys. (Phys. D), ser. 2, vol. 2 (1969).
[15] - Andreev S.I., and Vanyukov M.P., Sov. Phys. Techn. Phys., 6, 700 (1962).
[16] - Gallimberti I., XIVth I.C.P.I.G., Colloque C7, Grenoble (1979).
[17] - Davies A.J., Davies S.C., and Evans C.J., Proc. IEE, 118 (1971).
[18] - Bychkov Y.I., Korolev Y.D. and Gavrilyuk P.A., Sov. Phys. Techn. Phys., 17, 8 (1973).
[19] - Rompe R. and Weisel W., Z. Phys., 122, 636 (1944).
[20] - Tholl A., Z. Naturforch., 259-420 (1970).
[21] - Abbas I. and Bayle P., J. Phys. D, Appl. Phys., 14 (1981).
[22] - Hinnov E. and Hirschberg J.G., Phys. Rev., 125 (1962).
[23] - Uman M.A., "Lightning", Mc. Graw-Hill, New York (1969).
[24] - Labaune G., Ann. des Télécomm., 39, 5 (1984).

LIGHTNING MAGNETIC FIELD CALCULATION USING FINITE ELEMENT METHOD

P.R.P. Hoole and J.E. Allen

Department of Engineering Science, University of Oxford, Oxford, U.K.

Abstract - The ideal solution technique of magnetic fields from lightning should be characterised by a good leader/return stroke model and a versatile, efficient and user friendly field solution method. The finite element method is suitable for accurate magnetic field solution ; it also permits study of the effects of lightning channel tortuosity, branches, the presence of a scatterer ; magnetic fields very near to the channel could be determined, whatever the radius of the channel and wavelength of the source signals. In this paper, the solution of magnetic fields from a straight, vertical lightning channel using the finite element method is described. The finite element mesh may be generated manually, semi-automatically or automatically. Minimum effort is required from the user for the latter two modes of mesh generation. Using empirical approximations for the lightning leader and return strokes, magnetic fields are computed. Numerical errors are discussed. The studies presently being carried out are briefly described.

INTRODUCTION

The work reported in this paper is part of a program to study the physics of lightning and therby test and further the work done by the past two generations of lightning scientists on lightning modeling, and then compute lightning currents and related electromagnetic fields radiated from the channel. This work may be classified into six distinct steps as shown in Figure1. Return stroke modeling involved the investigation of the streamer theory[1] and shock wave theories[2] propounded for leader strokes, the transmission-line model[3] and the return stroke velocity and the application of Braginskii's theory of spark discharge[4] to lightning modeling. While gathering the experimental data currently available on lightning, the possibility of calculating lightning current magnitudes and rate of rise of current from electric field measurements[5] has been considered. However the immediate focus of this paper is on steps 4 and 5, dealing with the computation of radiated magnetic fields.

All computations presented in this paper make use of the empirical model for the return stroke; the 3km channel is divided into 25 sections. The earth is assumed to be a perfect conductor, with the mirror image of lightning channel replacing the earth. The currents in the mirror image flow in the same direction as the source current. The current decays with the channel height and travels at constant velocity.

Of the two finite element methods available, the differential formulation is preferred here in view of our desiring a solution everywhere over a large region of space; for integral formulations result in full matrices, as opposed to sparse ones with differential methods. Therefore integral methods are suitable only when a problem requires a solution at a few limited number of field points and prove unweildly when several nodes are involved. Futhermore, an integral solution may only be formulated for case of a straight, vertical conductor; the differential formulation is easily extended for more complex geometries which characterise a cloud to ground lightning flash.

OUTLINE OF COMPUTER PACKAGE

We intend solving for magnetic fields, radiated by the leader and return strokes, by Maxwell's equations for the magnetic flux density $\underline{B}$ governed by

$$\text{Curl}\,\mu^{-1}\underline{B} = \underline{J} + \frac{\partial \underline{D}}{\partial t} \qquad (1)$$

where μ is the permeability, $\underline{J}$ is the current density, t is time and $\underline{D}$ is the electric flux density. Now since

$$\text{Div}\,\underline{B} = 0 \qquad (2)$$

we intoduce the vector potential $\underline{A}$ so as to satisfy (2)

$$\text{Curl}\,\underline{A} = \underline{B} \qquad (3)$$

Now comparing (4) with the Maxwell equation

$$\text{Curl}\,\varepsilon^{-1}\underline{D} = -\frac{\partial \underline{B}}{\partial t} \qquad (4)$$

where ε is permittivity, we obtain

$$\underline{D} = -\varepsilon \frac{\partial \underline{A}}{\partial t} - \varepsilon\,\text{Grad}V \qquad (5)$$

where V is an electric potential.Putting these into (1), we get

$$\text{Div Grad}\,A - \mu\varepsilon \frac{\partial^2 A}{\partial t^2} = -\mu J_0 \qquad (6)$$

where J_0 is the lightning current inside the channel and zero outside the channel. This is the equation that is commonly solved for the vector potential from which, using (3), the magnetic flux density is obtained. For the cylindrical model of the lightning flash with axi-symmetry, the finite element formulation of (6) is[6]

$$\left\{2(c\Delta t)^{-2}[T]+[S]\right\}A^{t+\Delta t} = \mu[T]J_0^{t+\Delta t} + 5(c\Delta t)^{-2}A^{t} - 4(c\Delta t)^{-2}[T]A^{t-\Delta t} + (c\Delta t)^{-2}[T]A^{t-2\Delta t} \quad (7)$$

where A and J_0 are scalar values of vector potential and current density in the z direction; [T] is a metric tensor and [S] is the Dirchlet matrix.

The time stepping algorithm above may be started employing the fact that A is zero at $t \leq 0.0$. Strictly speaking the initial conditions depend on the leader stroke currents. Leader stroke vector potential and magnetic fields are also calculated. Expressions of the type (7) may be built up for all the triangles making up the region of solution and summed to correspond to the minimization of the full global funtional. The resulting set of linear, symmetric positive definite equations may then be solved at each time step by the preconditioned conjugate gradient method[7] or frontal solvers[8].

Any numerical method will necessarily involve the division of lightning channel into finite number of sections. Since no experimental data to date give the rate of decay of current along a lightning or spark channel, it is difficult to dogmatically set a maximum on the length of each section. In order to have some indication of the decay of current as it travels up the lightning channel, consider a current wave as it travels along a transmission-line. Considering the R,L,C elements only, the rate of decay of current for high frequencies (when $\omega L \gg R$), is given by[9]

$$I = I_1 \exp(-Rz/2Z_0) \quad (8)$$

$$Z_0 = \sqrt{L/C} \quad (9)$$

For an initial current I_1 = 40kA, with R = 1ohm/m, L = 2microH/m and C = 10picoF/m [3] the decay of current for a 3.5km long channel is given in Figure2. Approximate rates of decay are 40A/m for 0 - 1000m, 15A/m for 1000 - 1500m and 4.3A/m for 1500 - 3500m. These values are pessimistic values in that for lower frequency modes (less than 1MHz), which are most significant in lightning discharges, the rates of decay will be much lower. Using the above three values, the percentage error in assuming constant current in each segment for different number of channel sections is given in Table1.

Where the linear triangular mesh is to be wholly automatically generated, the input specifications required are the number of segments the lightning channel is to be divided into, the time step t and the time limit. The mesh generated in this manner proves to be fine and the accuracy is enhanced, but is very expensive in terms of the matrix size to be handled by the solver. Alternatively if fewer nodes are to be specified at distances away from the channel in a graded mesh, the horizontal distances from the channel and the number of nodes in each vertical line ought to be specified. The number of nodes above the channel are specified separately, and may be few in number.

RESULTS

The leader stroke pulse which resembles current due to charging of an RC circuit triggered by a constant voltage source, is given by the following empirical model:

$$I(t) = I_0 \exp(-(z/\lambda + t/\tau)) \quad (10)$$

where z is the height, λ = 1500m and τ = $3\times10^{-5}s^{-1}$. Computed magnetic fields ,for I_0 = 0.5kA, are given in Figure3. The fields are plotted from the instant at which they arrive at the respective points; the travel times are not shown.

This paper does not address itself to the task of return stroke modeling. Two widely used empirical models were tried out; namely, the Bruce-Golde type model (Model1)[10]

$$I(t) = I_0[\exp(-\alpha t) - \exp(-\beta t)] + I_1[\exp(-\delta t) - \exp(-\varepsilon t)] \quad (11)$$

with velocity

$$V(t) = V_0 \exp(-\gamma t) \quad (12)$$

where

I_0 = 30kA I_1 = 3 kA

$\alpha = 10^5 s^{-1}$ $\delta = 10^3 s^{-1}$

$\beta = 3\times10^6 s^{-1}$ $\varepsilon = 10^4 s^{-1}$

$V_0 = 10^8 m s^{-1}$ $\gamma = 3\times10^4 s^{-1}$

(The current does not decay with height). The most recent empirical model (Model2)[11] is where the current surge is prescribed to be composed of three components. The first is composed of four linearly varying components: (1) $t \leq$ 1microsec, 5kA/microsec (2) $1 < t \leq$ 2microsec, 20kA/microsec (3) $2 < t \leq$ 4microsec, -2.8kA/microsec, (4) $4 < t \leq$ 40microsec, -0.25kA/microsec. The second component is a 3.1kA uniform current and the third component, called corona component,is identical to the second term in (11), with I_0 = 31 Δ z, α and β as before; Δz is the length of each section the lightning channel is divided into. Both the first and third components decay as exp(-z/λ). (The numbere quoted above differ from those used in the original work). Space does not permit discussion of return stroke modeling[12].

For the straight, vertical lightning channel a semi-analytical solution for the vector potential at earth point P, due both to source and image elements, could be obtained from [15]

$$A = \frac{\mu_0}{4\pi}\int \frac{[j]}{R}\,dV \quad (13)$$

$$= \frac{\mu_0}{4\pi}\sum_{n=1}^{2N}\frac{[I_n]}{R_n}\Delta z \quad (14)$$

where

μ_0 = permeability of free space

R_n = the distant of the nth channel element from P

$[I_n]$ = retarded current in the nth element; i.e. at instant $(t-R_n/c)$, where c is the velocity of light.

N = total number of elements

The error in calculating vector potentials due to the division of the channel into finite elements is calculated from (14) and plotted in Figure4. For good accuracy, the minimum number of channel sections should be greater than 25 (see Table1). If 25 sections is assumed to give 100 percent accuracy, then an error of 12 percent for 1km and 8 percent for 25km will exist if the channel is divided into 10 sections. Magnetic fields for Model1 and Model2 near the lightning channel are given in Figure5(a) and 5(b) respectively. Magnetic fields at larger distances were calculated with a sparse grid system to keep the number of nodes below 300; retardation effects were not included. Calculated fields for Model2 are given in Figure6(a) and 6(b).

A compromise must always be reached between accuracy and cost of computation[14]. Further comparisons were made between the solution of A at ground level, from (7) and (14). The accuracy of the finite element method was found to be very good[6]. But for distances greater than 25km acceptable accuracies could not be reached for a mesh size which could be solved for A in 2 hours on a main-frame ICL2988 machine. A feature which was observed for Model2 when two few a sections are assigned for channel is fluctuations of the field, which are fine in structure. As such the distributed LCR model of the return stroke[3], which has only been solved for currents with 10 sections, needs further study.

Measured magnetic fields[15] for leader strokes agree with the computed fields in structure. Magnetic fields radiated from return stroke, peak at time instants greater than 3microsec, and this peak is on a slowly varyiing hump of the waveform. At distances far removed from the flash, the peak is dominated by the rapidly increasing component of the current. It is of interest to note that the magnetic fields calculated from Model1 (Figure5(a)) for near fields also agree with the measured pattern of the magnetic fields. Futhermore the magnetic field wavefront for Model1 is concave, a notable feature of fields on submicrosecond time scale.More discussion, with magnetic fields calculated with submicrosecond time step, is required before the old empirical model[16] is done away with, for more complex models.

For studies on the effects of branch currents and tortuosity of lightning channel, is it necessary to go for three dimensional computation? It is sufficient to carry out studies on a two dimensional cartesian problem to determine the possible high frequency effects of branch currents of the first stroke; but if accurate results are required a three dimensional simulation is necessary. It should be pointed out that an interactive graphics system[17] will greatly ease the burden on the user and permit mesh refinement techniques to increase accuracies when required. The $\underline{J} \times \underline{B}$ force could also be computed using the finite element method[18]. Force inside the channel could also be determined since fields inside the channel is calculated; the channel radius becomes an important parameter.This also makes the finite element method attractive as a multi-purpose computer package.

CONCLUSIONS

The finite element has been successfully used in civil engineering problems[19] and steady state electrical problems[20]. It proves to be a good tool in solving lightning associated problems. The application of the method for such transient and spatially large problems has much scope for improvement and application. All results reported here were limeted to a 2 hour computer run, which particularly limited the number of nodes assigned above the ground plane.Currents induced in a large scattering body near to the lightning flash and the contribution of branch currents to the magnetic fields are at present being considered using the program developed in FORTRAN77 language. Efficient and user friendly grid generating routines[21] will be necessary if expensive three dimesional simulation is required.

ACKNOWLEDGEMENTS

Dr.S.R.H.Hoole (Elect. & Comp. Eng. Dept.,Drexel University,Philadelphia, U.S.A.)has been the first author's sole tutor in the finite element method.Dr.N.St.J.Braithewaite (Dept. of Eng. Science,Oxford University,U.K.) has made many helpul suggestions to test and to develop the computer routines.

REFERENCES

[1] B.F.J.Schonland,The Lightning Discharge, in: The Encyclopaedia of Physics,22,(Spriger Verlag,1956),576
[2] R.G.Fowler,Lightning, in: Atomic Collision Physics,5,(Academic Press,1982),32
[3] P.F.Little,Transmission Line Representation of a Lightning Return Stroke,J.Phys.D,11,(1978),1893
[4] S.I.Braginskii,Theory of the Development of a Spark Channel, in: J.A.Rees(Editor), Electrical Breakdown of Gases,(Macmillan 1973),Paper16
[5] G.D.Weidman and E.P.Krider,The Fine Structure of Lightning Return Stroke Waveforms,J.Geophys.Res.,83,(1978),6239
[6] P.R.P.Hoole and S.R.H.Hoole,Finite Element Computation of Magnetic Fields from Lightning Return Strokes, To appear, J.Maths and Comp. in Simulation,(1985)
[7] S.R.H.Hoole, Z.J.Cendes and P.R.P.Hoole, Renumbering and Preconditioning in Conjugate Gradient Algorithm, To appear, J.M.C.S.,(1985)
[8] B.M.Irons,A Frontal Solution Program for Finite Element Analysis, Int. J. of Num. Meth. in Eng.,2,(1970),5
[9] B.M.Weedy,Electric Power System, 3rd Ed.,(John Wiley,1980)
[10] N.St.J.Braithwaite and M.J.Cooke, A Survey of the High Frequency Effects Associated with the Lightning Discharge, Oxford University Engineering Science Labcratory Report, No.1290/1979,(1979)
[11] M.J.Master,M.A.Uman and R.B.Standler, Calculation of Lightning Return Stroke Electric and Magnetic field above ground, J.Geophys.Res.,86,(1981),12127
[12] P.R.P.Hoole,Lightning - Earth Flash Return Stroke,M.Sc. Thesis, Dept. Eng. Sci., Oxford University,(1984)
[13] C.H.Durney and C.C.Johnson, Introdution to Modern Electromagnetics,(McGraw-Hill,1969)
[14] P.P.Sivester, Software Engineering Aspects of Finite Elements, in: M.V.K. Chari and P.P.Silvester(Editors), Finite Elements in Electric and Magnetic Field Problems, (John Wiley,1980)
[15] M.A.Uman and E.P.Krider, A Review of Natural Lightning: Experimental Data and Modeling,IEEE Trans.EMC,24,(May 1982),79

[16] C.E.R.Bruce and R.H.Golde, The Lightning Discharge,JIEE,88,(1941),487
[17] S.R.H.Hoole and P.R.P.Hoole,An Expert System for Interactive Finite Element Design, Proc.of 3rd Annual Workshop on Interactive Computing,CAE:Electrical Eng. Education, (IEEE Comp. Soc. Press,Oct 1984)
[18] S.R.H.Hoole and P.R.P.Hoole, On Finite Element Force Computation From Two and Three Dimensional Magnetostatic Field,To appear, J. of Applied Physics,April 15,(1985)
[19] O.C.Zienkiewicz,The Finite Element Method,3rd Edition,(McGraw-Hill,1977)
[20] P.P.Silvester and R.L.Ferrari,Finite Elements for Electrical Engineers,(Cambridge University Press,1983)
[21] S.R.H.Hoole,A Memory Economic 3-D Finite Element Mesh Generator, The Small Comp. (R)evolution,(Computer Soc. Press, Sept.1984),111

N / H (METRES)	5	10	20	25
0 – 1000	53	17.5	9.5	7.5
1000 – 1500	15	7	3.4	2.7
1500 – 3500	4	2	0.94	0.08

Table1. Percentage Error Due to Lightning Channel Sectioning

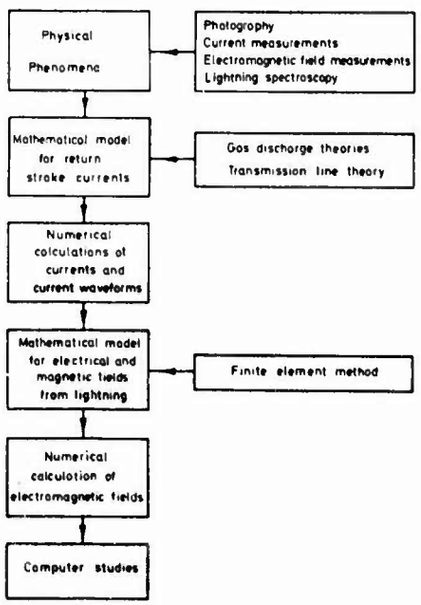


Fig. 1 Lightning Study Chart

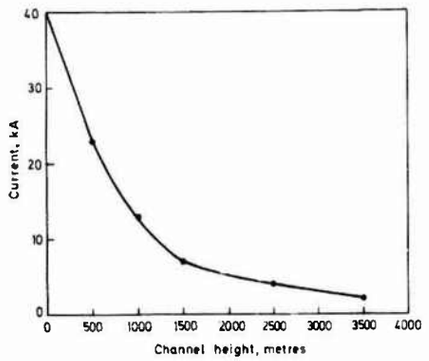


Fig. 2 Decay of Current along a transmission line

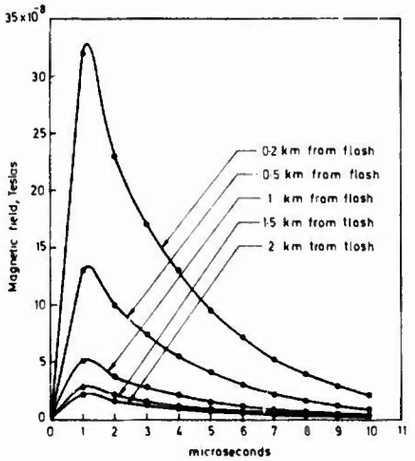


Fig. 3 Calculated Magnetic Fields from leader stroke; at ground level

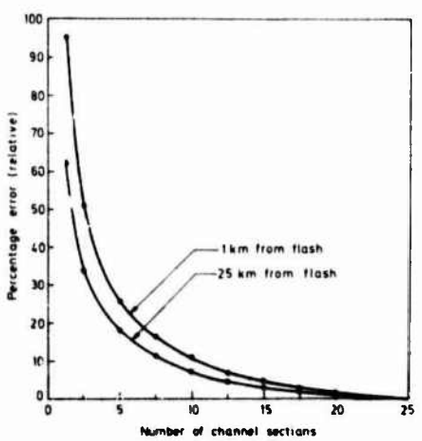


Fig. 4 Percentage error in Vector Potential Calculation

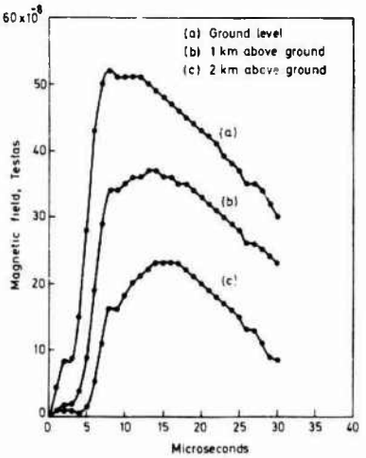


Fig. 5 (a) Magnetic Fields from Return Stroke Model 1 (1.6 km from flash)

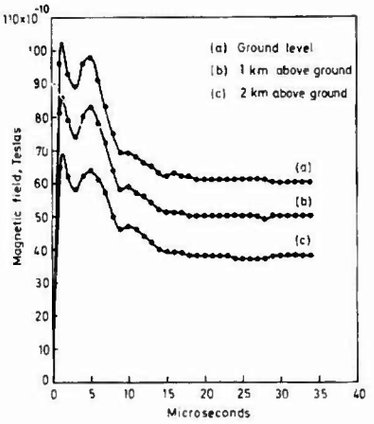
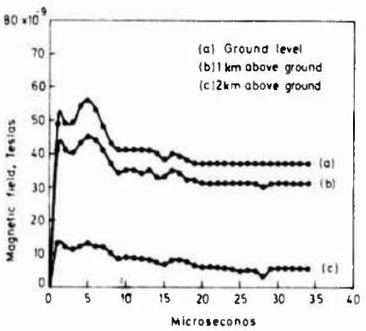
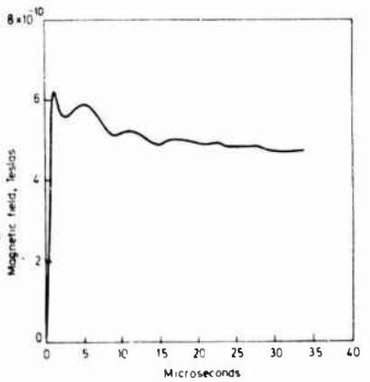


Fig. 6 Magnetic Field from Return Stroke Model 1 (a) 5 km from flash



(b) Magnetic Fields from Return Stroke Model 2 (1.6 km from flash)



(b) 25 km from flash (little difference in fields at different heights)

A NEW MODEL OF LIGHTNING SUBSEQUENT STROKE - CONFRONTATION WITH TRIGGERED LIGHTNING OBSERVATIONS

P. Hubert

Service d'Astrophysique, Centre d'Etudes Nucléaires de Saclay, 91191 Gif-sur-Yvette Cedex, France

Abstract - The electric current, the electric field and the magnetic field signals produced by a triggered lightning subsequent stroke are compared with the predictions of a model which assumes that the return stroke can be explained by the sole transportation to the earth of the negative charge carried by the leader. While the current and the magnetic field signals are satisfactorily explained, the model predicts, at a distance of 100m, an electric field jump, ΔE, 3.7 times larger than the observed value. The deficit in E seems to be common in big subsequent strokes, since the ratio of ΔE to the peak current, I_{max}, decreases with I_{max}. However, in first strokes the same ratio is appreciably larger. A more sophisticated model is needed to take care of these observations.

1 - INTRODUCTION

This work is an attempt to establish theoretically and to justify experimentally, a model describing as a function of space and time the displacement of electric charge and the flow of electric current along the channel during a lightning subsequent stroke. This model considers the descent of the dart leader and the upward progression of the return stroke. It has much in common with the model proposed by Lin et al /1/ and improved by Master et al /2/, but it differs in several respects. On the one hand it has the advantage to predict the electric field and the magnetic field variation during the descent of the dart leader and to avoid the seldom justified assumption of a straight vertical channel. On the other hand, it is drastically simplified at the present stage and will need further refinement before being fully acceptable.

Since it has been observed that the triggered lightning subsequent strokes are, as far as we know, exactly similar to natural lightning subsequent strokes /3,4/, triggered lightning offers an unprecedented occasion to check any theoretical prediction on the subject. This is the object of the present contribution.

A physicist's dream is a "typical" stroke observed with a full set of measuring equipment, cleverly adjusted and working perfectly. In spite of some obvious imperfections, the stroke considered below was initially considered as the best approximation to an ideal case among all the events observed up to now. As a first step it has been decided to limit the discussion to this sole event.

2. DATA COLLECTION

2.1 The observation was made in August 1981 during a triggered lightning campaign at LANGMUIR Laboratory (USA-New Mexico) /4/. The stroke considered below occured 825 ms after the beginning of the flash n° 8116. Information on this flash can be found in /4, 5, 6 and 7/.

2.2 The lightning current was measured with a coaxial shunt and the magnetic signal with a ferrite antenna. The technique is the same as described in /8/.

The electric signal measurement used a horizontal flat plate antenna /9/ facing upwards with an arrangement permitting a theoretical computation of the geometrical field enhancement factor. This factor is 1.63, a value small enough to avoid any excessive corona effet.

The distance from the lightning struck point to the magnetic sensor was 191m. The distance to the electric sensor was 102m.

2.3 The three dimensional geometry of the channel has been obtained with a pair of pictures interpreted following a stereographic method described in /10/. One picture of the pair (photo A) was kindly supplied by R.Orville, it appears on the left of fig 2 in ref /7/. The other picture (photo B) was obtained by the author's wife from a place such that an angle of 51.9 deg. exists between the two lines of sight. The field of photo A is limited to the lower part of the channel, from zero up to 620m above ground (channel length: 821m). Above this point, the photo B has been interpreted by assuming that on photo A the channel picture proceeds in the direction defined by the last visible segment. Using this procedure, the last visible point on photo B is 1025m above ground, the channel length being 1635m. Thereafter it has been assumed that the channel is a straight line in the same direction as the last computed segment.

2.4 The velocity, VL, of the dart leader and, VRS of the return stroke has been measured with an optoelectronic device developed at St Privat /11/. The results are :

$$VL = 3.0\ (\pm\ 0.3)\ 10^7\ m/s$$

$$VRS = 1.4\ (+\ 0.4, -\ 0.26)\ 10^8\ m/s$$

On the same flash, with a streak camera technique, velocity measurements have been performed simultaneously by R.Orville's team /7/. However their camera included a shutter which was open during a time too short for the late stroke considered here. For the earlier strokes, the agreement between the results obtained with both techniques is sufficient to give confidence in the figures given above.

An important fact quoted in /7/ is that in all the strokes observed with the streak camera an upward connecting streamer met the downward leader at the height of approximately 20m above ground. An observation made by A.Eybert-Berard and L.Barret with a slower streak camera /6/ seems to indicate that the same is probably true for the stroke considered here but the image of the leader is so faint that the interpretation is ambiguous.

3 - THEORY AND METHOD

The diameter of the channel is supposed small enough to consider it as a filament on which any point is defined by its curvilinear abscissa, s. At the ground s=0, above ground it is positive.

The model is expected to give the current, I (s,t) and the linear charge density, λ (s,t), where t is the time.

In the case of a filament, the classical Maxwell equations /12,13/, can be written:

$$\partial\lambda/\partial t = -\partial I/\partial s \qquad (1)$$

$$\vec{E} = -\vec{\nabla}\phi - \partial\vec{A}/\partial t \qquad (2)$$

$$\vec{B} = \vec{\nabla} \times \vec{A} \qquad (3)$$

$\vec{E}$ and $\vec{B}$ are the electric and the magnetic field.

ϕ and $\vec{A}$ are the retarded scalar and vector potentials.

At any place of observation:

$$\phi(t) = \frac{1}{4\pi\varepsilon_0} \int_{CHANNEL} \frac{\lambda(s, t-R/c)\, ds}{R} \qquad (4)$$

$$\vec{A}(t) = \frac{\mu_0}{4\pi} \int_{CHANNEL} \frac{I(s, t-R/c)\, \vec{ds}}{R} \qquad (5)$$

$\vec{ds}$ is a vector of length ds parallel to the channel at the point of abscissa, s, R is the distance between the same point and the observer, c is the speed of light.

Taking into account I and λ given by the model and the shape obtained as explained in § 2.3, a computing program has been developed which performs the integration of the equations (4), (5) and the derivations implied by (2) and (3) in order to obtain $\vec{E}$ and $\vec{B}$ at the position of their respective sensor. The computation takes care of the image principle, assuming that the ground is a flat, horizontal, perfectly conducting plane.

The altitude of the observer can be chosen at will in order to simulate a measurement on the ground or close to a flying aircraft. In the ground observation reported here, the vertical component E_z and the tangential component B_θ are considered only. For the sake of simplicity the subscripts Z and θ are omitted below.

Since the equations are quite general the method is valid for observation at any distance. The only approximations are related to the properties of the ground and to the imperfect knowledge of the shape of the channel.

4 - THE MODEL

4.1 The model described here has been developed completely with analytical expressions which are simple but too lengthy to be printed in this report where the basic ideas are more important for the reader's information.

At each step, use has been made of the charge conservation equation (1) in order to deduce λ when I is known and vice versa.

4.2.1 Concerning the dart leader the assumptions are as follows.

Initially, the negative charge Q is concentrated on a single point at the top of the channel where $s=s_T$. During the descent this charge expands in such a way that, as proposed by Golde /14/, the density has an exponential distribution:

$$\lambda = Q \exp(-s/L)/(L(\exp(-s_1/L) - \exp(-s_T/L))) \qquad (6)$$

L is a characteristic length, s_1 is for the lower end of the leader

$\lambda = 0$ if $s < s_1$

Taking into account the remark at the end of § 2.4 and adopting the point of view of Lin et al /1/, in what concerns subsequent strokes, the influence of the upward going connecting streamer is neglected.

4.2.2 After the time, t_L , when the leader reaches the ground and before the instant when the point under consideration has been reached by the return stroke (RS.) the current goes on flowing but it decays exponentially with a time constant which respects the continuity of I and of $\partial I/\partial t$ when $t = t_L$.

4.3.1 Concerning the return stroke, in conformity with the idea expressed in /1/, it is assumed that the arrival of the R.S. turns on distributed current sources which send a negative current downwards with the speed of light. For an element ds situated in s, the contribution to the current is:

$$dI = (\lambda_0/\tau) \exp(-\Delta t/\tau)\, ds \qquad (7)$$

λ_0 is the density of charge which exists when the R.S. arrives in s. This charge represents the charge deposited by the leader and modified by the process occurring before the arrival of the R.S. as described in § 4.2.2.

τ is an adjustable time constant.

Δt is the time elapsed between the passage of the R.S. and the instant when the point s is considered.

4.3.2 Another contribution to the current in the R.S. is the current which crosses the boundary at the top of the R.S. This current is evaluated in the same way as it is in § 4.2.2. After crossing the boundary it travels downwards with the speed of light.

5 - OBSERVATION VERSUS COMPUTATION

5.1. Figures 1,3,5 represent respectively the current, the magnetic and the electric signals recorded as explained above. Figures 2, 4, 6 are the same signals computed with the parameters L=15000 m and $\tau = 10^{-6}$s. On the computed curves, the vertical scale is normalized so that the maximum current I max = 20 kA is the same, on fig 1 and fig 2.

5.2. On the current curves (fig 1 and 2) the time to half value is approximately the same $t_{\frac{1}{2}} = 65\ \mu$s. This agreement is the result of the choice of L. The rise time is shorter on the computed curve, the main reason being that τ has been chosen too small. No attempt has been made for a better choice because this would be a vain effort as long as the model does not take the connecting streamer into account.

5.3. The observed and the computed magnetic signal (fig 3 and 4) are in rather good agreement in what concerns their shape. On both curves, it is interesting to remark the slow rise which precedes the steep part of the signal. This slow rise does not exist on the current curve: it is due to the current in the dart leader before it reaches the ground. This observation which validates the dart leader model has been made frequently on triggered lightning strokes.

The amplitude of the observed magnetic signal is 0.16 Gauss, versus 0.26 Gauss for the computed one, the difference is larger than the expected accuracy. An explanation can be found, probably in the non uniform conductivity of the

ground: the probe being only 2m above ground, it can be expected to be rather sensitive to this effect.

It is gratifying to note that the "rule of thumb" expression /4/:

$$B_{max} = \mu_o I_{max} / 2\pi D$$

where the distance D = 191m, gives B_{max} = 0.21 Gauss which is just midway between the observed and the computed value.

5.4.1 The observed and the computed electric field signal shown on fig 5 and 6 have an overall shape which is roughly the same. First the negative charge lowered by the dart leader produces an increase in the absolute value of the negative field. When the leader reaches the ground the charge is drained to the earth and the field recovers its initial value. Normally one would expect that after the stroke the curve should be higher than before because of the disappearance of the charge. This has been observed in many instances but in the present case the difference is unnoticeable because the charge is at a large distance initially.

The comparison between fig 5 and 6 reveals that on the computed curve the recovery is slower and, worse of all, that the amplitude of the computed signal is 3.7 times larger than the amplitude of the measured value.

5.4.2 In order to resolve this major discrepancy several simple hypothesis have been put forward; all but one can be rejected after examination.

A strong corona current occurring near the sensor or on the sensor itself would produce a screening effect but, in that case the positive charge deposited in the air would produce an overshoot on the signal because this kind of charge needs a relatively long time to dissipate.

The short connecting streamer and the tripod mentioned in §2.4 and in /4/, respectively are certainly responsible for some amount of electric field reduction. It is unlikely that the reduction factor would be so large at a distance of 102m with objects about 20m in height. However, as explained in § 2.4 the hypothesis of a longer connecting streamer cannot he excluded.

Changing the value of τ does not solve the problem because the maximum value of E occurs before the launching of the return stroke.

Changing L or using a linear mixture with several different L's has been attempted also without succes.

6 - ELECTRIC FIELD JUMP IN DIFFERENT STROKES

6.1. Considering all the strokes pertaining to four flashes which fell at nearly the same distance from the electric field sensor, an evaluation has been made of the ratio $R = \Delta E / I_{max}$ where ΔE is the field jump due to the return stroke and I_{max} is the peak current. The results are summarized on table I where R_{av} is the average value and c.c. is the coefficient of correlation between I_{max} and R.

Following the nomenclature in /4/, the flash 8123 is "anomalous" and the other three are "pseudo-classical". Consequently, the four flashes present a genuine "first stroke" but only the flash 8123 has a powerful one.

Two important facts emerge from table I:

6.2. In subsequent strokes there is a strong negative correlation between I_{max} and R. In other words, in big subsequent strokes, ΔE is lower than predicted by mere proportionality. This non linearity is probably due to the existence of a connecting discharge, the length of which is greater for powerful strokes. This is in contradiction with the currently held view that the connecting discharge is unimportant in subsequent strokes /1/.

In the flash 8116, the stroke considered above, for a check of the model, has a value R = 0.5 which is one of the lowest in the list. This circumstance explains the failure of the model to predict ΔE correctly.

6.3. In first strokes, the ratio R is larger than it would be in subsequent strokes with the same I_{max}. In fact, in the 1981 observations, the first stroke of most anomalous flashes saturated the E probe electronics. The probable explanation is that the launching of the upward propagating connecting streamer requires, an electric field higher in virgin air, than in the preionised conditions which prevail when the subsequent strokes occur.

7 - DISCUSSION AND CONCLUSION

The model of Lin et al /1,2/ includes three ingredients which they call: corona current, uniform current and break down pulse current. The model above uses only an equivalent to the first ingredient but, with a mixture of L's it incorporates also the second one if one of theL's is infinite. Then the only missing ingredient is an upward going current pulse which transfers a positive charge from the earth to the sky. A preliminary attempt to incorporate such a pulse in the computation indicates that it is not sufficient alone but that the trend is in the good direction. At the time of this writing it seems that a solution may exist by incorporating the effect of a connecting streamer combined with an upward pulse which carries a fraction of the total charge larger than the fraction estimated in /2/.

If one considers the number of measured parameters which have to be explained simultaneously, it is the first time that a lightning stroke model is subjected to a test so severe. In consequence it is not surprising if the first attempt to give a global explanation is only a step in that direction.

Acknowledgements

This research was supported by the "Direction des Recherches et Etudes Techniques" and by "Electricité de France".

References

/1/ Lin, Y.T., Uman, M.A., and Standler R.B.: Lightning return stroke models
J.Geophys.Res., 85, 1571-1583, 1980

/2/ Master, M.J., Uman, M.A., Lin, Y.T. and Standler R.B.: Calculations of lightning return stroke electric and magnetic fields above ground
J. Geophys.Res., 86, 12127-12132, 1981

/3/ Saint Privat d'Allier Research Group: Eight years of lightning experiments at St Privat d'Allier
Rev.Gen.Elec., 9, 561-582, 1982

/4/ Hubert, P., Laroche, P., Eybert-Berard A. and Barret L.: Triggered lightning in New Mexico
J. Geoph.Res.89, 2511-2521, 1984

/5/ Hubert, P. Triggered lightning at Langmuir Laboratory during Trip 81.. Note DPh-EP-8166 Commissariat à l'Energie Atomique Saclay, 1981.

/6/ Eybert-Berard, A., and Barret, L.: rapport de campagne Trip 81, Note CENG-DEMT-LASP-82-10, Commissariat à l'Energie Atomique Grenoble 1982

/7/ Idone, V.P., Orville, R.E., Hubert, P., Barret,L. and Eybert-Berard, A.: correlated observations of three triggered lightning flashes. J.Geoph.Res. 89, 1385-1394, 1984

/8/ Hubert, P., and Fieux, R. Mesure des courants de foudre à la station de St Privat d'Allier Rev.Gen.Elec.5, 344-349, 1981

/9/ Kitagawa, N., and Brook, M. A comparison of intracloud and cloud to ground lightning discharges J.Geoph.Res. 65, 1189-1201, 1960

/10/ Hubert, P. Methode stereographique pour calculer la forme géométrique du canal d'un éclair. Note DPh-EP-82.007, Commissariat à l'Energie Atomique, Saclay, 1982

/11/ Hubert, P., and Mouget, G. Return stroke velocity measurements in two triggered lightning flashes J.Geoph.Res., 86, 5253-5261, 1981

/12/ Uman, M.A., Mc Lain, D.K., and Krider E.P. The electromagnetic radiation from a finite antenna. Am.Journ.of Physics 43, 33-38, 1975

/13/ Levine, D.M., and Meneghini, R. A solution for the electromagnetic fields close to a lightning discharge 8th International aerospace and ground conference on lightning and static electricity, Fort Worth 1983, DOT-FAA-CT- 83-25, paper n°70

/14/ Golde, R.H. Lightning protection page 27 Edward Arnold publisher, London 1973.

TABLE 1

	FIRST STROKE		ALL SUBSEQUENT STROKES			SUBSEQUENT STROKES WITH $I_{max} > 5$ kA.		
FLASH N°	I_{max} kA.	R	n	R_{AV}	C.C.	n	R_{AV}	C.C.
8116	3	1,6	27	0,9	-0,74	14	0,67	-0,91
8120	2,2	2,6	23	1,0	-0,71	16	0,95	-0,60
8123	35	>1,6 ♦	20	1,5	-0,78	9	1,2	-0,79
8124	1,7	2,8	31	1,1	-0,74	21	0,95	-0,69

♦ Electric field sensor saturated

I_{max} : peak current

R : ratio $\Delta E / I_{max}$ where ΔE is the electric field jump

R_{av} : average R

c.c. : correlation coefficient between R and I_{max}

n : number of strokes

Fig.1. Measured current

6.4 kA/division

20 μs/division 2 μs/division

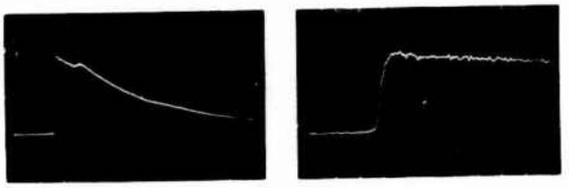


Fig.2. Computed current

5.8 kA/division

20 μs/division 2 μs/division

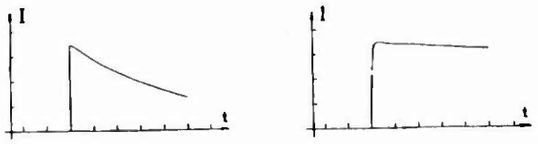


Fig.3. Measured magnetic signal

3.3. 10^{-2} Gauss/division

20 μs/division 2 μs/division

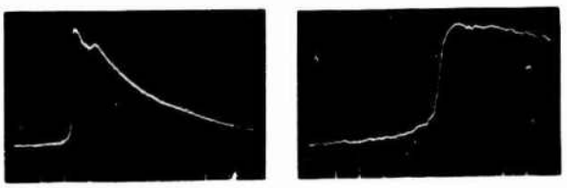


Fig.4. Computed magnetic signal

5.6 10^{-2} Gauss/division

20 μs/division 2 μs/division

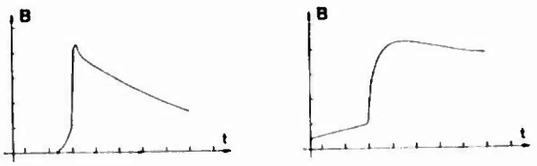


Fig.5. Measured electric signal

1.9 kV/m/division

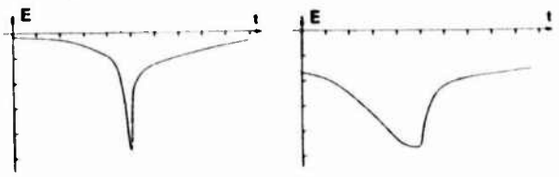
20 μs/division 2 μs/division



Fig.6. Computed electric signal

7.7 kV/m/division

20 μs/division 2 μs/division



THE ENERGY REQUIREMENTS OF AN AIRCRAFT TRIGGERED DISCHARGE

J.A. Bicknell and R.W. Shelton

Physics Department, University of Manchester Institute of Science & Technology, Manchester M60 1QD, U.K.

Abstract

The corona produced at aircraft surfaces requires an energy input before the corona can develop into a high current discharge and, thus, a possible lightning stroke. This energy must be drawn from the space charge field of the thundercloud and, since this is of low density, the unique propagation characteristics of positive corona streamers may be important. Estimates of the energy made available by the propagation are compared with laboratory measurements of the minimum energy input required to trigger a breakdown. The comparison indicates a minimum streamer range for breakdown of several tens of metres. Also estimated is the energy released as a consequence of streamer-hydrometeor interactions; this is shown to be significant so that breakdown could depend upon the precipitation rate within the cloud. Inhibiting streamer production may therefore provide an aircraft with a degree of corona protection.

INTRODUCTION

It is axiomatic that the lightning discharge draws energy from the electric field of the host thundercloud but the mechanism whereby this energy, which is of low density and large volume, is funnelled into a relatively small discharge channel, is not at all clear. A somewhat similar situation prevails in the consideration of charge movement and distribution as evidenced by the charged and uncharged leader controversy (Kasemir 1984). It is common to suppose that the breakdown of long non-uniform gaps provides a good analogy with that of the lightning discharge and certainly detailed studies such as those conducted by the Les Renardieres Group (1972, 1974) have revealed a marked similarity in the behaviour of the respective leader-return stroke phase. However we are here only concerned with the triggering of the discharge and, in this case, a comparison of the two reveals a number of discrepancies particularly with regard to the magnitude of the energies and energy densities.

Except for possibly plane-plane electrode geometry the first stage of a breakdown in a gap of laboratory dimensions involves the development of some form of corona and there is no reason to suppose this pattern will not be repeated in a lightning discharge. Suitable natural corona sites in a thundercloud include single hydrometeors (ice, water etc) and colliding water drops (Crabbe 1974) whilst aircraft and rockets provide artificial alternatives. Of course, the appearance of corona is not the sole requirement to ensure a breakdown; corona is a low current phenomona which requires an additional energy input sufficient to promote a transition to arc-like conditions characterised by a sharp increase in electron concentration. According to Barreto (1984) gas heating follows the formation of the weakly ionised plasma of a corona streamer channel. The increase in ionisation required may then be achieved in several different ways depending upon the size of the gap. In long gaps highly luminous ionisation waves are thought to be responsible. Marode (1979) and others have presented breakdown models based upon the joule heating of the streamer channel whilst Sigmond (1982) and Bicknell (1983) have estimated the energy input required to achieve the transition in small gaps of a few cm.

It is the availability of this energy which distinguishes the laboratory gap from the thundercloud. If the long gap is approximated by a concentric sphere arrangement (inner radius a, outer radius b) with the inner sphere raised to a potential V then for $b \gg a$, one half of the capacitative energy is contained within a sphere of radius 2a. For this region the energy ϵ and average energy density $\bar{\epsilon}$ are

$$\epsilon = \pi \epsilon_0 a V^2 \qquad \bar{\epsilon} = 3\epsilon_0 V^2/28a^2$$

For the Les Renardieres impulse generator with a = 0.3m, b = 10m the breakdown voltage is ~2MV or:

$$\epsilon = 34\,J \qquad \bar{\epsilon} = 42\,J\,m^{-3}$$

In practice, a is the radius of a hemispherically capped rod so that the approximation underestimates the average energy density in the vicinity of the rod. With such large energy densities, the corona originating at the electrode achieves the required increase in channel ionisation and the transformation to a corona leader which completes the initiation or triggering phase. Gibert (1984), using a Schlieren technique has captured the phenomena beautifully in long gaps. From

studies of surface breakdown Boulay (1984) has shown that the corona leader, consisting of a conducting stem with corona at the head, can propagate as a single entity once formed.

By contrast, in a thundercloud the energy densities available for corona growth are significantly lower. The ambient space charge field energy density is only $0.4 Jm^{-3}$ for a field of $3 kVcm^{-1}$. The enhanced fields near charged or uncharged hydrometeors provide larger densities but only in extremely small volumes. Charged aircraft may serve as rather large energy sources but to approach the values cited above would require an aircraft of, say 10^{3} pf capacitance to be raised to a potential well in excess of IMV if the space charge field is ignored. Clearly, corona from static wicks would prevent the necessary charge accumulation. In any case the mechanism which causes natural lightning would be equally applicable to any discharge triggered by aircraft. In the absence of large energy densities some means of tapping the energy stored in large volumes must be considered. Corona propagation provides an obvious possibility with dissipation increasing with range. We summarize briefly below the more relevant properties of corona together with the proposed energy requirements for breakdown. These are then used to estimate the necessary range of the corona.

Corona

Any conductor in a sufficient electric field displays ambipolar corona with the onset field generally inversely dependent upon the conductor length in the direction of the field. Both corona polarities can exhibit optical and current modulation; the positive frequency (1-10kHZ) is lower than the negative frequency (50kHZ-1MHZ) Humood (1984). There exists a minimum field E_o in which corona can propagate indefinitely - the critical or stability field. The value of this field is however significantly lower for positive corona streamers than for negative streamers (Tang 1982). At atmospheric pressure we have

$$E_o^{+} \simeq 4.5 \text{ kV/cm} \qquad E_o^{-} \simeq 18 \text{kV/cm}$$

with somewhat lower values at lower pressures. Since measured large scale electric fields in a thundercloud do not exceed ~4kV/cm (Winn 1971) then only positive streamer propagation is initially possible with some allowance being made for altitude. The negative corona remains essentially localised. The streamers branch as they travel away from the aircraft or hydrometeor at a velocity $>10^{5} ms^{-1}$ (Tang 1982); each active streamer consisting of a dense positive space charge ($>10^{-11}$ C) at the head of a trail of quasi-neutral plasma having a diameter ~50μm (Marode 1975). From Lichtenberg figures taken in small gaps the streamer number density at the front of the propagating system has been estimated to be $2 \times 10^{4} m^{-2}$ and approximately constant (Bicknell 1980).

Energy to Initiate a Breakdown

The corona propagation is dissipative, the energy being used for ionisation, required to extend the channel; excitation, with subsequent radiation; and channel heating. The newly created channel has an electron density of $\sim 10^{20} m^{-3}$; most of the energy released by the displacement being used in the creation of this plasma with the field at or near the stability level. Indeed a good estimate of the value of the stability field can be obtained from this proposition. For breakdown the electron density must be increased to $\sim 10^{23} m^{-3}$ and this requires a further energy input. Marode (1979) and others have put forward the idea, supported by model calculations, that joule heating of the channel gas, which leads to an enhanced ionisation coefficient, may be the possible mechanism. The joule heating results from the channel current which grows as the field increasingly exceeds the stability level. Sigmond (1982), using the current profile from corona onset to breakdown in small point-plane gaps has estimated this additional energy input. Bicknell (1983) has used the same procedure but with an electrode geometry which allows the streamers to propagate in a quasi-uniform field. In this case the energy input per unit length of channel required for a breakdown field E_B is just

$$J_o = E_B \int i dt.$$

and appears to saturate at a value of 10^{-1} Jm^{-1} for distances greater than $5 \times 10^{-2} m$. The integration is terminated when the current begins to increase again after the decay of the first corona current pulse. For this reason J_o is not comparable with the much larger values quoted by Israelsson (1984), Uman (1968) and others which refer to the completed arc phase.

Energy and Range Estimates

The propagating streamer system effectively introduces a dipole into the charged region of a thundercloud thus releasing a quantity of energy which increases with streamer range. Most of this energy is consumed in creating the increasing number of streamer channels but if it can be argued that some small fraction is available as an input to a given length of channel, probably located near the origin of the system (eg the aircraft) then at a given range the value of the energy input per unit length will exceed J_o and a breakdown may be triggered. Neither the fraction available nor the breakdown length are precisely known so that estimates made are necessarily only crude such as those at (i) below. An alternative approach is to consider energy inputs which arise as a result of streamer-droplet interactions. Although the amounts involved are much smaller than the dipole energy, the energy is not only more directly available to the channel but is also an input which would not normally occur in the absence of the interaction. For example, if ionising waves are important in long gap breakdown it is difficult to see how

they might arise in a thundercloud in the absence of a cathode unless one regards the hydrometeors as essentially representing an extended cathode. At (ii) the interactions are assumed to reduce the space charge density in the region of the thundercloud occupied by the streamer system and at (iii) the dissipation of the streamer tip electrostatic energy is considered.

(i) Dipole Energy

The negative region of the thundercloud is represented by a spherical volume of radius R_o and a space charge density ρ; the positive charge centre is ignored throughout. A streamer system initiated from an aircraft or hydrometeor at the perimeter of the charged volume where the field is greatest propagates radially into the cloud. If we assume that this deposits a charge +Q at $r = R_o - R$ and -Q at $r = R_o$ where R is the streamer range then the change in electrostatic energy is

$$\epsilon = Q\rho R_o R/3\epsilon_o \qquad \text{for } R \ll R_o$$

ignoring the small energy due to the dipole QR itself. For propagation to occur then the perimeter field must be $> E_o^+$ so

$$\epsilon \simeq QE_oR \qquad (1)$$

propagation continues until the field is $< E_o^+$. If the system is roughly conical of half angle α, a streamer density β and a mean charge per streamer tip of q then

$$Q = R^2 q \pi \beta \tan^2\alpha = aR^2 \quad \text{where } a = \pi q \beta \tan^2\alpha$$

$$\text{or } \epsilon = aE_o^+R^3 \qquad (2)$$

If a fraction f of this energy is made available to a channel of length kR then the unit energy input J is

$$J = faE_o^+R^2/k \geq J_o \text{ for a breakdown}$$

$$\text{or } R \geq \left[kJ_o/faE_o^+\right]^{\frac{1}{2}} = 2.75\left[k/f\right]^{\frac{1}{2}} \qquad (3)$$

for $J_o = 10^{-1}$ Jm^{-1} $E_o^+ = 3 \times 10^5$ Vm^{-1} $\beta = 2 \times 10^4$ m^{-3} $q = 10^{-11}$ C, $\alpha = 15°$. So if only 0.1% of the energy is available for a channel which is 10^{-1} of the streamer range then $f = 10^{-3}$, $k = 10^{-1}$ and the required minimum range is 27.5m.

(ii) Reduction of the Space Charge Density

Streamer-hydrometeor interactions will lead to the deposition on the larger hydrometeors of the tip charge and a reduction of the local negative space charge density. Although the energy involved is considerably less than that considered at (i) the direct interaction could provide a more efficient mechanism for the transfer of energy to a potential breakdown channel, all the interactions being linked by the weakly ionised trails of each streamer. To simplify the calculation we assume that the streamer, originating from an aircraft or hydrometeor near the surface of the spherical thundercloud of radius R_o, reduces the space density in a spherical volume of radius R' near the cloud surface. The electrostatic energy of this volume before the passage of the streamer system is

$$= C\rho^2 R'^5. \quad \text{where } C = 4\pi/15\epsilon_o \text{ for a sphere}$$

so that a reduction of $\Delta\rho$ in the density releases energy of

$$\Delta\epsilon = 8\pi E_o R'^5 \Delta\rho/5R_o \qquad (4)$$

where we have put, since $R' \ll R_o$.

$$\rho = 3\epsilon_o E_o/R_o$$

Making the pessimistic assumption that this energy is dissipated in a channel length of $2R'$ then to trigger a breakdown

$$J = \Delta\epsilon/2R' = 4\pi E_o R'^4 \Delta\rho/5R_o \geq J_o$$

$$\text{or } R'^4\Delta\rho \geq 5J_oR_o/4\pi E_o \simeq 4 \times 10^{-4} \qquad (5)$$

for the values already quoted in (i).

The change in space charge density will clearly depend on the number of interactions per unit volume and therefore on the size distribution of the hydrometeors N(d) and the streamer number density β as well as the tip charge q. From mean free path considerations

$$\Delta\rho = 0.25\pi\beta q \int_{d_s}^{\infty} (d_s + d)^2 N(d)\,dd \qquad (6)$$

Where only hydrometeors greater than the diameter d_s of the streamer channel are considered significant (Phelps 1971). N(d) may be represented by a Marshall-Palmer distribution (Pruppacher 1980) which expresses the rain droplet spectrum in terms of the precipitation rate $\mathcal{R}$.

$$N(d) = n_o \exp(-\Lambda d) \qquad (7)$$

where $\Lambda = 4.1\mathcal{R}^{-0.21}$ mm^{-1} and n_o is a constant, 8×10^3 m^{-3} mm^{-1}.

Thus substituting for N(d) we have

$$\Delta\rho = 2.5\times10^{-7}\pi\beta n_o q \int_{d_s}^{\infty} (d_s + d)^2 \exp(-\Lambda d)\,dd$$

which can be integrated to give (8)

$$\Delta\rho \simeq \frac{5 \times 10^{-7}\pi\beta q n_o \exp(-\Lambda d_s)}{\Lambda^3} \quad \text{for } d_s \ll \Lambda$$

Substituting for $\Delta\rho$ in condition (5) the value of R is

$$R' \geq 56.2\mathcal{R}^{-0.16} \exp(0.1\mathcal{R}^{-0.21}) \qquad (9)$$

where the precipitation rate $\mathcal{R}$ is expressed in units of mm hr^{-1}. R'_{min} is shown as a function of $\mathcal{R}$ in Fig. 1. Here R'_{min} is not the streamer range but the radius of the assumed spherical region which suffers a space charge density reduction; the two lengths are however clearly related so that a similar dependence of the range on $\mathcal{R}$ is to be expected.

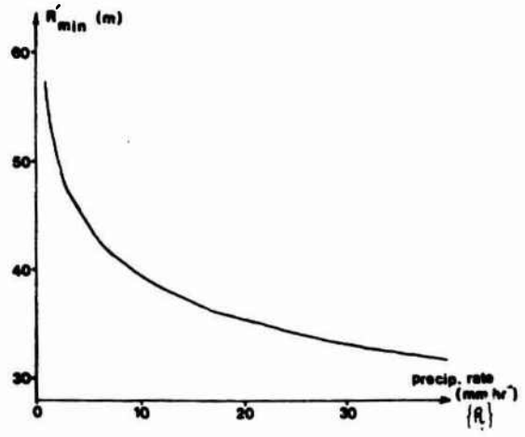


Figure 1.

(iii) Streamer Tip Energy

The dense blob of positive charge at the extremity of each propagating streamer has an electrostatic energy ϵ_t which is released when the tip strikes a hydrometeor. We shall assume that this energy is made available to a section of the streamer system near the origin as in (ii). Tang (1982) has certainly observed luminous waves travelling back along a streamer channel following an interaction with a large simulated hailstone but the microphysics of the process is not well understood. Taking a conical streamer system as in (i) of range R then the energy available is:

$$\pi R^3 \tan^2\alpha \; N(R)\epsilon_t \qquad (10)$$

Where $N(R)$ is the number of streamer-droplet interactions per unit volume. If here R is the streamer range required to trigger a breakdown in unit channel length assuming that all of the available energy is dissipated in this channel then

$$R \geq \left[J_o / \pi \tan^2\alpha \, N(R)\epsilon_t\right]^{1/3}$$

where

$$\epsilon_t = 3q^2/10\pi\epsilon_o d_s \text{ and}$$

$$N(R) = \frac{5\times10^{-7}\pi n_a \exp(-2\lambda d_s)}{\lambda^3} \qquad (11)$$

The lower integration limit for $N(R)$ is here $2d_s$. Taking the average tip charge to be 5×10^{-11} C in a sphere of radius $d_s = 6\times10^{-2}$ mm and with other values as before then typical minimum values for the streamer range are shown in Table 1.

	R mm. hr.$^{-1}$	N(R) m.$^{-3}$	R_{min} m.
Heavy Rain	10	11.5	32
Torrential Rain	50	34.7	22
Rain Gush	100	54.8	19

Discussion and Conclusion

1. Because of the unique propagation characteristics of positive streamers the growth of such a system, we suggest, is a prerequisite for a breakdown triggered by an isolated conductor such as an aircraft. The propagation is essential for the provision of the necessary breakdown energy whilst the relatively low density of the available electrostatic energy implies that the streamer range may be substantial (i.e., tens or hundreds of meters). Although the estimates made of the minimum range are subject to large errors based as they are on crude assumptions, extrapolation of small gap data and an imprecise knowledge of the physical processes involved, the concept of a minimum range remains, nonetheless, plausible.

2. It seems unlikely that thundercloud electric fields achieve magnitudes much in excess of the streamer stability field; the much favoured concept of the existence of pockets of high field must be ruled out on fundamental grounds. In these circumstances the energy input which results from streamer-droplet interactions may well be crucial in triggering a breakdown. Thus a dependence of the breakdown on the precipitation rate within a cloud may exist where, generally, the larger precipitation rates require smaller cloud volumes in which the ambient field exceeds the streamer stability field.

3. The largest ambient fields will be located at the periphery of the negative (or positive) space charge volume and it is here that the streamers are most likely to originate. If the field falls below the stability level before the minimum range is achieved, the breakdown would not materialise but a number of droplets or hydrometeors would be left carrying the positive streamer tip charge. This may explain the measurements of Christian (1983) who found a small number of graupel particles with an average charge of 2.9×10^{-10} C in the negative region of a thundercloud where particle charge was an average -3.7×10^{-11} C. The positive charge is typical of a streamer tip charge values.

4. The energy estimates have been based on a single positive streamer system. In practice the systems are repetitive at a frequency of ~1kHz so that, provided the ambient field is not reduced below the stability level, several systems may contribute to the total energy available with a corresponding reduction in the range. At a speed of 500mph an aircraft moves only ~25cm in the time interval between each system so that the position of the potential breakdown channel, which is most probably located adjacent to the aircraft at the base of the streamer system, is little changed allowing the energy input to be cumulative.

5. If positive streamers are indeed a prerequisite for a triggered breakdown, as suggested here, then inhibiting their production should prevent the breakdown and thus offer the aircraft some form of corona protection. Stabilising the positive glow corona mode (Bicknell 1984) may be a means of achieving

this desirable result.

References

Barretto, E. (1984)
VII Int. Conf. on Atmos. Elec. (ICAE) Albany, New York

Bicknell, J. A. and Humood, B. (1983)
8th Int. Aerospace and Ground Conf. on Lightning and Static Electricity (IAGCLS), 42.1., Fort Worth, U.S.A.

Bicknell, J. A. and Humood, B. Y. (1984)
9th IAGCLS, Orlando, U.S.A.

Bicknell, J. A. and Sadik, A. S. (1980)
VI ICAE, Paper V11-2, Manchester, U.K.

Boulay, J. L., and Larigaldie, S. (1984)
9th IAGCLS, Orlando, U.S.A.

Christian, H., Lillie, L., Saunders, C. P. R. and Hallett, J. (1983)
8th IAGCLS, Paper 25.1, Fort Worth, U.S.A.

Crabbe, J. A. and Latham, J. (1974)
Quart. J. Roy. Met. Soc., 100, 191-202

Humood, B. Y. (1984)
Ph.D. Thesis, University of Manchester Institute of Science & Technology, Manchester, U. K.

Gibert, A., Domens, P., and Dupuy, J. (1984)
VII ICAE, Albany, New York

Israelsson, S., Lundquist, S. and Scuka, V. (1984)
VII ICAE, Albany, New York

Kasemir, H. W. (1984)
VII ICAE, Albany, New York

Les Renardieres Group (1972)
Electra, 23

Les Renardieres Group (1974)
Electra, 35

Marode, E. (1975)
J. Appl. Phys. 46(5), 2005-2020

Marode, E., Bastien, F., and Bakker, M. (1974)
J. Appl. Phys., 50(1), 140-146

Phelps, C. T. (1972)
J. Geophys. Res., 77, 407-411

Sigmond, R. S. and Goldman, M. (1982)
III Int. Symp. on Gaseous Dielectrics, Knoxville, U.S.A.

Tang, T. M. (1982)
Ph.D. Thesis, University of Manchester Institute of Science & Technology, U. K.

Uman, M. A., Orville, R. E., Sletten, A. M. and Krider, E. P. (1968)
J. Appl. Phys., 39, 5162-5168

Winn, W. P. and Moore, C. B. (1971)
J. Geophys. Res., 76, 5003-5017

Acknowledgement

This work is supported in part by the European Office of Aerospace Research and Development (EOARD) on Grant AFOSR 83-0083.

ELECTROMAGNETIC RADIATION ASSOCIATED WITH THE BREAKDOWN OF AIR AT ATMOSPHERIC PRESSURE

A. Bondiou, G. Labaune and J.P. Marque

Office National d'Etudes et de Recherches Aérospatiales, B.P. 72, 92322 Châtillon Cedex, France

Abstract - Previous calculations have shown that the VHF-UHF radiation of lightning would be associated to the transient arc phase of breakdown of the air at atmospheric pressure. Current evolution can be described through the classical laws of the air conductivity variation during the transient arc, with the electric field in the breakdown zone as principal parameter. A first calculation of the radiated field based on a constant electric field during the breakdown and a constant length of the radiating zone revealed to be in good agreement with the experiment.
A more complete calculation is presented here: it is based on the resolution of the discharge propagation equation and thus allows a point by point representation of the conductivity evolution of the plasma. The results are in the form of the temporal and spatial variation of the current in the breakdown zone and lead to the calculation of the electromagnetic field.
Comparisons between this model, laboratory discharge and lightning will be discussed.

I - INTRODUCTION

Research on electromagnetic interference due to lightning is based on a large quantity of in-situ measurements of the level, spectral content and time history of the emitted radiation and on a fair knowledge of the physical processes leading to lightning propagation.
Since 1978, ONERA has undertaken a series of experiments to analyse the triggering and propagation mechanisms of discharges along a dielectric surface. These discharges present numerous analogies with the precursors of natural lightning (current, propagation velocity, plasma properties).
The study of these discharges has shown up triggering mechanisms followed by sharp current variations which may be the main source of VHF-UHF radiation.
In comparison, wideband measurements of natural lightning have shown the pulse nature of this radiation. The basic assumption of our analysis associates these pulses to the fast rising front (a few ns) of the ionization process brought into play by the streamer-leader transition.
A simplified calculation of the radiated field during discharge triggering can be made by studying the case of static breakdown; this assumes a constant emissive component length, conservation current on the interval and a constant electric field. The model, based on the laws governing the development the medium's conductivity at transition, has enabled a first approach to the problem and produces values of the maximum radiated field that are compatible with experiment.
A study carried out in a dynamic configuration (creation and propagation of the transient arc zone producing the radiation) requires calculation of a space-time profile of the current during transition to the arc. A model was developed for the surface discharge experiments.
We shall detail the assumptions and the calculation method along with its application to modelization of the radiated field in this paper.

II - SHOWING UP THE ROLE OF THE TRANSIENT ARC - CALCULATION USING STATIC APPROXIMATION

II.1 Experimental results

The TRIP 82 and TRIP 83 (Thunderstorm Research International Program) experiments carried out in the United States included study of lightning related electromagnetic radiation using wideband systems (600 MHz). The measurements made showed up very short rising front pulses (2 to 5 ns) for peak values included between 30 and 350 mV/m (see Fig. 1) [1]. These pulses are detected at the very beginning of storm activity and follow in succession at a rate of 1 to 20 per microsecond.
The pulse-like characteristic of the radiation observed in wideband has been reported by several authors [2-4] and Proctor [4] has stated that radio noise of this type detected during the various phases of the flash are probably related to the ionization processes of virgin air.

II.2 Basic Assumption - The Function of the Transient Arc

Experiments carried out at ONERA on sparks along a dielectric surface [5, 6] showed up a phase of discharge development forming the transition between a preionization zone (streamer) and the conducting channel. This phase of strong ionization, called the transient arc, involves very fast current variations (on the order of a 10 ns rising front) which can be associated with the pulse-like VHF-UHF radiation studied here [1].

II.3 Current Calculation in the Transient Arc Phase

The simplified model we shall present first consists of the evolution of the current i(t) and calculating of the electromagnetic field radiated during static breakdown, i.e. by assuming current conservation over the entire breakdown zone and a constant value for the electric field.

A theoretical calculation made by Rompe and Weizel [7] enables an approach to the development over time of the conductivity of a plasma created in air at atmospheric pressure, assuming that all the electric energy produced goes into ionization. This assumption is expressed by the following energy equation:

$$\frac{d}{dt}\left(n_e \left(\frac{3}{2} k\, Te + e\, \phi_i\right)\right) = j.E$$

n_e, Te : electronic density and temperature,
ϕ_i : ionization potential of the atom considered,
j : current density,
k : Boltzman constant.

With μ_e the electronic mobility, conductivity $\Gamma = n_e \mu_e e$ obeys the following differential equation:

$$\left(\frac{3}{2} k\, Te + e\, \phi_i\right) \frac{1}{\mu e e} \cdot \frac{d\Gamma}{dt} \qquad \frac{j^2}{\Gamma}$$

and

$$\Gamma^2(t) = 2A \int_o^t j^2\,(u)\, du$$

$$\text{with } A = p_o \frac{\mu o\, e}{\left(\frac{3}{2} k\, Te + e\, \phi_i\right)}$$

p_o : atmospheric pressure in atmospheres.
At atmospheric pressure, for ϕ_i = 15 V and $\mu_e = 4.10^{-2}\ m^2V^{-1}s^{-1}$. The theoretical value of coefficient A is $2.5x10^{-3}\ atm.m^2.s^{-1}V^{-2}$. Experimental verification of this law [8] by interelectrode breakdowns showed that the conductivity of the medium followed this law provided an ionization coefficient $A = 5.10^{-5} m^2 s^{-1} V^{-2} atm.$ is introduced. We shall use A in the rest of the calculation as a phenomenological coefficient, without trying to deduce its physical meaning.
The evolution of the resistance as a function of time of a channel of length δ through which a current i(t) flows is written as:

$$R(i,t) = \left(\frac{p_o\, \delta^2}{2A \int_o^t i^2(u)\, du} \right)^{\frac{1}{2}}$$

Furthermore, in the static case (typically the case of interelectrode breakdown with a field E_o imposed by an outside circuit), current development is as follows:

$$i(t) = E \left(\frac{2A}{p_o} \int_o^t i^2\,(u)\, du \right)^{\frac{1}{2}} + i_o$$

i_o represents the current produced by corona predischarge mechanisms which we shall not describe here.
For $i(t) \gg i_s$:

$$i(t) \simeq i_o \exp\left(\frac{AE^2}{p_o}\, t\right)$$

The transient arc formation time, Tmax, is expressed as:

$$Tmax = \frac{p_o}{AE}\ Log\ \frac{imax}{i_o}$$

For a peak current of 1000 A and a current i_o included between 10^{-7} and 1 A, the value of Tmax varies from 10 to 30 ns (taking E_o = 25 kV/cm, breakdown field in atmospheric air). The general expression of the electromagnetic field Erad radiated at a distance R by the current component of length δ orientated along axis 0x is:

$$\underset{(t)}{Erad} = \frac{\sin\theta}{4\pi\, \varepsilon_o\, RC^2} \int_o^t \frac{di}{dt}\, dx$$

Given the previous assumptions and assuming the current conservation i(t) along length δ:

$$\underset{(t)}{Erad} = \frac{\delta}{4\pi\, \varepsilon_o\, RC^2} \quad \frac{AE^2}{p_o}\, i_o \exp\left(\frac{AE^2}{p_o}\, t\right)$$

The value of length δ is given as a first approximation by the relation $\delta = v Tmax$, where v is the spark propagation velocity (typically for a flash precursor: $v = 5.10^5$ m/s hence δ is around a cm).
For t > Tmax, the transient arc zone is formed and the characteristic current imax of the propagation is reached. We shall assume that in propagation, a zone exists before discharge, whose geometry remains constant and which follows the same laws as the arc channel. Since this ionization front is nondeformable, current i(x,t) during propagation does not depend explicitly on time. Equation (7) becomes:

$$Erad\ (t) = \frac{1}{4\pi\, \varepsilon_o RC^2} \int_o^{\delta} \frac{\partial i}{\partial x}\, \frac{\partial x}{\partial t}\, dx$$

$$Erad\ (t) = \frac{1}{4\pi\, \varepsilon_o RC^2}\ v\ \Delta i$$

where $\Delta i = imax - io$ represents the total variation of current on the gradient zone. The assumption of a quasi nondeformable front in propagation would indicate that the spectral content of Erad is of low frequency.
The peak value of the radiated field during the transient arc phase is around 40 mV/m, for a current imax = 1000 A end an observetion range R = 10 km. The pulse r se time described by equation (8) is 4 ns, this velue is compatible with the measurements. The spectral densities celculated by this method are coherent with the Pierce synthetic curve (Fig. 2).
The description of the trensient erc triggered here corresponds to a stetic breekdown, the current is assumed to be conservative over the full gradient zone whoue length is set et its terminal value $\delta = v Tmax$ without prejudicing the dynamic espect of tront formation.
Implementation of e more accurate calculation would assume knowledge of profiles i(x,t) in the transient arc zone end calculetion of field E development. Develonment of e dynamic model will be based on a theoreticel epproach of transition to arc from a spark along e dielectric surfece.

III - THEORETICAL STUDY OF THE TRANSIENT ARC

III.1 Surface Discharge

Experiments carried out at ONERA, since 1978, involve experimental and theoretical study of discharges propagated through the air along a dielectric surface under the effect of a voltage pulse of around 100 kV [5]. The corresponding experimental device diagram is given in figure 3.

Analysis of the current at a point of discharge and high performance optical instrumentation (time resolved spectroscopy, holographic interferometer) have shown up the various phases of discharge development (Figs 4 and 5).

It should be emphasized that the peak current characteristic values (around one hundred amperes), propagation speed (10^5 to 10^6 m/s) and plasma descriptive parameters (T = 25000 K in the discharge channel [9]) provide the ground for significant analogies between surface discharge and the precursor of natural lightning.

Modelling of the transient arc zone which exists between the leader predischarge and the conducting channel (aee Fig. 5) is of twofold interest: it enables interpretation of the experimental laws of velocity and current, and provides the neceasary source terms for calculation of the radiated electromagnetic field under the hypothesis developed in Part 1.

III.2 Transient Arc Zone Modelling [10]

Experimental study of dischargea provides an estimate of potential distribution $v(x)$ along the propagation axia (see Fig. 4). The calculation described herein enables to predict the evolution of the potential at all points up to the stationary profile given in figure 4. The model is based on the following assumptions.

i) The entire profile is nondeformable during propagation as shown by the photographs, figure 5.

ii) The initial state of the aystem before the transient arc phase can be described as a preionization phaae characterized by a constant field E_0 = 11.2 kV/cm and producing a weak capacitive current io such that:

$$i_0 = CE_0 v l_0$$

C : linear capacity of the dielectric plate,
v : spark propagation velocity,
lo: leader zone length.

iii) The transient arc can be described using the Rompe and Weizel law giving the resistance per unit length R(x,t):

$$R(x,t) = \left[\frac{1}{2A \int_0^t i^2 (u)\, du} \right]^{\frac{1}{2}}$$

The single dimensional description of the spark along the propagation axis Ox allows the application of the classic propagation equation:

$$\frac{1}{R} \frac{\partial^2 V}{\partial x^2} - \frac{1}{R^2} \frac{\partial V}{\partial x} \frac{\partial R}{\partial x} = C \frac{\partial V}{\partial t}$$

Moreover, the condition of non deformability of the wavefront implies the following condition:

$$V(x,t) = V(t - \frac{x}{v(t)})$$

Resolution of the equation system (11) to (14) results in the current and potential profiles during transient arc formation (Fig. 6). Since the field in the conducting channel is very weak (E $\simeq$ 200 V/cm) it can be assumed that the transition zone is fully formed when the total potential available ($V_0 - V_s$: figure 4) is equal to the drop in voltage at the transient arc terminals.

Figure 7 allowa comparison of the experimental and theoretical current profiles in X = 0. In accordance with the experiment, the current rise time value 10 %-90 % is a constant of around 8 ns, independent of the voltage or the capacity of the line. This value Tmax only depends on the law of conductivity applied to the plasma's development over time.

This model, which provides predicted values of peak current and propagation speeds consistent with the experimental results, also permits the prediction of the time history of the electric field in the transition area. According to these resulta, E eatablishes itself very rapidly (in 1 to 2 ns) at a mean value of 25 kV/cm, or approximately at the breakdown field in air at atmoapheric pressure. It would also appear that the current rise time is independent of the local capacitance introduced into the linear equation. Hence, the temporal width of the transient arc phase only dependa on the coefficient appearing in the Rompe and Weizel law (equation 2).

We have, therefore, shown that the Rompe and Weizel law provides an adequate description of the transition phase common to both interelectrode breakdown and diacharge along a dielectric surface. The application of the model developed for surface discharge to the calculation of a field radiated by an analogous discharge propagating in the air seems possible to the extent that the space-time development of the emissive zone does not depend on the local capacitance of the system.

IV - APPLICATION OF THE RADIATED FIELD CALCULATION MODEL

The exact shape of the field radiated by a current component of length $\delta(t)$ is given by equation (15):

$$E_{rad}(t) = -\frac{1}{4\pi \varepsilon_0 RC^2} \int_0^{\delta(t)} \left(\frac{\partial i}{\partial t} + \frac{\partial i}{\partial x} \frac{\partial x}{\partial t} \right) dx$$

The formal structure developed in Part 3 allows calculation of the component $(\partial i/\partial x)(\partial x/\partial t)$, which does not appear in the static model, and the real developement of length $\delta(t)$ of the emissive element.

Figure 8a shows the time history of current i(t) at a point in the transient arc zone; the propagation current was assumed to be constant and equal to the value of imax defined previously for the first approximation.

Figure 8b reproduces the associated radiated field shape for an observation range R = 10 km and a current imax = 100 A.

The dynamic model confirms that the VHF-UHF radiation corresponds, under our assumption, to the transient arc formation phase and not to the later stationary propagation. The rise time 10 %-90 % of the pulse (T = 4.5 ns) and the peak value of the radiated field for R = 10 km (for imax = 1000 A, Epeak = 50 mV/m) are compatible with experimental data.
The radiated field calculated using the dynamic model does not differ significantly from the field calculated in static approximation until propagation current is well over 1000 A (Fig. 9).
A comparison of interest is that of the normalized spectral densities (frequency band: 0-400 MHz) obtained from the two models (Fig. 10). The correction made by the dynamic model is relatively insignificant in the spectral range considered here, which is suggested by the relatively good match of the static model with the Pierce synthetic curve (Fig. 2).

V - CONCLUSION

We have assumed that the pulses observed in the VHF-UHF bands at the beginning of storm activity can be associated with a transient arc phase common to various types of breakdown in air at atmospheric pressure. We have shown that the Rompe and Weizel conductivity law provides a satisfactory description of the strong ionization phase during the formation of a discharge along a dielectric surface. The development of the transient arc only depends on the Rompe and Weizel coefficient and not on local initial conditions.
Description of the phenomenon by a static model representing interelectrode breakdown leads to results similar to those obtained from a dynamic model describing breakdown zone propagation of surface discharge. The introduction of an additional propagation equation in the latter case enables calculation of the field value in the transient arc field (E $\simeq$ 25 to 30 kV/cm) as well as the development over time of the emissive element length.

VI - ACKNOWLEGDEMENTS

This work has been carried out with the support of the Direction des Recherches Etudes et Techniques of the Defense Ministry.

REFERENCES

[1] - G. Labaune, "Rôle de l'arc transitoire dans le rayonnement des ondes métriques et décimétriques de l'éclair", Ann. des Télécom. 39, Nos 5-6 (mai-juin 1984).

[2] - C. Baum, "Measurement of Electromagnetic Properties of Lightning with Ten Nanoseconds Resolution", Lightning Phenomenology Notes n° 3 (1982).

[3] - G. Labaune, A. Delannoy, P. Richard, P. Laroche, "Hypothèses sur les mécanismes de rayonnement VHF-UHF de l'éclair", 2ème Colloque International sur la Compatibilité électromagnétique, Trégastel, 1-3 juin 1983, Tiré à Part n° 1983-45.

[4] - D.E. Proctor, "VHF Radio Picture of Cloud Flashes", J. Geophys. Res., 86, n° C5, pp. 4041-4071 (May 1981).

[5] - S. Larigaldie, C. Labaune, J.P. Moreau, "Lightning Leader Laboratory Simulation by Means of Rectilinear Surface Discharges", J. Appl. Phys., 52 (12), pp. 7114-7120 (Dec. 1981).

[6] - S. Larigaldie, "Simulation d'un foudroiement - Analyse des mécanismes associés à la décharge", Rapport Technique ONERA n° 5/7236 PY (Août 1982).

[7] - B. Weizel, R. Rompe, "Theorie des elektrischen funkens", Annalen der Physik, 6 Folge, Band 1, 1947.

[8] - G.A. Mesyats, G.S. Korshunov, "Formation of Nanosecond Sparks in Static Breakdowns of a Gas", Soviet Physics, Technical Physics 13 (4), 483 (Oct. 1968).

[9] - M.C. Bordage, G. Hartmann, "Spectroscopic Measurements on Discharges along Dielecric Surfaces", J. Appl. Phys., 53, 12 (1982).

[10] - A. Bondiou, "Etude de la formation d'une décharge de surface et analyse spectroscopique de l'onde de retour associée", Thèse Ing. Docteur, Université d'Orsay, 18 Octobre 1984, n° 672.

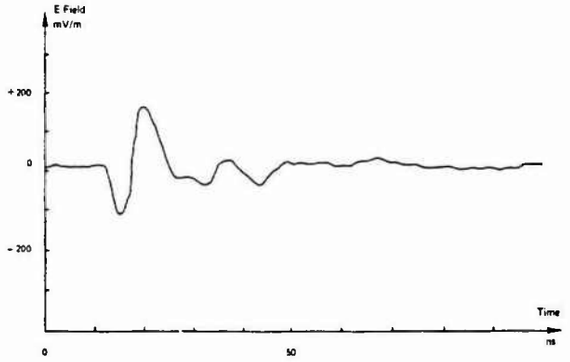


Fig. 1 - Characteristic signal of pulses recorded in wideband (600 MHz).

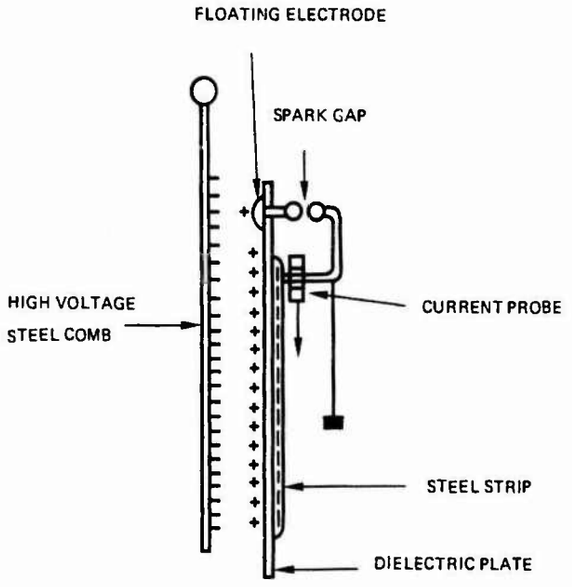


Fig. 3 - Experiment device.
The insulating support consists of an approximately 1 mm thick plexiglass plate, a narrow (width 1.5 cm) metal strip is located behind the plate. The plate is brought up to high voltage by a ion generator comb. The floating electrode is then brought down sharply to zero potential by a pressurized burster. Since an intense electric field occurs near the electrode, the sliding spark propagates from the top to the bottom of the plate guided by metal strip.

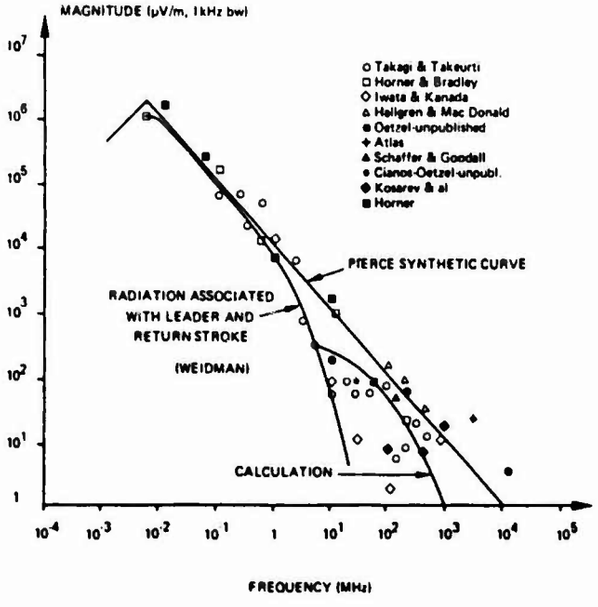


Fig. 2 - Comparison of the calculated spectral densities with the Pierce synthetic curve.

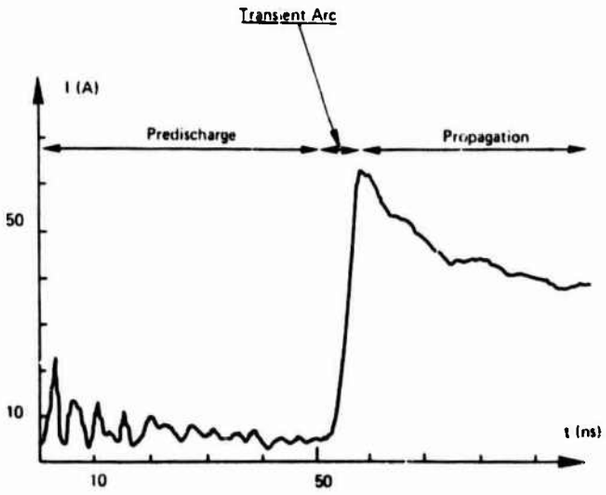


Fig. 4 - Current measured on the electrode by a Rogowski coil, response time $\tau \simeq 4$ ns.

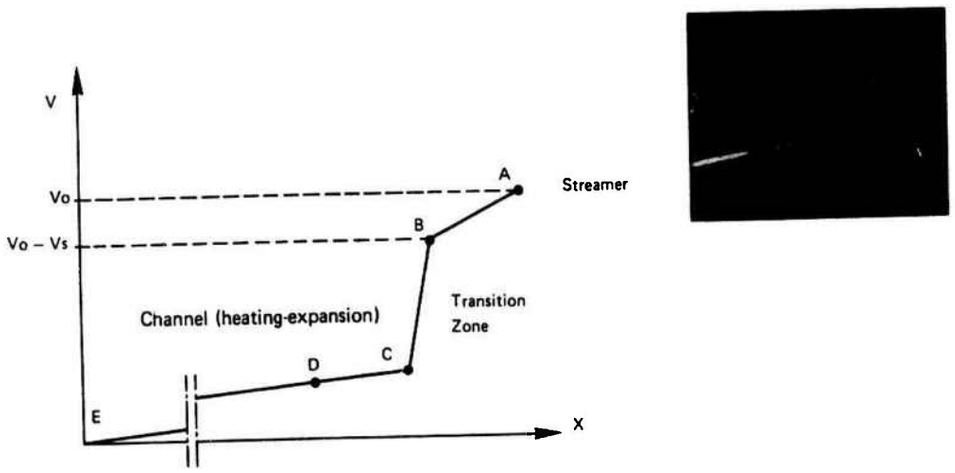


Fig. 5 - Distribution of potential along the propagation axis and photography of the discharge leader (exposition time: 3 ns).

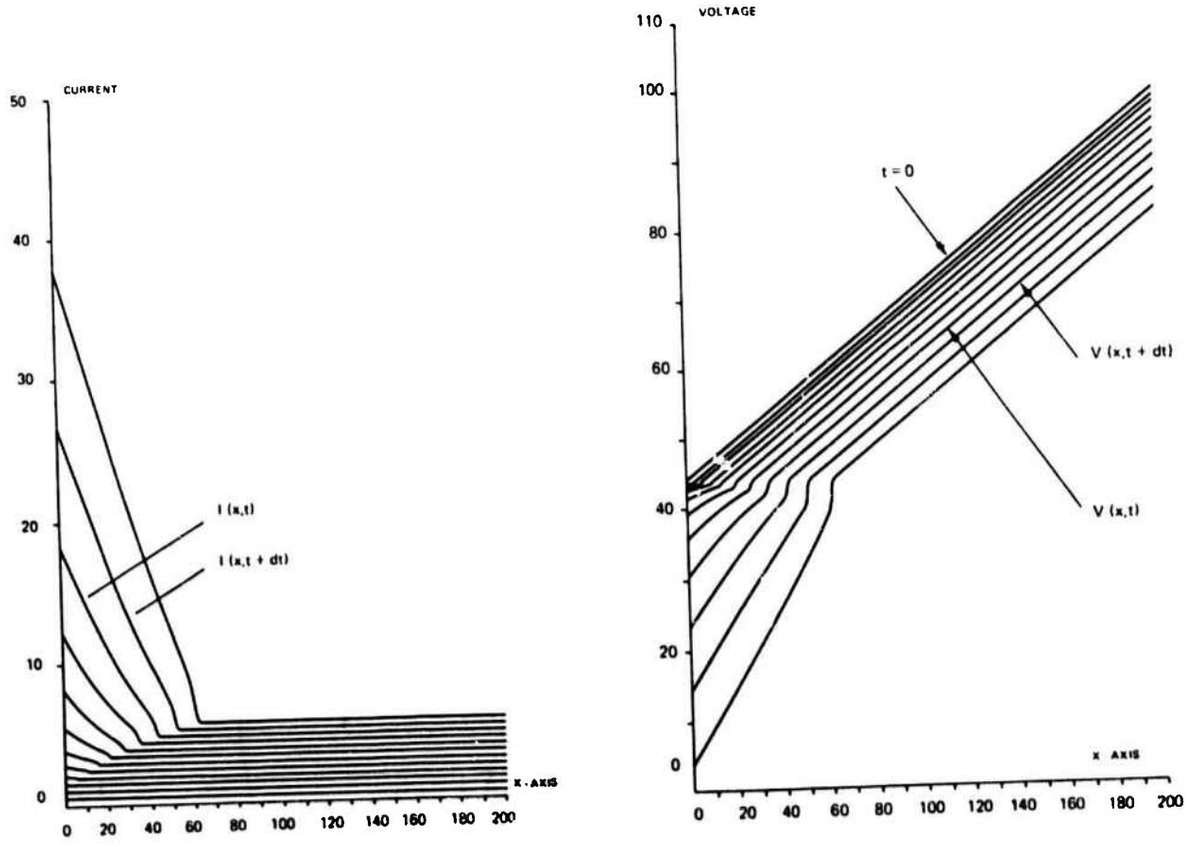


Fig. 6 - Development over time of current and voltage potential during transient arc. The propagation equation is solved numerically using a time interval $\Delta T = 2.5 \times 10^{-10}$ s and space interval of $\Delta X = 10^{-3}$ cm.

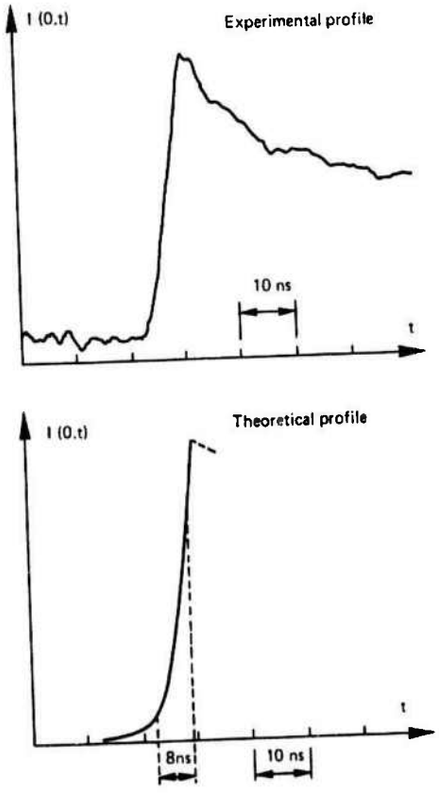


Fig. 7 - Comparison of theoretical and experimental profiles associated with the transient arc (current measured and calculated in X = 0).

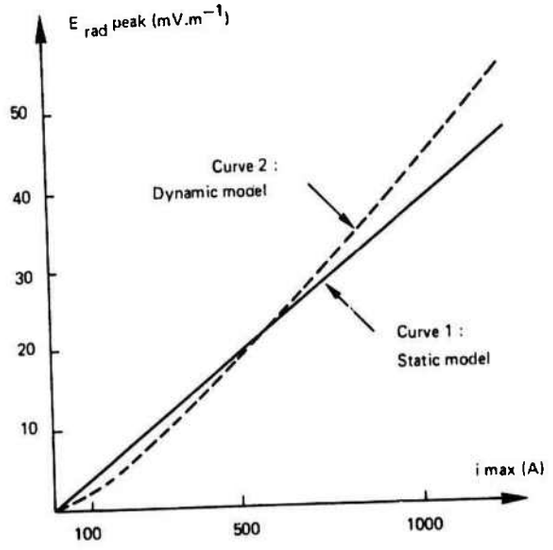


Fig. 9 - Comparison of the radiated field peak value (R = 10 km) calculated using both methods.

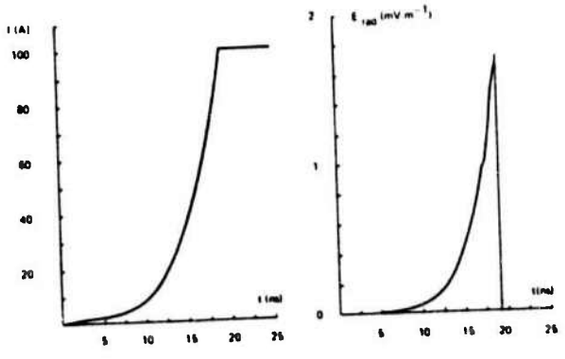


Fig. 8 - Current front I(t) at a given point in X and associated radiated field (Propagation current imax = 100 A; observation range R = 10 km).

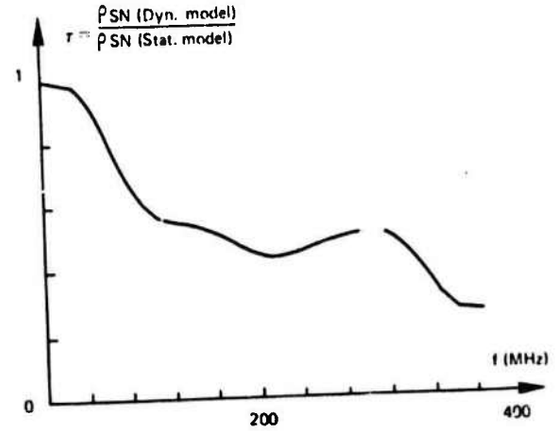


Fig.10 - Ratio of spectral densities normalized at continuum for both models (sampling frequency: 2 GHz; imax = 100 A).

TRIGGERED LIGHTNING FLASH CHARACTERIZATION

P. Laroche, A. Eybert-Bérard* and L. Barret*

Office National d'Etudes et de Recherches Aérospatiales, B.P. 72, 92322 Châtillon Cedex, France
**CENG, Avenue des Martyrs, B.P. 85X, 38041 Grenoble Cedex, France*

Abstract - Two triggered lightning experiments were performed in 1983 and 1984 in Florida, USA. The triggering system, rocket and wire, used a new technical arrangement which distinguishes it from systems used by French researchers since 1973. The flashes triggered with this new technique have properties which are somewhat different from those of flashes obtained with the former systems; in this paper, we will discuss the respective influence of triggering site and triggering system on the behavior of flashes.

1 - INTRODUCTION

Cloud-to-ground lightning flashes may be triggered by the fast ascent of a wire in a high electric field between a storm cloud and the ground. This method suggested by Brook et al. (1961) was first applied above sea by Newman (1965). The technique was greatly improved by French experimentalists who have studied triggered lightning above ground since 1973.

Since 1973, triggering experiments had been carried out with different technical devices and in various places by Japanese (Horii,1982), American (Stueberg, 1983) and French (Sparg, 1982; Hubert, 1984) experimentalists, the latest experiment, as far as we know, having taken place at Kennedy Space Center, Florida (Eybert et al., 1985).

Triggered flash behaviour may be vary greatly from one case to another, but the results of the 83 and 84 experiments indicate typical flash characteristics. Significant modifications in the properties of the triggering devices had been made two years ago and their influence on flash behaviour is open to question. Obviously, the most determining factor in the occurrence of a triggered flash is the storm itself and the aims of this paper is to discuss the respective influence of those two parameters.

After a short presentation of general results of 83 and 84 Florida experiments, we will describe the technical features of the two principal triggering devices used from 1973 to 1984.

We will then provide data on the measurements made at various sites in France and in New Mexico and describe the basic phenomena of triggered flashes. Finally, we will discuss differences in phenomena in terms of the effects of the triggering site and triggering device properties.

2 - GENERAL BEHAVIOUR OF A TRIGGERED FLASH

Positive upward leader development

Most of the flashes triggered in France and USA are initiated by the upward propagation of a positive leader. A few flashes with positive polarity had been obtained (Kerebel, Hubert, 1979) and in some cases the current became positive during the flash (Hubert et al., 1984, Walteufel et al., 1980).

During the ascent of the wire (figure 1), isolated pulses of less than 1A and width less than 1 ns, are observed. These correspond to positive streamers propagating from the wire tip. The velocity of the positive streamer may be between a few 10^5 m.s^{-1} to a few 10^6m.s^{-1} (Bicknell, 1984, Golde, 1977). The time interval between pulses may range between 10 ms and 100 ms; in the case of figure 5 it is about 25 ms and corresponds to a wire displacement of 5 m. Frequently, the pulse size increases over time.

The current from the last pulse does not go back to zero and we observed the onset of an upward leader corresponding to a continuous negative current. The velocity of the leader may range from a few 10^4m.s^{-1} to a few 10^5 m.s^{-1} (SPARG, 1980, P. Hubert, 1978). This occurs when the wire tip has reached an altitude of 100 m to 600 m AGL; the current collected at the flash foot when the wire melts is a few tens of amperes.

Continuous current process

A continuous current ranging from a few hundreds to a few thousands of amperes, and corresponding to a continuous illumination of the channel, occurs in most triggered flashes. This process may follow the upward leader or may appear after the occurence of downward leader-return stroke processes. The negative charge lowered to the ground by the continuous current process is large (few tens of Coulombs) and, in most cases, much greater than the charge lowered by the return strokes of the same flash.

Downward leader-return stroke process

This process is similar to those observed in downward cloud-to-ground natural flashes. It consists of the downward propagation of a stepped leader or of a dart leader, the short ascent of a junction leader and the propagation in the channel of ground-to-cloud current wave. Properties of subsequent return strokes in natural and triggered lightning are quite similar (P. Hubert et al., 1984).

Different kinds of triggered flashes

Depending on the overall triggering conditions, we may obtain the following kinds of events corresponding to different succession of the above processes.

Type A: The flash begins with a continuous current process corresponding to the development of a positive discharge; the process may last a few hundreds of milliseconds. The melting of the wire is visible through a typical fluctuation of the current (figure 2). It should be noted that regarding the low frequency current at the foot of the flash there is no distinction between the upward leader process and the continuous process. The electrical charge lowered to ground does not directly neutralize the charge of storm clouds; as pointed out by Vonnegut (1981), it corresponds to the charge displaced by the breakdown of an air medium where a high electric field exists.

During the continuous process or afterwards, the leader return stroke process may be observed.

Type B: (figure 9). After the onset of the propagation of a positive leader, the melting cause the current to go to zero and we have to wait few tens of milliseconds to observe a downward leader (stepped or dart) which the lower part generally follows the branches of the upward leader; when it approaches the ground a return stroke occurs. The flash carries on with several return strokes and often with a continuous current process.

In the case of an unsuccessfull triggering attempt, we may only observe an incomplete development of upward leader; the corresponding current signal is a pulse lasting a few tens of milliseconds with an intensity of a few tens of Amperes (figure 2).

3 - GENERAL RESULTS OF THE 83 AND 84 FLORIDA EXPERIMENTS

A joint experiment on triggered lightning was made during the summer of 83, 20 km south of Melbourne, Florida (Barret, Eybert, 1984). The objectives of the experiment were to characterize natural and triggered lightning and measure electromagnetic interactions between triggered flashes and an instrumented cylinder simulating an aircraft fuselage (Richmond, 1984). Twenty flashes were triggered in seven different storms. The keraunic level of Florida is very high but storms occur preferentialy in-land and seldom reach the coast (the triggering site was 10 km west of the coast line). Nevertheless, the events were numerous enough to obtain successful experiments with a high ratio of efficiency (66%).

Different measurements on the electrical properties of flashes were made but the most relevant, for our purpose, is the measurement of the current at the foot of the triggered flash. This was done with a coaxial resistive shunt with a resistance of one milliohm of 80 ns time constant, installed on the top of a double Faraday rage containing an electronic conditioner. Current signal was processed by fiber optic links and recorded in a shielded command shelter, some 50 m away from the launching pad. The main characteristics of current measurements are:

bandwidth: DC to 30 MHz.

Range: $\pm$ 60 KA over 80 dB dynamic range obtained by a log amplifier.

All the flashes began by a continuous current component; one of them exhibited a current inversion: it became positive after 350 ms of negative continuing current. The last flash was triggered in altitude by unspooling a conductive wire 100 m above ground. The table, figure 3, gives general data on the triggered flashes.

The Florida 84 experiment was made at the Kennedy Space Center (50 km north of the 83 experimental site). NASA, USAF and several laboratories of US universities were involved in the experiment; CEA and ONERA were involved, respectively, with triggered lightning and in flight lightning measurements (Eybert et al., 1985; Rustan, Moreau, 1985). An unusual low occurence of storms was observed in summer 84 and consequently we only obtained eight triggered flashes in three different storms.

The current measuring device was similar to the one used in 83, but its performance was significantly increased:

Range: $\pm$ 100 kA

Threshold level: < 1A

Bandwidth: DC to 20 MHz

Coaxial shunt: $10^{-3}\,\Omega$ ($\pm$ 1%) with s 50 ns time constant.

Fast components of the signal were displayed on a 100 MHz bandwidth oscilloscope whose screen was filmed with a 35 mm streak camera (30 Hz - 20 MHz channel). An intermediate frequency linear channel (DC to 1 MHz) was displayed on the same kind of device but with a lower sensitivity to record the highest pulses. High frequency linear and logarithmical frequency channels were recorded on a magnetic analog recorder, with a DC - 60 kHz bandwidth.

The general behaviour of the flashes recorded in 84 is quite similar to those triggered in 83. They are all negative and begin by a continuous current. Table on figure 4 gives the general characteristics of the flashes.

Main characteristics of the 83 and 84 results

The general characteristics of 83 and 84 triggered flashes are rather similar to those of flashes obtained previously. Nevertheless, we have evidence of systematic differences regarding current due to the upward leader and type of the flash.

The initial current rate, corresponding to the propagation of the upward leader is significanlty higher for 83 and 84 flashes than for others as illustrated by figure 5.

Almost all the triggered flashes are type A. They begin with a continuous process and end with one or several return strokes. The 83 and 84 experiments were conducted on new sites with a new triggering system (LRS). We will now examin the respective influences of the triggering site and of the triggering system on flash behavior.

4 - TRIGGERING SYSTEM INFLUENCE

Description of the triggering device

. Classical device (figure 6)

This system basically consists of a spool of wire installed at ground; its lower end is connected to the current measuring system. The upper end is mechanically connected to the rocket with a two-meter long insulating and elastic cap. This system was used by French experimentalists everywhere, with minor changes until the 83 and 84 Florida experiments. The wire is made of steel and is 0.18 mm in diameter; it is protected by cotton. The bottom of the spool is made of a dielectric material and a aluminium bond cylinder covers the spool to enable correct unspoooling of the wire which passes through a collecting ring about 30 cm above. A full spool has a total length at about 3 km and an inductance at 1000 Hz of about 3 H; the linear resistance of the wire is $8\,\Omega$/m.

The weight of the rocket and attachment system is 2.7 kg.

. Lightning Rocket System (LRS - Barret - Eybert 83)
The spool of wire is attached to the fin of the rocket (figure 7). The lower part of the wire is connected to the measuring system. The wire is made of copper; it is 0.2 mm in diameter and is coated with Kevlar. For ground triggering experiment, the spool contains 700 m of wire. For "altitude" triggering equipment, the first part of the spool is dielectric (adjustable from 0 to 300 m). The linear resistance of the wire is 0.45 Ω/m; the overall inductance of the spool is 350 m H at 1000 Hz.
The weight of the LRS is 2.5 kg including the spool (200 g).

. Main differences between the two systems
The electrical properties of the LRS and the standard system are different, see figures 6 and 7. The arrangement of the standard system allows electrical breakdown between the wire and the steel parts connected to the current measuring system. For instance, it can be deduced from electrical diagram, figure 6, that a current pulse of 1A with a 10 µs rise time applied at the lower part of the wire, produces a transient voltage of 330 kV at the collecting ring level. It is obvious that, neither the wire running through the collecting ring, nor the short air gap (few millimeters) between the spool box and ground can withstand a voltage this high. So when current pulses due to streamer development are emitted from the wire, we can infer that the lower part of the unspooled wire is connected to ground (via the current measuring system) by an arc. Traces of these breakdowns were, in many cases, actually found in the box after a triggering attempt.
Another major difference in the electrical characteristics of the two systems is that the wire resistance of the LRS is about twenty times lower than that of the standard system.
The fundamental mechanical difference between LRS and standard system is that, since the mobile part of the LRS is lighter, the velocity of the wire is 20% to 30% greater than the velocity obtained with the standard system. The typical maximum speed of the wire is 250 m/s with the LRS and 200 m/s with the standard system.

Discussion
Upward triggered lightning is similar to natural upward lightning occurring on top of a high lower or on the summit of a mountain. The action of the triggering system increases the electrostatic field produced by the storm cloud above the corona onset and enables the development of streamer from the wire tip by preventing the shielding effect from ions accumulation. Moore et al 1982, pointed out that the velocity required by a thin wire to obtain triggering must be greater than 150 ms^{-1} (this is approximately the drift velocity of ions in a 10 kV/cm electric field). The typical velocities of the two triggering systems satisfy this condition.
The initial low frequency dI/dt signal is dependent on upward leader velocity (P. Hubert, 1978). In the following, we use this parameter to characterize the onset of the leader. The values of dI/dt are determined either by the slope of the current curve or by the initial mean slope of the curve after the last streamer pulse has occurred (see exemple, figure 5).

. dI/dt variations during the same series of experiments
It is clear that flashes triggered in the same storm at an interval of a few minutes, in general, behave similarly. The type of the flashes, the duration and waveform of their continuous processes, and even the time lapse to observation of the first downward leader-return stroke process, are nearly identical. The question is to verify if these similarities correspond to initial leader development similarities. We have collected data, figures 8 and 9 on the initial dI/dt of ground flashes triggered during the 81 experiments in New Mexico where the standard triggering system was used. If there is a strong influence of the storms properties on leader behaviour, two flashes triggered at an interval of a few minutes, would have almost the same dI/dt values. We have plotted, figure 8, the ratio of these values versus time between the two flashes and we see no evidence of correlation: the ratio ranges from 0.05 to 1 randomly for time intervals from 0 to 92 minutes.
A local storm parameter which may influence the upward leader is the electrostatic field at ground when the rocket is fired. Figure 9 shows a tendency for the initial dI/dt to increase with field but the scattering around the best fitting curve is very high.
We think that as field strenght increases so does dI/dt, but that this point is no the most relevant. The velocity of the wire is higher but close to that required to trigger, and a statisticai variation of this parameter may influence the development of streamers and the initial propagation of the leader.

. Melting of the wire
The melting of the wire is always visible on the current curve for the standard system but it is never visible on an observation at a similar bandwidth for the LRS. The energy required to heat and melt the wire is 190 J/m for the stsndard system and 166 J/m for the LRS. Taking into account the electrical resistance of the wire we estimated that the melting current is three to four times greater for LRS than for the standard system. Hubert (1978), found that with the standard system the leader had reached an aititude greater than 1000 m AGL at the time of melting, hence, with the LRS, melting would occur at a higher altitude. The behaviour of the propagating positive discharge is dependent on the electric field conditions in the neighbourhood of the tip; it may not be directly affected by a rise in the resistance of a small portion of its channel more than one kilometer sway. This point is illustrated by two flashes, figure 10, for which the current has ceased to flow in the shunt, after the melting of the wire, for about 10 ms. The continuous current time history, before and after melting, does not seem to be affected at all by this event.
The effect ot the impedance of the standard system is limited to the unspooled part of the wire as pointed out above. At the triggering aititude - typically 200 m AGL - resistance is respectively 1600 Ω and 90 Ω for the standard system and the LRS; it is obvious that the corresponding voltage drop for current of less than 1A is negligible with respect to electrostatic field strength whose typical value above the thick space charge layer near ground may range from 20 kV/m to 50 kV/m.
From the data available at this date, we do not see any evidence of any electrical effects on the behaviour of flashes due to the differences in the two triggering devices. We infer that the discrepancy in the dI/dt values may be due, among others causes, to rocket speed variation from one firing to another.

5 - TRIGGERING SITE INFLUENCE

Since the early seventies we have used five different triggering sites. A distinction can be made between mountainous sites like Saint Privat d'Allier (1100 m ASL) in the center of France and Langmuir

Laboratory (3300 m ASL) in New Mexico, and flat plain sites like Le Barp in the southwest of France and the two Florida sites, which are all at sea level. We triggered 55 flashes in New Mexico, 98 at Saint Privat, 28 in Florida and we have data on 5 flashes triggered at Le Barp (more data have probably been acquired by others experimentalists at Le Barp).

The curves of figure 11 on the histograms of dI/dt values, determined as previously described, for four different series of experiments the following remarks may be made:

- there is a wide discrepancy in the dI/dt values obtained during the same series of experiments as already illustrated by results in figures 8 and 9,
- the curves on the New Mexico 81, Saint Privat 77 and 78 experiments are virtually identical,
- the curves plotted from Le Barp 79 and Florida 84 experiments are almost identical and correspond to values of more than one order of magnitude greater than in the three other cases.

We have found that initial low frequency dI/dt values are greater for flat plain sites than for mountainous sites. This is true regardless the type of triggering device used (standard for Le Barp, Saint Privat, New Mexico and LRS for Florida). This result holds for 85% to 90% of flashes obtained in 1977 and 1978 at Saint Privat, the other flashes exhibit dI/dt values identical with the highest values obtained in FLORIDA.

The onset conditions for the upward leader are prepared by the streamers occurring during wire ascent. A determining factor is the vertical electrostatic field strength between cloud and ground, which depends on storms cells.

Figure 12 is the table of the distribution of types of triggered flashes per site for six different series of experiments. We have considered that the melting of the wire simply happened (an upward leader has begun its ascent) and the event can be considered as a type B flash because had it been successful the only possibility is that it would have had a carry on due to a downward leader-return stroke process. For the Saint Privat and New Mexico experiments, a little more than 50% were type B flashes. For the Florida and Le Barp experiments 89% to 100% of flashes were of type A. These results clearly indicate that storms above flat sea level sites have different characteristics from those observed above mountainous sites.

Storms studied in New Mexico were always of horographic type. They form on top of the mountain and often the cloud base is at ground. Most of the flashes exhibit an upward branching at low altitude due to the proximity of the electrical charges.

Storms at Saint Privat are mostly horographic but a few of them are associated with a front; storm geometry varies with respect to altitude and value of charges separated in the clouds.

Florida storms are, in general, formed above land and are blown toward coast by a westerly wind. Due to low latitude, the cloud base is high and the electrostatic field at ground is weak (typical maximum value 8 kV/m in Florida and 12 kV/m in New Mexico). Triggered flashes do not exhibit low altitude branching. All storms concerned by Le Barp 1979 data are associated with a front; in most of the case the upward branching is not visible.

6 - CONCLUSION

We have found that the flashes triggered at two Florida sites with a new device present systematic differences from those obtained on montainous sites with a standard triggering device: the initial low frequency dI/dt corresponding to upward leader ascent, and strongly dependent of its velocity, is one or two orders of magnitude greater. It has been shown that the differences in the standard and LRS triggering devices may not induce any significant electical effect on the behavior of the leader of the flash. The overall characteristics of flashes are determined by the storm: Florida flashes are only of type A (continuous current process followed by return stroke processes).

Data concerning five different series of experiments clearly show that initial dI/dt depends of the nature of the site: this parameter is greater for sea level sites.

The onset of the leader, characterized by dI/dt, is influenced by streamer development for which the wire velocity and vertical electric field strength are determinant.

These results indicate that the field conditions between cloud and ground are more favorable at sea level sites and that the higher wire speed of the LRS may favor the occurrence of streamers.

The influence of the triggering system will be studied in more detail during the next Florida 85 experiments, for which both the standard system and LRS will be used under same storms conditions.

7 - ACKNOWLEDGEMENT

This work has been carried out with the support of the Direction des Recherches Etudes et Techniques of the Defense Ministry.

REFERENCES

L. Barret, A. Eybert-Bérard: "Système de déclenchement artificiel d'éclairs de foudre", Brevet n° 83.11281, July 1983.

L. Barret, A. Eybert-Bérard: "Campagne foudre aux Etats-Unis", Note CENG/DRE/SEEn-ASP n° 84-09.

J.A. Bicknell, B.M. Humood: "Bipolar Corona and Aircraft Triggered Discharges", Int. Aerospace and Ground Conference on Lightning and Static Electricity, Orlando, June 1984.

M. Brook, G. Armstrong, R.P.H. Winder, B. Vonnegut, C.B. Moore: "Artificial Initiation of Lightning Discharges", J.G.R. V.66, pp. 3967-3969, 1961.

A. Eybert-Bérard, L. Barret, J.P. Berlanois: "Campagne Foudre aux Etats-Unis", Note CENG/DRE/SEEn-ASP n° 85-02.

R.H. Golde: "Lightning", vol. 1, Physics of Lightning. Academic Press, 1977.

P. Hubert: "Eclairs déclenchés à Saint-Privat d'Allier en 1976", Note DPh-EP-78-518/PH/np, November 1978.

P. Hubert: "Triggered Lightning at Langmuir Laboratory during TRIP 81", Note CEN Saclay DPh/EP/81-66, November 1981.

P. Hubert, P. Laroche, A. Eybert-Bérard, L. Barret: "Triggered Lightning in New Mexico", J.G.R. V.89, n° D2, April 20, 1984.

M. Kerebel, P. Hubert: "Opération LANDES 79", Note CESTA/EX/ESP n° 80-170.

C.B. Moore, I.J. Caylor, D.L. Hall, T.F. Stueber: "Characteristics of the French Ruggieri Anti-Hail Rockets Used to Trigger Lightning", Measurement notes, Note # 27, November 25, 1982.

M.N. Newman: "Problems of Atmospherice and Space Electricity", in CORONITI edit ELSEVIER, 1965.

R. Richmond: "Rocket - Triggered Lightning - a comparison with natural lightning". Int. Aerospace and Ground Conference on Lightning and Static Electricity", Orlando, June 1984.

S.P.A.R.G. (St Privat d'Allier Research Group): "Huit ans d'expérience sur la foudre à Saint-Privat d'Allier", R GE n° 9, September 1982.

T.F Stueber: "Artificially Triggered Cloud-to-Ground Lightning Exhibiting Characteristics of Natural Lightning", DE 82016087, SAND-83-0745.

B. Vonnegut: "Deductiona concerning accumulations of Electrified particles in thunderclouds based on electric field changes associated with lightning", J.G.R., Vol. 88, n° C6, April 20, 1983.

P. Waldteufel, P. Metzger, J.L. Boulay, P. Laroche, P. Hubert: "Triggered lightning strokes originating in clear air", J.G.R., Vol. 85, n° C5, May 20, 1980.

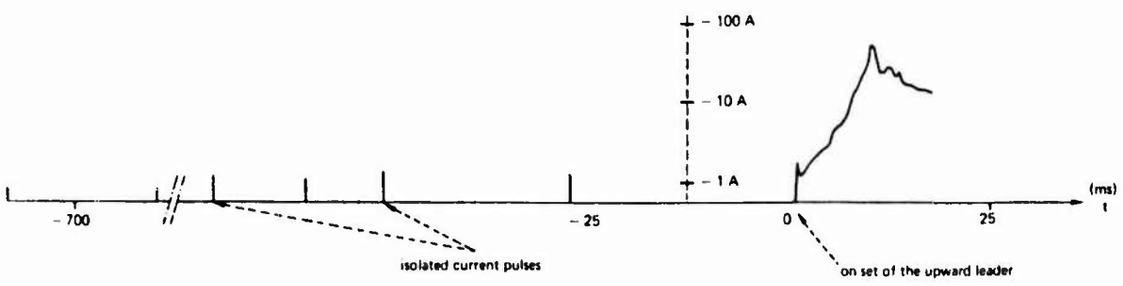


Fig. 1 - Triggered lightning flash n° 8401

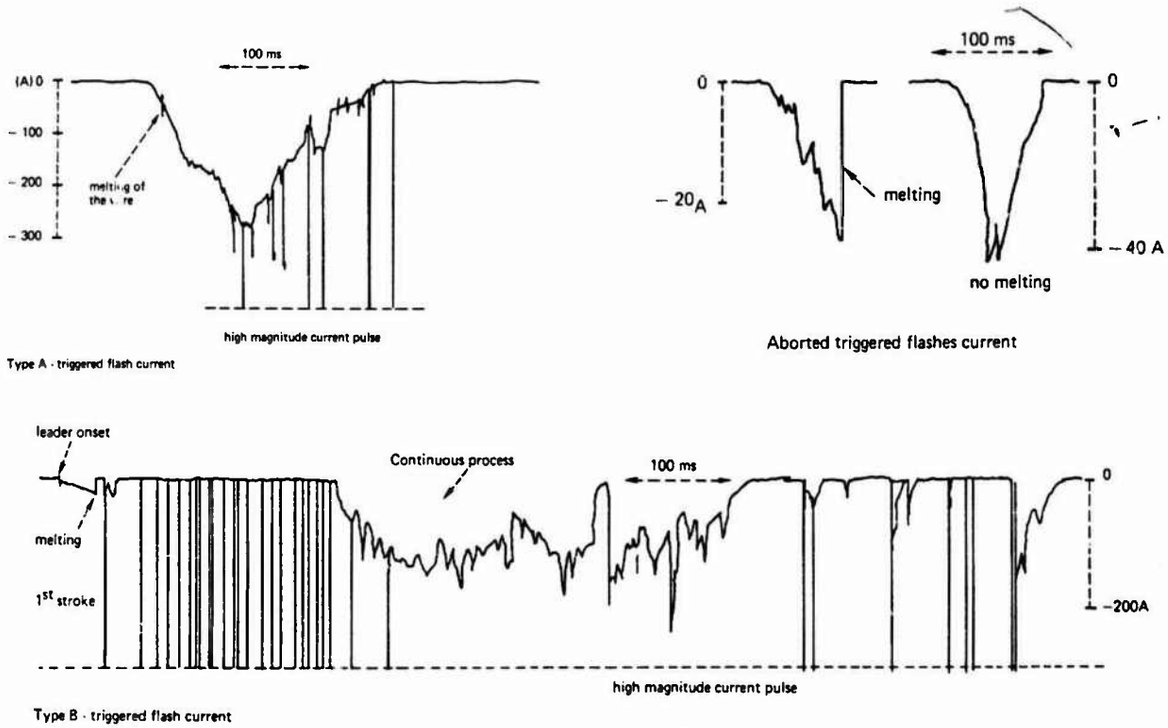


Fig.2 - Types of triggered flashes

	Flash duration ms	Triggering height m	Continuous charge C	I max kA	Field at ground kV/m
1	650	540	80	- 55	- 7.1
2	480	340	70	- 22	- 7.7
3	370	300	100	+ 10	- 7.7
4	270	210	20	- 1	- 8.1
5	600	230	40	- 10	- 6.4
6	535	260	50	- .5	- 6.4
7	1 055	330	60	- 12	- 6
8	100	440	1.4	- .03	- 2.6
11	855	390	40	- 16	- 6.1
12	50	420	.2	- .01	- 5.7
14	670	390	70	- 22	- 6.3
17	940	600	60	- 35	- 4.6
20	1 000	740	75	- 2	- 5.6
22	1 000	260	65	- 10	- 7.6
23	1 280	265	100	- 16	- 7.1
24	1 160	240	60	- 16	- 7.8
27	1 230	260	120	- 20	- 3.6
28	700	340	40	- 6	- 3.5
29	450	600	2.5	- 25	- 7.9
30	> 550	290			- 7.3

Fig. 3 - 83 Florida campaign general results

Launch #	Duration	I max	Field at ground
1	500	- 2.2	- 5.2
5	490	- 1.2	- 5.8
9	1 143	- 2.7	- 5.6
10	1 310	> - 30	- 6.5
11	1 188	- 26	- 5.9
12	828	- 21.6	- 6.7
13	1 034	- 21	- 5.
14	274	- 1	- 3.9

Fig. 4 - 84 Florida campaign general results

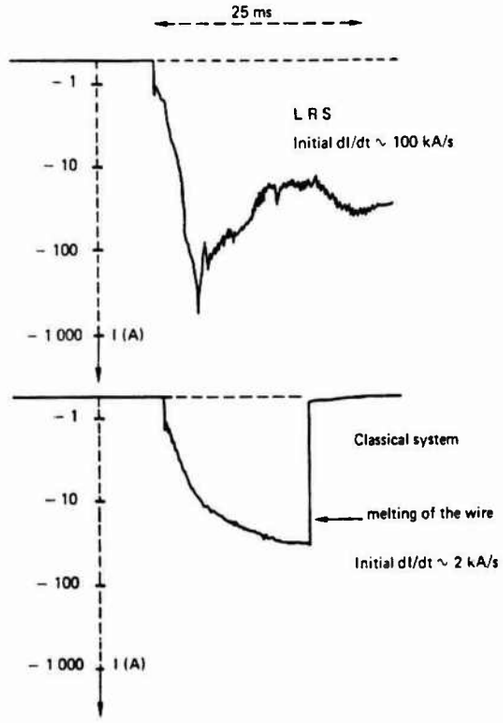


Fig. 5 - LRS and classical system current onset

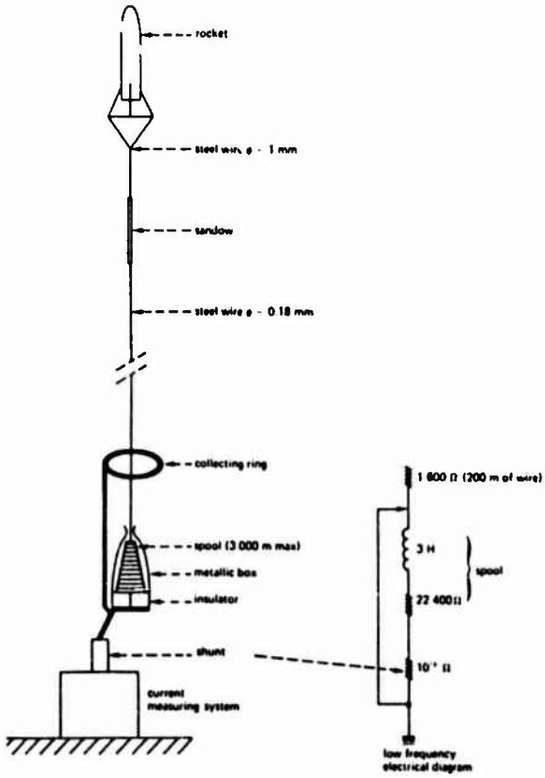


Fig.6 - Classical triggering system

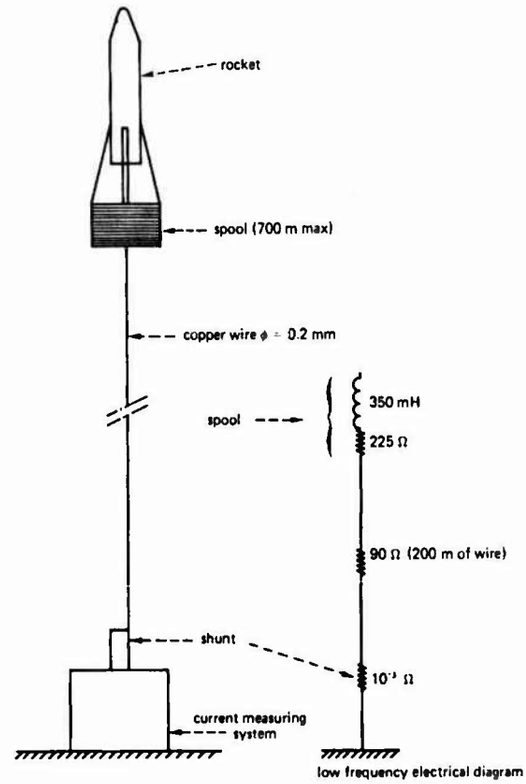


Fig. 7 - LRS triggering system

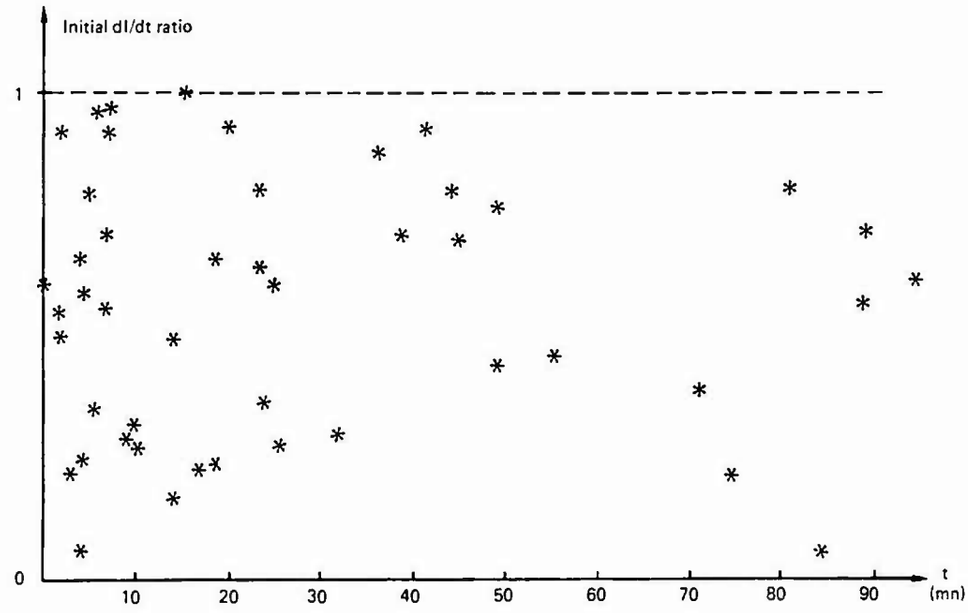


Fig.8 - New Mexico 81 : Initial low frequency dI/dt ratio versus time interval between flashes

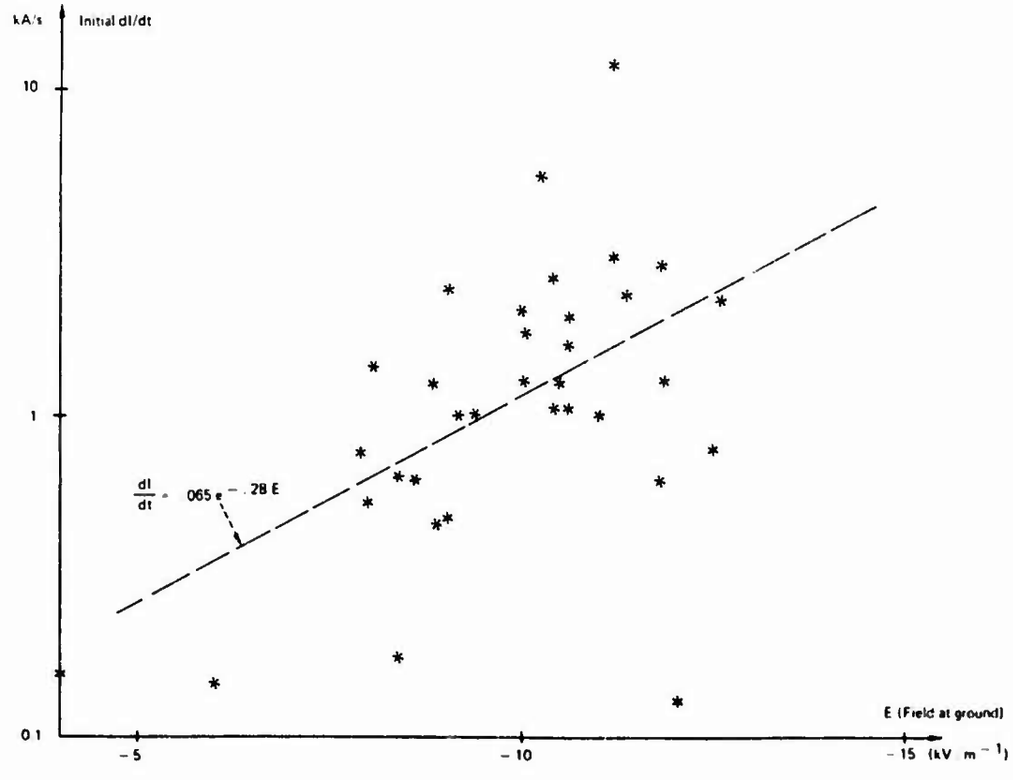


Fig. 9 - New Mexico 81: initial low frequency dI/dt versus electrostatic field at ground

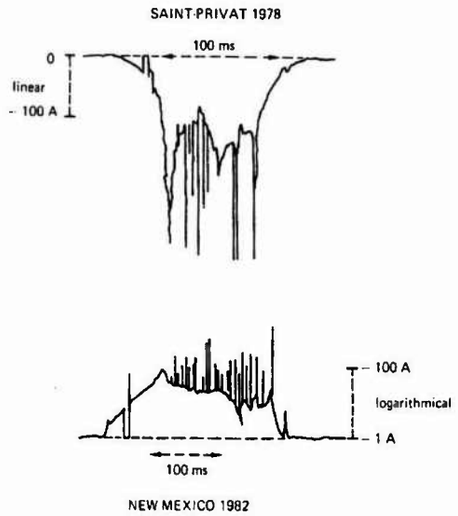


Fig.10 - Two cases of interrupted current after melting of the wire

	Saint Privat 1978	Le Barp* 1979	New Mexico 1981	New Mexico 1982	Florida 1983	Florida 1984
TYPE B	54 % with 8 % of melting	0 %	56 % with 8 % of melting	66 % with 8 % of melting	11 % of melting	0 %
TYPE A	46 %	100 %	44 %	34 %	89 %	100 %

* for this campaign we do not have data about melting of the wire

Fig.12 - Type of triggered flashes versus experimental sites.

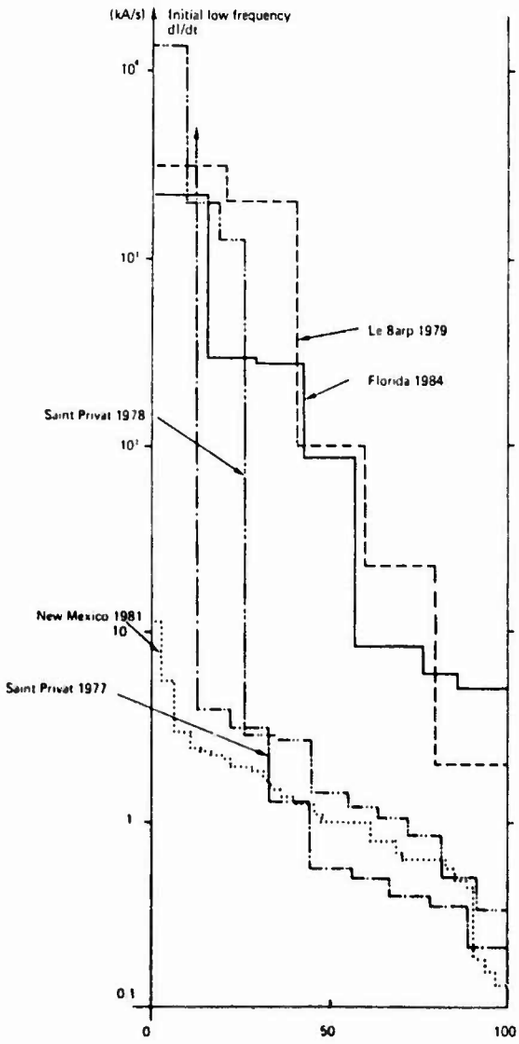


Fig.11 - Histogram of initial dI/dt

GROUP VELOCITY OF LIGHTNING RETURN STROKE CURRENTS

Z.I. Kawasaki, M. Nakano, T. Takeuti and T. Nakai

The Research Institute of Atmospherics, Nagoya University, 3-13 Honohara, Toyokawa, Aichi 442, Japan

Abstract - We have used a measuring system of luminous components during triggered lightning experiments at Hokuriku Coast of Japan. This system consists of two photodiodes and a two-channels broadband data recorder. With this system the luminous signals through a objective lense(f=50mm) from two different heights of return stroke channels have been recorded on magnetic tapes and we were able to observe 45 strokes during these experiments. The recorded luminous components were rather impulsive and much similar to the current shape of Lin-Uman-Standler's model. To obtain the two-dimensional return stroke velocities we defined "tip velocities" and "group velocities". About the former we decided the velocity with an arrival time difference of two luminous signals. About the latter we decided the velocity with a dispersion relation based on Fourier analysis. The mean of "tip return stroke velocity" was found to be 0.9×10^8 m/sec. and this value was almost same of the results of Idone and Orville's work. On the other hand the mean of "group return stroke velocity" was found to be 0.5×10^8 m/sec. and was in excellent agreement with the results of Schonland and McEachron. It should be noted, however, that the variation of the former was large in comparison with that of the latter. From this fact we assumed that Idone et al. was able to measure the "tip velocities", in spite of Schonland measured only "group velocities", owing to the progress of the sensitivity of measuring systems during these 50 years. To prove our hypothesis we executed a one-dimensional computer simulation with an electromagnetic fluid model based on plasma physics and got 1.3×10^8 m/sec. tip velocity and 0.7×10^8 m/sec. group velocity. Our computer simulation was able to explain the difference between recent results and previous results.

Introduction

The velocity of lightning return stroke currents is cosidered to be one of most important parameters[Boyle and Orville,1975;Hubert and Mouget,1980; Idone and Orville,1982;Nakano et al.,1983], not only from the view point of lightning physics but also from the view point of technical sense, such as protections of facilities from lightnings. in recent years, there has been a renewal of interest in the velocity measurements to be attributed to the need of use the accurate values for the return stroke velocity in the various new models[Uman and McLain,1969;Uman et al.,1975;LeVine and Meneghini,1973;Lin et al.,1980]. Historically, the measurements of the velocity of return stroke currents are never new topics and more than fifty years ago Schonland et al. reproted the velocities measured with Boys camera[Schonland and Collens,1934;McEachron,1939]. Recent obtained velocities with streak camera by Idone et al. are compaired with those by Schonland in detail and Idone concluded that the mean value of the former ($=1.0\times10^8$ m/sec) is about twice larger than that of the latter($=0.5\times10^8$ m/sec). The results of Hubert show the similar tendency and of course same to Nakano's results. On the other hand Jordan et al.[Jordan and Uman,1983] reprorted the relative light intensity as a function of height and time. According to their results return stroke current pulses are rather deformed as they are propagated along the channel perhaps bexause of its dispersive characteristics and we can consider that these phenomena are quite similar to the behaviour of an electromag netic pulse in a dispersive medium[Stratton,1941]. About the electromagnetic pulses in some dismersive medium, we know that various velocities are able to define, such as the phase velocity, the group velocity and the front velocity etc.,and we get to have a next question. "What kind of velocities has been mesured about lightning stroke currents until now ?"

Under above discussions,in this paper we present the two precise definitions on lightning return stroke current pulses according to the electromagnetic theory and try to explain the difference of previous Schonland's results and recent Idone's results. Moreover we excecute a computer simulation of return strokes with an electromagnetic fluid model based on plasma physics and estimate the return stroke velocity theoretically.

Experiment

We have already suggested and reported a measuring system of luminous signals from lightning channels. In this paper we will briefly describe it. As shown in Figure 1, luminous signals emitted from two different portions of a return stroke channel are observed with two photodiodes through an objective lense (f=50mm). These luminous signals are transformed into electric signals and recorded on magnetic tapes with a two channels data recorder. The bandwidth of this

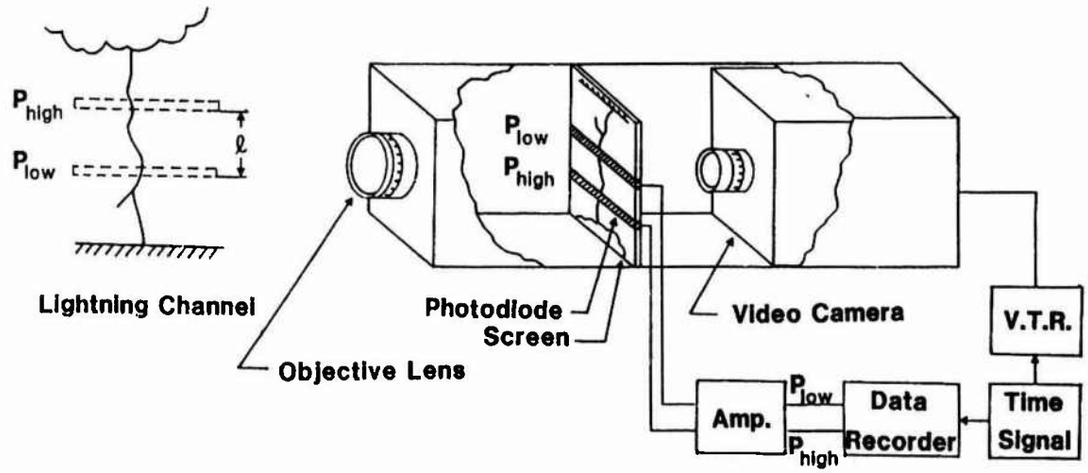


Figure 1. A schematic of the measuring sustem of luminous signals from lightning return stroke channels.

whole system is about 1 MHz. Of course, we simultaniously carry out the observations of electric field changes and magnetic flux densities to identify the type of discharge processes. The typical examples of these observed quantities, that is, an electric field change, magnetic flux density and luminous signals from two different height of a return stroke channel are shown in Figure 2. If we have some informations about the distance between the lightning striking point and the observation site, we are able to estimate the two dimensional velocity of return stroke current with the arrival time difference of two luminous signals.

Detail presentations of methods to estimate the velocities with measured data and discussions will be given in the following sections and here we show another example of luminous signals measured during triggered lightning experiments at Hokuriku Coast of Japan which were held in December, 1982. The distance between rocket launchers and our observation site is about 1.6 km and the altitude difference of two portions where two luminous signals were emitted each other is about 250 m. In Figure 3 a pair of traces of luminous signals measured by the lower and upper photodiodes are shown with the notations of (a) and (b) . We have observed 45 triggered lightning strokes during these experiments and all of them are negative ground flashes. From these examples we can find that the current pulse is deformed as it is propagated along the channel. Moreover the shapes of these signals are very similar to the shapes of currents based on Lin-Uman-Standier's new model.

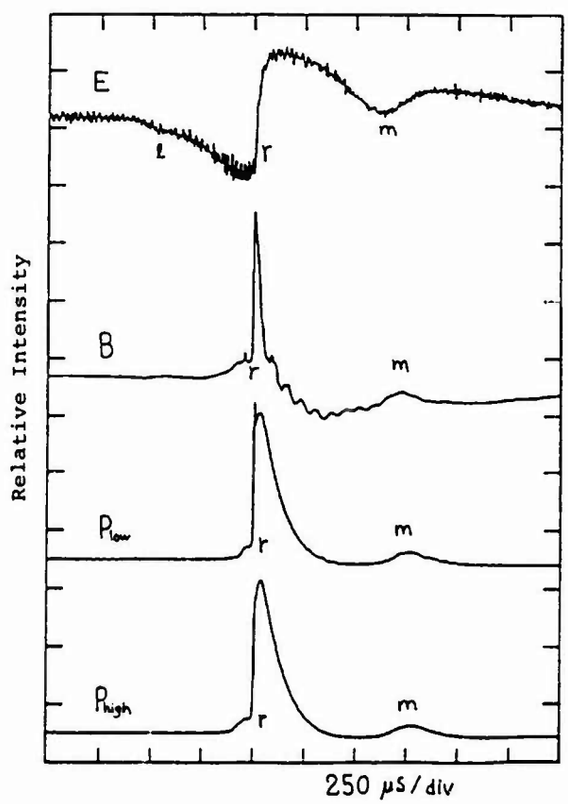


Figure 2. One of typical data measured during triggered lightning experiments in Japan.

Analysis

In this section we define what is called "the tip velocity" and "the group velocity" about return stroke currents and estimate two different velocities with two different procedure. The former should be estimated by the arrival time differnce of two luminous signals and this is a quite usual procedure. On the other hand the latter should be estimated with dispersion relations based on Fourier Analysis.

In all previous works, not only Hubert et al. but also Idone et al. of course Schonland, they measured the velocities with the arrival time difference. However as mentioned above, the shape of luminous signals is deformed very much with current's propagations along the channel, which means the deformations of current shape itself. So we can

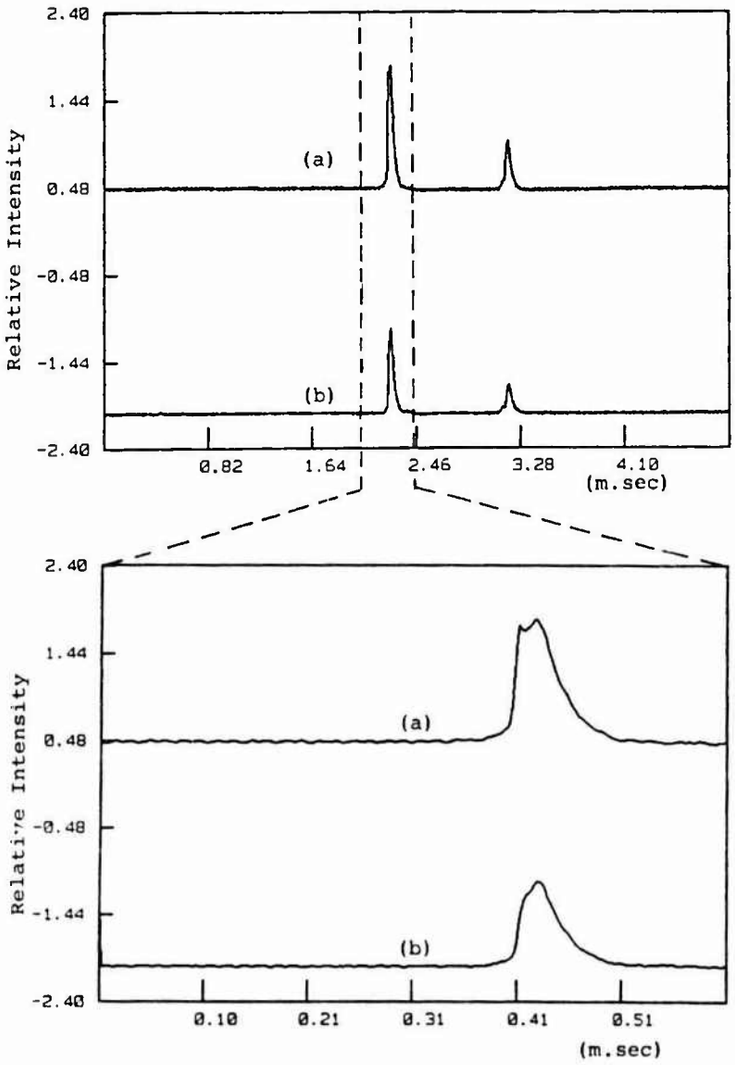


Figure 3. Measured luminous signals from different two heights.

consider that it is not sufficient to use only "the tip velocity" for the return stroke velocity. We think that it is necessary to define another velocity which maintain physical menings.

Return strokes are considered to be nonlinear break down phenomena which are propagated in an ionized leader channel to the opposite direction of leader strokes. These phenomena are understood to be a motion of ionizing potential waves been dominated by Poisson's equation for the electric field and by the equation of energy conservation[Albright and Tidman,1972]. So we are able to suppose that the velocity of return stroke current is concerned with the velocity of the potential wave. As mentioned above the behaviour of the ionizing potential wave is pretty similar to that of an electromagnetic pulse in a dispersive medium and we can conciude that the velocity estimated with the arrival time difference is a so called "the tip velocity" or " the front velocity'. Here after we use the term of the tip velocity. After Stratton the wave front velocity is always equal to the velocity of light in free space, c(=3.0 X 10^8 m/sec), no matter what the medium. He named this a precusor wave and the more sensitive measuring systems become, the faster velocities estimated with the arrival time differnce become. That is, recent results by Hubert, Idone and Nakano seem to be very different from previous results by Schonland and we would like to insist that these are due to progress of measuring systems, never due to the difference of phenomena. Moreover we insist we should difine another velocity for the velocity of return strokes which has physical significance because it is quite trivial that the front velocity is equal to c. In other word the time difference is not always equal about deformed wave train dpending on what level we can measure.

If a state of the medium is presented by the function $\Psi(z,t)$,where

$$\Psi(z,t) = A\exp[i(kz-wt)] \quad (1)$$

then the surfaces of constant state or phase are propagated with the velocity

$$V_p = w/k. \quad (2)$$

A wave train of finite length cannot be represented in the simple harmonic form (1), and a single group or pulse of any desired shape may be constructed upon the Theory of Fourier integral

$$\Psi(z,t) = \int_{-\infty}^{\infty} A(k)\exp[i(kz-wt)]\,dk. \quad (3)$$

After a little mathematical treatments we can find that the wave packet is propagated with the group velocity

$$V_g = dw/dk. \quad (4)$$

in case the medium is nondispersive, V_g coincides with the phase velocity V_p ,but otherwise it is a function of the wave number.

So far we have discussed about electromagnetic puises in some medium and same discussion is abie to adapted for the return stroke current puises. To estimate the group velocity of return stroke currents we must obtain a ω-k diagram of a pair of luminous signals. For this purpose we analyze measured luminous signals with FFT(Fast Fourier Transform) and with next equation (4) a ω-k diagram is given as shown in Figure 4.

$$\theta_d = k(z_1-z_2) - w(t_1-t_2) \quad (5)$$

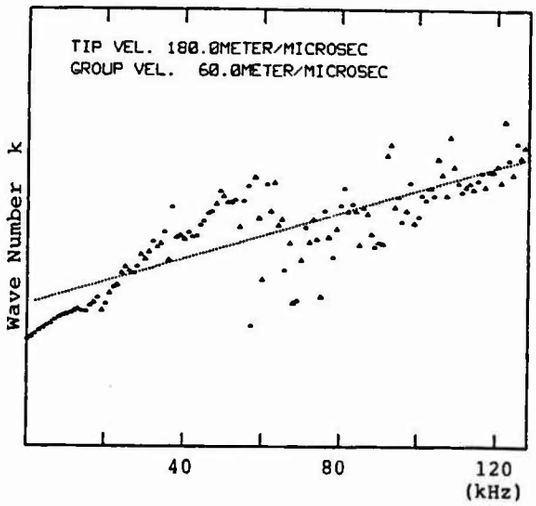


Figure 4. -k diagram coresponding to the measured data shown in Figure 3.

where θ_d, z_1-z_2 and t_1-t_2 are phase difference, altitude difference and time difference respectively.

A typical example of ω-k diagram shown in Figure 4 coresponds to the luminous signals shown in Figure 3. With this diagram we can estimate the group velocity by means of numerical derivative and in this paper we use a linear approxmation and estimate the group velocity with the gradient of dotted straigt line which is given with the least square method. About this example estimated group velocity is 0.6×10^8 m/sec and the tip velocity is 1.8×10^8 m/sec. All measured 45 pairs of luminous signals are analyzed respectively and decided the tip velocities and the group velocities. In Figure 5 the distributions of these quantities are presented. We can find that about the tip velocities the variation is rather wide. Moreover the mean value of tip velocities is very close to that of Idone and the mean value of group velocities is almost equal to that of Schonland.

Computer Simulations

After Albright et al., return strokes are able to be represented with electromagnetic fluid model based on plasma physics

$$\frac{\partial \mathcal{D}}{\partial t} = -e n_e \mathcal{V} \quad (6) \qquad \frac{\partial n_i}{\partial t} = S \quad (7)$$

$$\frac{\partial n_e}{\partial t} = -\nabla\cdot(n_e \mathcal{V}) + S \quad (8)$$

$$\frac{\partial (n_e \mathcal{V})}{\partial t} = -\nabla \frac{n_e T}{m} - \nabla\cdot(n_e \mathcal{V}\mathcal{V}) + \frac{e n_e}{m}\mathcal{E} - \nu n_e \mathcal{V} \quad (9)$$

$$\frac{\partial}{\partial t}\left(\frac{3}{2} n_e T + \frac{1}{2} m n_e |\mathcal{V}|^2\right) = -\nabla\cdot\left(\frac{5}{2} n_e T \mathcal{V} + \frac{1}{2} m n_e |\mathcal{V}|^2 \mathcal{V}\right) + e n_e \mathcal{E}\cdot\mathcal{V} - V_i S \quad (10)$$

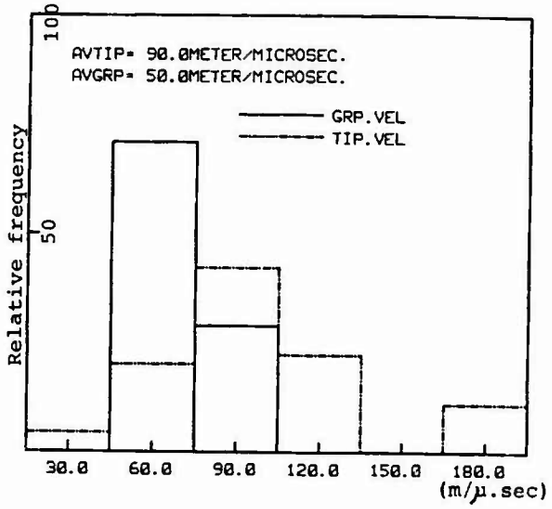


Figure 5. Velocity distributions of tip and group velocities for 45 negative flashes.

To simulate return strokes we must solve these equations numerically. The two-step Lax-Wendroff method is known to be the most conventional. We are now carrying out this simulation and will be able to present another paper at next chance. In this paper we derive the simplyfied one dimensional equations on the electric field and the electron density under a proper assumption, such as the temperature of the channel is constant etc.,

$$\frac{\partial E_z}{\partial t} = -n_e E_z - \rho \frac{\partial n_e}{\partial z} \quad (11)$$

$$n_e = 1 - |E_z|^2 - \frac{\partial E_z}{\partial z} \quad (12)$$

in Figure 6 we show the simulation results about the case of the channel's temperature of 20000°K and the channels be consisted of only N_2 for which the ionization threshold is about 17 eV. For the initial condition the electric field intensity at the tip of potential wave is assumed to be 5×10^5 V/meter. The arrow in Figure 6 indicates the direction

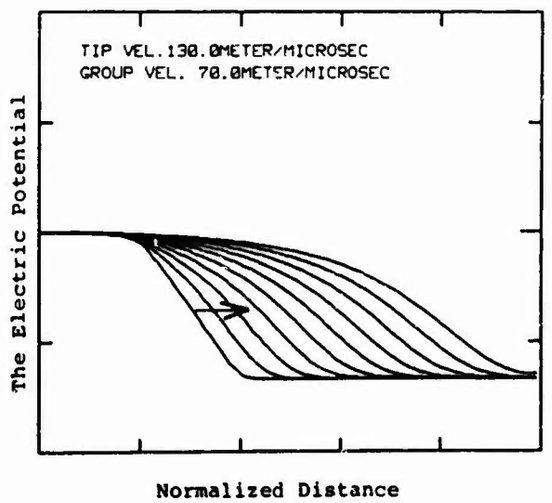


Figure 6. Simulation results for the potential wave as return strokes.

to which the potential wave is propagated. From this simulation result we can find the potential waves are propagated with deformation. For this case the tip velocity becomes 1.3×10^8 m/sec and the group velocity becomes 0.7×10^8 m/sec. Both of them are very close to the values obtained with measured luminous signals in the previous sections.

Conclusions

In this paper we started from a question, "What kind of velocities has been measured on lightning return stroke currens?" and defined two kinds of velocities, the tip velocity and the group velocity. We carried out the estimations of the tip velocity and the group velocity for 45 pairs of luminous signals measured during the rocket triggered lightning experiments in Japan. The mean value of tip velocity was 0.9×10^8 m/sec and the mean value of group velocities was 0.5×10^8 m/sec. The former are almost equal to the results of Idone and the latter are almost equal to the results of Schonland. To explain this difference we executed a one-dimensional computer simulation with an electromagnetic fluid model based on plasma physics. Experimental results were in excellent agreement with theoretical results. Our computer simulation was able to explain the difference between recent results and previous results. After Electromagnetic Theory in the dispersive medium the velocity which maintains the pysical significance is " the group velocity" and we concluded that we should use same concept for the return stroke velocity. We found that the mean of group velocities about rocket triggered lightnings was 0.5×10^8 m/sec.

Refernces

M.A.Uman and D.K.McLain,J.Geophys.Res.,74,6899-6909(1969)
M.A.Uman,D.K.McLain and E.P.Krider,Amer.J.Phys.,43,33-38(1975)
J.A.LeVine and W.L.Taylor,Radio Science,13,801-809(1978)
Y.T.Lin,M.A.Uman and R.B.Standler,J.Geophys.Res.,85,1571-1583(1980)
J.S.Boyle and R.E.Orville,J.Geophys.Res.,81,4461-4466(1976)
P.Hubert and G.Mouget,J.Geophys.Res.,86,5253-5261(1981)
V.P.Idone and R.E.Orville,J.Geophys.Res.,87,4903-4915(1982)
M.Nakano,T.Takeuti,Z-I.Kawasaki and N.Takagi,J.Mete.Soc.Japan,61,339-345(1983)
B.F.J.Schonland and H.Collens,London Ser.A.,143,654-674(1934)
K.B.McEachron,J.Franklin Inst.,227,149-217(1939)
D.M.Jordan and M.A.Uman,J.Geophys.Res.,88,6555-6562(1983)
J.A.Stratton,McGrawhil Book Company,London,330-340(1941)

SURVEY OF LIGHTNING HAZARD AND LOW ALTITUDE DIRECT LIGHTNING STRIKE PROGRAM

N.O. Rasch and M.S. Glynn

FAA Technical Center, Aircraft and Airport Systems Technology Division, Atlantic City Airport, New Jersey 08405, U.S.A.

Abstract - Modern aircraft designs are employing increasing amounts of poorly-conducting composite airframe materials and aensitive digital microelectronica to achieve greater performance levels. Unfortunately, these designs make aircraft potentially more susceptible to damage or impairment resulting from electrical interference. This interference can arise from static electricity, lightning dischargea, and nuclear EMP, among others. Composite materisls do not provide the high level of ahielding that was achieved by metal skinned aircraft. Microelectronics can be damaged or destroyed at far lower levels than previously used vacuum tubes. Thus, optimum protection levels must be provided to enaure safety of flight.

This paper provides a program to obtain quantitative and qualitative data on the electromagnetic characteristics of the lightning environment encountered by attschment to sn aircraft in flight at altitudes from 2,000 to 20,000 feet. Specific characteristics of cloud-to-ground lightning, simulated nuclear electromagentic pulse (NEMP), and the interaction with the aircraft will be defined.

Dsta acquisition flights are scheduled to be made in and nesr areas of active thunderstorms (not to exceed 40 dBZ of radar reflectivity) and will last approximately 2 or 3 hours. When weather allows, the aircrsft will be flown over an instrumented ground station to record associsted ground based electromagnetic field data. Approximately 100 flight hours are anticipated each year in support of this project. The flights are plsnned to occur over the Florida peninsula in the the vicinity of the Kennedy Space Center, Florida. An FAA Convair CV-580 aircraft inatrumented with wide-bsndwidth electromagnetic sensors snd recorders will be based at Patrick Air Force Bsse, Florida.

A two-year experimental phase will be conducted in 1984 snd 1985 to measure electromsgnetic parameters produced by a direct lightning strike to an aircraft in flight. Approximately one year will be required sfter completion of the data acquisition flights for snslysis and publication of the dste.

Introduction

Dr. Richard G. Fowler ststes that: It seems spparent, as one views that panorama of organized satisfaction of human curiosity we call science, thst one might reasonably cite the terror which lightning hss inspired in all ages to explain the singular fact that with very little exaggeration it can be said thst this oldest and most majestic of terrestrial electricsl phenomena is still less completely understood than the structure of the nucleus. [1]

The electromagnetic tranaients sssociated with a lightning strike pose a threat to the electrical systems of aircraft in the immediate vicinity. Because of the complex geometries involved, it is difficult to calculate the voltages and currents induced in aircraft internal wiring, but it is clear that both electric and magnetic fields are important in the coupling mechanism. The high current associated with a lightning strike gives rise to an intense, rapidly changing magnetic field, and the high voltage gives rise to an intense rapidly changing electric field. However, the electromagnetic field really needs to be treated as a whole in the overall coupling phenomenon.

In order to predict the nature snd magnitude of this threat, it is necessary to achieve an understanding of the lightning phenomenon, particulary the currents snd charges slong s tortuous discharge path.

A number of models have been proposed for the distribution of the lightning current and charges along the chsnnel and their relstionship to the radiated fields (far-field zone), but little has been published sbout the very near-fields of interest in a nearby strike, and the effects of chsnnel tortuosity on these induced fields. [2]

Purpose

This paper will discuss a procedure conducted to implement research in the technology area that will provide "lightning characterization and threat definition" information and data in support of specifications and criteria related to protection of current and new generation aircraft against atmospheric electricity hazards. The emphasis of the effort will be directed towards obtaining data on the effects of electromagnetic transients and the electromagnetic compatibility (EMC) of systems as influenced by atmospheric electricity hszards such as lightning (direct and indirect), static discharge, and other external factors causing electromagnetic interference (EMI) effects to an aircraft in flight.

Bsckground

The FAA has an interest in the study of stmospheric electricity effects to systems and structures of current snd new generation aircrsft. This interest is reflectd in the "FAA Engineering and Development Technical Program Plsn - Atmospheric and Aircrsft Electrical Hszsrds" dated October 1983. [3] The FAA is also conducting joint projects with the National Aeronautics snd Space Administration (NASA) and the United States Air Force in lightning snd ststic electricity resesrch.

Atmospheric electricity intersction with sn aircraft can result in numerous problems. For the case of lightning, physicsl dsmsge csn result from direct strikes on the sircraft. Such damage is chsracterized by burning, eroding, blasting, and is the consequence of either the extreme heat loading and accompanying acoustic shock wave or deforming by magnetic forces from the high current component of lightning. A further effect results from the fast changing electric and magnetic fields produced by the high currents of a direct or nesr strike. In both csses, these fields csn couple voltage transients into the internal sircraft wiring and subequently to the electronic flight critical snd flight essential control and avionics systems.

The emphasis of this activity is directed towards lightning characterization, hazard definition, and the sreas of research that deals with EMI/EMC/electromagnetic pulse (EMP) type problems in generic and new technology avionic systems. Concern for vulnerability of aircraft flight critical and flight essential systems to atmospheric electricity hazards has increased substantially over the past 15 years. Two primary factors have contributed extensively to this increased threat: (1) Increasing widespread use of sensitive microelectronic low voltage/low current/ high density solid-state devices in digital flight essential systems; and (2) the reduced physical protection and electromagnetic shielding afforded aircraft systems and crew by advanced technology airframe materials.

In order to provide a level of safety and to ensure that the full advantage of the rapidly expanding fields of microelectronics, digital systems, and composite structures, etc., is realized, the needed data and information must be acquired that will ensure full, unimpeded utilization of the advanced technologies while simultaneously providing validated hardening information and procedures.

Historically, the majority of lightning measurements have been made at ground level, and have provided most of the existing data on lightning. Recent cloud-to-cloud and intracloud airborne measurements above 20,000 feet have been made to obtain data typical of lightning experienced by aircraft in flight. Analysis indicates a different overall pattern in aircraft lightning data compared to ground strikes. It is not yet fully understood what type of lightning phenomena is interacting with the aircraft durng these strikes.

This well-designed experiment was needed to enable a better understanding of low-altitude lightning strikes to aircraft. This experiment includes measurements of current flow (both current transients snd continuing current), electric fields (both transient electric field changes and static electric fields), snd current distribution on the aircraft. Other data, such as aircrsft turbulence, airborne snd ground-bssed radar informstion, etc., also have been incorporated into the program.

Scope

This program hss been developed to obtain quantitative dsta on the electromsgnetic chsrscteristics of the lightning environment encountered by sn aircraft in flight from 2,000 feet to 20,000 feet. Specific characteristics of lightning snd nuclear EMP (NEMP) and interaction with the aircraft to be investigated include the following:

a. Incident magnetic fields from nesrby lightning flashes.

b. Surface currents, displacement currents, and current distributions on an aircraft resulting from s direct strike.

c. Totsl current flow on an aircraft resulting from a direct strike including low level continuing current.

d. Quasi-stati- electric field conditions existing near the aircraft for direct and nearby strikes.

e. Electric and magnetic field characteristics preceding aircraft lightning attachments.

f. Electromagnetic fields associated with NEMP.

g. Induced voltages and currents on actual aircraft wiring and instrumentation.

Other supplementary data such as radar patterns, turbulence, etc., will be gathered where possible to aid in the analysis and interpretation of the electromagnetic information.

The program consists of eight major phases:

a. Instrumentation design and procurement.

b. Aircraft modification, equipment installation, checkout, and calibration.

c. Data acquisition flights in a thunderstorm area.

d. Data acquisition flights in a simulated nuclear (NEMP) environment.

e. Ground-based lightning simulation (LEMP) tests.

f. Data Analysis.

g. Remove and replace instrumentation system (between seasons).

h. Aircraft restoration.

A 2-year experimental phase will be conducted with phases b through f. being repeated as necessary the second year. Approximately 1 year will be required after completion of the data acquisition flights for analysis of the data.

Data acquisition flights will be made in and near active thunderstorms and will last approximately 3 hours. When weather permits, the aircraft will be flown over an instrumented ground station to record associated ground based electromagnetic field data. Flights at altitudes between 2,000 and 20,000 feet will be made into areas of radar reflectivity not to exceed 40 dbz. Approximately 100 flight hours are anticipated each year in support of this project.

Ground based lightning electromagnetic pulse (LEMP) tests will be conducted at the Air Force Wright-Aeronautical Laoratory and nuclear electromagnetic pulse (NEMP) testing will be conducted at Kirkland Air Force Base. The data will be analyzed to determine if a common protection criteria can be established.

Anticipated Results

This comprehensive experimental program will yield information on:

a. Characterization of lightning.

b. Aircraft-Lightning hazards definition.

c. Initiation of lightning discharge to aircraft.

d. Possible triggering of lightning by the aircraft.

e. Electrostatic field thresholds for lightning attachment to aircraft.

f. Continuing current levels and charge transfer during aircraft attachments.

g. Transient current and field amplitudes and rates of change for direct and nearby strikes.

h. Current distribution over aircraft surfaces.

i. Current pulse repetition rates and durations.

j. Induced voltages and currents on actual aircraft wiring and instrumentation.

k. Associated ground based field levels and characteristics.

l. Define meteorological conditions conducive to lightning aircraft attachment.

m. Develop improved ground test techniques to better simulate lightning conditions.

The program is complex, it requires consolidation of resources (both monetary and expertise) and cooperation between the U.S. Air Force (Flight Dynamics Lab, Weapons Lab, Patrick Air Force Base), NASA (Kennedy Space Center), U.S. Navy (Naval Research Lab.), and ONERA (Office of National D'Etudes et de Recherches Aerospatiales).

A block diagram of the organizations involved is shown in figure 1. Also shown are the means by which they are administratively coupled.

A breakdown of the major components required for the airborne research are as follows:

o Research Aircraft - The selection of the aircraft was critical to the success of the entire program. The aircraft was required to be large enough to contain the entire instrumentation system including the data retrieval system and operators. Have the capability of remaining on station for periods of 3 to 4 hours at altitudes between 2,000 and 20,000 feet, yet have adequate speeds to be vectored to thunderstorms at distances up to 100 miles from the base station. The aircraft had to exhibit a history of extreme safety in the thunderstorm environment. The FAA Technical Center's Convair C-580 aircraft (N-49) (figure 2) exhibited all the aforementioned properties and most important was availble.

The aircraft was modified by having the special designed sensors installed to measure the effects of both direct- and near-lightning strike effects (figure 3). The addition of the wing booms (figure 4) required that the aircraft be placed into an experimental status, which precluded the transportation of passengers.

Note: It must be emphasized that an in-depth safety evaluation was conducted to ensure that the aircraft operations would be conducted safely. Lightning Technologies, Incorporated, was contracted (this company is under contract for the safety evaluation of the NASA F-106B aircraft) to conduct this evaluation.

o Research Instrumentation System - The instrumentation concept consists of a number of electromagnetic sensors which measure the electromagnetic fields during the lightning strike to the aircraft (figure 3). The instrumentation will be simultaneously triggered from either an I, I, B, or D signal. The Tektronic 7612 digitizer time window uses 2048 available samples with a basic 5 ns sampling rate.

This instrumentation system will be contained in the passenger compartment of the aircraft.

The following instrumentation systems will be installed on the aircraft:

- Lightning Characterization System - This will involve transient measurement sensors specifically designed for this project coupled to Tektronic 7612 digitizers and a 28-channel HP analog recorder (figure 5).

  Time correlation will be utilized.

- Static Field Mill Measurements - A total of four field mills will be installed on the aircraft. The field mill output will be fed into an analog computer which calculates E_x, E_y $E_z$and Q. These results will be stored on a 9-track digital recorder and presented in analog form in real-time on a strip-chart recorder (figure 6).

- VHF Radiation Field - ONERA conducted VHF radiation field measurements utilizing a 63 MH_z and 120 MH_z aircraft antenna (figure 3).

- E & H Field Measurements - ONERA has utilized "E" and "H" field sensors located on the wings inboard of the engines to measure the rate of change of the field in this area (figure 3).

- Thunderstorm Detection Measurement - Storm detection equipment has been installed on the aircraft, primarily to aid in vectoring the aircraft towards thunderstorms. The data has been recorded on a digital recorder.

- Television Monitor System - A television video system will be installed to continuously monitor both wing tips and the top of the aircraft.

- Turbulence Measurements - A turbulence measurement system will be installed on the aircraft to record the actual turbulence experienced by the aircraft.

Research Measurements

D-Dot, B-Dot, and I-Dot are the measurements of choice as determined by a group of technical experts representing industry, academe, and government. D-Dot is related to rate of change of electric field. I-Dot is rate of change of strike current to the boom; and B-Dot is rate of change of magnetic flux density. The amplitude ranges are based on a nominal strike with 10,000 amperes and 500,000 volts per meter change in 0.1 microsecond. The B-Dot range corresponds to the D-Dot generated by the above current at 1-meter radius (table 1).

o Turbulence Measurements - A turbulence messurement system was installed on the aircraft to record in real-time the actual turbulence the aircraft is subjected to during the thunderstorm penetrstions. The system will ultilize a time reference system and output from the Inertial Navigation System for data analysis purposes (figure 7). [4]

Electromagnetic Sensors

The sensors used in the lightning instrumentation system sre derived from designs developed for nuclear electromagnetic pulse measurements. The sensor response to rates of change of the lightning electromagnetic characteristics (as opposed to the current and fields, directly) accentuates the recording of the higher frequency components of the lightning process. Since the magnitudes of induced voltages (and currents) are proportional to rates of change of the lightning electromagnetic characteristics, enhanced definition of the more interesting (from an induced effects viewpoint) portion of the spectrum is obtained. The sensor sensitivity is calculated based on sensor geometry and then checked using a parallel-plate transmission line or simular type calibrator.

Measurement Locations

The electromagnetic sensors are located on the aircraft in regions where the field strengths are the greatest. Lightning currents contain frequency components high enough to excite the electromagnetic resonances of the aircraft; thus; the strongest fields occur at the antinode points of the resonances. For the lowest frequency resonances, the charge, and therefore the electric field antinodes occur at the extremities of the aircraft and the current and magnetic field antinodes occur at the center. Thus, the D-Dot sensors are located near the ends of the nose, tail, and wings, and the B-Dot sensors are located near the center of the fuselage. Practical considerations, such as the location of access panels, dictate the exact sensor locations (figure 3).

Summary

In summary, this program is expected to provide both qualitative and quantitative infromation to expand the understanding of lightning phenomena and to provide a data base for establishing aircraft lightning protection criteria. The data will be invaluable for the validation of the lightning characterization models previously developed.

The entire aircraft community will be provided with the data and information needed to ensure that the full advantages of the rapid expanding fields of microelectronics and advance technology structural materials are realized.

TABLE 1. RESEARCH MEASUREMENTS

MEASUREMENT	SYMBOL	AMPLITUDE RANGE	SENSOR TYPE
Rate of Change of Electric Flux Density	D	50 A/m^2	Flush Plate Dipole
Rate of Change of Magnetic Flux Density	B	2×10^4 Tesla/sec	Multigap Loop
Rate of Change of Current	I	10^{11} A/sec	Inductive Current Probe

References

1. Fowler, R. G., Applied Atoms Collision Physics, Volume No. 5, Lightning, pages 31-65, 1982.

2. Pearlman, R. A., Lightning Near Fields Generated by Return Stroke Current, McDonnell Aircraft Company, Proceedings EMC Conference, 1979.

3. Engineering and Development Technical Program Plan - Atmospheric and Aircraft Electrical Hazards; DOT/FAA/CT-83/4.

4. Lewis, W., Rasch, N., and Barile, A.,8th International Aerospace and Ground Conference on Lightning and Static Electricity, Fort Worth, Texas, June 21-23, 1983.

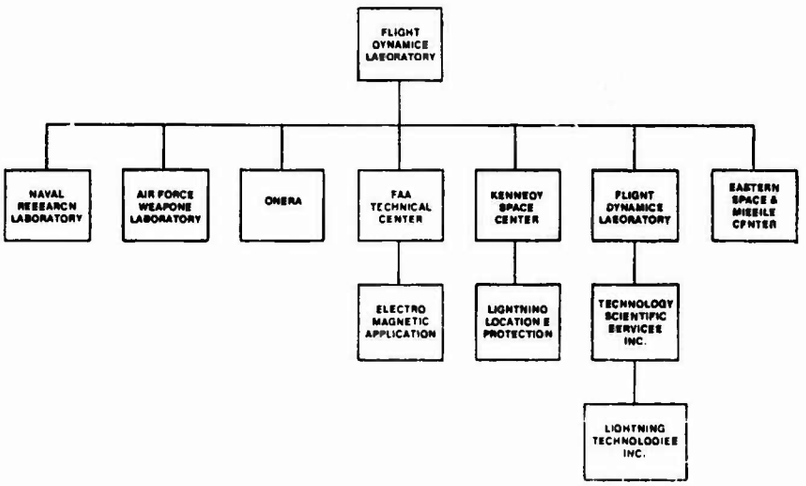


FIGURE 1. BLOCK DIAGRAM OF ORGANIZATIONS DISPLAYING ADMINISTRATIVE COUPLING

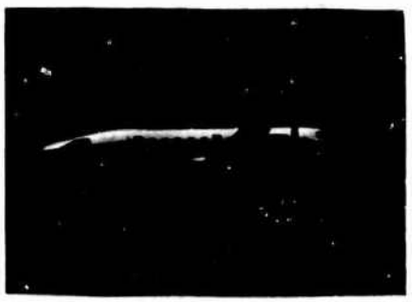


FIGURE 2. AIRCRAFT (N49)

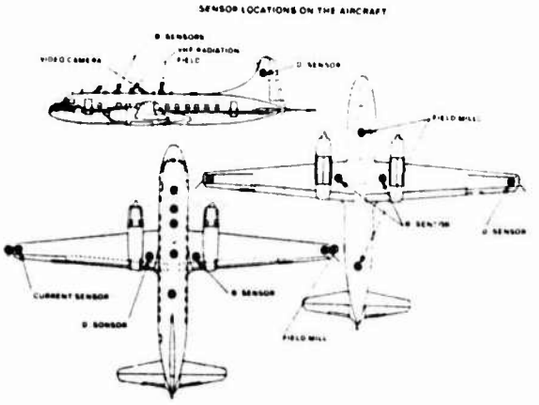


FIGURE 3. SENSOR LOCATIONS ON AIRCRAFT



FIGURE 4. WING BOOMS

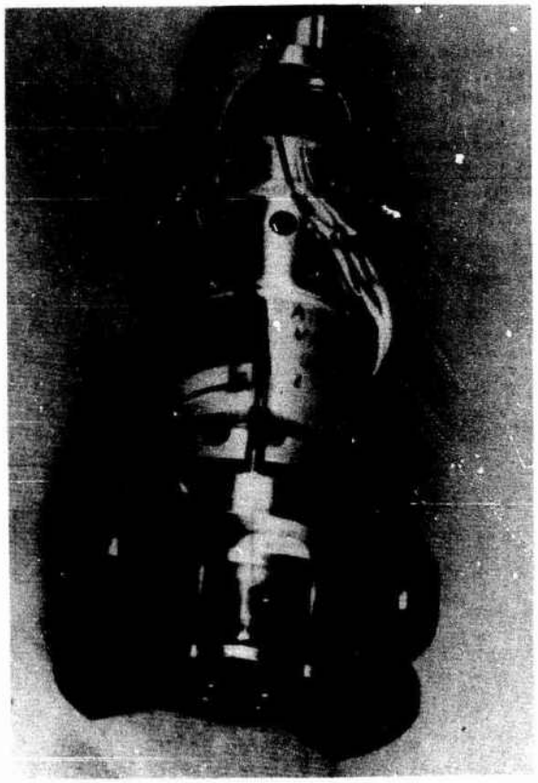


FIGURE 6. STATIC FIELD MILL MEASUREMENT

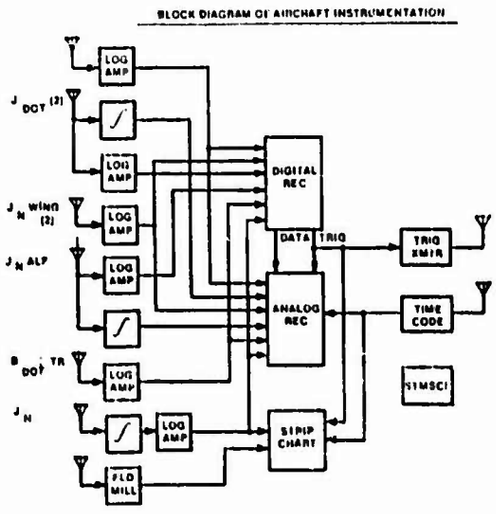


FIGURE 5. TYPICAL LIGHTNING CHARACTERIZATION DATA RETRIEVAL SYSTEM



FIGURE 7. TURBULENCE SYSTEM

AIRBORNE AND GROUND ELECTROMAGNETIC FIELD MEASUREMENTS OF LIGHTNING

P.L. Rustan Jr., B.P. Kuhlman and J.M. Reazer*

U.S. Air Force Wright Aeronautical Laboratories AFWAL/FIESL, Wright-Patterson AFB, Ohio 45433, U.S.A.
**Technology Scientific Services, Inc., Post Office Box 305, Overlook Branch, Dayton, Ohio 45431, U.S.A.*

Abstract

A CV-580 aircraft, instrumented with electromagnetic field and current sensors, was flown in central Florida during the summer of 1984. A ground test site located at the eastern tip of Cape Canaveral Air Force Station was also instrumented with electromagnetic field sensors. The ground sensors were mounted on the beach about 80 ft from the ocean. A ground plane was extended from the water to the sensors so that the fields, radiated by lightning discharges over the ocean, would propagate to the sensors without being affected by ground conductivity. Time code between the aircraft and the ground site was synchronized with an accuracy of one millisecond.

Twenty one lightning discharges attached to the aircraft. The electric and magnetic fields for one of these flashes were recorded simultaneously at the aircraft during the direct strike and at the ground site 68 km away. The airborne data show that the aircraft triggered an intracloud lightning discharge that lasted 1.2 s and consisted of an initial active phase for about 40 ms and 12 large isolated pulses during the remainder of the flash. Some of the pulses during the initial active discharge and two of the isolated pulses in the aircraft were correlated with the radiated fields measured at the ground site.

INTRODUCTION

During 1984 a Federal Aviation Administration (FAA) Convair 580 (CV-580) aircraft was inatrumented to measure the electromagnetic fields and currents produced by lightning attachment to the aircraft. The aircraft was flown in central Florida near and inside active thunderstorms at altitudes between 2,000 and 18,000 ft and regions of precipitation radar returns less than 40 dBz. The aircraft was instrumented externally with five magnetic field sensora, five electric field sensors, two current shunts, and two VHF antennas. Internally, three clip-on current probes were uaed to determine induced transients on aircraft wirea and a wire loop was monitored to measure induced voltages due to aperture coupling. Twenty eight channela of continuous analog data with a 2 MHz bandwidth in the direct channels and 500 kHz bandwidth in the FM channels were recorded in the aircraft. Six Tektronix 7612 waveform digitizera with a sample rate of 5 ns and two channels of 2048 aamples were also used in the aircraft.

A ground station waa placed at the eastern moat tip of the Cape Canaveral Air Force Station, Florida to record the electric and magnetic fields produced by the lightning diachargea that attached to the aircraft. Four flush plate dipole electric field antennas and two magnetic field loop antennas were uaed to detect the electric and magnetic fields produced by diatant lightning flashes which might attach to the aircraft. The electric and magnetic field signals were recorded continuoualy in an analog recorder with a 2 MHz frequency response. The derivatives of the electric and magnetic fields were also recorded by using two 7612 waveform digitizers. In this paper we analyze the simultaneous electric and magnetic field records from the aircraft and the ground station during a lightning strike to the aircraft on 5 Sept 84 at 23:30:36.

AIRCRAFT INSTRUMENTATION

Figure 1 shows the location of the external sensors mounted on the skin of the aircraft. Five surface current rate of change sensors designated as J_S were mounted on the aircraft at the forward upper fuselage (J_{SFUF}), aft upper fuselage (J_{SAUF}), bottom left wing (J_{SBLF}), bottom right wing (J_{SBRW}), and top left wing (J_{STLW}). Five displacement current aensors deaignated as J_N were mounted on the left wing tip (J_{NLWT}), right wing tip (J_{NRWT}), top right wing (J_{NTRW}), forward upper fuselage (J_{NFUF}), and verrical atabilizer (J_{NVS}). One current shunt was mounted on each wing tip (I_{RW} and I_{LW}).

All the aurface current rate of change sensors except the one mounted on the top left wing (J_{STLW}) were deaigned by EG&G (1). The EG&G J_S sensors were a modified version of the radial Multi-Gap Loop (MGL) ground plane B-dot Model 5 (MGL-5). This type of sensor has an equivalent area of 0.001 m^2, a frequency response in excess of 700 MHz and a riaetime of 0.5 ns. The J_{STLW} sensor was designed in France and provided by the Office National d'Edudes et de Recherches Aeroapatiales (ONERA). The physical dimenaiona and shape of the French sensor were comparable to the MGL-5 senaor.

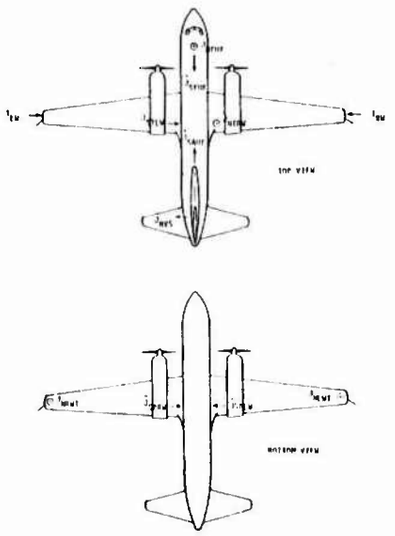


Fig. 1. CV-580 Transient electromagnetic sensor locations (Arrows indicate direction of positive current flow).

All the displacement current rate of change sensors except the one mounted on the top right wing (J_{NTRW}) were designed by EG&G (1). The J_{NLWT}, J_{NRWT}, and J_{NVS} were the EG&G Flush Plate Dipole (FPD) sensors with an equivalent area of .01 m^2. The J_{NFUF} was the same design but with an equivalent area of .005 m^2. These EG&G sensors have a frequency response in excess of 350 MHz and a risetime of 1 ns. The J_{NTRW} sensor was designed in France and provided by ONERA for this project. The French sensor was a Hollow Spherical Dipole (HSD) capable of detecting fields between 100 V/m and 316 kV/m with a frequency response from 100 Hz to 130 MHz, and a risetime of 3.5 ns.

The outputs of the surface and displacement current rate of change sensors were integrated and recorded in a 28 channel Honeywell 101 analog recorder. With the exception of the J_{NFUF} sensor, the J_S and J_N sensors were integrated using a 3.13 ms time constant and recorded on direct channels of the analog recorder (400 Hz to 2 MHz response) with a 40 dB dynamic range. The J_{NFUF} sensor output was integrated using a 220 ms time constant and recorded on three different channels. Two outputs with different ranges were recorded on FM modules of the analog recorder with a frequency response from DC to 500 kHz and the third output was monitored on a strip chart recorder. The electric field measurement range for the J_{NRWT}, J_{NLWT}, and J_{NVS} was from 4 kV/m to 1 MV/m and for the J_{NFUF} was from 22.5 kV/m to 2.25 MV/m. These electric field ranges were obtained from the integrated data in the analog recorder assuming the permittivity of free space. Similarly, the magnetic field measurement range for the J_{SEF}, J_{SAF}, J_{SBRW}, and J_{SBLW} was from 48 A/m to 4800 A/m, assuming the permeability of free space.

A solid shield semi-rigid 0.25 inch diameter heliax cable FSJ1-50 was used to carry the signals from the external J_S, J_N, and I sensors to the signal conditioner panels. The corrugated solid copper outer conductor of the heliax cables was grounded at intervals of no more than two feet throughout the aircraft to reduce coupling from electromagnetic fields. The splitters, attenuators, amplifiers, buffers, and integrators were located inside the signal conditioner panel.

A six channel Gould ES1000 electrostatic strip chart recorder was operated continuously during flight. The integrated channel of the J_{NFUF}, the two wing tip currents the aircraft time code, and a trigger signal were monitored in the six channels. The J_{NFUF} integrated signals monitored on the strip chart were sensitive to transient electric fields at the aircraft produced by lightning flashes within a few kilometers of the aircraft.

GROUND STATION INSTRUMENTATION

A US Air Force instrumentation trailer, 12 ft high and 36 ft long, was located at Cape Canaveral Air Force station about 100 ft from the ocean. Four flush plate dipole electric field antennas and two magnetic field loop antennas were used to detect the electric and magnetic fields produced by distant lightning. These antennas were located on the beach about 70 ft from the trailer. The signals from the antennas were transmitted through conduit to the instrumentation trailer. An 80x20 ft^2 aluminum wire mesh extending into the ocean for 20 ft was built to provide a highly conductive path from the ocean to the sensors.

The signals from the electric and magnetic field antennas were integrated and recorded in a Bell & Howell 3700B analog recorder using channels with different gains to increase the dynamic range. The overall dynamic range of the system was from 2 V/m to 100 kV/m for the electric field and 0.02 to 5 A/m for the magnetic field. All the ground field data presented in this paper was recorded in direct channels with a frequency response from 400 Hz to 2 MHz. IRIG B timing data available at the Cape Canaveral AFS/Kennedy Space Center complex was made available at the ground site, recorded on the analog recorder and the strip chart and transmitted to the aircraft during the first few minutes of flight. The aircraft was synchronized to the 1 kHz carrier in the IRIG B signal and time correlation better than one millisecond was maintained during the duration of the flight.

CORRELATED AIRBORNE AND GROUND DATA

On 5 Sept 84 at 23:30:36 Z, the CV-580 aircraft was struck by lightning while flying about 68 km south of the ground site. The aircraft was flying in clouds in an area of slight turbulence. Figure 2 shows a mapping of the precipitation returns as measured by the Daytona Beach, Florida weather radar station. The black areas indicate regions of precipitation returns in excess of about 30 dBz. The inner circle corresponds to a radius of 25 nautical miles. The location of the aircraft and the ground site are shown as A and G, respectively, on the weather radar picture. At the time of the strike the aircraft was flying at an altitude of 18,000 ft with an outside air temperature of -3°C.

Figure 3 shows some of the analog data recorded in the aircraft and on the ground site during the beginning of the discharge. The top six traces were played back from the analog recorder on the aircraft, whereas the bottom four traces show some of the

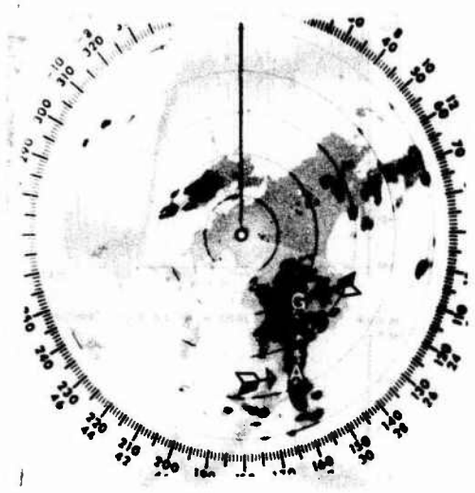


Fig. 2. Mapping of precipitation returns for the thunderstorm as measured by the Daytona Beach, Fl weather radar station. A is the location of the aircraft and G is the location of the ground site. The circular lines are 25 NM apart.

simultaneous far field data on the ground station 68 km away. The top trace is the integrated J_{NFUF} signal recorded on an FM channel. The second trace shows the time of the trigger signal for the digital data. The threshold level was set to 1500 Teslas/sec for any of the J_S sensors. The first pulse that exceeded the threshold level for digital signal acquisition occurred 4 ms after the initial attachment. The next three signals correspond to the integrated J_{NRWT}, J_{NLWT}, and J_{NLWT} recorded in direct analog recorder channels. The sixth signal from the top is the reference time code recorded in the aircraft. The bottom four signals are, from top to bottom, the vertical electric field, the north and east component of the magnetic field, and IRIG B time code signal from the ground site. The small sinewave in the time signal has a period of 1 ms.

The first indication of the discharge is seen as a slow rise of the electric field on the forward upper fuselage (E_{FUF}) on the top trace of Figure 3. The E_{FUF} rises to 320 kV/m in about 1.5 ms then decays slightly to 270 kV/m in the next 0.5 ms before undergoing a field change from 270 kV/m to -550 kV/m in 0.1 ms. This large field change corresponds to the time of the lightning attachment to the aircraft. The slow positive electric field change in the E_{FUF} prior to the discharge indicates a variation in the charge near the aircraft. Assuming an average leader velocity of 1.5×10^5 m/s (2), the initial 1.5 ms field change will correspond to a leader propagation of 300 meters. It appears that the aircraft triggered the discharge by flying about 300 m from a charge center. If a faster propagation velocity of 10^6 m/s is assumed, the leader would have to propagate 1.5 km before aircraft attachment. In that case the aircraft would have intercepted the discharge. On the contrary, for slower leader velocity the radius of aircraft influence might be only 100 or 200 m. For the first 40 ms after the initial attachment, there are a large number of pulses flowing throughout the aircraft as shown in Figure 3. The pulse repetition rate reaches a maximum of about 10^3 pulses/sec. This variable pulse repetition rate probably occurs due to the discharging of many pockets of charges during the initial active phase (3) of the intracloud discharge. The first pulse of the flash in the electric field record at the ground site corresponds to the 270 kV/m to -550 kV/m transient in the forward fuselage of the aircraft.

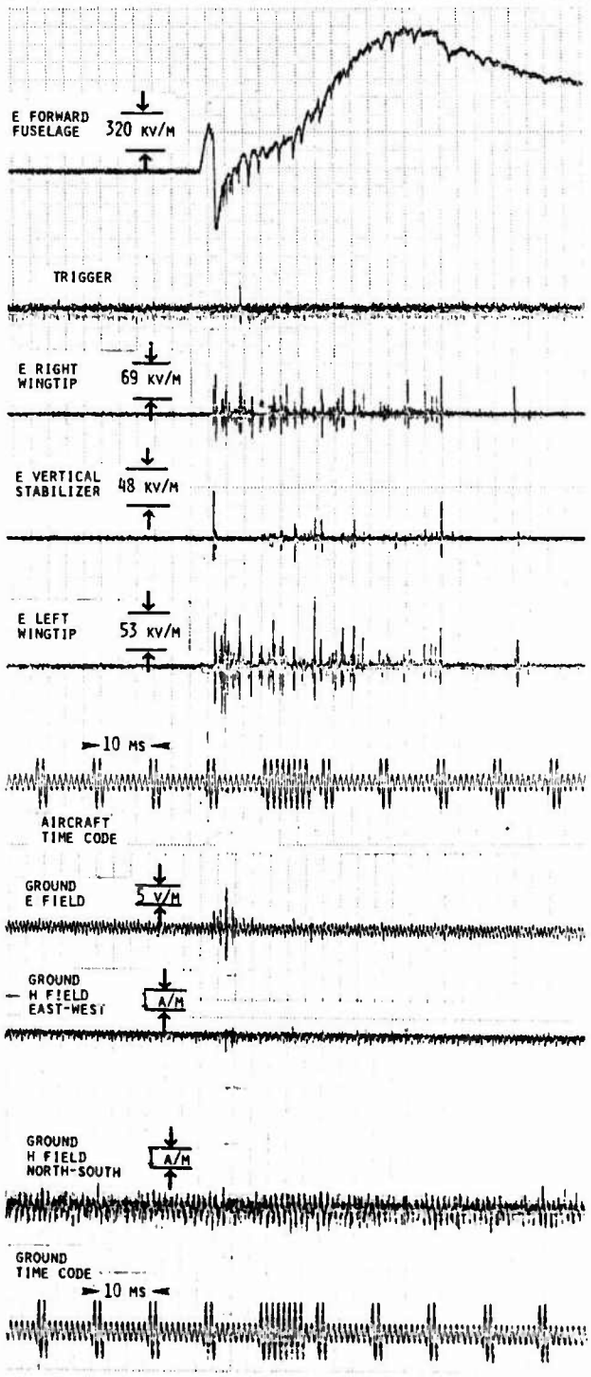


Fig 3. Simultaneous displays of the analog records during the beginning of the lightning flash. The top six traces were recorded in the aircraft and the bottom four traces were recorded at the ground site.

There are three other significant pulses on the ground site with a magnitude of at least twice the noise level of the recorder during the first few milliseconds. The largest of these pulses occurs about 2 ms after the initial lightning attachment.

Figures 4(a)-(d) show simultaneous electric field data in a one millisecond window recorded in the aircraft analog recorder at the time of the initial attachment. Figure 4(a) shows the 270 kV/m to -550 kV/m transient on the forward fuselage electric field record at the time of the initial attachment. Figures 4(b), (c), and (d) show the electric field on the vertical stabilizer, right wingtip, and left wingtip during the same period. The first large transient in the electric field record is about 100 kV/m and occurs about 245 μs from the beginning of the window of the vertical stabilizer data on Figure 4(b). The vertical stabilizer sensor measures the horizontal component of the electric field and, during this transient, the right wingtip electric field record shows a field change of about 65 kV/m with no correlated data on the left wingtip. These data show that there may have been a primarily horizontal discharge from the vertical stabilizer to the right hand side of the aircraft before the larger electric field change on the forward fuselage.

Figure 5 shows a one millisecond expansion of the left wingtip electric field analog data starting 1.2 ms after the large electric field transient in Figure 4(d). This figure is shown to illustrate the variable structure of the pulse trains during the initial lightning attachment. During the 1984 program, pulses with 30 ns risetime and a few hundred nanoseconds pulse width were recorded in the digital system (4). However, many of the pulses have a much slower risetime and wider pulse width. The first pulse at the beginning of Figure 5 has a risetime of 15 μs and a pulse width of 30 μs. However, the first pulse risetime is not shown in the picture. The second wide pulse has a risetime of 50 μs and a pulse width of 200 μs. The third pulse has a risetime and pulse width of 40 μs. Finally at the end of the one millisecond window there is another pulse with a risetime of 20 μs and pulse width of about 40 μs. The pulse width of the last pulse is not fully shown in the figure. None of these wider pulses appear to be bandlimited by the 2 MHz frequency response of the analog recorder channel. During this one millisecond expansion the pulse repetition rate is 4×10^3 pulses/sec; however, over a wider window in the active region the pulse rate is closer to 10^3 pulses/sec. The measured pulse width is related to the length of the channel and the velocity of the wave attaching to the aircraft. Assuming a leader velocity of 10^5 m/s the channel lengths neutralized by these four pulses were 300, 2,000, 400, and 400 meters, respectively. However, the channel length could have been much smaller if we assume a faster leader velocity.

Figures 6(a)-(d) show a 102 μs window of a fast transient pulse that occurred 438 ms after the beginning of the initial lightning attachment. The pulse is bandlimited by the analog recorder system. Figure 6(a) shows a 260 kV/m electric field transient at the forward fuselage which is bandlimited by the 500 kHz bandwidth of the FM channel. Figures 6(b),(c), and (d) show simultaneous electric field transients of -100 kV/m, -140 kV/m, and -70 kV/m on the vertical stabilizer, right wingtip, and left wingtip, respectively. Figures 6(b),(c), and (d) are

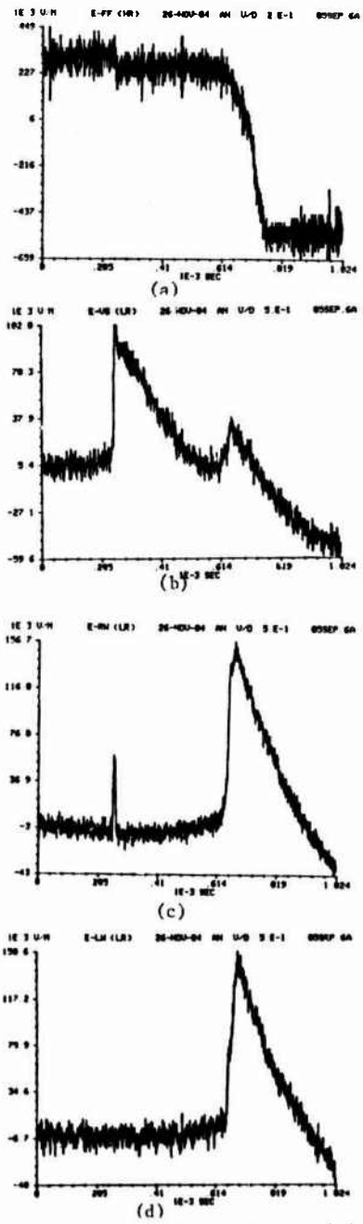


Fig 4. Simultaneous analog data recorded in the aircraft over a one millisecond window at the beginning of the lightning discharge. (a) Electric field on forward upper fuselage, (b) Electric field on the vertical stabilizer, (c) Electric field on the right wing, (d) Electric field on left wing.

bandlimited to the 2 MHz frequency response of the direct record channels. These isolated pulses during the junction phase of the intracloud discharge are often larger and faster than the pulses during the initial aircraft lightning attachment.

Figure 7 shows some of the analog records for the 1.2 sec duration of the flash. After the initial leader and aircraft lightning attachment, there was an active discharge phase that lasted about 40 ms with at least 42 pulses larger than twice the noise

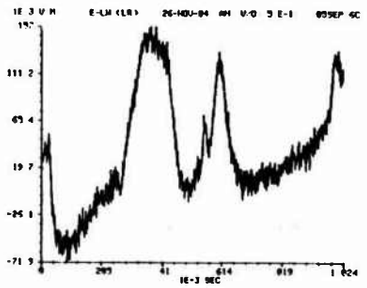


Fig 5. One millisecond time window of the electric field on the left wing starting 1.2 ms after the lightning attachment.

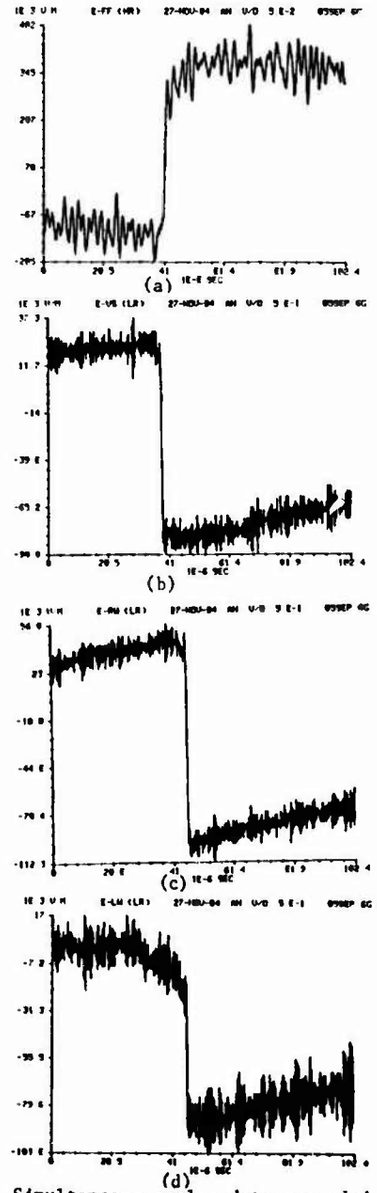


Fig 6. Simultaneous analog data recorded in the aircraft over a 102 μs window about 438 ms after the beginning of the discharge. (a) Electric field on forward upper fuselage, (b) Electric field on the vertical stabilizer, (c) Electric field on the right wing, (d) Electric field on left wing.

level. After completion of the initial active period, there were about 20 other pulses distributed over the entire duration of the flash. The pulse during the beginning of the aircraft attachment, some of the pulses during the active discharge phase and one of the isolated pulses in the junction phase of the discharge have been presented. Some of the pulses produced by the radiated fields on the ground site will now be discussed.

Figure 8 shows a 204 μs time window of the largest pulse measured at the ground site at the time of the lightning attachment. It is impossible to show simultaneous pulses with a microsecond resolution between the aircraft and the ground site because the IRIG B reference is only one millisecond.

Figures 8(a),(b), and (c) show the simultaneous vertical electric field and the two directions of the magnetic field records for the largest electric field pulse of the intracloud discharge. This pulse occurred about 3 ms after the initiation of the discharge and is the largest pulse on the seventh trace from the top in Figure 3. The electric field transient was 13 V/m and the correlated magnetic field transients were 0.459 A/m and 1.095 A/m in the North-South and East-West directions, respectively. Since the aircraft lightning attachment occurred over land about 68 km south of the ground site, most of the radiated fields produced by the discharge were attenuated by the ground propagation. The pulse shape of the electric and magnetic fields measured for this flash has similar characteristics to those reported by Weidman and Krider (1979), and Krider et al (1975), (4) and (5). However, their typical electric field magnitude for flashes between 15 and 30 km was 20 to 25 V/m (4). The reported (5) magnitudes of the magnetic flux density for intracloud flashes within 50 km were 5 to 10×10^{-9} Teslas. The pulse in Figure 8 has magnetic fields of 14×10^{-9} and 6×10^{-9} Teslas. This intracloud discharge had a much larger electric field level than would be obtained by extrapolating Weidman and Krider's and Krider et al's results for this distance. Some simultaneous radiated fields were also measured on the ground site during the isolated pulses of the junction phase of the intracloud discharge. Therefore, it is very clear that the lightning discharge that attached to the aircraft was a large, intracloud discharge.

CONCLUSION

We have presented simultaneous analog data on an aircraft and at a ground site 68 km away for an intracloud lightning discharge that attached to the aircraft. It is shown that this discharge is larger than the typical intracloud discharge data presented in the literature. This is an important point because there have been some claims reported at previous conferences that the lightning attachment to the aircraft might be produced by a "baby lightning", which implies a small discharge around the aircraft. This is not the case for this flash and our analysis indicates that this does not appear to be the case for any of the lightning discharges that attached to the CV-580 aircraft during the 1984 summer program.

It is also evident from the analog records that there are two different phases during the intracloud discharge as measured in the aircraft during lightning attachment: the initial and very active discharge phase with a pulse repetition rate of about 10^3 pulses/sec and duration near 40 ms and the

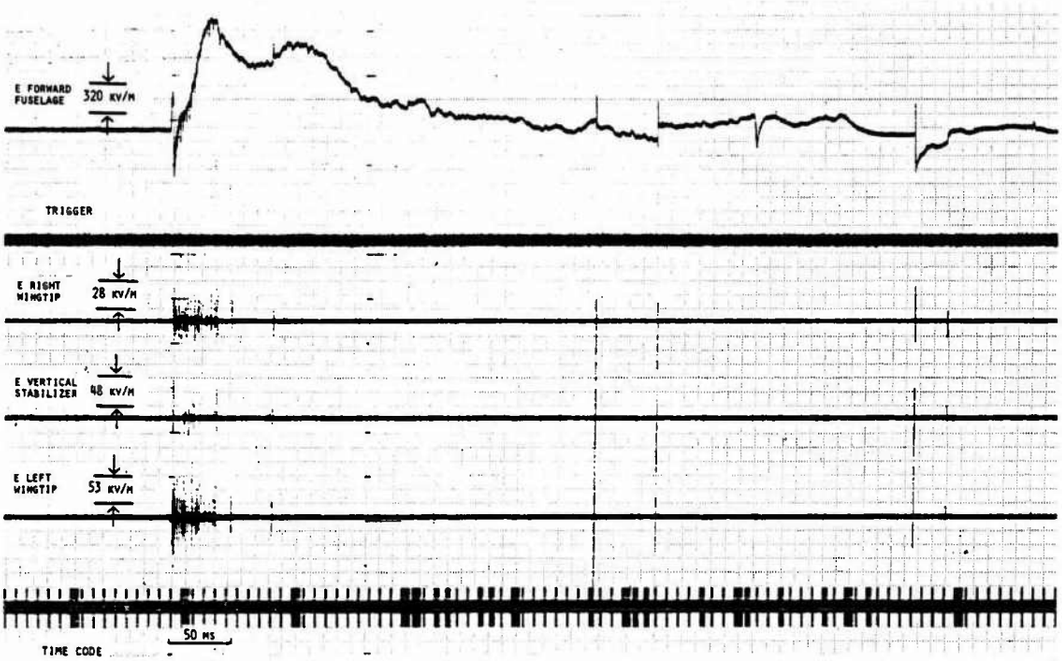


Fig 7. Simultaneous displays of six of the analog records in the aircraft during the lightning discharge.

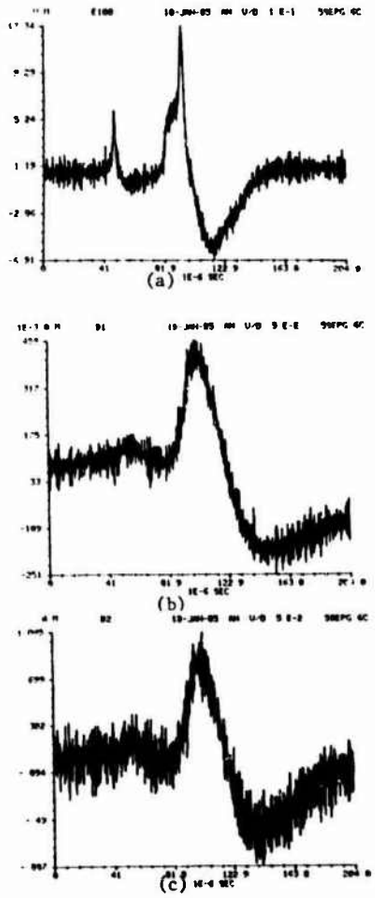


Fig 8. Simultaneous records of the vertical electric field (a) and the two magnetic fields (b) and (c) measured at the ground site 68 km away from the intracloud discharge.

junction phase which is characterized by isolated pulses. The largest pulses in the intracloud discharge are usually found in this junction phase. The risetime of the pulses in the discharge can be faster than the 350 ns step response of the analog recorder or as slow as 100 μs. The pulse width of the pulses in the discharge can also be quite variable and narrower than recorder bandwidth or as wide as several hundreds microseconds. We have related the width of the pulse to the length of the lightning channel.

We also analyzed the initiation of the discharge by examining the electric field data obtained with a 220 ms integration constant and recorded in a channel with a DC frequency response. From this data it appears that the aircraft triggered the discharge by flying within 300 m from an active charge center. If the leader velocity is near 1.5×10^5 m/s, it is highly likely that an intracloud discharge was about to happen in the next few seconds and the aircraft just happened to be the triggering source by enhancing the field in the proximity of the charge center.

REFERENCES

1. EG&G Wash Anal Sciences Center, Inc., 2450 Alamo Ave, S.E.,P.O. Box 9100, Albuquerque, NM 87119.

2. M. A. Uman, Lightning, Dover Pub, 1984.

3. N. Kitagawa, and M. Brook, "A comparison of intracloud and cloud-to-ground lightning discharges," J. Geophys. Res., Vol 65, pp 1189-1201, 1960.

4. C.D. Weidman, and E.P. Krider "The radiation fields wave forms produced by intracloud lightning discharge processes," J. Geophys. Res., Vol 84, pp 3157-3164, 1979.

5. E.P. Krider, G.J. Radda, and R.C. Nogle, "Regular radiation field pulses produced by intracloud discharges," J. Geophys. Res., Vol 80, pp 3801-3804, 1975.

AIRCRAFT LIGHTNING ATTACHMENT AT LOW ALTITUDES

P.L. Rustan Jr. and J.P. Moreau*

U.S. Air Force Wright Aeronautical Laboratories, AFWAL/FIESL, Wright-Patterson AFB, Ohio 45433, U.S.A.
**ONERA, 29, Avenue de la Division Leclerc, 92329 Châtillon, France*

Abstract -

This paper presents a characterization of lightning attachment to aircraft on the basis of a large amount of data collected during the C-130 1981 program (2 strikes), the CV-580 1984 program (21 strikes), and the C-160 Landes program (18 strikes). These data were collected in Florida (C-130 and CV-580) and in France (C-160) at altitudes ranging from 2000 to 18000 ft. The parameters being characterized are the variations of the currents and the electric and magnetic fields on the aircraft surface during aircraft lightning attachment.

The analog data for the electric and magnetic fields during lightning attachment are similar for all the flashes. Lightning attachment to the aircraft appears to be initiated by a leader process which lasts about one or two milliseconds. This process is usually followed by a fast pulse similar to those of ground return strokes. After this initial pulse, there is a very active period of 20 to 60 milliseconds which is characterized by a pulse repetition rate of 1000 pulses per second. The remainder of the flash contains isolated pulses similar to those obtained during the final or junction phase of intracloud discharges.

Typical pulse structures and the pulse repetition rates are described including the fine structure of some large pulses obtained with a 5 ns sampling rate for some flashes. These pulses show evidence of resonances due to the aircraft geometry.

INTRODUCTION

In May 1982 the IEEE Transactions on Electromagnetic Compatibility published a special issue on lightning and its Interaction with Aircraft. The articles in this volume contain a discussion of the lightning phenomenon, its interaction with the aircraft and the various aspects of lightning protection. These articles constitute a survey of the body of knowledge in this area of research. The paper "Triggered Lightning" (1) published in this issue contains an excellent discussion of the aircraft lightning interaction and summarizes the data collected during the various lightning research programs through 1981.

Since 1981 a significant amount of lightning attachment data has been collected and analyzed in four research programs in the WC-130, CV-580, C-160, and the F-106 aircraft. This paper summarizes some of the data collected in the first three programs. These aircraft were flown at altitudes between 2,000 and 20,000 ft near and on the edges of active thunderstorms. There are many similarities among the data collected in different flashes for the same aircraft and among the three types of aircraft to derive some conclusions about the overall characteristics of the aircraft lightning attachment process. Specifically, we have analyzed the analog data collected during the initial attachment of lightning to the aircraft and the digital pulse structure during the flash.

LIGHTNING INITIATION

Overall Characteristics.

During 1984 the CV-580 aircraft was instrumented with five surface current rate of change sensors, five displacement current rate of change sensors and two current sensors(2). The aircraft was flown in central Florida between 11 July and 5 Sept 84. The surface current and displacement current sensor readings were proportional to the rate of change of the magnetic and electric field, respectively. The outputs of all the electromagnetic field sensors were integrated and recorded in a wideband analog recorder. Whenever the derivative output of the electromagnetic field sensors exceeded a preset threshold level, a window of 10.24 us was acquired with a sample every 5 ns. The combination of the high resolution digital data for specified intervals and the lower frequency resolution analog data provided information on the processes during lightning attachment to the aircraft.

We studied the forward fuselage electric field records during the beginning of all the lightning attachments to the CV-580 aircraft for which analog data was recorded. This sensor instrumentation was designed to record electric field between 22.5 kV/m and 2.25 MV/m. Figure 1 shows a block diagram of the sensor instrumentation. The input signal to the 0.005 m^2 area sensor was integrated with a 220 ms time constant, split into two channels to increase the dynamic range and recorded in two FM channels of the Honeywell 101 analog recorder with a frequency response from DC to 500 kHz. This sensor does not detect electrostatic fields, but with this long time constant it can measure a very slowly varying field. A positive field change on the recorder corresponds to the lowering of negative charge for an identical field instrumentation on a ground site.

Figures 2, 3, and 4 show the electric field measured on the forward fuselage and recorded on the analog recorder during the beginning of the

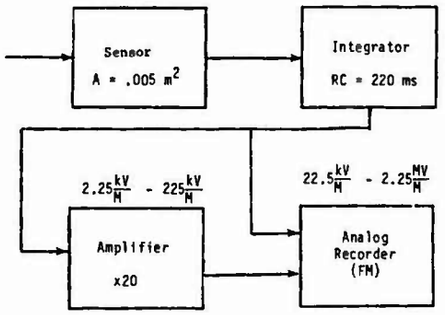


Fig 1. Block diagram of the forward upper fuselage electric field sensor used in the CV-580 aircraft.

lightning discharge. Figure 2 shows the electric field during the initiation of 10 different lightning discharges. The horizontal scale for all flashes is 3 ms per division and the vertical scale is 320 kV/m per division. Figures 2(a) and (b) occurred 11 July 84 at an altitude of about 14,000 ft prior to the beginning of the discharge, the electric field is saturated in the positive direction indicating negative charge on the aircraft. All the lightning strikes in Figure 2 were obtained with the aircraft flying at either 14,000 or 18,000 ft with an outside air temperature between 5°C and -7°C. Figures 2(c)-(j) start from zero electric field. During the beginning of all ten flashes there is a slow negative electric field change lasting about 2 ms followed by a positive, faster field change. The attachment to the aircraft occurs during the positive, faster field change. Figures 2(c)-(j) were obtained at the beginning of eight different lightning attachments on 13 July, 7 Aug, and 5 Sep 84. For flashes 2(c)-(j) there was no indication in any of the sensors being recorded

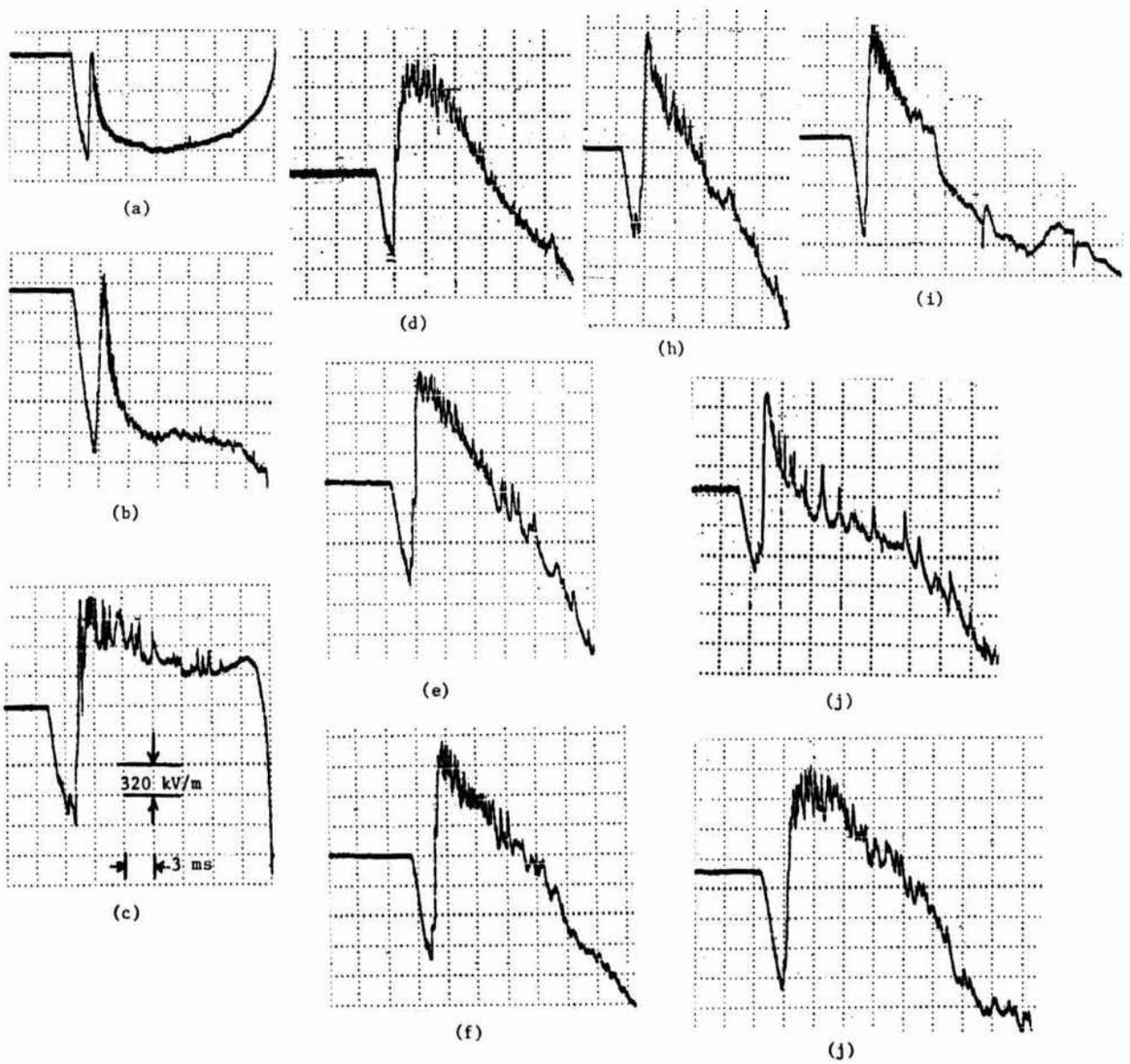


Fig 2. Forward fuselage electric field measurements during the initiation of 10 different lightning discharges. The horizontal scale is 3 ms per division. The vertical scale is 320 kV/m.

that a flash was going to occur prior to the negative-going field change. The slow negative field change in the 10 flashes represents a variation of the charge near the aircraft produced by a leader propagation. Even though the leader velocity is not known, the short duration of the negative leader prior to the discharge probably indicates that the distance over which the leader propagated did not exceed 300 m. The presence of the aircraft in a highly electrified field is sufficient to enhance the ambient electrostatic field to a level where breakdown occurs. All the ten aircraft lightning attachments in Figure 2 appear to be triggered by the presence of the aircraft. All these flashes show about the same leader duration indicating about the same distance from a high electric field region within the cloud.

Figure 3 shows the same type of data with three other lightning strikes on the aircraft while flying at 18,000 ft. Figure 3(a) corresponds to a strike on 7 Aug 84 and Figures 3(b) and (c) were recorded on 5 Sept 84. Figure 3(a) shows a variation of the electric field on the aircraft surface for over 30 ms prior to the lightning attachment. Figure 3(b) shows a variation of the rate of change of the field for about 15 ms prior to the discharge. Finally, Figure 3(c) shows a leader change for at least 3 ms prior to attachment. The traces shown in Figures 3(a) and 3(b) are substantially different than those in Figure 2. The fact that there is a substantial field change between 3 and 30 ms prior to the attachment appears to indicate that the aircraft did not trigger these discharges. Probably the aircraft intercepted a branch of a propagating lightning discharge instead of initiating the discharge as it appears to have done in the cases in Figure 2.

Figure 4 shows the forward fuselage field change during an aircraft lightning attachment at 4,000 ft. The aircraft was just above the bottom of the cloud, which was estimated at 3,500 ft. This discharge has different characteristics than the 13 flashes shown in Figures 2 and 3. First, a negative electric field change is detected for at least 5 ms, showing a leader propagation, then the attachment occurs. The only three fast pulses in the flash are shown in Figure 4. Unlike the other flashes where significant field changes are detected for hundreds of milliseconds after the initial attachment, most of the charge transfer in this flash occurred in the first tens of milliseconds. We could not confirm that this flash hit the ground. If the flash was a cloud-to-ground discharge, it probably consisted of only one return stroke. If the discharge did not make ground contact, it was a natural intracloud discharge in the lower levels of the clouds and transferred a small amount of charge. In any case, the long leader indicates that the aircraft did not trigger the lightning discharge.

Figure 5 shows the current flow on the left wing tip and the electric field on the right wing and the vertical stabilizer during the first 100 ms of a flash 7 Aug 84 at 18,000 ft in the CV-580 aircraft. The forward fuselage electric field for the first few milliseconds of this flash is shown in Figure 2(e). According to our interpretation of the data, this flash was probably triggered by the aircraft. The flash lasted 460 ms and transferred a charge of about 100 coulombs through the aircraft. The continuing current flow during the initial phase of the discharge shown in Figure 5(a) was about 250 A and the charge transferred was 30 C. There were

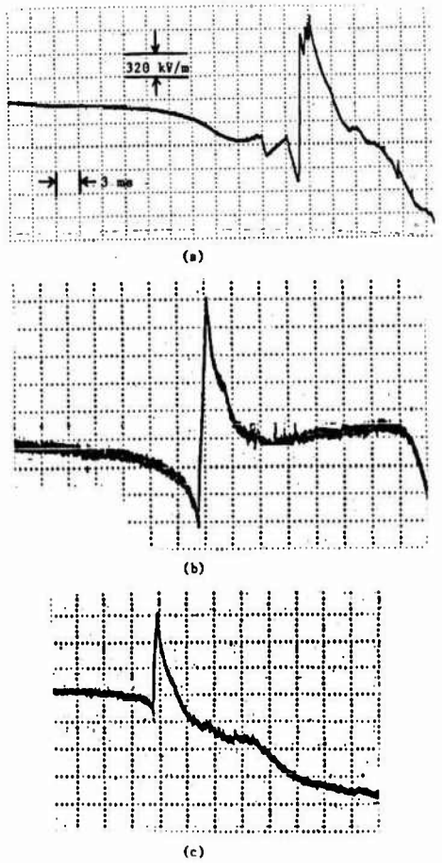


Fig 3. Forward fuselage electric field measurements during the initiation of 3 different lightning discharges. The horizontal scale is 3 ms per division. The vertical scale is 320 kV/m.

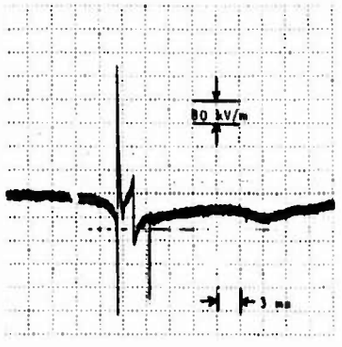


Fig 4. Forward fuselage electric field measurement during an aircraft lightning attachment at 40,000 ft. The horizontal scale is 3 ms per division. The vertical scale is 80 kV/m.

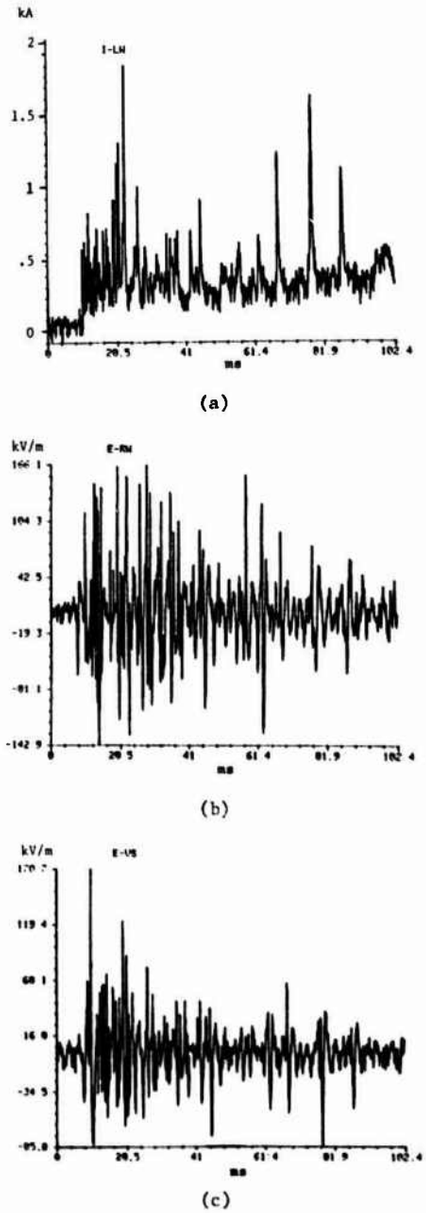


Fig 5. Current flow on the left wingtip(a), and electric field on the right wing (b), and vertical stabilizer (c) during the first 100 ms of a lightning attachment to the CV-580 aircraft.

many current pulses superimposed on the continuing current and the largest current pulse measured was 1.8 kA. However, after completion of the summer experiment, burn spots were noted near the current shunt due to arcing of the current in the channel. Our laboratory experiment showed that the inductance in the current shunt circuit was too large to measure rate of rise larger than 10^7 A/s. The current shunt measured correctly the continuing current levels but was limited to 10^7 A/s in the discrete current pulses before arcing occurred. Figures 5(b) and 5(c) show the simultaneous records of the electric field on the right wing and the vertical stabilizer for this flash. There are simultaneous electric field pulses on the right wing and the vertical stabilizer for all the discrete current pulses detected on the left wing, but there are many other field pulses which do not have large correlated current pulses. The largest electric field change pulse during the first 100 ms was 171 kV/m at the vertical stabilizer during the beginning of the discharge. However, the largest field changes in the flash occur during the isolated pulses near the end of the discharge where about 250 kV/m transients were measured on both wingtips and on the vertical stabilizer. Also there is a reversal of the polarity of all the electric field transients after the first 200 ms of the discharge. The junction phase (3) of the intracloud discharge has been characterized as containing large, isolated transients of opposite polarity as compared to earlier stages of the flash.

Figure 6 shows the overall characteristics of one of the direct strike lightning attachments on the WC-130 aircraft at 17,000 ft in southern Florida on 17 July 1981 (4). Figures 6(a) and (b) show the traces of the analog electric field field on the forward and aft fuselage. Figures 6(c) and (d) show the magnetic field analog records which are proportional to current flow in the nose to tail and wing to wing direction. The traces on Figures 6(a)-(c) are saturated because the aircraft instrumentation was designed primarily to measure the far fields produced by lightning. The flash lasted 295 ms and consisted of two phases. The first phase lasted 76 ms and had a pulse repetition rate greater than 10^3 pulses/sec. The second phase consisted of a few large, isolated pulses. The lightning strike swept across nine fastening screws spread along the upper fuselage from a spot outside the copilot's window to a spot near the wing. Also, one of the two HF antenna wires mounted between the upper fuselage and the stabilizer was burned in half. The magnetic field data on Figures 6(c) and (d) confirm the fact that most of the current propagated in the nose-to-tail direction.

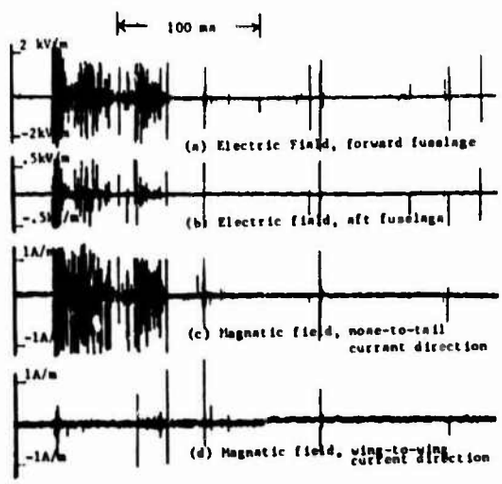


Fig 6. Electric (a), (b) and magnetic (c), (d) fields measured at four aircraft locations during a lightning attachment to the WC-130 aircraft.

The overall characteristics of the discharge on the analog records for the two lightning strikes recorded in the WC-130 aircraft in 1981 were similar to those recorded in the CV-580 aircraft in 1984. Both aircraft flashes last about the same amount of time as natural lightning discharges and have similar pulse repetition rate and overall characteristics.

The analog records of the Transall data (4) shown in Figure 7 are comparable to the data collected in the other programs and shows the large variability of the current pulses that propagate throughout the aircraft during lightning attachment.

The variations in the pulse width between about 100 ns and tens of microseconds indicate that the channel length may range between about 100 m and several kilometers. The Transall data does not appear to show current pulses larger than about 10 kA flowing on the aircraft. This result is also consistent with the C-130 and CV-580. Regardless whether we measure the current directly or we infer its magnitude from the electromagnetic field values, no large peak current levels comparable to cloud-to-ground discharges are determined.

Figures 7(a)-(e) show magnetic pulses detected in the Transall C-160 aircraft during some of the lightning attachment at altitudes between 14,000 and 18,000 ft Mean Sea Level (MSL). The magnitude of the current pulses on the aircrsft that produced these magnetic fields were between 3 and 7 kA. These pulses vary in risetime, pulsewidth and pulse repetition rate. Figure 7(a) and (b) show pulses with risetimes of about one microsecond and pulsewidths of about 15 μs. Figure 7(c) shows a double pulse with a pulse width of about 30 μs. Figure 7(d) shows the more complex structure of a slow negative pulse superimposed with faster positive pulses. Finally, Figure 7(e) illustrates the pulse repetition rate often encountered in all the airborne measurements of lightning attachment to aircraft. In Figure 7(e) the pulse repetition rate is greater than 10^4 pulses/sec.

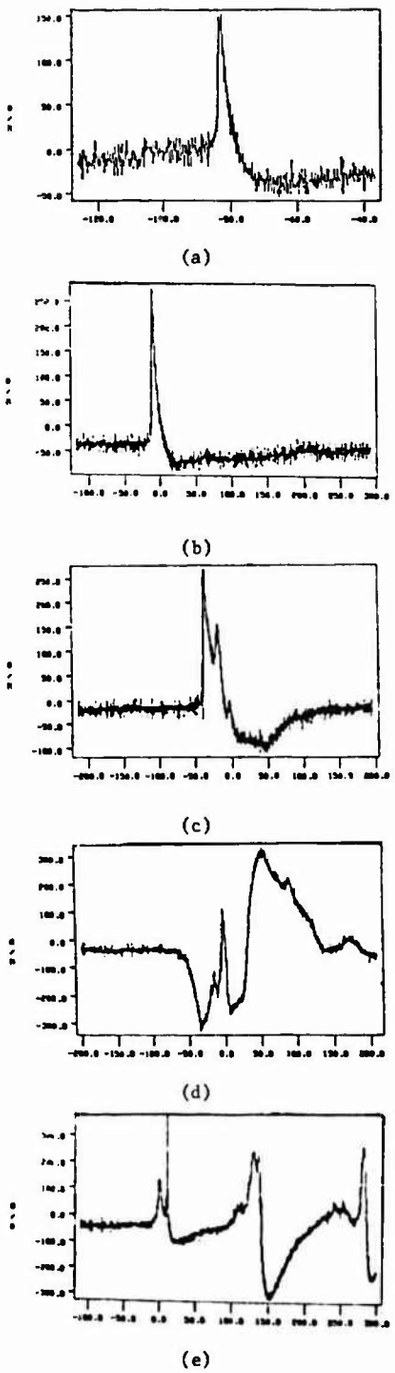


Fig 7. Typical magnetic field pulses measured on the surface of the Transall C-160 aircraft during lightning attachment. The horizontal scale is time in microseconds.

Detailed Pulse Structure.

So far we have discussed the lightning attachment characteristics derived from analyzing the wideband analog data with an upper frequency response of 2 MHz. All these lightning research aircraft were also instrumented to record higher frequency currents and electromagnetic fields during lightning attachment by selecting a threshold level and capturing the first interval in the flash that exceeded the threshold level.

Figure 8 shows four simultaneous digital data traces acquired by using Tektronix 7612 digitizers with 2048 data samples per channel and 5 ns between samples. This data was obtained during one of the isolated pulses about 100 ms after the beginning of the flash. This was the first pulse that exceeded the preset threshold level of 1500 T/s. Figures 8(a)-(d) show the displacement current density in A/m^2 recorded on the right and left wing and the surface current denaity on the right wing and aft fuselage, respectively. The largest field values of -21.7 A/m^2 and 2,065 T/s were measured on the right wing sensors. We subtracted the cable propagation delays from the data to determine the difference of the time of arrival of the pulse at the various sensors. The attachment occurred on the right wing and the right wing signals arrived first and had the largest magnitude. The time delay of the displacement current density pulse between the right wingtip and the left wingtip was 100 ns which corresponds to the speed of light propagation over a distance of 100 ft. The difference in the time of arrival of the displacement and surface current density first peak pulse between the right wingtip and all the sensors in the aircraft was roughly

equal to the time required for a pulse propagating at the speed of light of 1 ft/ns. After the initial first peak pulse on the displacement and surface current density in Figure 8, there is a decaying exponential pattern. The subsequent peaks on the waveforms are obtained from the reflection of the current waveform when it strikes an aircraft boundary with a different impedance. The subsequent peaks on the damped sinusoidal waveform in Figure 8(a) are obtained from the reflection of the initial current pulse as it propagates across and through the wings and fuselage and reflects from the opposite wingtip, the tail and the nose. The difference in the amplitude of the reflected pulse is due to the reflection coefficient of the boundaries. From this analysis and that of the digital data acquired in the summer 84 experiment, we concluded that the aircraft lightning channel propagated throughout the entire aircraft. Even though there may be a single entry and exit point in the aircraft, the electromagnetic fields propagate throughout the aircraft and reflect from all the boundaries. Additionally, there has to be a lightning channel at all the aircraft boundaries, otherwise the first peak of the field waveform in Figure 8(a) and others will be fully reflected when it reaches the wingtips, nose and tail of the aircraft. This type of analysis presents a new challenge to the standard lightning attachment patterns discussed on the SAE-4L Standards (5).

Figure 9 shows one of the lightning pulses recorded with the Transall digital acquisition system. The pulse has a risetime of about 80 ns, a pulsewidth of 150 ns and roughly corresponds to a current pulse of 3 kA. The reflections of these pulse as it propagated to the aircraft boundaries are smaller than those obtained in the CV-580 aircraft. These differences may be due to the differences of the aircraft impedances and the length of the lightning channel.

CONCLUSION

We have presented an analysis of the data collected in the C-130, CV-580 and Transall C-160 aircraft. Some of these data have been shown in time scales ranging from tens of nanoseconds to hundreds of milliseconds. To understand the mechanism of the lightning attachment to the aircraft, we have shown data about the overall structure of the flash and the individual pulses in the discharge. We show that continuous wideband analog recording of the lightning discharge is as important in this type of research as the high frequency resolution windows of the individual pulses. From the continuous analog data we can determine the role of the aircraft in the initiation of the discharge, and the overall structure of the flash. The latter provides some key parameters on aircraft lightning protection such as pulse repetition rate and total charge and energy transferred through the aircraft. From the individual high frequency pulses we can determine the peak magnitude and rate of rise of the currents and electromagnetic fields on the aircraft. The latter information is critical for protecting aircraft against indirect effects while the early information is needed to protect the aircraft against direct effects.

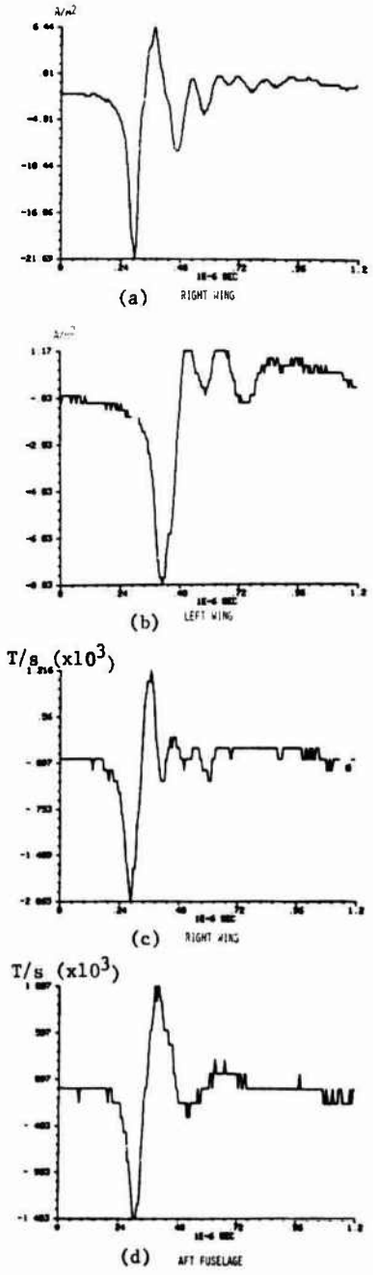


Fig 8. Displacement current density on the right wing (a) and left wing (b), and surface current density on the right wing (c), and aft fuselage (d) during the first pulse that exceeded the threshold level of 1500 T/s set for this flight. The total horizontal scale is 1.2 microseconds.

Our discussion of triggered lightning based on the data in Figures 2-3 indicates that the aircraft is highly likely to trigger the lightning discharge when flying in close proximity to a charged region. Our limited data from between 14,000 and 18,000 ft show that aircraft might trigger about 75% of all aircraft lightning attachments. However, this percentage probably becomes much less at lower altitudes where there is a smaller amount of charge and might become much larger at about 30,000 ft.

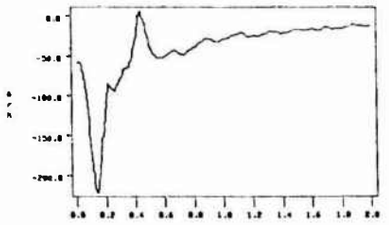


Fig 9. Magnetic field pulse measured with a sample of 2 ns on the C-160 aircraft during a lightning attachment. The total horizontal scale is 2 microseconds.

The variations in the analog electric field records in all the lightning discharges in the CV-580 can be used to infer that the current data shown in Figure 5 might be typical of the current in intracloud discharges. That is, charge transfer of tens and hundreds of coulombs appears to occur in intracloud discharges near the freezing level.

REFERENCES

1. D.W. Clifford and H.W. Kasemir, "Triggered Lightning," IEEE EMC Trans., May 1982.

2. P.L. Rustan, B.P. Kuhlman, and J.M. Reazer, "Airborne and Ground Electromagnetic Field Measurements of Lightning," 10th Int. Aerospace and Ground Conference on Lightning and Static Electricity, Paris, France, June 1985.

3. N. Kitagawa and M. Brook, "A Comparison of Intracloud and Cloud-to-ground Lightning Discharges," J. Geophys Res., Vol 65, pp 1189-1201, 1960.

4. P.L. Rustan, B.P. Kuhlman, A. Serano. J. Reazer, and M. Risley," Airborne Lightning Characterization," AFWAL-TR-83-3013, Jan 1983.

5. J.P. Moreau, and J.C. Alliot, "E and H Fields Measurements on the Transall C-160 Aircraft During Lightning Flashes," 10th Int. Aerospace and Ground Conference on Lightning and Static Electricity, Paris, France, June 1985.

6. J.A. Plumer, J.D. Robb, et al., "Lightning Test Waveforms and Techniques for Aerospace Vehicles and Hardware," Report of SAE Committee AE4L, 20 June 1978.

RESEARCH IN LIGHTNING SWEPT-STROKE ATTACHMENT PATTERNS AND FLIGHT CONDITIONS WITH THE NASA F-106B AIRPLANE

B.D. Fisher, P.W. Brown and J.A. Plumer*

NASA Langley Research Center, Hampton, Virginia 23665, U.S.A.
**Lightning Technologies, Inc., Pittsfield, Massachusetts 01201, U.S.A.*

Abstract - Lightning swept flash attachment patterns and associated flight conditions recorded from 1980 to 1984 during 1154 thunderstorm penetrations and 637 direct strikes with a NASA F-106B research airplane in Oklahoma and Virginia have been studied with an emphasis on lightning avoidance by aircraft and on aircraft protection design. The individual lightning attachment spots, along with crew comments and photographic data from a cockpit-mounted video camera and an aft-facing, fuselage-mounted 16-mm movie camera have been used to identify lightning swept-flash attachment patterns. The altitudes, ambient temperatures, turbulence and precipitation at which the strikes occurred are summarized and discussed. It was found that the peak strike rate (2.1 strikes/min) occurred at altitudes between 38 000 and 40 000 ft, corresponding to ambient temperatures colder than -40°C. Whereas only 34 strikes were experienced at altitudes below 20 000 ft (ambient temperatures warmer than -20°C), 603 strikes were experienced above 20 000 ft altitude. Finally, although the swept-flash attachment patterns fall into four general categories, it has been found that any exterior surface of this airplane may be susceptible to direct lightning attachment.

I - INTRODUCTION

The NASA Langley Research Center Storm Hazards Program [1-5] is being conducted to improve the state of the art of severe storm hazards detection and avoidance, as well as protection of aircraft against those hazards which cannot reasonably be avoided. The primary emphasis of the program is being placed on lightning hazard research, although research into such areas as wind shear and turbulence [6] also is being conducted. From 1980 to 1984, 1154 thunderstorm penetrations were made with an instrumented and lightning-hardened NASA F-106B airplane in Oklahoma and Virginia in conjunction with ground-based weather radar measurements by NOAA-National Severe Storms Laboratory (NSSL) and the NASA Wallops Flight Facility (WFF), respectively. During these penetrations, 637 direct lightning strikes were experienced; in addition, lightning transient data were recorded from 177 nearby lightning flashes. Since 1982, the UHF-band radar at NASA WFF has been used to guide the airplane through the upper electrically-active regions of thunderstorms [7]. In 1984, the UHF-band radar also was used to provide guidance to electrically-active regions in thunderstorms at altitudes below 20 000 ft.

Two purposes of the Storm Hazards Program, other than the detailed measurement of the electromagnetic characteristics of airplane lightning strikes, are to quantify those conditions which are conducive to lightning strikes to aircraft and to clarify some of the more questionable aspects of establishing lightning strike zones on aircraft. Since some new aircraft designs are incorporating large areas of skin and structure of composite materials, improved knowledge of the susceptibility of various parts of the aircraft surface to lightning strikes is essential. The present definitions of probable lightning strike zones [8 and 9] are based on past experience and tests in which scale models are subjected to simulated lightning strikes. Initial results from the present program verified the need for further clarification of probable lightning strike zones. To facilitate the determination of the lightning swept-flash patterns on the F-106B airplane, an extensive onboard photographic system is used [10 and 11]. The purpose of this paper is to update the lightning attachment point analysis and lightning strike condition data presented to this forum in 1983 [4] by summarizing the data from 1980-1984 [11].

II - TEST EQUIPMENT AND TEST PROCEDURES

II.1 Test Equipment

II.1.1 F-106B research airplane

A thoroughly instrumented and lightning-hardened F-106B "Delta Dart" airplane (figure 1) is used to make thunderstorm penetrations [2 and 3]. Based on the lightning experiences of this program, the lightning hardening procedures [2] now include removing paint from most most exterior surfaces of the airplane to reduce swept-stroke lightning dwell time, hence minimizing the chance of a lightning melt-through anywhere on the airplane. Prior to each thunderstorm season, the lightning hardening integrity is verified during ground tests in which simulated lightning currents and voltages of greater than average intensity are conducted through the airplane with the airplane manned and all systems operating [2].

II.1.2 Airborne cameras and optics

The lightning attachments to the airplane have been filmed by combinations of five onboard cameras [10,

11, and 12]. The characteristics of these cameras are given in table I, and the locations of the airborne camera systems are shown in figure 2.

Since 1980, aft attachments have been viewed by a 16-mm movie camera mounted under a fairing on the left side of the fuselage (figures 1(b) and 2), looking aft with a field of view including the left wing tip and vertical tail. From 1980-1983, this camera utilized a pin-hole instead of a lens, and was run continuously from cloud entry to cloud exit on each penetration [10]. Several improvements were made to the camera in 1984: a wide-angle lens (table I) replaced the pin-hole for the reasons given in [11]; a heated window was installed to reduce the number of instances of fogging and icing previously experienced [10]; and, later during the 1984 season, this movie camera was modified further so as to trigger automatically via inputs from two light-sensitive diodes mounted behind the pilot's rear-view mirror (see figure 2 and [11]), facing the nose boom. In the automatic mode, the movie camera could be preset prior to each flight to run at nominal frame rates of either 200 or 400 frames/sec, with a one second duration for each actuation. At the nominal 400 frames/sec rate, there were 126 exposed frames for each actuation, primarily due to the lag associated with camera motor start and motor acceleration/deceleration characteristics.

Also in 1984, a black and white video camera (table I) was selected and installed in the cockpit between the pilot's ejection seat and the flight test engineer's forward instrument panel (see figures 1(b) and 2). The only candidate camera acceptable, for the reasons given in [11], used a Charge Induction Device (CID) sensor. The camera faced aft with a field of view encompassing both wing tips. However, the vertical tail was not visible because of the blockage caused by the aft bulkhead in the cockpit and by the overhead canopy rail. The video recorder was located in the forward section of the weapons bay (see figure 2). The recorder and camera were operated continuously throughout the flight. The camera recorded 30 frames/sec, with each frame composed of alternating, interleaved rastor lines from the last 1/60 sec of the previous frame and the first 1/60 sec of the current frame.

II.1.3 Other airborne data systems

The direct-strike lightning instrumentation system (DLite) [5, 13-15] records electromagnetic waveforms from direct lightning strikes and nearby lightning flashes in flight by using electromagnetic sensors (figure 1) and a shielded recording system with 5 nanosecond time resolution located in the weapons bay. Outputs from several of the DLite sensors also were recorded on a Boeing Data Logger System [16] which was mounted in the weapons bay through the 1983 season. The airplane attitude, Mach number, altitudes, ambient temperatures, and other flight conditions were measured by the Aircraft Instrumentation System (AIS) and the Inertial Navigation System (INS) [4 and 6].

II.1.4 Ground-based systems at NASA Wallops Flight Facility

For the research flights in Oklahoma in 1980 and 1981, the NSSL Doppler radar at Norman was used to measure the precipitation reflectivity data [17] and wind velocity data [6]. Additionally, an incoherent 10-cm-wavelenoth surveillance radar [17] was used to provide air traffic control guidance to the airplane.

Instrumentation from the Atmospheric Sciences Research Facility at NASA WFF [12 and 18] was used to provide guidance to the F-106B during storm penetrations in Virginia. The facility includes a UHF- and an S-band (SPANDAR) radar with the capability of airplane tracking via inputs from a third radar which tracks a C-band transponder mounted on the airplane. These three radars are shown in figure 3. In 1981 and 1982, the SPANDAR was used to provide Doppler radar measurements showing mean radial wind velocity and spectrum width (a measure of turbulence) as well as precipitation reflectivity [19].

Since 1982, the NASA WFF UHF-band radar has been used to obtain the range, azimuth, and elevation angle of echoes from lightning channels in real time [7]. The lightning flash rate was estimated by use of an echo transient counter which counts the number of lightning echoes in a selectable range interval along the radar beam of the UHF-band radar.

II.1.5 NASA Langley Flight Service Station

The primary responsibility to launch and recall the airplane, select the storms and altitudes of interest, and provide real-time flight support and guidance to the aircrew was assigned to the Storm Hazards project personnel located in a dedicated area of the NASA Langley Flight Service Station. The equipment installed in this station to support the mission [11] included communications systems, lightning detection systems, time displays, satellite cloud imagery, airplane status displays, and an integrated video display which tied much of these data together.

The primary system was the integrated video display [11] which displayed color-coded precipitation reflectivity factor and geopolitical maps from National Weather Service weather radar sites. The manufacturer expanded the capabilities of the basic system to permit NASA-generated graphics overlays of cloud-to-ground lightning locations from the NASA cloud-to-ground lightning mapping system [18] and data telemetered to the ground from the AIS and INS onboard the F-106B airplane. The airplane overlay data included the airplane ground track and discrete digital readouts of several key flight parameters. Using the integrated video display system, it was possible for the NASA Langley personnel in Metro to better utilize the NASA WFF data in recommending safe headings to targets of interest. In fact, the display allowed the Metro staff to independently support flights when NASA WFF support was not available.

II.2 Test Procedures

II.2.1 Flight procedures

In the Storm Hazards Program, it has been assumed that storm regions containing the greatest natural lightning activity were the most likely regions in which to experience a direct strike. During 1980 and 1981, most thunderstorm penetrations were made by the F-106B airplane at altitudes corresponding to ambient temperatures between ±10°C, based upon data such as that shown in figure 4 (from [20] with more recent data from [21]) in which the altitudes at which commercial aircraft were struck during routine operations are plotted. The five basic thunderstorm penetration procedures established in 1980 [4 and 5] were supplemented in 1982, when real-time guidance to the lightning flash density centers in thunderstorms [22 and 23] became available from the NASA-WFF UHF-band radar. Since 1982, the lightning echo location data from the UHF-band radar and the storm's precipitation reflectivity data from SPANOAR have been used to select the storm of interest and the desired altitude for each penetration.

II.2.2 Data reduction

Static temperature and pressure altitude were determined from parameters measured and recorded by the AIS. The pressure altitude was determined from static pressure values which were corrected for position error. The ambient temperature was determined from the total temperature measurement. The relative intensities of turbulence and precipitation at the times of the lightning events were based on pilot observations as extracted from the cockpit voice transcripts.

The lightning events experienced by the F-106B airplane are categorized as direct strikes or as nearby flashes [11]. Following each flight in which there were direct lightning strikes, the lightning attachment points were located by careful inspection of the airplane surface. Using the procedure given in [4], an attempt was made to postulate, based on the various data types, the initial orientation of the lightning channel with respect to the airplane, the initial and final attachment points, swept-flash path(s), and direction(s) from which the flash exited the airplane (see [10] for definitions of swept-flash attachment terms). The motion picture sequences of lightning from the 16-mm movie cameras and the still photographs from the Hasselblad 70-mm camera (table I) were time-correlated with the other data via the AIS using the techniques given in [10 and 11].

III - DISCUSSION OF RESULTS

III.1 Flight Conditions Conducive to Lightning Strikes

The number of direct strikes and nearby flashes for the Storm Hazards '80-'84 Programs are summarized by year in table II, in which the numbers of penetrations and missions also are included along with the state(s) in which the F-1068 airplane was based. As shown in table II, five years of thunderstorm research in Virginia (VA) and Oklahoma (OK) have resulted in 637 direct lightning strikes and 177 nearby flashes during 1154 penetrations in 156 research missions.

Histograms showing the number of penetrations, duration of each penetration and the number of strikes and nearby flashes experienced from 1980-1984 are shown for altitude intervals of 2000 ft in figure 5, and for ambient temperature intervals of 5°C in figure 6. Penetrations were made at pressure altitudes ranging from 4000 ft to 40 000 ft with a mean penetration altitude of 24 300 ft (figure 5). Temperature data (mean value during the penetration) were available for 1046 penetrations, with values ranging from 20°C to -55°C, with an overall mean value of -22.5°C (figure 6). The distributions of penetration time with altitude and temperature are very similar to the corresponding penetration distributions.

Direct strikes were experienced at pressure altitudes ranging from 14 000 ft to 40 000 ft with a mean value of 30 800 ft (figure 5). The corresponding ambient temperatures ranged from 5°C to -55°C, with a mean value of -31°C (figure 6). The nearby flash data are very similar to the direct strike data.

The lightning strike statistics shown in this paper differ significantly from the published strike data from commercial aircraft [20 and 21], in which most lightning strikes were found to occur between ambient temperatures of ±10°C (figure 4). Most of the direct strikes to the F-1068 airplane occurred at pressure altitudes above 24 000 ft, corresponding to ambient temperatures colder than -25°C. Based on data such as that in figure 4, most penetrations in 1980 and 1981 were made at altitudes corresponding to ±10°C with little success in experiencing lightning strikes (see table II). Since 1982, the F-106B airplane has been making high altitude penetrations using the UHF-band radar at NASA WFF to provide guidance to the upper flash density center in thunderstorms [22 and 23], resulting in hundreds of direct lightning strikes [4, 7, 10, and 12]. Finally, in the last half of the 1984 thunderstorm season, the UHF-band radar was used to direct the airplane towards the lower lightning flash density center at altitudes below 20 000 ft. The low altitude research effort of 1980-81 and 1984 is shown in the low altitude/warm temperature peaks in the penetration and duration data in figures 5 and 6. Despite spending 760 minutes of penetration time at pressure altitudes below 20 000 ft (23 percent), only 34 direct strikes were experienced (5 percent). In fact, the peak strike rates of 12.3 strikes/penetration and 2.1 strikes/min occurred at pressure altitudes between 38 000 ft and 40 000 ft, corresponding to ambient temperatures colder than -40°C. On the other hand, the peak strike rate near the freezing level (0°C) was only 0.13 strike/min (in the interval between 18 000 ft to 20 000 ft). The NASA Storm Hazards data and the commercial data differ because the NASA data came from intentional thunderstorm penetrations, while the commercial data were derived from a variety of meteorological

conditions, mostly in nonstormy clouds. Commercial aircraft will normally deviate from course to avoid thunderstorms which reach to cruise altitudes, and only penetrate when required to do so in the terminal area, where typical assigned altitudes are near the freezing level. Thus, the distribution of direct lightning strikes with ambient temperature found in the Storm Hazards Program is different from that in nonstormy clouds because of the higher percentage of time spent by the F-106B research airplane in the upper flash density center, compared with the low percentage of time spent in storms at those altitudes by commercial aircraft in routine operations. However, lightning strikes have been encountered at nearly all temperatures and altitudes, indicating that there is no altitude at which aircraft are immune from the possibility of lightning strikes.

In figure 7, the percentage of direct strikes to the F-106B airplane are plotted as a function of the flight crew's opinion of turbulence and precipitation intensities at the time of the strikes. The data are plotted for strikes at all altitudes and for those strikes below 20 000 ft altitude. In the majority of cases, direct strikes occurred in the regions of thunderstorms in which the crew characterized the turbulence and precipitation as negligible to light. However, for the 34 strikes which occurred at altitudes below 20 000 ft altitude, the crew called a higher percentage of the strikes in light to moderate precipitation and turbulence than shown by the data for all altitudes. In both cases, though, the Storm Hazards Program data have shown that the number of direct strikes in thunderstorms do not show a positive correlation to turbulence and precipitation intensities. This finding is in agreement with commercial aircraft data [21].

In addition, some strikes and nearby flashes to the F-106B airplane occurred on the edges of the thunderstorm cloud mass. The distribution of lightning events with respect to airplane position relative to time of cloud entry and cloud exit is shown in figure 8. Although 98 percent of the lightning events occurred while the airplane was within the cloud, as shown for commercial aircraft [21], 10 percent of the events occurred at the cloud edges (±10 sec of cloud entry or cloud exit), and 2 percent actually occurred with the airplane outside the cloud mass.

Precipitation and turbulence also are not necessarily related. For example, the Doppler radar data recorded by the NASA-WFF SPANDAR during 1981 [19] showed that heavy turbulence was often found not only within high reflectivity cores of storm cells, but also between cells, near storm boundaries, and in innocuous-appearing low reflectivity factor regions. Finally, it has been found [7] that the average probability for the airplane to be struck was greater in storm regions with a flash rate of 0 to 10 flashes per minute than for regions with flash rates higher than 10 flashes/min.

The lower altitude flash density center in thunderstorms is closely associated with high reflectivity cores [22 and 23]. In order to minimize the chances of encountering hail, the F-106B airplane was not flown into the reflectivity cores of storms where the reflectivity values exceeded 50 dBZ. Therefore, no comments can as yet be made on the probability of direct lightning strikes occurring in such areas. The data obtained during the Storm Hazards Program show that the greatest probability of experiencing a direct lightning strike in the upper portions of a thunderstorm occurred in regions where the ambient temperature was colder than -40°C, where the relative turbulence and precipitation intensities were characterized as negligible to light, and where the lightning flash rate was less than 10 flashes/min. These data also indicate that the presence and location of lightning do not necessarily coincide with the presence and location of hazardous precipitation and turbulence.

III.2 Lightning Attachment Patterns

Four general strike scenarios have been found in the swept-flash attachment patterns on the F-106B airplane [4, 10, and 12]. The terms used in describing lightning attachment scenarios (i.e., entry and exit points) are defined in [10]. The four general strike scenarios are:

1. Flashes which initially attach to the nose of the aircraft and subsequently "sweep" alongside it, reattaching at a succession of spots along the fuselage. In these cases, the initial and final exit point is usually the trailing edge of an extremity such as a wing or vertical fin tip. The final entry point is a trailing edge of the fuselage, because the flash is usually still alive by the time the aircraft has flown completely through it.

2. Similar to (1) except that the entry channel sweeps aft across the top or bottom wing surface instead of the fuselage.

3. Strikes in which the initial entry and exit points occur at the nose. In this case, the lightning flash appears to "touch" the aircraft nose but continues on from this point to another destination. The aircraft then flies through the flash, resulting in successive entry points along one side of the fuselage or wing and exit points along the other. Again, because the flash usually exists for a longer time than it takes the aircraft to fly its length, the final entry and exit points are located along trailing edges.

4. Strikes in which the initial and final entry and exit points are confined to the aft extremities.

With most of these general scenarios, swept-flash channels frequently have been found which rejoin behind the airplane after the airplane has flown through the channel [4]. Prior to the Storm Hazards Program, it had been believed that once a strike occurred, the channel would remain attached to the aircraft until the flash died out naturally (see [20], for example).

The onboard photographic systems used in 1984 have been able to document general strike scenarios 1, 2, and 4 and examples of scenarios 1 and 2 will be discussed in this paper. For example, strike 210 of 1984 (figures 9-11) represents general strike scenario 1. This strike, discussed in detail in [11], resulted in an unusual positioning of the lightning channel alongside the airplane fuselage and canopy and over the wing, followed by a detachment of the channel from the airplane and a small restrike (or second strike) to the left wing tip. Selected frames from the aft-facing, fuselage-mounted movie camera, which was automatically triggered by light-sensing diodes at a nominal frame rate of 400 frames/sec (see table I) are shown in figure 9, while selected frames from the cockpit-mounted video camera (30 frames/sec) for the same strike are presented in figure 10. The lightning channel was visible in the first 58 of the 126 frames exposed in the 1 sec movie film interval and in 13 frames on the videotape. The lightning strike scenario for strike 210 is given in figure 11, with the chronological sequence shown schematically in figure 11(b).

Referring to figure 11(b), the strike scenario may be summarized in nine phases:

1. Strike initiation (movie frames 1 and 2, video frames 1-3): lightning channel oriented as shown in figure 11(a), with entry channel located above the airplane and to the left of the airplane centerline; initial entry point at nose boom; initial exit at left wing tip (see video frame 1, figure 10(a)).

2. Sweot flash (movie frame 3, video frame 4): as the airplane flew forward through the lightning channel, the entry portion of the channel swept back down the left side of the fuselage across the overhead canopy rail (video frame 4, figure 10(b)) to the trailing edge of the rudder; the exit channel trailed aft from the left wing tip.

3. Entry and exit channel convergence (movie frames 4-8, video frames 5-8): as the airplane continued to fly forward, the entry channel hung onto the rudder and the exit channel hung onto the left wing tip; the entry and exit channels were converging on the left wing tip (see movie frame 4, figure 9(a) and video frame 5, figure 10(c), for example).

4. Entry and exit channel converge (movie and video frame 9): when the airplane reached the point where the entry channel was below its flight path (figure 11(a)), the entry channel came in contact with (or very close to) the left wing tip; the entry channel can be seen brushing the left wing tip and making contact with the exit channel in movie frame 9 (figure 9(b)) and video frame 9 (figure 10(d)).

5. Rejoined channel behind the airplane (movie frame 10): at the instant the entry channel brushed against the left wing tip, charge transferred directly to the entry channel, thereby omitting the airplane from the electric circuit (see figure 9(c)); the initial and final lightning channel entry and exit points thus established for strike 210 of 1984 are shown in figure 11(c).

6. Detached lightning channel recedes behind the airplane (movie frames 11-22 and video frames 10 and 11).

7. Restrike to left wing tip (omitted from figure 11 for clarity) (movie frames 23 and 24 and video frames 12 and 13): entry channel of restrike (or new strike) at left wing tip; the exit channel was not in the field of view of either camera; remnants of the first strike channel were still visible in the movie frames, but were blocked by the fuselage in the video frames (see movie frame 24, figure 9(d) and video frame 13, figure 10(e)).

8. Decay of both strike channels (movie frames 25-27, no video frames): both channels faded away behind airplane.

9. Decay of original channel (movie frames 28-58, no video frames): remnants of original channel remained visible as two unusually bright spots which were either channel segments viewed "end on," or detached segments or "balls" of channel plasma which remained luminous after the rest of the channel had decayed - "ball lightning."

As early as the 1980 research program [3], strikes were found which swept back over the midspan areas of the delta wing (general strike scenario 2), and such strikes have been found in each research season. Strikes in this area of the wing were not expected since attachments across swept wings on airplanes without upstream attachment points such as engine nacelles or drop tanks are extremely rare. Their discovery led to the removal of all paint from the top and bottom wing surfaces prior to the 1981 season to minimize the chance of a melt through or hot spot in the wing fuel tanks from lightning attachment. Strike 80 of 1984 is the only strike to date in which the lightning channel has been photographed sweeping back over the wing. In figure 12, the entry channel, which is sweeping aft from the nose boom, can be seen on the top surface of the left wing and the exit channel can be seen trailing back from the left wing tip. Figure 12 is the second frame of two taken by the aft-facing, fuselage-mounted movie camera, which was running continuously at 14 frames/sec (see table I). The cockpit video camera was not installed on this flight.

The significance of strikes 80 and 210 is that by flying into or through the lightning channel, the channel may become positioned or attached to the aircraft at locations that would be deemed highly improbable by electric field theory alone. Heretofore, lightning attachment patterns or "zones" [8 and 9] have been thought of as originating at extremities of the aircraft where electric field gradients are sufficient to form junction leaders. The present case illustrates that, whereas attachment patterns do indeed originate at high field locations,

the subsequent patterns are dependent solely on relative positions of the entry and exit channels with respect to the moving aircraft. It is, therefore, possible to imagine other scenarios in which the channel can reattach to almost any surface of the aircraft. This leads to the conclusion that orotection designs which depend upon the existence of "Zone III" areas (defined in airworthiness regulations as aircraft surfaces where lightning attachments are very improbable) must now be considered at risk, especially if such surfaces or structures would suffer significant damage if subjected to a strike.

These two encounters also show that an aircraft may be subject to radiated effects from lightning channels uncommonly close alongside its surface, as well as to the effects of direct attachment. Although no adverse effects were noticed or reported by the F-106B crew in this case (the intensity of currents in this particular flash are known to have been relatively minor and the airplane has been provided with unusually thorough protection measures), a similar encounter of a conventional aircraft with a severe flash might have more frightening consequences. Protection designers must, therefore, deal with the effects of close-in nearby flashes as well as direct attachments, both of which apparently may occur at almost any spot or region of the aircraft.

Unfortunately, no photographic evidence exists of strike scenario 3, although there is other evidence from pilot descriptions and lightning attachment points for several such strikes to have occurred on the F-106B airplane [3 and 10]. Even though such strikes are rare, they are significant, as they probably verify the lightning incident hypothesis shown in figure 13 from [24]. In [24], a lightning strike incident to a twin-engine business jet is described in which both of its engines flamed out at an altitude of 31 500 ft, and in spite of repeated attempts, the engines would not restart until the airplane had descended to an altitude of 13 000 ft. No mechanical or electrical damage was found. It was hypothesized in [24] that the engine flameouts were caused by the disruption of inlet air which results when the lightning channel and its attendant shock wave are swept in front of the engine inlet. For both engines to fail, the lightning channel would have to have swept down both sides of the fuselage, as shown in figure 13. The findings of the Storm Hazards Program now indicate that such a strike pattern is possible. In the case of the F-106B airplane, however, no engine roll-backs or flame-outs from lightning have been experienced, probably because of the robustness of the J-75 turbojet engine, even though there is an inlet on each side of the fuselage feeding the single engine.

A high percentage of the strikes experienced in the Storm Hazards Program are confined to the aft extremities of the airplane [3, 10, and 11] (strike scenario 4). In fact, the cockpit-mounted video camera has detected a number of strikes which were not seen in the cockpit or were not within the field of view of the aft-facing, fuselage-mounted movie camera. Strikes have been found to any combination of aft extremities.

The lightning attachment point data have provided further insights into the validity of the assumptions used in establishing lightning strike zones on aircraft [8] by showing the manner in which an airplane interacts with a lightning strike channel, especially the manner in which flashes sweep aft from initial lightning attachment points. The data from 1984 confirm the previous findings [12] that initial entry and exit points most frequently occur at airplane extremities, in this case the nose boom, the wing tips (individually and simultaneously), the vertical fin cap, and the afterburner. It also has been confirmed that swept-flash attachment points can occur along the full length of the fuselage, as is common in other airplanes of this general size, following initial strike attachments at the nose. The 1984 data also have confirmed the three unexpected results found earlier [12]: lightning attachments in the afterburner [4]; swept flashes across the midspan surface of the delta wing [3, 4, 11, and 12]; and, the existence of lightning channels which rejoin and persist after passage of the airplane through them. Finally, the 1984 data have provided new evidence that the entire surface of the airplane may be susceptible to lightning attachment [11].

Preliminary DLite data indicate that there has been at least one strike with a peak current amplitude of 54 kA. Even with strikes of this magnitude, the adverse physical effects of the lightning on the F-106B airplane have been confined to minor surface cosmetic damage to the metal exterior of the airplane [12] and to the three research composite fin caps [25] erosion of metal from both wing tips [12]; three small holes melted completely through the 1-mm (0.05-in.) thick aluminum skin near the trailing edge of the vertical tail beneath the composite fin cap [11]; and several small punctures in the fiberglass radome [12]. Adverse electrical effects have been confined to a few momentary outages on the airborne x-band weather radar [12], two failures of a Distance Measuring Equipment (DME) unit [12], and several false commands to the DLite recording system. These electrical problems have been remedied by installing improved shielding on the wiring and circuits and by use of a properly-grounded DME antenna. It should be emphasized that these relatively benign results are for a metal airplane using a hydraulic control system. The same results will be more difficult to achieve on a composite-structure airplane using digital avionics.

IV - SUMMARY OF RESULTS

During the NASA Langley Reseach Center Storm Hazards Program, 637 direct lightning strikes were experienced by an F-106B research airplane from 1980-1984. This study produced the following results:

1. The peak strike rates (2.1 strikes/min and 13 strikes/penetration) occurred at altitudes between 38 000 ft and 40 000 ft, corresponding to ambient temperatures colder than -40°C. The peak strike rate near the freezing level, where most previously

reported strikes have occurred, was only 0.1 strike/min.

2. Although lightning strikes have been encountered at nearly all temperatures and altitudes, the regions of highest risk for an airplane to experience a direct lightning strike were those areas of thunderstorms where the ambient temperature was colder than -40°C and where the relative turbulence and precipitation intensities were characterized as negligible to light. Therefore, the presence and location of lightning do not necessarily indicate the presence and location of hazardous precipitation and turbulence.

3. The onboard data confirm that the lightning attachment patterns on this airplane fall into four general categories and that flashes can rejoin after passage of the airplane. However, the 1984 data have shown that the entire surface of this airplane may be susceptible to lightning attachment.

REFERENCES :

1. Fisher, B. D.; and Crabill, N. L.: Summary of Flight Tests of an Airborne Lightning Locator System and Comparison With Ground-Based Measurements of Precipitation and Turbulence. 1980 Aircraft Safety and Operating Problems, Joseph W. Stickle, compiler. NASA CP-2170, Part 1, 1981, pp. 251-277.
2. Fisher, B. D.; Keyser, G. L., Jr.; Deal, P. L.; Thomas, M. E.; and Pitts, F. L.: Storm Hazards '79 - F-106B Operations Summary. NASA TM-81779, Mar. 1980.
3. Fisher, B. D.; Keyser, G. L., Jr.; and Deal, P. L.: Lightning Attachment Patterns and Flight Conditions for Storm Hazards '80. NASA TP-2087, Dec. 1982.
4. Fisher, B. D.; and Plumer, J. A.: Lightning Attachment Patterns and Flight Conditions Experienced by the NASA F-106B Airplane. Procs. Addendum, Eighth Inter. Aero. and Ground Conf. on Lightning and Static Elec., Ft. Worth, TX, June 1983. DOT/FAA/CT-83/15(A), pp. 26-1 - 26-14.
5. Neely, Maj. W. R., Jr.; and Fisher, B. D.: The NASA F-106B Storm Hazards Program. Procs., Twenty-Sixth Annual Symp., Soc. of Exper. Test Pilots, Los Angeles, CA, Sept. 1983, pp. 242-256.
6. Usry, J. W.; Dunham, R. E. Jr.; and Lee, J. T.: Comparison of Wind Velocity in Thunderstorms Determined From Measurements by a Ground-Based Doppler Radar and a F-106B Airplane. NASA TM-86348, 1985.
7. Mazur, V.; Fisher, B. D.; and Gerlach, J. C.: Lightning Strikes to an Airplane in a Thunderstorm. J. Aircraft, Vol. 21, No. 8, Aug. 1984, pp. 607-611. (Supercedes AIAA-84-0468.)
8. Protection of Aircraft Fuel Systems Against Lightning. AC No. 20-53, FAA, Oct. 6, 1967.
9. SAE Committee AE4L: Lightning Test Waveforms and Techniques for Aerospace Vehicles and Hardware. Soc. Automot. Eng., Inc., June 20, 1978.
10. Zaepfel, K. P.; Fisher, B. D.; and Ott, M. S.: Direct Strike Lightning Photographs, Swept-Flash Attachment Patterns and Flight Conditions for Storm Hazards '82. NASA TM-87647, 1985.
11. Fisher, B. D.; Brown, P. W.; and Plumer, J. A.: NASA Storm Hazards Lightning Research. Thirtieth Corporate Aviation Safety Seminar, Flight Safety Foundation, Inc., Dallas/Fort Worth Airport, Texas, Apr. 1985.
12. Fisher B., D; and Plumer, J. A.: Lightning Attachment Patterns and Flight Conditions Exerienced by the NASA F-106B Airplne from 1980 to 1983. AIAA-84-0466, Jan. 1984.
13. Pitts, F. L.: Electromagnetic Measurement of Lightning Strikes to Aircraft. J. Aircraft, Vol. 19, No. 3, March 1982, pp. 246-250. (Supercedes AIAA-81-0083.)
14. Thomas, M. E.: Direct Strike Lightning Measurement System. AIAA-81-2513, Nov. 1981.
15. Lee, L. D.; Finelli, G. B.; Thomas, M. E.; and Pitts, F. L.: Statistical Analysis of Direct-Strike Lightning Data (1980 to 1982). NASA TP-2252, Jan. 1984.
16. von Bokern, G. J.: In-Flight Lightning Data Measurement System for Fleet Application-Flight Test Results. Proc., National Aero. and Elec. Conf., Dayton, OH, Vol. 1, May 1982, pp. 25-31.
17. Doviak, R. J., ed.: 1980 Spring Program Summary. NOAA Tech. Mem. ERL NSSL-91, Apr. 1981. (Available from NTIS as PB81-23494D.)
18. Gerlach, J. C.; and Carr, R. E.: Wallops Severe Storms Measurement Capability. Preprint Vol. - Fifth Symp. on Met. Obs. and Instr., Toronto, Canada, Apr. 1983. Amer. Met. Soc. and Canadian Met. and Oceanographic Soc.
19. Bohne, A. R.: Joint Agency Turbulence Experiment Interim Report. AFGL-TR-83-0180, July 1983.
20. Fisher, F. A.; and Plumer, J. A.: Lightning Protection of Aircraft. NASA RP-1008, 1977.
21. Plumer, J. A.; Rasch, N. O.; and Glynn, M. S.: Recent Data From the Airlines Lightning Strike Reporting Project. AIAA-84-2406, Oct./Nov. 1984.
22. Gerlach, J. C.; Mazur, V.; and Rust, W. D.: UHF and S-Band Radar Observations of Electrically Active Storm Cells. Procs., 21st Conf. on Radar Meteor., Edmonton, Canada, Sept. 1983, pp. 238-241.
23. Taylor, W. L.; Rust, W. D.; MacGorman, D. R.; and Brandes, E. A.: Lightning Activity Observed in Upper and Lower Portions of Storms and Its Relationship to Storm Structure From VHF Mapping and Doppler Radar. Procs., Eighth Inter. Aero. and Ground Conf. on Lightning and Static Elec., Ft. Worth, TX, June 1983. DOT/FAA/CT-83/25, pp. 4-1 - 4-9.
24. Plumer, J. A.: Lightning Strike Feedback: Some Trends Emerge. Flight Operations, Vol. 69, No. 2, Feb. 1979, pp. 23-29.
25. Howell, W. E.; and Fisher, B. D.: Observations of Severe In-Flight Environments on Kevlar/Epoxy and Graphite/Epoxy Composite Structural Components. SAE Paper No. 830767, Apr. 1983.

TABLE I.- CHARACTERISTICS OF AIRBORNE PHOTOGRAPHIC SYSTEMS

Location	Camera				Lens	
	Type	Orientation	Type	Film or Imager Size	Make/Type	Description
Forward of Cockpit	Movie	Forward-facing	Milliken DBM-54	16 mm	Dallmeyer	Triple anastigmat, f/2.9, 15 mm
Cockpit	Movie	Forward-facing	Milliken DBM-54	16 mm	Kinoptik	Tega. F/1.8, 5.7 mm
Aft of Cockpit: I	Movie	Aft-facing	Milliken DBM-54	16 mm	Pinhole	f/67, 5.1 mm
II	↓	↓	↓	↓	Century	f/1.8, 5.7 mm
III					↓	↓
IV						
Cockpit	Video	Aft-facing	GE4TN2505	0.67 in.	Century	f/1.8, 5.7 mm
Cockpit	Still	Aft-facing	Hasselblad 500 EL/M	70 mm	Zeiss	Distagon, f/4,40 mm

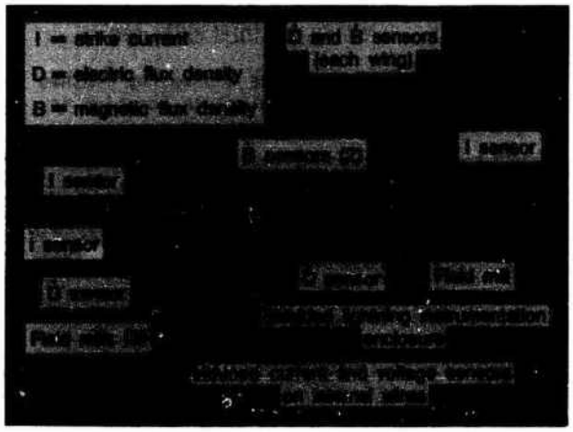
Camera Location	Film/Sensor		Mode of Operation	f Stop	Neutral density filter	Frame rate, frame/sec (c)
	Type	Sensitivity				
Forward of Cockpit	Kodak Ektachrome 7256	ASA64	Manual	f/11	0.6	14
Cockpit	Kodak Ektachrome 7256	ASA64	Manual	f/11	-	16
Aft of Cockpit: I	Kodak Ektachrome 7256	ASA64	Manual	f/67	-	14
II	↓	↓	Manual	f/11	1.5	16
III			Automatic(b)	↓	↓	200
IV			Automatic(b)			400
Cockpit	CID(a)	Full output at face plate. Illumination of 0.8 f.c.	Manual	f/11	1.5	30
Cockpit	Vericolor II or III	ASA125 or 160	Automatic(b)	f/8 or f/11	-	(f)

Camera Location	Shutter			Years
	Type	Rotary shutter ang., deg.	Speed, msec	
Forward of Cockpit	Rotary	72	14	1980 - 1982
Cockpit	Rotary	195	34	1983
Aft of Cockpit: I	Rotary	200	39	1980 - 1983
II	↓	195	34	1984
III		180	2.5	1984
IV		180	1.25	1984
Cockpit	(d)	Unshuttered. See note (d)	(d)	1984
Cockpit	Electro-mechanical (e)	(e)	30	1983

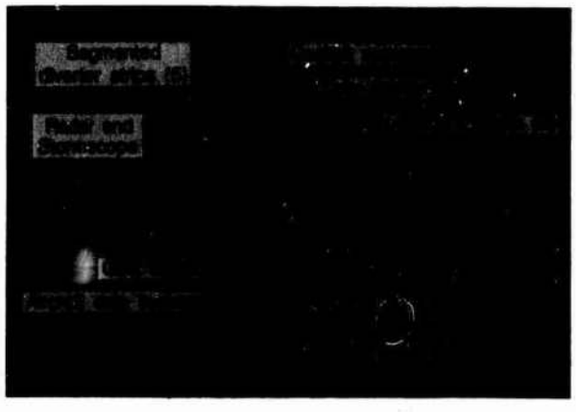
Notes: (a) General Electric Charge Injection Device (CID). Silicon 248 x 388 pixel array.
(b) Automatic mode uses photographic diode for lightning-tripped camera actuation.
(c) Movie camera frame rates are for steady-state operation. Acceleration/deceleration characteristics results in 126 frames in 1 sec at 400 frames/sec.
(d) 1:1 field interlace for video frame; frame integration time of 33 msec.
(e) Electromechanical between-the-lens shutter with 5 msec response time.
(f) Not applicable.

TABLE II - STORM HAZAROS MISSION SUMMARY

Year	Strikes	Nearby Flashes	Penetrations	Missions	States
1980	10	6	69	19	VA & OK
1981	10	22	111	24	VA & OK
1982	156	26	241	35	VA
1983	214	112	324	40	VA
1984	247	11	409	38	VA
TOTALS	637	177	1154	156	



(a) Location of electromagnetic sensors on the F-106B.



(b) Location of additional research sensors and equipment on the F-106B.

Figure 1.- NASA Langley Research Center Storm Hazards '84 research vehicle.

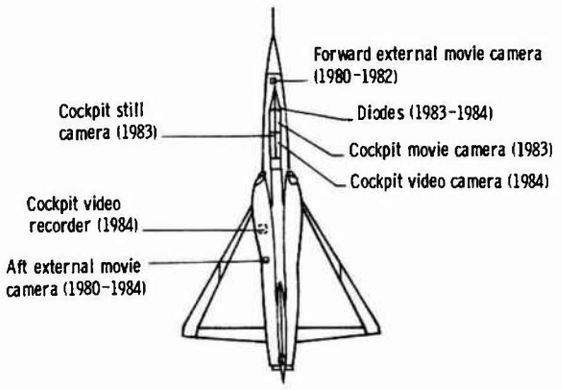


Figure 2.- Location of airborne camera systems.

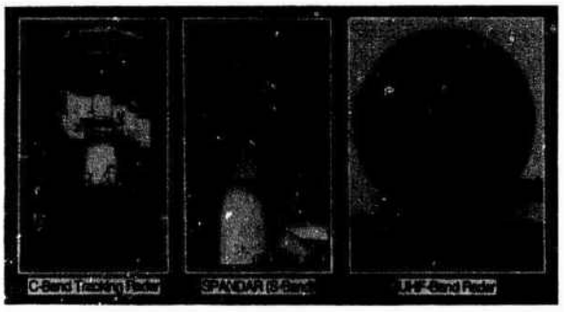


Figure 3.- Storm Hazards radar support at NASA Wallops.

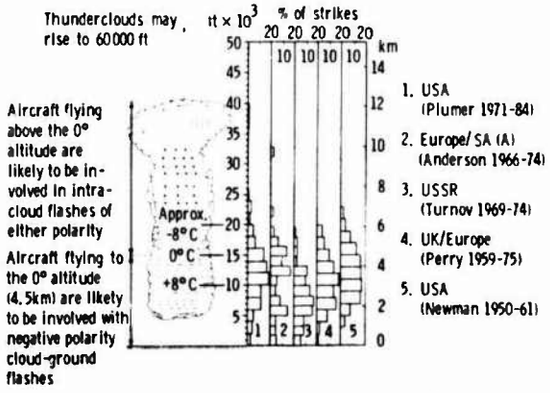


Figure 4.- Aircraft lightning strike incidents as a function of altitude. From reference 24 with updated data from reference 25.

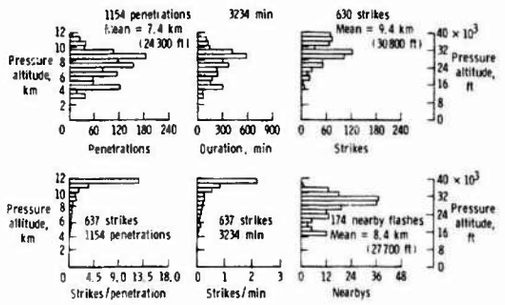


Figure 5.- Thunderstorm penetrations and lightning statistics as a function of pressure altitude for Storm Hazards '80 - '84.

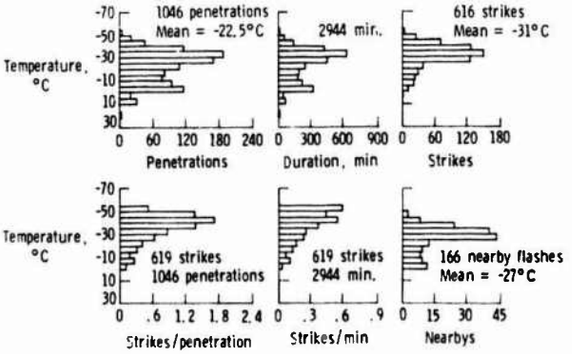


Figure 6.- Thunderstorm penetrations and lightning statistics as a function of ambient temperatures for Storm Hazards '80 - '84.

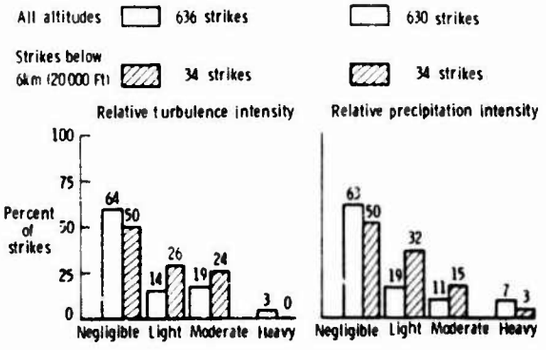


Figure 7.- Relationship of lightning strikes to relative turbulence and precipitation intensities for Storm Hazards '80 - '84.

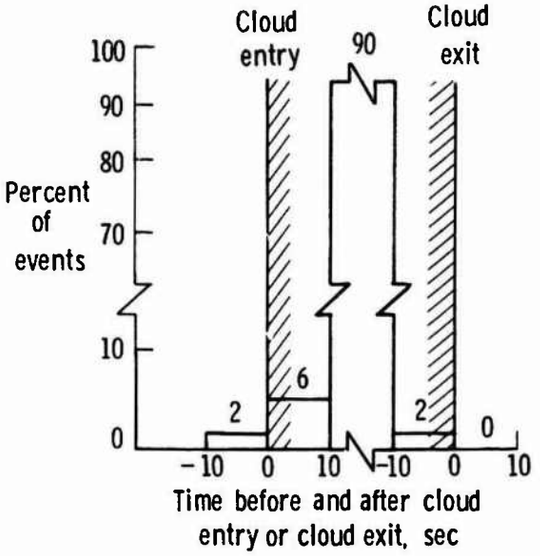
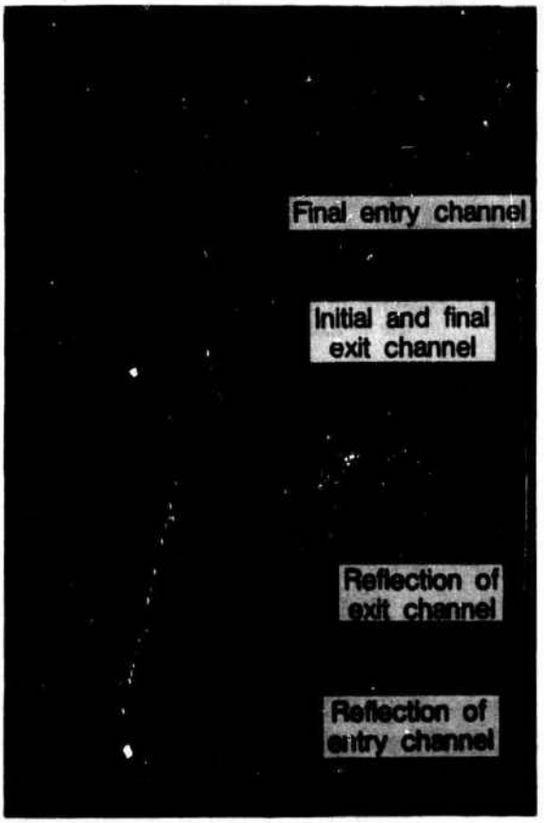
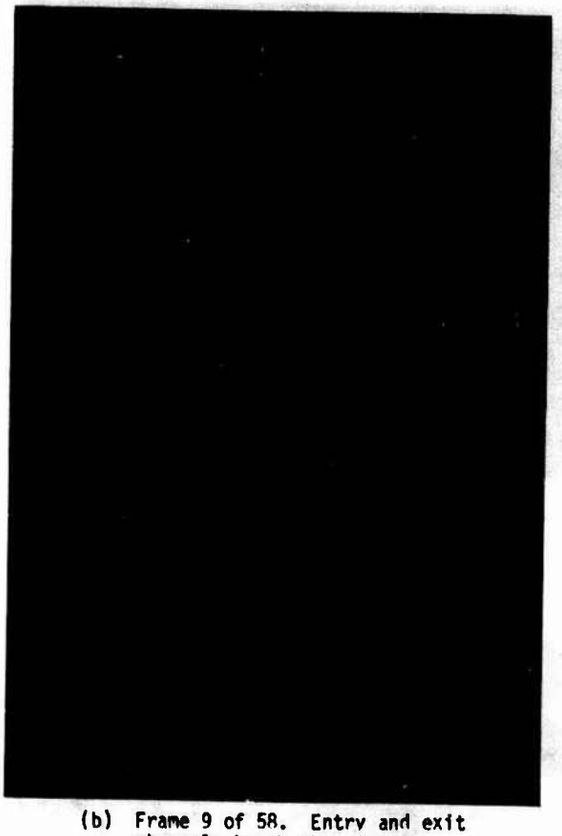


Figure 8.- Lightning strikes and nearby flashes in relation to airplane location in the cloud mass.

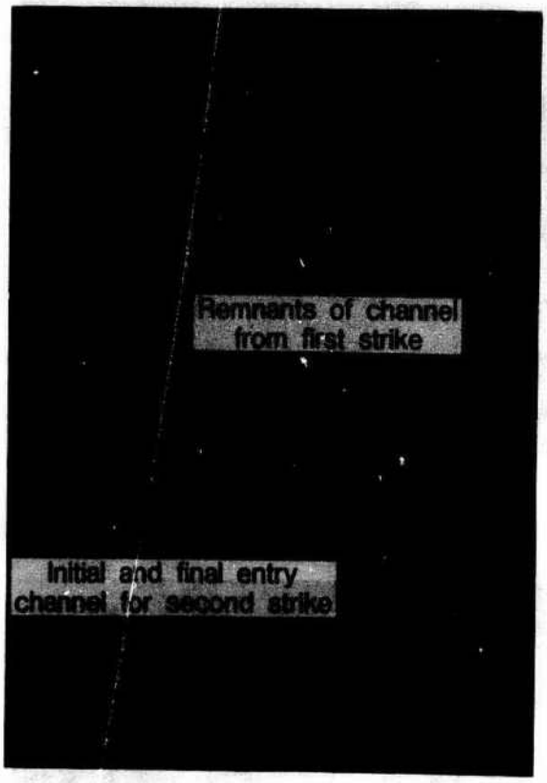


(a) Frame 4 of 58.

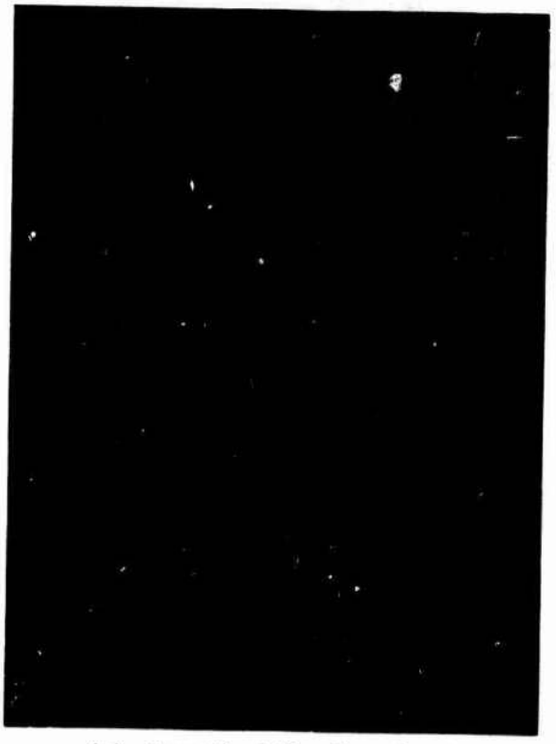
Figure 9.- Photographs of direct strikes to vertical tail & left wing tip of F-106B airplane from aft-facing, fuselage-mounted movie camera. Strike 210 of 1984; flight 84-047; Aug. 13, 1984; 19:50:05.5 GMT; 17 900 ft altitude near Sunbury, NC. Nominal frame rate of 400 frames/sec.



(b) Frame 9 of 58. Entry and exit channels brush the wing tip.

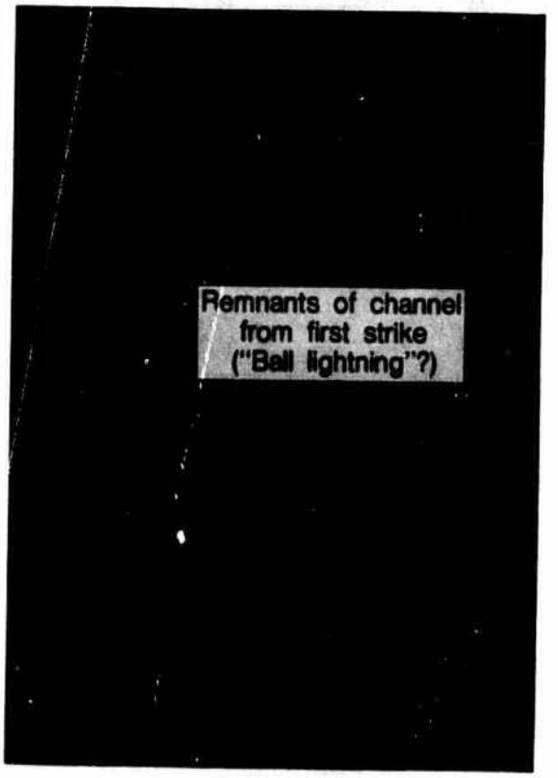


(d) Frame 24 of 58. Exit channel of second channel not in field of view of onboard cameras.



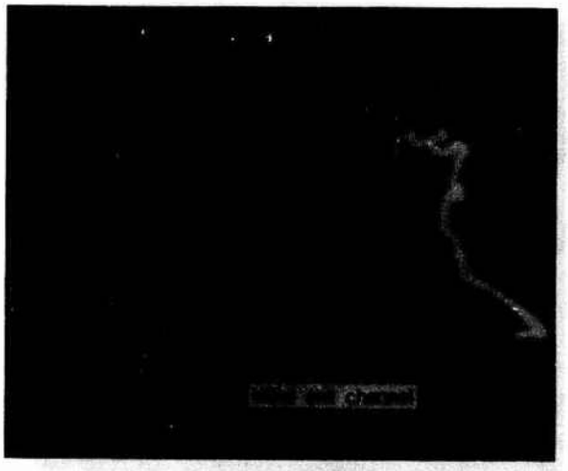
(c) Frame 10 of 58. Channel not attached to airplane.

Figure 9.- Continued.

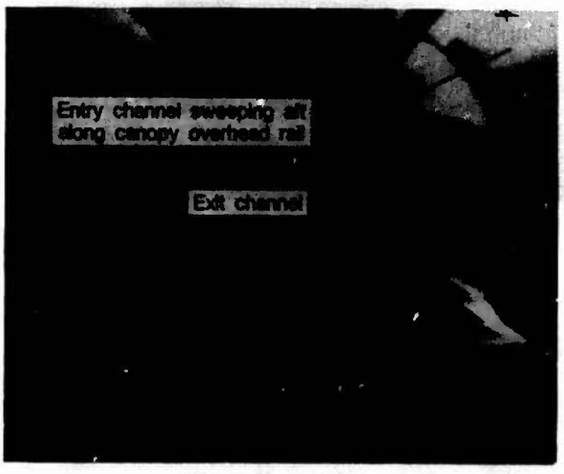


(e) Frame 34 of 58.

Figure 9.- Concluded.



(a) Frame 1 of 13.



(b) Frame 4 of 13.

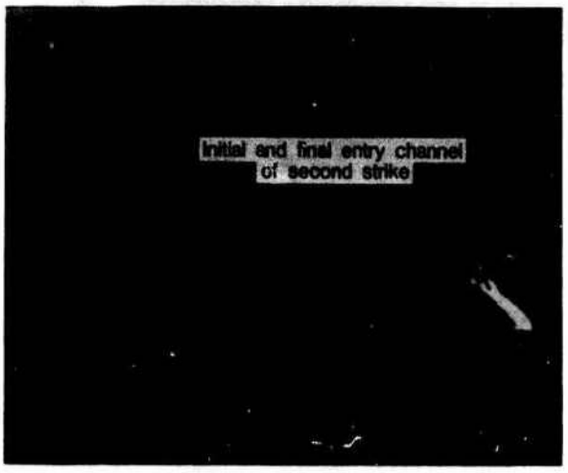


(c) Frame 5 of 13.

Figure 10.- Photographs from cockpit-mounted video camera of strike 210 of 1984.



(d) Frame 9 of 13. Final frame with lightning channel attached to airplane.



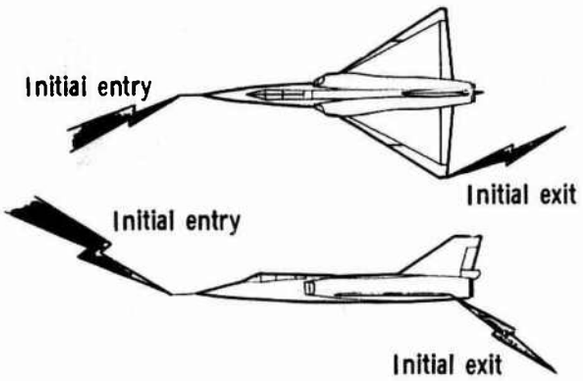
(e) Frame 13 of 13. Exit channel of second strike not within field of view of onboard cameras.

Figure 10.- Concluded.

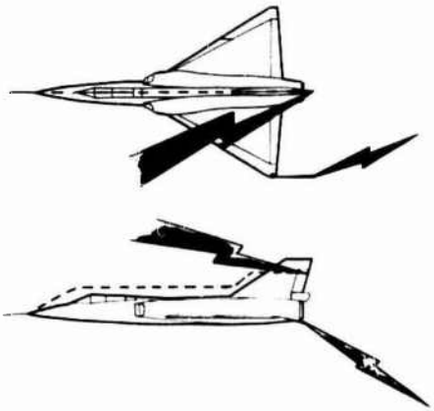


(a) Inferred channel orientation with respect to airplane.

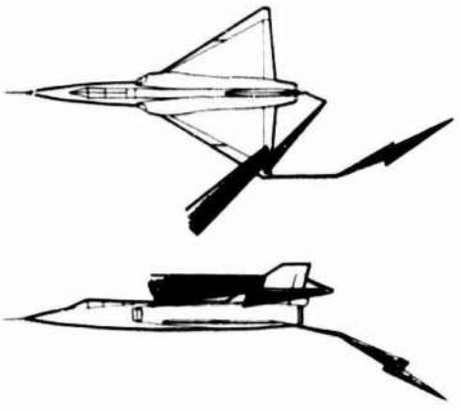
Figure 11.- Lightning strike scenario for strike 210 of 1984; flight 84:047; Aug. 13, 1984.



Initial entry at nose boom; initial exit at left wingtip
Movie frames: 1 and 2
Video frames: 2 and 3 (fig. 10(a))



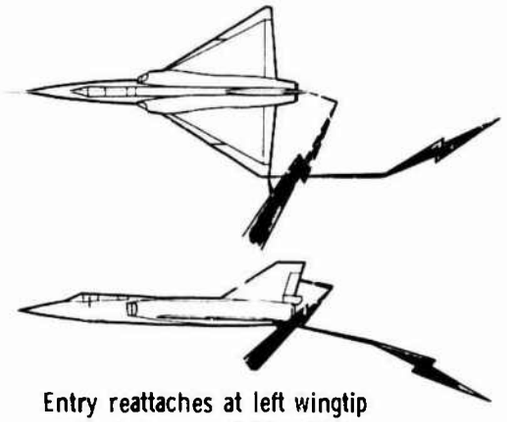
Entry swept back over canopy and attaches to trailing edge of rudder
Movie frames: 3 and 4 (fig. 9(a))
Video frames: 4 and 5 (figs. 10(b) and (c))



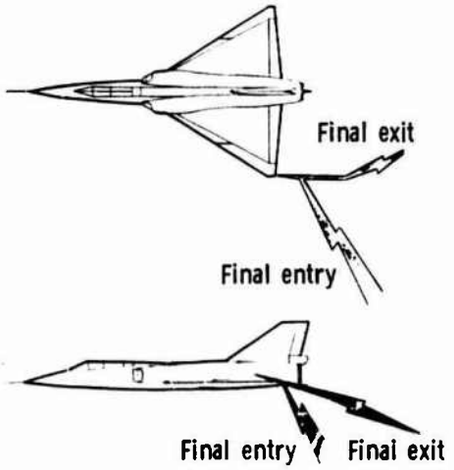
Entry hanging onto rudder; exit hanging onto wingtip
Movie frames: 5 - 7
Video frames: 6 - 8

(b) Sequence showing F-106B airplane flying through lightning channel. Restrike to left wing tip omitted for clarity.

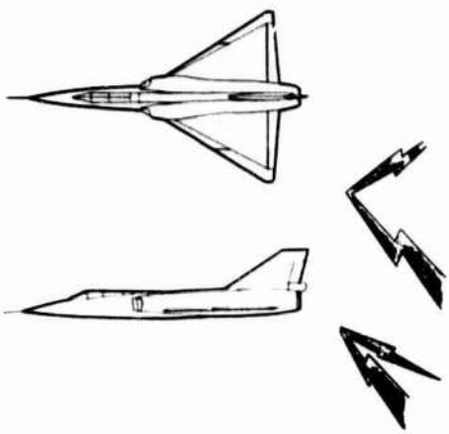
Figure 11.- Continued.



Entry reattaches at left wingtip
Movie frames: 8 (fig. 9(b))
Video frames: 9 (fig. 10(d))



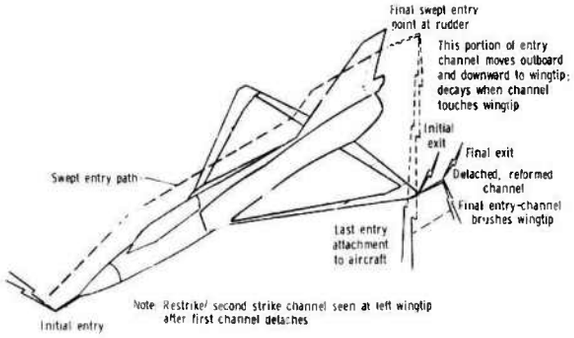
Entry combines with exit; final entry and final exit
Movie frames: 9 (fig. 10(c))
Video frames: 10 and 11



Entry and exit detach from aircraft
Movie frames: 10 - 58
Video frames: None

(b) Concluded.

Figure 11.- Continued.



(c) Lightning attachment point summary.

Figure 11.- Concluded.

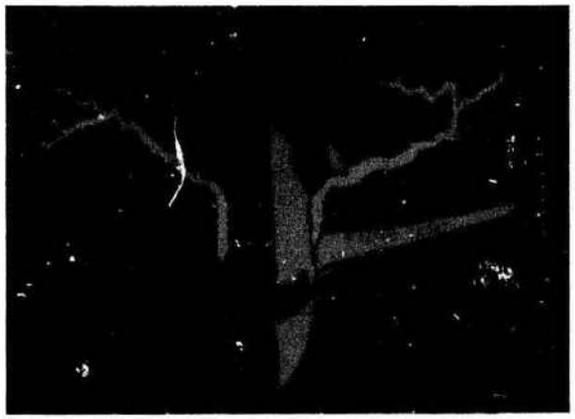


Figure 13.- Possible scenario for a dual flame-out from a lightning strike.

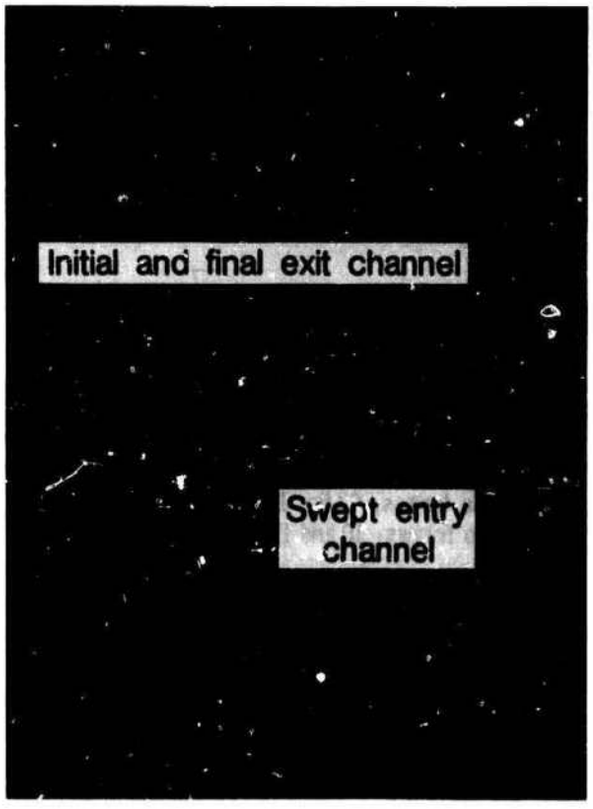


Figure 12.- Photograph of direct strike to left wing tip and wing upper surface of F-106B airplane from aft-facing, fuselage-mounted movie camera. Strike 80 of 1984; flight 84-031; July 7, 1984; 16:28:57 GMT; 25 700 ft altitude over Atlantic City, NJ. Frame rate of 16 frames/sec. Frame 2 of 2.

E AND H FIELDS MEASUREMENTS ON THE TRANSALL C160 AIRCRAFT DURING LIGHTNING FLASHES

J.P. Moreau and J.C. Alliot

Office National d'Etudes et de Recherches Aérospatiales, B.P. 72, 92322 Châtillon Cedex, France

Abstract - An experimental campaign was carried out in the South West of France during Spring 1984; two main objectives were pursued:
- a best understanding of the microphysic, dynamic and thermodynamic properties of frontal systems,
- a characterization of the main parameters of electric and electromagnetic phenomena associated with cloud discharges.

The present paper is essentially devoted to the analysis of measurements obtained with the Transall aircraft which was set up during the campaign.
Electromagnetic fields due to direct lightning flashes on the aircraft are presented in details:
a - typical E and H waveforms obtained during the whole duration of the flashes and recorded by analog device with a 2 MHz bandwidth,
b - typical E and H waveforms obtained on transient digitizers with a large bandwidth (100 MHz); the E and H pulses are ranged either with their spectral content or with their amplitude characteristic,
c - electromagnetic transfer function of a well-defined aperture installed on the aircraft fuselage; experimental results are compared with numerical calculations.

In conclusion the moderate AEHP threat value is compared to experimental results and the importance of VHF measurements for understanding the physical process is emphasized.

I - INTRODUCTION

Lightning is one of the most severe and most unknown electromagnetic hazards to which aircraft may be exposed. For many years specialized laboratories have tried to find a characterization of the lightning processes with increasing interest since the advanced technology aircraft give, if no special treatement is applied, less protection to electronic devices than the previous entirely metallic ones. ONERA has conducted an airborne experiment on a Transall C160 for indirect effects characterization of lightning. This has been carried out during spring 1984 in the South of France. Previous studies specially in the NEMP field have shown that indirect effects could be evaluated if the repartition of the electric and magnetic fields on the aircraft skin is known [1]. The C160 was instrumented with magnetic and electric field sensors and also with VHF and UHF receivers. The output of these sensors were simultaneously recorded with a "fieldmill" signal which gives the electrostatic situation of the aircraft and the evolution of the external atmospheric field.
In this paper, electromagnetic fields due to direct lightning flashes on the aircraft are presented in details: typical E and H field waveforms obtained during the whole duration of the flashes and recorded by analog device with a 2 MHz bandwidth, typical E and H waveforms obtained on transient digitizers with a 100 MHz bandwidth, electromagnetic transfert function of a well defined aperture installed on the aircraft fuselage and a comparison between experimental results and calculation. We have analyzed 18 flashes and we give for the measured parameters the mean value and the standard deviation. The characteristics derived include risetimes, peak amplitude and frequency content.

II - SENSORS AND INSTRUMENTATION

The results presented hereby correspond to the following setups of the instrumentation. E and H sensors designed for the measurement of the fast electromagnetic field variations are installed under a radome. The electric field sensor measures the normal to the surface component of the field located on the right side of the aircraft at three meters from the nose and the magnetic field sensor measures the tangential component of the magnetic field. The E sensor is a hollow spherical type dipole which includes an active integrator device such that the output signal is directly proportional to E. The total measuring range of this sensor spreads from 30 mV/m to 316 kV/m in selectable attenuations with a dynamic range of 70 dB and a bandwidth of 100 Hz to 130 MHz (± 1 dB).
The H sensor is a loop including an active integrator device such that the output signal is directly proportional to H. The total measuring range of this sensor spreads from 0.8 mA/m up to 839 A/m in 8 selectable attenuations with a dynamic range of 50 dB and a bandwidth of 6 kHz to 130 MHz (± 1 dB).
Inside the aircraft, located at a distance of 50 cm from the outside skin on the axis of a 38 cm diameter circular window is a free field H sensor.
The characteristics of this sensor are the following: measuring range 1 to 100 A/m in 3 selectable attenuations of 50 dB dynamic range and a bandwidth of 30 kHz to 100 MHz (± 1 dB). In addition, the measurement of the aircraft potential is made by means of 5 "field-mills"; we only used the output of one of them to follow the evolution of the discharge processes. The main characteristics of this sensor is an operating range of ± 100 kV/m and a bandwidth from DC to 20 Hz.

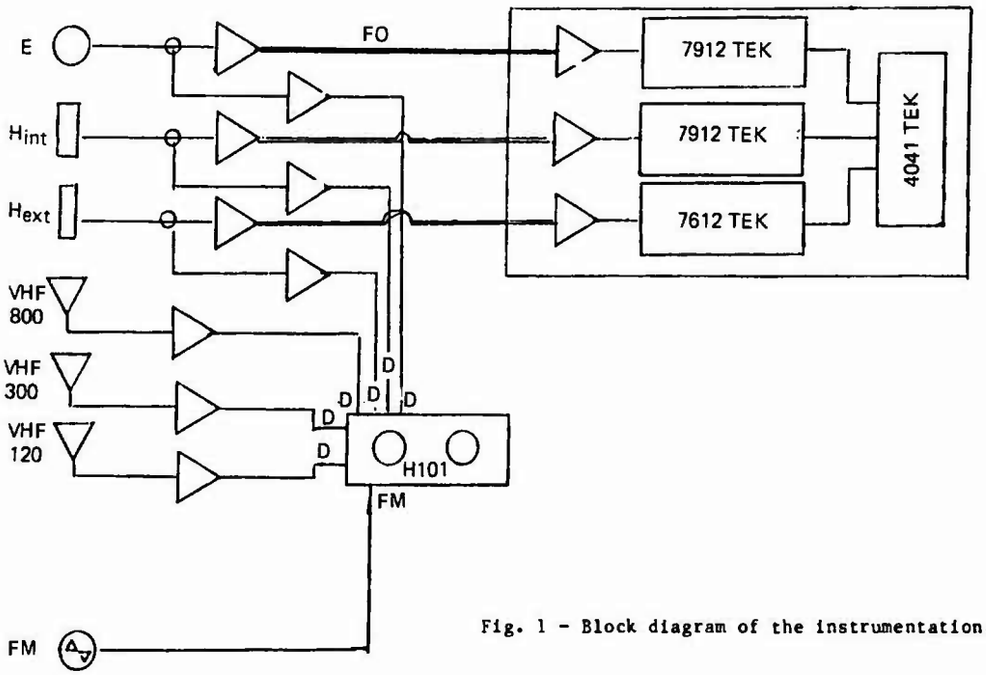


Fig. 1 - Block diagram of the instrumentation.

The VHF and UHF antennas tuned at frequencies of 120, 300 and 800 MHz are connected directly by means of solid coax to the receivers which basically contain one filter with a 4 MHz bandwidth and a log-amplifier.

The whole instrumentation follows the block diagram on figure 1. Signals from the two magnetic sensors and the electric field sensor are transmitted over fiber optic cables to the shelter instrumentation inside the aircraft. These links have a bandwidth of 200 MHz and a dynamic range of 40 dB.

Analog records are carried out by a H101 analog recorder on direct and FM channels set on a WBII standard.

Digital records are made on Tektronix 7612 and 7912 transient digitizers with a 10 µs window for the 7612 and 2 µs window for the 7912 and an equivalent bandwidth of 100 MHz. Theae digitizers are under control of a Tektonix 4041 system controller. The operating program allows a train of 4 acquisitions of 10 µs window every 50 ms, then a deadtime of 4 minutes is necessary to transfer the digital data from the computer memory to the mass storage device (DC 100 Tape).

III - RESULTS

The measurements were carried out during the period of time spreading from the 16th of June to the 28th June 1984 and concern 18 lightning flashes. The aircraft has been flown over the South of France at an altitude ranging from 3200 to 6400 m most of the time between 0°C and -8°C. There have been 7 lightning impacts on the front boom, 4 lightning impacts on the wings and 7 non-localized lightning impacts.

III.1 - Flash characteristics

A flash which consists of one or more sequential discharges lasts several hundreds of milliseconds; the mean value is 300 ms with a standard deviation of 251 ms, the extreme values are 80 and 800 ms. These durations are approximatively evaluated by looking at the relatively fast variations of the electrostatic field. These fast variations cannot be confused with the slow variations due to the charge cloud distribution because of the aircraft speed which implies that during 100 ms the aircraft has only moved by 10 m. The mean value of these variations is 70 kV/m with a standard deviation of 37 kV/m; the slope of the first electrostatic field variation is 0.8 kV/m/ms with a atandard deviation of 270 V/m/ms. During the process, every change of slope in the electrostatic field record is associated with a series of electromagnetic pulses. This situation is shown on figure 2; the two analyzed events correspond to front boom impacts; figures 2a and 2c are "field-mill" messurements, figures 2b and 2d are the simultaneous records of the external magnetic field. It can be seen that the first pulses are gathered in a train form lasting some milliseconds (points T_1, T_2). This situation has occurred in 75% of the analyzed cases; in the 25% other cases isolated pulses start the process. The typical succession of pulses during the first period of the attachment process is shown on figure 3. On that picture, the first train T lasts 2 ms and is followed by sharp isolated pulses P occurring several milliseconds after and during the whole process. This situation has already been described by Fitzgerald in December 1968 [2], by NASA [3] and by USAF/FDDL in 1981 [4].

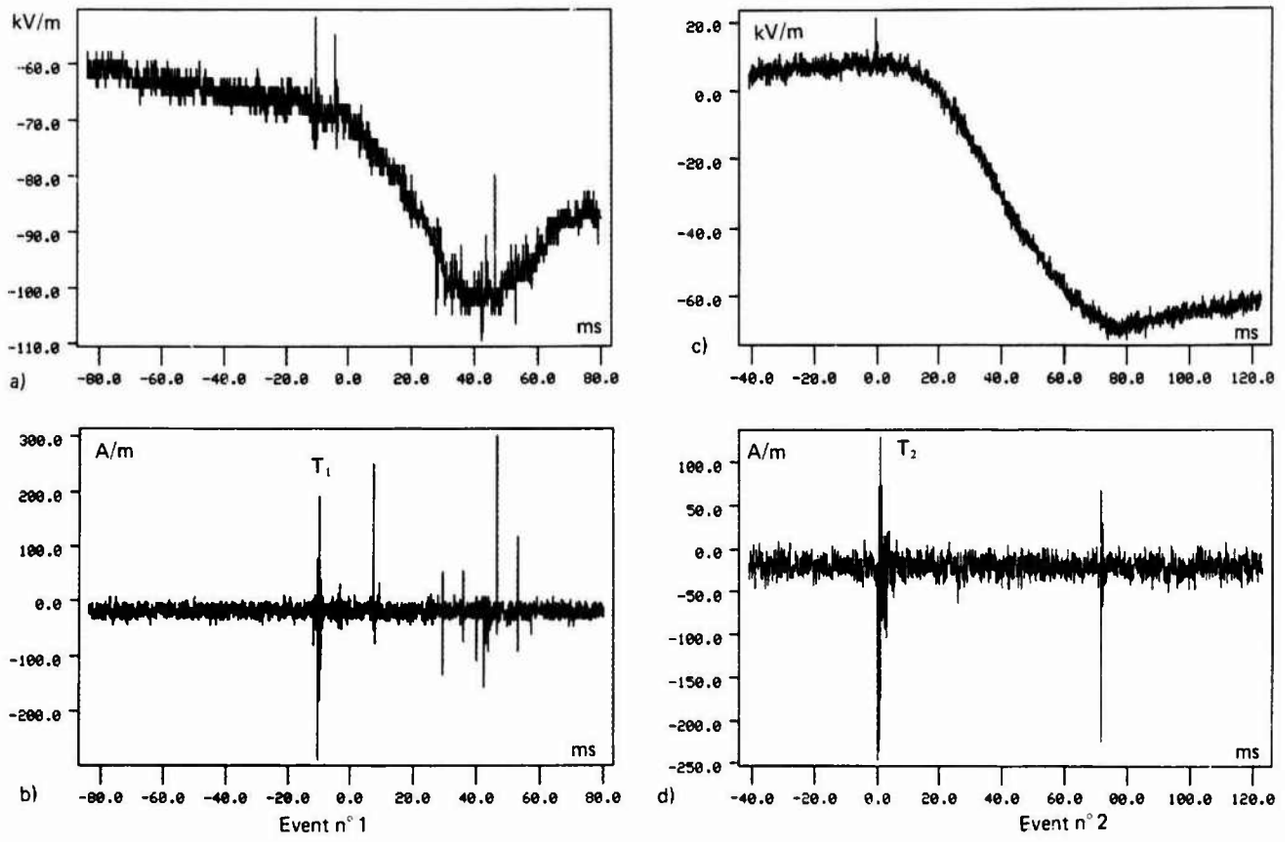


Fig. 2 - Electrostatic and magnetic fields.

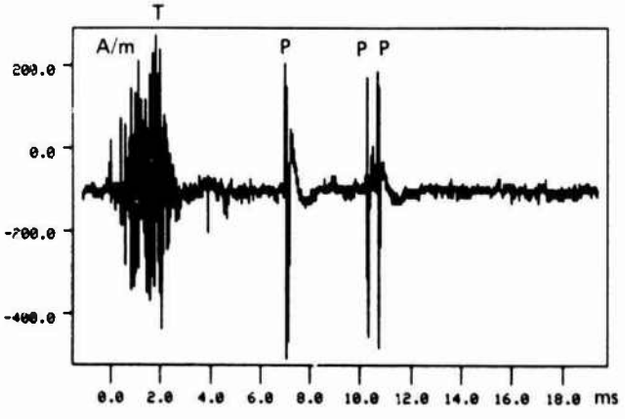


Fig. 3 - Typical succession of electromagnetic pulses.

This shows that the first contact of the discharge with the aircraft is different from the following ones and suggests some kind of triggering process. Flashes not preceeded by this phenomena may be natural flashes.

A detailed analysis of these trains can be observed on figure 4 where four of them are shown. As an hypothesis, these records suggest the growth of a leader merging from the aircraft by steps separated by some 100 µs up to a point where a connexion occurs between this leader and the cloud leader. The first pulses are unipolar and are immediately followed by bipolar pulses as soon as the contact has been realized. These first pulses are number 1 to 4 on figure 4a, 1 and 2 on figure 4b, 1 to 4 on figure 4c and 1 and 2 on figure 4d. The following pulses in these trains may be oscillatory like back and forth travel of the current wave between the aircraft and the cloud, assuming a velocity of the wave front of 10^7 m/s (velocity usually assumed for a 10 kA arc). The distance between the aircraft and the end of the arc in the cloud would be 1 km. The rise time of these pulses is several microseconds or several tens of microseconds with a repetition rate of 10^4 pulses/s.

The following isolated pulses are probably due to sequential attachments of the arc or swept strokes. These isolated pulses are separated by several milliseconds which correspond to attachment points separated by some 10 cm which is seen looking at the pits that the strikes left on the booms and on the skin of the aircraft. The rise times of these pulses are much faster, about 100 ns.

III.2 - V.UHF records

The records on figure 5 show the interest of VHF measurements from two different viewpoints:

- from a designer point of view, the measurement of VHF field magnitude is useful for the evaluation of the disturbances induced on radiocommunication systems and on automatic radionavigation devices. On figure 5b which shows a record of the 120 MHz radiation with a 2 MHz bandwidth, the peak value of the field is evaluated at 2.2 V/m which corresponds to a value of 50 mV/m/kHz. On figure 5c, for 300 MHz the peak value of the field is evaluated at 5 mV/m which correspond to a value of 100 µV/m/kHz. These values, much higher than the usual radiocommunication levels, should not destroy the

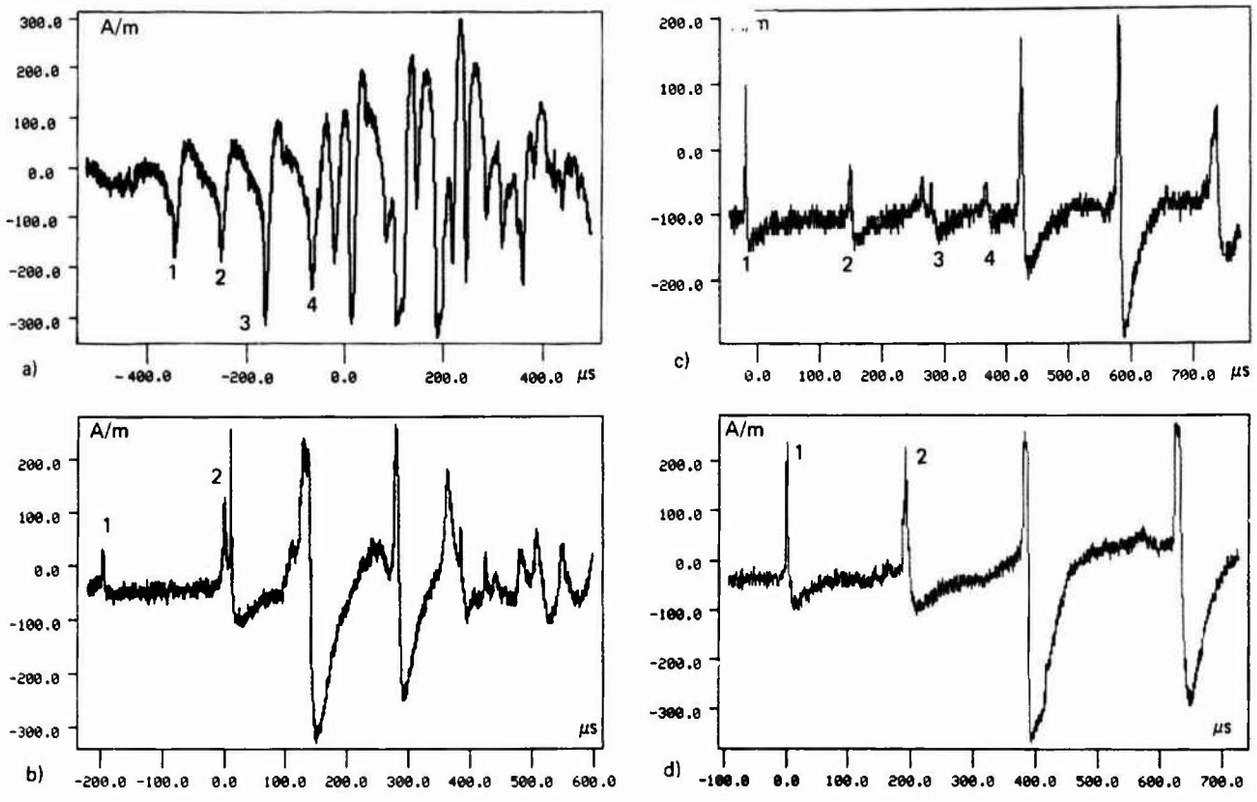


Fig. 4 - Trains of magnetic field pulses.

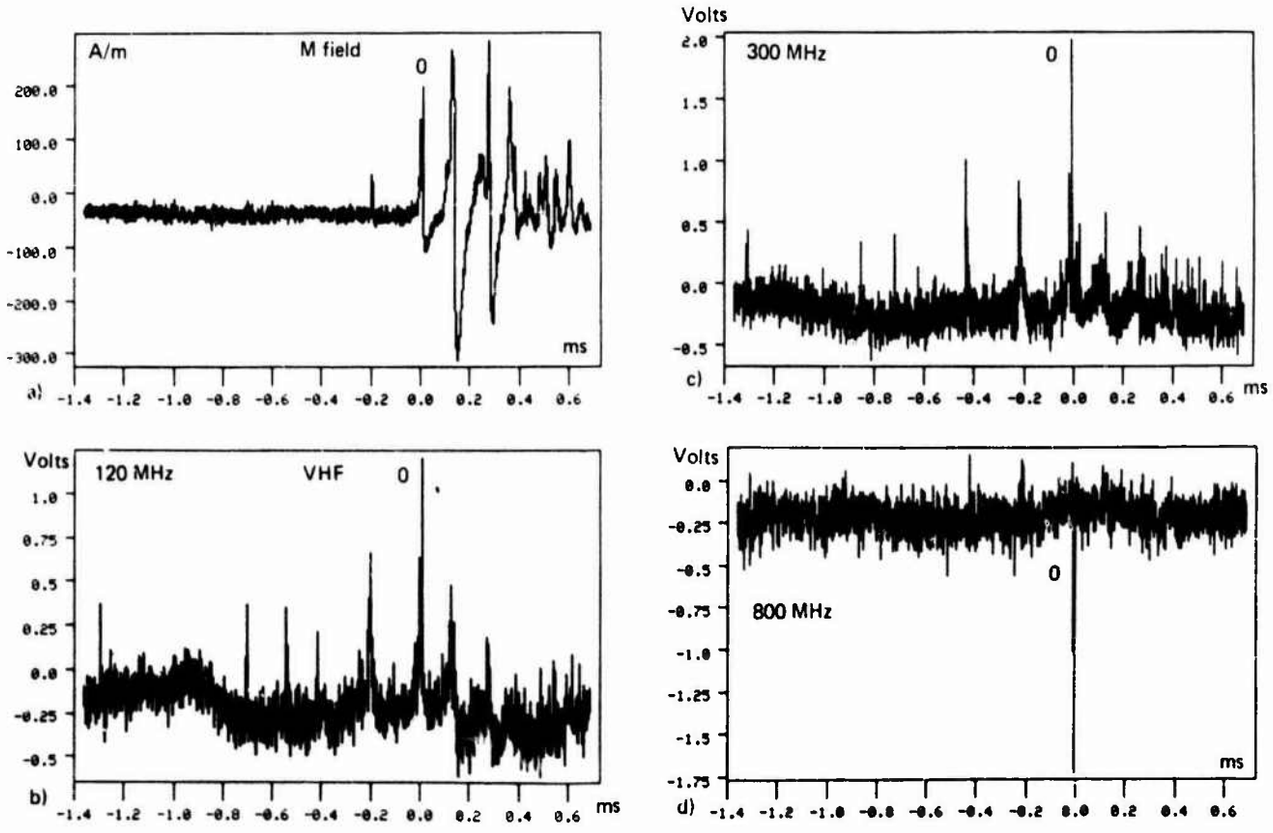


Fig. 5 - Simultaneous VHF and magnetic fields on the aircraft.

hardware, but disturb the operating mode;
- from a characterization point of view and for physical understanding of the process, VHF records show two important points: there is significant VHF radiation before the attachment process defined by point 0; this can be seen if a comparison between figure 5a (H field) and figure 5b or c is made. This point is not only due to the fact that VHF records have typically 40 dB dynamic range instead of 40 dB for the H field but also to the fact that the radiation coming from a preliminary process has a high frequency content that field measurements cannot show. Besides, during the attachment itself, H field shows rise times equal to 100 ns (cf. 3.3) but VHF records shows significant values at 300 MHz meaning that some very fast physical processes are involved with 3 ns or less rise times; figure 5d which monitors 800 MHz radiation shows that the frequency content of the process does not go up to that value.

III.3 - Wide band field measurements with 2 μs windows

This type of measurement concerns the fields which exist on the skin of the aircraft during the attachment process. The acquisition device is designed for the study of single pulses and figure 6 shows the results of two acquisitions. Figures 6a and 6b are electric field measurements; figures 6c and 6d are magnetic field measurements. The mean value of the peak amplitude of the electric field variation is 18 kV/m with a standard deviation of 13 kV/m. The mean rise time is 180 ns with a standard deviation of 200 ns. For the magnetic field, the mean value is 150 A/m with a stsndard deviation of 250 A/m, the mean rise time is also equal to 180 ns. These important values of the standard deviation on risetimes is due to the fact that some pulses have rise times less than 10 ns, and some 600 ns, depending on the time when the acquisition has been completed during the whole process. The highest value encountered for the peak magnetic field is evaluated at 400 A/m. This would correspond to an estimated current of 5 kA if the current had been uniformly distributed around the fuselage. This relatively low value in regards to what is found in the literature is due to two main reasons. The first and the most important one is that the digitizers are working from a trigger level and did not capture the highest pulse but the first one above the trigger level.

Looking at analog records, the first pulses above the trigger level are about three times smaller than the most important ones. This will lead to maximum values of the current between 10 and 20 kA. The second reason is that the current does not flow uniformly along the fuselage, the path of the current depending on the points of entry and exit. The ratio between the peak value of the electric field and the peak value of the magnetic field has a mean value of 360 Ω with a standard deviation of 200 Ω which shows that the field is not in a TEM mode at the position of the sensors. The frequency content of the acquisition is shown on figure 7. Figures 7a and b concern the FFT of figures 6a and b waveforms which are rather slow pulses (100 ns rise time) and the frequency content has no significant value beyond 20 MHz. Figures 7c and d give the FFT of one of the fastest pulses, with a 5 ns rise time non shown here. The FFT shows that energy exists up to 60 MHz and a periodicity of pulses is seen. Looking closer on figure 7b it is possible to see a spike between 4 and 5 MHz merging 3 dB above the mean spectrum; this may be representative of a longitudinal mode of resonance of the C160 aircraft.

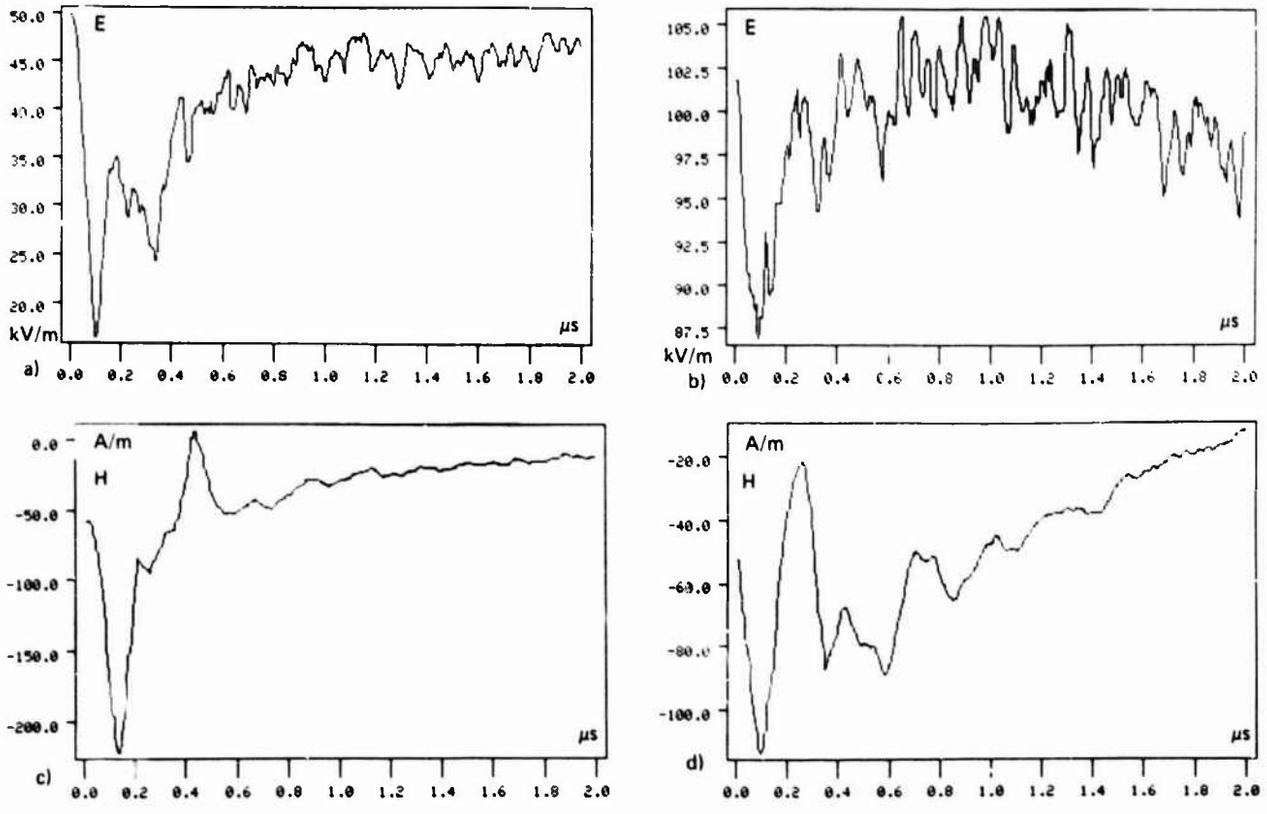


Fig. 6 - Magnetic and electric field pulses (wide band).

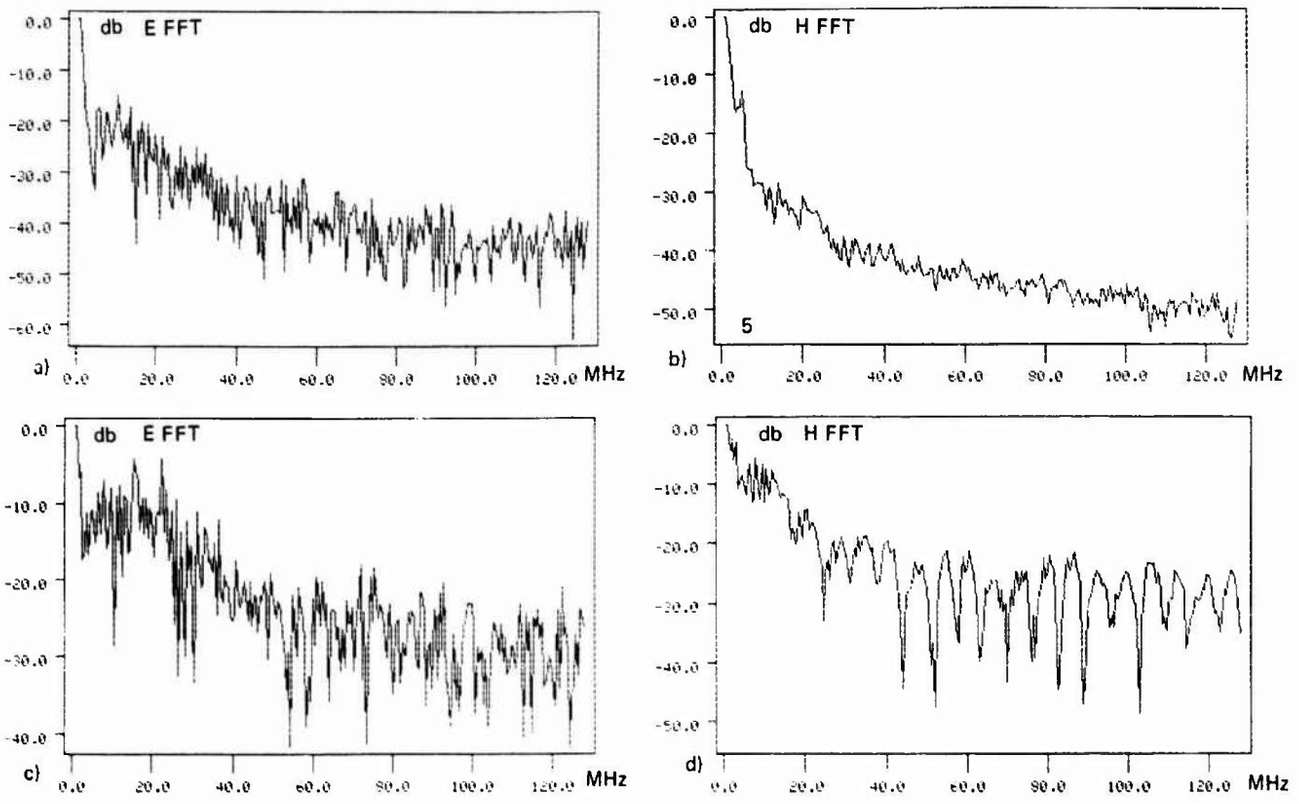


Fig. 7 - Fast Fourier Transform of magnetic and electric field pulses.

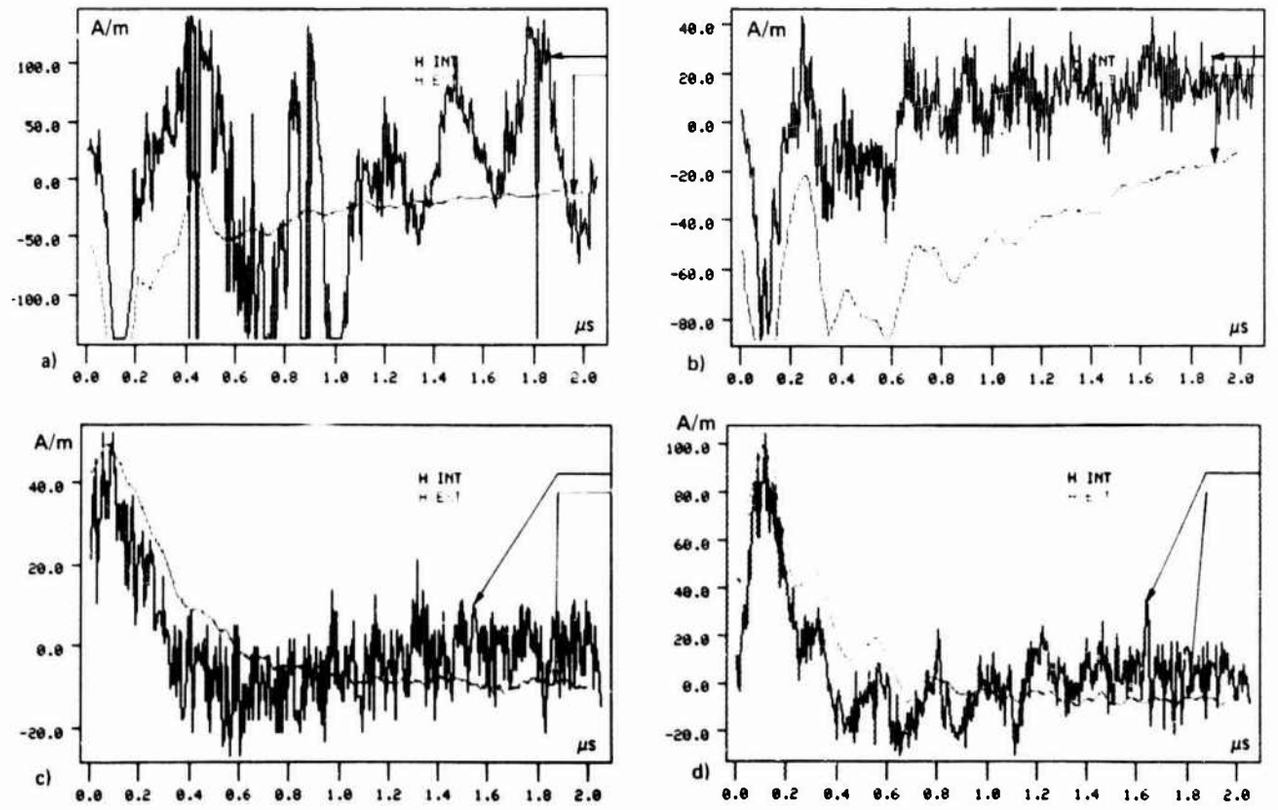


Fig. 8 - External magnetic and internal magnetic fields 50 cm behind a 38 cm diameter window.

III.4 - Penetration through the aperture.

The C160 aircraft has six 38 cm diameter circular windows; behind one of them, at 1 m from the external magnetic and electric field sensors and at a distance of 50 cm inside the aircraft, is set a free magnetic field sensor. Unfortunately this sensor is not exactly in a free field situation because of others experiments. The response of this sensor can be seen on figures 8 (a to d) which show different acquisitions. These pictures are the superposition of the external magnetic external field, Hext, and the internal magnetic field, Hint. The amplitude of the internal field has been multiplied by a factor of 20 for all these pictures in order to obtain the two curves on the same graph. It is easy to see a good correspondence between Hint x 20 and Hext at least at the beginning of the waveform for about the first 400 ns; after this period, and if the frequency content of the excitation has got enough energy in high frequency, some internal resonances of the C160 may be excited. That is the case on figure 8a for instance where the 5 MHz resonance lasts longer on the Hint than on Hext. The mean peak value of the internal field is 6 A/m with a standard deviation of 4 A/m. Such a field has a significant magnitude since it can produce a voltage of some volts on a rectangular loop of 10 x 20 cm which may be the ground line of a printed circuit board. It may be of some interest to compare these experimental values to the calculations found in the literature based on the dipole equivalence of an aperture. Starting from Maxwell's equations and writing:

$$\overrightarrow{Hint} = - \vec{\nabla} \times (\vec{m} \times \vec{\nabla} G) - j\omega \vec{p} \times \vec{\nabla} G \qquad (5)$$

with G: Green's function such as $G = \frac{e^{-jkr}}{4\pi r}$
$\vec{m}$: magnetic dipole moment,
$\vec{p}$: electric dipole moment.

with the assumptions $\omega/c \ll 1/R$ and calculating $\overrightarrow{Hint}$ on the axis of the aperture, p is colinear to $\vec{\nabla} G$.

So $\overrightarrow{Hint} = - \vec{\nabla} \times (\vec{m} \times \vec{\nabla} G)$
with $m = - 2 \alpha m . \vec{H}_{sc}$
αm = magnetic polarisability
($\alpha_m = d^3/6$ for a d-diameter aperture)
$\vec{H}sc = \overrightarrow{Hext} = \vec{H}$ short circuit.
It can be shown that Hint is equal to:

$$|\overrightarrow{Hint}| \quad \frac{d^3 |\overrightarrow{Hsc}|}{12 \pi R^3}$$

with the data corresponding to the experiment this gives an attenuation factor of 100 between the external and the internal fields; the experiment gives a factor of twenty. This difference may be probably explained by the fact that the sensor is not actually in a free field environment.

IV - CONCLUSION

This airborne experiment has given a good set of data for characterization and analysis of the indirect effects of a lightning strike and gives some confirmation on process already seen by previous experiments.
The most important results are the followings: from an electromagnetic viewpoint a flash lasts several hundred of milliseconds, there are two kinds of flashes: those which begin by a train of pulses lasting some milliseconds and followed by solitary pulses (75% of the cases) and those which begin by solitary pulses.
The magnitude of the fast field variation on the skin of the aircraft does not exceed 600 A/m for the H field and 50 kV/m for the E field. The rise time for the majority of the pulses is about 100 ns. These value may lead to reconsider the moderate threat value given in the AEHP program [6] (50 kA/µs and 20 kA peak) since the values found there are 15 kA peak and 150 kA/µs).
Digitizers and VHF experiments have shown pulses of a few nanoseconds rise time occurring along the whole process. The penetration of the measured fields through the aperture is 5 times greater than predicted, which means that one has to be cautious while applying this type of model to actual situations; nevertheless calculations are not going too far and give an idea of what could be expected.
The experiment has shown the great interest of studying VHF radiations for by this mean it is possible to analyse the high frequency content of the radiation during the whole process [7].
Although the characterization of the field on the skin of the aircraft is well known by the C580 and the C160 experiments, the relationship between the arc current and the fields is still unknown. The little number of sensors disposed on the C160 does not allow to study the current path. Future experiments will be necessary to work on that point in order to determine how much of the current flows directly through the aircraft and what is the importance of the impedance mismatch between the aircraft and the arc.

REFERENCES

[1] - C.E. Baum, "Coupling into coaxial cables from currents and charges on the exterior", presented at the 1976 URSI Meeting, Amberst (Mass., USA).

[2] - D.R. Fitzgerald, "Aircraft and rocket triggered natural lightning discharges", Lightning and Static Electricity Conference, AFAL Rep. TR-68-290, Part II, December 1968.

[3] - F.L. Pitts and M.F. Thomas, "1980-1981 direct strike lightning data", NASA Tech. Memorandum 81946 and 83273, February 1981 and March 1982.

[4] - P.L. Rustan, B.P. Kuhlam, A. Serrano, J. Reazer and M. Risley, "Airborne lightning characterization", AFWAL TR 83/3013.

[5] - K.S.M. Lee, "EMP-interaction, principles, techniques and reference data", AFWL-TR 80/402, December 1980, pp. 184-186.

[6] - J.R. Lippert, Lt Jayme, E. Lavoie and R.C. Beavin, "Progress of the atmospheric electricity hazards protection program", International Aerospace and Ground Conference on Lightning and Static Electricity, June 26-28, 1984, Orlando (Flor., USA).

[7] - J.P. Moreau, "Caractérisation du rayonnement électromagnétique des précurseura de la foudre", Thèse de Doctorat d'Etat (décembre 1983), Paris VI.

IMPLICATIONS ASSOCIATED WITH THE OPERATION OF DIGITAL DATA PROCESSING IN THE PRESENCE OF THE RELATIVELY HARSH EMP ENVIRONMENTS PRODUCED BY LIGHTNING

R. Hess

Principal Engineer, Sperry Corporation, Aerospace & Marine Group, Phoenix, Arizona 85027, U.S.A.

ABSTRACT

Much of the extensive capability associated with military and commercial aerospace vehicles is provided by avionic equipment that electronically processes relatively large amounts of data. Although such capability exists in vehicles now in service, future vehicles will require substantially more extensive data-processing capability. The two methodologies used for electronic data processing are: 1) analog, and 2) digital, but two processing faults (disruptions of data flow and undesired operations on data) significantly compromise the integrity of processed data. This paper identifies fundamental differences between the two methodologies, and discusses the implications relative to the immunity of the electronic equipment within an aerospace vehicle to any detrimental effects produced by lightning.

I – INTRODUCTION

Much of the extensive capability associated with military and commercial aerospace vehicles is provided by avionic equipment that electronically processes relatively large amounts of data. Although such capability exists in vehicles now in service, substantially more extensive data processing capability will be required in future vehicles.

The two methodologies used for electronically processing data are 1) analog, and 2) digital, but two processing faults (disruptions of data flow and undesired operations on data) significantly compromise the integrity of processed data.

II – DISCUSSION

Analog Computers

When data is processed by analog computers, the data is simultaneously applied to many dedicated computing elements. The data flow is then confined to specific, well-defined paths when these element are connected in the configuration to meet the design objectives for the specified operation of a particular analog computer. The computing elements within an analog computer are individual circuits along a computing path.

Undesired operations on data occur in analog computers when data paths are merged in an unspecified manner or when an electronic circuit malfunctions. Disruptions in data flow are the result of disruptions in the normal operation of some electronic circuit, and the circuit disruptions can be permanent due to the failure of a circuit element, or they can be transient because of interference by illegitimate signals. Since data paths in an analog computer are limited to specific, well-defined connections of dedicated electronic circuits, virtually all possible data paths are identifiable. Therefore, circuit malfunctions/failures can be identified with relatively high confidence by applying test methodologies that have been proven by extensive experience with such equipment. In other words, because of the very structured control of data flow inherent in analog computers, such special-purpose equipment can be predicted to fail in a special or specifically predictable manner. As a result, verification tests have proven effective in establishing proper equipment operation and revealing any significant malfunctions attributable to exposure to external environments.

Analog computation for aerospace vehicle feedback control is generally unsusceptible to external interference signals of relatively short duration (less than 1 ms transients) because the feedback control signals of such vehicles (feedback control of the mechanical/hydraulic systems within them) change relatively slowly (as compared to lightning-induced transients), and because of the special-purpose nature of their computing elements (specific dedicated electronic circuits).

Within an analog computer, only the data whose construction requires significant time to be produced (state variables) can be irreversibly compromised by transients (the term transient is intended to mean that class of short duration illegitimate signals which possess the agency to interfere/disrupt). In addition, within an analog computer a state variable will be unique to a dedicated computing element. Data associated with other variables may be scrambled momentarily by transients, but will return to normal after the transients die out. The information provided by state variables derived in computing elements used for feedback control (control state variables) is usually stored in circuit elements that require relatively large amounts of energy, or orders of magnitudes greater than that encountered in interfering transients, to cause significant changes in the information (outputs change slowly for electronic integrators and the lag/filter circuits that have large time constants). So even though control state variables appear to drastically change

when transients penetrate complex active devices (operational amplifiers, etc), they will immediately return to the value that existed before the transient after the transient has passed.

The state variables in analog computers that are most susceptible to transients are logic states that are latched. Latches provided by high-speed, integrated circuits (flip-flops, counters, etc.) can be toggled (change state) by relatively small amounts of energy.

In an analog computer designed to provide feedback control within aerospace vehicle, there should be no fundamental requirement for high-speed control of logic states. Susceptibility of latch circuits to transients could be virtually eliminated by adopting storage elements, which require energy that is orders of magnitude greater than that encountered by interfering transients to be changed (lags with relatively large time constants), as part of the latch feedback path or memory. Thus, because of the inherent nature of the computing elements within this kind of special-purpose computer, it is possible, to design an analog computer that is unsusceptible to interfering transients if a moderate degree of design emphasis is placed on susceptibility immunity.

Digital Computers

When data is processed by digital computers, the data is applied to one general-purpose computing element known as an arithmetic logic unit (ALU). Eventually, data to be processed must be directed along the common paths or data buses that transmit it to/from the ALU. Data either waiting to be processed or data that is already processed is held in the computer's memory. Data processing is directed by a set of general-purpose instructions (instruction set), and this general method of data processing is tailored to a specific application by a collection of individual instructions from the instruction set. In state-of-the-art digital avionic computers, this list of instructions or program can contain more than 100,000 instructions that are to be executed in many different sequences and, like data, this program must also be stored in memory. The subelements of the ALU and memory are electronic circuits. However, unlike analog computers, it is not possible to restrict data flow to the specific paths associated with dedicated computing elements since, when executed, virtually all instructions, control data flow and, in this respect, the ALU, memory and data buses, should be considered part of the total data path.

Integrated circuit technology provides the interconnection of many of the various logic circuits "cells" that compose the ALU and memory as a single electronic device. Within representative digital computers, the actual ALU and memory area result when the appropriate devices from various types of digital integrated circuits are connected together. The degree of circuit integration can range from hundreds of individual solid-state active - pn junction, FET - and passive circuit elements (LSI) to thousands of such elements (VLSI). Even larger-scale integration is anticipated for the electronic devices within future digital avionic computers.

Obviously, a digital computer intended for avionic application has a complex program with a larger number of instructions. It is therefore virtually impossible to identify all possible data paths, and extreme care must be taken to avoid any undesirable operations on data or the merging of data in an unspecified manner because of software faults. Also, while failures of the electronic circuits (hardware) within the computer will often be obvious because of the resulting wholesale disruption of data processing, device/circuit complexity defies conventional failure-mode analysis. It is virtually impossible to predict the effects of all possible circuit disruptions, whether they are permanent and caused by circuit element failure, or transient and caused by illegitimate signal interference. Therefore, disruptions in data flow can either be permanent due to the destruction of a software instruction or the failure of a circuit element, or transient due to illegitimate signal interference.

Because of the relative newness of digital technology, the corresponding inexperience with digital data processing, and the hardware and software complexities of digital avionics, test methodologies that establish an acceptable confidence level of proper equipment operation are still evolving. As a result of the generalized nature of the data-flow control inherent in digital computers, such general-purpose equipment can fail in a general manner (failure manifestation can range from wholesale and obvious to subtle, unpredictable, and insidious). Because of this, the effectiveness of verification tests to reveal significant equipment malfunctions attributable to external exposure are limited.

Since all data to be processed in a digital computer passes through the ALU, high-speed data transmission is fundamental to the operation of digital avionic equipment that executes large numbers of instructions in a computation cycle. The need for high-speed data handling translates into high-speed electronic devices that by nature respond to rapidly changing signals, whether the signals are legitimate or not. As a result, because very fast, intense transients can penetrate past the input interface into interior circuits, both memory and data control within a digital computer are susceptible to transient disruption. To eliminate the threat of destroying or permanently scrambling program instructions stored within digital avionic equipment memories, software resides in read-only memory (ROM) so that even if the logic states of ROM elements are momentarily changed by transients, they will return to normal after the transients die out.

In addition to momentary logic state changes, device damage may also be of concern relative to both memory and the ALU because, as the degree of integration increases in that devices contain more and more circuit components, the geometries of individual circuit elements decrease. Smaller geometries mean lower damage energies as well as lower switching energies (faster switching times).

In addition to the ROM elements associated with digital avionic equipment, all digital computers must provide random access memory (RAM-write/read) elements to store data that is always being updated. Unlike ROM, RAM (logic latches) states can be permanently changed by transients and, as observed during the discussion of analog computers, loss of state variable information is a key issue associated with the inherent upset susceptibility of RAM since state variables represent the class of processed data that can be irreversibly compromised when changed in an unorthodox manner.

The preceding discussion has been centered around the characteristics of digital avionic equipment as they

relate to the impact of transients (upset susceptibility, hardware complexity, software complexity). To attempt to anticipate/neutralize all possible or specific ways this general-purpose approach to computing can be upset by transients would be an exercise in futility. Because of the general nature of digital computer susceptibility to transients, the solutions to this problem must also be general, as in the example of ROM usage in digital avionic equipment.

Lightning is an external environment producing transients that are sufficently fast and intense to both damage and upset electronic equipment. Since lightning can induce transients on wiring throughout an aerospace vehicle, it can also be a threat to functions based on the use of redundant electronic equipment. The interaction of lightning with aerospace vehicles and the subsystem equipment within is a situation that is extraordinarily complex. Therefore, a complementary cycle of testing and analysis will play a critical role in programs involving the development of such equipment when the eletromagnetic environment produced by lightning is a significant issue.

If the electronic equipment being considered uses an analog computation approach, the testing and analysis methods to demonstrate that equipment will not be damaged or that the duration of any interference will not be significant already exist and are relatively straightforward. These methods have been applied to a broad spectrum of aerospace vehicle electronic equipment. This spectrum ranges from government-furnished equipment that has been part of government inventory for an extended period of time, and which was not specifically designed to be compatible with a lightning environment, to state-of-the-art equipment whose design included requirements for lightning/EMP compatibility. Essentially, these established methods use the direct or specific approach to verify that lightning or EMP requirements have been satisfied. The direct approach entails a detailed investigation of every computing element and data path. This approach can even be used in assessing digital equipment to verify that lightning-induced transients will not reach levels sufficient to cause device damage. When circumstances are amenable to such an approach, verification testing can be used with a relatively high level of confidence that such tests will establish conformance to requirements.

Unfortunately, it is not clear that the direct approach will be effective when immunity to lightning-induced transient interference of digital computations is the requirement to be resolved. The issues associated with this situation are so general and so complex that verification of this requirement will critically rely upon interpretation of development test and analysis data. The analysis should not only include a detailed explanation of the candidate design but, more importantly, the rationale that underlies and justifies the design concepts.

For example, if the design is based on the general position that transient penetration can be suppressed to the point where interference/damage levels of the critical internal circuitry will never be approached, then the analysis would have to clearly establish a high level of confidence that this objective has been achieved. Immunity to the effects of internal transients is another general position upon which a design could be based. In that instance, the analysis should contain component safety-margin information and a description of computation recovery (reset, initialization, and restart of the computation cycle). When assessing digital computer susceptibility to interference, another key analysis contribution would be the identification of any critical windows in the computation cycle.

When lightning is an environmental consideration, analysis will be the fundamental means by which verification of the conformance of digital avionic equipment to lightning requirements is achieved. Any apparent discrepancies in verification conformance that cannot be resolved with confidence could be included as part of the justification for the performance of verification tests. Conditions that produce such discrepancies should be closely monitored during verification testing to show that equipment does indeed conform to lightning requirements.

But even if there are no apparent discrepancies, intelligently performed verification tests will play an effective and important corroborative role in establishing an additional margin of confidence in the analysis conclusion that shows conformance.

III – CONCLUSIONS

Several technology trends associated with aerospace vehicle design in the direction that impact lightning vulnerability in a negative manner are listed below (Ref.1):

- Dramatically increase the use of carbon-fiber reinforced plastics (CFRP) for the vehicle skin and primary structures.
- Steadily lower susceptibility/vulnerability (S/V) levels of electronic devices.
- Substantially increase the volume of data processed by digital electronics.

The inherent conductivity of CFRP is significantly lower than aluminum. As a result, shielding afforded by vehicle surfaces and internal structural members will be significantly reduced. Thus, more of the burden for the attenuation of the electromagnetic (EM) environment, both external and internal, will have to be assumed by subsystem elements and structures, such as shielded bays, shielded wiring, equipment enclosures, and fiber optics. In addition, the immunity of electronic equipment to the substantial transients caused by lightning will have to be enhanced through appropriate design techniques. For analog computers, this may include judicial application of high-speed logic devices and, when they are used, careful treatment of latch circuits. For digital computers, the measures used to achieve designs that provide immunity to such transients will be substantially more complex, involving appropriate architectural elements and proper application of design techniques associated with high-speed data processing.

It is interesting to note that original work to characterize digital computer upset is being pursued by the sector of the technical community concerned with the effects of lightning on aerospace vehicles (Ref. 2, 3, 4, 5). The investigation of monitors to detect upset is included. The potential threat to high-speed data processing posed by EM environments is illustrated by the following qualitative assessment which anticipates that transients induced into subsystem interface cables will be controlled to

values that are consistent with those defined as Level 3 (300/600 volts) in document AE4L-81-2. The energy in an interface cable associated with the double exponential pulse is on the order of 10 millijoules (mJ); it would be on the order of 1 mJ for the damped sinusoid pulse. Such broadband waveforms represent the type of signals that can be induced on cables by lightning or other EM enviroments (which can also penetrate into buried electronic computing and storage elements).

Extensive testing of electronic devices has revealed that damage thresholds of LSI devices are on the order of 100 nanojoules when they are exposed to short duration pulses of 1 microsecond or less (Ref. 7, 8). Oevice upset occurs for energies an order of magnitude lower or more. The damage energy corresponding to VLSI devices is projected to be on the order of 1 nanojoule. This is consistent with the order of magnitude or more reduction in device geometries. Thus, inception of VLSI device upset would occur for energies less than 1 nanojoule. This wide disparity between threat levels and upset levels (10^7 or greater) clearly highlights the potential for the wholesale disruption of data processing and the corruption of stored data. Obviously, device damage is also an issue of concern.

The ability to automatically detect significant disruption of data processing, initialize the processing cycle, recover all critical variables and reinstate processing would result in a digital data processor that is as immune to significant disruption of computed functions as an analog data processor. In addition, this high degree of computing integrity could be further enhanced by the application of fiber-optic data transmission between electronic computers.

REFERENCES

1. D. T. Auckland, R. F. Wallenberg, and J. A. Birken. "The Effects of New Technology Trends on Aircraft Lightning Vulnerability and the Capability to Identify Technology Deficiencies," International Aerospace and Ground Conference on Lightning and Static Electricity, Fort Worth, Texas (June 1983).

2. M. E. Schmid, R. L. Trapp, G. M. Mason, and A. E. Davidoff. "Monitors for Upset Detection of Computer Systems," International Aerospace and Ground Conference on Lightning and Static Electricity, Fort Worth, Texas (June 1983).

3. G. M. Mason, "Upset Experimentation in Computer-Based Systems," International Aerospace and Ground Conference on Lightning and Static Electricity, Fort Worth, Texas (June 1983).

4. V. A. Carreno, "Upset Susceptibility Study Employing Circuit Analysis and Digital Simulation," International Aerospace and Ground Conference on Lightning and Static Electricity, Orlando, Florida (June 1984).

5. C. M. Belcastro, "Data and Results of a Laboratory Investigation of Microprocessor Upset Caused by Simulated Lightning-Induced Analog Transients," International Aerospace and Ground Conference on Lightning and Static Electricity, Orlando, Florida (June 1984).

6. "Test Waveforms and Techniques for Assessing the Effects of Lightning-Induced Transients," AE4L Committee Report AE4L-81-2, SAE (December 1981).

7. Semiconductor Vulnerability, AFWL-TR-73-119, Volume 1, Air Force Weapons Laboratory, Kirtland AFB, New Mexico (July 1973).

8. D. R. Alexander, C. R. Jenkins, and J. J. Schwarz. "EMP Susceptibility of Semiconductor Components," D224-13042-1, The Boeing Company, Seattle, Washington (September 1974).

A NEW FORM OF TRANSIENT SUPPRESSOR

B.I. Wolff and R.A. Earle

General Electric Company - PESD, EP7, P.O. Box 4840, Syracuse, NY 13221, U.S.A.

Abstract - A new tubular extrusion form of transient suppressor made from metal-oxide-varistor (MOV) material could improve the effectiveness of transient suppression systems. The new component was designed for installation directly on the pins of system wiring connectors minimizing added bulk and weight. The physical construction lends itself to relatively large conducting areas and inherent heat-absorbing mass, thereby aiding the ability to divert transient peak current and to sustain deposited energy. The electrical characteristics of the new connector pin varistors have been shown to be generally similar to commercial disc varistors of comparable voltage and active physical volume. Electrical ratings were first estimated by projection from other forms and then empirically verified by evaluation testing. It was concluded that these devices, which also exhibit resistance to the stress of radiation, have a manifest potential to improve transient voltage protection of both aerospace and ground electronic systems.

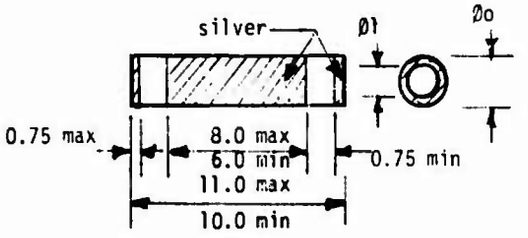
I - INTRODUCTION

The advance of microelectronics has brought powerful new capabilities to aerospace and ground electronic systems. An obvious effect is miniaturization which has greatly increased functional density within a given volume or mass. Reliability is potentially better because of fewer and shorter interface connections, and the reduction of size and conductor length also can improve response speed or extend bandwidth. However, the sophisticated semiconductor chips which lie at the heart of new-generation electronics require more elaborate protection against damage or upset by voltage transients. Hence, the need for transient protection has been multiplied.

The installation of transient suppression within system cable connectors is a relatively new approach to the implementation of transient voltage protection, and one which imposes new requirements on the suppressor components themselves. Most existing forms of transient suppressors have limitations of one kind or another. These drawbacks might relate to their physical size and shape, to their electrical performance, or to their resistance to possible environmental stresses when used in some applications. And because, in general, some compromise or balance of performance characteristics will be necessary certain design features might be weighted more heavily than others. This paper describes the results of a program to develop a new form of transient suppressor intended to best fill a particular set of requirements.

II - DEVICE MODEL

Extruded tubular form capacitors have been widely used for some time as high frequency RF filtering elements within multi-pin connectors. The advantage of this hollow cylindrical shape is that the component can be slipped over connector pins without requiring major redesign or size increases in the connector bodies. Experimental transient suppressors of this form also were made some years ago by machining them from blocks of metal-oxide-varistor material.[1] Since that time materials have been significantly improved in electrical performance and extended in range of available voltages. But extensive effort was still required to develop MOV materials suitable for the production of extrusion shaped parts on a high volume scale. The wire sizes used in medium and high density connectors, American wire guage numbers 20 and 22, presented the greater challenge because of smaller diameters and narrower wall thicknesses. The part dimensions used are shown in Figure 1.



Part Size	Øo Min	Øo Max	Ø1 Min	Ø1 Max
20 AWG	2.03	2.18	1.09	1.52
22 AWG	1.73	1.90	0.86	1.32

Figure 1. Outline Dimensions - Millimeters

The material composition of MOV's consists of over 90% zinc oxide, bismuth oxide, and other metal oxides. These materials can be prepared and processed into specific forms by techniques parallel to those used to make ceramic capacitors of similar form such as discs, chips and extruded tubes. However, despite a mechanical similarity to some passive devices MOV's are active semiconductor devices. Zinc oxide is widely recognized as a semiconductor material [2]. The properties of single junction zinc oxide-bismuth oxide semiconductor diodes have been studied and reported [3]. That study revealed a breakdown voltage different from silicon diodes, as expected, and demonstrated a sharp transition from the non conducting to the conducting region with a highly non linear

I-V characteristic typical of a good semiconductor material. These characteristics tend to carry over into large MOV forms which typically contain many thousands of semiconducting junctions.

As is well known zinc-oxide metal-oxide-varistor material consists of many individual grains of Zno separated by a thin intergranular layer containing oxides of bismuth and other elements. This structure usually is irregular in actual configuration but for didactic purposes it is conventional to represent it as a more uniform layout. [4] Figure 2 represents the idealized microstructure of a segment of the cross-section of a tubular varistor form. Effectively, each ZnO grain is a resistor and each grain boundary is a miniature varistor. Hence, MOV's internally are complex series parallel networks of semiconducting diodes and resistors. In turn, each diode will have an associated capacitance and leakage resistance element. The reduction of this network leads to the varistor equivalent circuit model of Figure 3.

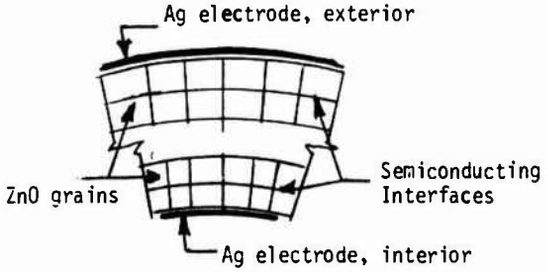


Figure 2. Idealized MOV Microstructure

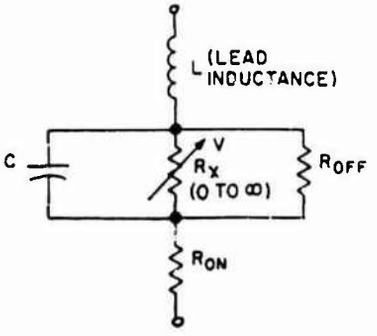


Figure 3. Varistor Equivalent Circuit

For many practical applications, perhaps most, it is possible to further reduce the equivalent circuit of a varistor. Device capacitance and parallel leakage resistance have negligible effect on transients except those of very low energy. Provided that connecting leads are short, preferably less 1 cm in length, the lead inductance also has negligible effect under typical 8/20 and 10/1000 μs transient current waveshapes. [5] In such cases the varistor model reduces to a simple fixed resistance in series with a current dependent resistance.

It has been shown empirically that the voltage response to current stimuli of typical MOV's can be closely approximated by a behavioral equation of two terms. [6] This equation usefully is founded on the simple, but meaningful, electrical and physical model of the device and its variable design parameters, as follows:

$$V_C = aI^b + R_S I \qquad (1)$$

where V_C is the varistor clamping voltage, a is a device constant, b is the exponent of nonlinearity, I is the operating current, and R_S the fixed series bulk resistance of the device. Since estimated values of R_S typically are a small fraction of one ohm the second term of equation (1) can be ignored when operating current is below one ampere. Specifically, if current is expressed in units of milliamperes, and the nominal varistor voltage V_N is defined as the voltage at a test current of one milliampere, then it is apparent that V_N has the same numerical value as the device constant, a.

$$V_N = aI^b = |a|, \text{ if } I = 1. \qquad (2)$$

EFFECTS OF PHYSICAL GEOMETRY

The physical dimensions of the varistor can be related to the electrical model. First, let p represent the voltage gradient characteristic of varistor material as described in units of V/mm at a test current of 1 mA, where numerical values of p in the range of about 10 to 500 are practical. (Dimensionally, the material gradient would be correctly measured as kilohms/mm, but the usage of V/mm is common and intuitively meaningful.) By definition the device constant, a, of any varistor then can be given by; where t is the thickness of the varistor section in mm:

$$a = pt \qquad (3)$$

Also, by the conventional formula for resistance in terms of material resistivity, ρ, and conductor areas A:

$$R_S = \rho t/A \qquad (4)$$

Substitution of (3) and (4) into (1) gives:

$$V_C = t\,(pI^b + \rho I/A) \qquad (5)$$

To find the effect of material and design variables on voltage clamping performance it is useful to define a characteristic called clamping ratio C.R., as below.

$$C.R. = V_C/V_N \qquad (6)$$

For varistors of a given nominal voltage the ratio C.R. depends only on the values of b, p, ρ of the material used and the conducting area A as the sole design variable. This may be demonstrated by substitution of (5) for V_C and (2) for V_N in equation (6). The resulting form can be reduced as below.

$$C.R. = I^b = \rho I/pA \qquad (7)$$

As would be expected the clamping ratio depends, first of all, on the nonlinear exponent, b. The effect of material variables on this exponent can be grasped intuitively by considering the relation of the varistor microstructure to its terminal behavior. Each semiconducting grain boundary tends to act as an ideal miniature varistor in series with a fixed resistance of the adjacent ZnO grain. A complete structural model of a metal-oxide-varistor would represent the device as the series-parallel combination of a very large number of these individual elements. Equations (1) and (7) effectively are reduced forms of a complex system, in which exponent b may be regarded as a proxy measure of the homogeneity of the material.

The voltage drop across the series fixed resistance, as represented by the second term of (5) and (7), can be minimized first by advanced materials with a low value of resistivity. Secondly, it can be minimized by selecting a material with a high voltage gradient p; but this choice is limited by the fragility of a thin section. Thirdly, it can be minimized by a larger size part with greater area. This is the most common variable used to design or choose varistors for the best clamping performance. Practical considerations of space and cost limit the range of options.

OTHER DESIGN CONSIDERATIONS

Like other devices, varistors have finite limits of electrical stress which they can withstand. The limits of a given class of materials are proven by evaluation testing. Once established these can be used to design devices to meet some rating goals by varying section thickness and conducting area over some range.

At first glance it might appear that the surge withstand capability could be increased simply by using a material with a low value of voltage gradient, p, thereby allowing a thicker part. However, because the resistance of the material itself adds to the power dissipated at high current this design approach is of limited value in practice. Also, any added resistance tends to degrade the clamp ratio. Hence, the goals of better clamping voltage and greater energy capability tend to be mutually exclusive. A well-designed varistor is a judicious compromise of these goals as well as other technical and cost factors.

The preceding proposition can be demonstrated by deriving an expression for peak power density. Let PP represent peak power, and let PPD be peak power density. By substitution of equation (5) into the definition of peak power:

$$PP = VI = t\,(pI^{1+b} + \varrho I^2/A) \qquad (8)$$

Recalling that the volume is given by At the peak power density is:

$$PPD = pI^{1+b}/A + \varrho I^2/A^2 \qquad (9)$$

If values representative of commercial radial disc varistors are assigned to all variables except p then clamping ratio and power density can be compared in their dependence on the voltage gradient using equations (7) and (9). As illustrated by Figure 4 these characteristics change oppositely with variation of p. Also, there may be side-effects in the material electrical properties resulting from changes in the material formulation which are needed to vary p. The best compromise will depend on the specific needs of the application.

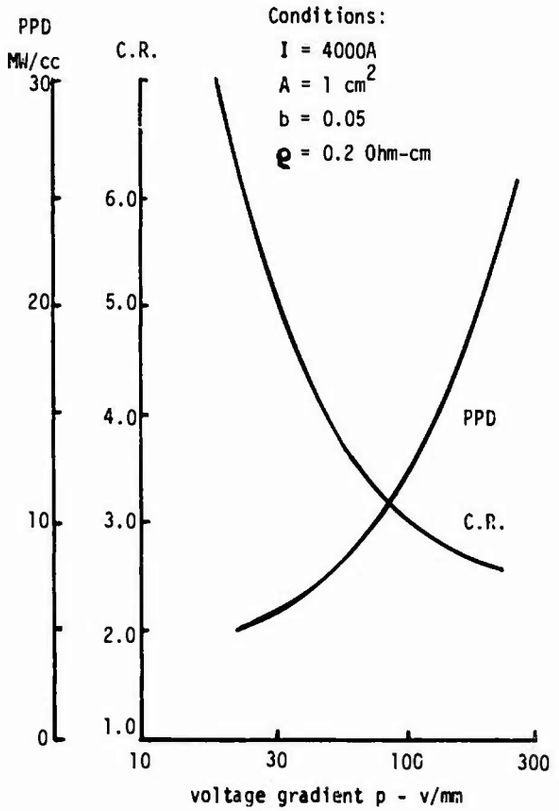


Figure 4. Variation of C.R., PPD with p.

Generally, it is desirable to minimize and control the varistor standby current I_D, which is defined as the current measured with the maximum rated continuous dc voltage V_M (dc) applied. In metal-oxide-varistors the region of highly nonlinear conduction extends down to currents on the order of 20μA. Below this the V-I characteristic becomes increasingly affected by the value of the parallel leakage resistance R_{OFF} in Figure 3. This characteristic is also affected by temperature. Both the nonlinear characteristic and the resistivity of the parallel path tend to be inherent properties of a varistor material. Changes to the material formulation might help to reduce standby current somewhat but would tend to compromise clamping voltage and peak current capability.

The parallel resistance can be modeled as dependent on device geometry. Let r be the resistivity of the varistor material in the off state with other terms as defined previously. Then simply:

$$R_{OFF} = rt/A$$

If the values of r and t are fixed by the material and the application voltage then R_{OFF} can be increased by using the smallest feasible varistor area. This may somewhat reduce typical values of I_D. However, the affect on maximum I_D is less because its value is determined mainly by the nonlinear region of conduction.

Both typical and maximum standby currents can be reduced by using a higher voltage varistor if a higher protective level is acceptable to the application. Alternatively, a narrower tolerance could be specified

for the varistor voltage but this would raise the cost. Special testing to select only varistors with better values is another approach, again affecting cost.

Capacitance may be the most difficult to adjust of MOV characteristics. Firstly, because the principal role of varistors is to suppress transients they are designed to be cost-effective in providing the best protective level and required surge withstand capability. Capacitance therefore tends to be a residual after other objectives have been satisfied. In many applications varistors are connected across ac or dc power lines, where the magnitude of capacitance or its device to device variation are not important. In fact, the varistor capacitance may be helpful in suppressing transients and filtering noise. Data transmission lines, however, are an important exception, and control of capacitance values is of concern.

If the applied voltage is zero, or well below the threshold of nonlinear conduction, a varistor can be regarded simply as a ceramic capacitor whose value is given by the familiar formula for a parallel-plate capacitor. If C represents capacitance and ϵ is the dielectric constant of the particular material used:

$$C = \epsilon A/t$$

It should be noted that the measured value of capacitance is somewhat dependent on the frequency of the test signal, and could be 25-50% higher at 1 KHz than at 1 MHz.

From the expression above it is evident that a thicker section of a given material will reduce capacitance, but also will raise the varistor voltage. For the same voltage capacitance perhaps could be reduced by changing the material but this may compromise other properties such as peak current rating. The one sure way to minimize capacitance is to use the smallest disc size feasible for the application.

TUBULAR GEOMETRY CONSIDERATIONS

The preceding discussions were intended to be general ones applicable to MOV's of common shape such as round discs or rectangular chips. The new tubular form can be approached with the same analysis, excepting that the effective conducting area and volume are a special case which might require some interpretation. Unlike typical disc varistors the new tubular form, made as described in this paper, had different electrode configurations on its conducting faces. As shown in Figure 1 the interior wall was completely coated with a fired silver paste electrode, and this electrode was permitted also to lap slightly over onto the exterior ends of the tube. However, the actual exterior electrode was isolated from the tube ends by a distance of roughly twice the wall thickness. Hence, the expected path of conduction was through the thin wall of the tube with current flowing between the exterior electrode and the segment of interior electrode directly opposite. This fact leads to a model of effective electrode area A which uses the circumference of the interior electrode of diameter $\emptyset_1$ times the length l of the exterior electrode; i.e.

$$A = \pi \emptyset_1 \, l$$

The effective volume for dissipation of deposited transient energy in the form of heat also might require some interpretation. This volume can be calculated precisely as the volume of the hollow cylinder of length l; i.e., as the volume of the exterior cylinder minus the interior one. However, it might be intuitively satisfying to be able also to approximate the volume directly in terms of the wall thickness t. Let $\emptyset_o$ represent the outside diameter of the tube, with $\emptyset_1$ and l as the inside diameter and length, so that the volume L of the tube then will be described by the expression:

$$L = \pi \, l(\emptyset_o^2 - \emptyset_1^2)/4 \qquad (13)$$

Note that:

$$\emptyset_o = \emptyset_1 + 2t \qquad (14)$$

If the typical wall thickness for a given tubular part is some multiple of the inner diameter, then equation (13) can be solved in terms of t; and it can be shown that, if:

$$\emptyset_1 = 2.5t$$

$$L = 8.6t^2 \qquad (15)$$

and if:

$$\emptyset_1 = 3t$$

$$L = 10.2t^2 \qquad (16)$$

Equations (15) and (16) provide approximations for the typical active volume of parts made for wire guage sizes 22 and 20 respectively.

CONSTRUCTION OF SAMPLES

Experimental tubular varistors had been made some years ago, not from extruded forms, but by machining of pieces from blocks of sintered MOV material. Also, with the limited choice of materials then available a wide range of voltage types could not be attained. Although a greater variety of materials has since been developed these have been intended for disc varistors which typically are thicker in cross-section. Some new formulations had to be developed to achieve voltage gradients compatible with the thin walls of the tubular form. This made it possible to produce sample groups with nominal varistor voltages of 8, 33, 220 and other values. Furthermore, these pieces now were made by methods suitable for expansion to high volume production.

In the manufacture of MOV's raw materials are processed into sintered forms by methods parallel to passive ceramic components. However, MOV's are active semiconductor devices, as indicated by evidence of depletion layers in varistors with the same type of behavior observed for silicon semiconductor abroup p-n junction diodes. (7) The semiconducting characteristics of varistors in any form are sensitive to processing conditions; and the new tubular shape, with a surface-to-mass proportion very different from a disc, required development of new processing conditions. The bodies were fired at peak sintering temperatures of about 1200°C or higher. Electroding was by means of thick film silver paste fired onto the interior and exterior walls of the tube in the pattern of Figure 1.

TEST METHODS

With the use of design knowledge as described in the preceding sections the electrical behavior of a new form or size can be largely predicted. Still, the actual performance needs verification by tests using industry standard methods. For electrical characteristics the key parameters are nominal voltage V_N; clamping voltage V_C and dc standby current I_D. For some applications capacitance also is important. In electrical rating assurance tests the vital maximum ratings are continuous voltage $V_{m(ac)}$ or $V_{m(dc)}$, peak current I_{tm} and energy W_{tm}. To compare characteristics before and after a stress the nominal voltage V_N often

is sufficient as the single end-of-life criterion; because, if the V_N values initially were within specification, and if the values were not shifted more than 10% by the stress, then there is indication that V-I characteristics were not shifted beyond usefulness. In the development of the new tubular form varistors all the above tests reported in this paper were conducted in accordance with IEEE Standard C62.33-1982. A description of most of the definitions and terms of that standard also is available in the commercial literature. [8]

In addition to electrical performance the resistance of the new component to mechanical and environmental stresses was tested also. The most interesting of these was the exposure of the metal-oxide-varistor material to gamma radiation, with results as reported in a later section.

EMPIRICAL TEST RESULTS

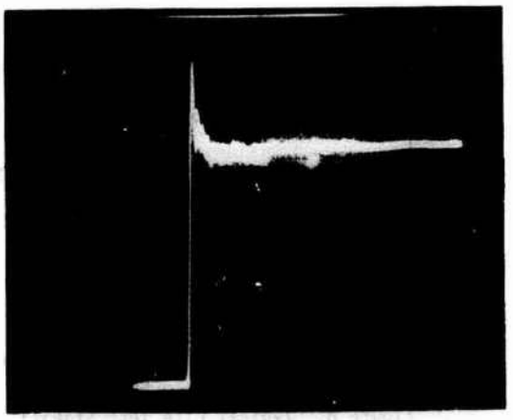
The typical electrical characteristics measured on groups of test samples with nominal varistor voltages of 8, 33 and 220 volts are listed in Table 1. These electrical values are generally similar to those which might be observed on disc varistors of comparable conducting area.

Table 1 - Typical Characteristics Observed @ 20-25°C

Type	V_N @ 1 mA (Volts)	V_C @ I (Volts)	(A)	I_D @ V_m(dc) (μA)	(Volts)	C (pf)
V8CP22	8	20	5	50	6	10,000
V33CP22	33	63	10	5	26	3,500
V220CP20	220	363	20	2	180	240

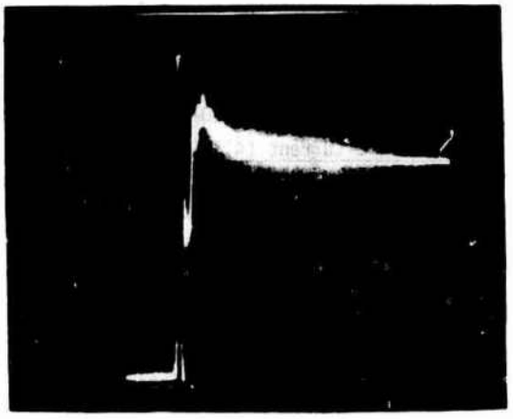
The new varistor form shows reduced voltage overshoot in response to very fast rising transients. This stems from its design as a leadless, direct-connected component. The inductance of leaded components on the other hand, in combination with high values of current rate-of-rise can cause an inductive voltage drop across the device leads which adds momentarily to the clamping voltage. The overshoot phenomenon and its reduction by leadless connection is illustrated by the sequence of waveform photos of figures 5, 6 and 7. Figure 5 shows the open circuit voltage waveform of a fast rising transient and Figure 6 shows the clamping voltage response when a leaded disc varistor type V12ZA1 is inserted in the circuit. The leading edge of this clamping voltage waveform gives evidence of the effect of lead inductance causing a short-lived overshoot followed by a damped undershoot. Still, leaded varistors have been shown to adequately protect typical integrated circuits. [9] Figure 7, which is the response of a typical tubular varistor type V8CP22 in the same circuit, shows how the new leadless form has virtually eliminated lead inductance overshoot.

The results of operating life testing are shown in Figure 8. This graph displays power dissipation average readings observed on two groups of different type samples. One group was tested under dc power line conditions, the other with ac voltage applied. These power dissipation values were observed by insitu measurements; i.e., with the test pieces in a chamber at elevated temperature and with the continuous voltage applied. Both groups demonstrated relatively low power dissipation and stable behavior over the test period.



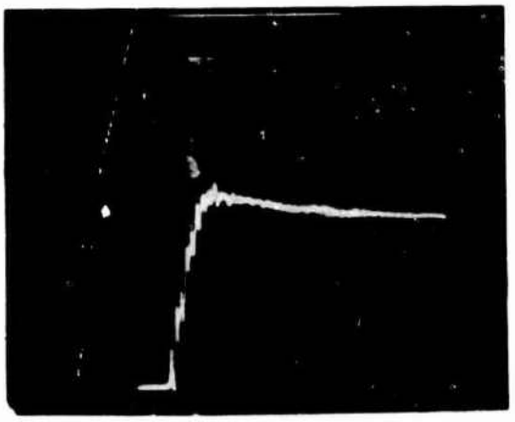
Vert: 200V/div. Hor: 50 ns/div.

Figure 5. Open Circuit Transient Voltage



Vert: 5V/div. Hor: 50 ns/div.

Figure 6. Suppressor Lead Inductance Overshoot



Vert: 5V/div. Hor: 50 ns/div.

Figure 7. Transient Suppressed by V8CP22

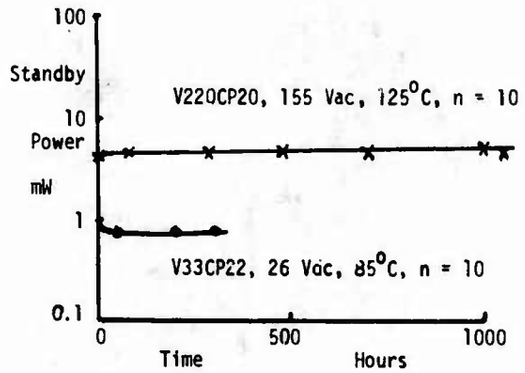


Figure 8. Typical Life Test Stability

The results of pulse testing are shown in Table 2. This lists the test stresses and the typical effect on nominal varistor voltage. It should be noted that these stress levels were intended to reflect rating conditions producing a very low rate of failure. The levels required to reach the threshold of catastophic failure might be several times higher.

Table 2. Pulse Test Typical Results

Type Tested: V220CP20, T_A = 20-25°C

# Pulses	Wave Current (A)		Energy (J)	V1mA Shift
2	8/20 us	180	1.5	-3.0 %
1	10/1000 us	7	3.2	+1.1 %

Commercial MOV material, similar to that used in the new form varistors, showed a most interesting result when exposed to gamma radiation. The current voltage characteristics and admittance spectroscopy measurements, at 1 KHz to 10 KHz from 10°K to 300°K, showed no significant change after irradiation with 10^6 rads Co^{60} gamma radiation. (10) These findings are consistent with earlier tests on experimental tubular form varistors. (1)

SUMMARY AND CONCLUSIONS

The new tubular form of transient suppressor utilizes metal-oxide-varistor technology, which combines the electrical advantages of active semiconductor devices with mechanical properties often associated with passive components. The physical construction of MOV's lends itself to relatively large conducting areas with inherent heat-absorbing mass. In turn this leads to relatively greater capability to carry transient peak current and to absorb the deposited energy. The semiconducting characteristic of the material also helps clamping voltage performance. To permit transient suppression to take place on the outside enclosing shield of the equipment module, rather than on internal circuit lines, the new component was designed for installation directly on the pins of electrical connectors. Hence, the new tubular form helps greatly to reduce the added bulk and weight previously associated with transient protection hardware, and the leadless construction reduces voltage overshoot due to lead inductance.

Special ceramic processing techniques were adapted for application to MOV materials in order to make the new tubular form a practical reality suitable for production in potentially high quantities. In addition, the formulation and processing of existing commercial MOV materials were adapted for use with the new form. The electrical characteristics of the connector pin varistors were shown to be similar to commercial disc varistor products of comparable voltage and physical active volume.

It was concluded that these connector pin varistors are a viable new form of transient supporessor with a manifest potential to fill an open need for better transient protection of both aerospace and ground electronic equipment.

ACKNOWLEDGEMENT

The authors are indebted to many colleagues for invaluable aid in the theory, design, preparation and testing of the new form varistors; especially G. Dumais, S. Korn, L. Levinson and J. May.

REFERENCES

1. Tasca, D.M. and Peden, J.C., EMP Surge Suppression Connectors Utilizing Metal Oxide Varistors, Report HDL-TR-179-1, U.S. Army, Harry Diamond Laboratories, Washington, D.C. 20438, 1974.

2. Hannay, N.B., Semiconductors, Reinhold Publishing Corp., New York, 1959, P. 300.

3. Lou, L.F., "Current-Voltage Characteristics of ZnO-Bi_2O_3 Heterojunction," Journal of Applied Physics, Vol. 50, 1979, p. 555.

4. Levinson, L.M. and Philipp, H.R., "Metal Oxide Varistor - A Multijunction Thin Film Device," Appl. Phys. Lett., 24 No 2, Jan 15, 1974.

5. Fisher, F.A., "Overshoot - A Lead Effect in Varistor Characteristics," Report 78 CRD, General Electric, Schenectady, N.Y., 1978.

6. Wolff, B.I., "Analyzing Surge Protective Devices within a Common Framework," Federal Aviation Administration-Florida Institute of Technology Workshop on Grounding and Lightning Technology, FAA-RD-79-6, March 6-8, 1979, Melbourne, Florida, U.S. Dept. of Transportation, Washington, DC 20590.

7. May, J.E., "Carrier Concentration and Depletion Layer Model of Zinc Oxide Varistors," Bulletin of the American Ceramic Society, Vol. 57, No. 3, 1978, p. 335.

8. Transient Voltage Suppression, Fourth Edition, General Electric Company, Auburn, NY, 1984.

9. May, J.E. and Korn, S.R., "Metal Oxide Varistors for Transient Protection of 3 to 5 Volt Integrated Circuits," Electrical Overstress/Electrostatic Discharge Symposium, Sept. 26, 1983, Reliability Analysis Ctr, RADC/RBRAC, Griffiss AFB, NY 13441.

10. Cordaro, J.F. and May, J.E., "Low Temperature Admittance Spectroscopy of ZnO Varistors," Bulletin of the American Ceramic Society, Vol. 64, No. 3, March 1985.

A 12 YEAR STUDY OF LIGHTNING STRIKE PREVENTION SYSTEMS

R.B. Carpenter Jr. and M.D. Drabkin*

Lightning Eliminators & Consultants, Post Office Box 3628, Santa Fe Springs, California 90670, U.S.A.
**LEA Dynatech Inc., Santa Fe Springs, California 90670, U.S.A.*

Abstract - The Dissipation Array System (DAS) was designed by Roy B. Carpenter, Jr. to prevent lightning strikes to the objects protected by DAS. During the last 12 years, hundreds of DAS have been installed within the USA and many other parts of the world. The statistical study of their performance gave the following results: 90% of the installed systems did not have a single lightning strike; 9% showed about 90% reduction in the number of the strikes; less than 1% reported little or no changes. The study continued to analyze the successes and failures, comparing site and array characteristics with the histories of performance, i.e. before and after data. The results of the study were conclusive: (1) They vindicate the premise that lightning strikes to a given facility can be prevented, regardless of the apparent difficulty; (2) They demonstrate the need for careful attention to the site and facility character, as well as the array configuration itself; (3) They reveal some design weaknesses that require further clarification to permit achievement of almost 200 percent successful system design.

BACKGROUND

In June 1971, the author introduced a new form of lightning protection called the Dissipation Array system (DAS). On December 25, 1979, U.S. Patent No. 4180698 was awarded covering this system design in its final concept. Since that time, over 550 DA Systems have been installed in many parts of the world. Additionally, some copies of the concept have been created by others with varying degrees of success. The author has recently surveyed all of the installations still in use to date, to determine their status and effectivity. This paper represents our understanding of the DAS operational concept; and a summary of the data derived from the survey of past customers. The results vindicate the premise that in contrast to lightning rods, lightning can be prevented from striking the areas of concern, and the protector itself. In summary, the DAS dissipates a little energy throughout the storm as opposed to the rod system that is subject to a deluge of current in a matter of a few microseconds. Note that the average lightning strike is only 300 milliamperes for one minute; or, 180,000 amperes for 100 microseconds.

Summary of Operational Concept

Dissipation Array System (DAS) consisting of thousands of sharpened points enhanced by the electrostatic field always presented in any weather condition. Figure 1 presents a conceptual example. When fair weather conditions, DAS, as well as the ground, is charged negatively with respect to the ionesphere and produces very small (tens nanoamperes) negative charges flow into surrounding DAS air, particularly from tall structures. Under the influence of the thunder cloud's dipole, which in most cases, has a negative charge near the base of the cloud and a postive charge in the upper part of the cloud, DAS becomes positive charged system as does the surrounding earth. The charge is accumulated in DAS by means of the ground collector system. This buildup of the positive charge on DAS creates local corona when ionization of air by collision starts around everyone of the thousands of sharpened points of DAS; commonly referred to as point discharge. As a result, the positive charges, stream from the DAS into the surrounding air creating a space positive charge. This space charge that is carried away from the DAS by thundercloud field and wind, changes the resulting electrostatic field so that the potential gradient at ground level (DAS has the



Figure 1, Dissipation Array System Concept

same potential as ground) decreases substantially, thus preventing any further development of ionization by collision which would develop into the stepped streamer, etc. Thus, the likelihood of the direct lightning stroke to DAS and the protected facility is in fact eliminated because the conditions conducive to the stroke are eliminated.

A detailed analysis of the operational concept and its theoretical derivation are presented within the appendix to this paper. Factors wuch as ionizaer shape, size, height, point separation and environment must all be considered in concert to assure a successful system.

Performance Assessment Criteria

Assessing the performance of any form of lightning strike protectors is not an exacting science for the DAS. There are only two parameters that can be evaluated. These are: The dissipation current and the site statistical history. We have collected data from both of these sources.

Figures 2 and 3 are copies of segments of dissipating current recordings made for two separate sites. Figure 2 is a slow speed recording, about 1.0 cm per minute. Figure 3 is a high speed recording of about 1.0 cm per second on a fast reacting chart recorder. In both cases, the displacement from the baseline is proportional to the dissipation current. Full scale is 2 milliamperes. These data present a histogram of the storm motivated dissipation current; they prove the Dissipator dissipates energy, but not much more. One fact is obvious, the integral of the total dissipation current throughout the life of a storm, equals more than the charge contained in an average stroke.

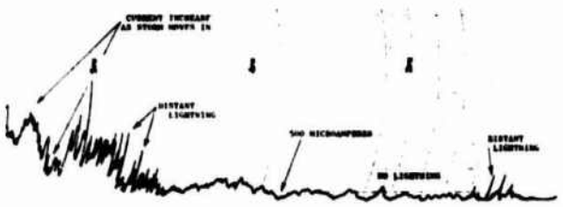


Figure 2, Slow speed recording



Figure 3, High speed recording

Figure 4 presents a TV photograph of the corona plasma, taken from a 366 meter tower under an intense storm.

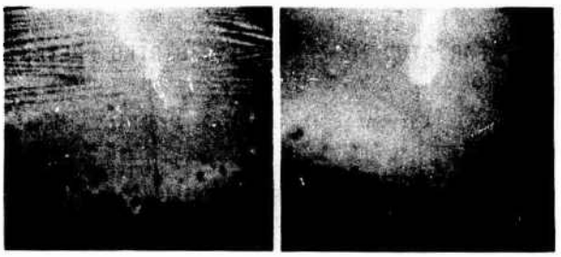


Figure 4, Corona Plasma from a large array system.

Typical Installation History

Of the over 550 installations of DA Systems installed to date, some typical examples were selected to demonstrate the DAS effectiveness. History is important as it contributes to the statistical evidence; but also contributes contrasting information with respect to the before and after status. The following are of particular interest:

1. AM Radio Station CKLW Windsor, Ontario, Canada, (Figure 5). The antenna system is composed of five well grounded towers 92 meters high. For over 20 years the station log recorded an average of 25 outages per year due to direct lightning strikes. In 1972, a disk type DAS was installed. There have been no strikes recorded in over 11 years.

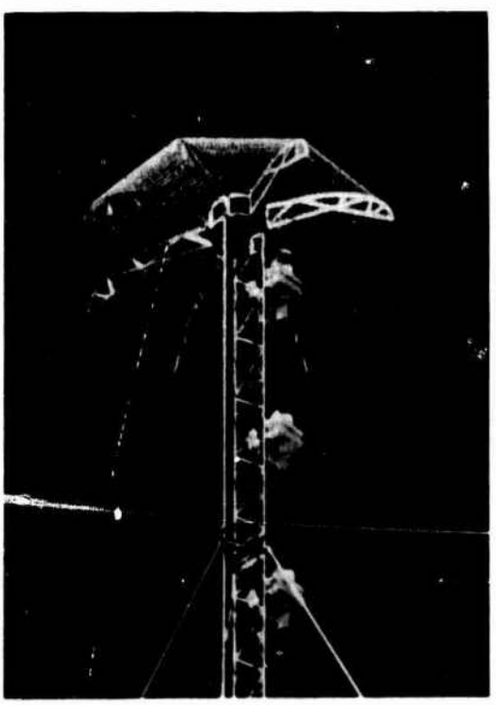


Figure 5, CKLW Array Installation

2. WBBH-TV, Ft. Myers, Florida (Figure 6) in a keraunic level of 100, the antenna is mounted on a tower over 300 meters in height. The records indicated over 48 outages per year due to direct strikes to the antenna. In 1975 a Trapazoidal shaped DAS was installed. No strikes have been recorded in 9 years.



Figure 6, WBBH-TV Array, Ft. Myers, FL



Figure 7, Peachbottom Nuclear Station

3. Philadelphia Electric has a Nuclear Generating plant at Peachbottom, Pennsylvania. The plant occupies over 100 hectors along the banks of the Susquehanna River. The "off gas" stack rises to 720 feet above the plant (Figure 7). Plant history records between 2 and 5 lightning related incidents per year. In 1976, the Hemispheric shaped dissipator illustrated was installed. In the 8 years, no further outages were recorded.

4. In Memphis, Tennessee, a company known as Federal Express (FEC) occupies over a square kilometer of the airport facility. Each night between 11 P.M. and 3 A.M., up to 100 aircraft come into the hub to discharge and pick up packages. Time is critical and lightning was a problem to the whole operation. No records of the number of strikes were available. The Keraunic number is 65. The results of the DAS installation (Figure 8) were dramatic. No further lightning activity was noted in or near the area - at first the corona disturbed the personnel. Subsequently, the FAA control tower people noted that there was no lightning at the FEC end of the field and much less even at the far end of the field. An unsolicited report was filed with Hq. in Washington, D.C. They now intend to buy systems.



Figure 8, Part of Federal Express Array system, Memphis, TN

5. PPG Chemical occupies several hundred hectors of land on the southern coast of Louisiana, Keraunic No. 70. Lightning was creating a problem in the chlorine generating cells. A DAS was installed over two cells; several years later, over two more. Later much more of the plant was protected, not so much because of direct lightning; but, because they observed that the Hydrogen flare stacks under the arrays were not set on fire by nearby strikes, but the ones outside the DAS were. The DAS had reduced the electrostatic field to below the secondary arcing level, as well as preventing the direct strike.

Statistics

There are many other outstanding success stories. All may be verified by personal calls. There have been very few "failures". Failures are herein defined as not preventing the strike to the protected area. The most convincing data is the cumulative records of

successes. There are now over 550 DAS installations scattered in many parts of the world, plus some are unauthorized copies. In late 1984, a survey of all known DAS installations was made, as to their state and performance. The results were as follows:

1. Over 90% reported complete success, i.e. no strikes.
2. 9% reported at least a 90% reduction; in the recorded strikes.
3. Less than 1% reported little to no perceptible change.

An assessment of those sites having problems indicated the following problems:

1. Constraints established by the customer prevented a proper or optimum system design or installation.
2. Poor design (older systems only).
3. Losses caused by power main surges, not strikes to the tower.
4. Poor installation technique.

In summary, from the past 12 years, there is an abundance of evidence available to the intellectually honest inquirer that substantiates the premise that lightning can be eliminated from area of concern. As in all R & D programs, failures do happen. However, the preponderance of date is overwhelming in favor of the Dissipation Array system for lightning prevention. The study results were conclusive:

1. Lightning strikes can be prevented.

2. It did demonstrate the need for careful attention to the site and facility character, as well as the array configuration itself.

3. It did reveal some design weaknesses that require further clarification to permit achievement of a 100 percent successful system design every time.

Appendix

The Operational Concept of the DAS

The Dissipation Array System is composed of three basic elements: the array of sharpened thin conductors (the dissipator), the ground current collector and the service wires connecting the dissipator to the ground current collector.

It is a well proven fact that an electrostatic field near a pointed conductor tends to concentrate at the point, enhancing the electric field. An electric field exists over the entire fine weather areas of the earth. At an altitude above 50 km, the air has such a high conductivity that it may be considered to be the equivalent to a good conductor and any electrical charge reaching a point at this altitude will soon become uniformly distributed around the whole earth. So the atmosphere above 50 km and the surface of the earth, which is also a good conductor, in effect, constitute the plates of a concentric spherical capacitor, having at fair weather conditions the negatively charged earth and the positively charged ionosphere. Because of its ionization, the air is not a perfect dielectric, so that the plates of the capacitor are not completely insulated from each other and electric currents will flow between them when they are charged to different potentials. The average value of the fair weather positive field at ground level is about 130 v/m.

The lines of the electric field cloud-earth will be deflected from their generally vertical direction near any elevated pointed conductor. And, if the electric field enhanced by the concentration of its lines of force ending on the conductor's point is sufficiently strong, there is a possibility of ionization by collision confined to the very small volume near the point. An electric current starts to flow from the tip of the conductor to the air. Electricity flow from the point is normally a quiet, invisible process, but if the electric field becomes sufficiently great, ions collisions yield enough energy to excite particles of the air and make them luminous and sound. This visible ionization is termed corona (also known as St. Elmo's fire) and can be seen in darkness as a bluish glow. The likelihood of producing corona on the tip of a conductor depends upon three major factors: the height of the conductor, the radius of curvature or the sharpness of the point and the electric field. When the conductor is connected to the ground, it has the same potential as the earth; but the air is at different potentials at different heights. So the tip of the conductor and the air around have the potential difference. This difference is increased as the conductor is made taller and the lower initial electric field is required to initiate corona.

At disturbed weather conditions, when thunder clouds are formed, the base of a thundercloud has in most cases the negative charges concentration and the upper part of the thundercloud is charged positively. The negatively charged base of the thundercloud attracts positive charges from the under cloud earth surface, thus negatively charged at fair weather elevated pointed conductor or array of such conductors will change the sign of charge and become positively charged as the results of the presence of the thundercloud. The point-discharge current from the array of the pointed conductor will carry away positively charged ions. Moved away from the array, these ions will form a space charge which reduces the electric field near the points, since lines of force will end on these ions instead of on the points. This process will progress until electric field will be so much reduced that it prevents further ionization and corona ceases. Then, as the space charge is carried away by wind, the electric field near the points again is increasing and the new corona discharge starts. Thus the point-discharge currents have the pulsed nature which has been proved by measurements of point-discharge currents both in natural and laboratory conditions. It was found that

wind velocity has a great influence on the current flow, increasing the interval between pulses and the charge per pulse.

Figure A-1 shows a simplified model of thundercloud and the positive space charge situated as some horizontal distance from the thundercloud dipole. The electrostatic field at ground level, at the given moment, can be calculated from the following equation:

$$Eg = 2Q \frac{H_1}{(H_1^2 + D^2)^{3/2}} - \frac{H_2}{(H_2^2 + D^2)^{3/2}} + \frac{2P}{H_3^2}$$

Where: H_1 and H_2 - heights of the centers of the positive and negative charges Q in the thundercloud.

H_3 - heights of the positive space charge P situated horizontally D from the thundercloud dipole.

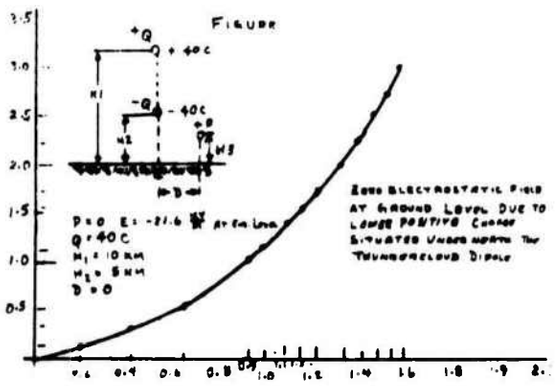


Figure A-1

Although it is known, in fact, that the charge distribution is not strictly uniformly but the actual distribution is so variable that it is difficult to justify more precise calculations.

Figure A-2 presents the calculated size of the positive space charge required to zero, the electric field at ground level when D=0. Based on such calculation, the only 0.1c at height about 300 m above the earth will be sufficient to neutralize the negative field of thundercloud at ground level. Assuming the total point-discharge current about 100 μA, it will take about 17 min to constitute such charge. Curve shown on Figure A-2 represents the calculated electric field at ground level as function of the heights of the positive space charge of 0.1c situated at 2 km from thundercloud dipole. As may be seen from this figure, the electric field decreases with increase of the height of the space charge, becomes zero at about 330 m and changes sign from positive to negative with progressing increase of the space charge's height.

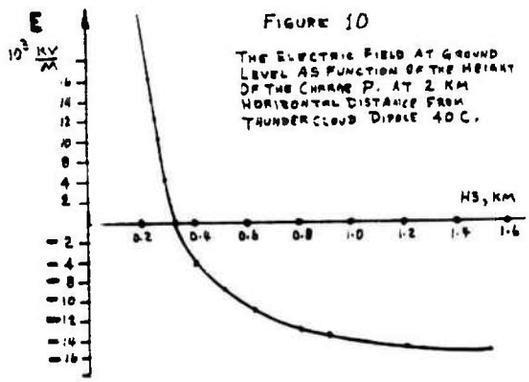


FIGURE 10
THE ELECTRIC FIELD AT GROUND LEVEL AS FUNCTION OF THE HEIGHT OF THE CHARGE P, AT 2 KM HORIZONTAL DISTANCE FROM THUNDERCLOUD DIPOLE 40 C.

Figure A-2

The lightning discharge initiated by upward leaders goes through the states of point discharge to streamer, due to glow to arc transition when the current exceed some critical value.

To reduce the likelihood of the transition from a glow to arc discharge, which would initiate an upward directed leader, a multitude of the points have to be arranged and placed on the large electrode which shape is designed as a uniform electric field electrode used in high voltage apparatus to suppress corona. It is conceivable that no single point of such array will discharge current enough for the transition to the arc regime. As a result, the initiation of an upward leaders would not take place under the conditions found during normal storm situations. In such circumstances the lightning strikes to the DAS and object protected by the DAS would be in practice, eliminated.

A NUMERICAL CALCULATION OF SPACE CHARGE LAYER CREATED BY CORONA DUE TO A GROUND ARTIFICIAL POINT BENEATH THUNDERSTORM

Yan Muhong

Lanzhou Institute of Plateau Atmospheric Physics, Academia Sinica, China

ABSTRACT - Using a two-dimensional, time-dependent, axisymmetrical model, we have calculated numerically the time and space distribution of the electric field and space charge density within 300m height above ground under the thunderstorm. A 60m high artificial point was introduced to calculate the corona current and field close to a point from the time-dependent formula. The model contains various transfers between ions and the ion transfer of conduction and turbulence but neglects advective transfer. The calculation shows that when the initial field is 9kv/m and neutral particle concentration is $10^4/cm^3$, the corona current will reduce to 1/70 in 10 secords, and will reach its final value-1/130 of its initial value in about 34 seconds. At that time, the space charge density close to a point is $2.1nc/m^3$, while the density of $0.2nc/m^3$ will reach 200m high, its horizontal extent will be more than 80m. The density radio of large and small ions will increase to 1/10. The space charge density near or under the point is quite high and is about 1nc/m , this will weaken the electric field, make it much lower than its initial value to about 80m away or even make it reverse when very close to the surface. The electric field will be higher than its initial value above the point. The higher the concentration of neutral particles, the thinner the space charge layer and consequently, the higher the space charge density will be. For example, when the neutral particle concentration is $10^5/cm^3$ the concentration radio of large and small ions will reach 10.

1. INTRODUCTION

The electric charges released by point discharges at ground level, under the influence of high thunderstorm electric fields, play an important part on the electric current that flows between cloud and ground. This process forms a positive charge accumulation zone above ground level. It has the screening effect forming space charge. Standler and Winn (1-2) showed the fact of evident reduction of electric field at ground level due to this effect. Electric field intension at ground level is four or five times lower than that at a few hundred meters above it.

Chauzy et al (3-4) numerically calculated the distribution of space charge due to point corona at ground level. The model they used was one-dimension. This paper discusses space and time distribution of electric field and charge under the effect of corona created by a isolated artificial point at ground.

2. THE MODEL

2.1 The basic characteristics and the parameters

A two-dimensional, time-dependent, axisymmetric model has been applied to compute space charge and electric field profiles under the effect of isolated artificial point discharges beneath a thunderstorm. The model has following characteristics:

2.1.1 The model mainly discusses discharge process of a isolated artificial point, and the effect of nature points is neglected. A metallic needle connected to ground is putted at 60 meters height along central axis. The needle length is 4.5 meters. it produces corona discharges due to negative electric field beneath a thunderstorm. Average effect area A' of corona can be approximately represented by a semispherical area about $31.6m^2$ with diameter equal to needle length.

2.1.2 Let n_+ and n_- be the positive and negative small ions concentration, N_+ and N_- the corresponding of large ions respectively. The mobilities of small and large ions of each sign, μ_+, μ_-, μ'_+ and μ'_-, are the function of height and have following values separately:

$$\mu_+ = 4.2*10^{-4} e^{0.14z} \quad cm^2/s/esuV$$

$$\mu_- = 5.7*10^{-4} e^{0.14z} \quad cm^2/s/esuV$$

$$\mu'_+ = 4.2\ e^{0.14z} \quad cm^2/s/esuV$$

$$\mu'_- = 5.7\ e^{0.14z} \quad cm^2/s/esuV$$

where z is height in km and 1esuV is equal to 300v.

2.1.3 The model has only considered ions transportation by electrical conduction and eddy diffusion, and it assumes that the eddy diffusion coeficient Kv is constant, uniform and equal to 50 m^2/s for all particles.

2.1.4 The transportation of advection is neglected in the model.

2.1.5 The model takes into account the small ions capture by neutral aerosol particles, its attachment by opposite sign large ion and recombination between the opposite sign small ions. The different attachment coefficients are difined as follows:
α is the small ions recombination coefficient, equal to $1.6*10^{-6} cm^3/s$, β_{+-} and β_{-+} are the small ions attachment coefficients by the opposite sign large ions and equal to $10^{-5} cm^3/s$, β_{+0} and β_{-0} are the small ions attachment coefficients by the neutral aerosol particles, and equal to $2.0*10^{-6} cm^3/s$.

2.1.6 Recombination of large ions and attachment by the neutral aerosol particles are neglected compared to the other coefficients.

2.1.7 The initial neutral aerosol particle concentra-

tion N_0 is uniform and aqual to $10^4/cm^3$ for clean air or $10^5/cm^3$ for polluting air.

2.2 Tha axpression of corona current dansity

Obsarvation shows that alectric fiald intension is commonly lass than 10kv/m (5) on tha land, while it can be mora than 50kv/m (6) on the ocaan. Tha formar is in consequanca of corona discharge of points at ground laval. The expression of corona current density inducad by the alactric fiald E_b closa to a point whan it exceeds tha onsat valua Ec has baan chosan:

$$Ic = a(Eb^2 - Ec^2) \qquad (1)$$

with Ec=0.78kv/m. Where a is constant of corona, depanding on property of the point, and approximataly equates to $\varepsilon\mu_+ h/A'$, whare ε is dielactric constant of air, h is the height of the point and aqual to 60m. Tharafora $a=1.2*10^{-15}$ A/v^2.

The formula (1) is commonly obtained in staady stata. As a mattar of fact, whan ions producad by corona transport outwards, tha alactric fiald close to a point also changas. Tharafore, Ic varias with time. Tha spaca charge dansity closa to tha point, ρ_T, obays following equation of continuity:

$$\frac{\partial \rho_T}{\partial t} = -\nabla\cdot\vec{I}_c - \nabla\cdot\vec{I}_\lambda$$

and Poisson"s aquation $\nabla\cdot\vec{E}_b = 4\pi\rho_T$

It can ba obtainad from abova two equations:

$$\frac{\partial \vec{E}_b}{\partial t} = -4\pi(\vec{I}_c + \vec{I}_\lambda)$$

whara $\vec{I}_\lambda$ is tha conduction current dansity due to the downward motion of the nagative ions in alectric fiald and obeys tha Ohm's law, $\vec{I}_\lambda = -\lambda\vec{E}_b$, whare λ is avarage conductivity of air banaath a thunderstorm and equal to $6*10^{-13}$ /m/Ω. E_b and Ic have sama direction in the region close to tha point. Tharefora, tha scalar aquation can be obtainad:

$$\frac{\partial E_b}{\partial t} + 4\pi Ic = 4\pi\lambda E_b \qquad (2)$$

According to relations (1) and (2), let $E_b=E_{b0}$ for t=0, E_b and Ic are calculated as follows:

$$E_b = \frac{P(B+\lambda) - Q(B-\lambda)\,e^{-4\pi Bt}}{2a(P + Qe^{-4\pi Bt})} \qquad (3)$$

$$Ic = \lambda E_b - \frac{PQB^2 e^{-4\pi Bt}}{a(P+Qe^{-4\pi Bt})^2} \qquad (4)$$

whara $B=\sqrt{\lambda^2 + 4a^2 Ec}$, $P=B+2aE_{b0}-\lambda$, $Q=B-2aE_{b0}+\lambda$. E_{b0} is the ambient alactric field intension at t=0, and assumad to ba uniform and aqual to 9kv/m in the calculation of tha modal.

2.3 The aquations of the calculation

All parameters make use of CGSE unity system in tha calculation. From the equation of continuity wa can daduce the temporal and spatial evolution of the four types of ions concentrations as well as the neutral aerosol particles concentration. The temporal and spatial evolutions of the electric field can be daducad from Poisson's equation. The following six equations in axisymmetric coordinate system with two dimansions can be writtan:

$$\frac{\partial n_+}{\partial t} = -\frac{1}{r}\frac{\partial}{\partial r}(r n_+ \mu_+ E_r) - \frac{\partial}{\partial z}(n_+\mu_+ E_z) + G - \alpha n_+ n_- - \beta_{+,0} n_+ N_0 - \beta_{+,-} n_+ N_- + D_{n_+}$$

$$\frac{\partial n_-}{\partial t} = +\frac{1}{r}\frac{\partial}{\partial r}(r n_- \mu_- E_r) + \frac{\partial}{\partial z}(n_-\mu_- E_z) + G - \alpha n_+ n_- - \beta_{-,0} n_- N_0 - \beta_{-,+} n_- N_+ + D_{n_-}$$

$$\frac{\partial N_+}{\partial t} = -\frac{1}{r}\frac{\partial}{\partial r}(r N_+ \mu'_+ E_r) - \frac{\partial}{\partial z}(N_+\mu'_+ E_z) + \beta_{+,0} n_+ N_0 - \beta_{-,+} n_- N_+ + D_{N_+}$$

$$\frac{\partial N_-}{\partial t} = +\frac{1}{r}\frac{\partial}{\partial r}(r N_- \mu'_- E_r) + \frac{\partial}{\partial z}(N_-\mu'_- E_z) + \beta_{-,0} n_- N_0 - \beta_{+,-} n_+ N_- + D_{N_-}$$

$$\frac{\partial N_0}{\partial t} = \beta_{-,+} n_- N_+ + \beta_{+,-} n_+ N_- - \beta_{-,0} n_- N_0 - \beta_{+,0} n_+ N_0 + D_{N_0}$$

$$\frac{1}{r}\frac{\partial}{\partial r}\left(r\frac{\partial\varphi}{\partial r}\right) + \frac{\partial^2\varphi}{\partial z^2} = -4\pi e(n_+ + N_+ - n_- - N_-) = -4\pi\rho_T$$

$$Er = -\frac{\partial\varphi}{\partial r} \qquad Ez = -\frac{\partial\varphi}{\partial z}$$

whare E_z is tha vartical alactric field intansion, and tha sign convention adoptad in the modal is that tha upward diraction is positive. E_r is the radial alactric field intension, φ tha potantial, a the alemantary charga, G tha rata of formation by cosmic rays and aqual to 15.4/cm^3/s, ρ_T tha space charga density. $D_{n\pm}$, $D_{N\pm}$ and D_{N_0}, tha eddy transportation tarm of each kind of particles can ba writtan:

$$D_X = \frac{1}{r}\frac{\partial}{\partial r}\left(K_v r\frac{\partial X}{\partial r}\right) + \frac{\partial}{\partial z}\left(K_v\frac{\partial X}{\partial z}\right)$$

Adding aquations (3) and (4) to abova-mention equation leads to a eight equation system. This system was numarically solvad using finita-diffaranca and iterativa mathod.

3. THE RESULTS

Fig.1 displays the avolution of corona current density closa to a point for E_{b0}=9kv/m and $N_0=10^4/cm^3$.

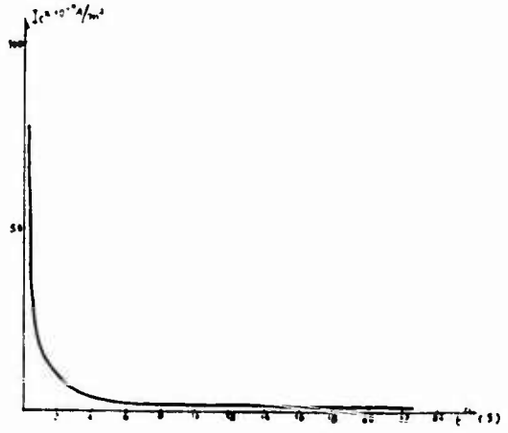


Fig.1: Corona current density variation closa to a point (Ic), for $N_0=10^4/cm^3$ and E_{b0}=9kv/m.

It claarly shows that corona current density Ic decays rapidly with tima, tha initial valua is $77.4*10^{-9}$ A/m^2, it is 10^{-8} A/m^2 aftar two seconds. Ic varies slowly with tima aftarwards, its valua is $0.64*10^{-9}$A/m^2 aftar 34 seconds and tends to ba staady. The distribution of spaca charga dansity during 34 seconds is shown on fig.2.

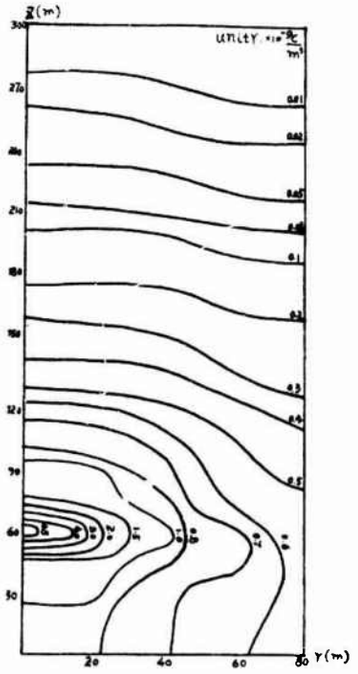


Fig.2: Distribution of space charge density (ρ_T) at 34 seconds for $N_0=10^8/cm^3$.

The charge density in the region arround the point is maximal and equal to $4.5*10^{-9}$ C/m³. The local space charge screening layer is formed with the transportation of charge. The charge density gradully decreases with the increase of height. The charge layer, in which the charge density is more than or equal to $0.2*10^{-9}$ C/m³, can vertically extends to the height of 190 meters, while its radial extent will be more than 80 meters. Below the height of the point(60 meters), the charge density is larger and equal to 10^{-9} C/m . Afterward, the space charge layer continuously extends outwards with the increase of time. At this time the transportation of space charge mainly depends on eddy diffusion due to the decrease of electric field, so that the charge layer extends very slowly. For example , after one minite, it only reaches to 210 meters.

Though the advection was neglected in the model, the radial transportation of the space charge is strong still (see fig.2). This is in consequence of the effect of radial electric field. Calculation shows that the radial electric field is 10kv/m close to a point during 34 seconds. The space charge are transported by the radial electric field. Afterward, the radial electric field intension decreases due to the opposite effect of transported space charge. For example, after one minite, the electric field intension is equal to 3kv/m. The transportation of charge mainly depend on eddy diffusion with the increase of time. Therefore the radial extension of the space charge layer is weakened.

Fig.3 diaplays the evolutiona of space charge density ρ_T , the concentration of small positive ions n_+, and of large positive ions N_+ at the height of 60m and 30m above ground level respectively. It clearly shows that ρ_c and n_+ decay rapidly with the increase of time close to a point, and reach to a steady value of $4.5*10^{-9}$ C/m³ and $27*10^9/m^3$ reapectively at 34 seconds. However the concentration of large positive ions increases with time, and the ratio N_+/n_+ increases from zero to 1/10. Thus it can be seen that small positive ions produced by corona are rapidly captured by neutral aerosol particles and transform into large positive ions with lower mobility. Below the height of the point (see fig.3-b) ρ_c and n_+ rapidly increase with time at the beginning, then gradually decrease tend to a steady value after 10 seconds. The ratio N_+/n_+ obviously increases with time, being 1/2 at 34 seconds and 1 at 90 seconds. More small positive ions are captured by the neutral aerosol particles. The large positive ions are dominant gradually in the space charge layer.

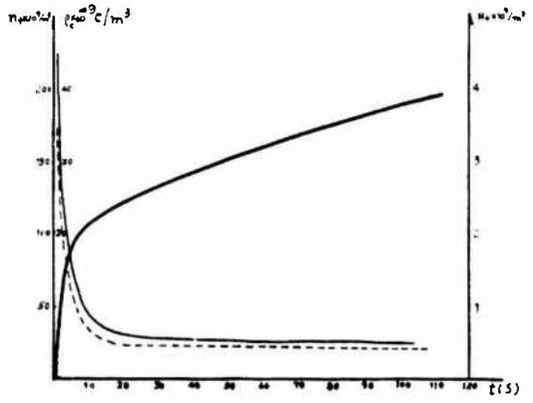


Fig.3-a Evolution of space charge density ρ_c, the concentration of small positive ions n_+, and of large positive ions N_+ close to a point.

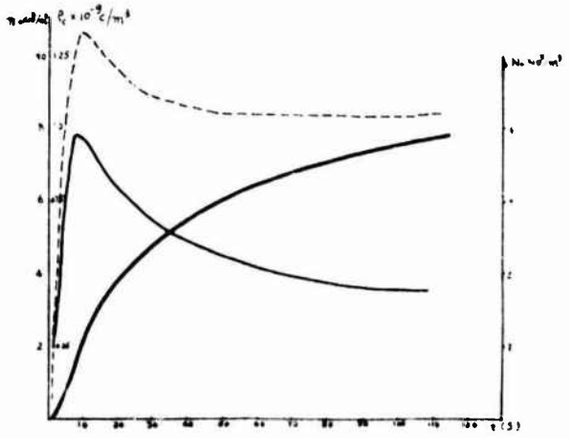


Fig.3-b The same as fig.3-a, but at 30m above ground level and radial distance 20m.

The distribution of vertical electric field is shown on fig.4. It clearly shows that the area in which the value of the electric field is less than that of initial external electric field is limited to the height below 100m. Below the height of the point(60m), the electric field intension is very low and appears to be opposite sign in the local area below 30m. The maximum electric field of opposite sign is -500v/m at the beginning and increases to -1000v/m after one minite. The area extends radially to more than 80 meters.

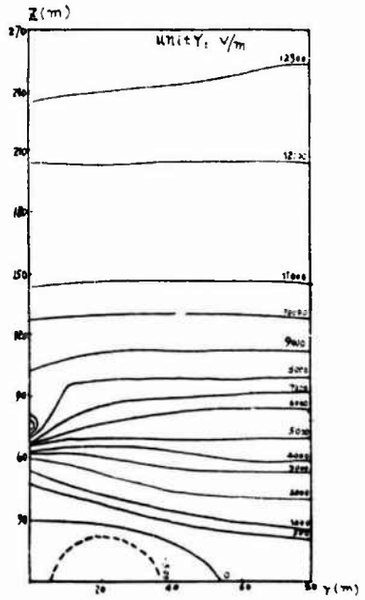


Fig.4: Distribution of vertical eiectric fieid at 34 seconds for $N_0=10^4/cm^3$ and t=34s.

The vertical electric field evolutions at three ieveis are shown on fig.5. The area of decreasing electric field, induced by space charge, is limited to beiow the height of the point. The sign of eiectric field changes from positive to negative at ground after 9 seconds and at the height of 30m after 30 seconds. However the eiectric field is always positive above the height of the point and can exceed ambient electric field intension.

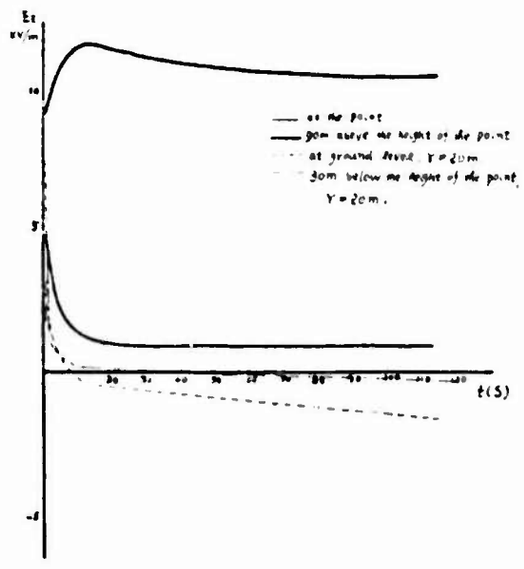


Fig.5: Evolution of the vertical electric field at three levels for $N_0=10^4/cm^3$.

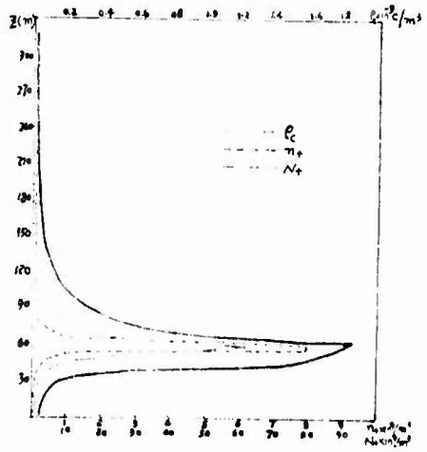


Fig.6: Vertical profiles of charge density ρ_c and small as well as large positive ions concentrations n_+, N_+ at radial distance r=20m for $N_0=10^5/cm^3$ and t=34s.

Fig.6 displays the vertical profiles of charge density ρ_c, small and large positive ions concentration n_+, N_+ for $N_0=10^5/cm^3$ and t=34s. It clearly shows that the charge density increases obviously, but soon decreases rapidly with the increase of height. More small positive ions are captured by the neutral aerosol particles and transform into the large positive ions with lower mobility. The ratio N_+/n_+ is 3 close to a point, and increases rapidly to 10 with the increase of height. So that the thickness of the space charge layer decreases remarkablely. The charge layer in which the charge density is more than or equal to $0.2*10^{-9}$ C/m^3 is limited to below the height of 100 meters.

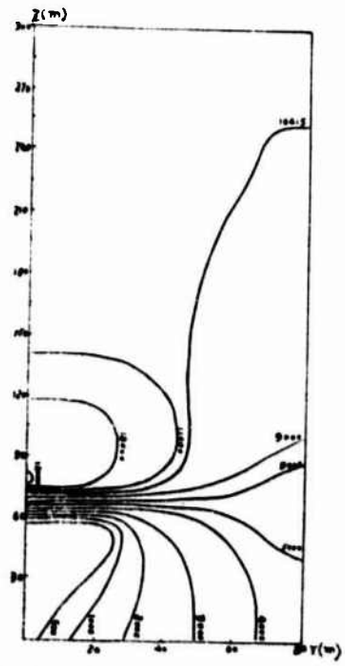


Fig.7: Distribution of vertical electric field for $N_0=10^5/cm^3$ and t=35s.

Fig.7 is corresponding distribution of vertical electric field. As compared with fig.4, we can see that the area of lower electric field is very small, and the negative sign electric field disappears below the height of the point. Therefore, the screening effect, produced by corona discharge of the isolated metallic point, is more effective in clean air than in pollutive air.

The results also show that when the corona current density produced by a artificial point increases, the area of lower electric field will be extended. The electric field becomes negative below the height of the point, and can reach to a maximum value of -3000v/m at steady state.

4. REFERENCES

(1) Standler, R. B. and Winn, W. P., 1979:
Effects of corona on electric field beneath thunderstorms. Quart. J. R. Met. Soc., 105, 285-302.

(2) Standler, R. B., 1980:
Estimation of corona current beneath thunderstorms. J. Geophys. Res., 85, C8, 4541-4544.

(3) Chauzy. S. and Raizonville. P., 1982:
Space charge layers created by corona at ground level below thunderclouds: measurements and modeling. J. Geophys. Res., 87, C4, 3143-3148.

(4) Chauzy, S. and Rennela, C., 1984:
Response of the space charge layer created by corona at ground level to external electric field variations beneath a thundercloud. VII International conference on atmospheric electricity, Albany, N. Y.

(5) Vonnegut, B., 1963:
Some facts and speculations concerning the origin and role of thunderstorm electricity. Meteor. Monogr., 5 224-241.

(6) Toland, R. B. and Vonnegut, B., 1977:
Measurements of maximum electric field intensity over water during thunderstorm. J. Geophys. Res. , 82, 438-440.

(7) Kasemir, H. W., 1978:
Corona discharge and thunderstorm fields. Coference on cloud physics and atmospheric electricity of the AMS 1978, Issaquah, Washington.

INVESTIGATION OF THE LIGHTNING VULNERABILITY OF NUCLEAR EXPLOSIVE TEST SYSTEMS AT THE NEVADA TEST SITE *

R.T. Hasbrouck

Lawrence Livermore National Laboratory, Livermore, California 94550, U.S.A.

Abstract—At the U.S. Depsrtment of Energy's Nevada Test Site, the Lswrence Livermore Nstionsl Laborsrtory (LLNL) conducts operations involving the underground detonation of nuclear explosive test devices. Nuclear explosive safety is a very important consideration during these operations. To assure ssfety, sll components, systems snd procedures are anslyzed by LLNL and are subjected to an inter-agency Nuclesr Explosive Safety Study. These studies consider all sources and psths of energy thst could conceivably initiste an unwsnted detonstion. One of the energy sources considered is lightning. Over the years, several lightning hszard studies have been carried out. They each concluded that the msgnitude of lightning energy reaching the high explosive or the detonators wss smsll compared to thst required to produce s detonstion. In 1983, sn LLNL tssk force was estsblished to reexamine the lightning vulnerability of the nuclesr explosive test systems, taking into account the previous studies and current knowledge. As s resulc of this investigstion seversl improvements are being implemented. Also, simulated lightning tests will be used to provide verificstion of the safety claims. Although underground nuclesr testing is unique, the oversll method and results of this investigation should be of use to those fsced with a lightning threat in a large, csble-inter-connected system.

INTRODUCTION

The purpose of this psper is to present the results of recent studies to evaluate the vulnerability of a nuclear explosive test device system to a direct or nearby lightning strike.

In 1973, F. A. Fisher, General Electric Co., conducted sn extensive analytical study (Ref. 1) of the effects of lightning on nuclear explosive systems located at the bottom of an emplacement hole. Calculations were made to determine the downhole voltage and current waveforms resulting from lightning strikes directly to or nearby the interconnecting cables. The calculations were done in the time domain, using, a general network-analysis computer program, ECAP (Electronic Circuit Analysis Program). A significant facet of this study was the development of a statistical assessment of the probable exposure of the systems to lightning effects.

In 1974, J. P. Luette, Sandia National Laboratoriss, used an electromagnetic analysis program to study the response to a direct lightning strike of several different distributed models of the system (Ref. 2).

both of these studies conclude that the magnitude of lightning energy produced by a direct or nearby strike to the device system cables, and reaching the high explosive, or its dstonators, was small compared to the ensrgy required to produce a detonation. These studies served as the principal refersnces for a 1975 Nuclear Explosive Safety Study (NESS) committee (Ref. 3), which concluded that the proposed nuclear explosive operations (which were the subject of that NESS) "provided adequate nuclear explosive safety" where lightning was a threat.

In 1982, a NESS committee requested (Ref. 4) that LLNL reevaluate, using current information, the effects of lightning energy on the test system. Their contention was that the "predicted response of a test device system to lightning is predicated on snalyticsl studies thst evaluate the transient response of the downhole csbles to the postulated lightning model." It wss also noted that the esrlier studies presented calculations snd a grounding scheme that had not been substantiated sxperimentally.

In response to this request, LLNL established s three-person task force to investigate the lightning vulnersbility of nuclear explosive test dsvice systems at the test site. Because of the complsx nature of the nuclear test environment and the fact that the members of the task force possessed only limited knowledge about lightning, services were secured of two acknowledged lightning experts: S. R. Crawford, Ford Aerospace and Communications Corp. and J. D. Robb, Lightning and Transient Research Institute (LTRI).

Prior to meeting with Crawford and Robb, the task force prepared the following list of objectives that served as their charter:

- Immediately identify any serious deficiencies.
- Determine if the 1973 and 1974 studies were still valid in light of present-day knowledge.
- Identify the most vulnerable phase of the nuclear test operation.
- Recommend improvements to enhance system safety (specifically from a nuclear explosive safety standpoint).
- Recommend a method for verifying the effectiveness of those improvements.

* Work performed under the auspices of the U.S. Department of Energy by the Lawrence Livermore National Laboratory under contract No. W-7405-ENG-48.

Crawford and Robb conducted an investigation and prepared a report containing the details considered, conclusions, and recommendations (Ref. 5).

It should be emphasized that the sole issue of this investigation was nuclear explosive safety. Required personnel safety practices were already implemented. It was agreed that if a decision had to be made between the extremely remote possibility of a lightning-initiated detonation and the possibility of the system becoming inoperative because of lightning, the latter was the only acceptable choice.

Before presenting the results of the investigation, I will, for background information, describe the test site and the nuclear explosive test device system, including some procedures. Following that, I will present the method employed to achieve the fulfillment of the objectives, as well as pertinent system details. I intend to present an organized process for dealing with the problem of evaluating the lightning vulnerability of, and implementing improvements in, a large and complex system.

DESCRIPTION OF TEST ENVIRONMENT

The Natural Environment

Within an area of approximately 3000 km^2 of remote high desert country 180 km north of Las Vegas, Nevada, the United States Department of Energy conducts its underground nuclear test program. Designated as the Nevada Test Site (NTS), this area consists of wide flat valleys, flat top mesas, and mountains. Specific tests are conducted at locations whose elevations vary from 1.2 km, for the valleys, to 2.2 km on the mesas.

Although the NTS experiences most lightning activity from May through September, it is not unusual to observe occasional lightning throughout the balance of the year. During summer the mountainous terrain and hot desert produce strong updrafts of heated air that contribute to the formation of cumulonimbus clouds. Summer's frontal storms generally move up the Colorado River Valley, bringing moisture from the Gulf of California. The large cyclonic storms of winter typically approach from the mountains that lie to the northwest. Referring to the isokeraunic chart for this region, one observes that the NTS should, on the average, experience 20 thunderstorm days per year. During the summers of 1971 and 1972, a study was carried out to characterize lightning activity at the NTS (Ref. 6). The overall results indicated the same order of magnitude of thunderstorm days as presented by the isokeraunic chart. However, lightning flash densities to ground for the mesas were found to be 50 to 100 times greater than for the valleys. Actual observations at McCarran International Ariport, Las Vegas, Nevada, reported 23 thunderstorms days in 1978 and 23 in 1980.

The Test Environment

The University of California, Lawrence Livermore National Laboratory (LLNL) is one of two national laboratories responsible for the Department of Energy's test operations at the NTS. Each test operation (commonly referred to as an "event") takes place on either a valley or mesa, at a site containing an area known as ground zero (GZ) which is approximately centered around the point of test detonation (see Fig. 1).

The nuclear explosive test device is assembled at a special facility located on the NTS and then delivered to the appropriate GZ. At GZ the device is installed—along with related arming and firing, instrumentation, and control systems—into a structure, which is designated the "test assembly"; this operation takes place within a metal installation building whose height can vary from 8 to 30 m. The completed test assembly—which may reach a length of 30 m—is then lifted from the installation building, suspended by a string of drill pipe and lowered to the bottom of an emplacement hole.

Lowering is accomplished by crane, whose height may reach 37 m. (The combined weight of the test assembly and pipe string may be as much as 3.6×10^5 kg.) Emplacement holes range from 1.5 to 3.0 m in diameter and from 180 to 1,100 m in depth. They incorporate a steel casing that extends from the surface to a depth of 37 m and is grouted in place.

Following completion of the lowering operation, the emplacement hole is backfilled with a combination of gravel, grout, and epoxy plugs. This procedure, referred to as "stemming," prevents dispersal of radioactive debris produced by the detonation by containing it underground.

The uphole (ground-level) portions of the arming and firing, instrumentation, and control systems are housed in large metal-bodied trailers located in the recording trailer park (RTP), approximately 300 m from GZ. These trailers are connected to the downhole experiment by a large number (25 to 100) of coaxial and multiconductor cables, which are laid out on the surface of the ground.

Nuclear Explosive Safety

To satisfy the important requirement for nuclear explosive safety, a rigorous review process is carried out for every event. The objective is to ensure that the nuclear explosive cannot be unintentionally detonated. First, LLNL conducts a safety analysis of all components, procedures, and operations that could conceivably lead to the application of energy (electrical, mechanical, thermal, etc.) to the high explosives, detonators, or their associated electrical circuits. Then, prior to receiving authorization to assemble the nuclear explosive, a Department of Energy interagency NESS is conducted. Lightning is one credible energy source that is considered. While the probability of a lightning-initiated detonation is believed to be exceedingly small, the consequences of such an occurrence are considered to be totally unacceptable. It was this ongoing emphasis on nuclear explosive safety that led to the formation of the task force.

Ground Zero

Over the several months required to prepare for an event, the GZ area undergoes many changes. At the time of device delivery, approximately two weeks prior to the scheduled shot day, one or two tall installation buildings and cranes are present (Fig. 2). A multitude of cables, having an end-to-end length of up to 1.4 km, are laid out on the ground. A trailer (referred to as the "Red Shack"), through which all downhole cables must pass, is initially located in the vicinity of the emplacement hole. Figure 3 depicts GZ at the start of a downhole operation, while Fig. 4 shows a test assembly suspended from the crane. The device system is



Figure 1. Aerial view of typical event site.

contained within the white painted steel canister at the bottom of the test assembly.

The area in proximity to the emplacement hole is gradually cleared until, on shot day, only a short length of drill pipe sticks out of the stemmed emplacement hole. The unburied surface run of cables terminates 300 m away at the RTP. The Red Stack has been moved to the RTP. The varying configuration of the event site during the final two weeks was taken into account during the investigaion to identify the most vulnerable phase of the GE operation.

Grounding System

A well designed, carefully implemented, low-resistance grounding system is installed at every GE. Typical steady-state values of 5 ohms or less

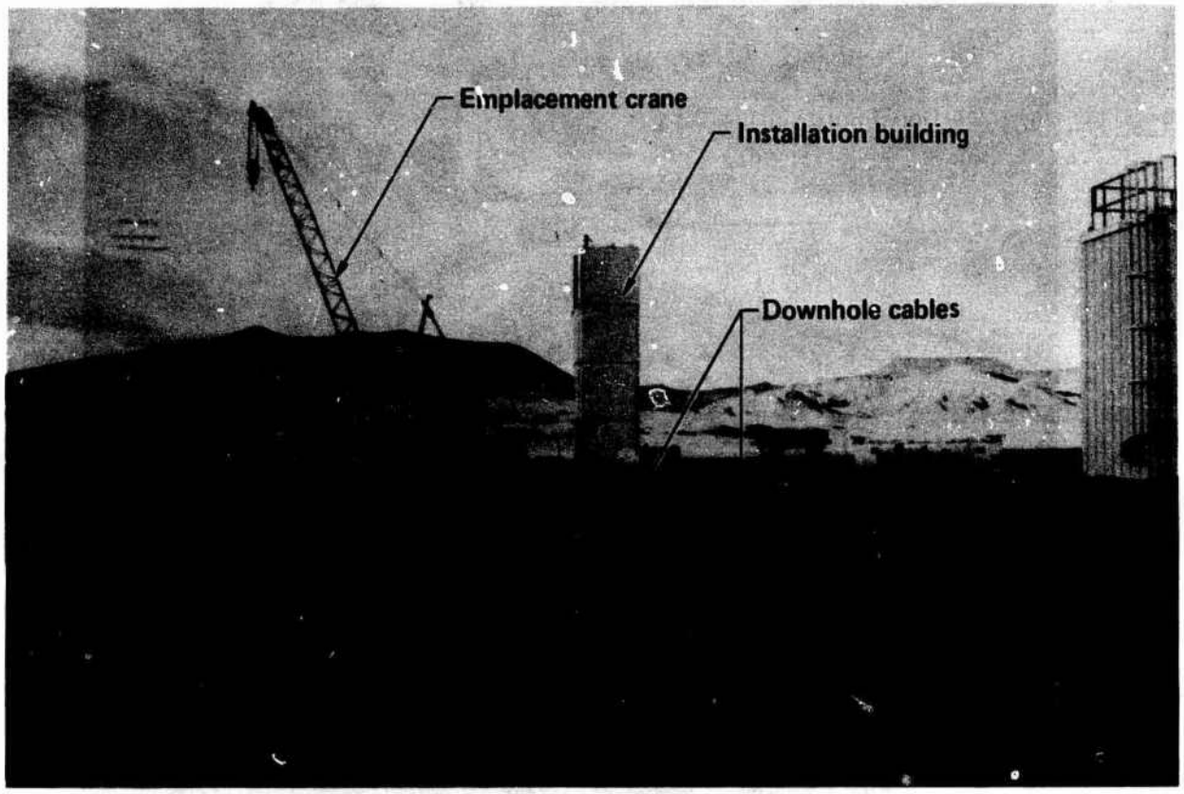


Figure 2. Ground-level view of GZ, showing installation building, emplacement crane, and cable runs.

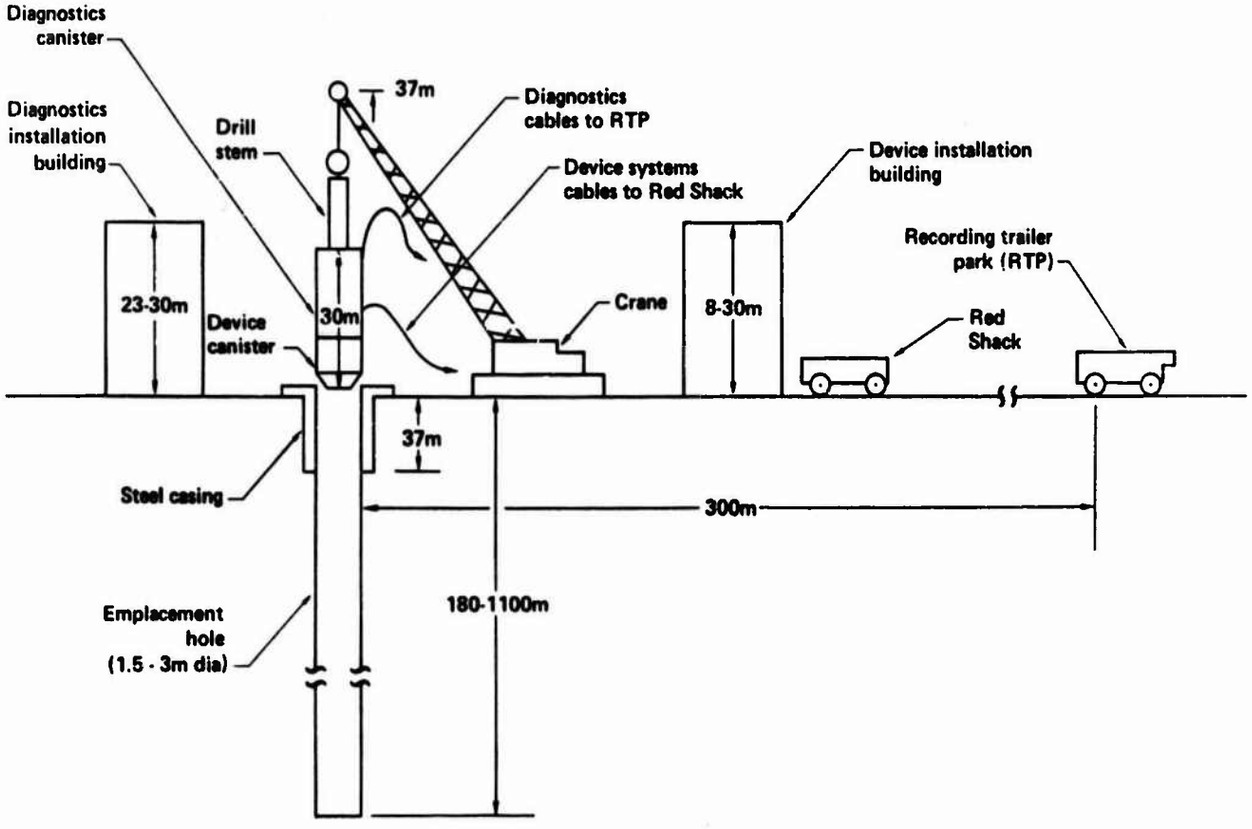


Figure 3. Simplified elevation sketch of GZ facilities at start of down-hole operation.

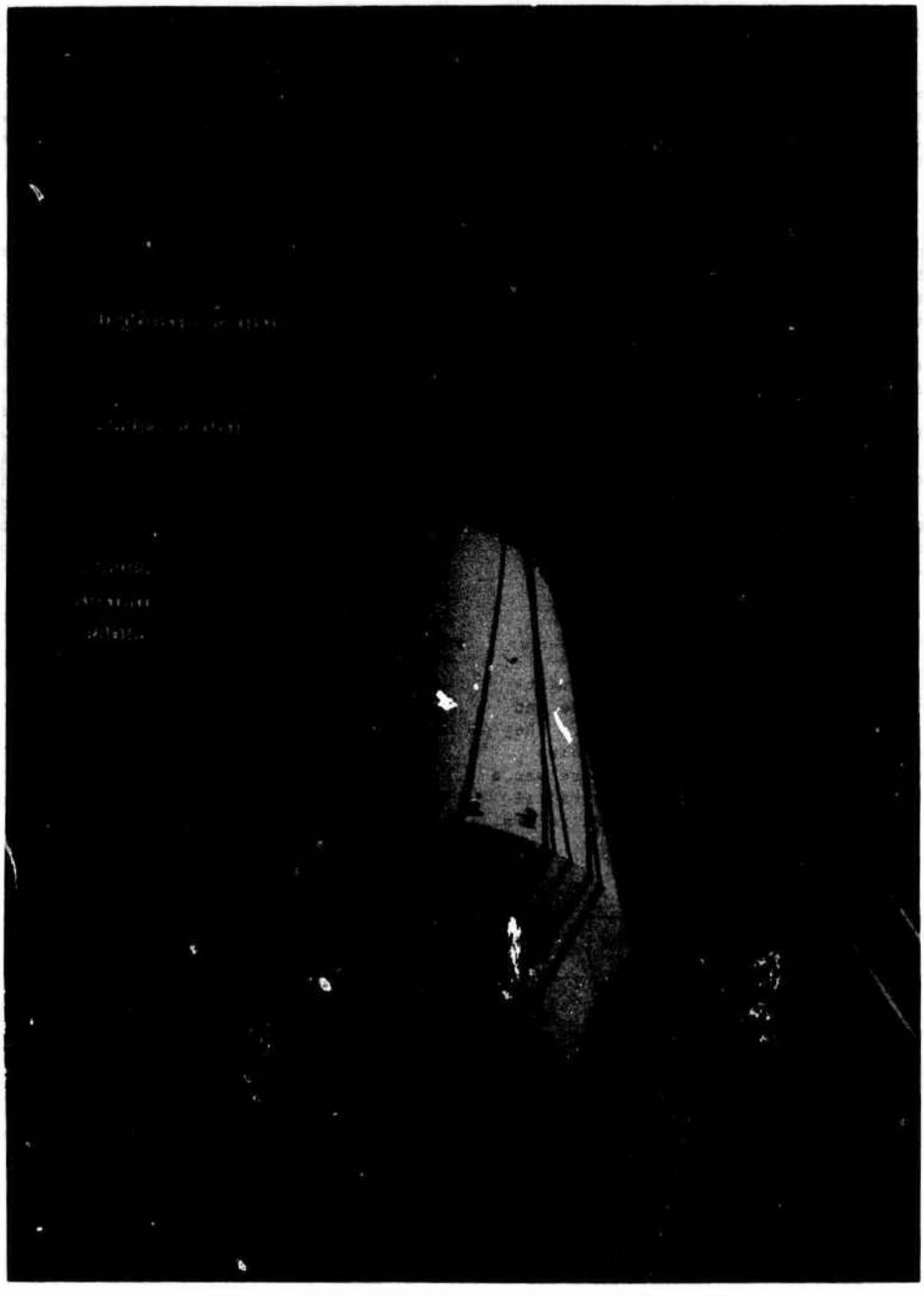


Figure 4. Test assembly ready for amplacamant.

ara maasurad batwaan tha casing and surrounding aarth, using the thraa-point fall-of-potantial mathod. This systam must providа personnal safaty, lightning protaction, and low alactrical noisa. The amplacamant hola casing is usad for "aarthing" tha GE single-point grounding systam. Building and aquipmant intarconnactions to the casing ara via bara AWG No.-2/0 coppar wira. At the RTP, savaral salt pits providа local low rasistanca grounds.

The Davica Canistar

In tha davica installation building, the nuclaar axplosiva tast davica is mountad within an opan cylindrical structura known as the "davica padastal."

Also containad within tha padastal ara tha arming and firing (A&F) and ancillary componants. During axacution of tha avant, tha A&F componants taka ramotaly controllad alactrical powar from tha Rad Shack and produca tha signals raquirad to fira the axploding bridgawira datonators that initiata tha datonation.

The davica systam cablas (typically nina) antar the padastal through its staal lid and ara tarminatad with tarminal strips and connactors. Smallar gauga conductors than carry signals and powar to thair final dastination. An insulatad AWG-No.-2/0 solid-coppar-conductor safaty grounding cabla is boltad to tha padastal in the vicinity of tha othar cablas.

The Intended Firing Path

While an actual A&F system is much more complex, Fig. 5 provides a simplified but accurate representation. All cables that enter the device canister must originate, or pass through, the Red Shack. Positive control is maintained through security and administrative procedures. The A&F cables are disconnected and their connectors locked-up until the last few hours prior to shot time. While disconnected, the ends are not terminated, so that in the event of a lightning strike, the resulting voltage peak will occur in the Red Shack rather than in the device canister.

A&F signals that are generated at the remote Control Point (and transmitted to the event site by the Command Microwave system) actuate relays in the Red Shack at specific times during the automatic countdown sequence. These relays control a dc voltage that is used to charge, and subsequently trigger, the capacitive discharge unit, which then fires the bridgewire detonators. A major portion of each nuclear explosive safety study is devoted to ensuring that the A&F system can only be powered intentionally.

PRELIMINARY FINDINGS

Approximately six weeks after an orientation meeting, Crawford and Robb met with the task force and others to discuss their preliminary findings. They reported that they found no serious deficiencies that would require immediate attention. There was a considerable amount of discussion regarding radial counterpoise grounding systems and what LTRI refers to as the "fortress concept." Overhead diverters were also discussed, with the conclusion that they would not be cost effective since GZ sites are not permanent, and the nuclear explosive residence time is only approximately two weeks. This two-day meeting allowed Crawford and Robb to finalize their information gathering prior to preparing their final report.

The key points, as well as the LLNL plan to implement their recommendations are presented in the next section.

As a separate but related item, Crawford and Robb were asked to evaluate a proposal to eliminate the air terminal down-conductors from the multi-deck installation buildings. The rationale was that current from a strike to the building would preferentially flow through the metal exterior walls of the building and into the building's grounding system. The experts agreed that this would be an acceptable practice. While bonding between the vertical modules of the building was considered to be inherent because of their great weight, the proposal called for copper jumpers at each corner to enhance the inter-module bonding. Proper bonding of metallic objects adjacent to the interior side of the walls is a standard practice.

RESULTS OF THE INVESTIGATION

Validity of the Earlier Reports

While new data exist regarding lightning channel mechanisms and structure and faster current rates of rise, the basic conclusions of the Fisher and Luette

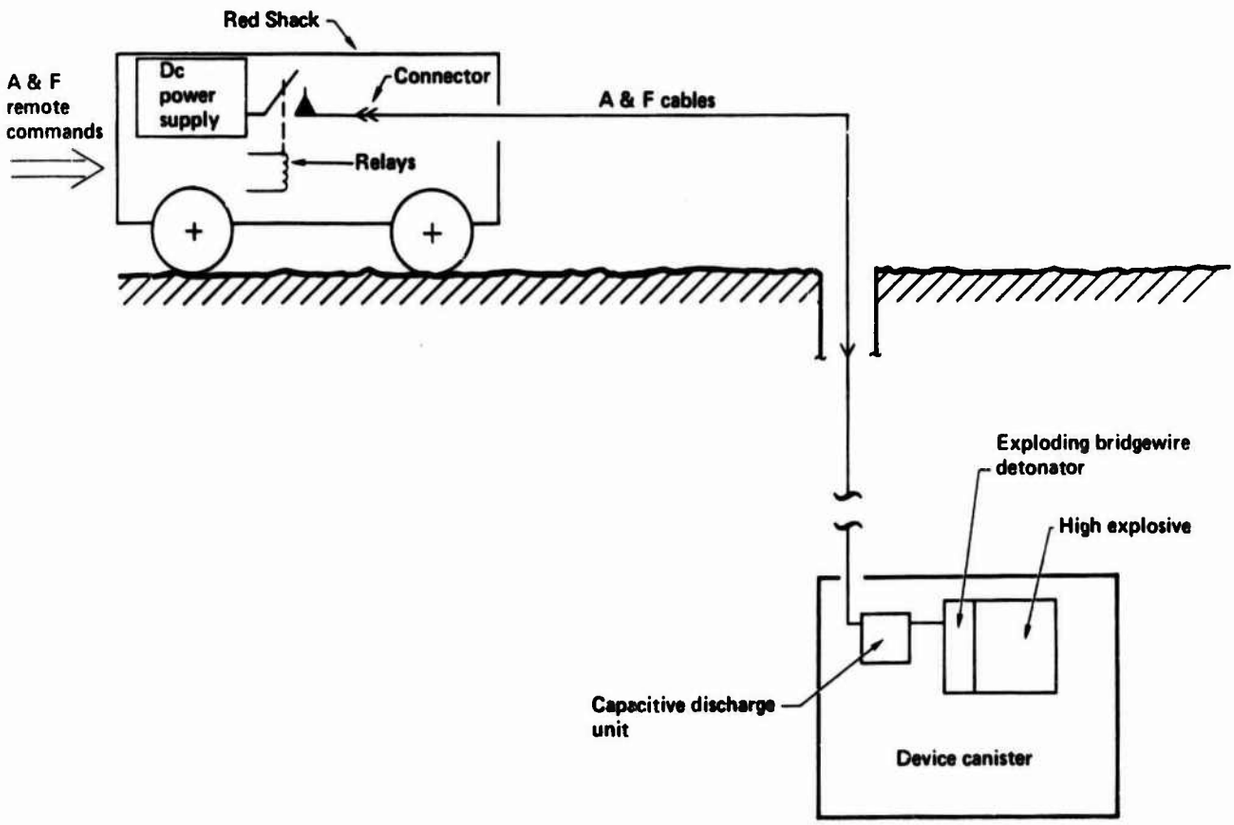


Figure 5. Simplified diagram of the intended device-firing pathway.

reports were considered to be esentially correct. The exception was the slower lightning current risetimes used in their calculations. As mentioned earlier, those conclusions were hased on models that considered lightning effects on a device system located at the hottom of the emplacement hole.

Crawford and Robh concurred with the NESS suggestion that testing of the system was important.

The Most Vulnerable Operational Phase

The greatest hazard was considered to exist when the test assemhly was suspended hy the crane and just entering the emplacement hole. A direct strike to the crane or test assembly could result in puncture of one or more of the device system's cahles, very near the point where they enter the canister. The system would not henefit from the high surge impedance provided hy the long cables when the system is emplaced downhole. Current division remote from the device canister, resulting from multiple-path arcing through the cahle insulation to ground, could not take place.

Care is taken to avoid carrying out the emplacement operation when a threat of lightning exists. The probability of a lightning strike during this oparation is considered to he exceedingly small. Again, the consequences of an accidental detonation are ahsolutely unacceptahle.

Inter/Intracloud Lightning Threat

Inter/intracloud lightning oftens induces large transient voltages in power lines and long cahles that can damage unprotected electrical and electronics components. Also, a person working on the unterminated end of a long cahle may receive a shock. A conservative analysis was carried out in which the effects of a 10-kA discharge, 1-km high and 1-km long, were considered. It was concluded that the magnitudo of induced voltage reaching the device system was small compared to that required to cause a detonation.

RECOMMENDATIONS

Several recommendations were made relating to both nuclear explosive safety and uphole electronic systems protection. Since the sole purpose of this investigation was nuclear explosive safety, only those recommendations pertaining to that topic were considered for implementation at this time. Once the safety recommendations have heen incorporated, additional protection for enhanced operational survival can be considered.

Radial Counterpoise Grounding System

During the initial period of a strike to a "grounded" system, the lightning current encounters a surge impedance that can exceed the steady-state value by 10 times or more. This causes the ground system potential to be significantly higher than the surrounding earth. A 20-kA stroke (50 percentile amplitude) passing through an 80-ohm surge impedance produces a 1.6-Mv transient. Electrical insulation becomes virtually nonexistent, large transient currents flow unpredictably, and significant damage can occur.

A major reduction in the surge impedance is required in order to reduce transient voltages to a controllahle range. By incorporating a radial counterpoise grounding system, ground resistance and therefore surge impedance, can be greatly reduced.

Crawford and Rohh proposed a system consisting of eight hare-copper AWG-No.-2/0 conductors, 60-m long, which would be bonded to the well casing. Equally spaced, at 45-degrees, they would extend radially and he buried 0.3-m deep. The net surge impedance of this radial counterpoise ground was calculated to he 11 ohms. Using the same parameters, the steady-state resistance of the casing alone was calculated to he 8 ohms. Assuming a 10-times increase, the casing surge impedance would he at least 80 ohms. While the method used to arrive at this value is not considered by Crawford and Rohh to be "exact science," it does demonstrate the henefit derived from this type of grounding technique. The radials also allow the system surge impendance to decay rapidly to the steady-state value. Thus, the peak amplitude of the transient voltage is greatly attenuated, and it exists for a much shorter period of time.

While this system represents an ideal approach, it introduces cost and construction prohlems. The existing GZ system has evolved over the years and satisfies a variety of independent and sometimes conflicting requirements.

Following a closer look at the existing system, it was determined that it closely approximates the recommended counterpoise system. The Red Shack, installation huildings, crane and several other GZ facilities are grounded to the casing via individual, buried AWG-No.-2/0 hare-copper conductors. The length, quantity, distrihution and depth of hurial of the radials are not the same as indicated for the ideal system. In the opinion of Crawford and Robh, the present GZ design does provide a surge impedance lower than that of the casing alone. This is supported hy actual GZ resistance measurements, mentioned earlier, which indicate a typical steady-state value of 5 ohms.

Difficult-to-verify protection techniques, such as overhead diverters, radial counterpoise grounding, and "the cone of protection" could not he relied upon to ensure nuclear explosive safety in a lightning environment. Thus, it was decided not to modify the existing GZ grounding system. Rather, the decision was made that the device canister should provide all of the necessary protection.

Fortress Design

While a topologically closed surface, i.e., a Faraday cage provides perfect protection, practical systems require penetration of the cage by electrical signal and power conductors. This penetration represents the worst compromise of an otherwise impervious barrier (Refs. 7, 8). With the LTRI "fortress approach," sensitive components are contained within a volume enclosed by a metallic skin. Cables containing penetrating conductors possess overall shields that are bonded to the outer surface of the fortress by means of 360-degree backshell connectors. Within the fortress, and close to the feed-through connectors, each conductor passes through a hybrid transient limiting network prior to being routed to its final destination.

Hybrid Transient Limiters

The input portion of the hybrid limiter network consists of either a metal oxide varistor (MOV) or a gas filled spark gap tube, shunt-connected from the

conductor to a low impedance ground (Fig. 6). Where balanced pairs are involved, a line-to-line transient limiting component is also employed. Next is a series component (inductor or resistor) followed by a shunt-connected, bipolar avalanche diode (TranZorb). Under normal opereting conditions, the shunt components present extremely high impedances to ground, and the series component offers a very low impedance.

When a lightning stroke attaches itself to one or more of the cables, the current divides. The path from an outer shield to the outer skin of the fortress represents a significantly lower surge impedance than that provided by the conductors and their transient limiter networks. A major portion of the current will flow from the shield to the outer skin and from there find its way to earth. Even if the canister rises momentarily to a very high potential with respect to earth the interior will remain in an essentially equipotential state.

The remaining current (an estimated 10%) present on the inner conductors will see the impedance of the limiter series element plus the surge impedence of the conductors beyond the limiter. Once the voltage appearing across the TranZorb exceeds the breakdown value, the series impedance element is essentially grounded. The TranZorb responds in nanoseconds, long before the lightning current reeches its peak, and is capable of carrying a sizeeble amount of transient current. As the current continues to rise, the voltage caps across the series impedance quickly reach the gas tube or MOV breakdown value. Essentially all of the remaining current is then conducted to ground. While slower to act, the MOV and gas tube are capable of accommodating very large amounts of transient energy.

Modified Device Canister

A modified device canister, referred to as the Lightning Invulnerable Device System (LIDS), has been designed and fabricated. It incorporates the fortress concept as described above. Figure 7 shows a simplified comperison of the LIDS to the present design. The coaxial end multiconductor cables heve their outer shields bonded to the lid of the canister vie 360-degree beckshell connectors. The sefety ground cable is bolted to the outside of the lid. A thru-bolt is not permitted, end to ensure this, the ground ceble inside the cenister is bolted to e different portion of the lid's inner surface. Special transient limiter modules (for the multiconductor cables) and coaxial transient limiters (for the coaxial cables) are being developed by several manufacturers. Gas tube and MOV input limiters, and resistor and inductor series impedances will be evaluated.

A Comment on Fiber-Optic Cables

From the isolation standpoint, fiber-optic cables represent an ideal way to penetrate the fortress. However, until the problem of transmitting sufficient power optically has been solved, copper cables will continue to penetrate the fortress. Ironically, reducing the number of copper cables, without eliminating them altogether, does not meke matters any better. Fewer copper cables means there are fewer parallel paths to ground for arcing currents. Thus, a greater magnitude of current will appear at the lid penetration point. If a metallic jacket is used to provide mechanical protection for the fiber-optic cable, it should be bonded to the outside of the lid. The metallic jacket also provides a parallel arcing path to ground.

Simulated Lightning Tests

Objectives of these tests will be to evaluate the several hybrid transient limiter designs, determine the most vulnerable lightning attachment point, and obtain data tc substantiate the "lightning invulnerable" claim. Subsequent tests may be performed at the Sandia National Laboratories' lightning simulator facility in order to observe the lightning invulnerable device system performance using a double-exponential current pulse, combining high current with a fast current risetime.

The LIDS will be subjected to a series of simulated lightning tests, conducted by LTRI. The limiter designs will first be tested to verify their performance at the specified limiting levels. Several will then be tested at increasing levels, up to 50 kA, to determine failure levels and modes.

The final tests will be made on the complete LIDS, with the limiters being terminated by typical load impedances. Low-level coupling tests (20 kA and 20 kA/μsec) will permit determination of mutual inductance end resistence perameters for the system. Increasing peak currents and retes of rise, up to maximums of 200 kA end 200 kA/μsec, will be seperetely

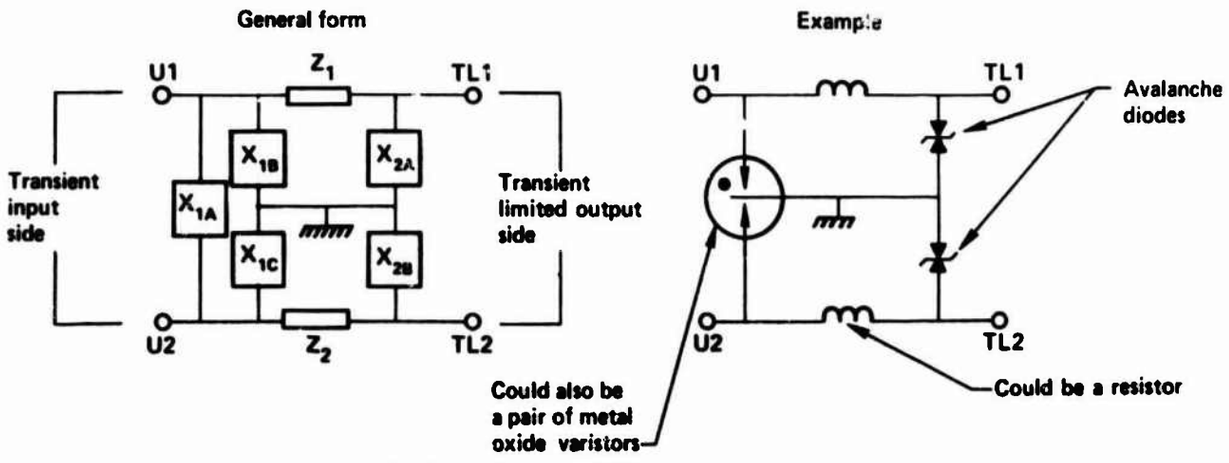


Figure 6. Block diegram of hybrid trensient limiter

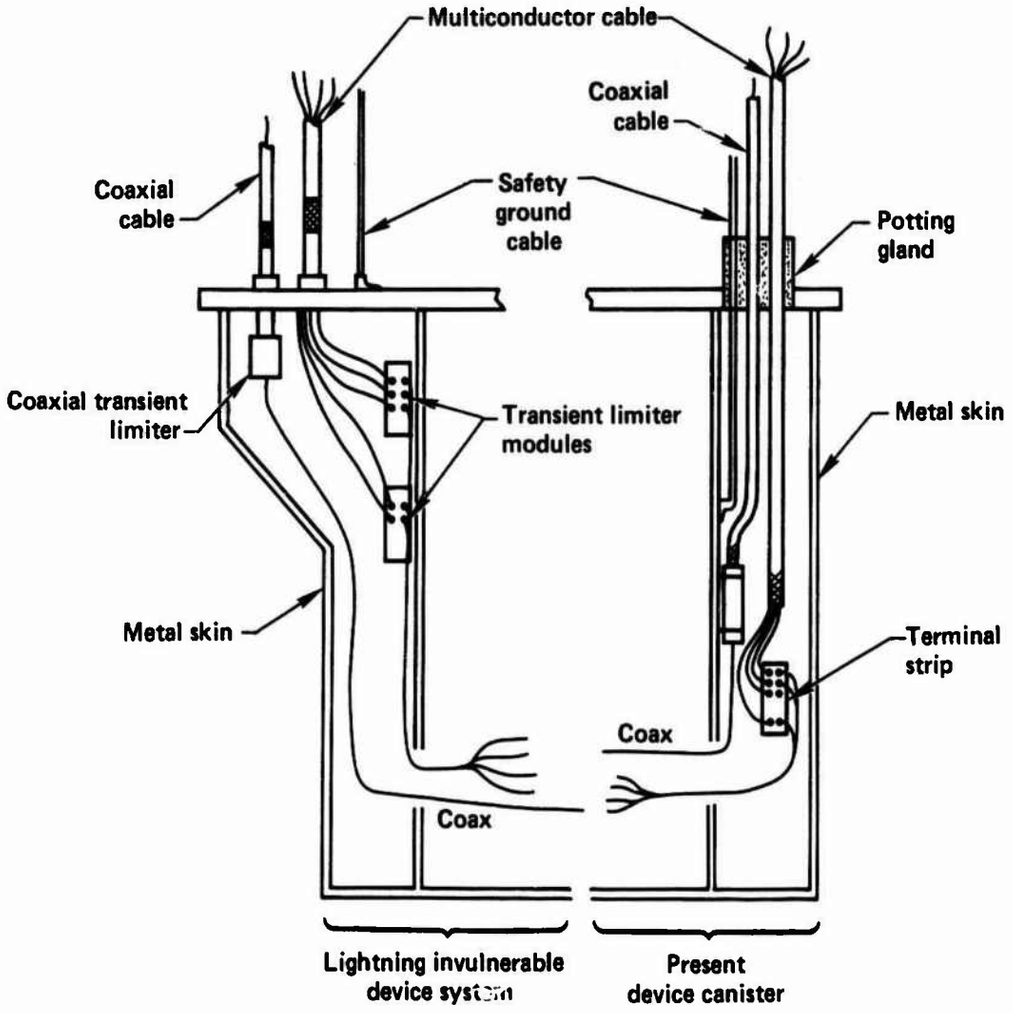


Figure 7. Simplified sketch showing comparison of lightning-invulnerable device system and present device canister.

applied. A damped oscillatory current pulse will be used in order to avoid the damaging effects of the more lightning-like double-exponential current pulse. Lightning attachments will be made, approximately 1 m from the lid, to various configurations of cable shields and conductors.

SUMMARY

The task of evaluating the lightning vulnerability of a large and complex operation and making recommendations for improvements has been successfully carried out. Because of the absolutely unacceptable consequences of a lightning-induced detonation of a nuclear test device, several commonly used protection techniques were determined to be of little use. From what the task force learned, the decision was made to concentrate primarily on designing a lightning invulnerable environment for the test device system. The effectiveness of this design will be tested later this year, using full-threat-level simulated lightning. As time and funds permit, the portions of the event system that are not nuclear-safety-critical will also receive improved protection.

ACKNOWLEDGEMENTS

The timely and successful completion of this task would not have been possible without the efforts of R. J. Burton, LLNL consultant, J. P. Johnson, Sandia National Laboratories Albuquerque, and our experts, S. R. Crawford and J. D. Robb. The excellent state of the existing GZ grounding system can be attributed to the conscientious efforts of A. G. Brown, LLNL Nevada, and P. J. Thompson, Holmes & Narver, Inc.

REFERENCES:

1. F. A. Fisher, *Lightning Hazard Study*, General Electric Co., Environmental Electromagnetics Unit, Corporate Research and Development, Pittsfield, MA, Prepared for U.S. Atomic Energy Commission, Nevada Operations Office, Las Vegas, NV, Contract No. AT(26-1)-594 (1973).

2. J. P. Luette, *Lightning Hazards Study of Nevada Test Site Arming and Firing System*, Sandia Laboratories, Albuquerque, NM SLA-74-0070 (1974).

3. No author cited, *Nuclear Explosive Safety Study of the Effect of Lightning on LLL Nuclear Explosive Operations at the NTS*, U.S. Energy Research and Development Administration, Las Vegas, NV (1975).

4. No author cited, *Nuclear Explosive Safety Study of the LLNL Arming & Firing and Timing & Control Systems and Operations at the NTS*, U.S. Department of Energy, Nuclear Operations Branch, Las Vegas, NV (1982).

5. R. T. Hasbrouck, J. P. Johnson, R. J. Burton, S. R. Crawford, and J. D. Robb, *Final Report of the Nuclear Explosive Lightning Vulnerability Task Force*, Lawrence Livermore National Laboratory, Livermore, CA, UCRL-15618 (1984).

6. K. Buset and K. W. Price, *Lightning Flash Densities and Calculation of Strike Probabilities to Certain Vulnerable Installations at the Nevada Test Site (NTS)*, Los Alamos Scientific Laboratory, Los Alamos, NM, LA-UR-74-1953.

7. W. Graf, J. Hamm, and E. F. Vance, "Relative Importance of Electromagnetic Shield Violations," *8th International Aerospace and Ground Conference on Lightning and Static Electricity, Lightning Technology Roundup, June 21-23, 1983* (U.S. Department of Transportation, Fort Worth, Texas, 1983), p. 8-1.

8. W. Graf and J. E. Nanevicz, "Topological Grounding Anomalies," *8th International Aerospace and Ground Conference on Lightning and Static Electricity, Lightning Technology Roundup, June 21-23, 1983* (U.S. Department of Transportation, Fort Worth, Texas, 1983), p. 9-1.

STEPPED LEADER AND STRIKING DISTANCE

I. Mladenović and A. Vorgučić*

Tehnološki Fakultet, 16000 Leskovac, Yugoslavia
**Elektronski Fakultet, 18000 Niš, Yugoslavia*

Abstract - In this paper is pointed out of that movement of the stepped leader may have influence of the estimation of the striking distance lenght.This estimation being founded on the photos of the lighting channel. The influence is as much greater as the final jump(starting movement of the return streamer) takes place at the begining last step movement of the stepped leader along the channel already prepared by the pilot streamer.

1. INTRODUCTION

In intention to protect from the lighting stroke, the phenomenon of the lighting discharge is subject of many investigations. The spectrum of this investigations is large, from measuring many characteristics of lighting, recording, taking of photographs to the statistical elaboration of all collected data.

The lighting research includs a large number of characteristic quantities which depends from many parameters and whose magnitudes are in a very broad measuring volume. For example, the lighting current measuring equipment should have the frequency range from 1 to 10^6 Hz and current range from 1 to $5 \cdot 10^5$ A |1|.

Collecting and comparing all of this data, got on any way, acquires every day more complete picture about this casual process.

In this paper would be given a sugestion for a discussion or a consideration which bounds stepped leader and striking distance meaning on the possible influence the velocities of the stepped leader motion on the (estimate) evaluating of the striking distance from the photographs of lighting stroke channels.

2. STEPPED LEADER

Most og the lighting discharges are toward earth with the negative charge. According to the photographs from the Boys camera and measuring the electrical field on the earth, the cloud - ground discharge is initiated by a streamer that develops downwards in a series of steps. Each of this steps is observed as a sudden increase in luminosity of the channel of the ionized air at the tip of the streamer. This streamer is called stepped leader. The spark in its moving toward ground get over some distance, stops and after short time interval continue to move. The lenght of each step is about 50 m. After completing a step the tip of the streamer appears to pause for a time of the order 50 μs, and the new step being much brighter then the rest of the streamer |2,3|. When stepped leader, in its moving, approaches the ground, starts the positive conecting leader from the earth to the stepped leader. This conecting leader, which is initiated by the critical electrical field from the electrical field from the electrical charge in the channal of the downmoving stepped leader, conects striking point with leader channel. Trough the ionized channel moves upward positive charge (return stroke) with velocity of $5 \cdot 10^7$ m/s. The downmoving stepped leader has two velocities. First, the stepped leader approaches the ground at an average velocity at about $1.5 \cdot 10^5$ m/s. The second one is velocity of the individual step motion value of $5 \cdot 10^7$ m/s |2,3,4| .

Fig.1 shows shematic diagram for ilustration of the first discharge (stepped leader) recorded by a moving cammera.

One of the first theory of the stepped leader are due to Schonland (1938). Schonland's model of the stepped leader has a channel of uniform cross-section with radius of the order of the meter. The fact that the average velocity of the stepped leader agrees fairly closely with the calculated minimum velocity of an electron cloud that is abble to perpertuate itself by ionization, led Schonland to suggest that the insulation of the air is broken down by apilot leader, that adv-

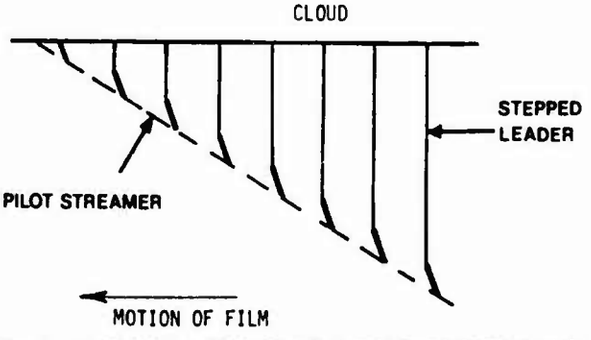


Fig.1. Ilustrating diagram of the stepped leader with step and pilot leader.

ances continuously. Schonland defined the pilot leader as "a true negative virgin air streamer that travels continuously downward in front of the step streamer processes with a velocity equal to the effective velocity of these". The pilot leader progressing some tens of metres, causes the current in the lihgtning channel to increase and produce a luminous step. Support for existance of pilot leader come from the laboratory exeminations.

The pilot leader, which continualy progresses, prepares the way for the step process by ionizing the air. Upon the ionizing channel moves the speedy step. When this speedy process reaches the tip of the pilot leader one step of stepped leader is completed. The pilot

leader continue to move during the pause between steps.

Bruce (1941) explained the stepped leader like Schonland. According Bruce the stepped leader has a arc channel at the center of leader on high potential. Becouse of large potential difference, the radial corona current flow to the core of channel. The current increases with increasing of the channel. When the corona current excels a value of the order of 1A a sudden transition from glow to arc discharge occurs. This is the step in the stepped leader.

It could be concluded that all theories of the stepped leader includes that the average velocity for a negatively charged downmoving stepped leader is about $1.5 \cdot 10^5$ m/s, like the velocity of the pilot leader. The pilot leader, which prepares the way for the step process by ionizing the air, moves continualy. The mean velocity of individual steps is $5 \cdot 10^7$ m/s, much higher than average velocity of the stepped leader. Time intervals between individual steps is about 50μs. The velocity of the return stroke is much greater than average velocity of the stepped leader.

Some characteristics of lihgtning discharge (mean value) |2,3,4| :

velocity of:

stepped leader	$1.5 \cdot 10^5$	m/s
individual steps	$5 \cdot 10^7$	m/s
conecting leader	$5 \cdot 10^7$	m/s
return stroke	$5 \cdot 10^7$	m/s

duration of:

stepped leader	10 - 30	ms
individul steps	1	μs
interval between steps	50	μs
return stroke	100	μs

current of:

stepped leader	100	A
individual steps	500 - 2500	A
return stroke	10^4 - 10^5	A

length of individual steps	50	m

3. STRIKING DISTANCE

The distance between the tip of the downmoving leader and the point on the earth or structure when, under elektrical charge deposited in leader channel, a electrical field on the earth or structure reaches a critical value. From point on earth or structure where electrical field exceeds critical value, starts positive conecting leader (return stroke), which conects striking point and the tip of the downmoving negative leader. This is the length of the last step in the lightning channel development. This length depends, generaly of the electrical charge in the leader channel. The striking point is not by anything determined in advance, but only by critical electrical field intensity due to downmoving leader. The electrical field strenght above ground, due to the charge along the leader channel, initiate the positive conecting leader from the striking point. The charges in the leader channel are neutralized during the return stroke process. The crest of the lightning depends on this charge. From the integration of current oscilograms it is concluded that an average lightning current of 20 kA coresponds to a charge of 1C |5| . From the foregoing considerations it follows that the striking distance could be introduced like function on crest lihgtning current. The detrmination of striking distance in function of lightning current was given by Golde (1945) as a numerical solution and as many others authors. For example, relationship suggested by Love is

$$r = 2I + 30 \left|1 - \exp(I/6.25)\right| \quad (m)$$

where r - striking distance in m and I lightning crest current in kA. This relation like relations from other autors, can be presented in the simplified form

$$r = kI^p .$$

Constans k and p have different values, what depends on the autors, and start from 3.3 to 10.6 for k and from 0.51 to 0.85 for p.

In Fig.2 are given curvs of the striking distance versus the crest current of the lihgtning stroke from named authors. The different values of the striking distance results from the different consideration of critical value of electrical field, distribution of the electrical charge in the leader channel and so on. More about striking distance in |5| .

The point where the leader channel and the upward streamer meet, could be seen in same photographs according the sharp bend in the lightning channel. From such a photographs taken from two directions and stimultaneous measurements current or estimated from the lightning current effect, the striking distance could be determinated - estimated.

4. SOME CONSIDERATION

They are two velocities in the stepped leader : v_1 - velocity of the pilot leader propagation also average velocity of the stepped leader and v_2 - the velocity of the individual step trough the already prepared channel by the pilot leader. The mean values are: $v_1 \approx 1.5 \cdot 10^5$ m/s and $v_2 \approx 5 \cdot 10^7$ m/s.

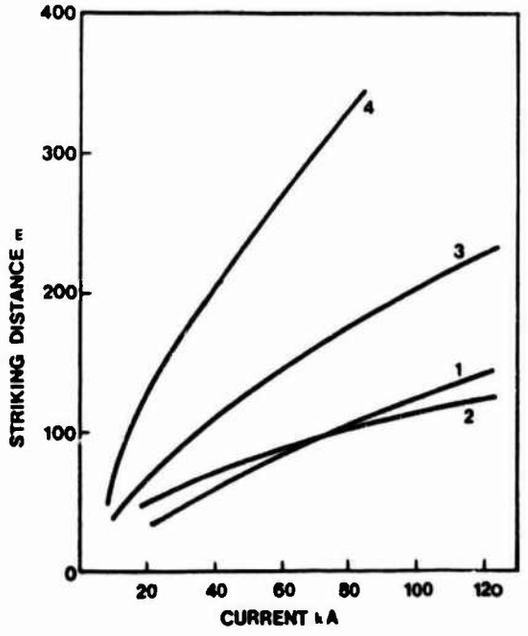


Fig.2. Striking distance versus the negative crest lightning current|5| , 1 - Golde, 2 - Wagner, 3 - Love, 4 - Ruehling.

Striking distance is distance the tip of downmoving leader from the striking point, when the charge in the leader channel due critical electrical field on the striking point to initiate the conecting leader.

Now we have to distinguish two tipes: tip of the pilot leader moving with the velocity v_1 and tip of the individual step in the stepped leader moving with velocity v_2 . It is possible that position of both tipes may initiate the conecting streamer from striking point because the both of them bears the charge. It is not the same which tip and from which position due the critical field on the striking point. If it is a tip of the individual step we have to take in consideration that it has the velocity like the conecting streamer and it has already prepared way for its motion.

Fig.3b. shows position of individual step tip inicia-ting conecting streamer, when the tip is in the begining of its motion. The both step and conecting streamer moves with equal velocity ($v_s = v_2$). The way of downmoving leader is determinated, meeting point of two leaders "2", which is seen on the photograph like bend of channel, is nearer to the striking point and the striking distance on the photograph is D instead D'.

Fig.3a. shows position of individual step neer to the end of prepared way by pilot leader, when is conected streamer iniciated. Bending of channel could be much sooner.

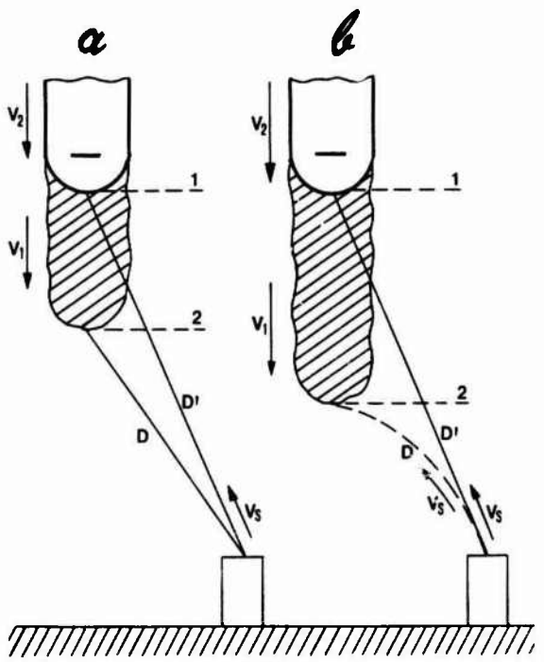


Fig. 3.

5. CONCLUSION

The negative downmoving stepped leader has two velocities. The average velocity of stepped leader is aqual to velocity of the pilot leader mean value of $1.5 \cdot 10^5$ m/s. The second one is velocity of the individual step into the stepped leader value of $5 \cdot 10^7$ m/s. According to this velocities in the paper are introduced two tipes. Tip of the pilot leader and tip of the individual step. It is pointed out that on the photographs of the lightning channel the distance from channel bend to the striking point, should not to be striking distance. This length depends from which tip and from which position in the channel due electrical field of critical value on the striking point. The difference the real and seen distance which could appear comes from speeds of stepped leader, conected streamer and prepared way for individual step by pilot leader.

6. REFERENCES

|1| Bazeljan, E.M., Gorin B.H., Levitov V.I., Fizičeskie i inženernye osnovy molniezasity, Gidrometeizdat, Leningrad, 1978.

|2| Berger K., The Earth Flash, in Golde R.H.,(Ed): Lightning, Academic Press, London, 1977.

|3| Uman M., Lightning, McGraw Hill, New York, 1969.

|4| Mason B.J., The Phisics of Clouds, Clarendon Press, Oxford, 1971. II ed.

|5| Golde R.H., The Lihgtning Conductor, in Golde R. H. (Ed.): Lightning, Academic Press, London,1977.

EXPOSITION TO THE LIGHTNING CURRENT OF OBJECTS SITUATED NEAR TO THE VERTICAL LIGHTNING ROD

A. Vorgučić and I. Mladenović*

Elektronski Fakultet, 18000 Niš, Yugoslavia
**Tehnološki Fakultet, 16000 Leskovac, Yugoslavia*

Abstract - In the paper is given the method of estimating, namely, the determinating the maximum value of lightning current an object or equipment could be exposed to, when placed to the lightning rod or any other object having the function of the lightning rod. This estimation of possible maximum value of lightning current a lover object is exposed to, is based on the evalution of the more protected spaces of the lightning rod. The maximum value of the lightning current an equipment or an object could be exposed to, is the function of the height of the lightning rod, the dimensions of the object and their reciprocal distance.

1. INTRODUCTION

The lightnig rod, which should protect a specified ground area from lightning strokes by causing all strokes to hit the rod, was introduced by Benjamin Franklin in 1753. During the more than 200 years since its introduction, many theories and hundreds of papers were presented to define the zone protected by the lightning rod. This large number of theories was occasioned doubtlessly by the fact that the principal processes associated with lightning were not well known. But each of these theories,coupled with experience obtained from observation and experimental evidence, contributed to the fund of collected knowlege. The conformation and extent of the zone protected by the lightning rod was determined principally from experience. But this evidence differed from place to place as evidenced by the variability in national electrical codes relative to lightning protectors.

New and new lightning strokes on the objects already protected, aspecialy at high structure, makes conviction, that there is no absolutely sure lightning protection. The better knowlege, of atmospheric electrical discharge, in the recent time, lead to the new vision and new theories. The developpment of new theories, which include numerous protected spaces around one lightning rod, allows better evalution of the protected spaces of the lightning rod.

2. PROTECTIVE ZONE OF THE LIGHTNING ROD

In lightning protection, a very important matter was what was the nature of the space protected by the lightning rod. It has been assumed that the protected space is either conical or cylindrical. The base of the cone or cylindar is a circle having a radius which depends on the hight of the lightning rod and experience of the observer. The appropriate was often changed. The conformation of the protected zone included cones and cylinders with considerable variations in the radius. Current practice in many countries indicates that the protective zone is defined either by an angle from the vertical or by a radius which depends on rod heighth. For example, in electrical codes of some contries the single mast protective angle is specified as 45° while with two masts the protective angle between them is 60°. In the other codes, the base-to-heighth ratio is 1 for important cases of protection and 2 for less important cases.

One the first theoretical determinations of the protected zone was based on the "principle of the shortest distance". At this time, it was assumed that the lightning stroke seeks out the point of the earth's surface which is nearest to the place at which it exits the cloud. It was assumed that the exit points

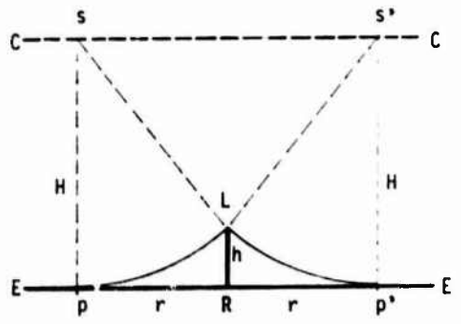


Fig.1. One of the first derivation of the radius of protection zone of the lightning rod

for all earth-bound lightning discharges lie in a place (CC' on Fig.1) which is parallel to the surface of the earth (EE) [1]. In Fig. 1 it is easy to see that the protected range PP' of the lightning rod LR is obtained by finding the points S and S'. All strokes leaving the cloud at points in a circle with the diameter SS' under this assumption seek out the point L. All those strokes leaving the

cloud outside the circle of diameter SS´ will strike points outside of the protected surface (circle with diameter PP´). This radius of the protected zone according to this consideration was

$$r = (2H - h)^{1/2}. \qquad (1)$$

To exam the values of this radius Walter [1] used the findings of the Hamburg Fire Insurance Office on buildings damaged by lightning strokes over a period of 20 years. Significantly he found out that the protected zone is much smaller than the radius in Eq.1. He concluded that the basic assumption that when the lightning leaves the cloud it is directed to the nearest point on the earth´s surface, must be false. From other observations he concluded that the altitude at which the lightning definitely seeks the tower is very near the top of the tower. Also many direct observations and photographs show that the point from which the lightning seeks the stroke point, is not in the cloud but is much nearer to the stroken point [2].

The optimum solution approach and physical model to the last steps of the leader (which are very important in protected zones) were developed by Golde [3,4,5], using the results of breakdown experiments of long spark gaps excited by an impulse generator. Using the supposition that the last step of leader moving toward the ground could be compared with long sparks, he defined the last dischargin distance. In the initial discharge the negative leader moves from the cloud toward earth in steps. The main stroke, which builds up from the earth toward the cloud, is initiated by the electrical field from the downcoming leader. The main stroke, which propagates with much greater velocity than the leader originates at the stroke point.The electrical field strenght above ground, due to the charge along the leader channel. The critical field strength which can initiate the main stroke from the earth is larger for negative impulses then for positive. The charges in the leader channel are neutralized during the return stroke process. The magnitude of the lightning current depends on this charge. From the integration of current oscilograms it is concluded that an avarage lightning current of 20 kA corespondens to a charge of 1 C. The point where the leader channel and the upward streamer meet can be seen in some photographs which thereby support this theory [2,4]. From foregoing considerations it follows that the striking distance to a lightning rod cannot be described by just one value. Golde introduced a new concept of the attractive effect and protected zone of a vertical lightning rod. The protective zone of a freestanding vertical lightning rod he described by a cylinder about the rod [4].

Protected spaces of the lightning rod two methods, based on "electrogeometric" theories will be heir mention. The "lightning sphere" method [6,7] deals with propability of lightning strokes in the object which is in protected space. Protected space is determined with sphere of radius which depends on propability. For a given propability the sphere must not tuch the protected object, as is showen in Fig.2. Another method for evaluation of the protected spaces of the lightning rod [8] showes more protected spaces of the lightning rod depending of the crest current of lightning stroke. The second one will be described more.

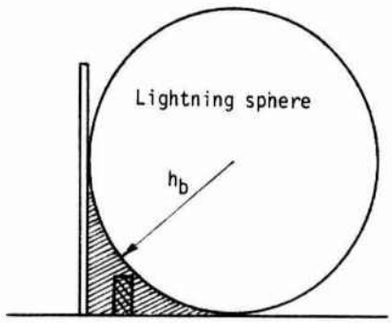


Fig.2. Protected space according "lightning sphere" method.

3. STRIKING DISTANCE

The distance between the tip of the downmoving leader and the point on the earth or structure when, under electrical charge deposited in leader channel, reaches a critical field value on the earth or structure. From point on earth or structure, where electrical field reach critical value, starts positiv conecting leader (return stroke), which conects striking point and the tip of the downmoving negative leader. This is the length of the last step in the lightning development. It depends, generaly of the electrical charge in the leader channel. The striking point is not by anything determined in advance, but only by critical electrical field intensity due to downmoving leader. There is possible to start two or three positive leaders from the earth, what brings to the branching the lightning channel near to the earth.

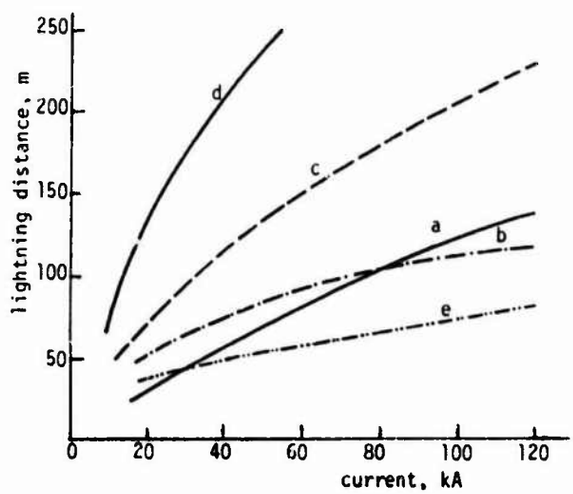


Fig.3. Striking distance versus the negativ crest lightning current [4,5] a-Golde, b-Wagner, c-Love, d-Rühling, e-Horváth.

The critical distance depends from the channel charge in relation to the crest current of the first stroke in the flache. For the practical calculation, the generally form of this dependance is given by

$$R = kI^p \qquad (2)$$

where R is in meter and I crest value in kA. Constants k and p have different values, what depends on the authors, and start from 3.3 to 10.6 for k and from 0.51 to 0.85 for p.

In Fig.3 are given striking distances versus the crest current of lightning stroke from named authors. The different values of striking distance results from the different consideration of critical value of electrical field, distribution of the electrical charge in the leader channel and so on. More about striking distance in [5]. After some photographs of lightning discharge and current measuring, it seems that the best conformation has the curve a in the Fig.3.

4. EVALUTION OF THE PROTECTING SPACE OF THE LIGHTNING ROD

If we accept the "striking distance", one from Fig.3, for example developed by Golde [5], it is possible to evaluate the protected space of high lightning rods and also explain the lateral strokes in the proximity of tall structures. According to Fig.4, if the leader approaches a long vertical rod or a tall structure, it will be struck at a point on the structure or earth and that the shortest distance from the leader tip will be equal to the striking distance. The striking distance depends on the charge in the leader channel namelly lightning crest current R= f(I). The radius of the protection zone for each current is equal to the striking distance.

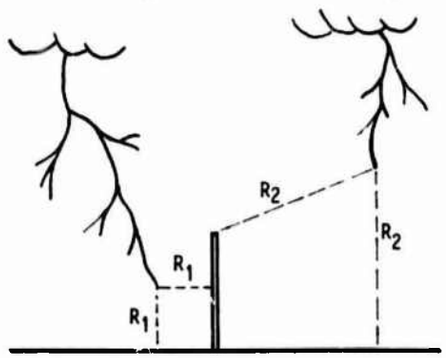


Fig.4. Negative leader approaching to the tall structure seek the striking point

Fig.5. shows the protected spaces of high vertical lightning rod (or high structure) for a five different values of the crest lightning currents. On the lefthand side are given the protected spaces for lightning currents of lower crest value and on the righthand side for the currents of higher values. Case on the righthand side cann deseribe also lower objects with average lightning currents. According to the principle of the "chortest distance", protected space is inside the cone, which has circle shaped envelope radius approximate equal to the striking distance.

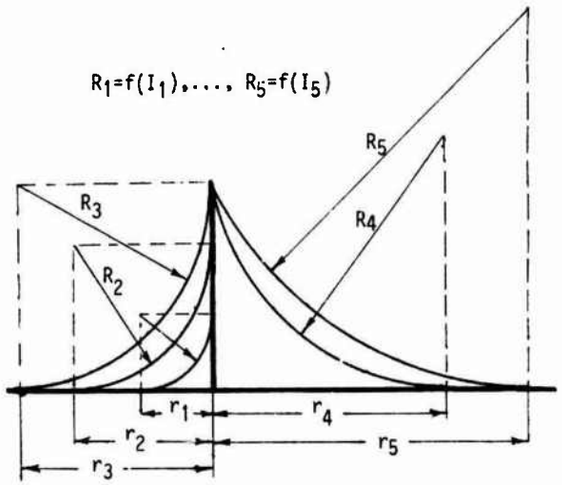


Fig.5. Protective spaces in function of lightning current magnitude ($I_1<I_2<I_3<I_4<I_5$).

5. EXPOSITION TO THE LIGHTNING CURRENT

According to the more protected spaces treatman of the lightning rod which dependens on the lightning current crest value, it is passible with electrogeometrical method, to evaluate the lightning current to which is exposed some object near to the vertical lightning rod.

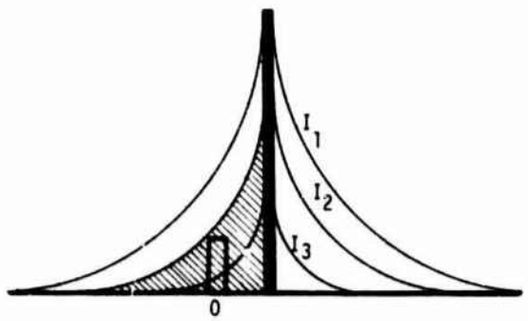


Fig.6. Object O near the lightning rod is not protected from lightning crest current less than I_2.

Fig.6. shows the vertical lightning rod of hight h with three protected spaces according to the three currents like in the Fig.3. O is the object which should be protected. This object is, according Fig.6, inside the protected spaces the currents greater than I_2. It means that the object O is protected from lightning current magnitude greater then value I_2. For all other lightning crest currents less then I_2 (say I_3 in Fig.6) the object O is not protected.

For the object of hight h on distance r the lightning rod the high of H, determining the radius of the circle which form the cone

of the protected space, which is approximately equal to the striking distance, it is possible to determine the currents the object is exposed to.

In analysis of the determining of the striking distance in the first approximation the highst influence of the object or lightning rod would not be taken into consideration.

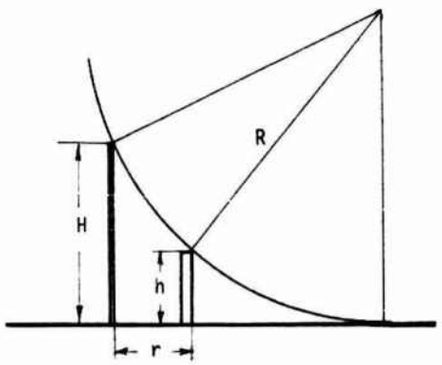


Fig.7. Derivation the striking distance of the maximum crest lightning current the object is exposed to. Case lower lightning rod (H<R).

According to the Fig.7. in the case for the lightning rod height H less then striking distance R (case of lower lightning rods), the striking distance is

$$R = \frac{H + h}{2(H-h)^2}\left[(H-h)^2 + r^2\right] + \frac{Hr}{(H-r)^2}\sqrt{\frac{h}{H}\left[r^2 + (H-h)^2\right]}. \qquad (3)$$

In case of hight and very hight lightning rod and object near to them (Fig.8.) the striking distance for the maximale crest lightning current is

$$R = (r+h) \pm \sqrt{2rh}. \qquad (4)$$

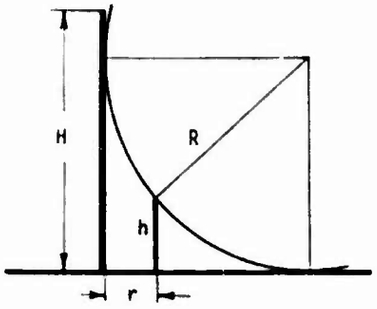


Fig.8. Derivation the striking distance of the maximum crest lightning current the object is exposed to. Case higher lightning rod (H>R).

The striking distance obtained by geometrical way give opportunity to determine-estimate the maximum crest current toward curves in Fig.3, the object may be exposed.

6. CONCLUSION

The protected space of a lightning rod or a tall structure depends on the magnitude of the lightning current. A single lightning rod has many different protected spaces each one determined largely by the current magnitude. The protected space is approximately conical with a circularly shaped envelope as shown in Fig.5, the radius of the envelope being nearly equal to the striking distance.

For a object (or equpment) of the hight h on the distance r from the lightning rod the hight H (or other hight structure having the function of the lightning rod) it is possible to determine the maximale striking distance by the geometric methode. According to the maximale striking distance, got in this way, it may be determined maximale lightning current the object could be exposed to. The object is now exposed to all lightning current less and equal to the this maximale current. This boundary value is the function of the hights of the lightning rod and object and their reciprocal distance.

7. REFERENCES

[1] Walter,B., Ueber Blitzschutz durch "Fernblitzableiter", Z.für techn.Physik, 14, No 3, 1933, s.118-126.

[2] Walter,B., Von wo ab steuert der Blitz auf seine Einschlagstelle zu?, Z.für techn. Physik, 18, 1937, s. 105-109.

[3] Golde,R.H., Teoretische Betrachtungen über den Schutz von Blitzableitern, ETZ-A, 82, 1961, s. 273-277.

[4] Golde,R.H., Lightning Protection, Edward Arnold, London, 1973.

[5] Golde,R.H., The Lightning conductor, in Golde R. H. (Ed): Lightning, Academic Press, London, 1977.

[6] Horváth,T., Praktische Methode für Standardizirung der Schutzwirkungen von Fangvorichtungen, 14. Int. Blitzschutzkonferenz, Gdansk, 1978, R-4.06.

[7] Hasse,P., Wiesinger J., "Blizkugel" - Verfahren zur Ermittlung des Schutzbereich von Fanganordnungen, 14. Int. Blitzschutzkonferenz, Gdansk, 1978, R-4.08.

[8] Vorgučić A., Condition for Evalution of the Protective Zone of the Lightning Rod, FAA/Georgia Institute of Technology Workshop on Grounding and Lightning Protection, FAA-RD-78-83, Atlanta, May 1978, pp. 115-129.

LIGHTNING AND LOGISTICS
CAPE CANAVERAL - A PROVING GROUND FOR LIGHTNING RESEARCH

C.N. Golub

USAF Eastern Space and Missile Center, Patrick Air Force Base, Florida 32925, U.S.A.

Abstract - One of the problems encountered in lightning research is finding a suitable location where both lightning and logistics are accessible and affordable. One of the most favorable sites in these respects is the Cape Canaveral area of the Eastern Test Range in Florida, USA. In the summer of 1984 a number of organizations engaged in lightning research took advantage of this situation and acquired one of the largest amounts and greatest variety of data ever gathered during one season at one location. This paper describes what facilities were available and how they were utilized by the research organizations. The experiments performed ranged from conventional electric and magnetic field measurements to rocket-triggered lightning and coordinated measurements of lightning phenomena made simultaneously from ground stations and from an instrumented aircraft.

I. INTRODUCTION

A large number of lightning research projects are taking place in various locations around the world, especially where lightning activity is high. This situation is evident from even a casual perusal of the subject [1]*.

However, what is not so evident in the literature are the difficulties of performing such research, in particular in the area of logistic support. The moment a research project goes beyond simple observations and starts involving availability of electrical power, synchronized timing, landline or radio communications, and weather forecasts, the complexity of obtaining such support increases rapidly. If one goes one step further and starts flying instrumented aircraft or launching lightning triggering rockets, the business of obtaining air space clearance and providing liability coverage insurance is enough to discourage the hardiest soul and deplete the best stocked pocketbook.

As an example, a joint ONERA-U.S. Air Force project to do triggered lightning research in a public area of Florida for two months involved among other expenses a $30,000 premium for liability insurance to indemnify personal or property damage that might have been caused by a triggering rocket.

On the other hand, interest in lightning research is such that if an organization is planning a unique approach to obtain original data, it is very likely that once this plan becomes known, other organizations will volunteer support in the form of instrumentation, aircraft, or test sites as their share of the research effort. When I say "volunteer", it may be that there is some cost involved, but even then it will be much less than if the lead organization were to provide such facilities by itself.

A case in point, and the subject of this paper, are the test facilities available in the Cape Canaveral area in Florida. They have been used to develop mesocale weather prediction capabilities and for the second year they are also being used for lightning research. There are indications that this kind of work will continue for years to come and I am here to encourage you to join us and make use of these facilities. Let me make it clear that we are not a research facility--we are operations. But we encourage activities from which we hope to derive benefits.

What I want to describe for you in this presentation is the environment in which you can perform a variety of research projects.

*Numbers in brackets designate references at end of paper.

II. LOCALE

Around Cape Canaveral people often refer to "This side of the river or the other side of the river." Well, the river in question is the Banana River (Fig 1) and one side belongs to the U.S. Air Force and the other side to NASA. The Air Force side (east of the Banana River) is the Cape Canaveral Air Force Station and includes Cape Canaveral proper and Port Canaveral. Cape Canaveral is the headwaters, so to speak, of the 10,000 mile Eastern Test Range. The NASA side is the J.F. Kennedy Space Center or KSC. All launch pads, both NASA and Air Force, are on Cape Canaveral except for the Space Shuttle launch pads (complexes 39 A & B) which are on KSC. The NASA launch pads on Cape Canaveral are used for satellite launches (using Atlas Centaur and Delta vehicles) and are leased from the Air Force. Other users of Air Force launch pads are the Army, the Navy and whoever else has a legitimate need. The overall area of both sides of the Banana River covers about 417 square kilometers. The air space above is restricted to space launch and allied operations. In effect we have our own three-dimensional world extending 20 km from the Indian River to the Atlantic Ocean, 29 km from Port Canaveral to the north bounds of the Kennedy Space Center and 100 km high. And last but not least, we are in one of the highest isokeraunic areas of the world.

III. THE SUPPORT FACILITIES

1. There are two industrial areas, one for KSC and one for the Cape. Each one has shop and laboratory facilities and all the support you might want ranging

from cafeterias to physical standards laboratories. We have tracking radars, tracking optics (with video recording capabilities), telemetry, and our own air traffic controllers working in conjunction with the Federal Aviation Administration (FAA) controllers. But more to the point for weather and lightning researchers we have the following to offer:

2. The "piece de resistance" is the McIDAS-lineage MIDDS. Let me explain this mumbo-jumbo. McIDAS stands for "Man-computer Interactive Data Access System." It is the brain child of the Space Science and Engineering Center of the University of Wisconsin for integrating a variety of meteorological data sets into one display. MIDDS stands for "Meteorological Interactive Data Dispiay System" which is a local adaptation of the McIDAS for Space Center activities. Eventualiy there will be a network of such systems, at the Cape, at the NASA Johnson Space Center in Houston, Texas, and the Marshall Space Flight Center in Huntsviile, Alabama, at the Western Test Range, at the Air Force Consolidated Space Operations Center, at the University of Wisconsin, and elsewhere.

Most of these systems will have access to one another's data sets as weii as to global meteorological data systems such as GOES, Meteosat, and other such remote sensors.

The MIDDS at Cape Canaverai (also known as MIDDS I) is a particularly weii honed system for "nowcasting"; it is designed to give accurate weather conditions for time intervals of up to two hours from the time the forecast is issued in a cross-section of atmosphere a few kiiometers wide, about 300 kiiometers long and 100 kilometers high. These are the dimensions of the Orbiter's landing approach during which it is very sensitive to the presence of the slightest amount of moisture in condensed form in the surrounding atmosphere. If the conditions are not right for an immediate landing, the Orbiter is waived off for another orbit. If adverse conditions are expected to persist for a ionger period of time, the Orbiter is rerouted to Edwards Air Force Base in California. It is then brought back piggyhack on a 747 aircraft to the Kennedy Space Center, an expensive proposition.

In addition to the demanding requirements for shuttle landing, there are numerous needs for accurate "nowcasting" in the various phases of preparation for a space iaunch, such as transfers of payloads from preparation site to launch site, various weather sensitive tasks on-site, threats of direct and induced effects of lightning, etc.

3. Available Meteoroiogical Data

In its sophisticated task of precision noweasting in addition to its capabiiity for more conventionai but stiil high accuracy forecasting, the MIDDS is supported by the following data sets:

a. Two GOES local earth stations (for COES East and a GOES yet to be launched) indicating cloud cover in the visibie and infrared.

b. An extensive mesonetwork of sixteen stations in the Cape/KSC area for surface observation (between ground and the 150 meter level) supplying wind speed and direction, temperature, and dew point. Additional stations are being installed on the mainland to the west.

c. An upper air data acquisition system consisting of rocketsondes, rawinsondes, jimspheres, and windsondes, both at the Cape and at downrange stations, and two ground-based telemetry and tracking systems.

d. A local 5cm weather radar with backup from other weather radars located 130 kilometers to the north, 220 kilometers to the west and 300 kilometers to the south. Next fall we shall have the added capability of a volumetric display of weather radar data; in this mode we shall be storing conventional data scanned in azimuth and elevation for the whole three-dimensional space and then display it along any desired cross section of the atmosphere, such as, for instance, the Shuttle landing approach.

e. An extensive network of field mills (a total of 34 scattered over the Cape/KSC area).

f. A dual array lightning location system which in conjunction with the field mill network supplies a very complete picture of lightning activity in an area of about 300 kilometers around the Cape.

g. In addition to the above local or near-local data sources, we receive the conventionai worldwide weather services from the National Weather Service, the National Oceanic and Atmospheric Administration, the Federal Aviation Administration, etc.

4. Available Dispiays

All of the above are ingested in the MIDDS and can be displayed with or without preprocessing and with the proper navigation and scaling appiied to the data for correct overiaying; these data can he displayed in a variety of presentations such as:

a. Cloud cover in two or three dimensions, in visible or infrared or computer enhanced comhination with a resolution of up to one km. The three dimensional presentation gives you a feeling of depth as you observe the cioud configuration from above.

b. The cloud imagery can be color enhanced or color coded to provide precipitation (from the weather radar), lightning and other information.

c. Severai such images taken at different times can be looped to give you the actual motion and evolution of weather conditions over a given period of time.

d. Streamlines of wind direction and velocity can be overlayed on this imagery.

e. Isotherms and isohars and other contours can also be overlayed or displayed separately.

f. Other information availiable includes atmospheric temperature profiles, Skew-T and Stuve thermodynamic diagrams, etc.

IV. THE PROVING GROUND AND ITS OPERATIONS

Now that I have described some of the technicai resources to be found at Cape Canaveral, let me teli you some of the uses researchers have made of them.

a. This is the second season that an FAA instrumented aircraft will be flying in the area, being vectored in and out of thunderstorms by Cape Canaverai ground instrumentation. Some of the video cameras and

timing units used on board to recrod lightning striking the aircraft and the time of the events are on loan from the Cape. It has also flown over lightning triggering rockets and their launch by a French crew was synchronized with the aircraft position overhead.

b. Ground instrumentation for lightning research from the Wright Flight Dynamics Laboratory was used to make observations synchronized with those made by the FAA aircraft. It was also used to make other observations, including electromagnetic propagation over the ocean.

c. Other lightning research was conducted either independently or in coordination with the above projects by various research organizations, including the Universities of Florida and Arizona and by the State University of New York at Albany.

d. Currently the NASA Marshall Space Flight Center has a wind profiler doppler radar being tested at the Cape with weather data and logistics support being supplied by the Air Force.

If you personally have an interest in taking advantage of our resources, describe your needs in a letter to me and I shall be able to tell you how we can support you and supply you with additional details that would be of interest to your specific needs.

CONCLUSION

The meteorological community in general and the lightning community in particular are often looking for hard to find resources to perform their research under better controlled conditions and at less cost. The Cape Canaveral area constitutes a proving ground with almost limitless capabilities for this type of research. Although not engaged in research itself, the Eastern Test Range encourages such research from which it hopes to glean practical results needed in its operations.

References

[1] "International Aerospace and Ground Conference on Lightning and Static Electricity", Proceedings 1983, 1984

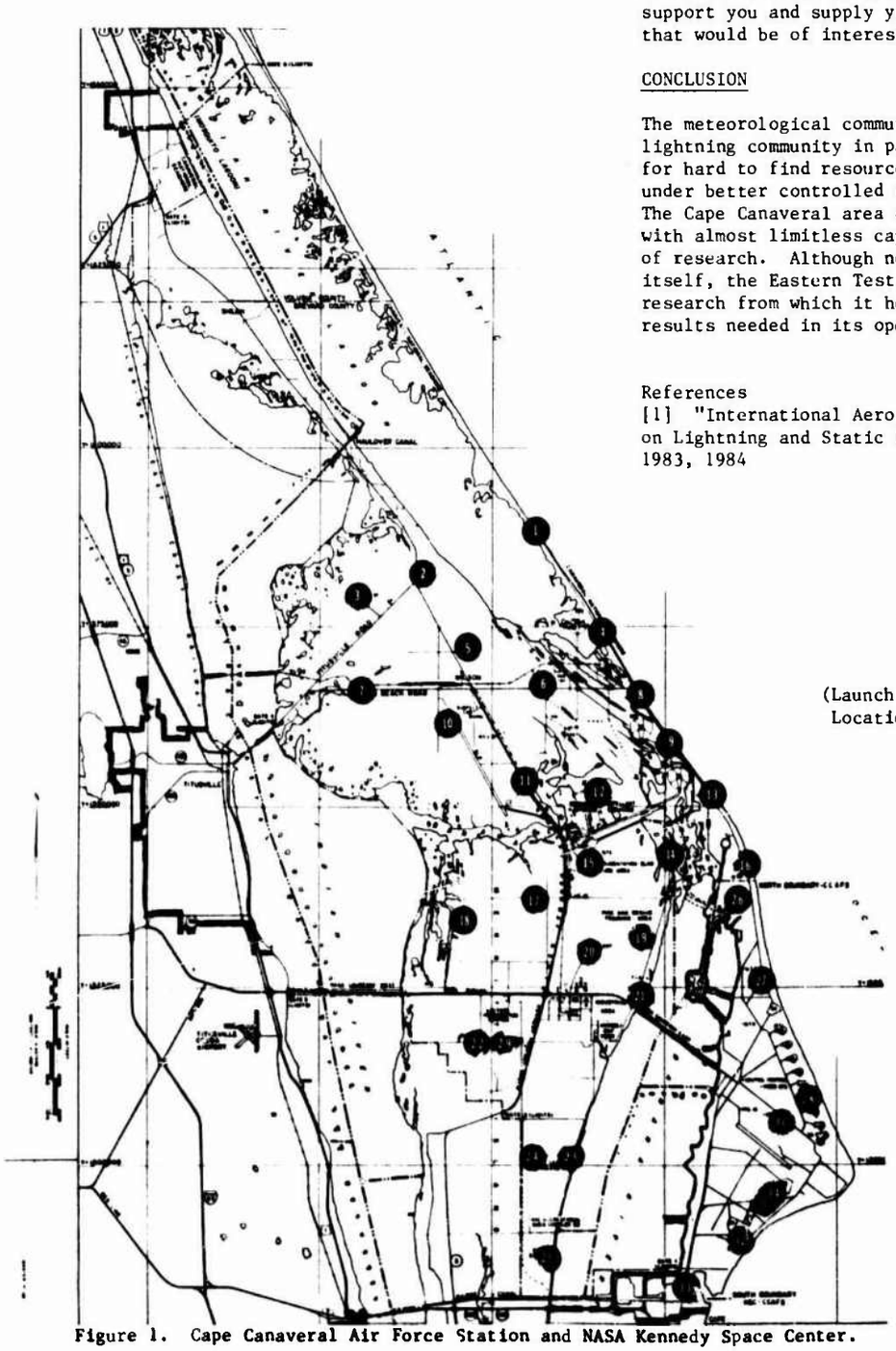


Figure 1. Cape Canaveral Air Force Station and NASA Kennedy Space Center.

CHARACTERISTICS OF CLOUD-TO-GROUND LIGHTNING FLASHES ALONG THE EAST COAST OF THE UNITED STATES

R.E. Orville Sr., R.B. Pyle, R.W. Henderson, R.E. Orville Jr. and R.A. Weisman

Department of Atmospheric Science, State University of New York at Albany, Albany, New York 12222, U.S.A.

Abstract - A magnetic direction-finding network for the detection of lightning cloud-to-ground strikes has been installed along the east coast of the United States. Most of the lightning occurring from Maine to Florida and as far west as Ohio is detected. Time, location, flash polarity, stroke count, and peak signal amplitude are recorded in real time. Flash locations, time, and polarity are displayed routinely for research and operational purposes. Flash density maps have been generated for the summers of 1983 and 1984, when the network only extended to North Carolina, and show density maxima in northern Virginia and Maryland.

I.- INTRODUCTION

The detection and location of lightning by a new magnetic direction-finding technique (1) must be considered one of the more interesting instrumental developments in recent years. Extensive networks of lightning direction-finders (DF) have been established for forest fire detection in the western United States, Canada, and Alaska, and research systems have been used in Florida and Oklahoma.

Principles of the direction-finding system

The lightning direction-finding system has been described previously (1). The basic system consists of an orthogonal magnetic-loop antenna, a flat plate antenna, and associated electronics to process the incoming signals. The bandwidths of the antenna systems are wide (approximately 1 kHz-1MHz) so that the shapes and polarities of the lightning field waveforms are preserved. The orthogonal magnetic-loop antenna senses the magnetic field from lightning and a voltage is induced in each loop that is proportional to the magnetic field derivative multiplied by the cosine of the angle between the plane of the loop and the direction of propagation of the incoming field. The ratio of the integrated voltages in the orthogonal loops provide the direction to the lightning flash. A 180° ambiguity in direction is removed by an electric field antenna that senses the polarity of the charge lowered to the ground. The processing electronics are designed to respond only to those field shapes that are characteristic of return strokes in cloud-to-ground flashes.

EAST COAST NETWORK

Nine high gain direction finders have been installed along the east coast to record lightning ground strikes, Fig. 1

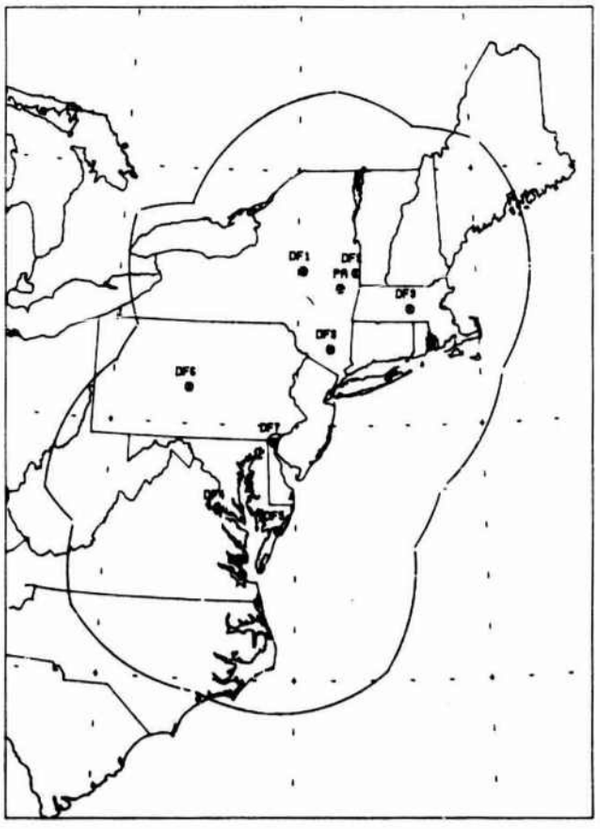


Fig. 1 The location of nine high gain lightning direction finders are shown in the east coast lightning detection network for the summers of 1983 and 1984.

The nine direction finders are located in New York (at Little Falls, Cambridge, and Newburgh) three in Virginia (at Dahlgren, Wallops Island, and Langley), one in Pennsylvania (at State College), one in Delaware (at the Greater Wilmington Airport), and one in Massachusetts (at the Worcester Airport). Each direction finder has a nominal range of 400 km and where two or more direction finders overlap in their coverage, we have sketched a line to enclose the area covered by the network. Within this region, we estimate that 70 to 80 percent of the ground strikes are detected. Outside this region, a smaller percentage of lightning ground strikes are detected.

All 9 DF's are controlled by a position analyzer microcomputer that is located in the operations room at the State University of New York at Albany. This is labeled as PA in Fig. 1. Communications between the position analyzer and the DF's are over a full duplex, 2400 baud, synchronous-leased circuit that operates continuously throughout the year. The position analyzer monitors the status of each remote DF and the data link by polling the DF's at a rate of five stations per second.

When a DF senses a lightning ground flash, the signals for up to 14 return strokes are processed by the DF microcomputer. The time, angle, signal amplitude, and polarity of the first return stroke, and the stroke count (multiplicity), then are stored in memory until it is polled by the position analyzer. When two or more DF's record a flash within a programmed time interval (typically 6 msec) the location of the flash is computed and plotted. The data associated with the flash are displayed on video graphic terminals, and recorded on nine-track tape. The results can then be analyzed for flash characteristics such as flash density as a function of location and time.

Flash density results

At the request of the Electric Power Research Institute (EPRI), the ground strike flash density has been monitored since June of 1983. Two summers of observations have been completed. Figure 2 shows a flash density map that is produced by combining the ground flash data for June 1983 and June 1984. The contour interval is 500 ground flashes over an area of 50 x 50 km. Thus the first contour represents a flash density of 500 flashes per 2 500 km^2 or 0.2 flashes per km^2. The first dark contour is the fifth one and corresponds to 2 500 flashes or a flash density of 1 per km^2. The origin of the plot is at the lower left corner and is at 35 degrees north latitude and 85 degrees west longitude. The size of the plot is 1 500 by 1 500 km. Significant maxima appear where the Potomac River enters the Chesapeake Bay along the Virginia -Maryland border and near the Pennsylvania, New Jersey, New York border. Lesser maxima occur in southwestern

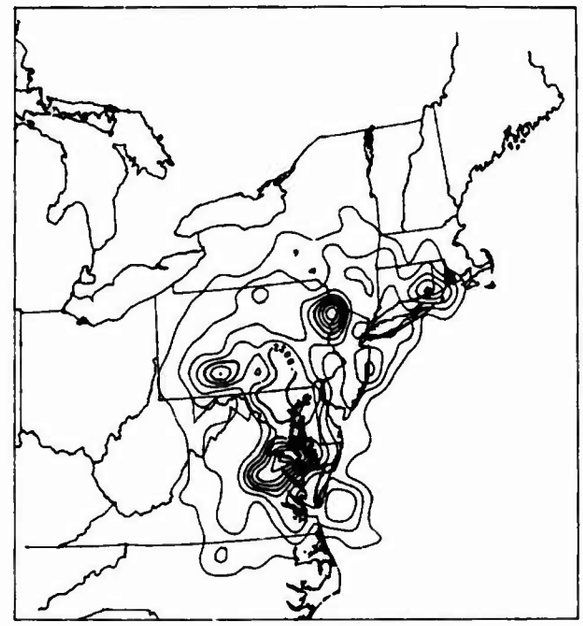


Fig. 2 Contours are shown for the composite flash density for the months of June 1983 and 1984.

Pennsylvania and southeastern Connecticut. The decrease of the flash density along the periphery of the network, see Fig. 1, is the result of the decreasing sensitivity of the network. The local maxima over the Atlantic Ocean to the southeast of Delaware is the result of a site error and will be removed in future plots as soon as the corrections are evaluated.

The flash density for the combined months of July 1983 and July 1984 is shown in Fig. 3. The parameters of the plot are the same as for Fig. 2. Note that the maximum flash density occurs near the Virginia - Maryland border where the Potomac River enters the Chesapeake Bay. The highest flash density is 1.8 flashes per km^2 for this composite plot. The maximum along the Pennsylvania - New Jersey border in June (Fig. 2) has now shifted to northern New Jersey. Other less prominent maxima occur along the east coast.

The flash density plot for the final month of summer is shown in Fig. 4 where we have combined the ground flash density values for August of 1983 and 1984. The maximum flash density has shifted to central Virginia where values exceeding 5 000 ground flashes per 50 by 50 km are shown. This corresponds to ground flash densities exceeding 2 per km^2 for the two combined months. A maximum appears in the eastern New York area with values reaching 1.8 flashes per km^2. A smaller maximum occurs in West Virginia and indicates the influence of the Applachian Mountains.

The total number of flashes recorded in the summer months of 1983 and 1984 exceeds 1 000 000. The detection efficiency of the

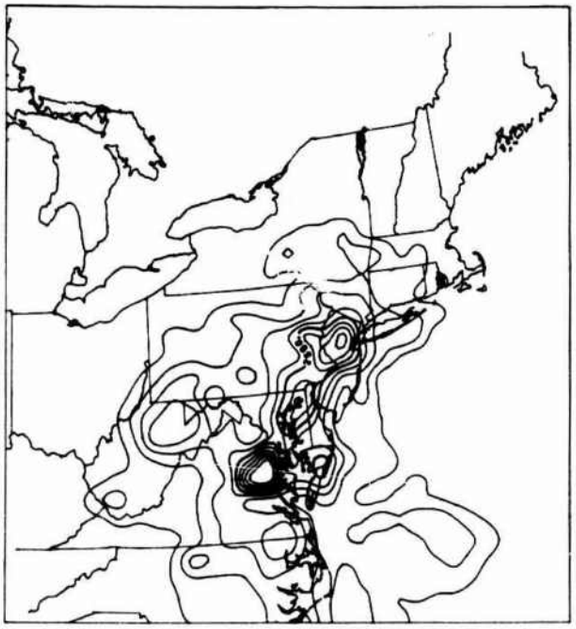


Fig. 3 Lightning ground flash density for the months of July in 1983 and 1984.

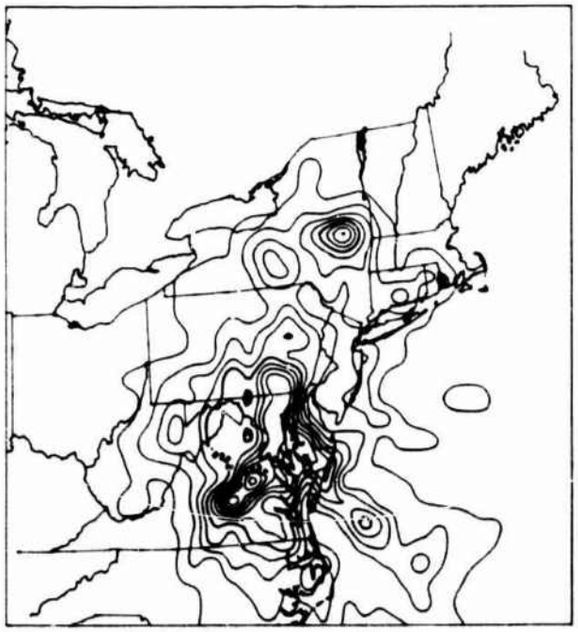


Fig. 4 Lightning ground flash density for the months of August in 1983 and 1984.

network as a function of space is unknown at this time, but studies in parts of the network suggest that it ranges from 50 to 70 percent in 1983 to much higher values in 1984 because of the installation of improved software in the position analyzer microcomputer. We believe that the relative values of the flash densities show significant variations that are real. Flash density maps for smaller areas to meet the needs of utilities can be generated from our data base over a grid size as small as a few kilometers.

Peak current estimates and polarity

The network records the peak amplitude of the magnetic field and the polarity of the charge lowered to ground in each lightning flash. We have summarized these data for the summers of 1983 for both negative and positive lightning ground flashes.

Figure 5 shows a histogram of the normalized radiation values to a distance of 100 km for all negative flashes detected in the summer of 1983. Nearly 500 000 cloud-to-ground flashes lowering negative charge were recorded. The abscissa has a median value of 162 and this can be related to the median value of the peak current reported by Berger (2) for negative flashes to the instrumented towers of the Mt. San Salvatore. Berger's median value was 30 kA and is assumed to match the median value for the ground flashes recorded by the East Coast Network. Since the peak magnetic field is linearly related to the peak current, a value of 500 on the abscissa corresponds to approximately 100 kA and a value of 1 000 corresponds to approximately 200 kA. We note that few flashes lowering negative charge exceeded a peak current of 100 000 amps.

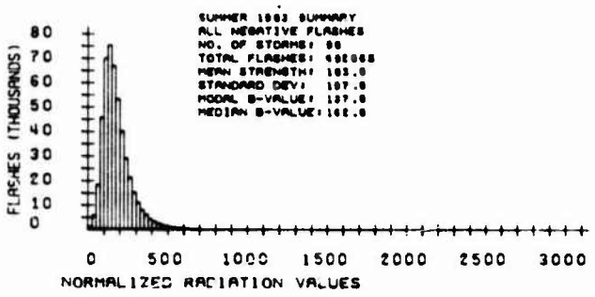


Fig. 5 Distribution of the peak magnetic field values for first strokes in negative flashes to ground. The units are high gain values from the direction finders normalized to 100 km.

A similar histogram plot for 16 000 ground flashes for the summer of 1983 lowering positive charge is shown in Fig. 6. Note that the width of the histogram is significantly broader than the histogram for negative flashes shown in Fig 5. Also, note that the median magnetic field value is approximately 50 per cent higher implying a median peak current of 45 kA for positive flashes. It appears that lightning lowering positive charge has significantly higher peak currents. Perhaps it is these flashes that are the most damaging.

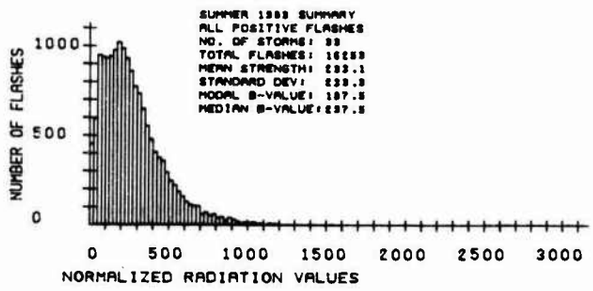


Fig. 6 Distribution of the peak magnetic field values for first strokes in positive flashes to ground. The units are high gain values from the direction finders normalized to 100 km.

Network expansion

During the fall of 1984 and the spring of 1985, the east coast network is doubling its size as lightning direction finders are installed along the east coast to Florida. Figure 7 shows the extent of the network.

It will be possible to monitor the development of thunderstorms throughout the network from one location at the State University of New York at Albany and to provide these data to any user within the network area. Data will be available in real time or from a file to aid in the operation use or the research use of the lightning data.

II-CONCLUSION

The results of this study show that the installation of a ground strike lightning detection network along the East Coast provides the first opportunity to monitor the flash density as a function of space and time. Flash density plots have been shown for combined months. It is also possible to plot the seasonal and annual distribution of lightning ground flashes. Peak normalized radiation values for first return strokes have been plotted for the summer of 1983 for flashes lowering negative charge and for flashes lowering positive charge. The median peak magnetic field for negative flashes indicates that the median peak current is 30 kA. The median peak magnetic field for positive strokes is 50 per cent higher implying a median peak current of 45 kA for positive flashes.

ACKNOWLEDGEMENTS - The establishment of a large lightning detection network requires the cooperation of many individuals and organizations who share our common research interests. We thank Andrew Landor and Vincent Idone for assistance with the direction finder site installations. We thank Cynthia Erdt for the preparation of the manuscript. This research was supported in part by the Electric Power Research Institute as part of a contract for lightning ground flash density measurements, by the National Science Foundation (ATM8400207) and the National Aeronautics and Space Administration (NAS833380).

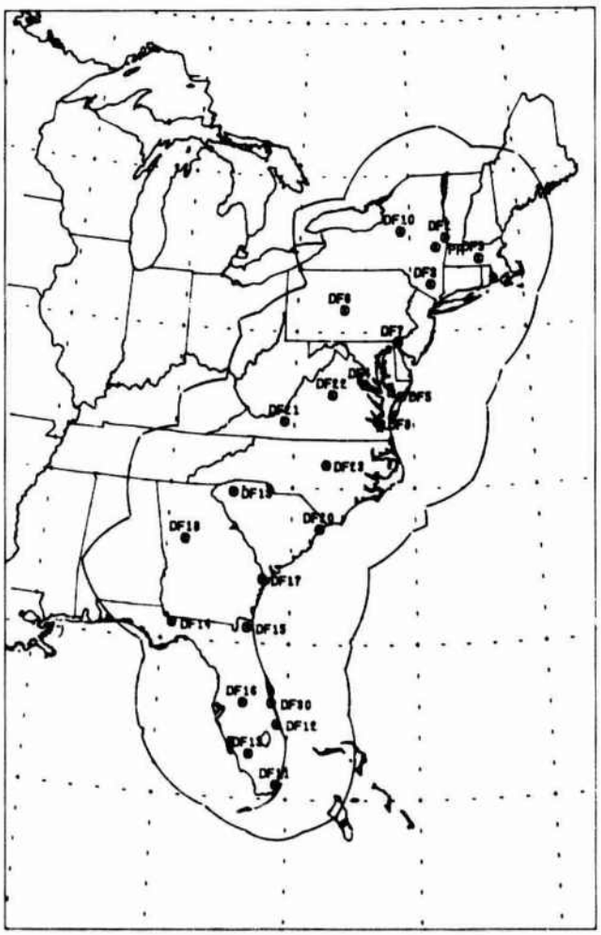


Fig. 7 The extent of the east coast lightning detection network is shown for the summer of 1985.

REFERENCES

1. Krider, E.P., A.E. Pifer, and D.L. Vance, 1980: Lightning direction-finding systems for forest fire detection. **Bull. Amer. Meteor. Soc., 61, 980-986.**

2. Berger, K., R.B. Anderson and H. Kroninger, 1975: Parameters of lightning flashes. **Electra, 41, 23-37.**

LOCATING ROCKET TRIGGERED LIGHTNING USING THE LLP LIGHTNING LOCATING SYSTEM AT THE NASA KENNEDY SPACE CENTER

M.W. Maier and W. Jafferis*

LLP Inc., 1001 South Euclid Ave, Tucson, Arizona 85719, U.S.A.
**NASA/SO, Kennedy Space Center, Florida 32899, U.S.A.*

ABSTRACT - Five rocket triggered cloud-to-ground lightning flashes were detected by the operational lightning locating system at the NASA Kennedy Space Center on August 17, 1984. The locating system, which was designed to detect natural lightning, detected at least 2 and as many as 5 strokes in the triggered flashes suggesti g that some of the strokes in the triggered lightning had signal amplitude and waveshape characteristics similar to natural lightning. However, not all triggered strokes were detected indicating that some strokes were atypical in nature. Since the ground strike point of the triggered flashes were known quite precisely, the accuracy of the lightning locating system was also evaluated. The 3 direction finders were found to have a mean bearing accuracy of $\pm$ 0.5-0.6^0. The distance error of the real-time position solutions of the locating system on the triggered flashes were in the range of 195-770 m with a mean of 460 m.

1. INTRODUCTION

During the summer of 1984 a team of scientists from the Centre d'Etudes Nucleaires (CEN), Grenoble, France triggered 8 lightning flashes during 3 separate thunderstorms at the NASA Kennedy Space Center (KSC) in Florida. The flashes were triggered using small ground launched hail- suppression rockets which trail a grounded conducting wire. The triggering technique and earlier results are described elsewhere (Fieux et al., 1975; Hubert and Mangas, 1983).

During one thunderstorm on August 17, 6 rockets were launched between 2003 and 2041 UT[1] triggering 6 cloud-to-ground lightning flashes. Five of the 6 lightning flashes were detected by the LLP Lightning Locating System which is operated for NASA by the U.S. Air Force at the Cape Canaveral Air Force Station (CCAFS). Of the 5 triggered flashes detected by the LLP Lightning Locating System, 4 flashes were located in real-time by triangulation from 2 or more of the responding direction finding stations. In the remaining case, only a single direction finding station responded to the triggered lightning so that no position could be calculated.

The detection of 5 of the 8 triggered lightning flashes by the LLP Lightning Locating System is significant for at least 2 reasons - (i) since the LLP Lightning Locating System is designed to detect only natural lightning return strokes, detection of the triggered lightning indicates that at least 1 stroke in the triggered flashes had waveshape and intensity characteristics similar to natural lightning return strokes (ii) since the location of the ground strike point of the triggered lightning is known quite precisely, comparison of the real-time positions determined by the LLP Lightning Locating Systems with the location of the trigger site provides a unique opportunity to make an undisputable evaluation of the operational accuracy of this lightning locating system.

In this paper, we examine in detail the real-time data generated by the LLP Lightning Locating System to better define the morphology of the storm during which the lightning flashes were triggered and to study the measured characteristics of the rocket triggered lightning flashes themselves. Special attention will be given to estimating the accuracy of the operational lightning locating system using the rocket triggered lightning. The measured accuracy data are then used as input to a simple model which graphically depicts the locating accuracy of the lightning system throughout its full operational range.

2. LOCATING SYSTEM

The lightning locating system installed at the NASA Kennedy Space Center is a commercial system developed and manufactured by Lightning Location and

1All times given here are Universal Time (UT). Eastern Daylight Time (EDT) is UT minus 4 hours.

Protection, Inc. (LLP) of Tucson, Arizona. The system was first installed on a trial basis during the summer of 1978 as part of the Federal Evaluation of Lightning Tracking Systems (FELTS) conducted for the U.S. Navy by Southwest Research Institute (Johnson, 1980). Based on the successful performance of this system during the FELTS test, a complete locating system was subsequently purchased and permanently installed to support the detection and warning of thunderstorm hazards at the Space Center. The LLP Lightning Locating System and a network of 34 electric field mills serve as the primary lightning hazard inputs to the Meteorological Interactive Data Display System (MIDDS) now being implemented to support the weather sensitive launch, landing, and ground operations of the Space Shuttle at KSC (Erickson et al, 1985).

The LLP Lightning Locating System at KSC is composed of 3 medium gain lightning direction finding stations installed in a roughly triangular array as shown in Figure 1. Each direction finder automatically detects the radio impulse generated by any lightning return stroke within a nominal range of 200 km and measures the bearing angle to the lightning ground strike point. Radio impulses from non-lightning background noise sources (e.g. radio, radar, ignition noise, etc.) and intra-cloud lightning are rejected by the direction finder electronics. Based on previous measurements, it is thought that the angular accuracy of the direction finder is approximately $\pm 1^0$ (Krider et al., 1978).

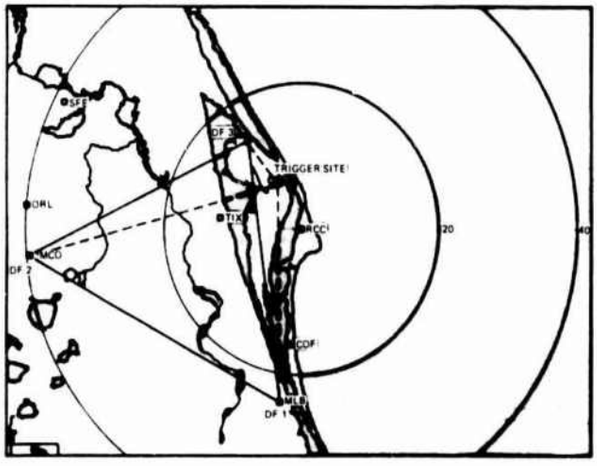


Figure 1. - Map of the Kennedy Space Center area showing the position of the 3 direction finding stations (DF) and the Rocket Trigger Site.

Once a lightning flash has been detected by the direction finder the azimuth, first stroke signal intensity, signal polarity, and the stroke multiplicity of the detected flash are transmitted to a central position analyzer using dedicated data lines. The position analyzer computes the location of each lightning flash in real-time by a triangulation of the time coincident inputs from 2 or more direction finders. The computed lightning location and raw direction finder data are transferred to a conventional hardcopy printer and magnetic tape recording system for archival and later analysis. The processed lightning data are also disseminated to high-resolution color displays which graphically show the location and evolution of lightning storms near the Space Center to aid the forecasting and warning of lightning and thunderstorm hazards. The maximum delay from the time of occurrence of a lightning flash to display, using this system, is 2 seconds. The overall lightning locating system configuration and operation is described by Krider et al. (1980) and Maier et al. (1984).

3.STORM MORPHOLOGY

Magnetic tape records for the storm of August 17, 1984 began at 1822. A plot of all 2083 cloud-to-ground lightning flashes detected and located by the LLP Lightning Locating System between 1822 and 2100 (when the storm ended) are shown in Figure 2. The bulk of the lightning occurred in a

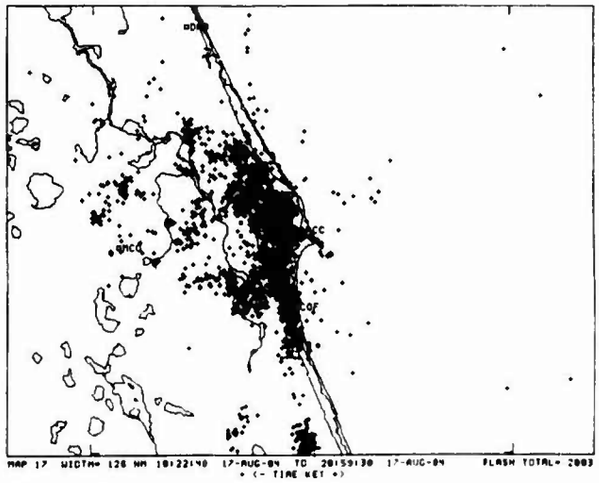


Figure 2. - Map of all cloud-to-ground lightning strike locations between 1822 and 2058 on August 17, 1984. 2083 flashes are plotted.

roughly north-south line extending down the Indian River from just north of the Space Center to over Melbourne. Surface wind data from the KSC wind tower network (not shown) indicates a strong seabreeze convergence zone moved inland from the Atlantic Ocean starting about 1640. The seabreeze convergence zone reached the Indian River about 1820 and probably initiated the development of the major north-south storm complex over and just west of the Space Center during the afternoon of August 17.

A histogram of the rate of occurrence of cloud-to-ground flashes within 56 km (30 NM) of the Range Control Center (RCC) at the Cape Canaveral Air Force Station is given in Figure 3. The storm was already producing cloud-to-ground lightning when the tape records began at 1822. The lightning rate quickly increased to a sustained level exceeding 10 flashes/min by 1840. The lightning rate remained above 10 flashes/min until 1950. The 10 flash/min storm cloud-to-ground lightning rate threshold is generally regarded as a reliable indicator of the transition from a moderate to severe thunderstorm. The average storm cloud-to-ground lightning rate in Florida is generally 1-2 flashes/min (Pakham,et al., 1984; and Maier and Krider, 1982). The 5-min average peak lightning rate of 28 flashes/min occurred between 1805-1810. This is one of the highest peak storm cloud-to-ground lightning rates yet detected using the LLP Lightning Locating System (Peckham et al., 1984 and Maier and Krider,1982).

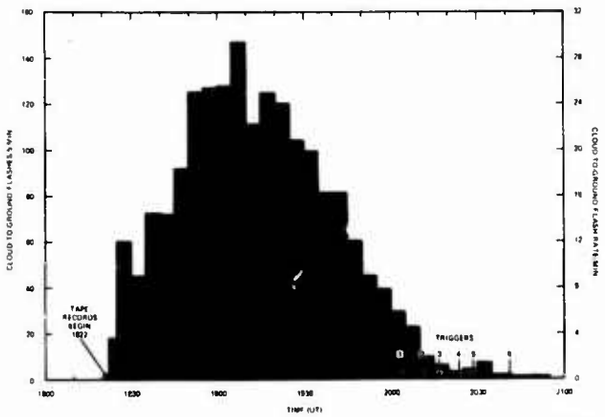


Figure 3. - Histogram of the cloud-to-ground lightning rate in the Kennedy Space Center area on August 17, 1984.

All 8 of the rocket launches and subsequent triggered lightning events occurred near the end of the storm (Figure 3). The storm cloud-to-ground lightning rate was about 5 flashes/min when the first rocket was launched decreasing to below 2 flashes/min for the last 5 launches. The last cloud-to-ground flash from the storm occurred about 2065.

The spatial evolution of the storms on the afternoon of August 17 are depicted in a series of cloud-to-ground lightning maps each covering successive 30 minute intervals (Figure 4). The major clusters of lightning (presumably the individual storms) have been identified and labeled on Figure 4. The major storm cluster (identified as C_1) is already active at the time of the first panel (Figure 4a) over the north end of the Indian River. In the subsequent maps (Figures 4b-4e) the storm either moves or develops to the southeast and passes over the north part of the Space Center and dissipates just off the east tip of Cape Canaveral. The storm reaches peak intensity between 1900 and 1929 (Figure 4c) while the storm is centered just east of the Shuttle Landing Facility (SLF).

The second major storm (C_2) forms over the Indian River southeast of the Space Center prior to 1830. Initially this storm strengthens and develops eastward (Figure 4b) and then shifts southward down the coast. Very few of the lightning flashes from this storm strike east of the coastline over the Atlantic Ocean. The storm dissipates near Melbourne after 2000. A second storm (C_3) forms just east of storm C_2 and move eastward over Lake Washington. This storm dissipates just as storm C_2 reaches peak intensity.

A number of other storms are also detected during this period. Storms C_4, C_5, C_6, and C_8 form progressively farther eastward from the Atlantic coastline. Storms C_7 and C_8 form inland from the coast well south of storm C_2.

The overall evolution of storms on this afternoon exhibit a high degree of organization. The initial activity occurs northeast of the Space Center with the major storms (C_1, C_2, and C_7) developing or progressing southward along the coast presumably in the zone of strong seabreeze induced convergence. Storms C_4, C_5, C_6, and C_8 develop inland in a west to southwest direction. The 7 storms which form well inland from the coast on this afternoon have shorter durations and produce far fewer flashes than the 2 major storms which form along the coastline.

4. TRIGGERED LIGHTNING EVENTS

The 8 triggered lightning events occurred during the dissipating stages of storm C_1 between 2003 and 2042. The only natural cloud-to-ground lightning from storm C_1 during this time occurred just southeast of the RCC approximately 10-12 km southeast of the trigger site. Approximately 4 natural cloud-to-ground flashes are detected on the Space Center following the last triggered flash.

The triggered lightning were identified using the lightning locating system records by their close proximity to the rocket launch site and time of launch. Since the background (non-triggered) lightning rate was quite low at this time, we don't believe there is any significant ambiguity in identifying the triggered flashes using the locating system records.

A list of the times of the first triggered lightning stroke as seen on KSC video tape records and the time of the first stroke recorded by the locating system are given in Table 1. The first stroke locating system times are between 467 and 860 milliseconds later than the first stroke times from the video tape. A mean delay of this magnitude can be accounted for by a difference in the relative time synchronization between the locating system and video system clocks. No special effort was made to synchronize these 2 clocks very precisely and a constant difference of from 467 to 850 milliseconds is not unexpected. However, since both clocks are known to be capable of maintaining time to an accuracy of from 2-8 milliseconds over durations comparable to the period during which the flashes were triggered, the large range in time differences between the two systems is an indication that the locating system may not have detected 1 or more of the first strokes in the triggered lightning events. If the relative time difference between the 2 clocks were in the range of 467-473 milliseconds, then the first stroke in flashes 3 and 6 would have been detected by the locating system and the first strokes detected by the locating systems in flashes 1, 2, and 4 would have occurred 285, 266, and 360 milliseconds, respectively, after the first triggered stroke appearing on the video tape records. These interstroke intervals are much longer than the normal interstroke intervals in natural lightning (Uman, 1969). However, return strokes with atypical waveshapes or those producing very small signal intensities may have occurred during these long interstroke intervals which were not detectable by the direction finders in the locating system.

4.1 Direction Finder Measurements

The original real-time direction finder data for all detected triggered lightning flashes are reproduced in Table 2. The data consists of the time of the first detected stroke, the bearing angle of the first stroke (in degrees from true north), the peak signal intensity of the first stroke (in relative units), and the number of strokes detected in the entire flash. This information is the standard data recorded on magnetic tape for each flash detected by the LLP Lightning Locating System. All 3 direction finders responded to triggered flash 1 and 2, while only direction finders 1 and 3 responded to triggered flash 4 and 5. Only direction finder 3 responded to flash 3. None of the direction finders responded to flash 8 (therefore, no data are shown for this event).

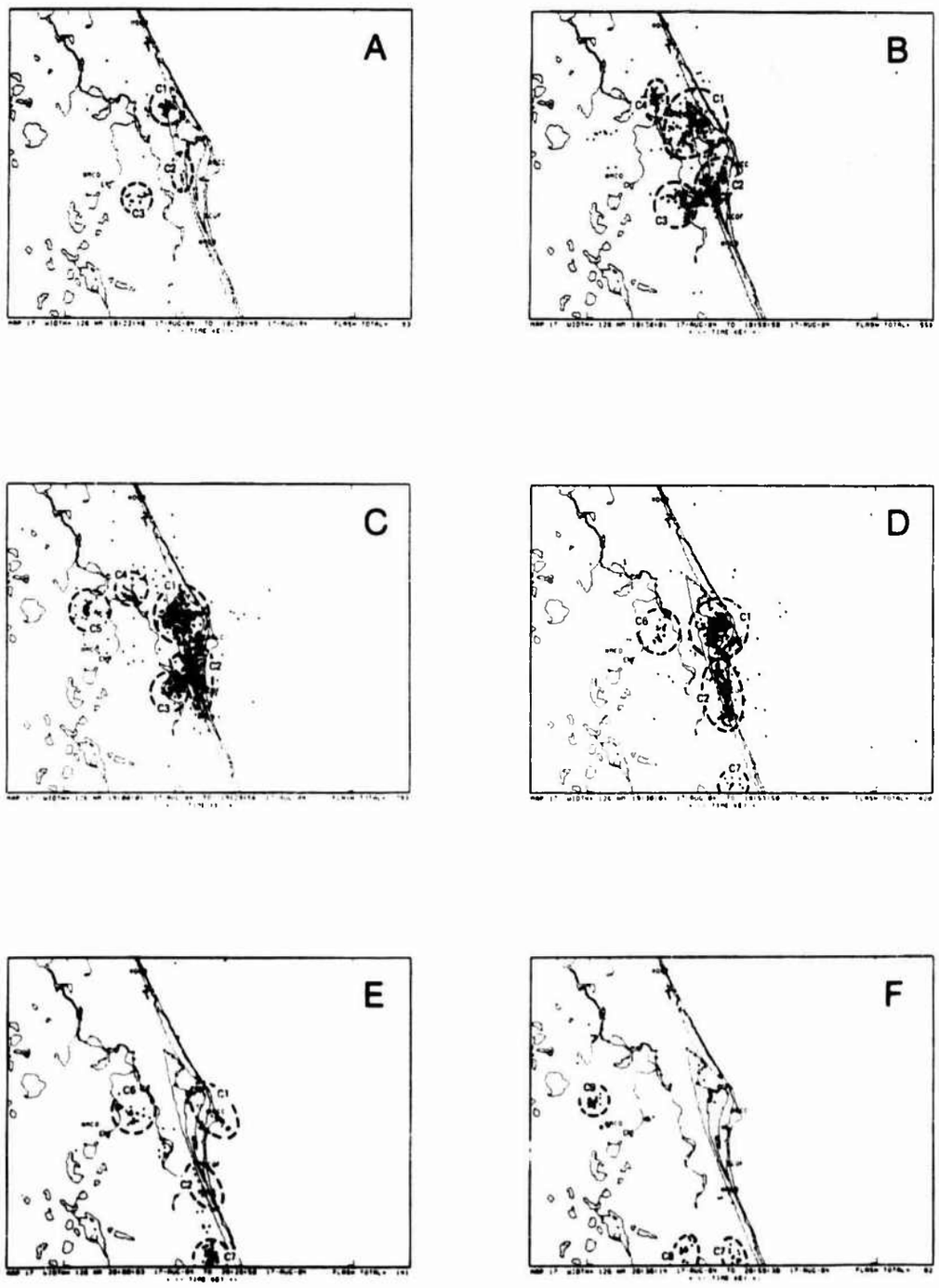


Figure 4. - Cloud-to-ground lightning maps for successive 30-min intervals on August 17, 1984. Major storm clusters are identified.

Table 1. - Times of the first detected stroke from both the KSC video tape records and the lightning locating system.

FLASH	CEN EVENT	KSC VIDEO	LOCATING SYSTEM
1	84-09	2003:41.87	2003:42.835
2	84-10	2010:57.07	2010:57.805
3	84-11	2017:44.20	2017:44.887
4	84-12	2023:58.85	2023:58.854
5	84-13	2028:48.82	2028:48.083
6	84-14	2041:02.88	-

The direction finders all detected different combinations of return strokes in each of the triggered flashes. In flash 1, direction finder 3 only detected one stroke 204 ms prior to the first stroke detected by direction finder 1. Direction finder 1 and 3 both detected three strokes later in this flash. Altogether, the direction finders detected a minimum of 4 strokes in flash 1. In flash 2, direction finders 1 and 2 both responded nearly simultaneously to the first detectable stroke although direction finder 2 only detected 1 stroke. Direction finder 3 did not detect its first stroke until 40 milliseconds after direction finders 1 and 2. It appears that a total of 4 strokes were detected in this flash. Only direction finder 3 responded to flash 3 and detected 4 return strokes. In flash 4, direction finder 3 detected 2 strokes starting 165 ms prior to the only stroke detected by direction finder 1. In flash 5, direction finder 1 responded first and detected 8 strokes while direction finder 3 first responded 72 ms later and only detected 5 strokes.

4.2 Direction Finder Bearing Accuracy

The bearing angles from each direction finder site to the triggered lightning flashes show excellent consistency from flash to flash. The differences between the actual and measured bearings from the direction finder sites to the triggered lightning site is given in Table 3. The accuracy of the actual (ground truth) bearing is limited only by our knowledge of the geographic positions of direction finder sites and the rocket trigger site, a value which we estimate to be $\pm.1^0$ or less given the small uncertainties in the surveyed coordinates of

Table 2. - Real-time direction finder data for the triggered flashes.

SITE	PARAMETER	FLASH 1	FLASH 2	FLASH 3	FLASH 4	FLASH 5
DF 1	Time	2003:42.831	2010:57.805	-	2024:59.818	2029:49.093
	Azimuth	059.6^0	359.0^0	-	058.4^0	359.5^0
	Sig Amp	50.5	196.6	-	42.4	67.0
	Strokes	3	4	-	1	6
DF 2	Time	2004:43.030	2010:57.810	-	-	-
	Azimuth	75.6^0	75.6^0	-	-	-
	Sig Amp	40.5	145.6	-	-	-
	Strokes	3	1	-	-	-
DF 3	Time	2003:42.665	2010:57.841	2017:44.887	2026:58.854	2028:48.165
	Azimuth	166.6^0	166.6^0	141.1^0	136.2^0	136.0^0
	Sig Amp	66.2	137.0	186.4	361.1	282.2
	Strokes	1	3	4	2	5

Table 3. - Direction finder bearing error (in degrees) for the triggered flashes.

Direction Finder	Flash 1	Flash 2	Flash 3	Flash 4	Flash 5	Mean Error
DF 1	0.4	-0.2	-	0.2	0.3	0.28 (0.10)
DF 2	-0.2	-0.2	-	-	-	0.20 (0)
DF 3	0.7	0.7	1.9	-1.0	-0.2	0.80 (0.63)

the sites. The mean bearing error (determined using the absolute value of the measured bearings) for the 11 direction finder measurements is 0.55 degrees with a standard deviation of 0.53 degrees. These errors are substantially less than the 1 standard deviation error of 1.8^0 measured by Krider et al. (1978), although Krider did report that the ground truth technique included an estimated error of approximately $\pm$ 1^0 so that the direction finders could have actually performed somewhat better in that test.

It is interesting to note that the mean bearing error of direction finder 3 is approximately twice that observed from either direction finders 1 or 2. We believe this direction finder exhibits slightly larger bearing errors than the other direction finders because it is located only 12.8 km from the trigger site compared to the 55.4 and 69.1 km ranges of the other 2 sites. As shown by Uman et al. (1980), magnetic direction finders of the type used at KSC are likely to exhibit larger bearing errors on close lightning due to polarization effects from lightning channels which are not exactly vertical. In fact, Uman's estimate of the polarization component of the direction finder bearing errors are in almost exact agreement with the observed bearing errors on the triggered lightning flashes. Not only does this tend to confirm Uman's calculations, but it is strong evidence that polarization effects from non-vertical channel sources are the dominant source of random error in magnetic direction finders of the type used here.

4.3 Triangulated Lightning Strike Locations

The positions of the 4 triggered flashes which were detected simultaneously by 2 or more direction finding stations were calculated by triangulation at the position analyzer in real-time. These locations are shown relative to the triggering site in Figure 5. Since flashes 1 and 2 were detected by all 3 direction finders, 3 position solutions are possible and each are shown. Flashes 4 and 5 were only detected by 2 direction finders so only a single position solution is displayed.

In cases where 3 or more direction finders respond to any lightning flash, several slightly different position solutions are possible since each combination of 2 direction finders yields a unique intersection. The position analyzer is programmed to use the pair of direction finders which yield the intersection having the highest probability of being nearest to the actual lightning strike location (Maier et al., 1984). Other more elaborate procedures for determining the optimum location of a lightning flash using multiple direction finder bearings have been developed but have not been implemented in the real-time system as yet (Hiscox et al., 1984).

The horizontal distance between the rocket trigger site and the real-time location determined by the position analyzer based on its selection of the best 2 direction finder intersections ranged from 195 to 770 m with a mean 485 m.

The 3 position solutions shown for both flashes 1 and 2 are calculated using the 3 sets of 2 direction finder bearings available for each flash. Accuracy triangles are drawn for each flash with the 3 position solutions serving as vertices. The size of these accuracy triangles are a useful measure of the probable accuracy of the lightning position solution offered by the position analyzer. For example, in flash 1 the position analyzer solution was based on the direction finder 1 and 3

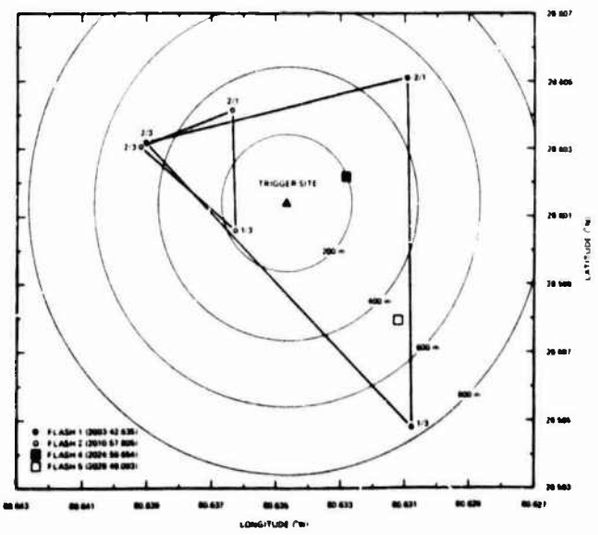


Figure 5. - Triangulated locations of the 4 triggered lightning flashes. Accuracy triangles are drawn for all three intersections in flashes 1 and 2 since all 3 direction finders responded in these 2 cases. Only single fixes available for flashes 4 and 5.

Table 4. - Estimated Peak Current [in kiloamperes] for the triggered flashes. Asterisks denote first detected strokes.

DIRECTION FINDER	FLASH 1	FLASH 2	FLASH 3	FLASH 4	FLASH 5
DF 1	18.7	73.7*	-	15.7	24.8
DF 2	18.7	87.3*	-	-	-
DF 3	7.0*	11.5	18.7	30.4*	24.6*

intersection which is approximately 770 m from the triggered lightning strike location. In flash 2, the position analyzer solution was based on the direction finder 2 and 3 intersection about 480 m from the triggered lightning strike location. In both cases, the size [length of the sides] of the accuracy triangles is approximately the same as the position error of the real-time solutions. Thus, the size of the accuracy triangles appears to provide a good first-order estimate of the uncertainty of the real-time position solutions determined by the lightning locating system.

4.4 Peak Current Estimates

As mentioned earlier, the direction finders also measured the peak magnetic field of the first detected return stroke of each flash. Since the absolute calibration of the signal amplitude measurement circuits in the direction finders are known with some certainty, the peak current of the first detected stroke can be estimated using an appropriate model which relates peak measured magnetic field intensity to peak current. Here we use the transmission line model of Lin et al. [1980] and a return stroke velocity of 1×10^8 m/s. The model is incorporated into the position analyzer and prints the estimated peak current in kiloamperes for each flash.

The accuracy of this peak current estimation technique is not well known. Errors can result from uncertainties in the absolute calibration of the direction finder, direction finder digitization errors, data transmission errors, uncertainties of the transmission line model itself and errors in the estimate of the lightning return stroke velocity. To judge the possible size of these errors in a collective sense, we have tabulated the estimated peak current for all natural lightning flashes detected by all three direction finders during storm C_1 within 12 km of the rocket triggering site [Figure 6]. The sample includes 222 measurements of which all [or most] are presumed to be first strokes of the flash. The median estimated peak current is found to be 35 kA which is within $\pm$ 20% of the generally accepted median first stroke peak current for natural cloud-to-ground lightning flashes [Anderson and Eriksson, 1980].

The estimated peak currents for the rocket triggered lightning flashes are given in Table 4. As mentioned earlier, the first strokes detected by all direction finders for the five triggered flashes were different strokes with the exception of flash 2 for which both direction finder 1 and 2 detected the same stroke [2010:57.805-810]. For this stroke, direction finder 1 reported an estimated peak current of 73.7 kA and direction finder 2 an estimated peak current of 87.3 kA. These two measurements agree within 10% which is about half of the estimated error of our peak current measurements.

With the exception of the direction finder 1 and 2 measurements on flash 2, all of the other estimated peak currents are less than the median peak current for natural lightning in storm C_1 of 35 KA. In fact, some of the peak currents are rather small [7-15 kA] which is in general agreement with the earlier direct measurements of the peak current of rocket triggered lightning flashes.

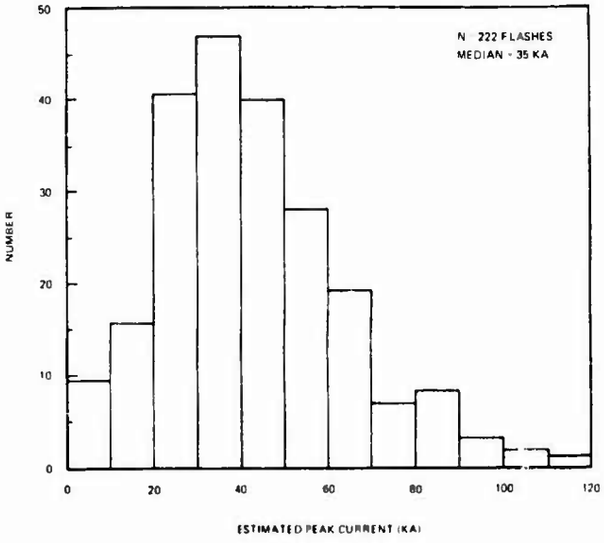


Figure 6. - Estimated peak currents for all natural lightning first strokes detected within 12 km of the rocket trigger site during storm C_1.

5. OVERALL LIGHTNING LOCATING SYSTEM ACCURACY

The position accuracy of the lightning locating system throughout its entire operating area can be estimated knowing that the direction finders exhibit a mean bearing error on lightning of ± 0.5-0.6^0 using a technique similar to that of Stansfield [1947].

Figure 7 shows an array of ellipses which enclose the estimated one standard deviation location error for lightning flashes detected by the Kennedy Space Center lightning locating system throughout central Florida [an area which is about twice the nominal operating range of this particular system]. These ellipses were generated assuming the standard deviation of the bearing error from each direction finder were 0.8^0 and were constant with range.

The 0.8^0 standard deviation used to generate the error ellipses shown in Figure 7 is slightly larger than the 0.5-0.6^0 standard deviation measured on the triggered lightning. The larger standard deviation was used to compensate for the slightly larger bearing errors observed on lightning close to the

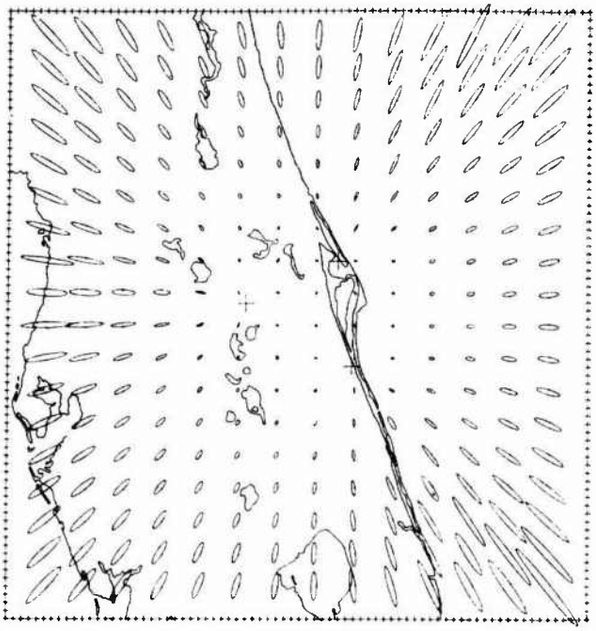


Figure 7. - One standard deviation error ellipses for the Kennedy Space Center Locating System assuming a normally distributed direction finder error having a standard deviation of 0.8^{0}.

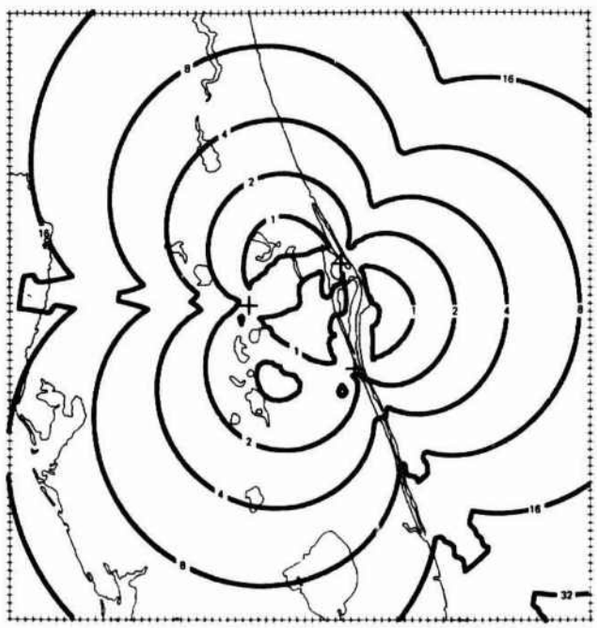


Figure 8. - Isopleths of the longest axis of the error ellipses shown in Figure 7 in kilometers.

direction finder stations and uncertainties in the long-term stability of the alignment of the direction finding antennas. Thus, the error ellipses presented in Figure 7 are conservative in the sense that they are larger than would be expected given the actual performance of the direction finders on the 5 triggered lightning events reported above.

Inside the triangle formed by the 3 direction finders which form the Kennedy Space Center Network, the lightning locating system errors are quite small and basically circular in shape (Figure 7). Outside the triangle, the errors gradually change from circular to elliptical and increase in size. The ellipticity of the locating system position errors increases with range particularly along the three baselines formed by the direction finder pairs. This effect is due to small random direction finder errors which produce larger position errors when the direction finder bearings intersect at a small angle.

We have quantified the locating system errors by generating a plot of the one standard deviation position error isopleths throughout central Florida (Figure 8). Because of the elliptical nature of the locating system errors, the position error isopleths are half the length of the major axis of the error ellipse. Thus, this is the largest position error expected (at the one standard deviation level) at any given location throughout the network. Typical errors will be smaller than those shown in most cases.

Within 40-80 km of the center of the KSC Lightning Locating System (an area which includes the Space Center itself), the position errors are generally circular with a 1 standard deviation radius of 1.0 km or less. As expected, these errors are in good agreement with the direct measurements on the triggered lightning as reported earlier. In fact, if a 1 standard deviation direction finder bearing error of $0.6-0.8^{0}$ were used instead of the 0.8^{0} value, the system position errors over and near the Space Center would be in the 500 m range, a value which agrees very closely with the measured mean horizontal error observed on the 4 triggered flashes detected in real-time by the Lightning Locating System.

The maximum locating system errors increase with range primarily due to the increasing ellipticity of the lightning location fixes. Within 2 baseline lengths (roughly 120 km) the largest errors are no worse than 16 km , and are 8 km or less where the lightning flashes occur roughly perpendicular to any of the 3 direction finder baselines. Better locating accuracy at longer ranges can be obtained by increasing the direction finder baselines at the expense of locating accuracy inside the network.

6. SUMMARY

The rocket triggered lightning flashes during the summer of 1984 were successfully detected by the operational lightning locating system at the Kennedy Space Center. This lightning locating system is normally used to help detect, locate, and warn of lightning hazards which might impact Space Center operations. The Lightning Locating System data provided a unique opportunity to better understand some of the characteristics of the triggered lightning flashes and at the same time evaluate the overall performance of the lightning locating system itself. Some of the significant findings based on the analysis of the 5 triggered lightning events include:

1. The direction finders, which were designed to detect natural lightning return strokes, detected at least 2 and as many as 8 return strokes in 5 of the 9 triggered lightning flashes. No strokes were detected from the sixth flash. Thus, at least 2 and as many as 8 strokes in each of the last 5 triggered flashes had signal amplitude and waveshape

characteristics typical of natural lightning.

2. Four of the 9 triggered lightning flashes were detected by 2 or more of the direction finding stations and were subsequently located by triangulation for a system detection efficiency of 0.67. This is slightly less than the 0.84 detection efficiency measured earlier for the same lightning locating system on natural lightning (Johnson,1980). Also, the first strokes detected by the locating system for at least 3 of the flashes followed the first stroke seen on the video records by 295 to 390 ms. Thus, not all of the strokes produced by the triggered lightning had signal amplitude and waveshape characteristics typical of natural lightning and were not detected by the locating system. There is some indication that these atypical strokes occur earlier in the flash rather than later.

3. We estimate that the peak currents produced by the first detected strokes of the triggered flashes had a range of from 25-71 kA. The later strokes had an estimated peak current range of from 7-24 kA. The median first stroke peak currents for natural lightning during this storm was 35 kA. The peak currents are estimated to be accurate to within 10-20%.

4. The overall evolution of the storms on August 17, 1984 near the Space Center were well depicted by the operational lightning locating system. The triggered lightning flashes occurred late in the lifecycle of one of the longest lived, strongest storms detected that day. This and another strong storm formed and grew in a narrow north-south band along the Atlantic coast in an area of presumed strong seabreeze convergence. The consistent pattern of new storm (or cell) development or motion southward along the coast and southwestward inland during the course of the afternoon is further evidence of the utility of real-time lightning locating systems as an aid to the improved short term warning of lightning and thunderstorm hazards.

5. The direction finders exhibited a mean bearing error of 0.55^0 (standard deviation of 0.53^0 on 11 measurements) on the triggered lightning flashes. The bearing errors were slightly larger when the direction finder was closer to the lightning, presumable due to polarization effects from non-vertical channel segments.

6. The locations of the triggered lightning flashes computed in real-time by triangulation from 2 or more of the direction finding stations were in the range of 195 to 770 m from the rocket launch site. The mean error was 460 m. These position errors are in excellent agreement with the expected errors for a direction finding network having a sensor configuration like that used at the Space Center with direction finder bearing accuracy in the range of 0.5-0.8 degrees.

Because of the relatively small number of rocket triggered lightning flashes upon which these results are based, we advise caution when drawing any firm conclusions from the above observations. However, additional rocket triggered lightning experiments at the Space Center are desirable in order to increase the number of measurements so that these initial results can be confirmed. It would also be desirable to launch the triggering rockets at several other locations within the operating range of the locating system to learn more about the effects of range on direction finder accuracy and to confirm the overall system accuracy plots given in Figures 7 and 8. Finally, the lightning triggering capability appears to offer an excellent opportunity to test the accuracy and reliability of new lightning locating systems and techniques which may be developed.

REFERENCES

Anderson, R.B., and A.J. Eriksson, A Summary of Lightning Parameters for Engineering Applications, Electra, 69, 65-102, 1980.

Erikson, J.E., B.F. Boyd and J.W. Oliver, Meteorological Interactive Data Display System (MIDDS) Data Base, Preprints, International Conference on Interactive Information and Processing Systems for Meteorology, Oceanography, and Hydrology, Amer. Meteor. Soc., Boston, MA, 1985.

Fieux, R., C. Gary and P. Hubert, Artificially Triggering Lightning Above Ground, Nature, No. 257, 212-214, 1975.

Hubert, P. and P. Mouget, Return Stroke Velocity Measurements in Two Triggered Lightning Flashes, J. Geophys. Res., 86, 5253-5261, 1981.

Johnson, R.L., Federal Evaluation of Lightning Tracking Systems (FELTS), Final Report, Prepared for Office of Naval Research under contract N00014-79-C-0223 with Southwest Research Institute, San Antonio, TX, 1980.

Krider, E.P., R.C. Noggle and M.A. Uman, A Gated, Wideband Magnetic Direction Finder for Lightning Return Strokes, J. Appl. Meteor., 15, 301-308, 1976.

Krider, E.P., R.C. Noggle, A.E. Pifer, and D.L. Vance, Lightning Direction-Finding Systems for Forest Fire Detection, Bull. Am. Meteor. Soc., 61, 980-986, 1980.

Lin, Y.T., M.A. Uman, and R.B. Standler, Lightning Return Stroke Models, J. Geophys. Res., 85, 1571-1583, 1980.

Meier, M.W., and E.P. Krider, A Comparative Study of the Cloud-to-Ground Lightning Characteristics in Florida and Oklahoma Thunderstorms, Preprints, 12th Conference on Severe Local Storms, Am. Meteor. Soc., Boston, MA, 1982.

Meier, M.W., L.G. Byerley, R.C. Binford, W.L. Hiscox, E.P. Krider, A.E. Pifer, and M.A. Uman, Gated, Wideband Magnetic Direction-Finders for Locating Cloud-to-Ground Lightning, Preprints, VII International Conference on Atmospheric Electricity, Am. Meteor. Soc., Boston, MA, 1984.

Peckham, D.W., M.A. Uman, and C.E. Wilcox, Jr., Lightning Phenomenology in the Tampa Bay Area, J. Geophys. Res., 89, 11783-11805, 1984.

Stansfield, R.G., Statistical Theory of D.F. Fixing, J. IEEE, Part IIA, 762-770, 1947.

Uman, M.A., Y.T. Lin, and E.P. Krider, Errors in Magnetic Direction Finding Due to Non-Vertical Lightning Channels, Radio Sci., 15, 35-39, 1980.

OPERATIONAL USES OF DATA FROM SEVERAL LIGHTNING POSITION AND TRACKING SYSTEMS (LPATS)

W.A. Lyons, R.B. Bent* and W.H. Highlands*

*R*SCAN Corporation, 511 Eleventh Avenue South, Minneapolis, MN 55415, U.S.A.*
**Atlantic Scientific Corporation, 2711 S. Harbor City Blvd, Melbourne, FL 32901, U.S.A.*

Abstract - LPATS - the Lightning Position and Tracking System - is an operationally deployed lightning ground strike detection network that utilizes a time-of-arrival (TOA) technique. Atmospheric convective phenomena can be monitored in real-time from the mesoscale (10 km or less) to the subsynoptic scale (over 1000 km across). Theoretical estimates of locational accuracy suggest mean errors on the order of 100 m near the network center, slowly degrading to several thousand meters at distances beyond 800 km range. Numerous indirect indications suggest a slow fall-off of detection efficiency with range. The first LPATS network became operational over the Florida peninsula in July, 1982. Two additional civilian subscription-funded networks have been added in the ensuing two years. In addition to the military, LPATS data are employed by utilities, private meteorological firms, industrial organizations, and commercial broadcasting stations. LPATS data have undergone intensive meteorological analysis. It has become apparent that lightning occurs in highly organized patterns more often than as randomized events embedded within storms. A series of case studies will be presented showing the patterns documented to date. At times, lightning ground strokes appear to be concentrated within relatively small "generating cells", most likely associated with active updraft cores. At the other extreme of convective systems, lightning associated with a mesoscale convective complex (MCC) appeared to be highly organized, advancing almost as a solid "wall" associated with the gust front that characterizes the leading edge of such systems. Observations of Hurricane Diana revealed a well defined banded structure. More interestingly, a lightning generating cell was observed to rotate about the eye wall. Observations of winter lightning associated with snow storms in the Upper Midwest are detailed. Thunderstorms forming along a stationary front extending from Nebraska to Wisconsin produced over 31,500 strokes in 4 hours in a narrow corridor.

I - INTRODUCTION

Lightning and atmospheric electrical phenomena have been investigated using a wide variety of sensors and platforms. In addition to acoustic and optical studies, storm electricity has been monitored using devices ranging from relatively simple flash counters (Anderson, et al, 1979) to spherics monitors (Kohl, 1980), to VHF interferometric techniques (Proctor, 1980; Hayenga and Warwick, 1981). Lightning has been observed via conventional radar (Ligda, 1956; Mazur and Rust, 1983). Even before the possible deployment of a lightning mapping satellite (Christensen, et al, 1980), lightning has been studied from above using aircraft (Christian, et al, 1983), the DMSP polar orbiting satellite (Orville, 1983), and the Space Shuttle (Vonnegut, et al, 1985).

For the operational location of lightning cloud-to-ground (CG) strokes, however, there are essentially two accceptable approaches: 1) magnetic direction finding (MDF) (Krider, et al, 1976), and 2) time-of-arrival (TOA) (Bent, et al, 1983). The MDF technique has been in widespread operational use since the late 1970s (Orville, et al, 1983). While it certainly represents a major advance over the highly limited lightning detection capabilities of past systems, MDF systems are subject to problems of site errors due to 1) maintaining exact antenna orientation, and 2) the presence of metal in buildings, buried cables, and other similiar obstacles (Horner, 1954; Darveniza and Uman, 1983; Mach, 1984; Hiscox, et al, 1984). As noted by Pierce (1982), a time-of-arrival (TOA) technique is by far the most accurate way of fixing the source of an individual spheric, if an interstation timing of at least 10 microseconds can be attained. The dramatic revolution in microelectronics has resulted in the availability of low cost receivers for easily available timing signals (such as LORAN-C), obviating the need for such expensive timing sources as atomic clocks. A four station prototype TOA network was designed by Atlantic Scientific Corporation and established over the Florida peninsula in the spring of 1982. Earlier papers by Bent, et al (1983; 1984), and Lyons and Bent (1983) have described the basic system operations and presented initial examples of data collected by the network. At this writing, there are either operating or under installation three



Fig. 1. Coverage area for the three civilian LPATS networks operating in the United States: the Florida, Upper Midwest, and West Gulf.

civilian networks covering portions of over 20 states in the eastern U.S. (Fig. 1). This paper will summarize the techniques that are currently being employed to display and interact with this newly available data base, as well as present representative case studies obtained from operational networks. At this time, there are approximately two dozen on-line users for LPATS data including television and radio stations, utilities, military bases, and industrial facilities.

II - PRINCIPLE OF OPERATION

A TOA Lightning Position and Tracking System network consists of three to six antennas, each connected by a dedicated full duplex data link to a central analyzer (CA) (Fig. 2). At each antenna site, there are two simple whip antennas (1.2 to 5.0 meters in height). One antenna receives LORAN-C signals, while the second monitors the electric field. These have no special siting requirements and can be placed in the vicinity of metal objects, other conductors, or atop conventional buildings. No alignment checks or frequent periodic maintenance are necessary. The electronics at each site include a lightning strike detector and a timing signal generator sychronized to within a few hundred nanoseconds of the output of the timing signal generator at each of the other respective locations. Electric field measurements in the 2 to 500 KHz (3 dB) range are sampled continuously. The timing of the peak of the CG wave form is ascertained within a few hundred nanoseconds. A minimum of three stations must detect the CG strike in order for a location to be calculated. For a three station solution, the central analyzer solves the complex spherical hyperbolic explicit non-interative equations necessary for stroke location. The data are output in latitude and longitude coordinates. Custom built hardware allows for extremely fast hardware trigonometric calculations. LPATS can monitor individual return strokes in a multiple lightning flash only 15 milliseconds apart, discriminating more than 50 strokes per second (a rate unlikely to be approached in nature). When all four stations detect the CG stroke, the algorithm for determining the location of the ground strike is reduced to a set of linear equations. The nominal time for locating a strike and displaying it on the video monitor is 0.3 seconds.

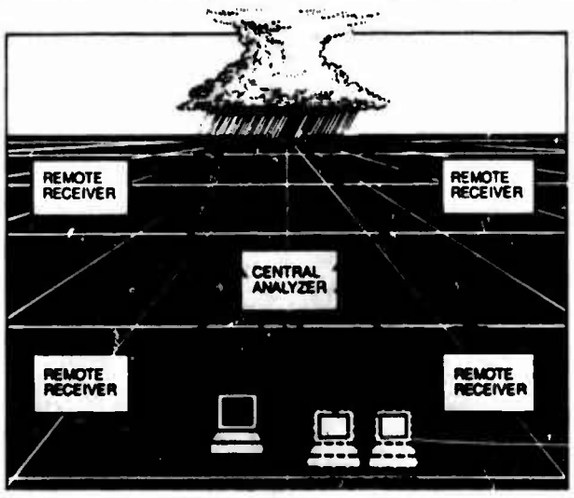


Fig. 2. The LPATS system consists of three or four remote receivers that monitor lighting stroke characteristics over a wideband frequency range. Each receiver obtains the data from a small vertical antenna. Waveform analysis is performed in the receivers and pertinent information is passed over telephone or microwave links to a central analyzer. The central analyzer then computes the strike location. This information is time tagged and made available to several output ports for communication to a monitor.

The precise timing requirements for TOA systems can be met by using the LORAN-C navigation signal which is available over much of North America and indeed, over large portions of the globe. Only the ground wave portion from a single station of the LORAN-C signal is utilized. The sky wave signal rejection is

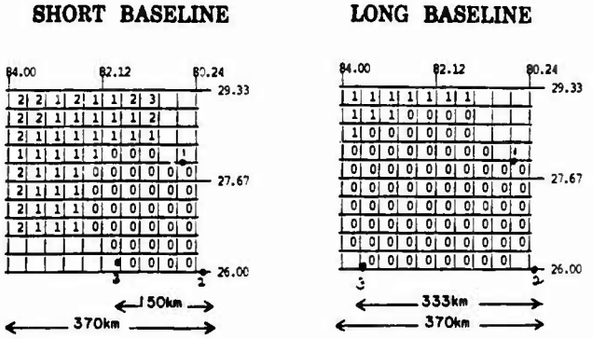


Fig. 3. (left) Computed mean locational error for three station LPATS configuration (black dots) with a 80 nm (150 km) east west baseline; (right) for a 180 nm (333 km) east west baseline. Calculations assume 40 strokes per cell, with random errors of +/- 1000 nanoseconds. Error code: 0 = less than 925 m, 1 = 926 to 1850 m, 2 = 1851 to 2775 m, 3 = 2776 m or more. Domain size is 370 km on a side, or 136,900 km^2.

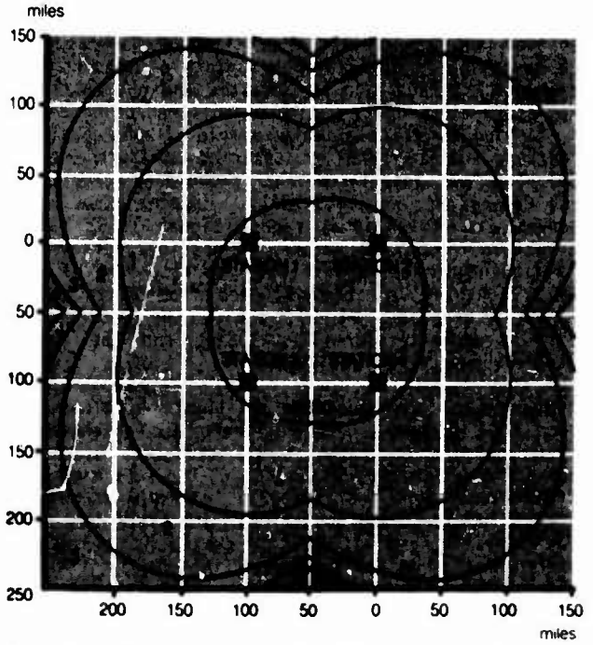


Fig. 4. Mean CG strike location error under worst case conditions, for a four station LPATS network, using the three station solution, and a square form network with 180 km baseline. The inner isopleth is the 750 m mean error, with outer isopleths being about 1500, 3000, and 4500 m respectively.

accomplished within the receiver electronics. While the LORAN-C signals may not always be reliable for navigation in many areas, it must be emphasized that LPATS does not use LORAN-C for navigation. Only the signal from one station in a chain need be acquired. Over water reception can be at ranges up to 2600 km and over land about 2200 km. The availability of the LORAN-C signal is in fact inconsequential. In those cases where a timing signal is unavailable from a single LORAN-C station, additional LPATS equipment is offered which will generate or receive timing from other sources, as is done for the Electricity Supply Commission (ESCOM) of the Republic of South Africa.

A typical LPATS network might have a 150 to 350 km baseline. Experience has shown that the thunderstorm detection capability of an LPATS network covers an area with a radius four or more times the baseline. Short baseline systems are essentially as accurate as long baseline networks near their center, but have a diminished operative range. The impact of increasing the baseline from about 150 km to 333 km is shown in Fig. 3. The area of high locational accuracy (better than 925 m average error) greatly expands as the baseline increases, rather contrary to what might be initially expected. Naturally, base lines cannot be increased ad infinitum due to diminishing network detection efficiency. It should be noted that if communication to the CA via land lines is not practical, a short baseline system, on the order of 10-40 km, can be installed and operated using radio or other communication channels.

III - THE VIDEO INFORMATION SYSTEM (VIS)

LPATS users in the U.S. do not need to purchase, maintain, or operate a lightning detection network. At this time, the most commonly used device to acquire LPATS data is the Video Information System (VIS). The VIS consists of a color monitor, keyboard, and special purpose microcomputer. The VIS contains pre-programmed geographical maps of the network and has the capacity to store a minimum of 3000 lightning strokes (time, latitude, longitude, stroke polarity) in addition to the map features. All pre-programmed software is retained in non-volatile memory so that when a power outage occurs, no software reloading is required. Typically, a seven color RGB-TTL monitor (512 x 480) is used to depict both lightning stroke and base map features.

Users may access LPATS data in several ways: 1) dedicated full duplex telephone lines (3002 conditioning) to either the network central analyzer or to an antenna site which is equipped with a communications multiplexer, 2) on a dial-up basis into the central analyzer, using either a dedicated or contended port, or 3) by satellite communications to the user's own low cost earth station.

Data can be acquired in much the same manner as from color remote dial-up radar systems. There is an important difference, however. When interrogating a radar, only current information may be acquired. The LPATS CA stores at least the last 3000 lightning strokes (augmentable to 50,000) so that the user may obtain a history of the recent network lightning strokes.

The VIS display has many useful characteristics. Included among these are: 1) keyboard selectability of the shape and color of the lightning stroke pixel and line width of the geographical map background, 2) a cursor which allows the determination of the exact latitude and longitude of each strike, the time (to the nearest minute) of the strike, and the azimuth and range of that strike from any arbitrarily selected point in the network's domain, 3) the ability to perform a dynamic zoom to any point on the base map by simple keyboard control, 4) a base map using up to 7 individual colors to specify such features as coastlines, highways, city boundaries, weather stations, etc. - each of which are selectably removable or displayable, 5) a recall of data within a given time period (the last 20 minutes, from six to four hours ago, etc.), 6) a time-lapse animation of storm lighting strokes over any arbitrary time period.

Direct interfacing into the customer's own computer requires a simple RS-232 connection. Among the most important attributes of LPATS data are the relatively low data rates involved. While storm stroke rates on the order of several thousand per hour are not uncommon, this represents a miniscule amount of data compared to many other meteorological remote sensing systems. Lightning has the interesting characteristic of having a very high information value and a low data rate, as opposed to the very high data rates and low information value of such systems as satellites and radar. Thus, it becomes a simple, straight forward matter to integrate lightning data onto satellite image displays, conventional and Doppler radar systems, and onto McIdas-based interactive displays.

IV - SYSTEM EVALUATION

There has been a very limited number of studies evaluating the accuracy of the several available lightning detection systems available (Johnson, et al, 1982). Naturally, the lack of any routinely available primary data base for lightning ground strokes is at the root of the difficulty in evaluating the performance of an LPATS TOA system. The two parameters of primary concern are CG stroke detection efficiency, and locational accuracy. Many of the factors contributing to these are described in great detail in Bent, Highlands, and Lyons (1984). It has been estimated that near the center of an LPATS network, the CG stroke detection efficiency is approximately 85%, as determined by actual visual observations during storms. It is felt that the detection efficiency of an LPATS network falls off very slowly with range. At the current time, analyses of internal data coherence and consistency are one of the main tools for LPATS evaluation. It can be easily noted through ongoing inspections of the VIS display that there is little difference in the cohesiveness of lightning clusters plotted near the center of the network compared to those at the far fringes of the display (beyond 800 km range). In an experiment conducted on 3 February 1984, a cell located over the Gulf of Mexico (26°N, 85°W) was moritored from the U.S. Navy's East Gulf network (680 km distant) and simultaneously from the peninsular Florida network (385 km distant). All strokes over a 2.5 minute period were noted. Fully 61% of the s rokes noted by the Florida network were detected by the more distant East Gulf network. In another case an isolated thunderstorm in the Kansas City area was tracked by the Florida, East Gulf, and Upper Midwest networks simultaneously, with all strokes falling in clusters within 20 km of each other. These and many other comparisons suggest a significant degree of stroke detection efficiency at long ranges (Bent, et al, 1984).

With regards to locational accuracy, a theoretical simulation of the system performance has been used to determine accuracy statistics for a typical LPATS net-

work (Bent, et al, 1984). In order to investigate the accuracy of the system on a theoretical basis, it is hypothesized that the total system timing errors will not exceed 2 microseconds as a worst case situation. A computer program was written to simulate a TOA network's performance on a 40 x 40 matrix centered over any predetermined array of four antennas. At each of the 1600 grid points, the timing from a theoretical flash to each receiver was distorted by a random number less than 100% of the anticipated worst case error. The positional error for each theoretical lightning stroke was calculated for 50 iterations in each grid point. For the Florida network, which is quite typical, the predicted errors in locating lightning strokes in the center of the state about 140 km from each of the receiving stations are as follows: mean error 97 m, maximum error 411 m, and standard deviation 76 m. At a distance of 560 km from the center of the network, the predicted values are as follows: mean error 2300 m, maximum 6800 m, and standard deviation 1800 m. Figure 4 is a map typical of a network's locational accuracy isopleths.

The internal consistency of the stroke data attests to the probable reliability of these estimates. In one particular study, fourteen strokes were observed within one flash at a distance of over 200 km from the network centroid. The variation in successive stroke locations was less than 1100 meters. It can also be observed on the VIS display that lightning clusters do not tend to "smear" or become dispersive at ranges in excess of 500 or 600 km. These results have been confirmed by field tests conducted by the U.S. Naval Oceanographic Command [1]. Other theoretical evaluations have strongly suggested that LPATS will not be perturbed by the impact of mountains. A 2000 meter mountain range traversing a network would introduce fixed (and therefore removable) locational errors on the order of 30 to 300 meters at the worst. The impact of a 60 km long power line within 100 m of an antenna would introduce errors no greater than 7 m, which are essentially inconsequential (Olsen, et al, 1982; Bent, et al, 1984).

V - CASE STUDIES

It has become apparent from the routine use of LPATS that lightning is often a far more organized phenomenon than had previously been anticipated. Lightning strokes are not necessarily a randomly scattered "act of God" type of event, but show distinct patterns and morphologies in some cases similar to those from radar studies. Just as the typical radar echo is smaller than the cloud in which it is embedded, more often than not LPATS lightning clusters are significantly smaller than the overall radar echo with which they are associated. A series of case studies follow which reveal some of the patterns observed.

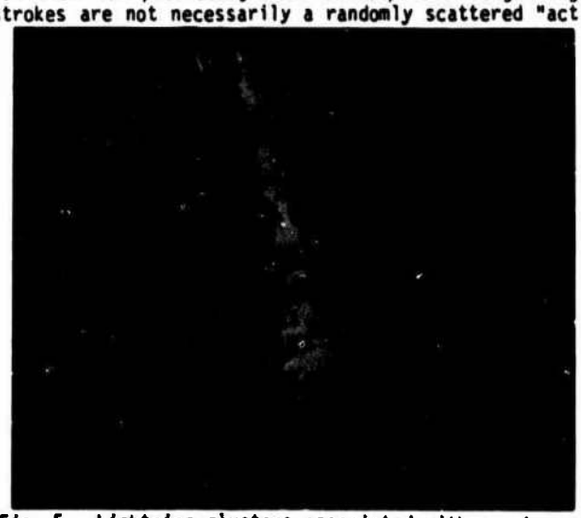


Fig. 5. Lightning clusters associated with sea breeze thunderstorms over peninsular Florida late on the afternoon of 5 May 1984.

Air Mass Thundershowers

The term "air mass" thundershower connotes a randomness and lack of organization to atmospheric convection. While there is clearly a broad spectrum in the degree of organization of mesoscale convective precipitation events, the more any given series of convective events is examined, the more at least some degree of patterning will emerge. The original study of "air mass" storms, The Thunderstorm Project (Byers and Braham, 1949), concentrated on small non-severe storms



Fig. 6. Lightning "lineaments" associated with small air-mass thundershowers over Iowa and Illinois, 2000-2100 GMT, 4 September 1984. The curvilinear path directly reflects the strong relative cyclonic vorticity within the circulation of a storm centered well north of the area.

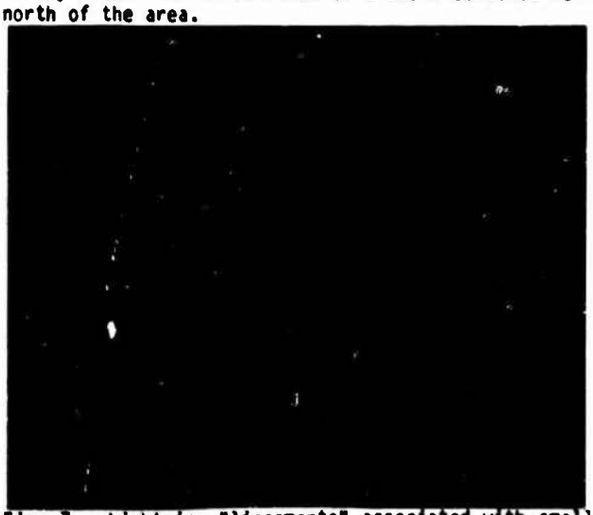


Fig. 7. Lightning "lineaments" associated with small thundershowers embedded within the strong southwesterly flow in advance of a cold front moving through the Great Plains during an early spring storm, afternoon and early evening, 20 February 1985.

in Ohio and Florida. In subsequent years it has become apparent that afternoon summer showers in Florida are strongly influenced by the sea breeze (Byers and Rodebush, 1949; Pielke, 1974). Thunderstorms will routinely form along the sea breeze convergence zone as it propagates inland during the day. Satellite imagery has presented vivid illustrations of the high degree of organization of sea breeze storm events. Figure 5 displays a very typical display from the Florida LPATS network. A strong sea breeze convergence zone along the eastern shore of Florida triggered a chain of contiguous storm centers. Lightning activity was moderate, exceeding 6000-7000 strokes per hour during the late afternoon.

Figure 6 represents the LPATS display from a totally different convective regime, which could still be loosely categorized as an "air mass" shower system. On 4 September 1984, unseasonably cool air was being swept into the Upper Midwest by the strong cyclonic flow associated with a deep cyclone north of the Great Lakes. Afternoon instability showers developed over Iowa, Wisconsin, and Illinois. GOES satellite imagery revealed charasteric well-defined cyclonically curved cloud streets. Small (less than 20-30 km) cumulonimbus clouds formed within these cloud streets and moved southeastward, steered by the strong low level flow. The LPATS display shows the lightning "lineaments" associated with these storms. Individual "lightning generating cells", smaller than their parent cumulonimbus, maintained themselves often for 100 to 200 km, yet with widths on the order of 10 km. This tendency for lightning "lineaments", long-lasting narrow lightning coridors associated with the electrically active point of a larger convective cloud, has been noticed on many occasions.

Figure 7 shows another set of lightning "lineaments" monitored during synoptic conditions quite dissimilar to the case described above. On the afternoon of 20 February 1985, an early spring cyclone was advecting unseasonably warm air over large portions of the Midwest, much of which was still snow covered. Scattered thunderstorms developed in the broad southwesterly flow ahead of a slowly advancing cold front. While the GOES satellite imagery did not reveal any obvious patterning in the dappled cloud field moving northeastward over Kansas, Iowa, Missouri, and into Minnesota, LPATS (Fig. 7) showed otherwise. Distinct lightning "lineaments" with aspect ratios on the order of 20 to 1 indicated discrete lightning generating cells moving northeastward at over 20 m/sec, some lasting up to several hours.

Cold Frontal Thunderstorms

The classic "Polar Front Cyclone" model of the Bergen School assigns the synoptic cold front as perhaps the principal thunderstorm generating factor at mid-latitudes. Several LPATS displays of cold frontal storms follow below.

On the afternoon of 15 August 1984, a weak cold front extended from Minnesota into northern Nebraska. As indicated in the GOES imagery, this cloud band was quite narrow, less than about 100-150 km across (Fig. 8). In a one hour time span, approximately 2500 strokes were recorded in a very narrow (25-50 km) band directly beneath this cloud line and its associated radar echoes (Fig. 9). A close up of this lightning cluster is shown in Fig. 10. It should be noted that the western edge of this cluster was more than 900 km southwest of the centroid of the Upper Midwest network. There appears to be relatively little



Fig. 8. GOES KB8 images (visible), at 1730 GMT, 15 August 1984, showing narrow band of cold frontal thunderstorms along the South Dakota-Nebraska border.

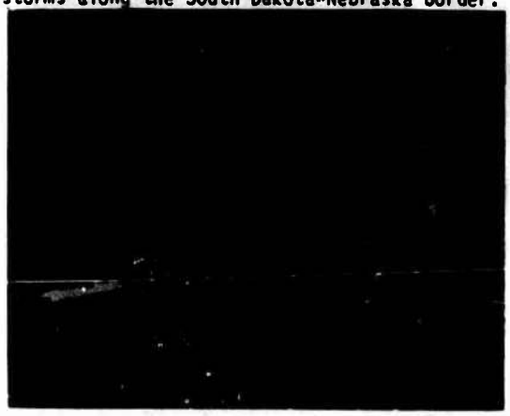


Fig. 9. VIS display, 1630-1730 GMT, 15 August 1984, with about 2500 strokes.



Fig. 10. Detail of lightning cluster shown in Fig. 9, showing 2200 strokes from 1545 to 1645 GMT, 15 August 1984.

"smearing" of the lightning stroke patterns as a result of decreased locational accuracy or detection efficiency with range. It is common to find such densely packed lightning clusters even at the edge of the Upper Midwest and other networks.

Figures 11-13 reveal a "classic" pre-cold frontal squall line event. On 20 November 1983, a cold front was sweeping across the east Gulf of Mexico, generating a typical squall line ahead of the surface position of the front. In Fig. 11, about 700 strokes are plotted over a 20 minute period, displaying a

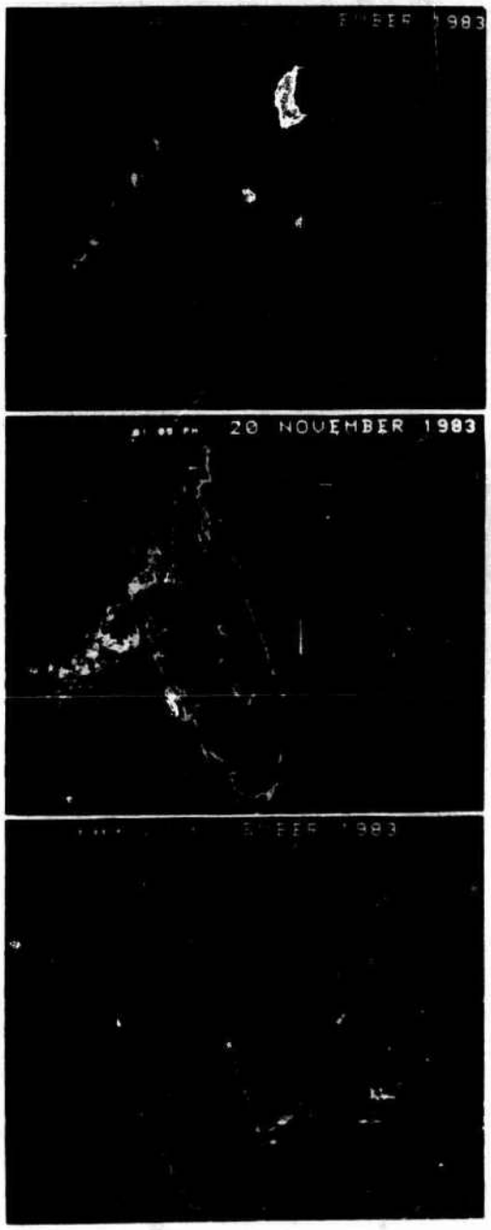


Fig. 11. About 700 CG strokes, 1702-1722 GMT, 20 November 1984, as a well defined pre-cold frontal squall line approaches the west coast of Florida.

Fig. 12. Squall line lightning activity continues with about 3000 strokes between 1705 and 1905 GMT.

Fig. 13. The squall line, after crossing Florida, gradually weakened, with about 3000 strokes between 2300 and 0400 GMT. Discrete lightning cells could still be discerned within the overall thunderstorm line.

clear, well-defined squall line approaching the west coast of Florida. As the front pushed southward and more moisture became available, a high level of lightning activity was maintained, with Fig. 12 showing 3000 strokes occurring over a two hour period. In Fig. 13, the same squall line about 10 hours later had traversed the Florida peninsula. Thunderstorm activity had decreased and the attendant lightning had diminished considerably. The original picture, color coded in one hour increments, showed about 3000 lightning strokes over a 6 hour period. Particularly in the original photograph, the organized progressive motion of the squall line and of its constituent lightning cells is immediately apparent.

Stationary Frontal Storms

During the spring and summer in the eastern U.S., the stationary front is a most vigorous thunderstorm generating mechanism. Cells often form in broad east-west belts with activity persisting for days. As shown in Fig. 14, an intense temperature gradient was present over Iowa and surrounding states late on the afternoon of 1 September 1984. Surface maximum temperatures ranged from over 100°F (38°C) in southeast Iowa to 70°F (21°C) in southwest Minnesota. A line of thunderstorms erupted along this quasi-stationary front after about 2200 GMT (Fig. 15). The line itself showed very little motion over the ensuing several hours, while individual cells were noted tracking rapidly northeast and then eastward along the frontal boundary. In the period between 2300 GMT and 0000 GMT, 1 September 1984, a total of 9500 strokes were plotted on the VIS within this very narrow band. In the four hours between 2300 GMT and 0300 GMT, a total of 31,500 strokes were concentrated in a band about 75-150 km wide and 1300 km long (Fig. 16). It should be noted that in order to monitor this event using radar, a minimum of four WSR-57 radar systems (Neenah, Minneapolis, Des Moines, Grand Island) had to be accessed via dial-up displays to provide a complete

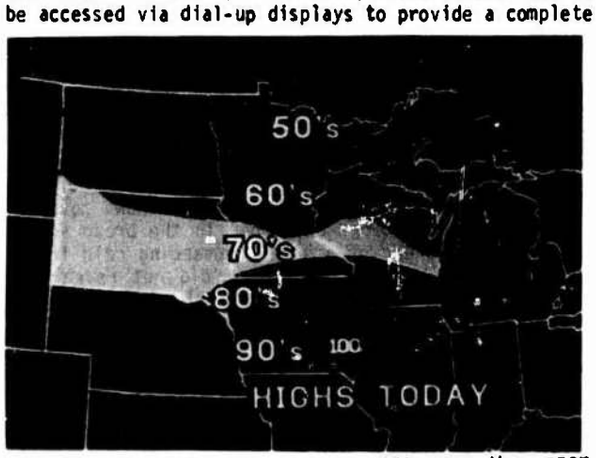


Fig. 14. High temperature map (°F) over the upper Midwest, 1 September 1984. Temperatures range from 12°C to 38°C over region.



Fig. 15. GOES KB8 infrared image (MB curve) at 0000 GMT, 2 September 1984, showing thunderstorm clusters forming along the quasi-stationary frontal boundary.

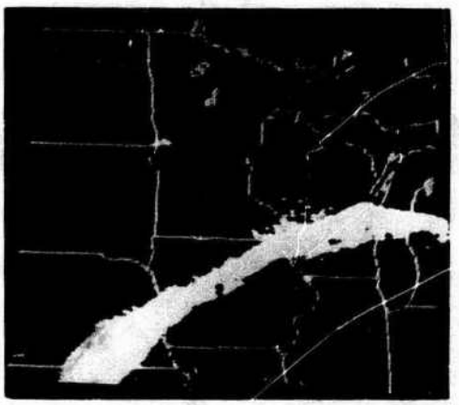


Fig. 16. Accumulated CG strokes between 2300 GMT and 0300 GMT, 1-2 September 1984. Approximately 31,500 individual strokes were plotted.

Mesoscale Convective Complexes

Over the years, researchers (Maddox, 1980) have discovered a new form of highly organized mid-latitude convection, the mesoscale convective complex (MCC). Covering hundreds of thousands of square kilometers and lasting 12 to 72+ hours, the MCC is a prodigious producer of severe weather, including flash flooding and tornadoes. Two case studies suggest lightning is another notable characteristic of the MCC.

Late on the afternoon of 24 May 1984, a rapidly moving cold front was sweeping through Minnesota and Wisconsin. GOES satellite imagery detected a cluster of thunderstorms forming in Minnesota. These moved rapidly east-southeastward into eastern Wisconsin, where they coalesced into an MCC-like cloud mass. Figure 17 shows the GOES infrared image (MB curve) at 0100Z, 25 May 1984. While clearly linked to a cold front and somewhat smaller than a typical MCC, this cloud cluster did appear to have many of the characteristics of an MACC. Note the broad V-shaped pattern of the cold cloud tops in the GOES imagery over Wisconsin and Lake Michigan. Compare this with Fig. 18, which shows the regional view of lightning in a one hour period from 2352 to 0052 GMT. A close-up view of the storm cell (Fig. 19) shows a 31 minute summation of the lightning strokes associated with this cloud cluster. Figure 20 reveals it in greater detail. Both in the original color coded displays and on the VIS screen animation it was apparent that the CG strokes associated with this storm were advancing almost as a solid "wall" of lightning, most likely in conjunction with the gust front. At the peak of activity, this cluster generated 5000 strokes per hour as it moved through central Wisconsin.



Fig. 17. GOES KB8 infrared image (MB curve), 0100 GMT, 25 May 1985, showing MCC-like thunderstorm cluster over the Milwaukee area.

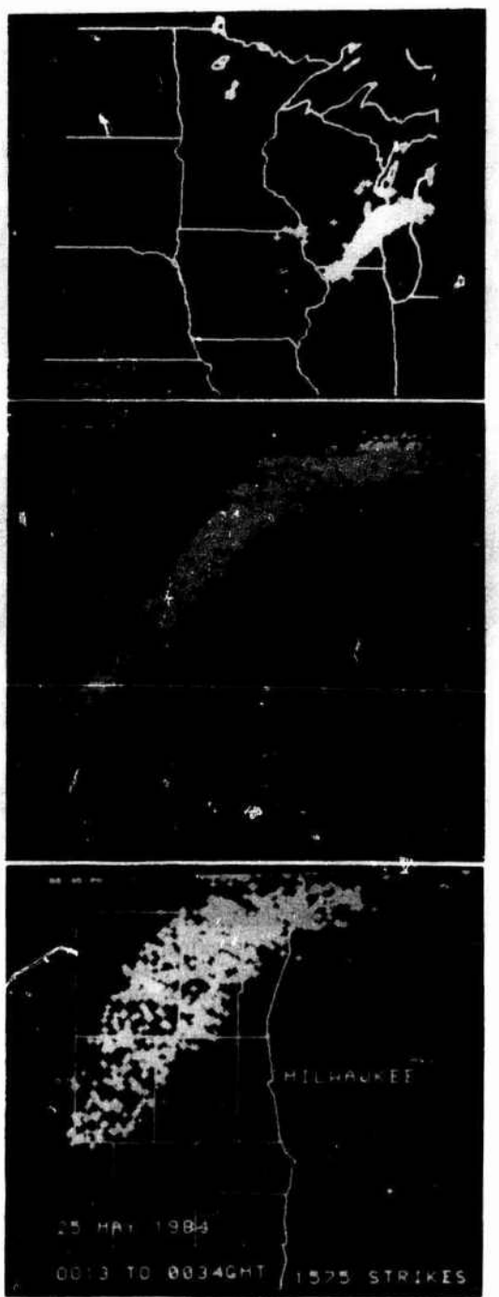


Fig. 18. Upper Midwest network VIS display showing one hour of CG strokes, ending 0100 GMT, 25 May 1984.

Fig. 19. Detail of the storm shown in Fig. 18, with 1575 strikes between 0013 and 0034 GMT, 25 May 1984.

Fig. 20. Close-up view of Milwaukee metropolitan area. All displays generated in real-time using the LPATS VIS system.

On 14 June 1984, a broad upper atmospheric ridge stretched across the upper Midwest. Highly unstable air was present in the maritime tropical air mass to its south. These are highly favorable conditions for MCC formation and in fact a series did develop in North and South Dakota and propagated eastward over a several day period. Figure 21 shows a portion of a



Fig. 21. GOES 4 km resolution infrared image, 1600 GMT, 14 June 1984, showing large convective cloud system in eastern South Dakota.



Fig. 22. LPATS display showing 2500 CG lightning strokes from 1545 GMT to 1712 GMT, 14 June 1984. The bulk of the cluster is found over southeastern South Dakota.

GOES infrared image showing the classic MCC cloud signature revealed by the enhancement employed in the image processing. Even in its declining stage, this MCC was continuing to produce a rather intense and highly organized lightning CG display (Fig. 22). Again, the new CG strokes were found at the eastern and southern edge of the cluster, advancing with the probable gust front. Note that the slight discrepancy between the LPATS CG locations and the cloud pattern is due to a gridding error on the satellite image which displays the South Dakota border about 30 km to the north.

Winter Lightning

It is a developing realization that lightning is not an exclusively summertime phenomenon. It has been noted during every week of the year along the eastern seaboard of the U.S. (Orville, et al, 1983). Winter lightning is often found within intense occluded winter cyclones. These are frequently associated with intense snowfalls in the central and eastern U.S. On several occasions during the winter of 1984, the Upper Midwest network used lightning to track apparent convective snowbursts producing snowfall accumulations in excess of 4" (10 cm) per hour. These played a most useful role in local snowfall forecasting in Minnesota during the record setting snowfall season of 1983-84.



Fig. 23. GOES KB8 image (MB curve), 0230 GMT, 19 February 1984, showing cloud pattern associated with a major upper Midwest snowstorm.

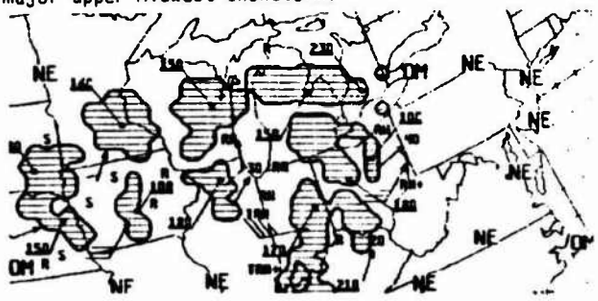


Fig. 24. Radar summary, 0235 GMT, 19 February 1984. Light rain and/or snow showers, with maximum echo tops to 18,000 ft (5600 m) are noted from Nebraska into Iowa and northern Illinois.

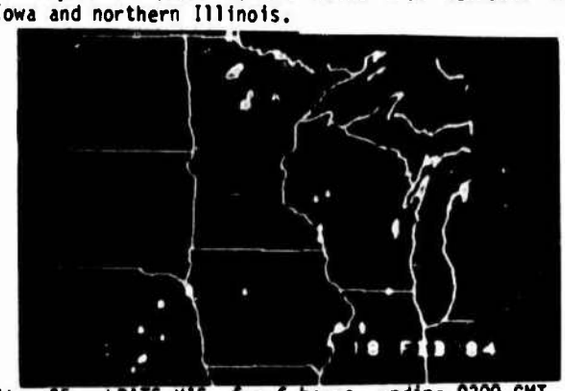


Fig. 25. LPATS VIS, for 6 hours, ending 0300 GMT, 19 February 1984, showing scattered CG strokes, including one on IL-WI border northeast of Rockford, IL (RFD).

STATION: RFD TODAY'S DATE: 19-FEB-84

TIME	DATE	PRS	TMP	DEW	WIND	G	VIS	WE	SKY
6AM(127)	18	169	35	35	0608		1 1/4	F	C 2 OVC
7AM(135)	18	165	35	34	1405		1	F	C 3 OVC
8AM(142)	18	176	36	36	1004		1/2	F	C 3 OVC
9AM(152)	18	184	36	36	1408		3/4	F	C 3 OVC
10AM(162)	18	181	36	36	1508		3/4	F	C 2 OVC
11AM(173)	18	165	37	37	1415		1	F	C 3 OVC
12PM(182)	18	147	38	37	1514		1	R-F	C 5 OVC
1PM(197)	18	131	39	38	1214		3	R-F	C 5 OVC
2PM(207)	18	104	39	38	0914		3	R-F	C 6 OVC
3PM(217)	18	080	40	39	0815		3	R-F	C 6 OVC
4PM(227)	18	062	40	40	0912		4	R-F	C 5 OVC
5PM(237)	18	060	40	40	0817		4	R-F	C 6 BKN 20 OVC
6PM(002)	18	049	42	42	1308	24	2	R-F	C 5 OVC
7PM(012)	18	139	35	33	3109	15			C 14 OVC
8PM(022)	18	027	43	43	1220		3	R-F	C 6 OVC
9PM(032)	18	023	44	44	1410		3	TRW-F	C 7 OVC
10PM(042)	18	022	47	47	1816		3	F	10 SCT C 14 BKN
11PM(052)	18	016	44	44	1610		3	F	14 SCT 41 SCT
12AM(062)	19	014	41	41	1809		6	F	CLR

Fig. 26. Listing of airways observations at RFD, 18-19 February 1984. Remarks (not shown) noted "LTGCG NE" at 0300 GMT.

On 19 February 1984, a large occluded low was centered in northeastern Iowa with its associated high cloud tops stretching from South Dakota into Minnesota, Wisconsin and Michigan (Fig. 23). As shown in Fig. 24, widespread snow covered the Upper Midwest, with rain showers reported from Iowa into northeastern Illinois. Maximum echo tops as observed by radar were under 18,000 feet (5600 m). Certainly, there is nothing in the satellite radar imagery to suggest lightning in Nebraska, Iowa, or Illinois. Yet as shown in Fig. 25, there was scattered lightning activity reported throughout the region. Interestingly enough, a log of the hourly observations at the Rockford, IL airport revealed CG lightning northeast at 0300 GMT (Fig. 26). These satellite images and radar observations would normally be interpreted to suggest only the presence of moderate rainshowers in Illinois and Iowa, with the nearest thunderstorms being in southern Indiana. LPATS, however, has frequently noted that lightning can occasionally occur from DVIP Level 1 or 2 radar echoes during both winter and summer. Thus, the use of radar as a direct indicator of thunderstorms can upon occasion be quite misleading.

Hurricane Lightning

Hurricanes, while essentially comprised of spiral bands of convective clouds, are generally not thought to be associated with significant lightning. Studies have found, however, that intense convection, sufficient to produce embedded tornadoes, especially within the outer convective rainbands, is not uncommon (Gentry, 1983). This makes the paucity of lightning observations within tropical cyclones all the more intriguing. Johnson, et al (1984) do report a significant amount of electricital activity emanating from the vicinity of Hurricane Alicia, using a 2 MHz interferometer located at the Marshall Space Flight Center, Alabama. More recently, however, the Florida LPATS network has documented lightning CG strokes associated with tropical cyclones. Ouring the formative stages of Tropical Storm Barry in late August, 1983 off the east coast of Florida, significant lightning activity was noted. Even more interesting are the observations made on 9-10 September 1984 prior to the rapid intensification phase of soon-to-be Hurricane Diana. Figure 27 shows the LPATS dislay along the Florida east coast between Cape Kennedy and Palm Beach on the afternoon of 9 September 1984. Tropical Storm Diana was gaining strength at this time, with its circulation center near 80°W, 29.5°N. The spiral convective bands were clearly visible on the GOES satellite imagery. The LPATS data, representing about 2 hours of activity, were directly aligned with these outer convective rainbands. By mid-day on 10 September 1984, Diana was intensifying east of Jacksonville, FL. Figure 28 shows the accumulated lightning strokes over about a 15 hour period. In addition to the outer spiral bands, a definite concentration of CG strokes was found in and near the eye wall. Figure 29 shows a close-up of the eye wall lightning events. CG strokes began in the western part of the eye wall and slowly (at speeds far less than the presumed ambient low level winds) rotated in a counterclockwise manner more than 180° around the eye. This pattern was in fact repeated several times, resulting in a cycloidal-shaped trail of CG strokes on the VIS display over a many hour period. This case is under detailed study at this time. It would appear that the CG strokes rotating about the eye are associated with a "convective hot spot" that has been noted by hurricane researchers on several occasions prior to rapid hurricane intensification [2]. Satellite studies of hurricanes have also noted massive cumulonimbus build-ups developing above the general eye wall clouds, which similarly rotate slowly about the circulation center (Gentry, et al, 1970). With the ability of LPATS to detect lightning activity for almost 1000 km offshore, perhaps a new tool in tropical storm diagnosis could be emerging.

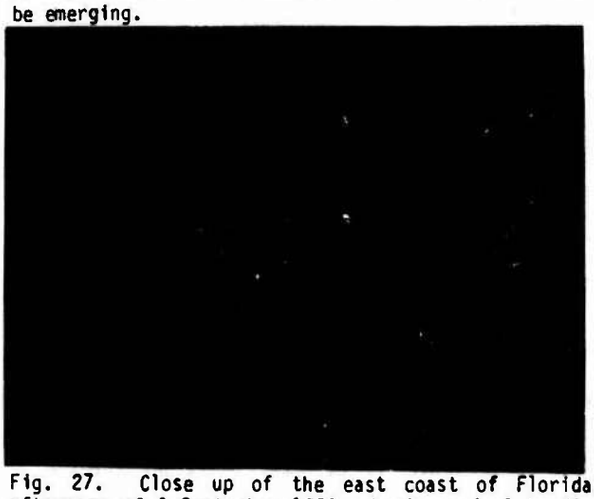


Fig. 27. Close up of the east coast of Florida, afternoon of 9 September 1984, showing spiral banding in the lightning data, here summarized for a two hour period. The center of Tropical Storm Diana's circulation was located well to the northeast of Cape Kennedy (top of picture).



Fig. 28. LPATS CG data summarized over a 15 hour period ending late on 10 September 1984. This was just before the major intensification of the storm.



Fig. 29. Close-up of lightning strokes associated with convection embedded within the eye wall of the hurricane. The lightning began in the western portion of the eye wall and slowly rotated counterclockwise into the northeast quadrant.

VI - SUMMARY AND CONCLUSIONS

The display of instantaneous CG lightning stroke data has found applications in local forecasting as well as various aspects of meteorological research. Individual four station networks can serve as a reliable real-time detector and tracker of thunderstorms over an area some 1800 km on a side. Since LPATS is a unique discriminator of lightning and therefore thunderstorms, its use avoids the necessity of inferring thunderstorm occurrences from either satellite or from radar reports. The ability to animate and recall historical data (over a period of several hours) allows an easy determination of storm motion and morphology, thus greatly assisting short-range nowcasting. LPATS provides an instantaneous sub-synoptic view of atmospheric convective events on a single display, whereas perhaps as many as ten radars would necessarily need to be composited to provide the same thunderstorm tracking capability. Lightning data are devoid of ground clutter and anomalous propagation problems that plague radar. Needless to say, LPATS is not seen as a replacement for radar, but as a highly valuable augmentation. Furthermore, the relatively low data rates associated with lightning detection systems and its time/latitude/longitude data format make it extremely straight forward to integrate lightning into already existing digital and satellite data bases. The documented coherence of lightning in time and space has important implications both for mesoscale nowcasting and lighting climatological studies.

[1] Geitz, W.C., 1983: Evaluation of the Lightning Position and Tracking System. Prepared by Navel Oceanographics Command Oetachment, Pensacola, for Commander, Naval Air Systems, Washington, D.C.

[2] P.G. Black, NOAA, personal communication.

VII - REFERENCES

Anderson, R.B., H.R. Van Niekerk, S.D. Prentice, and O. MacKerras, 1979: Improved Lightning Flash Counters. CIGRE J. ELECTRA, 66, 85-98.

Bent, R.B., W.F. Highlands, and W.A. Lyons, 1984: Description and Theoretical Evaluations of LPATS (Lightning Position end Trecking System) to Monitor Lightning Ground Strikes Using a Time-of-Arrival (TOA) Technique. Preprints, Seventh Intl. Conf. on Atmospheric Electricity, AMS, Albany, 317-324.

Bent, R.B., P.W. Cesper, T.H. Scheffler, and R. Leep, 1983: A Unique Time-of-Arrival Technique for Accurately Locating Lightning over Lerge Arees. Reprints, Fifth Symposium on Meteorological Observations and Instrumentation. Toronto, AMS, 505-511.

Byers, H.R., and R.R. Braham, Jr., 1949: The Thunderstorm. U.S. Government Printing Office, Washington, D.C.

Byers, H.R., end H.R. Rodebush, 1948: Causes of the Thunderstorms of the Florida Peninsula. J. Meteorol., 5, 275-280.

Christien, H.J., L. Frost, P.H. Gillaspy, S.J. Goodman, O.H. Veughen, M. Brook, B. Vonnegut, end R.E. Orville, 1983: Observetions of Opticel Lightning Emissions From Above Thunderstorms Using U-2 Aircreft. Bull. Amer. Meteor. Soc., 64, 120-123.

Christensen, L.S., W. Frost, and W.W. Veughan (Eds.), 1980: Proceedings: Workshop on the Need for Lightning Observations from Space. NASA CP-2095, Weshington, D.C.

Darvenizia, M., and M.A Uman, 1983: Reseerch Into Lightning Protection of Distribution Systems II - Results from Florida Field Work, 1978 and 1979. IEEE, 83 SM454-6.

Gentry, R.C., 1983: Genesis of Tornadoes Associated with Hurricanes. Mon. Wea. Rev., 111, 1793-1805.

Hayenga, C.O., J.W. Warwick, 1981: Two-Dimensional Interferometric Positions of VHF Lightning Sources, J. of Geophys. Res., 86, 7451-7462.

Hiscox, W.L., E.P. Krider, A.E. Piter, and M.A. Uman, 1984: A Systematic Method for Identifying and Correcting "Site Errors" in a Network of Magnetic Oirection Finders. Proceedings, Int'l. Aerospace and Ground Conference on Lightning and Static Electric, National Interagency Coordinating Group, Orlando, June 36-38, 1984, Paper 7-1.

Horner, F., 1954: Influence of Buried Conductors on Bearings. Wireless Engineer, 30, p. 186, 191.

Johnson, R.L., D.E. Janota, and J.E. Hay, 1982: An Operational Comparison of Lightning Warning Systems. J. Appl. Meteor., 21, 703-707.

Kohl, D.A., 1980: An Evaluation of the Area Thunderstorm Monitor in an Operational Application. Bull. Amer. Meteor. Soc., 61, 993-997.

Krider, E.P., R.C. Noggle, and M.A. Uman, 1976: A Gated, Wideband Magnetic Direction Finder for Lightning Return Strokes. J. Appl. Meteor., 15, 301-306.

Ligda, M.G.H., 1956: The Radar Observation of Lightning. J. of Atmos. and Terrestrial Physics, 9, 329-346.

Lyons, W.A., and R.B. Bent, 1983: Evaluation of the Time-of Arrival (TOA) Technique for Real-Time Ground Strike Measurements Using the Lightning Position and Tracking System (LPATS). Preprints, 13th Conf. on Severe Local Storms, AMS, Tulsa, 37-40.

Mach, O.M., 1984: Evaluation of an LLP Ground Strike Locating System. MS Thesis, School of Meteorology, University of Oklahoma, 54 pp.

Maddox, R.A., 1980: Mesoscale Convective Clusters. Bull. Amer. Meteor. Soc., 108, 1108-1121.

Mazur, V., and W.O. Rust, 1983: Lightning Propagation and Flash Density in Squall Lines as Determined with Radar. J. Geophys. Res., 88, 1495-1502.

Olsen, R.G., and A. Aburwein, 1982: LORAN-C Positioning Errors Caused by Scattering from Wires Above the Earth. IEEE, Transactions on Electromagnetic Compatibility.

Orville, R.E., 1981: Global Distribution of Midnight Lightning - September to November 1977. Mon. Wea. Rev., 109, 391-395.

Orville, R.E., R.W. Henderson, and L.F. Bosart, 1983: An East Cost Lightning Detection Network. Bull. Amer. Meteor. Soc., 64, 1029-1037.

Pielke, R.A., 1974: A Three-Dimensional Numerical Model of the Sea Breezes over South Florida. Mon. Wea. Rev., 102, 115-135.

Pierce, E.T., 1982: Spherics and Other Electrical Techniques for Storm Investigations. In, Thunderstorms: A Social, Scientific, and Technological Documentary, Vol. 3, E. Kessler, Ed., USDOC, NOAA, U.S. Gov. Printing Office, 135-148.

Proctor, D.E., 1981: VHF Radio Pictures of Cloud Flashes. J. Geophys. Res., 86, 4041-4071.

Vonnegut, B., D.H. Vaughan, Jr., M. Brook and P. Krehbiel, 1985: Mesoscale Observations of Lightning from Space Shuttle. Bull. Amer. Meteor. Soc., 66, 20-29.

RANGING AND AZIMUTHAL PROBLEMS OF AN AIRBORNE CROSSED LOOP USED AS A SINGLE-STATION LIGHTNING LOCATOR

L.W. Parker and H.W. Kasemir*

M-S 31, GTE Government Systems Corp., One Research Drive, Westborough, Massachusetts 01581, U.S.A.
**Colorado Scientific Research Corp., 1604 S. County Road 15, Berthoud, Colorado 80513, U.S.A.*

Abstract - Data from recent flight tests, useful for assessing the lightning-location capability of a commercial airborne crossed loop mounted on a C-130 aircraft, are analyzed under a novel interpretation. The new interpretation identifies data from individual flashes. These and associated airborne radar cloud data lead to an improved assessment of the instrument's range and azimuth errors. The value of identifying individual discharges lies in the fact that the multiple return strokes of the same flash may be assured tc originate in the same location. Therefore, if each dot on the display is asscciated uniquely with one return stroke, the radial distance and azimuth are the same for all return-stroke dots caused by the same lightning. The radial and azimuthal spreads can then be determined. The results obtained show (a) large radial spreads that severely deteriorate the instrument's ranging capability, (b) reasonably good azimuth capability for distant lightnings, and (c) deterioration of azimuth capability for nearby lightnings, but also for all single-stroke flashes. A novel method is also suggested as a hopeful possibility for overcoming the ranging difficulty. It should be investigated in future work.

1.0 INTRODUCTION

In our recent survey [1], we analyzed many lightning warning systems suitable for airborne use. The present paper is concerned with the accuracy of one of these systems, a single-station crossed loop used as an on-board lightning locator [1,2]. The data were obtained with Stormscope, a commercially-available instrument (operating in the 50-kHz region) that represents this type of detector. In flight tests performed by the Air Force in 1981 [3,4], the instrument was installed on a WC-130 Lockheed Hercules transport aircraft, operated by NOAA. The primary mission of the joint NOAA-Air Force program was to characterize the radiation emitted by lightning and its coupling to the aircraft. The aircraft was suitably instrumented with electric and magnetic field sensors for this purpose [5], and Stormscope was "piggy-backed" thereon.

To our knowledge, these data constitute the first available of their kind suitable for assessment of an instrument mounted on a large aircraft. Data obtained prior to 1981, including the Air Force's own tests[6] and experiences of operators of small private aircraft [7], have involved small or mid-sized aircraft. (New data involving a Convair 580 is anticipated from 1984 tests.)

The Stormscope data in conjunction with airborne radar data were acquired along a flight path toward and around an isolated storm located by the airborne radar. (An additional valuable feature is that the Stormscope display screen was manually cleared frequently during the flight.) These data, and our own analysis associating Stormscope dots with return strokes of individual lightning flashes, allowed an assessment to be made of the instrument's azimuth and ranging, and therefore also lightning-location, capabilities [3]. This association (suggested also in the preliminary study by J. Reazer [4]) represents an advance in that the analysis and statistical procedures are thus applicable to individual lightning discharges where the Stormscope data are correlated in time, as opposed to the usual Stormscope display where clusters of dots are accumulated over many lightning discharges. The value of identifying individual discharges lies in the fact that the multiple return strokes of the same flash may be regarded as originating in the same place. Therefore, the radial distance and the azimuth should be the same for all return-stroke dots caused by the same lightning, and the radial or azimuthal spread can be determined.

In order to make clear why we can relate the individual Stormscope dots to lightning strokes, it will be helpful to review here the temporal phenomenology of a cloud-to-ground discharge. (This information may be found for example in Ref. 8.) The average lightning discharge (or flash) to ground is multiple, i.e., includes a series of several individual component strokes, i.e., return strokes. (The terms "flash" and "stroke" are attributable to Schonland.) During a moderate storm the average interval between flashes is 20 seconds. The overall duration of a flash is of the order of one second, and the duration of an individual component stroke is of the order of one millisecond. The multiplicity of a flash (number of strokes) has an average value between 3 and 4, but can vary from one to more than 20. The probability of any given number occurring decreases as the number increases. Each stroke consists of a high-current pulse, and is preceded by a low-current leader process. The mean time interval between strokes is about 30 ms or longer, and tends to increase with the number of strokes. Positive flashes, as opposed to negative ones, usually are single-stroke flashes.

Hence, the multiple strokes of a flash can easily be resolved in time if the resolution capability of the instrument is under a millisecond. We believe that the Stormscope instrument resolves the component return strokes of a single flash, and displays these strokes as individual dots, occurring within a time interval of one second. This interpretation leads to new types of results. The results to be presented are based on our recent report [3].

2.0 STORMSCOPE DATA ANALYSIS

The types of data obtained in the 1981 measurements that are relevant here are as follows:

a. Airborne video tape record of Stormscope displays, which provided the Stormscope data used here.

b. Timing data from an on-board time code generator (synchronized to the ground station time base).

c. Digitized airborne weather radar data, stored on flexible disk or magnetic tape. This radar data was valuable for the present purposes.

No independent "ground-truth" lightning location data were available. It should be mentioned that the data from the other on-board sensors with which the aircraft was heavily instrumented (B-dot, D-dot, I-dot) to measure submicrosecond-time-scale lightning-induced transients were tailored to a different investigation and were generally not suitable for the problem of interest here.

It should also be noted that the data-reduction effort, by Reazer and ourselves [3,4], was considerable, requiring manual timing, hand measurements, and copying of individual Stormscope dots from the video monitor screen onto drawings, from the video tape, frame by frame. (This laborious procedure can be avoided in the future by automatically digitizing the Stormscope data.) Using the same video tape and radar data as Reazer [4], we have extracted additional valuable data and reorganized all of the data to obtain new types of results, to be described below.

Figures 1 and 2 summarize the principal results obtained with respect to azimuth and ranging capability, as follows.

We organized the Stormscope dot data into about 50 individual cloud-to-ground flashes, with an average of about 4 dots (strokes) per flash, corresponding to a particular time period on 25 August 1981. During this time period, there was essentially a single storm cloud indicated by the radar. Combining radar data (digitized) with aircraft position and heading data at several positions allowed us to locate the ground position of the cloud and to reconstruct the aircraft flight path. Figure 1 shows the inferred cloud position and the flight path toward and around the cloud. The cloud is defined to have a circular shape with a typical diameter of 2.5 nmi. The flight path and the instantaneous Stormscope dot displays at various positions along the path allowed a test of how well Stormscope could track a well-defined lightning source. The numbers at positions along the path (from 1 to 41) not only label the positions, but also denote the "Flash Indices" [3] of the individual flashes occurring when the airplane was at those positions. The encircled indices (Flashes 1, 5, 7, 16, 20, 22) designate the flashes giving rise to the selected Stormscope displays that will be discussed below, together with the "rays" (azimuth lines) emanating from various points along the path. Figure 2 presents range data for the 41 flashes and shows how the range data compare with the true cloud position. We will discuss Fig. 2 in detail later.

2.1 Combined Cloud-Dot Displays

Figures 3-8 are diagrams of simulated compass-rose displays of Stormscope dot data with superimposed radar cloud data for the six selected individual flashes mentioned above. The cloud is represented diagrammatically by quadrilaterals whose vertices lie on ovals drawn by us around the densest portions of the radar clouds (not shown). The diagonals of the quadrilaterals correspond roughly to the major and minor axes of the ovals. Greater detail in defining the cloud shape is not warranted for the present purposes. The inference of the cloud position was not a trivial task in view of shortcomings in the available data (see Ref. 3). All six displays to be discussed have a maximum range of 50 nmi and a 360-degree azimuthal view. The cloud range and radial spreads of the dots can be estimated from the figures, but can also be read off directly from Figure 2.

Figure 3 (Flash 1, at 14:14:03) shows a single dot on the 264-degree radial, at a range of 43 nmi. The cloud (lightning source) on the other hand is near the 0-degree radial, at a range of about 30 nmi. This represents a poor azimuth detection which appears to be typical of single-dot (single-stroke) flashes.

Figure 4 (Flash 5, at 14:15:48) shows 7 dots on the 0-degree radial, with ranges distributed from 10 to 30 nmi. The cloud is near the 0-degree radial (straight ahead of the airplane) and at a range of 22 nmi. In this case, the azimuth detection is good. The radial spread is not good (as also indicated in Figure 2) and is mostly inward.

Figure 5 (Flash 7, at 14:16:24) shows 5 dots on the 0-degree radial, aligned with the cloud. The ranges are distributed from 18 to 45 nmi, with the cloud at 18 nmi. Thus, the azimuth detection is good, while the radial spread is poor and entirely outward.

As Figure 1 indicates, Flashes 1, 5, and 7 all occur while the airplane is heading directly toward the cloud.

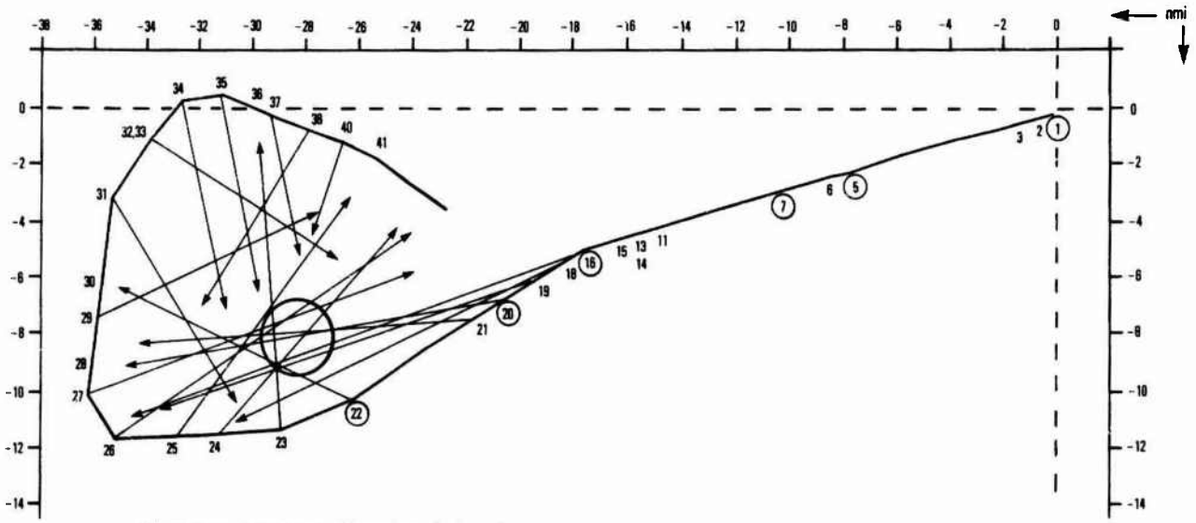
Figure 6 (Flash 16, at 14:18:08) shows 3 dots, one on the 0-degree radial and two on the 12-degree radial, aligned with the cloud. The radial spread is from 21 to 50 nmi, with the cloud at 11 nmi. The azimuthal detection is still quite good, while the radial spread is poor, and entirely outward. At this time the airplane has begun its turn to circle around the cloud (Figure 1). The good azimuth defined by the two inner dots is also shown by the ray emanating from Point 16 in Figure 1.

Figure 7 (Flash 20, at 14:18:56) shows 6 dots, the outermost 4 of which are well aligned with the cloud (8 nmi) on the 25-degree radial. The radial spread is from 3 to 26 nmi, that is, inward and outward but predominantly outward. The azimuthal detection is still good.

Figure 8 (Flash 22, at 14:20:34) shows 13 dots, spread over 90 degrees in azimuth and over 3 to 26 nmi in range. The cloud is at 3 nmi, that is, nearby on the 75-degree radial. This occurs at the position of closest approach (Figure 1). This striking degradation in azimuth detection is associated with the closeness of the lightning, as will be discussed.

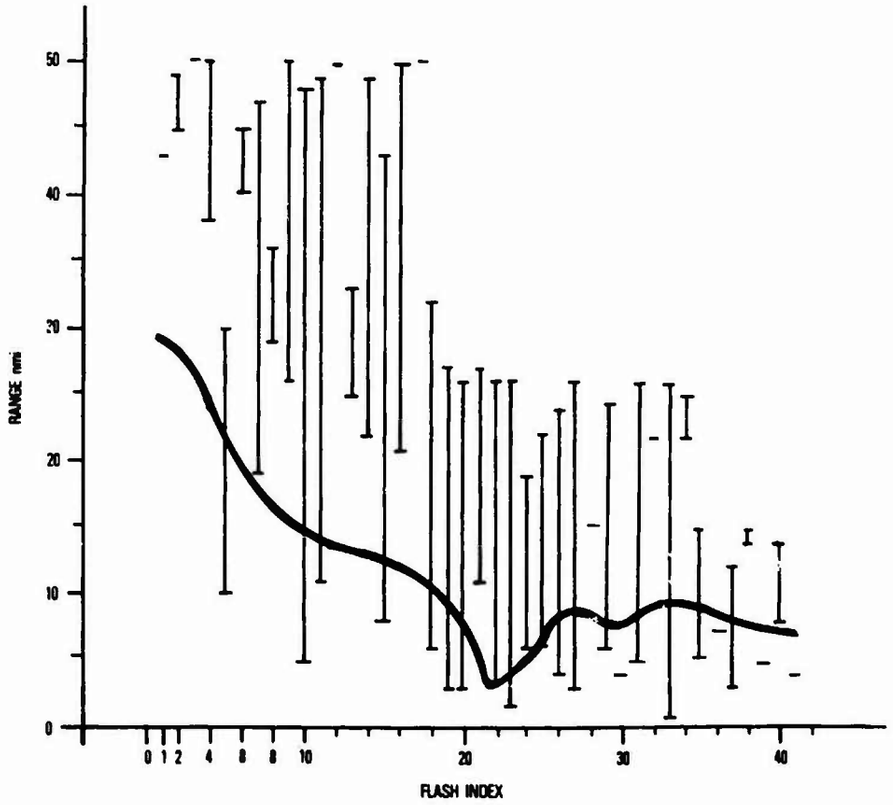
3.0 SITE ERRORS

Reference 3 [App. C; see also Refs. 1 and 2] presents an original 3-D computer model and numerical computations of the site error at the Stormscope location and at other locations on the C-130 aircraft. (These correction factors have to be determined only once, since they depend only on aircraft geometry. The azimuth errors due to real lightning sources cannot be calculated precise-



Circle = cloud of diameter 2.5 nmi.
Encircled numbers denote selected flashes discussed in text and in Figs. 3-8.
Arrows denote mean azimuths (see text).

FIGURE 1. FLIGHT PATH AND STORMSCOPE AZIMUTHS AT VARIOUS POSITIONS WHERE INDIVIDUAL FLASHES OCCUR (25 August 1981).



Heavy curve = cloud position
Single horizontal bar denotes range of a single-dot flash.
Vertical bars represent radial spread of dots caused by individual flashes.

FIGURE 2. STORMSCOPE RANGE SPREADS versus FLASH INDEX and CLOUD POSITION ALONG FLIGHT PATH (25 August 1981).

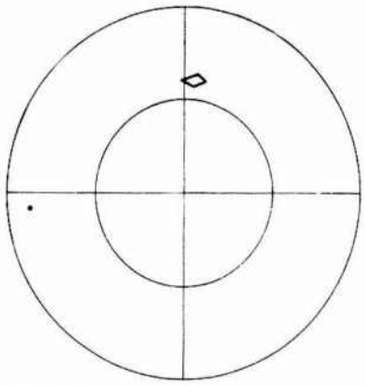


FIGURE 3. FLASH 1. 1 DOT. 25 August 1981. 14:14:03.
Airplane at origin of coordinates.
Cloud quadrilateral: azimuth = 0°,
range = 30 nmi.
Stormscope single dot: azimuth = 264°,
range = 43 nmi.

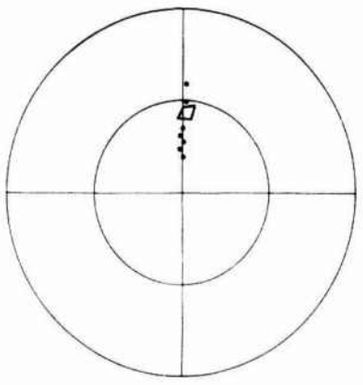


FIGURE 4. FLASH 5. 7 DOTS. 25 August 1981. 14:15:48.
Airplane at origin of coordinates.
Cloud quadrilateral: azimuth = 0°,
range = 22 nmi.
Stormscope dots: azimuth = 0°,
average range = 20 nmi.
range spread = 20 nmi.

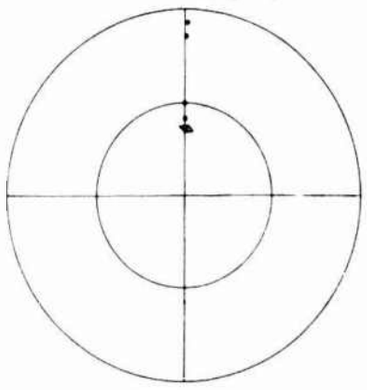


FIGURE 5. FLASH 7. 5 DOTS. 25 August 1981. 14:16:24.
Airplane at origin of coordinates.
Cloud quadrilateral: azimuth = 0°,
range = 18 nmi.
Stormscope dots: azimuth = 0°,
average range = 32 nmi,
range spread = 27 nmi.

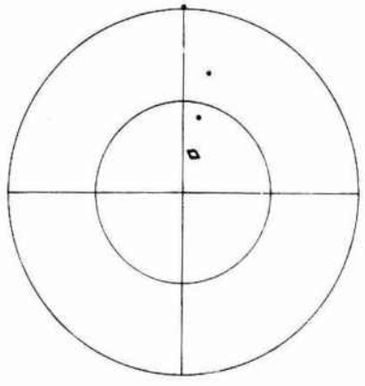


FIGURE 6. FLASH 16. 3 DOTS. 25 August 1981. 14:18:08.
Airplane at origin of coordinates.
Cloud quadrilateral: azimuth = 15°,
range = 11 nmi,
Stormscope dots: azimuth = 0°-12°,
average range = 36 nmi,
range spread = 29 nmi.

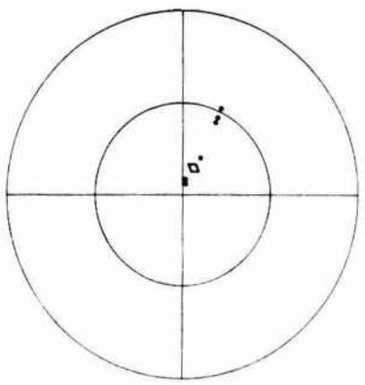


FIGURE 7. FLASH 20. 6 DOTS. 25 August 1981. 14:18:56.
Airplane at origin of coordinates.
Cloud quadrilateral: azimuth = 25°,
range = 8 nmi,
Stormscope dots: azimuth = 10°-25°,
average range = 15 nmi,
range spread = 23 nmi.

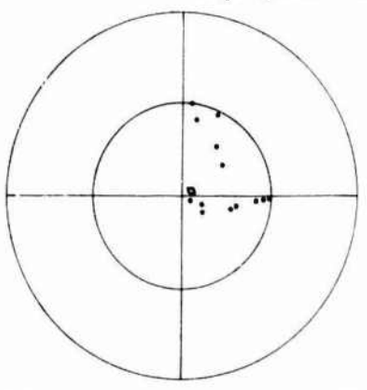


FIGURE 8. FLASH 22. 13 DOTS. 25 August 1981. 14:20:34.
Airplane at origin of coordinates.
Cloud quadrilateral: azimuth = 75°,
range = 3 nmi.
Stormscope dots: azimuth = 6°-125°,
average range = 15 nmi,
range spread = 23 nmi.

ly, but can be determined by measurement.) An interesting result is that for the location chosen, under the "platypus" or "beaver tail," the site error is essentially identical to that of a crossed loop centered on a long cylinder. This problem has a known analytic solution. Hence, the site error calibration function for a crossed loop at the Stormscope location can be represented analytically, by

A_o = arc tan (2 tan A),

where A denotes the apparent azimuth angle and A_o denotes the true azimuth angle.

This site-error formula predicts that there is no error in the forward and backward directions (zero and 180 degrees), and at 90 degrees. Also, the observed azimuth is more nearly in the forward (or backward) direction than the true azimuth. In the first four example flashes (Flashes 1, 5, 7, 16,) shown in Figs. 3-6 all azimuths are in the forward direction. Hence, there is no site error. There is also no significant site error in Flash 20, which occurs near the forward direction. In Flash 22, however, the extreme azimuthal scatter dominates the site errors. In other cases [3] the large errors in azimuth (greater than 20 degrees) when they occur cannot be explained as site errors.

4.0 DISCUSSION

In this section the Stormscope ("SS") data are analyzed to assess the capability of a crossed loop to track lightning activity, in particular cloud-to-ground flashes. First we consider the ranging capability, and next the azimuth capability. Then we will discuss the significance of the results.

4.1 Stormscope Ranging

Most of the data reveals severe radial spreading of the dots. To quantify this spreading effect, we consider the minimum and maximum ranges of the dots in the 41 flashes [3] associated with the aircraft trajectory in Fig. 1. (These minimum and maximum values can be obtained from the data given in Ref. 3.) Figure 2 shows a set of vertical "range-spread" bars defining the spread for each flash. Ten flashes consisting of only one dot/stroke (i.e., Flashes 1, 3, 12, 17, 28, 30, 32, 36, 39, 41) have no vertical range-spread bars, only a short horizontal "tick" mark representing the range of the single dot. Also included is the range of the radar cloud in each flash, denoted by the heavy curve.

For Flashes 1-18, the SS display range was 50 nmi. After Flash 18 the SS display range was switched to 25 nmi, which is the display range for the remaining Flashes 19-41. It is evident that in none of the flashes does the SS range reasonably approximate the cloud distance. Also, the maximum SS range in most cases overestimates greatly the cloud range. This could lead a pilot to infer that the electrical discharges are considerably further than they actually are. On the other hand, the inward spread may alarm the pilot unnecessarily. The inward spread could also account for the high "false alarm" rates experienced in the mining-operations warning tests of Ref. 9. It should be noted that there is a tendency for the radial spread to occupy the available display range. Thus, for Flashes 1-18, the maximum range tends to cluster around the 50 nmi limit of the display, while for Flashes 19-34, it tends to cluster around the 25 nmi limit. It is interesting that some improvement in ranging seems to occur in Flashes 35-41.

4.2 Stormscope Azimuths

Stormscope (SS) sensing of lightning flash azimuths should be reasonably good, in view of the well-established technology of magnetic crossed loops, in the absence of site errors, and when the radiator (lightning channel) is vertical and the magnetic vector of the electromagnetic field is perpendicular to the crossed-loop axis (that is, lies in the horizontal plane and is perpendicular to the line joining the radiator position and the sensor position)[2]. The following SS characteristics are evident:

a. In most cases, particularly at large distances, say 20-30 nmi, from the cloud (lightning source), with the aircraft headed generally toward the cloud, the SS dot azimuths track the cloud azimuth reasonably well. There should be no site error when the source is in the forward direction.

b. When the aircraft is near the cloud, say within 3-4 nmi, the SS dot azimuth sensing capability deteriorates. The azimuths either are wrong or fan out to the extent that they become indeterminate (e.g. Fig. 8). For example, at the aircraft flight path positions nearest to the cloud, the azimuths are fanned out over 90 degrees. Moreover, the multiplicity of dots increases, to as many as 17 per flash. The spread in azimuths cannot be explained as site errors.

c. Of the 10 single-dot flashes, 7 give erroneous azimuths. These are not explainable as site errors.

4.3 Continuous Triangulation on Aircraft Trajectory

Figure 1 shows the cloud and the aircraft flight path, with Stormscope (SS) azimuth lines emanating from various "flash positions" along the flight path. Each azimuth line represents an average of dot azimuths taken from the appropriate figure of Ref. 3. A single azimuth line has been selected here to represent each flash, whereas there are in many cases fans of azimuths.

The collection of azimuth lines generally and clearly point toward the cloud region. As the aircraft circles around the cloud, the SS azimuth lines generally point to the interior of the region. However, the distance to the source is still unknown due to the large radial spread. This figure suggests that an improved method of locating a lightning source using an airborne crossed loop is to accumulate successive azimuths (by an onboard computer) and compute their points of intersection continuously. The spread of ranges thus obtained by this "continuous triangulation" method should be much reduced, even though some remaining scatter is to be expected.

5.0 CONCLUSIONS

The principal results and conclusions, that should be valid for any crossed-loop lightning direction finder, are as follows.

Crossed-loop azimuths are reasonably good for distant lightnings, but deteriorate for nearby lightnings. The large errors in azimuth when they occur cannot be explained as site errors. The azimuthal spread is of the order of ± 3 degrees (for distant lightnings, beyond about 20 nmi) , while the radial spread is of the order

of 20 nmi. Thus, the radial spread of dots is excessive, and the ranges indicated by the dots are therefore fair at best, but generally poor to nonexistent. This is one of the main problems for single-station crossed-loop lightning locators.

The presence of site errors is suggested in relatively few cases. In most cases there was either no site error, or the azimuthal errors were excessive and not systematic (nearby lightning or single-stroke flashes).

A possible method is suggested for processing the azimuth data (of Stormscope or any other airborne azimuth detector) in such a way as to infer range while reducing the effective radial spread. This involves a technique of "continuous triangulation", whereby (using an on-board computer) one accumulates successive azimuths along the flight path and computes their points of intersection continuously. The system thus operates effectively as a two-station system, and the spread of ranges thereby obtained should be much reduced even though some remaining scatter is to be expected.

The outstanding feature of this research is as follows:

One can be sure that all the Stormscope dots that are generated by one lightning flash originate at the same location. This is always questionable if one tries to evaluate clusters.

5.1 Unanswered Questions

Several questions remain unanswered, but tentative explanations are offered, as follows:

a. Why does the azimuth capability deteriorate when the aircraft is near the lightning? Perhaps we are no longer in the "radiation zone" of the radiator. At 50 kHz the wavelength is 6 km or 3.2 nmi. Within this range we are in the induction zone of a point-dipole radiator. Moreover, since the length of a lightning channel is of the order of 6 km, the channel no longer appears as a point dipole at a range of 6 km. Also, the lightning channels may have horizontal components that can make significant contributions at close ranges. This effect (nonvertical lightning) would degrade the azimuth-detection capability of a crossed loop[2].

b. Why does the multiplicity of dots increase greatly near the lightning source? There may be, in addition to the strong pulse of a return stroke, many weak pulses radiated by the lightning channel, for instance, K-changes or electromagnetic reflections at the branch points of the channel. These weak pulses may be picked up at close range. Another possibility is the contribution of intracloud discharges to SS data; this cannot be clearly ruled out, particularly at close ranges. The manufacturer, however, appears to have designed the instrument to detect only cloud-to-ground discharges.

c. Why do single-dot flashes tend to give erroneous azimuths? We have no obvious explanation for this. There may be other storms not seen by the radar that could account for odd azimuths.

6.0 ACKNOWLEDGEMENT

We are grateful to C. Mashburn of Warner Robins Air Logistics Center for his encouragement and support, and to G. duBro, J. Reazer, P. Rustan, A. Serrano, and L. Walko of the Atmospheric Electricity Hazards Group at Air Force Wright Aeronautical Laboratories for providing the data and many helpful discussions. This work was sponsored by the U.S. Air Force under Contract F09603-83-C-1680.

7.0 REFERENCES

1. Parker, L. W. and H. W. Kasemir, Airborne warning systems for natural and aircraft-initiated lightning, IEEE Trans. Electromagnetic Compatibility EMC-24, 137-158 (1982).

2. Parker, L. W., Errors in lightning direction-finding by airborne crossed loops, International Aerospace and Ground Conference on Lightning and Static Electricity, Ft. Worth, DOT/FAA/CT-83/25, Paper #57 (1983).

3. Parker, L. W. and H. W. Kasemir, Assessment of a lightning detector as an aid in strike avoidance by a C-130 aircraft, Lee W. Parker, Inc. Final Report to Warner Robins ALC under Contract F09603-83-C-1680 (Sept. 1984).

4. Reazer, J., Data acquisition for evaluation of an airborne lightning detection system, Draft Report (Sept. 1982); Walko, L. C. and J. Reazer, Air Force Flight Dynamics Laboratory Report AFWAL-TR-83-3083 (Sept. 1983).

5. Rustan, P. L., B. P. Kuhlman, A. Serrano, J. Reazer and M. Risley, Airborne lightning characterization, Air Force Flight Dynamics Laboratory Report AFWAL-TR-83-3013 (Jan. 1983).

6. Baum, R. K. and T. J. Seymour, In-flight evaluation of a severe weather avoidance system for aircraft, AFFDL Report AFWAL-TR-80-3022 (1980).

7. Rozelle, R., Weather avoidance, an alternative to radar, The AOPA Pilot, November (1979), pp. 95-105. (Also, personal communication, 1980).

8. Uman, M., Lightning, Dover Publications, New York (1984). See also Uman, M., A review of natural lightning: experimental data and modeling, IEEE Trans. Electromagnetic Compatibility EMC-24, 79-112 (1982).

9. Johnson, R. L., D. E. Janota and J. E. Hay, An operational comparison of lightning warning systems, J. Appl. Met. 21, 703-707 (1982).

SPECIAL PROTECTION CIRCUITS AGAINST TRANSIENT CURRENTS FOR AIRCRAFT SYSTEMS

J.L. ter Haseborg and H. Trinks

Technical University Hamburg-Harburg, Harburger Schlossstrasse 20, 2100 Hamburg 90, F.R.G.

Abstract - Concerning the time domain of the response of protection circuits, containing non-linear electrical components, it is necessary to distinguish between the "early-time-response" and the "late-time-response". For example in case of multistage circuits with arresters as coarse and suppressor diodes as fine protection the early-time-response, caused by the responding arresters, may show extreme residual pulses independent of the breakdown voltage of the diodes. Responsible for the response particularly for the early-time-response are the electrical dimensions, shieldings, and mainly the arrangement of the components inside of the protection circuit. Particularly circuits with small mechanical dimensions show a typical early-time-response because all circuit components are narrow neighbouring. This may be a problem for electronic aircraft systems to be protected since here a minimum weight and minimum size for protection circuits is required.

I - INTRODUCTION

It is difficult to realize non-linear protection circuits for signal and control lines which show comparatively low residual pulses at the output terminals, e.g. voltages less than 1oV. The reason for this behaviour are the comparatively steep edges which are produced by responding non-linear components, especially arresters.

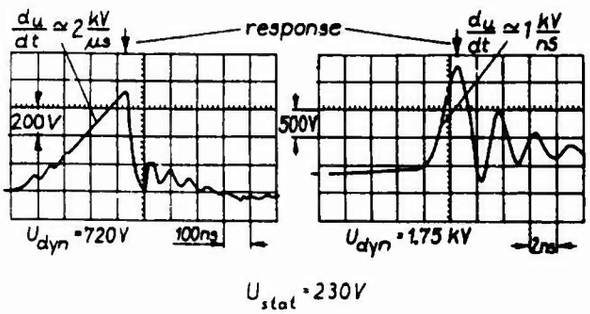


Fig. 1: Response of a gas arrester dependent on the edge steepness of the applying surge

Fig. 1 represents the response of a gas arrester applied by a surge with 2 kV/µs or with 1 kV/ns respectively, s. [1] Fig. 9, [2], [3]. The value 2 kV/µs is typical for LEMP-induced surges. In this case even the falling edge, caused by the responding gas arrester, is steeper than the rise. Changes in current are proportional to changes in magnetic field and therefore a high edge steepness may cause extreme induced voltages in loops (wiring) of protection circuits particularly in the low-voltage parts. The amplitudes of these interfering, induced voltages (early-time-response) show values, dependent on the circuit design and the edge of the pulse, of the order of several hundred volts at the output terminals of the protection circuit.

Multistage protection circuits with arresters e.g. as coarse protection and suppressor diodes e.g. as fine protection are of special interest. In this case the early-time-response (approx the first 5o ... loo ns after response of the arresters) shows extreme residual pulses and oscillations with amplitudes which are largely independent of the breakdown voltage of the suppressor diodes. These pulses or oscillations respectively show rise times down to approx. 3 ns or frequencies of 5o ... loo MHz respectively. Only the late-time-response subsequent to the early-time-response shows values identical with the breakdown voltage of the components. Concerning the development and realization of protection devices with residual pulses which are bound by the breakdown voltages - e.g. of suppressor diodes - for the early-time-response as well as for the late-time-response, a special test facility is required for measuring the response.

II - TEST FACILITY

The registration - particularly of the early-time-response - requires sensors and recording instruments which allow a reproducible detection of edge steepness up to several kV/ns.

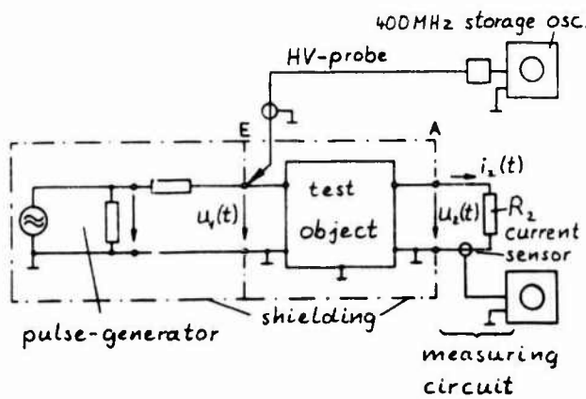


Fig. 2: Test facility for measuring the response of protection circuits

Fig. 2 shows the test facility consisting of a pulse-generator, a device containing the test object (protection circuit) to be tested, and the measuring circuit. The pulse-generator, coaxially constructed, as well as the test object are arranged in two separate shielding boxes to prevent field coupling from the generator to the test object and the measuring circuit. This is important particularly for test objects with comparatively low residual pulses < 1o V. In principle there exist two possibilities for measuring the response:

- frequency-compensated HV-probe
- current sensor

whereby both types of probes can be used in connection with a storage oscilloscope or a transient recorder (transient digitizer) respectively. In order to detect the pulses and oscillations of the early-time-response, mentioned above, a measuring circuit with a high 3 dB-frequency cutoff of 15o MHz is developed. Special current sensors are used for measuring the response $i_2(t)$ which are considerably smaller compared with typical HV-probes. Concerning protection circuits of small size, e.g. for aircraft systems, a small size of the sensors is absolutely required. The test pulse $u_1(t)$ is measured by means of a frequency-compensated HV-probe.

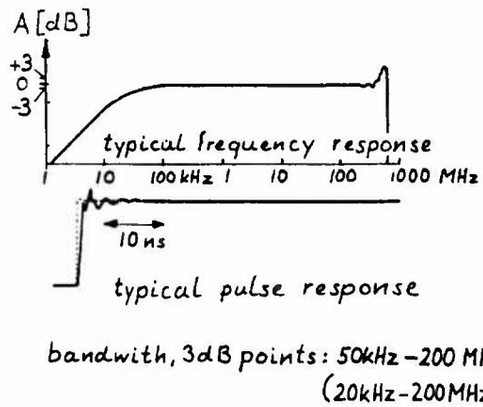


Fig. 3: Frequency response and pulse response of the current sensors

Fig. 3 shows the typical frequency response and the typical pulse response of the current sensors.

In order to measure the output current in a coaxially terminated protection circuit (e.g. 5oΩ) a special current sensor is used in order to minimize pertubation of the current to be measured.

III - MEASUREMENT RESULTS

Fig. 4 and 5 show the early-time-response and the late-time-response of two different protection circuits - terminated with 3oo Ω - consisting of two stages (gas arrester and suppressor diode) decoupled by an ohmic resistor or inductance respectively. The edge steepness of the applying surge $u_1(t)$ has a value of about 3oo kV/µs causing a dynamic threshold voltage of about 2 kV as shown in Fig. 4a and 5a. The Fig. 4b - c and 5b - c represent the early-time-response (in this case $t_{etr} \leq$ 1oo ns*)). Although the breakdown voltage of the suppressor diodes amounts to 31,4 ... 34,7 V according to the data sheet the amplitudes of the oscillations with a frequency of about 8o MHz show values of 6oo V. In Fig. 4d and 5d the late-time-response for $t_{ltr} >$ 1oo ns*) is represented. Fig. 4d evidently shows the limitation of the output current to i_2 = 11o mA or u_2 = 33 V respectively, this is exactly within the range of the breakdown voltage of the suppressor diode according to the data sheet mentioned above. The differences between the curves showing the late-time-response in Fig. 4d and 5d are due to the different series impedances R and L in the protection circuits. The two curves in Fig. 5d belong to two different terminations R_2, The shapes of these curves are dependent on the time constant L/R_2.

A special protection circuit has been developed. The following parameters for this with 3oo Ω terminated circuit were given: starting from an applying surge with an edge steepness up to 1 kV/ns a limitation of the output voltage - for both the early-time- and late-time-response - to u_2 = 9 V (i_2 = 3omA) was required. According to Fig. 6 the maximum amplitude of the early-time-response is even considerably less than 9 V. The differences between the protection circuits shown in Fig. 5 and 6 besides different breakdown voltages of the suppressor diodes and different values for L, essentially consist in a particular arrangement of the arrester, the suppressor diode, and the wiring.

IV - CONCLUSIONS

This presentation has shown that the arrangement of the components and the wiring in protection circuits may influence the output voltage (residual pulse) considerably. This is particularly a problem in the case of protection circuits with small dimensions as required for electronic aircraft systems to be protected. For low frequency systems or transmission lines respectively to be protected which are not capable to transmit the oscillations and pulses of the early-time-response only the limitation in the late-time-response is of interest and the early-time-response may be neglected.

V - REFERENCES

[1] J.L. ter Haseborg: "Transient Response of Multiconductor Transmission Lines", International Aerospace and Ground Conference, Orlando, USA, June 26-28, 1984

[2] P.A. Merz: "Lightning and NEMP-Surges on Gas Arresters. A Computation Procedure for the Transient Response", 4th Symposium on EMC, Zurich, March 1o-12, 1981

[3] J.L. ter Haseborg, H. Trinks: "Protection of Electronic Systems against Surge Voltages caused by Lightning", 17th International Conference on Lightning Protection, The Hague, Sept. 6-9, 1983

*) Indexing: "etr" → early-time-response;
"ltr" → late-time-response

Fig. 4

Fig. 5

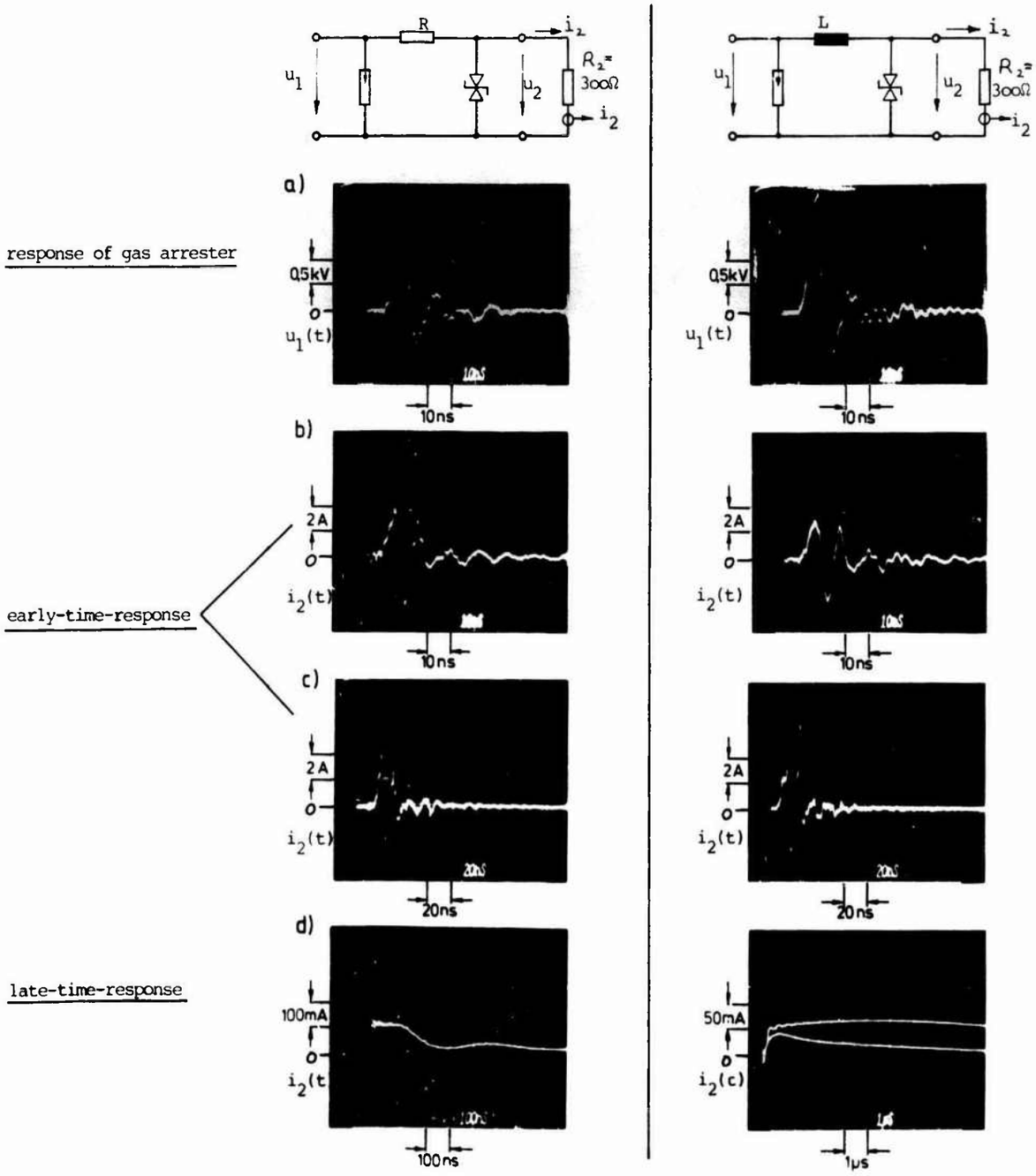


Fig. 4/5: Response of two different protection circuits
a) Applying surge (response of gas arrester)
b), c) Early-time-response
d) Late-time-response

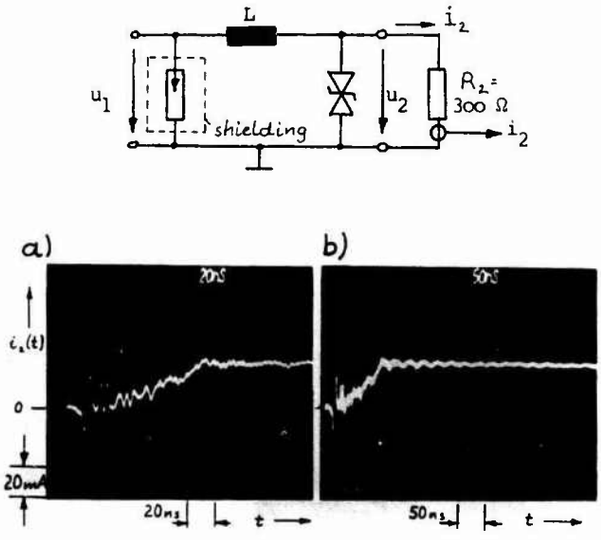


Fig. 6: Response of a special protection circuit - terminated with 300 Ω - with a voltage limitation to 9 V for early- and late-time-response
a) early-time-response
b) late-time-response

LIGHTNING-INDUCED TRANSIENT TEST ON A TRANSPORT AIRCRAFT

C. King

Boeing Commercial Airplane Company, Systems Technology Engineering, P.O. Box 3707, M/S 9R-52, Seattle, Washington 98124, U.S.A.

Abstract — Modern transport aircraft use advanced technology which incorporates multiple digital systems and makes extensive use of composite materials for secondary structure. Aircraft power, signal, and control wiring are routed through structures covered by composite materials. Shielding afforded by composite materials is often not sufficient to reduce the lightning-induced transients on aircraft wiring to acceptable levels. Wire shielding and structural shielding using foil applied to composite panels can be used to reduce the transient voltage levels on the wiring to below the damage threshold level of the equipment. The induced transient voltage levels may be assessed using analytical and/or measurement techniques.

The lightning protection design of a modern jetliner is discussed, along with details of an airplane ground test used to validate the lightning protection design. Measured engine control wiring voltage and current responses are compared with calculated values obtained using an analytical/empirical computer model.

1.0 PROTECTION OF ELECTRONIC SYSTEMS

The design of lightning-induced voltage transient protection for avionics and electrical equipment is a multi-step process. First, the lightning current threat waveform (amplitude and time history) that might strike the aircraft must be defined. There are currently two documents that detail test levels for aircraft lightning tests. These documents are the FAA Advisory Circular 20-53 and the SAE Committee AE4L report. The SAE AE4L report was released in 1978 and is accepted internationally as a valid lightning test document. The work reported in this article is based upon a lightning stroke with a peak current of 200 kA and a probable maximum rate of current rise of 2×10^{11} A/sec (airplane threat), as defined in Table II of FAA Advisory Circular 20-53.

Note: The Advisory Circular is presently being revised (AC 20-53A) to use a peak rate of current rise of 1×10^{11} A/sec and is consistent with the SAE AE4L document.

Second, the airplane design is surveyed to identify airframe apertures where electromagnetic fields can be created by the lightning current flow. At the completion of the aperture survey, the voltages induced by a specified lightning strike in wires located in an idealized aperture are calculated. We say that the aperture is idealized because its geometry, material properties, joint impedances, etc. are simplified to make the problem tractable. The voltages calculated, using the idealized model, are later modified by revising the model capacitances, inductances, and resistances to fit the measured data. Once this has been done for one wire across an aperture, there is enough assurance of the models' effectivity that voltages induced in other wires across the aperture can be calculated. Aperture analysis involves calculating the open-circuit voltage (V_{oc}) for a representative unshielded wire crossing the aperture. Shielding effects due to aircraft and foil are considered before a final open-circuit voltage value is derived. Measured results of aircraft with similar geometry and apertures are also used to help determine if the initial model provides data that is in the right range. The contributions of all apertures along a wire run are added to give a total open-circuit voltage value.

Third, the levels to which the internal wiring is exposed are established. The actual voltage induced in wiring is controlled by one or more design techniques. The simplest is to route wiring away from the aperture. Also, the use of metallic material such as aluminum foil or appropriately spaced bonding straps can be used to electromagnetically close the aperture. The most often used technique is to shield the wiring with conductive braid.

Even though at this stage of development there have been no measurements taken to validate or update the model, comparative assessments of various protection schemes can be conducted at this time. Thus, a baseline design can be developed prior to the availability of an aircraft, but the system designers and wiring engineers must be made aware that changes may be required as a result of the model update. Because the baseline may be either overdesigned (overly complex, costly, or heavy) or underdesigned, the model update phase, using actual airplane measured data, is very important (details of modeling methods are given in the reference).

It is almost inevitable that there will be changes to the design as a result of the initial airplane test and resulting model update, especially if critical control systems are involved. Wiring separation and system isolation are important considerations, and their specifications must be available to the protection system developer. The developer must also know the upset and damage voltage qualification levels of the electronic units; he or she may even influence the development of new specifications if systems trade studies (cost, weight, maintainability, etc.) show that this could be desirable.

The final step is to verify the analytical model and the protection design by testing the production airplane. When test time is limited and the aircraft is large, it may not be practical to locate the test item in a coaxial configuration to produce uniform current flow over the structure. Also, the large size of the airplane makes it difficult to test to the full threat level with respect to the peak current and maximum rate of rise.

The approach is to configure the model with a ground plane and analytically excite it with high current test pulses. This model is thus used to determine the responses that would be expected on the test airplane and the voltages expected on the wiring to the electronic units.

For the airplane discussed, the test current waveforms were chosen to be consistent with the 1978 SAE AE4L report for oscillatory waveforms G1 and G2. The G1 waveform is used to investigate resistive or diffusion flux effects, and was conducted at 2.5 kHz with a peak current of 20,000 A. The G2 waveform is used to investigate aperture coupling. An oscillatory discharge of 160 kHz, with a peak current of 20,000 A, has a maximum rate of current rise of 2×10^{10} A/sec.

The peak currents of the G1 and G2 waveform and the maximum rate of current rise of the G2 waveform are 1/10 full-scale threat. The justi-

fication for using these two waveforms to validate the lightning protection is shown in Figure 1, where the spectrum of the test currents is compared with the spectrum of 1/10 the design threat; i.e., the G1 waveform simulates the lower frequencies of lightning and the G2 waveform simulates the higher frequencies.

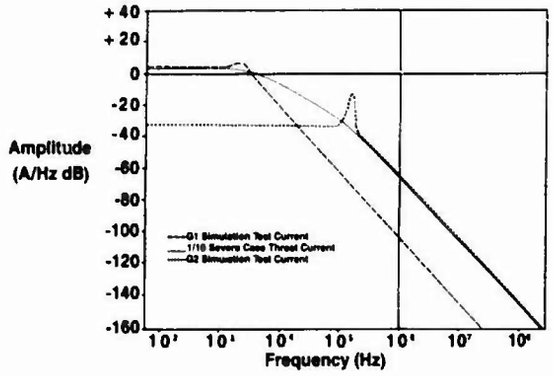


Figure 1. G1, G2 and 1/10 Severe Threat Frequency spectrum Comparison

1.1 High Current Lightning Test

Figure 2 shows the test setup. Current is driven into one wing of the aircraft by the current generators. The nacelle on the opposite wing is connected to the ground plane. This setup simulates the worst-case current path through the aircraft with respect to induced transients on the wiring of the struck engine.

The voltage and current responses on selected wiring are monitored through a fiberoptic link. Both the response current and the drive current are recorded on the programmable digitizer.

Five circuits between the fuselage and engine nacelle were selected to be monitored during the high current discharges. For convenience, it was desirable that at least one wire in each circuit be grounded in the nacelle. This allows measurement of open-circuit voltage or short-circuit current by proper termination at the fuselage end of the wire. Three circuits ran from the electronics bay in the fuselage to widely

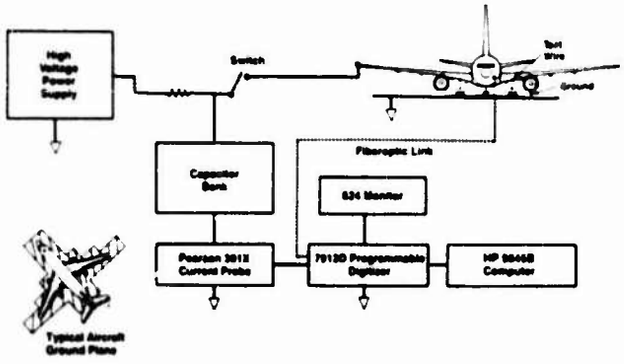


Figure 2. Pulse Generator and Measurement Test Setup

separated locations on the engine; one to the bottom of the fan cowl, one to the engine core, and one to the electronics engine control (upper fan cowl). The fourth circuit monitored was the electrical throttle link between the cockpit and the electronic engine control. In the case of the throttle link, both primary and secondary (fifth circuit) wiring of the dual redundant system was measured for induced transients.

1.2 Comparison of High Current Test Results and Model Calculations

The measured responses are shown on Tables 1 and 2 for the G1 and G2 generators respectively. The responses on Table 1 were measured with a peak current very near 23 kA for all tests. The G2 peak current varied from 8.8 to 19.7 kA during the testing. All responses on Table 2 have been linearly extrapolated to a peak current level of 19.25 kA for ease of comparison with the calculated data. On both tables, the maximum response of all circuits is listed next to the calculated values.

	Engine rpm	Oil Temperature	Oil Quality	Throttle Position	Throttle Position	Maximum Response Measured	Model Calculation
Struck Engine							
V_{oc} I_{sc}	8.8V 3.4A	4.5V 2.4A	4.5V 2.3A	4.1V 3.0A	5.0V 2.5A	5.0V 3.4A	38.0V 13.0A
Unstruck Engine							
V_{oc} I_{sc}	.68V 45A	1.2V .62A	3.0V 1.7A	1.6V .82A	.71V .33A	3.0V 1.7V	3.0V 2.5A

Table 1. Circuit Responses to G1 (23 kA) Aircraft Excitation

	Engine rpm	Oil Temperature	Oil Quality	Throttle Position	Throttle Position	Maximum Response Measured	Model Calculation
Struck Engine							
V_{oc} I_{sc}	6.3V 0.46A	6.2V 0.35A	3.9V 0.17A	4.6V 0.13A	7.6V 0.34A	7.6V 0.46A	52.2V 3.2A
Unstruck Engine							
V_{oc} I_{sc}	4.7V 0.06A	4.3V 0.06A	3.1V 0.06A	7.3V 0.16A	0.4V 0.06A	7.3V 0.16A	34.0V 0.37A

Table 2. Circuit Responses to G2 (19.25 kA) aircraft Excitation

Examples of the test data are compared with analytically derived waveforms from the computer model in Figures 3 through 6.

Figures 3a and 3b show the voltage and current response waveforms respectively measured on the engine rpm wiring circuit, as a result of the test waveform 3c produced by the G2 Marx generator. Figures 4a and 4b show the voltage and current response waveforms predicted from the model for the threat waveform shown in Figure 4c. A similar set of measured and model waveforms for the G1 test waveform are shown in Figures 5 and 6.

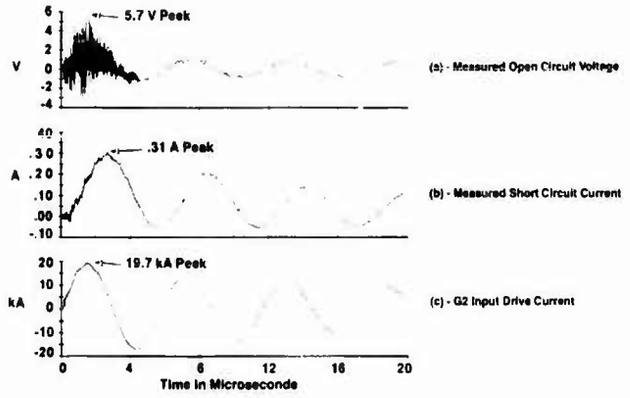


Figure 3. Measured Waveform Responses for Engine Circuit Test When Airframe Was Subjected to Output of G2 Marx Generator

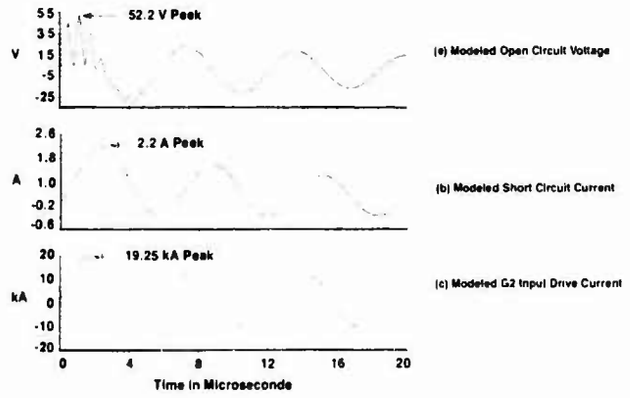


Figure 4. Calculated Waveform Responses for Engine Circuit Test When Model Was Subjected to Simulated Output at G2 Marx Generator

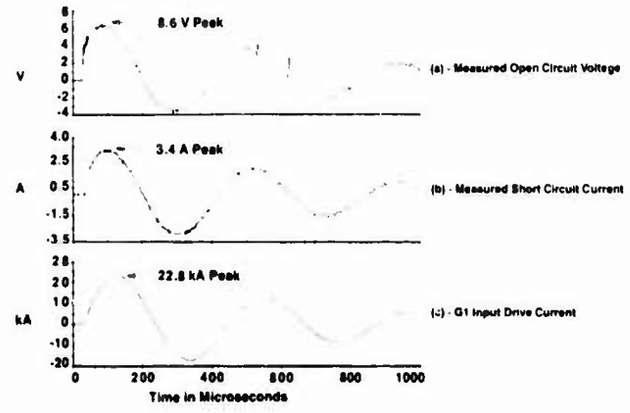


Figure 5. Measured Waveform Responses for Engine Circuit Tent When Airframe Was Subjected to Output at G1 Capacitor Bank

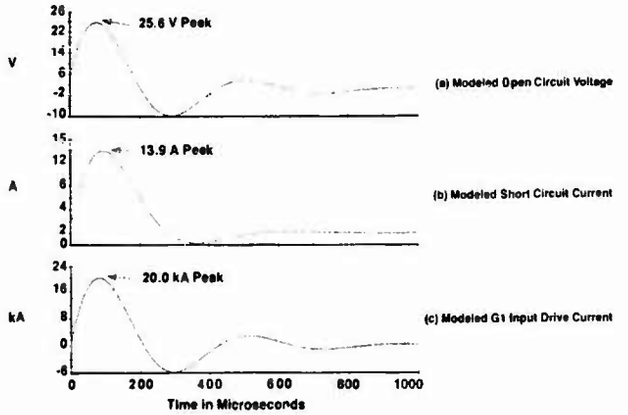


Figure 6. Calculated Waveform Responses for Engine Circuit when Modul Was Subjected to Simulated Output of G1 Capacitor Bank

The measured response waveforms have a shape similar to the calculated waveform, but of lower amplitude.

1.3 Updated Model

It is a goal to eliminate the expensive, time consuming pulse tests for protection design validation and to use the analytical/empirical model instead. The calculated responses are expected to be larger than the measured results because worst-case connector and bonding strap contact resistances are used in the model to account for production variations and aging effects. Thus, this approach may be more realistic than pulse testing because it is not economically feasible to test a statistically sufficient number of airplanes to account for the production and aging variations.

Swept-CW tests were conducted concurrently with the pulse tests on the production aircraft. The swept-CW measurements were used to update the analytical model of the production airplane. Figure 7 shows the open-circuit voltage response for both the post-test model and the pre-test model as the result of a lightning attachment of a severe stroke to the engine nacelle. The severe threat waveform is also shown for reference.

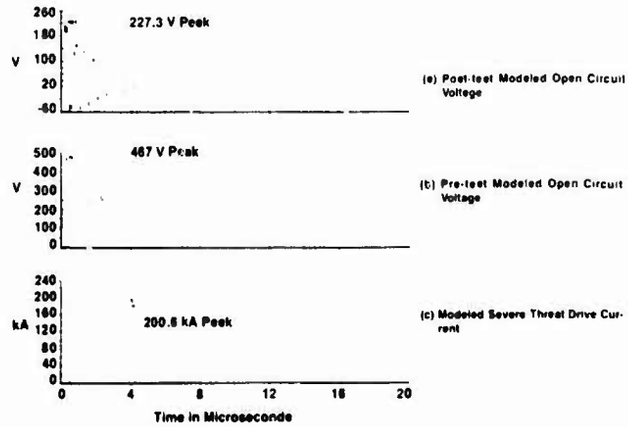


Figure 7. Calculated Waveforms Which Show Pretest and Post-Test Model Results for a Severe Lightning Threat

This waveform was derived by changing the ground test structure parameters (L, C, radiation resistance) to the inflight parameters (analytically derived) and loading the attachment points with the assumed threat impedance of 500 ohms. The approximately 2-MHz core wire resonance is close to the resonant frequency of the 600 V 1-MHz test waveform used to qualify the electrical equipment.

2.0 CONCLUSIONS

Extensive use of composite materials in structure and increased reliance on critical electrical/electronic controls requ:re a comprehensive effort to protect aircraft wiring and systems from the effects of lightning-induced transient voltages and currents.

Lightning apertures on the aircraft were identified. Detailed analysis at each aperture calculated the voltages to be induced on signal wiring. Shielding, cable overbraid, bonding jumpers, and aluminum foil were used to provide the necessary levels of protection. Line replaceable units (electronic units) were designed and proof-tested to a specified voltage waveform.

For the design described herein, the analytical model updated by swept CW measurements indicates a maximum lightning-induced transient of 220 V open circuit. Linear extrapolation of the pulse test measurements results in an open-circuit voltage of 78 V on a typical engine wire. The results of both methods show the transient voltages to be well below the 600-V equipment qualification requirement.

REFERENCE

East, D.A., "Lightning-Induced Transient Protection for Commercial Aircraft, Using Frequency Domain Analysis and Low-level Test Methods." International Aerospace and Ground Conformance on Lightning and Static Electricity, page 52-1, June 26-28, 1984.

TIME-CONVOLUTED HOTSPOT TEMPERATURE FIELD ON A METAL SKIN DUE TO SUSTAINED ARC STROKE HEATING

T.S. Lee* and W.Y. Su

Institute of Technology, University of Minnesota, Minneapolis, Minnesota 55455, U.S.A.

Abstract - For the heat-conduction problem of frontal arc strike on a metal skin, the response of hotspot temperature field to impulse heating was recently analyzed (Proc. 1984 International Aerospace & Ground Conference on Lightning & Static Electricity, p. 27-1). The results as developed apply whenever the arc dwell time is insignificant compared against relevant heat diffusion times. This last requirement is not met in many field and/or laboratory conditions. In this work, we extend the theory to the more general time-dependent source prescription by taking advantage of the system linearity and introducing a formulation based on time convolution. Integral formulas are formally derived and their utilization in practical arc-heating work is examined. The results have been applied to experiments on Titanium and Aluminum plates subjected to sustained heating due to step switch-on DC arc sources with reasonable agreements.

INTRODUCTION

By way of an initial-value problem, the diffusion in a finite plate of spark-stroke or pulsed-laser heating away from the surface strike region was analytically treated in a previous work [1]. Formulated in the natural cylindrical geometry as shown in Fig. 1., the results apply to experimental situations in which the characteristic time of thermal conduction through the plate far exceeds that of the heat release. In essence, we regard the predicted temperature rise in the plate as a response to a total impulse excitation power of $\delta(t)$ calories/sec. This causal relationship, based on inherent system linearity, is illustrated in Fig. 2, with the corresponding unit impulse response given by

$$h(r,z,t) = (\rho c \pi a^2)^{-1} F(r,t) G(z,t) \quad \text{deg.C/cal.,(1)}$$

where

$$F(r,t) = \sum_{s=0}^{\infty} \frac{(-1)^s}{s!(s+1)!} \left(\frac{a^2}{4K^2 t}\right)^{s+1} M_s(r,t)$$

$$G(z,t) = 1 + 2\sum_{n=1}^{\infty} (-1)^n \operatorname{sinc}\left(\frac{n\pi\beta}{b}\right) \cos\left(\frac{n\pi z}{b}\right) \exp\left[-\left(\frac{n\pi K}{b}\right)^2 t\right]$$

$$M_s(r,t) = \sum_{p=0}^{\infty} \frac{(-1)^p (s+p)!}{(p!)^2} \left(\frac{r^2}{4K^2 t}\right)^p$$

and

$$\operatorname{sinc} x = \sin x / x \quad .$$

In the particular case of hotspot (r = 0, z = 0), the result simplifies to

$$F(r,t) = 1 - \exp\left(-\frac{a^2}{4K^2 t}\right) \quad . \qquad (2a)$$

In addition, if a "thin-disk" model ($\beta \to 0$) for the heating cell is used, we further have

$$G(z,t) = 1 + 2\sum_{n=1}^{\infty} (-1)^n \exp\left[-\left(\frac{n\pi K}{b}\right)^2 t\right] \quad . \qquad (2b)$$

TIME-CONVOLUTED RESPONSE

In many situations involving arc spot heating, the energy input is not instantaneous. Rather, it may prolong over a scale of time on the same order of, or greater than, the characteristic heat conduction time through the plate. Under those circumstances, the initial-value-problem approach is inadequate. In its place, an approach based on time convolution for prediction of temperature response to a time-dependent continuous heating is required.

Consider in Fig. 3 the overall input-output relationship. If we denote by p(t), in cal./sec., the instantaneous input heating power starting at an initial t = 0 instant, then the temperature response at a general field point in the plate is

$$T(r,z,t) = p(t) * h(r,z,t) \quad . \qquad (3)$$

where the symbol * stands for convolution integration [2]. Expressed explicitly, this is

$$T(r,z,t) = \int_0^t p(\tau) h(r,z,t-\tau)\, d\tau \quad . \qquad (4)$$

An alternate form of this response is

$$T(r,z,t) = \int_0^t p(t-\tau) h(r,z,\tau)\, d\tau \quad . \qquad (5)$$

*Consultant, Lightning & Transients Research Institute, St Paul, Minnesota 55113, U.S.A.

ARC HEATING

The instantaneous input power p(t) for arc heating may be written as

$$p(t) = \frac{v(t)\, i(t)}{J} \qquad (6)$$

In equation (6), i(t) is the instantaneous arc current. J is a constant linking heat unit to mechanical unit. For example, J = 4.17 Joule/Calorie. In stable operations of an electric arc, the voltage supply is typically insensitive to changes in current i(t). In the case of a cathode electrode heating, it is often practicable to regard the "cathode drop" voltage (typically 10 to 30 volts) as a quantity indicative of the level of power being introduced. However, in most high-current arc work situations, it is the metal evaporation on the front surface which accounts for most of the heating power available. Thus, being associated with heat conduction in the plate, the nominal voltage v(t) in equation (6) can conceivably be taken as a moderate fraction of the total cathode-drop voltage.

CONSTANT ARC-CURRENT HEATING

In applications where a constant-current I is turned on at an initial time, the nominal voltage v(t) may be regarded a constant, V. Consequently,

$$p(t) = P\, u(t) \quad , \qquad (7)$$

where u(t) = unit step function

$$P = VI/J \quad ,$$

as illustrated in Fig. 4.

By inserting equation (7) into equation (5), we have

$$T(r,z,t) = P \int_0^t u(t-\tau) h(r,z,\tau)\, d\tau = P \int_0^t h(r,z,\tau)\, d\tau \qquad (8)$$

Typical predictions using equation (1) or equation (2) and equation (8) are of a form illustrated in Fig. 5, in which the temperature T at any field point is shown to approach its long-term asymptotic value

$$T_m(r,z) = P \int_0^{\infty} h(r,z,\tau)\, d\tau \quad . \qquad (9)$$

corresponding to an ultimate steady-state stabilization.

COMPARISION WITH EXPERIMENTS

High-current DC power sources have been routinely used to provide sustained arc heating to metal plates (principally Al) at the Lightning and Transients Research Institute. Tne results obtained here have been found to predict the overall heating characteristics well.

For a more systematic comparison, we use test data measured by Kofoid [3].In his experiments, the temperature attained at the backside of the test metal sheet was determined by the use of "Tempilaq" temperature-indicating coatings. (For details of the tests performed, the reader is referred to Reference 3.) The discharge currents ranged from 20 to 2900 A. For Ti and Al test sheets of selected thickness, the time it takes to reach a melting temperature of respectively 1320 degrees C and 620 degrees C is called critical temperature time and is denoted by T_c .In Table I, parameters pertinent to Ti and Al sheets, one each, are listed. The current levels in successive tests are 160, 220, 800, 900, 1800, and 2800 Amperes for the 0.225 cm Ti plate and 420, 480, 600, 710, 900, 1100, 1450, 1900, and 2300 Amperes, respectively. The critical-temperate time T_c for each test is duely recorded and shown in Fig. 6. Reference 4 also discussed the stroke sizes based on empirical observation. It was recommended that for most arc work an average invariant current density $J_0 = I/\pi a^2$ of 50,000 A/cm^2 and 17,000 - 36,000 A/cm^2 for Ti and Al respectively. In our use, we choose the value of 36,000 A/cm^2 for the Al plate.

For theoretical prediction we have used equations (1-2) and (8) or the hot spot temperature based on a "thin-disk" source model. For each plate a suitable nominal voltage V is chosen to match the experimental results. In Figure 6, the prediction curves have been drawn, corresponding to V = 23 volts for Ti plate and V = 3.5 volts for Al plate used.

It can be seen that the experimental and theoretical variations of T_c with I are generally in reasonable agreement. The apparent disagreement for the lower current case (I = 160 A,Ti) can be attributed to the fixed choice of J_0 = 50000 A/cm^2. This value is quite reliable for high currents. For a low arc current, it tends to underestimate the stroke size a. For the Aluminum plate, a rather small 3.5 volts for V appears to be necessary for simulation. This aspect may be attributed to the fact that the boiling temperature for Al is not too high. Before the backside temperature reaches melting at the hotspot, considerable heat may have gone into evaporating the surface metal in a total energy balance. Thus, the nominal power left for heat conduction P is accordingly reduced.

CONCLUSION

A time-convoluted heat-conduction theory has been presented for use when the source power for heating a metal plate is

sustained in time. Limited comparison with experimental data shows that, used judiciously, it can lead to reasonable agreement.

Glossary of Symbols

F	defined in eq. (1)
G	defined in eq. (1)
I	current level
J	work-heat equivalence constant
J_0	arc current density
K	square root of thermal diffusity $(k/\rho c)^{1/2}$
M_s	defined in eq. (1)
P	power level
T(r,z,t)	temperature at field point
T_c	critical-temperature time
$T_m(r,z)$	asymptotic temperature, eq. (9)
V	voltage level
a	radial dimension of heating cell
b	plate thickness
c	specific heat
h(r,z,t)	impulse response
i(t)	current
k	heat conductivity
p(t)	heating power
r	radial coordinate
z	axial coordinate
β	heating cell depth
ρ	mass density

ACKNOWLEDGEMENT

Support by the USAF Wright Aeronautical Laboratories, Wright-Patterson Air Force Base, Ohio and the Naval Air Development Center, Warminster, Pennsylvania, in the area of optical detection techniques is appreciated.

REFERENCES

1. T. S. Lee and W. Y. Su, "Transient Spark-Arc Hotspot Surface Heating on Metallic and Reinforced-Composite Skins", Proceedings of the Nineth International Conference on Lightning and Static Electricity, Orlando, Florida, U.S.A., June 1984, p. 27-1.

2. P. M. Morse and H. Feshbach, Methods of Theoretical Physics (McGraw-Hill, 1953).

3. M. J. Kofoid, "Lightning Discharge Heating of Titanium Aircraft Skins", Boeing Scientific Research Laboratories, Document D1-82-0752, (September, 1968).

Table I Parameters Related to Titanium and Aluminum Sheets Used in Tests

Parameters	Ti	Al
mass density (g/cm^3)	4.4	2.7
specific heat c (cal./g/°C)	0.16	0.217
heat conductivity k (cgs)	0.04	0.504
Critical temperature T_c (°C)	1320	620
Arc current density J_0 (A/cm^2)	50,000	36,000
Thickness b (cm)	0.225	0.203

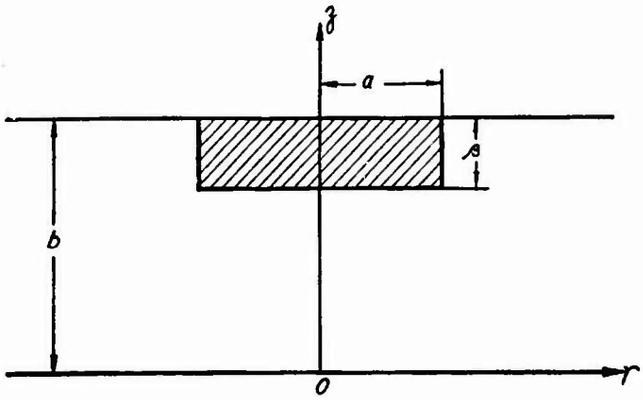


Fig. 1 - Model of initial spark-arc heating in a plate.

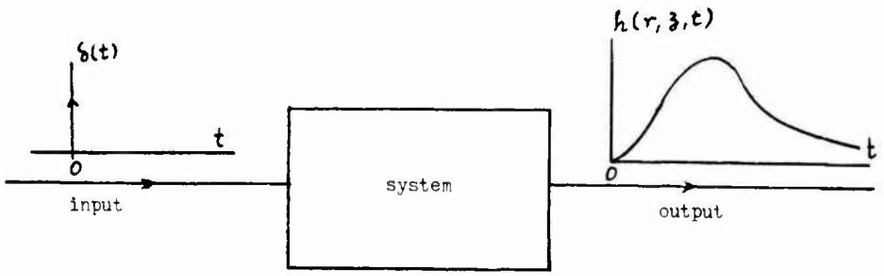


Fig. 2 - System impulse responce.

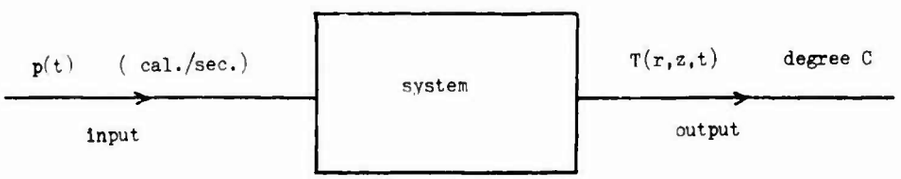


Fig. 3 - Input-output relationship governing the sustained heating of a finite plate.

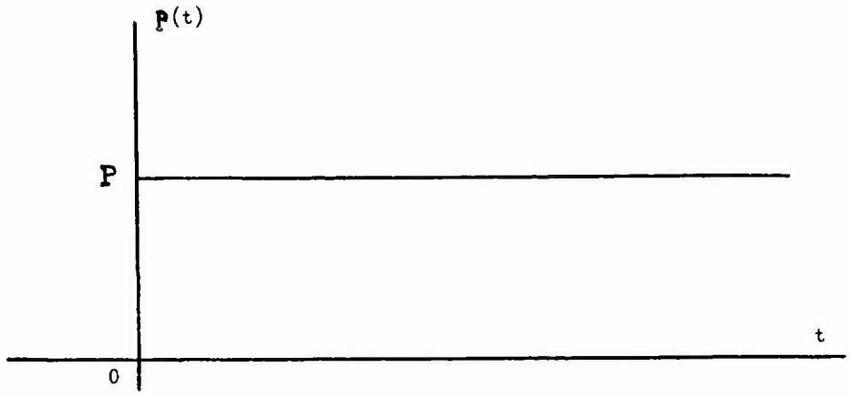


Fig. 4 - Heating power input for a constant-current arc.

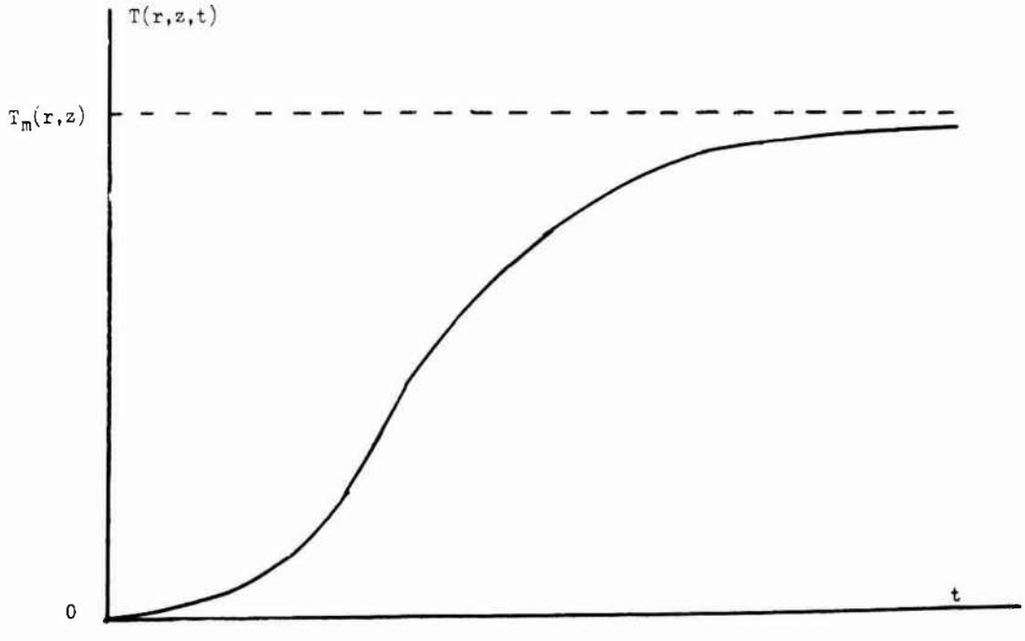


Fig. 5 - Temperature responce at a field point to constant-current arc heating.

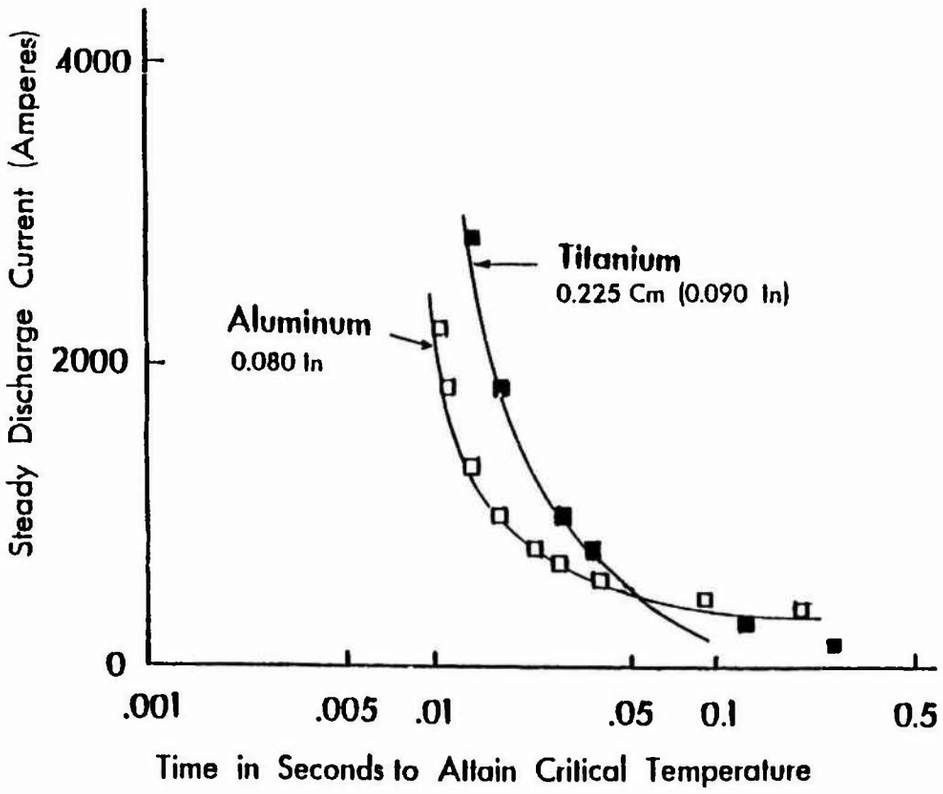


Fig. 6 - Relation between the critical-temperature time T_c and the current level I. Experimental data points are from Ref. 3 and the theoretical curves are calculated from equation (8).

RING DISCHARGE ON THE BACKSURFACE OF A COMPOSITE SKIN WITH OHMIC ANISOTROPY IN RESPONSE TO FRONTAL HIGH CURRENT INJECTION

T.S. Lee and J.D. Robb*

Institute of Technology, University of Minnesota, Minneapolis, Minnesota 55455, U.S.A.
**Lightning and Transients Research Institute, St. Paul, Minnesota 55113, U.S.A.*

Abstract - Backsurface discharge on a composite fuel tank skin under lightning strike conditions has been previously identified [Proc. 1984 Intern. Aerosp. and Ground Conf. on Lightning and Static Electricity, p. 32-1] as a potential hazard to aircraft independent of those investigated in the past. Whenever the stroke current exceeds a fixed level in amplitude, surface breakdown in the shape of a ring centered around the hotspot at a radial dimension on the order of that of the stroke becomes possible.

Conventional composite skins contain impregnated fiberous layers, resulting in anisotropic electrical properties. In the present work we have investigated the influence of this anisotropy through a simplifying model using a longitudinal conductivity $\sigma_\perp$ (perpendicular to skin) and a separate transverse conductivity $\sigma_\parallel$ (parallel to skin). It is demonstrated that the axially symmetric field can be dealt with by methods of the conventional potential theory (Laplace equation in governance) through a transformation of cylindrical coordinates in which the longitudinal length scale is expanded by a factor of $(\sigma_\parallel/\sigma_\perp)^{1/2}$. By centering attention on the region near the backsurface, we have reached two important conclusions:

1. The current flow pattern contains a stagnation-dominated near-field region and a geometry-dominated far-field decaying region. Furthermore, such a pattern is unaltered by anisotropy in conductivity. The accompanying non-colinear electrical field pattern is markedly distorted, however.

2. All conclusions concerning ignition hazard derived from the model of a uniform scalar conductivity for the skin previously examined remain intact.

INTRODUCTION

Carbon Reinforced Composites (CRC) are extensively employed in advanced aircraft structures. Their susceptibility to lightning strikes when used in fuel tank skins is of major concern. It has long been intimated that a lightning attachment to an unprotected CRC tank skin may cause internal sparking at fasteners and hot spots inside the tank with a peak temperature in excess of the autoignition temperature of the fuel vapor. In a recent work [1], hazard mechanisms based on combined mechanical - electrical considerations were suggested to account for observations in actual pulsed-arc tests of CRC skins.

Actually, in the same work [1], quite apart from thermal and/or mechanical sources, a potential ignition hazard of a purely electric origin was identified. According to this model mechanism, lightning current injection introduces electric field in the skin. With highly resistive materials like graphite, current relaxation time is far smaller than the characteristic time of the current variation. In consequence, the electric field is largely ohmic and a quasistatic picture suffices. The field on the exposed inner surface near the center of symmetry is small at small radii due to current stagnation and small again at large radii due to radial current dispersion. Near an intermediate radius on the order of the lightning arc dimension, this surface field peaks. With the inner surface exposed to a fuel-vapor mixture, a potential hazard exists when the local potential gradient on the surface exceeds its breakdown value. This corresponds to a situation in which the total lightning current rises above a certain minimum level with the result that the pattern of radial surface breakdown will be in the shape of a finite ring with a mean radius comparable to the stroke channel dimension. Figure 1 illustrates the topology of such a "ring discharge".

Modern CRC skins utilize layers of impregnated fibers for strength reinforcement. As a result, material properties are significantly anisotropic, both mechanically and electrically. In Ref.

1, the hazard due to ring discharge on the back surface was treated on the assumption of uniform isotropic conductivity, σ, throughout the skin. The degree of reasonableness of that assumption was not investigated. In this work, we shall reexamine the ring hazard problem by adopting a model of anisotropy in electric conductivity. Specifically, if we designate the direction in which current is injected as the longitudinal direction ($\hat{z}$) and with it a conductivity value of $\sigma_{\perp}$. Concurrently, we allow a separate conductivity value of $\sigma_{\parallel}$, for transverse directions. Hence, a Cartesian conductivity matrix $[\sigma]$ may be defined through

$$\underline{J} = [\sigma] \cdot \underline{E} \quad , \tag{1}$$

where

$$[\sigma] = \begin{bmatrix} \sigma_{\parallel} & 0 & 0 \\ 0 & \sigma_{\parallel} & 0 \\ 0 & 0 & \sigma_{\perp} \end{bmatrix} .$$

$\underline{E}$ is the electric field and $\underline{J}$ is the current density. The lightning current field has solenoidal symmetry. Thus, we readily relate the radial and the axial components of both $\underline{J}$ and $\underline{E}$ through (1) as

$$\begin{bmatrix} J_r \\ J_z \end{bmatrix} = \begin{bmatrix} \sigma_{\parallel} & 0 \\ 0 & \sigma_{\perp} \end{bmatrix} \begin{bmatrix} E_r \\ E_z \end{bmatrix} \tag{2}$$

in a cylindrical coordinate system. Implicit are a field structure and a current structure in the form

$$\underline{E} = E_r \hat{r} + E_z \hat{z} \tag{3}$$

$$\underline{J} = J_r \hat{r} + J_z \hat{z} \quad . \tag{4}$$

As vector fields, they are not locally colinear.

EQUATIONS

The charge conservation law as applied to a quasistatic field is

$$\nabla \cdot \underline{J} = 0 \quad , \tag{5}$$

which imposes the divergence-free constraint on $\underline{J}$. In view of (4), this equation is equivalent to

$$\frac{1}{r} \frac{\partial}{\partial r}(r J_r) + \frac{\partial}{\partial z}(J_z) = 0 \quad . \tag{6}$$

By (2), we have

$$\frac{\sigma_{\parallel}}{r} \frac{\partial}{\partial r} (r E_r) + \sigma_{\perp} \frac{\partial}{\partial z} (E_z) = 0 \quad . \tag{7}$$

At this point, let us introduce a scalar electric potential V (r,z) such that

$$\underline{E} = - \nabla V \tag{8}$$

or

$$E_r = - \frac{\partial V}{\partial r} \tag{9}$$

$$E_z = - \frac{\partial V}{\partial z}$$

Equation (9) transforms (7) into

$$\frac{\partial^2 V}{\partial r^2} + \frac{1}{r} \frac{\partial V}{\partial r} + \left(\frac{\sigma_{\perp}}{\sigma_{\parallel}}\right) \frac{\partial^2 V}{\partial z^2} = 0 \quad . \tag{10}$$

COORDINATE TRANSFORMATION

Equation (10) is a linear, homogenious, second-order, partial differential equation governing V. Its solution may be facilitated by replacing the system of cylindrical coordinates (r, ϕ, z) with a new system of cylindrical coordinates (R, $\bar{\Phi}$, Z). Specifically, we use

$$\begin{aligned} R &= r \\ \bar{\Phi} &= \phi \\ Z &= (\sigma_{\parallel} / \sigma_{\perp})^{1/2} z \quad , \end{aligned} \tag{11}$$

in effect contracting the longitudinal length scale. At the same time, if we write

$$V(r,z) \equiv \bar{V}(R,Z),$$

equation (10) becomes

$$\bar{\nabla}^2 V = 0 \quad , \tag{12}$$

where $\bar{\nabla}^2$ is a Laplacian operator in the new coordinate system. Solutions to this Laplace equation are better documented and known than those to (10).

SOLUTION DESCRIBING CURRENT FIELD NEAR BACKSURFACE

1. Nearfield: - Field in the current-stagnation region (r << a).
   Equation (12) has the special solution

$$\bar{V}(R,Z) = S \left[(R^2/2) - Z^2 \right] + P \quad , \tag{13}$$

where S and P are constants. By (11), this is

$$V(r,z) = S \left[(r^2/2) - (\sigma_{\parallel}/\sigma_{\perp}) z^2 \right] + P \quad . \tag{14}$$

In correspondence, (2) and (9) help yield

$$E_r = - Sr$$

$$E_z = 2S(\sigma_{\parallel}/\sigma_{\perp}) z$$

$$J_r = -S\sigma_{\parallel} r$$
$$J_z = 2S\sigma_{\parallel} z \quad . \qquad (15)$$

In Fig. 2(a), constant $\overline{V}$ curves are hyperbolas in the new (R,Z) coordinates. The corresponding constant V curves are also hyperbolas, when plotted in the physical coordinates (r,z). These are now shown in Fig. 2(b), in which we have also shown the $\underline{E}$ fluxlines as dotted curves and the $\underline{J}$ fluxlines as solid curves. The non-colinearity between $\underline{E}$ and $\underline{J}$ fluxes are readily apparent.

In Ref. 1, we constructed the current field for the case of an isotropic conductivity, out of an analogy with the fluid velocity field for an axially symmetric steady incompressible stagnation flow. In the present case, no convenient analogy is apparent. Nevertheless, an examination of (15) reveals that

$$J_r(0, z) = 0$$
$$J_z(r, 0) = 0 \quad ,$$

satisfying precisely the kinds of boundary conditions required of a stagnation flow. Hence, the choice of the particular solution (13) or (14) for representation is justified.

The constant S used in (13)-(15) may be judiciously estimated by the following scheme: The current injection takes place over an effective area of πa^2 on the outer surface at an elevation of z = b. We identify $J_z(o,b)$ with the mean injection density, i.e.,

$$J_z(0, b) = -I/\pi a^2 \quad ,$$

which, by (15), determines

$$S = -I/2\pi a^2 b \sigma_{\parallel} \quad ,$$

resulting in

$$E_r = Ir/2\pi a^2 b \sigma_{\parallel}$$
$$E_z = -Iz/\pi a^2 b \sigma_{\perp}$$
$$J_r = Ir/2\pi a^2 b$$
$$J_z = -Iz/\pi a^2 b \quad . \qquad (16)$$

2. Far field in the skin (r >> a).

In this limit, the physical expectation is that the injected current will be conducted radially away. The cross-skin flow will cease and the radial conduction will be uniform. Thus, at larger r, we have

$$J_r = I/2\pi br$$
$$J_z = 0$$
$$E_r = I/2\pi b\sigma_{\parallel} r \qquad (17)$$
$$E_z = 0$$
$$V = -\frac{I}{2\pi b \sigma_{\parallel}} \ln r + q \quad ,$$

where q is a constant.

The field strength on the backsurface is given by $E_r(r,o)$. Its characterizations in the near field and the far field are now in hand, in (16) and (17), respectively. To appreciate the overall distribution, we have sketched these in Figure 3. Peaking of the field strength occurs near r = a at a magnitude on the order of $I/2\pi ab\sigma_{\parallel}$. If the breakdown strength of the contiguous fuel vapor is E_c, then there is a critical current level

$$I_c = 2\pi ab\sigma_{\parallel} E_c \quad , \qquad (18)$$

above which a hazard by way of ring-shaped surface discharge must definitely be reckoned with. To obtain a nominal value for I_c under operating conditions, let us assume that the aircraft is at an altitude of 30,000 ft., for which we use E_c approximately equal to 6 KV/cm. For a painted skin of thickness $b \simeq 1$mm, the typical stroke size is on the order of a=1 mm. Equation (18), thereupon, gives $I_c \simeq 80$ kamps, a value within the experiences of natural lightning phenomena.

Discussions

1. The model is based on the assumption that the lightning current I(t) is specified a priori, as, for example, may be provided by an idealized current source.

2. As seen in (16) and (17), the current field distribution is unaffected by anisotropy in resistivity. The corresponding electric field is markedly distorted, however.

3. The constants P in (13) and q in (17) are immaterial to immediate discussions. However, they are meant to be chosen in such a way as to lead to mutual compatibility in global mapping.

Conclusions

The backside discharge hazard to a CRC fuel tank skin under lightning strike conditions has been investigated for a model utilizing anisotropy in resistivity. Whenever the instantaneous current exceeds a fixed amplitude, surface discharge in the form of a ring centered around the hot spot with a dimension on the order of that of the stroke is expected to occur. The skin curent distribution is independent of resistive anisotropy.

Conclusions on global backsurface field strength drawn from previous work on an isotropic model are unchanged by the

introduction of anisotropic resistivity. The surface field pattern depends for quantitative evaluation on the strike current, the skin thickness, the stroke size and the transverse conductivity only.

The new hazard mechanism of backsurface ring discharge is totally separated from hazard mechanisms based on thermal-conductions, mechanical, fastener-sparking, or, ohmic-heating concepts which have been advanced and investigated in the past. It may exist in combination with one or more of those named in a realistic lightning strike situation. Depending on the stroke characteristics, the electrical, mechanical, and thermal properties as well as the thickness of the skin, its relative effect could well prove significant in specific hazard situations.

Acknowledgement

Support by the USAF Wright Aeronautical Laboratories, Wright-Patterson Air Force Base, Ohio and the Naval Air Developemt Center, Warminster, Pennsylvania, in the area of optical detection techniques is appreciated.

References

1. J. D. Robb, and T. S. Lee, "Combined mechanical-electrical ignition hazards to carbon-reinforced composite fuel tanks," Proc. 1984 Intern. Aerospace and Ground Conf. on Lightning & Static Electricity, p. 32-1.

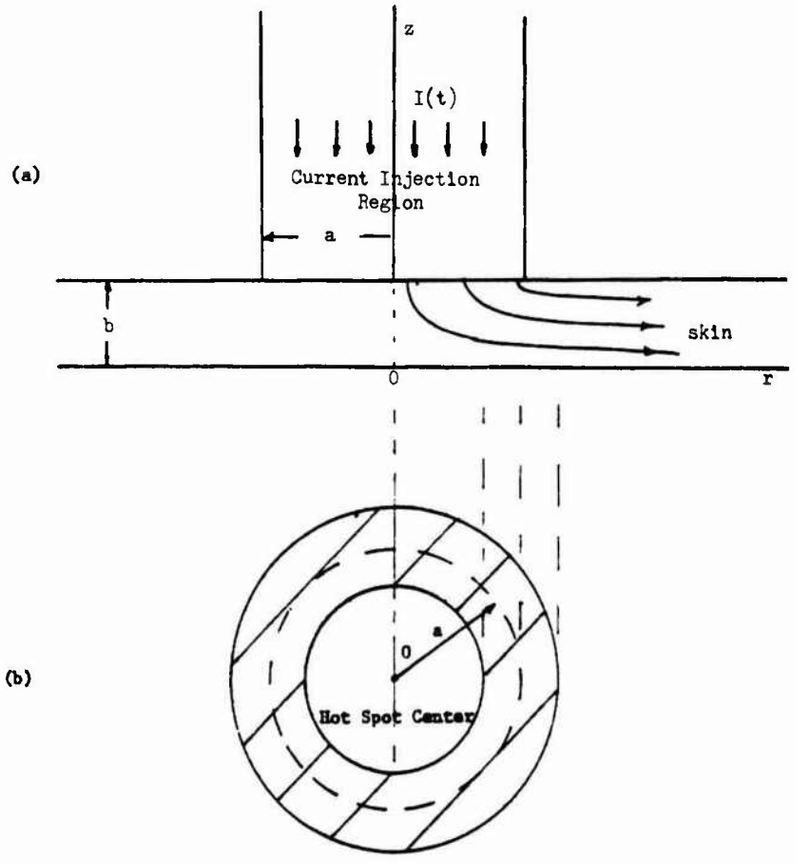
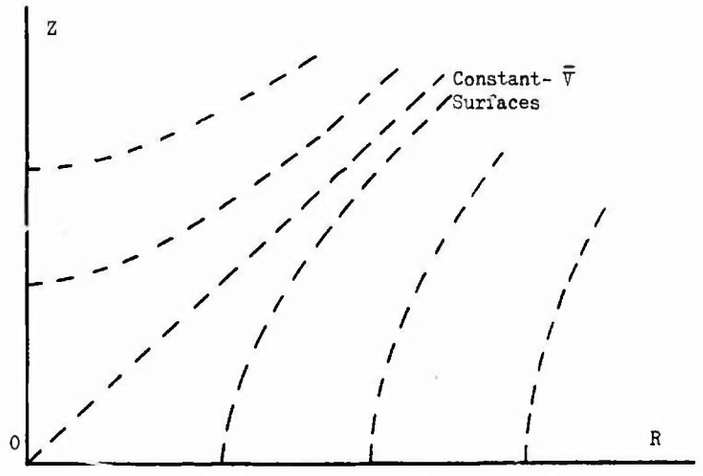


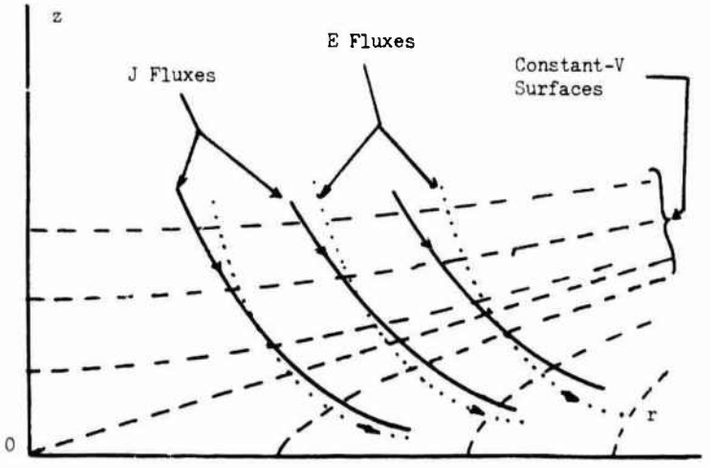
Figure 1. Ring Discharge.

(a) Lightning-Arc Current Injection. b is the skin thickness and a is an effective radius of the frontal stroke.

(b) Hazard Band on Backside of Skin in Which the Surface is Vulnerable to Local Gaseous Breakdown.



(a)



(b)

Figure 2. Axially Symmetric Stagnation Current Flow Field.

(a) Constant Potential $\bar{V}$ Surfaces Displayed in the Plane with Contracted Vertical Coordinate.

(b) Potential Current Flow in the Physical Coordinate Plane($\sigma_{\parallel}/\sigma_{\perp} > 1$): - - - - constant V surfaces; ····· electric flux lines; _____ current flux lines.

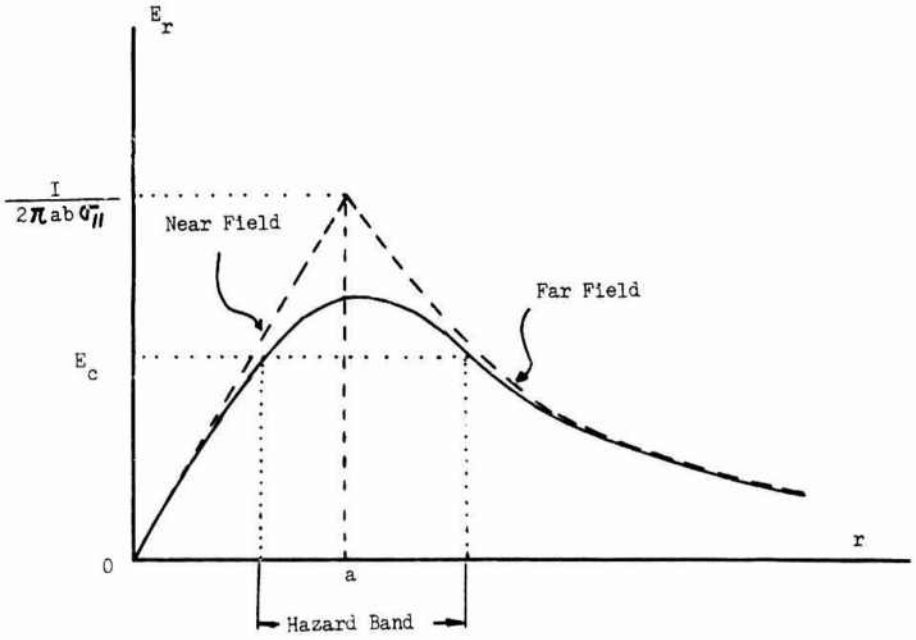


Figure 3. Radial Variation of Back Surface Field Strength. Indicated Hazard Band Corresponds to the Range of Radii over Which this Field Strength Exceeds Local Breakdown Threshold.

DEVELOPMENT AND TESTING OF PROTECTION MEASURES FOR REINFORCED COMPOSITES AGAINST LIGHTNING STRIKE

H.-P. Wentzel, C.M. Herkert*, Th. Thiele** and G. Boes***

Messerschmitt-Bölkow-Blohm GmbH, Unternehmensbereich Transporter, Postfach 10 78 45, D-2800 Bremen 1, F.R.G.
**Messerschmitt-Bölkow-Blohm GmbH, Unternehmensbereich Hubschrauber und Flugzeuge, Postfach 80 11 40, D-8000 München 80, F.R.G.*
***Dornier GmbH, Postfach 14 20, D-7990 Friedrichshafen, F.R.G.*
****Institut für Plasmaphysik der Universität Hannover, Callinstr. 38, D-3000 Hannover, F.R.G.*

ABSTRACT

The paper gives the results of a programm performed under contract to the German Ministry of Defence by German Aerospace Companies. (Messerschmitt-Bölkow-Blohm GmbH, Dornier GmbH, Industrieanlagen - Betriebsgesellschaft mbH and the Institute of Plasmaphysik, UNI-Hannover).

It covers surface lightning protection systems and electrical bonding measures for carbonfiber - reinforced composites (CFC) structures.

Furthermore, the influence of humidity on CFC (solid- and sandwichplates) by lightning strike has been investigated. Only direct effects, that means influences on the structure itself, have been considered.

As protective materials aluminum mesh and aluminum mesh with a dielectric material (Kevlar-fabric) have been regarded. In the test rig at the Institute of Plasmaphysik (University of Hannover) specimens with the above mentioned protective materials were tested. The different types of specimens were loaded with simulated lightning discharges:

- Solid CFC-plates (1 mm) protected with aluminum mesh/ Kevlar-fabric

- Electrical bonding test specimens composed of a solid CFC-plate with/without metal protection system and CFC-substructure

- Solid CFC-plates and sandwich-plates with different core materials (aluminum and Nomex) with a height of 10 mm and 50 mm and the effects of the influences of humidity in these specimens have been investigated, tested and evaluated.

In a further step electrical bonding test specimens composed of a solid CFC-plate with different structure parameters have been investigated, tested and evaluated.

Lightning discharges applied to the specimens were:

100 kA ($0.25 \cdot 10^6$ A^2s), 200 kA ($0.6 \cdot 10^6$ A^2s),
200 kA ($2.0 \cdot 10^6$ A^2s).

Test results will be presented with the aid of damage diagrams, showing specimens type, applied actual electrical discharge, residual strength, test number and damaged area on protection system, electrical bonding measures on composite structure.

I - INTRODUCTION

CFC structures for secondary and primary aircraft components will be increasingly used at present and in future. These parts are mainly located on the surface of the aircraft and, therefore, may possibly be struck by lightning, depending on where they are located on the aircraft.

Basically, such a lightning strike can have two different influences on the aircraft:

indirect effect caused by electromagnetic fields introduced in cables and electronic equipment and direct effects on the structural component itself. In the following paper discussions will be limited to direct effects.

II - SPECIMEN GEOMETRY AND MANUFACTURING

(A) - Solid CFC-plates (1 mm)

The dimensions of the solid plates (Fig. 1) are 400 x 400 x 1,3 mm. These plates are composed of a CFC-structure coated with protection system aluminum mesh (100 g/m^2) and Kevlar-fabric (Interglas No. 98 605).

The aluminum mesh and Kevlar-fabric were laid up on wet CFC-prepreg and cured in one-shot at 175 °C.

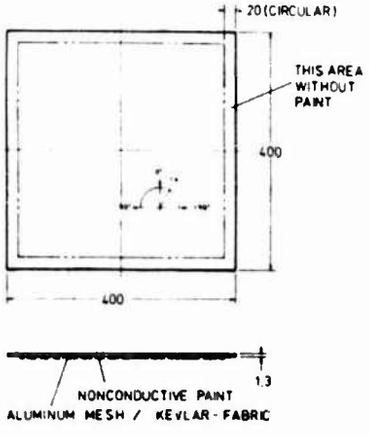


Fig. 1 Dimension of solid CFC specimen

(B) - Electrical bonding test specimen with CFC-substructure

The aim of the investigation was to find a difference between titanium-screws and blind-rivets as well as wet or dry assembled to divert the current from the protection into the CFC-substructure. For the electrical bonding several designs were selected, of which the following types shall be demonstrated (see Fig. 2 and 3)

- bonding type
  - ° titanium screws (Fig. 2)
  - ° blind-rivets (Stainless Steel) (Fig. 3)
- assembly type
  - ° wet
  - ° dry
- protection
  - ° aluminum-mesh
  - ° no protection

The dimensions of the electrical bonding test specimens are 402 x 200 x 3,1 mm and it is composed of a CFC-structure either coated with aluminum-mesh or not. The CFC-structures (plates) were drilled, countersunk, screwed and riveted with the CFC-substructure (overlap-joint, C-profile).

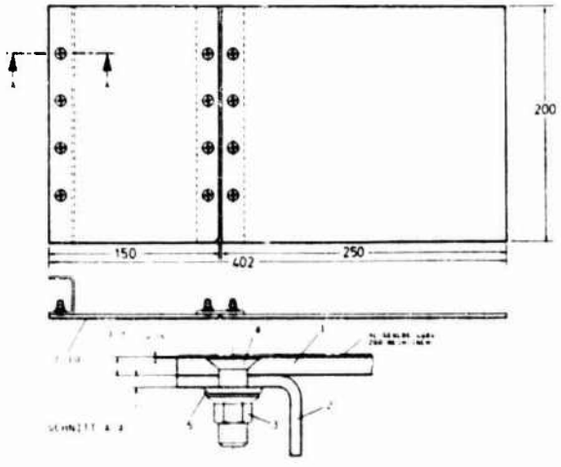


Fig. 2 Bonding type titanium screws

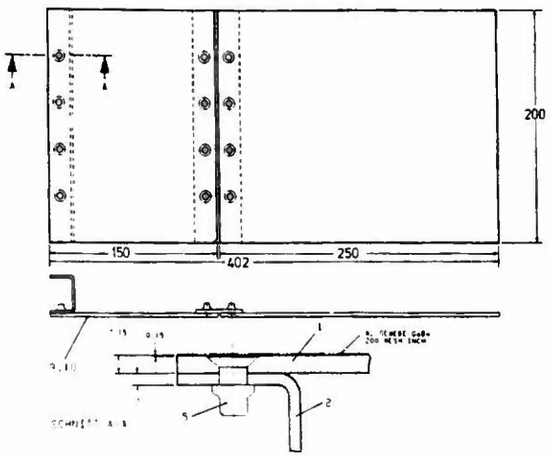


Fig. 3 Bonding type blind-rivets

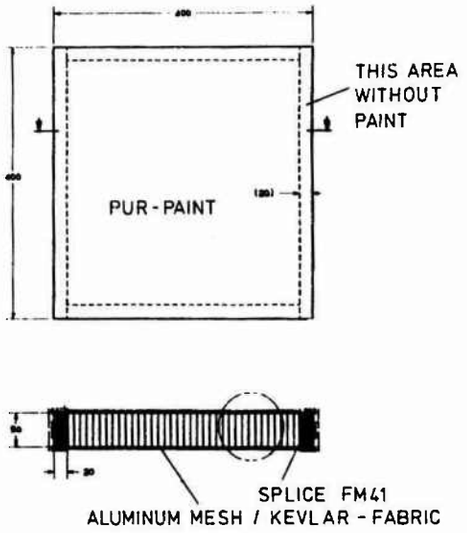


Fig. 4 Dimension of CFC sandwich specimen

(C) - Solid CFC-plates and sandwich-plates

The aim was to investigate the effects of the influences of humidity of the damage area in the CFC-structure after simulated lightning strike. The dimensions of the solid plates are 400 x 400 x 1 and 3 mm. The plates are composed of a CFC-structure coated with the protection systems aluminum mesh and aluminum mesh with Kevlar-fabric (similar Fig. 1).

The dimensions of the sandwich-plates are 400 x 400 mm with a core thickness of 10 mm and 50 mm. The different core materials (aluminum and Nomex) were cut and bonded with CFC-facings (thickness 1,0 mm) by a high temperature adhesive film cured at 175 °C (Fig. 4).

All sandwich-plates were coated with the protection systems aluminum mesh and aluminum mesh with Kevlar fabric on both facings.

(D) - Electrical bonding test specimen with different structure parameters

The aim was to find a solution to divert the current through the overlap joints. The following 4 types shall be demonstrated (see fig. 5, 6, 7, 8).

- bonding type ° CFC-CFC without intermediate insulating layer
- bonding type ° CFC-Al with intermediate insulating layer GFRP + Sealing
- bonding type ° CFC-Al with intermediate insulating layer GFRP, Sealing + liquid shim
- bonding type ° CFC-CFC with intermediate insulating layer Sealing PR 1403G

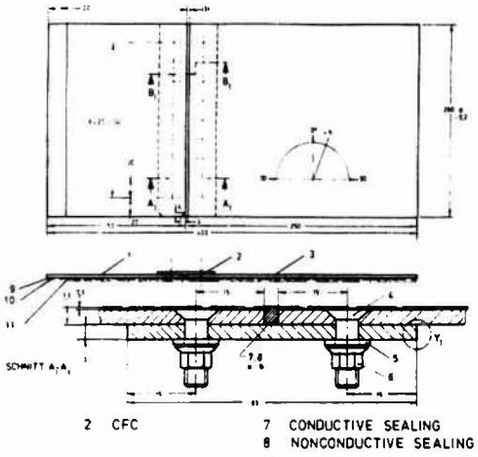


Fig. 5 CFC-CFC without intermediate insulating layer

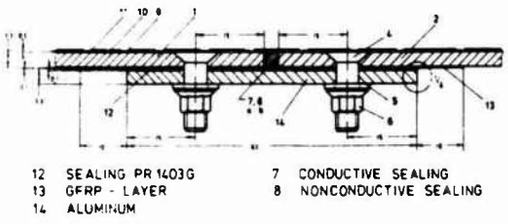


Fig. 6 CFC-Al with intermediate insulating layer GFRP + sealing

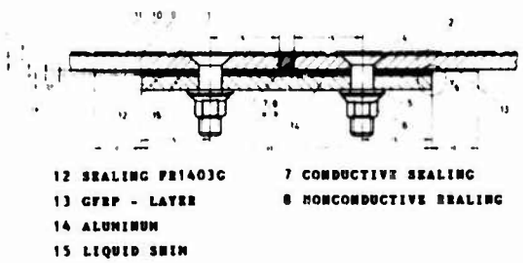


Fig. 7 CFC-Al with intermediate insulating layer GFRP, Sealing + liquid shim

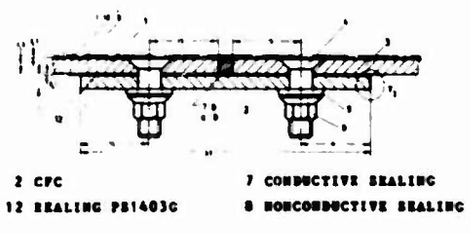


Fig. 8 CFC-CFC with intermediate insulating layer Sealing PR 1403G

The dimensions of the electrical bonding specimen are 403 x 200 x 3 mm and it is composed of a CFC-structure coated either with aluminum mesh and Kevlar fabric or not. The CFC-plates were drilled and countersunk and screwed with titanium-bolts (Ø 5 mm). For the gapsealing conductive as well as nonconductive sealing were used. At these electrical bonding specimens the residual strength after lightning strike were investigated.

All specimens were painted with a nonconductive polyurethane paint.

The peripheries of all solid plates and sandwich-plates were freed from paint and adhesive (electrically conductive area to the testframe).

For the manufacturing of the CFC-structure prepreg, Fibredux 914C/T300 Ciba-Geigy was used. The CFC-structure was the same for all specimens $(0/90/+45/-45)_s.n$.

III - TEST FACILITY AT THE UNIVERSITY HANNOVER

- Peak current facility

The current facility (Fig. 9) enables simulation of the components of the stroke current of a natural lightning discharge. The source is set up to generate pulses from 10 to 200 kA at a maximum action integral $\int i^2 \cdot dt = 2.5 \times 10^6 A^2 s$. The capacitor bank consists of 96 capacitors (4.6 µF each) arranged in couples connected in series. There are 4 sections which can be electrically separated from one another, each section consisting of 12 groups. One of the sections can be subdivided into any number of groups from 1 to 12. The peak current is switched by means of an encapsulated central spark gap, the operating voltage of

which is controlled over a wide range of variation of the gas pressure. Moreover, the damping of the shock circuit can be influenced by changing the number of coaxial conductor cables (a maximum of 15) between the capacitor bank and the work table. Thus the set up can be used for a large field of parameters.

- Continuing current facility

As soon as the discharge initiated by the current pulse impinges upon the test specimen, a second circuit is closed which provides a current of 100 to 500 A drawn from 120 car batteries at a total voltage of 1440 V. The current and its duration, i.e. the amount of charge, can be predetermined by using appropriate series resistors (24 x 6.05 Ω) and a timer (25 ms to 6 s). A current of 500 A is still obtained with extended test samples having a higher resistance (maximum 1 Ω).

In order to definitely avoid interruption of the current during this phase of the discharge - usually the arc lengths are 50 mm - a low resistance air coil of 20,5 mH has been inserted in the circuit. The inductive voltage will sustain the arc. Since there may be 50 kV between the test specimen and the electrode opposite to it, the car battery assembly has to be protected against the high voltage pulse. The protective device is a two-stage LC filtering network which acts as a voltage divider at the frequency of the shock discharge. Additional protection is provided by the low pressure protection gap having a triggering voltage 200 V above the battery voltage.

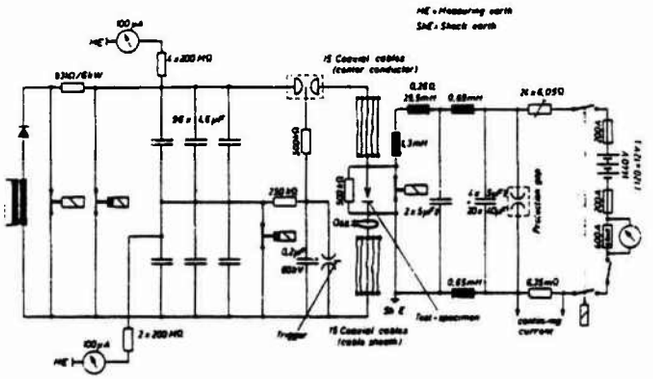


Fig. 9 Circuit of the lightning simulation facility

- Electrode, dimensions of test specimen

The electrode can be pointed toward any region of the test specimen, thus permitting several loads for a given specimen.

The electrode is a tungsten rod (10 mm diameter) held in a brass receptacle. The bottom end of the electrode is tipped by an insulating sphere made of Araldite. Thus the current will flow from an electrode surface perpendicular to the surface of the specimen, and the plasma jet emanating from the electrode (containing electrode material) will not hit the specimen and affect the visual appearance of damage. In order to facilitate breakdown, a carbon fiber protruding from the electrode is used which ends about 10 mm above the sample.

The maximum dimension of the specimen is limited by the size of the test room and its doors. The entrance has a height of 1.95 m and a width of 2.35 m. The test room will accommodate lengths up to 9 m. Objects up to 2.65 m x 2.55 m x 6 m may be tested on an adjacent platform which can be locked up. For still larger objects, outdoors tests can be arranged.

- Measuring technique

In the experiments the peak current is measured as a function of time using a calibrated Rogowski coil including a calibrated integrating unit. In addition, the continuing current is measured using a insulated amplifier and a digital recorder. The data are then fed into a desk computer for calculation of the action integral, the peak current, the rate of rise of current from 0 % to 90 % of the pulse amplitude, the amount of charge and the average of the continuing current. The curve can be displayed on an oscilloscope screen.

IV - PERFORMANCE TEST

The tests were carried in following phases:

	Test specimen type
Phase 1: 200 kA peak current, 2 . $10^6 A^2s$ action integral	(A) (B) (C) (O)
Phase 2: 200 kA peak current, 0,6 . $10^6 A^2s$ action integral	(A) (B)
Phase 4: 100 kA peak current, 0.25 . $10^6 A^2s$ action integral	(C)

The solid plates and the sandwich plates were loaded several times per specimen. The electrical bonding specimen was loaded in the center of the specimen.

The specimen was stretched in a rectangular frame, so that a good electrical contact about the four edges from the solid plates and sandwich plates was guaranteed. For the connection of the electrical bonding specimen at the test frame, brass frames were used. Because of the large number of tests, a small selection of test results is presented.

V - RESULTS OF LIGHTNING TESTS

- General

Test results are shown in damage diagrams. In the top of these diagrams the intended actual loading of the specimen is given. On the left-hand side of the diagrams the information about the damage area classification (in width and depth) with respect to protection system and CFC-structure is shown. From the right-hand side of these diagrams remarks on the abbreviations used and information about used materials can be taken. On the bottom of the diagrams the relationship between test number and specimen type can be seen.

(A) - Solid CFC-plates (1 mm)

The test results (Fig. 10) with the solid CFC-plates of 1 mm protected with aluminum mesh and Kevlar-fabric shows that the CFC-structure could be effectively protected by the insulating layer Kevlar-fabric between CFC-structure and aluminum mesh.

Furthermore, the Kevlar-fabric-layer prevents the contact corrosion between CFC and aluminum mesh.

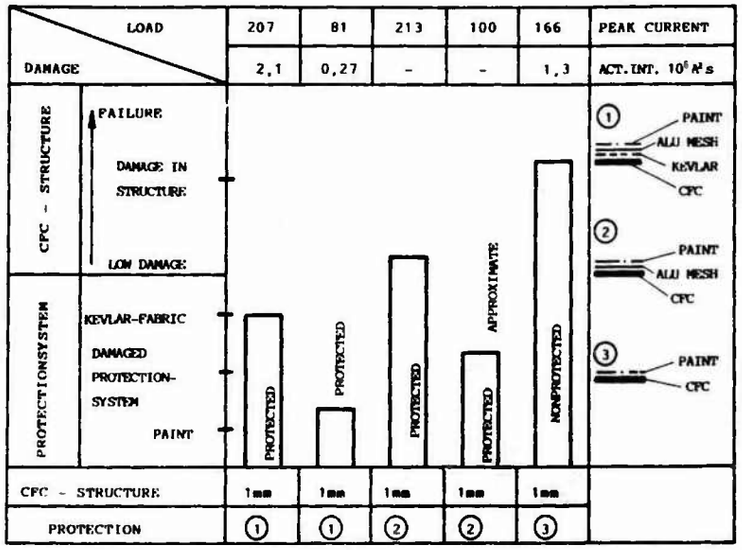


Fig. 10 Lightning test results of solid plates (1 mm) protected with aluminum mesh and Kevlar-fabric compared with aluminum mesh protected and non-protected CFC-structure

(B) - Electrical bonding test specimen with CFC-substructure

° Electrical resistance measurements

The test results (Fig. 11) show that the protection system aluminum mesh has only a little influence on the electrical resistance measurements and that the dry assembled rivets are better then wet assembled. The measurement results of the specimen types Ti-screws are the same, whether dry or wet assembled.

The electrical resistances R have been determined by the measurement of voltage drop at a constant current of 10 A.

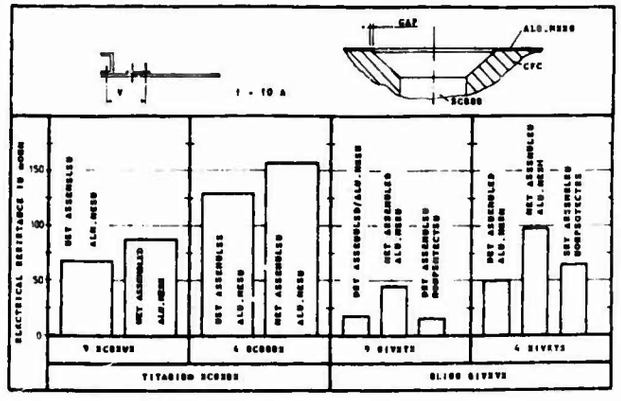


Fig. 11 Electrical resistance R in mΩ

° lightning strike test results

A lot of electrical bonding specimens consisting of 3 mm thick CFC solid plates covered/noncovered with protection system and bonded via bolts to the CFC substructure were tested.

The design of the specimen type with titanium screws (wet or dry assembled) successfully passed all tests 200 kA, $2 \cdot 10^6 A^2s$; 200 kA, $0.6 \cdot 10^6 A^2s$ (see Fig. 12 and 13).

The design of the specimen type with blind rivets (wet or dry assembled) was not satisfying (see Fig. 14 and 15).

All specimen types with blind rivets, which were loaded with 200 kA, 2 . $10^6 A^2s$, were damaged. Only the specimen type with 9 blind rivets in row passed successfully the test 200 kA, 0.6 . $10^6 A^2s$. The lightning strike test results were given in Fig. 16.

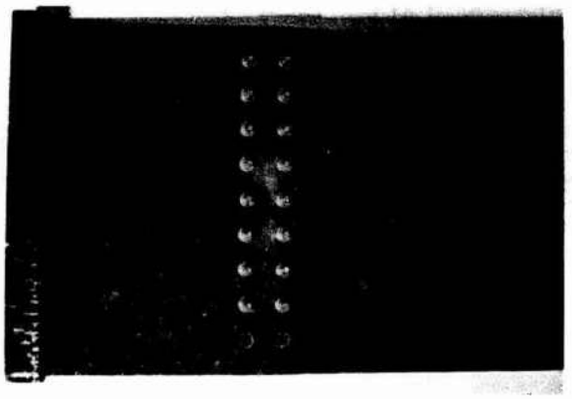


Fig. 12 Specimen type with titanium screws, 9 bolts in row

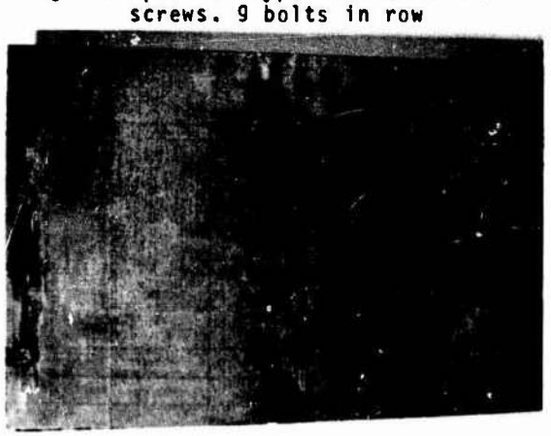


Fig. 13 Specimen type with titanium screws, 4 bolts in row

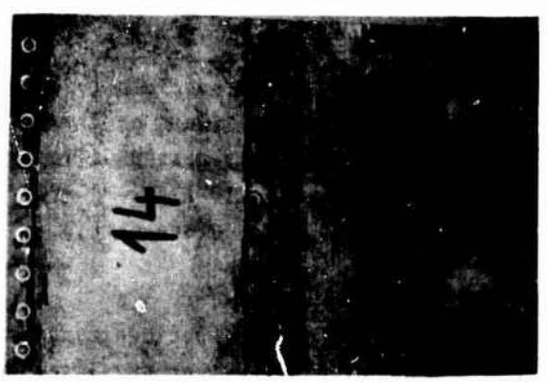


Fig. 14 Specimen type with blind rivets, 9 rivets in row



Fig. 15 Specimen type with blind rivets, 4 rivets in row

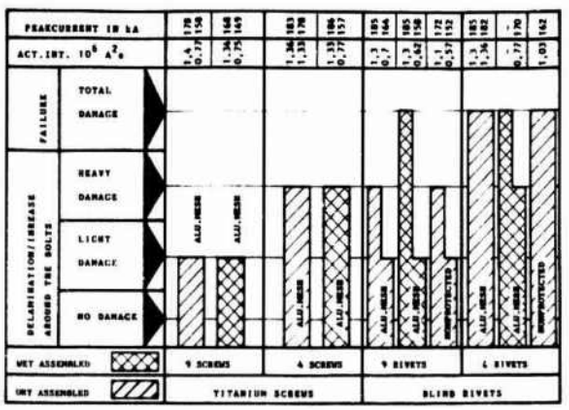


Fig. 16 Lightning test results of electrical bonding specimens

(C) - Solid CFC-plates and sandwich-plates

° Moisture pick-up of CFC-plates

The ag ing was carried out to ACOTEG-proposal chap. 5.1 (pre-drying) . The CFC-plate moisture pick-up is shown in Fig. 17 and 18.

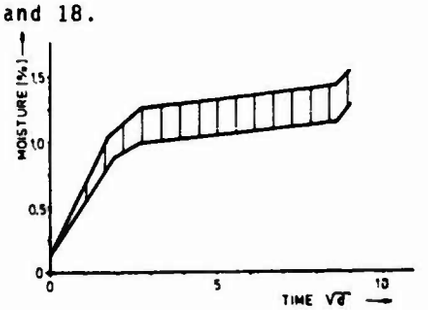


Fig. 17 Moisture pick-up of CFC-plate 1 mm

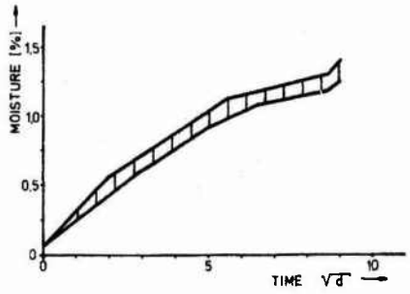


Fig. 18 Moisture pick-up of CFC-plate 3 mm

° Moisture pick-up of sandwich-plates

The ag ing was carried out to ACOTEG-proposal chap. 5.1 (pre-drying) . The sandwich-plate moisture pick-up is shown in Fig. 19 and 20.

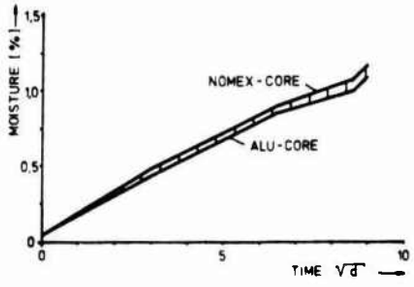


Fig. 19 Moisture pick-up of sandwich-plates with 10 mm core

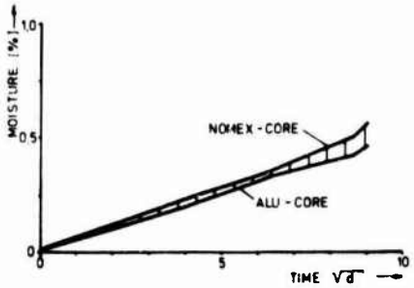


Fig. 20 Moisture pick-up of sandwich-plates with 50 mm core

The ag ing procedure was 70 °C/95 % RH. One of the specimens included normal humidity (laboratory)

° Lightning strike test results

Solid CFC-plates

Test results with the solid CFC-plates demonstrated that there is no significant increase in damage area of the CFC-structure when the specimens have been aged (Fig. 21 and 22).

Hence it follows that it is not necessary for lightning strike test to use aged specimens.



Fig. 21 CFC-solid plate protected with CFC/Kevlar-fabric/aluminum mesh 208 kA, 1.9 . $10^6 A^2 s$

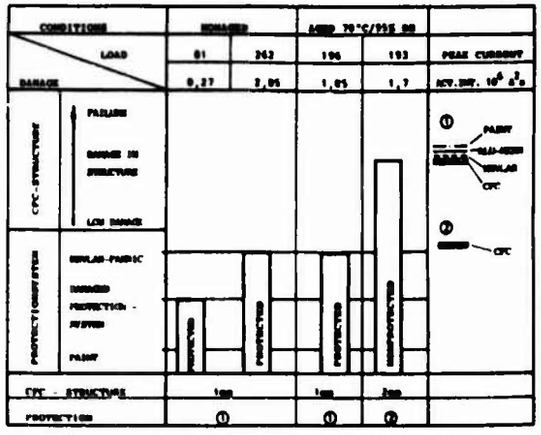


Fig. 22 Lightning test results of solid CFC-plates

° Lightning strike test results

Sandwich-plates

The test results of sandwich specimen with CFC-facings and aluminum or Nomex core material (10 mm + 50 mm) can be obtained in detail from Fig. 25. The diagram shows the results for sandwich plates in dry and wet conditions.

In summary the conditioned sandwich-plates show less or same damages after lightning strike than nonconditioned plates.

The aluminum honeycomb were in both cases damaged (crashed). The Nomex honeycomb (10 mm) in dry conditions have been heavily damaged. The reason is that the Nomex honeycomb in wet conditions are likely more flexible. The damage at protected sandwich plates with 50 mm core height were smaller after lightning strike than sandwich plates without protection (Fig. 23 and 24).

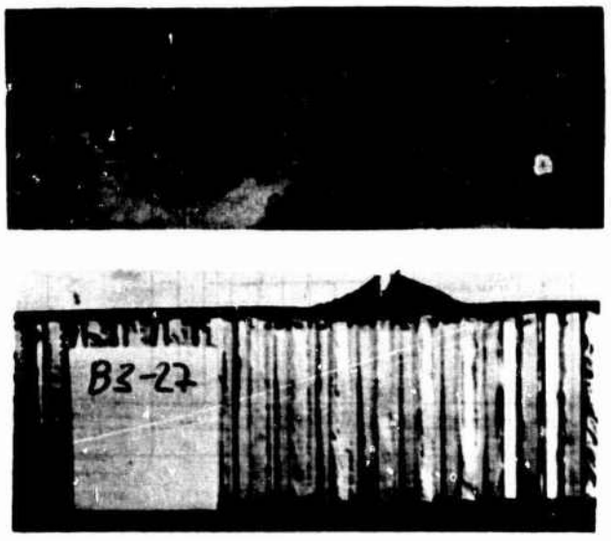


Fig. 23 Sandwich plate with 50 mm aluminum core, protected

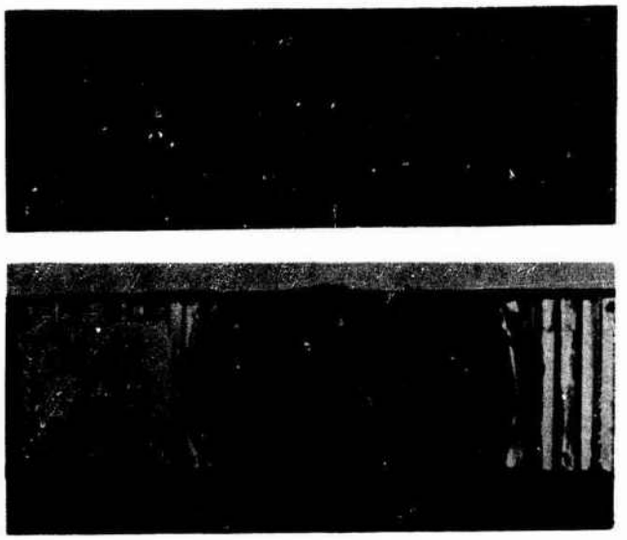


Fig. 24 Sandwich plate with 50 mm aluminum core, unprotected

(D) - Electrical bonding test specimen with different structure parameters

° Lightning strike test results

A lot of electrical bonding specimen consisting of 3 mm thick CFC solid plates covered/noncovered with protection system and provided with different structure parameters

- conductive sealing in the gap (current transfer improvement via conductive sealing in opposite to nonconductive sealing)

- insulating materials between Aluminum-CFC- and CFC-CFC-connections (influence of current transfer properties)

- liquid shim and sealing between Aluminum-CFC connections (influence of current transfer properties)

were tested.

CONDITIONS	NON	AGED	NON	AGED	NON	AGED	NON	AGED
PEAK CURRENT kA	203	200	200	201	203	200	205	200
ACT.INT. 10^6 A^2s	1,8	1,9	1,8	1,9	1,8	1,9	1,8	1,9
DAMAGE IN CFC-STRUCTURE								
FAILURE								
DAMAGE IN HONEYCOMB								
NO DAMAGE								
HONEYCOMB	NOMEX 10mm		ALU 10mm		NOMEX 50mm		ALU 50mm	
PROTECTION	① ② ① ②		① ② ① ②		① ② ① ②		① ② ① ②	

① ALU-MESH WITH KEVLAR-FABRIC

② ALU-MESH WITHOUT KEVLAR-FABRIC

* BY 100kA ; 0,3 10^6 A^2s THE DAMAGES ARE SMALLER

Fig. 25 Lightning test results of sandwich plates

In all cases the CFC-skin (1.5 mm) was not damaged.

In addition to the lightning strike test the specimen residual tensile strength of the specimens was determined.

The test results of electrical bonding specimens were given in Fig. 28.

All specimen types were loaded with 200 kA, 2 . $10^6 A^2 s$.

In summary the protection system (aluminum mesh and Kevlar) protected the CFC-structure effectively against lightning strike.

By using conductive sealings in the gap the damage in the connection area of protected specimen was insignificant.

A current transfer improvement by using conductive sealings in unprotected specimens were not detected.

By using insulating material in the connection area the influence of the current transfer was insignificant.

An influence by using liquid shim in the connection area was not detectable (Fig. 26 and 27).



Fig. 26 Electrical bonding specimen, protected

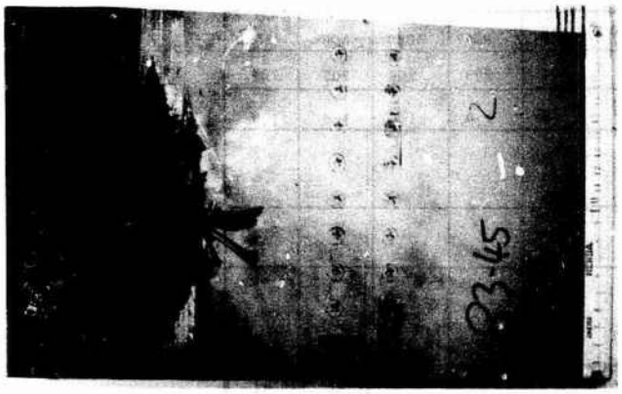


Fig. 27 Electrical bonding specimen, unprotected

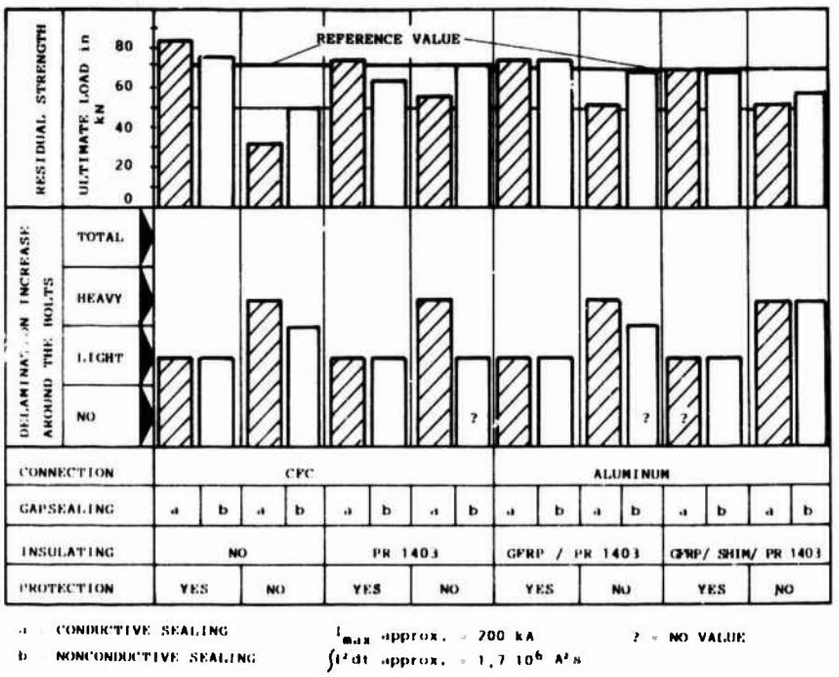


Fig. 28 Lightning test results and residual strength of electrical bonding specimens

VI - SUMMARY

These tests have demonstrated

- that the CFC-structures by using aluminum mesh and Kevlar-fabric (insulating layer between CFC and aluminum mesh) could be effectively protected against lightning strike (200 kA, 2 . $10^6 A^2s$).
- that conditioned CFC-plates and sandwich-plates show less or same damages after lightning strike than nonconditioned plates.
- that the design of the specimen type with titanium screws (wet or dry assembled) successfully passed all tests (200 kA, 2 . $10^6 A^2s$ and 200 kA, 0.6 . $10^6 A^2s$).
- that by using insulating material in the connection area the influence of the current transfer was insignificant and an influence by using liquid shim in the connection area was not detectable.
- that all specimen types with few blind rivets in row (<4), which were loaded with 200 kA, 2 . $10^6 A^2s$ were heavily damaged.

LIGHTNING STROKE TESTS AT THE CFRP HORIZONTAL STABILIZER OF ALPHA JET

Th. Thiele and G. Boes*

Dornier GmbH, Postfach 14 20, D-7990 Friedrichshafen, F.R.G.
**Institut für Plasmaphysik der Universität Hannover, Callinstr. 38, D-3000 Hannover, F.R.G.*

Abstract - The horizontal stabilizer of the Alpha Jet is the first german horizontal stabilizer made of CFRP.

A special lightning protection system was developed because of the difference in electrical behaviour of CFRP and metal. This system and the compliance test are described in this paper.

I - INTRODUCTION

Between 1974 and 1981, a horizontal stabilizer, made of CFRP, was developed and built for the weapon system Alpha Jet. The project was promoted by the German Federal Ministry of Defense (BMVg). See fig. 1.

In addition to the static and dynamic tests destined to prove the sufficiency of the structural design BWB-ML (the flight approval authority of the BMVg) required the proof of a sufficient protection against lightning stroke of the horizontal stabilizer.

It had to be demonstrated that the aircraft can terminate its flight safely on the nearest airport after having been struck by lightning. Apart from the compliance test for the flight approval, further tests were carried out to gain knowledge of the lightning stroke behaviour of the various components and material types.

The tests were performed in cooperation with the Institute for Plasma Physics of the University in Hanover.

II - CASE HISTORY

The left half of the CFRP horizontal stabilizer, which had already undergone the compliance tests, was available for the lightning tests. Fig. 2 gives a general view of the performed compliance tests.

As opposed to the protective system described in chapter 4, the horizontal stabilizer, used to perform the compliance tests, was not equipped with the lightning protection system on the spar box. The reason was to avoid that the strain gauge recording was influenced by the Al-mesh during compliance tests.

For the ligthning tests the Al-mesh protective system was added to the upper and lower sides of the spar box. Comperative microcuts showed that there was no decisive difference between the protective system fixed with co-curing process and the subsequently fixed protective system with respect to the electric contact between carbon fibres and aluminium wire. The fracture of the spar box was covered with the later attached protective system so as to obtain original conditions with regard to the protective system. The broken leading edge section with the available protection system was covered with Al-mesh over a large area. A non-conductive resin system curing at room temperature was used for bonding. To simulate the fuselage rear section an Al-plate of the same thickness was attached to the horizontal stabilizer at the original distance.

III - DESCRIPTION OF THE COMPONENT

The CFRP horizontal stabilizer is identical with the series horizontal stabilizer made of metal with regard to geometry, profile and bearing points.

Main components of the horizontal stabilizer are (fig. 3) :

- o 1 spar box
- o 2 leading edge sections with integrated ribs
- o 2 trailing edge sections with integrated ribs
- o 2 stabilizer tips

The spar box consists of 2 U-shells and 11 ribs. The load transfer ribs are made of titanium, the two end ribs of aluminum. The U-shells and the other ribs are manufactured from CFRP-UD material.

For the panelling of the leading edge sections a hybrid of GFRP and CFRP fabrics was selected as a stone impact protection. The integrated ribs consists of CFRP fabric except for the end rib which is made from aluminum. The trailing edge section with the integrated ribs is made of CFRP fabric except for the aluminum end rib and trailing edge.

The stabilizer tips correspond to the series stabilizer tips and consists of GFRP fabrics with 2 aluminum ribs.

IV - LIGHTNING PROTECTION SYSTEM OF THE CFRP HORIZONTAL STABILIZER

The lightning protection system of the CFRP horizontal stabilizer (fig. 4) comprises:

a. surface protection for the leading edge section and the spar box and

b. frame protection for the spar box, the leading edge and trailing edge sections

The surface protection of the leading edge section and the spar box consists of Al-mesh which was applied by means of the co-curing process. The Al-mesh of the leading edge section and the spar box neither have a direct electric contact with each other nor with the airframe.

The frame protection is composed of the aluminum end ribs of the leading and trailing edge sections and of the sparbox as well as of the trailing edge. This system is electrically connected with the airframe.

The design of the lightning protection system was based on the following philosophy:

- Lightnings hitting the outer zone of the horizontal stabilizer shall be conducted to the fuselage, distributed over large areas, via the spar box, the leading edge section and the frame protection. This large-area discharge of the lightnings shall prevent these load-carrying and aerodynamically important assemblies rom being severely damaged.

- Lightnings hitting the trailing edge section shall be conducted into the fuselage via the frame protection or exit via the metal part of the trailing edge section.

  A severely damaged trailing edge section represents no direct risk for the horizontal stabilizer.

The horizontal stabilizer is suspended in the same bearings as the metal version. It is, however, connected with copper braided strips of 10 mm^2 each from every rib to the fuselage.

V - TEST PROGRAM

A test program was established in coordination with the flight approval authority BWB-ML.

In total, 27 lightning strokes of varying intensity were planned, based on the STANAG standard lightning curve. Fig. 5 shows the striking points on the horizontal stabilizer. The roman numeral denotes the load value (fig. 6), the arabic numeral the order.

The actual compliance test was the lightning stroke I/1. The remaining tests served the purpose to gain a general impression and knowledge of the efficiency of the system applied and the lightning stroke behaviour of the materials used.

VI - TEST PERFORMANCE AND RESULTS

The tests were carried out in the laboratory of the Institute for Plasma Physics of the University in Hanover.

Fig. 7 shows the compliance test set-up with the electrode directed to the load point. The switching-on of the direct voltage for the charge transfer caused a direct ignition which slightly damaged the protection system. In the course of the second test the following values were measured:

- Peak amplitude: 197 kA
- Action integral: $1.93 \cdot 10^6 A^2 s$
- Charge transfer: 161 C

The striking point can be seen from fig. 8. This figure shows that the charge transfer took place from the hitting point to the corner of the protective system. The current was transferred partly from the upper and the lower side of the leading edge section to the fuselage simulation (fig. 9, 10). Further transfer points were not discovered. At the striking point the material was damaged up to the third layer, the diameter was 60 mm.

For the further performance of the test program the order of the test steps was changed so as to avoid frequent modification of the test set-up.

First, the low loads were applied and afterwards the next higher ones. It was agreed with the flight approval authority BWB-ML to continue the tests for the load values II and III without charge transfer, since this current causes no damage which adversely affects the stability of the component.

The figure 11 show a typical damage in the trailing edge section in the case of load value I.

After the performance of all program items,

the outer area of the leading edge section was tested applying the highest possible lightning value that could be realized at that time by the test installation.

This final test resulted in the following values:

- Peak amplitude: 227 kA
- Action integral: $2.4 \cdot 10^6 A^2 s$
- Charge transfer: 184.7 C

Figure 12 gives an impression on the striking point. The colour of the resin in the area had slightly changed.

VII - RESULT

The result of the lightning tests and the subsequent non-destructive tests proved that the lightning protection system selected for the CFRP horizontal stabilizer fulfils its task. None of the lightning strokes applied to the component caused any damage which could have reduced the flight safety to a great extent.

The figures 13 and 14 show an overall view of the upper and the lower side of the horizontal stabilizer after the performance of all tests.

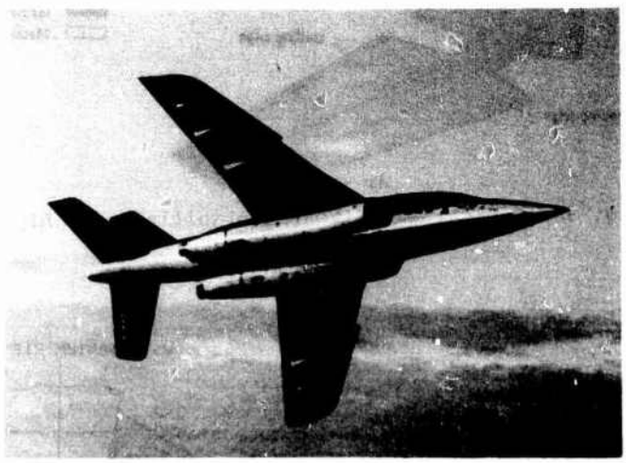


Fig. 1 : Alpha Jet with CFRP Horizontal Stabilizer in Flight

Nr.	Test Mode	Load [xL.L.]	Test-temperature[°C]	Moisture Content
1	static	1,25	RT	normal
2	static	1,15	-55°C	normal
3	static	1,15	+70	≤ 1%
4	dynamic, test program per flight, 20.000 simulated flight hours		RT	
5	static	1,0	RT	
6	static	1,0	-55	
7	static	1,0	+70	
8	static, interrupted fracture test	1,0	+70	
9	static, fracture test right side	1,18*	+70	
10	static, fracture test left side	1,48*	+50	≤ 1%

* proved

Fig. 2 : Test Program CFRP Horizontal Stabilizer

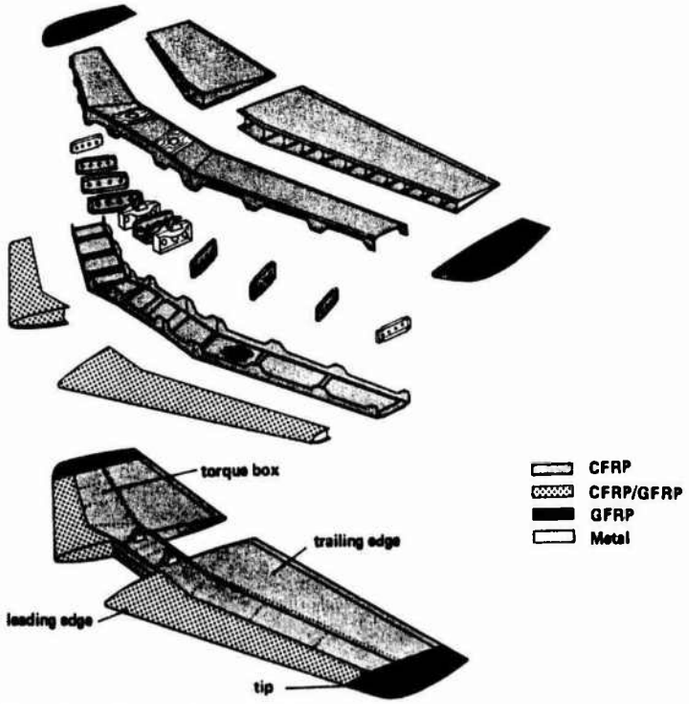


Fig. 3 : Composite horizontal stabilizer for Alpha Jet

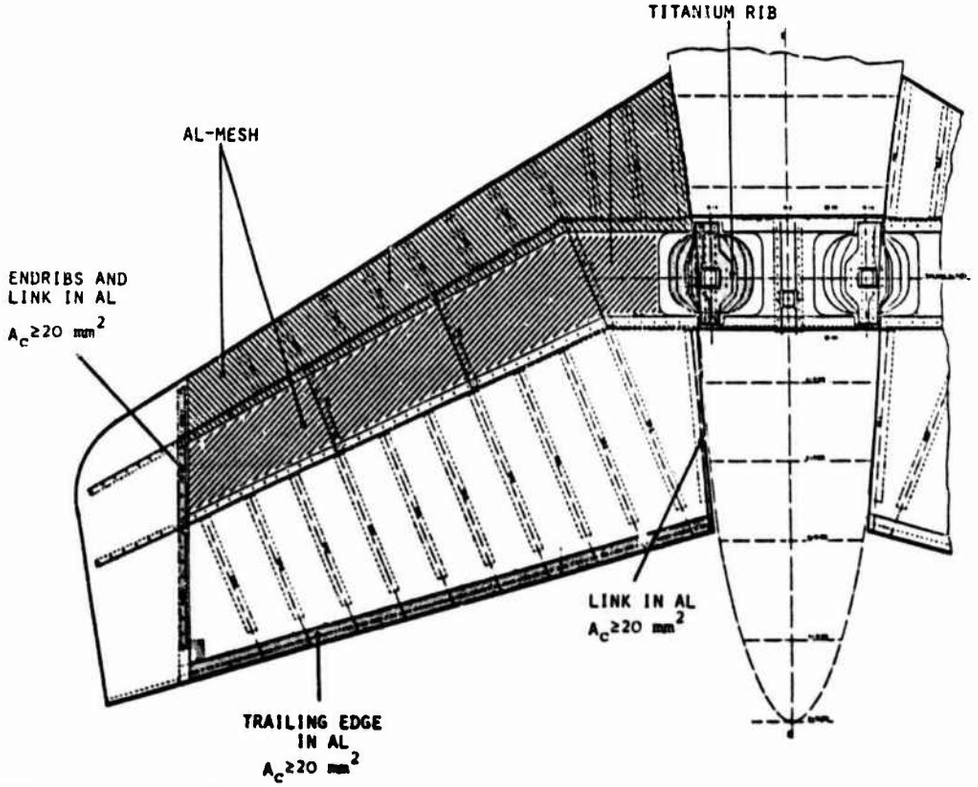


Fig. 4 : Lightning protection system CFRP Horizontal Stabilizer Alpha Jet

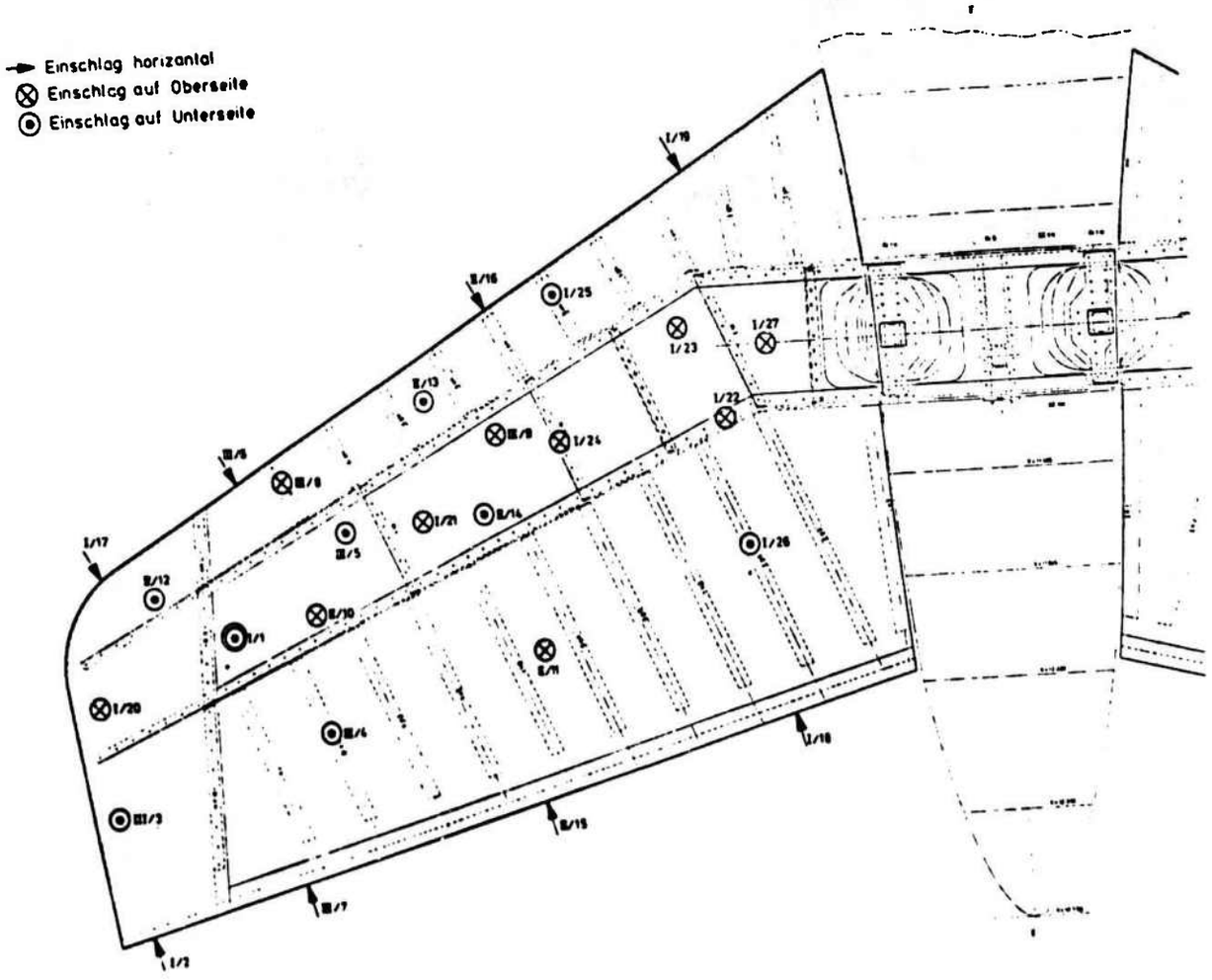


Fig. 5 : Lightning stroke test program

	I	II	III
Peak Amplitude I [kA]	200	100	50
Action Integral $\int i^2 dt$ [$10^6 A^2 s$]	>1,5	-	-
Charge Transfer $\int idt$ [C]	200	200	50

Fig. 6 : Test values

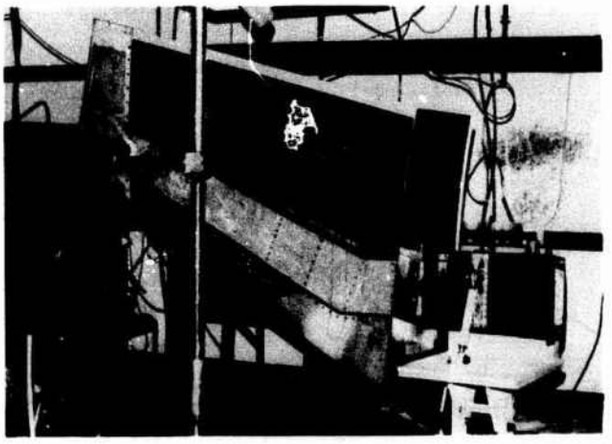


Fig. 7 : Test set-up



Fig. 10 : Current transport to fuselage



Fig. 8 : Damage compliance test

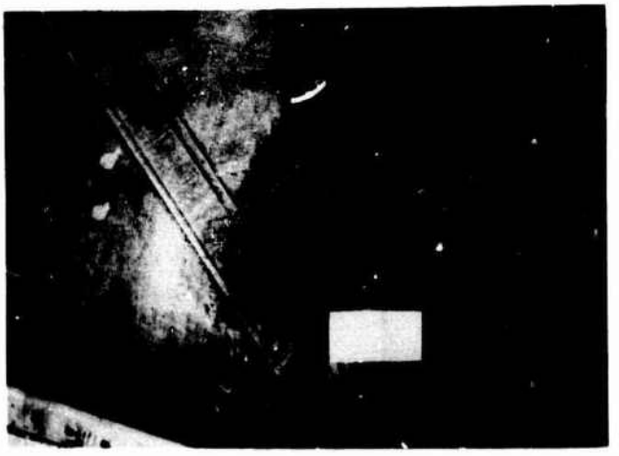


Fig. 11 : Striking point T. E.



Fig. 9 : Current transport to fuselage

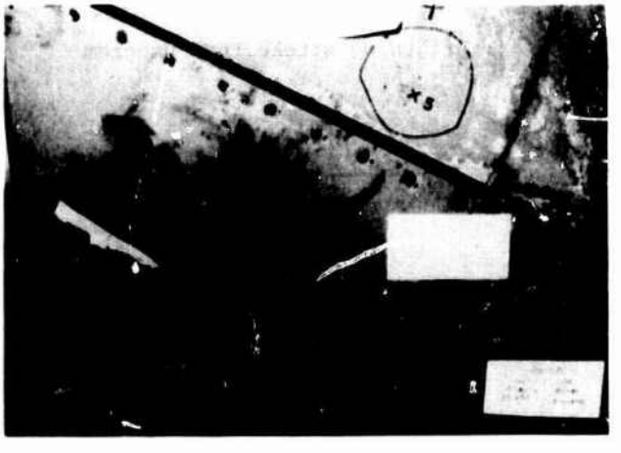


Fig. 12 : Striking point L.E. high lightning value

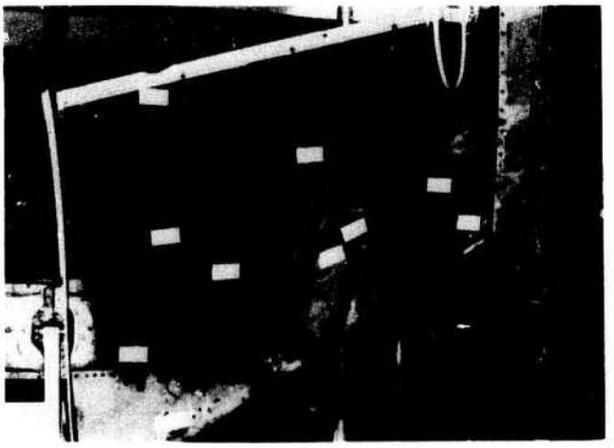


Fig. 13 : Overall view, upper side



Fig. 14 : Overall view, lower side

SIMULATED LIGHTNING TESTS ON BAYMETEX C PROTECTED GRAPHITE-EPOXY LAMINATES

H. Ebneth

Bayer AG Leverkusen, Central Research Department Application of New Products, 5090 Leverkusen, Bayerwerk, F.R.G.

Abstract - Highly nickel-coated graphite fabrics will provide adequate composite structure protection from Zone 1 A and 2 A lightning strikes, as simulated lightning tests showed. The coating level used will depend on the damage tolerance and structural make-up of the part to be protected. Mechanical tests show that the nickel-coated graphite fabric has an positive effect in compression of the panels. The compressive strength is about 25 % better than the panel with a non-metallized fabric ply.

INTRODUCTION

This report summarizes work of Bayer AG and its subsidiary Mobay Chemical Corporation in 1984. The scope of the work included fabrication of eight graphite/epoxy composite laminates; four panels for Zone 1 A lightning strike and four panels for Zone 2 A lightning strike. Physical damage assessment and mechanical testing of the lightning struck panels was performed. The first section of this report describes panel fabrication and mechanical testing. The second section covers lightning strike testing and physical damage assessment.

A previous paper was published at the International Aerospace and Ground Conference on Lightning and Static Electricity (June 26 - 28, 1984), Orlando, Florida, USA [7].

SUMMARY

Test results confirm the value of Baymetex C metallized fabric for structural composite lightning strike protection. Baymetex is the trademark used by Bayer AG and Mobay Chemical Corporation to denote its unique line of metallized fabric materials. When incorporated as the outer ply in a laminate, the Baymetex C protected underlying tape plies from severe damage resulting from Zone 1 A, 200,000 ampere lightning current attachment. This protection capability was shown in that no punctures were sustained on the protected halves of the test panels while all of the unprotected samples were punctured.

Struck panels protected with Baymetex C exhibited approximately 85 percent retention of tension and compression strength when compared to the normalized strength of unprotected control specimens. Results of these Zone 1 A tests indicate that the nickel-coated fabric outer ply will probably suffer damage over a larger area than an unprotected fabric, but the damage depth, area and volume in underlying plies is substantially reduced.

The Zone 2 A test results provide a more quantitative damage comparison between protected and unprotected panel halves. One prominent trend in the data is that the protected halves sustained a more shallow damage depth and a smaller damage volume than the unprotected laminate. A second trend shown in the data is that the surface area damage was greater for the protected panel. This would seem to indicate that Baymetex C metallized fabric allows the attachment current to spread over a larger area. This results in a lower current density at the attachment point resulting in less damage to underlying plies in the laminate. As was also the case in Zone 1 A lightning strikes, mechanical test results agreed with the physical damage assessment after Zone 2 A, 100,000 ampere simulated lightning strikes. The half of the panels protected with the metallized fabric retained a much higher percentage of strength, both in tension and in compression, than the half of the panels containing a normal fabric ply. In fact, when compared to the unprotected control specimens, laminates containing Baymetex C retained virtually 100 percent strength retention in tension and compression after a Zone 2 A simulated lightning strike.

A final conclusion of the test program was that incorporation of Baymetex C does not seem to adversely impact laminate mechanical properties. Among the control specimens, both nickel-coated and normal laminates had similar tensile strength. In compression, the Baymetex C samples exhibited 25 percent greater strength than the normal panels.

PANEL FABRICATION AND MECHANICAL TESTING

MATERIALS

Bayer AG via Mobay Chemical Corporation supplied a nickel-coated graphite fabric to the test-lab exhibiting the following properties:

	BAYMETEX C STYLE 100
Warp Yarn	3000 filament Thornel® T-300 graphite
Fill Yarn	3000 filament Thornel® T-300 graphite
Weave	Plain
Yarn Count	12.5 x 12.5 ends/inch
Fabric Weight	190 gm/sq meter
Metal Weight	115 gm/sq meter
Total Weight	305 gm/sq meter
Metal	Nickel

The metallized fabric was impregnated with Fiberite® 934 epoxy resin. Resin content of the impregnated fabric was 33.0 percent.

The control fabric prepreg had the following properties:

Warp Yarn	3000 filament Thornel® T-300 graphite
Fill Yarn	3000 filament Thornel® T-300 graphite
Yarn Count	12.5 x 12.5 ends/inch
Fabric Weight	196 gm/sq meter
Resin	Fiberite® 934 epoxy resin
Resin Content	41.0 percent

The tape material employed in the underlying plies had the following properties:

Fiber	Thornel® T-300 graphite
Style	Unidirectional Tape
Weight	145 gm/sq meter
Resin	Fiberite® 934 epoxy resin
Resin Content	37 percent

FABRICATION

Eight composite panels, each measuring 20 inches x 24 inches, were fabricated using the above mentioned materials. Each panel was layed up with 24 plies of unidirectional tape in the following orientation:

$$\left[(+45/0/-45/0)(+45/90/-45/0)_2\right]_S$$

One half of each side of the panel was covered with the Baymetex C lightning strike protection fabric while the other half was covered with the control fabrics as shown in Figure 1. All eight panels were cured in one autoclave for two hours at 350°F (177°C). The panels were cured with the fabric side against the tool resulting in a smooth surface for painting. After cure, the panels were painted on the fabric side with the conventional paint system used in commercial aircraft ($\frac{1}{2}$-1 mil of an epoxy primer and 3 - 5 mils of a polyurethane topcoat), air dried overnight and subsequently cured at 160°f (71°C) for two hours.

After the panels were scanned for internal flaws and delaminations using the Through Transmission Ultrasonic scanner, they were cut to give 16 inch x 16 inch panels for lightning strike testing and test specimens as controls for mechanical testing. The scheme for cutting is shown in Figure 2 and the configuration of the test specimen is shown in Figure 3. All eight 16 inch x 16 inch panels were submitted for lightning strike testing, four for Zone 1 A and four for Zone 2 A lightning strike. The second section of this report details the particulars of the lightning strike tests and damage assessment.

MECHANICAL TESTING

After lightning strike, three test specimens were cut from each half of the panel as shown in Figure 4. The specimens were tested in tension and compression for residual mechanical integrity. The test matrix is shown in Table 1. The control specimens were also tested under the same test matrix. Compression specimens were supported in a test fixture as shown in Figure 5 during compression. Both the tension and compression specimens were tested with a MTS hydraulic machine with a loading rate of .05 in./min.

RESULTS AND DISCUSSION

The physical appearance of the panels after cure was good. Although the resin content of the nickel-coated fabric was significantly lower than that of the normal fabric, no resin starvation nor surface defects were detected. Through Transmission Ultrasonic scans also showed no internal defects in the panels.

Mechanical test results are shown in Tables II to VI, and graphically depicted in Figures 6 and 7. Specimen identification is coded as follows:

$$\underbrace{X\,X\,X\,X}_{A} - \underbrace{X\,X}_{B\,C};\ \underbrace{X\,X}_{D}$$

Where A $\triangleq$ Panel Number

B $\triangleq$ C = Control Specimen
1,2,3, = Specimen Nos.

C $\triangleq$ T = Tension
C = Compression

D $\triangleq$ NF = Nonmetallized Fabric = nickel free
NC = Baymetex C Style 100 = nickel coated

For comparison purposes, test specimens and controls with the normal fabric ply were compared in one group while those with the nickel-coated fabric ply were compared in another group.

Since after the lightning strike test, the top fabric ply may be totally or partially detached and the laminate may be severely damaged, the thickness of the lightning strike tested specimens may vary a great deal from that of the control specimens. To get a fair comparison of the residual mechanical property of the lightning strike tested specimens with the control specimens, an average thickness of the corresponding control specimens were used to calculate the ultimate strength. The values are listed under the normalized Ultimate Strength column. For example, panels 7990, 7991, 7992, and 7993 were tested in tension. The thickness of the half of the panel with a normal fabric ply (NF) has a slightly different thickness than the half of the panel with a nickel fabric ply (NC). So the average thickness of 7900-CT; NC, 7991-CT; NC, 7992-CT; NC and 7993-CT; NC was used to calculate the strength of the specimens with the same panel number and NC fabric. The average thickness of 7990-CT; NF, 7991-CT; NF, 7992-CT; NF, and 7993-CT; NF was used to calculate the strength of the specimens with the same panel number and NF fabric.

The compression panels 7994 and 7988 were layed up with an extra ply of prepreg tape by mistake. These two panels were, therefore, slightly thicker and they were distinguished from the compression panels 7995 and 7989 when average thicknesses were calculated .

A seperate column showing the Actual Ultimate Strength which was calculated from actual measured thickness is also included.

Where damage is severe resulting in a non-uniform thickness is also included. Where damage is severe resulting in a non-uniform thickness across the specimen a median thickness was used. Based on 100 % retention of strength for the control, the percent of strength retention were calculated for the corresponding lightning strike tested specimens. The last two columns indicate whether the top fabric ply is intact or detached and the location where the specimen failed as measured from one end of the specimen.

As noted in the lightning strike testing and damage assessment section of this report, the half of the panels with a normal fabric ply was damaged severely after the Zone 1 A lightning strike. No mechanical testing was performed for the Zone 1 A NF specimens as shown in Tables II and IV.

It was indicated in the Fabrication Section that the layup orientation was $\overline{(+45/0/-45/0)(+45/90/-45/0_2)}_S$. This layup orientation would have been quasi-isotropic if the second ply from the top and bottom of the panel had been 90°. The reason for substituting a 0° ply for a 90° ply near the outer surfaces of the panel is to increase the sensitivity of the mechanical test for lightning strike damage. Since the fiber is the primary load carrying component, especially in tensile tests, any damage to the outer 0° plies due to lightning strike would reduce the mechanical performance more drastically.

In general, mechanical test results show that the panels with nickel-coated fabric have better strength retention than the panels with normal fabric. The results agree with the physical and visual assessment of the lightning struck panels. It should be noted that among the control specimens, both the nickel-coated panel and the normal panel have similar tensile strength while the nickel-coated panel has a compressive strength of about 25 % higher than the normal panel. It shows that nickel does not seem to affect the composite strength adversely. In fact, the observed increase in compressive strength could be due to the increased stability of the nickel-coated fiber under compression loading. It should be noted that the -2 specimen, which was cut from the area with the worst damage, has the lowest residual strength.

The average mechanical teat results of two panels tested under the same conditions are shown in Figures 6 and 7. In tension, the strength retention of the NC panels was much better than that of the NF panels. In compression, the strength retention of the NC panels was much better than that of the NF panels after Zone 1 A lightning strike, but was about the same for both the NC and NF panels after Zone 2 A lightning strike. By visual inspection, the NF panels were damaged much more than the NC panels. This discrepancy was probably due to the much higher strength of the NC control over the NF control.

After lightning strike, the top fabric ply was destroyed in both the NC and NF panels. The residual strength measured was from the basic panel, so the effect of the possible added stability from the nickel-coated fiber was removed. It may be more enlightening to compare the normalized strength retention. In that case, a strength of 79.9 ksi for the NF panel was compared to a strength of 90.9 ksi for the NC panel. This is equivalent to 14 % higher strength for the NC panel over the NF panel.

CONCLUSIONS

The following points may be concluded based on this portion of the study:

1. Mechanical test results agree with the physical damage assessment of panels after lightning strike.
2. The half of the panels with a nickel-coated fabric ply retained a much higher percentage of strength both in tension and in compression over the half of the panels with a normal fabric ply.
3. For pre-lightning strike testing, nickel has no effect on the tensile performance of the panels, while in compression the half of the panels with a nickel-coated fabric ply performed 25 % better than the half of the panels with a normal fabric ply.

LIGHTNING STRIKE TESTING AND DAMAGE ASSESSMENT

INTRODUCTION

A lightning laboratory in the US was utilized for generating the simulated lightning discharges required for these tests. Figure 8 summarizes the lightning strike waveform components as set forth in "Lightning Qualification Test Techniques for Aerospace Vehicles and Hardware", MIL-STD-1757. The laboratory is capable of reproducing lightning current discharges which contain the amplitude levels, time durations, and energy transfers, called out as recommended test values by MIL-STD-1757. In the lab, lightning generators and general lab equipment are arranged so that the high voltage power supply controls, the switching and grounding controls, and all electronic test equipment are located in a protected control room separated from the testing area inside the test chamber. The test article is fitted onto a test stand where all the necessary connections for completing the lightning discharge current paths are made.

Depending upon the lightning strike zone being simulated, the test articles may be hard-wired at both the current entry and exit points of just hard-wired at the current exit point with an air gap between the test article and a discharge electrode at a predetermined current entry (attachment) point.

Through these tests, we were seeking to find whether or not the nickel-coated graphite fabric on the test panels would provide protection for the test panels against damage caused by the simulated lightning current attachment.

TEST METHODS AND PRACTICES

For these tests, simulated lightning discharge currents were generated by discharging banks of charged capacitors through the test panels. The capacitors in each bank are configured in predetermined series parallel combinations to provide the required amount of capacitance. The capacitor banks are identified according to the component part of the lightning current waveform that they are capable of producing. For example, the "D-Bank" produces the "D" component shown in Figure 8. Therefore, the "A", "D", and "B-C Mod" component parts of the lightning current waveform are produced by reapective capacitor banks. These capacitor banks make up the lightning generator and are per-

manently mounted in the laboratory.

Within the lab, the test area is arranged to allow for maximum flexibility in test setups. A wide variety of test articles can and have been lightning tested using this method.

For this series of Zone 1 A and Zone 2 A current attachment testing, the discharge electrode was positioned close to the test panel front surface at the point where attachment was desired. An air gap, 2.75 inches long, was established between the tip of the discharge electrode and the test panel front surface. The lightning current discharge electrode was positioned to inject simulated lightning current into the test panel so that the current was forced to flow to the bottom of the test panel to ground. The electrode was a $\frac{1}{4}$-in. diameter tungsten rod, with a rounded end to reduce blast shock waves that might unrealistically intensify the current attachment damage. The electrode was held rigidly in place to prohibit mechanical impact of the test panel. The tests were conducted with the discharge electrode at a negative potential relative to the positive test panel.

When simultaneous current component testing is being done, such as "A-B" (Zone 1 A) or "D-B-C" (Zone 2 A) discharges, a programmable timer is used to control the discharge sequence of the current component parts. In these tests the "A" bank and "D" bank discharges were initiated by the discharge of a "trigger" bank (a separate charged capacitor) used to ionize the air gap between the discharge electrode and the test panel. The flash produced by the discharge of the trigger bank is detected by an optical sensor. This signal is then used to turn on the programmable timer unit. Then, according to the present time, the timer unit generates a signal for turning on the "B" bank (for Zone 1 A) or the "B-C Mod" bank (Zone 2 A) in the proper sequence.

The lightning discharge current is sensed by a current transformer. An output voltage, proportional to the sensed current level, is connected to a computerized oscilloscope from the current transformer. The input to the computerized oscilloscope is stored and then analyzed. After analysis, the oscilloscope displays the test wave form along with numerical values for peak current, action integral, time duration, circuit resistance and inductance, and other selectable information. A typical circuit test setup is illustrated in Figure 9.

TEST EQUIPMENT

1. Norland 2001A, Computerized Oscilloscope
   Four input channels
   Sample Interval: 1 microsecond to 1000 (± 0.01%)
   Voltage Range: ±0.1 to ± 100 Volts full scale

2. Hipotronics Model 830-830, DC High Voltage Power Supply
   Output in three ranges:
   Low 0-6 kVolts at 0-250 milliamperes
   Med 0-12 kVolts at 0-500 milliamperes
   High 0-30 kVolts at 0-1000 milliamperes

3. Pearson 2093, Current Transformer
   Output = 0.101 Volt per Ampere

4. Ten Channel Programmable Timer Unit, (Boeing built)
   Channels 1 through 4: 0-9999 microseconds in 1 microsecond increments
   Channels 5 through 10: 0-9999 milliseconds in 1 millisecond increments
   Output Voltage: each channel, 0 to +60 Volts dc

5. Universal Voltronics, Corp. (Labtrol)
   High Voltage Power Supply
   Output in three ranges:
   Low 0-10 kVolts at 0-2 milliamperes
   Med 0-60 kVolts at 0-6 milliamperes
   High 0-250 kVolts at 0-20 milliamperes

6. "A" - Bank (Laboratory installation)
   Series Parallel Combination of 165 μF, 6 kV capacitors
   Total Calculated Capacitance = 531 μF
   Maximum Charge Voltage = 30 kV

7. "B-C Mod" Bank (Laboratory installation)
   Series Parallel Combination of 165 μF, 6 kV rated capacitors and 250 μH and 7 mH inductors.
   "B" Segment:
   Total Calculated Capacitance = 2475 μF
   Total Calculated Inductance = 1500 μH
   "C Mod" Segment:
   Total Calculated Capacitance = 5600 μF
   Total Calculated Capacitance = 56 mH
   Maximum Charge Voltage = 6 kV

8. "D" Bank (Laboratory installation)
   Parallel combination of 5.08 μF, 30 kV rated capacitors
   Total Calculated Capacitance = 81.28 μF
   Maximum Charge Voltage = 30 kV

DAMAGE ASSESSMENT TECHNIQUE

This series of eight graphite epoxy laminated test panels were subjected to Zone 1 A (panels 7988, 7989, 7990, and 7991) and Zone 2 A (panels 7992, 7993, 7994, and 7995) simulated lightning currents. The panels were photographed after being lightning tested. These photographs document the lightning testing and provide a record of the test panel's appearance before the damaged areas were cleaned out.

Each panel was then cleaned by scraping of the damaged areas. The scraping was done to clear the damaged area of loose fabric and tape debris. Damaged fabric and tape in the layup was scraped away to the point where the undamaged laminate was still intact.

The quantitative damage assessment began after the test panels were scraped and wiped clean. This damage assessment started with the making of a test panel pencil tracing. Two example copies of these pencil tracing are shown in Figures 10 and 11. To make the pencil tracings, a piece of paper was taped into position over the test panel damaged area. A dull pointed pencil was then rubbed over the paper. Enough pressure was applied to the pencil to make the damage patterns appear on the paper, but not so much pressure as to tear holes in the paper. This pencil tracing technique produces a one-for-one, generally well defined, replica of the test panel damage area. These pencil tracings add to the test documentation and were used in the measurement of the test panel damage area.

The damage area was measured by using a planimeter on the pencil tracing. Usually, the test panel damage prevents using the planimeter directly on the test panel because the planimeter requires a continuous smooth surface on which it can roll. To measure the damage surface area, the planimeter was used to trace around the damage area perimeter on the pencil tracing. The planimeter then provided a readout of the area in square inches.

A dial indicator mounted on a bridge was used to measure the damage depth. The bridge was positioned so

that it was over and spanning the damage area. It was then moved until the dial indicator pointer rested in the spot having the greatest depth. This measurement was referenced to the top surface of the panel. Figure 12 illustrates the damage depth measurement.

By assuming that the damage volume approximates the volume of a cone, a value for the damage volume was calculated by using the formula for the volume of a cone. The measured area and depth values were substituted in the cone volume formula as follows:

V = Damage Volume = (1/3)AD
Where, A = Damage Area in square inches,
D = Damage Depth in inches, and
V = Damage Volume in cubic inches.

TEST RESULTS

Eight 15''x 16''x 0.15 '' graphite epoxy test panels were lightning tested. Four of the test panels were exposed to Zone 1 A ("A" and "B" componente) and four of the panels were exposed to Zone 2 A ("D", "8", "C-Mod" components) simulated lightning current attachments. The simulated lightning current waveforms used are illustrated in Figure 13. Each test panel was subjected to two current attachments, one to the protected (nickel-coated graphite fabric) half and one to the unprotected (normal graphite fabric) half of the panel. This current attachment approach is shown in Figure 14.

Two of the test panels (7988 and 7944) had one extra ply in their layups. Panel 7988 was tested at the 200,000 ampere Zone 1 A level and panel 7994 was tested at the 100,000 ampere Zone 2 A level. The extra ply in these two panels did not appear to cause them to respond differently to the lightning currents than the other panels.

ZONE 1 A RESULTS

Panels 7988, 7989, 7990, and 7991 were subjected to Zone 1 A lightning current attachments. In every case, the unprotected half (coded NF), of the test panel was punctured during testing. None of the nickel-coated fabric protected halves (coded NC) of the panels were punctured during testing.

While the nickel-coated fabric lightning protection system prevented puncturing, the protection system itself sustained heavy damage. Large portions of the nickel-coated fabric were blown away by the current attachment. The nickel-coated fabric remaining on the panel after the current attachment was only lousely bonded to the panel and was completely removed during the scraping process.

Only the NC half of the Zone 1 A test panels were scraped for damage assessment. Due to total laminate puncture, the NF halves were not scraped. The lightning damage assessment for the NF halves of the Zone 1 A test panels is simply that they suffered punctures and a puncture is considered to be a failed condition.

The Zone 1 A simulated lightning current test values are tabulated in Table VII. A summary of the damage values for the Zone 1 A test panels is given in Table VIII.

ZONE 2 A RESULTS

Panels 7992, 7993, 7994, and 7995 were subjected to Zone 2 A lightning current attachments. These panels suffered less surface area damage than did the Zone 1 A panels. The unprotected half (NF) of panel 7993 was punctured by the current attachment.

The puncture damage of panel 7993 was not as severe as that of the Zone 1 A punctures. Because of this, the damage to the NF half of 7993 was scraped and assessed in the same manner as the other Zone 2 A panels.

Table IX presents the Zone 2 A simulated lightning current test values. The Zone 2 A panel damage values are summarized in Table X.

CONCLUSIONS

For this particular panel layup configuration, the nickel-coated fabric outer ply demonstrates the ability to protect the underlying tape plies from severe damage resulting from Zone 1 A 200,000 ampere lightning current attachment. This protection capability was shown in that no punctures were sustained in the protected halves of the panels while all of the unprotected halves of the Zone 1 A panels were punctured. Results of these Zone 1 A tests indicate that the nickel-coated fabric outer ply will probably suffer damage over a larger area than an unprotected fabric, but the damage depth, area and volume in the underlying plies will be substantially reduced.

The Zone 2 A test results provide a more quantitative damage comparison between the protected and unprotected panel halves. One prominent trend in the data is that the protected halves sustained a more shallow damage depth and a smaller damage volume than the unprotected halves. A second trend shown in the data is that the surface area damage was greater for the protected than unprotected halves. This data seems to indicate that the nickel metallized fabric allows the attachment current to spread over a larger area. This means there is a lower current density at the attachment point resulting in less damage to the protected underlying plies of the laminated panel.

REFERENCES

[1] Harold Ebneth, "Nickel-coated graphite and aramide fabrics as part of composite for lightning strike protection of aircraft", International Aerospace and Ground Conference on Lightning and Static Electricity (June 26-28, 1984), Orlando, Florida, USA, pages 55-1 to 55-5.

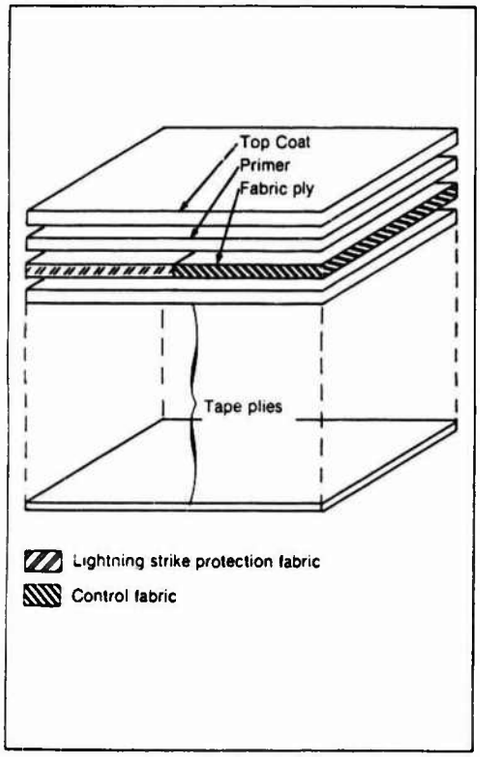


Figure 1. Panel stack up sequence

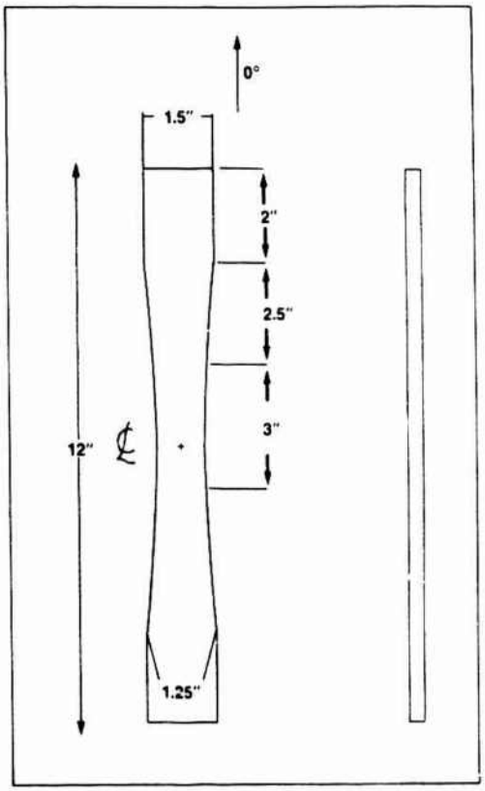


Figure 3. Configuration of test specimens

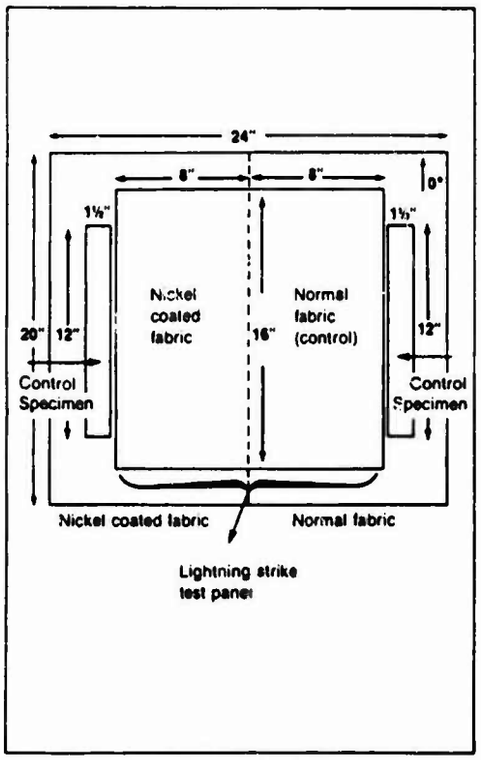


Figure 2. Scheme for machining lightning strike panel and control specimens

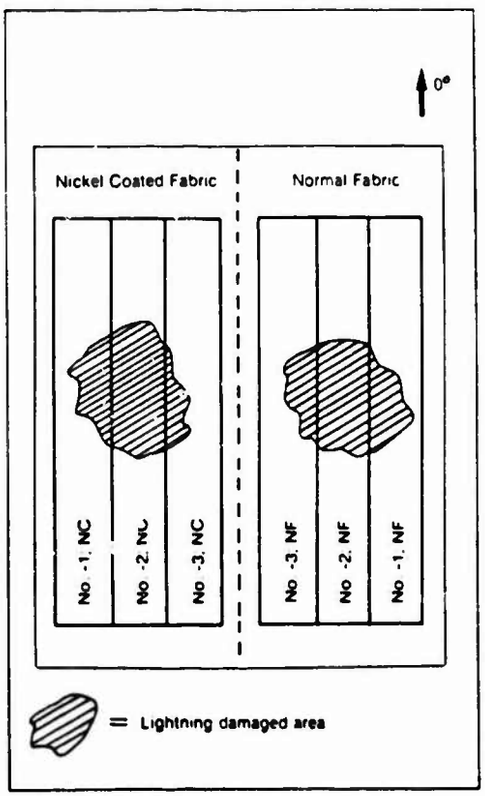


Figure 4. Scheme for machining test specimens from lightning struck panels

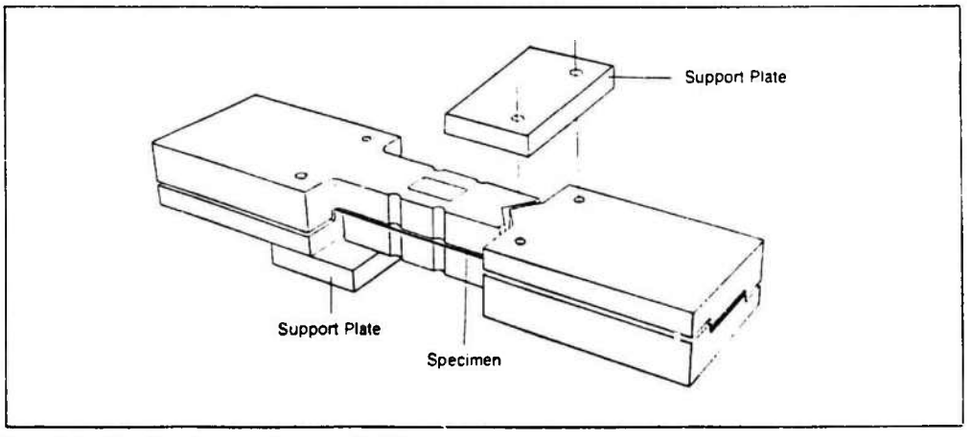


Figure 5. Configuration of compression support test fixture

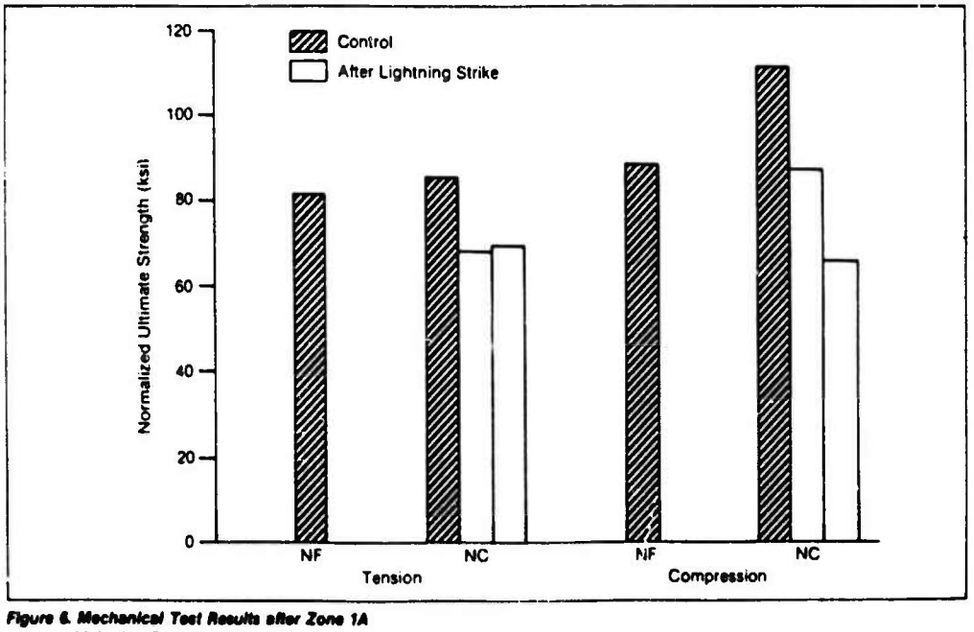


Figure 6. Mechanical Test Results after Zone 1A Lightning Strike Test

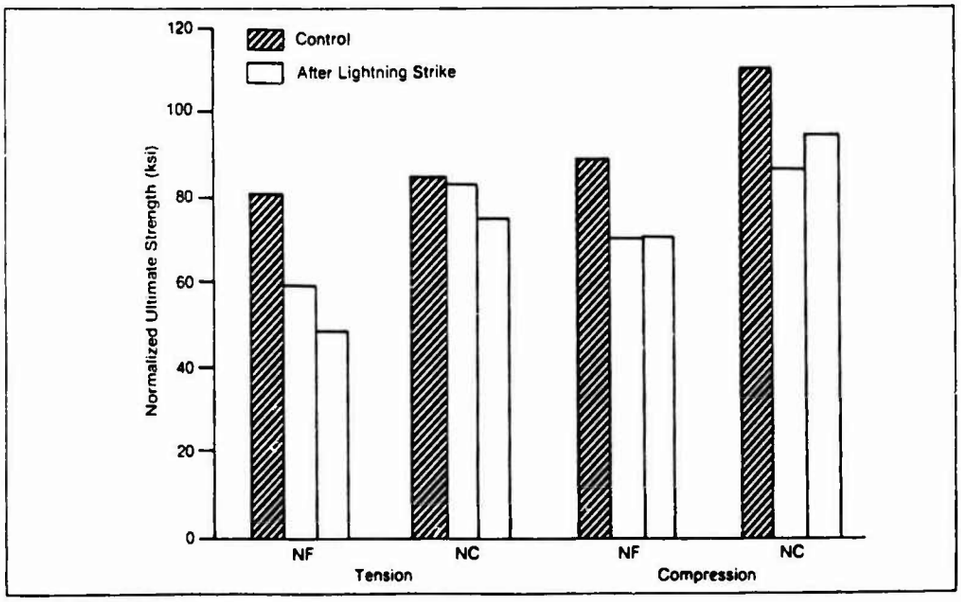


Figure 7. Mechanical Test Results after Zone 2A Lightning Strike Test

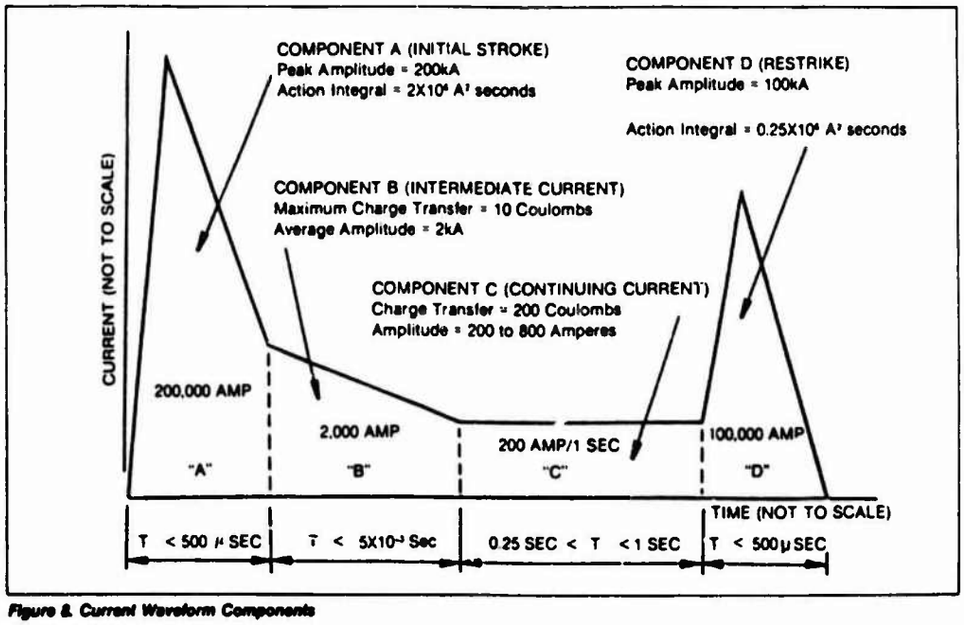


Figure 8. Current Waveform Components

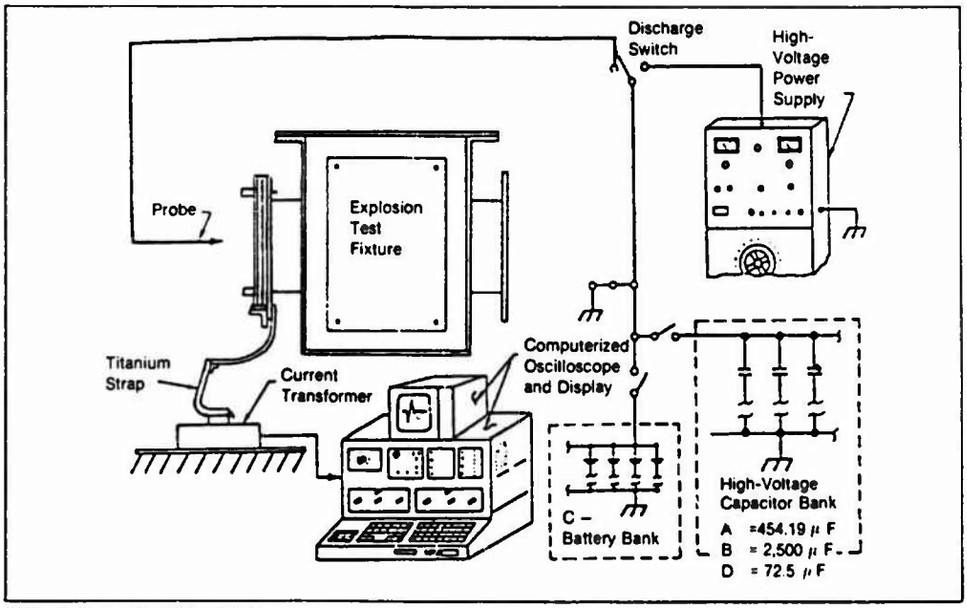


Figure 9. Typical Test Circuit Setup

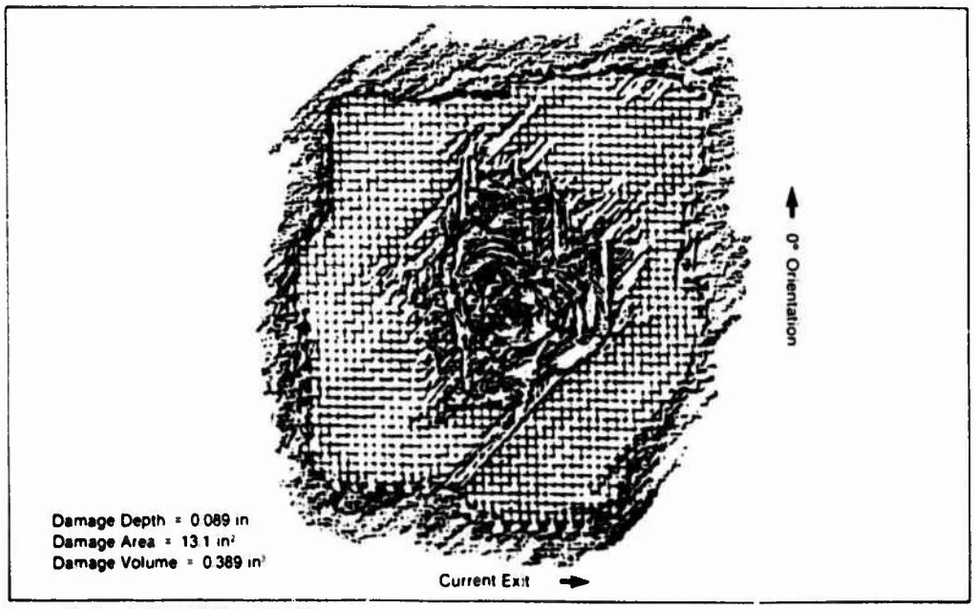


Figure 10. Panel #7992-NF Pencil Rubbing Zone 2A Lightning Strike

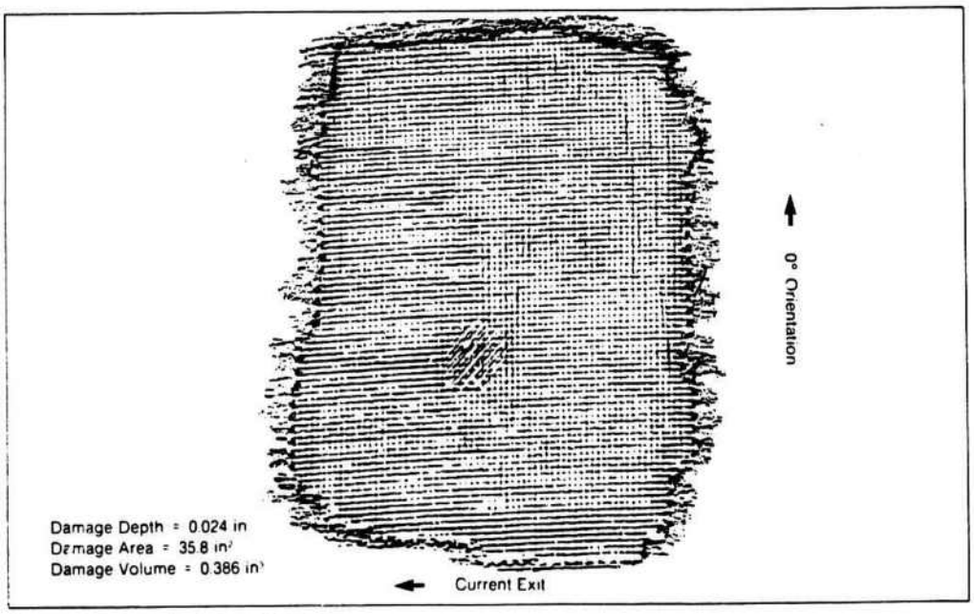


Figure 11. Panel #7992-NC Pencil Rubbing Zone 2A Lightning Strike

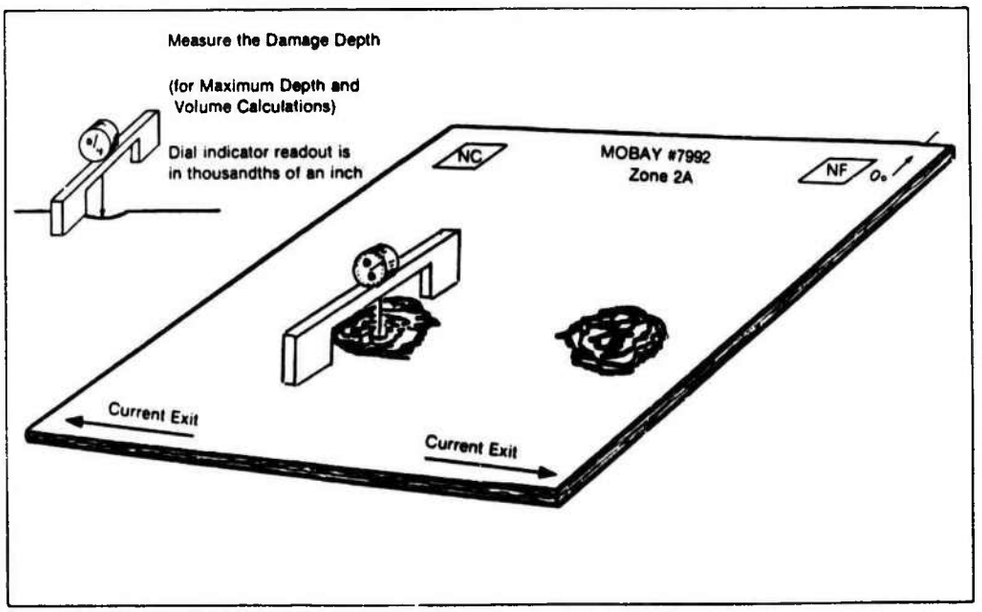
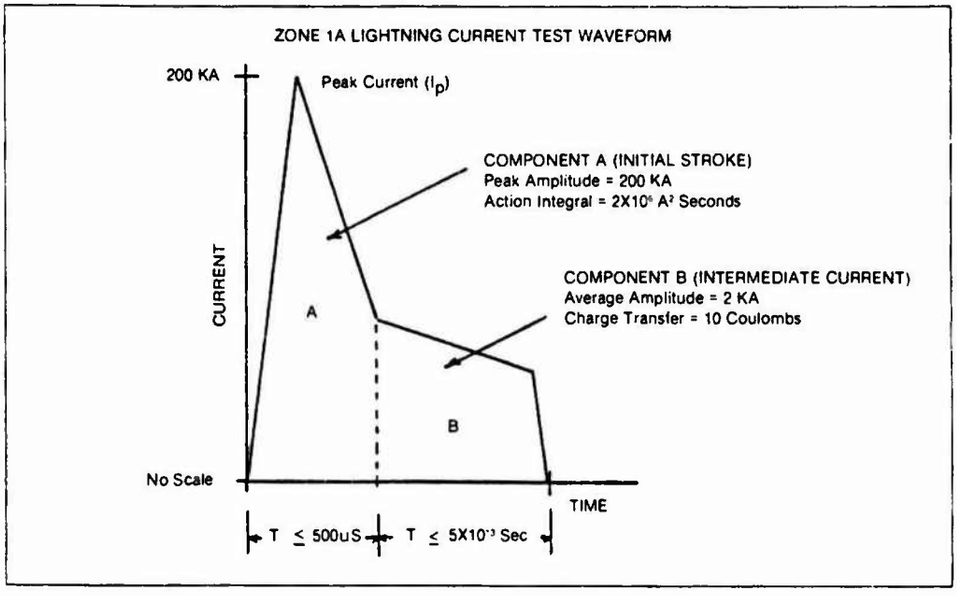


Figure 12. Damage Depth Measurement



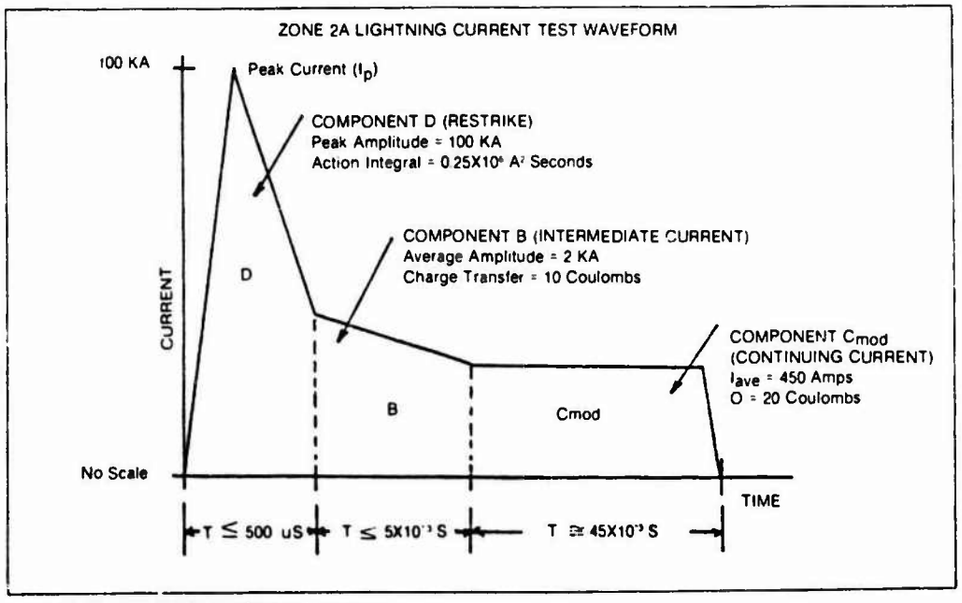


Figure 13. Simulated Lightning Current Waveforms

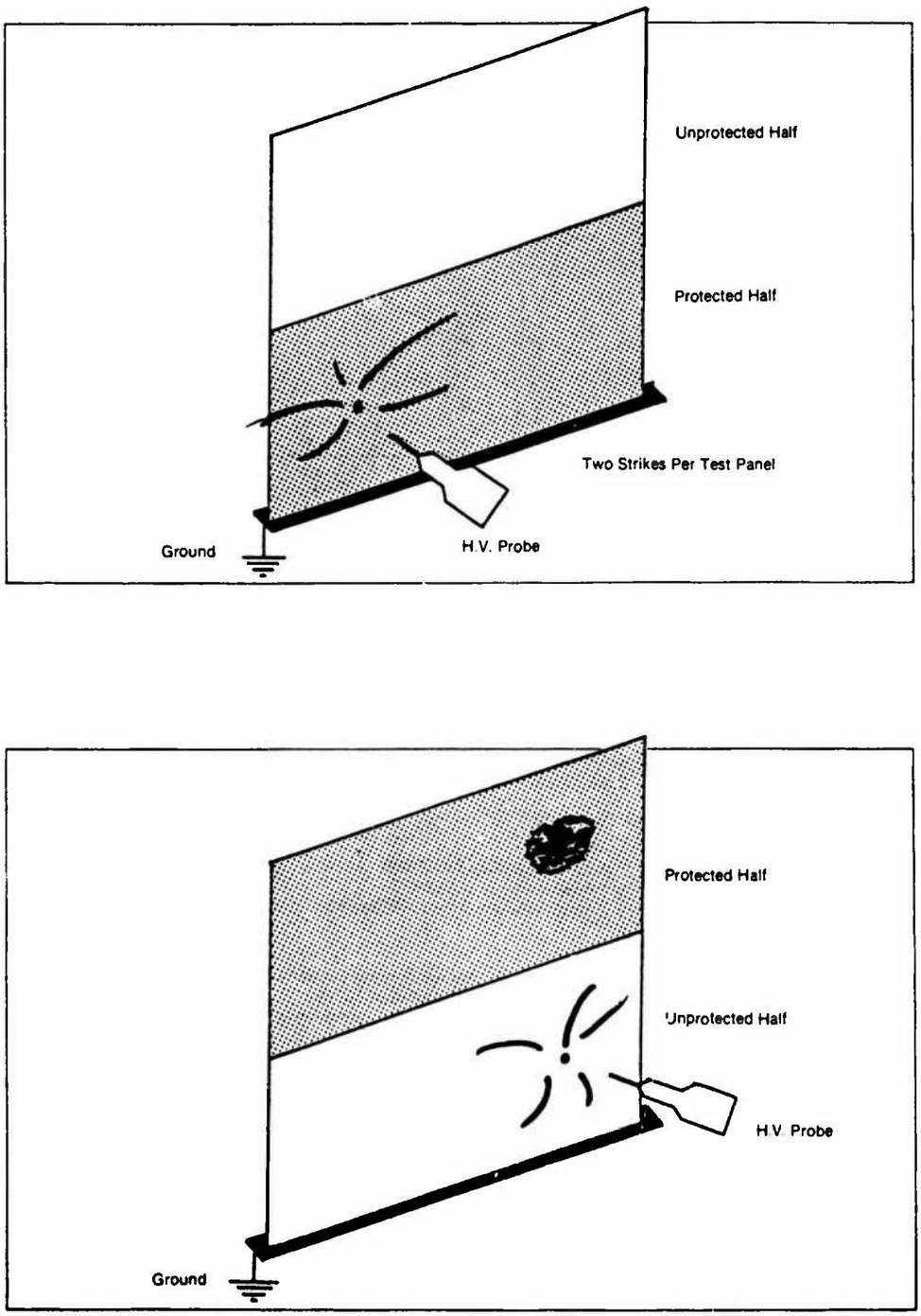


Figure 14. Test Panel Current Attachment Approach

TABLE I

TEST MATRIX

Panel ID	Lightning Strike Test Type	Mechanical Test Type
7988 [1]	Zone 1A	Compression
7989	Zone 1A	Compression
7990	Zone 1A	Tension
7991	Zone 1A	Tension
7992	Zone 2A	Tension
7993	Zone 2A	Tension
7994 [2]	Zone 2A	Compression
7995	Zone 2A	Compression

[1] Panel 7988 was laid up by mistake with one extra ply of tape oriented at 0° and located between the 14th and 16th ply, counting from the tool side or fabric side of the panel.

[2] Panel 7994 was laid up by mistake with one extra ply of tape oriented at 45° and located between the 7th and 8th ply, counting from the tool side or fabric side of the panel.

TABLE II

TENSION RESULTS OF PANELS AFTER ZONE 1A LIGHTNING STRIKE

Specimen ID	Measured Width (in)	Measured Thickness (in) [3]	Average Thickness of Control (in)	Ultimate Load (kip)	Actual Ultimate Strength (ksi) [1]	Retention of Strength (%)	Normalized Ultimate Strength (ksi) [2]	Retention of Strength (%)	Top Fabric Ply Intact or Detached [3]	Specimen Failure Location (in) [4]
7992-CT; NC	1.2512	0.1566	0.1557	17.33	85.5	100	89.0	100	I	6.0
7993-CT; NC	1.2505	0.1572	0.1557	15.97	81.2	100	82.0	100	I	4.0
7990-CT; NC	1.2507	0.1547	0.1557	16.02	82.8	100	82.3	100	I	4.75
7991-CT; NC	1.2521	0.1542	0.1557	17.52	90.7	100	89.9	100	I	4.75
Average					85.8	100	85.8	100		
STD DEV					4.52		4.22			
7990-1T; NC	1.2504	0.1416	0.1557	14.80	63.6	97.4	76.0	88.6	D	2.75
7990-2T; NC	1.2485	0.1229	0.1557	10.60	69.0	80.4	54.5	63.5	D	6.0
7990-3T; NC	1.2505	0.1447	0.1557	14.49	80.1	93.4	74.4	86.7	D	5.0
Average					77.6	90.4	68.3	79.6		
STD DEV					7.58	6.88	11.98	14.0		
7991-1T; NC	1.2504	0.1406	0.1557	14.79	84.1	98.0	76.0	88.6	D	4.5
7991-2T; NC	1.2453	0.1243	0.1557	10.01	64.7	75.4	51.6	60.1	D	6.0
7991-3T; NC	1.2432	0.1420	0.1557	15.63	88.5	103.1	80.7	94.1	D	4.5
Average					79.1	92.2	69.4	80.9		
STD DEV					12.70	14.8	15.61	18.2		

[1] Stress calculated based on measured thickness and width.
[2] Stress calculated based on measured width and average thickness of corresponding control specimens.
[3] I = Intact; D = Detached; P = Partially Intact.
[4] Measured from one end of specimen.
[5] In specimens where the fabric ply is partially intact, the thinner measurement is recorded. In specimens where damage is severe, e.g., with a hole, a median thickness is recorded.

TABLE III

TENSION RESULTS OF PANELS AFTER ZONE 2A LIGHTNING STRIKE

Specimen ID	Measured Width (in)	Measured Thickness (in) [5]	Average Thickness of Control (in)	Ultimate Load (kip)	Actual Ultimate Strength (ksi) [1]	Retention of Strength (%)	Normalized Ultimate Strength (ksi) [2]	Retention of Strength (%)	Top Fabric Ply Intact or Detached [3]	Specimen Failure Location (in) [4]
7992-CT; NF	1.2529	0.1566	0.1569	12.65	64.5	100	64.4	100	I	5.5
7993-CT; NF	1.2528	0.1592	0.1569	15.79	79.2	100	80.3	100	I	5.0
7990-CT; NF	1.2516	0.1560	0.1569	18.63	95.4	100	94.9	100	I	4.75
7991-CT; NF	1.2520	0.1543	0.1569	17.15	88.8	100	87.3	100	I	4.5
Average					82.0	100	81.7	100		
STD DEV					13.43		13.01			
7992-CT; NC	1.2512	0.1566	0.1557	17.33	88.5	100	89.0	100	I	6.0
7993-CT; NC	1.2505	0.1572	0.1557	15.97	81.2	100	82.0	100	I	4.0
7990-CT; NC	1.2507	0.1547	0.1557	16.02	82.8	100	82.3	100	I	4.75
7991-CT; NC	1.2521	0.1542	0.1557	17.52	90.7	100	89.9	100	I	4.75
Average					85.8	100	85.8	100		
STD DEV					4.52		4.22			
7992-1T; NF	1.2529	0.1467	0.1569	14.39	78.3	95.5	73.2	89.0	P	3.25
7992-2T; NF	1.2489	0.0974	0.1569	8.03	66.0	80.5	41.0	50.2	D	4.0
7992-3T; NF	1.2474	0.1467	0.1569	12.68	69.3	84.5	64.8	79.3	P	4.25
Average					71.2	86.8	59.7	73.0		
STD DEV					6.37	7.76	16.73	20.4		
7993-1T; NF	1.2499	0.1472	0.1569	12.44	67.6	82.4	63.4	77.6	P	5.5
7993-2T; NF	1.2476	0.0733	0.1569	2.67	29.3	35.7	13.7	16.8	D	6.0
7993-3T; NF	1.2504	0.1457	0.1569	13.30	73.0	89.0	67.8	83.0	P	4.75
Average					56.6	69.1	48.3	59.1		
STD DEV					23.85	29.1	30.07	36.8		
7992-1T; NC	1.2510	0.1483	0.1557	17.10	92.2	107.5	87.8	102.3	D	4.75
7992-2T; NC	1.2482	0.1399	0.1557	16.78	96.1	112.0	86.4	100.7	D	5.75
7992-3T; NC	1.2504	0.1463	0.1557	15.11	82.6	96.3	77.6	90.4	D	4.5
Average					90.3	105.2	83.9	97.8		
STD DEV					6.94	8.10	5.49	6.44		
7993-1T; NC	1.2505	0.1445	0.1557	15.75	87.2	101.6	80.9	94.3	D	6.0
7993-2T; NC	1.2458	0.1360	0.1557	12.42	73.3	85.4	64.0	74.6	D	6.25
7993-3T; NC	1.2504	0.1455	0.1557	15.68	86.2	100.5	80.5	93.8	P	4.5
Average					82.2	95.8	75.1	87.6		
STD DEV					7.73	9.04	9.63	11.2		

[1] Stress calculated based on measured thickness and width.
[2] Stress calculated based on measured width and average thickness of corresponding control specimens.
[3] I = Intact; D = Detached; P = Partially Intact.
[4] Measured from one end of specimen.
[5] In specimens where the fabric ply is partially intact, the thinner measurement is recorded. In specimens where damage is severe, e.g., with a hole, a median thickness is recorded.

TABLE IV

COMPRESSION RESULTS OF PANELS AFTER ZONE 1A LIGHTNING STRIKE

Specimen ID	Measured Width (in)	Measured Thickness (in) [1]	Average Thickness of Control (in)	Ultimate Load (kip)	Actual Ultimate Strength (ksi) [1]	Retention of Strength (%)	Normalized Ultimate Strength (ksi) [2]	Retention of Strength (%)	Top Fabric Ply Intact or Detached [3]	Specimen Failure Location (in) [4]
7994-CC; NC [5]	1.2494	0.1628	0.1624	21.50	105.7	100	105.9	100	I	5.25
7995-CC; NC	1.2506	0.1562	0.1557	22.43	114.8	100	115.2	100	I	4.5
7988-CC; NC [6]	1.2504	0.1619	0.1624	23.46	115.9	100	115.5	100	I	4.75
7989-CC; NC	1.2520	0.1552	0.1557	21.10	108.6	100	108.2	100	I	4.75
Average					111.2	100	111.2	100		
STD DEV					4.92		4.87			
7988-1C; NC [6]	1.2499	0.1522	0.1624	16.53	86.9	78.1	81.4	73.2	D	4.75
7988-2C; NC [6]	1.2496	0.1351	0.1624	14.70	87.1	78.3	72.4	65.1	D	5.5
7988-3C; NC [6]	1.2479	0.1531	0.1624	21.65	113.2	101.8	106.8	96.0	D	5.0
Average					95.7	86.1	86.9	78.1		
STD DEV					15.16	13.6	17.83	16.0		
7989-1C; NC	1.2489	0.1430	0.1557	13.97	78.2	70.3	71.8	64.6	D	5.5
7989-2C; NC	1.2465	0.1231	0.1557	10.30	67.1	60.3	53.1	47.8	D	5.0
7989-3C; NC	1.2476	0.1436	0.1557	14.00	78.2	70.3	72.1	64.8	D	4.75
Average					74.5	67.0	65.7	59.1		
STD DEV					6.39	5.76	10.91	9.79		

[1] Stress calculated based on measured thickness and width.
[2] Stress calculated based on measured width and average thickness of corresponding control specimens.
[3] I = Intact, D = Detached, P = Partially Intact.
[4] Measured from one end of specimen.
[5] Panel 7994 was laid up by mistake with one extra ply of tape oriented at 45° and located between the 7th and 8th ply counting from the tool side or fabric side of the panel.
[6] Panel 7988 was laid up by mistake with one extra ply of tape oriented at 0° and located between the 14th and 16th ply counting from the tool side or fabric side of the panel.
[7] In specimens where the fabric ply is partially intact, the thinner measurement is recorded. In specimens where damage is severe, e.g., with a hole, a median thickness is recorded.

TABLE V

COMPRESSION RESULTS OF PANELS AFTER ZONE 2A LIGHTNING STRIKE

Specimen ID	Measured Width (in)	Measured Thickness (in) [7]	Average Thickness of Control (in)	Ultimate Load (kip)	Actual Ultimate Strength (ksi) [1]	Retention of Strength (%)	Normalized Ultimate Strength (ksi) [2]	Retention of Strength (%)	Top Fabric Ply Intact or Detached [3]	Specimen Failure Location (in) [4]
7994-CC; NF [5]	1.2511	0.1613	0.1628	17.38	86.1	100	85.3	100	I	5.0
7995-CC; NF	1.2520	0.1568	0.1569	18.95	96.5	100	96.5	100	I	6.0
7988-CC; NF [6]	1.2505	0.1642	0.1628	17.58	85.6	100	86.4	100	I	4.25
7989-CC; NF	1.2517	0.1585	0.1569	17.02	85.8	100	86.7	100	I	5.75
Average					88.5	100	88.7	100		
STD DEV					5.35		5.21			
7994-CC; NC [5]	1.2494	0.1628	0.1624	21.50	105.7	100	105.9	100	I	5.25
7995-CC; NC	1.2506	0.1562	0.1557	22.43	114.8	100	115.2	100	I	4.5
7988-CC; NC [6]	1.2504	0.1619	0.1624	23.46	115.9	100	115.5	100	I	4.75
7989-CC; NC	1.2520	0.1552	0.1557	21.10	108.6	100	108.2	100	I	4.75
Average					111.2	100	111.2	100		
STD DEV					4.92		4.87			
7994-1C; NF [5]	1.2489	0.1500	0.1628	16.23	86.7	98.0	79.8	90.0	P	6.0
7994-2C; NF [5]	1.2488	0.1059	0.1628	10.59	80.1	90.5	52.1	58.7	D	6.0
7994-3C; NF [5]	1.2482	0.1465	.628	16.27	89.0	100.6	80.1	90.3	D	6.0
Average					85.2	96.4	70.7	79.7		
STD DEV					4.62	5.24	16.09	18.1		
7995-1C; NF	1.2524	0.1504	0.1569	16.66	88.4	99.9	84.8	95.6	P	4.0
7995-2C; NF	1.2479	0.0861	0.1569	7.82	72.8	82.3	39.9	45.0	D	5.5
7995-3C; NF	1.2496	0.1466	0.1569	17.34	94.7	107.0	88.5	99.8	P	5.75
Average					85.3	96.4	71.1	80.1		
STD DEV					11.27	12.7	27.00	30.5		
7994-1C; NC [5]	1.2521	0.1510	0.1624	19.29	102.0	91.7	94.9	85.3	D	5.5
7994-2C; NC [5]	1.2477	0.1413	0.1624	15.28	86.7	78.0	75.4	67.8	D	6.0
7994-3C; NC [5]	1.2482	0.1545	0.1624	18.55	96.2	86.5	91.5	82.3	D	5.0
Average					95.0	85.4	87.3	78.5		
STD DEV					7.75	6.95	10.40	9.37		
7995-1C; NC	1.2512	0.1437	0.1557	17.56	97.7	87.9	90.2	81.1	D	5.0
7995-2C; NC	1.2487	0.1416	0.1557	18.58	105.1	94.5	95.5	85.9	D	5.0
7995-3C; NC	1.2498	0.1471	0.1557	19.08	103.?	93.3	98.1	88.2	D	5.75
Average					102.2	91.9	94.6	85.1		
STD DEV					3.94	3.55	4.03	3.62		

[1] Stress calculated based on measured thickness and width.
[2] Stress calculated based on measured width and average thickness of corresponding control specimens.
[3] I = Intact; D = Detached, P = Partially Intact.
[4] Measured from one end of specimen.
[5] Panel 7994 was laid up by mistake with one extra ply of tape oriented at 45° and located between the 7th and 8th ply counting from the tool side or fabric side of the panel.
[6] Panel 7988 was laid up by mistake with one extra ply of tape oriented at 0° and located between the 14th and 16th ply counting from the tool side or fabric side of the panel.
[7] In specimens where the fabric ply is partially intact, the thinner measurement is recorded. In specimens where damage is severe, e.g., with a hole, a median thickness is recorded.

TABLE VI

AVERAGE MECHANICAL TEST RESULTS OF PANELS AFTER LIGHTNING STRIKE [1]

	Tension		Compression	
	Normalized Strength (ksi)	Strength Retention (%)	Normalized Strength (ksi)	Strength Retention (%)
Control NF	81.7 (13.0)	100	88.7 (5.2)	100
Control NC	85.8 (4.2)	100	111.2 (4.9)	100
Zone 1A NF	0	0	0	0
Zone 1A NC	68.9 (12.5)	80.3 (14.6)	76.3 (17.6)	68.6 (15.8)
Zone 2A NF	54.0 (22.6)	66.0 (27.6)	70.9 (19.9)	79.9 (22.5)
Zone 2A NC	79.5 (8.5)	92.7 (9.9)	90.9 (8.1)	81.8 (7.3)

[1] Average value of the results of 4 specimens for the control and 6 specimens for the lightning strike tested panels. Data from Tables II, III, IV, and V.

( ) Standard Deviation

NF = Panels with Normal Fabric

NC = Panels with Nickel Coated Fabric

TABLE VII

ZONE 1A TEST VALUES

	"A" Component		"B" Component		
Panel No.	Peak Current (10^3 Amps)	Action Integral ($10^6 A^2$ Sec)	Average Current (10^3 Amps)	Energy Transfer (Coulombs)	Panel Puncture
7988-NC	184	2.4	1.7	8.5	NO
7988-NF	168	2.1	1.7	8.5	YES
7989-NC	207	3.0	1.8	8.8	NO
7989-NF	188	2.5	1.8	8.8	YES
7990-NC	199	2.9	1.6	8.2	NO
7990-NF	199	2.7	1.7	8.5	YES
7991-NC	203	2.9	1.7	8.3	NO
7991-NF	195	2.8	1.7	8.5	YES

Note: NC = Nickel Coated Fabric (protection system)
NF = Normal Fabric (unprotected)

TABLE VIII

ZONE 1A DAMAGE VALUES

	Damage*			
Panel No.	Depth (inch)	Area ($in.^2$)	Volume ($in.^3$)	Maximum** Depth (inch)
7988-NC	0.017	6.5	0.037	0.034
7988-NF	PUNCTURE	--	--	(0.150)
7989-NC	0.026	7.6	0.066	0.043
7989-NF	PUNCTURE	--	--	(0.150)
7990-NC	0.026	9.6	0.083	0.043
7990-NF	PUNCTURE	--	--	(0.150)
7991-NC	0.028	6.3	0.059	0.045
7991-NF	PUNCTURE	--	--	(0.150)

*Damage Values referenced to the 2nd ply as the 1st ply (128-in^2 nickel coated fabric) was totally removed.

**Maximum Depth = (2nd ply reference depth) + (outer ply thickness, 0.017-in.)

N- = Nickel Coated Fabric (protection system)
N- = Normal Fabric (unprotected)

TABLE IX

ZONE 2A TEST VALUES

	"D" Component		"B" Component		
Panel No.	Peak Current (10^3 Amps)	Action Integral ($10^3 A^2$ Sec)	Average Current (10^3 Amps)	Energy Transfer (Coulombs)	Panel Puncture
7992-NC	83	2.4	1.7	8.5	NO
7992-NF	78	2.0	1.9	9.5	NO
7993-NC	97	2.8	1.8	9.0	NO
7993-NF	102	2.6	1.8	8.8	YES
7994-NC	102	3.3	1.8	9.0	NO
7994-NF	97	2.9	1.7	8.6	NO
7995-NC	98	3.2	1.8	9.0	NO
7995-NF	103	2.9	1.8	9.0	NO

Note "C-mod" Component values for all Zone 2A panels
Average Current = 450 Amps, Energy Transfer = 20 Coulombs

NC = Nickel Coated Fabric (protection system)
NF = Normal Fabric (unprotected)

TABLE X

ZONE 2A DAMAGE VALUES

Panel No.	Damage			
	Depth (inch)	Area ($in.^2$)	Volume ($in.^3$)	
7992-NC	0.024	35.8	0.286	
7992-NF	0.089	13.1	0.389	
7993-NC	0.032	23.2	0.247	
7993-NF	(0.150)	(12.3)	(0.617)	(PUNCTURED)
7994-NC	0.023	29.6	0.227	
7994-NF	0.087	15.2	0.440	
7995-NC	0.020	26.2	0.188	
7995-NF	0.105	12.3	0.431	

Note: NC = Nickel Coated Fabric (protection system)
NF = Normal Fabric (unprotected)

FIELD OBSERVATIONS OF AIRCRAFT CHARGING IN CONVECTIVE CLOUDS

B. Gardiner, J. Hallett and C.P.R. Saunders*

Atmospheric Sciences Center, Desert Research Institute, P.O. Box 60220, Reno, Nevada 89506, U.S.A.
**Department of Physics, U.M.I.S.T., P.O. Box 88, Manchester, U.K.*

ABSTRACT

Aircraft charge was measured during penetrations of summer convective clouds in Montana as part of the Desert Research Institute involvement in the Cooperative Convective Precipitation Experiment. An Aerocommander was instrumented to measure electric field, aircraft charge, ice particle type and concentration, precipitation particle charge and the usual meteorological parameters. Preliminary results are presented which point to the importance of ice particles in aircraft charging and are compared with laboratory results at lower impact velocity. Evidence is presented to show that temperature, liquid water content and electric field may affect the sign and magnitude of charging. No evidence was found to link sudden changes in aircraft charge or local electric field to lightning strikes on the aircraft.

INTRODUCTION

Laboratory studies of graupel charging [1 - 3] have demonstrated that charging only occurs in the presence of ice crystals and supercooled water. Charging was also found to be a function of temperature, liquid water content and the concentration of impurities [$(NH_4)_2SO_4$ and NaCl] in the liquid water. Of particular importance, Jayaratne et al. [3] found that the sign of the graupel charging changed sign at a temperature between -10°C and -20°C depending on the liquid water content. The charge separated per collision-separation event for 100 μm diameter ice crystals (the largest used in laboratory studies) is typically 1fC, though this can be 10x larger in the presence of impurity concentrations typical of the atmosphere. Gardiner et al. [4], from observations of Montana convective storms, have found that so long as it is possible to extrapolate laboratory results to ice crystal sizes more typical of convective clouds, many aspects of thunderstorm electrification may be explained in terms of graupel-ice charging. Furthermore, the observations suggest that the conditions suitable for charging may only occur in very specific regions of the clouds where graupel, vapor grown crystals and supercooled water are co-located and these regions are likely to be at the boundary between updrafts and downdrafts [5].

Field mills mounted on the top and bottom of an aircraft fuselage provide the charge carried on the aircraft. The measurement of aircraft charge, along with that of electric field, ice type and concentration, particle charge, liquid water content and temperature, are analyzed in order to reveal details of the mechanism for aircraft charging and its possible role in initiating lightning strikes. In particular it is important to understand how aircraft become charged, with what magnitude and sign, and whether by being charged aircraft more likely to be struck by lightning. Although circumstantial evidence from the increase in radio static during flights through precipitation shafts points to the importance of ice collisions in aircraft charging, the connection has not been well established by detailed observation. If ice is important, a number of questions are raised. Is it possible to extend what has been learnt about graupel-ice and ice-metal [6] charging in the laboratory at low impact velocities (~ 10 m s^{-1}) to charging at aircraft speeds (100 - 150 m s^{-1})? Does the aircraft become charged by acquiring charge already carried by the ice particles or simply by virtue of the collisions themselves? Does the trail of charged ice cloud left by the aircraft act as a channel for lightning strokes?

FIELD OBSERVATIONS

An instrumented Aerocommander aircraft was operated for the Desert Research Institute during the CCOPE[1] project. The CCOPE project [7] was a cooperative project involving various University groups, NCAR[2], the Bureau of Reclamation, the Illinois State Water Survey, NASA[3], NOAA[4] and the National Research Council of Canada which took place in Eastern Montana during the summer of 1981. 14 aircraft, 8 radars, 2 mesoscale surface data networks and a radiosonde network were used to make an extremely thorough investigation of all aspects of convective storms.

The Aerocommander was equipped to measure the following parameters:

a) Vertical Electric Field and Aircraft Charge.

Rotating shutter-type field mills were mounted on the top and bottom of the aircraft fuselage. These were flush to the surface and located just behind the trailing edge of the wings. The field mills operated on both a sensitive and insensitive range, full scales of 1.2 ± 0.4 kv m^{-1} and 50 ± 2 kv m^{-1} respectively. Both field mills were calibrated on the ground between parallel plates with corrections for edge effects. The field measured by each

---

1 Cooperative Convective Precipitation Experiment
2 National Ocean and Atmospheric Administration
3 National Center for Atmospheric Research
4 National Aeronautic & Space Administration

mill when mounted on the aircraft is the sum of the atmospheric electric field and the field produced by charge residing on the aircraft skin. Therefore the field measured by the upper and lower field mills, E_U and E_L respectively, is given by

$$E_U = aE_F + cE_Q \quad (1)$$

$$E_L = -bE_F + dE_Q \quad (2)$$

where E_F is the vertical atmospheric electric field, E_Q is the field due to the aircraft charge and a, b, c and d are factors due to the aircraft shape which have to be determined. To simplify the problem consider the aircraft to be represented by a horizontally orientated prolate spheriod with rotational symmetry, length 2ℓ and diameter 2r. It can be shown [8] that the field on the vertical axis at the surface (E_{PS}) due to a charge q_A residing on such a body is given by

$$E_{PS} = -\frac{q_A}{4\pi\varepsilon_o \ell r} \quad (3)$$

This provides the factors c and d in equations (1) and (2). However, the solution for the distortion of the external field E_A by a prolate spheriod is extremely complex and it is simpler for these purposes to now consider the aircraft as a cylinder stretching to infinity in both directions. It can be shown [8] that the field measured at the top surface of such a body (E_{CU})is given by

$$E_{CU} = 2E_F \quad (4)$$

and the field on the lower surface (E_{CL}) by

$$E_{CL} = -2E_F \quad (5)$$

This provides the factors a and b. Note that in this paper fields are measured in the opposite direction to the conventional physics sense, i.e., positive points to the direction a negative charge will move.

Finally, a test was made of the non-symmetry of the aircraft by self-charging the aircraft by means of a high voltage supply on a day with a low ambient field. The ratio of upper to lower field mills was found to be given by $E_U/E_L = 0.77 \pm .03$, mainly due to the fact that the wings are mounted flush with the upper surface of the fuselage. Therefore combining all these factors gives

$$\frac{E_U}{(0.77)^{1/2}} = 2E_F - \frac{q_A}{4\pi\varepsilon_o \ell r} \quad (6)$$

$$(0.77)^{1/2}\ E_L = -2E_F - \frac{q_A}{4\pi\varepsilon_o \ell r} \quad (7)$$

Rearranging and substituting values for ℓ and r gives

$$E_F = 0.285E_U - 0.219E_L \text{ V m}^{-1} \quad (8)$$

$$q_A = -(0.364E_U + 0.280E_L) \times 10^{-9} \text{ C} \quad (9)$$

b) Particle Charge

The individual charge carried by precipitation (graupel) particles was measured by means of the voltage induced during passage through an induction ring. Spurious charges arising from impact with the induction tube were excluded from analysis by examination of the pulse shape and time of flight through a second ring in series with the first. The percentage of all particle passages which impact on the induction ring was found to be less than 10%. The voltage levels were stored on audio tape after a voltage to frequency conversion. Analysis was then performed by playing the tape back into a microcomputer configured as a storage oscilliscope, which allows a time resolution of 1 ms. The charge particle device provides information on the sign and magnitude of individual charges, the ratio of positive to negative charge densities, the ratio of the numbers of positive charged particles to those charged negative and the ratio of the total numbers of charged particles to the total ice concentration (see (c) below). The sample volume of the device is 165 $\ell\ s^{-1}$ at a flight speed of 100 m s^{-1} and individual particles carrying charges within the range ±5-100 pc can be detected. Since the aircraft itself sweeps out a volume of approximately $6.6 \times 10^5\ \ell\ s^{-1}$, it is obvious that for low ice concentrations the charge particle detector may miss particles which are nonetheless affecting the aircraft.

c) Particle Size, Shape and Concentration

Measurement of particle type and sizes in the range 6 - 3000 μm was made using a formvar replicator [9] which has a sample volume of 1 $\ell\ s^{-1}$, horizontal resolution 1 m. In addition, a standard Knollenberg 2D-C probe was used [10]. This measures particles in the range 25 - 800 μm and has a sample volume, on average, of 5 $\ell\ s^{-1}$. Once again the problem of not detecting particles for low ice concentrations, as discussed in (b), is relevant.

d) Cloud Droplet Characteristics

Details of the cloud droplet spectra were obtained from an FSSP[5] probe [10] operating on the 2 - 47 μm (15 channels) range and the formvar replicator. The cloud liquid water content (LWC) was obtained by integrating over the entire size range of the FSSP and from a Johnson-Williams (JW) liquid water meter.

e) Temperature

Temperature to an accuracy of ±0.2°C was obtained using both Rosemount and reverse flow thermometers.

f) Vertical Velocity

Vertical velocity was computed in the manner described by Lawson [11] from measurements of true airspeed, pressure, vertical acceleration, pitch, roll, angle of attack and temperature.

g) Pressure and Position

[5] Forward Scattering Spectrometer Probe

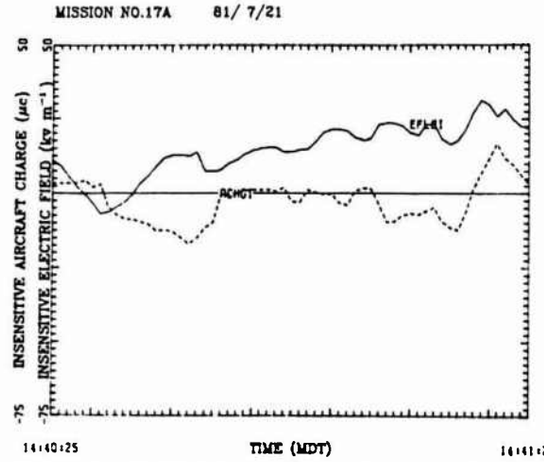


Figure 1a: Insensitive electric field (solid line) and aircraft charge (dashed line), 1440:25 - 1441:25, 21 July 1981.

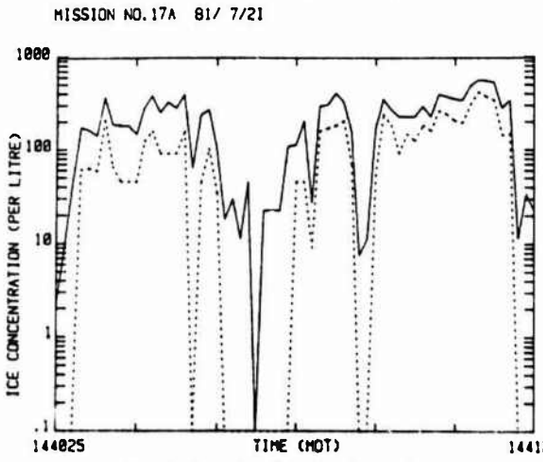


Figure 1b: Total ice (solid line) and vapor grown crystal (dashed line) concentrations, 1440:25 - 1441:25, 21 July 1981.

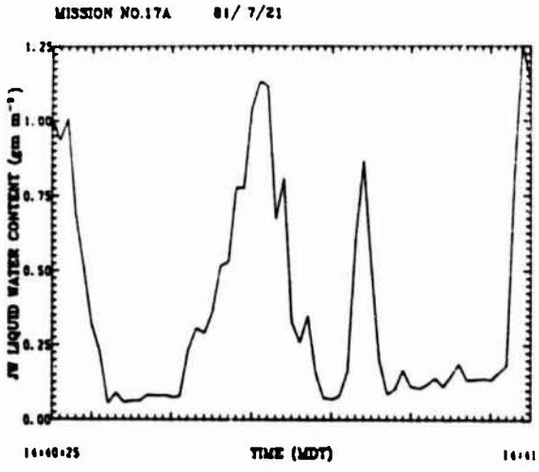


Figure 1c: JW measured liquid water content, 1440:25 - 1441:25, 21 July 1981.

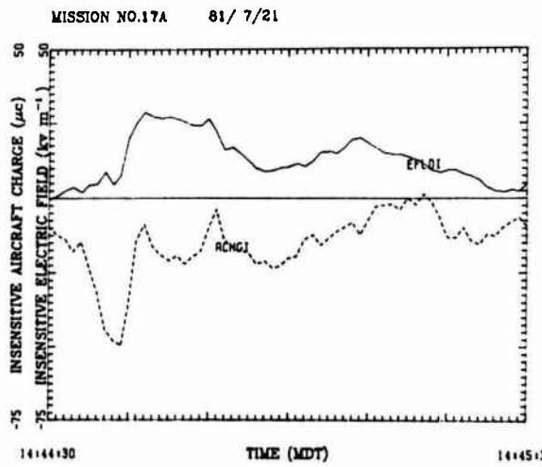


Figure 2a: Insensitive electric field (solid line) and aircraft charge (dashed line), 1444:30 - 1445:30, 21 July 1981.

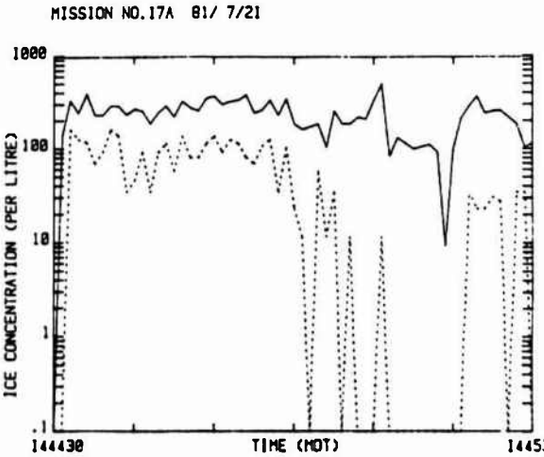


Figure 2b: Total ice (solid line) and vapor grown crystal (dashed line) concentrations, 1444:30 - 1445:30, 21 July 1981.

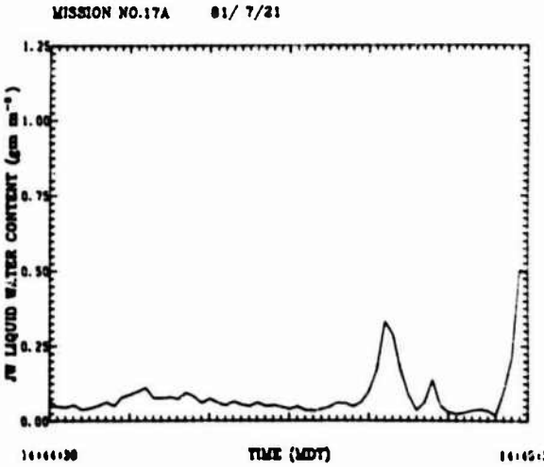


Figure 2c: JW measured liquid water content, 1444:30 - 1445:30, 21 July 1981.

The FSSP operated at 100 Hz in cloud, 10 Hz out of cloud whilst most other parameters were gathered at 10 Hz in cloud and 1 Hz out of cloud.

RESULTS

Table 1 presents a summary of the cloud passes used in the analysis of aircraft charging. Cloud passes have been chosen so as to provide a matrix of conditions; different ice types and concentrations, different liquid water contents and different temperatures.

a) Mission 17A-Graupel and Vapor Grown Crystals

A series of penetrations were made through a line of cumulus congestus which were rapidly glaciating. Penetrations were made at an altitude of 6800 m and a temperature of -21°C. The highest ice concentrations and aircraft charging observed during the CCOPE project were found in these clouds. Figure 1a shows the electric field (solid line) and aircraft charge (dashed line) for a one minute period during the first pass through one of these clouds whilst Figure 1b gives the measured total ice (solid line) and vapor grown crystal (dashed line) concentrations over the same period. Both graupel and vapor grown crystals were observed during this pass in total concentrations as high as 600 ℓ^{-1}. Generally in periods of high ice concentration (> 100 ℓ^{-1}), liquid water contents (see Figure 1c) were low (< 0.1 gm m^{-3}) though there are short periods, such as around 1440:28 and 1440:55, when the cloud was a mixture of vapor grown crystals, graupel and supercooled water, conditions previously argued as ideal for graupel charging. The aircraft on the other hand becomes most highly charged in the periods with the highest ice concentrations, 1440:30-1440:40 and 1441:05-1441:20 even though liquid water contents were low. In general the aircraft was negatively charged during this pass though between 1441:18 and 1441:25 the aircraft charge is strongly positive. A possible reason is that the predominant ice form changes from graupel at the beginning of the period to vapor grown crystals by 1441:10. This hypothesis can be checked by studying passes were the predominant ice forms are graupel and vapor grown crystals respectively.

Part of the second pass through this cloud is shown in Figure 2 a, b, c. Note the abrupt increase in aircraft charge as soon as ice is encountered at 1444:30. Charging during this pass is always negative and the predominate ice form is graupel. Furthermore the strongest charging appears superficially to be associated with weak values of the electric field. During this pass extremely large values of space charge density were measured by the particle charge sensor, reaching a maximum of -8C km^{-3}.

b) Mission 14A - Vapor Grown Crystals

Let us examine a cloud where vapor grown crystals are the predominant ice form. On 17 July 1981 flights were made through the feeder cells of an extremely complicated storm system which was somewhere between a supercell and a squall line. Five penetrations were made at an altitude of 5600 m and a temperature of -14°C. Liquid water contents were extremely low throughout these passes (~ 0.07 gm m^{-3}). Figure 3b shows the total ice (solid line) and vapor grown crystal (dashed line) concentrations for a one minute period during the second pass. The majority of the ice was found to be small (< 100 μm) plates and very little graupel was detected. Figure 3a shows that charging was predominantly negative in contrast to our initial observations in Mission 17A which suggested that vapor grown ice charged the aircraft in a positive sense. Two differences that may have contributed to this are the warmer temperature of these penetrations and the almost total lack of any liquid water. Even though in Mission 17A liquid water contents were low during the periods (~ 10 s) with the highest ice concentrations, between these periods water contents were as high as 1 gm m^{-3}.

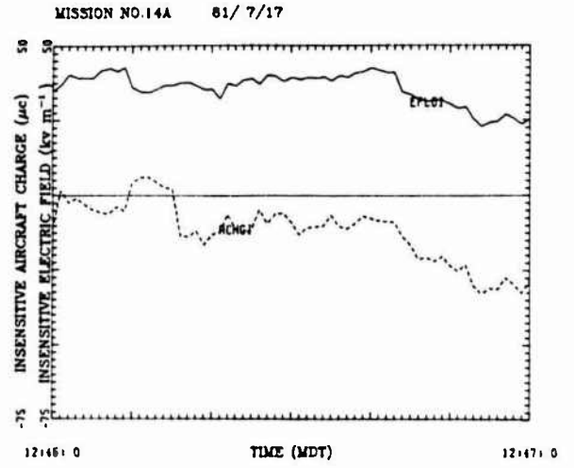


Figure 3a: Insensitive electric field (solid line) and aircraft charge (dashed line), 1246:00 - 1247:00, 17 July 1981.

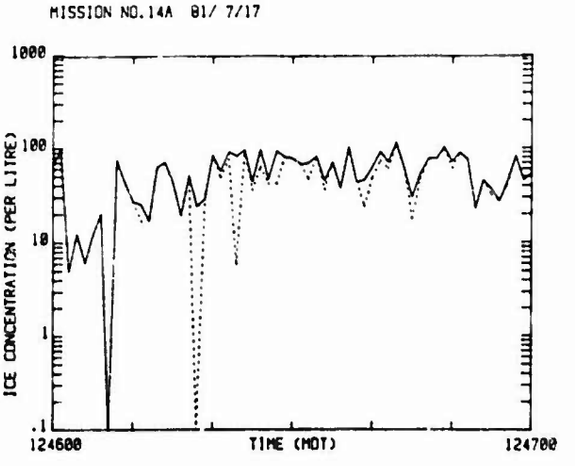


Figure 3b: Total ice (solid line) and vapor grown crystal (dashed line) concentration, 1246:00 - 1247:00, 17 July 1981.

c) Mission 10A - Graupel

A series of penetrations were made through a large decaying system on 11 July 1981. These penetrations were at an altitude of 4700 m and temperatures close to the freezing level (-2°C). No vapor grown crystals were detected in this cloud, the ice was either graupel or possibly wet growth graupel. Two distinct charging patterns are presented in Figures 4 and 5 which are separated by 2 minutes. Between 1824:30-1825:30 the charging is exclusively positive whilst between 1826:20-1827:20 the charging is negative. Two differences between these periods are apparent. In the first period a majority of the ice is wet graupel (dashed line, Figure 4b) whereas very little was detected in the second period (Figure 5b). Since this could be due to melting in the replicator at these high temperatures, the results should be viewed with caution. More significant is the change in the sign of the electric field, positive in the first period, negative in the second, suggesting that the electric field may have some influence on the charging process as was the case in Buser and Jaccard's [6] experiments.

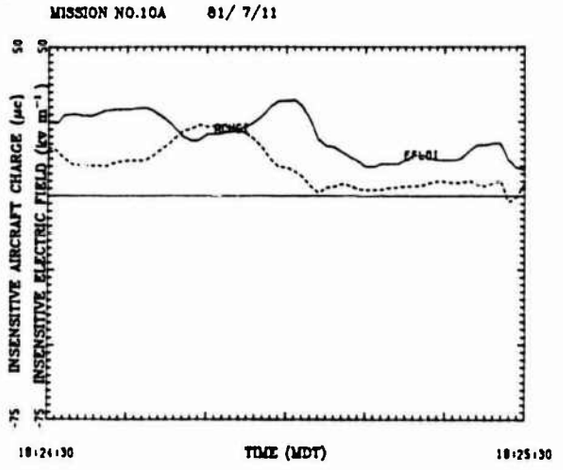


Figure 4a: Insensitive electric field (solid line) and aircraft charge (dashed line), 1824:30 - 1825:30, 11 July 1981.

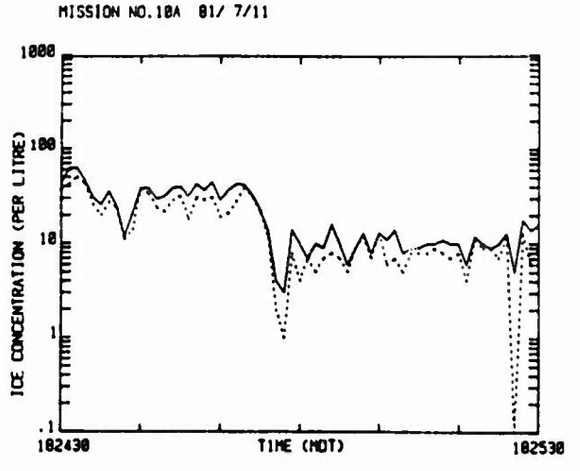


Figure 4b: Total ice (solid line) and wet growth graupel (dashed line) concentrations, 1824:30 - 1825:30, 11 July 1981.

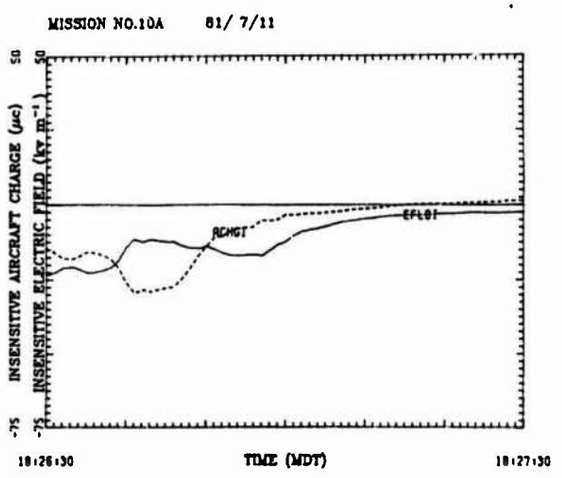


Figure 5a: Insensitive electric field (solid line) and aircraft charge (dashed line), 1826:30 -1827:30, 11 July 1981.

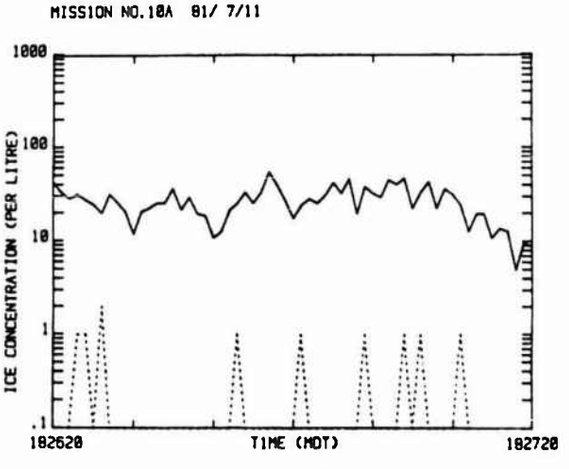


Figure 5b: Total ice (solid line) and wet growth graupel (dashed line) concentrations, 1826:30 - 1827:30, 11 July 1981.

d) Mission 29A - Supercooled Cloud Droplets

To verify the role of ice in aircraft charging, a cloud pass in which no ice was detected was studied. A number of moderate sized cumulus were investigated which in general were fairly ice free. Penetrations were at an altitude of 4800 m and a temperature of -8°C. Figure 6 shows the electric field and aircraft charge for both the insensitive and sensitive ranges during one such pass. The aircraft entered cloud at 1552 and immediately a weak electric field (long dashes) was detected and the aircraft became charged. This is particularly obvious in the sensitive aircraft charge (very short dashes), but even so the magnitude of charging is significantly reduced (~ -2.5 μC) compared to the previous cases studied. The small amount of charging that did take place was probably still the result of ice collisions. As discussed in the Field Observations section, it is possible for the replicator to miss ice particles at low concentrations because of its small sample volume (1 $\ell\ s^{-1}$) whereas the airplane sweeps out a much larger volume ($6.6 \times 10^5\ \ell\ s^{-1}$). The particle charge detector, which has a sample volume of 166 $\ell\ s^{-1}$, did detect some charged precipitation particles during this pass (see Table 1).

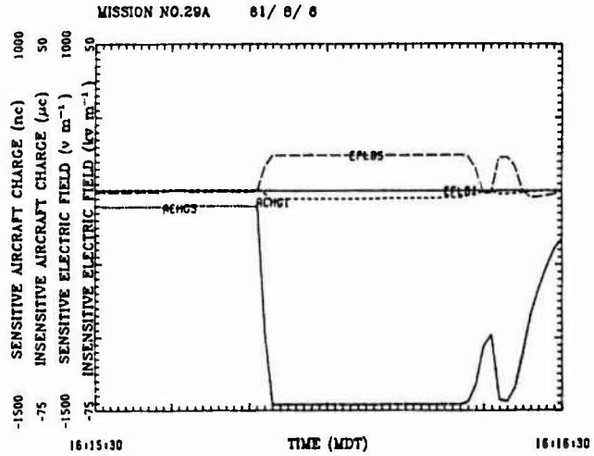


Figure 6: Insensitive electric field (solid line), insensitive aircraft charge (medium dashes), sensitive electric field (long dashes) and sensitive aircraft charge (short dashes), 1615:30 - 1616:30, 6 August 1981.

e) Lightning Strikes

Between 1900-1935 on 11 July 1981, penetrations were made through a highly electrified large scale storm system. There was intense lightning activity and on a number of occasions the aircraft was struck by lightning. Two such occasions are shown in Figure 7, the lightning hit the aircraft at 1904:12 and 1906:55 at which times the on-board computer failed. The highest electric field (saturated at 50 kv m^{-1}) and space charge density (-9.4 C km^{-3}) observed during the CCOPE flights were found in this cloud.

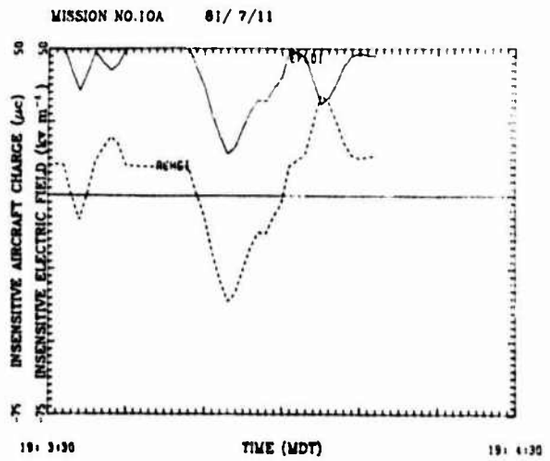


Figure 7a: Insensitive electric field (solid line) and aircraft charge (dashed line), 1903:30 - 1904:30, 11 July 1981. Lightning struck the aircraft at 1904:12.

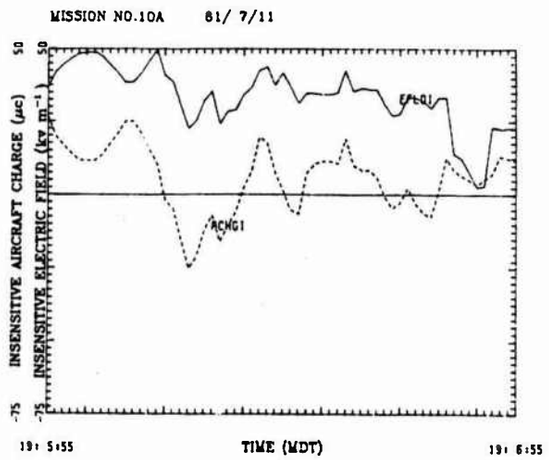


Figure 7b: Insensitive electric field (solid line) and aircraft charge (dashed line), 1905:55 - 1906:55, 11 July 1981. Lightning struck the aircraft at 1906:55.

DISCUSSION

Significant aircraft charging appears to occur only in the presence of ice. Is this charge due to the aircraft-ice collisons or does the aircraft acquire the charge already carried by the ice particles? During Mission 17A (1444:30-1445:30) space charge densities carried by precipitation particles reached -8C km^{-3}. A quick calculation can be made to test whether it is feasable for the aircraft charge to have been acquired from these precipitation particles. The volume swept out by the aircraft in 1 sec is given by the true air speed multiplied by the cross-sectional area $\simeq$ 660 m^3 s^{-1}. The maximum possible rate of charge gain (dq_g/dt) is given by

$$\frac{dq_g}{dt} = -8 \times 660 \times 10^{-9} \text{ C s}^{-1} \qquad (10)$$

The charge decay is given by an exponential where the 1/e time is 4 secs (see 1632:42 in Figure 8, the time at which the aircraft emerged from a cloud). Therefore the rate of charge loss (through ionic neutralization) at any instant in time is given by

$$\frac{dq_L}{dt} = \frac{-q_A}{4} \qquad (11)$$

where q_A is the aircraft charge.

For equilibrium

$$\frac{dq_g}{dt} + \frac{dq_L}{dt} = 0 \qquad (12)$$

which gives,

$$q_A = -4 \times 8 \times 660 \times 10^{-9} \text{C}$$

$$= -20 \ \mu\text{C}$$

The maximum aircraft charge observed during this pass was approximately -50 μC (1444:39), and some other mechanism is therefore needed to explain the charging.

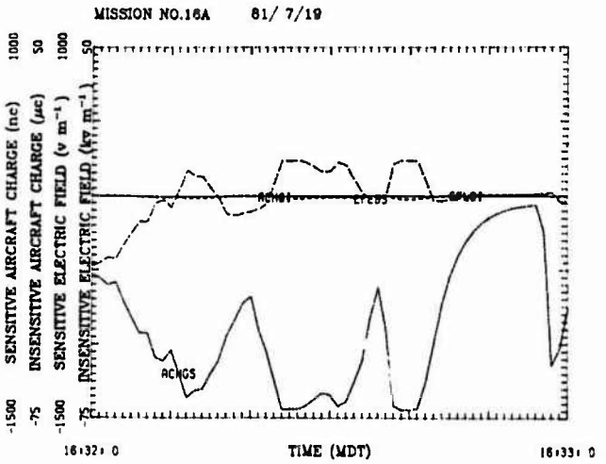


Figure 8: Insensitive electric field (solid line), insensitive aircraft charge (medium dashes), sensitive electric field (long dashes) and sensitive aircraft charge (short dashes), 1632:00 1633:00, 19 July 1981.

From Figure 8 it is obvious that because of the decay time for charge carried by the aircraft, the aircraft effectively integrates over a four or five second time period. Therefore the affect of changes in ice type, ice concentration or liquid water content on time scales shorter than this will not be resolved. Significant changes on time scales less than 5 secs are observed to occur quite frequently in Figures 1 and 2 and therefore it will be impossible to determine the affect of these sudden changes on the aircraft charge.

The measurements presented also allow some insight to be gained into the reasons for lightning strikes on aircraft. The question is posed as to whether the lightning strikes were correlated with an increase in either aircraft charge or electric field in the vicinity of the aircraft. From Figure 7 no such causality is evident in either case and this was also true for other lightning strikes. Therefore it would seem from this very preliminary investigation that the aircraft was hit due to being in the natural path of the lightning rather than because of some increase in electric field intensity at its surface. Because only measurements of vertical electric field were made it is possible that large changes in the horizontal electric field went unnoticed.

CONCLUSIONS

The results presented here are an extension to work first presented by Christian et al [12]. Although the work is still somewhat preliminary in nature, several conclusions can be drawn.

The presence of ice appears to be necessary for significant charging to take place. On the 6 August 1981 (Mission 29A) when very little ice was present, much weaker charging was observed than on the other days studied. The form of the ice does not appear to be critical, both vapor grown crystals and graupel charge the aircraft. However, there is some evidence that under different conditions (temperature and/or liquid water content) the sign of the charging may be reversed. For example, on the 17 July 1981 (low LWC, warm temperatures), vapor grown crystals charged the aircraft negatively whilst on the 21 July 1981 (higher LWC, lower temperatures) the aircraft charged positively. The direction of the electric field appears on occasion to influence the sign of the charging (Mission 10A) though this needs to be investigated more thoroughly before any definite conclusion can be drawn.

Calculation suggests that charging is a result of aircraft-ice impacts rather than by stripping of the charge already carried by the ice particles. Laboratory studies of ice-ice collisional charging [1-3] although applicable to convective storm electrification [4] do not appear to be relevant to aircraft charging (e.g., charging occurs without the presence of liquid water). However, some aspects of the laboratory studies of ice-metal [6] charging do appear relevant (influence of electric field).

The large variations in particle type and concentration over small distances in convective clouds make interpretation of the data somewhat difficult. It would be useful to repeat these measurements under more uniform conditions such as in precipitating stratiform clouds.

Finally, no evidence was found for a correlation between lightning strikes on the aircraft and either the charge carried by the aircraft or the local electric field.

ACKNOWLEDGEMENTS

Work reported here was suported under grants #ATM 8020415 and 8209684, Meteorology Program National Science Foundation, Washington, D.C.

REFERENCES

[1] Reynolds, S.E., M. Brook and M.F. Gourley, 1957: Thunderstorm charge separation. J. Met., 14, 426-436.

[2] Takahashi, T., 1978: Riming electrification as a charge generation mechanism in thunderstorms. J. Atmos. Sci., 35, 1536-1548.

[3] Jayaratne, E.R., C.P.R. Saunders and J. Hallett, 1983: Laboratory studies of the charging of soft hail during ice crystal interactions. Q. J. R. Meteor. Soc., 109, 609-630.

[4] Gardiner, B., D. Lamb, R. Pitter, J. Hallett and C.P.R. Saunders 1985: Measurements of initial potential gradient in a Montana summer thunderstorm. J. Geophys. Res., in Press.

[5] Hallett, J., B. Gardiner, D. Lamb. R. Pitter and C.P.R. Saunders, 1984: Natural variability of particle charge in Montana summer cumuli. Transactions American Geophysical Union, 65, p. 849.

[6] Buser, O. and C. Jaccard, 1978: Charge separation by collision of ice particles on metals: electronic surface states. J. Glac., 21, 547-557.

[7] Knight, C.A., 1982: The Cooperative Convective Precipitation Experiment (CCOPE), 18 May - 7 August 1981. Bul. Amer. Met. Soc., 63, 386-398.

[8] Sommerfeld, A., 1952: Electrodynamics. Academic Press, New York, 371 pp.

[9] Hallett, J., 1976: Measurements of size, concentration and structure of atmospheric particulates, by the airborne continuous particle replicator. Air Force Geophys. Lab., Mass., U.S.A. Report No. AFGL-TR-76-0149.

[10] Knollenberg, R.G., 1981: Techniques for probing cloud microstructure. Clouds: their formation, optical properties and efects. P.V. Hobbs and A. Deepak, Eds., Academic Press, New York, 495 pp.

[11] Lawson, R.P., 1979; A system for airborne measurement of vertical air velocity. J. Appl. Met., 18, 1363-1368.

[12] Christian, H., L. Lillie, C.P.R. Saunders and J. Hallett, 1983: Laboratory and field observations related to ice particle and aircraft charging in convective storms. Intl. Conf. on Lightning and Static Electricity, Fort Worth, Texas.

TABLE 1

Date	Mission No.	Time (MDT)	Alt (m)	Temp (°C)	Average LWC (gm m^{-3})	Average Particle Charge (C km^{-3})	Maximum Particle Charge (C km^{-3})
11 July 81	10A	1823-1854	4700	-2	<0.05	-0.4	-1.9
11 July 81	10A	1900-1935	4800	-3	0.2	-3.3	-9.4
17 July 81	14A	1244-1254	5600	-14	0.07	+0.08	
21 July 81	17A	1439-1441	6800	-21	0.35	-2.6	-5.9
21 July 81	17A	1444-1446	6800	-21	0.1	-4.5	-8.1
6 August 81	29A	1615-1617	4800	-8	1.8	+0.04	

DUST ELECTRIFICATION DURING LARGE EXPLOSIONS

M.L. Price, R.A. Perala*, G. Edlin+ and C.B. Moore‡

Electro Magnetic Applications Inc., 8200 South Memorial Parkway, Suite D, Huntsville, AL 35802, U.S.A.
**Electro Magnetic Applications Inc., 1978 South Garrison, Denver, CO 80227, U.S.A.*
+Ballistic Missile Defense Systems Command, Advanced Technology Center, Huntsville, AL 35807, U.S.A.
‡New Mexico Institute of Mining & Technology, Socorro, NM 87801, U.S.A.

ABSTRACT - Six electric-field-measuring instruments were placed, flush with the earth's surface, in a line radially outward from Ground Zero during the DIRECT COURSE high explosive test on 26 October 1983. Large electric field excursions (in excess of +22 kV/m) were observed above each instrument after the passage of the explosion shock wave. The polarity of the excursions indicates that negative charges were elevated above the instruments. These negative charges came from the earth, apparently as a result of contact electrification during the turbulence following the explosion. The observed electrical excursions were short-lived; it appears that positive-ion point discharges from the earth, induced by the strong concentrations of negatively-charged dust, acted quickly to limit and then to reduce the electrical perturbations. No enhancement in the atmospheric electrification was observed as the dust particles fell back to earth but local effects were observed as dust particles struck the sensing electrodes. The local charge concentrations residing on the dust particles exceeded 200 nC/m^3 which is more than tenfold greater than that residing on cloud particles producing thunderstorm electrification. Despite these high local concentrations of charges, no significant, lightning-like, electrical discharges were observed except at the time of shock wave passage near one of our recorders. We infer that the observed high concentrations of charge were not accumulated sufficiently in organized volumes. If accumulations were to occur or if point discharge were suppressed, vigorous electrical discharges might be expected.

I - INTRODUCTION

Dust electrification can occur under many different sets of physical conditions. One well-known case due to volcanic eruptions produces large dust plumes in which spectacular displays of lightning have been reported.[1] Measurements made of the Mount St. Helens' plume show that large amounts of electrical charge were present for many hours after the initial large eruption of 18 May 1980 and numerous electrical discharges were observed over this period.[2] Another area in which dust electrification can be a serious, and in some cases catastrophic, concern occurs within storage silos such as grain elevators.[3]

In this report, we consider a different cause of dust electrification, viz., that produced behind the shock wave due to the detonation of a large amount (5.5×10^5 kgm) of high explosive. The resulting dust cloud extended over a relatively large area, i.e., $\sim$ 1 km in radius from Ground Zero, and persisted for several minutes before the larger particles fell to earth and the smaller particles were lofted high into the atmosphere. A series of measurements were made of the electric fields generated inside this dust layer.

The main purpose of our experiment was to measure in situ local electric fields and their changes on a time scale of $\sim$ micro-seconds. This required the design and construction of an electric field change meter capable of responding to such effects and also built to survive, operate and record during the event. Of particular interest to our group was the recording of the electric field strength and polarity with moderately high resolution before, during and after the explosion. Other undocumented reports have been made of electrification sufficiently vigorous as to cause major radio disturbances. We wished, therefore, to observe the onset of any electrical disturbances, to measure the peak strength and to determine whether or not the observed electrification intensified as any charged dust particles fall out, possibly leaving a residual charge of the opposite polarity in the atmosphere.

II - EXPERIMENTAL DESIGN

The high explosive test, code-named DIRECT COURSE, was conducted on the White Sands Missile Range near Socorro, New Mexico. It consisted of a fiberglass sphere 12.6 meters in diameter, filled with 5.45×10^5 kgm of Ammonium Nitrate mixed with Fuel Oil (ANFO) that was placed on top of a 45.9 meter steel tower. Upon detonation, a spherical shock wave was created and propagated through the atmosphere and over the desert-like terrain surrounding Ground Zero. This produced a highly turbulent region containing dust lofted behind the shock wave. At distances close to Ground Zero, the dust layer extended tens of meters in the air while, further out, the dust layer raised only a few meters before settling back onto the ground.

Five eletric-field change-measuring sensors and one electric-field meter of the rotating vane type (a field mill) were placed radially outward from Ground Zero. The locations of the instruments are shown in Figure 2-1. All of the instruments were placed so that absolute electric calibrations could be made without the need for application of a corrective "form factor."

For the four regions with expected large over-pressures after the explosion, electric-field-change instruments of the type shown in Figure 2-2 were prepared. Each of these consisted of a heavy walled, cubical steel box with an open top and a sensing electrode mounted inside the box on the wall closest to Ground Zero. The electrode was a rectangular aluminum plate, 6 mm thick, with a sensing area of 223 cm^2. An overhang and an inclined ramp deflector were arranged to protect each sensor from the direct impact of flying debris. The electrode was elevated about 14 cm above the bottom of the box so as to keep it above most of the fallout

material collected by the box. A battery-operated electronic circuit that measured any displacement currents flowing to the recessed, sensing electrode was located underground in a compartment adjacent to the sensor. A silicone-lacquer-treated, fiberglass insulator was chosen to support the sensing electrode because it was less microphonic than better insulators such as Teflon.

Four 6 volt alkaline lantern batteries provided the ±12 V supply needed to power the electronics. The current drain by the systems was about ±25 mA which allowed the batteries to provide useable power for a period in excess of 75 hours, much longer than the eight hours that elapsed between initial turn-on and the calibrations after the explosion.

The operational amplifier (National Semiconductor type LF356) used in the circuit was arranged to have a risetime of about 0.5 microseconds or a frequency response of about 300 kHz. An integrating time constant of 30 milliseconds (R_f = 3.0 x 10^8 ohms and C_f = 100 pF) was then used to obtain wide dynamic-range measurements of discrete changes in the electric field. Use of this feature convolves any incident electric field changes with the instrumental relaxation but it allows a measure of the fast changes in electric field normally associated with lightning, relatively unaffected by any earlier changes which will have relaxed. Data obtained in this manner must be "de-convoluted" to remove the instrumental relaxation effects. The technique for deconvolution was reported in Reference 4. If charge is transferred to or from the sensing electrode during the recording period, it too is detected and can be estimated by a variation of this technique. Instead of interpreting the deconvoluted response as a field change, it can be treated as a charge change.

The signals from the sensing amplifier were passed through a wideband, fast, single-ended, driver amplifier (National Semiconductor type LH0033) and then sent to South Instrumentation Park through RG-213 cables. At South Instrumentation Park the signal cables were terminated by 50 ohm GR resistors, isolated from the earth.

The signals appearing across the 50 ohm termination were sensed differentially with the use of LF356 operational amplifiers that drove a 14 channel, analog, magnetic-tape recorder having an FM recording response of 0.5 MHz.

In a clearing northeast of South Instrumentation Park, the electric field meter and another field change meter were buried so that their upper surfaces also were flush with the surrounding earth. The outputs from these instruments also went through the differential amplifier bank and were recorded on magnetic tape.

Each of the six instruments was calibrated, in place, by the use of a 1 meter, square metal plate supported on bakelite (i.e., charge-free) insulators at a height of 11.1 cm above the level of the box or instrument top. A ±68.0 volt potential was applied between the isolated plate and the earth through a double-pole, double throw, reversing switch. Use of the equipment applied a ±612.6 V/m electric field to each instrument and the resulting square-wave signal was transmitted to South Instrumentation Park where it was recorded as a calibration. The system response to magnitude and polarity was determined before and after the DIRECT COURSE explosion.

These calibrations indicate that the field change measuring instruments were quite sensitive to the direct input of charge to the sensing electrode with saturation responses on the order of ±6 V for input charges of as little as 0.6 nC or an equivalent charge density of 27 nC/m^2 on the sensing electrode. In the sensing of external electric fields, the recessed and shielded locations of the electrodes caused great attenuation so that very strong, external electric field changes were required to saturate each instrument. Accordingly the instruments were useful for sensing strong external electric fields, but they also were vulnerable and easily saturated by direct charge transfers to their sensing electrodes.

III - RESULTS

Recordings were obtained from all six instruments during the DIRECT COURSE explosion. Plots of the actual data are shown in Figures 3-1 and 3-2. Examination of the data indicates that strong, positive electric fields (indicating negative charge above) were developed over each instrument but only after the explosion shock wave passed by. The electric fields so produced were very strong, but transient, with rapid relaxations until new disturbances occurred.

An instrumental problem was found in the field change meter used at Station 3. A monopolar Tranzorb (instead of a bipolar one) was incorrectly used to protect the driver amplifier's output and this clipped the instrumental response to positive electric fields at the +0.3 volt level. Despite this limitation, the positive field contributions strongly outweighed the negative ones so that a lower bound for the negative charge transfers could still be determined after the deconvolution process. This problem developed only at positive field strengths in excess of 5 kV/m, which provides an explanation as to why the positive field limitation was not detected with the ±612.6 V/m calibration pulse.

After allowance for this limitation, the results for the outer five instruments are qualitatively similar but the field change indications at Station 1, the closest site, show an anomaly starting about three seconds after the explosion. During this period, there are indications of strong positive charges arriving at the sensor electronics. After the test, 4.85 kg of dirt were found deposited in the cubical box at Station 1. Both the sensor and its supporting insulator were found coated heavily with fine talcum-like powder. It was also found that this instrument was driven downward 5 cm in the well-tamped earth by the explosion pressure.

IV - DISCUSSION

The deconvoluted plot for the electric-field-change that was recorded at Station 5, 1,976 m from GZ, is shown in Figure 4-1 in a comparison with the actual electric field recording obtained with the field mill located about 1.5 m distant to the southwest. The reconstructed electric field data initially agree, at least qualitatively, with the actual recording, but there are some differences. The field change instrument had a much higher frequency response (~300 kHz) than did the field mill (~1 Hz) so that the indications of sudden field changes do not appear in the filtered output of the field mill. It appears that after passage of the shock wave at South Instrumentation Park, the local electric field strength became so great that local, positive, point discharge emissions occurred from the earth and these rapidly counteracted many of

the effects of the levitated, negatively-charged dust particles. While these emissions of point discharge were not measured directly, the initial strong fields relaxed far more rapidly than can be explained either by atmospheric conductivity or by fallout of the dust. It is interesting to note that a video recording of the shock wave passage shows an electrical transient similar to that produced by short lightning discharges within 60 ms of the shock wave passage.

The drift toward negative values in the reconstructed electric field plot at Station 5 after 1206:15 MDT suggests either the arrival of positive charges at the exposed field change sensor as a result of dust fallout or an accumulation of positive charge in the atmosphere over the instrument. Since the electric field meter shows a decrease in the field strength (toward zero) during this period, it appears that a charged dust fallout of about 0.7 nC/m^2 can account for the charging of the field change sensor.

In recognition of the differences in the instrumental response to external fields and to charge transfers at the sensing electrode, two different ordinate scales are plotted in Figures 4-1, 4-2 and 4-3. The other significant finding from the observations at Station 5 is that the initial portions of the reconstructed field change recording give a fairly useful indication of the actual electric field excursion and, therefore, some useful results may be extracted from the results obtained with the four battery-operated field change instruments located closer to Ground Zero where electric field mills could not be operated.

Deconvoluted records of the field changes from these four instruments are shown in Figures 4-2 and 4-3. All of these show the lower bounds for the strong concentrations of negative charges levitated after the passage of the shock wave and produced strong, positive (upwardly-directed) electric fields. The fields so produced were much stronger than can exist near the earth's surface. We infer, therefore, that strong emissions of positive point discharge ions must have occurred from the earth nearby, just as appeared to occur at South Instrumentation Park.

These deconvoluted field changes do not return to zero after the initial excursions. This suggests that transfers of negative charges to or positive charges from the sensing electrodes must have occurred during the sensing period. Emission of positive point discharges from the field sensing electrodes are unlikely because they are so well shielded in their recesses. It is also unlikely that neutral particles rebounding from the sensing electrode carried away positive charge, for dielectric materials usually acquire negative charges in contact with metals. Accordingly, we are inclined to the view that local turbulence caused the impacts of negatively charged dust particles and transferred net negative charges to each electrode.

Since the recordings at all four of the inner stations went off scale, only the lower bounds can be estimated for any charge transfers here also. At Station 3 (233 m distant from GZ), we estimate that negative charge transfers to the sensing electrode of more than 31 nC/m^2 took place while the figure for Station 4 (695 m distant from GZ) is 27 nC/m^2.

A somewhat different behavior was observed at Stations 1 and 2, the closer stations, Initially, at these stations the field indications were also of negative charge being levitated after the shock wave passage, followed by negative charge arrival at the sensing electrodes. After 1206:03 MDT, the output from Station 1 indicated that positive charges were arriving at the sensing electrode. Over the next minute about +270 nC/m^2 of positive charges were collected.

These indications may have been the result of the impact on the electrode of dust particles charged positively by collection of positive point discharge ions or they may be an effect of particles rebounding from the electrode, carrying more negative charge away. It is clear that a dust maelstrom occurred within the cubical box and that many charge transfers, unrelated to lightning production, did occur. At Station 2 (170 m distant from GZ) the dominant indications for the first thirty seconds were of negative charge aloft and then of negative charges arriving at the sensing electrode. Initially, about -5 nC/m^2 of negative charge was collected. After 1206:30, the reconstructed record indicates that positive charges began to arrive at the sensing electrode and about +2.2 nC/m^2 of positive charge were collected.

V - SUMMARY

The significant findings from the electric field measurements were:

1. Passage of the displacement disturbance and of the outgoing shock wave lifted large amounts of negative charge into the air from the earth. The elevated charge densities exceeded 200 nC/m^2 at all stations and 500 nC/m^2 at the close stations.

2. Strong, short-lived, positive electric fields were created locally: >56 kV/m at Station 1, 128 m, and 22 kV/m at Station 5, 1976 m distant from GZ.

3. There is little correlation between the electric field disturbances observed at adjacent sites (which indicates that the charges affecting each sensor were close to it). There are indications that negative charges impinged on the sensing electrodes of the field change meters.

4. Small dipole moments were generated (i.e., the charges were not separated by an appreciable height). The maximum field change of 1060 V/m observed before shock wave passage at Station 5 (1976 m from GZ) could have been produced by a dipole moment of less than 0.5 C-km over GZ.

5. There is one indication of a brief electrical discharge resembling lightning when the shock wave passed South Recording Park.

6. Three seconds after detonation, the indications at the closest site were of the arrival of positive charge amounting to more than 260 nC/m^2. This may be the result of the collisions of dust particles with the sensing electrode. The observed effects could have been caused either by the rebound of neutral particles from the electrode or by the arrival of dust, charged positively by collection of point discharge ions.

7. All of the electrical disturbances were short-lived, lasting less than 20 seconds. Large excursions in field strength were followed by rapid relaxations, presumably aided by strong point discharges from the local vegetation.

8. There were no indications of significant electric charges remaining aloft and there were no increases in the surface field strength as the dust particles fell

out. The relaxation time constant of the final electric field recovery at Station 5 was >6 seconds.

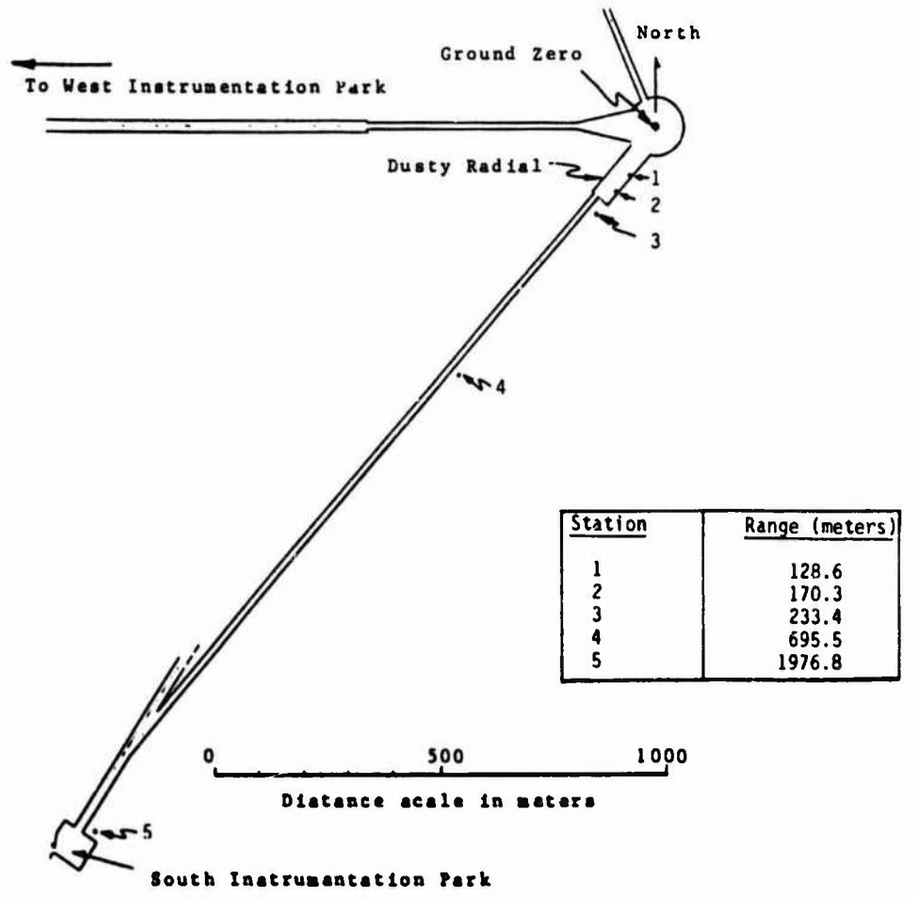
REFERENCES

1. Pounder, C., "Volcanic Lightning," Weather (GB), Vol. 35. No. 12, pp. 357-360, December 1980.

2. Hobbs, P.V., Radke, L.F., Eltgroth, M.W., and Hegg, D.A., "Airborne Studies of the Emissions from the Volcanic Eruptions of Mount St. Helens," Science, Vol. 211, No. 4484, pp. 816-818, February 20, 1981.

3. Maurer, B., "Discharges Following Electrostatic Charging in Large Storage Silos," Report No. Conf-7809151-2, BASF A.G., Ludwigshafen am Rhein Corp., 1978.

4. Price, M.L., Moore, C.B., Hayenga, C.O., Hall, D.L., and Caylor, I.J., "Dust Cloud Electrification Measurements," EMA-84-R-18, Electro Magnetic Applications, Inc., Huntsville, AL, January 1984.



Station	Range (meters)
1	128.6
2	170.3
3	233.4
4	695.5
5	1976.8

Figure 2-1. A map showing the locations of the electric-field change-measuring instruments used during the DIRECT COURSE explosion on 26 October 1983.

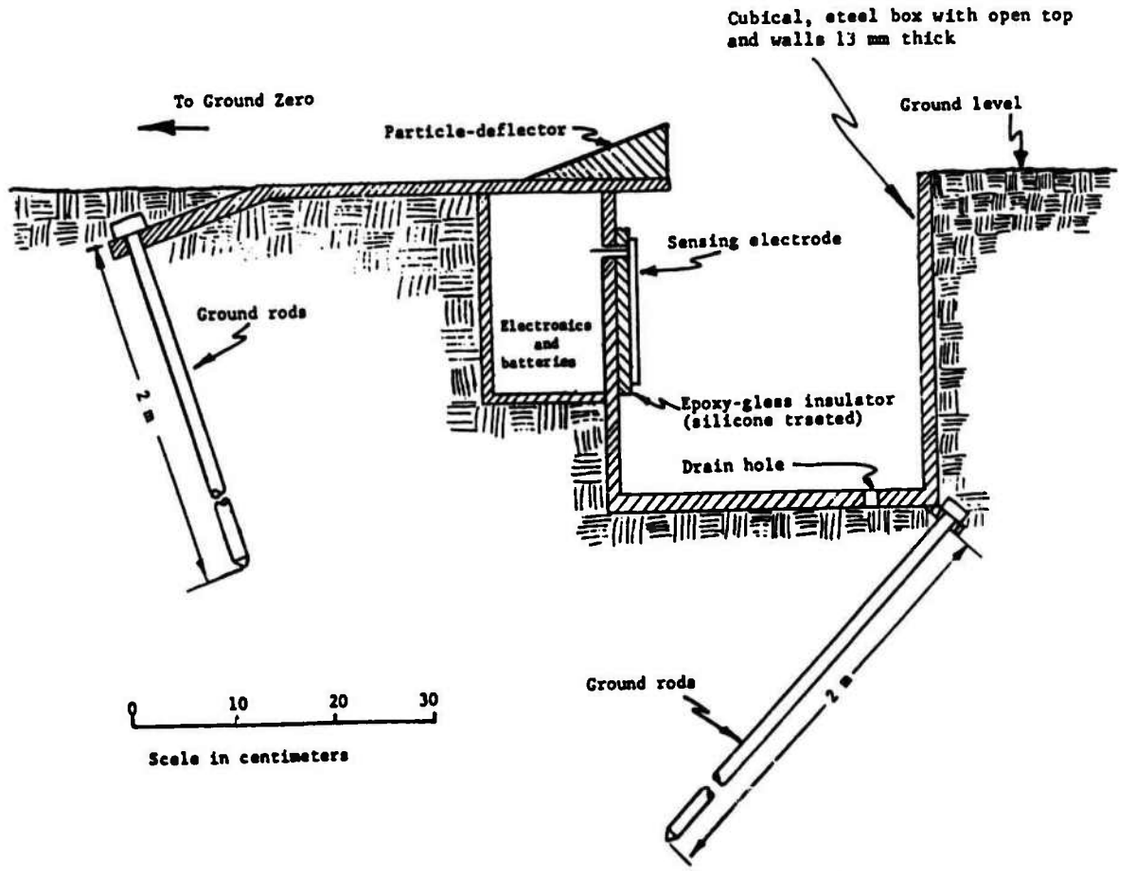


Figure 2-2. Electric field-change measuring sensor used in the DIRECT COURSE experiment

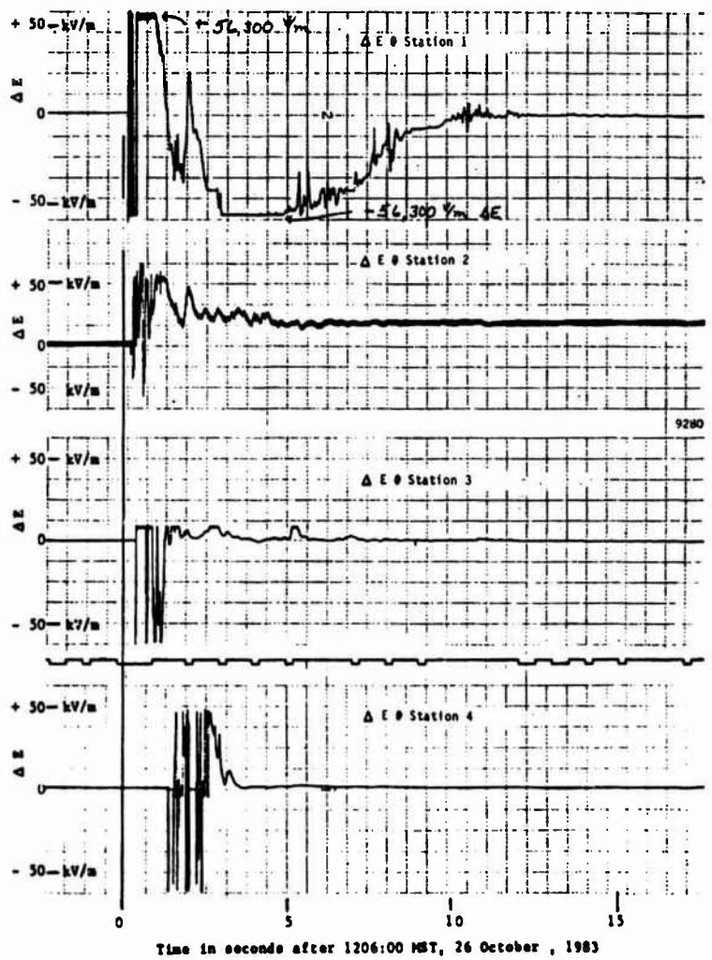


Figure 3-1. Changes in the electric field at various distances from Ground Zero during DIRECT COURSE at White Sands Missile Range

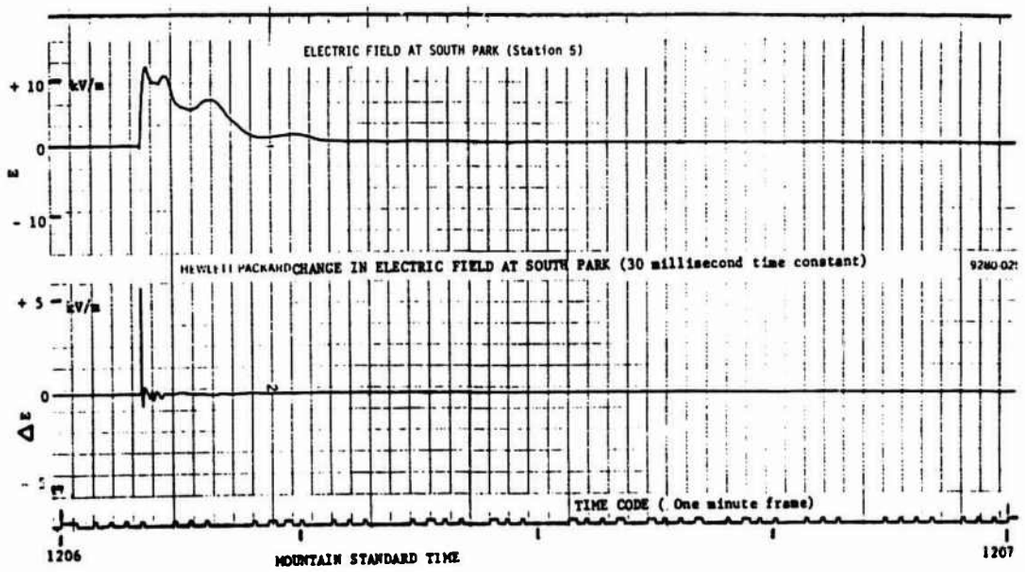


Figure 3-2. Electric field and its change at South Instrumentation Park, White Sands Missile Range on 26 October, 1983 during the DIRECT COURSE test.

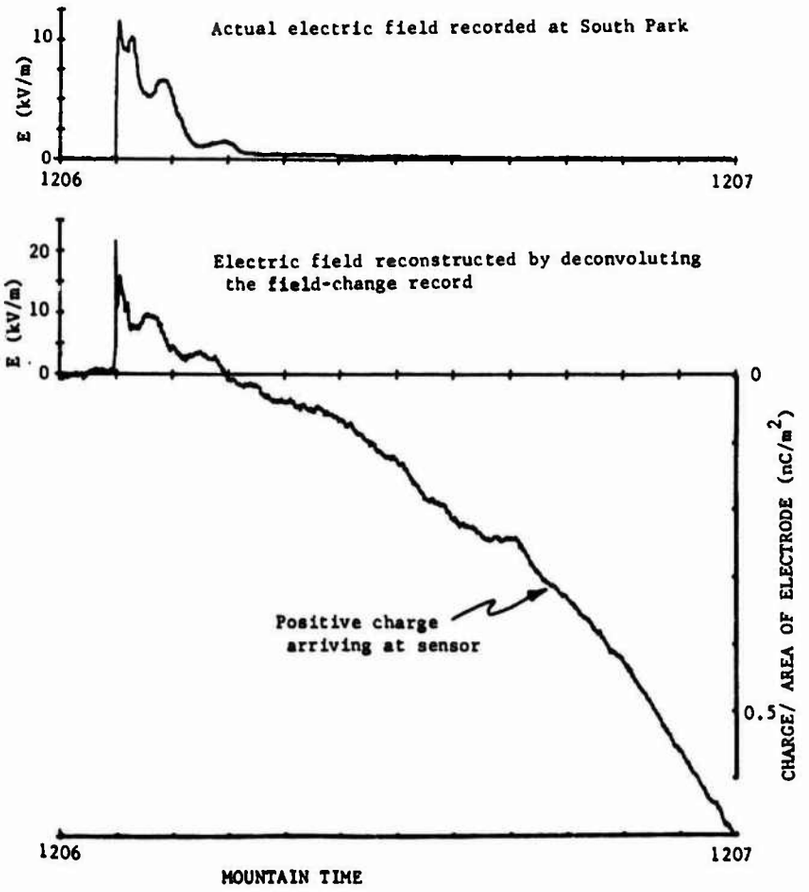


Figure 4-1. Comparison of the deconvoluted electric-field-change recording with the actual field recorded at South Instrumentation Park

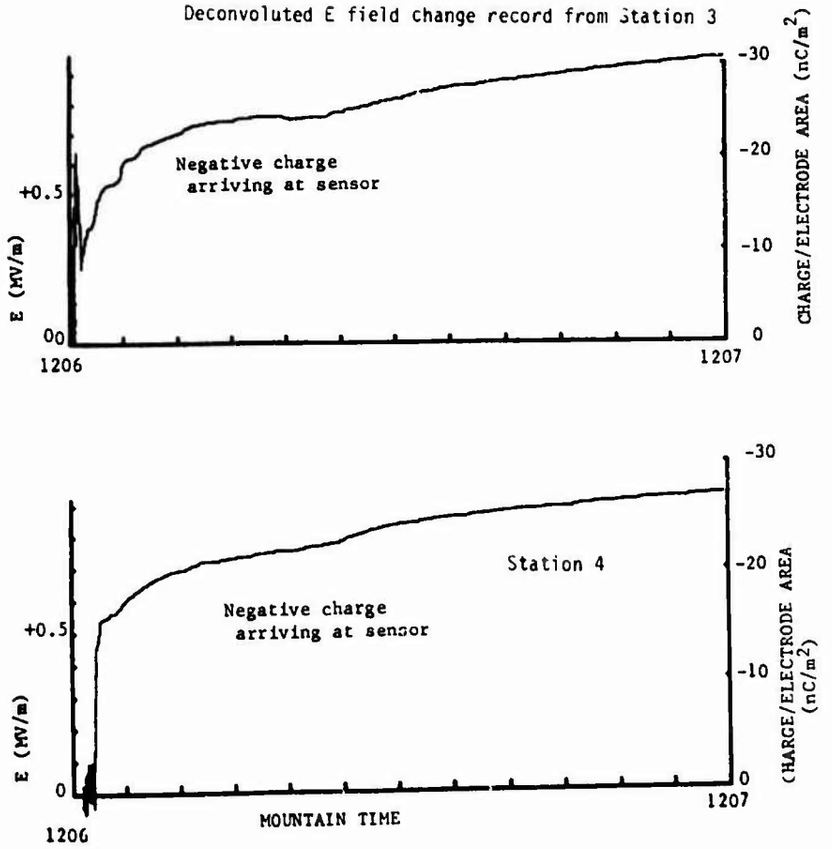


Figure 4-2. A comparison of the reconstructed electric-field-change records at stations 3 and 4. The magnitudes of the reconstructed fields are far greater than the atmosphere will allow and therefore the indications must be interpreted as charge transfers to the sensors.

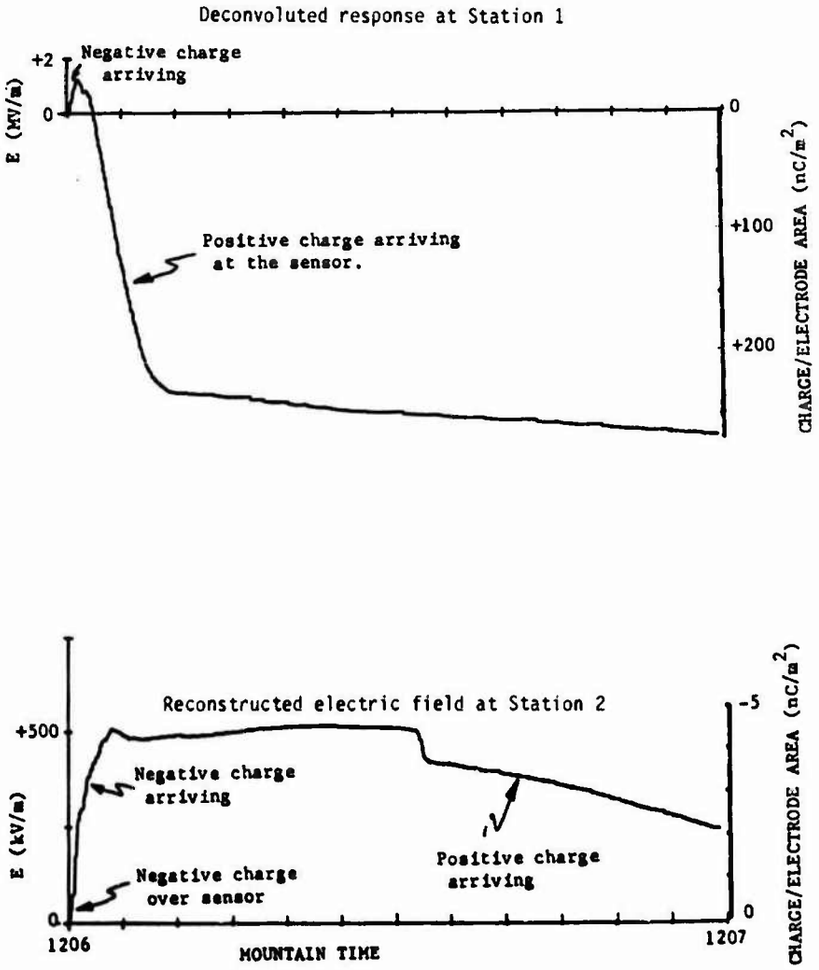


Figure 4-3. Deconvoluted responses of the field-change measuring instruments at Stations 1 and 2.

CORONA THRESHOLD DETERMINATION BY THREE-STAGE PHYSICAL MODELLING OF AIRCRAFT

J.E. Nanevicz and E.F. Vance

SRI International, Menlo Park, California 94025, U.S.A.

ABSTRACT

The Problem - At what aircraft potential will the VHF blade antenna protruding from the belly of an aircraft reach corona threshold? Problems of this type frequently arise in connection with the design of passive discharger installations for new aircraft. Similar questions also come up when an engineer is faced with the need to track down an elusive noise source on an existing aircraft. Ground tests or flight tests on an actual aircraft to obtain the answer can be very time-consuming and expensive.

The Solution - An accurate determination of the corona threshold of a protuberance can be made in the laboratory at very low cost. The measurement techniques described in the paper use a scale model of the aircraft (1/25 to 1/100 scale is satisfactory) together with a sample of the protuberance in question (often a blade antenna). Through a succession of at most 3 measurements — one on the aircraft model, and two on the sample -- it is possible to determine the corona threshold of the protuberance as installed on the aircraft.

By expanding the aircraft model measurements, it is possible to explore alternate sites on the aircraft to minimize the likelihood of corona discharge. Also, investigation can be made of possible modifications to the protuberance (such as rounding of edges) to increase corona threshold potential.

The appropriate laboratory techniques are described and examples of results are presented.

I - BACKGROUND

Frequently, engineers involved with the development and troubleshooting of communication systems on aircraft are faced with the need for determining the corona threshold potential of a protuberance from the mold lines of an aircraft. (For example, a blade antenna, a vent, a pitot tube etc.). The need for this information follows from the fact that noise-free reception of radio signals on the aircraft is dependent upon the proper functioning of the passive discharger system installed on the aircraft, and the avoidance of corona discharges from any element of the airframe itself. [1,2] Thus the engineer must contrive to ensure that, at the highest expected charging rates of the aircraft (as the result of flight through precipitation containing ice crystals), the aircraft potential does not exceed the value at which some protuberance might experience air breakdown.

In general, the engineer must be able to determine the potential at which breakdown of a proposed design will occur. If this is unacceptably low, he must devise ways to increase the threshold potential (by rounding edges or by relocating the protuberance to a less prominant position on the aircraft). He must also be able to test the effectiveness of any fixes he devises.

II - STRAIGHTFORWARD APPROACHES USING FULL-SCALE AIRCRAFT

The problem of threshold determination can be approached head on using several techniques as shown in Figure 1. In (a) the aircraft is instrumented to permit detection of corona discharge from the protuberance and to define aircraft potential. The aircraft is operated in precipitation conditions leading to static charging of the aircraft. If the charging encountered in flight is sufficiently severe to induce corona from the protuberance, the determination of its threshold is made. If not, all that can be established is that the threshold exeeds the maximum potential attained during the flight tests.

Experienced engineers recognize immediately that flight test programs in general tend to be

expensive and unwieldy. For example, investigating the effect of modifying the protuberance, or relocating it, requires additional flying. In general, flight testing is best confined to either proof testing or to the gathering of information regarding the basic properties of the charging environment. The use of flight tests, of course, does have the virtue of duplicating all facets of the problem.

An alternate approach that might be considered is illustrated in Figure 1 (b). Here the full-scale aircraft (including protuberance) is mounted on insulating blocks and charged to a high dc potential (100's of kilovolts) using a high-voltage power supply. Measurements of discharge current from the protuberance of interest are used to determine the aircraft potential at which discharge onset occurs.

Although the method of Figure 1(b) appears at first glance to duplicate the important features of an aircraft in flight, it, in fact, suffers from serious drawbacks. The proximity of the ground tends to distort the field structure about the aircraft, and the effects of wind flow on corona threshold are not duplicated. In addition, implementing the tests is expensive because insulating structures capable of supporting the aircraft must be built, and the fuel system must be specially treated ("pickled") to avoid the possibility of vapor ignition by electrical discharges from the aircraft. Although exploring design changes is easier than in an actual flight test it is still quite ponderous and time consuming.

III - LABORATORY MODELLING APPROACH

The problem of corona threshold determination can be attacked in the laboratory by recognizing at the outset that a one-step laboratory modelling program cannot be made to succeed, and that attention must be focussed on the facets of the overall problem that the various possible modelling schemes can accurately duplicate.

The general concepts of procedures for threshold determination are shown in Figure 2. The concept of measurements employing a full-scale aircraft (discussed in connection with Figure 1) is shown in (a). Here we note that, whether the aircraft is in flight or mounted on insulating blocks, the aircraft potential is measured together with the discharge current from the protuberance to determine, in a single step, the potential at which discharge is initiated. The laboratory modelling concept of Figure 2 (b), on the other hand, involves a series of measurements each of which provides insight into a specific facet of the problem. By combining the results of the measurements of (b) it is possible to relate airplane potential to the occurrence of corona discharge. The measurement techniques involved in carrying out the individual steps of Figure 2(b) will be discussed together with an indication of the way in which the diverse measurements are combined to yield the desired relationship between aircraft potential and corona discharge onset. Consideration will also be given to ways in which the measurements can be expanded to permit the investigation of the effects of location on the aircraft and design details of the protuberance.

In general, the laboratory-measurement approach involves breaking down the problem of threshold determination into several steps. In considering step (1) we note that the relationship between aircraft potential and the ambient electric field in the general vicinity of the protuberance is determined entirely by the geometry of the aircraft involved. Further, it is true that this same relationship exists on a scale model of the aircraft in question. Thus, if we contrive to measure the relationship between ambient field and aircraft potential on a scale model of the aircraft, we have also determined this relationship for the full-scale aircraft.

The technique for carrying out the determination of step (1) is shown schematically in Figure 3. A scale model of the aircraft of interest is suspended in the laboratory as shown in the photograph of Figure 4 -- well away from any structures, to simulate an aircraft in flight. A high-voltage power supply of voltage V is connected to the model via a wire to a remote element (such as a wing tip). Thus the model is electrically charged and an electric field structure is established on its surface and in its general vicinity. The magnitude of the electric field, E_m, at points of interest on the skin of the aircraft model can be determined by means of charge

transfer measurements described by Maxwell.[3] With this technique, a small conductive probe (located at the end of a thin insulating rod) is touched to the model, and acquires a charge q proportional to the magnitude of the electric field, E_m, at the point of contact and to the induction area A_p of the probe.

$$q = E_m A_p \quad (1) \ .$$

The magnitude of the charge is measured by means of an electrometer equipped with a Faraday "ice pail" to receive the charge. The relationship between ambient field and transferred charge (the probe induction area, A_p,) can be determined by repeating the measurement in a known field (i.e. the field between the pair of parallel plates shown in Figure 3). Details of the charge-transfer measurements and certain critical considerations are discussed in Appendix A.

From geometric scaling arguments, the fields on the full-scale aircraft are smaller than they are at corresponding points on the model by a factor equal to the model scale n. Thus the aircraft field E_a is related to the model field E_m at the corresponding point by the relationship

$$E_a = E_m/n \quad (2)$$

where n is the scale factor of the model.

Thus, at the end of the model measurements of atep (1), we have determined the coupling parameter k_1, relating the ambient field E_a, where the protuberance will be located, and aircraft potential V:

$$V = k_1 E_a \quad (3) \ .$$

It ahould be noted that while the aircraft model is suapended in the laboratory, it is possible to explore alternate possible locations on the aircraft surface to determine if there are alternative locations for the protuberance where ambient field E_a is significantly lower.

A schematic of the setup for carrying out the determinstion of step (2) is shown in Figure 5. A full-scale sample of the protuberance (antenna) under investigation is mounted on a large metal plate simulating the aircraft skin. A second metal plate is placed parallel to the first at a spacing d (several antenna heights away), and a high voltage is applied between the two plates. This establishes a uniform field E_o between the two plates, except in the vicinity of the antenna where the field is distorted and concentrated by the presence of the antenna as suggested in the figure. A photograph of the "electrostatic cage" used for this purpose is shown in the background of Figure 4. The cage shown has guard rings installed between the metal plates to assure a uniform electrostatic field inside the "cage".

Essentially, the argument for the measurement illustrated in Figure 5 is that it duplicates very closely the electrostatic situation on the belly of a charged aircraft. The radius of curvature is large compared to the dimension of the antenna blade so that the field structure over the volume of interest in the vicinity of the aircraft skin is closely approximated by the uniform field between a pair of parallel conducting sheets. Thus, the field distortions produced by the antenna in the test setup in the laboratory are virtually identical to those produced when the antenna is immersed in the ambient field of the charged aircraft.

In principle, one could increase the voltage of the power supply in Figure 5 until corona discharge occurred from the antenna. Unfortunately, in practice, it is usually found that unacceptably high voltages are required to produce corona and that the requirements for insulation and rounding of the edgea of the platea to avoid electrical breakdown from them are extremely difficult to achieve. Thus, it ia usually best, inatead, to use the set up of Figure 5 simply to determine the field enhancement produced by the antenna blade. Thia can be done by choosing a reference point on a flat region of the antenna blade near the sharpest metal corner from which corona will first occur (a point roughly 3-cm in and 3-cm down from the corner is appropriate and convenient), and determining the relationship between the ambient field E_a and the reference point field E_r

$$E_a = k_2 E_r \quad (4) \ .$$

The determination is made simply by energizing the system of Figure 5 and making charge transfer

measurements touching the probe to the left plate to determine E_a and to the reference point to determine E_r.

Finally, the determination of step (3) can be made using the set up of Figure 6. Here a full-scale operational sample of the antenna blade under consideration is placed within an electrode structure which is sufficiently compact that corona discharge can be induced from the antenna with reasonable values of applied voltage. The test begins with some modest level of voltage applied. A charge-transfer measurement is made to determine the relationship between the voltage applied to the "bathtub" geometry and the reference point field E_r on the antenna. Since the system is linear, the same relationship between field and voltage will exist independent of applied voltage. Once this relationship has been determined, the voltage applied to the antenna blade is increased until corona discharge onset is detected on the power supply current meter. The value of voltage is noted and used to calculate E_{rt}, the reference point field at corona threshold. This value of field can be substituted into equation (4) to determine the value of ambient field

$$E_{at} = k_2 E_{rt} \qquad (5)$$

required for corona threshold of the antenna under investigation.

It should be noted that E_{at} is characteristic of the antenna, and can be measured and tabulated independently of the aircraft on which the antenna is to be used. For example, two antennas — one a 9-inch stub typical of UHF antennas, and the second a 17-inch blade typical of VHF antennas -- were studied in the laboratory, and had corona thresholds as shown in Table I.

Table I
Ambient Fields For Antenna Corona Threshold

Antenna	E_{at}--Ambient Field For Threshold kV/M
9-inch stub	181
12-inch blade	112

It should also be noted that, once the set up of Figure 6 is in place in the laboratory, it is possible to experiment with ways in which the antenna corona threshold E_{at} can be raised -- e.g., by rounding edges. Such experiments can be completed quickly and at relatively little cost.

Once the ambient threshold field E_{at} for an antenna has been determined, this result can be substituted into E_q (3) to determine the threshold potential

$$V_t = k_1 E_{at} \qquad (6)$$

for the antenna under consideration installed at the location in question. The results of a set of such determinations for various stations on the fuselage center line on wide-body aircraft are shown in Figure 7. From charge transfer measurements (of the sort illustrated in Figure 3) the value of the parameter k_1 was determined, and is plotted at the lower curve in Figure 7. Next, using the values of E_{at} for the two antennas in Table I, the corona threshold potentials for these antennas installed at the various fuselage stations was determined using E_q. (6). The resulting thresholds are plotted as the upper two curves in Figure 7.

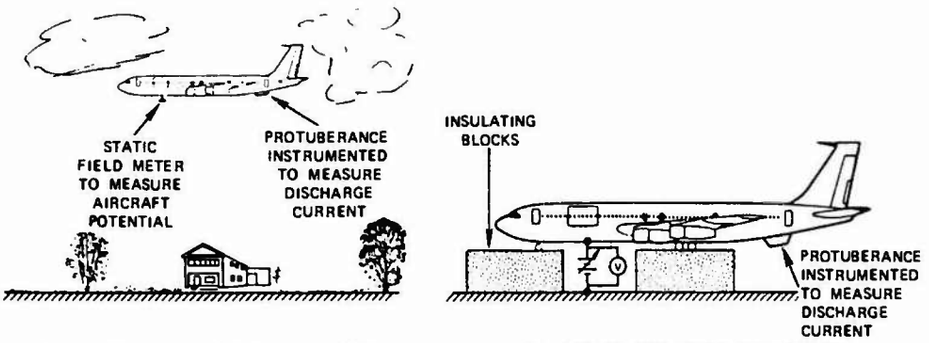
It should be noted that the value of the parameter k_1 is a function of aircraft geometry alone. It can be determined using model measurements without regard for the threshold properties of the antennas being considered for installation. Thus, once the setup of Figure 3 has been assembled, it is prudent to explore the aircraft surface and determine k_1 at all locations where protuberances, such as antennas, might ultimately be located.

VI - SUMMARY

Laboratory techniques can be applied to the determination of corona thresholds of odd protuberances from the body of an aircraft. These measurements require only a full-scale sample of the protuberance and a scale model of the aircraft (often a plastic toy model coated with electrically-conducting paint will do). The laboratory technique does not incur the costs of a flight test program, and does not suffer from the inaccuracies normally introduced in test-stand measurements on a full-scale aircraft. The effects of air flow in modifying threshold are not

simulated using the laboratory techniques (they are not simulated in the test stand measurements either).

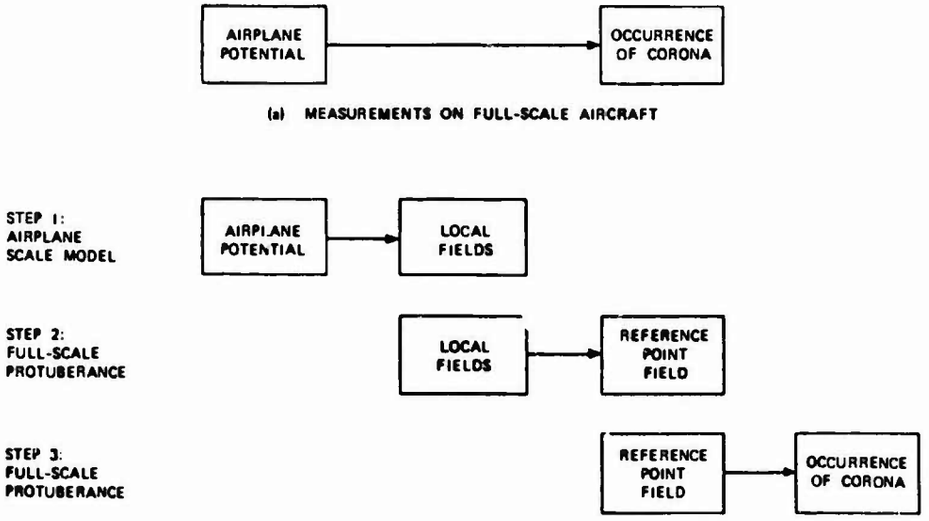
In general, the laboratory techniques discussed here are remarkably flexible and powerful. They permit the exploration of virtually all of the issues important in the siting of antennas and other protuberances on an aircraft. They permit the engineer to explore the effects of modifications in antenna design and placement at very little cost. Furthermore, the form of the measurements is such that the question of antenna design can be investigated independently of the issue of placement (the converse is also true). Thus, using very inexpensive instrumentation, the engineer is able to resolve a number of difficult questions arising in aircraft design and troubleshooting.



(a) USE OF INSTRUMENTED FLIGHT TEST AIRCRAFT

(b) USE OF FULL-SCALE AIRCRAFT ON INSULATING STRUCTURE

FIGURE 1 DIRECT METHODS FOR CORONA THRESHOLD ESTIMATION



(a) MEASUREMENTS ON FULL-SCALE AIRCRAFT

(b) MEASUREMENTS USING REDUCED-SCALE MODEL OF AIRCRAFT

FIGURE 2 CONCEPTUAL COMPARISON OF TECHNIQUES FOR THRESHOLD DETERMINATION

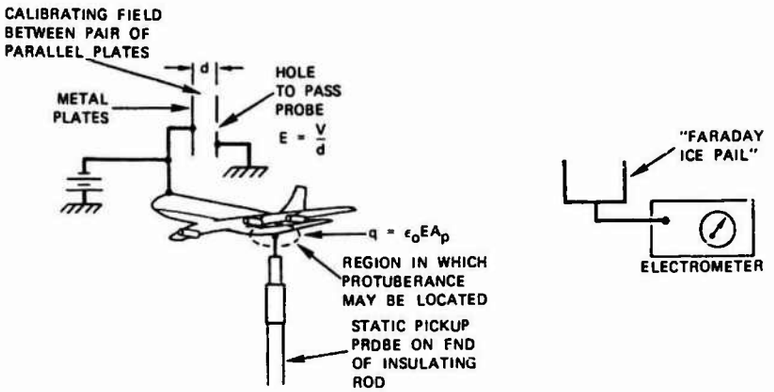


FIGURE 3 LABORATORY DETERMINATION OF RELATIONSHIP BETWEEN AIRCRAFT POTENTIAL AND AMBIENT ELECTRIC FIELD (step 1)

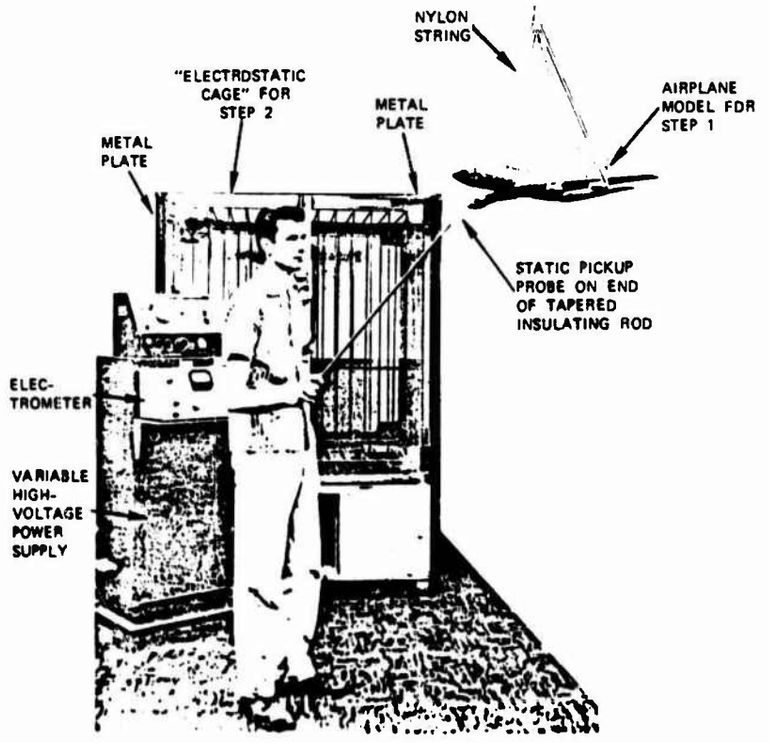


FIGURE 4 LABORATORY SETUP USED FOR CORONA THRESHOLD DETERMINATION (steps 1 and 2)

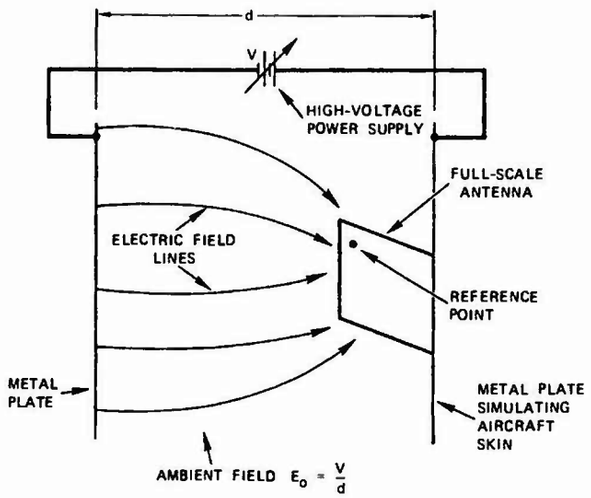
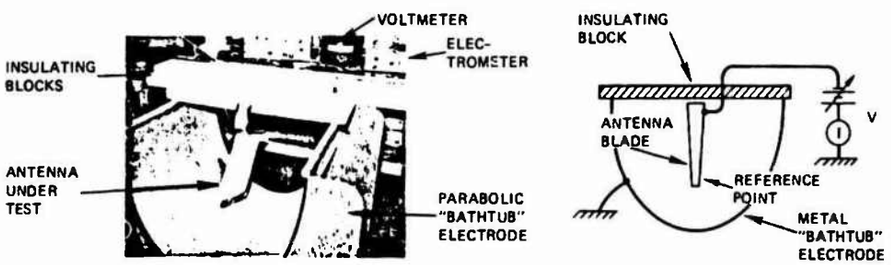


FIGURE 5 SETUP TO DUPLICATE FIELD ENHANCEMENT CAUSED BY ANTENNA (step 2)



(a) PHOTOGRAPH OF SETUP (b) SCHEMATIC DIAGRAM OF SETUP

FIGURE 6 SETUP TO INDUCE CORONA FROM ANTENNA (step 3)

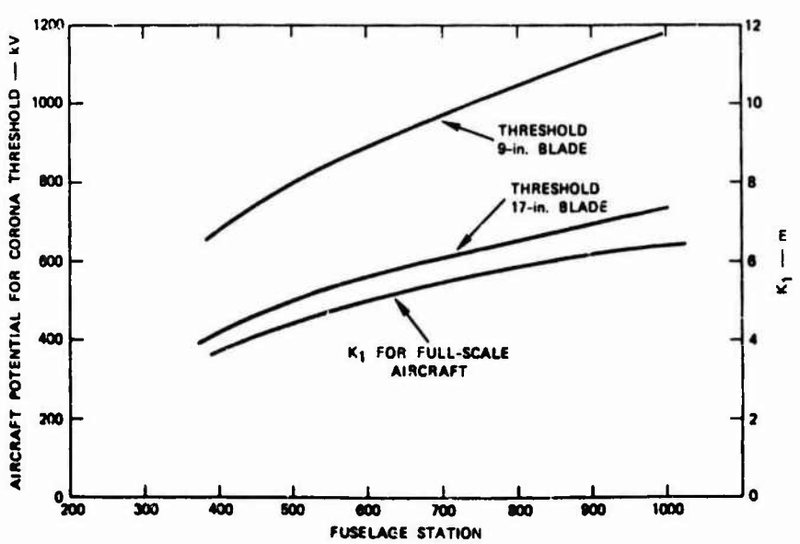


FIGURE 7 THRESHOLD POTENTIALS OF BLADE ANTENNAS ON AIRCRAFT FUSELAGE

APPENDIX A

STATIC ELECTRIC FIELD DETERMINATION USING CHARGE TRANSFER MEASUREMENTS

If a small, uncharged metal probe is placed in the field E_o near the surface of a conducting sheet the field will assume the form shown in Figure A-1(a) where it is evident that a potential difference exists between the probe and the conductor. When the probe is placed in contact with the conductor as in Figure A-1(b), therefore, charge will flow onto the probe. If the probe is now removed from the conductor as in Figure A-1(c), the probe is left with an excess of charge, q. The magnitude of this charge is determined by the geometry of the probe and the field intensity in the region. By measuring the charge q_o acquired by the same probe in a region of known field intensity E_o, one can determine the ratio of the charge to the field intensity at the plane surface. The probe can then be used to measure the magnitude of an unknown field E at other plane conducting surfaces, since

$$E = \frac{E_o}{q_o} q ,$$

where q is the charge acquired by the probe when placed in contact with the plane surface where the field E is to be determined.

The charge acquired by the probe is measured with an electrometer such as that illustrated in Figure A-2. The charged probe is brought in contact with the bottom of the Faraday "ice pail" charge receptacle, whereupon the charge leaves the probe and flows to the outside surface of the receptacle. Part of the charge flows through the resistor and onto the motor-driven variable capacitor, which develops an alternating voltage proportional to the charge deposited on it. This alternating voltage is amplified and measured with a high-impedance voltmeter. The voltage developed across the capacitor is proportional to the charge deposited on it, which is proportional to the potential of the charge receptacle, which in turn is proportional to the charge deposited on it by the probe; thus the deflection of the voltmeter indicates the amount of charge placed in the receptacle.

The charge-pick-up probe used for these measurements consists of a 1.6-mm long piece of 20 gauge wire forced into the end of a 1.6-mm diameter Teflon rod. A small diameter rod is necessary near the model to minimize the field distortion caused by the presence of the dielectric. To obtain mechanical strength and rigidity, the diameter of the Teflon rod used to hold the conducting probe tip was increased with increasing distance from the model.

The dimensions of the conducting probe tip are dictated by the dimensions of the object on which field measurements are being made. In order that the probe calibration made in a plane geometry be valid, field measurements should be made only on surfaces such that the radius of curvature is substantially larger than the greatest dimension of the probe. If, for example, as in Figure A-3 the field at the surface of a cylinder were to be measured using two probes calibrated in a uniform field, the value obtained using the small probe would be very nearly correct, but the value obtained using the large probe would be low.

Shown in Figure A-4 are the electrometer used for charge measurements, and the field free ionized region used to discharge the probe before taking a reading on the model. Several 500 microcurie polonium sources (of the type commonly sold with phonograph record dusting brushes), were placed on the inside of a 15-cm diameter metal tube which was connected to ground. Thus a field-free ionized region existed inside the tube. When the probe is placed inside the tube, the fields produced by charges residing on the probe will extract ions of the appropriate sign from the ionized region, thereby neutralizing the charge on the probe.

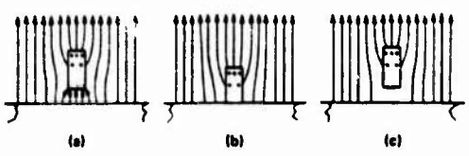


FIGURE A-1 ILLUSTRATION OF CHARGE SEPARATION

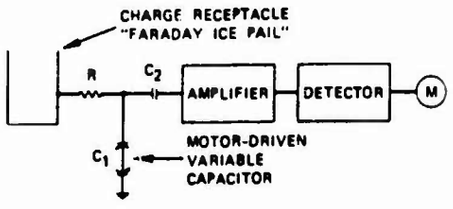


FIGURE A-2 BLOCK DIAGRAM OF ELECTROMETER

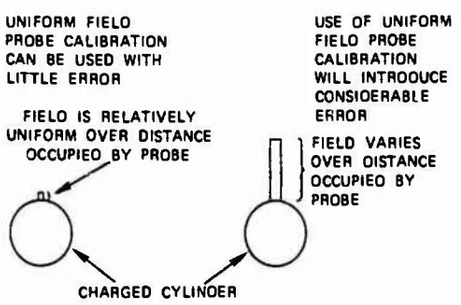


FIGURE A-3 PROBE IN A NON-UNIFORM FIELD

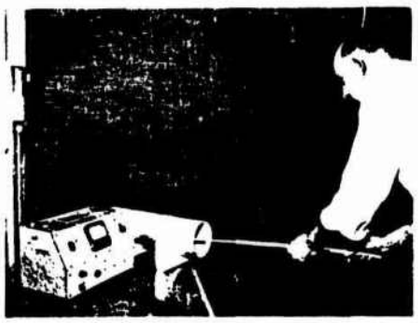


FIGURE A-4 PROBE BEING DISCHARGED OVER RADIOACTIVE POLONIUM

REFERENCES

1. R. L. Tanner and J. E. Nanevicz, "An Analysis of Corona-Generated Interference in Aircraft", Proceedings of the IEEE, Vol. 52, No. 1, pp. 44-52, (January 1964).

2. J. E. Nanevicz and R. L. Tanner, "Some Techniques for the Elimination of corona Discharge Noise in Aircraft Antennas", Proceedings of the IEEE, Vol. 52 No. 1, pp. 53-64, (January 1964).

3. J. C. Maxwell, "A Treatise on Electricity and Magnetism", Third Edition, Carendon Press, Oxford, (1892).

LIVE TESTS ON STATIC ELECTRICITY IN FUELLING OF AIRCRAFT

H Schneider

Flight Test Center of the German Armed Forces, 8072 Manching, F.R.G.

Abstract - A test program on the build-up of static charges on jets being fuelled was carried out in 1984 at German Flight Test Center.
During handling operations refined distilled fuels can become electrostatically charged due to the dissociation of ionizable materials.
These charges will enter the aircraft being fuelled and generate an electrostatical voltage between a/c and refueller and ground, respectively.
Resulting discharges could trigger an explosion of fuel vapor.
To prevent such discharge hazards bonding and grounding procedures have been established.
Because of the complexity of servicing operations and due to different national grounding and bonding regulations there is considerable confusion.
Main purpose of this program was to solve questions arising from the required Electrical Safety Connections commonly used to prevent static hazards.

INTRODUCTION

During fuel transfer, mixing or filtering operations charges are generated within the fuel by ionization that can cause a high strength electric field between fuel-surface and its environment inside the tank. When exceeding a particular threshold sparks will occur that can trigger explosions in the vapor space. These processes have been investigated by Oil Companies and other institutions (Ref. 1, 2, 3 et alt).

In order to increase the conductivity of distilled fuels additives are used resulting in a faster dissipation of electrostatic charge, and consequently the risk of electrostatical ignition has been decisively reduced.

Another correlated problem is the charging of airframes during fueiling due to the ionized fuel.
Fatal explosions can be triggered by sparks when coupling or removing fuel hoses.
To prevent these hazards bonding and grounding procedures have been established.

This report exclusively covers our tests that were aimed to obtain information on the degree of charging during actual fuelling of a/c.

It is not intended to discuss items such as ignition energies, flammability, influences of temperature, accident statistics and other problems that relate to the process of aircraft fueiling.

CHARGE GENERATION during Aircraft Fuelling

Refined distilled fuels are excellent insulators. At the interface between fuel and its environment (e.g. lines, filters, hoses) charges are generated within the fuel that are due to ionic trace contaminants.

The fuel flow collects the ions of one polarity while the ions having the opposite polarity are fed to the chassis.

The mechanism of charge generation is not yet completely investigated.
The ions in the fuel flow represent a current which is characterized by the charge density of the fuel and the volumetric flow rate:

$$I = Q \times V$$

- I Current Flow
- Q Charge Density
- V Flow Rate

The charge density Q is a function of the flow rate V, the area A and the particular charging conditions of the fuel/surface interface X

$$Q = f(V, A, X)$$

RELAXATION

Because of its conductivity fuel will simultaneously be discharged by relaxation.

The rate of charge drop is defined by an exponential function

$$Q(t) = Q_0 e^{-t/\tau}$$

- $Q(t)$ Charge after time t ($\mu C/m^3$)
- Q_0 Initial Charge ($\mu C/m^3$)

$$\tau = \frac{\varepsilon}{\varkappa}$$

- τ Relaxation Time Constant (sec)

$$\varepsilon = \varepsilon_0 \times \varepsilon_r$$

$\varepsilon_o = 8{,}85 \times 10^{-12} \frac{As}{Vm}$

Absolute Dielectric Constant

ε_r Relative Dielectric Constant (for Hydro-carbons about 2)

$\varkappa$ Fuel Conductivity ($\frac{pS}{m}$)

The relaxation time for undoped fuels ranges from approx. 1 to 10 seconds.
After this time the charge within the fuel itself has been reduced by 63 % and after 3τ it will be reduced by 95 %.

A balanced condition is established within the hose after some meters that results from the initial charge and the typical charging of the hose on the one side and from the relaxation on the other side.

The corresponding current is approximately given by

$i_\infty = \beta \times (\bar{V} \times R)^2$

I_∞ current for a long pipe
$\bar{V}$ average flow velocity
R inner radius of pipe
$\beta = 1.5 \times 10^{-13} \frac{As}{cm^4}$

This equation has been empirically found, and it applies to undoped fuel (Ref. 3).

For doped fuels a rough estimation can be made, only.
This balanced current i_∞ characteristic for a certain type of hose finally will reach the aircraft being fuelled.

It will return to the refueller chassis through the conductive hose and in parallel through the grounding and bonding cables.

DOPING

To obtain a faster dissipation of electrostatic charges Oil Companies dope the aviation fuels with conductivity improvers (e.g. Shell ASA lii, Du Pont Stadis 450).

We know from experience that levels of 100pS/m are sufficient to achieve satisfactory discharging. In this case the relaxation time is approx. 0.2 secs. The conductivity of doped fuel depends on the temperature and will decrease as the fuel temperature drops. Long storage times will also reduce the conductivity.

To allow a safety margin Shell therefore recommends to provide flammable products with conductivities in the order of 200-360 pS/m.

Standardized doping rates for German Air Force are 150 - 700 pS/m.
For practical measurements see Fig. 1

An ambivalent result of doping should be pointed out:
Doping chemicals are contaminants and they intensify the charge build-up within the fuel.

On the other hand these chemicals increase the conductivity of the fuel and cause a considerably faster dissipation of the charge.

TEST PROGRAM

In former tests (Ref. 3) the charge build-up in aircraft tanks has been investigated to obtain data on the risk of discharges inside the tanks. These tests have led to the recommendation that fuels be doped.

Our objective was to examine the charge build-up on the frames of aircraft being fuelled with doped JP 4 under live conditions.

Main purpose was to gather information on bonding and earthing philosophy and whether bonding between refueller and aircraft is sufficient to prevent a static discharge during fueiling with doped JP 4.

Mock-up Tests

In a first step mock-up tests were performed in cooperation with TÜV Rheinland (Industrial Supervisory Board, Cologne, W-Germany).

A 6000 ltrs tank truck was installed on 10mm Teflon insulation plates and then refuelled from another 24000 ltrs tank truck (Fig. 2 and 3).

Fuel was flowing from the refueller through a 20 m hose (Table 1, hose 8) to the Charge Density Measuring Unit (CDMU) and from here through a 3 m hose (Table 1, hose 9) into the insulated tank. The 3 m hose was insulated at both ends with an insulation coupling (iso 1 resp. iso 2, 10 mm Teflon each).
The conductivity of the two hoses was in compliance with German Standard VG 95955, i.e. the resistance of hoses up to 40 m in length should not exceed 1 M Ohm (see Table 1).

Throughout the fueiling process the charge ($\mu C/m^3$) of the fuel was measured by the CDMU and the current entering the 3 m hose was monitored at iso 1. The value of the current leaving the hose at iso 2 represents the charging current entering the tank.

The tests were carried out at temperatures of approx. 4°C, with a fuel conductivity of about 360 pS/m.

The test installation was available for a two-days test period, only. Nevertheless the results show some interesting aspects:

The charge passing through the CDMU was nearly 50 $\mu C/m^3$ (see Fig. 3 and 4) and the resulting current was about 0.9 µA. This is nearly

1.3 times the value to be expected for I_∞ when using the above equation for undoped fuel.

The returning current across Iso 1 was reduced by ten percent, i.e. about 0.8 µA.

The returning current across Iso 2 was still 0.1 µA.
The charge drop between Iso 2 and Iso 1 is presumably caused by relaxation. After all, it took more than 3 C for the fuel to pass through the short hose.

The reason for the relatively high charge density of fuel entering the CDMU might be due to a particular charging tendency of the hose and the doping.

To demonstrate the charge build-up on the tank truck simulating the aircraft we interrupted the measuring path across Iso 2 and registered the voltage build-up relative to the grounded refueiler chassis (see Fig. 3 and 5).

The tank ground resistance was 1.5×10^{10} Ohms and the capacity to earth appr. 1.3 nF.
In the test we found a voltage build-up of

$$\frac{\Delta U}{sec} = \frac{Ixt}{C} = 100 \frac{V}{sec} \quad \text{(see Fig. 4)}$$

To prevent any risks the increasing voltage was shorted at 500 V_{max}.

Then we earthed the mock-up with 2.2 M Ohms and found the voltage across it to be 0.3 V.

(The input resistance of the voltmeter was 10^{14} Ohms).

Several months later the mock-up test results were confirmed by a simplified installation: The 6000 ltrs tank truck was installed in the some way as before, but the 20 m hose was directly fitted to the insulation coupling Iso 2.
Temperature was about 2°C, and the conductivity of the fuel 250 pS/m.

We measured the returning current across Iso.2 to be nearly 1 µA (see Fig. 6). Then we bridged Iso 2 with a 2.2 MOhms resistance and found the voltage between tank and refueller to be below 1V (The resistance of the teflon insulation between tank and refueller was less when compared with the first mock-up tests because of high humidity).

Live Tests (see Fig. 7)

Next step was to transfer the principle to live tests on several aircraft. To simulate worst case conditions the aircraft was installed on 10 mm Teflon plates insulating it from ground (appr. 5×10^9 Ohms without attached hose).

The earthed refueller pumped JP4 into the a/c tanks through a 20 m hose (Table 1, hose 8). The resistance of this hose was in compliance with Standard VG 95955.

Since there was no insulation coupling available for the interface aircraft/single point of the hose, we had to register the voltage drop between a/c and refueller while pumping, to measure the actual resistance between a/c and refueller, in order to calculate the returning current.

Conductivity of the JP4 was measured prior to the individual tests and it ranged from 200 to 360 pS/m within the corresponding temperature range from -25° to + 25°C.

The measured resistance of the connecting hose across which the voltage drop occurred was in the range of 60 - 550 KOhms. The voltage between a/c and refueiler never exceeded 0.5 V.

With the examined voltage drop and the actual hose resistance the corresponding current could be derived:

- At flow rates of about 800 l/min charging current was approx. 0.8 µA.
- At flow rates of about 1200 l/min charging current was approx. 1 µA.

HIFR (Helicopter In Flight Refuelling)

Estimation of charging

This special procedure of fuelling a hovering helicopter is used for ship-based helicopters which are to be supplied at sea.
In the German Navy this method is not yet established. Therefore, no tests were possible and consequently we can give an estimation, only.

Concerning electrostatical charging we have to distinguish among several aspects. In flight a helicopter is mainly charged by tribo-electrification (dust, rain, snow etc.) natural electrical fields, running engines, and HIFR:

The amount of tribo-electric charging current primarily depends on gross-weight and meteorological conditions and can range for medium helicopters from 10 to 30 µA according to tests performed at Manching in the seventies (UH-1D/CH-53).

This current will charge the capacity helicopter-earth to high voltages (tens of kilovolts).

The natural electrical field has a value of about 100 V/m at clear skies.

For atmospheric disturbances fields up to 20 kV/m were reported.

The theoretical value for a hovering height of 20 m would be 400 kV. However, the value measured at the Manching trials was 50 kV_{max} and Ref. 7 gives the following estimation: "Aircraft voltages will vary considerably as with other forms of charging but are unlikely to reach 100 kV, (contrary to earlier be-

iiefs), and will more frequentiy vary between 10-50 kV."

Charging by the running engines can be neglected since their influence is very low.

Fueiiing charge during HiFR

In addition to the above mentioned constant negative or positive charging current the fuelling current must be superimposed.

The latter will be in the same range as found in our above tests.
Aii these currents have to be grounded while fueliing in order to prevent dangerous sparks.

The capacity of a helicopter with the iift cable dangling near ground ranges from 500-1000 pF (UH-1D/CH-53) and it is nearly constant for different cable iengths and helicopters at the time of first discharging (see Fig. 8).

After short cut of stored energy the permament current will cause a voltage drop across the cabie or hose iength, respectiveiy.The standardized hovering height for HIFR Operations is 15 to 20 m; the bonding resistance between the ship and the a/c fuel coupling should not exceed 1 M Ohm (Stanag 3847).

For assumed data 50 KV and 1000 pF the energy to be shortened initially via earthing connections will amount to

$$E = \frac{1}{2} \times CU^2 = 1250 \text{ mJ}.$$

For the above data and a permanent current of 30 µA the voltage drop of the hose across 1 MOhm wiii be

$$U = RxI = 30\ \mu A \times 1\ \text{MOhm} = 30\ V.$$

The maximum voitage for a minimum ignition energy of W = 0.25 mJ using the above data is given by the following equation

$$U = \sqrt{\frac{2xW}{C}} = \sqrt{\frac{2x0.25\ mJ}{1000\ pF}} = 700\ V$$

The time constant

$$\tau = RxC = 1\ M\ Ohm \times 1000\ pF = 1\ m\ sec.$$

Within a 3 m Secs. shorting heiicopter will be discharged.

Voitage build-up in the case of bonding interrupt for above data:

$$\frac{\Delta U}{sec} = \frac{Ixt}{C} = \frac{30\ \mu A}{1000\ pF} \times t = 300\ \frac{V}{sec}$$

CONCLUSION

In a aircraft/refueller system insulated to ground a refuelling process should not generate a voltage to ground because charge buiid-up, reiaxation and return via bonding cabie occur within this system.
The process wiii not be influenced by grounding procedures.

Bonding through the hose or the bonding cabie with 1 M Ohm is vital and should be sufficient for normal conditions.
To prevent a charge build-up due to transients of electric fieids for thunderstorm conditions earthing by cabie is recommended.

However, these considerations appiy to electrostatical charging,oniy.

HIFR

After the first discharge of the stored electrostaticai charge at initiai bonding contact, it has to be guaranteed that ship and heiicopter are kept at the same potential during refueiiing. For ali bonding connections a resistance of 1 M Ohm shouid be sufficient. Immediately before, during and shortiy after the refueliing process a bonding connection has to be maintained.

Under thunderstorm conditions the use of a bonding cable is recommended.

REF.

(1) J.T. Leonhard

"Generation of Eiectrostatic Charge in Fuei Handling Systems. A Literature Survey"
Naval Research Laboratory Report 8484, 1981

(2) K.C. Bachmann and W.G. Dukek

"Static Electricity in Fueliing of Superjets"
Esso Products Research Division 1972

(3) K. Hömberg, Effelsberg, Köntje

"Elektrostatische Aufiadung beim Betanken von Fiugzeugen"
TÜV Rheinland 1978 (Industriai Supervisory Board).

(4) Köntje

"Report on Requirements in Aircraft Bonding and Grounding"
TÜV Rheinland 1982 (Industrial Supervisory Board).

(5) Naval Air Systems Command

"Airframe Electrical Grounding Requirements Program"
Final Report 1981

(6) Central Servicing Development Establishment
Royal Airforce Swanton Marley
Servicing Investigations 1980

(7) M.E. Rogers
Interim Report on Helicopter Static Electrification Hazards
Royal Airforce Establishment
Technical Report 67292, 1967

Table 1 Resistance of extracted fuel hoses from refueller chassis to single point

Refueller-Hose	Resistance of Fuel Hose/ Ohms	Remarks
1	750	20 m Hose
2	100	
3	20K	
4	125	
5	250	
6	350	
7	300K	
8	550K	
9	30	3 m Hose

Hoses 8 and 9 respectively were used for the tests

Table 2 Resistance of refuellers to adjacent earth point (through tires, no earthing cable attached)

Refueller Chassis	Resistance to Earth Point/Ohms	Remarks
1	30K	on asphalt
2	25K	
3	50K	
4	50K	
5	25K	
6	55K	on anti-skid
7	50K	coating
8	100K	

Refueller 6 was used for all tests

Table 3 Resistance and capacity to earth point for parked aircraft

A/C	Resistance via Tyres/ Ohms	Capa-city/ nF	Remarks
F104	5-1,3 M	2,2	on anti-skid
F4	5- 7 M	3,5	coating
α-Jet	1-1,5 M	2	
MRCA	0,2-1,2M		

Above values (Table 1-3) highly depend on particular earthing conditions, aircraft configuration and relative humidity, they are mean values.

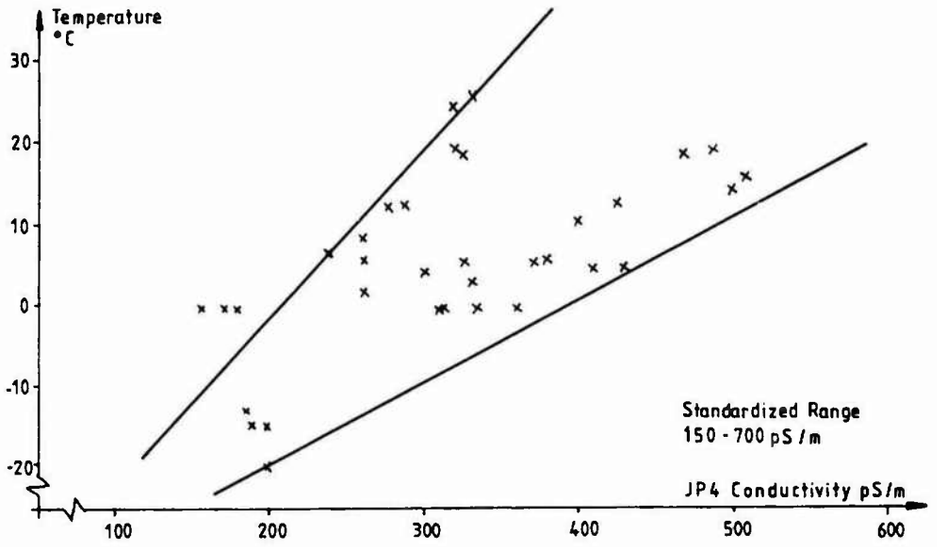


Fig. 1 Conductivity of doped JP 4 as function of temperature (Random samples of refuellers and storage tanks at different airports).



Fig. 2 Photograph of mock-up test configuration

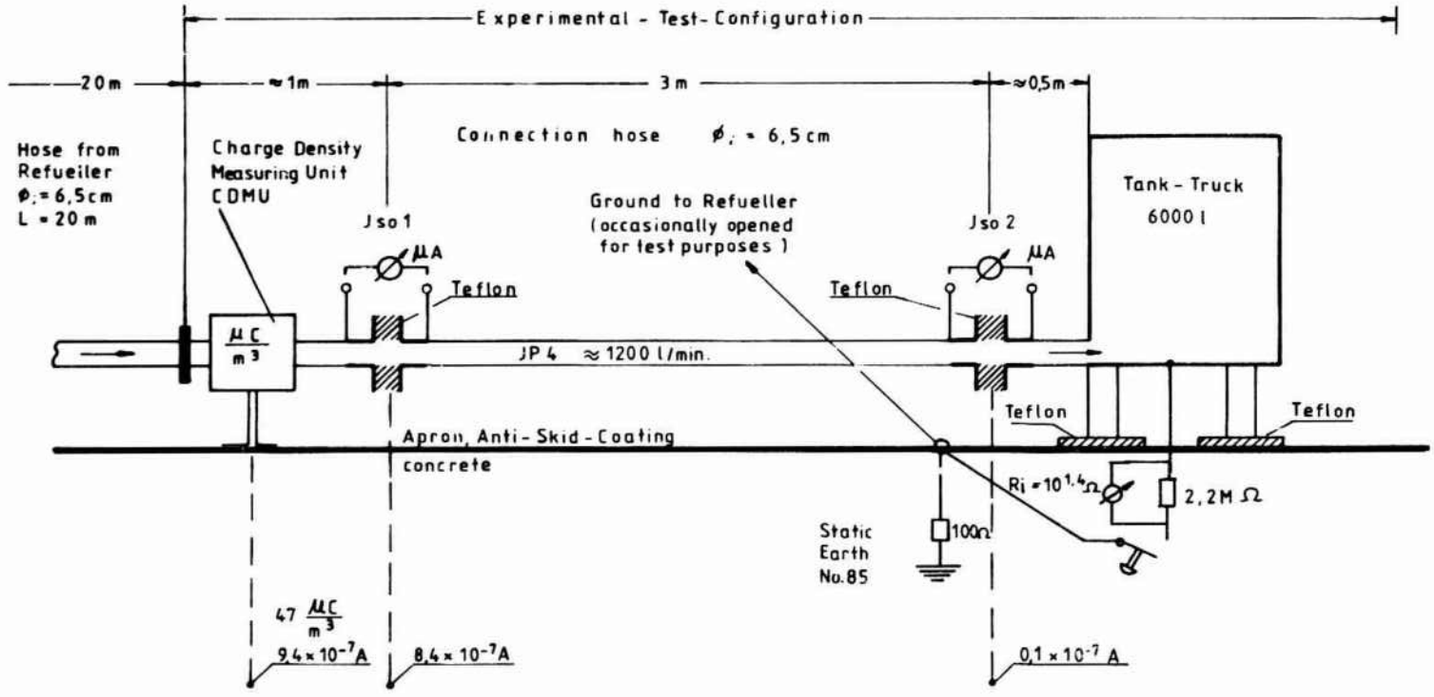


Fig. 3 Test-configuration for refuelling of aircraft with measured currents, Mock-up installation

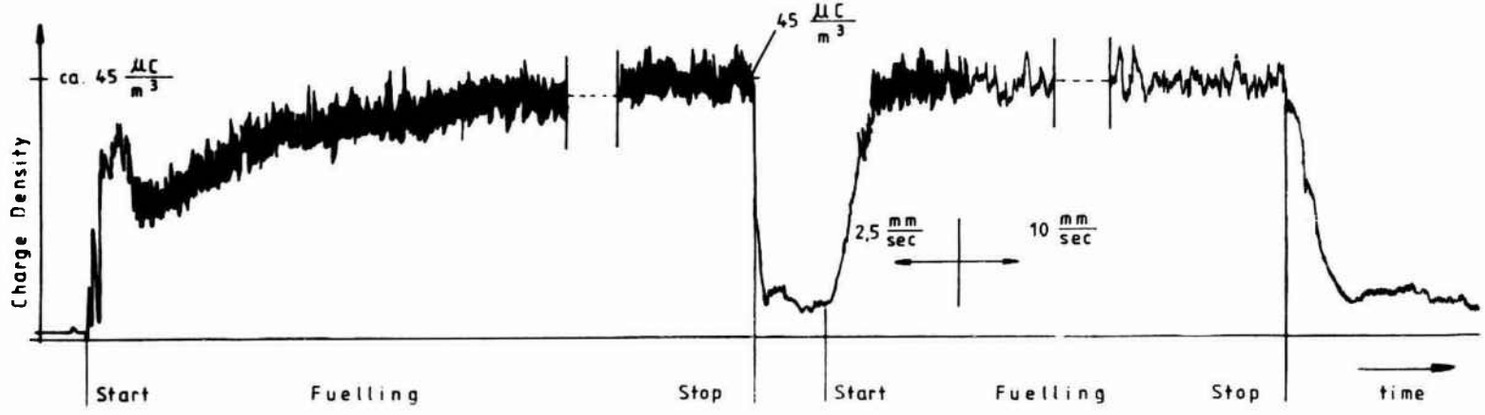


Fig. 4 Charge densitiy of the fuel passing the CDMU (Flow rate 1200 l / min)

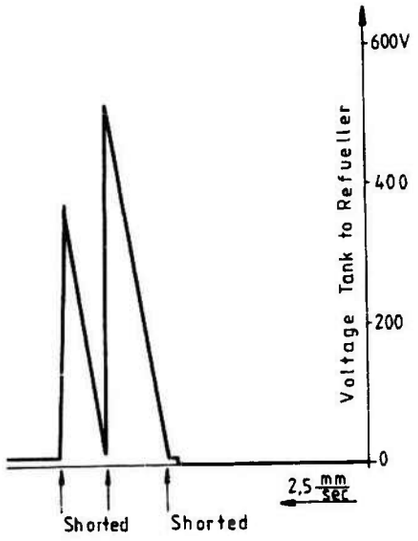


Fig. 5

Voltage build-up between tank and refueller
(Tank insulated 5 x 10^9 Ohms)

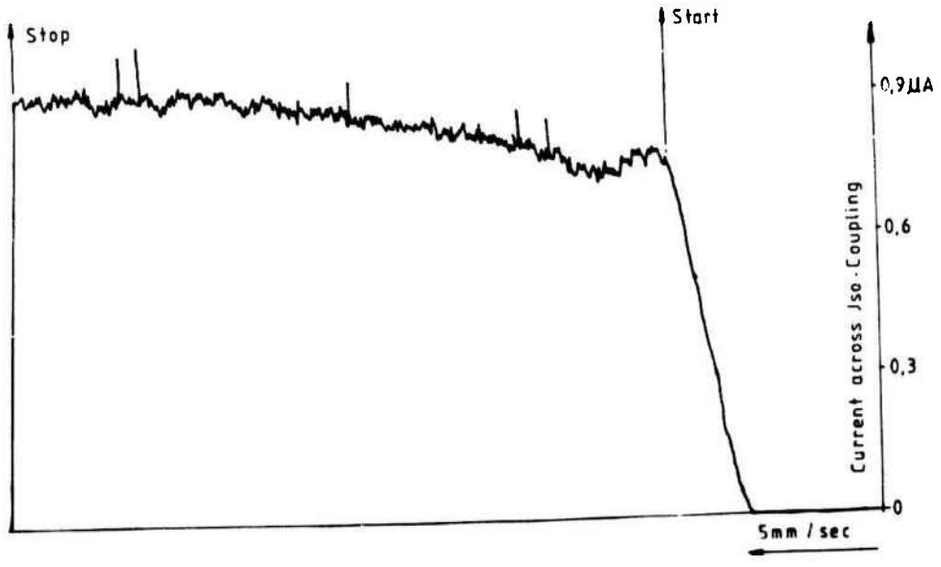


Fig. 6 Current across Iso-coupling, simplified mock-up installation

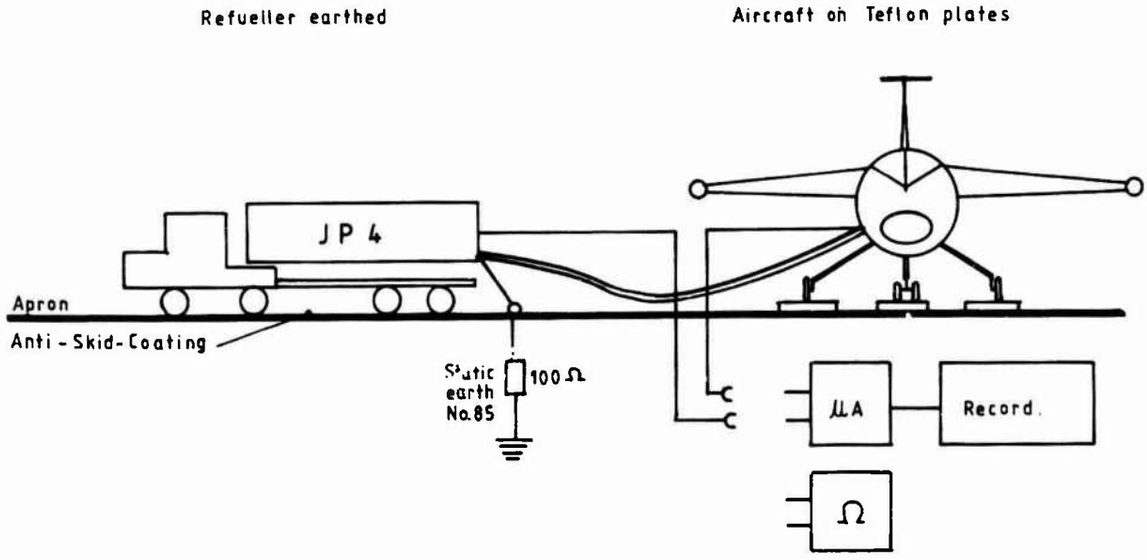


Fig. 7 Live tests configuration

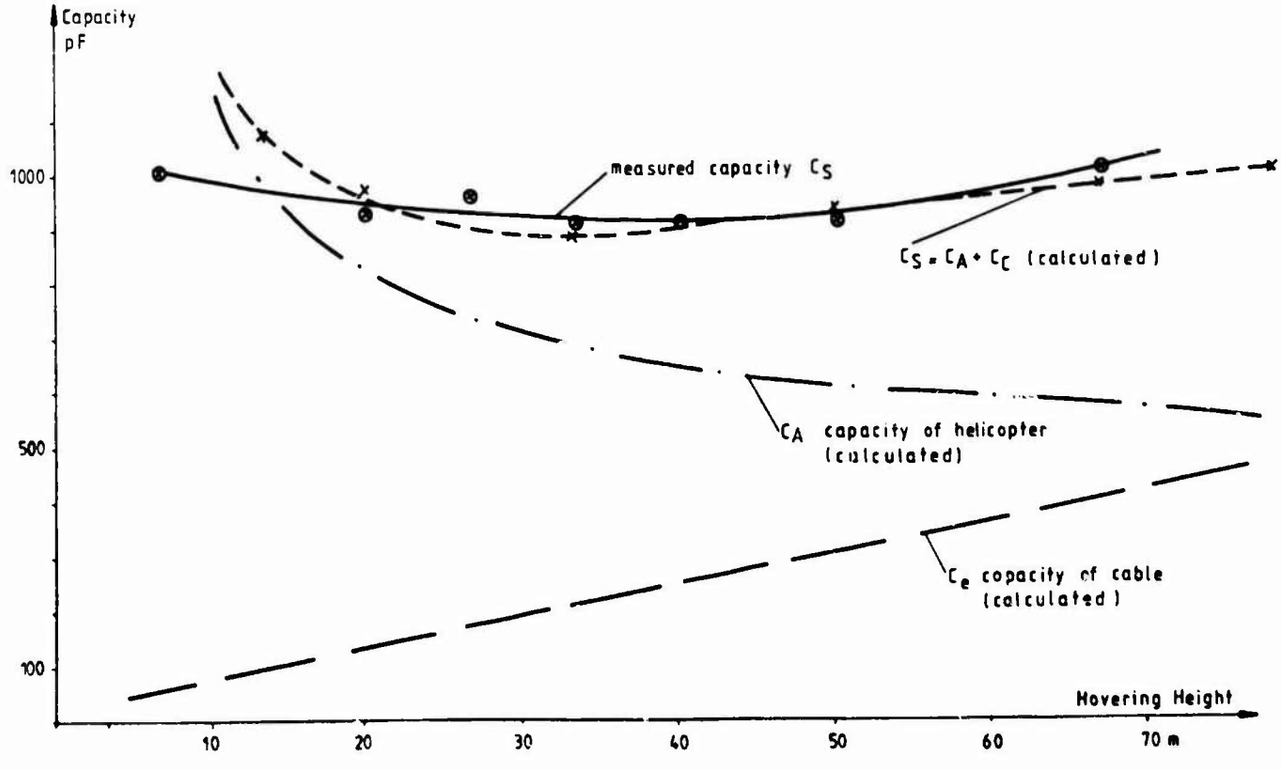


Fig. 8 Capacity of hovering helicopter CH-53 picking up loads immediately prior to ground contact of cable

HAND-HELD ELECTROSTATIC CHARGE DISTRIBUTION MEASURING SYSTEM

D. Königstein

Hochschule der Bundeswehr Hamburg, P.O. Box 70 08 22, D-2000 Hamburg 70, F.R.G.

Abstract - A hand-held field-meter (HFM) was developed for the purpose of measuring electrostatic charge distributions outside the laboratory without the need for expensive or bulky equipment. It consists of a sensor-device, which is moved along the structure of interest by hand and a battery-operated minicomputer connected to it by simple two wire connection. Presentation of the entire local charge distribution on a graphic-screen and on a small printer as well as evaluation of interesting data like medium, maximum and minimum surface charge density are possible on location. The system is expected to improve electrostatic testing of large objects or components in and outside the laboratory.

1. INTRODUCTION

It is known that any insulating material or insulated conducting structure can be electrostatically charged. Especially thin layers of high resistivity, applied on the conductive structure or lightning protection system of aircraft parts may cause electrostatic problems. Charge densities of some hundreds of nanocoulombs per square centimeter may be stored and discharged by breakdown of the insulating layer or by surface flashover. Surface streamer produced by static charging of the fuselage of an aircraft on the ground were shown by Taillet [1] and are related to charge densities in the mentioned range.
In preceeding works [2,3] the entire resulting electrostatic charge distribution due to several methods of simulated charging was measured in the laboratory on samples of fixed size and shape. The damage of insulating superficial layers due to the discharge of the stored energy could be demonstrated. With the help of the computer-controlled measuring system it was found that the local surface charge distribution was not necessarily uniform but large differences in surface charge density at short local distances were possible. Thus it was desirable to be able to measure the true local surface charge distribution not only in the laboratory but also in the field.

2. MEASUREMENT OF SURFACE CHARGES BY CAPACITIVE PROBE

The measurement of the surface charges σ on an insulating superficial layer or an insulated object has to be done by the static electric field E. To do this, several kinds of probes are known, e.g. the field mill [4], the vibrating probe [5] or the active or passive capacitive probe. The basic mechanism, that is producing a sensor signal, is in any case the electric field strength on the sensor surface. So the relation between field strength and surface charge have to be considered carefully. On the other hand for a true static measurement some effort is necessary to handle the drift problem of the active capacitive probe if the mechanical problems of the moving sensors shall be avoided.

2.1 The static field of a charged layer or insulated object

Figure 1 shows the basic principle of operation of an active capacitive field probe in the outer electric field of a charged layer of thickness d. If the distance between probe and surface is a, the surface charge density σ and the dielectric constant of the considered material ε_r, the measured field strength E will be:

$$E = \frac{\sigma}{\varepsilon_o\left(1 + \frac{a}{d}\,\varepsilon_r\right)} \qquad (1)$$

This equation is only valid if the backplane of the insulated layer has the same potential as the sensor (usually grounded). It is important to realize that high surface charge densities may have relatively low external fields if the measuring distance is high compared with the thickness of the layer. As described in [3] the limiting value for σ is the possible inner field strength $E_{i\,max}$ following eq. (2):

$$\sigma_{max} = \varepsilon_o \cdot \varepsilon_r \cdot E_{i\,max} \qquad (2)$$

For good insulators, especially thin layers, charge densities in the range of microcoulombs per square centimeter are possible. If a capacitive probe is calibrated in a homogeneous field, the true charge density on the surface is given by:

$$\sigma = \varepsilon_o \cdot E \cdot \left(1 + \frac{a}{d}\,\varepsilon_r\right) \qquad (3)$$

If the field strength in the vicinity of a conducting charged object is to be measured the whole stray capacitance of the object has to be known, as the surface charge density

changes, when the probe is approaching the surface.

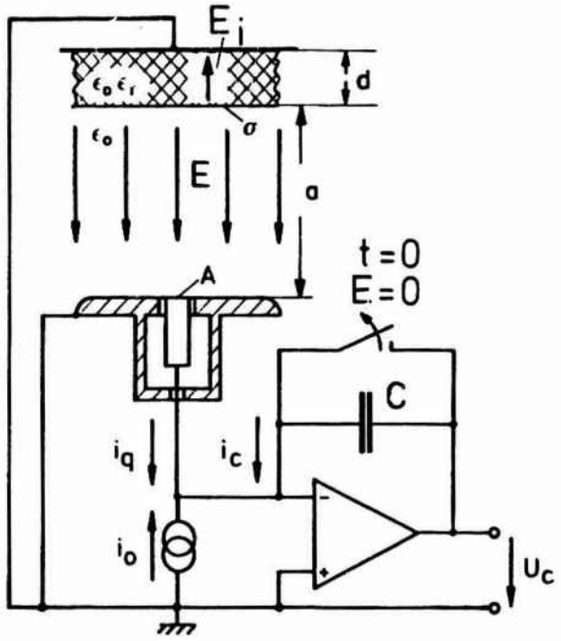


Figure 1: Basic principle of operation of an active capacitive field probe in the vicinity of a charged layer

2.2 Elimination of the integrator drift

For high resolution and low distortion of the measured field the active capacitive probe is the best solution. However, the electronic integrator implicates a problem of time dependent drift error. As indicated in fig. 1 not only the displacement current i_q is integrated in the capacity C, but also the offset current i_o and thus the output voltage of the integrator U_c follows eq. (4):

$$U_c = \frac{\varepsilon_o \cdot A \cdot E}{C} + \frac{i_o}{C} \cdot t \qquad (4)$$

If the offset current i_o is constant, a drift error increasing linearly with time is to be expected. Figure 2 shows an example of the drifting output signals with E = 0 at room temperature for 16 different sensor channels. As the sensor area A and the integration capacity C is chosen for an output signal of approx. 2 volts at maximum field strength, an error of less than 10 % during a measuring time of 100 seconds can be observed. This error is related to an offset current of approx. 1 pA. It could be reduced by choosing much more expensive operational amplifiers, but as the value is increasing significantly with temperature the error would never be neglectible. Since i_o is a constant value during the considered time (linear slope of the curves) it is better to correct it mathematically if the first and the last value of the drift error and the timing of the measurement is known. This has the additional advantage to eliminate also the offset voltage which was not considered in eq. (4) but is yet existing as fig. 2 shows.

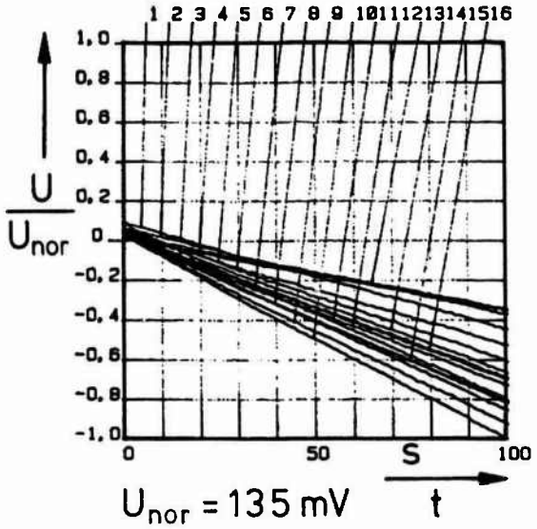


Figure 2: Typical offset current drift of 16 different integrator channels at room temperature

3. REALIZATION OF THE HAND-HELD CHARGE DISTRIBUTION MEASUREMENT SYSTEM

Two main components were used to develop a lightweight, hand-held charge measurement system. First, a sensor device with the ability to measure the static electric field along a line parallel to a surface of interest, moved by hand in the direction of the second coordinate. Second, a commercially available minicomputer to be carried with a shoulder-belt by the operator. Together with appropriate machine-language programs the fast serial (38400 Baud) interface of the computer is used for simple two-wire data transfer between the two components. The total weight of the system is approx. 3 kg. If desired, the sensor device can be operated stand-alone with an oscilloscope display and without data storage and drift correction but with automatic drift reset at fixed intervals. The measuring ranges are ± 25, 10 and 5 kV/cm with a resolution of 200, 80 and 40 V/cm. The related charge values are computed for the individual test objects as described in 2.1.

3.1 Sensor device

The principle of operation of the hand-held sensor device is shown in a block diagram in fig. 3. 16 active capacitive field probes are arranged in a sensor cylinder, which can be rotated 45° by means of a reset-servo to achieve a shielded position before and after measurement. Thus the condition E = 0 allows to reset the integration capacitors at the beginning, and to store the drift error values at the end of a measurement. The distance between the single probes was chosen to be 12.5 mm to cover a measured length of 200 mm in the x-coordinate. The 16 field strength signals are multiplexed and transmitted serially to an analog to digital converter of

Some other kinds of presentations will be shown in the next figure with an example of simulated field data. First, a 3-dimensional presentation, which is simulating the resolution of the LCD-display on a matrix printer. Second, the same data, presented with an intensity variation related to the local value of the field strength. The third picture shows the lines of equal field strength for the same data. These examples demonstrate the variety of possible evaluations which can be used for the different purposes.

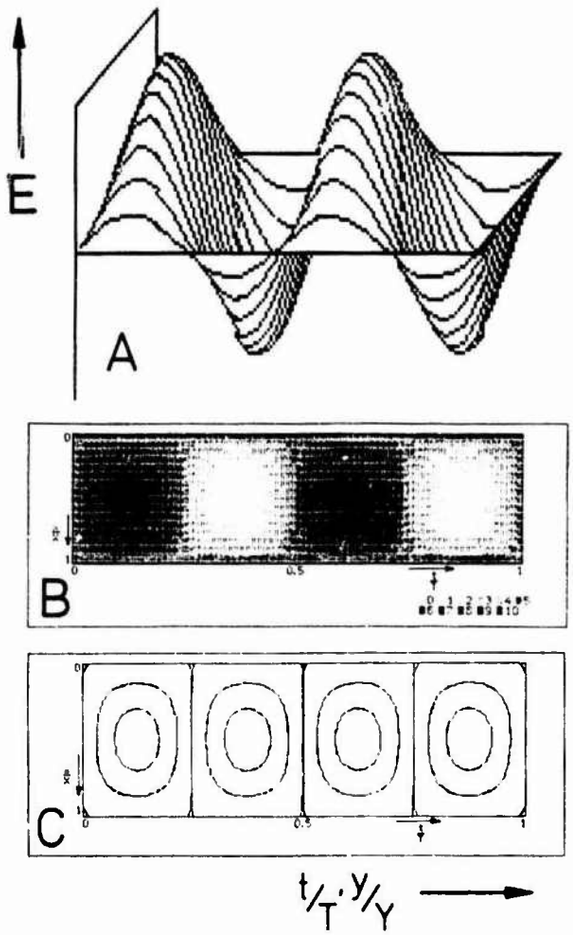


Figure 7: Different examples of field data presentation
A: 3-dimensional
B: Intensity variation
C: Lines of equal field strength

For the first qualitative impression the 3-dimensional presentation is definitely the best solution. On the other hand it does not allow to localize an anomaly exactly. For this purpose the other presentations are more useful. It is also possible to plot a line of measured data along a single coordinate. From the field strength differences on different points along the surface, the surface field strength across the insulating layer can be determined, too.

Finally, the digital storage of all measured data allows evaluation of interesting values, such as true local surface charge Q, maximum charge density $\hat{\sigma}$ or medium and minimum charge density if the thickness and the dielectric constant of the surface layer are given as described in 2.1.

5. CONCLUSIONS

As known from previous work, electrostatic charge distribution on insulating layers can be very inhomogeneous. Thus local charge values may be much higher than the result of an integral measurement suggests. On the other hand the interpretation of the local charge distribution can give valuable information about the measured material (resistivity, layer thickness, bonding quality).

With the developed hand-held field-meter it is possible to make a true charge distribution measurement outside the laboratory including data storage and error correction. Thus it will be possible to control the properties of surface layers during operation, without the need for laboratory samples. The system will improve electrostatic testing of large objects and shall be used on aircraft parts or similar objects in the near future.

6. REFERENCES

[1] Taillet, J.: "Basic Phenomenology of Electrical Discharges at Atmospheric Pressure". AGARD Lecture Series No. 110, "Atmospheric Electricity Aircraft Interactions", June 1980

[2] Königstein, D.: "Local Charge Distribution and Development on Insulating Surfaces". ICOLSE, Oxford, 23-25 March 1982, Proceedings report E 8

[3] Königstein, D.: "Damage of RFC Surface Layers by Electrostatic Charging". ICOLSE, Ft. Worth, Texas, USA, 21-23 June 1983, Proceedings report No. 7

[4] Waddel, R.C.: "An Electric Field Meter for Use on Airplanes". The Review of Scientific Instruments 1948, Vol. 16, No. 1, p. 31-35

[5] Danyluk, S.: "A UHV Guarded Kelvin Probe". Journal of Physics E: Scientific Instruments 1972, Vol. 5, p. 478-480

8-Bit resolution. As the 16 signals are converted and transmitted within 4.8 ms they can be considered as measured at equal times compared with the measuring velocity in the y-coordinate. Three different modes of operation can be chosen.

1. X/Y-mode: A friction wheel (fw) initiates a new set of data after a movement of 12.5 mm in the y-coordinate (Δy). Thus an area of 200 mm times 1 m can be scanned by hand as the 16 field probe signals are stored 80 times. The time of this measurement may be between 0.4 and 20 seconds as desired by the user.

2. X/t-mode: This mode is used if it is difficult or not desired to use the friction wheel, or if the object itself is moving or if the time-dependent development of the charges along one line is to be measured. A new set of data is stored each 5 ms to 250 ms as desired, resulting in a total measuring time as in X/Y-mode.

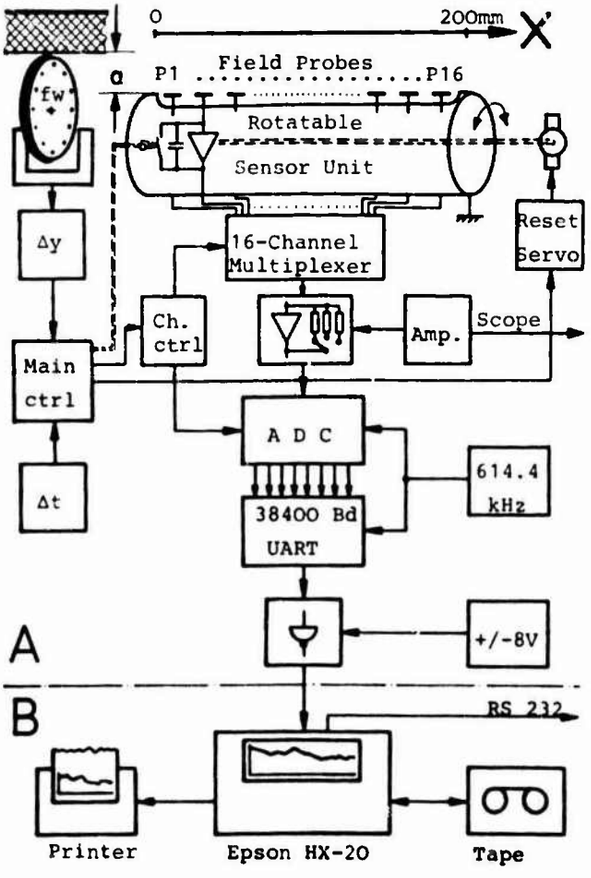


Figure 3: Principle of operation of the hand-held field-meter (HFM)
A: sensor device
B: Minicomputer with built-in printer and recorder

3. Scope-m: In this mode the 16 multiplexed analog channel signals can be displayed permanently by an oscilloscope as demonstrated in fig. 4. The sensor unit closes and opens at 20 s intervals for drift reset. Thus a local monitoring of charge development or a control of general charge distribution can be done in the laboratory without data storage for later use.

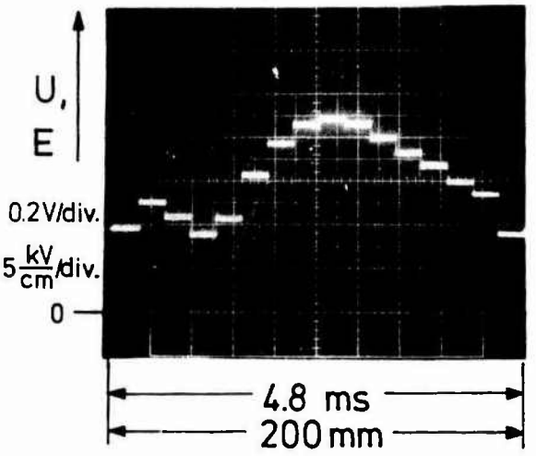


Figure 4: Example of the field-strength distribution along a line parallel to the surface of an artificially charged insulator (PMMA, 5 mm)

In the first two modes the 16 channel signals are transmitted to the computer for the first time immediately after integrator reset and and with the sensor unit in the shielded position (E=0). During the measurement the computer checks the actual time of a data transmission for later drift correction. For the same reason a set of data is transmitted at the end of the measurement with shielded probes. Thus a complete measurement consists of (80+2)· 16 = 1 312 charge values which are transmitted to and stored by the computer.

As the sensors are arranged on a cylinder of 60 mm diameter and are to be used in a distance of 12.5 mm from the surface, the shape of the test object should be nearly straight in one direction. In the second coordinate a radius of the surface down to 10 to 20 cm is possible. Thus big objects with a limited curvature of the surface in only one direction can be measured like the fuselage, wings or windscreen of an aircraft or similar objects.

3.2 Minicomputer

All measuring data from the sensor device can be transmitted to a small and lightweight minicomputer, able to store the necessary amount of data, handle the data transmission and display the results on a built-in LCD screen and a small miniprinter. With a weight of approx. 2 kg the computer is able to operate 24 hours in stand-by, waiting for data,

and 1 hour in permanent data transmission. For data display and transmission machine language programs were developed. A simple utility program just asks the user for the measuring range and tells him how many files are free on the tape-casette. When the computer is prepared for data transmission, the measurement begins by pressing the start button on the sensor device or moving the friction wheel in the X/Y-mode.

After measurement any stored data can be transmitted via RS 232 interface to other computers or storage equipment if desired. Additional presentation of data on matrix-printer or plotter at the office is possible as well. A lot of programs were developed for this purpose.

4. RESULTS AND PRESENTATION OF MEASUREMENTS

4.1 Immediate presentation

Immediately after measurement the computer presents a small 3-dimensional picture on the printer and the LCD-screen with low resolution and no drift correction. The user can decide whether he wants to get a better presentation and data storage or start a new measurement. Fig. 5 shows the information that he will receive.

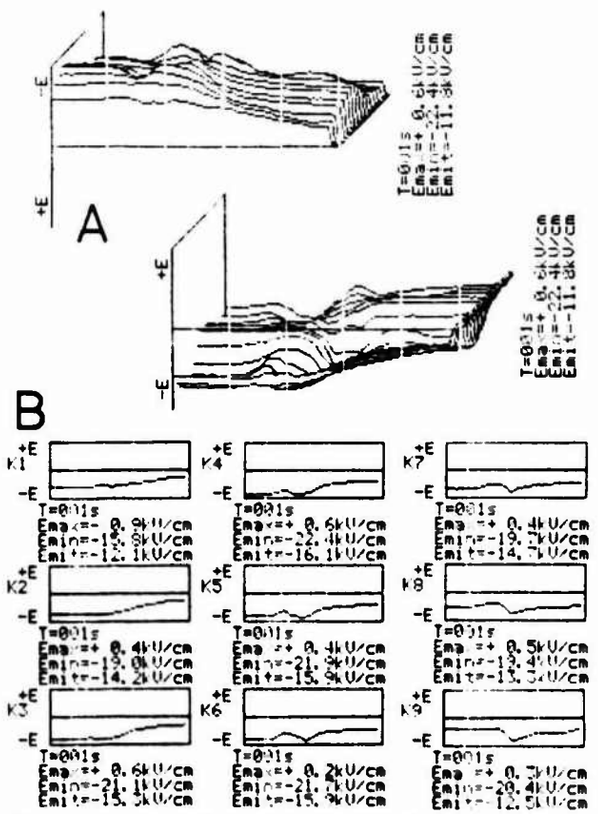


Figure 5: Results of a measured charge distribution as presented by the miniprinter (and LCD-display) (PMMA, 5 mm, corona-charged)
A: 3-dimensional presentation of the entire measured data
B: Presentation of the different sensor channels (Ch 1 to 9 only)

In this case the sensor device was moved along the surface of a piece of corona-charged plexiglass. The measured field strength distribution is presented once with positive polarity up and once with negative polarity up. In this way curves can be seen, which otherwise might be hidden behind others. In addition, the different sensor channels are presented separately to ease the exact localization of any anomaly. For each single picture the measuring time, the maximum, minimum and medium measured field strength is given.

4.2 Improved presentation

The resolution of the built-in LCD-display and miniprinter is limited, as fig. 5 showed. However, as the measured data are stored on magnetic tape, improved presentation with the help of additional hardware at the laboratory or at the office is possible. Fig. 6 shows the resolution which can be achieved for the same data as in fig. 5 by the use of a usual matrix-printer. The different measuring time positions are connected in this presentation by a line and the time axis is turned around.

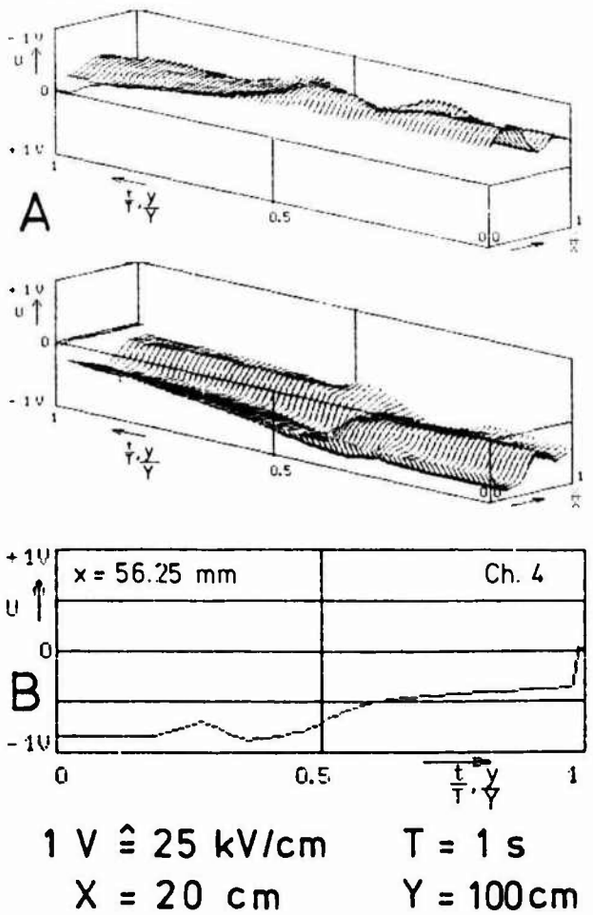


Figure 6: Measured charge distribution of fig. 5 as presented with improved resolution
A: 3-dimensional presentation
B: Data of one selected channel (Ch. 4)

A NEW UNDERSTANDING OF BREAKDOWNS IN THE DAY SECTIONS OF GEOSYNCHRONOUS ORBIT

L. Levy

Centre d'Etudes et de Recherches de Toulouse, Département "Technologie Spatiale", B.P. 4025, 31055 Toulouse Cedex, France

Abstract - Spacecraft anomalies all around the geostationary orbit are tentatively explained as the result of a material-dependent worst case environment. In the midnight-to-dawn section of the geostationary orbit, differential charging is understood as a consequence of particle injection during the occurrence of substorms. In the day section, spacecraft anomalies have been rather explained by charging of internal dielectrics due to penetrating high energy electrons.

The exposed theory is an attempt to a unified conception of spacecraft charging. It is aimed at demonstrating that the concept of worst case environment is dependent on materials properties: worst-case for "conductive" dielectrics is the occurrence of substorms and is to be found in the midnight-to-dawn section. Conversely, poorly conductive materials, or floating structures will experience worst case charging in the day-section provided they are in the shadow.

I - INTRODUCTION

It has become well known that dielectric materials used as satellite external coatings can be differentially charged by the ambient environment at geosynchronous orbits.

The current understanding is to associate the possibility of such charging with the development of geomagnetic substorms which affect the electron and ion population in a given section (midnight-to-dawn) of the geosynchronous orbit. This theory is supported by the numerous anomalies that a lot of satellites underwent precisely in this orbit section when geomagnetic activity was high.

Nevertheless, the anomalies distribution is not always so clear, and many other satellites present a different pattern. Not always correlation is found with the satellite location, nor with geomagnetic activity.

We propose a new theory so as to contribute to explain these unexpected behaviors. It is built in the light of both personal experience (on conductivity properties, breakdown criteria drawned from ground-tests) and published literature on environment and satellite anomalies. The approach of the paper comes out from the two questions: which is the most significative worst case environment parameter : Energy or Intensity? The further question is where on the orbit are the highest energies or intensities encountered?

We show that there is not simply a unique "worst case". Day side environment will be the worst case for pure dielectrics (no conduction), night side will be the worst for dielectrics with a certain amount of conductivity.

II - THE LOCAL TIME DEPENDENT OF THE ANOMALIES

The local time dependence of anomalies is often presented in the form of Figure 1 from Ref. (1).

The figure 1 distribution is typical of what is well understood by the current theory on spacecraft charging which associates the charging and discharging probability with the encountering of injected electrons (in the 1 to 50 keV energies) in the midnight-to-dawn Section of the orbit during substorm periods. Correlation is found with location and also with geomagnetic activity. The number of anomalies occurrences is maximum precisely at the very injection location

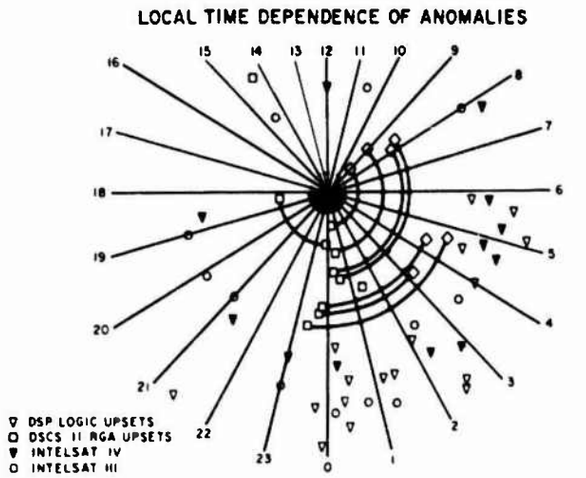


Figure 1 - Typical local time dependence of anomalies (Ref.1) (radial distance has no meaning)

The figure 2, from Ref. (2) exhibits a quite different pattern.

There is not any obvious maximum: anomalies are as frequent in day-side than in the night-side. The anomalies outside the midnight-to-dawn section are not yet completely understood. Suppositions are that they may be caused by discharging (for unknown reasons) long time after that charge has occurred in the night-side. Another hypothesis is that they may be due to high energy penetrating electrons. These electrons would charge dielectrics (like insulating cable sheaths) inside the satellite.

This paper is an attempt to a unified conception of spacecraft charging and induced anomalies in terms of

material properties (mainly conductivity) and local time dependent environment.

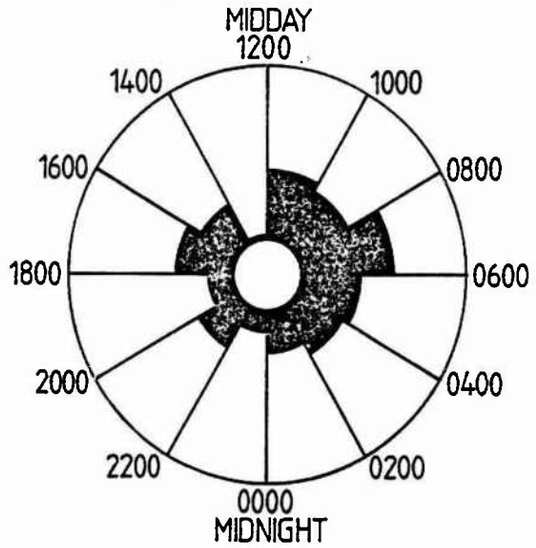


Figure 2 - Meteosat F1 anomalies local time dependence (Ref. 2) - Radii scale 0-25 indicates Nos of events

3. THE SPACECRAFT CHARGING THEORY

Very complete reviews papers (3,4) deal with the spacecraft charging theory. Only major characteristics are reported here.

3.1. Absolute charging

Absolute charging refers to the entire spacecraft potential with respect to the ambient plasma. It is the result of the charge collected from the environment. The basic physical law governing the potential of a surface is that it takes the value which annuls charge exchanges. The net current to surface is then zero, and when it is not, a potential variation is induced in such a way to satisfy the current balance.

The ambient plasma consists of electrons and ions, mainly protons. The plasma characteristics, energy and density, are dependent on the location on the orbit and on the state of the magnetosphere, quite or disturbed. The substorm is a disturbed state which makes higher the intensities (in the 1 to 30 keV energy range) in the antisolar side of the magnetosphere. As a rapid statement, absolute potential will depend on the density (temperature) of the plasma. Photoemission due to extreme ultraviolet sun light will have also a major importance.

At equilibrium, the following equation applies to a floating surface :

$$Je = Ji + Jsec + Jph \qquad (1)$$

Je is the electron incident current, termed as the charging current. Je is a fonction of the potential V of the collecting surface. Je decreases when the surface potential increases negatively.

Ji is the ion incident current. It is only slightly dependent on the negative surface potential. For a plasma where electrons and ions are in thermal equilibrium, the electron incident current exceeds that of the ions by a factor $\sqrt{Mi/Me}$, Mi and Me being the ion and electron mass. Je ~ 40 Ji for a surface at zero potential.

Jph is the photoemission current. When a material is exposed to sunlight radiation, its most energetic photons (with quanta energies $h\nu > 4$ eV, E-U-V domain) can extract electrons from the surface material, depending on its work function. Photoemitted electrons are in the 1 eV range, which makes photoemission very sensitive to barrier effects. Phctoemission from a kapton surface under normal solar incidence is about 2 nA/cm^2 (in the absence of barrier effects)(value of 2 nA/cm^2 is taken in the Nascap Library, see for instance Ref. 5).

Jsec is the secondary emission current from a surface due to impact of primary particles. The yield δ (true secondary emission) or σ (total secondary emission) is the number of emitted electrons per incident electron. It is a function of the primary energy and for dielectrics and metal oxydes it may exceed unity.

For a given primary energy, $Jsec = \sigma(Ep)Jp$.

Secondary electron energies are in the 0 to 50 eV range.

Absolute charging by itself is not considered to be the first reason of discharges and anomalies on-board satellites.

3.2. Differential charging

Differential charging occurs because of the existence of many dielectric materials used as external coatings. These materials are selected for thermal control properties first. They are dielectrics accidently except in certain cases on solar generators for instance.

The reason for a given dielectric to charge differentially (with respect to the structure or ground of the satellite) lies both on material properties and on locally varying situation on the satellite. When isolated surfaces have different material properties (conductivity, secondary emission) or are exposed to different environments, different potentials will be induced.

Shadowing of a surface (by the body of the satellite) is a source of differential charging by preventing photoemission.

Differential charging is thought to be the first reason of concern on satellites. It gives rise to strong local electric fields at the edges of the thin dielectrics used as thermal coatings.

At equilibrium, the balance equation (1) must then include a term of leakage current as a consequence of the differential voltage ΔVs.

$$Je(Vs) = Ji(Vs) + Jsec(Vs) + Jph(Vs) + Jl(\Delta Vs) \qquad (2)$$

with

Vs = absolute structure (ground) potential

ΔVs = differential voltage of a dielectric with respect to structure

$Jl(\Delta Vs)$ = leakage current depending only on material conductivity properties

Equation (2) simplifies for a surface in shadow and for pure dielectriccs

. SURFACE IN SHADOW (Jph = 0)

$Je(Vs) = Ji(Vs) + Jsec(Vs) + Jl(\Delta Vs)$

and with the approximation Je > Ji

$Je(Vs) = Jsec(Vs) + Jl(\Delta Vs)$ (3)

. SURFACE IN SHADOW AND PURE CAPACITORS (Jl=0)

$Je(Vs) = Jsec(Vs)$ (4)

Equations 3 and 4 apply to electron charged dielectrics in the laboratory conditions where the samples under tests are layed on grounded holders. Results of such laboratory experiments are discussed in the following sections.

4. THE CAPACITIVE MODEL IN GROUND TEST CONFIGURATION

The situation of a dielectric in laboratory tests is rather different from the in-orbit situation.

. The metallized side (rear side) of the sample is at ground experiment potential. In space, the metallized side is at the frame "absolute" potential.

. The charging environment is very simplified : monoenergetic electron beams are used instead of distributed energy electrons and ions beams.

Nevertheless, this simplified approach is experimentally easy and much has been learned about electrostatic behavior and material properties of electron bombarded dielectrics.

The following section emphasizes two of these properties, namely secondary emission and conductivity, which are keys of existing differential potentials. (Photoemission is another important key but it will be not dealt with).

4.1. The capacitive charging model:

The dielectric is considered to be a capacitor loaded by its own leakage resistor.

The basic equation is the following

$C(dv/dt) = Je(V) - (Jsec(V) + Jl(V))$

V surface potential in Volts
C capacity in F/cm^2
Je incidence electron current in A/cm^2
Jsec secondary electron current in A/cm^2
Jl leakage current or conduction current in A/cm^2.

At equilibrium, $C(dv/dt) = 0$

$Je(Vseq) = Jsec(Vseq) + Jl(Vseq)$,

that is equation (3) with $Vs = \Delta Vs$.

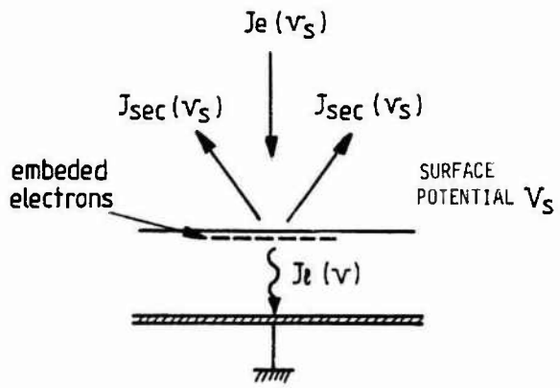


Figure 3 - The capacitor ground test charging model

4.2 Idealized dielectrics : pure capacitors

For pure capacitor Jl = 0 and equation (3) turns into (4).

$Je(Vseq) = Jsec(Veq)$.

Secondary emission is then the only physical process by which charge is removed from the surface. The equilibrium potential will be the one for which the secondary emission yield is unity.

Let us consider the secondary emission yield of kapton as a function of primary energy. Figure 4 shows two curves. One is from Ref. (6). The other was obtained with home facilities.

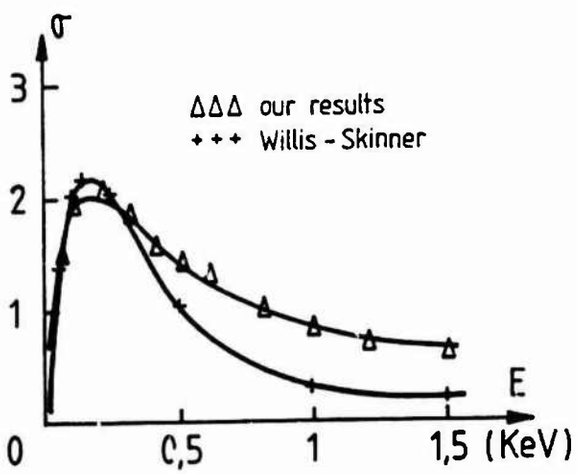


Figure 4 - Secondary emission yield of kapton

The curve is very typical of secondary emission of dielectrics. It shows that the yield can be higher than unity for energy ranging from 50 to 500/800 eV. These values are termed as Eland E2, cross over energies for which $\sigma = 1$.

Let us suppose now that an irradiation is started with $E > E2$. σ is lower than unity and charge is stored on the surface.

As the surface potential grows, the effective energy of the incoming electron is reduced by an effect of potential repelling. "True" incoming energy is : $E - qVs$.

When Vs is high enough that

$$E - qVs = E2 \qquad (5)$$

$\sigma = 1$, and no more charge can be further brought to the surface.

Very important consequences outcome from equation (5).

. The first is that the plot of surface potential at equilibrium against energy Vseq(E) will be a straight line. This has been widely verified by most experimentations. See Ref.(8).

. The second is that equation (5) is not dependent on beam intensity. Only the energy determines the surface potential Vseq at equilibrium. It will be grown more or less rapidly depending on intensity but saturation value will not be changed.

In terms of worst case environment, this leads to the statement : "the potential of such a dielectric in space will be governed essentially the mean energy of the encoutered electrons, even if the associated intensities are low" provided that :

. it is in the shadow (no photoemission, Jph = 0),

. it is thick enough to stop the energetic incoming electrons.

Figure 5 shows the range energy relation for electrons in kapton (Ref. 7), Figure 6 from Ref. (8) is the surface versus potential curve versus Energy beam in the case of idealized dielectrics (Figure 6a) and in the case of conductive dielectrics (Figure 6b).

4.3. Evidence for some degree of conduction

It is this section's purpose to illustrate that most dielectrics always exhibit some degree of conductivity. Plots of surface potentials against energy depart from idealized straight lines for high values of the potential. It is clearly the consequence of an increasing leakage current existence.

4.3.1. DARK CONDUCTIVITY

Conductivity of kapton, cerium doped glass, pure silica and teflon was studied at the laboratory by the "decreasing surface potential" method :

. First, the dielectric is charged my means of electron beam,

. then, the irradiation is stopped while continously monitoring the surface potential,

. the decreasing surface potential is then ascribed to the leakage current of the dielectric considered as a capacitor loaded by its own leakage resistance.

An elementary treatment leads to the expression of the conductivity :

$$(1/\rho) = -\varepsilon(dVs/dt)/Vs$$

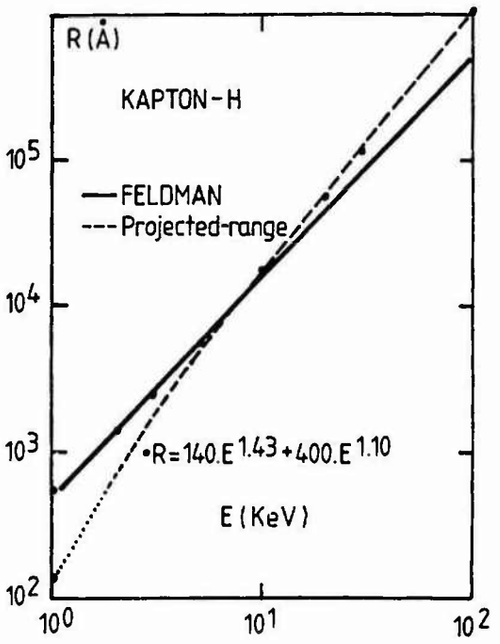


Figure 5 - Range Energy relation for electrons in kapton (Ref. 7)

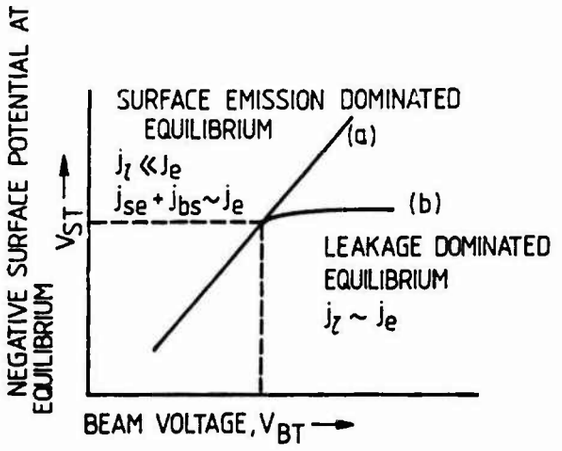


Figure 6 - Charging response for idealized (a) and conductive dielectrics (b) (Ref. 8)

. ρ = resistivity in (Ω.cm)

. ϵ = permittivity in F. cm^{-1}

. Vs = Volts

. t = seconds

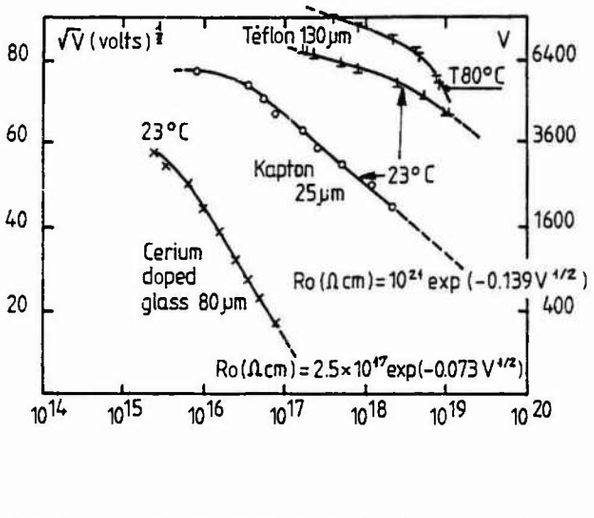


Figure 7 - Voltage dependent resistivity of kapton cerium doped glass, teflon (in dark)

Figure 7 shows the resistivity of kapton, cerium doped glass and teflon against the square of measured Vs. The interest of such a presentation is that a straight line is the evidence for field-assisted conductivity (Poole-Frenkel effect).

Dielectrics materials are not ohmic and we propose analytical expression for kapton and cerium doped glass resistivities as a function of the applied potentials.

The general expression is :

$$\rho = \rho_o \exp\left[-\alpha(Vs^{1/2})\right]$$

with { Vs = surface potential (in volts)
{ ρ_o and α are dependent on the material

For kapton 50 µm (temperature 23°C):

$$\rho(\Omega.cm) = 10^{21} \exp(-0.139)\ Vs^{1/2}$$

For cerium doped glass 80 µm (temperature 23°C):

$$\rho(\Omega.cm) = 2.5\ 10^{17} \exp(-0.073)\ Vs^{1/2}$$

4.3.2. Environment induced conductivity

Conductivity of dielectric materials is not independent on in-orbit general environment.

It has been shown for instance that the kapton samples of the SCATHA experiments SSPM 1 and SSPM 2 became more and more conductors and this was due to a sunlight photoconduction effect : Ref. (9).

This effect was also illustrated in ground tests where conductivity effects on sunlightened kapton was studied.

Dielectrics in space exhibit also the well known radiation induced conductivity phenomenon.(r.i.c.) Energetic trapped electrons of the geosynchronous orbit penetrate completely the rather thin used materials. They create the r.i.c. which adds to the dark conductivity.

R.i.c. can be even much higher than dark conductivity. Again the decreasing surface potential method was used to study the r.i.c.: the sample was not left to discharge by "its own means" : it was exposed to the penetrating electrons of a bêta strontium source. The conductivity was found to be very sensitive upon radiation presence for kapton and pure silica. See Figure 8. No effect was found for cerium doped glass, but cerium doped glass is intrinsically already rather conductive. R.I.C. was not studied on teflon.

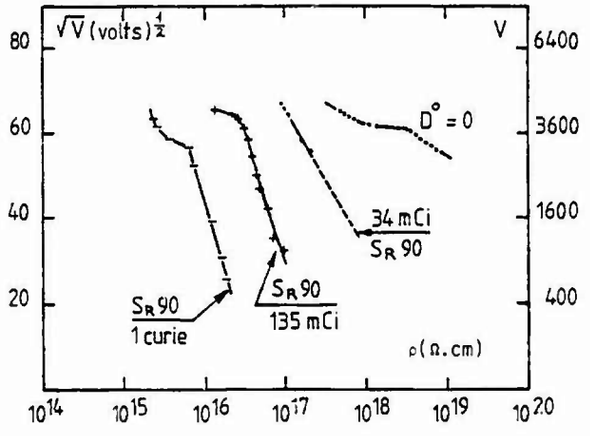


Figure 8 - R.I.C. evidence in Kapton 50 µm. (Sr90 1 curie corresponds to ∿10 rad/s for a sample to source distance = 8,8 cm).

So, it is obvious that most dielectrics in space will exhibit a certain amount of conductivity and of leakage current under differential voltage. It makes sense to compare the leakage currents magnitudes with respect to the maximum incident electron currents that are to be met in orbit.

Let us compute the leakage current value assuming a resistivity $\rho = 10^{15}\Omega.cm$ and a differential voltage ΔVs = 1000 Volts for a material with thickness 50 µm.

$$Jl(nA/cm^2) = (1000)/(10^{15}.50.10^{-4}) = 0,2\ 10^{-9}$$

This leakage current is quite important with respect to the maximum intensities that are available on the orbit. The very important consequences of the existence of rather large leakage dielectric currents are the following :

. leakage currents act to limite effective differential voltages: the thinner the dielectrics, the lower the achieved potentials.

. Worst case environment will be the occurrence of the maximum available currents in the 1 to 50 keV energy range. The intensity as well as the mean associated energy will be the keys of the most severe charging.

This worst case environment is to be found in the midnight to dawn section of the geosynchronous orbit during the disturbed periods of the magnetosphere.

This will be shown in the following section.

5. WHEN AND WHERE WILL "CONOUCTIVE" AND "PURE" DIELECTRICS UNDERGO THE MOST SEVERE CHARGING IN ORBIT

5.1. The local time dependence of the environment and anomalies.

Data environment have been gathered in space by electrons and ions spectrometers flown on the ATS5, ATS6, GEOS, METEOSAT and SCATHA satellites.

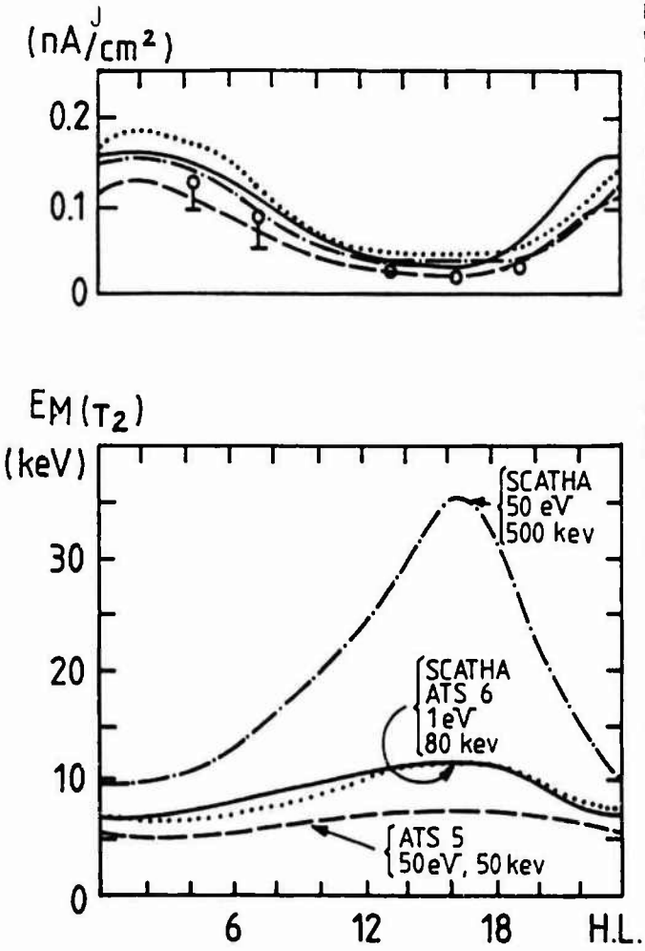


Figure 9 - Local time variation of mean electron energies and intensities from ATS 5/6 and SCATHA in-flight measurements (Ref. 10)

The Figure 9 taken from Ref. (10) shows the average of the mean energy and intensities local time variations. Thousands of spectra collected from the SCATHA; ATS5 and ATS6 spectrometers have been compiled and averaged.

These spectra are in good agreement with each other. The discrepancy on the SCATHA mean energy distribution is only apparent and comes from the enlarged energy domain analyzed by the SCATHA experiment. (up to 500 keV).

Figure 9 reveals a remarkable characteristic of the electron local time energy and intensity distribution: the higher intensities are to be found in the night-side (midnight-to-dawn) and the higher energies are to be found in the day-side.

Anticorrelation exists between energies and intensities : in the night-side low energies (< 10 keV) are associated with high intensities (0,1 nA/cm^2) and in the day-side high energies (up to 35 keV) are associated with low intensities (0,08 nA/cm^2).

5.2 Day-side worst case for "pure dielectrics in the shadow"

Figure 9 is suggestive that the day-side environment will constitute the worst case environment for pure dielectrics (if they do exist at the surface of the satellite). Additional conditions to propose them as good candidates for being sources of arcing and anomalies are that they are in the shadow, thick enough to stop the incoming electrons, and that they do effectively arc when charged by the environment. Another condition is that their capacity with respect to the structure should be very low (this should be the case for thick materials).

We have tested such an element that is likely to be used as a strut to ensure mechanical fixations of thermal shields.

We have found that very little intensity beam was necessary to charge it. It could be considered as a pure capacitor, a piece of material (fiber glass material) held above the structure of the satellite. See Figure 10 for the test results and details of the tested elements. The value of the leakage current for such an element was lower than 5 pA/cm^2. The capacitor value was less than 5 pF/cm^2.

Figure 10 gives the surface potential achieved during a test with two monoenergetic beams of values E1 = 4 keV and E2 = 20 keV. The ratio between the two associated intensities I_1 et I_2 was varied during the test while keeping the total beam I1 + I2 constant = 0,1 nA/cm2. The result was a variation of the mean incoming energy and an increasing surface potential with the mean energy.

The strut was covered with metallized kapton which was found to exhibit arcing if not grounded.

So, in the author's think, there is at least one category of elements for which day-side environment constitute the worst case, we could call them: "pure thick dielectrics in the shadow". The proposition is opened for further evaluation.

5.3 Nigth-side worst case for "conductive dielectrics"

The night-side environment is considered since the earliest investigations on spacecraft charging as a worst environment.

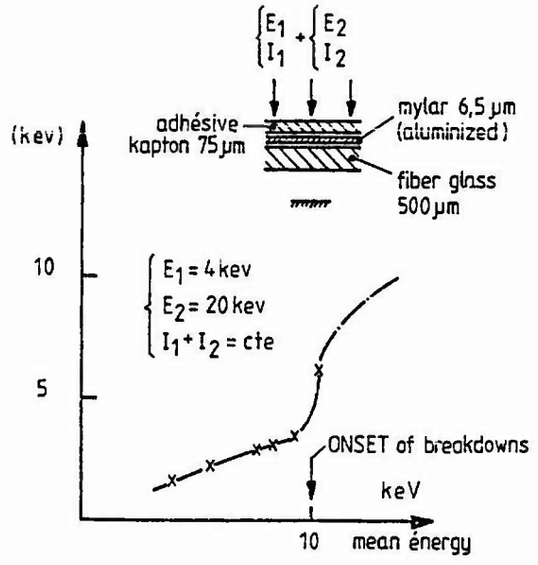


Figure 10 - Floating surface response to combined energy irradiation with two beams : mean energy is $(E_1 I_1 + E_2 I_2)/(I_1 + I_2)$

The paper purpose is only to emphasize that this fact is connected to the conductivity properties of the used materials. Two figures from the literature will be proposed. First is Figure 11 from (Ref. 9) that shows the differential charging distribution of the kapton as a function of local time. Differential charging occurs when the higher intensities are available on the orbit in the midnight-to-dawn section.

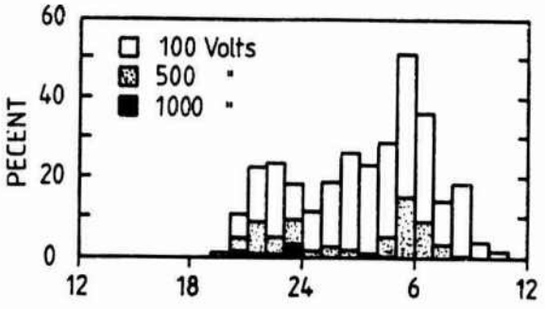


Figure 11 - One hour local time histograms of charging probabilities for the near geosynchronous orbit (L = 6.6 ± 0.4 Re). (Ref. 09)

The second is Figure 12 from Ref (11). It shows the local time anomalies distribution on-board the MARECS-A satellite. It shows simultaneously the probability of occurrences of intensities higher thar a certain value (500 pA/cm^2). That is exactly in the paper conception a case of "intensity governed potential". The similarity between Figures 11 and 12 is remarkable. MARECS-A outer surface was mainly Kapton (75 micrometers).

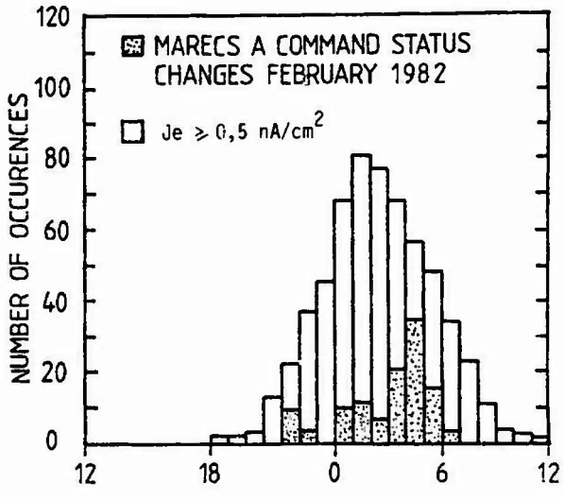


Figure 12 - one hour local time occurrences of electron fluxes 500 pA/cm^2 and anomalies (Ref. 11)

6. CONCLUSION

The exposed theory is an attempt to a unified conception of spacecraft charging and induced anomalies.

It was aimed at demonstrating that the concept of worst case experiment could be dependent on material properties. Discharges in the day-side of the geostionary orbit had never been thought before as the consequence of locally built, higher surface potentials. The most widely proposed explanation was to explain there discharges as the result of internal dielectric charging by penetrating high energy electrons through shielding defects due to thinner skin.

The data from SCATHA showing that maximum average energy occurred in the day-side section make pure dielectrics (or floating structures in the shadow) good candidates to exhibit locally higher potentials than in the night-side.

The exposed theory is very simple. It postulates that significant potentials on conductive dielectrics will require rather high incoming electron fluxes that are present only on the midnight-to-dawn section of the orbit (this was already known). Conversely, pure dielectrics or floating structures will present their highest possible potential in the noon section of the orbit where maximum electron energies are encountered.

How a given satellite behave, where and when does it discharge will obviously depend on how it is made.

REFERENCES

(1) Mc Pherson, D.A. and Schober, W.R., Spacecraft charging at high altitudes, the Scatha satellite program, Progress in Astronautics and Aeronautics Spacecraft charging by magnetospheric plasmas, Vol. 47; Ed. A. Rosen, AIAA N.Y. 1976

(2) Météosat spacecraft charging investigation, A. Robbins, Esa Contract 3561/78F/GG/SC, march 1979

(3) H.B. Garret, A.F.G.L. Hanscom Afb, Mass. Bedford, Spacecraft charging a review, Space Systems and their interaction with earth space environment Progress in Astronautics and Aeronautics, Vol. 71, Martin Summerfield series, Ed. H.B. Garret, C.P. Pike

(4) N. John Stevens, Interactions betwwen spacecraft and the charged particle environment, Spacecraft charging technology 1978, Nasa Conference Publication 2071, Afgl/TR-79-D082

(5) G.W. Schnuelle, D.E. Parks, I. Katz, M.J. Mandell, P.G. Steen, J.J. Cassioy (Systems science and software), A. Rubin (AFGL), Charging analysis of the Scatha Satellite, Spacecraft charging technology, 1978, Afgl-Tr-79-0082

(6) R.F. Willis and D.K. Skinner, Secondary electron emission yield behaviour of polymers, Solid State Communication, Vol. 13, pp. 685,688, 1973

(7) J. Bourrieau, L. Levy, A. Paillous, Onéra/cert Derts Toulouse, Détermination of material characteristics, TV Sat Contract, n° 241

(8) Carolyn K. Purvis, L.R.C., Status of materials characterization studies, Spacecraft charging technology, 1978, AFGL-TR-79-0082

(9) P.F. Mizera and G.M. Boyd, The Aerospace Corp. El Segundo, CA, a summary of spacecraft charging results, AIAA 82-0268

(10) E. Gary Mullen, David A. Haroy, AFGL, Henry B. Garret, JPL California Institute of Technology Elden C. Whipple, University of California at San Diego, P78-2 Scatha environmental data-atlas, Spacecraft charging technology conference, 1980, AFGL-TR-81-0270

(11) R. Grard, K. Knott and Pedersen, ESA, Spacecraft charging effects, Space Science Review, 32, (1983), p. 289

STATUS OF CRITICAL ISSUES IN THE AREA OF SPACECRAFT CHARGING

J.E. Nanevicz and R.C. Adamo

SRI International, Menlo Park, California 94025, U.S.A.

Abstract - Over the past decade, a aubatantial effort haa been made to increase the available knowledge relating to the causes and effecta of the spacecraft charging phenomenon. To thia end, numerous theoretical studies, laboratory tests, computer simulations, aa well aa limited in-orbit meaaurements, have been performed.

In general, the phenomenon of spacecraft charging involves the complex space environment interacting with a structure made up of regions of metal and dielectric materials whoae electrostatic properties are not generally conaidered in spacecraft deaign and fabrication. The charge stored by tne dielectrics may, in turn, lead to electrical dischargea.

Although considerable progress has been made in the three technical areas mentioned above:

- Environment definition
- Interaction
- Discharge characteristics,

it appears that certain critical questions have not yet been adequately answered, particularly in the areas of interaction and discharge characteristics.

This paper discusaes several of these questions, the reasons for their importance, and posaible approaches to their resolution.

I - INTRODUCTION

Spacecraft charging occurs when the exterior aurfaces of a satellite interact with the orbital environment and become electrically charged. The process is of great interest to satellite builders and operators because electrical discharges can result, generating electromagnetic noise, releaaing contaminants, and causing degradation of the insulating materials from which the dischargea occur.

Some of the major technical considerations important to spacecraft charging are illustrated in Figure 1. Firstly, the process is critically dependent upon the presence and properties of the orbital charged particle environment. From the scale on the left of the figure, we note that the ambient particle environment is highly general (i.e., independent of the characteristics or even presence of a satellite).

In the next step, the orbital particles interact with the satellite aurfacea to produce electrical charging of the satellite frame and of insulating materials on the surface. (It should be noted that insulating materials are used because of their sometimes critical thermo-optical propertiea, so that the designer muat proceed with extreme caution in replacing theae materials or modifying them in any way.) From the left side of the figure we note that, since the material propertiee affect the outcome of the interaction, the results are somewhat less general, although they ahould be reasonably applicable to all satellites using the same materials in similar configurations.

In the third atep, electrical discharges occur producing various deleterioua effects on the satellite and its syatema. From the left side of the figure, we note that these processea are even more vehicle specific. The occurrence of

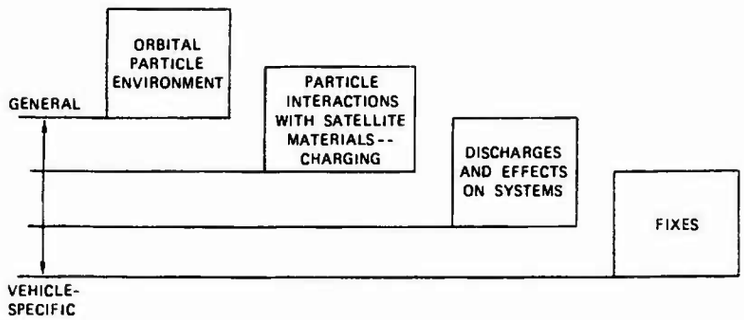


FIGURE 1 TECHNICAL CONSIDERATIONS IN SPACECRAFT CHARGING

discharges depends not only upon surface material properties, but also upon details of installation. Coupling of noise and its effects on systems depend on satellite construction details and on system vulnerability levels.

In the fourth area--the development of fixes--consideration must be given to all of the specific features of the satellite in question including: materials, construction techniques, and basic system susceptibility. Thus, at the left side of the figure we note that this technical area is highly vehicle specific.

II - STUDIES OF THE SPACECRAFT CHARGING PROBLEM

A. Experimental Studies

As indicated in Figure 2, spacecraft charging to large potentials was first reported by DeForest in 1972[*1] and the resulting discharging was detected on an orbiting satellite by Nanevicz, Adamo and Shaw in 1973[2]. Since that time, however, the study of the charging processes involved and their effects has proceeded in a random and uneven manner. Much of the reason for the lack of continuity and balance in the study of spacecraft charging stems from the fact that experiments on synchronous-orbit aatellites are substantially more difficult than are laboratory experiments. Thus, since the orbital experiments of Ref 2, only the P78-2 (SCATHA) satellite[3] has been instrumented specifically for the in-orbit study of spacecraft charging. In the interim, experimental activity has focused on the conduct of laboratory experiments[4,5], and on the development of improved simulation techniques[6,7].

A further reason for the uneven development of a more complete understanding of spacecraft charging is that, as shown in Figure 3, the overall problem has several facets that may very legitimately be studied independently. The principal technical areas of significance in spacecraft charging and their roles may be summarized as follows:

1. Environment

A description of the particle types and their energies present during a substorm is important strictly on a scientific basis and because it provides insight into what may be required to properly simulate the space envrionment in the laboratory.

2. Interaction of Environment with Satellite Materials

Proven techniques to account for and quantify the electrical behavior of aggregates of conducting and insulating materials during a magnetic substorm are important in predicting available stored energies and behavior of specific materials.

3. Characteristics of Discharges Resulting from Spacecraft Charging

The characteristics of the discharges produced on spacecraft materials are important in several regards. Knowing which materials are responsible and understanding their electromagnetic characteristics allows the designer to choose between several alternativea such as:

- Avoiding their use
- Controlling their placement

* References are listed at the end of the paper.

1972	• ATS 5 SATELLITE--DE FOREST — DEMONSTRATED SATELLITES CAN CHARGE TO HIGH POTENTIALS
1973	• NON-NASA SYNCHRONOUS ORBIT SATELLITE--NANEMICZ, ADAMO, SHAW -- DEMONSTRATED OCCURRENCE OF DISCHARGES DURING SUBSTORMS — SHOWED DISCHARGES CORRELATED WITH OPERATIONAL ANOMALIES
BEGINNING 1973	• LABORATORY AND ANALYSIS--MANY WORKERS — SIMULATORS ASSEMBLED AND USED FOR EXPERIMENTS -- CHARGE DEPOSITION IN MATERIALS -- DISCHARGE CHARACTERIZATION — ANALYSES MADE OF CHARGE DEPOSITION AND DISCHARGE TRIGGERING -- NASCAP CODE
1979	• SCATHA SATELLITE PROGRAM--MANY EXPERIMENTERS — SUBSTANTIAL STRESS ON DEFINING SPACE ENVIRONMENT -- GENERATED DATA ON CHARGE DEPOSITION — LIMITED DATA ON DISCHARGE SOURCE CHARACTERISTICS
TODAY	• NEEDS (EXISTING VOIDS) — INFORMATION FOR ENGINEERS AND DESIGNERS -- DISCHARGE CHARACTERISTICS -- MATERIAL BEHAVIOR IN SPACE -- ADEQUACY OF SIMULATION TECHNIQUES

FIGURE 2 HISTORY OF SPACECRAFT CHARGING STUDIES

- Electromagnetically hardening the satellite to render it immune to the effects of the discharges.

In addition, information on the properties of the discharges occurring in space is essential to the development and validation of schemes for the simulation of spacecraft charging in the laboratory, and for the development of standards and specifications.

4. Coupling to Systems

The design engineer needs to know how electromagnetic pulses generated by discharges on the outside of the vehicle excite the structure and couple to the satellite wiring system on the interior. Although, strictly speaking, the electromagnetic coupling is not caused by spacecraft charging, the way the vehicle is excited and coupling occurs is very sensitive to the location and character of the discharges.

5. Systems Affected

The susceptibility of satellite electronic systems to the pulse interference stemming from spacecraft charging is of importance to the designer in devising schemes for assuring system immunity. Here again, although susceptibility cannot be attributed to spacecraft charging, the degree of susceptibility of systems is affected by the properties of the signal radiated by the discharge.

B. Degree of Understanding of the Technical Areas

As was mentioned earlier, progress in the various technical areas comprising spacecraft charging has been uneven. The various facets of the problem pose varying degrees of difficulty in

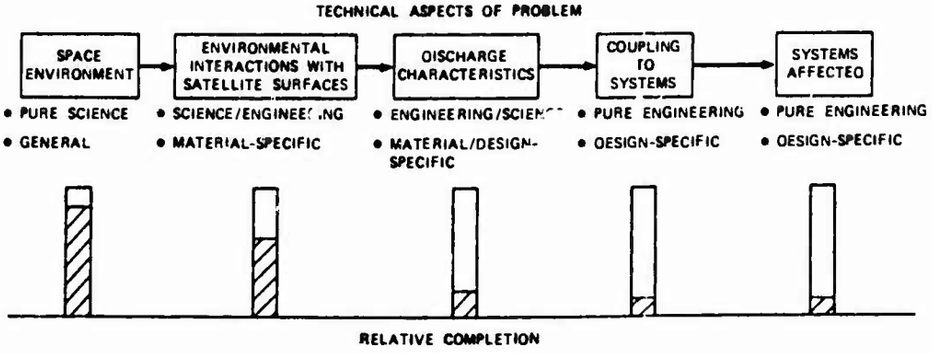


FIGURE 3 PERSPECTIVES ON SATELLITE CHARGING PROBLEM

their study. Also, developments in the underatanding of one area (such as interaction processes) must wait for the prior work in another (such as definition of the basic charging processes). Thus, as indicated graphically in the lower part of Figure 3, the several technical areas have developed generally as follows:

1. Environment

The study of this area is very fundamental in that it involves carrying sensors designed to sample the environment at the orbits of interest. Care must be taken to assure proper calibration of the sensors and to avoid data contamination by the presence of the aatellite and its sensors. Adequate instruments have been orbited for sufficient time to provide substantial insight into the properties of the environment. In general, this facet of the spacecraft charging problem is most completely defined.

2. Interaction

This area is more material- and design-specific since it involves material properties as well as the characteristics of the environment. The problem has been studied in the laboratory--beginning with the studies of Adamo and Nanevicz[8] and continued by Stevens and Purvis[9] and many others. Analytical studies were carried out by Katz et al[10] culminating in the NASCAP code for predicting charge accumulation on various satellite surfaces. Unfortunately, orbital experiments to verify the validity of the laboratory work and analyses have been very few. Data from the SCATHA satellite reported by Mizera et al[11] verified the general behavior observed in the laboratory studies with modulated illumination.[8] Laboratory work by Adamo and Nanevicz[12] indicating that Kapton should become progressively more conducting--and less able to store charge--with exposure to sunlight in orbit has been verified by experiments on SCATHA as reported by Vampola.[13] The SCATHA satellite carried provisions for the study of the charging behavior of a carefully selected set of material samples. Doing more extensive material studies on a single satellite would probably be out of the question. In general, making an effort to enlarge the material sample base, and to refine the measurement scheme would be worthwhile if launch opportunities present themselves. Experiments should be designed to answer questions raised in connection with the application of NASCAP and in connection with normal satellite operation.

3. Discharge Characteristics

This problem is substantially more difficult and less well understood since it presupposes an understanding of both the environment and of the way it deposits charge in satellite materials. Given that sufficient charge is stored in a material, a discharge is triggered at a unique place in the material. The discharge taps the stored charge causing currents to flow and generating plasmas which combine to produce an electromagnetic pulse.

The properties of these pulses were first studied by Nanevicz and Adamo[14] in connection with the development of instrumentation for the satellite measurement program described in Ref 2. Later they studied the electromagnetic signals generated by discharges in a special "electromagnetically clean" setup in the laboratory.[5]

The instrumentatiou on the P78-2 SCATHA satellite included provisions for periodically measuring the transient pulse signals induced in a short dipole antenna at the end of a 2-meter-long boom on the exterior of the satellite.[3] The sophisticated instrumentation used for this measurement precluded its dedication solely to the study of external fields. As a result, the instrumentation spent three-quarters of its available time monitoring signals existing at three points on the interior of the satellite.

The location of the external-transient sensor antenna at the end of a boom on P78-2 SCATHA was unfortunate since it violated the fundamental sensor size requirements for transient signal study, i.e., that the "sensor" must be sufficiently small that antenna ringing occurs at frequencies above the range of interest.[15] Thus, the exterior discharge data from SCATHA are complicated by the presence of antenna/boom ringing.

Since P78-2 SCATHA carried only one sensor to measure the exterior transient electromagnetic environment, it is not possible to determine where on the exterior of the satellite a discharge

occurred. This lack of information about discharge source locations also makes it impossible to infer absolute discharge source strength from the data.

Finally, it must be recognized that P78-2 SCATHA is only a single satellite made using the materials and fabrication processes selected by the builder. Since the charge storage and discharge processes are both material specific and since the triggering of discharges is highly dependent on the mechanical arrangement, the discharging behavior observed on this satellite may differ substantially from what would have been observed had SCATHA been assembled by another contractor. Thus,, there are major uncertainties remaining in our ability to describe the discharging behavior of satellites in general.

4. Coupling to Systems

The problem of coupling transient electromagnetic pulses into systems is not unique to spacecraft charging. Problems of this sort arise in connection with the assessment of system vulnerability to lightning and the nuclear EMP, and a great deal of work has gone into the study of these problems. In general, it is found that coupling is critically dependent on the design details of the system in question--design of shields, penetration treatments, aperture treatments etc.--as well as upon the physical location and electromagnetic properties of the source. For example low frequencies penetrate a system most readily along penetrating electrical conductors, while high frequencies can propagate easily through apertures in the shield structure.

Thus, although many of the experimental and analytical tools for the determination of discharge coupling to systems are available in principle, progress in this area is being held back by the lack of orbitally confirmed information on the electromagnetic properties of spacecraft discharges and on their probable locations on satellites. Such information is needed for inclusion in the standards and specifications applied during the evolution of a satellite. The same sort of information is needed to guide the development and application of pulse simulation sources for ground testing of satellites and their subsystems.

5. Affected Systems

This facet of the spacecraft charging problem also is not unique. In general, electronic systems must be designed to function in an environment including electromagnetic interference sources. Specifications are levied on the designers of the satellite system (e.g. MIL STD 1541) and its subsystems (e.g. MIL STD 461/462) in an effort to assure that they will not be adversely affected by the operational environment. Care must be exercised to assure that these specifications are as representative as possible of the actual environment in order that the systems not be either overdesigned or underdesigned.

In this regard, it is important to recognize that modern spacecraft electronic systems depend to a great extent on digital components, and, as a consequence, are particularly vulnerable to pulsed interference of the sort generated by the electrical discharges associated with spacecraft charging. Accordingly, designers require accurate information regarding the characteristics of the pulse signals they can expect on their systems as a consequence of spacecraft charging. The problem of system upset and damage by transient pulses is currently receiving a great deal of attention by the lightning and nuclear EMP communities. Thus, many of the tools and concepts needed to attack this facet of the problem are available. The principal need at this time is accurate information about the characterisitics of the electromagnetic threat caused by spacecraft charging.

III-THE INTERFERENCE CONTROL PROBLEM

The general interference control problem is shown in Figure 4. A source of electromagnetic interference exists, and interacts with a victim system via one or more coupling paths. The degree to which the designer must be concerned with this problem depends upon the strength of the source, the susceptibility of the victim and the character of the coupling path.

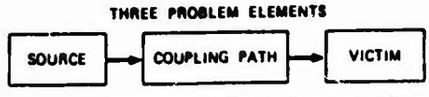


FIGURE 4 ENGINEERING VIEW OF INTERFFRENCE CONTROL PROBLEM

TYPICAL OPTIONS:

ELIMINATE SOURCE	REDUCE COUPLING	HARDEN VICTIM
— NEW MATERIALS	— SHIELDING	— PIN TREATMENT
— MODIFIED SURFACES	— CONTROL OF ELECTROMAGNETIC PENETRATIONS	— BOX SHIELDING
— MODIFIED CONFIGURATIONS	— CLOSURE OF GAPS IN SKIN	— CIRCUIT TREATMENT
— ELECTRICAL BONDING	— APERTURE TREATMENTS	— ERROR CORRECTION TECHNIQUES

FIGURE 5 CONSIDERATIONS IN DEVELOPING FIXES

Since the severity of the overall problem depends upon the properties of the three principal elements it follows that the problem of assuring immunity can be attacked, at any one or all of the elements, by striving to:

- eliminate the source
- control the coupling
- harden the victim.

In general, a properly engineered solution requires information on each of the major elements. In particular, the properties of the source are highly critical since they establish the levels and frequency characteristics which must be considered in the design.

A list of some of the options one can consider in devising schemes to assure system immunity to spacecraft charging is shown in Figure 5. In general, it is prudent to consider all of the possible options in evolving a design.

1. Source Elimination

First, the designer can strive to eliminate the discharge source through various approaches. For example, he can attempt to prevent charge storage in the dielectrics on the exterior of the satellite. This can be accomplished by increasing the conductivity of the bulk material or by applying optically-transparent, electrically-conductive films on the outside surface. Since modifying the material in any way is likely to affect its thermo-optical properties, these modifications must be restricted to the minimum possible extent consistent with achieving the desired goal. This, in turn, implies that laboratory charging simulators must be available that are capable of duplicating the critical facets of the orbital environment with adequate fidelity to ensure that the desired system behavior will be ultimately obtained in space. (In fact, we must first determine which features of the environment it is important to duplicate.)

Alternatively, the designer may choose to permit charge accumulation, but to install the dielectrics in such a way as to inhibit the occurrence of discharges. For example, in laboratory experiments, discharges generally initiate at the edges of materials, and it is often found that surrounding the dielectric with a metal frame with rounded edges tends to inhibit discharges. Again, to test this scheme it is necessary to have available an adequate laboratory charging simulator. (We must know that behavior in the simulator duplicates behavior in orbit.)

Finally, the designer must ensure that all electrically-conducting elements of the satellite are electrically bonded to each other. This includes parts of the thermal control materials such as the layers of thermal blankets. If the satellite includes unbonded conductors, they can charge to potentials different from their surrounding elements leading to sparking between adjacent conductors. The measures taken to ensure bonding are sufficiently gross that relatively unsophisticated simulation and testing techniques may be used to verify their adequacy.

2. Coupling Control

As was indicated earlier, the designer may choose to apply electromagnetic coupling control techniques to achieve immunity to spacecraft

charging. In general, even if other techniques, (such as source elimination,) are also pursued, it is useful to pay attention to coupling control because many of the major interference distributors (such as ground wires penetrating shields) can be treated for virtually zero cost.

Modern approaches to transient interference control have been described by Vance,[16] and can be applied to satellites. Conceptually, the modern approach consists of establishing one or more closed electromagnetic barriers between the source and the victim. Each barrier consists of a topologically closed metallic shield with special treatments at all of the imperfections such as penetrating wires, joints, and openings. Essentially, the designer needs to assure himself that he has taken every reasonable step to "close" the barrier.

Some of the barrier violations such as penetrating ground conductors can be treated by simple expedients at virtually no cost. Others, such as the installation of filters or limiters on penetrating power conductors, impose penalties including cost, weight, space, and--perhaps most important--decreased reliability or the potential for a single-point failure. Thus the designer is faced with the need to apportion his efforts at coupling control intelligently. He needs to know where on the satellite the discharge sources are likely to occur, and he must be able to define their electromagnetic properties in order that he neither overdesign nor underdesign the coupling control system.

3. Victim Hardening

Finally, it is possible to take steps to make the victim circuits more immune to the transient electromagnetic environment. One approach is to establish a small electromagnetic barrier at the subsystem box level. Metal boxes are used to establish the barrier topology, pin treatments (filters and limiters) may be installed on penetrating conductors, or shields may be used on interconnecting cabling. In addition, basic circuit design may be reviewed and modified to eliminate particularly susceptible circuits. Software changes can be used to incorporate error correction techniques. In general, consideration must be given to basic system hardness as satellite design progresses, but often it is difficult to make major changes in system hardness at this level. Many units are affected, and the ramifications of any change must always be carefully reviewed.

Since satellite electronic systems are built to function in a specified electromagnetic environment, the satellite designer/builder needs to be able to specify this anticipated environment with substantial accuracy in order that he provide the subsystem contracter with reasonable specifications. The environment on the inside of the satellite is determined by the characterisitics of the discharge source and the coupling paths. Although analytical and experimental techniques exist to estimate this environment, it would be highly profitable to make provisions on orbiting satellites to define this interior electromagnetic environment, and to compare it to the discharge properties. Such orbital data would provide a check on our ability to predict satellite electromagnetic behavior. Measurements on internal circuits would also provide valuable information on ambient noise levels in typical satellites.

Very little orbital information of this sort exists today. Satellites do not ordinarily carry instruments to characterize the electromagnetic environment. Even on SCATHA it was difficult to correlate internal noise pulses with external discharges.

IV-ORBITAL DATA REQUIREMENTS

As was indicated earlier in connection with the discussion of Figure 3 in Section IIB, the engineering aspects of the spacecraft charging problem could benefit from additional orbital data. In particular, it appears that great benefit would accrue from data in three basic areas:

1. Identification of Materials Displaying Susceptibility in Orbit

This information would alert designers of particularly susceptible materials, and would define likely discharge locations on satellites using the same materials. Localization of dishcarge sources coupled with measurements of pulse amplitude at a known location on the exterior

of a satellite allows the absolute source intensity to be estimated.[15]

Identification of susceptible materials together with the definition of absolute source intensity would serve to prioritize the development of noise coupling controls or the replacement of materials.

2. Quantify Discharge Characteristics in Orbit

This information is essential for the definition of the noise source to be used in system vulnersbility assessments, either analytical or experimental. Orbital discharge source characteristics are needed to guide the development of ground testing techniques--in particular, the development of discharge simulators. This same information is also needed to update the standards and specificiations used in the development of satellites.

Note: A comparison of the data of items 1 and 2 with the results of laboratory simulations serves to provide a number of important insights. First, it helps to define the fidelity required in ground simulations. The orbital environment is complex, and it is very costly to duplicate all features of that environment. Second, such comparisons are needed to develop assurance that laboratory simulations adequately duplicate orbital behavior. Third, such information would be valuable in determining areas in which ground simulations must be improved.

3. Characterize Internal Noise Pulse Environments on Typical Satellites

This information is useful in establishing the "noise-floor" levels typically found in satellites as the result of satellite system operations such as power switching. (It doesn't make sense to strive to reduce externally-generated noise appreciably below this level.)

Information on the level and character of noise coupled from known external sources would be extremely valuable in permitting an assessment of our ability to predict the coupling of signals from the exterior. This is a complex process involving satelite resonances, aperture/penetrator coupling (which acts as a filter), and finally wiring resonances, so that the pulse is greatly modified in coupling to the interior--both in amplitude and in form. Orbital confirmation of the accuracy of available prediction techniques is badly needed.

V - ORBITAL MEASUREMENTS

In considering possible approaches to obtaining orbital engineering data, it is important to bear in mind that the measurement system will undoubtedly have to be carried at the last minute on a "piggy back" basis on operational satellites. Accordingly, both the electronics and the sensors required should be small, simple, reliable, flexible, and require little power and little telemetry.

An approach based on the SRI Transient Pulse Monitor flown on the SCATHA satellite[3] is shown in Figure 6. Provisions are made to characterize pulses both on the inside and on the outside of the satellite. The external measurements are made at several locations to permit source localization of the sort described in Ref. 15. (A system to accomplish discharge localization on a satellite in orbit is presently being developed by Taillet and Boulay at ONERA in Paris.[17].) Thus, the system will provide information on the relative susceptibility of different satellite materials. Since the source is localized and its properties are measured at several known positions on the surface of the satellite, a first order quantification can be made of absolute source characteristics.

Various internal measurements can be made to obtain data of varying degrees of fidelity. If a system is known to be susceptible in orbit, a sensor can be arranged to monitor this specific system "sensitive box." Other sensors can be used to monitor parameters of more general interest. For example, one or more can be arranged to record data useful in assessing our prediction capabilities.

The system of Figure 6 can be simplified to incorporate the barest minimum number of sensors monitored, and parameters measured, for use as a housekeeping monitor to be routinely carried on satellites. Currently, there are sufficient uncertainties about many facets of spacecraft charging that carrying such monitors in the immediate future would be highly useful in

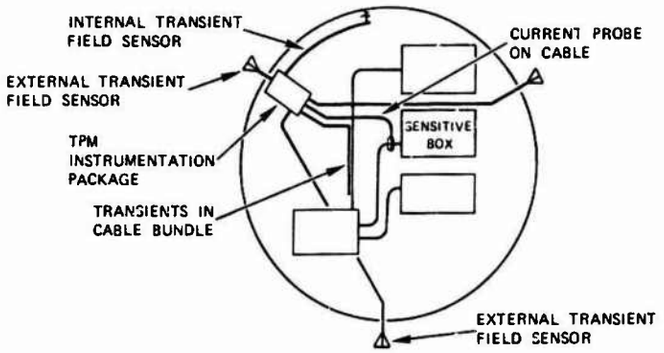


FIGURE 6 INSTRUMENTATION/SENSOR CONFIGURATION

resolving. Now, when a satellite experiences anomalies, the investigating team is forced to use second and third level inferences regarding the possibility of spacecraft charging. Many important decisions are made on the basis of such incomplete data. Presently, many satellite operating agencies depend on ground commanded circumventions to avoid possible operational problems stemming from spacecraft charging. Developing a network to permit operators to alert one another of the occurrence of substorms and spacecraft charging would therefore be extremely useful.

VI-SUMMARY & CONCLUSIONS

Based upon the above discussions, it appears that a key requirement for improving the overall effectiveness of presently available spacecraft-charging control techniques is to obtain a better understanding of the actual in-orbit discharge process and its characteristics. This information is criticaly needed to improve ground-test techniques and facilities and to allow more meaningful noise coupling and circuit susceptibility analyses and design improvements.

This information could most reliably and accurately be obtained by taking advantage of payload opportunities, to the greatest extent possible, to incorporate appropriate, properly-designed discharge detection and characterization instrumentation on present and future spacecraft programs.

REFERENCES

1. S. E. DeForest, "Spacecraft Charging at Synchronous Orbit," J. Geophys. Res., Vol. 77, No. 4 (February 1972).

2. J. E. Nanevicz , E. C. Adamo and R. R. Shaw, "Electrical Discharges Caused by Satellite Charging at Synchrounous Orbit Altitudes," 1975 Lightning & Static Electricity Conference, Culham Laboratory, England (1975).

3. J. R. Stevens and A. L. Vampola, "Description of the Space Test Program P78-2 Spacecraft and Payloads," Final Report SAMSO TR-78-24, Space and Missile Systems Organization Air Force Systems Comand, (October 1978).

4. N. J. Stevens, F. D. Berkopec, J. V. Staskus, R. A. Blech, and S. J. Narcisio, "Testing of Typical Spacecraft Materials in a Simulated Substorm Environment," Proceedings of the Spacecraft Charging Technology Conference, AFGL-TR-77-0051, Air Force Geophysics Laboratory, (February 1977).

5. J. E. Nanevicz, R. C. Adamo, B. L. Beers and T. N. Delmer, "Electromagnetic Fields Produced by Simulated Spacecraft Discharges" AFGL-TR-81-0270, 1980 Spacecraft Charging Technology, NASA Conference Publication 2182, (November 1980)

6. J. E. Nanevicz and R. C. Adamo, "A Rugged Electron/Ion Source for Spacecraft Charging Experiments" Proceedings of the Spacecraft Charging Technology Conference, AFGL-TR-77-0051, Air Force Geophysics Laboratory, (February 1977).

7. R. C. Adamo and J. E. Nanevicz, "Development of a Continuous Broad-Energy-Spectrum Electron Source," Proceeding of the Spacecraft Envionmental Interactions Conference, NASA/Lewis Research Center, (October 1983).

8. R. C. Adamo and J. E. Nanevicz, "Chemical Phsics of Charge Mechanisms in Nonmetallic Spacecraft Materials," Final Report, Contract F49620-77-C-0113, SRI Project 6402, SRI International, Menlo Park, Calif. (May 1979).

9. C. K. Purvis, N. J. Stevens, and J. C. Oglebay, "Charging Characteristics of Materials: Comparison of Experimental Results with Simple Analytical Models," Proceedings of the Spacecraft Charging Technology Conference, AFGL-TR-77-0051, Air Force Geophysics Laboratory, NASA TMX-73537, (February 1977).

10. I. Katz, D. E. Parks, S. Wang, and A. Wilson, "Dynamic Modeling of Spacecraft in a Collisionless Plasma," Proceedings of the Spacecraft Charging Technology Conference, AFGH-TR-77-0051, Air Force Geophysics Laboratory, (February 1977).

11. P. F. Mizera, et al, "First Results of Material Charging in the Space Environment," Aerospace Report No. TOR-0081(6506-01)-1, Contract No. F04701-80-C-0081, Space Division Air Force Systems Command Los Angeles Air Force Station, (March 1981).

12. R. C. Adamo and J. E. Nanevicz, "Effects of Illumination on the Conductivity Properties of Spacecraft Insulating Materials", Final Report NASA CR-135201, Contract NAS3-20080, SRI Project 4904, SRI International Menlo Park, Calif., (July 1977).

13. A. L. Vampola, "P78-2 Engineering Overview, "AFGL-TR-81-0270, 1980 Spacecraft Charging Technology, NASA Conference Publication 2182, Air Force Geophysics Laboratory, (November 1980).

14. R. C. Adamo and J. E. Nanevicz, "Spacecrsft-Charging Studies of Voltage Breakdown Processes on Spacecraft Thermal Control Mirrors", Progress in Astronautics and Aeronautics, Volume 47, American Institute of Aeronautics and astronautics New York, New York, (1976).

15. J. E. Nanevicz and R. C. Adamo, " Laboratory Studies of Spacecraft Response to Transient Discharge Pulses," Proceedings of the Spacecraft Environmental Interactions Conference, NASA/Lewis Research Center, (October 1984).

16. E. F. Vance, "Electromagnetic Interference Control", IEEE Trans. EMC, Vol. EMC-22 No. 4 pp. 319-328 (November 1980).

17. J. Taillet, J. Boulay, private communication.

SPACECRAFT MATERIALS TEST IN A CONTINUOUS, BROAD ENERGY-SPECTRUM ELECTRON BEAM*

M. Blez, J. Thayer and J.E. Nanevicz

SRI International, 333 Ravenswood Avenue, Menlo Park, California 94025, U.S.A.

Abstract - The electrostatic charging and subsequent discharging of external spacecraft thermal-control materials is a result of complex interactions with the temporally and spatially varying ambient space environment. The validity of laboratory studies of these interactions may be highly dependent upon how well the important features of that environment are simulated.

In the past, various practical limitations have caused most simulation experiments to be conducted using a constant, monoenergetic electron beam to simulate the charging processes occurring in space during a magnetic aubstorm. During the past year, the confluence of several events provided an opportunity to conduct laboratory experimenta under more realistic conditions: The development of the SRI multienergy multipactor electron gun was completed, diagnostic instrumentation was on hand, and one of the authors (Blez) was available for a period of 8 months as an SRI International Fellow to conduct the experiments.

This paper describes some of the observed similarities and differences in the behavior of several typical apacecraft thermal control materials when exposed to a mono-energetic electron beam and to a more realistic continuous broad energy-spectrum electron beam.

I - INTRODUCTION

As indicated in a companion paper, the various disciplines given the collective title of "Spacecraft Charging" have evolved in an uneven wsy.[1] As a reault, the understanding of important issues in a number of areas is substantially deficient. The measurement program discussed here wss undertaken to provide insight into one facet of the spacecraft charging problem. This program became possiole as the result of the fortuitous confluence of several events: The development of a multienergy electron gun at SRI,[2] and the presence of one of the authors, Blez, as an SRI International Research Fellow for most of 1984.

The choice of topic for this investigation stemmed from the observation that the electrostatic charging and subsequent discharging of external thermal-control materials on spacecraft is a result of complex interactions of these materials with the temporally and spatially varying ambient space environment.[3,4] As a result, the validity of laboratory studies of these interactions may depend highly upon how well the important features of that environment are simulated.

To date, many independent laboratory studies of the charging and discharging properties of spacecraft materials have been performed using monoenergetic electron sources (initially such sources were used because they were the only ones resdily available). Although a great deal has been learned from these studies, a disturbing number of discrepancies remain between the test results and actual in-orbit observations of spacecraft charging and discharging. For example, SRI discharge-detection instrumentation on a non-NASA geosynchronous satellite during 1974[5] indicated that electrical discharges (and in some cases resulting anomalies) occur at times when they would not be expected according to the results of laboratory tests. Also, the behavior of a particular fabric material sample in orbit on P78-2 (SCATHA) differed substantially from its behavior in laboratory tests using a monoenergetic electron source.[6]

Preliminary tests at SRI using a rudimentary multienergy electron gun indicated that there could be substantisl differences in the charging and discharging behsvior of spacecrsft materials when

*The work reported here was conducted under an element of SRI's internal research and development (IR&D) program. This element focuses on the development of laboratory techniques and instrumentation for the study of flight vehicle electrification.

illuminated with a multienergy source rather than with a monoenergetic beam.[7] Similarly, the results of material charging tests performed using two separate monoenergetic electron guns at two discrete energies differed significantly from those obtained using a monoenegetic electron source.[8,9] These differences raise questions regarding the degree of confidence that should be placed in the results of various ground tests.

Despite the engineering importance of dielectric charging and discharge characterization data, the information gathered in ground-based simulations has never been adequately validated by similar measurements in space. Since planning and conducting orbital experiments is costly and time consuming, SRI concluded that a laboratory experiment tailored to provide insights into possible reasons for the spparent disparities between orbital and laboratory behavior of spacecraft materials would be very useful at this time.

The current theories of dielectric charging imply that the exact profiles of the internal chsrge distributions and, therefore, the magnitudes of the internal electric fields are determined by the details of the incident electron energy distribution.[10] These theories also suggest that the magnitude of the internal electric fields determine whether s discharge will take place. Accordingly, it was decided thst it would be highly instructive (and feasible at this time) to conduct a systematic study contrasting the electrical behavior of materials under monoenergetic (generally used in simulations) and multienergetic (more typical of the true orbital environment) electron beam illumination. Such measurements would provide insights into the degree to which imperfect simulation of the electron energy spectrum affected the credibility of laboratory experiments.

Reported here are the first results from an ongoing series of laboratory studies being conducted at SRI to investigate critical issues associated with laboratory simulations of spacecraft charging.

II EXPERIMENT DESIGN

A. General Concept

In concept, the experiments consisted of (1) illuminating identical samples of typical spacecraft materials alternately with monoenergetic and multienergy beams, and (2) looking for differences in the way the materials charged and discharged. This approach used existing instrumentation and facilities available at SRI and afforded an opportunity to investigate the degree to which deviations in the simulation of the orbital environment affected material behavior.

The test setup used in these experiments (Figure 1) is similar to the setup used earlier by Nanevicz et al.[11] to study the electromagnetic fields radiated by discharges from spacecraft materials illuminated by a monoenergetic electron beam. A cylindrical glass bell jar was mounted on a ground plane simulating the spacecraft frame and was evacuated to a few x 10^5 torr. A large-area electron source providing uniform illumination over the test sample was mounted at the top of the bell jar, and test samples were placed on a special test jig at the bottom of the jsr.

The inside of the jar was coated with an electrically conductive "radome" paint to prevent ststic chsrge accummulation on the jar wslls. However, the paint was of sufficiently high resistivity to be electromagnetically transparent at the frequencies of interest.

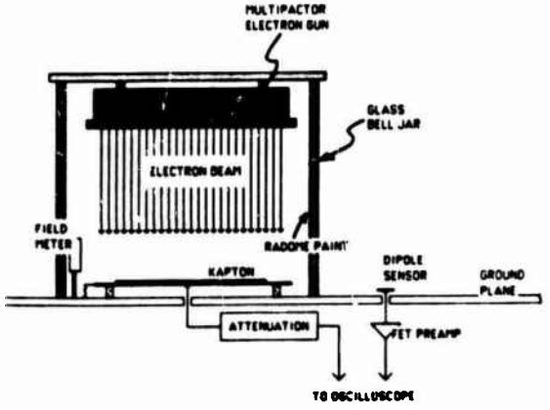


FIGURE 1 EXPERIMENTAL SETUP

Instrumentation included a small dipole E-field sensor (located in the near field, 30 cm from the bell jar center), which measured the electromagnetic field radiated by the discharge. A field meter located adjacent to the sample provided a reading proportional to the surface potential of the test sample. Also monitored were sample return current, electron beam current, and beam accelerating potential.

Simultaneous records were made of all measurements for later comparison.

B. Electron Source

The special electron source used in this experiment was developed at SRI International for use in spacecraft charging studies.[12,2] This source provides a large-area beam with independently controlled beam current, beam energy, and energy spectrum. Electrons are produced by multipactor breakdown between two large-area parallel plates and are extracted from between the plates by introducing a pattern of holes in one plate and biasing both plates negatively with respect to ground. A control grid was provided to control beam current, and a grounded accelerating grid was used to obtain the desired beam energies.

To produce monenergetic electrons, we used a simple copper screen as the accelerating grid.[12] A continous energy spectrum was produced by replacing this accelerating screen with a specially prepared foil sheet that provided scattering centers in the beam path. Incident electrons are scattered in traversing the target and give up energy to the target material. By the proper selection of foil materials, the probability of electron scatter can be manipulated and the desired energy spectrum can be produced.[2]

The electron energy spectrum used in these experiments represented a generic spectrum (Figure 2) and was not intended to simulate the details of any particular spectrum measured at geosynchronous orbit. This form was chosen because it is easy to produce with resonable beam efficiency and because it includes electrons with low energies that are typical of the orbital environment. The form of the spectrum at low energies, however, deviates considerably from the orbital environment. The absolute energy level of the eloctron spectrum could be adjusted by simply varying the voltage applied to the accelerating grid/foil.

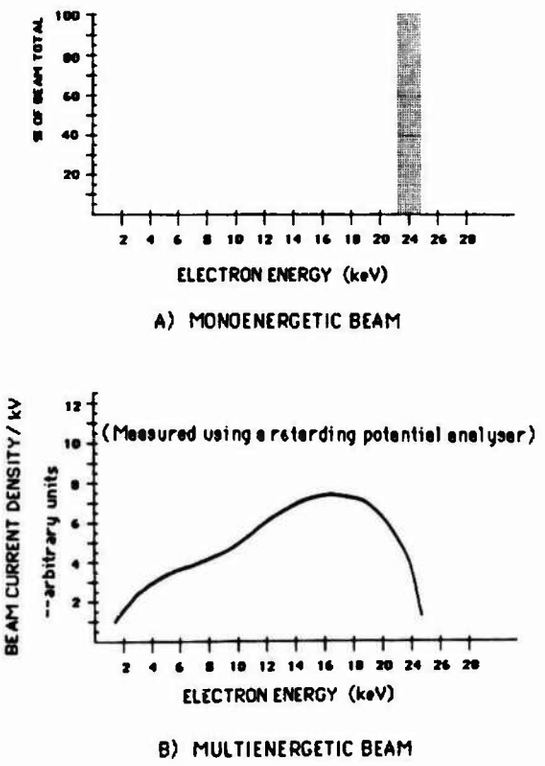


FIGURE 2 ILLUMINATING ELECTRON BEAM SPECTRA USED IN EXPERIMENTS

C. Electromagnetic Transient Measurements

For the measurements of radiated electric fields, we used instrumentation developed orginally for the work of Reference 11, but we refined and modified it for this program. The electric field probe consistsd of a small, capacitively loaded, electric dipole antenna with a self-contained FET preamplifier, so that the sensor output was directly proportional to the magnitude of the electric field at its location.[13] Thus, the sensor output provided a direct time waveform of the radiated electric field, E(t).

The sample-base return current was monitored by mounting the sample on a 33 cm diameter plate (Figure 1). The plate, in turn, was connected to the ground plane through 24 parallel, 50-ohm resistors equally spaced around its periphery. The terminating resistors installed in this way

minimized the tendency of the plate to ring when excited by a transient signal. To record the current, one resistor was removed and replaced by a 50-ohm coaxial cable leading to the 50-ohm input on a high-speed (1 GHz bandwidth) oscilloscope.

Sample surface potentials were monitored using a vibrating-reed electrostatic field meter (also developed at SRI). This device is an improved version of those sold commercially, since it is designed to function in a plasma environment and indicate ion current as well as local static electric field. Its output was fed into a 5 kHz bandwidth chart recorder.

D. Sensor Calibrations

Each sensor used in this investigation was calibrated by subjecting it to known transient or static fields. The radiated electric field sensor was placed in a 50-ohm parallel-plate transmission line driven by a pulse generator to produce a known transient field within. By reducing the length of the calibration pulse, we checked the frequency response of the sensor. The sensor was found to track the driving pulse to 5 ns.

The static field meter was calibrated by replacing the sample in the testing jig with a metal sheet connected to a power supply of known potential. A calibration of the base current sensor was not necessary, since the arrangement described constitutes a simple current divider.

III - EXPERIMENTAL PROCEDURE

Two spacecraft-charging simulation techniques were compared in this study. The first technique used a monoenergetic electron beam, typical of those used widely in earlier simulations of the space charging environment.[11,14,15] The second simulation technique used a continuous-spectrum, multienergy electron beam more typical of the orbital environment. Current densities of 0.3, 1.0, and 2.9 nA/cm^2 (typical of substorm conditions) were used. Beam energies were as shown in Figure 2.

Test material samples were made of Kapton, obtained from the normal suppliers of the aerospace industry. Samples were 75- and 127-μm- thick rectangles, 250 cm^2 in area, that were aluminized on one side. The results of preliminary experiments showed wide variation in the various sample responses to identical test conditions. Accordingly, a preparatory treatment was instituted for new samples to enssure that all samples had been identically conditioned prior to testing. Samples were peripherally bonded to the test jig using a border of conducting (copper) adhesive tape. (Discharge triggering is sensitive to edge treatment, and this was the mounting procedure used at SRI in the past.) The samples were then cleaned with pure ethyl alcohol, rinsed with deionized water, dried, and placed in the bell jar.

Either the mono- or multienergy accelerating grid was installed on the electron gun, and the chamber was evacuated to approximately 1×10^{-5} torr. Each sample was subjected to one particular energy spectrum, and the current densities were stepped through the range of values stated above. Simultaneous oscillograms were made of the radiated field and return current from each individual discharge. The discharges were numbered in chronological order. At each current density, testing continued until roughly ten discharges had been observed or until discharges from the sample stopped occurring. As a rule, tests with each energy spectrum were repeated three times, each time with a fresh material sample.

An additional test was performed to compare the samples' rates of charging and discharging under the two different simulations. A single large sample of 127-μm Kapton material was divided in half, and each half was exposed to one of the simulations. Beam current density in both cases was 5 nA/cm^2, and beam spectra were as shown in Figure 2. The static field meter installed in the bell jar was used to monitor the samples' charging and discharging behavior in the two test environments.

IV - EXPERIMENTAL RESULTS

During the study, substantial variation was seen in important parameters of the material responses investigated. However, not all of the differences observed could be attributed to changes in controlled parameters.

Figure 3 shows plots of the rise time and peak value measured for the return current and radiated

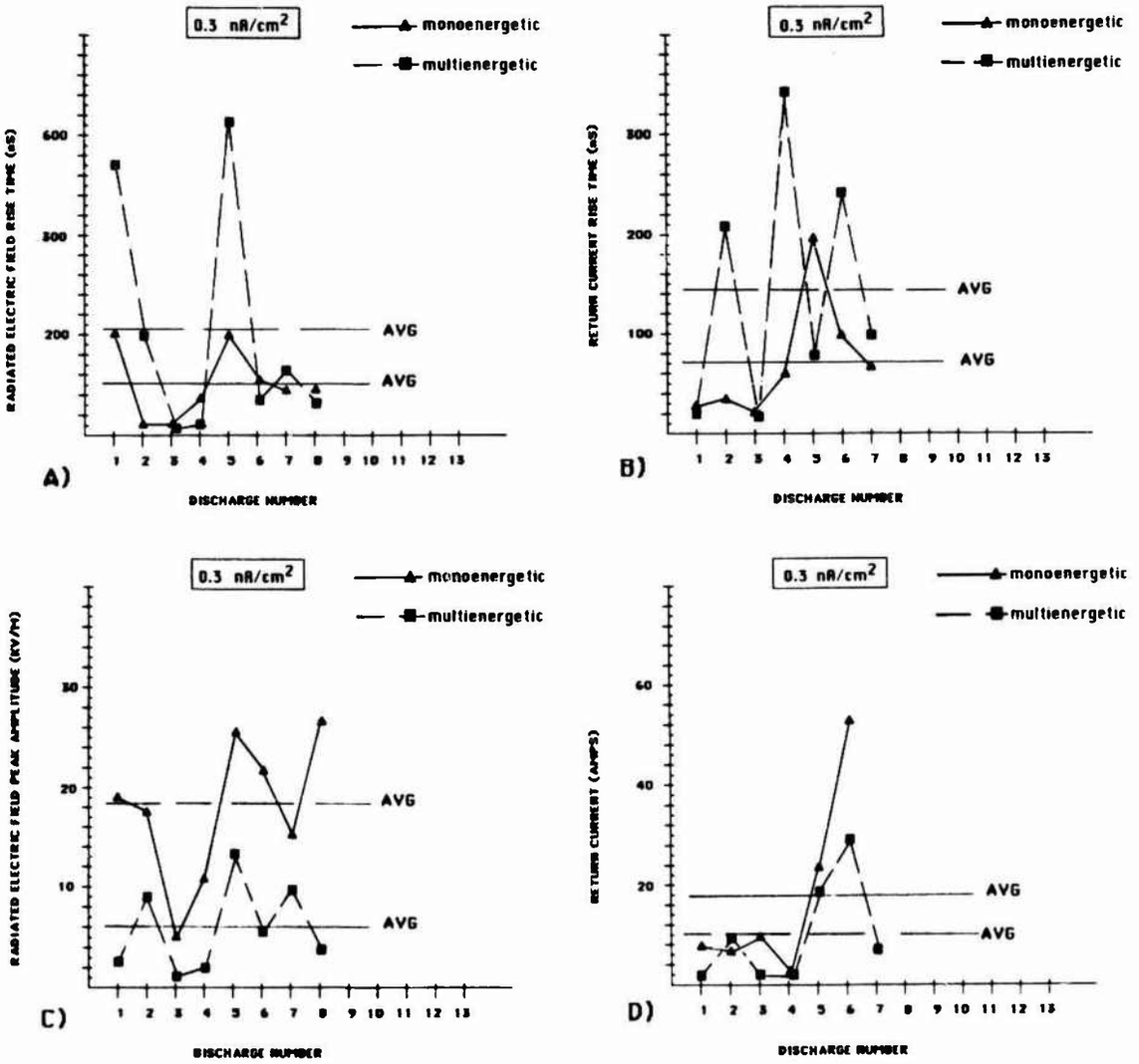


FIGURE 3 RESPONSE HISTORY FOR TYPICAL SAMPLES OF 75 μm KAPTON AT 0.3 nA/cm² AND TWO ENERGY SPECTRA

field on sucessive dischargea from a aample during a pair of tests conducted at a current density of 0.3 nA/cm^2. Similar data from teats at beam current densities of 1.0 and 3.0 nA/cm^2 are shown in Figures 4 and 5, respectively.

Figures 3 through 5 clearly show great differences in the properties of succeasive dischargea from a given sample. As discussed below, these differencea exiat because a wide variety of discharges are possible — ranging from those that (from visual observation) involve the entire sample to those confined to a small point on the surface of the sample. In spite of the wide variations observed, it is instructive to look for systematic differences in the behavior of the aamples under the two environments. To aasist in this process, the average value of each parameter waa calculated and ia shown on each of the graphs.

Our aearch for general trends in Figurea 3 through 5 revealed that the most obvious and consistent difference between mono- and multienergy behavior is observed in the pulse rise timea (panels [a] and [b] of each Figure). In particular, the radiated field rise time (panel [a]) generaly appears to be shorter (faster rising pulse) for monoenergetic illumination (on the average by roughly a factor of two) at all current densities. A similar, but less clear difference ia

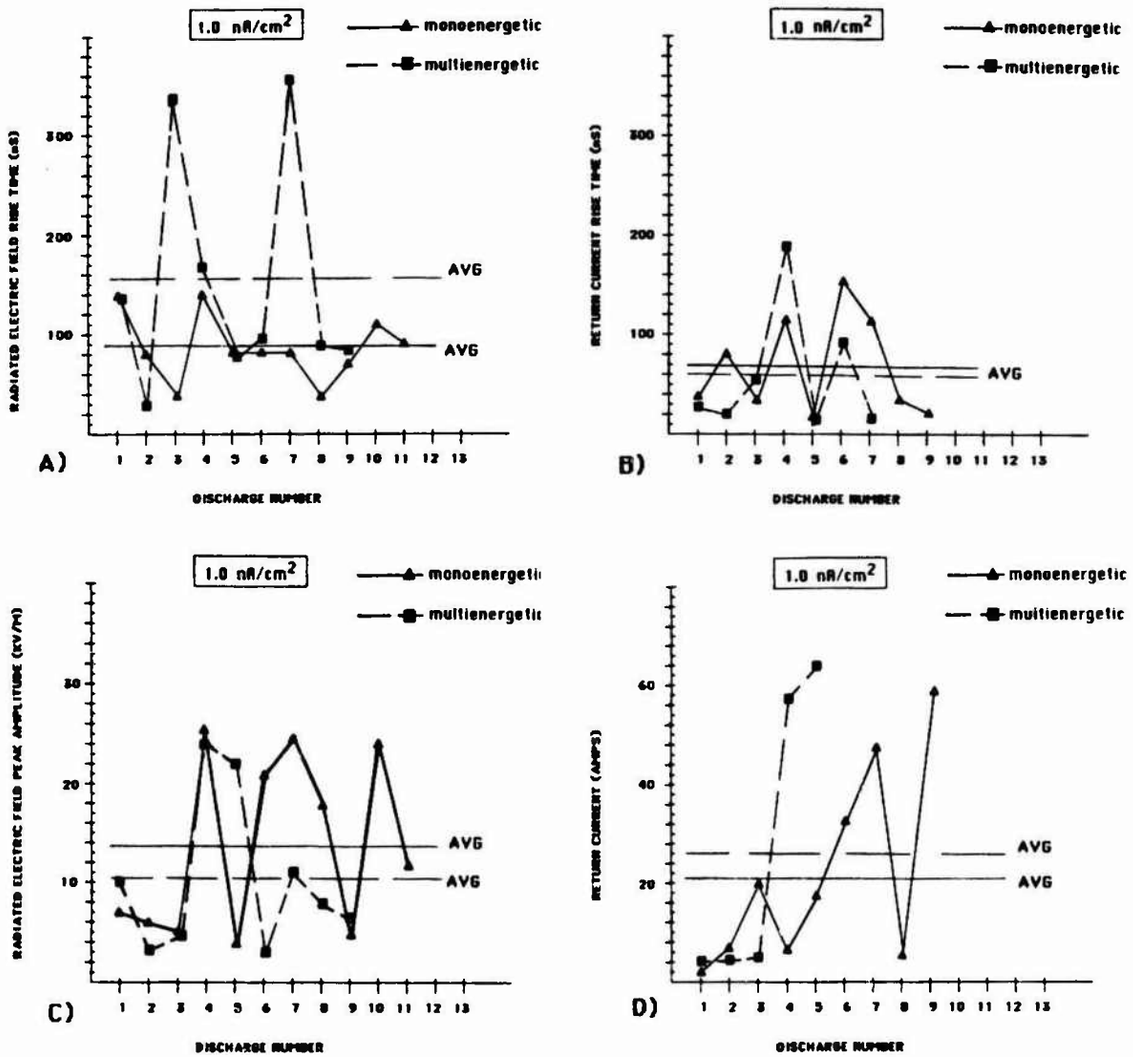


FIGURE 4 RESPONSE HISTORY FOR TYPICAL SAMPLES OF 75 µm KAPTON AT 1.0 nA/cm² AND TWO ENERGY SPECTRA

observed in the return current rise time (panel b). Again, discharges under monoenergetic illumination tended to show a shorter return current risetime, except in Figure 4b, where there appears to be no substantial difference.

In the case of the peak return current and peak radiated field (panels c and d), on the other hand, there appears to be no consistant difference. In fact, for the peak radiated field (panel c), multienergy illumination resulted in higher amplitude pulses at low beam currents (Figure 3c), while monoenergetic illumination resulted in higher amlplitude pulses at high beam currents (Figure 5c).

For the sake of completeness, response histories obtained with samples exposed at 10 nA/cm^2 beam current density are shown in Figure 6. Although this current density is at or above the maximum densities reported from space, testing is frequently done at this level in an effort to accelerate the test program. Thus, behavior of materials at these charging rates is of interest, since it provides insights into the distortions in material behavior one is likely to experience with accelerated testing. The great variation in the values of the parameters in Figure 6, makes it difficult to discern any systematic differences between material behavior with multi- and

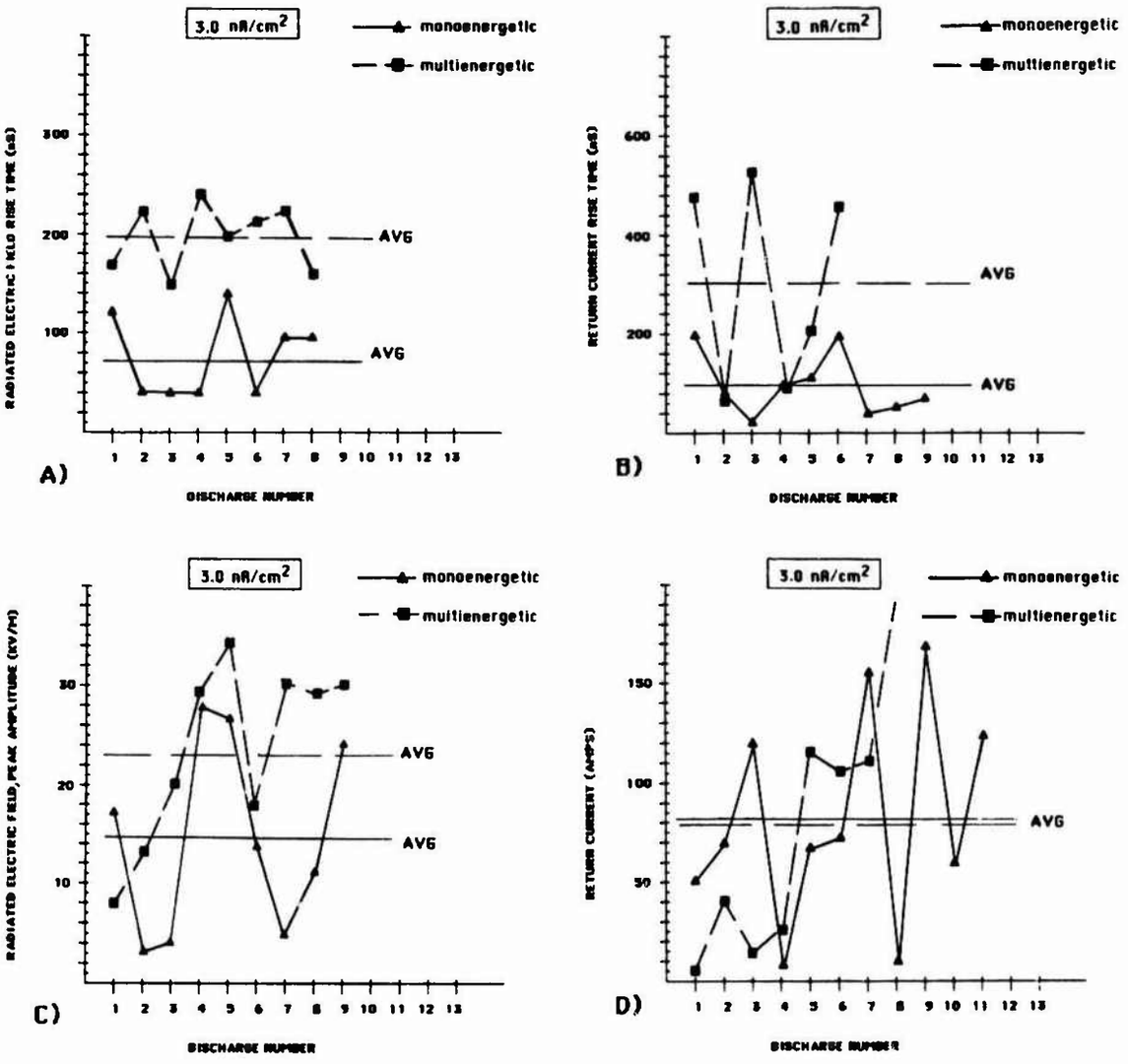


FIGURE 5 RESPONSE HISTORY FOR TYPICAL SAMPLES OF 75 μm KAPTON AT 3.0 nA/cm² AND TWO ENERGY SPECTRA

monoenergetic illumination. However, when the average values for the parameters in each panel of Figure 6 are compared, it appears that the same general relationships between multi- and monoenergetic data observed in Figure 5 also exist in Figure 6, but they are not so clear cut.

The results of the experiments presented in Figure 6 imply that the temptation to test materials only at high current densities should be resisted. The data presented here suggest that important differences in behavior can be masked or can disappear entirely when the beam current density is increased to 10 nA/cm².

A further graphic indication of the great randomness observed in discharge parameters at high beam current densities is shown for radiated field rise time in Figure 7. Here, the time histories from two successive samples exposed to a multienergy beam are plotted together with the history from a sample exposed to a monoenergetic beam. The two tests with the multienergy beam show no more similarity with each other than do either of them with the monoenergetic test.

The reason for the wide range of discharge pulse parameters observed in the tests can be come evident from a review of some of the pulses that

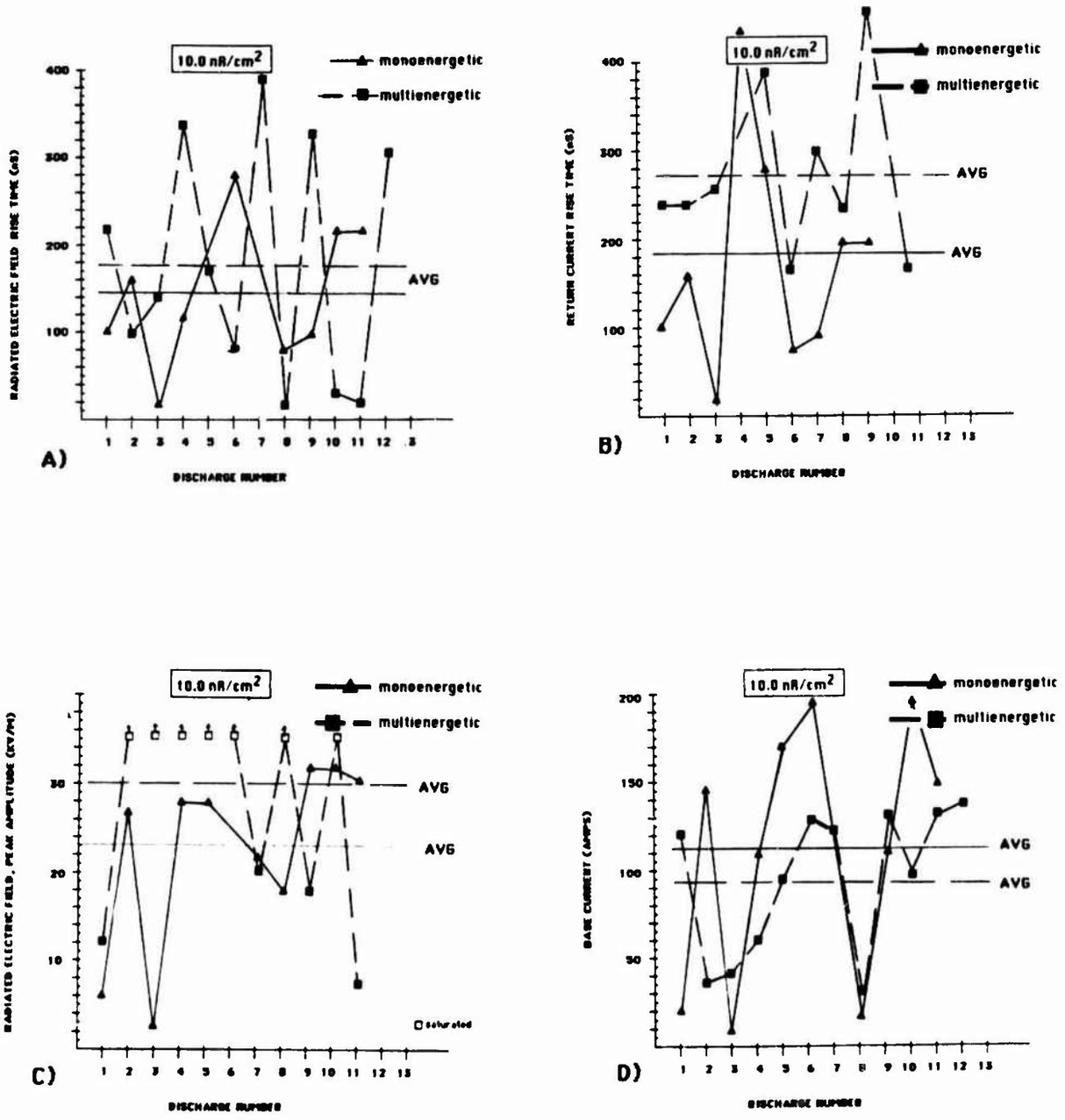


FIGURE 6 RESPONSE HISTORY FOR TYPICAL SAMPLES OF 75 μm KAPTON AT 10 nA/cm² AND TWO ENERGY SPECTRA

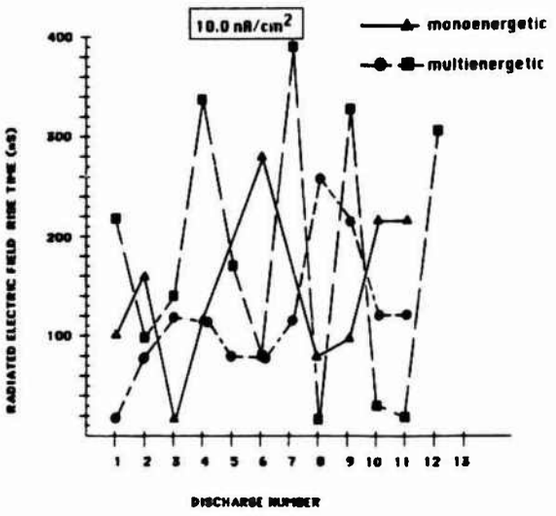


FIGURE 7

RESPONSE HISTORIES OF TWO MULTIENERGETIC TEST CASES AND ONE MONOENERGETIC TEST CASE (75 μm kapton)

were recorded during the test program. The three more or less distinct "general" types of pulse observed are shown in Figure 8. Waveforms such as those in Figure 8a were generated by a discharge shown visually to be confined to a single point on the sample. Pulses typified by Figures 8b and 8c were observed on discharges that appeared to envelope the entire sample.

A discharge confined to a single point would presumably tap only the charge stored in its immediate vicinity. Accordingly, the pulse should form quickly and dissipate as soon as the region was discharged, generating a single short pulse of the sort shown in Figure 8a.

If a substantial portion of the test sample is involved, time is required to propagate the discharge over the surface, and the pulses generated by such discharges should last longe, as shown in Figures 8b and 8c. If the extended

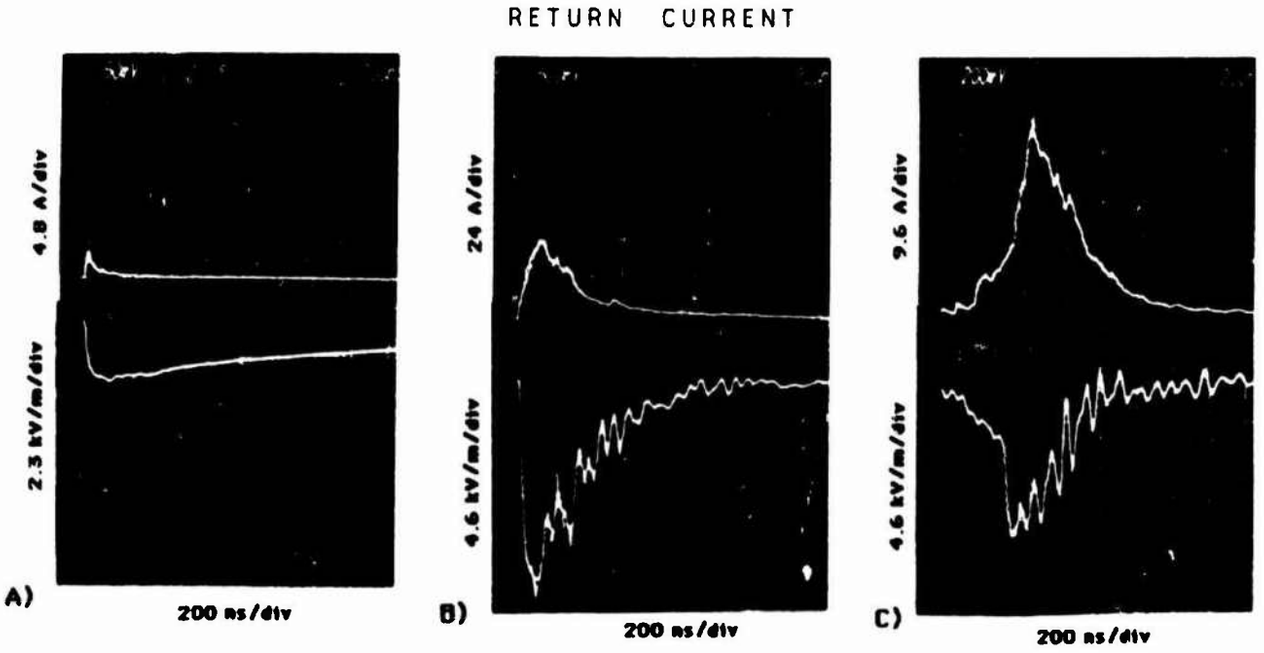


FIGURE 8
TYPICAL WAVEFORMS OBSERVED IN THREE DISCHARGES USING EITHER ENERGY SPECTRUM

discharge originates in a region a of high, easily tapped charge, a pulse with a fast leading edge (as shown in Figure 8b) will be generated. If, on the other hand, the extended discharge must propagate over the surface a substantial distance before reaching a region of easily tapped charge, a pulse such as that shown in Figure 8c will be generated. The period of propagation to the high-charge region results in the slowly rising leading portion of the pulse. Once the propagating discharge reaches the easily tapped charge, an abrupt change in base current and radiated field is produced.

In general, exposure to the multienergy beam tended to produce discharges of the general type illustrated in Figure 8c. However, all of the waveform types illustrated in Figure 8 were observed with both simulations.

A major shortcoming associated with the use of laboratory simulations to study discharge parameters is illustrated by the return current waveform of Figure 8c, which represents the current blown away from the test sample. Approximating the discharge current pulse by a triangular wave with amplitude 50 A and a base of 1000 ns, we find that the charge blown away is roughly

$$q = \int i\,dt \simeq 1/2\ 50\ (1000 \times 10^{-9})$$

$$= 25 \times 10^{-6}\ \text{coulomb}$$

If we estimate the spacecraft to have a self-capacitance of about C = 250 pF, the voltage to which the spacecraft would charge as the result of such a net removal of charge is given by

$$V = q/C = \frac{25 \times 10^{-6}}{250 \times 10^{-12}} = 100\ \text{kV}$$

which is not possible. Thus we must conclude that either the discharge will choke off much sooner than it does in the laboratory or that a mechanism must exist in space for the blow-away current to be recovered by the spacecraft virtually as rapidly as it is ejected. Thus, it is very likely that the discharges occurring in space will differ substantially from those generated in the laboratory. (This problem was identified by Nanevicz and Adamo in connection with an earlier laboratory study of discharge properties.[11] The problem of removing blown away current does not arise in the laboratory, because it can be collected by the ground electron gun located above the test sample [Figure 1]).

With monenergetic illumination, the test samples produced discharges at about twice the rate of the multienergetic case, even though the overall beam current from the gun was the same in each test. This result is reasonable according to the following arguments: For the monenergetic beam, all the incident electrons (total beam current) left the gun with 24 keV of energy. In the multienergetic case, however, only about 5% of the total beam current had energy of 24 keV. During irradiation, the beam deposits charge in the sample, which produces a repelling static electric field. In the monoenergetic case, this field slows the incident electrons, but the overall beam current remains essentially unchanged. In the multienergy case, on the other hand, some of the incident electrons have small velocities (energies) and cannot penetrate the field. For example, if the sample is charged to 5 keV, an electron leaving the gun with less than 5 keV of energy will not reach the sample. This effect continually reduces the incident beam current of the multienergetic simulation. Thus, the multienergetic simulation of the geosyncronous environment charges dielectrics more slowly and produces fewer discharges per unit time than its mononergetic counterpart.

Samples under multienergy illumination generally continued discharging for a longer period of time than those exposed to a monoenergy beam [Figure 9]. Some samples under the multienergy beam continued to discharge for over two hours, while samples under a monoenergy beam would quit discharging after a few minutes. The physical processes responsible for this behavior have not yet been investigated. It is not clear, for example, whether the bulk conductivity of the material is increased by the high-energy component of the electron illumination, or whether the discharge triggering mechanism is inhibited by the effects of the monoenergetic illumination.

It is interesting to note from Figure 9 that, following most discharges, the sample voltage dropped to a small fraction of its initial voltage, indicating that a substantial fraction of the surface had been discharged. Such discharges

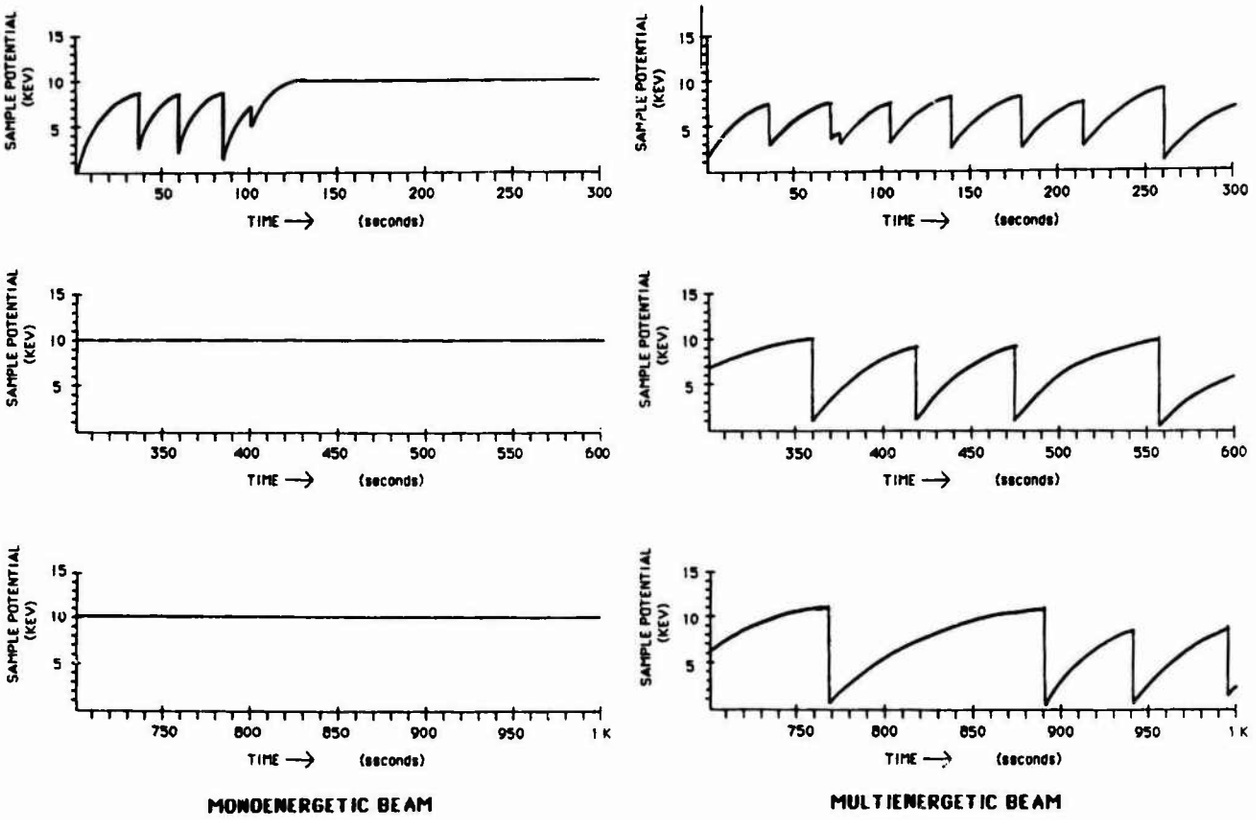


FIGURE 9
CHARGING AND DISCHARGING OBSERVED WITH MONO AND MULTIENERGY SIMULATIONS (127 μm kapton)

generated transient pulses of the sort shown in Figures 8b and 8c. In the top line of Figure 9 shows that one discharge each, for both mono- and multienergy illuminations, produced a small perturbation in effective surface potential, indicating that only a small portion of the surface had been discharged. Such discharges produced pulses of the sort illustrated in Figure 8a.

V - EXPERIMENTAL OBSERVATIONS

During the experimental program, a variety of observations provided significant insights into the issue of spacecraft charging and its simulation.

As indicated in Section III, sample mounting techniques have a great effect on the ease with which discharges are triggered. An investigation of various edge treatments revealed that discharges encompassing more than a single point always involved a grounded edge. This implies that consideration of installation details is important, not only in laboratory simulations, but also in the application of results from such simulations to spacecraft (design).

In preparing the test samples for the experiments, each sample was wiped clean. It was often observed that the direction of the discharge paths followed the direction of wiping the sample. The physical processes involved were not investigated, but the observation seems significant.

In conducting the present set of experiments, it was generally necessary to use a higher-energy monoenergetic beam to secure discharges than was true in the past. This might be because from the stocks of Kapton samples used in previous experiments at SRl had been exhausted and because new material was ordered for the present experiments. No time was available to investigate variablity between different batches of Kapton. This should be pursued in future work.

IV - CONCLUSIONS

The study results show that some significant differences exist in Kapton's response to monoenergetic and multienergetic simulations of the geosychronous charging environment. Particularly significant is the fact that samples exposed to a multienergy beam continue discharging (apparently indefinitely), while samples from the same batch of material exposed to a monoenergetic beam stop discharging after a few minutes. Thus, an experimenter working with a monoenergetic electron beam may falsely believe that spacecraft charging will not be a problem for his materials in orbit.

A second apparently consistent difference in the behavior of Kapton with multi- and monoenergetic electron illumination is in the rise time of the discharges produced. In general, the discharges observed with monoenergetic illumination had shorter rise times (by roughly a factor of two) than did the discharges observed in the multienergy experiments. Since short rise-time pulses are most effective in penetrating apertures and other electromagnetic imperfections in a satellite, the use of data generated in experiments with a monoenergetic beam will result in a slight overspecification of the severity of the orbital electromagnetic environment.

A particularly significant finding of this study was that parameters not normally considered as important experimental variables in the study of material charging and discharging have as great (or greater) influence on the material's response as do those parameters that are normally closely controlled. For example, the way in which a sample was cleaned (direction of cleaning strokes) affected the orientation of the Lichtenberg patterns. While some samples would discharge two or three times, other "identical" samples under "identical" test conditions might discharge twenty times or more. It may be that the details of how the material is attached to the satellite, from what production run the material originated, and other as yet unknown variables have a greater influence on how a given craft behaves in a charging environment, than do the details of the charging environment itself. Further investigation is needed in this area to adequately identify, describe, and characterize the critical parameters involved in a material's response to charging conditions.

In general, the cost of accurately duplicating the known charging environment at geosynchronous altitude becomes increasingly expensive as the required accuracy of that simulation increases and the number of controled parameters increases. The present study was undertaken to investigate the effects of modifying one of these parameters -- the electron beam spectrum. It was found that differences did exist between material behavior under mono- and multienergetic illumination. In addition, found that significant difficulties exist in our ability to apply our laboratory results to actual satellites. For example, the amplitude and duration of the blow-off current pulse observed in the laboratory (Section IV) will probably not be duplicated in orbit. Also discharge behavior is significantly affected by uncontrolled variations in material properties and handling. These results indicate that further progress in the area of ground simulation and in the general understanding of spacecraft charging would benefit enormously from in-orbit measurements designed to validate the results of laboratory work and to provide guidance for future efforts.

REFERENCES

1. J. E. Nanevicz and R. C. Adamo, "Status of Critical Issues in the Area of Spacecraft Charging," 1985 International Aerospace and Ground Conference On Lightning and Static Electricity, Paris, (10-12 June 1985).

2. R. C. Adamo and J. E. Nanevicz, "Development of A Continuous Broad-Energy-Spectrum Electron Source," in 1982 International Conference on Spacecraft Charging Colorado Springs, (1983).

3. H. B. Garrett, "Spacecraft Charging: A Review," in Space Systems and Their Interactions with Earth's Space Environment, H. G. Garrett and C. P. Pike, eds., Vol. 71, pp. 167-226 (American Institute of Aeronautics and Astronautics, 1980).

4. J. E. Nanevicz and R. C. Adamo, "Occurrence of Arcing and Its Effects on Space Systems," in Space Systems and Their Interactions with Earth's Space Environment, H. G. Garrett and C. P. Pike, eds., Vol. 71, pp. 252-275 (American Institute of Aeronautics and Astronautics, 1980).

5. J. E. Nanevicz, R. C. Adamo, and R. R. Shaw, "Electrical Discharges Caused by Satellite Charging at Synchrounous Orbit Altitudes," 1975 Lightning & Static Electricity Conference, Culham Laboratory, England (1975).

6. P. F. Mizera et al., "Spacecraft Charging in the Spring of 1981," prepared for Space Division, Air Force Systems Command, Los Angeles Air Force Station, Contract No. F04701-80-C-0081, Aerospace report No. TOR-0081(6508-05)-1, The Aerospace Corporation, El Segundo, California (30 September 1981).

7. R. C. Adamo and J. E. Nanevicz, "Preliminary Comparison of Material Charging Properties Using Single-Energy and Multienergy Electron Beams," in Spacecraft Charging Technology Report No. NASA CP-2182, AFGL-TR-81-0270, (1981).

8. M. S. Leung, M. B. Tueling, and E. R. Schanauss, "Effects of Secondary Electron Emission on Charging," in Spacecraft Charging Technology, NASA Conference Publication 2182, pp. 163-178 (1980).

9. M. Treadaway et al., "Dielectric Discharge Characteristics in a Two-Electron Simulation Environment," in Spacecraft Charging Technology, NASA Conference Publication 2182, pp. 4-16 (1980).

10. B. L. Beers and V. W. Pine, "Electron-Beam-Charged Dielectrics--Internal Charge Distribution," in Spacecraft Charging Technology, NASA Conference Publication 2182, pp. 17-32 (1980).

11. J. E. Nanevicz, R. C. Adamo, B. L. Beers, and T. N. Delmer, "Electromagnetic Fields Produced by Simulated Spacecraft Discharges," AFGL-TR-81-0270, 1980 Spacecraft Charging Technology, NASA Conference Publication 2182 (November 1980).

12. J. E. Nanevicz and R. C. Adamo, "A Rugged Electron/Ion Source for Spacecraft Charging Experiments," Proceedings of the Spacecraft Charging Technology Conference, AFGL-TR-77-0051, Air Force Geophysics Laboratory (February 1977).

13. J. E. Nanevicz and R. C. Adamo, "Laboratory Studies of Spacecraft Response to Transient Discharge Pulses," Proceedings of the Spacecraft Environmental Interactions Conference, NASA/Lewis Research Center (October 1984).

14. N. J. Stevens, F. D. Berkopec, J. V. Staskus, R. A. Blech,and S. J. Narcisio, "Testing of Typical Spacecraft Materials in a Simulated Substorm Environment," Proceedings of the Spacecraft Charging Technology Conference, AFGL-TR-77-0051, Air Force Geophysics Laboratory (February 1977).

15. C. K. Purvis, N. J. Stevens, and J. C. Oglebay, "Charging Characteristics of Materials: Comparison of Experimental Results with Simple Analytical Models," Proceedings of the Spacecraft Charging Technology Conference, AFGL-TR-77-0051, Air Force Geophysics Laboratory, NASA TMX-73537 (February 1977).

ASPECTS OF LIGHTNING PROTECTION SCHEMES FOR RADOMES

J. Bishop, A. Aked*, C.W. Powell** and H.M. Ryan**

Flight Systems Department, Q.153 Bldg., Royal Aircraft Establishment, Farnborough, Hants GU14 6TD, U.K.
**Strathclyde University, Glasgow, U.K.*
***NEI Reyrolle Ltd., Hebburn, Tyne and Wear, U.K.*

Abstract - This paper describes a programme of work, funded by the UK MOD, to investigate the design of aircraft radome lightning protection based upon the concept of lightning striking distance. A simple mathematical model describing the protection is derived and experimental results designed to test the theory are given. It is concluded that within the limits of unpredictability of high voltage discharges, the model goes some way towards explaining the performance of a cylindrical cage of protective conductors in terms of their pitch and distance from the internal metalwork being protected.

1 INTRODUCTION

Aircraft radomes are vulnerable to damage by lightning strike; trends in radome design have reduced their electrical strength so that their vulnerability and hence the need for lightning protection has increased. The normal method of lightning protection consists of a cage of conductors placed around the radome, with one end of each conductor earthed at the airframe end. The number of conductors used, and their spacing, has to be a compromise between the degree of lightning protection given and the amount of radar degradation allowed. Radar degradation occurs due to the microwave scattering action of each protection strip and the combined effect of the cage of conductors. The scattering depends upon the direction of illumination of the strips by the radar beam, and hence this will vary as the radar antenna is scanned to the left, right, up and down. The implications for the radar system are that the side lobe performance is degraded with a consequent reduction of radar range and noise immunity. Hence the number of protection strips must be kept to the minimum required for adequate radome protection (ref 1).

The conductor spacing design criterion used in the UK, has been based upon the concept of puncture/flashover (ref 2). This assumes that if a lightning leader touches the radome it can either flashover to an adjacent protection strip or puncture the radome wall to attach to the internal metalwork. The conductor spacing is such as to ensure that flashover rather than puncture occurs. Using this concept the strip spacing must be closer for a weak dielectric material than for a strong one, and considering the trends in radome design more strips are required than has been the case in the past.

High voltage tests of a large radome showed that the use of the puncture/flashover criterion had produced a significant degree of over protection, since a large number of strips could be removed before radome puncture occurred. During the tests it was observed that discharges went straight to a protection strip rather than to the radome surface and then flashed over. These observations were the reason for initiating this research programme with the objective of determining the geometric criteria of protection provided by a cage of conductors surrounding internal metalwork. It is obvious that a single conductor surrounded by a symmetrical cage of protection conductors must be protected if there are sufficient conductors in the cage - this must apply whether the protection conductors are on a dielectric surface or in air. What is required is a theory that relates the geometry of this situation to the degree of protection provided, the electrogeometric theory given below attempts to do this.

2 ELECTROGEOMETRIC THEORY OF RADOME PROTECTION

In the electrogeometric method of determining suitable positions for the earthed conductors in lightning protective schemes, the basic assumption is that there exists a 'lightning striking distance' r_s (ref 3). If a lightning leader, developing along a tortuous path determined by the local physical conditions, extends to within a distance r_s from an earthed conducting object then it is assumed that the subsequent lightning strike will terminate on that object. Thus protective conductors must be positioned so that for every possible direction of approach of the lightning leader, it must always reach a distance r_s from some part of the protective system or the earth, before coming within r_s from the object being protected. In the absence of any contrary experimental evidence it is assumed that the striking distances to different objects are equal, although there is much uncertainty about the

magnitude of r_s . The striking distance is considered to be dependent upon the charge density in the lightning leader and consequently of the peak current in the resulting lightning strike.

In the present study of the protective properties of lightning conductors on non-conductive areas on the surface of an aircraft in flight, we have assumed that the concept of the 'lightning striking distance' is still valid. In other words if a lightning leader extends by chance to within such a distance from any point on the surface of an aircraft then the resulting lightning channel will strike that point. We have at present no knowledge of the magnitude of this distance, here symbolised by r_s' .

Taking a simplified model with cylindrical symmetry, Fig 1 shows the arrangement of n conductors equally spaced around the circumference of a cylinder of radius r_1 which represents the radome. The internal radar equipment is here represented by a coaxial inner cylinder of radius r_2 . The protection afforded by these n protective conductors depends on the probability of a lightning leader getting within a distance r_s' from the inner cylinder.

In Fig 1 the curve AB is the locus of points equidistant from the protective strip PS1 and the surface of the inner cylinder. Curve AC is the corresponding locus of points equidistant from PSn and the inner cylinder. These two curves intersect at the point A, which lies on the radial line mid-way between the two protective strips and is distant L_1 from the surface of the outer cylinder, ie the radome surface. If L_1 is less than the lightning striking distance r_s' then, before any lightning leader can enter the region bounded by the lines AB and AC, it will be less than r_s' from one of the protective strips and hence the lightning will strike this strip rather than the inner cylinder. The inner cylinder can be struck if L_1 is greater than r_s' . In this case a lightning leader developing by chance into the region bounded by lines AB and AC may thereafter develop within this region to be within r_s' from the inner cylinder and hence strike it.

Fig 2 shows the form of the loci AB and AC in more detail. In this figure the origin 0' corresponds to the point O' in Fig 1 and the y-axis lies along the radial line O'A in Fig 1. As an alternative to representing the equipment within the radome as a coaxial cylinder the most vulnerable region could be simulated by siting a single conductor at the point D. In this case the loci are the straight lines AE and AF but the length L_1 is unchanged. In Fig 2 it can be seen that there is little difference between these lines and the curves AB and AC for distances from the outer cylinder in excess of $L_1/2$.

The ratio of L_1 to R_1 is a function of the ratio of R_2 to R_1 , ie of $F = R_2/R_1$. The variation of the magnitude of L_1/R_1 as a function of F , is shown in Fig 3 for n , the number of protective strips, equal to 6, 10 and 16. Assuming that the theory is valid then the smaller is L_1 , then the greater the degree of protection, Fig 3, shows as the number of strips is increased, then for R_1 constant L_1 falls. Thus as would be expected the protection increases by adding conductors.

L_1 increases rapidly as the value of F approaches the value cos (180°/n) which corresponds to the point D lying at the centre of the straight line joining adjacent protective strips. For this condition the loci are asymptotic to the radial line ODA (Fig 1) and $L_1 = \infty$. This is to be expected since when the conductor to be protected lies on the same surface as the protection strips - protection is not possible.

If n = 10 this critical value of F equals cos (180°) = 0.951 . A reduction of F to 0.945 reduces L_1/R_1 to approximately 7.8 while a reduction to 0.94 halves it to about 4 and a further reduction to F = 0.93 results in $L_1/R_1 = 2.25$. As an example for an outer radius R_1 of 1 metre, the radial separations between inner and outer cylinders for the above conditions are 49, 55, 60 and 70 millimetres respectively.

If F is greater than the critical value then each locus is asymptotic to the radial line through the point of contact of the tangent from the corresponding protective strip to the inner cylinder as shown in Fig 4. For this condition it is possible for a lightning leader to approach directly to within r_s' from the inner cylinder for any value of r_s' .

As an example, in the 10 protective strip arrangement of Fig 4, if F = 0.99 , the angle of the 'inner cylinder vulnerable' wedge is 19.8°. Thus the probability that an approaching leader will by chance be in one of the 10 such wedges is 55%. This probability falls as the value of F is reduced. For the 10-strip arrangement the probabilities for F = 0.98, 0.97 and 0.96 are 36%, 22% and 10% respectively.

As stated earlier if F is less than the critical value, cos 180°/n) then the loci meet and it is the relative values of R_s' and L_1 which will determine whether or not the inner cylinder can be struck. This is only possible if L_1 is greater than R_s' .

As a lightning leader approaches an aircraft in flight, discharges may develop from different points on the surface. Any such discharge developing from a protective strip on a radome will result in the 'apparent' position of the strip being further from the equipment within the radome and hence the protection afforded to such equipment would be expected to increase. The presence of the insulating wall of the radome will inhibit the development of discharges from the internal structures. If such discharges

alone were to develop then they could reduce the protective effect of the strips. However if the conditions were such as to cause significant discharges to develop within the radome then even greater discharges would be developing from the protective strips and effective protection should still be achieved.

3 EXPERIMENTAL STUDIES

3.1 Mock Radome

This model was constructed from lightweight metal-angle which accommodated seven hardboard sheets (1.22 metres wide x 3.2 millimetres thick) bowed to semi-cylindrical shape. Alignment of the boards at their abutments was obtained by means of small insulating screws and washers, while crossed wood lath supports underneath the boards maintained the semi-cylindrical shape. Thin 12.7 millimetre wide tinned copper strips were pulled taut longitudinally over the external surfaces of the boards to represent the lightning conductors. A 12.7 millimetre square section mild-steel bar 4.5 metres in length, was mounted centrally under the boards on two, vertically adjustable metal supports to represent apparatus to be protected inside the mock radome. This bar (A_m) and the protective copper strips were connected to the metal-angle structure and earthed. Other dimensions are given in the end elevation, Fig 5.

3.2 Test Equipment and Procedure

The model was positioned on the laboratory floor to give clearances of > 10 metres, to nearby wall, or equipment. The test equipment comprised an impulse generator and, voltage divider with associated two beam transient recorder. Test voltages were applied to a 2 metre long 20 millimetre diameter rod suspended centrally over the model from a long string insulator. The lower end of the rod was cone shaped to 60° and spaced approximately 3 metres above the radome.

Photographic records with corresponding oscillograms were obtained for every impulse voltage applied to the test piece. Two cameras were used, situated at a height above floor level equal to the centre of the main gap between the high voltage rod and the upper radome surface; one camera being in line with the major axis of the mock radome while the other was mutually displaced by 90°. The cameras were synchronized to open with operation of the impulse generator.

Two double exponential impulse voltage waveshapes were chosen for the investigation designated short (S) and long (L). In accordance with IEC-60 recommendations these were measured as 1.4/40 μs and 120/1725 μs for S and L waves respectively.

Earlier experimental work using a roughly comparable model [Ref4], indicated that only a small difference would occur in the spread of long-spark attachment points on the model, between tests performed at the V_{50} voltage level and tests at the V_{90} level. Small differences in voltage level was therefore considered relatively unimportant for the present work; nevertheless sparkover levels are included in the table of results (Table 1). Variations in values of ambient air density correction factor Kd and absolute humidity.

3.3 Test Results

Preliminary tests on the mock radome (see Fig 5) for strip angles Q_D of both 36 and 45° showed that the hardboard sheets were effective in preventing negative polarity strikes to the inner electrode 'A_m'. But for comparable conditions, some positive discharges punctured the hardboard sheets and attached on to 'A_m'. Thus positive polarity was considered the more onerous and therefore used in the present short investigation, involving four test conditions 1, 2, 3 and 4, as shown in Fig 5 and 6. In Fig 6, the loci of points in the main gap equidistant from electrode 'A_m' and both adjacent protective strips are drawn in dotted for different values of h . Thin wood lath structures were made to these calculated wedge dimensions - forming the dotted lines - and constructed vertically on either side of the centre board on the model. Prior to testing, still photographs of these structures were taken for the four experimental conditions so providing formats on which subsequent photograph negatives could be accurately superimposed to determine the trajectories of the long sparks relative to these wedge shaped outlines.

Approximately 20 sparkovers to the model were obtained using positive polarity short-waves then repeated using long-waves, for each of the four test conditions given in Fig 5. The trajectories recorded for each flashover were then related to the wedge shaped outlines. The results arepresented in Table 1.

4 EXPERIMENTAL RESULTS

The first important result of the mock radome experiments was the effect of the radome wall - simulated in the test arrangement by hardboard sheet. The test conditions were set so that all the sparks produced by positive short-fronted impulses hit the central rod electrode whether or not the hardboard sheet was present in the central test section of the model. Tests using negative short-fronted impulses also produced 100% flashover to the central rod when there was no hardboard sheet. With the sheet present however all the flashovers were to the protective strips. Consequently all the subsequent tests were undertaken using only positive impulses.

In the main series of tests approximately 20 flashovers were observed under each of eight different conditions; four different radial positions of the central electrode and for two different impulse voltage wavefronts. The hardboard sheet was not present on the central 1.2 metre wide section of the test model.

For the four positions of the central rod the radial distances to the outer surface were 20, 48, 64 and 78 millimetres. The corresponding values of 'h' in Fig 1 were +28, 0, -16 and -30 millimetres. In Table 1 these conditions are indicated as electrode conditions 1, 2, 3 and 4. In this Table the impulse voltage wavefront duration is indicated by an 'S' or ' ' beside each observation. For each electrode configuration the number of flashovers to the central electrode and to the protective strips are indicated both as totals and as percentages.

As the central conductor was moved further from the outer surface the efficacy of the protective strips increased. The proportion of the flashovers which went to the central electrode fell as shown in Fig 6. The two scales on the horizontal axis indicate the radial separation and also the ratio $F = R_2/R_1$.

Included in the figure are two 0% values observed in an earlier test for radial separations of 103 and 118 millimetres.

From records of the spark paths viewed along the axis of the model, it was determined whether or not the path crossed the surface of the wedge formed by the loci of points equidistant from the protective strips and the central rod.

For the first configuration this wedge was inverted as indicated in Fig 9, because F exceeded the critical value of 0.951. For the second rod position F was equal to the critical value and hence the height of the wedge tip was infinite and the wedge took the form of a rectangular block or an 'infinite wedge'. The final two positions of the rod corresponded to F being less than the critical value and the wedges had tip heights of L_1 = 2752 millimetres and 1435 millimetres respectively.

For the first two configurations the high voltage electrode, 3048 millimetres from the cylindrical surface, was contained within the wedge and so flashover to the central electrode could develop entirely within this region. If this occurred then at every point in its development the spark was nearer to the central electrode than to either protective strip. The proportion of the sparks to the central electrode which developed in this way is shown in Fig 6 and the corresponding number of sparks is recorded in Table 1.

As the wedge encloses the high voltage electrode it is impossible for a spark to develop to either protective strip without crossing the surface of the wedge. There can therefore be no entries in the Table under the heading "sparks to the protective strips/developing entirely within the wedge". The last row of Table 1 shows the number of sparks which crossed the surface of the wedge either as they developed to hit the central electrode or to strike one of the protective strips.

When the wedge does not enclose the high voltage electrode as in the final two configurations, there must again be a blank in the table of results as it is impossible for a spark to terminate on the central electrode without crossing the surface of the wedge. Those sparks which struck the protective strips and which developed entirely outside the wedge were, at every point, closer to the strip than to the electrode. The proportion of sparks striking the protective strips which developed in this manner is shown in Fig 7.

The number of sparks which crossed the wedge surface as they developed is shown in Table 1.

5 DISCUSSION OF RESULTS

In the present study the radome has been simulated by a hemi-cylindrical mock radome some 8 metres in length. The approaching lightning is here represented by a spark approximately 3 metres in length, and the conductors in and on the radome are earthed. Thus the conditions are not similar to those of an aircraft in flight. Nevertheless the tests should be able to indicate whether the analysis based on the concept of a lightning striking distance has sufficient merit to warrant continued study. The use of the cylindrical model has allowed comparison to be made between the actual spark paths and the path limits implied by the electro-geometric model.

Long spark studies in high voltage laboratories have shown that the spark path between two widely separated electrodes has a greater apparently random component when the applied impulse voltage has a long wavefront.

The forms of the wedges for the configurations studied are shown in Fig 9. For condition 1 and short-fronted impulses 95% of the sparks struck the central electrode and of those 95% developed entirely within the wedge, ie the spark developed to the electrode nearest to it.

One spark which hit the central electrode was for part of its development nearer to the protective strip. This occurred at some 1½ metres from the cylindrical surface. With long-fronted impulses applied only 59% of the sparks hit the central electrode but every one of these sparks developed entirely within the inverted wedge. All the remaining 41% of the sparks which hit the protective strips crossed the wedge surface within 1 metre of the high voltage electrode.

The critical gap length for the long-fronted impulse breakdown was therefore less than 3 metres. When the inner electrode was situated at the critical radius the wedge became an infinite one. For short-fronted impulses applied for this test condition one spark divided into two channels. One branch hit the central electrode while the other struck one of the protective strips. Sixteen out of 17 sparks to the central conductor developed entirely within the wedge.

When long-fronted impulses were used 59% struck the central electrode - as in the previous long-fronted case. Nine of these were contained within the wedge and seven crossed the wedge surface as they developed.

These paths therefore are not compatible with the assumptions of the electrogeometric model that the spark will develop to the conductor nearest to it. Once again the sparks which developed to the strips crossed the wedge surface within a metre of the HV electrode.

For the third electrode configuration and short-fronted impulses, two of the 20 sparks split near the radome surface and hit both the central electrode and a protective strip. Eight strikes occurred to the rod and 14 to the protective strips. Half of these developed entirely outside the wedge but the other half criss-crossed the wedge surface before finally striking the protective strip, in conflict with the assumed model. This also occurred when long-fronted impulse voltages were used. Five out of 11 sparks exhibited this behaviour. Only 20% of the sparks hit the central rod.

In the fourth configuration, where the height of the wedge tip was 1435 millimetres, the number of sparks striking the central rod was only two for each form of voltage. Over three-quarters of the sparks hitting the protective strips developed outside the wedge.

The results of this attempt to compare the spark forms observed with the limits set by the very simple electrogeometric model are encouraging.

6 CONCLUSIONS

The application of the electrogeometric model to a cage of protection strips surrounding some internal metalwork, produces a model which offers an explanation of facts that would be expected to apply. For example increasing the number of protection strips increases the degree of protection given and that the protection depends upon the value of the striking distance. Ref 3 shows striking distance to be a function of change in the lightning leader and hence of peak lightning current. It follows that if the model is valid then the probability of an attachment to protected metalwork is also a function of the lightning current.

It would also be reasonable to assume, as the model shows, that reducing the spacing between the protective cage and the internal metalwork requires a closer conductor pitch to achieve protection. What is of interest is that as this spacing is reduced the number of conductors required increases quite sharply.

A useful concept for the design of protection schemes is the critical value of R_2/R_1 . This ratio will be fixed for a given problem since it depends upon the radius of the radome and the closest distance of approach of the radar antenna, the critical number of protection strips can be found by equating R_2/R_1 to cos (180/n) . According to the theory the number of strips required will be greater than this and dependent upon the degree of protection required. It does however give a starting point for the design and a method of evaluating an existing design.

Fig 3 shows the protection given to be a function of L_1/R_1 and the requirement for protection is that L_1 is less than the striking distance. Assuming striking distance to be independent of the size of the radome and L_1 is required to be some proportion of the striking distance, then the larger the radome the greater the degree of protection for a fixed R_2/R_1 and constant number of protection strips. Hence the model predicts a size factor of increased protection for increasing radius even though the pitch of the protection strips has increased. A similar application of the puncture/flashover criterion would require more protection strips to keep the required distance between strips. This apparent difference arises because of the assumption that the lightning leader touches the radome surface does not hold, since the discharge goes straight to a protective conductor for the number of strips greater than the critical number. If the number of strips is less than this, the the leader may touch the surface and protection depends upon the dielectric strength of the radome.

The test results are in general agreement with the model predictions but not totally so. This is not surprising since the model assumes that a discharge will go to the nearest conductor, this can only be approximately true since we are dealing with probabilities and not absolute. It is reasonable to expect there to be a greater probability of an attachment to the nearest conductor rather than a certainty, the probability will be a function of extra distance to be travelled to the further conductor as well as of the electric field distribution, etc. This represents an error in the basis of the model and can be expected to reduce the degree of protection predicted. This variation would also be expected to be a function of the rise time and polarity of the test waveform used. Additional complications would arise due to the conditions pertaining to an aircraft in flight such as the lack of an earth connection, effects of airflow and radome dielectric charging.

ACKNOWLEDGEMENT

The work report here was sponsored by the Ministry of Defence under contract A81A/2093.

REFERENCES

1 Waterman, S W, "The calculation of diffraction effects of radome lightning protection strips".
International Aerospace Conference on Lightning & Static Electricity, March 1982, Oxford.

2 Waterman, S W, "Flashover voltage reduction by proximate conductors". Ibid.

3 Golde, R H, "Lightning". Academic Press, May 1977.

4 Phillpot, J, et al, "Lightning Strike point location studies on scale models". Lightning & Static Electricity Conference, Culham Laboratory, April 1975.

TABLE 1 RESULTS OF POSITIVE POLARITY SPARK TESTS

		CONDITION 1			CONDITION 2			CONDITION 3			CONDITION 4		
TOTAL NUMBER OF SPARKS OBSERVED		20			20 +			20 #			20		
VOLTAGE LEVEL		17			21			20			24		
	S	V83			V80			V83			V71		
	L	V85			V73			V87			V75		
			A_m	$B_1 - B_2$	A_m	$B_1 - B_2$		A_m	$B_1 - B_2$		A_m	$B_1 - B_2$	
TOTALS	S	17	85%	5%	17	85%	4	8	40%	16	2	18%	18
	L	18	59%	7	16	59%	11	4	20%	16	2	8%	22
LONG SPARK PATHS ENTIRELY WITHIN WEDGE	S	18	90%		16	80%							
	L	18	59%		9	33%							
LONG SPARK PATHS ENTIRELY OUTSIDE WEDGE	S							2	35%	16	15	75%	
	L							18	54%		20	83%	
LONG SPARK PATHS CROSSING WEDGE SURFACE	S	1	5%	1	1	5%	4	1	35%	1	3	15%	
	L	0	0	2	2	6.7%	11	6	30%	4	2	8%	
	S	1	5%	1	1	5%	4	8	40%	16	2	10%	
	L	0	0	2	2	6.7%	11	4	20%	4	2	8%	

AIR DENSITY CORRECTION FACTOR δ₀ VARIED BETWEEN 1.02 AND 1.03 DURING THE TESTS
HUMIDITY H VARIED BETWEEN 5 AND 5.5 g/m³

+ ONE LONG SPARK WAS FORKED - STRIKING A_m AND B_1 OR B_2
# TWO LONG SPARKS WERE FORKED - STRIKING A_m AND B_1 OR B_2

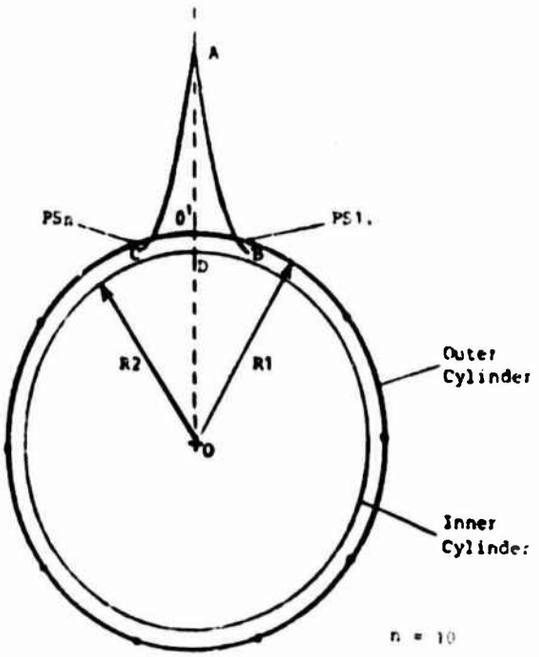


Fig.1 Loci of points equidistant from the protective strips PS1 and PSn and the inner cylinder.

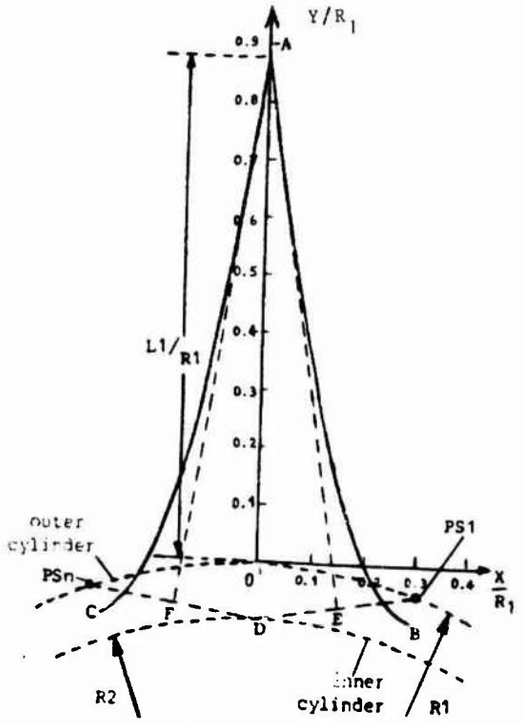


Fig. 2 Loci of points equidistant from protective strips PS1 and PSn
n = 10 $R_1/R_2 = 0.9$

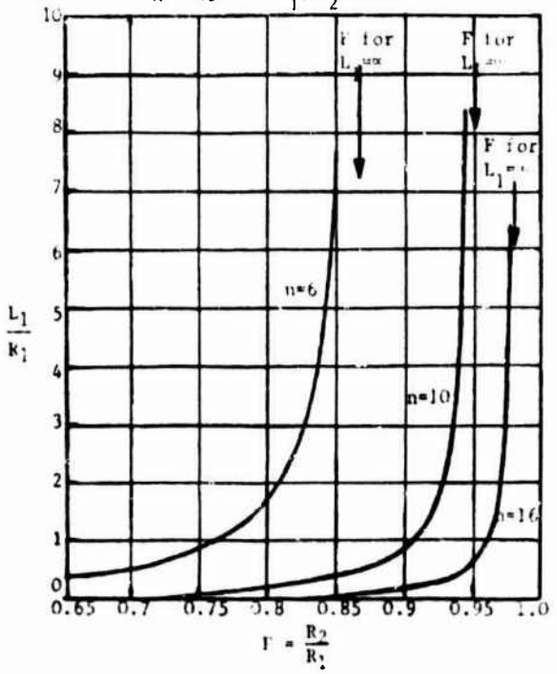


Fig.3 Ratio of wedge length L_1 to the radius of the outer cylinder R_1 for 6, 10 and 16 protective strips and a range of values of $F = R_2/R_1$

Copyright © Controller, Her Majesty's Stationery Office, London, 1985.

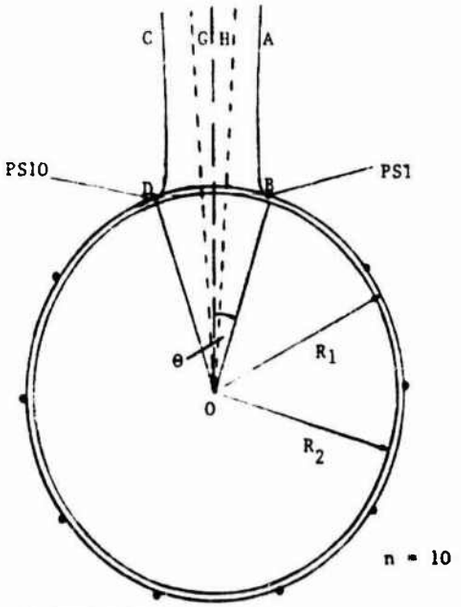
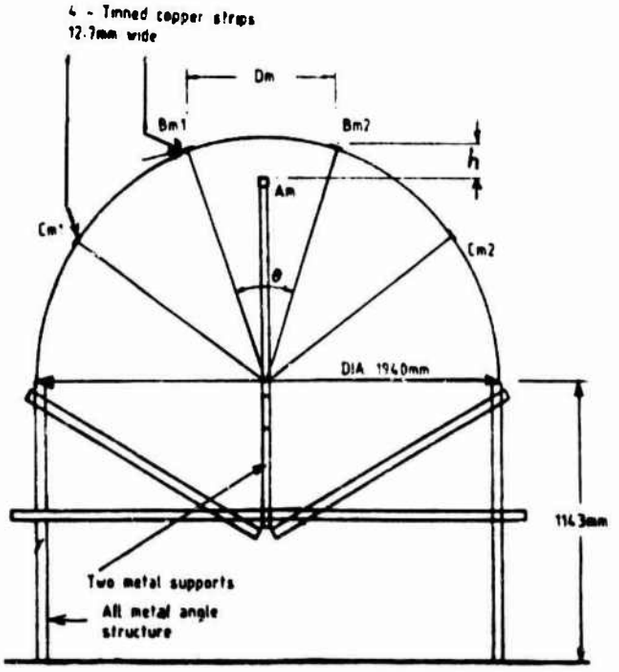


Fig. 4 Loci of points equidistant from protective strips PS1 and PS10 and the inner cylinder if

$$F = \frac{R_2}{R_1} > \cos\theta \qquad \theta = \frac{180}{n}, \quad F = 0.97$$

n = number of protective strips

GOH - 'inner cylinder vulnerable' wedge, angle GOH = 7.86°



- θ Angle subtended by strips Bm1 and Bm2
- Am, was a ½ square section MS bar, 15 feet long, resting horizontally on top of the two metal supports. A ½ round glass fibre rod supported Am in the centre of the model to prevent sag
- Overall length of model was 28', comprising SEVEN 4' wide sections

Fig. 5 Mock Radome (end elevation)

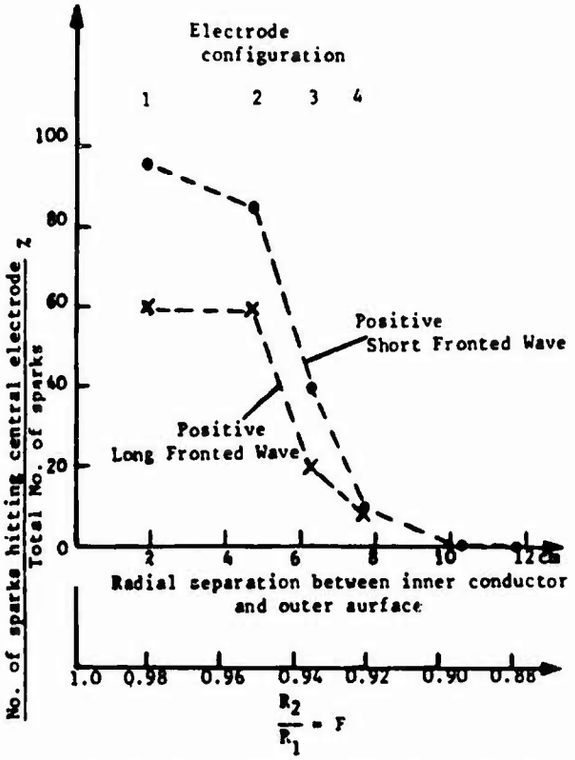


Fig. 6 The observed probability of sparking to the central electrode to a base of the radial separation between this electrode and the outer surface

R_1 = 0.97 m

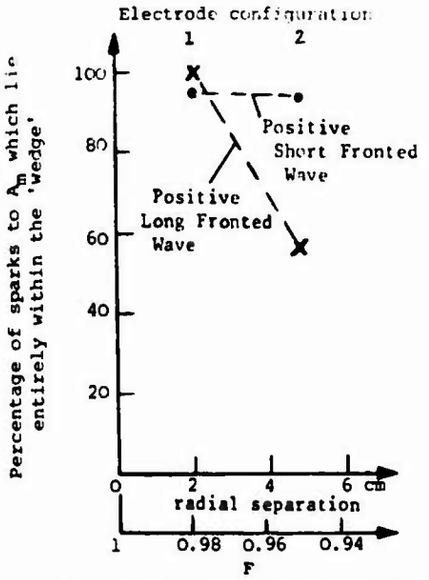


Fig. 7 Proportion of the sparks to the central electrode which lay entirely within the 'wedge', to a base of the radial separation between the central electrode and the outer surface.

R_1 = 0.97 m

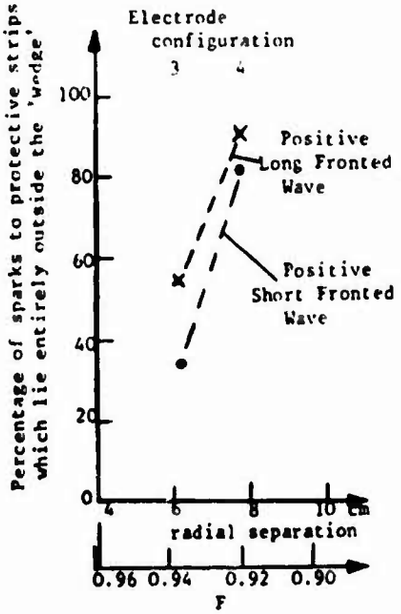


Fig. 8 Proportion of the sparks to the protective strips which lay entirely outside the 'wedge', to a base of the radial separation between the central electrode and the outer surface.

R_1 = 0.97 m

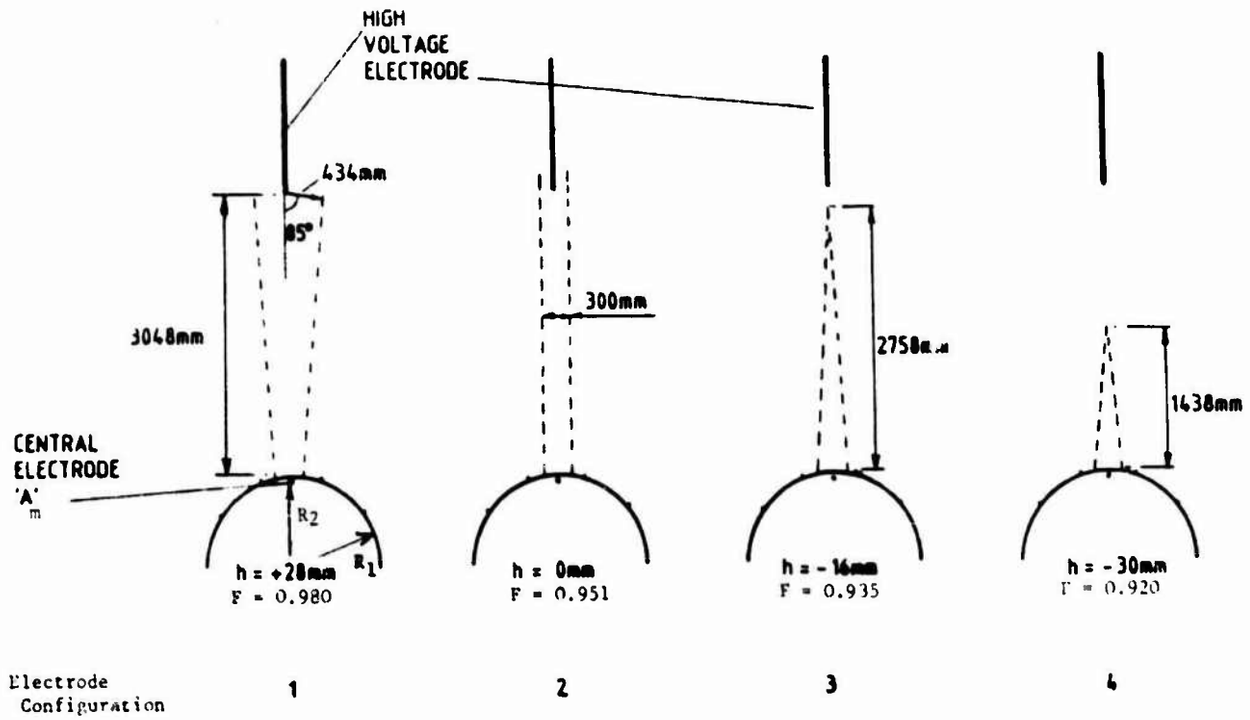


Fig. 9 'Wedge' forms corresponding to four positions of the central electrode

$R_1 = 0.97m$ $\qquad F = \frac{R_2}{R_1}$

AUTHOR INDEX

Adamo (R.C.).- See Nanevicz (J.E.)..... 475

Aked (A.).- See Bishop (J.)..... 499

Allen (J.E.).- See Hoole (P.R.P.)..... 205

Alliot (J.C.).- See Levesque (P.)..... 29

Alliot (J.C.).- See Moreau (J.P.)..... 281

Andersh (D.J.).- See Gardner (R.L.)..... 1

Anderson (F.J.), Freier (G.D.), Lee (T.S.) and Robb (J.D.).- Optical detection methods for testing of fuel tank lightning ignition hazards..... 157

Baker (L.).- See Gardner (R.L.)..... 1

Bala (M.), Mathpal (K.C.) and Rai (J.).- Ground electrostatic field changes due to lightning..... 89

Barret (L.).- See Laroche (P.)..... 231

Baum (C.E.).- See Gardner (R.L.)..... 1

Beniguel (Y.).- Induced current surface density after a direct lightning strike on an aircraft..... 25

Bent (R.B.).- See Lyons (W.A.)..... 347

Bicknell (J.A.) and Shelton (R.W.).- The energy requirements of an aircraft triggered discharge..... 217

Bishop (J.), Aked (A.), Powell (C.W.) and Ryan (H.M.).- Aspects of lightning protection schemes for radomes..... 499

Blakeslee (R.J.).- See Krider (E.P.)..... 83

Blez (M.), Thayer (J.) and Nanevicz (J.E.).- Spacecraft materials test in a continuous, broad energy-spectrum electron beam..... 485

Boes (G.).- See Thiele (Th.)..... 395

Boes (G.).- See Wentzel (H.-P.)..... 383

Bondiou (A.), Labaune (G.) and Marque (J.P.).- Electromagnetic radiation associated with the breakdown of air at atmospheric pressure..... 223

Brick (R.O.).- Multipath lightning protection for composite structure integral fuel tank design..... 149

Brown (P.W.).- See Fisher (B.D.)..... 267

Brüns (H.D.) and Singer (H.).- Electromagnetic interaction of external impulse fields with aircraft..... 13

Carpenter Jr. (R.B.) and Drabkin (M.D.).- A 12 year study of lightning strike prevention systems..... 299

Corbin (J.C.).- Military standard for lightning protection of aerospace vehicules..... 9

Delannoy (A.).- See Gondot (P.)..... 71

Dill (M.).- See Laroche (P.)..... 59

Drabkin (M.D.).- See Carpenter Jr. (R.B.)..... 299

Dunkley (V.P.).- See Hardwick (C.J.)..... 127

Duroure (C.).- See Gayet (J.F.)..... 67

Earle (R.A.).- See Wolff (B.I.)..... 293

Ebneth (H.).- Simulated lightning tests on Baymetex C protected graphite-epoxy laminates..... 403

Edlin (G.).- See Price (M.L.)..... 431

Eybert-Bérard (A.).- See Laroche (P.)..... 231

Fisher (B.D.), Brown (P.W.) and Plumer (J.A.).- Research in lightning swept-stroke attachment patterns and flight conditions with the NASA F-106B airplane..... 267

Freier (G.D.).- See Anderson (F.J.)..... 157

Friedlander (M.).- See Laroche (P.)..... 59

Funayama (R.).- See Goto (Y.)..... 97

Gardiner (B.), Hallett (J.) and Saunders (C.P.R.).- Field observations of aircraft charging in convective clouds..... 423

Gardner (R.L.), Baker (L.), Gilbert (J.L.), Baum (C.E.) and Andersh (D.J.).- Comparison of published HEMP and natural lightning on the surface of an aircraft..... 1

Gayet (J.F.), Duroure (C.), Soulage (R.G.) and Laroche (P.).- Location of lightning strokes on aircraft in storm field with measured electrical, microphysical and dynamical properties..... 67

Gayet (J.F.).- See Laroche (P.)..... 59

Gilbert (J.L.).- See Gardner (R.L.)..... 1

Glynn (M.S.).- See Rasch (N.O.)..... 247

Golub (C.N.).- Lightning and logistics. Cape Canaveral - A proving ground for lightning research..... 329

Gondot (P.) and Delannoy (A.).- In-flight electrical conductivity measurements..... 71

Goto (Y.), Narita (K.), Naito (M.) and Funayama (R.).- Electric fields produced by winter thunderstorms. 97

Grorud (E.) and Soiron (M.).- Induced surface currents and fields on a conducting body by a lightning strike (frequency domain)..... 21

Hallett (J.).- See Gardiner (B.)..... 423

Hamelin (J.).- See Weidman (C.)..... 175

Hardwick (C.J.) and Dunkley (V.P.).- The observation of high frequency Ḃ and Ḋ transients excited on a fuselage by an impulse generator..... 127

Hasbrouck (R.T.).- Investigation of the lightning vunerability of nuclear explosive test systems at the Nevada test site..... 311

Hebert (J.L.), Walko (L.C.) and Schneider (J.G.).- Design of a fast risetime lightning generator..... 115

Hebert (J.L.).- See Walko (L.C.)..... 137

Henderson (R.W.).- See Orville Sr. (R.E.)..... 333

Herkert (C.M.).- See Wentzel (H.-P.)..... 383

Hess (R.).- The effects of finite linear characteristics inherent in the physically realizable devices associated with cable injection tests..... 37

Hess (R.).- Implications associated with the operation of digital data processing in the presence of the relatively harsh EMP environments produced by lightning..... 289

Highlands (W.H.).- See Lyons (W.A.)..... 347

Hoole (P.R.P.) and Allen (J.E.).- Lightning magnetic field calculation using finite element method..... 205

Hubert (P.).- A new model of lightning subsequent stroke - Confrontation with triggered lightning observations..... 211

Hutzler (B.), Riquel (G.) and Riu (J.P.).- High voltage laboratory tests and lightning phenomena 191

Jafferis (W.).- See Maier (M.W.)..... 337

Jayaratne (E.R.).- See Saunders (C.P.R.)..... 77

Johnson (J.).- See Thomson (E.M.)..... 167

Kasemir (H.W.).- See Parker (L.W.)..... 357

Kawasaki (Z.I.), Nakano (M.), Takeuti (T.) and Nakai (T.).- Group velocity of lightning return stroke currents..... 241

King (C.).- Lightning - induced transient test on a transport aircraft..... 367

Königsteln (D.).- Hand-held electrostatic charge distribution measuring system..... 461

Krider (E.P.), Blakeslee (R.J.) and Maier (L.M.).- Thunderstorm currents and lightning charges at the NASA Kennedy Space Center..... 83

Krider (E.P.).- See Leteinturier (C.)..... 185

Kuhlman (B.P.).- See Rustan Jr. (P.L.)..... 253

Labaune (G.).- See Bondiou (A.)..... 223

Labaune (G.).- See Levesque (P.)..... 29

Larigaldie (S.).- High current surface discharge propagation analysis - Application to the lightning leader..... 197

Larigaldie (S.).- See Levesque (P.)..... 29

Laroche (P.), Dill (M.), Gayet (J.F.) and Friedlander (M.).- In-flight thunderstorm environmental measurements during the Landes 84 campaign.... 59

Laroche (P.), Eybert-Bérard (A.) and Barret (L.).- Triggered lightning flash characterization..... 231

Laroche (P.).- See Gayet (J.F.)..... 67

Le Boulch (M.).- See Weidman (C.)..... 175

Lee (T.S.) and Robb (J.D.).- Ring discharge on the backsurface of a composite skin with ohmic anisotropy in response to frontal high current injection..... 377

Lee (T.S.) and Su (W.Y.).- Time-convoluted hotspot temperature field on a metal skin due to sustained arc stroke heating..... 371

Lee (T.S.).- See Anderson (F.J.)..... 157

Leteinturier (C.), Krider (E.P.) and Willett (J.C.).- Submicrosecond structure of the radiation fields produced by lightning..... 185

Levesque (P.), Taillet (J.), Labaune (G.), Larigaldie (S.) and Alliot (J.C.).- A study of the physical mechanisms and the perturbations created by the attachment of an arc to a conducting cylinder..... 29

Levy (L.).- A new understanding of breakdowns in the day sections of geosynchronous orbit..... 467

Lyons (W.A.), Bent (R.B.) and Highlands (W.H.).- Operational uses of data from several lightning position and tracking systems (LPATS)..... 347

McKenna (P.M.).- See Perala (R.A.)..... 121

Maier (M.W.) and Jafferis (W.).- Locating rocket triggered lightning using the LLP lightning locating system at the NASA Kennedy Space Center..... 337

Maier (L.M.).- See Krider (E.P.)..... 83

Marque (J.P.).- See Bondiou (A.)..... 223

Mathpal (K.C.).- See Bala (M.)..... 89

Medelius (P.).- See Thomson (E.M.)..... 167

Mladenović (I.) and Vorgučić (A.).- Stepped leader and striking distance..... 321

Mladenović (I.).- See Vorgučić (A.)..... 325

Moore (C.B.).- See Price (M.L.)..... 431

Moreau (J.P.) and Alliot (J.C.).- E and H fields measurements on the transall C160 aircraft during lightning flashes..... 281

Moreau (J.P.).- See Rustan Jr. (P.L.)..... 259

Nakai (T.).- See Kawasaki (Z.I.)..... 241

Nakano (M.).- See Kawasaki (Z.I.)..... 241

Naito (M.).- See Goto (Y.)..... 97

Nanevicz (J.E.) and Adamo (R.C.).- Status of critical issues in the area of spacecraft charging..... 475

Nanevicz (J.E.) and Vance (E.F.).- Corona threshold determination by three-stage physical modelling of aircraft..... 441

Nanevicz (J.E.).- See Blez (M.)..... 485

Narita (K.).- See Goto (Y.)..... 97

Orville Sr. (R.E.), Pyle (R.B.), Henderson (R.W.), Orville Jr. (R.E.) and Weisman (R.A.).- Characteristics of cloud-to-ground lightning flashes along the east coast of the United States..... 333

Orville Jr. (R.E.).- See Orville Sr. (R.E.)..... 333

Parker (L.W.) and Kasemir (H.W.).- Ranging and azimuthal problems of an airborne crossed loop used as a single-station lightning locator..... 357

Perala (R.A.), McKenna (P.M.), Rudolph (T.H.) and Robb (J.D.).- Implementation of a crowbar switch in a Marx generator/peaking capacitor lightning simulator system..... 121

Perala (R.A.).- See Price (M.L.)..... 431

Plumer (J.A.).- See Fisher (B.D.)..... 267

Powell (C.W.).- See Bishop (J.)..... 499

Pradeep Kumar (P.) and Rai (J.).- Electric field changes due to lightning in tropical thunderstorms..... 105

Price (M.L.), Perala (R.A.), Edlin (G.) and Moore (C.B.).- Dust electrification during large explosions..... 431

Pyle (R.B.).- See Orville Sr. (R.E.)..... 333

Rai (J.).- See Bala (M.)..... 89

Rai (J.).- See Pradeep Kumar (P.)..... 105

Rasch (N.O.) and Glynn (M.S.).- Survey of lightning hazard and low altitude direct lightning strike program..... 247

Reazer (J.M.).- See Rustan Jr. (P.L.)..... 253

Riquel (G.).- See Hutzler (B.)..... 191

Riley (L.H.).- United States Army missile command lightning simulation test facility..... 111

Riu (J.-P.).- See Hutzler (B.)..... 191

Robb (J.D.).- See Anderson (F.J.)..... 157

Robb (J.D.).- See Lee (T.S.)..... 377

Robb (J.D.).- See Perala (R.A.)..... 121

Rubinstein (M.).- See Thomson (E.M.)..... 167

Rudolph (T.H.).- See Perala (R.A.)..... 121

Rustan Jr. (P.L.), Kuhlman (B.P.) and Reazer (J.M.).- Airborne and ground electromagnetic field measurements of lightning..... 253

Rustan Jr. (P.L.) and Moreau (J.P.).- Aircraft lightning attachment at low altitudes..... 259

Ryan (H.M.).- See Bishop (J.)..... 499

Saunders (C.P.R.).- See Gardiner (B.)..... 423

Saunders (C.P.R.) and Jayaratne (E.R.).- Electric charge transfer during riming..... 77

Schneider (H.).- Live tests on static electricity in fuelling of aircraft..... 451

Schneider (J.G.).- See Hebert (J.L.)..... 115

Shelton (R.W.).- See Bicknell (J.A.)..... 217

Singer (H.).- See Brüns (H.D.)..... 13

Soiron (M.).- See Grorud (E.)..... 21

Soulage (R.G.).- See Gayet (J.F.)..... 67

Stone (J.W.).- See Thomson (E.M.)..... 167

Su (W.Y.).- See Lee (T.S.)..... 371

Takeuti (T.).- See Kawasaki (Z.I.)..... 241

Taillet (J.).- See Levesque (P.)..... 29

ter Haseborg (J.L.) and Trinks (H.).- Special protection circuits against transient currents for aircraft systems..... 363

Thayer (J.).- See Blez (M.)..... 485

Thiele (Th.) and Boes (G.).- Lightning stroke tests at the CFRP horizontal stabilizer of alpha jet..... 395

Thiele (Th.).- See Wentzel (H.-P.)..... 383

Thomson (E.M.), Medellus (P.), Rubinstein (M.), Uman (M.A.), Johnson (J.) and Stone (J.W.).- Horizontal electric fields from lightning return strokes..... 167

Trinks (H.).- See ter Haseborg (J.L.)..... 363

Uman (M.A.).- See Thomson (E.M.)..... 167

Vance (E.F.).- See Nanevicz (J.E.)..... 441

Vorgučić (A.) and Mladenović (I.).- Exposition to the lightning current of objects situated near to the vertical lightning rod..... 325

Vorgučić (A.).- See Mladenović (I.)..... 321

Walko (L.C.) and Hebert (J.L.).- Lightning simulation tests on FAA CV-580 lightning research aircraft. 137

Walko (L.C.).- See Hebert (J.L.)..... 115

Weidman (C.), Hamelin (J.) and Le Boulch (M.).- Lightning VHF and UHF emissions and fast time resolved measurements of the associated electric field variations..... 175

Weisman (R.A.).- See Orville Sr. (R.E.)..... 333

Wentzel (H.-P.), Herkert (C.M.), Thiele (Th.) and Boes (G.).- Development and testing of protection measures for reinforced composites against lightning strike..... 383

Willett (J.C.).- See Leteinturier (C.)..... 185

Wolff (B.I.) and Earle (R.A.).- A new from of transient suppressor..... 293

Yan Muhong.- A numerical calculation of space charge layer created by corona due to a ground artificial point beneath thunderstorm..... 305

Commission paritaire N° 26.741

© Les Editions de Physique 1985

Directrice de la Publication : Jeanne BERGER

Imprimé en France. – JOUVE, 18, rue Saint-Denis, 75001 PARIS
N° 14216. Dépôt légal : Mai 1985